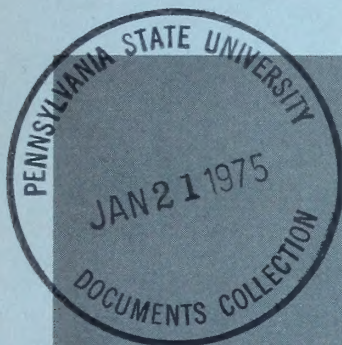




U.S. DEPARTMENT OF COMMERCE

National Oceanic and Atmospheric Administration



COLLECTED REPRINTS-1973

**ATLANTIC OCEANOGRAPHIC
AND METEOROLOGICAL LABORATORIES**



U.S. DEPARTMENT OF COMMERCE

Frederick B. Dent, Secretary

NATIONAL OCEANIC AND ATMOSPHERIC ADMINISTRATION

Robert M. White, Administrator

ENVIRONMENTAL RESEARCH LABORATORIES

Wilmot N. Hess, Director

Collected Reprints-1973

ATLANTIC OCEANOGRAPHIC AND METEOROLOGICAL LABORATORIES

ISSUED JULY 1974

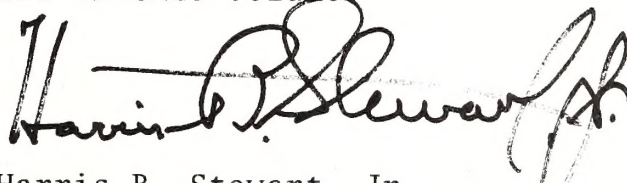
Atlantic Oceanographic and Meteorological Laboratories
Miami, Florida 33149

For sale by the Superintendent of Documents, U. S. Government Printing Office, Washington, D. C. 20402




FOREWARD

This annual volume, the eighth in the series, brings together the results of research of NOAA's Atlantic Oceanographic and Meteorological Laboratories which appeared in various scientific journals during 1973. The one-volume format is used this year in the interest of saving money, but it also reflects the fact that the National Hurricane Research Laboratory and the Experimental Meteorology Laboratory have transferred from AOML to NOAA's new Office of Weather Modification. A new AOML laboratory, the Ocean Remote Sensing Laboratory, came into being in 1973, and their first papers are included in this volume.

A handwritten signature in dark ink, appearing to read "Harris B. Stewart, Jr.", with a large, stylized flourish at the end.

Harris B. Stewart, Jr.
Director, Atlantic Oceanographic
and Meteorological Laboratories

NOAA-AOML
15 Rickenbacker Causeway
Virginia Key
Miami, Florida 33149, U. S. A.



Digitized by the Internet Archive
in 2012 with funding from
LYRASIS Members and Sloan Foundation

<http://archive.org/details/collectedreprint1973atla>

CONTENTS

Page

General

1. Stewart, Harris B., Jr.
A Caribbean Cruise with a Difference, Marine
Technology Society Journal 7, No. 5, 16-20,
Aug. 1973 1
2. Stewart, Harris B., Jr.
Federal Research Bucks Still Available if Ideas
are Innovative, Muse News 5, No. 1, 7-9, May, 1973 6
3. Stewart, Harris B., Jr.
NOAA/Carib: An Experiment that Worked, Environmental
Data Service, 3-11, Apr. 1973 9
4. Stewart, Harris B., Jr.
The International Ocean, Science and Public Affairs
29, No. 8, p. 38, Oct. 1973 18

Physical Oceanography

5. Charnell, R. L. and G. A. Maul
An Oceanographic Observation of New York Bight from
ERTS-1, NOAA Tech Report, ERL 262-AOML 9, 8 pages,
Feb. 1973 19
6. Charnell, R. L. and G. A. Maul
Oceanic Observation of New York Bight by ERTS-1,
Nature 242, No. 5398, 451-452, Apr. 1973 27
7. Charnell, R. L., D. V. Hansen, and R. I. Wickland
Surface and Bottom Water Movement in New York Bight,
Final Report on The Effects of Waste Disposal in
the New York Bight, for the Coastal Eng. Res. Ctr.,
U.S. Army Corps of Eng., by National Marine Fisheries
Service, Sandy Hook Laboratory, February 1972, 6-1
thru 6-30, 1973 30

8. Maul, G. A.
Infrared Sensing of Ocean Surface Temperature, The
Second Fifteen Years in Space, Science and Technology
31, 451-463, 1973 61
9. Maul, G. A.
Remote Sensing of Ocean Currents Using ERTS Imagery,
Symposium on Significant Results Obtained from the
Earth Resources Technology Satellite-1 1, Sect. B,
1365-1375, Aug. 1973 75
10. Maul, G. A. and M. Sidran
Atmospheric Effects on Ocean Surface Temperature
Sensing from the NOAA Satellite Scanning Radiometer,
Journal of Geophysical Research 78, No. 12, 1909-
1916, Apr. 1973 86
11. Molinari, R. L.
Buoy Tracking of Ocean Currents, The Second Fifteen
Years in Space, Science and Technology 31, 431-444,
1973 94
12. Molinari, R. L.
Data from the Lagrangian Current-Measurement Project
Conducted Aboard the NOAA Ship RESEARCHER During
CICAR Survey Month I, NOAA Tech Memo ERL AOML-19,
81 pages, Apr. 1973 108
13. Molinari, R. L. and D. V. Hansen
Formulation of Drifting Limited Capability Buoy
Placement and Retrieval Concepts, NOAA Tech Memo
ERL AOML-18, 29 pages, Apr. 1973 190
14. Pashinski, D. J. and G. A. Maul
Use of Ocean Temperature While Coasting Between
the Straits of Florida and Cape Hatteras, Mariners
Weather Log 17, No. 1, 1-3, Jan. 1973 219

Marine Geology and Geophysics

15. Bennett, R. H.
Palaeotemperature and Cohesion in Globigerina Ooze
Sediment Cores from the Caribbean Sea, Nature Physical
Science 240, No. 101, 114-116, Dec. 1972 222

16. Bennett, R. H. and G. H. Keller
Physical Properties Evaluation, Initial Reports
of the Deep-Sea Drilling Project XVI, 513-519,
1973 227
17. Dietz, R. S.
Book Review: Carbonate Sediments and Their
Diagenesis, Marine Technology Society Journal 6,
No. 5, 57-58, Oct. 1972 234
18. Dietz, R. S.
The Bahamas Enigma, Sea Frontiers 19, No. 6, 330-
336, Nov.-Dec. 1973 235
19. Dietz, R. S.
Morphologic Fits of North America/Africa and
Gondwana: A Review, Implications of Continental
Drift to the Earth Sciences 2, 865-872, 1973 242
20. Dietz, R. S.
New Global Tectonics and "The New Geometry": Dis-
cussion, the American Association of Petroleum
Geologists Bulletin 57, No. 12, 2452-2456, Dec.
1973 250
21. Dietz, R. S. and B. M. French
Two Probable Astroblemes in Brazil, Nature 244,
561-562, Aug. 1973 255
22. Dietz, R. S. and J. C. Holden
Continents Adrift: New Orthodoxy or Persuasive
Joker? NATO Symposium on Continental Drift, Univ.
Newcastle-upon-Tyne, England, April 10-14, 1972,
1105-1121, 1973 257
23. Dietz, R. S. and J. C. Holden
Geophysical Illusions of Continental Drift: A
Discussion, The American Association of Petroleum
Geologists Bulletin 57, No. 11 (Pt. I of II),
2290-2296, Nov. 1973 274
24. Dietz, R. S. and J. C. Holden
Geotectonic Evolution and Subsidence of Bahama
Platform: Reply, Geological Society of America
Bulletin 84, 3477-3481, Oct. 1973 280

25. Dietz, R. S., J. C. Holden, and W. P. Sproll
 Antarctica and Continental Drift, Proc. SCAR
 Symp. on Antarctic Geology and Solid Earth Geo-
 physics, Oslo, Norway, Aug. 1970, 837-842, 1973 285
26. Dorman, L. M. and B. T. R. Lewis
 Experimental Isostasy 3, Inversion of the Iso-
 static Green Function and Lateral Density Changes,
 Journal of Geophysical Research 77, No. 17, 3068-
 3077, June 1972. 291
27. Dorman, L. M. and B. T. R. Lewis
 The Isostatic Green's Function and the Inverse
 Potential Problem, Geophysical Journal of the
 Royal Astronomical Society 35, 375, 1973 301
28. Dorman, L. M., et al.
 Caribbean Atlantic Geotraverse, NOAA/IDOE 1971,
 Report No. 3, Gravity, NOAA Tech Report ERL 277-
 AOML 11, 35 pages, Aug. 1973 302
29. Freeland, G. L. and R. S. Dietz
 Rotation History of Alaskan Tectonic Block,
 Tectonophysics 18, No.3/4, 379-389, July 1973 322
30. Harbison, R. N. and B. G. Bassinger
 Marine Geophysical Study off Western India,
 Journal of Geophysical Research 78, No. 2, 432-
 440, Jan. 1973 333
31. Harbison, R. N., R. K. Lattimore, and P. A. Rona
 Structural Lineations in the Canary Basin, Eastern
 Central North Atlantic, Marine Geology 14, 269-275,
 Feb. 1973 342
32. Heath, G. R., R. H. Bennett, and K. S. Rodolfo
 Introduction, Initial Reports of the Deep Sea
 Drilling Project XVI, 3-17, 1973 349
33. Keller, G. H. and R. H. Bennett
 Sediment Mass Physical Properties - Panama Basin
 and Northeastern Equatorial Pacific, Initial
 Reports of the Deep Sea Drilling Project XVI,
 499-512, 1973 364

34. Keller, G. H. and D. N. Lambert
 Geotechnical Properties of Submarine Sediments,
 Mediterranean Sea, Mediterranean Sea, ed. by
 Daniel J. Stanley ©Dowden, Hutchinson and Ross,
 401-415, 1972 378
35. Keller, G. H., D. Lambert, G. Rowe, and N. Staresinic
 Bottom Currents in the Hudson Canyon, *Science*
 180, No. 4082, 181-183, Apr. 1973. 393
36. McGregor, B. A., P. R. Betzer, and D. C. Krause
 Sediments in the Atlantic Corner Seamounts:
 Control by Topography Paleo-winds, and Geochem-
 ically-Detected Modern Bottom Currents, *Marine*
 Geology 14, 179-190, Feb. 1973 396
37. Peter, G.
 Marine Magnetic Anomaly Lineations and Paleomag-
 netic Research: Preliminary Thoughts, NOAA Tech
 Report ERL 223-ESL 19, 37-38, Jan. 1972 405
38. Peter, G., O. E. DeWald, and B. G. Bassinger
 Caribbean Atlantic Geotraverse, NOAA/IDOE 1971,
 Report No. 2, Magnetic Data, NOAA Tech Report ERL
 228-AOML 12, 19 pages, Oct. 1973 407
39. Peter, G., G. Merrill, and S. Buck
 Caribbean Atlantic Geotraverse, Proj. Intro -
 Bathymetry NOAA/IDOE 1971 Report #1, NOAA Tech
 Report ERL 293-AOML 13, 29 pages, 1973. 420
40. Peter G., R. K. Lattimore, O. E. DeWald, and G. Merrill
 Development of the Mid-Atlantic Ridge East of the
 Less Antilles Island Arc, *Nature Physical Science*
 245, No. 148, 129-131, Oct. 1973 440
41. Richards, A. F., V. J. McDonald, R. E. Olson, and
 G. H. Keller
 In-place Measurement of Deep Sea Soil Shear Strength,
 Underwater Soil Sampling, Testing, and Construction
 Control, STP 501, American Society for Testing and
 Materials, 55-68, 1972 443

42. Rona, P. A.
Marine Geology, McGraw-Hill Yearbook of Science
and Technology, 1972, 252-256, 1973 457
43. Rona, P. A.
New Evidence of Seabed Resources from Global
Tectonics, *Ocean Management* 1, 145-159, 1973 462
44. Rona, P. A.
Plate Tectonics and Mineral Resources, *Scientific
American* 229, No. 1, 86-95, July 1973 477
45. Rona, P. A.
Relations between Rate of Sediment Accumulation
on Continental Shelves, Sea-Floor Spreading, and
Eustacy Inferred from the Central North Atlantic,
Geological Society of America Bulletin 84, 2851-
2871, Sept. 1973 487
46. Rona, P. A. and H. S. Fleming
Mesozoic Plate Motions in the Eastern Central
North Atlantic, *Marine Geology* 14, 239-252, Feb.
1973 508
47. Rona, P. A., A. Parvulescu, W. Liang, and
C. A. Lauter, Jr.
Development and Preliminary Test of a 1000 Hertz
Pulse Compression Seismic Reflection Profiling
System, *Journal of Geophysical Research* 78, No.
35, 8577-8583, Dec. 1973 522
48. Swift, D. J. P.
Delaware Shelf Valley: Estuary Retreat Path,
Not Drowned River Valley, *Geological Society of
America Bulletin* 84, 2743-2748, Aug. 1973 529
49. Swift, D.J. P., D. B. Duane, and T. F. McKinney
Ridge and Swale Topography of the Middle Atlantic
Bight, North America: Secular Response, *Marine
Geology* 15, 227-247, 1973 535

50. Swift, D. J. P., J. W. Kofoed, F. P. Saulsbury, and P. Sears
 Holocene Evolution of the Shelf Surface, Central and Southern Atlantic Shelf of North America, Shelf Sediment Transport, Process and Pattern, ©Dowden, Hutchison and Ross, Ch. 23, 499-574, Nov. 1972 556

Ocean Remote Sensing

51. Apel, John R.
 A Hard Look at Oceans from Space, Amer. Inst. of Aeronautics and Astronautics, 9th Annual Meeting and Technical Display, Washington, D. C., Jan. 8-10, 1973, AIAA No. 73-11, 1973 632
52. Apel, John R.
 On a Dedicated Oceanographic Satellite, The Second Fifteen Years in Space, Science and Technology 31, American Astronautical Society, 445-450, 1973 641
53. Apel, J. R. and J. W. Sherman, III
 Monitoring the Seas from Space (NOAA's Requirements for Oceanographic Satellite Data), Report AOML-LORS 6.73.1, 38 pages, 1973 647

Sea-Air Interaction

54. Augstein, E., H. Riehl, F. Ostapoff, and V. Wagner
 Mass and Energy Transports in an Undisturbed Atlantic Trade-Wind Flow, Monthly Weather Review 101, No. 2, 101-111, Feb. 1973 690
55. Brummer, B., F. Ostapoff, and H. Schmidt
 Upper Air Soundings During Atlantic Trade-Wind Expedition (1969) (ATEX), Published by NOAA, Vol. I, II, and III, 1973 (*Text only*). 701
56. Carlson, T. N., J. M. Prospero, and K. J. Hanson
 Attenuation of Solar Radiation by Windborne Saharan Dust Off the West Coast of Africa, NOAA Tech Memo ERL WMPO-7, 27 pages, Sept. 1973 731

57. Hanson, K. J., F. Hebard, and R. Cram
Oceanographic Features in the Lee of the Windward
and Leeward Islands, ERTS and Ship Data, Symposium
on Significant Results Obtained from the Earth
Resources Technology Satellite-1, Vol. I, Technical
Presentations, Section B, National Aeronautic and
Space Administration, 1357-1363, 1973 757
58. Ostapoff, F., Y. Tarbeyev, and S. Worthem
Heat Flux and Precipitation Estimates from Oceano-
graphic Observations, Science 180, 960-961, June
1973 764
59. Ross, D. B. and V. Cardone
Observations of Oceanic White Caps for Moderate to
High Wind Speeds, Fourth Annual Earth Resources Pro-
gram Review, MSC-05937 IV, Section 85/1-20, Dec.
1972 767

A Caribbean Cruise With A Difference

BY HARRIS B. STEWART, JR.

Cdr. Jimmy Lyons and
some new friends.



"The only instance that I have witnessed that exceeded the person-to-person impact of the *DISCOVERER* was the good ship *HOPE* off the Peruvian coast."

**Dr. James M. Lammons
Texaco Trinidad, Inc.**

The Cooperative Investigation of the Caribbean and Adjacent Regions (CICAR) is a 15-nation oceanographic effort aimed at developing a better understanding of the Caribbean system and providing a mechanism whereby the Caribbean Basin community of nations can increase their own involvement and capabilities in marine science.

A cooperative program of the Intergovernment Oceanographic Commission of United Nations Educational, Scientific and Cultural Organization (UNESCO), CICAR has sponsored regular meet-

ings of the several national coordinators to review accomplishments and to make future plans. At meetings held in Washington, D.C., Mexico City, Mex., Port of Spain, Trinidad, and most recently in Havana, Cuba, the message came through loud and clear: What the Latin American nations wanted most was an opportunity for their students and faculty members to get at-sea training and instruction in the full spectrum of oceanographic observations.

The concept of NOAA-Carib developed gradually within NOAA's Atlantic Oceanographic Meteorological Laboratories (AOML) in Miami. The primary goal was a two-month oceanographic expedition aboard the NOAA ship *DISCOVERER* on which Latin American scientists and students would carry out their own research work. They would plan

Reprinted by permission of Environmental Data Service, published by the National Oceanic and Atmospheric Administration.

what they wanted to do in their own waters, and select the people to go along to do it and to get training while so doing. They would keep all the data collected during their phase of the operation, and work up and publish the results. NOAA's role would be to provide the fully equipped *DISCOVERER*, plus a basic cadre of experienced seagoing scientists to assist the Latin Americans in the various operations they wished to carry out.

When the concept of NOAA-Carib was put forward by the U.S. Delegation at the Trinidad CICAR meeting in 1971, it was greeted with enthusiasm. Planning then got underway on an intensive scale, and Mexico, Jamaica, Puerto Rico, Trinidad and Tobago, Venezuela, and Colombia all began putting together their own programs to be accomplished on the *DISCOVERER* during the NOAA-Carib cruise scheduled for October, November, and December 1972.



Mike Sunray of NOAA's National Weather Service explains the recorder trace of meteorological observations taken by the radio instrument package attached to the weather balloon.

After mountains of correspondence, partly in Spanish, several last-minute cables, and a few panicky telephone calls, nine Mexicans arrived in Miami to sail October 9th on the first leg of NOAA-Carib. Cdr. Donald Florwick, Jack Kofoed, and Harris Stewart, all of AOML, alternated as Chief Scientists for portions of the trip. UNESCO provided about \$2,000 to assist Latin Americans in their travel to and from the ship.

There were numerous changes in personnel in the scientific party at seven Caribbean ports—Veracruz, Montego Bay, Kingston, San Juan, Port



Lt. Lawrence Keister discusses the intricacies of position location with Mexican Navy cadets.

of Spain, La Guaira (Caracas), and Cartagena. In each country, the *DISCOVERER* held an "open house" for streams of school children, college students, local officials, dock workers, and the local curious.

The visitors listened to short lectures on what we were up to as they filed past exhibits of our equipment at work, through the bridge, the laboratories, the computer room, the meteorological "shack," the plotting room, and the flying bridge. They stared curiously at the big winch and coring gear, and with fascination watched themselves on closed-circuit television in the electronics shop.

In each country, a one-day cruise was arranged for up to 50 or so local people. The local NOAA-Carib coordinator was told that he could invite whomever he wanted but that preference should be given to students and faculty members who could most benefit by a one-day demonstration trip. Most of the "cruisees" were students, but there was also a fair sprinkling of members of the local press, as well as a few local administrators.

In every instance but one, the one-day cruise was highly successful. Out of San Juan harbor, however, the *DISCOVERER* encountered rough seas, and most of the visitors were shortly indisposed. Soon attendance at the lectures and demonstrations was sparse, and almost every bunk aboard held a groaning occupant who, although swearing he would never go to sea again, certainly left with considerable respect for those who do so routinely.

One each of the one-day trips, much of the briefing was done by marine scientists from the country concerned who had already been onboard for the previous leg. Thus, in the Spanish-speaking

ports, explanations were made in Spanish by their own countrymen.

The real accomplishments of NOAA-Carib, however, were the individual national projects planned to meet local needs and carried out essentially by local scientists in their own waters. The enthusiasm of the Latin Americans was contagious. Alfonso Lopez Reina, for example, a geologist from Colombia, stayed at the seismic reflection recorder for 26 hours straight as the *DISCOVERER* ran profiles across the Aguja Submarine Canyon off Colombia. When asked if he didn't need some sleep, his response was "Yes, of course, but I can sleep when I get ashore; why waste this valuable time by sleeping?"



John Proni explains the use of underwater sound to detect subsurface water movements.

Aside from an occasional case of seasickness when the bunk looked better than anything else aboard, the Lopez reaction was essentially that of all who took part in NOAA-Carib. It was a rewarding experience for the U.S. participants to see that the seagoing work we tend to take for granted was highly valued by our Latin American colleagues.

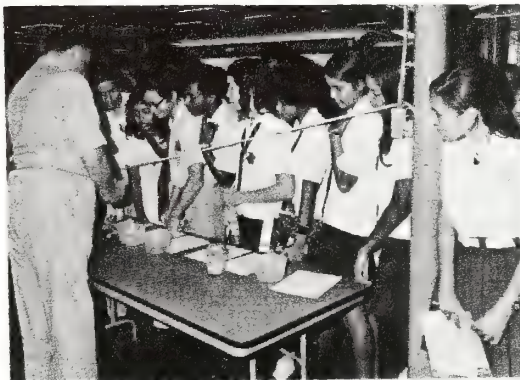
Specific scientific results? There were quite a few. Out of Veracruz the Mexican geologists and geophysicists, under Dr. Robert Lankford, managed to fill in some holes in the geophysical knowledge of the Mexican shelf.

Off Jamaica, scientists from the Mona Campus of the University of the West Indies recovered cores from the Cayman Trough, obtained seismic

reflection profiles of the Jamaican shelf, and specified where they wanted bottom current measurements made off the eastern tip of the island. The *DISCOVERER* planted bottom current meters at the location specified. The instruments were retrieved by acoustic signals some two months later as the *DISCOVERER* was enroute from Cartagena to Miami. One of the systems flooded out shortly after it was planted, but the records from the other were flawless and are now being analyzed to fill a glaring gap in the knowledge of the circulation around Jamaica.

The Puerto Rican work centered heavily on chemical investigations made under the direction of Dr. Donald Atwood of the University of Puerto Rico, who has since accepted the position of CICAR Subject Leader for Chemistry. Dr. Atwood is establishing a set of standard chemical observations for the remaining CICAR operations.

Between Puerto Rico and Trinidad, the *DISCOVERER* made a successful recovery of the deep-sea, bottom-mounted tide gage that had been em-



Bob Starr discusses bottom biological samples with schoolchildren from Trinidad.

planted in water over 4,000 meters deep some six months previously. So far as is known this marked the longest deep-sea tide record yet obtained in the open sea. Additional work on this leg also provided ground truth data for Earth Resources Technology Satellite (ERTS-I) observations of the "wakes" in the lee of the Antillean islands.

With the exception of one oil company geologist and one officer from the Trinidad and Tobago Coast Guard, all of the Trinidad scientific party, under Professor Jake Kenny, came from the St.

Augustine campus of the University of the West Indies. They were an eager and enthusiastic group and kept those of us from the United States hopping during the entire week that we worked with them on the Trinidad shelf.

Our bottom dredgings recovered benthic species that had the Trinidad biologists actually collecting tens of samples of specimens that were previously known only from one single museum specimen. Ranges were also extended and, as Professor Kenny put it, "NOAA-Carib has more than doubled the existing knowledge of the bottom fauna of the Trinidad shelf."

Using oil company maps of the known offshore geology of the east Trinidad shelf, the *DISCOVERER* went directly to critical areas to examine apparent anomalies. One strange topographic high turned out to be a classic example of the diapiric that so often provide structural traps for the accumulation of petroleum.

On our return to Port of Spain, the data went ashore with the Trinidad scientists and, hopefully, the results of the analyses now in progress will shed new light on the origin of features on the Trinidad



Robert Marak of NOAA's National Marine Fisheries Service shows plankton samples to Mexican students.



David Howard (left) and Benjamin Culverhouse of NOAA give Mexican schoolchildren a lift.

Photo by the United States Information Service.

shelf—and perhaps even assist in assessing the local petroleum potential.

The cruise wasn't all work, however. The night before the ship left Trinidad, Professor Kenny held a big dinner party. It was the U.S. Thanksgiving Day, and the buffet combined traditional turkey and cranberry sauce with delicious Trinidad-Chinese food. We listened to Trinidad calypso singing and told sea stories. There were comparable evenings at the other ports, and the people-to-people aspects of NOAA-Carib are perhaps as important for the future as the scientific results achieved.

At La Guaira, the Venezuelans had just completed an overland gravity traverse from Caracas to the coast, and the *DISCOVERER*'s ship-board gravimeter was able to extend this line some ten miles out to sea. With the Venezuelan geologists under Perez Nieto, we traced seaward for some 50 miles the seafloor extension of the large fault that underlies the city of Caracas and plunges into the sea at La Guaira.

Off Colombia, the *DISCOVERER* made a

string of east-west plankton stations and was able to spot the higher productivity in the area of upwelling which the Colombians had wanted to investigate. This was further studied by three lines of stations where salinity-temperature-depth observations were made for the Colombian physical oceanographer, Dr. Jaime Hernandez. There were also meteorological balloon releases; more plankton tows; miles of air-gun, gravity, magnetic, and bathymetric profiles;



A weather balloon launch draws a crowd.

sea-water chemistry analyses; and a boomerang core taken from the axis of Aguja Canyon before the ship arrived at Cartagena.

At the ancient walled city of Cartagena, Capitan de Fragata Gustavo Angel Mejia—the former CICAR Coordinator for Colombia and recently assigned as the new Commanding Officer of the Colombian oceanographic ship, *A.R.C. SAN ANDRES*—acted as our host for the three-day visit.

In looking at statistics for NOAA-Carib, it was found that the ship had provided at-sea training for periods ranging from one day to two weeks for some 401 Latin Americans. They participated in all

phases of oceanographic observations at sea—physical, chemical, geological and geophysical, biological, fisheries, and meteorological. Several thousand others came aboard to inspect the ship and its equipment, and Walt Disney Studios and the U.S. Information Agency each had a film crew aboard for one or more legs.



Following their two-day scientific cruise, the students from Mexico City's University present a pinata to Capt. Floyd Tucker, Jr., the *DISCOVERER's* Commanding Officer (left), and Cdr. Donald Florick.

The Mexicans, Jamaicans, Trinidadians, Venezuelans, and Colombians received some 23 reconditioned mechanical bathythermographs provided by the U.S. Navy for their retention and use. Most of all, however, NOAA-Carib showed that the United States is concerned about marine science in the Caribbean and is willing to help others in the area in a way that they themselves feel is the most productive. The post-expedition letters of appreciation from all over the Caribbean lead us to believe that on NOAA-Carib we did indeed meet our stated goals. □

HARRIS B. STEWART, JR. is director of the Atlantic Oceanographic Meteorological Laboratories in Miami, Florida. He has an undergraduate degree in geology and received his M.S. and Ph.D. in oceanography from Scripps Institution of Oceanography, University of California. Dr. Stewart, one of the founding members of MTS, was elected to the office of vice president for exploration and ocean operations by the members in July of this year. He is the author of three books and numerous technical papers.



Fed. Research Bucks Still Available If Ideas Are Innovative Enough

BY HARRIS B. STEWART JR., PHD

We are extremely proud of the Virginia Key marine science complex that's developing out here: a very nice university-federal lab melding, a mutually beneficial, synergistic operation that so far has worked very well.

Now, if the system really is to continue to work, the university and the federal labs have got to move forward, it seems to me, hand-in-hand.

Over the last months, the federal research activity and the federally supported research activities have taken a fair fiscal beating.

We're going through a traumatic period — not only for those who are directly funded federal laboratories such as Atlantic Oceanographic and Meteorological Laboratory, but also for those who are supported by many of the federal programs, as in the University of Miami.

It is a time of belt-tightening, which is a nice way of saying budget cutting, and how do you combat this? How do you alert the powers that be of the importance to the nation of understanding the ocean and the processes that go on in it, above it, and under it? How do we get the message across? How do we keep the federal establishment sufficiently concerned about the importance of the oceans to the United States that a viable ocean program is, in fact, underway in this country?

A LOT OF US have thought about this for more years than we care to count. Let me suggest some ways that we as scientists and scientist-administrators can perhaps get this message across.

For those of us who depend on the

taxpayer's dollar for our very livelihood, and for doing the work that we so desperately feel needs doing, we've got to find some new approach, some new way to get our message across, some way to show the federal establishment that the ocean is, in fact, incredibly relevant to solving some of the problems facing the nation today — let alone building up the pool of knowledge to help solve the problems that will face the nation tomorrow.

I have three suggestions on how we as scientists can perhaps improve the situation.

One is to find some way whereby the United States can make a total policy commitment to the oceans. This was done in space a number of years ago. President Kennedy said we will have a man on the moon by 1970 — period.

That was a policy commitment, something to which our national treasures were going to be devoted. And it was accomplished ahead of time. One such policy commitment by the United States could very easily be that the total environmental understanding of the nation's nearshore areas will, in fact, be accomplished in ten years.

NOW THAT'S a big order. Putting a man on the moon was a big order. What would this mean? This would mean all-out attack by physical ocean-

ographers on the nearshore processes, the mechanisms, the ability to predict what goes on. It would entail full-scale work on the biological aspects of the coastal zone, the ecological aspects, the geological aspects, the chemical aspects, the sociological aspects, the energy aspects — the whole spectrum of the coastal zone.

Let's assume that the United States at the highest levels made a policy decision that in ten years we would have a "complete environmental understanding" of the nearshore area and that the United States was willing to plow one billion dollars per year into this effort.

You may say that we don't have the people to do it, but when one billion dollars is put on the barrelhead, capable people to do the job will come up out of the woodwork. Ships that are being laid up, scientists that are pumping gas would come back into the system and my contention is that if we couldn't accomplish it, we would make one whale of a good attempt.

But again, this would entail a national policy decision relating to the ocean, one that I do not now see about to be made.

What can be done other than on the national level?

One thing that I think can be done is to inject new ideas, exciting concepts, ideas that on one hand would be fun for us to work on, and on the other hand would be highly relevant to the solution of problems of the type that can garner today's federal funds.

I'D LIKE very quickly to throw out two such ideas that are almost uniquely south Florida oriented. One is the concept of offshore, man-made islands. I've pushed this before, so I'll push it very briefly this trip.

The concept basically is this: First, South Florida is short on waterfront; secondly, South Florida coastal areas are subject to the damage related to wave action on top of hurricane storm-surges; the rising water doesn't do quite so much damage as those miserable waves on top of it.

Thirdly, South Florida has very real problems with its beach erosion.

Now, what if the proper engineering and environmental studies were done and a string of offshore islands — man-made islands — were constructed seaward of and parallel to Miami Beach, say in depths of 50 to 60 feet.

The technology for building offshore islands is here. They're being built in other parts of the world with considerable success. These will then be sodded and planted with sea grape, palms, and other things that would stand the rigors of the environment.

So we would have (1) esthetic enhancement of the environment, (2) additional recreation beaches — places to sail to or swim to or go to for picnics, (3) it would indeed reduce the force of storm surge waves on man-made structures on the beach.

Finally, and perhaps most importantly, it would, in all probability, reduce wave action at the beach, therefore reducing the tossing of the sand into suspension and the literal movement of beach sand which is denuding those beaches.

THERE IS A LARGE beach replenishment project about to get started along Miami Beach. Offshore islands would in no way compete with that but would perhaps retard the rate at which that new sand was removed.

Now, is something like this feasible? Very possibly. But what it takes is good minds and good ocean engineering.

How far apart would the islands have to be?

What sort of effects would there be on the beach insofar as increasing sand accumulation is concerned?

The Corps of Engineers knows that sand accumulates on the beaches behind what they call detached breakwaters. It happened at the Santa Monica breakwater, it happened at the Winthrop breakwater, north of Boston — the mechanism works.

Would we have to bypass sand under Haulover Cut in order to keep it coming into Miami Beach? I don't know. There are engineering problems and there are environmental problems that would have to be solved.

But who's working on them, who's looking ahead at this sort of thing?

THERE IS a second idea: this one originally proposed by Bill von Arx at Woods Hole as a possible solution to our growing energy crisis. Again, it falls within the criteria of being oceanic, of being exciting, of being relevant.

The idea comes from the fact that nature has very cleverly concentrated solar energy in the western boundary currents in our oceans on the order of 50 to 1. The major one of these western boundary currents is the Gulf Stream; and, as the Florida Current, it flows right out here.

"Bill von Arx and John Apel of NOAA have run through the

computations on this, and it appears that the extractable power over the submerged Miami Terrace on the Florida side of the Stream amounts to some 1200 megawatts or about two Turkey Points."

Fine.

Nice statement.

But how do you do it? Once you have the energy, how do you utilize it?

Well, if it went into power lines, there would be problems with phase shift and line losses. So what Bill has been doing is some very imaginative thinking.

HIS CONCEPT briefly stated is this: what you do is tap this offshore energy and convert it to DC, then use it to break down water to produce cryogenic hydrogen and oxygen. This cryogenic hydrogen and oxygen would then be shipped all over the country as packaged "cold power."

(Continued on Page 25)

Research

Continued from Page 9.

It wouldn't go on power lines, it wouldn't go in pipe lines, but in all probability it might be the saving of U.S. railroads, for example.

In other words, at the places where the energy was required, it would be delivered in little packages. The end product of this as the cryogenic oxygen and hydrogen boil off and combine is power, and the only waste by-product is pure water.

So there's no pollution problem . . . your by-product is water.

That, basically, is the concept. The energy in our Gulf Stream would probably be trapped by some sort of large ducted fans as submerged generators which would be floated out, submerged below navigation depth, anchored somehow, and just allowed to churn away out there.

SURE, THERE are problems. What do you do about fouling organisms? Do you use acoustic techniques to keep the fouling organisms off the equipment? What happens downstream if you begin removing heat from the system? How much heat would be removed?

It's the sort of thing that's going to take a lot of thought and an incredible amount of engineering, but so did putting a man on the moon.

I think the point is that these are the sorts of things that should be thought about, because if we're going to bail out of this, hopefully temporary, support slump that we're all in in the marine sciences, it is going to take innovative ideas and capable people.

I'm still convinced that in the system there is funding to support innovative ideas that look as though they might have a payoff and are indeed relevant. This is the way to get funding support today.

Reprinted from Environmental Data Service, 3-11, Apr. 1973.



Lt. Lawrence Keister discusses the intricacies of position location with Mexican Navy cadets.

NOAA-Carib: An Experiment That Worked

BY HARRIS B. STEWART, JR.

"The only instance that I have witnessed that exceeded the person-to-person impact of the DISCOVERER was the good ship HOPE off the Peruvian coast."

DR. JAMES M. LAMMONS
TEXACO TRINIDAD, INC.

The Cooperative Investigation of the Caribbean and Adjacent Regions (CICAR) is a 15-nation oceanographic effort aimed at developing a better understanding of the Caribbean system and providing a mechanism whereby the Caribbean Basin community of nations can increase their own involvement and capabilities in marine science.

A cooperative program of the Intergovernment Oceanographic Com-

mission of United Nations Educational, Scientific and Cultural Organization (UNESCO), CICAR has sponsored regular meetings of the several national coordinators to review accomplishments and to make future plans. At meetings held in Washington, D.C., Mexico City, Mex., Port of Spain, Trinidad, and most recently in Havana, Cuba, the message came through loud and clear: What the Latin American nations wanted most was an opportunity for their students and faculty members to get at-sea training and instruction in the full spectrum of oceanographic observations.

The concept of NOAA-Carib developed gradually within NOAA's Atlantic Oceanographic Meteorological Laboratories (AOML) in Miami. The primary goal was a 2-month oceano-

graphic expedition aboard the NOAA ship DISCOVERER on which Latin American scientists and students would carry out their own research work. They would plan what they wanted to do in their own waters, and select the people to go along to do it and to get training while so doing. They would keep all the data collected during their phase of the operation, and work up and publish the results. NOAA's role would be to provide the fully equipped DISCOVERER, plus a basic cadre of experienced sea-going scientists to assist the Latin Americans in the various operations they wished to carry out.

When the concept of NOAA-Carib was put forward by the U.S. Delegation at the Trinidad CICAR meeting in 1971, it was greeted with enthusiasm. Planning then got underway on

an intensive scale, and Mexico, Jamaica, Puerto Rico, Trinidad and Tobago, Venezuela, and Colombia all began putting together their own programs to be accomplished on the *DISCOVERER* during the NOAA-Carib cruise scheduled for October, November, and December 1972.

After mountains of correspondence, partly in Spanish, several last-minute cables, and a few panicky telephone calls, nine Mexicans arrived in Miami to sail October 9th on the first leg of NOAA-Carib. Cdr. Donald Florwick, Jack Kofoed, and Harris Stewart, all of AOML, alternated as Chief Scientists for portions of the trip. UNESCO provided about \$2,000 to assist Latin Americans in their travel to and from the ship.

There were numerous changes in personnel in the scientific party at seven Caribbean ports—Veracruz, Montego Bay, Kingston, San Juan, Port of Spain, La Guaira (Caracas), and Cartagena. In each country, the *DISCOVERER* held an "open house" for streams of school children, college students, local officials, dock workers, and the local curious.

The visitors listened to short lectures on what we were up to as they filed past exhibits of our equipment at work, through the bridge, the laboratories, the computer room, the meteorological "shack," the plotting room, and the flying bridge. They stared curiously at the big winch and coring gear, and with fascination watched themselves on closed-circuit television in the electronics shop.

In each country, a 1-day cruise was arranged for up to fifty or so local people. The local NOAA-Carib coordinator was told that he could invite whomever he wanted but that preference should be given to students and faculty members who could most benefit by a 1-day demonstration trip. Most of the "cruisees" were students, but there was also a fair sprinkling of members of the local press, as well as a few local administrators.

In every instance but one, the 1-day cruise was highly successful. Out of San Juan harbor, however, the *DISCOVERER* encountered rough seas, and most of the visitors were shortly indisposed. Soon attendance at the





Above: The DISCOVERER's NOAA-Carib cruise, October 9 to December 15, 1972.
Left: A weather balloon launch draws a crowd.

lectures and demonstrations was sparse, and almost every bunk aboard held a groaning occupant who, although swearing he would never go to sea again, certainly left with considerable respect for those who do so routinely.

On each of the 1-day trips, much of the briefing was done by marine scientists from the country concerned who had already been onboard for the previous leg. Thus, in the Spanish-speaking ports, explanations were made in Spanish by their own countrymen.

The real accomplishments of NOAA-Carib, however, were the individual national projects planned to meet local needs and carried out essentially by local scientists in their own waters. The enthusiasm of the Latin Americans was contagious. Alfonso Lopez Reina, for example, a geologist from Colombia, stayed at the seismic reflection recorder for 26 hours straight as the DISCOVERER ran profiles across the Aguja Submarine Canyon off Colombia. When asked if he didn't need some sleep, his response was "Yes, of course, but I can sleep when I get ashore; why waste this valuable time by sleeping?"

Aside from an occasional case of seasickness when the bunk looked better than anything else aboard, the Lopez reaction was essentially that of all who took part in NOAA-Carib. It was a rewarding experience for the U.S. participants to see that the sea-going work we tend to take for granted was highly valued by our Latin American colleagues.

Specific scientific results? There were quite a few. Out of Veracruz the Mexican geologists and geophysicists, under Dr. Robert Lankford, managed to fill in some holes in the geophysical knowledge of the Mexican shelf.

Off Jamaica, scientists from the Mona Campus of the University of the West Indies recovered cores from the Cayman Trough, obtained seismic reflection profiles of the Jamaican shelf, and specified where they wanted bottom current measurements made off the eastern tip of the island. The DISCOVERER planted bottom current meters at the location specified. The instruments were retrieved by acoustic signals some two months later as the DISCOVERER was enroute from Cartagena to Miami. One of the systems flooded out shortly after it

was planted, but the records from the other were flawless and are now being analyzed to fill a glaring gap in the knowledge of the circulation around Jamaica.

The Puerto Rican work centered heavily on chemical investigations made under the direction of Dr. Donald Atwood of the University of Puerto Rico, who has since accepted the position of CICAR Subject Leader for Chemistry. Dr. Atwood is establishing a set of standard chemical observations for the remaining CICAR operations.

Between Puerto Rico and Trinidad, the DISCOVERER made a successful recovery of the deep-sea, bottom-mounted tide gage that had been emplaced in water over 4,000 meters deep some six months previously. So far as is known this marked the longest deep-sea tide record yet obtained in the open sea. Additional work on this leg also provided ground truth data for Earth Resources Technology Satellite (ERTS-1) observations of the "wakes" in the lee of the Antillean islands.

With the exception of one oil company geologist and one officer from

the Trinidad and Tobago Coast Guard, all of the Trinidad scientific party, under Professor Jake Kenny, came from the St. Augustine campus of the University of the West Indies. They were an eager and enthusiastic group and kept those of us from the United States hopping during the entire week that we worked with them on the Trinidad shelf.

Our bottom dredgings recovered benthic species that had the Trinidad biologists actually collecting tens of samples of specimens that were previously known only from one single museum specimen. Ranges were also extended and, as Professor Kenny put it, "NOAA-Carib has more than doubled the existing knowledge of the bottom fauna of the Trinidad shelf."

Using oil company maps of the known offshore geology of the east Trinidad shelf, the DISCOVERER went directly to critical areas to examine apparent anomalies. One strange topographic high turned out to be a classic example of the diapiric traps that so often provide structural traps for the accumulation of petroleum.

On our return to Port of Spain, the data went ashore with the Trinidad

Below: Mike Sunray of NOAA's National Weather Service explains the recorder trace of meteorological observations taken by the radio instrument package attached to the weather balloon (see previous page). Right: Cdr. Jimmy Lyons and some new friends.







Bob Starr (above) discusses bottom biological samples with schoolchildren from Trinidad. Right: Robert Marak of NOAA's National Marine Fisheries Service shows plankton samples to Mexican students.

scientists and, hopefully, the results of the analyses now in progress will shed new light on the origin of features on the Trinidad shelf—and perhaps even assist in assessing the local petroleum potential.

The cruise wasn't all work, however. The night before the ship left Trinidad, Professor Kenny held a big dinner party. It was the U.S. Thanksgiving Day, and the buffet combined traditional turkey and cranberry sauce with delicious Trinidad-Chinese food. We listened to Trinidad calypso singing and told sea stories. There were comparable evenings at the other ports, and the people-to-people aspects of NOAA-Carib are perhaps as important for the future as the scientific results achieved.

Between Trinidad and La Guaira, the port for Caracas, Venezuela, the Venezuelans, under Dr. Hernan Perez Nieto, were concerned mainly with the geological and fisheries aspects of their offshore waters. Hector Lopez and Antonio Muchado of Venezuela stayed with the ship through Cartagena and, with Ken Honey of NOAA's National Marine Fisheries Service (NMFS), made regular tows

using the standard CICAR bongo and neuston nets and the Isaacs-Kidd mid-water trawl. During port stops, the Venezuelans gave regular lectures in Spanish on the biological and fisheries work of NOAA-Carib and instructed others in taking standard observations.

Through NMFS, it had been arranged that the plankton nets and frames would remain with Venezuela and Colombia. These were left aboard the Colombian ship, A.R.C. SAN ANDRES when the DISCOVERER sailed from Cartagena in mid-December. By then, Ari Brogman and the other Colombians aboard were fully checked out on their use, and two more CICAR countries are now using standard gear.

At La Guaira, the Venezuelans had just completed an overland gravity traverse from Caracas to the coast, and the DISCOVERER's shipboard gravimeter was able to extend this line some ten miles out to sea. With the Venezuelan geologists under Perez Nieto, we traced seaward for some 50 miles the seafloor extension of the large fault that underlies the city of Caracas and plunges into the sea at La Guaira.





Top: John Proni explains the use of underwater sound to detect subsurface water movements. Below: Following their 2-day scientific cruise, the students from Mexico City's University presents a pinata to Capt. Floyd Tucker, Jr., the DISCOVERER's Commanding Officer (left), and Cdr. Donald Florick. Right: Harris Stewart, the author, explains some of DISCOVERER's oceanographic gear to students from the University of the West Indies, Trinidad.

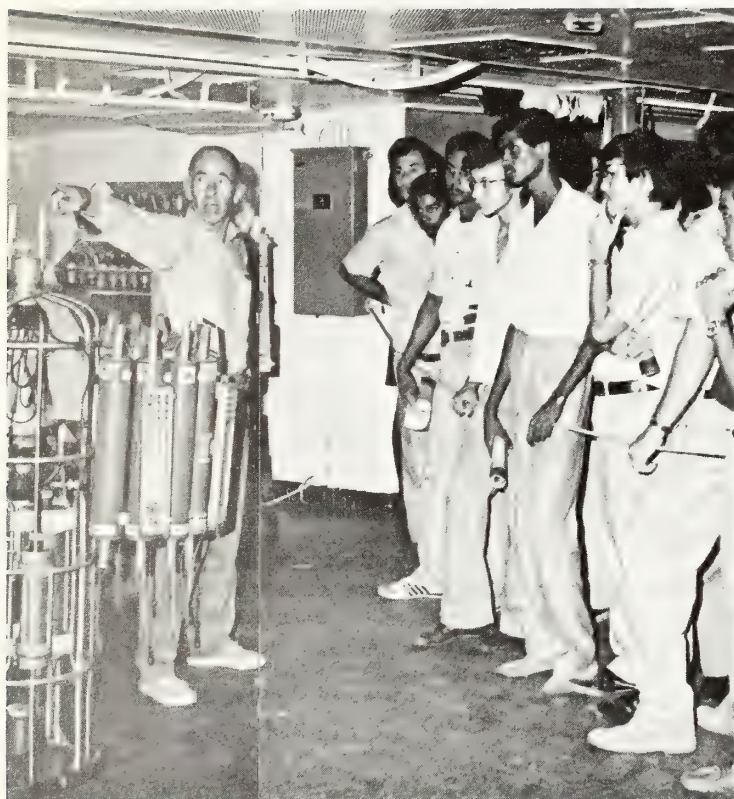


Off Colombia, the *DISCOVERER* made a string of east-west plankton stations and was able to spot the higher productivity in the area of upwelling which the Colombians had wanted to investigate. This was further studied by three lines of stations where salinity-temperature-depth observations were made for the Colombian physical oceanographer, Dr. Jaime Hernandez. There were also meteorological balloon releases; more plankton tows; miles of air-gun, gravity, magnetic, and bathymetric profiles; sea-water chemistry analyses; and a boomerang core taken from the axis of Aguja Canyon before the ship arrived at Cartagena.

At the ancient walled city of Cartagena, Capitan de Fragata Gustavo Angel Mejia—the former CICAR Coordinator for Colombia and recently assigned as the new Commanding Officer of the Colombian oceanographic ship, A.R.C. *SAN ANDRES*—acted as our host for the 3-day visit.

In looking at statistics for NOAA-Carib, it was found that the ship had provided at-sea training for periods ranging from 1 day to 2 weeks for some 401 Latin Americans. They participated in all phases of oceanographic observations at sea—physical, chemical, geological and geophysical, biological, fisheries, and meteorological. Several thousand others came aboard to inspect the ship and its equipment, and Walt Disney Studios and the U.S. Information Agency each had a film crew aboard for one or more legs.

The Mexicans, Jamaicans, Trinidadians, Venezuelans, and Colombians received some 23 reconditioned mechanical bathythermographs provided by the U.S. Navy for their retention and use. Most of all, however, NOAA-Carib showed that the United States is concerned about marine science in the Caribbean and is willing to help others in the area in a way that they themselves feel is the most productive. The post-expedition letters of appreciation from all over the Caribbean lead us to believe that on NOAA-Carib we did indeed meet our stated goals. □



The International Ocean

HARRIS B. STEWART, JR.

*National Oceanic and Atmospheric Administration
Miami*

Because the oceans cover so much of our Earth, it is important that we who live on the relatively dry one-third of this planet develop cooperatively a much better understanding of that watery other two-thirds.

One valid reason for international cooperation in marine science is that no nation by itself can ever hope to learn all about the sea or to understand its processes. That this is a viable mechanism was proven by the International Cooperative Investigation of the Tropical Atlantic some 10 years ago and by the International Indian Ocean Expedition in 1964. In 1974, we will again prove this concept with the GARP Atlantic Tropical Experiment. Even now we are proving it with the Cooperative Investigation of the Caribbean and Adjacent Regions (CICAR).

The mission of CICAR as we interpreted it was to increase our understanding of the Caribbean Sea and the Gulf of Mexico—their physical oceanography, fisheries, biology, geology, marine chemistry and meteorology. As the field phase of CICAR developed, it became evident that the four major areas where international cooperation was needed were: field operations, particularly where synoptic or multi-ship projects were involved; data exchange among the participants; planning; and education and training.

There is one item of potential international non-cooperation about which I am personally most concerned. This is the question of freedom to do research at sea. Within another nation's territorial seas, it is becoming increasingly difficult to obtain official permission to do oceanographic research. The currents of the sea and the life in the sea recognize no man-made boundaries, and the ocean scientists who seek to understand the magnificent complexities of the processes and the life within the sea should not be hampered in their search for understanding these processes.

AN OCEANOGRAPHIC OBSERVATION OF NEW YORK BIGHT FROM ERTS-1

Robert L. Charnell and George A. Maul
Atlantic Oceanographic and Meteorological Laboratories
Physical Oceanography Laboratory
Miami, Florida

The Earth Resources Technology Satellite (ERTS-1), made a transit over New York Bight on August 16, 1972. Imagery from this transit shows several oceanographic features that demonstrate the usefulness of remote sensing over a large area for the synoptic observation of changes in water quality in the coastal zone. Both the extent and turbulent character of the Hudson River plume are discernible in the image. Residue from a dump of waste acid is visible over a 5-mile area in the apex of the bight. Little dispersion of this residue has occurred, suggesting that this feature will be a persistent signature in images from future satellite transits.

On August 16, 1972, the multispectral scanner (MSS) aboard the first Earth Resources Technology Satellite (ERTS-1) obtained a set of images of the New York Bight which contains information of oceanographic significance. The images demonstrate the effectiveness of using satellites to observe surface features that indicate changes in water quality. The impact of this technique on coastal-zone oceanographic analysis will be widespread.

The MSS aboard ERTS has four channels, with band-pass filters covering the visible and near infrared bands. Channel 4 covers the 0.5- to 0.6- μm (green-yellow) band; channel 5 covers the 0.6- to 0.7- μm (orange-red) band; channel 6 covers the 0.7- to 0.8- μm (red) band; and channel 7 covers the 0.8- to 1.1- μm (infrared) band. An understanding of the manner by which solar energy is reflected across the spectrum is needed to determine which bands contain the most information relating to ocean phenomena.

Reflectance of solar energy from the sea surface, as measured by a spacecraft, is a function of atmospheric state, water depth, water-mass

characteristics, sea-bottom characteristics, and sea state. To insure that information about the ocean was being observed, calculations were performed to determine the percent of energy that penetrated the sea surface, that was reflected from a perfect reflector, and that was subsequently seen at the surface. These calculations were made by solving the intensity equation

$$I = \int_0^{\infty} \phi_{\lambda} I_{0\lambda} e^{-\alpha_{\lambda} z} d\lambda$$

where I is the intensity observed at a depth z through a band-pass filter ϕ_{λ} , which is normalized over the region of wavelength λ for the appropriate ERTS channel; $I_{0\lambda}$ is the intensity at the sea surface; and α_{λ} is the spectral attenuation coefficient.¹

Calculations show that a perfect reflector at a depth of 1 m (3 ft) returns 86 percent of the incident energy for the 0.5- to 0.6- μm band, 55 percent for the 0.6- to 0.7- μm band, 11 percent for the 0.7- to 0.8- μm band, and 0.2 percent for the 0.8- to 1.1- μm band. These results suggest that an oceanographic feature will not be seen in the 0.8- to 1.1- μm band (reflected infrared). Hence, comparison of suspected water features observed in the visible bands with those observed in the infrared band insures that above-surface features such as clouds are not mistaken for surface and subsurface oceanographic features. (A comparison of these calculations for all four bands is shown in fig. 1.)

Calculations on energy penetration also provide a first estimate of the depth of a feature. For example, a perfect target at 5 m (16 ft) will reflect 50 percent in the green-yellow band, will reflect 7 percent in the orange-red band, and will essentially reflect no percent in the red or near infrared bands.

MSS imagery, presented in figure 2, shows an area of approximately 100 x 100 mi in the New York Bight. The body of water in the upper

¹The attenuation coefficient for pure water was used in this calculation. This provides a conservative estimate because α , for even the cleanest sea water, is much larger.

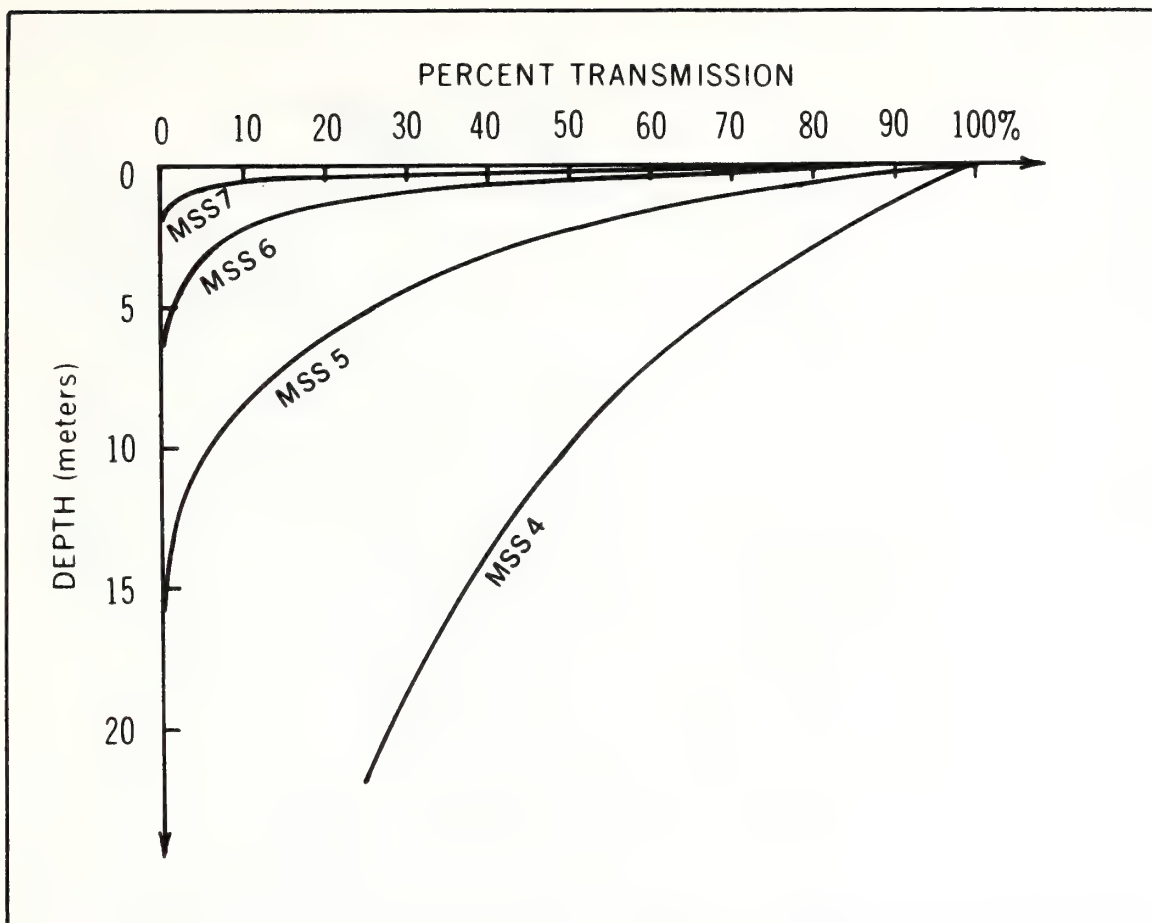


Figure 1. Theoretical calculation of the percent of solar energy penetrating the sea surface that reaches a given depth for each of the four channels of the ERTS MSS.

center left of the image is Raritan Bay; the land mass at the top is a portion of Long Island. The image extends along the coast of New Jersey (land mass on the left) to just beyond Barnegat Inlet. The picture in the figure is the bulk-processed imagery of the MSS 5 channel (0.6- to 0.7- μ m) just as it is received from the National Aeronautics and Space Administration (NASA) data-processing facility. Imagery was obtained at 1507 GMT when the elevation of the sun was 53° and the azimuth was 130°. For this transit, the MSS 5 channel was the most sensitive to oceanic features; MSS 4 band was obscured by haze induced by atmospheric



Figure 2. Bulk-processed imagery in the 0.6- to 0.7- μ m band of ERTS-1 from the New York Bight transit of August 16, 1972.

scatter; and the other channels showed much less detail in sea-surface features, as the calculations would suggest.

The large white features present in the right side of the image (fig. 2) are clouds. They are present in all bands. The dark areas (to the northwest) adjacent to these white features are shadows cast on the sea surface by the clouds. The haze present over New York City comes from smoke and dust produced in the metropolitan area.

The most prevalent oceanic feature in this New York Bight frame (fig. 2) is the existence of visibly turbid surface water near the coast. The light-colored water extends a few miles offshore and is produced by the action of waves and tides at the land-ocean boundary in maintaining suspended sediment. Farther from shore, the settling of sediment and mixing with shelf water decrease the turbidity. An evaluation as to the extend of this turbid surface water adjacent to the southern coast of Long Island is hindered by the existence of high clouds. The general turbid nature of the nearshore water precludes detection of the sea bottom with MSS. Lateral extent of coastal turbid water increases in the area of high-water velocities, such as would be encountered in Barnegat Inlet (lower left-hand portion of the image) where a tidal plume is clearly visible.

A plume of light-colored water extends from the mouth of the New York Harbor complex south along the New Jersey coast. The plume, which is approximately 29 km (18 mi) long and 11 km (7 mi) wide, represents the core of lower salinity water from the Hudson River. Characteristically at this time of year (August), the Hudson River plume is relatively small because of reduced fresh water outflow and is pushed onto the New Jersey coast by the predominant winds. Surface winds for the preceding day were less than 10 kt and were generally from the east.

Clearly, the plume is not homogenous. Patchiness is indicative of the turbulent mixing process by which the plume water is absorbed into the ambient bight water. The relatively sharp eastern boundary of the plume indicates that dispersion processes are not isotropic.

Fortuitously, surface salinity data were collected in the general area of the plume.² A transect on approximately August 10 and another on August 22 were made perpendicular to Sandy Hook. Although the data are too few to define the shape and size of the plume, they indicate that the low-salinity Hudson plume was in this general area as depicted in the MSS 5 image and that the plume was about two part per thousand lower in salinity than the ambient bight water.

There is an unusual and interesting feature in the apex of the bight about 32 km (20 mi) southeast of the harbor entrance that apparently is a manifestation of man's activity in the area. The feature consists of a fairly sharp wavy line and a more diffuse circular patch north of the line. These features are located in the general area for waste disposal (NOAA, 1972).

The two major dump sites in the bight are for sewer sludge and for waste acid. Between five and six bargeloads of sewer sludge are dumped daily at a point about 8 km (5 mi) southeast of Ambrose Light Station. An average of about two bargeloads of waste acid are taken each day for disposal to a site some 16 km (10 mi) southeast of Ambrose Light Station. Disposal of waste acid is made while the vessel is in transit: one-half the load is dumped over a distance of approximately 8 km enroute to the turning point; the remainder is dumped on the way back. Surface color of waste acid is yellow-green, optimally detected in the MSS 4 band; because of atmospheric dispersion, the MSS 5 band (as processed by NASA) affords higher contrasts in surface features. The acid is slow to mix with the sea water because the waste is of near-equal density and hence maintains sharp boundaries for substantial periods of time.

The distinct wavy line is the result of waste acid disposal. The northwest-southeast dimension of the feature is approximately 8 km. The less distinct portion of the line may be residue from an earlier dump. A minor discrepancy occurs in that the turning point in the

²Salinity data were kindly supplied by the Ecosystems Investigations, NOAA National Marine Fisheries Service, Middle Atlantic Coastal Fisheries Center, Sandy Hook Laboratory, Highlands, N.J.

image frame is approximately 8 km nearer the harbor than the authorized dump site.

Normally, dumping occurs on a semidaily basis. Thus, the relic dump must be at least 12 hr old, and the dispersion was very slow. The fact that the recent dump may have drifted some 8 km implies that it was made several hours before the satellite transit. Even though wind mixing was low for this day, the implication for dump durability is that dumping of this magnitude generally will produce a persistent surface feature.

The diffuse circular patch to the north of the waste acid dump is close to the sewer sludge dump site. Surface manifestation of a sewer sludge dump is much less noticeable than that of waste acid; only a gray-brown slick will remain. Initial low intensity of the reflected image makes the character of the surface patch less discernible.

This single image (fig. 2), taken in an area of complex oceanography and high population density, demonstrates the utility of satellites (such as ERTS) that are equipped to survey the water-quality changes (such as location of river discharge plumes) and to measure the effectiveness of waste-dumping procedures. It seems likely that satellites with sensors, optimized to view the ocean in visible and infrared wavelengths, will supply synoptic wide-area data and will make management of the coastal zone on a broad scale much more realistic.

ACKNOWLEDGMENTS

We acknowledge the description of waste-dumping procedures provided by John B. Pearce of the NOAA National Marine Fisheries Service, Middle Atlantic Coastal Fisheries Center, Sandy Hook Laboratory, Highlands, N.J.

This research was, in part, supported by the Earth Resources Program of the National Aeronautics and Space Administration. The imagery for ERTS proposal C315 was supplied by the NASA Data Processing Facility at Goddard Space Flight Center, Greenbelt, Md.

REFERENCE

National Oceanic and Atmospheric Administration (1972), The effects of waste disposal in the New York Bight, *A Summary Final Report*. Prepared by the National Marine Fisheries Service, Middle Atlantic Coastal Fisheries Center, Sandy Hook Laboratory, Highlands, N.J., 70 pp.

Oceanic Observation of New York Bight by ERTS-1

ON August 16, 1972, the multispectral scanner (MSS) aboard the first Earth Resources Technology Satellite (ERTS) obtained images of New York Bight which contain information of oceanographic significance. The images demonstrate the effectiveness of satellite use in observing surface features that indicate variations of water quality.

The MSS measures reflectance of solar energy in four channels with band pass filters that cover visible and near infrared bands from 0.5 to 1.1 μm . Because solar energy penetrates ocean water further for the shorter observed wavelengths, features characteristic of the water mass, such as turbidity, are more predominant in the lower bands; features on or above the sea surface, such as clouds, tend to appear with uniform strength in all channels (Fig. 1). A nearly perfect

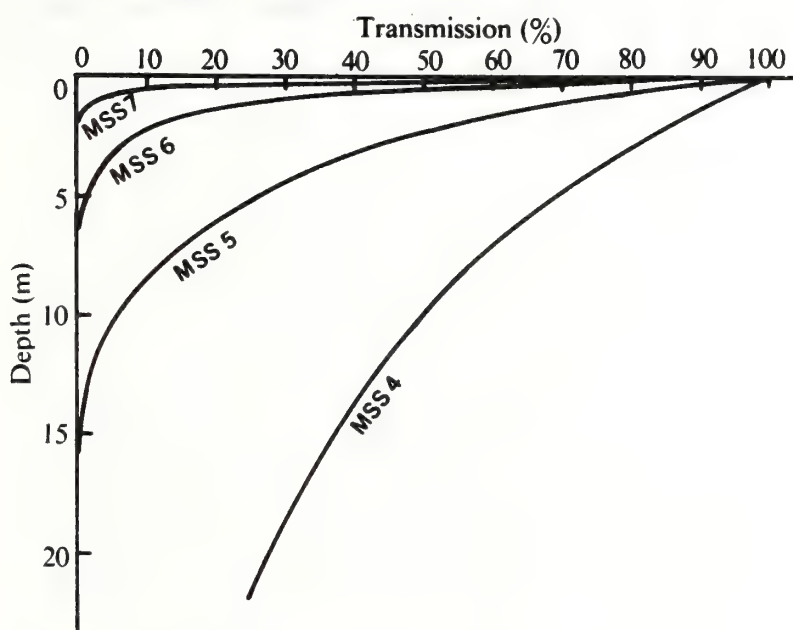


Fig. 1 Theoretical calculation of the proportion of solar energy penetrating the sea surface that reaches a given depth for each of the four channels of the ERTS MSS. Calculations used the attenuation coefficient for pure water. This provides a conservative estimate because for the cleanest sea water α is much larger.

target at 5 m will reflect 50% of the energy in the lowest band and essentially none in the highest band.

Fig. 2 shows imagery from the band most sensitive to ocean features—MSS-5; MSS-4 is partly obscured with haze induced by atmospheric scatter. The most prevalent oceanic feature in this frame is visibly turbid surface water near the coast. A plume of light-coloured water extends from the New York harbour complex south along the New Jersey coast. The plume, approximately 18 mile long and 7 mile wide, represents the offshore Hudson River effluent. The Hudson River plume is relatively small at this time of year owing to reduction in the outflow of fresh water and is pushed on to the New Jersey coast by the prevailing winds.

Inhomogeneities in the plume indicate the turbulent mixing processes by which plume water is absorbed into ambient Bight water. The relatively sharp eastern boundary of the

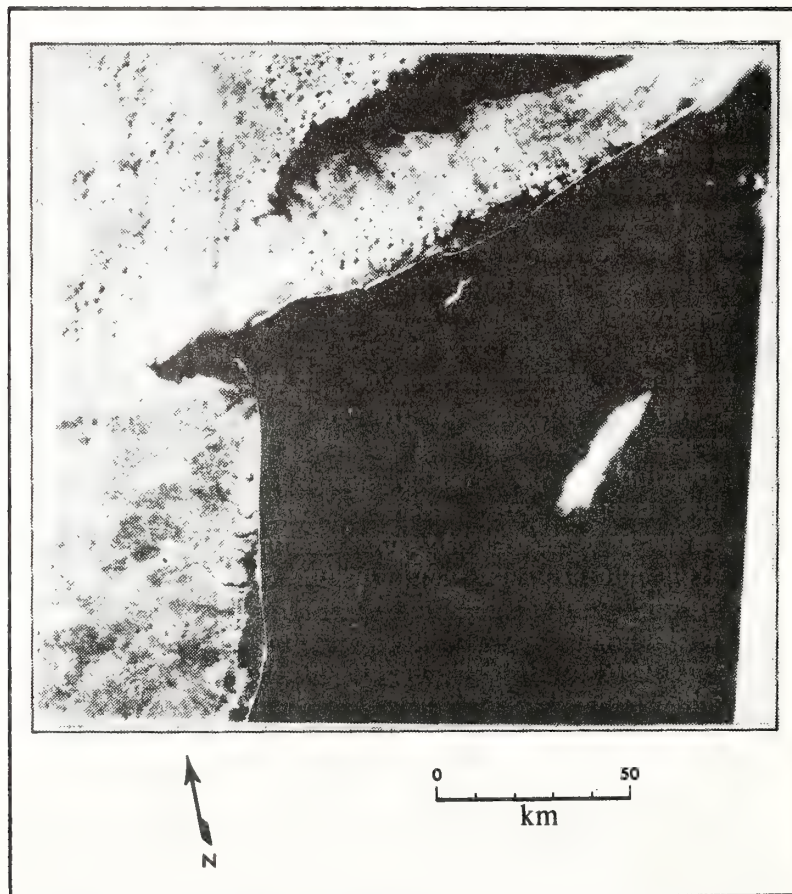


Fig. 2 Bulk processed imagery in the 0.6 to 0.7 μm band of ERTS-1 from the New York Bight transit of August 16, 1972.

plume suggests that dispersion processes are not isotropic.

There are features in the Bight apex about 20 mile southeast of the harbour entrance, seemingly manifestations of human activity in the area. A line and a more diffuse circular patch north of the line are seen in this frame. These features are located in the general area used for waste disposal¹.

The line resulted from the disposal of waste acid. Less distinct portions of the line may be the residue of an earlier dump, at least 12 h before; dispersion has evidently been slow. Even though wind mixing was low for that day it is apparent that dumping of this magnitude will usually produce a persistent surface feature. Subsequent ERTS images all show dump residues.

The diffuse circular patch to the north of the waste acid dump is close to the sewer sludge dump site. Surface vestige of a sewer sludge dump is much less noticeable than waste acid; only a grey-brown slick remains. Initial low intensity of reflected light makes the character of the surface patch less discernible.

It seems likely that satellites with sensors optimized to view the ocean in visible and infrared wavelengths, supplying synoptic data over large areas, will materially aid management of the coastal zone on a broad scale.

This research was sponsored in part by NASA. Imagery from Goddard Space Flight Center.

ROBERT L. CHARNELL
GEORGE A. MAUL

*National Oceanic and Atmospheric Administration,
Atlantic Oceanographic and Meteorological Laboratories,
Physical Oceanography Laboratory,
Miami, Florida*

Received November 27, 1972.

¹ *Effects of Waste Disposal in the New York Bight* (National Marine Fisheries Service, Sandy Hook, New Jersey, 1972).

Reprinted from the Final Report on the Effects of Waste Disposal in the New York Bight, for the Coastal Eng. Res. Ctr., U. S. Army Corps of Eng., by National Marine Fisheries Service, Sandy Hook Laboratory, February 1972, 6-1 thru 6-30, 1973

SURFACE AND BOTTOM WATER MOVEMENT
IN NEW YORK BIGHT

by

R. L. Charnell

D. V. Hansen

R. I. Wicklund

Prepared for Sandy Hook Sport Fisheries Marine Laboratory
National Marine Fisheries Service
Sandy Hook, Highland, New Jersey 07732

Prepared by National Oceanic & Atmospheric Administration
Atlantic Oceanographic & Meteorological Labs.
Miami, Florida 33130

February 15, 1972

TABLE OF CONTENTS

SECTION

6	Surface and Bottom Water Movement in New York Bight	.. 6-1
6.1	The Drifters	.. 6-3
6.2	Near-Bottom Transport	.. 6-5
6.2.1	Seabed Drifter Returns	.. 6-5
6.2.2	Direct Current Measurements	.. 6-12
6.2.3	Density Patterns	.. 6-15
6.3	Surface Drifter Returns	.. 6-18
6.4	Temporal Changes in Circulation	.. 6-20
6.5	Summary	.. 6-23

SECTION 6. SURFACE AND BOTTOM WATER MOVEMENT IN NEW YORK BIGHT.

For several years, the Sandy Hook Sport Fisheries Marine Laboratory has collected data on temperature and salinity between Cape Cod and southern Florida to learn how these features of the marine environment affect distribution of marine organisms. This long-range study is continuing. In 1968, the U. S. Army Corps of Engineers provided additional support to augment these observations in a part of the New York Bight extending from Jones Inlet, N. Y., to Monmouth Beach, N. J. These new observations were to provide details of the near-shore water circulation as it relates to movement and dispersal of sewage sludge and dredging spoils deposited in the area.

To meet these objectives a sampling grid of 23 stations was established in a part of the Bight (Figure 6-1). Periodically at these stations, measurements were made to determine values for temperature and salinity at depth intervals of four meters, and for dissolved oxygen near the bottom. See Table 1-1 for the calendar of these cruises and the appendix to this chapter for description of these instruments.

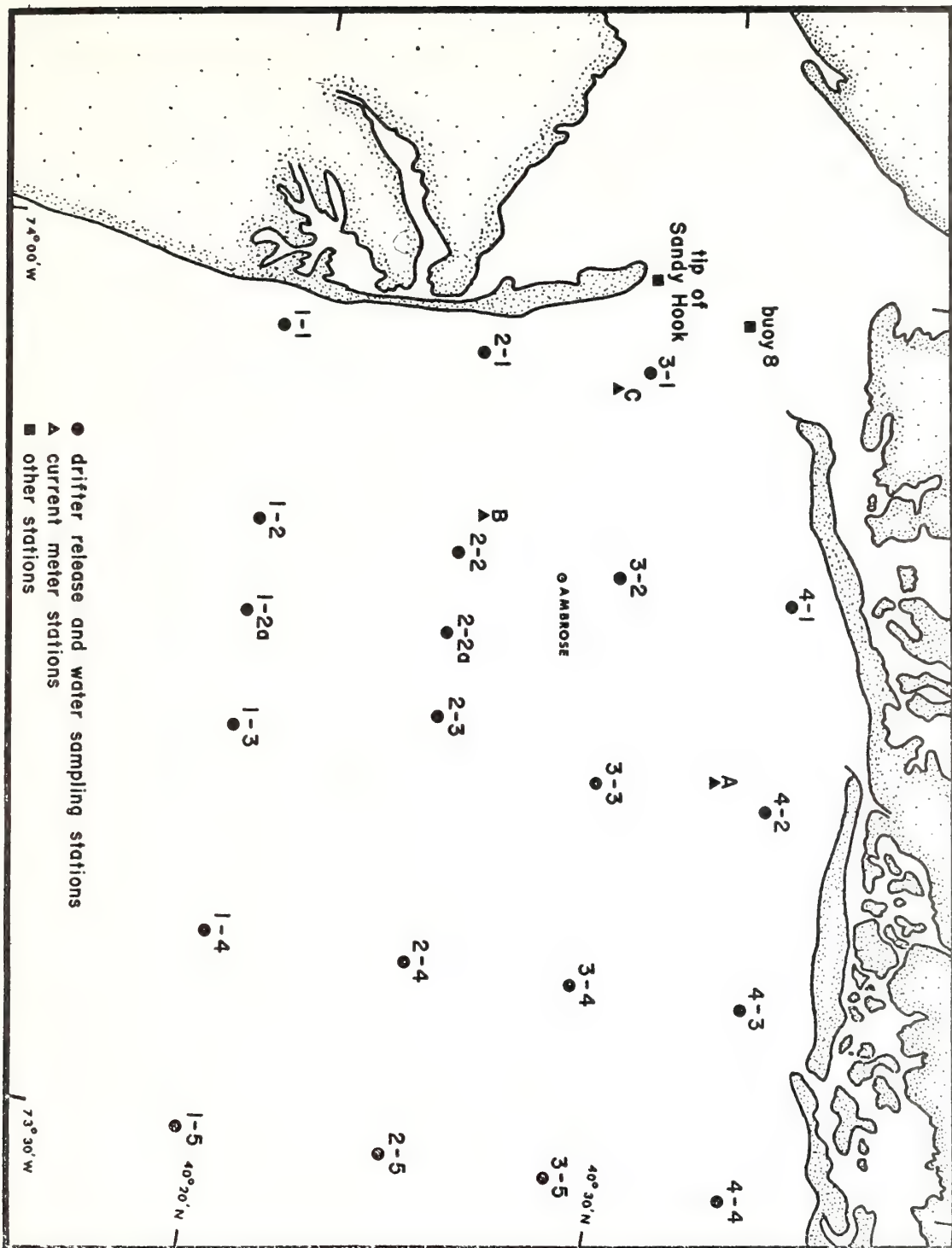


Figure 6-1. New York bight waste disposal study area.

In addition several attempts at direct measurement of currents and particulate transports were made. Current meters were placed at four fixed stations within the study area to measure current speed and direction near the bottom and at approximately 40 feet above the bottom. These observations were beset with problems, but yielded four usable records from three of the stations (See Figure 6-1 for current meter station location). Estimates of surface and bottom particulate transport were made with the use of seabed and surface drifters. These drifters were released at 21 of the fixed grid stations on each of the regular cruises.

Reaction of these drifters to water movement closely approximates that of other small movable objects at the surface and near the seabed. Their behavior thus provides the best estimate of the effect of water movement on the transport and dispersal of sewage sludge and dredging spoils. Consequently, discussion of circulation in this chapter is based primarily on the documented return of these drifters.

6.1 The Drifters

The heart of this study was the seabed drifter, whose movement provides a direct measure of the fate of

movable material deposited on the sea floor. Basically the drifter is a positively buoyant plastic saucer (diameter 18 cm) fastened to a small diameter stem 54 cm long. The free end of this stem is weighted so that the whole drifter has slight negative buoyancy. Surface drifters were small bottles, ballasted to float vertically and yet present a low above-surface profile to minimize unwanted wind effects. Details of construction and operation of these drifters can be found in Bumpus (1965), or Harrison et al. (1967).

A study of this sort relies on the public to return information on the time and location for each drifter found. Thus, positive results are obtained only when drifters move into areas accessible to the public. This may be an important consideration in an area like New York harbor where there are limited areas for drifters to wash up on a beach. Response to the drifter program has been high. Of the 1886 surface drifters released, 497 or about 26% were returned. Of the 2190 seabed drifters released in 1969, 710 or about 32% were recovered. These rates of return are exceptionally high for this type of investigation and are attributable to a combination of vigorous onshore transport mechanisms and

the intensity of traffic on the adjacent beaches. Results of our analysis reported here are based primarily on spatial and temporal patterns in return of those drifters released during 1969.

6.2 Near Bottom Transport

Several studies using seabed drifters have been made on the continental shelf in the middle Atlantic Bight area. The study by Bumpus (1965) indicates that nearshore, the tendency for flow is westerly or southerly with a component toward the coast; but the onshore-offshore component is difficult to distinguish from more or less isotropic dispersion because only those drifters carried onshore yield any information. His study, like that of Harrison et al. (1967), indicates that there is definite residual bottom drift toward the mouths of estuaries. Such inflow to the estuary mouth is expected as a normal consequence of estuarine circulation driven by fresh water outflow and has been observed in a wide variety of situations (Conomos et al., 1970, Gross et al., 1969).

6.2.1. Seabed Drifter Returns

Data from the present study tend to show the same pattern as described by Bumpus. However,

local and seasonal effects obscure much of the circulation detail. Long range trends are more easily seen if the returns are presented in relation to their point of origin. For example, Figure 6-2 presents the percentage returns of drifters released from each station for the entire year. Values for the individual stations are contoured to provide a visual impression of the pattern of returns. As might be anticipated from simple dispersion considerations, areas closer to land have a higher percentage return. A significant feature of these data is that minimum percentage return occurs along the axis of the Hudson-Ambrose Channels rather than from the farthest station from shore. This might imply that drifters placed in this area are moved rapidly seaward and are lost or that this area is a 'dead area' of little motion. Neither of these views is consistent with the observation of Bumpus or the principles of estuarine circulation.

It appears to us more likely that drifters from this region are preferentially drawn into the New York-Hudson River estuarine system. Stewart (1958) showed that upstream flow of bottom water occurs in at least the lower 50 miles of the Hudson River estuary. This

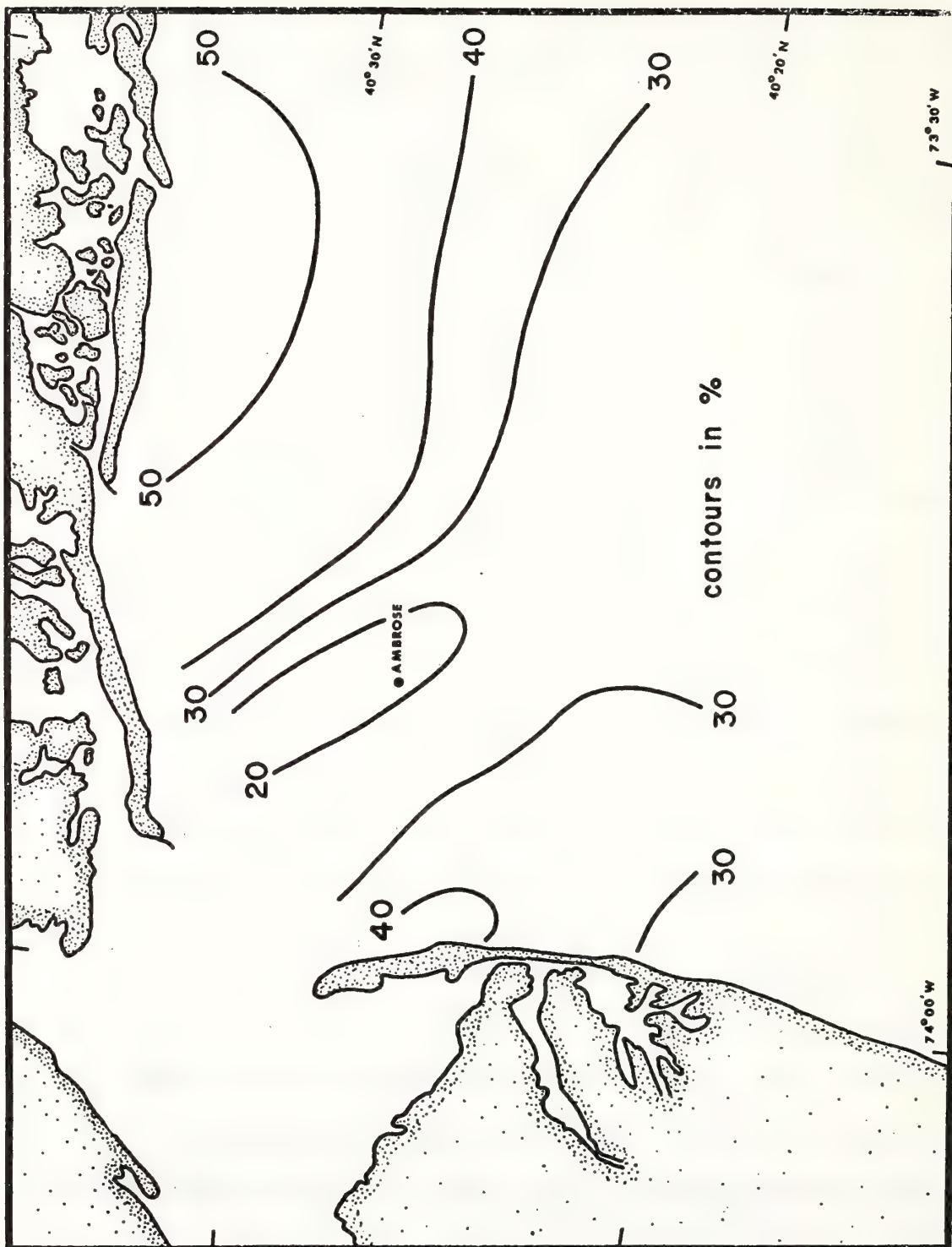


Figure 6—2. Seabed drifter returns.

phenomenon probably will have a seaward continuation.

Examination of a chart of the Upper Bay and Hudson River north of the Narrows reveals few areas that are suitable for beaching of these drifters. In time they will become covered with marine growth and will deteriorate, as well as become less buoyant as they are carried into less saline water. It is quite probable that the low return rate near Ambrose reflects upchannel migration and subsequent loss to the investigation rather than a seaward flushing of the drifters.

This view is also consistent with the fact that there are higher return rates from stations further out to sea. A drifter moving along the bottom is subjected to two processes; advection and dispersion. Advection may correspond to the main return flow into the estuary while dispersion is induced by tidal oscillation. Thus drifters further from the harbor entrance are more likely to be spread out and be beached before going through the bay mouth.

The hypothesized flow into the estuary may be tested by looking at the origin of all those drifters that were found somewhere within the New York harbor system. A total of 81 drifters or 3.7% of all those released were

Figure 6—3.

Origin of seabed drifters recovered in Hudson estuary expressed and contoured as percentage of all returns from individual stations.

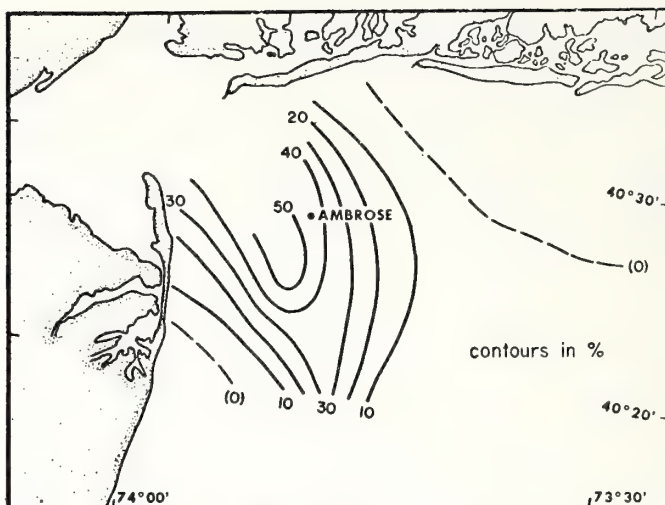


Figure 6—4.

Origin of seabed drifters recovered on Long Island.

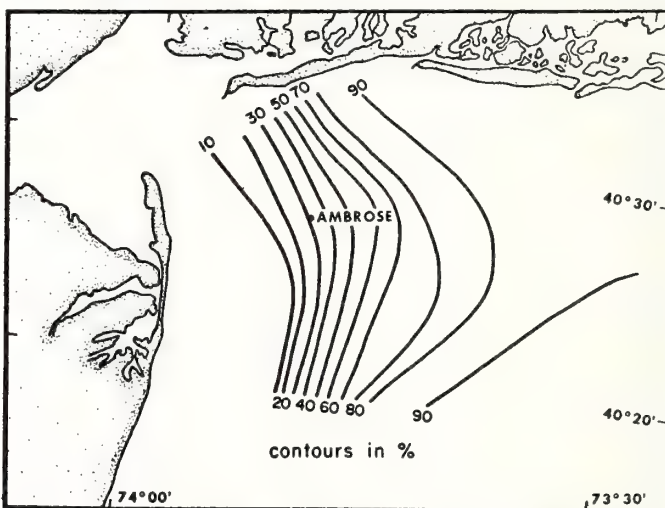
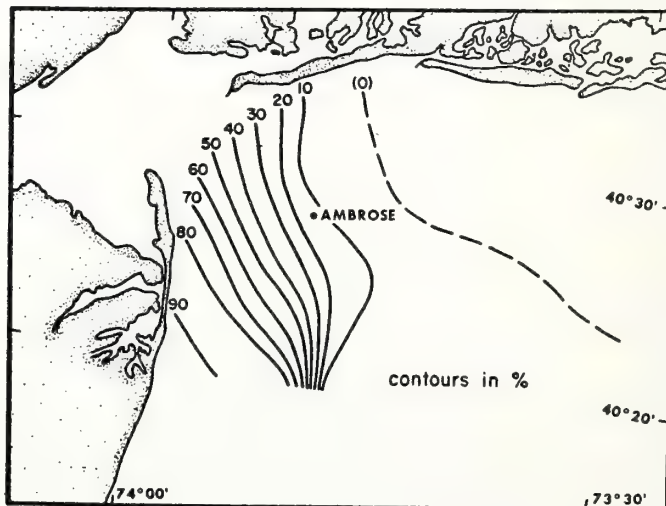


Figure 6—5.

Origin of seabed drifters recovered on New Jersey coast.



found within the bay. Greater sensitivity to origin is obtained by relating bay recoveries to total returns from a station rather than to total releases. Figure 6-3 presents these data. For these conditions, highest relative rate of return corresponds to the area with the lowest overall rate of return. In this case, however, the area closer to the mouth has higher estuary return than those stations further out. The axis of maximum relative return corresponds in a general sense to the Hudson-Ambrose Channel.

Drifters were found predominantly in two other areas; 477 drifters were recovered along the south coast of Long Island, while 127 drifters beached along the eastern coast of the mainland from Sandy Hook to Cape May. The remaining 35 drifters were found at miscellaneous locations not germane to the study area and have not been included in our analysis. For comparison to estuary returns, origin data for drifters recovered in these two areas are presented in Figures 6-4 and 6-5, respectively. For the mainland recoveries (Figure 6-5) return is clearly dependent upon distance from shore. Orientation of contours generally follows the proposed axis of bottom flow into the estuary. A significant feature of this distribution is that almost no drifters released in

the northeast section of the grid moved southwest onto the New Jersey coast.

Returns of drifters beached on Long Island also show a dependence of drifter release on distance from shore (Figure 6-4). Drifters appear to be carried ashore here more efficiently from a large part of the sampling grid. Contours for these data also are generally parallel to the proposed axis of bottom flow into the estuary in the western portion of the sampling grid. Returns are high from the south central portion of the grid and from the northeast section of the grid. The general impression conveyed by this year of bottom drifter data is of a general clockwise circulation in the bight, upon which is superimposed an estuarine circulation into the estuary and dispersion by tidal currents. This is probably not a contradiction of the circulation suggested by Bumpus (1965) because the present study is confined to an area closer to shore than that used by Bumpus.

Examination of bathymetry for this area shows that the Hudson channel greatly widens as it nears the Ambrose light. There are indications that the upstream channel bifurcates with a branch oriented to the northeast. This split in the channel may provide a mechanism for producing eastward flow along Long Island as a consequence of bottom water movement up the Hudson Channel.

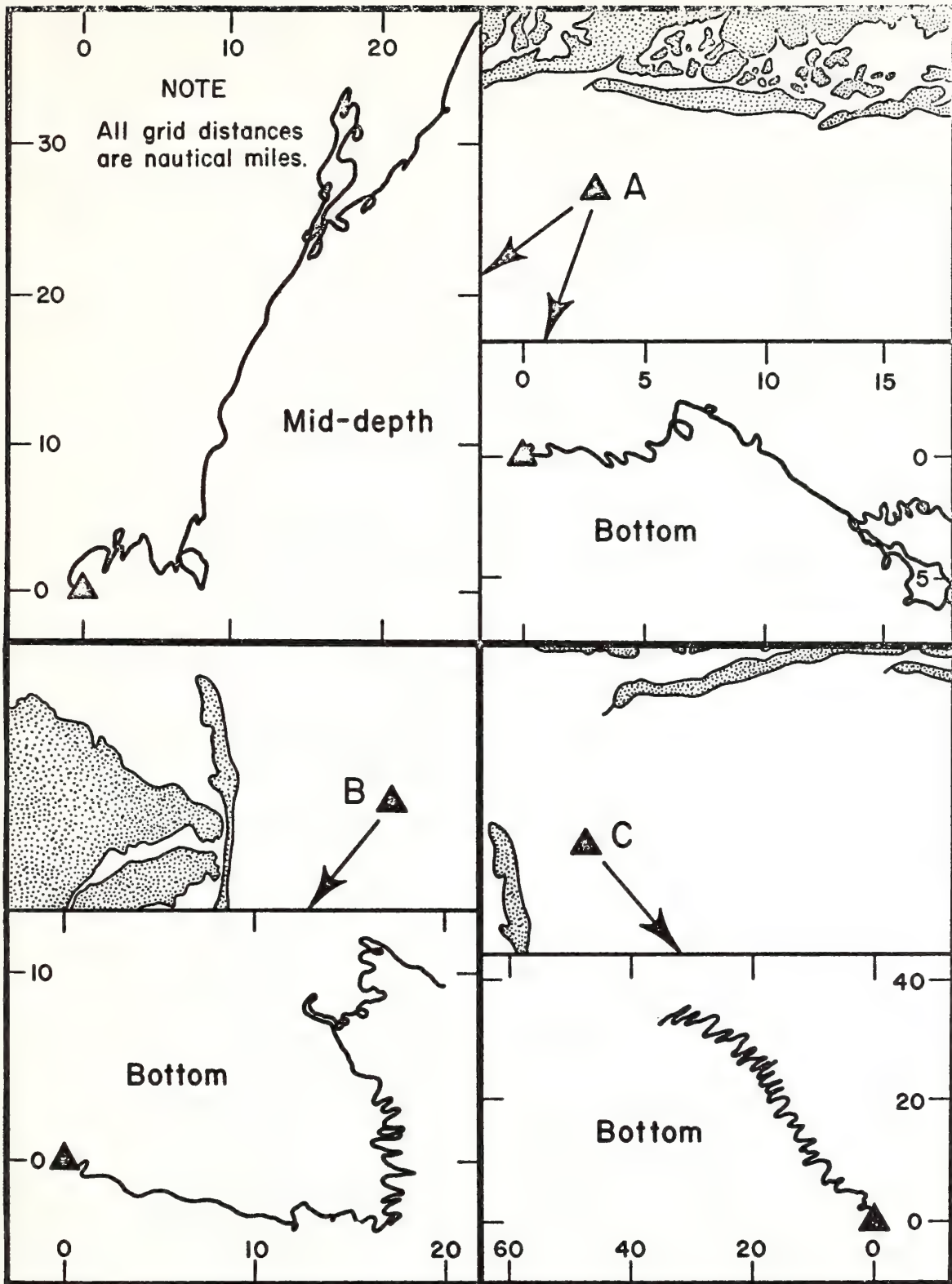


Figure 6-6. Progressive vector representation of current meter data.

6.2.2 Direct Current Measurements

Evidence for the bottom circulation pattern also includes the direct current measurements made during the study. While the records are few, non-synoptic, and for only short periods, they do provide evidence for bottom water movement similar to that inferred from bottom drifter returns.

All current meters set out for this study rapidly developed marine growth that eventually interfered with their operation. For the four reliable records, at least two weeks of observations can be considered valid. These four records were taken at three stations: (1) bottom and mid-depth observation in late June, 3.5 miles south of Atlantic Beach (Station A); (2) bottom observations in late February at location 2.5 miles southwest of Ambrose (Station B); (3) bottom observations in late May-early June at location 3.5 miles east of Sandy Hook (Station C). Locations of these stations are indicated on Figure 6-1. A summary of these measurements is presented in Figure 6-6; for each station the progressive vector diagram is presented for the valid segment of each record.

The southernmost station, B, is not situated in an area that, on the basis of drifter data, is in the main zone of upchannel return flow. Wind during this period was predominantly from the west. The record for Station B in February shows flow generally eastward away from the coast for the first four days; subsequently, net drift was toward the north until the record becomes invalid. Average net drift for the entire period was 3.9 miles/day.

Station A is situated in an area which, based on seabed drifter analysis, should have bottom flow predominantly to the east. For this period local winds were variable but generally from the south. The current records show for both bottom and mid-depth that flow tended to follow bottom contours away from the estuary mouth in a generally eastward direction. After about one week net flow at mid-depth swung northeast toward the shore while net bottom drift shifted to southeast away from the shore. Average net drift was 3.3 miles/day at mid-depth and 1.9 miles/day at the bottom.

Station C was situated almost in the path of inferred bottom flow into the estuary mouth. Here, bottom water is inferred to flow northwest into the Bay. This is in

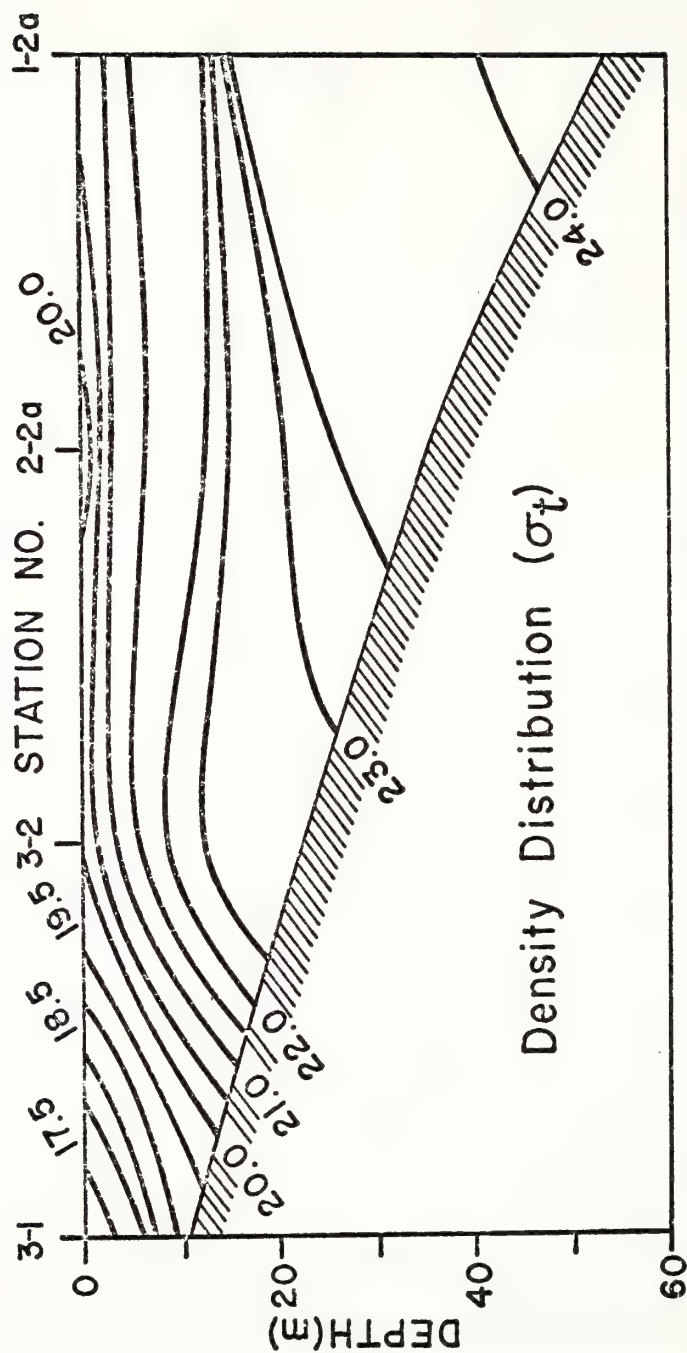


Figure 6—7. Density section along Hudson—Ambrose channel axis.

fact what the current record shows for late May and early June. There was substantial tidal oscillation but net drift followed a heading of about 320° True. Average net drift over the period was 4.2 miles/day.

6.2.3 Density Patterns

As further evidence, temperature and salinity values from this area are indicative of an estuarine circulation pattern. Data from the four stations most nearly aligned to the Ambrose-Hudson Channel can be used as a section along the most likely axis of flow. Bathymetry tends to confine flow along the axis, and tidal currents tend to conform to this axis. Even though the study area is an open ocean segment, there are bounds on the system that suggest estuarine behavior. Figure 6-7 presents a vertical section of density up this axis about the time current Station C was occupied. The data clearly suggest a pattern characteristically found in estuaries. The pitfalls of attempting to infer circulation from temperature and salinity distribution in estuaries and coastal areas are legion, but we have developed a semi-quantitative argument that landward flow near the bottom should occur preferentially in the Hudson Channel region of the Bight. A ubiquitous force for driving estuarine and coastal circulation is the horizontal

pressure gradient. The horizontal pressure gradient is expressible as

$$\frac{\partial P}{\partial \ell} = g \left[\rho S - \int_0^d \frac{\partial \rho}{\partial \ell} dz \right]$$

where

P is pressure

ℓ is horizontal direction

g is gravitational constant

ρ is density

S is surface slope

z is vertical direction

d is a particular depth of interest

In estuarine circulation a near-surface seaward flow is driven by the pressure gradient associated with surface slope. At greater depths the surface slope term is opposed by the vertically intergrated horizontal density gradient, $\partial \rho / \partial \ell$, typically reversing it to drive a counter flow at intermediate or great depths.

Figure 6-7 shows that horizontal density gradient is significant to the greatest depths found in the region. Hence, by virtue of the fact that the Ambrose and Hudson channels have more than twice the depth of adjacent regions, we expect that the estuarine circulation, well-documented within the estuary, must preferentially

occur also within the channelized portion of the New York Bight.

In a similar manner, the density distribution for the entire spring (March-June) suggests characteristic estuarine circulation: outflow at the surface accompanied by bottom return flow up the channel into the Bay.

6.3 Surface Drifter Returns

To add to the picture of Bight Circulation, the surface drifter data can be used to infer surface movement. There is somewhat more variability in these data due to wind effects. As might be expected, there was almost no evidence that surface drifters went upstream into the Bay; only one drifter was found in this area.

Data on the origin of recovered surface drifters are presented in Figure 6-8. It is evident that drifters released closest to Long Island south-shore had the greatest incidence of recovery ashore. For a clearer picture of drifter migration the data can be grouped by Long Island or New Jersey recovery as was done for the seabed drifters. Origin of release for the 406 drifters collected on the south shore of Long Island is shown in Figure 6-9. Again recoveries on Long Island are

Figure 6—8.

Surface drifter returns.

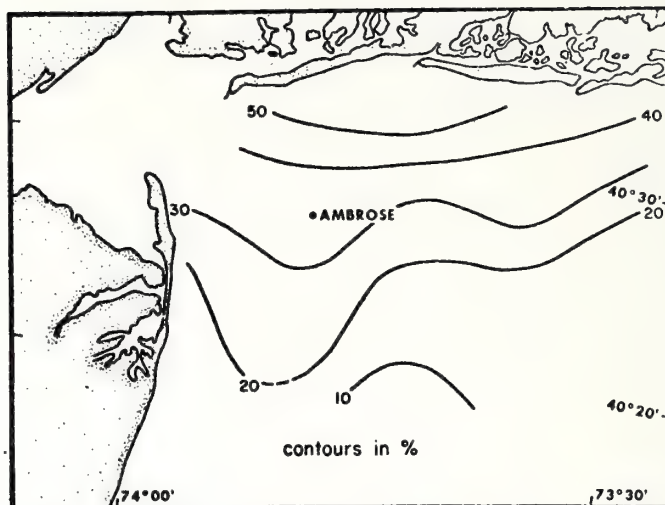


Figure 6—9.

Origin of surface drifters recovered on Long Island.

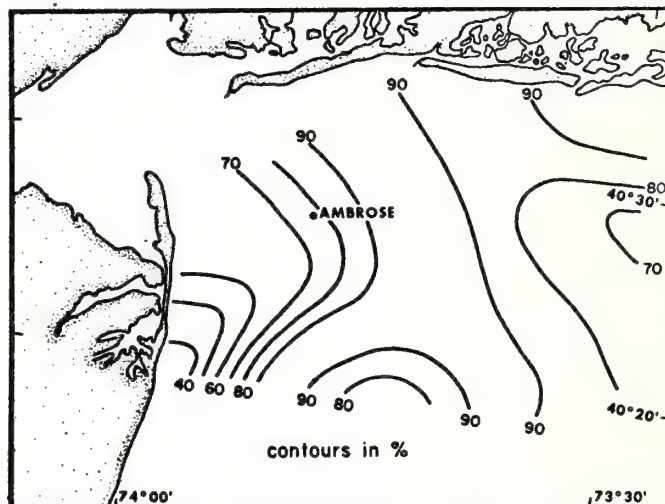
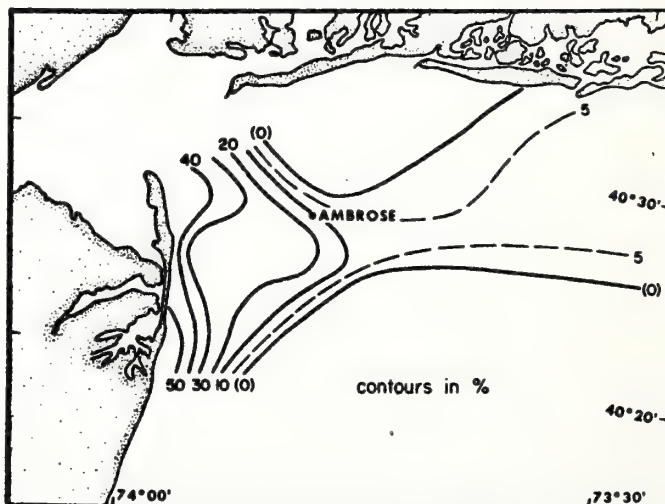


Figure 6—10.

Origin of surface drifters recovered on New Jersey coast.



related to total recoveries. Here there appears to be a ridge of high return to the north shore with areas of low return on either side. During most of the year winds from the south and west predominated. Winds from these points move the drifters to the north and tend to ground them on Long Island.

The area of low return to the west can be accounted for by the shift in recovery to the east coast mainland. Origin of release for these 37 recoveries is presented in Figure 6-10. The data show two features; overall low return to the mainland, and a very small area from which drifters are likely to beach on the mainland. These two figures clearly indicate, at least for 1969, that the predominant character of surface flow was a tendency for floating material to move in a northward direction. The 53 drifters not accounted for in these return areas were found in miscellaneous locations not germane to the study area and have not been included in our analysis.

6.4 Temporal Changes in Circulation

It would be desirable to examine the time dependent aspects of both surface and near bottom flow by interpreting data from the individual cruises. This type of analysis, however, would require release of substantially more drifters each month than were used for this study. Because of the stochastic nature of the processes controlling drifter movement, returns for too few releases

are not significant. Another problem is indicated by the low recovery rate of up-channel seabed drifter migrations. Ordinarily, at a given station, direction of drift is inferred from all returns for releases at one time; if a substantial number of drifters is not found (as is clearly the case for those that are carried offshore and is believed to be the case for those carried into the estuary) their direction is not represented and resultant flow estimates are in error.

One means of examining temporal aspects of the circulation is to follow the total rate of return from all stations as a function of time. These data are presented in Figure 6-11. The upper portion of the figure indicates return of surface drifters while the bottom portion indicates return of seabed drifters. It is apparent that there is considerably more seasonal effect at the surface than at the bottom. The peak in the surface returns corresponds in general to the maximum in Hudson River discharge. During this peak period the average wind direction swung from out of the west in February to generally from the south by June. During the winter (November-February) there were almost no recoveries of surface drifters, indicating a probable southeast transport of drifters. It is not likely that decreased beach traffic

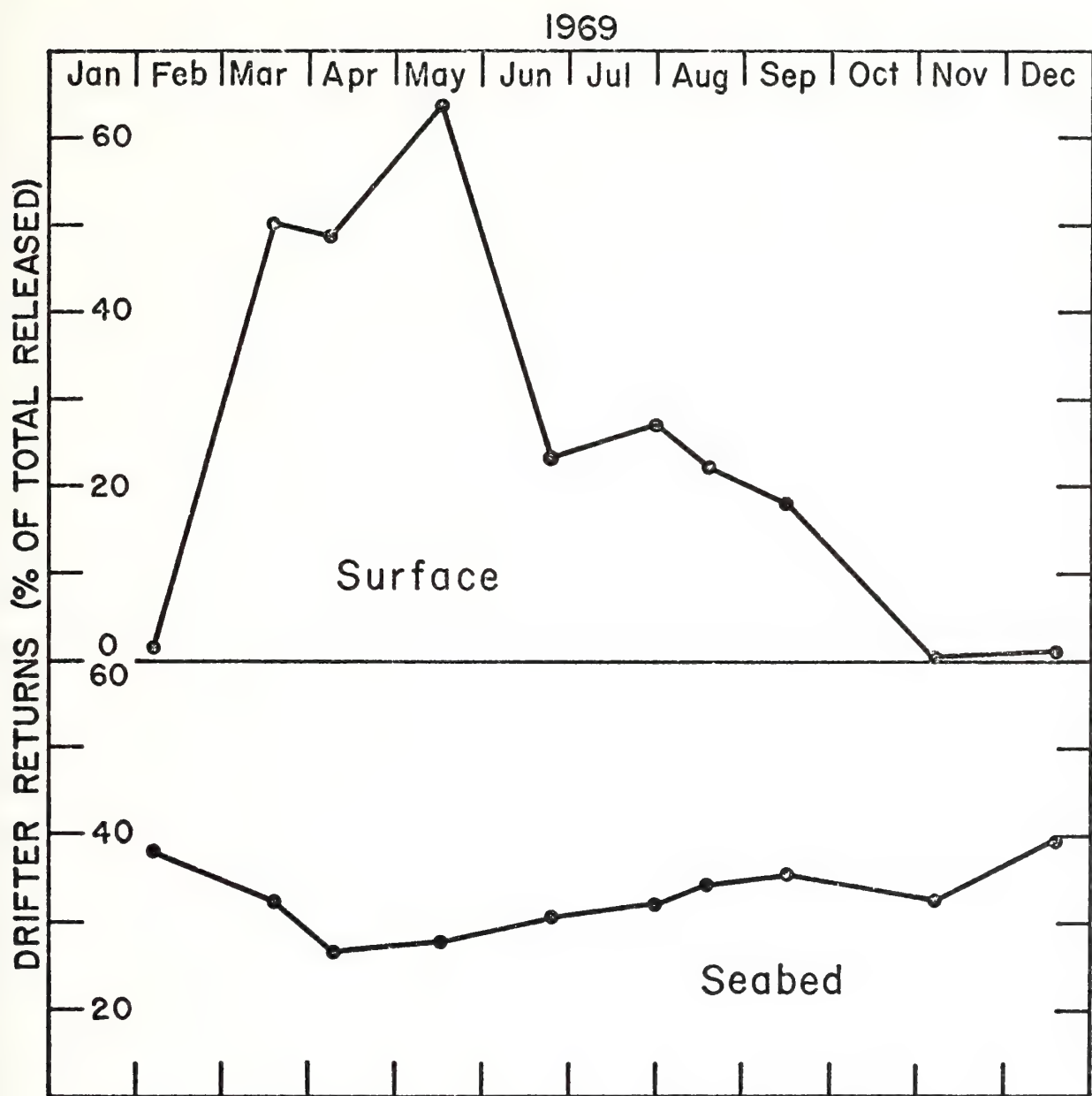


Figure 6-11. Time history of drifter returns.

in winter months accounts for diminished returns of surface drifters because return of bottom drifters has a slight maximum for this period. In general, however, return of seabed drifters showed only slight seasonality. There was slight decrease during the period of high surface return. This suggests that during the spring when outflow at the surface is strongest, more seabed drifters return up the Hudson and hence are lost. Actual estuary recoveries of the seabed drifters do show a slightly different picture; for just two months, August and September, recoveries were much higher than any other period with 17 and 20 returns respectively. This is nearly three times the recovery rate for the more nearly average months of April and May which had recoveries of five and eight drifters respectively.

6.5 Summary

This section presented results of an analysis of observations made in 1969 to provide details of the nearshore water circulation as it relates to movement and dispersal of sewage sludge and dredging spoils deposited in the New York Bight. The analysis was based primarily on return from over 4000 surface and seabed drifters released during the year and direct current measurements

made at three locations within the Bight. The data tend to support four major conclusions.

- 1) There is substantial shoreward migration of drifters deposited at the surface or on the bottom. Over 29% of all drifters released found their way to shore.
- 2) The data suggest a strong flow at the bottom along the axis of the Hudson-Ambrose Channel into the mouth of the Hudson estuary. Few drifters were recovered in the bay; low return may be due to public inaccessibility, reduced drifter buoyancy or other forms of drifter trapping.
- 3) There is some indication of a general clockwise circulation in the Bight which may be associated with a bifurcation in the head of the Hudson channel.
- 4) While surface drift patterns suggest strong seasonality, there is only mild seasonal variation in the bottom returns. During winter, surface flow seems to be predominantly southeast out of the study area. At other times flow tended northward onto Long Island.

REFERENCES

- Bumpus. D. F., 1965, Residual drift along the bottom on the Continental Shelf in the middle Atlantic Bight area. *Limnology & Oceanography*. Vol. 10, Supplement, p. R50-R53.
- Conomos, T. J., D. H. Peterson, P. R. Carlson, and D. S. McCulloch, 1970, Movement of seabed drifters in the San Francisco Bay estuary and the adjacent Pacific Ocean. *Geological Survey Circular* 637-B, p. B-1-B8.
- Gross, M. G., B. A. Morse, and C. A. Barnes, 1969, Movement of near-bottom waters on the Continental Shelf off the north-western United States. *Journal of Geophysical Research*, Vol. 74, No. 28, p. 7044-7047.
- Harrison, W., J. J. Norcross, N. A. Pore, E. M. Stanley, 1967, Circulation of shelf waters off the Chesapeake Bight; surface and bottom drift of Continental shelf waters between Cape Henlopen, Delaware, and Cape Hatteras, North Carolina June 1963 - December 1964, ESSA Professional Paper No. 3, p. 1-81.
- Stewart, H. B., Jr., 1958, Upstream bottom currents in New York Harbor, *Science*, Vol. 127, No. 3306, p. 1113-1115.

APPENDIX

Instrumentation

Temperature

- 1) Bucket Temperature - The mercury thermometers used for measuring bucket temperature had a precision of 0.05°C and were calibrated to an accuracy of $\pm 0.1^{\circ}\text{C}$. The temperatures obtained from bucket samples were used to check the validity of those taken with the RS-5-3 using the surface readings as a reference. Salinity was also measured in the bucket samples to verify the salinity readings of the RS-5-3 and the CM² salinometer.
- 2) Electrical Resistance Thermistor - The electrical resistance thermistor is incorporated in the sensing probe of a Beckman RS-5-3. This instrument gives temperature readings of 0.01°C and is accurate to $\pm 0.1^{\circ}\text{C}$. The RS-5-3 was calibrated in the laboratory and found accurate within these limits, which were specified by the manufacturer. Its accuracy was rechecked at each sampling location by comparing surface readings with a mercury thermometer and bottom readings with a reversing thermometer attached to a Nansen bottle.

- 3) Temperature Recorders - We placed Geodyne Temperature Recorders (Model A-119-4) along with the current meters referred to below at fixed locations. These instruments recorded temperature to an accuracy of $\pm 0.25^{\circ}\text{C}$.

Currents

- 1) Currents were estimated in the study area by using surface drift bottles (Bumpus, 1951), seabed drifters (Woodhead and Lee, 1960), and permanently fixed recording current meters (Jones, 1968).
- 2) Surface drift bottle and seabed drifter data were sent directly to the Woods Hole Oceanographic Institution where they were processed and entered into the computer program directed by Dean Bumpus. The results were returned to the Sandy Hook Sport Fisheries Marine Laboratory monthly.
- 3) Model A-100 Woods Hole current meters were installed at fixed stations for current measurements. Current velocity and direction were recorded every half hour for various time periods.
- 4) Current meters were pretested and calibrated in the laboratory following directions of the manufacturer.

Salinity

- 1) Salinity was measured with a Beckman RS-5-3 salinometer, and a CM² salinometer. The RS-5-3 is a portable, battery operated, inductively coupled instrument, giving a direct reading of salinity in parts per thousand. The accuracy of the instrument is rated at $\pm 0.3\%$ for salinities in the 0-400/00 range over a temperature range of 0-27°C.
- 2) Accuracy of the RS-5-3 and the CM² was checked by taking surface samples at each station with a bucket and bottom samples with a Nansen bottle and determining the salinity of each titration, using the Harvey Method. Field calibration was maintained by using a fifty-ohm calibration loop.

Dissolved Oxygen

- 1) The Alsterberg Modification of the Winkler Method was used to determine the dissolved oxygen (ppm) in sea water collected near the bottom with a Nansen bottle.

LIST OF FIGURES

- 6-1 New York Bight Waste Disposal Study Area.
- 6-2 Seabed Drifter Returns.
- 6-3 Origin of Seabed Drifters Recovered in Hudson Estuary expressed and contoured as percentage of all returns from individual stations.
- 6-4 Origin of Seabed Drifters Recovered on Long Island.
- 6-5 Origin of Seabed Drifters Recovered on New Jersey coast.
- 6-6 Progressive Vector Representation of Current Meter Data.
- 6-7 Density Section Along Hudson-Ambrose Channel Axis.
- 6-8 Surface Drifter Returns.
- 6-9 Origin of Surface Drifters Recovered on Long Island.
- 6-10 Origin of Surface Drifters Recovered on New Jersey Coast.
- 6-11 Time History of Drifter Returns.

INFRARED SENSING OF OCEAN SURFACE TEMPERATURE

George A. Maul*

Synoptic maps of ocean surface temperature are beneficial to marine transportation, fisheries operations, weather forecasting, and the marine science community. Data from infrared scanners on meteorological satellites such as NIMBUS and ITOS and analogous devices on aircraft are currently being used to generate experimental and operational products. Reviewed in brief are the theoretical background for this technology, instrumentation used, the direction of the research effort, and future work requirements.

INTRODUCTION

Remote sensing has provided oceanographers with a tool capable of acquiring quasi-synoptic global information on the near surface (< 100 meters) ocean environment. These data are forcing the marine science community to revise their views on circulation dynamics¹ which in turn affects the geology, biology, and chemistry of a water mass. Observations of the ocean are being made in several wavelength regions of the electromagnetic spectrum: visible, infrared, and microwave. Hanson² has made an excellent review of the field of passive remote sensing; the present discussion will be limited to the infrared sensing of surface temperature.

During the early 1960's experimental flights with airborne infrared thermometers were made notably by the U.S. Navy and the (now) National Marine Fisheries Service. These were low altitude (300 meter) flights designed to obtain surface temperature information over the Gulf Stream and along the coast, which led to operational programs. In 1964 the first

*Research Oceanographer, National Oceanic and Atmospheric Administration, Atlantic Oceanographic and Meteorological Laboratories, Miami, Florida.

NIMBUS experimental meteorological satellite was launched with an infrared scanner aboard; a synoptic view of terrestrial radiation was at last available. In 1970 the NOAA series of ITOS was started and operational vehicles were orbiting with scanning radiometers.

A schematic of a single channel scanner such as used on NIMBUS I, II, and III is shown at the top of Fig. 1³. A scan mirror is inclined 45° to the axis of rotation which is coincident with the spacecraft velocity vector. The mirror rotates at a rate (44.7 rpm for NIMBUS) such that contiguous scans on the earth's surface are obtained for the field of view and spacecraft altitude; scan spots are approximately 8 kilometers at the nadir. A modified Cassegrainian telescope with a chopper at the focus provides the electro-optics

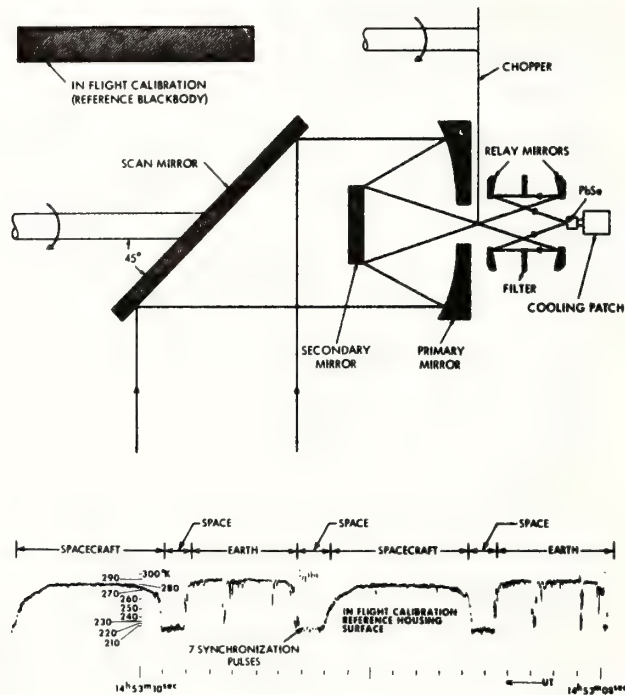


Fig. 1. Scanner optics (upper); analog scan trace of infrared radiometer (lower) from NIMBUS I Data Catalog and Users Manual³

for a lead selenide photo conductive cell. An example of the system output is given at the bottom of Fig. 1. Inflight calibration is accomplished by monitoring the output of thermistors in the reference blackbody with the space portion of the scan serving as a zero reference point. The radiometer output voltage is converted to FM signals for taping on-board and finally telemetering to ground stations.

INFRARED THEORY

Planck, at the turn of the century, formulated the basic law of blackbody radiation from quantum theory. The energy L emitted by a blackbody is related to the absolute temperature T and wavelength λ by

$$L(\lambda, T) = \frac{2c^2h}{\lambda^5 [\exp(hc/\lambda kT) - 1]}$$

where c is the speed of light in a vacuum, h is Planck's constant, and k is Boltzmann's constant. Considering the earth as a blackbody with a temperature of $290^\circ K$, the wavelength of maximum emission is at $10 \mu m$ and has an energy density of $840 \mu W cm^{-2} ster^{-1} \mu m^{-1}$.

True blackbodies do not exist in nature. However, many objects such as water which are opaque in infrared ($3 - 15 \mu m$), behave like graybodies. That is, they obey Kirchhoff's law in the form

$$\rho(\lambda, \theta') + \epsilon(\lambda, \theta') = 1$$

where ρ is the specular reflectivity (given by Fresnel's equation for a flat surface) and ϵ the specular emissivity (defined as the ratio of the emittance of a body to that of a blackbody at the same temperature and wavelength). Emissivity has angular (θ) dependence (see Fig. 2 for geometry).

Several emissivities from Bramson et al.⁴ are summarized below:

λ (μm)	$\theta' = 90^\circ$	$\theta = 40^\circ$
10.5	$\epsilon = 0.9916$	$\epsilon = 0.9833$
3.8	$\epsilon = 0.9752$	$\epsilon = 0.9608$

These facts suggest that observations should be constrained to lower nadir angles (θ) and that longer wavelength observations are preferable. Reflected radiation makes the 3.8 μm window useful only at night whereas the 11 μm region can be used both day and night.

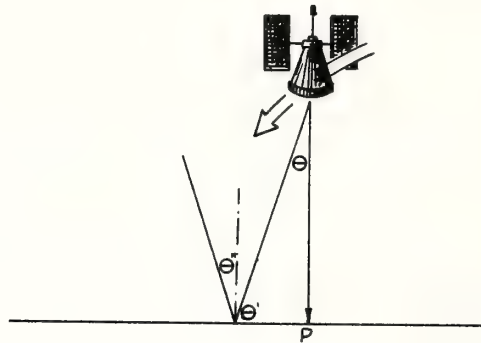


Fig. 2. Equation geometry: Nadir angle θ , emission angle θ' and reflectance angle θ'' .

Because water is essentially opaque in the infrared, the energy emitted comes from a thin surface layer less than 1 mm thick. Ewing and McAlister⁵ showed that this surface layer has a different temperature from that at 15 cm deeper in the water column. Saunders⁶ quantified this skin-bulk temperature difference (ΔT_w) using dimensional analysis and obtained

$$\Delta T_w = \frac{\Lambda q v}{\kappa \sqrt{\tau_w / \rho_w}}$$

where q is the sum of sensible, latent, and long wave radiative heat flux from the ocean, ν is the kinematic viscosity, K is the thermal conductivity of sea water, $\sqrt{\tau_w/\rho_w}$ is the kinematic stress, Λ is the constant of proportionality.

Hasse⁷ found that $-1.5^\circ\text{C} < \Delta T_w < 0.5^\circ\text{C}$ with typical values of -0.6°C being reported by other investigators. It is not clear from the literature if studies of emissivity took ΔT_w into account when the observations were made.

The radiation emitted by a blackbody $L(\lambda, T_s)$ at the ocean surface temperature T_s is attenuated by the atmosphere. Atmospheric transmissivity $\tau(\lambda, \theta)$ depends on the amount and temperature T_a of absorbing gases. Fig. 3⁸ gives absorption ($= 1 - \tau$) spectra for the principle absorbers and the solar

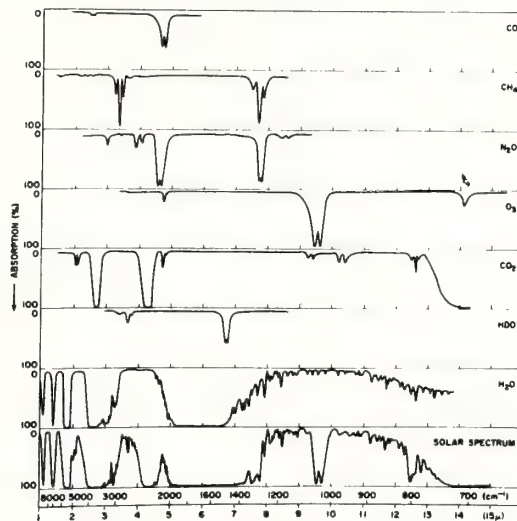


Fig. 3. Spectra of atmospheric gases and the solar spectrum (after Valley⁸).

spectrum through one atmosphere. Several "window" regions are apparent: $3.5\text{--}4.0\text{ }\mu\text{m}$, $8\text{--}9\text{ }\mu\text{m}$, and $10\text{--}12\text{ }\mu\text{m}$. Note that the maximum in the emission spectra for a 290°K blackbody and a minimum in reflectivity for water occur within the $10\text{--}12\text{ }\mu\text{m}$ transmissivity maximum. The NOAA series satellites use a filter with a bandpass response $10.5\text{ }\mu\text{m} < \lambda < 12.5\text{ }\mu\text{m}$

for sensing terrestrial radiation.

The integral form of the radiative transfer equation through a non-scattering atmosphere is

$$\begin{aligned}
 N(\theta) = & \int_0^{\infty} \phi(\lambda) \epsilon_s(\lambda, \theta') L(\lambda, T_s) \tau(\lambda, \theta) d\lambda \\
 & + \int_0^{\infty} \int_0^{P_s} \phi(\lambda) L(\lambda, T_a, P) \frac{\partial \tau(\lambda, P, \theta)}{\partial P} dP d\lambda \\
 & + \int_0^{\infty} \phi(\lambda) \rho_s(\lambda, \theta') N_{a,s}(\lambda, \theta'') \tau(\lambda, \theta) d\lambda
 \end{aligned}$$

where $N(\theta)$ is the radiance received at the satellite, P is atmospheric pressure, $N_{a,s}$ is the radiance of the atmosphere (a) at the surface (s) from the direction θ'' ; the other terms being defined as before. The first term on the right-hand side represents the emission of a graybody ϵL as attenuated by the transmission of the entire atmosphere τ , integrated over the spectral response ϕ of the instrumentation. The second term is the contribution to the radiance caused by the emission of the atmospheric absorbers (the result of another form of Kirchhoff's law); the integration in pressure coordinates is from the satellite to the surface P_s . The last term is analogous to the first for the reflected component of the sky radiance $N_{a,s}$. For a horizontally homogeneous atmosphere and in a direction away from the sun, $N_{a,s}$ is given by the interior integral of the second term with the limits reversed along the vector given by θ'' . The angles θ' and θ'' are effective angles which are functions of the earth's curvature and the slope of the wave surfaces.

Solutions to the equations are obtained by numerical techniques. Smith et al.⁹ report nadir viewing temperature departures (ΔT) of 1°-3°K for dry and moist atmospheres respectively using the 3.5-4.0 μm response of the early NIMBUS radiometers. Maul and Sidran¹⁰ report 2°-10°K departures for the 10.5-12.5 μm filter on NOAA-1 and 2 for similar atmospheres. Temperature departures increase very rapidly for

high nadir angle viewing ($> 45^\circ$) because the radiometer views proportionally more sky radiance.

AIRBORNE RADIATION THERMOMETRY

Airborne ocean surface temperature flights are usually made at altitudes of 300 meters. Low level flights are necessary in order to minimize the atmospheric correction. Fig. 4 shows a set of theoretical calculations based on solutions to the radiative transfer equation in which it is assumed that the ocean is a blackbody, i.e., $\epsilon = 1$. The calculations are for $8 \mu\text{m} < \lambda < 14 \mu\text{m}$, an altitude of 300 meters ($\Delta P = 36$ mbars), and assuming a standard atmosphere with a moist adiabatic lapse rate of -6.5°C per kilometer. Temperature departure ΔT is a function of both the amount of pre-

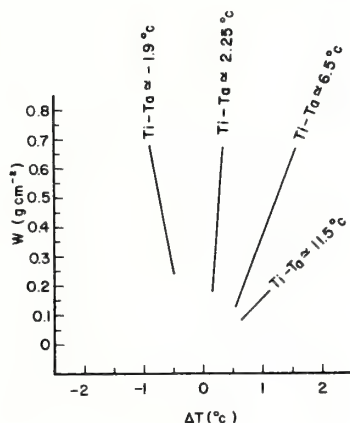


Fig. 4. Atmospheric effects for 300 meter altitudes on a 8-14 μm airborne radiation thermometer.

cipitable water vapor (w) in the air column below the instrument and the air temperature T_a measured at flight level; T_i is the equivalent blackbody temperature indicated by the instrument. Saunders¹¹ noted that over small temperature ranges the radiance can be approximated by a linear function of temperature. Carrying the linearization further by expanding the exponential dependence of τ and rearranging the

algebra, a correction equation for the data of Fig. 4 can be written

$$\Delta T = 0.015 m (T_i - T_a)$$

where m is the mixing ratio (g/kg) measured at flight level and 0.015 is the least squares fit to the calculations. The numerical coefficient could be rewritten $0.015 = 4.2 \times 10^{-4} \Delta P$ (where ΔP is the difference in pressure in millibars from the surface to flight level) if moderate departures from the 300 meter level are used. Thus if the aircraft monitors the ambient air temperature and mixing ratio, corrections for atmospheric effects can be made in real time.

McAlister¹² and McAlister and McLeish¹³ report on making heat flux measurements by using dual channel infrared radiometers. A radiometer measuring at $2.2 \mu m$ has an effective depth of $500 \mu m$; at $3.8 \mu m$ the effective depth is $75 \mu m$. If it is assumed that conduction is the dominant heat transfer process, then the equivalent blackbody temperature difference between the channels is linearly proportional to the heat flux. Aircraft measurements of this and surface temperatures have been made; surface temperature accuracies of the order of one tenth of a degree are reported.

SINGLE BAND SATELLITE DATA ANALYSIS TECHNIQUES

Some of the early work with the NIMBUS II is summarized by Warnecke et al.¹⁴. These investigations were oriented towards data display techniques, gridding and location, and to a lesser extent quantifying the results. Vukovich¹⁵ and McMillin¹⁶ devised filters to eliminate several noise sources in NIMBUS II data. LaViolette and Chabot¹⁷ proposed a method of eliminating cloud interference by compositing for a given grid point only the highest value observed in a given period. Since clouds are colder than the surface, the clear readings would be represented by high values. An example of this technique, called the High Daily Average (HDA), is given in

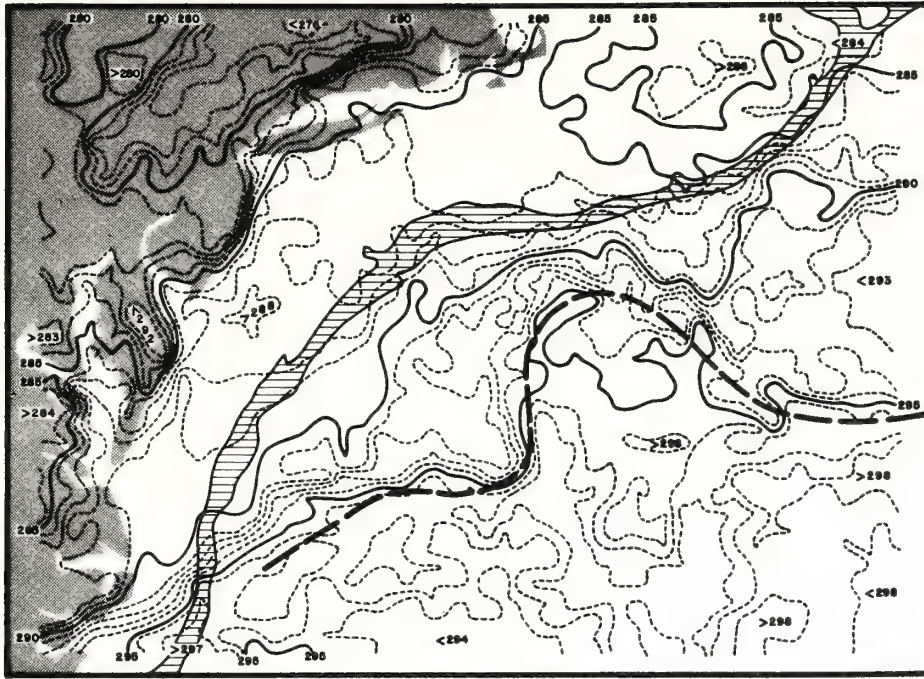


Fig. 5. Surface temperatures ($^{\circ}\text{K}$) from NIMBUS II using High Daily Average technique, off the east coast of U.S.A. for October 1966. Area of the continental slope is hatched.

Fig. 5. Fig. 5 is a HDA composite of seven days over the Gulf Stream in October 1966 from NIMBUS II nighttime data. The temperature values are uncorrected for atmospheric effects; the location of the Gulf Stream (heavy dashed line) is from Hansen¹⁸. Since this was the only successful application of this approach in six attempts, it is concluded that in general it is not widely applicable in mid-latitudes.

Smith et al.⁹ devised a statistical histogram method to discriminate against cloud contaminated data. If a frequency distribution (f) is Gaussian, the maximum slope occurs at ± 1 standard deviation from the mean. Subtracting the standard error of the radiometer from the value (v) at the maximum change ($d^2f/dv^2 = 0$) on the high side of the mean, theoretically recalculates the mean. When actual data are used, a bimodal distribution may be encountered if part of

the population are cloud observations. An example of typical histograms is given in Fig. 6⁹ for NIMBUS II where the standard error is reported as 1.5°K. This method requires

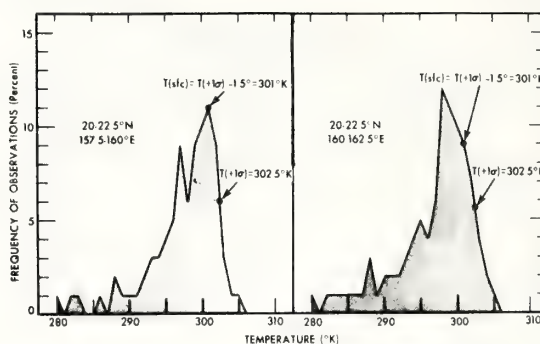


Fig. 6. Histograms of NIMBUS data (after Smith et al.⁹).

compositing the data in $1^\circ \times 1^\circ$ squares or larger, and while it is objective, the low spatial resolution (100×100 kilometers for $1^\circ \times 1^\circ$) makes it unattractive for certain applications. The authors report RMS differences of $1.7^\circ K$ between ship observations and their approach. A procedure being developed by Leese et al.¹⁹ at the National Environmental Satellite Service utilizes statistical principles such as described above to produce world coverage on a weekly basis.

MULTIBAND SATELLITE DATA ANALYSIS TECHNIQUES

The multiband techniques take advantage of the wavelength dependence of atmospheric transmissivity. A multispectral scanner is similar in principle to the scanner in Fig. 1, except that a beam splitter is required so that the same scan point is seen through several filters at the same time. The selection of the filters is a subject of current research.

Water vapor corrections can be made by using two channels

which are in two different regions of the water vapor absorption continuum. Then the only difference in the radiance in channels is due to the difference in the absorption coefficient (see again Fig. 3). Numerical solutions to these two equations in two unknowns are given in Fig. 7 from Anding and Kauth²⁰. The radiance in a band centered at $11.9 \mu\text{m}$ is

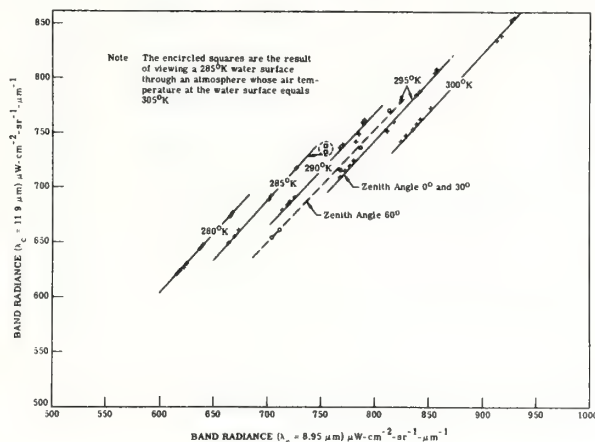


Fig. 7 Spectral radiance in two bands as a function of atmospheric state (after Anding and Kauth²⁰).

plotted against a band centered at $8.95 \mu\text{m}$. All the points for five model atmospheres and low nadir angles lie along one straight line for the same T_s . For larger nadir angles a new line is defined. The authors report standard errors of about 0.45°K with this two-band model using the known nadir angle for reasonable environmental conditions. Thus when a clear view of the ocean's surface is available, this work suggests that no other atmospheric corrections are needed.

Several other channels are required in this approach, notably a visible channel ($0.4\text{--}0.7 \mu\text{m}$) and one in the H_2O absorption region around $6.7 \mu\text{m}$. The visible channel can be used to detect tropospheric clouds because their reflectance is much higher than the ocean. The $6.7 \mu\text{m}$ region band is used to detect cirrus clouds at and above the tropopause. These ice crystal clouds are transparent to visible radiation but can

introduce 2-3°K errors if uncorrected for. Shenk and Salomonson²¹ used three channels from the NIMBUS II medium resolution radiometer (55 kilometer spot size at nadir) to make the first attempt at the multispectral approach with real data. Frequency distributions of temperatures from 6.4-6.9 μm channel and reflectances from the 0.2-4.0 μm channel were analyzed to obtain clear/not clear thresholds for the radiance in the 10-11 μm channel. Using "cloud free" scan spots, Shenk and Salomonson were able to get RMS comparisons with ship reports of 1.5°K, after correcting for atmospheric attenuation.

Very High Resolution Radiometers (VHRR) with two channels (0.5-0.7 μm and 10.5-12.5 μm) are operating aboard the NOAA-2 satellite. These instruments have spatial resolution at nadir viewing of less than 1 kilometer and are revealing many details in the ocean surface temperature structure. Fig. 8 is VHRR infrared imagery from 30 April 1973 showing the Loop Current in the Gulf of Mexico and the Gulf Stream up to the Carolinas. The warmer water of the current appears darker. The dual channel instrumentation allows tropospheric cloud discrimination and along with an infrared sounding device, estimates of the atmospheric variables needed to compute a correction. Maul and Sidran¹⁰ estimate accuracies of about 2°K from theoretical considerations of this system.

CONCLUSIONS

Ocean surface temperature mapping from space is a reality and may be an operational product on a low spatial resolution scale very soon. High resolution mapping is required for detailed studies in physical oceanography. Experiments on advanced test vehicles such as SKYLAB and NIMBUS G will add to our knowledge of optimum system designs, channel selection, and data processing.



Fig. 8. NOAA-2 VHRR infrared imagery of Gulf of Mexico.
Dashed line is location of Loop Current by ship.

REFERENCES

1. P. L. Richardson, A. E. Strong, and J. A. Knauss. J. Phys. Oceanogr., (in press), 1973.
2. K. J. Hanson. "Remote Sensing of the Troposphere," (V. E. Derr, ed.), U.S. Gov't. Printing Office, Washington, pp 22-1 to 22-56, 1972.
3. NIMBUS I HIGH RESOLUTION RADIATION DATA CATALOG AND USER'S MANUAL. N.A.S.A., Goddard Space Flight Center, Greenbelt, Maryland, 1965.
4. M. A. Bramson, I. L. Zel'manovich, and G. I. Kuleshova. English Translation: F-319, N.A.S.A., Washington, April 1965, 41 pp, 1964.
5. G. Ewing and E. D. McAlister. Science, 131(3410), pp 1374-1376, 1960.

6. P. M. Saunders. J. Atmos. Sci., 24, pp 269-273, 1967.
7. L. Hasse. Tellus, 15, pp 363-366, 1963.
8. S. L. Valley, Editor. Handbook of Geophysics and Space Environments, A.F.C.R.L., U.S. Air Force, pp 10-3, 1965.
9. W. L. Smith, P. K. Rao, R. Koffler, and W. R. Curtis. Mon. Wea. Rev., 98(8), pp 604-611, 1970.
10. G. A. Maul and M. Sidran. J. Geophys. Res., 78(12), pp 1909-1916, 1973.
11. P. M. Saunders. J. Geophys. Res., 75(36), pp 7596-7601, 1970.
12. E. D. McAlister. Appl. Opt., 3(5), pp 609-612, 1964.
13. E. D. McAlister and W. L. McLeish. J. Geophys. Res., 74(13), pp 3408-3414, 1969.
14. G. Warnecke, L. J. Allison, L. M. McMillin, and K.-H. Szekiolda. J. Phys. Oceanogr., 1, pp 45-60, 1971.
15. F. M. Vukovich. Mon. Wea. Rev., 99(11), pp 807-811, 1971.
16. L. M. McMillin. N.A.S.A. CR 9 G45-32, 16 pp 1969.
17. P. E. LaViolette and P. L. Chabot. Deep-Sea Res., 15, pp 617-622, 1969.
18. D. V. Hansen. Deep-Sea Res., 17, pp 495-511, 1970.
19. J. Leese, W. Pichel, B. Goddard, and R. Brower. Proc. of Int'l. Symp. on Remote Sensing of Environ., Vol. 1, Univ. of Michigan, pp 625-646, 1971.
20. D. Anding and R. Kauth. Remote Sensing of Environ., 2, pp 170-172, 1972.
21. W. E. Shenk and V. V. Salomonson. J. Phys. Oceanogr., 2(2), pp 157-167, 1972.

REMOTE SENSING OF OCEAN CURRENTS USING ERTS IMAGERY

George A. Maul, *National Oceanic and Atmospheric Administration, Atlantic Oceanographic and Meteorological Laboratories, Miami, Florida*

ABSTRACT

Major ocean currents such as the Loop Current in the eastern Gulf of Mexico have surface manifestations which can be exploited for remote sensing. A time series to study certain aspects of the surface expression of this current was begun in August 1972. Surface chlorophyll-a concentrations, which contribute to the shift in color from blue to green in the open sea, were found to have high spatial variability; significantly lower concentrations were observed in the current. The cyclonic edge of the current is an accumulation zone which causes a peak in chlorophyll concentration. The dynamics also cause surface concentrations of algae, which have a high reflectance in the near infrared. Combining these observations gives rise to an "edge effect" which can show up as a bright lineation on multispectral imagery delimiting the current's boundary under certain environmental conditions. Frequently the sea-state in the current is higher than in surrounding water due to differential shear. When high seas introduce bubbles, white caps, and foam, the reflectance is dominated by scattering rather than absorption. This has been detected in ERTS imagery and used for current location.

INTRODUCTION

The major circulation feature of the Gulf of Mexico is the so-called Loop Current. This flow enters the basin as a well formed western-boundary current through the Yucatan Straits. It penetrates into the Gulf to a varying latitude before it exits through the Straits of Florida. Transporting vast amounts of heat, salt and momentum, the current significantly affects circulation on the shelf, local fisheries, marine transportation, and is thought to be associated with hurricane intensification.

The current boundary separates two water masses. Across the boundary there is a difference in temperature, salinity, color, velocity, and biomass. These surface manifestations can be used for remote sensing in our efforts to monitor the current's variability. However, surface temperature difference, one of the best indicators, is not usable in the subtropics due to summer insolation which makes the sea surface isothermal. Other surface features, such as ocean color and evidences of horizontal current shear, probably have less seasonal variability.

This paper is a preliminary report on a time series of observations across the surface boundary layer of the Loop Current, and its detection by remote sensing, using several aspects of the surface features. The research is designed to investigate the seasonal variability of the juxtaposed water masses, both temporally and spatially, and the detection by ERTS of their boundary.

FIELD EXPERIMENTS

The field work began in June 1972 with a ship/aircraft experiment designed to detect the color boundary of the Loop Current front south of Dry Tortugas. The NASA C-130 flew over the research vessel track which was oriented in the same azimuth as ERTS suborbital track. Seven altitudes were flown, at 100 mb decrements, over the ship. Aircraft data collection included RC-8 color and color IR photography as well as multispectral photography to simulate the ERTS MSS imagery, PRT-5 sea surface temperature profiles, Bendix 24 channel scanner data, and inflight recordings of atmospheric temperature, pressure and moisture.

Prior to the aircraft overflights the scientific crew aboard R/V BELLOWS located the boundary. Measurements of

ocean temperature, chlorophyll-a, volume scattering function, and salinity were made every ten meters down to 50 meters; Forel color, and upwelling and downwelling spectral irradiance were taken at each of the five stations that bracketed the front. During the overflights on the following day, closely spaced surface measurements of the same variables (except irradiance) were taken. All measurements were made using standard oceanographic techniques or analyzed by methods detailed by Strickland and Parsons (1968).

In August 1972 a time series of the Loop Current by ship and satellite was begun. The cruise plan is to occupy the suborbital track of ERTS that crosses the west Florida shelf approximately 200 kilometers west of Tampa and terminates in the center of the Yucatan Straits. Every 36 days, the R/V VIRGINIA KEY is on the suborbital track. Continuous surface observations of radiometric temperature (in conjunction with the NOAA-2 IR sensors) and chlorophyll-a (by the fluorometric method of Lorenzen, 1966) are made; at approximately 12 kilometer intervals XBT's are taken, and samples are drawn for salinity, bulk temperature, volume scattering function, and biomass analysis. At appropriate daylight stations, measurements of upwelling and downwelling spectral radiance are made using a 1/4 meter Ebert scanning spectro-radiometer. A standard hydrographic section of the Yucatan Straits is made in order to estimate the geostrophic transport relative to 800 db. After the section, the cyclonic edge of the current is tracked by following the pathline of the 22° C isotherm at 100 meters; this pathline loops from the western edge of Yucatan to the Florida Straits south of Dry Tortugas and is in close proximity to the surface front. Finally another hydrographic section is observed along the sub-orbital track of ERTS that passes from Key West to Havana.

It is planned to continue the cruises to collect one year of data in order to obtain an evaluation of the seasonal variability. The final field experiment, planned for the autumn, is a SKYLAB/EREP mission involving a ship and an aircraft.

PRELIMINARY RESULTS

The cyclonic edge of the Loop Current tends to concentrate flotsam and jetsam. Natural materials, such as surface marine algae, were seen from the June photo-

graphy to have a pinkish cast on color IR (SO 397) film; this is confirmed in black and white IR photography (type 2424 film and a 89B Wratten Filter). When these algae are present, they appear as a bright lineation marking the edge of the current in ERTS MSS-6 (0.7-0.8 μ m).

A second consequence of the boundary layer dynamics is to concentrate chlorophyll bearing organisms. A typical profile across the current boundary is given in figure 1. This transect is from Key West harbor, out the channel into the coastal water, and across the front. The feature of interest is the peak in chlorophyll-a concentration just at the boundary. This is a phenomenon noticed in each of the six cruises to date and occurs to a varying degree in the deep sea as well as near shore. Details of the variability will have to await further sampling because of expected seasonal and biological dependence. One would expect however that a shift towards the green would occur and enhance the boundary in MSS-4(0.5-0.6 μ m). This does indeed happen as will be discussed below.

A third observation is the usual change in sea state across the boundary. When winds and associated waves cross into zones of high current velocity with an opposing set, the seas generally build up rapidly. It is not uncommon for the sea state to increase from 1 to 2 meters when crossing into the current. Thus an increase of white caps, foam, and bubbles is encountered near the edge which increases the reflectance in the current. This raises the reflectance in all channels, but in a non-uniform (wavelength dependent) manner.

The term "edge effect" (Maul, 1972) was coined to describe these phenomena which can be exploited to detect the boundary of major ocean currents. Other streaming events, such as sediments being entrained by the Gulf Stream after passing source regions such as Cape Hatteras (ERTS 1132-15092), can be considered part of this edge effect. It allows a multispectral approach to recognize the boundary of these currents in the absence of sea surface temperature changes.

To understand the physics of reflection from the ocean, consider a simple model of an ocean of semi-infinite depth (Z) with spherical scattering. The spectral reflectance $R(Z,-)$ is defined as the ratio of the

upwelling irradiance $H(Z,+)$, i.e. that from the ocean, to the downwelling irradiance $H(Z,-)$, i.e. that from the sky and sun:

$$R(Z,-) \equiv \frac{H(Z,+)}{H(Z,-)}$$

The reflectance is tacitly assumed to be a function of wavelength. From scattering theory the reflectance at the sea surface ($Z=0$) can be shown to be

$$R(0,-) = 1 - H(\mu) \sqrt{1 - \omega_0}$$

where ω_0 is the ratio of the scattering coefficient (b) to the attenuation coefficient (a), $H(\mu)$ is the so-called H-function for various scattering albedos (ω_0) as tabulated by Chandrasekhar (1960) and μ is the cosine of the zenith angle. It should be emphasized that this model does not include multiple scattering or the angular dependence of scattering such as the Monte Carlo calculations of Gordon and Brown (1973). Nevertheless it provides an analytic solution to the radiative transfer equation which illustrates the fundamental variables in reflectance.

An example of calculated reflectance from a plane water surface with the sun in the zenith [$H(\mu_0)$] is given in figure 2. The curves are based on scattering and attenuation coefficients given by Jerlov (1968) for natural ocean water bodies; a and b are chosen to exemplify the behavior of reflectance. Curve 1 is the spectral reflectance for pure water. Curve 2 is generated by changing the attenuation coefficient due to an increased absorption coefficient ($a=a-b$) due to yellow substance. Note that the reflectance is lower and that the peak has shifted to a longer wavelength. Curve 3 is generated by increasing the scattering coefficient due to isotropic scatters whose b is twenty times the Rayleigh (molecular) scattering at 450 nm.; only the magnitude of the scattering increases, in a wavelength dependent manner, with the peak invariant. Curve 4 combines the effects of absorption and scattering. The reflectance is lower than pure scattering and the wavelength of the peak is shifted to the green.

Curves 1 and 4 can be likened to the change in reflectance encountered when crossing an ocean front. An example of an observed reflectance pair is taken from

the June aircraft experiment and given in figure 3. These are uncorrected for the immersion effect and the reflectances are approximately 20% too high. The zenith angle was $\sim 20^\circ$ in each case. $H(Z,+)$ was measured 1 meter below the surface. The Loop Current water (marked 2) is lower in chlorophyll-a ($< 0.1 \text{ mg m}^{-3}$) and lower in volume scattering coefficient ($\beta(45)=2.6 \times 10^{-3} \text{ m}^{-1}$) than the coastal water (marked 4) with 0.4 mg m^{-3} chlorophyll-a and $\beta(45)=5.4 \times 10^{-3} \text{ m}^{-1}$. If one assumes that the absorption coefficient is proportional to the chlorophyll-a concentration and the scattering coefficient is proportional to the volume scattering coefficient at 45° (Beardsley et al, 1970) then a qualitative confirmation of reflectance theory is given.

The curves further suggest that changes in ocean color will be reflected in MSS-4. Figures 4a and b are images from ERTS-1 taken over the eastern Gulf of Mexico during times of surface observations. Figure 4a is MSS-4 data showing the higher reflectance of water from Florida Bay pouring over the Keys and being entrained by the Gulf Stream. This image confirms the discussion in the previous paragraph.

Figure 4b is MSS-5 data taken north of the Yucatan Straits during a period of surface observations. The curving discontinuity in the water masses outlines the edge of the current. However, the blue waters of the current are brighter than the adjoining waters in contradiction to the results in figure 3. The explanation must come from figure 2, where we see the effect of increased scatterers. A marked increase in sea state was encountered in the current, which can account for a much higher scattering coefficient due to entrapped air.

An additional explanation of this is offered through consideration of sea state alone. Ross and Cardone (1972) observed that with 15 m s^{-1} winds, 10% of the surface of the sea is covered with white caps, and white caps reflect approximately 90%. If reflectance of the ocean is assumed to be 5% in the absence of white caps and 10% of the sea is covered with white caps, then reflectance is $R=5\%(.9) + 10\%(.9)=13.5\%$ or 270% higher than without white caps.

The spectrum of total upwelling irradiance from above the ocean $H_T(0,+) = [R(0,-) + R_s]H(0,-)$ where R_s is the

reflectance of the surface (both diffuse and direct). For the case $R_s = \text{constant}$ and a given $H(0, -)$, H_T depends on ω_0 . From figure 2 we estimate that the ratio of $R(0, -)$ at 450 nm to that at 525 nm for pure water is ~ 4.5 (curve 1). The same ratio with scatterers only in the water (curve 3) is 2.0. Quantitative confirmation with realistic scattering phase functions will have to be calculated using the Monte Carlo code. Theoretically, the signal of a differential radiometer (Arvesen, 1972) is subject to such variation in ω_0 . If it is fortuitous that ω_0 always varies in the ocean such that $R(0, -)_{525}$ is constant (Duntley, 1972), then a dual channel instrument will work in the absence of sea state changes.

The solar spectrum is fairly flat in the visible region ($H(0, -)_{450}/H(0, -)_{700} \sim 1.3$). Hence, higher sea states, which reflect high percentages of white light, proportionally add more long wavelength energy to the upwelling irradiance. In terms of a chromaticity diagram, this means that the purity changes but not the dominant wavelength. To correct for sea state a channel in a multispectral scanner near 1 μm appears useful. At this wavelength there is a maximum in the attenuation coefficient of pure water (i.e. $\omega_0 \rightarrow 0$), a maximum in atmospheric transmissivity, and the influence of chlorophyll seems low.

CONCLUSIONS

ERTS imagery has been successful in providing information on the ocean in both the nearshore and deep sea environment. As the result of an edge effect the cyclonic side of the Gulf Stream can reflect in several ERTS bands as a prominent feature paralleling the current's edge. It is found however that sea state is a significant variable that can dominate the reflectance and change the spectral signature of surface waters. The prospect is therefore raised that passive remote sensing using ERTS may be used to quantitatively estimate sea state and near surface winds in areas of homogeneous water masses. Further, the sea state problem must be considered a dominant variable in the determination of ocean color from aerospace sensors.

REFERENCES

- Arvesen, J. C. (1972). Fourth Annual Earth Resources Review, Vol. IV, NASA MSC-05937, pp. 104-1 to 104-2.
- Beardsley, G. F., H. Pak, K. Carder, and B. Lundgren (1970). Journal of Geophysical Research, 75 (15), pp. 2837-2845.
- Chandrasekhar, S. (1960). Radiative Transfer, Dover, New York, 393 pgs.
- Duntley, S. Q. (1972). Fourth Annual Earth Resources Review, Vol. IV, NASA MSC-05937, pp. 102-1 to 102-25.
- Gordon, H. R. and O. B. Brown (1973). Applied Optics. (in press).
- Jerlov, N. G. (1968). Optical Oceanography, Elsevier, New York, 194 pgs.
- Lorenzen, C. J. (1966). Deep Sea Research, 13, pp. 223-227.
- Maul, G. A., (1972). Interim Report on Remote Sensing of Ocean Currents from ERTS, NASA-CR-12907, National Technical Information Center, E72-10233.
- Ross, D. B. and V. Cardone (1972). Fourth Annual Earth Resources Review, Vol. IV, NASA MSC-05937, pp. 85-1 to 85-20.
- Strickland, J. D. H., and T. R. Parsons (1968). A Practical Handbook of Seawater Analysis. Fisheries Research Board of Canada, Ottawa, 311 pgs.

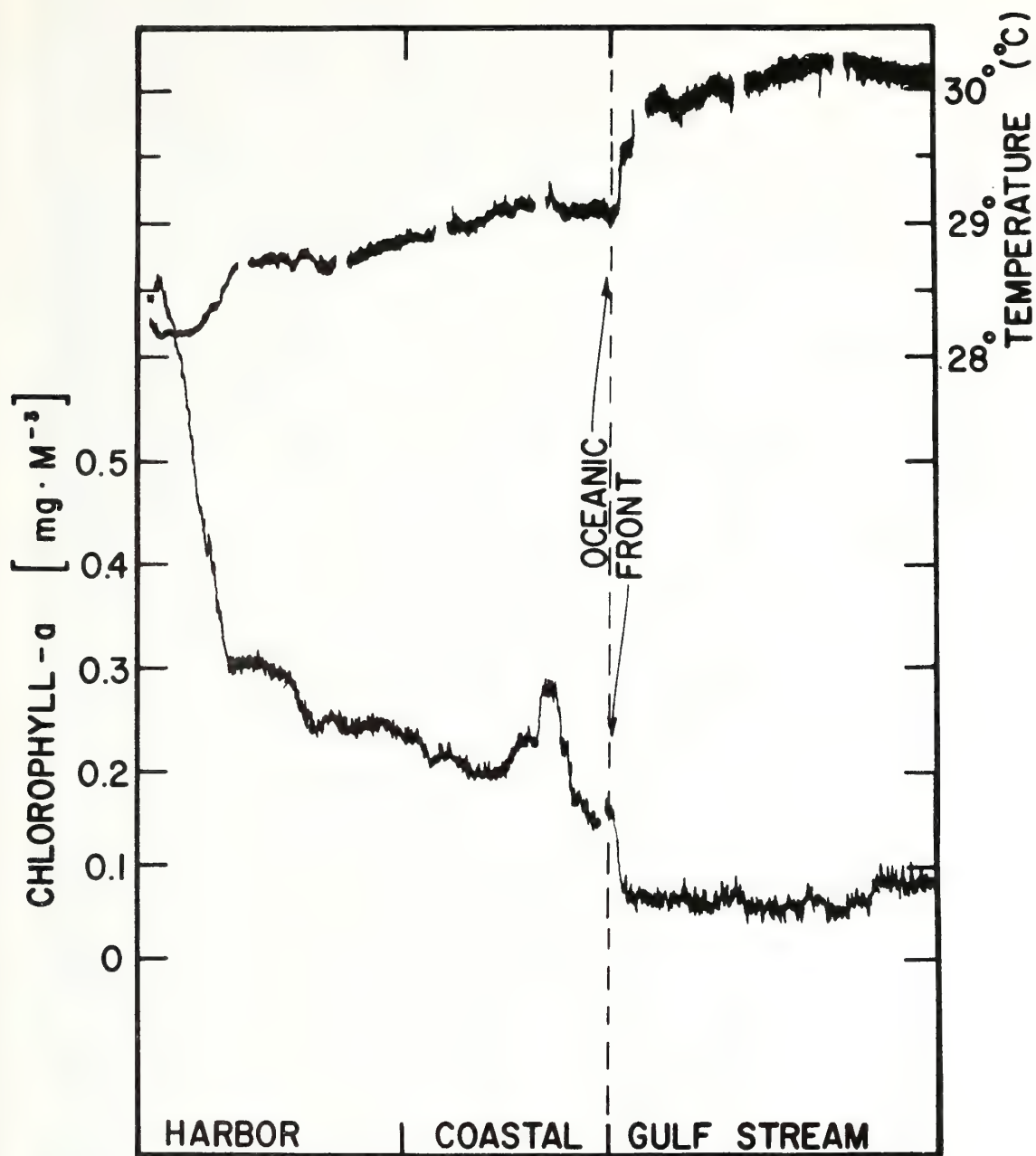


Figure 1: Surface temperature trace (upper) and surface chlorophyll-a profile (lower) across the Loop Current front and into Key West harbor. Horizontal scale across the figure is approximately 75 kilometers.

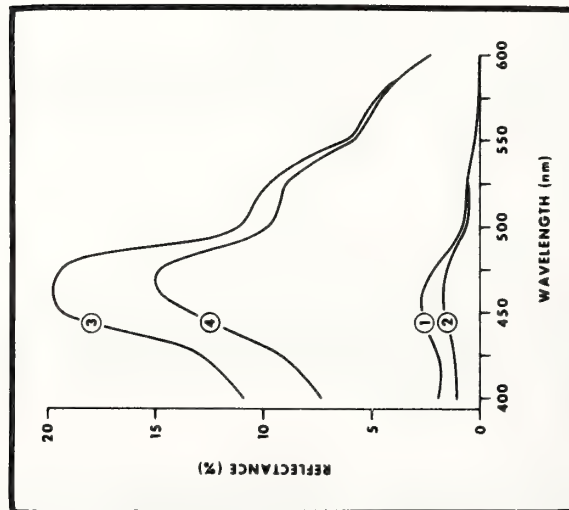


Figure 2: Results of theoretical calculations of reflectance from the water. 1 pure water, 2 pure water plus absorption due to yellow substance, 3 pure water plus isotropic scattering, 4 scattering plus absorption.

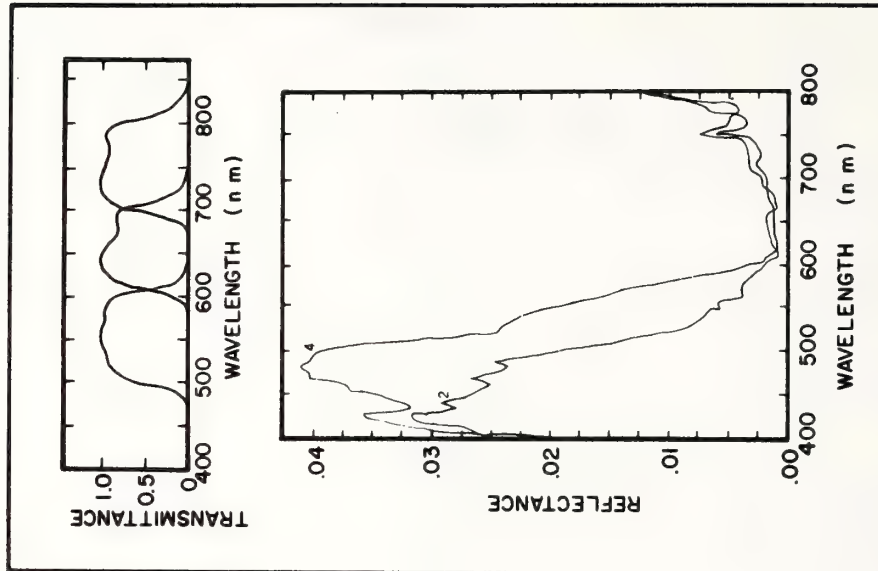


Figure 3: Observed reflectance across the Loop Current boundary. 2 current; 4 coastal water. Bottom depth exceeded 100 meters. Zenith angle about 15° in each case. The upwelling irradiance was measured at 1 meter depth. Upper panel has the spectral response of MSS 4, 5, and 6.



Figure 4a: MSS 4 imagery of the western Florida Keys showing water from Florida Bay being entrained by the Loop Current. The greener water from the bay appears brighter.

Figure 4b: MSS 5 imagery of the Loop Current exiting from the Yucatan Straits into the Gulf of Mexico. The blue water of the current appears brighter due to a higher sea state.

Atmospheric Effects on Ocean Surface Temperature Sensing from the NOAA Satellite Scanning Radiometer

GEORGE A. MAUL

*Physical Oceanography Laboratory, Atlantic Oceanographic and Meteorological Laboratories
National Oceanic and Atmospheric Administration, Miami, Florida 33149*

MIRIAM SIDRAN¹

*NSF Science Faculty Fellow, National Marine Fisheries Service
National Oceanic and Atmospheric Administration, Miami, Florida 33149*

Theoretical effects of atmospheric state, nadir angle, cloud amount, cloud height, and random noise on temperature data from the NOAA series satellites are investigated. These satellites have a dual-channel (visible and infrared) scanning radiometer. Temperature departures for nadir viewing range from 2.2°K for a dry winter atmosphere to 10.5°K under moist subtropical summer conditions. An 8°K temperature difference at the sea surface when viewed at zero nadir angle through the 30° N-July standard atmosphere registers less than 3°K at the satellite and is further compressed to 1°K when viewed at a 60° nadir angle. A 10% cloud cover can introduce errors that range from 0.5°K to 4°K depending on cumuloform cloud height; hence clouds must be completely eliminated in the analysis. Random noise in radiosonde data can introduce errors greater than 1°K for any given sounding; however, compositing and smoothing will eliminate most of this error source. A correction scheme for cloud-free conditions is developed that is essentially free of bias. A reasonable error estimate for the total system is of the order of 2°K.

The National Oceanic and Atmospheric Administration (NOAA) series of meteorological satellites will have two instruments aboard that can be used in collaboration to determine sea surface skin temperature (T_s) from space. A dual-channel scanning radiometer (SR) obtains simultaneous radiances in both the visible (0.5–0.7 μm) and infrared (10.5–12.5 μm) regions of the spectrum. The subpoint resolution of the SR is 4 km for the visible regions and 8 km for the infrared. The visible channel will provide geographically registered measurements of reflected radiation, useful for detection of all but cirroform clouds in the infrared channel. In addition, a vertical temperature profiling radiometer (VTPR) will obtain information on atmospheric state and hence is a necessary step in providing concurrent data for calculating T_s from the equivalent black-body temperature inferred by the SR.

Using data from the SR and the VTPR, a T_s analysis scheme is envisioned that corrects the cloud-free measurements for variations in atmospheric temperature and humidity profiles and then composites these daily values for 5 days or so to produce a map. In this context the effects of atmospheric state, nadir angle, cloud cover, cloud height, and random noise on infrared measurements in this window region were investigated.

The procedure suggested here for determining T_s from a spacecraft differs from previous approaches in several aspects. The high daily average method of *LaViolette and Chabot* [1969], the filter technique of *Vukovich* [1971], and the statistical approach used by *Smith et al.* [1970], do not attempt to reject cloud-contaminated data on a scan-spot by scan-spot basis; these methods tend to spatially smooth the results. *Shenk and Salomonson* [1972], on the other hand, use a multispectral approach that allows rejection of cloudy data from the Nimbus 2 medium resolution infrared radiometer on a resolution element scale, but the subpoint resolution of Nimbus 2 is too coarse

¹ Now at Department of Physics, Baruch College, City University of New York, N.Y.

for use in dynamical oceanography. *Anding et al.* [1971] suggest a multispectral approach that may surmount these problems, but the instrumentation is not yet available. As with the above approaches, the method we suggest is also instrument limited; this will be discussed below.

DESCRIPTIONS OF CALCULATIONS

The integral form of the equation of radiative transfer in an absorbing and emitting but non-scattering atmosphere is

$$N(u_0) = \int_0^\infty \phi_\nu N_\nu(u_\nu) \tau_\nu(u_0) d\nu \\ + \int_0^\infty \int_{u_0}^u \phi_\nu N_\nu(u) \frac{\partial \tau_\nu}{\partial u} du d\nu$$

where the optical depth u is positive downward from the height of the satellite u_0 to the sea surface u_s , N is the radiance received by the SR, N_ν is the spectral radiance of the blackbody at a wave number ν and is given by Planck's law, $\tau_\nu(u_0)$ is the spectral transmissivity of the entire atmosphere at u_0 , and ϕ_ν is the normalized spectral response of the NOAA-2 filter. To convert from radiance units to equivalent blackbody temperature T_{bb} , $N = \int_0^\infty \phi_\nu N_\nu(T_{bb}) d\nu$ is solved in an iteration scheme. It is implicit in this formulation that the emissivity of the sea surface is unity in this region of the spectrum, which is in essential agreement with measurements by *Buettner and Kern* [1965].

Spectral response of the NOAA-2 SR is approximately 950–800 cm^{-1} . This is outside the strong ozone absorption band centered at 1040 cm^{-1} ; hence water vapor is the major variable in this region of the window with a minor contribution from CO_2 .

The atmospheric transmissivities used are those of *Davis and Vievee* [1964]. In their work the infrared transmissivity through water vapor and carbon dioxide can be computed for 25- cm^{-1} intervals from analytic expressions. For the 800–1200- cm^{-1} region, *Davis and Vievee* fitted an expression of the form

$$\tau_\nu = \exp [-(k_\nu w p)^{a_\nu}]$$

to the observations of *Roach and Goody* [1958]. In this equation w is the precipitable water (g cm^{-2}), p is the ratio of in situ pres-

sure to standard pressure, and k_ν and a_ν are coefficients for each 25- cm^{-1} interval. The *Davis and Vievee* formulations were chosen for their simplicity in programming and because of the success *Saunders* [1970] and others have had in the lower atmosphere for correcting broad band (700–1250 cm^{-1}) airborne radiometers.

Atmospheric data input to the program is in radiosonde format, i.e., temperature and relative humidity as a function of pressure. The relative humidity is converted into precipitable water for use in *Davis and Vievee's* equations by using the empirical expressions given in the *Smithsonian Meteorological Tables* [1939] and solving

$$w = \frac{1}{g} \int_{p_1}^{p_2} m(p) dp$$

where m is the mixing ratio of water vapor, p is pressure, and g is gravity. The atmosphere-centimeters (atm-cm) of CO_2 were calculated by assuming that this gas is well mixed at 0.031% by volume. (An atmosphere-centimeter is a measure of the number of molecules of an absorbing gas at normal temperature and pressure.) By using the perfect gas laws, assuming hydrostatic equilibrium, and replacing the temperature with the virtual temperature, the CO_2 absorbers can be expressed as

$$u = 0.245 \int_{p_1}^{p_2} \left[\frac{1 + 1.609m}{1 + m} \right] dp$$

where u is the (atm-cm)_{STP} of CO_2 in the air column between pressures p_1 and p_2 (expressed in millibars) and m is again the mixing ratio.

Transmissivities are calculated from the independent variables in 1-mbar increments from the surface up to a height of 1 mbar (~ 48 km). This produces an 11 by 1020 matrix of transmissivities for the eleven 25- cm^{-1} intervals of ϕ_ν that are used to solve the radiative transfer equations. Special care was taken to avoid truncation errors, especially in calculating $\tau_\nu(u_0)$. The integrations were made on NOAA's computer facility at Suitland, Maryland, using the trapezoidal rule.

EFFECTS OF VARYING ATMOSPHERIC PROFILES

Calculations were made to determine the temperature departure $\Delta T = T_s - T_e$, where T_e is the equivalent blackbody temperature of the calculated radiance at a height of 1 mbar.

For these calculations, seven atmospheric profiles were chosen from the *U.S. Standard Atmosphere Supplements* [1966] for oceanographically meaningful latitudes; these are given in the first column of Table 1. The calculated temperatures T_e in this table are all for cloud-free conditions and zero nadir angle viewing. Sea surface temperatures were chosen to be equal to the surface air temperature T_a in every case except the 60° N-January atmosphere where T_a was well below the freezing point of sea water at 35‰ salinity.

Temperature departures for the cases chosen range from <2.5°K for dry winter atmospheres to >10.5°K under moist subtropical summer conditions. All the values of ΔT reported here are positive, but it is easy to imagine cases with negative values, especially where a large air-sea temperature difference exists. The variable $\Delta T(p)$ is a nearly linear function of $w(p)$ for a given atmosphere (a fact useful for correction of airborne radiation thermometers flown at low altitudes).

Recently, questions about the model dependence of ΔT calculations of this type have been raised [Maul and Sidran, 1972; Anding and Kauth, 1972]. The values of ΔT reported here are in substantial agreement with those of Rao *et al.* [1972] but are higher than those reported by Salomonson [Sabatini *et al.*, 1971] for the Nimbus 4 radiometer, which has a ϕ_e similar to that of the NOAA SR. Each of the above investigators used different transmissivity models.

A comparison between T_e and satellite-observed temperature was made for T_e values obtained by the R. V. Knorr in the Gulf Stream in June 1971. A frequency distribution of observed NOAA-1 temperatures for 3 clear days at the time and in the region of interest was

computed. With the use of Bermuda radiosonde data, T_e for the averaged T_a was calculated. The theoretical value was within 1°K of the mode observed in the histogram of satellite values. Encouraged by such agreement, the effects of random noise, nadir angle, cloud height, and cloud cover were computed.

EFFECTS OF RANDOM NOISE IN THE ATMOSPHERIC PROFILES

Since the correction procedure envisioned utilizes atmospheric profiles, it is interesting to study the effects of random errors in the input data. Random numbers were used to introduce controlled levels of temperature and humidity errors into the profiles. To ensure that the computer's random number generator was unbiased, a spectral analysis of the output was performed. The spectrum had reasonably uniform energy at all frequencies (white noise) and hence was unbiased.

The 30° N-July atmosphere was used in the random noise experiment because of the large ΔT (Table 1) and because field work is planned in the Gulf of Mexico to test this radiative transfer model. Results of adding temperature and/or relative humidity errors are summarized in Figure 1. For example, in the calculation for $\pm 5\%$ relative humidity error the range of the random numbers is set to ± 5 . Then elements of the column matrix of errors are sequentially added to the relative humidity data. If the new relative humidity is >100 or <0 , it is set to 100 or 0, respectively. T_e' , the calculated temperature with random errors, is then computed and stored. The process is repeated nine more times using different random numbers. The mean \bar{T}_e and the variance $\sigma^2 = \sum (T_e' - T_e)^2/n$ are calculated; the usual factor of $1/(n-1)$ is replaced

TABLE 1. Summary of Calculations of Equivalent Blackbody Temperature for the NOAA Scanning Radiometer

Atmosphere	T_a , °K	T_e , °K	$\Delta T (= T_a - T_e)$, °K	Precipitable H ₂ O, g cm ⁻²	CO ₂ , atm-cmSTP
15° N to Annual	299.6	291.1	8.6	4.0	248.5
30° N to Jan.	287.2	283.1	4.1	2.1	250.2
30° N to July	301.2	290.6	10.5	4.4	248.8
45° N to Jan.	272.6	270.4	2.2	0.8	249.3
45° N to July	294.2	287.7	6.4	3.0	248.6
60° N to Jan.	271.2	268.7	2.5	0.4	248.2
60° N to July	287.2	281.6	5.6	2.1	247.5

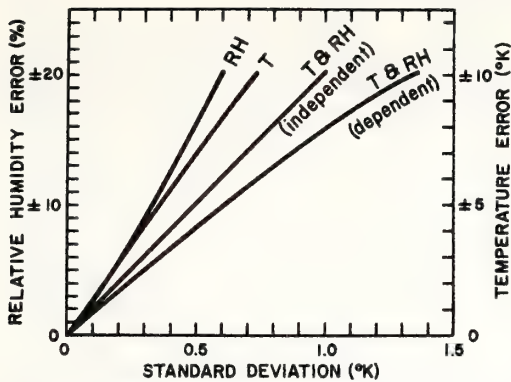


Fig. 1. Effect of random errors in relative humidity and atmospheric temperature on the calculated temperature at 1 mbar. The curve marked RH means the errors were applied to the relative humidity profile only; similarly T is for temperature error only. T & RH means that both parameters were degraded by the amount shown on the appropriate ordinate; i.e., when $\pm 10\%$ relative humidity error was introduced, a $\pm 5^\circ\text{K}$ temperature error was introduced.

by $1/n$ because the true mean of the population is known. The \bar{T}_e was always within 0.1°K of T_e in these experiments.

In the standard atmosphere tested the effect on T_e of temperature error alone was slightly greater than that of relative humidity error alone; the standard deviation σ in \bar{T}_e for $\pm 10^\circ\text{K}$ temperature error was $\pm 0.7^\circ\text{K}$. When random errors were added to both temperature and relative humidity, two conditions were investigated. In the first case, two independent series of random numbers were used to generate temperature and relative humidity errors; in the second case, the dependent case, the same random numbers were used to generate both types of errors. The calculations clearly show that when the errors are dependent a 30% larger standard deviation occurs. This is an important consideration in choosing the system that will measure the independent atmospheric variables.

Ostapoff *et al.* [1970] report realistic error maximums in radiosondes to be $\pm 10\%$ in relative humidity. This implies that the standard deviations in T_e to be expected are $\pm 0.3^\circ\text{K}$. This magnitude combined with the need to composite data (which would tend to cancel out errors) implies that this effect will not be a large source of error in these analyses; the error should not exceed 0.5°K .

EFFECTS OF VARYING NADIR ANGLE

Nadir angle, or limb-darkening effects, is studied for the 30°N -July (cloud-free) atmosphere. The sphericity of the earth is taken into account. For the NOAA vehicle in a sun-synchronous orbit a normalized path length factor L is derived from geometric considerations

$$L = b - |(b^2 + c)^{1/2}|$$

where $b = (a + r) \cos \theta$, $c = [r^2 - (a + r)^2]/\alpha^2$, θ is the nadir angle, r is the earth's radius, and a is the altitude of the satellite. At this orbital altitude and at a 60° nadir angle, for example, the path length is 20% longer than if the earth were assumed to be planar.

The effect of the nadir angle on T_e is seen in Figure 2. The five curves from top to bottom are for five values of T_s from 303.2°K to 295.2°K in 2°K decrements ($T_s = 301.2^\circ\text{K}$). These values represent the range of T_s to be expected for this standard atmosphere. For any given T_s , calculated temperatures decrease with increasing path length. The decrease is larger for higher T_s .

Sea surface temperature range for this study is 8°K . At the top of the atmosphere for zero nadir viewing this temperature range is reduced to 2.7°K . At 60° nadir angle it is further compressed to only 1°K . This has an im-

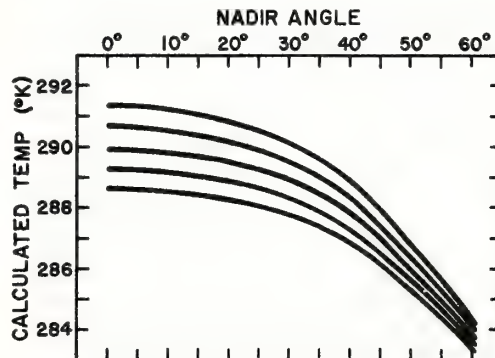


Fig. 2. Calculated temperature at 1 mbar as a function of nadir angle. The topmost line is for a surface temperature of 30°C (303.2°K), and each line below is decremented by 2°K . Note that the 8°K surface temperature difference represented by these curves is compressed to 2.7°K at 1 mbar with nadir viewing and further compressed to 1°K at 60° nadir angle.

portant implication when noise equivalent temperature difference (NE Δ T) is considered. If the NE Δ T of the radiometer system is determined to be $\pm 1^\circ\text{K}$, this implies a $\pm 8^\circ\text{K}$ uncertainty in measuring T_s at $\theta = 60^\circ$ for this standard atmosphere; even at $\theta = 0^\circ$, this NE Δ T gives rise to a question of $\pm 3^\circ\text{K}$. NE Δ T therefore must be considered in the geophysical as well as the instrumental sense. A reasonable compromise is to use data for $\theta \leq 40^\circ$; this provides 100% daily ground coverage at the latitude of the Gulf of Mexico and a fourfold effect of NE Δ T for this severe atmospheric condition.

EFFECT OF CLOUD COVER AND CLOUD HEIGHT

Trade wind regions typically have cumulus humilis or fractocumulus clouds that are about 1 km above the surface and are spaced several kilometers apart; their diameters average $\frac{1}{2}$ to 1 km. For the SR this means that cloud contamination in these regions is to be routinely expected. The effect of such cloud cover was investigated for the 30°N -July standard atmosphere.

Cirroform clouds cannot be detected by this instrument because of the low albedo and this constitutes an unknown source of error. Cumuloform clouds were simulated in the model by assuming that they are opaque to terrestrial radiation and radiate at their own temperature as a blackbody with emissivity equal to 1. The cloud's temperature was assumed to equal the air temperature T_a at its altitude. For a given T_s , a $T_{c|1000}$ was obtained at 1000 meters and a new T_s' was defined for x decimal fraction of cloud cover by $T_s' = T_{c|1000}(1 - x) + T_a|_{1000} \cdot x$. $T_{c'}$ was determined at the satellite by using T_s' and integrating through the remaining atmosphere. Temperature error, defined as the difference in computed temperatures ($T_c - T_{c'}$), is plotted on the abscissa versus percent cover at 1000 meters for the same five T_s values as before.

Figure 3a summarizes the results of these calculations. The temperature error is dependent on T_s ; higher errors are introduced for the same atmospheric state and percent of cloud cover for higher values of the surface temperature. The cloud cover for a nadir-viewing resolution element of 8 kilometers with

two smaller cumuloform clouds in the field of view would be approximately 20%. This corresponds to a temperature error of 0.2° – 0.8°K depending on T_s . This is an error that may have to be corrected in a statistical manner in the trade wind region because of the persistent cloudiness.

Hanson [1970] studied the frequency distribution of albedo measurements in an attempt to detect clouds. Shenk and Salomonson [1972] used an analogous approach and set the cloud-contaminated cutoff at the albedo value on the high side of the mode equal to the difference between the mode and the lowest value. If that cutoff is at the 10% cloud-contaminated level, a 0.5°K error is introduced for 1000-meter altitude clouds. Choosing a lower cloud/no-cloud criterion would improve this somewhat, but the amount of acceptable data there may be too small to accomplish the goal.

The effect of cloud height is calculated in a manner analogous to that described above. Results of this experiment are illustrated in

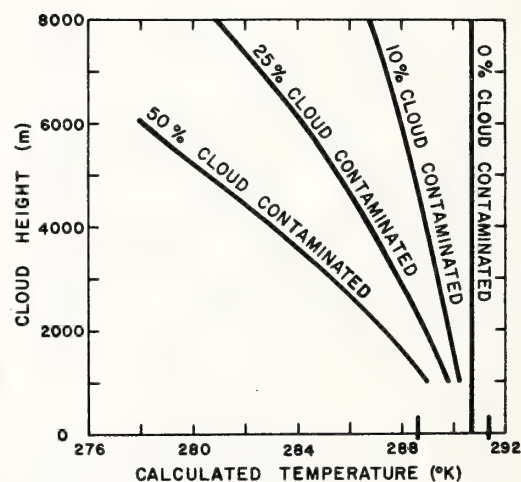


Fig. 3a. Temperature error introduced by clouds in the field of view as a function of the percent of the subsatellite resolution element filled with clouds at 1 km. Calculations are for the 30°N -July atmosphere which has a surface air temperature of 28°C . The temperature error is the difference between the calculated temperature for cloud-free conditions (for a given ocean surface temperature) and that computed for various percent cloudiness. Under typical trade wind conditions the suborbital resolution element of NOAA will have approximately 10% contamination.

Figure 3b, which uses $T_s = 301.2^\circ\text{K}$. For a given cloud cover the calculated temperature decreases with increasing cloud height because of the lower temperatures at higher altitudes. Note that a towering cumuloform that intercepts 10% of the field of view at 8 kilometers introduces a temperature error of 4°K , whereas at 1 km the error is 0.5°K . The percent of cloudiness can be estimated from the visible channel, but the mean height can only be calculated if the field of view is filled [Rao, 1970]. Therefore, cloud-contaminated scan spots must be completely rejected from the analysis.

CORRECTION SCHEME

Scan spots that are considered cloud free must be corrected for atmospheric transmissivity in order that the skin temperature of the ocean's surface may be determined. Compositing over several days and averaging values at the same grid intersections can then be accomplished. The assumption is made that the satellite obtains radiosonde-type data as it proceeds along its orbit and that this sounding is representative of the swath width of the SR ($0^\circ \leq \theta \leq 40^\circ$). NOAA-2 will be able to obtain temperature profiles, and future satellites will be able to acquire humidity as well.

To investigate the variability in T_c , twenty consecutive days of radiosonde data from Key West, Florida, were obtained. The standard

deviation in \bar{T}_c for these April data was 1.4°K ; when the two 8/8 cloud cover days were disregarded, σ was 0.8°K . The frequency distribution was bimodal with means differing by 1.2°K and equaling 0.4°K for the mode with the larger variance. The bimodal distribution appears to be caused by different air masses since the modes are time dependent. Assuming that advection of an air mass would appear as a temporal variability, the error in using a single radiosonde to represent the swath width of the SR is of the order 0.4°K . If a large horizontal inhomogeneity exists, e.g., the passage of a front, cloudiness will be associated with it and no useful observations will be obtained anyway. In this example, temporal compositing would have introduced an uncertainty greater than 1°K without atmospheric corrections.

In Figure 4 the surface temperature is plotted as a function of the calculated temperature for seven nadir angles from 0° to 60° ; the 30°N -July atmosphere is used. Smith *et al.* [1970] first reported a linear relationship between ΔT and T_c for a given nadir angle. From the figure one immediately notices that

$$\left. \frac{\partial T_s}{\partial T_c} \right|_\theta = f(\theta)$$

Upon integrating this expression, the desired

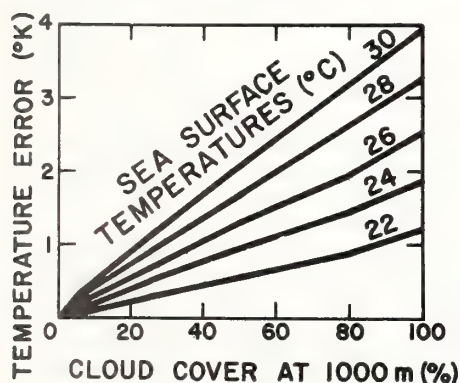


Fig. 3b. Calculated temperature at 1 mbar as a function of percent and height of low and middle clouds. The same atmosphere as Fig. 3a is used; sea surface temperature is 28°C (301.2°K). The two vertical bars on the right of the ordinate represent the 8°K range used in Figure 2.

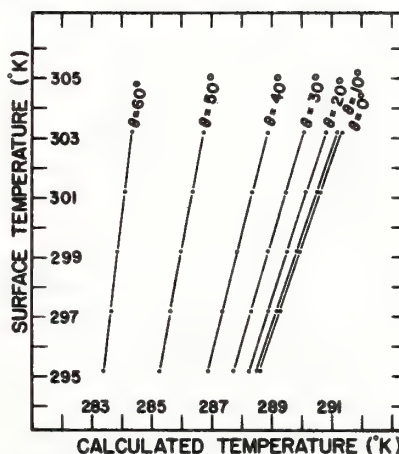


Fig. 4. Ocean surface temperature as a function of temperature calculated at 1 mbar. The 30°N -July atmosphere was used; range of ocean temperature is $22^\circ\text{--}30^\circ\text{C}$. The linearity for a given nadir angle θ between surface temperature and calculated temperature is used in a correction scheme. The maximum nadir angle suggested for use is 40° .

functional form must be $T_s = T_o \cdot f(\theta) + g(\theta)$, where $f(\theta)$ and $g(\theta)$ are the slope and intercept, respectively. Linear least squares were used to fit the curves; $f(\theta)$ and $g(\theta)$ were found to have nonlinear dependence on nadir angle. Several schemes were employed to fit nonlinear functions to $f(\theta)$ and $g(\theta)$, all of which led to complicated and unsatisfactory results.

Smith *et al.* [1970] employed an equation of the form $\Delta T = (a + b \cdot T_o) \exp [c\theta^2]$, where a , b , and c are constants, to compute the atmospheric corrections. A number of equations of this form were fitted to the data by least squares, but errors of 0.5°K persisted. Even fourth-order polynomials in θ were employed, but rms errors of 0.2°K remained. On the basis of these experiments and an estimation of the computer time required to correct large blocks of data, a linear interpolation scheme was devised that introduced errors no larger than 0.04°K.

The correction scheme is to first calculate T_o for a given atmosphere for all integer θ 's between 0° and 40°. This is done twice, once each for the lowest and highest T_s anticipated for a region. This provides a 3 by 41 matrix in θ , T_o (lowest), and T_o (highest). Then the nadir angle of the cloud-free scan spot is truncated to the nearest integer, and a simple linear interpolation scheme is used to calculate T_s from the matrix.

SUMMARY AND CONCLUSIONS

Several sources of error in the radiometric determination of sea surface temperature cannot be corrected for when using the NOAA SR. High thin cirroform clouds will not be detectable in the visible channel; a 6.7- μ m channel seems to provide the measurements for upper level clouds [Anding *et al.*, 1971; Shenk and Salomonson, 1972]. Variations of atmospheric state within the sweep of the scanner cannot be accounted for, but this will be about 0.4°K for a local region such as the southeastern Gulf of Mexico. Although errors of >1° may be expected from random errors in a given radiosonde, temporal and spatial compositing of the data tends to cancel this source.

Cloud detection remains the principal problem when using the SR for ocean surface tem-

perature determination. Errors as large as 4°K can be expected if the radiometer's field of view is only 10% cloud contaminated. The magnitude of this error depends on cloud height. Under fractocumulus conditions an error of <1°K is anticipated for clouds at <2-km altitude. Experience with actual data may allow statistical corrections for these error sources with cognizance for seasonal variability. The correction scheme for converting T_o to T_s yields interpolation errors of no greater than 0.04°K.

A summation of the error sources indicates that accuracies in ocean surface temperature determination are of the order of 2°K with the NOAA SR. This is marginally useful for certain fisheries applications but certainly adequate for weather forecasting and surface current boundary location studies in dynamical oceanography.

Acknowledgments. The assistance of A. Herman and D. V. Hansen is gratefully acknowledged.

This research was in part supported by the National Aeronautics and Space Administration Earth Resources Survey Program through the National Environmental Satellite Service Environmental Science Group.

REFERENCES

- Anding, D., R. Kauth, and R. Turner, Atmospheric effects on infrared multispectral sensing of sea surface temperature from space, *NASA CR-1858*, 1971.
- Anding, D., and R. Kauth, Reply to 'Comment on estimation of sea surface temperature from space,' *Remote Sensing Environ.*, 2(3), 171-173, 1972.
- Buettner, K., and C. Kern, The determination of infrared emissivities of terrestrial surfaces, *J. Geophys. Res.*, 70(6), 1329-1336, 1965.
- Davis, P., and W. Viezee, A model for computing infrared transmission through atmospheric water vapor and carbon dioxide, *J. Geophys. Res.*, 69(18), 3785-3794, 1964.
- Hanson, K., Applications for bispectral radiance measurement from a satellite, Ph.D. dissertation, Dept. of Meteorol., Univ. of Wisc., Madison, 1970.
- LaViolette, P., and P. Chabot, A method of eliminating cloud interference in satellite studies of sea surface temperature, *Deep Sea Res.*, 16(5), 539-548, 1969.
- Maul, G., and M. Sidran, Comment on 'Estimation of sea surface temperature from space' by D. Anding and R. Kauth, *Remote Sensing Environ.*, 2(3), 165-169, 1972.

- Ostapoff, F., W. Shinnars, and E. Augstein, Some tests on the radiosonde humidity error, *Tech. Rep. ERL 194-AOML 4*, 50 pp., Nat. Oceanic and Atmos. Admin., Boulder, Colorado.
- Rao, P., Estimating cloud amount and height from satellite infrared radiation data, *Tech. Rep. NESC 54*, 11 pp., Environ. Sci. Serv. Admin., Washington, D.C.
- Rao, P., W. Smith, and R. Koffler, Global sea surface temperature distribution determined from an environmental satellite, *Mon. Weather Rev.*, 100(1), 10-14, 1972.
- Roach, W., and R. Goody, Absorption and emission in the atmospheric window from 770 to 1250 cm^{-1} , *Quart. J. Roy. Meteorol. Soc.*, 84, 319-333, 1958.
- Sabatini, R. R., G. A. Rabchevsky, and J. E. Sissala (Eds.), in *Nimbus Earth Resources Observations, NASA TR-2*, p. 214, Allied Res. Ass. Inc., Concord, Mass., 1971.
- Saunders, P., Corrections for airborne radiation thermometry, *J. Geophys. Res.*, 75(36), 7596-7601, 1970.
- Shenk, W., and V. Salomonson, A multispectral technique to determine sea surface temperature using Nimbus 2 data, *J. Phys. Oceanogr.*, 2(2), 157-167, 1972.
- Smith, W., P. Rao, R. Koffler, and W. Curtis, The determination of sea surface temperature from satellite high resolution infrared window radiation measurements, *Mon. Weather Rev.*, 98(8), 604-611, 1970.
- Smithsonian Meteorological Tables, 5th revised ed., 282 pp., Smithsonian Institution, Washington, D.C., 1939.
- Vukovich, F., Detailed sea surface temperature analysis utilizing Nimbus HRIR data, *Mon. Weather Rev.*, 99(11), 812-817, 1971.

(Received October 20, 1972;
revised December 28, 1972.)

BUOY TRACKING OF OCEAN CURRENTS

Robert L. Molinari*

The use of free-drifting platforms to track ocean currents is discussed. The evolution of Lagrangian measurement techniques from ship-tracking to satellite-tracking of platforms is considered by describing specific drifter studies. Discussions of these studies include the uniqueness of the Lagrangian results, and other possible uses for the data. Future uses for buoy tracking also will be suggested.

INTRODUCTION

In the past, oceanographers have not used free drifting Lagrangian platforms to obtain fluid trajectories as extensively as their atmospheric colleagues. Meteorologists have recognized the utility of drifters in obtaining data on upper air currents and the value of these data in developing theories on the dynamics of these flows. However, recent oceanographic experiments have shown that Lagrangian techniques can be effective in the ocean environment. In particular, many of the results from these experiments could not be predicted from historical knowledge, nor could they be obtained from conventional Eulerian measurements.

The following sections will describe some of the steps in the continuing evolution of oceanographic Lagrangian techniques. Both ship tracked and satellite tracked drifter studies will be discussed. In each case an attempt will be made to specify the uniqueness of the Lagrangian results, and the concepts that were derived from these results. Finally, future uses for buoy tracking techniques will be suggested.

* Research Oceanographer, National Oceanic and Atmospheric Administration, Atlantic Oceanographic and Meteorological Laboratories, Miami, Florida.

STUDIES USING SHIP TRACKED BUOYS

Ship tracked Lagrangian drifters have been used in experiments investigating many spatial scales of ocean phenomena. Small scale (tens of kilometers) studies require accurate navigation only available from land based systems, and thus frequently consider nearshore processes. A large number of short drogue tracklines are obtained to describe statistically the feature being studied. To compensate for the lack of accurate positioning away from land stations, large scale (hundreds of kilometers) studies, which consider regional circulation patterns, use longer tracklines.

The studies of Chew and Berberian (1970, 1971, and 1972) are an example of the use of drifters to study small-scale features. Many buoys were tracked over short distances in the Florida Current off Miami (Fig. 1), and in the Gulf Stream off Cape Lookout to obtain data on the kinematics of these

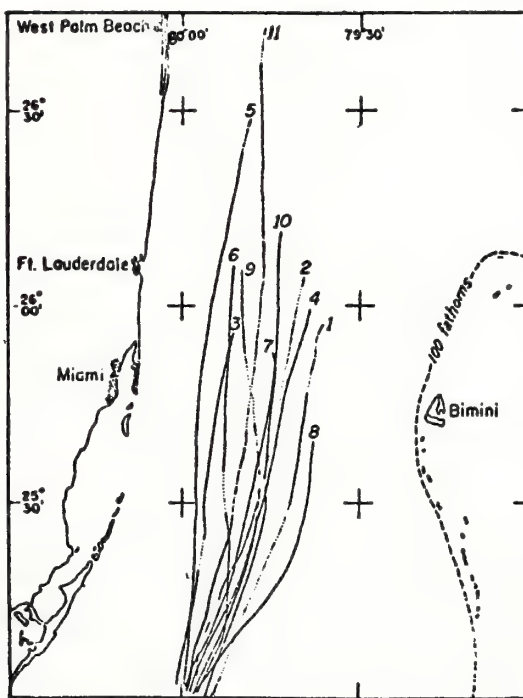


Fig. 1 Drogue trajectories obtained in the Florida Straits.

flows. The change in area with time of drogue triads represented by the triangle apexes of Fig. 2, can be equated to such kinematical properties of the flow as divergence, vorticity, and deformation.

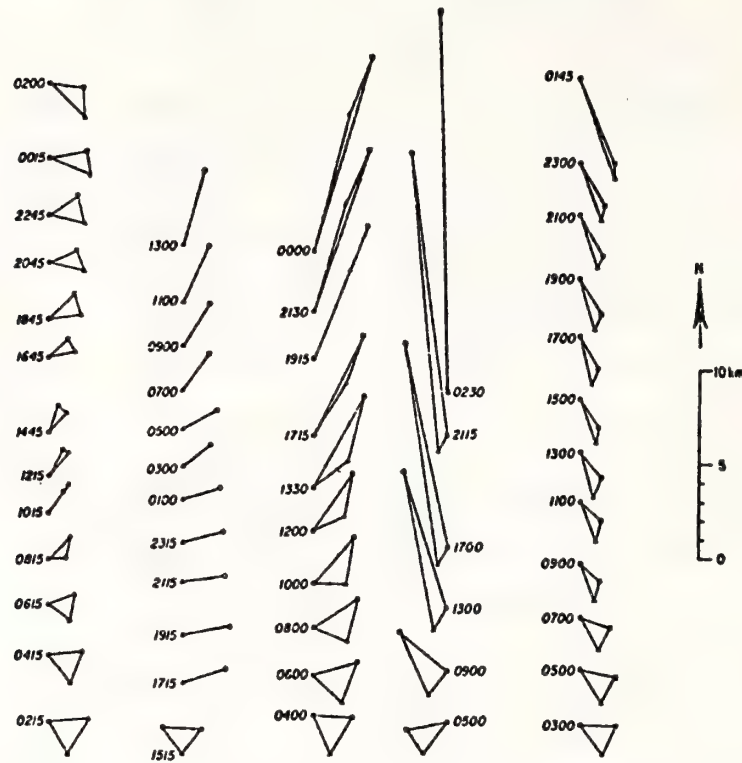


Fig. 2 Drogue diads and triads as a function of time obtained from the drogue trajectories of Fig. 1.

The quantification of these kinematical properties is a necessary step towards determining the dynamical processes occurring in ocean currents, and developing models to predict their course. To obtain such quantities of data from fixed point Eulerian experiments would require much greater expenditures of time and money. Furthermore, mooring techniques in regions of intense flow, such as the Florida Current, are not sufficiently developed to insure a successful experiment.

Chew (1972) and Molinari and Starr (1972) used surface drifters to determine regional current patterns. The Lagrangian drifter tracked by their ships is shown in Fig. 3. A satel-

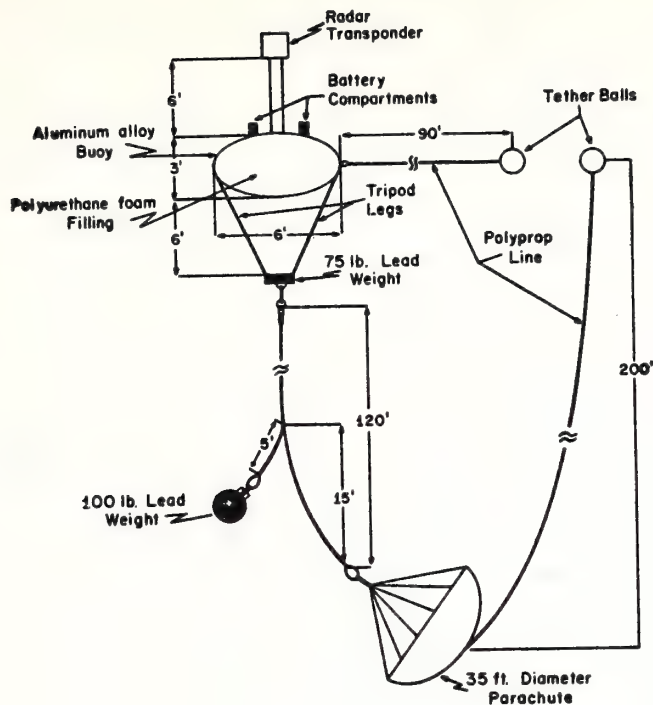


Fig. 3 Schematic diagram of the Lagrangian drifter used in the experiments of Chew (1972), and Molinari and Starr (1972).

lite navigation system was used as the ship positioning control for their experiments. To compensate for the one to two mile positioning accuracy of the satellite system, long tracklines were obtained. This method reduces the importance of a single fix, and provides a better representation of the circulation.

The drogue tracklines of Chew (1972) in the Gulf of Mexico are given in Fig. 4. The current pattern described by the drogue tracklines has been observed previously (Nowlin 1972), but never by Lagrangian measurements. The drogues accelerated from a velocity of 1.2 knots at the initial deployment position to 4 knots in the Florida Strait. As the drogues

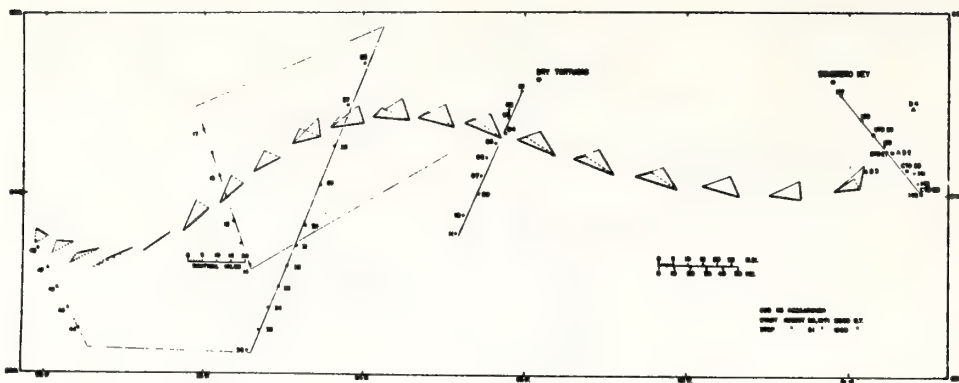


Fig. 4 Drogue trajectories, as given by the apexes of the triangles, obtained in the Gulf of Mexico during August 1971.

drifted along the wavelike pattern, they crossed the current axis, suggesting that water parcels also have a component of velocity normal to the mean current. This last feature could not have been measured by Eulerian techniques except at great expense, and the measurement of the acceleration phenomenon would have required an extensive Eulerian array. Again, the implantation of a current Eulerian mooring array would be impractical in the observed velocities.

Molinari and Starr (1972) obtained, in the Caribbean Sea, the drogue tracklines given in Fig. 5. Once again an area of current intensification was delineated by the surface drifters. In the vicinity of Cozumel Island, the drogues doubled their speed within an arclength of sixty nautical miles. Speeds obtained indirectly from conventional density measurements are much lower than the drogue velocities. Also, the current directions suggested by these density measurements do not reproduce the drogue directions, as the drogues accelerate across the density streamlines (Fig. 6).

STUDIES USING SATELLITE TRACKED BUOYS

The spatial and temporal coverage possible using ship tracked drifters is limited by the availability, endurance, and expense of the participating vessels. Satellite tracked buoys can

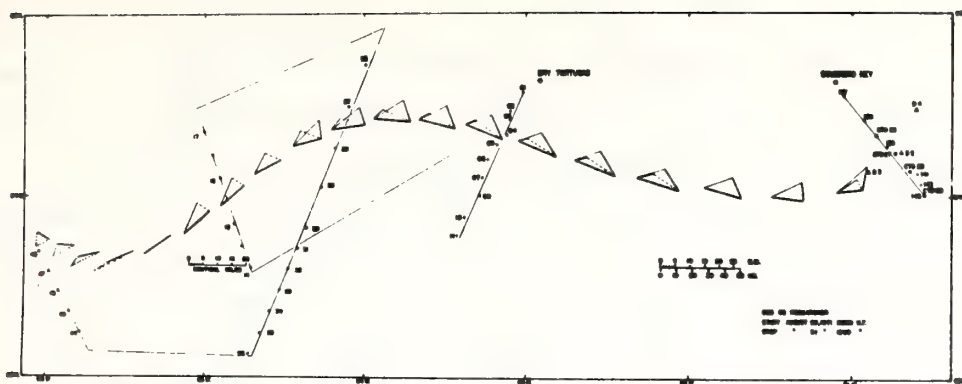


Fig. 4 Drogue trajectories, as given by the apexes of the triangles, obtained in the Gulf of Mexico during August 1971.

drifted along the wavelike pattern, they crossed the current axis, suggesting that water parcels also have a component of velocity normal to the mean current. This last feature could not have been measured by Eulerian techniques except at great expense, and the measurement of the acceleration phenomenon would have required an extensive Eulerian array. Again, the implantation of a current Eulerian mooring array would be impractical in the observed velocities.

Molinari and Starr (1972) obtained, in the Caribbean Sea, the drogue tracklines given in Fig. 5. Once again an area of current intensification was delineated by the surface drifters. In the vicinity of Cozumel Island, the drogues doubled their speed within an arclength of sixty nautical miles. Speeds obtained indirectly from conventional density measurements are much lower than the drogue velocities. Also, the current directions suggested by these density measurements do not reproduce the drogue directions, as the drogues accelerate across the density streamlines (Fig. 6).

STUDIES USING SATELLITE TRACKED BUOYS

The spatial and temporal coverage possible using ship tracked drifters is limited by the availability, endurance, and expense of the participating vessels. Satellite tracked buoys can

lengthen the time scales studied, as well as increase the spatial coverage possible. Satellite systems also permit a larger number of drifting platforms to be used in an experiment.

The OPLE (Omega Position Location Equipment) system was designed to evaluate the performance of the Omega navigational system in conjunction with synchronous satellites (Young 1970). The evaluation included the tracking of a drift buoy in the Florida Strait by the relaying of Omega signals through the Applications Technology Satellite (ATS-3). Upon command, the buoy transmitted stored Omega data through the satellite to a ground station, where buoy positions were calculated. Although the short two-day trackline of the buoy precluded an evaluation of the navigation system, the feasibility of a satellite-to-buoy link was demonstrated.

Most satellite positioning systems were originally designed for use in atmospheric balloon studies. It was soon realized that with minor modifications the balloon electronics packages could be modified for use in a buoy. Crumpler and Bivins (1971) reported an experiment using a modified balloon system, the IRLS (Interrogation, Recording, and Locating System) electronics package.

The IRLS system was used aboard the polar orbiting Nimbus IV satellite to position a buoy set adrift north of the Gulf Stream. The IRLS package uses a two-way communications link between satellite and platform to position the drifter and to accept other data collected by the buoy (see Fig. 7).

The satellite interrogates a platform with a coded signal. If the platform recognizes its signal it responds to the satellite with a transmission that includes the platform data. The distance from satellite to platform is determined from two successive buoy transmissions, and used by the satellite to position the platform. These data are stored until the satellite is commanded to transmit them to a ground station.

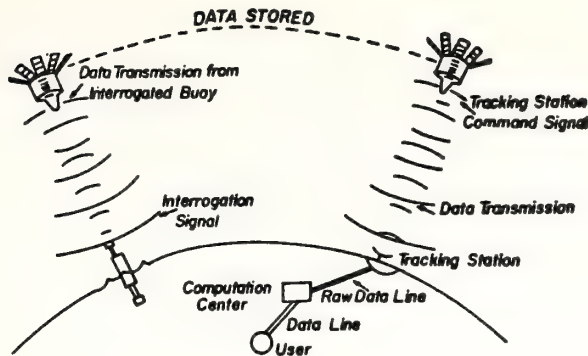


Fig. 7 Schematic diagram of the IRLS communication links between ground stations, satellite and platform.

The IRLS experiment further demonstrated the feasibility of tracking ocean drifters by satellite.

Results from a drifting buoy experiment presently being conducted by personnel of the National Oceanic and Atmospheric Administration's Atlantic Oceanographic and Meteorological Laboratories (AOML), NASA, and the French government's counterpart to NASA, the Centre National d'Etudes Spatiales (CNES), provide further evidence for the utility of Lagrangian drifters. The global pattern of ocean currents, particularly in regions of weak surface flow, has been determined primarily by ship drift reports. Upon the completion of a journey, differences between course steered and course made good (a function of the surface current) are forwarded to agencies such as the United States Coast Guard AMVER group. These data are then smoothed, usually by averaging all the reports for a particular month or season, and presented on surface current charts and atlases.

Fig. 8 is an example of a chart produced from ship drift reports. The figure is adapted from the AMVER November Pilot Chart of the North Atlantic. Areas with current direction given by solid arrows contain more data points than areas with dashed arrows. Numbers above the arrows indicate average velocity.

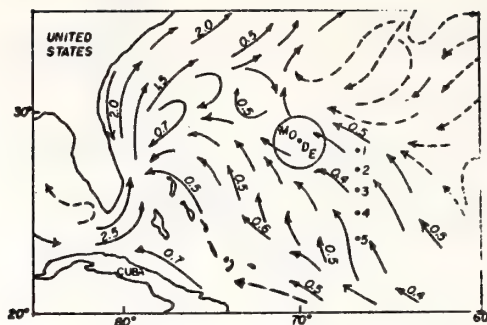


Fig. 8 Surface currents as adapted from the November Pilot Chart of the North Atlantic.

The joint AOML-NASA-CNES experiment is being conducted within the area bounded by 65°W and 70°W , and 20°N and 30°N . Preliminary results from this experiment have been presented by Hansen, et al. (1973). Drifting platforms were deployed along 67°W , from $23^{\circ}30'\text{N}$ to $28^{\circ}00'\text{N}$ (see Fig. 8), with the expectation that they would drift through the area of the Mid-Ocean Dynamics Experiment (MODE), also shown on Fig. 8. This expectation and the projected path of the buoys given on Fig. 9 were based on the Pilot Chart representations of the currents in the area.

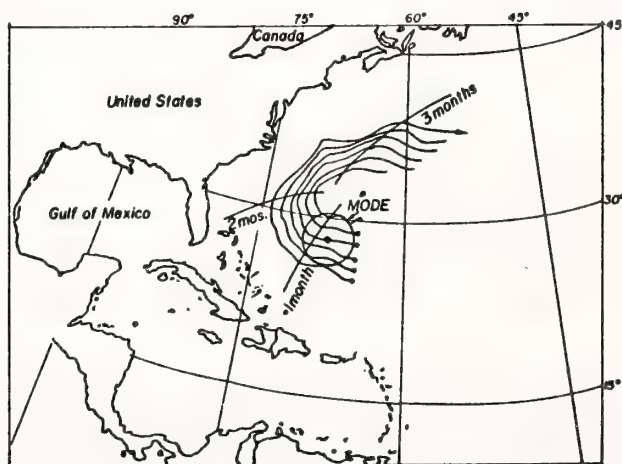


Fig. 9 Projected trajectories of the EOLE buoys.

The French EOLE tracking system was originally designed to track balloons from a NASA launched satellite. The communi-

cations link between satellite and platform is similar to the IRLS system, in that the satellite interrogates the buoy, and the buoy responds with a signal derived from the satellite transmission. The Doppler shifting of the buoy transmission is used to position the platform. Also included in the buoy signal is ancillary data collected by the drifter.

The buoy electronics package was housed in the drifter shown in Fig. 10. The spar buoy is approximately forty feet long,

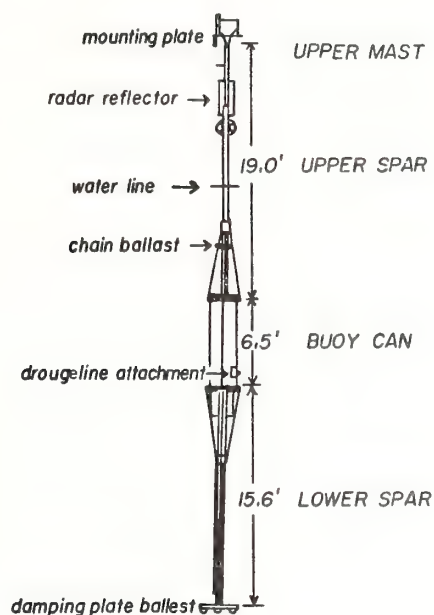


Fig. 10 Schematic diagram of the Lagrangian drifter used in the AOML-EOLE experiment.

with the upper mast extending ten feet out of the water. A parachute drogue is attached at thirty meters to reduce the effect of wind on the buoy. The drifter also is instrumented with a surface water temperature sensor and a temperature and pressure sensor at a depth of one hundred meters.

Fig. 11 gives the buoy tracklines from launch to mid-November. An obvious use for these Lagrangian data is to describe the surface currents in this area, during the study period. The

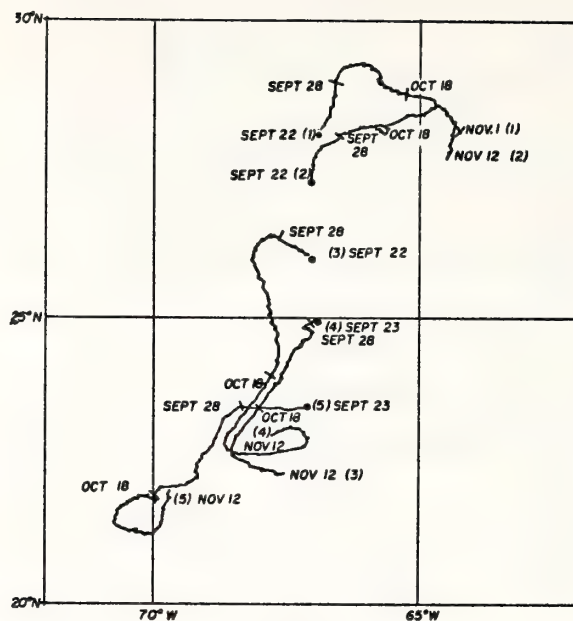


Fig. 11 Drift of the EOLE buoys from mid-September to mid-November.

surface currents derived from the buoy paths bear little resemblance to the surface drifts originally predicted from the Pilot Charts (Fig. 9). To define the observed trajectories from a fixed Eulerian array would require a very large number of current meter moorings. As the implantation of current meter moorings in deep water is still an expensive undertaking, the Lagrangian data provide a relatively inexpensive indicator of the surface flow.

Lagrangian statistic parameters also are to be obtained from these measurements. These parameters have been used in meteorological balloon studies to describe the turbulence field and to determine the spatial coherence of the flow, for instance. The parameters have not yet been quantified for oceanic flows, because of the short time scale of most drift-er experiments, and the small number of simultaneous moorings that have been successfully operated.

FUTURE USES OF BUOY TRACKING

The Williamstown Report of NASA and MIT (1969), which described possible applications of space and astronomic techniques, presented some questions that could be answered by Lagrangian methods. These questions extended beyond the obvious and important use of tracking surface currents, to tracing the flow, both surface and deep, of pollutants and biological resources.

Satellite tracked buoys could be planted in regions of high concentration of fish larvae, for instance, which drift at the surface. The distribution of the larvae at a later time can be obtained from the buoy drift. The same procedure also could be applied to trace pollutants emitting from a river mouth.

Subsurface drifting buoys that return to the surface at fixed intervals are being developed. If tracked by satellite they could provide long time histories of deep currents, information necessary for the prediction of the spread of pollutants that are dumped in ocean areas of great depth.

If deployed prior to an oceanographic experiment, drifters could provide data on the important time and space scales to be studied. These data could then be used to determine the most efficient station spacing and data collection interval. If used during an experiment, buoys deployed in triads can be used to determine kinematical properties of the flow as described previously. They also provide the advective field which is necessary for the determination of property fluxes.

If equipped with meteorological sensors the buoys serve as floating weather stations. If placed in strategic areas, such as hurricane intensification regions, they greatly increase the spatial coverage available to meteorologists.

Many of the uses for satellite tracked buoys just described are planned for experiments to be conducted in the near future. For instance, in the GARP Atlantic Tropical Experiment (GATE) some thirty to forty satellite tracked buoys are pro-

posed to be used in the oceanographic property flux studies, and to increase the area of meteorological measurements. Water quality studies are also planned in the Caribbean Sea and Gulf of Mexico, in which satellite tracked buoys are to be used with ships to determine the trajectories of pollutants in this region. Drifting buoy experiments have also been proposed to study the currents in the Antarctic Ocean and the North Pacific. The past successes of this Lagrangian technique suggest that oceanographers are acquiring a valuable addition to the list of oceanographic sensors.

REFERENCES

1. Chew, F. and G. A. Berberian (1970). "Some Measurements of Current by Shallow Drogues in the Florida Current," Limnol. Oceanogr., 15, 88-99.
2. Chew, F. and G. A. Berberian (1971). "A Determination of Horizontal Divergence in the Gulf Stream off Cape Lookout," J. Phys. Oceanogr., 1, 39-44.
3. Chew, F. (1972). "A Drogue Measurement of Downstream Acceleration in the Florida Current off Cuba," abstract in Trans. Am. Geophys. Union, 53, 392.
4. Chew, F. and G. A. Berberian (1972). "Neighbor Diffusivity as Related to Lateral Shear in the Florida Current," Deep-Sea Res., 19, 493-506.
5. Crumpler, A. and L. Bivins (1971). "An IRLS Drift Buoy Experiment," abstract in Trans. Am. Geophys. Union, 52, 240.
6. Hansen, D. V., D. J. Pashinski, R. L. Charnell, and T. R. Bartholomew (1973). "Mesoscale Motions in the Sargasso Sea: A Result from the EOLE Complementary Program," abstract in Trans. Am. Geophys. Union, 54, 313.
7. Molinari, R. L. and R. B. Starr (1972). "Lagrangian Current and Hydrographic Measurements in the Western Caribbean Sea," abstract in Trans. Am. Geophys. Union, 53, 392.

8. National Aeronautics and Space Administration (1969). Report of a study at Williamstown, Massachusetts to the National Aeronautics and Space Administration. Application of Space and Astronomic Techniques.
9. Nowlin, W. D. and J. M. Hubertz (1972). "Patterns for the Eastern Gulf-Loop Current Contrasting Summer Circulation Patterns for the Eastern Gulf-Loop Current versus Anticyclonic Ring-Contributions on the Physical Oceanography of the Gulf of Mexico," Texas A&M University Oceanographic Studies, Volume II, Reid and Capurro Editors, 119-138.
10. Young, H. M. (1970). "Summary of Test Results for the OPLE Experiment," Computer Sciences Corporation Report 4031-17, 169 pp.

Reprinted from NOAA Tech Memo NOAA ERL AOML-19, 81 pages, Apr. 1973.

DATA FROM THE LAGRANGIAN CURRENT-MEASUREMENT PROJECT
CONDUCTED ABOARD THE NOAA SHIP RESEARCHER DURING
CICAR SURVEY MONTH I

Robert L. Molinari

The NOAA ship RESEARCHER conducted, during July and August 1971, a physical oceanographic experiment in the northwestern Caribbean Sea and the southeastern Gulf of Mexico as part of CICAR (Cooperative Investigation of the Caribbean and Adjacent Regions) Survey Month I. The primary objective of the RESEARCHER cruise was to investigate the dynamics of the formation of the Yucatan Current, utilizing Lagrangian current-measurement techniques. This report describes the measurements taken and the methods applied to analyze the resultant data. It also makes available data to other researchers who are working on problems in the CICAR program to which these data may be relevant.

1. INTRODUCTION

Scientists from the Atlantic Oceanographic and Meteorological Laboratories (AOML) of the National Oceanic and Atmospheric Administration (NOAA) conducted a two-ship investigation in the northwestern Caribbean Sea (Cayman Sea) and the southeastern Gulf of Mexico (fig. 1) during July and August 1971. The study was undertaken as part of the Declared National Program, CICAR (Cooperative Investigation of the Caribbean and Adjacent Regions), and was funded by the International Decade of Ocean Exploration Office of the National Science Foundation. July 1971 was designated CICAR Survey Month I by the participating nations in an attempt to coordinate ship schedules.

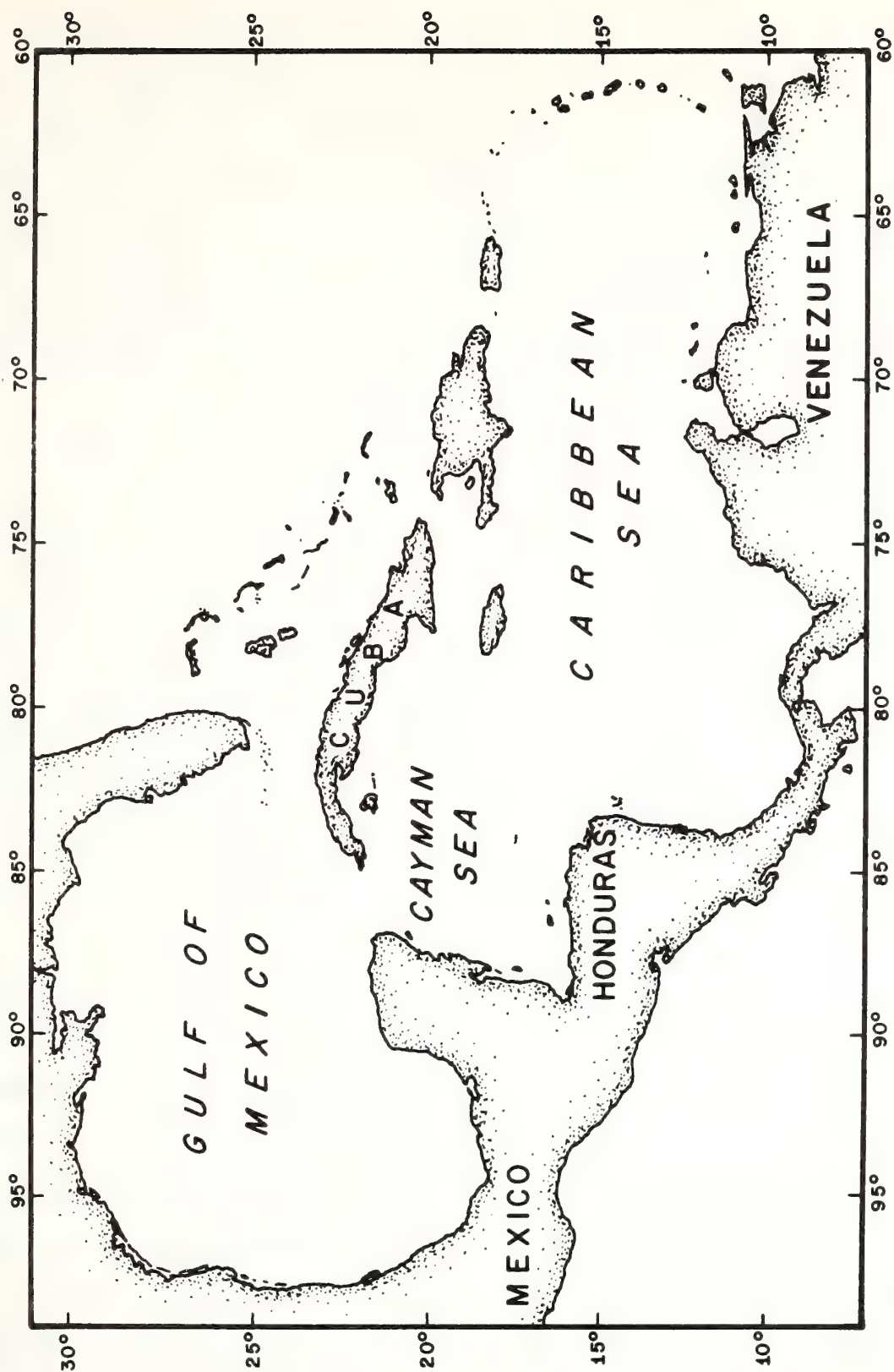


Figure 1. The Gulf of Mexico and Caribbean Sea (the northwestern Caribbean Sea study-area is also called the Cayman Sea).

Two ships of the NOAA National Ocean Survey were used in the AOML investigation. The NOAA ship DISCOVERER occupied hydrographic stations in the Caribbean Sea. The NOAA ship RESEARCHER collected both Lagrangian current and density data in the Caribbean Sea and the Gulf of Mexico. The primary objectives of the study were to investigate the formation of the Yucatan Current by Lagrangian measurements and to map the distribution of various chemical elements.

This report provides measurements and data taken by the RESEARCHER during the Lagrangian drifter portion of the experiment. The sections that follow describe the collection and analytical procedures applied. These techniques are presented to inform other users of these data, to describe the steps performed before the measurements were submitted to the National Oceanographic Data Center (NODC) of the NOAA Environmental Data Service, and to present data that are not archived by NODC.

2. DATA COLLECTION

Initially two 3-week cruises were planned to obtain the desired data. However, a hurricane threat shortened the second leg and necessitated an unscheduled stop in Miami, Fla. A third leg was then made in the Gulf of Mexico after the hurricane left the area.

The Lagrangian drifter tracked by the RESEARCHER is shown schematically in figure 2. The entire package weighed approximately 1,200 lbs (0.55 t). Each battery-powered Motorola radar transponder (model number SST-119XA) transmitted a coded signal, permitting radar screen identification of the buoy at ranges of 18 n. mi. (33 km) from the ship. The parachute drogue was deployed at 40 m (131 ft) to reduce the wind effect on the surface buoy.

As the RESEARCHER drifted with the buoys, ship positions were obtained every 15 minutes by an Omega system during legs I and II, and by a Loran system during leg III. Positions from a satellite navigation unit (International Telephone and Telegraph Aerospace Satellite Doppler Navigation Systems model 4007AB) were obtained, on the average, every 90 minutes. Concurrent relative drogue positions were obtained by the ship's gyrostabilized radar at each fix.

Density measurements were made while drifting, using the Edgerton, Germeshausen, and Grier Environmental Equipment Division Conductivity/Temperature/Depth (CTD) meter (model number 775-24, serial number 2), and Nansen bottle casts. Sippican Corporation System model R-203, expendable bathythermographs (XBT), and mechanical bathythermographs (MBT) were also used to obtain temperature data.

The positions of the four hourly CTDs and once-per-day Nansen casts of leg I (July 14 to August 2) and leg II (August

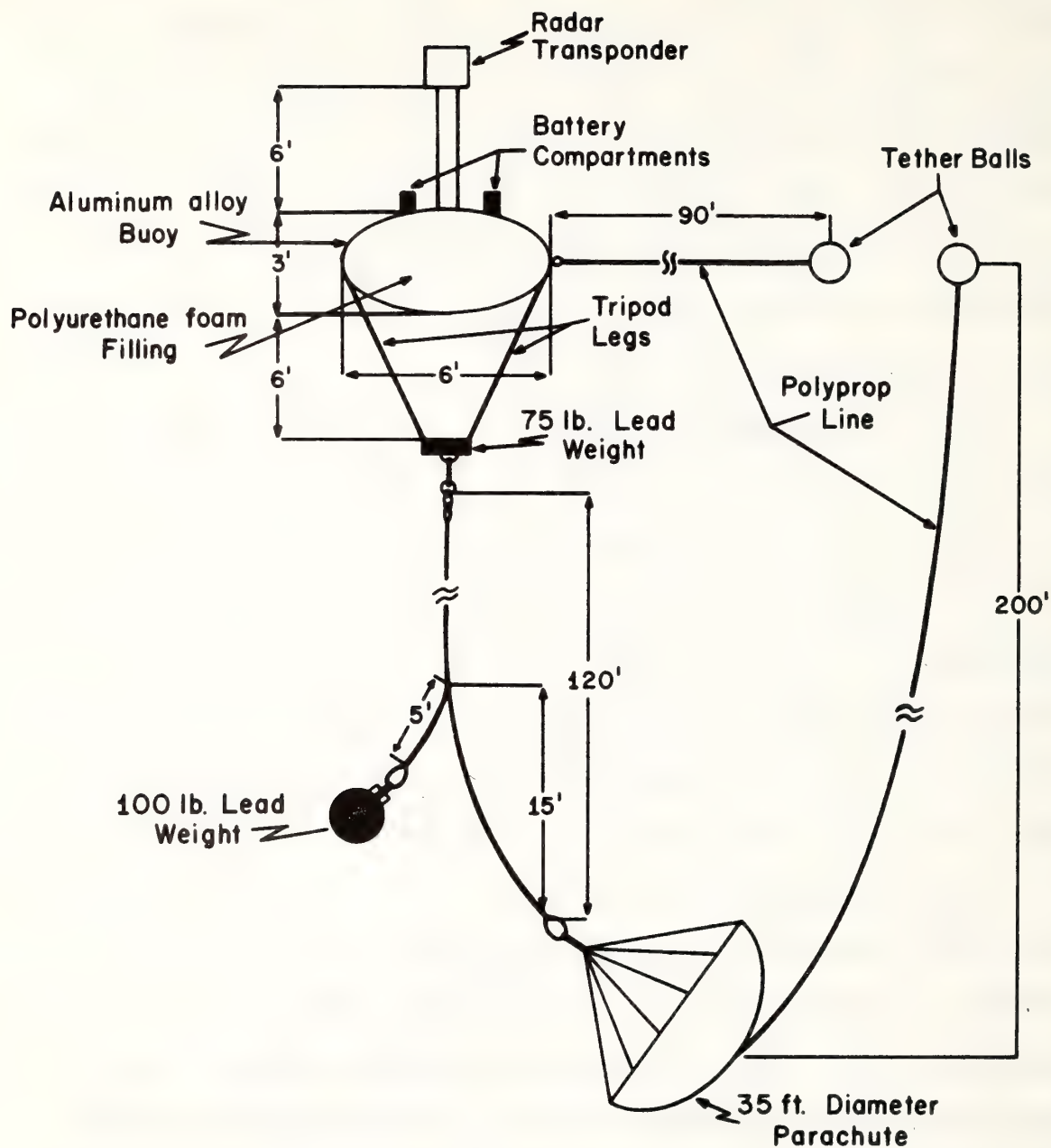


Figure 2. A schematic diagram of the Lagrangian drifter used in the experience.

10 to 21) are plotted in figure 3. Leg III (August 25 to September 1) stations are given in figure 4. Leg I and II XBTs are plotted in figure 5, and those of leg III are also in figure 4.

3. NAVIGATION AND BUOY DATA

Before launching the buoys, an XBT survey was made to determine the best deployment position. During these tracklines and the following drogue drift tracklines, satellite fixes were considered to be the prime navigational control. As these positions were obtained, they were checked to eliminate the obviously bad fixes. The accepted fixes were input to the ship's computer facility to produce a plot of the trackline, using dead-reckoning between the satellite positions. The plots produced for the predeployment lines were visually inspected for inconsistencies and, if none were found, the positions were accepted.

A more refined technique was necessary to produce the final drogue tracklines, as both Omega and satellite positions were used. The satellite fixes were further edited, considering four variables produced by the navigational package: the elevation of the satellite with respect to the horizon, the difference (residual) between the theoretical and measured slant ranges, the number of Doppler counts received, and the stability of the system's frequency standard. Fixes

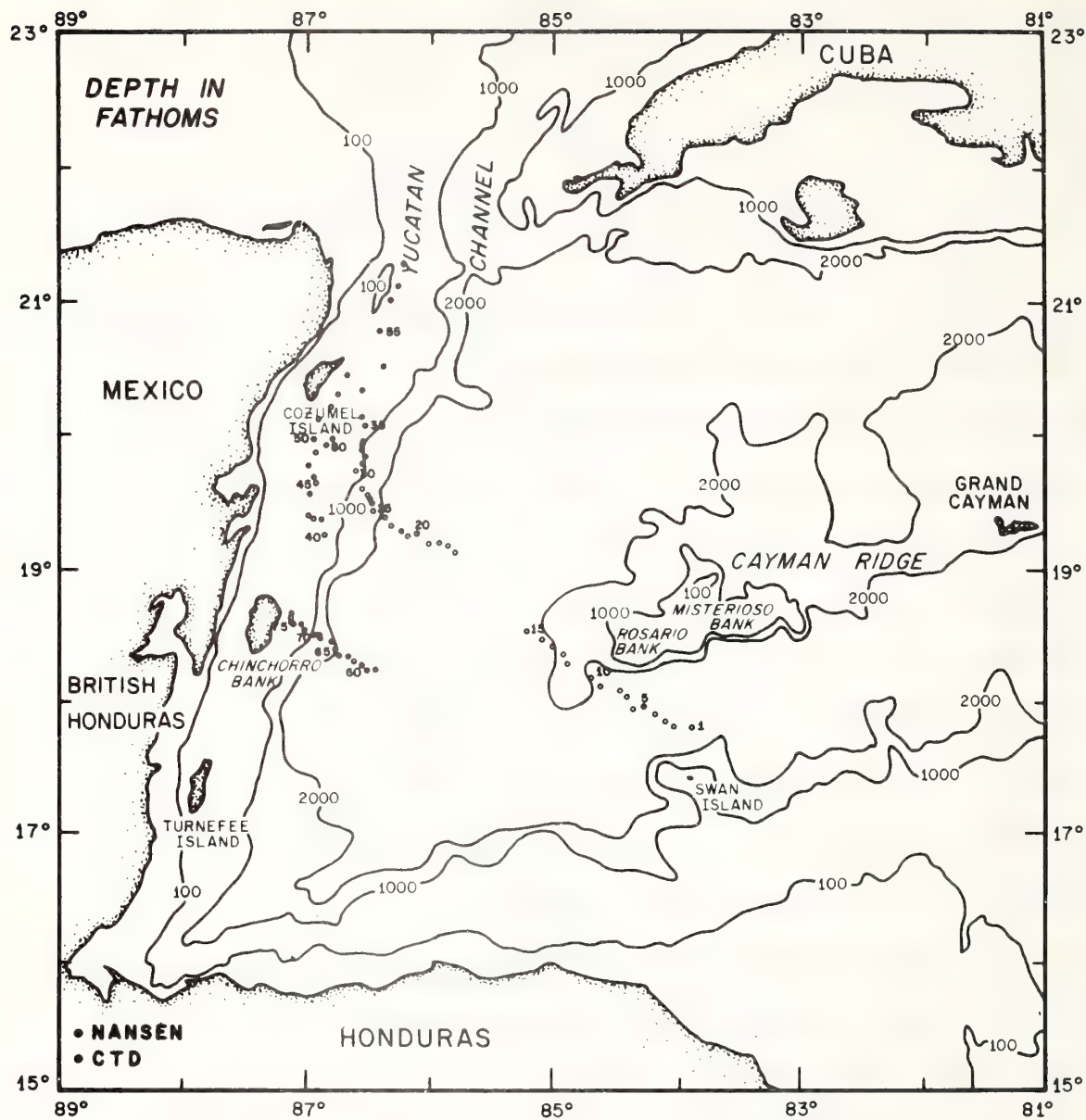


Figure 3. Positions of leg I and II CTD and Nansen casts. Station numbers 1 to 58 were occupied during leg I, and station numbers 59 to 81 during leg II.

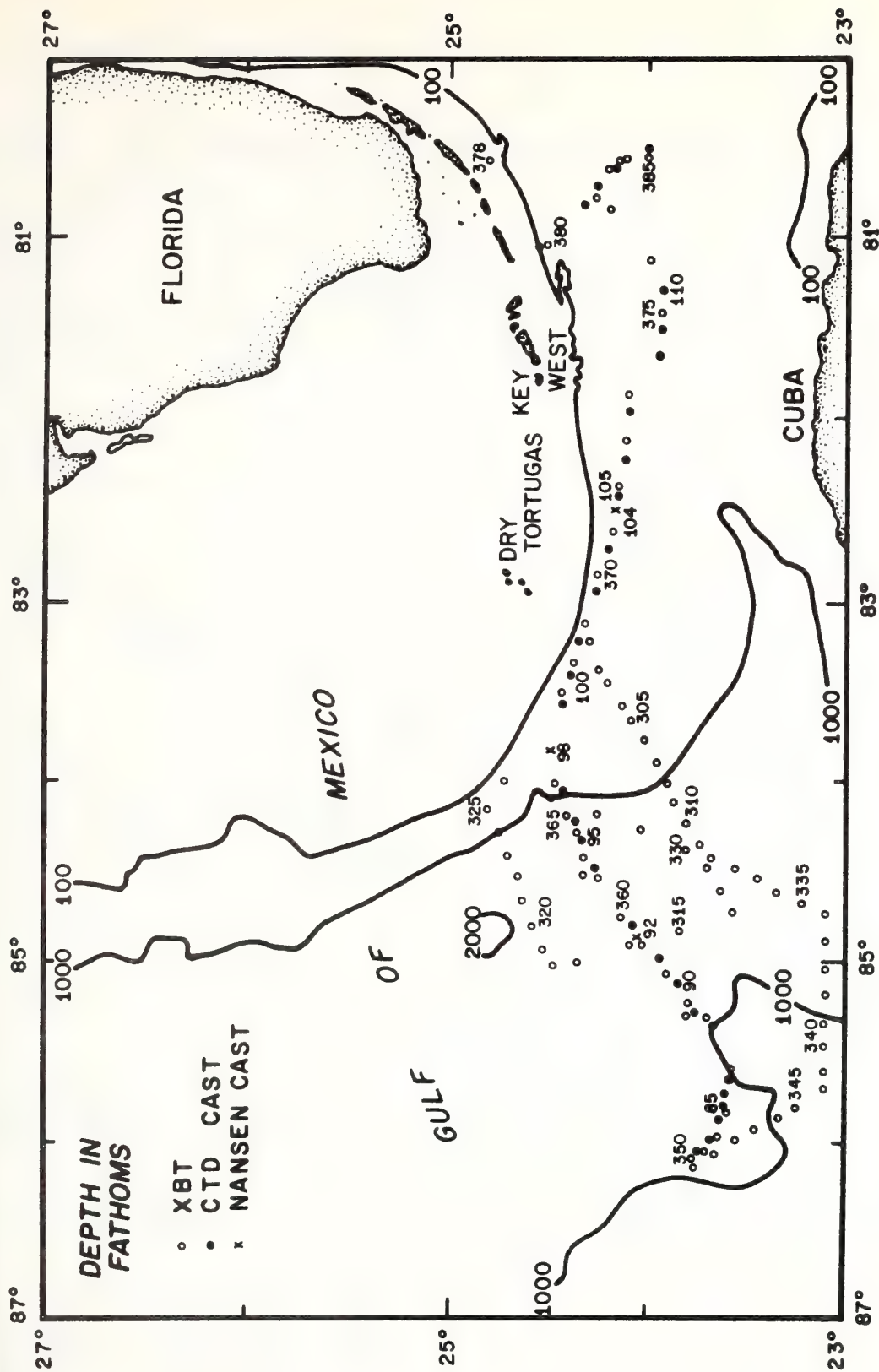


Figure 4. Positions of leg III CTD and Nansen casts and XBT lowerings.

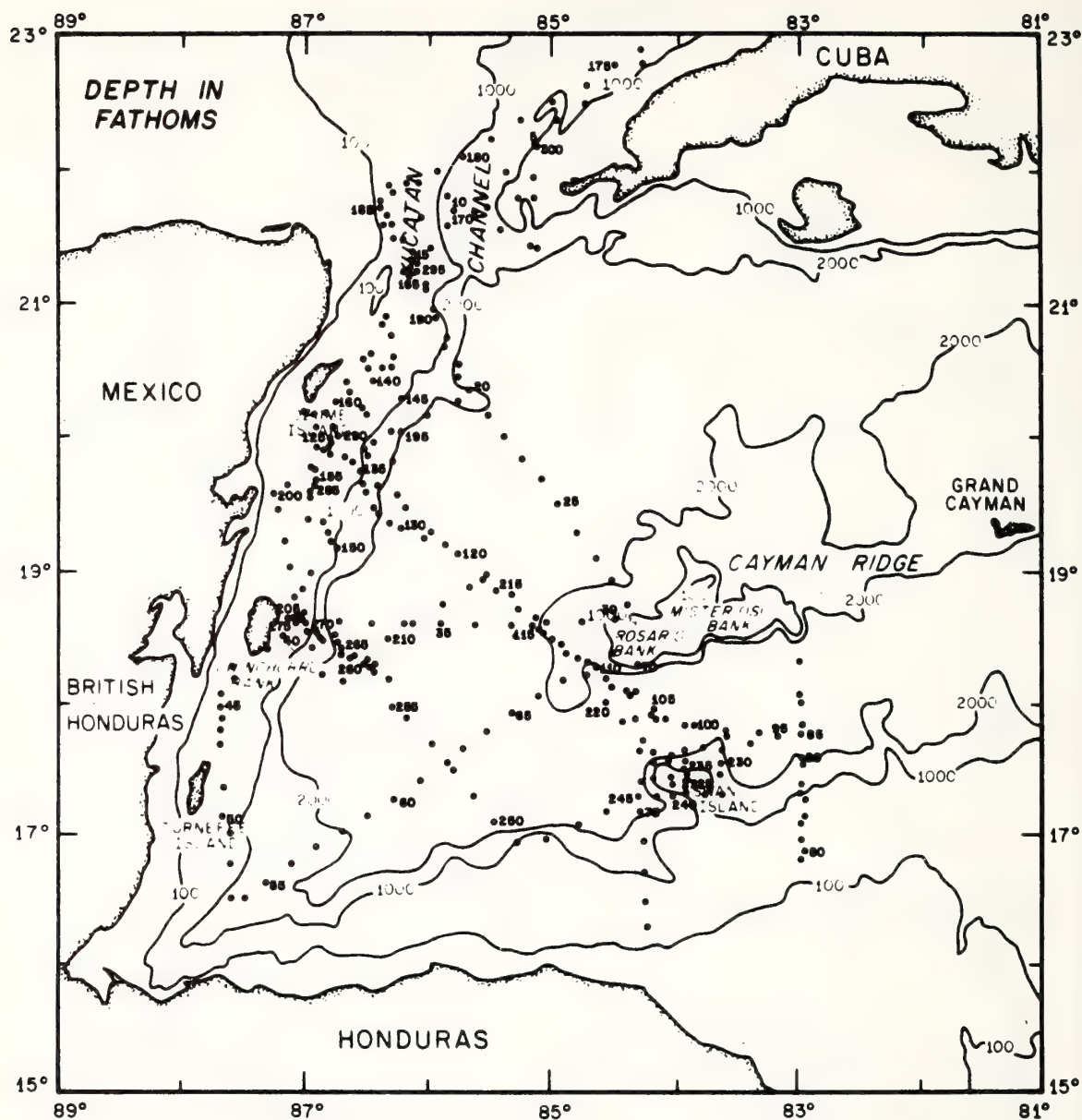


Figure 5. Positions of leg I and II XBT lowerings. Position numbers 1 to 175 were occupied during leg I, and position numbers 176 to 300 during leg II.

with Doppler counts of less than 4, satellite elevation angles of less than 15° and greater than 70° , residuals greater than 50, or instabilities in the frequency oscillator are suspect. These fixes were given closer scrutiny to determine their validity. Five satellites were monitored throughout the cruise, and plots similar to figure 6 were constructed to facilitate the edit.

The Omega positions were then adjusted to the accepted satellite data. The east-west and north-south component differences between the satellite and Omega fixes were computed and averaged to arrive at a corrector to apply to the Omega data. No significant variance existed between data collected when the ship was drifting and those collected while it was steaming. The mean longitude error was 1.416 km to the east, and the mean latitude error was 0.834 km to the south. Figure 7 gives the histogram of the difference data with a zero mean.

A further navigation edit was necessary to eliminate spurious relative-drogue positions and Omega fixes. The drogue data were verified to eliminate values that were incorrectly entered. To edit the navigation data, first a polynomial fit of the combined data was made. The latitude differences between the actual fixes and the polynomial-fit curve were computed and plotted (fig. 8). The erroneous positions appear as spikes on the curves.

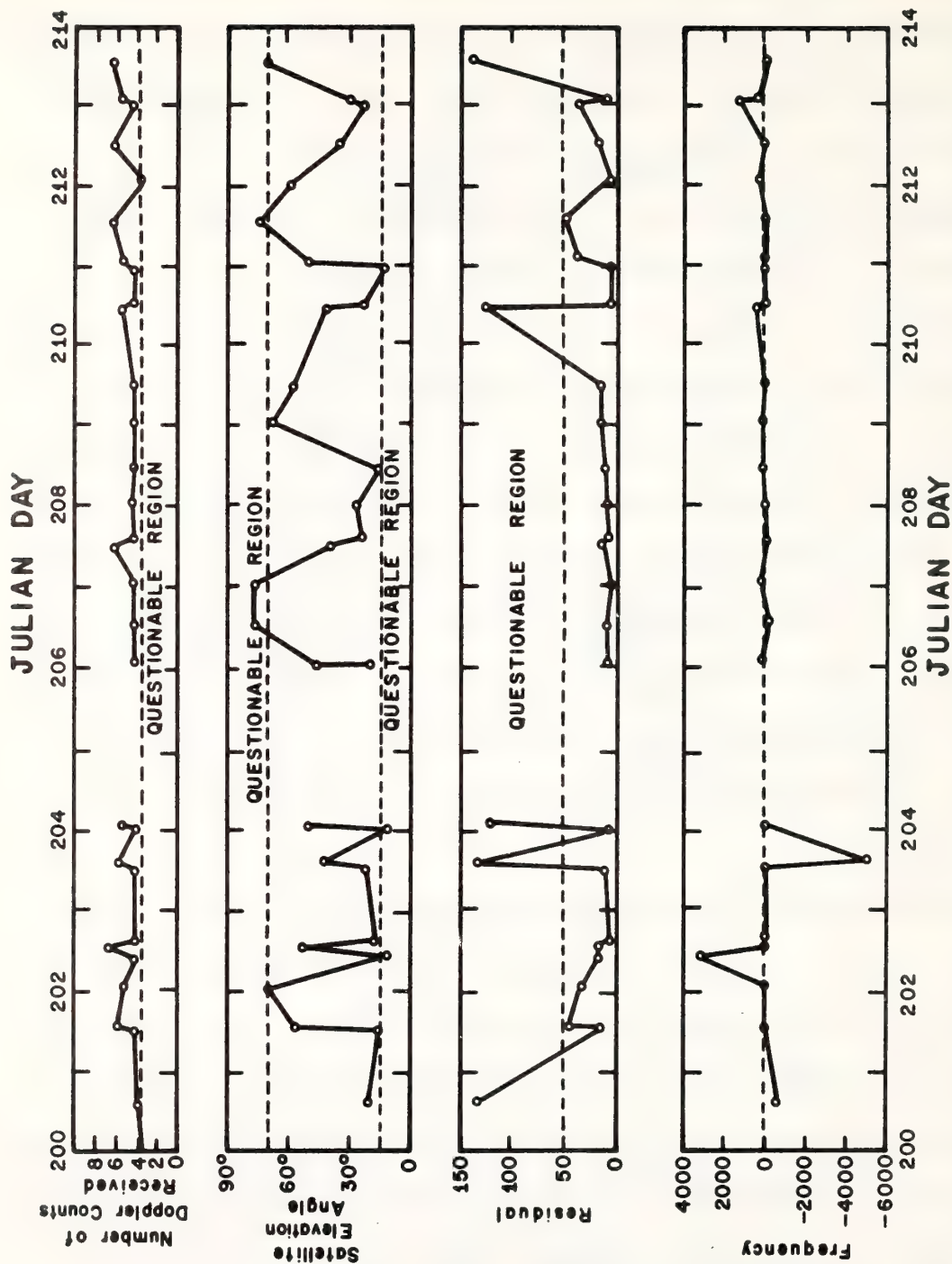


Figure 6. Time history of the four variables used to verify the satellite fixes. Variable values which can indicate questionable fixes are noted.

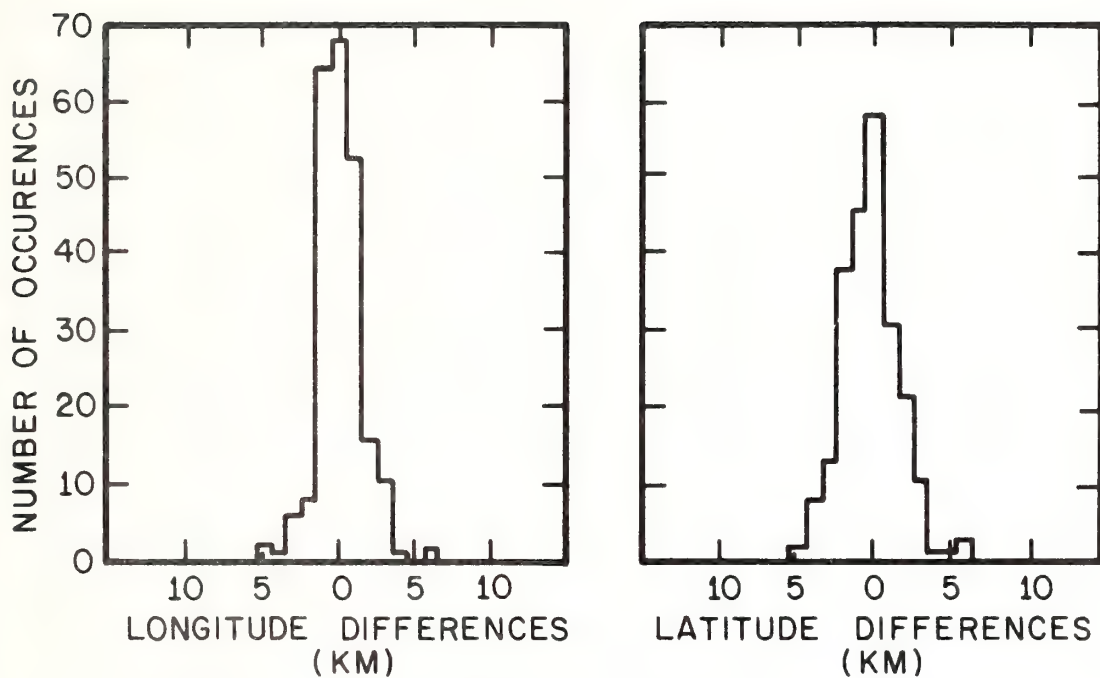


Figure 7. Zero-mean histograms of the component differences between satellite and Omega fixes.

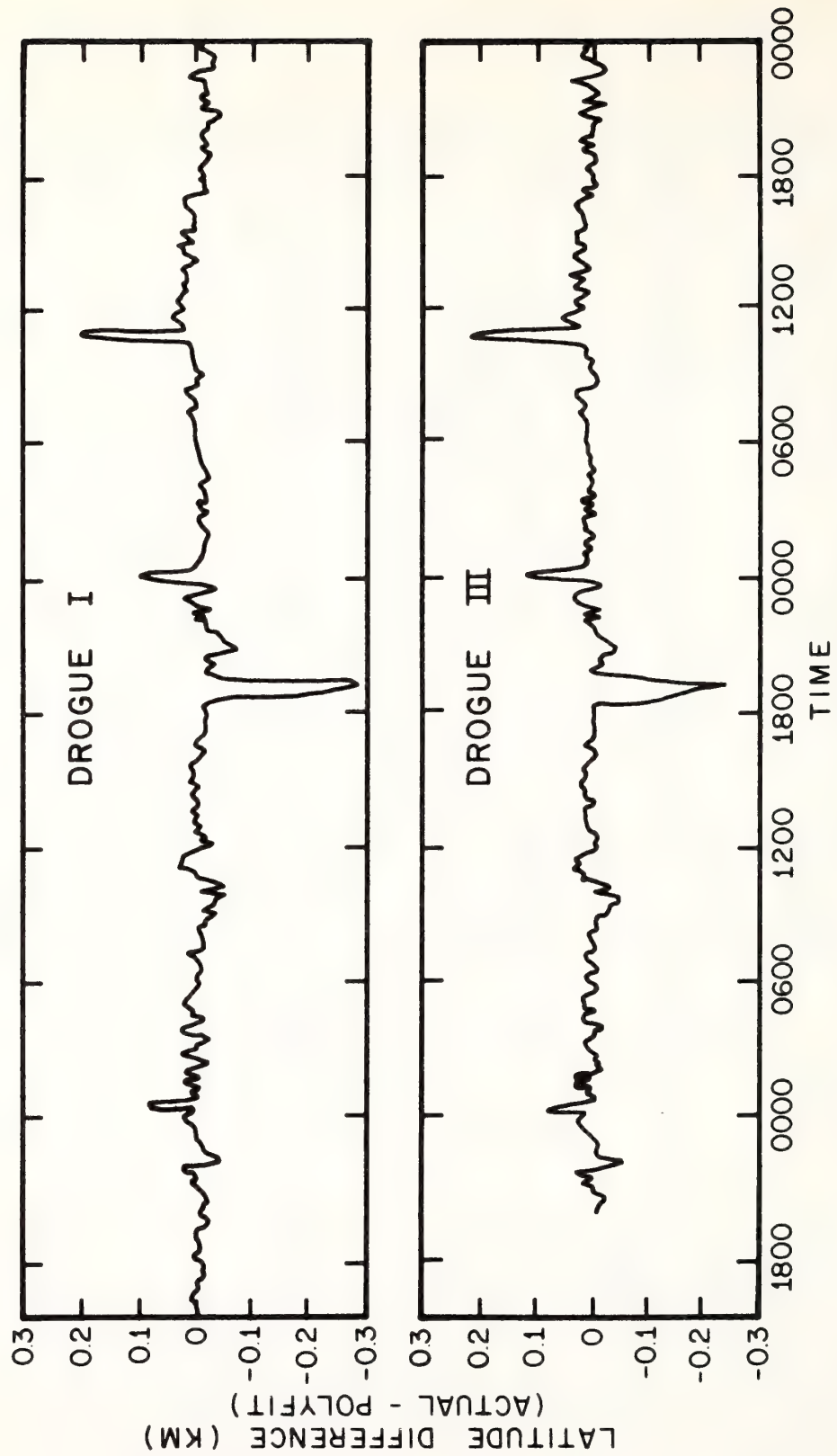


Figure 8. Latitude differences between actual fixes and a polynomial-fit curve as a function of time.

However, this procedure did not eliminate inconsistent fixes which were close to the polynomial-fit curve. The second scheme is based on the computation of component displacement distances between successive fixes. Those fixes which produced large distances were checked. Fifty percent of the inconsistent positions were caused by spurious Omega rates. This is approximately 4 percent of the total number of ship-drift Omega fixes. Mispunched data were corrected.

Appendix 1 lists the deployment, redeployment, and retrieval times of the four drogues used. Appendix 2 lists the times, ship positions, and drogue positions relative to the ship for the Caribbean Sea leg data. The questionable fixes are noted by an asterisk before the Julian Day, and satellite fixes are indicated by an S after the time.

Appendix 3 gives the ship and drogue data for the Gulf of Mexico leg. Although Loran rates were taken on this leg, no edit has yet been performed on these data. The satellite fixes have been edited in the manner previously described. The 15-minute positions listed were obtained by the ship's computer dead-reckoning program, discussed earlier.

4. DENSITY DATA

Standard physical oceanographic procedures, given in U.S. Navy Hydrographic Office Publication No. 614 (LaFond, 1951), were used to analyze the Nansen cast data. Salinity samples were analyzed on an inductive salinometer.

The temperature-salinity (T-S) curves for the Caribbean Sea and Gulf of Mexico are well documented, and T-S points, particularly in deep water, show little scatter from the curves. This consistent T-S relation was used to eliminate obviously bad temperature or salinity points. Figures 9 and 10 contain the Nansen bottle T-S data for the Caribbean Sea and Gulf of Mexico legs, respectively.

The CTD meter measures conductivity, which is converted to salinity on the ship's computer, using the equations of Bradshaw (Bradshaw and Schleicher, 1965). Bradshaw claims a salinity accuracy of 0.02 parts per thousand with the use of his expressions.

The CTD meter required calibration for what appeared to be a pressure effect on the conductivity sensor. The calibration was performed by comparing the CTD salinities with those values obtained from Nansen bottles hung on the CTD wire and from an adjacent Nansen cast. A T-S calibration rather than a salinity-depth calibration was used because of the time differences between CTD data collection and Nansen bottle tripping.

The uncorrected temperature-depth and salinity-depth values for each CTD station were smoothed by a linear regression computation. The regression was performed in overlapping 20-m segments to obtain salinity and temperature values every 10 m. Figure 11 gives some sample comparisons of smoothed and nonsmoothed data. The CTD meter was lowered at a rate

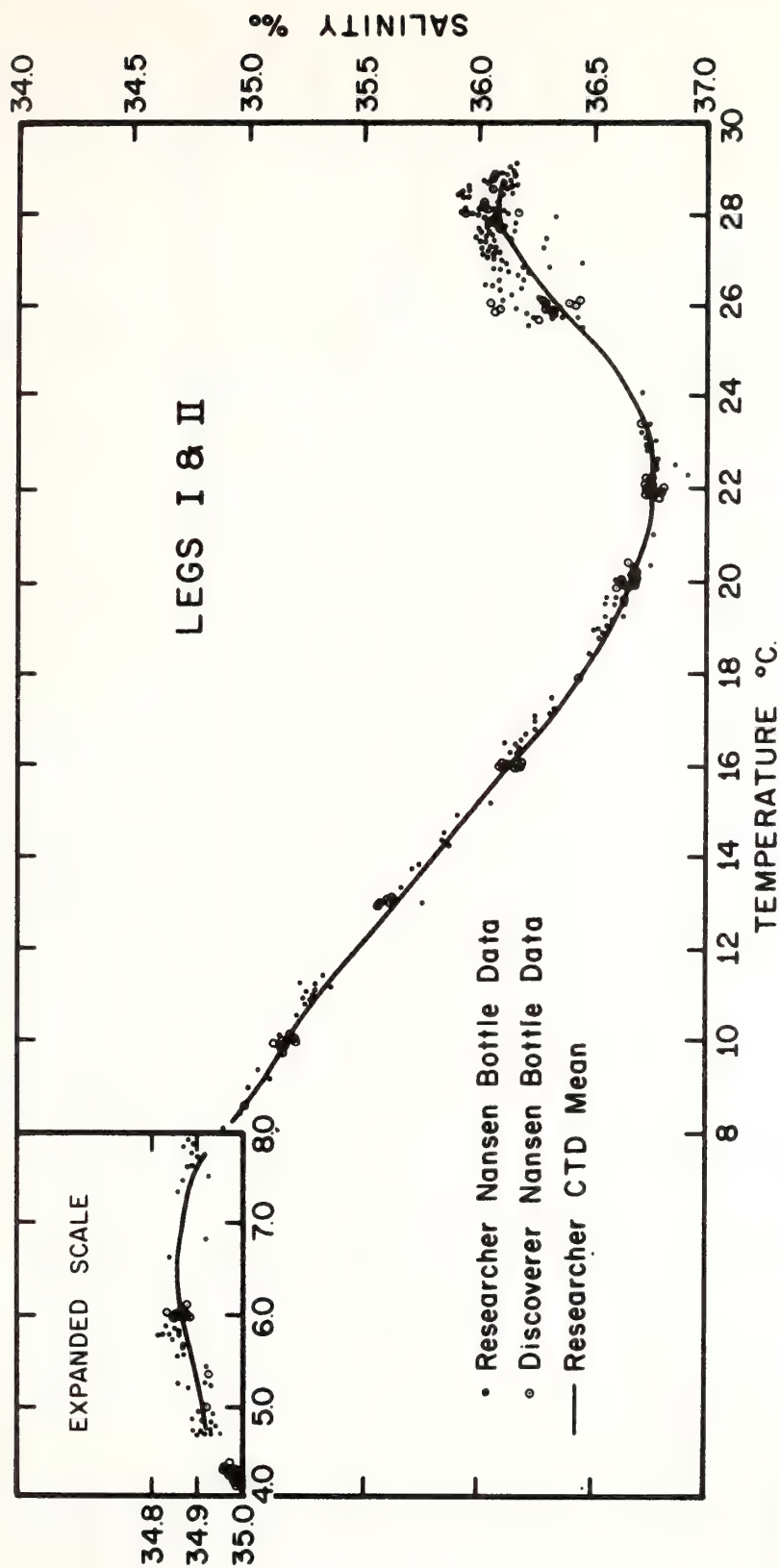


Figure 9. Nansen bottle T-S points obtained by the RESEARCHER and DISCOVER in the Caribbean Sea (legs I and II). Also plotted is the T-S curve obtained by averaging the corrected-CTD salinity values in 0.5°C-temperature increments for the Caribbean Sea.

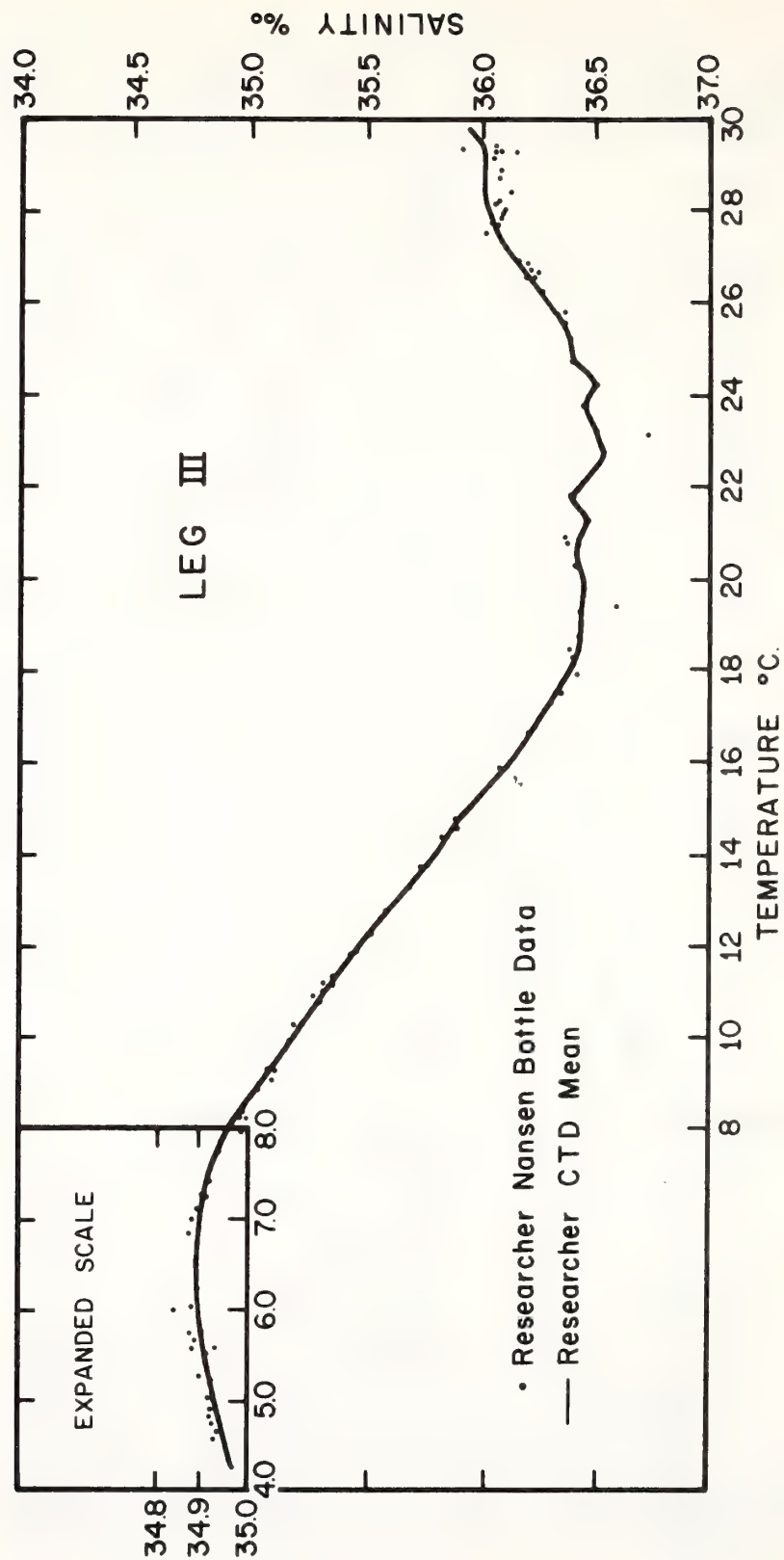


Figure 10. Nansen bottle T-S points obtained by the RESEARCHER in the Gulf of Mexico (leg III). Also plotted is the T-S curve obtained by averaging the corrected-CTD salinity values in 0.5°C-temperature increments for the Gulf of Mexico.

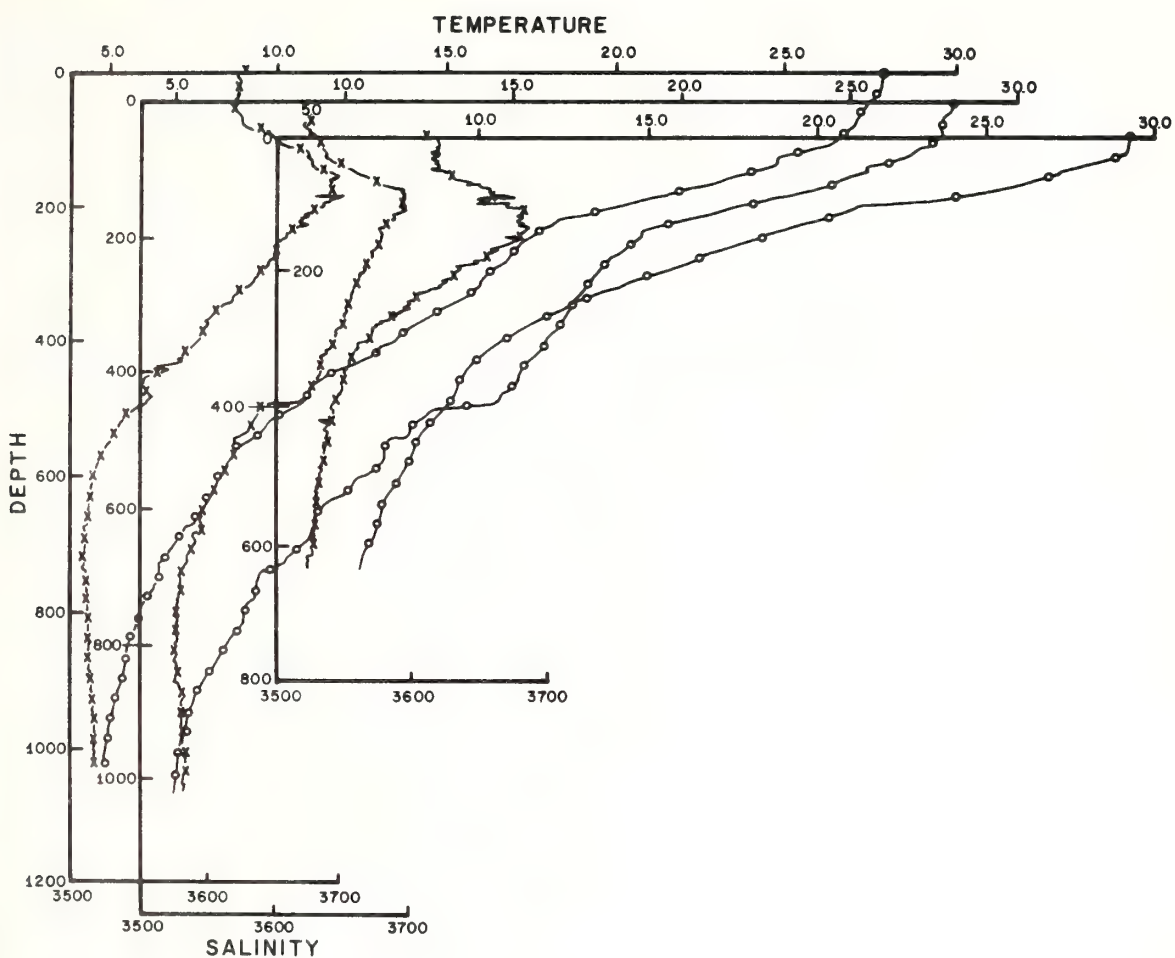


Figure 11. Comparison of smoothed temperature-depth and salinity-depth data points and nonsmoothed temperature-depth and salinity-depth curves.

of 3 m/min above 300 m and at 60 m/min below 300 m; samples were recorded every 3 seconds. Thus, approximately 13 points per 20 m in the upper 300 m and 7 points per 20 m below that depth were used in the regression.

The salinity error was not constant with time; the calibration of the conductivity sensor was drifting both slowly and in jumps. Figure 12 is a time-history of the salinity at the Antarctic Intermediate Water (AIW) and at 5.10°C , as obtained by the CTD meter. Historical data and those collected on the RESEARCHER (fig. 9) indicate a smaller salinity range at these values. This fact permits identification of periods of constant sensor calibration.

Four correction curves were developed for the four intervals of apparently constant-conductivity sensor calibration. The T-S data obtained from the Nansen bottles were compared to the corresponding CTD values. A second-degree polynomial fit of the CTD-Nansen salinity differences, as a function of temperature, was made to arrive at the calibration curve. Figure 13 gives the temperature and salinity-difference values used to determine the corresponding curve.

The CTD temperature-depth values have been compared with XBT and Nansen bottle data. The comparison indicates that individual CTD temperature values probably are accurate to $\pm .02^{\circ}\text{C}$.

The Nansen bottle and corrected-CTD salinity values at

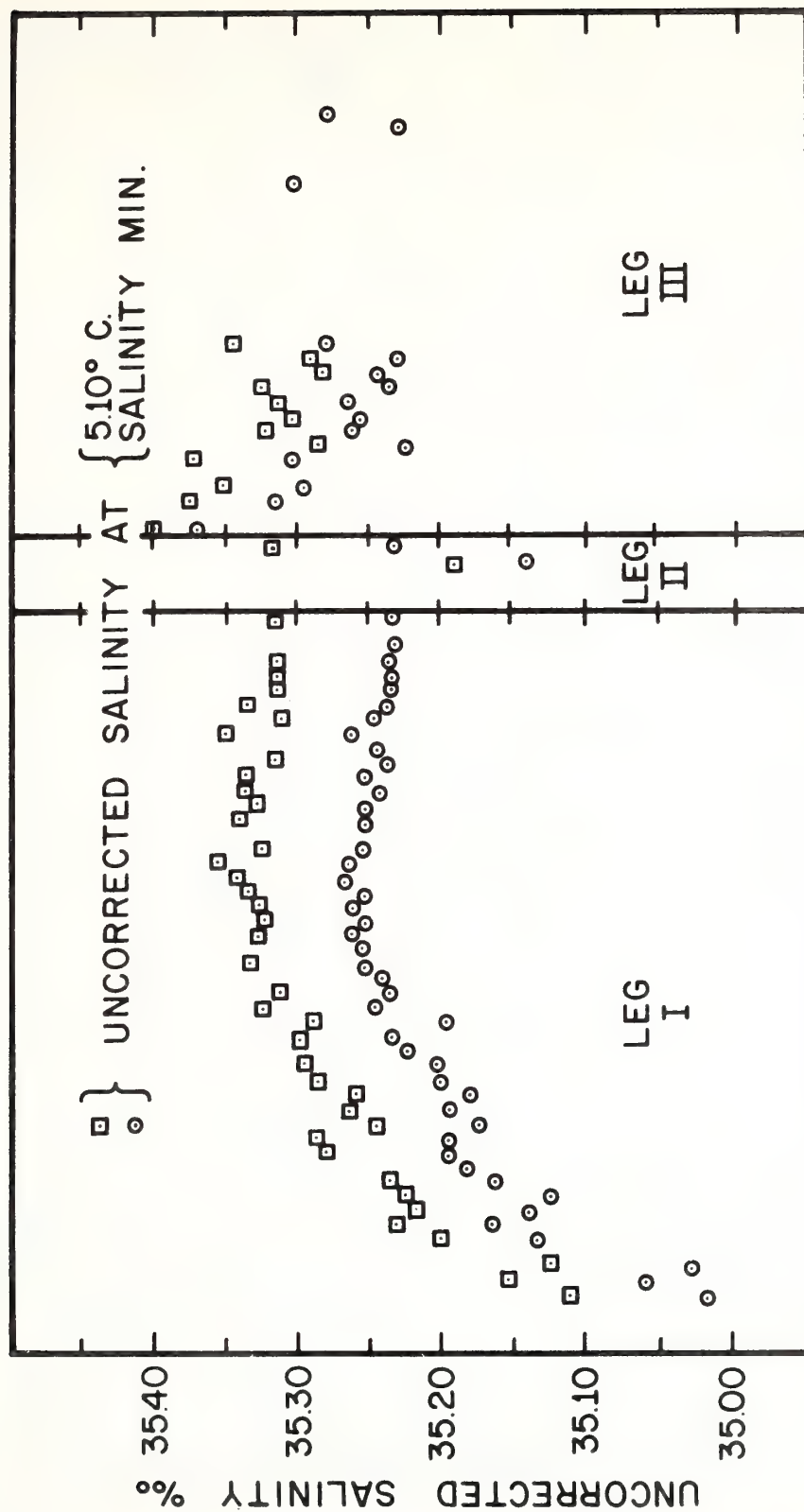


Figure 12. Uncorrected salinity data at the AIW salinity minimum and at 5.10°C, as measured by the CTD meter.

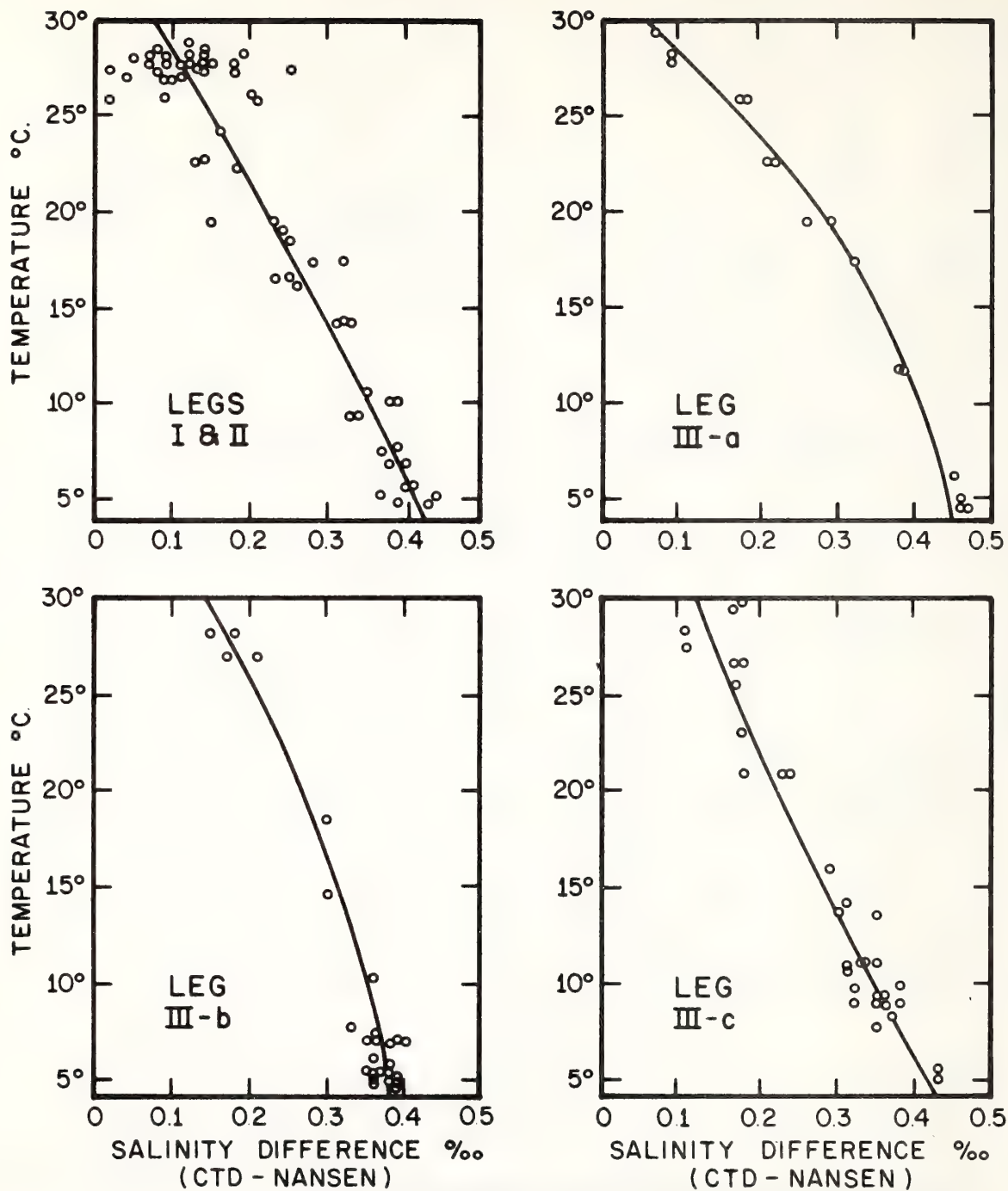


Figure 13. CTD-Nansen salinity-difference points and the corresponding second-degree polynomial-fit curves for the four periods of constant-conductivity sensor calibration.

constant temperature were compared. Nansen bottle and CTD salinity-value differences were averaged to arrive at the following difference means and standard deviations.

Leg	CTD stations	Number of points	Mean	Standard deviation
			‰	‰
I and II	18, 19, and 21 to 81	62	+ .001	0.04
III-a	82 to 86	25	0.000	0.02
III-b	87 to 96	38	- .001	0.03
III-c	97 to 114	43	- .012	0.05

During leg III-c, the CTD became erratic, causing the higher mean and higher standard deviation. The standard deviations can be considered a measure of the accuracy of an individual salinity value.

Mean T-S curves for the Gulf of Mexico and Caribbean Sea were obtained by averaging CTD salinity values in $\frac{1}{2}^{\circ}\text{C}$ intervals. The Caribbean Sea curve is given in figure 9 and the Gulf of Mexico curve in figure 10. The curves are within the envelope of Nansen bottle T-S points.

Appendix 4 lists in chronological order the Nansen and CTD depth, temperature, and salinity values. Only temperature-depth values are given for stations with suspect salinity data. As no surface bottles were used on the Nansen casts,

the salinity and temperature listed were collected from bucket samples. The CTD was normally turned on at 5 m; therefore, surface-bucket salinities and temperatures are listed for these casts.

5. EXPENDABLE AND MECHANICAL BATHYTHERMOGRAPHS

Periodic checks were made during the cruise legs to ensure that the XBT system remained in calibration. Comparison of CTD and XBT temperature traces indicated no systematic XBT malfunctions.

The XBTs were edited to find those without a check-cycle and to eliminate the obviously bad traces. The check-cycle initiated at the start of an XBT launch indicates the system is ready to be activated by the launch. Although XBTs with no ticks can be valid, tickless traces were compared with the preceding and following profiles to ensure their consistency.

The XBT traces were forwarded to NODC and now are filed under reference number 31-41898. A further edit of the XBTs was performed after their submittal to NODC, resulting in some position changes and in identification of some additional bad traces. Results of this edit will be forwarded to NODC.

The MBT temperature values were also checked for shifts in the instrument's calibration. Although the CTD-MBT

temperature differences increased somewhat with time, they remained within the accuracy of the MBT system. The temperature traces are filed at NODC under reference number 23472.

6. ACKNOWLEDGMENTS

The author expresses his thanks to the officers and crew of the RESEARCHER for the long and diligent hours they devoted to collecting these data. The manuscript was typed by Leola Williams and the figures were drawn by Robert Carrodus. The work was funded by the National Science Foundation under International Decade of Ocean Exploration grant AG-253.

7. REFERENCES

- Bradshaw, A., and K. E. Schleicher (1965), Effect of pressure on the electrical conductance of sea water, Deep-Sea Research, 12(2), 151-162.
- LaFond, E. C., (1951), Processing Oceanographic Data, U.S. Navy Hydrographic Office Publication No. 614, U.S. Government Printing Office, Washington, D.C., 114 pp.

APPENDIX 1. DROGUE DEPLOYMENT HISTORY

Day (Julian)/hour	Drogue 1	Drogue 2	Drogue 3	Drogue 4
July 19(200)/1800Z		Deploy	Deploy	Deploy
July 20(201)/1315Z	Deploy			
July 20(201)/2145Z				Retrieve
July 20(201)/2345Z				Deploy
July 22(203)/1430Z			Retrieve	
July 23(204)/1500Z				Retrieve
July 24(205)/1900Z	Redeploy		Deploy	
July 28(209)/1200Z	Retrieve	Retrieve	Retrieve	
July 29(210)/0245Z	Deploy	Deploy	Deploy	
July 29(210)/1315Z				Deploy
July 31(212)/1900Z		Retrieve		
August 1(213)/1200Z	Retrieve			
August 1(213)/1400Z			Retrieve	
August 1(213)/1530Z				Retrieve
August 16(228)/1530Z	Deploy	Deploy		Deploy
August 16(228)/1945Z			Deploy	
August 19(231)/2000Z			Retrieve	
August 20(232)/0745Z	Retrieve			
August 20(232)/1215Z		Retrieve		Retrieve
August 20(232)/2230Z		Deploy	Deploy	Deploy
August 21(233)/1215Z		Retrieve	Retrieve	Retrieve

APPENDIX 1. DROGUE DEPLOYMENT HISTORY--continued

Day (Julian)/hour	Drogue 1	Drogue 2	Drogue 3	Drogue 4
August 26(238)/2045Z		Deploy	Deploy	Deploy
August 27(239)/1945Z				Retrieve
August 27(239)/2030Z				Deploy
August 28(240)/0030Z	Deploy			
August 28(240)/1615Z				Retrieve
August 28(240)/1845Z				Deploy
August 30(242)/2145Z	Retrieve			
August 31(243)/1515Z			Retrieve	
August 31(243)/1645Z		Retrieve		
August 31(243)/1745Z				Retrieve

APPENDIX 2. CARIBBEAN SEA DRIFTING DATA

Column 1	* = Questionable fix		
Column 2	Julian Day		
Column 3	Greenwich time		
Column 4	S = satellite fix		
	Blank = Omega fix		
Column 5	Ship's latitude		
Column 6	Ship's longitude		
Columns 7	Range in n. mi. from ship to buoy 1		
	9		2
	11		3
	13		4
Columns 8	True bearing of buoy 1 from ship		
	10	2	
	12	3	
	14	4	

200	1800	17.6815	83.1411	-1.00	-1.0	1.39	237.5	2.40	88.0	1.65	31.0
200	1815	17.6605	83.1591	-1.00	-1.0	1.60	224.0	2.09	102.0	1.46	43.0
200	1830	17.6730	83.1525	-1.00	-1.0	1.88	223.5	1.99	113.0	1.40	51.5
200	1845	17.6572	83.1688	-1.00	-1.0	2.06	225.0	2.03	113.0	1.25	42.0
*200	1900	17.6584	83.2046	-1.00	-1.0	2.00	230.0	2.04	108.0	1.42	36.0
*200	1915	17.5702	83.2875	-1.00	-1.0	1.91	235.0	2.06	102.5	1.53	32.0
*200	1930	17.5385	83.1960	-1.00	-1.0	1.78	232.5	2.14	100.0	1.60	38.0
*200	1945	17.6852	83.2558	-1.00	-1.0	1.70	232.5	2.23	98.0	1.70	42.5
200	2000S	17.6748	83.1887	-1.00	-1.0	1.60	237.3	2.24	95.0	1.79	38.6
*200	2015	17.5942	83.2153	-1.00	-1.0	1.53	238.4	2.31	92.2	1.88	39.6
*200	2030	17.5689	83.2258	-1.00	-1.0	1.42	236.1	2.44	91.0	1.96	43.1
200	2045	17.6727	83.2133	-1.00	-1.0	1.41	231.0	2.52	93.0	2.01	47.2
200	2100	17.6640	83.2361	-1.00	-1.0	1.30	222.2	2.69	93.8	2.10	51.4
*200	2115	17.7044	83.2486	-1.00	-1.0	1.23	209.5	2.83	95.5	2.18	57.8
200	2130	17.6469	83.2400	-1.00	-1.0	1.22	196.5	2.96	94.7	2.32	62.9
200	2145	17.6800	83.2458	-1.00	-1.0	1.26	184.2	3.00	95.6	2.39	66.9
200	2146S	17.6776	83.2452	-1.00	-1.0	1.26	184.2	3.00	95.6	2.39	66.9
*200	2200	17.6150	83.2770	-1.00	-1.0	1.33	167.5	3.00	97.4	2.54	71.0
*200	2215	17.7407	83.1463	-1.00	-1.0	1.45	157.1	3.60	97.4	2.67	75.0
*200	2230	17.5790	83.2646	-1.00	-1.0	1.48	159.0	3.60	98.8	2.65	77.2
200	2245	17.6494	83.2811	-1.00	-1.0	1.47	180.5	3.00	101.0	2.43	76.2
*200	2300	17.5829	83.2881	-1.00	-1.0	1.49	207.6	2.83	102.2	2.12	72.8
200	2315	17.6667	83.2658	-1.00	-1.0	1.46	232.5	2.57	96.2	2.16	61.2
*200	2330	17.6272	83.3730	-1.00	-1.0	1.64	247.0	2.30	95.0	1.85	52.8
200	2345	17.6576	83.3328	-1.00	-1.0	1.65	245.6	2.36	97.8	1.91	57.2
201	0	17.6880	83.2926	-1.00	-1.0	1.53	239.0	2.58	99.5	2.04	65.2
201	15	17.7180	83.2661	-1.00	-1.0	1.68	241.8	2.44	100.2	1.96	63.3
201	30	17.7065	83.3015	-1.00	-1.0	1.77	248.1	2.27	101.5	1.92	59.2
201	45	17.6712	83.3106	-1.00	-1.0	1.92	256.0	2.21	98.0	1.92	52.0
201	46S	17.6747	83.2966	-1.00	-1.0	1.92	256.0	2.21	98.0	1.92	52.0
201	100	17.7050	83.3005	-1.00	-1.0	1.75	252.5	2.39	99.0	2.04	59.0
201	115	17.6935	83.3170	-1.00	-1.0	1.65	243.5	2.58	103.0	2.17	68.0
201	130	17.7072	83.3345	-1.00	-1.0	1.60	234.0	2.75	104.5	2.32	74.0
201	145	17.7020	83.3360	-1.00	-1.0	1.63	244.0	2.50	104.0	2.22	70.5
201	200	17.6992	83.3296	-1.00	-1.0	1.93	245.0	2.35	114.0	1.86	74.0
201	215	17.6772	83.3305	-1.00	-1.0	2.18	257.5	1.80	112.5	1.62	59.5
201	230	17.6872	83.3318	-1.00	-1.0	2.14	254.0	1.84	114.5	1.57	68.0
201	245	17.7024	83.3431	-1.00	-1.0	1.96	250.4	2.05	114.2	1.73	75.2
201	300	17.6954	83.3553	-1.00	-1.0	1.86	244.9	2.23	115.0	1.93	83.0
201	315	17.7105	83.3551	-1.00	-1.0	1.76	240.0	2.40	115.0	2.16	86.0
201	330	17.7029	83.3575	-1.00	-1.0	1.88	249.8	2.16	114.0	1.98	82.0
201	345	17.6992	83.3600	-1.00	-1.0	2.20	261.8	1.70	112.0	1.70	69.0
201	400	17.6854	83.3692	-1.00	-1.0	2.26	258.0	2.01	112.0	1.99	76.0
201	402S	17.6800	83.3805	-1.00	-1.0	2.26	258.0	2.01	112.0	1.99	76.0
201	415	17.6715	83.3785	-1.00	-1.0	2.09	255.0	2.24	112.0	2.22	80.0
201	430S	17.6742	83.3933	-1.00	-1.0	1.96	256.5	2.32	109.5	2.37	80.0
201	445	17.6649	83.3978	-1.00	-1.0	1.88	263.0	2.33	104.0	2.47	76.0
201	500	17.6779	83.4055	-1.00	-1.0	1.87	271.0	2.30	100.0	2.52	73.0
201	515	17.6804	83.4163	-1.00	-1.0	1.75	274.5	2.42	96.0	2.70	73.5
201	530	17.6864	83.4246	-1.00	-1.0	1.60	276.0	2.62	97.0	2.88	77.5
201	545	17.6750	83.4295	-1.00	-1.0	1.42	277.0	2.81	97.0	3.02	78.0
201	600	17.6475	83.4246	-1.00	-1.0	2.67	292.0	1.68	65.0	2.26	47.5
201	615	17.6457	83.4050	-1.00	-1.0	4.40	299.0	2.12	345.0	2.68	357.5
201	630	17.6594	83.4038	-1.00	-1.0	4.50	294.0	1.94	341.5	2.48	357.0
201	645	17.6539	83.4098	-1.00	-1.0	4.35	296.0	2.05	339.0	2.58	358.0
*201	700	17.6235	83.4175	-1.00	-1.0	4.33	298.0	2.12	358.0	2.63	2.0
*201	715	17.6850	83.4611	-1.00	-1.0	4.25	300.0	2.14	356.0	2.68	7.0
*201	730	17.6259	83.4515	-1.00	-1.0	4.00	301.0	2.12	2.5	2.68	15.0
201	745S	17.6581	83.4631	-1.00	-1.0	3.80	303.0	2.10	10.5	2.68	19.5
201	800	17.6467	83.4755	-1.00	-1.0	3.65	306.0	2.28	20.8	2.86	27.2
201	815	17.6454	83.4933	-1.00	-1.0	3.00	313.0	2.47	38.0	3.02	38.1
201	830	17.6635	83.4995	-1.00	-1.0	3.02	313.1	2.54	45.1	3.03	45.2
201	845	17.6787	83.5108	-1.00	-1.0	2.90	315.6	2.61	51.2	3.00	50.0
201	900	17.6604	83.5278	-1.00	-1.0	2.60	320.5	2.80	58.0	3.04	55.6

*201	915	17.8062	83.4868	-1.00	-1.0	2.40	330.2	3.00	62.5	3.51	59.6
201	930S	17.6719	83.5471	-1.00	-1.0	2.18	340.0	2.98	68.0	3.82	63.2
*201	945	17.6457	83.4888	-1.00	-1.0	2.06	348.5	3.44	72.7	4.16	68.2
201	1000	17.6822	83.5733	-1.00	-1.0	1.92	358.7	3.75	75.0	4.30	70.2
201	1015	17.6874	83.5716	-1.00	-1.0	1.82	12.0	3.92	78.9	4.60	73.2
201	1020S	17.6781	83.5939	-1.00	-1.0	1.82	12.0	3.92	78.9	4.60	73.2
201	1030	17.6915	83.5835	-1.00	-1.0	1.80	23.1	4.20	80.9	4.80	75.3
201	1045	17.6930	83.5960	-1.00	-1.0	1.82	36.5	4.42	83.0	5.05	77.5
201	1100	17.6765	83.6140	-1.00	-1.0	1.91	45.5	4.70	85.0	5.31	79.4
201	1115	17.6995	83.6230	-1.00	-1.0	2.15	55.0	4.90	86.6	5.60	81.0
201	1130	17.6904	83.6431	-1.00	-1.0	2.20	62.5	5.22	85.9	5.91	82.2
201	1145	17.7024	83.6525	-1.00	-1.0	2.40	66.1	5.40	87.0	6.13	83.0
201	1200	17.6977	83.6568	-1.00	-1.0	2.20	65.5	5.30	86.7	6.10	83.1
201	1212S	17.7196	83.6599	-1.00	-1.0	2.05	62.0	5.10	87.5	5.80	83.0
201	1215	17.6990	83.6621	-1.00	-1.0	2.05	62.0	5.10	87.5	5.80	83.0
201	1230	17.7085	83.6491	-1.00	-1.0	1.30	244.0	3.60	105.0	4.10	97.0
201	1245	17.7252	83.6081	-1.00	-1.0	2.85	252.5	2.03	140.0	2.33	114.3
201	1300	17.7280	83.6145	-1.00	-1.0	2.79	256.0	1.93	135.4	2.30	108.0
201	1315	17.7255	83.6036	1.65	290.5	3.75	270.3	1.20	186.0	1.22	116.0
201	1330	17.7112	83.6138	1.38	326.4	3.60	275.0	1.38	132.0	1.87	97.0
201	1345	17.7410	83.6338	.62	182.0	2.80	250.5	2.25	137.6	2.63	117.8
201	1354S	17.7297	83.6686	2.10	84.0	1.26	232.6	3.30	106.6	4.10	98.5
201	1400	17.7220	83.6711	2.10	84.0	1.26	232.6	3.30	106.6	4.10	98.5
201	1415	17.7220	83.7058	3.20	81.6	-1.00	-1.0	4.35	101.0	5.20	95.9
201	1430	17.7275	83.6883	1.88	64.6	1.63	271.0	2.99	101.1	3.60	95.0
201	1445	17.7254	83.6500	1.90	322.0	3.45	279.1	-1.00	-1.0	1.74	77.0
201	1500	17.7185	83.6390	2.88	294.0	4.60	275.0	1.26	259.2	-1.00	-1.0
201	1515	17.7325	83.6218	3.40	285.0	5.40	272.0	2.03	256.9	1.10	256.0
201	1526S	17.6958	83.6339	4.40	308.5	5.90	290.0	2.52	311.0	2.15	334.4
201	1530	17.7047	83.6330	4.40	308.5	5.90	290.0	2.52	311.0	2.15	334.4
201	1545	17.6874	83.6483	4.37	311.0	5.70	291.9	2.50	317.4	2.16	343.0
201	1600	17.6899	83.6591	4.30	313.3	5.70	293.0	2.48	322.5	2.22	349.7
201	1612S	17.7050	83.6613	4.20	315.0	5.50	293.6	2.37	327.0	2.22	356.0
201	1615	17.6957	83.6718	4.20	315.5	5.47	294.3	2.35	328.5	2.23	357.0
201	1630	17.7002	83.6791	4.10	317.0	5.30	295.3	2.27	335.8	2.23	6.3
201	1645	17.6967	83.6931	3.90	321.0	5.10	298.0	2.19	344.0	2.26	15.0
201	1700	17.6810	83.7095	3.80	322.5	4.90	299.0	2.14	353.0	2.34	22.5
201	1710S	17.7093	83.7064	3.75	324.5	4.75	301.0	2.10	356.0	2.36	27.0
201	1715	17.7220	83.7058	3.70	325.0	4.70	301.0	2.12	359.5	2.40	28.0
201	1730	17.6989	83.7315	3.65	328.0	4.55	302.0	2.08	7.0	2.49	35.0
201	1745	17.7142	83.7313	3.65	331.0	4.40	304.0	2.20	13.0	2.68	37.0
201	1800	17.7030	83.7433	3.80	332.0	4.50	307.5	2.37	13.0	2.76	36.0
201	1815	17.7087	83.7488	3.90	333.0	4.50	311.0	2.47	15.0	2.90	36.0
201	1830	17.7034	83.7620	3.95	336.0	4.50	311.0	2.60	17.0	3.00	36.0
201	1845	17.7382	83.7618	3.80	335.0	4.30	310.0	2.44	20.0	2.93	41.0
201	1900	17.7077	83.7853	3.40	335.0	4.40	309.5	2.23	27.5	2.80	47.0
201	1915	17.6790	83.7938	3.45	335.5	3.95	309.0	2.28	29.0	2.89	47.5
201	1930	17.7119	83.7855	3.55	333.0	4.05	309.0	2.27	25.0	2.87	46.5
201	1945	17.7019	83.8071	3.65	332.0	4.10	310.0	2.29	21.0	2.84	44.0
201	2000	17.6885	83.8155	3.78	331.2	4.24	310.0	2.32	17.5	2.82	39.4
201	2015	17.6969	83.8158	3.88	331.2	4.39	309.4	2.36	14.8	2.80	37.0
*201	2030	17.8139	83.7580	3.90	331.0	4.40	309.3	2.35	13.4	2.76	38.0
201	2045	17.7580	83.7920	3.50	328.8	4.00	306.9	1.96	14.0	2.45	41.5
201	2052S	17.7407	83.7880	3.50	327.5	4.00	307.1	1.90	15.9	2.40	43.1
201	2100	17.7494	83.8191	3.51	326.1	4.08	304.5	1.94	16.5	2.46	47.0
201	2115	17.7364	83.8345	3.35	324.2	3.98	301.3	1.72	21.0	2.30	52.0
201	2130	17.7230	83.8428	3.05	321.0	3.82	298.1	1.55	27.3	2.17	59.1
201	2145	17.7620	83.8081	3.10	308.0	4.10	289.4	1.14	353.2	1.60	65.0
*201	2200	17.6104	83.9425	3.49	299.1	4.55	283.9	1.44	308.5	-1.00	-1.0
201	2215	17.7565	83.8256	3.88	290.3	5.00	278.4	1.73	263.9	-1.00	-1.0
*201	2230	17.6620	83.8623	3.58	294.2	4.70	280.2	1.36	268.0	-1.00	-1.0
*201	2245	17.6807	83.8755	3.05	302.0	4.18	284.1	-1.00	-1.0	-1.00	-1.0
201	2300	17.7602	83.8693	2.82	308.6	3.53	285.6	-1.00	-1.0	-1.00	-1.0
*201	2315	17.8294	83.8618	2.55	320.4	2.98	292.0	1.66	79.0	-1.00	-1.0
201	2330	17.7707	83.9010	2.74	329.3	3.00	300.4	1.82	65.0	-1.00	-1.0
201	2332S	17.7718	83.8777	2.74	329.3	3.00	300.4	1.82	65.0	-1.00	-1.0
201	2345	17.7690	83.8885	3.15	324.5	3.48	298.3	1.67	51.8	1.08	312.8

202	0	17.7745	83.8940	3.10	321.0	3.70	296.0	1.54	39.0	1.38	303.5
202	15	17.8260	83.8713	3.50	313.9	4.10	293.0	1.36	9.5	1.79	294.5
202	30	17.7962	83.8860	3.80	308.0	4.50	290.5	1.39	336.0	2.17	289.0
202	45	17.7927	83.8770	4.20	306.5	5.00	290.0	1.71	316.0	2.60	288.0
202	100	17.7825	83.8756	4.60	303.0	5.50	288.5	2.08	304.0	3.10	287.0
202	115	17.7674	83.8875	4.55	304.0	5.40	290.0	1.95	309.5	2.88	289.0
202	130	17.7570	83.9021	4.40	306.0	5.30	291.0	1.86	316.0	2.78	291.5
202	142.5	17.7769	83.8938	4.50	309.0	5.20	292.5	1.94	321.0	2.77	297.0
202	145	17.7745	83.8940	4.55	311.0	5.25	293.5	1.95	326.0	2.79	298.0
202	200	17.7540	83.9073	4.60	314.0	5.30	297.0	2.16	334.5	2.84	305.0
202	215	17.7550	83.9171	4.50	316.0	5.05	299.0	2.12	344.0	2.70	312.0
202	230	17.7730	83.9276	4.20	319.0	4.80	301.0	2.01	357.5	2.48	316.0
202	245	17.7639	83.9361	4.15	321.0	4.60	301.0	2.04	6.0	2.36	320.0
202	300	17.7589	83.9491	4.00	324.0	4.80	302.0	2.06	17.0	2.22	326.0
202	315	17.7684	83.9593	3.80	327.0	4.20	303.5	2.08	23.5	2.10	331.5
202	316.5	17.7613	83.9599	3.80	327.0	4.20	303.5	2.08	23.5	2.10	331.5
202	330	17.7687	83.9665	3.70	329.0	3.95	305.0	2.18	33.0	2.02	340.0
202	345	17.7820	83.9813	3.60	331.5	3.80	307.4	2.33	40.5	1.94	350.0
202	400	17.7860	83.9860	3.43	336.0	3.58	310.0	2.49	46.4	1.91	.7
202	415	17.7775	83.9971	3.70	340.0	3.80	312.3	2.62	52.3	1.92	11.0
202	430	17.7829	84.0135	3.28	343.5	3.10	313.8	2.82	57.0	1.94	20.0
202	445	17.7869	84.0231	3.10	351.0	2.90	317.0	3.00	60.0	2.00	30.0
202	500	17.7854	84.0338	3.00	352.0	3.00	321.0	2.90	62.0	2.09	37.3
202	515	17.7907	84.0438	2.95	357.5	2.84	326.2	3.28	65.5	2.22	45.5
202	530	17.8044	84.0426	3.10	2.5	2.72	331.0	3.48	67.5	2.39	50.0
202	545	17.7920	84.0491	2.75	6.5	2.59	335.5	3.60	68.0	2.52	55.0
202	600	17.7979	84.0618	2.90	12.0	2.51	342.0	3.90	71.5	2.70	59.0
202	615	17.8065	84.0738	2.95	17.0	2.43	349.5	4.15	72.0	2.90	62.5
202	630	17.8069	84.0808	3.25	22.5	2.39	357.5	4.40	74.5	3.15	65.0
202	645	17.8047	84.0888	3.35	26.5	2.37	5.0	4.60	74.0	3.00	67.5
202	700	17.8149	84.1016	3.50	30.5	2.42	14.0	4.90	75.0	3.50	69.0
202	715	17.8140	84.0758	3.60	356.5	3.00	330.5	3.40	55.0	2.48	32.0
202	730	17.8117	84.0331	5.10	314.0	5.50	297.0	2.57	243.0	3.04	309.0
202	745	17.8062	84.0391	5.10	316.0	5.45	299.0	2.40	249.5	3.00	313.0
202	800	17.8102	84.0438	4.85	318.5	5.23	300.0	2.36	357.2	2.87	316.2
202	815	17.8050	84.0453	4.71	321.0	5.05	301.4	2.40	5.8	2.74	321.6
202	830	17.8094	84.0570	4.58	323.8	4.80	303.5	2.42	15.7	2.60	326.5
202	834.5	17.8200	84.0786	4.58	323.8	4.80	303.5	2.42	15.7	2.60	326.5
202	845	17.8289	84.0685	4.40	325.2	4.60	306.0	2.45	22.2	2.46	332.2
202	900	17.8287	84.0845	4.30	328.5	4.40	306.4	2.50	31.0	2.36	340.0
202	915	17.8227	84.0993	4.32	329.0	4.40	307.4	2.58	31.5	2.44	341.1
202	930	17.8267	84.1040	4.40	331.5	4.40	308.9	2.71	31.3	2.50	344.0
202	934.5	17.8253	84.1144	4.40	331.5	4.40	308.9	2.71	31.3	2.50	344.0
202	945	17.8291	84.1191	4.30	334.2	4.18	313.0	2.82	38.3	2.45	352.0
202	1000	17.8353	84.1274	4.17	337.2	4.02	315.0	3.00	41.2	2.44	.8
202	1015	17.8435	84.1321	4.02	340.7	3.88	319.3	2.96	45.2	2.44	8.3
202	1030	17.8352	84.1548	3.91	344.5	3.53	323.9	2.99	50.4	2.46	15.8
202	1045	17.8405	84.1648	3.85	348.2	3.43	325.9	3.42	55.8	2.54	24.7
202	1100	17.8185	84.1771	3.79	355.8	3.25	329.5	3.64	59.0	2.69	32.2
202	1115	17.8557	84.1690	3.75	358.4	3.00	337.2	3.92	62.0	2.87	37.0
202	1118.5	17.8481	84.1898	3.75	358.4	3.00	337.2	3.92	62.0	2.87	37.0
202	1130	17.8295	84.2041	3.69	2.0	3.00	339.9	4.20	64.4	2.94	43.8
202	1145	17.8550	84.2053	3.71	6.5	2.94	345.4	4.45	63.8	2.97	48.2
202	1200	17.8564	84.2106	3.90	7.1	3.10	347.0	4.60	64.9	2.80	45.5
202	1215	17.8507	84.2211	4.50	4.0	2.90	346.0	4.70	67.0	3.30	43.0
202	1230	17.8564	84.1716	4.90	319.5	4.95	302.0	2.36	15.0	2.80	325.1
202	1245	17.8575	84.1381	6.30	304.6	6.70	292.0	2.59	320.5	3.90	298.0
202	1300	17.8584	84.1523	6.21	306.5	6.60	293.0	2.50	326.0	3.80	301.0
202	1306.5	17.8702	84.1467	6.20	306.8	6.50	292.5	2.48	329.5	3.70	303.0
202	1315	17.8655	84.1588	6.00	307.4	6.25	293.0	2.85	332.0	3.60	303.0
202	1330	17.8719	84.1671	5.85	309.4	6.05	294.0	2.26	339.0	3.40	305.0
202	1345	17.8732	84.1725	5.85	309.0	6.00	294.0	2.24	341.5	3.35	306.0
202	1400	17.8772	84.1771	5.90	310.0	6.00	295.5	2.24	345.5	3.30	308.1
202	1415	17.8830	84.1783	5.90	310.0	6.10	295.0	2.35	345.0	3.45	309.0
202	1430	17.8809	84.1861	6.10	310.0	6.20	295.5	2.45	343.0	3.60	308.0
202	1445	17.8757	84.1876	6.15	311.0	6.20	297.0	2.49	346.0	3.65	301.0
202	1454.5	17.8812	84.2028	6.15	312.0	6.15	298.0	2.51	351.0	3.55	313.5
202	1500	17.8742	84.1981	6.05	313.5	6.10	299.0	2.53	354.0	3.45	314.0

202	1515	17.8792	84.2126	5.90	315.0	5.85	300.0	2.50	1.5	3.30	319.5
202	1520S	17.8886	84.2222	5.85	315.0	5.75	301.0	2.48	4.0	3.30	320.0
202	1530	17.8882	84.2201	5.70	317.0	5.60	301.5	2.50	8.5	3.00	322.0
202	1545	17.8880	84.2360	5.55	319.0	5.40	303.5	2.60	17.0	3.00	326.0
202	1600	17.8835	84.2403	5.35	320.5	5.15	306.0	2.65	25.0	2.96	331.5
202	1615	17.8974	84.2506	5.15	321.5	4.90	307.0	2.66	33.0	2.82	335.0
202	1630	17.8864	84.2625	5.00	324.5	4.65	308.5	2.74	37.5	2.70	339.5
202	1645	17.8960	84.2726	4.80	325.5	4.45	310.0	2.86	44.5	2.58	345.0
202	1700	17.9030	84.2836	4.60	329.0	4.15	312.5	3.00	51.0	2.49	353.0
202	1715	17.9025	84.2925	4.40	330.0	3.95	313.0	3.00	54.0	2.37	359.0
202	1730	17.9004	84.3003	4.30	330.0	3.90	313.5	3.00	55.5	2.38	2.0
202	1745	17.8990	84.3065	4.45	330.5	3.95	315.0	3.00	53.5	2.42	.5
202	1800	17.9229	84.3066	4.50	331.0	3.90	314.0	2.90	53.0	2.50	0.0
202	1815	17.9107	84.3131	4.52	329.5	4.03	315.0	3.00	53.0	2.59	359.0
202	1830	17.9234	84.3138	4.68	329.0	4.13	315.6	2.90	51.0	2.66	358.6
202	1845	17.9222	84.3198	4.50	328.0	4.00	315.0	2.95	55.0	2.53	358.0
202	1900	17.9180	84.3311	4.30	328.0	3.82	312.4	2.98	57.8	2.40	0.0
202	1915	17.9220	84.3358	4.30	327.0	3.80	312.7	2.97	60.0	2.40	1.0
202	1930	17.9490	84.3265	4.38	327.3	3.80	312.3	3.00	58.0	2.49	0.0
202	1945	17.9432	84.3368	4.50	326.0	3.90	312.5	2.96	55.0	2.65	358.5
202	1956S	17.9468	84.3274	4.60	327.6	3.98	313.0	2.97	56.0	2.66	358.4
202	2000	17.9492	84.3380	4.60	327.5	4.00	312.5	2.92	54.5	2.66	358.5
202	2015	17.9307	84.3476	4.65	326.4	4.00	312.1	2.93	54.4	2.71	358.1
*202	2030	17.9762	84.3400	4.62	325.0	3.96	311.0	2.87	54.2	2.72	356.0
202	2045	17.9484	84.3511	4.55	325.5	3.88	311.2	2.79	56.0	2.67	357.3
*202	2058S	17.9641	84.3438	4.55	323.6	3.95	310.6	2.72	56.0	2.66	356.5
202	2100	17.9264	84.3635	4.53	324.1	3.90	309.5	2.69	56.0	2.64	355.0
202	2115	17.9587	84.3481	4.52	322.1	3.88	307.0	2.64	58.0	2.64	353.5
202	2130	17.9369	84.3603	4.43	321.1	3.78	307.0	2.58	60.0	2.54	355.1
*202	2145	18.0882	84.3255	4.47	321.0	3.78	305.3	2.50	60.9	2.51	355.0
202	2200	17.9744	84.3593	4.48	318.9	3.84	303.9	2.38	61.1	2.50	351.8
202	2215	17.9585	84.3685	4.50	317.0	3.81	301.7	2.25	62.1	2.38	350.0
202	2230	17.9707	84.3618	4.50	314.0	3.88	300.9	2.17	61.8	2.38	347.9
202	2245	17.9757	84.3648	4.50	313.7	3.91	299.8	2.09	64.0	2.36	344.3
202	2300	17.9947	84.3736	4.51	310.9	3.95	296.8	1.95	64.7	2.36	341.1
202	2315	17.9925	84.3725	4.50	310.0	4.00	293.7	1.78	67.2	2.28	339.1
202	2330	18.0099	84.3778	4.60	307.5	4.10	293.2	1.73	68.5	2.32	335.3
202	2345	18.0017	84.3845	4.60	305.9	4.10	291.8	1.64	72.0	2.24	334.0
203	0	18.0135	84.3868	4.60	305.0	4.30	290.5	1.64	76.0	2.25	331.0
203	15	18.0312	84.3903	4.60	303.6	4.25	289.0	1.62	81.4	2.20	330.0
203	30	18.0380	84.3896	4.65	301.5	4.30	287.5	1.57	83.1	2.18	325.5
203	45	18.0377	84.3941	4.70	300.0	4.35	287.0	1.43	86.5	2.20	323.5
203	100	18.0229	84.4013	4.62	299.2	4.30	285.0	1.52	94.2	2.17	323.0
203	115	18.0382	84.4011	4.65	299.0	4.35	285.5	1.48	96.0	2.18	322.6
203	130	18.0329	84.4071	4.70	315.5	4.40	302.5	1.48	107.5	2.16	337.5
203	145	18.0312	84.4061	4.80	309.9	4.50	296.5	1.43	103.0	2.18	333.0
203	200	18.0319	84.4088	4.53	313.0	4.40	299.0	1.54	113.0	2.08	337.2
203	215	18.0572	84.4100	4.30	316.0	4.13	312.5	1.66	136.5	1.92	351.0
203	230	18.0460	84.4148	4.40	336.5	4.20	321.0	1.74	152.0	1.80	359.0
*203	245	18.0035	84.4288	4.52	317.2	4.38	303.0	1.64	133.0	1.82	337.5
203	300	18.0287	84.4185	4.65	298.0	4.55	285.0	1.54	115.0	1.92	312.5
203	315	18.0384	84.4126	4.60	292.0	4.60	278.0	1.54	117.0	1.90	310.0
203	330	18.0384	84.4286	4.60	300.0	4.56	288.0	1.62	115.5	1.83	312.0
203	345	18.0349	84.4311	4.60	298.5	4.55	282.0	1.58	100.3	1.83	312.2
203	400	18.0497	84.4396	4.40	267.5	4.40	274.0	1.77	107.0	1.66	305.0
203	415	18.0529	84.4438	4.50	296.0	4.60	283.0	1.70	110.0	1.77	311.0
*203	416S	18.0546	84.4886	4.50	296.0	4.60	283.0	1.70	110.0	1.77	311.0
203	430	18.0560	84.4480	4.60	295.5	4.63	281.5	1.66	108.4	1.84	311.4
*203	432S	18.0564	84.4939	4.75	304.0	4.86	293.0	1.50	113.0	1.98	317.0
203	445	18.0480	84.4546	4.90	294.0	5.00	281.8	1.42	96.3	2.08	307.5
203	500	18.0572	84.4578	5.05	300.0	5.20	290.0	1.32	99.0	2.22	315.0
203	515	18.0519	84.4636	5.00	285.0	5.20	283.0	1.35	69.5	2.17	30.5
203	530	18.0647	84.4598	5.10	293.5	5.25	286.0	1.35	79.0	2.16	304.0
203	545	18.0652	84.4670	5.00	303.0	5.20	293.0	1.49	61.0	2.12	319.5
203	600	18.0680	84.4776	5.00	302.5	5.20	292.0	1.60	85.5	2.15	323.0
203	615	18.0730	84.4805	5.05	312.5	5.25	297.5	1.71	83.0	2.18	328.5
203	630	18.0689	84.4963	4.85	308.0	4.90	296.0	2.09	79.0	2.12	337.0
203	645	18.0789	84.5135	4.30	304.0	4.30	291.0	2.90	70.5	2.22	9.0

203	700	18.0617	84.5331	3.90	349.0	3.70	321.0	3.70	60.0	2.70	27.0
203	715	18.0727	84.5530	3.35	333.0	2.90	314.0	4.25	82.0	2.91	49.3
203	730	18.0757	84.5593	3.25	348.0	2.90	326.0	4.50	86.0	3.00	60.0
203	740S	18.0785	84.5807	3.20	346.3	3.10	326.0	4.60	90.0	3.00	60.3
203	745	18.0729	84.5645	3.12	343.1	3.00	324.2	4.62	89.2	3.00	60.8
203	800	18.0757	84.5751	3.00	344.6	2.92	325.8	4.71	88.0	3.00	60.1
203	815	18.0874	84.5820	3.12	343.0	2.95	320.5	4.85	81.0	3.00	55.0
203	830	18.0750	84.5885	3.00	338.0	2.94	317.4	4.86	79.8	3.00	55.0
203	845	18.0680	84.5935	3.30	338.2	3.00	317.0	4.78	82.3	3.00	55.2
203	848S	18.0908	84.6008	3.30	338.2	3.00	317.0	4.78	82.3	3.00	55.2
203	900	18.0761	84.6026	3.40	340.0	3.00	319.0	4.70	85.8	3.00	58.0
203	915	18.0837	84.6046	3.60	341.0	3.00	319.2	4.60	85.5	3.00	55.6
203	930S	18.0853	84.6011	3.70	357.0	3.40	317.5	4.50	83.7	3.00	51.0
203	945	18.1064	84.6270	3.90	333.1	3.65	315.5	4.45	79.5	3.02	44.6
203	1000	18.0989	84.6248	4.05	331.1	3.88	313.8	4.32	78.5	3.00	42.0
203	1015	18.1172	84.6150	4.01	331.2	3.99	313.9	4.40	78.1	3.15	42.0
203	1030	18.1040	84.6233	4.12	331.7	4.00	312.9	4.29	79.1	2.98	40.9
203	1045	18.1142	84.6246	4.12	330.6	4.10	312.4	4.22	79.0	2.93	39.3
203	1100	18.1115	84.6253	4.24	330.1	4.20	312.3	4.28	78.8	3.12	39.1
203	1115	18.1320	84.6236	4.32	328.5	4.30	313.7	4.18	78.4	2.89	36.6
203	1130	18.1177	84.6380	4.28	330.6	4.35	313.5	4.45	79.5	3.00	39.8
203	1145	18.1604	84.6355	4.30	331.0	4.20	313.0	4.60	79.9	3.20	42.0
203	1200	18.1402	84.6488	4.25	332.0	4.20	316.0	4.70	79.0	3.00	41.5
203	1215	18.1364	84.6556	4.30	333.0	4.25	316.0	4.75	80.0	2.80	43.0
203	1218S	18.1369	84.6703	4.30	333.0	4.25	316.0	4.75	80.0	2.80	43.0
203	1230	18.1430	84.6617	4.20	332.5	4.15	315.5	4.90	81.0	3.10	46.0
203	1245	18.1495	84.6676	4.20	330.0	4.15	315.0	4.95	80.0	3.15	46.5
203	1300	18.1505	84.6818	4.20	333.0	4.15	316.0	5.05	80.5	3.25	47.0
203	1315	18.1520	84.6873	4.20	344.0	4.15	316.0	5.12	80.0	3.30	47.0
203	1330	18.1517	84.6916	4.30	333.7	4.30	317.0	5.15	80.0	3.35	45.5
203	1345	18.1584	84.6955	4.45	333.0	4.42	316.5	5.12	77.0	3.40	43.0
203	1400	18.1589	84.7025	4.60	333.5	4.56	317.4	5.20	78.0	3.50	42.0
203	1415	18.1615	84.7018	4.70	333.5	4.66	318.0	5.21	77.0	3.55	40.5
203	1430S	18.1714	84.7003	5.50	310.5	6.00	299.0	2.81	81.0	2.12	0.0
*203	1445	18.1582	84.6796	7.75	293.8	8.40	284.8	-1.00	-1.0	3.30	299.0
203	1500	18.1902	84.6325	7.85	294.0	8.60	287.0	-1.00	-1.0	3.40	301.0
203	1515	18.1979	84.6345	7.75	294.0	8.50	287.0	-1.00	-1.0	3.25	295.0
203	1530	18.1932	84.6431	7.95	293.1	8.70	287.0	-1.00	-1.0	3.40	297.0
203	1545	18.2040	84.6471	7.88	291.8	8.60	285.5	-1.00	-1.0	3.20	293.5
203	1600	18.2104	84.6553	7.75	292.0	8.50	286.0	-1.00	-1.0	3.00	291.0
203	1615	18.2187	84.6601	7.75	290.0	8.40	284.0	-1.00	-1.0	3.00	290.0
203	1616S	18.2178	84.6546	7.75	290.0	8.40	284.0	-1.00	-1.0	3.00	290.0
203	1630	18.2209	84.6681	7.60	289.5	8.35	283.5	-1.00	-1.0	3.05	287.0
203	1645	18.2180	84.6733	7.85	293.0	8.65	286.0	-1.00	-1.0	3.00	296.5
203	1700	18.2122	84.6723	8.50	295.0	9.20	288.0	-1.00	-1.0	3.70	299.0
203	1715	18.2254	84.6798	8.20	294.0	8.95	288.0	-1.00	-1.0	3.30	296.0
203	1730	18.2295	84.7366	5.20	303.0	5.80	293.5	-1.00	-1.0	1.40	28.0
203	1745	18.2382	84.7935	2.70	338.0	2.85	314.0	-1.00	-1.0	3.80	80.0
203	1800	18.2417	84.8111	2.58	341.0	2.74	314.0	-1.00	-1.0	3.90	82.0
203	1815	18.2557	84.7810	3.90	309.5	4.54	295.0	-1.00	-1.0	1.94	72.3
203	1830	18.2689	84.7726	4.00	307.3	4.60	293.0	-1.00	-1.0	1.83	78.0
203	1845	18.2710	84.8010	2.60	327.0	2.95	302.5	-1.00	-1.0	3.50	88.0
203	1900	18.2817	84.8095	2.59	333.0	2.86	308.0	-1.00	-1.0	3.70	86.0
203	1915	18.2479	84.8238	2.66	333.0	2.74	309.0	-1.00	-1.0	3.70	82.0
203	1930	18.2621	84.8297	2.66	333.0	2.74	309.0	-1.00	-1.0	3.70	82.0
203	1945	18.2602	84.8331	3.02	338.8	3.04	317.0	-1.00	-1.0	3.92	78.0
203	2000	18.2745	84.8391	3.20	341.7	3.19	321.0	-1.00	-1.0	4.03	76.0
203	2015	18.2802	84.8446	3.38	344.6	3.34	325.0	-1.00	-1.0	4.14	74.0
203	2030	18.2680	84.8511	3.55	347.5	3.50	329.0	-1.00	-1.0	4.24	72.0
203	2045	18.2755	84.8533	3.70	348.0	3.70	329.4	-1.00	-1.0	4.35	71.0
203	2100	18.2605	84.8650	3.81	351.0	3.77	332.0	-1.00	-1.0	4.42	71.2
203	2115	18.2724	84.8673	4.82	356.1	3.78	336.9	-1.00	-1.0	4.50	73.8
203	2130	18.2652	84.8766	3.80	12.6	3.78	353.4	-1.00	-1.0	4.60	89.2
203	2145	18.2695	84.8768	3.95	9.0	3.82	349.0	-1.00	-1.0	4.62	83.0
203	2200	18.2910	84.8690	4.01	7.2	3.95	347.6	-1.00	-1.0	4.61	81.6
203	2215	18.2969	84.8745	4.12	23.0	4.00	3.5	-1.00	-1.0	4.70	95.3

203	2230	18.2834	84.8915	4.11	39.5	4.00	20.3	-1.00	-1.0	4.78	111.9
203	2238S	18.2961	84.8941	4.03	49.3	3.95	29.7	-1.00	-1.0	4.78	122.4
203	2245	18.3047	84.8880	3.90	55.3	3.84	36.4	-1.00	-1.0	4.70	129.5
*203	2300	18.2984	84.9001	3.53	313.8	3.49	289.3	-1.00	-1.0	4.62	37.3
203	2315	18.3107	84.8892	3.48	352.6	3.51	330.3	-1.00	-1.0	4.44	77.8
*203	2330	18.3288	84.9041	3.41	349.4	3.57	327.5	-1.00	-1.0	4.24	77.0
203	2345S	18.3325	84.8956	3.42	347.3	3.67	324.5	-1.00	-1.0	4.08	78.1
204	0	18.3682	84.8953	3.45	340.0	3.80	319.0	-1.00	-1.0	3.85	76.0
204	85	18.3393	84.8979	3.40	338.5	3.80	317.0	-1.00	-1.0	3.75	77.0
204	15	18.3592	84.8878	3.40	340.1	3.80	320.3	-1.00	-1.0	3.75	80.1
204	30	18.3684	84.9111	3.40	338.0	3.85	313.1	-1.00	-1.0	3.60	84.6
204	45	18.3579	84.8983	3.30	328.1	3.90	305.5	-1.00	-1.0	3.50	75.5
204	100	18.3362	84.9106	3.30	328.0	3.80	311.0	-1.00	-1.0	3.50	73.5
204	115	18.3452	84.9180	3.32	338.2	3.85	317.0	-1.00	-1.0	3.40	89.0
204	130	18.3679	84.9040	3.50	333.0	3.90	314.4	-1.00	-1.0	3.40	82.0
204	145	18.3482	84.9085	3.40	327.0	4.00	308.3	-1.00	-1.0	3.20	77.0
204	200	18.3647	84.9180	3.35	329.5	3.90	313.5	-1.00	-1.0	3.35	82.5
204	215	18.3765	84.9203	3.30	346.5	3.95	322.5	-1.00	-1.0	3.30	90.5
204	230	18.3787	84.9328	3.25	329.5	3.90	311.0	-1.00	-1.0	3.30	83.5
204	245	18.3909	84.9218	3.25	330.0	3.90	311.0	-1.00	-1.0	3.30	85.0
204	300	18.3805	84.9293	2.94	329.0	3.70	310.5	-1.00	-1.0	3.35	87.0
204	315	18.3905	84.9306	2.83	310.5	3.60	295.0	-1.00	-1.0	3.40	78.0
204	322S	18.3943	84.9502	2.80	337.5	3.50	315.0	-1.00	-1.0	3.55	91.5
204	330	18.3805	84.9495	2.73	332.5	3.50	309.5	-1.00	-1.0	3.50	92.2
204	345	18.3690	84.9631	2.68	328.0	3.45	306.0	-1.00	-1.0	3.50	91.0
204	400	18.3924	84.9518	2.20	322.0	3.50	303.5	-1.00	-1.0	3.00	88.0
204	415	18.4080	84.9631	2.76	324.0	3.55	305.0	-1.00	-1.0	3.20	87.5
204	430	18.4190	84.9671	2.76	325.5	3.50	309.5	-1.00	-1.0	3.30	94.0
204	445	18.4119	84.9765	2.73	332.5	3.45	312.0	-1.00	-1.0	3.40	93.5
204	500	18.4080	84.9878	2.74	329.0	3.50	310.0	-1.00	-1.0	3.50	88.0
204	512S	18.4227	84.9848	2.70	338.0	3.40	318.0	-1.00	-1.0	3.60	92.0
204	515	18.4145	84.9960	2.74	339.5	3.35	318.0	-1.00	-1.0	3.60	97.0
204	530	18.4285	84.9816	2.74	336.0	3.40	315.0	-1.00	-1.0	3.60	89.5
204	545	18.4284	84.9860	2.88	326.5	3.60	305.0	-1.00	-1.0	3.45	76.0
204	600	18.4299	84.9958	2.94	349.0	3.60	327.5	-1.00	-1.0	3.55	99.5
204	615	18.4315	84.9966	2.98	337.5	3.60	318.5	-1.00	-1.0	3.60	86.0
204	630	18.4300	85.0135	3.10	339.0	3.60	320.0	-1.00	-1.0	3.70	87.0
204	645	18.4291	85.0165	3.20	341.0	3.60	320.0	-1.00	-1.0	3.85	84.0
204	700	18.4280	85.0195	3.20	342.0	3.55	323.0	-1.00	-1.0	4.00	83.0
204	715	18.4340	85.0206	3.05	343.0	3.60	322.0	-1.00	-1.0	4.00	82.5
204	730	18.4360	85.0330	3.30	344.0	3.50	323.0	-1.00	-1.0	4.10	82.5
204	745	18.4535	85.0453	3.30	345.0	3.50	323.8	-1.00	-1.0	4.21	80.4
204	800	18.4634	85.0553	3.40	346.3	3.80	324.8	-1.00	-1.0	4.30	79.5
204	815	18.4530	85.0585	3.45	349.0	3.54	327.6	-1.00	-1.0	4.40	79.3
204	830	18.4560	85.0691	3.51	349.0	3.59	329.5	-1.00	-1.0	4.49	78.5
204	832S	18.4606	85.0681	3.52	349.0	3.60	329.7	-1.00	-1.0	4.50	78.4
204	845	18.4540	85.0770	3.50	350.2	3.60	330.7	-1.00	-1.0	4.58	77.3
204	900	18.4625	85.0773	3.50	355.0	4.63	334.0	-1.00	-1.0	4.60	80.0
204	915	18.4710	85.0776	3.60	353.6	3.70	334.7	-1.00	-1.0	4.60	81.3
204	930	18.4670	85.0731	3.60	352.0	3.72	334.1	-1.00	-1.0	4.60	77.2
204	945	18.4632	85.0845	3.53	349.9	3.65	331.7	-1.00	-1.0	4.71	75.8
204	1000	18.4694	85.1015	3.48	352.1	3.52	333.1	-1.00	-1.0	4.80	76.6
204	1015	18.5017	85.1020	3.40	352.4	3.48	332.3	-1.00	-1.0	4.89	78.6
204	1018S	18.4856	85.1035	3.40	352.4	3.48	332.4	-1.00	-1.0	4.89	78.6
204	1030	18.4789	85.1246	3.38	354.4	3.40	333.0	-1.00	-1.0	4.91	79.3
204	1045	18.5012	85.1151	3.02	354.9	3.09	333.4	-1.00	-1.0	4.92	79.4
204	1100	18.4984	85.1246	3.36	358.0	3.24	336.6	-1.00	-1.0	5.10	80.3
204	1115	18.5105	85.1181	3.29	.1	3.03	337.0	-1.00	-1.0	5.21	83.0
204	1130S	18.5030	85.1386	3.28	1.2	3.03	336.0	-1.00	-1.0	5.30	81.8
204	1145	18.5167	85.1351	3.30	1.0	3.10	339.0	-1.00	-1.0	5.40	80.5
204	1200	18.5037	85.1478	3.25	.5	2.95	337.5	-1.00	-1.0	5.50	79.0
204	1215	18.5034	85.1566	3.20	3.0	2.90	341.0	-1.00	-1.0	5.65	82.0
204	1230	18.5150	85.1633	3.25	1.0	2.89	339.0	-1.00	-1.0	5.75	81.0
204	1245	18.5157	85.1703	3.25	8.0	2.87	344.0	-1.00	-1.0	5.90	82.5
204	1300	18.5117	85.1860	3.20	7.1	3.00	345.2	-1.00	-1.0	5.95	80.3
204	1315	18.5144	85.1851	3.30	7.8	2.83	343.6	-1.00	-1.0	6.00	77.7
204	1330	18.5192	85.1925	3.54	13.0	2.93	350.0	-1.00	-1.0	6.10	80.4
*204	1342S	18.5697	85.2231	3.40	358.0	3.15	339.5	-1.00	-1.0	6.15	80.5

204 1345	18.5189	85.2013	3.50	10.6	3.02	349.0	-1.00	-1.0	6.15	80.5
204 1400	18.5197	85.2040	3.45	11.1	3.25	347.2	-1.00	-1.0	5.96	80.5
204 1415	18.5290	85.2026	3.50	355.5	3.30	335.9	-1.00	-1.0	5.85	74.1
204 1430	18.5280	85.2086	3.50	359.5	3.30	336.5	-1.00	-1.0	5.70	77.0
204 1445	18.5299	85.2053	3.60	349.5	3.80	328.5	-1.00	-1.0	5.00	74.5
204 1500	18.5360	85.1686	4.60	316.5	5.35	304.0	-1.00	-1.0	2.64	65.0
*204 1515	18.5492	85.1313	6.00	291.5	7.05	283.5	-1.00	-1.0	-1.00	-1.0
*204 1530	18.5704	85.1321	5.90	28.0	7.00	22.0	-1.00	-1.0	-1.00	-1.0
*204 1545	18.5769	85.1405	5.80	81.0	6.87	72.0	-1.00	-1.0	-1.00	-1.0
204 1600	18.5809	85.1493	5.70	291.0	6.75	280.0	-1.00	-1.0	-1.00	-1.0
204 1615	18.6150	85.1711	4.00	281.0	5.20	273.0	-1.00	-1.0	-1.00	-1.0
204 1630S	18.6617	85.2167	2.65	213.0	3.85	225.5	-1.00	-1.0	-1.00	-1.0
204 1645	18.7020	85.2743	5.00	167.0	5.30	182.0	-1.00	-1.0	-1.00	-1.0
204 1700	18.7515	85.3291	8.00	147.5	7.85	158.5	-1.00	-1.0	-1.00	-1.0
204 1714S	18.8022	85.3897	10.90	149.5	11.40	142.5	-1.00	-1.0	-1.00	-1.0
204 1715	18.7892	85.3861	11.05	152.5	11.60	144.0	-1.00	-1.0	-1.00	-1.0
204 1730	18.8270	85.4431	14.30	143.0	14.80	138.0	-1.00	-1.0	-1.00	-1.0
204 1745	18.8589	85.4988	18.00	137.0	17.90	141.0	-1.00	-1.0	-1.00	-1.0

205 1900	19.0680	85.7516	2.50	182.0	6.30	220.0	4.45	262.0	-1.00	-1.0
*205 1915	19.0374	85.7653	2.58	177.0	6.20	217.5	4.40	263.0	-1.00	-1.0
205 1930	19.0894	85.7481	2.52	186.0	6.30	220.0	4.40	263.6	-1.00	-1.0
*205 1945	19.1547	85.7298	2.48	184.0	6.30	220.0	4.55	265.0	-1.00	-1.0
205 2000	19.1037	85.7453	2.49	187.0	6.50	221.0	4.75	265.5	-1.00	-1.0
205 2015	19.1207	85.7460	2.44	201.0	6.50	227.0	4.95	267.0	-1.00	-1.0
*205 2030	19.0629	85.7663	2.39	204.9	6.60	228.0	5.06	266.8	-1.00	-1.0
205 2045	19.0917	85.7693	2.70	202.0	6.90	223.5	5.35	259.0	-1.00	-1.0
205 2050S	19.1084	85.7587	2.70	302.0	6.90	225.5	5.35	261.5	-1.00	-1.0
205 2100	19.1282	85.7611	2.88	206.9	7.25	228.0	5.50	261.0	-1.00	-1.0
205 2115	19.1137	85.7685	3.22	215.5	7.45	232.0	5.50	256.1	-1.00	-1.0
205 2130	19.1199	85.7433	3.29	201.3	7.38	223.2	5.50	257.1	-1.00	-1.0
205 2145	19.1129	85.7615	3.23	199.1	7.47	227.4	5.60	260.0	-1.00	-1.0
205 2200	19.1322	85.7833	2.92	216.0	7.41	227.6	5.61	260.0	-1.00	-1.0
205 2215S	19.1289	85.7719	2.89	207.7	7.50	228.5	5.80	263.0	-1.00	-1.0
*205 2230	19.0662	85.8630	2.88	205.0	7.50	227.4	5.91	267.0	-1.00	-1.0
205 2245	19.1322	85.7833	3.00	221.5	7.62	232.6	6.07	259.5	-1.00	-1.0
205 2300	19.1365	85.7703	2.88	217.0	7.60	231.4	6.00	263.5	-1.00	-1.0
*205 2315	19.1780	85.7736	2.64	222.8	7.30	233.7	5.97	266.2	-1.00	-1.0
205 2330	19.1405	85.7968	2.36	228.9	7.02	236.7	5.85	269.6	-1.00	-1.0
205 2345	19.1710	85.8006	2.22	233.0	6.96	237.2	5.88	272.7	-1.00	-1.0
206 0	19.1735	85.7955	2.30	235.2	7.00	237.0	6.00	272.0	-1.00	-1.0
206 15	19.1489	85.8103	2.30	239.2	7.00	239.0	6.05	269.0	-1.00	-1.0
206 18S	19.1288	85.8041	2.30	238.0	7.05	236.8	6.10	267.3	-1.00	-1.0
206 30	19.1634	85.8116	2.34	235.0	7.15	236.5	6.00	271.0	-1.00	-1.0
206 45	19.1684	85.8145	2.38	235.2	7.20	239.0	6.05	273.4	-1.00	-1.0
206 100	19.1624	85.8266	2.36	240.0	7.15	243.0	5.95	274.2	-1.00	-1.0
206 115	19.1580	85.8351	2.36	231.5	7.10	236.0	6.00	270.3	-1.00	-1.0
206 130	19.1454	85.8390	2.64	235.0	7.20	238.0	6.05	271.0	-1.00	-1.0
206 145	19.1479	85.8383	2.47	217.4	7.25	219.0	6.20	256.5	-1.00	-1.0
206 200	19.1444	85.8408	2.52	242.0	7.40	248.5	6.30	272.7	-1.00	-1.0
206 215	19.1402	85.8406	2.87	246.0	7.50	240.5	6.45	272.0	-1.00	-1.0
206 230	19.1452	85.8478	2.87	246.5	7.50	241.5	6.52	272.8	-1.00	-1.0
206 245	19.1630	85.8468	2.54	251.2	7.60	243.6	6.55	275.5	-1.00	-1.0
206 300	19.1417	85.8766	2.65	249.0	7.60	242.5	6.50	273.0	-1.00	-1.0
206 315	19.1570	85.8675	2.52	250.5	7.40	242.5	6.40	275.0	-1.00	-1.0
206 330	19.1562	85.8650	2.42	250.0	7.35	243.0	6.25	276.0	-1.00	-1.0
206 345	19.1680	85.8693	2.23	246.2	7.30	241.0	6.10	269.0	-1.00	-1.0
206 346S	19.1646	85.8665	2.28	247.5	7.20	243.0	6.20	274.0	-1.00	-1.0
206 400	19.1799	85.8738	2.14	244.0	7.10	233.5	6.00	269.0	-1.00	-1.0
206 415	19.1444	85.8845	2.14	229.0	7.15	242.0	5.90	277.0	-1.00	-1.0
206 430	19.1722	85.8761	2.28	255.0	7.25	244.0	6.10	276.5	-1.00	-1.0
206 445	19.1577	85.8878	2.42	259.0	7.30	246.0	6.30	278.5	-1.00	-1.0
206 500	19.1722	85.8848	2.49	267.0	7.35	248.5	6.50	280.0	-1.00	-1.0
206 515	19.1594	85.8843	2.42	265.0	7.25	238.0	6.50	275.0	-1.00	-1.0
206 518S	19.1724	85.8911	2.42	265.0	7.25	248.0	6.50	275.0	-1.00	-1.0
206 530	19.1645	85.8828	2.50	268.0	7.32	243.0	6.57	278.0	-1.00	-1.0
206 545	19.1832	85.8800	2.59	271.0	7.40	249.0	6.65	281.0	-1.00	-1.0
206 600	19.1772	85.8833	2.58	276.0	7.40	250.0	6.75	278.0	-1.00	-1.0
206 615	19.1679	85.8935	2.58	278.0	7.40	251.5	6.70	284.0	-1.00	-1.0
206 630	19.1737	85.8990	2.54	282.0	7.40	251.0	6.70	283.0	-1.00	-1.0
206 645	19.1797	85.8956	2.80	279.0	7.70	252.5	7.10	282.0	-1.00	-1.0
206 700	19.1704	85.8970	3.25	285.5	7.85	256.0	7.40	285.5	-1.00	-1.0
206 715	19.1625	85.9213	2.64	294.0	7.15	252.0	6.90	286.5	-1.00	-1.0
206 730	19.1642	85.9441	1.92	302.0	6.30	249.0	6.00	288.0	-1.00	-1.0
206 745	19.1599	85.9570	1.35	328.5	5.50	243.0	5.20	292.0	-1.00	-1.0
206 800	19.1725	85.9751	1.16	23.3	5.24	244.9	4.70	295.6	-1.00	-1.0
206 815	19.1759	85.9813	1.17	3.4	5.20	245.2	4.70	296.0	-1.00	-1.0
206 830	19.1810	85.9886	1.27	.9	5.16	247.2	4.80	299.1	-1.00	-1.0
206 845	19.1827	85.9895	1.42	358.2	5.25	249.2	4.95	299.0	-1.00	-1.0
206 900	19.1709	85.9785	1.56	355.1	5.10	252.1	4.83	301.7	-1.00	-1.0
206 915	19.1775	85.9998	1.68	356.9	5.12	253.1	5.00	302.5	-1.00	-1.0
206 930	19.1775	86.0041	1.85	358.6	5.20	263.1	5.16	308.1	-1.00	-1.0
206 945	19.1877	86.0135	1.96	4.9	5.25	254.6	5.28	305.3	-1.00	-1.0
206 1000	19.1970	86.0041	2.13	355.0	5.33	253.3	5.44	303.2	-1.00	-1.0
206 1015	19.2012	86.0135	2.29	357.7	5.29	260.4	5.52	306.1	-1.00	-1.0
206 1030	19.2275	86.0430	2.36	1.2	5.08	257.0	5.40	308.3	-1.00	-1.0
206 1045	19.1443	86.0360	2.31	8.1	4.83	264.2	5.22	313.8	-1.00	-1.0

206 1100	19.1910	86.0293	2.24	10.7	4.75	260.8	5.62	310.0	-1.00	-1.0
206 1115	19.2122	86.0258	2.34	7.8	4.84	263.0	5.20	312.0	-1.00	-1.0
206 1130	19.2122	86.0301	2.51	2.1	5.08	265.9	5.64	313.0	-1.00	-1.0
206 1145	19.1927	86.0301	2.82	354.8	5.40	270.8	6.02	313.9	-1.00	-1.0
206 1200	19.1877	86.0273	3.40	345.9	5.80	275.0	6.58	312.2	-1.00	-1.0
206 1215	19.1885	86.0228	3.80	348.0	6.30	272.5	7.07	313.0	-1.00	-1.0
206 1230	19.1935	86.0285	4.20	340.5	6.10	277.0	7.52	314.0	-1.00	-1.0
206 1245	19.1910	86.0248	4.60	338.0	7.00	280.3	8.00	314.8	-1.00	-1.0
206 1300	19.1825	86.0245	4.90	333.0	7.00	280.8	8.45	312.0	-1.00	-1.0
206 1315	19.1885	86.0168	5.04	332.0	7.90	281.2	8.60	311.5	-1.00	-1.0
206 1330	19.1850	86.0193	5.30	326.0	8.25	277.5	8.19	310.0	-1.00	-1.0
206 13325	19.1942	86.0142	5.30	326.0	8.25	277.5	8.19	310.0	-1.00	-1.0
206 1345	19.2055	86.0176	5.18	327.0	8.26	279.0	8.90	308.0	-1.00	-1.0
*206 13485	19.2028	86.0197	5.20	205.0	8.32	156.5	8.92	187.5	0.00	0.0
206 1400	19.2149	86.0135	5.30	324.0	8.50	277.2	9.10	306.6	-1.00	-1.0
206 1415	19.2055	86.0176	5.40	322.5	8.65	276.5	9.22	306.5	-1.00	-1.0
206 1430	19.2020	86.0156	5.50	322.6	8.86	277.7	9.35	308.3	-1.00	-1.0
206 1445	19.2132	86.0196	5.60	322.8	9.00	279.5	9.46	308.1	-1.00	-1.0
206 1500	19.2080	86.0300	5.41	321.8	8.96	277.5	9.30	306.0	-1.00	-1.0
206 1515	19.2139	86.0355	5.25	322.5	8.70	277.4	9.11	307.0	-1.00	-1.0
206 15285	19.2117	86.0319	5.10	325.0	8.55	277.0	8.94	308.0	-1.00	-1.0
206 1530	19.2072	86.0491	5.10	326.2	8.55	277.0	8.92	307.0	-1.00	-1.0
206 1545	19.2130	86.0590	4.98	327.8	8.35	277.8	8.70	308.7	-1.00	1.0
206 1600	19.2199	86.0628	4.75	329.5	8.10	276.0	8.50	310.0	-1.00	-1.0
206 1615	19.2164	86.0740	4.60	331.0	7.90	276.0	8.30	311.0	-1.00	-1.0
206 1630	19.2224	86.0840	4.50	333.0	7.80	276.0	8.20	309.0	-1.00	-1.0
206 16405	19.2245	86.0880	4.40	336.5	7.60	275.5	8.05	309.5	-1.00	-1.0
206 1645	19.2207	86.0918	4.35	336.0	7.60	276.0	8.00	310.5	-1.00	-1.0
206 1700	19.2275	86.1043	4.15	339.5	7.30	275.0	7.70	313.0	-1.00	-1.0
206 1715	19.2479	86.0981	4.05	341.0	7.10	275.5	7.60	314.0	-1.00	-1.0
206 1730	19.2334	86.1141	4.00	341.0	6.95	271.0	7.40	309.0	-1.00	-1.0
206 1745	19.2385	86.1213	4.20	349.0	7.65	280.5	7.65	318.0	-1.00	-1.0
206 1800	19.2334	86.1185	4.40	343.5	7.20	277.5	7.85	315.5	-1.00	-1.0
206 1815	19.2232	86.1303	4.40	344.2	7.17	278.0	7.80	316.5	-1.00	-1.0
206 1830	19.2257	86.1426	4.40	345.0	7.15	278.5	7.75	317.5	-1.00	-1.0
206 1845	19.2447	86.1358	4.35	347.0	7.10	276.5	7.65	317.5	-1.00	-1.0
206 1900	19.2470	86.1435	4.40	348.0	7.30	273.0	7.80	313.0	-1.00	-1.0
206 1915	19.2360	86.1483	4.50	343.0	7.50	277.0	7.95	317.5	-1.00	-1.0
206 1930	19.2709	86.1436	4.60	344.0	7.60	280.0	8.10	317.0	-1.00	-1.0
*206 1945	19.3895	86.1091	4.65	342.0	7.65	276.0	8.10	315.5	-1.00	-1.0
206 19505	19.2504	86.1454	4.65	342.0	7.65	276.0	8.10	315.5	-1.00	-1.0
206 2000	19.2589	86.1590	4.60	349.9	7.50	283.2	7.90	320.8	-1.00	-1.0
206 2015	19.2674	86.1636	4.50	350.8	7.38	281.5	7.82	323.0	-1.00	-1.0
206 2030	19.2394	86.2026	4.45	351.0	7.17	280.0	7.65	324.0	-1.00	-1.0
206 2045	19.2555	86.1788	4.29	351.1	6.82	278.9	7.38	322.2	-1.00	-1.0
206 2100	19.2445	86.2011	4.20	350.0	6.67	273.2	7.20	327.0	-1.00	-1.0
*206 2115	19.2029	86.1976	4.20	358.6	6.62	282.3	7.18	315.4	-1.00	-1.0
*206 2130	19.2122	86.1570	4.30	355.6	6.67	284.0	7.30	327.5	-1.00	-1.0
206 21385	19.2711	86.1855	4.42	358.4	6.72	284.5	7.41	328.0	-1.00	-1.0
206 2145	19.2522	86.2076	4.50	357.0	6.80	284.0	7.42	329.0	-1.00	-1.0
206 2200	19.2522	86.1858	4.70	356.3	6.92	284.9	7.62	329.0	-1.00	-1.0
*206 2215	19.2147	86.2043	4.90	354.8	7.02	285.7	7.87	328.0	-1.00	-1.0
206 2230	19.2980	86.1850	5.00	2.3	7.10	288.5	7.98	332.1	-1.00	-1.0
206 2245	19.2717	86.2120	5.13	358.3	7.15	288.6	8.03	330.5	-1.00	-1.0
206 2300	19.2880	86.2186	5.20	359.6	7.00	287.0	8.00	332.6	-1.00	-1.0
206 2315	19.2930	86.2128	5.22	3.0	6.83	290.7	7.91	335.1	-1.00	-1.0
206 2330	19.2675	86.2336	5.13	6.2	6.56	292.4	7.72	336.0	-1.00	-1.0
*206 2345	19.2574	86.2366	5.13	4.6	6.44	289.4	7.60	335.0	-1.00	-1.0
207 0	19.3297	86.2485	5.15	8.0	6.30	293.0	7.60	341.0	-1.00	-1.0
207 15	19.3162	86.2583	5.20	12.0	6.15	294.0	7.60	342.0	-1.00	-1.0
207 30	19.3162	86.2627	5.35	13.0	6.10	293.5	7.60	338.0	-1.00	-1.0
207 45	19.3222	86.2725	5.35	14.1	6.00	295.9	7.50	343.8	-1.00	-1.0
*207 100	19.3434	86.2560	5.40	15.8	5.86	296.0	7.50	345.7	-1.00	-1.0
*207 1155	19.3008	86.2753	5.49	17.0	5.72	296.5	7.45	349.1	-1.00	-1.0
207 130	19.3239	86.2778	5.60	19.2	5.67	298.9	7.50	350.4	-1.00	1.0
207 145	19.3205	86.2846	5.80	19.0	5.80	299.0	7.75	351.0	-1.00	-1.0

207	200	19.3350	86.2906	6.00	19.0	5.90	303.2	7.95	349.9	-1.00	-1.0
207	215	19.3205	86.2891	6.20	17.5	6.10	303.8	8.10	350.4	-1.00	-1.0
207	230	19.3137	86.2896	6.43	18.0	6.25	306.2	8.35	351.0	-1.00	-1.0
207	244S	19.3086	86.3069	6.43	18.0	6.25	306.2	8.35	351.0	0.00	0.0
207	245	19.3240	86.2996	6.48	16.5	6.20	306.5	8.40	351.0	-1.00	-1.0
207	258S	19.3083	86.3064	6.42	18.7	6.00	307.0	8.30	351.0	-1.00	-1.0
207	300	19.3104	86.3008	6.45	19.3	6.00	306.0	8.33	352.0	-1.00	1.0
207	315	19.3062	86.3095	6.51	19.3	5.60	305.0	8.13	353.1	-1.00	-1.0
207	330	19.3172	86.3135	6.48	23.0	5.20	305.0	7.90	356.2	-1.00	-1.0
207	345	19.3412	86.3310	6.45	25.5	4.71	308.0	7.60	359.0	-1.00	-1.0
207	400	19.3387	86.3361	6.60	32.0	4.45	309.0	7.50	2.0	-1.00	-1.0
207	415	19.3327	86.3438	6.00	29.0	4.60	303.0	7.10	359.5	-1.00	-1.0
207	430	19.3455	86.3311	5.30	31.0	4.70	295.0	6.65	358.0	-1.00	-1.0
207	445	19.3590	86.3343	4.60	35.5	4.90	287.0	6.10	353.0	-1.00	-1.0
207	500	19.3795	86.3281	4.60	36.0	5.00	289.5	6.00	357.0	-1.00	-1.0
207	515	19.3947	86.3236	4.60	32.0	4.90	288.0	5.95	357.5	-1.00	-1.0
207	530	19.3940	86.3341	4.70	33.0	4.90	291.5	6.10	358.0	-1.00	-1.0
207	545	19.3839	86.3371	5.00	31.0	5.00	294.0	6.40	359.5	-1.00	-1.0
207	600	19.3830	86.3431	5.00	30.0	5.10	295.0	6.50	358.0	-1.00	-1.0
207	615	19.3814	86.3510	5.20	29.1	5.20	298.0	6.65	359.2	-1.00	-1.0
207	630	19.3857	86.3643	5.30	29.0	5.20	299.0	6.75	0.0	-1.00	-1.0
207	645	19.3739	86.3751	5.35	31.0	5.00	300.5	6.70	1.0	-1.00	-1.0
207	700	19.3815	86.3771	5.40	33.0	4.80	302.0	6.70	3.0	-1.00	-1.0
207	715	19.3790	86.3823	5.50	35.0	4.75	304.0	6.65	5.5	-1.00	-1.0
207	730	19.3892	86.3793	5.65	35.5	4.70	305.5	6.70	8.0	-1.00	-1.0
207	734S	19.3884	86.3919	5.65	35.5	4.70	304.5	6.70	8.0	-1.00	-1.0
207	745	19.3757	86.3891	5.88	30.0	4.70	301.2	6.87	.5	-1.00	-1.0
207	800	19.3757	86.3980	5.90	29.5	4.50	302.1	6.85	.5	-1.00	-1.0
207	815	19.3842	86.4026	6.00	30.0	4.42	303.0	6.82	2.2	-1.00	-1.0
207	830	19.3962	86.4093	5.80	33.8	4.13	301.7	6.52	3.5	-1.00	-1.0
207	845	19.4015	86.4208	5.59	46.2	3.84	308.0	6.21	14.5	-1.00	-1.0
207	900	19.4204	86.4311	5.65	45.5	3.93	307.9	6.25	14.2	-1.00	-1.0
207	915	19.4049	86.4270	5.70	43.1	4.19	308.9	6.41	13.4	-1.00	-1.0
207	930	19.4219	86.4190	5.72	41.4	4.33	310.8	6.60	12.0	-1.00	1.0
207	945	19.4237	86.4331	5.81	39.8	4.52	313.3	6.82	11.1	-1.00	-1.0
207	1000	19.4295	86.4211	6.00	38.0	4.72	314.6	6.94	10.4	-1.00	-1.0
207	1015	19.4160	86.4266	6.14	36.4	4.94	316.2	7.22	10.1	-1.00	-1.0
207	1030	19.4194	86.4155	6.14	37.3	4.96	316.8	7.22	10.9	-1.00	-1.0
207	1045	19.4482	86.4140	5.87	37.2	4.93	314.0	7.02	10.0	-1.00	-1.0
207	1100	19.4407	86.4295	5.60	36.5	4.94	311.0	6.79	8.5	-1.00	-1.0
207	1115	19.4320	86.4116	5.41	36.3	4.99	308.1	6.61	5.9	-1.00	-1.0
207	1130	19.4567	86.4056	5.12	36.9	4.97	305.8	6.38	8.1	-1.00	-1.0
207	1145	19.4380	86.4258	4.90	36.5	5.01	303.0	6.12	6.0	-1.00	-1.0
207	1200	19.4670	86.4200	4.65	36.0	5.10	310.2	5.95	5.0	-1.00	-1.0
207	1215	19.4755	86.4203	4.35	35.0	5.19	296.9	5.63	4.1	-1.00	-1.0
207	1230	19.4704	86.4220	4.15	35.0	5.20	295.0	5.62	3.0	-1.00	-1.0
207	1240S	19.4776	86.4248	4.00	35.0	5.30	294.5	5.55	1.5	-1.00	-1.0
207	1245	19.4814	86.4171	3.70	35.0	5.35	293.5	5.49	1.0	-1.00	-1.0
207	1300	19.4909	86.4245	3.80	34.5	5.35	292.5	5.30	1.0	-1.00	-1.0
207	1315	19.4890	86.4236	3.85	33.0	5.50	294.0	5.50	0.0	-1.00	-1.0
207	1330	19.4874	86.4226	4.00	30.0	5.70	296.0	5.70	358.0	-1.00	-1.0
207	1345	19.4857	86.4216	4.10	28.0	5.88	297.0	5.90	357.0	-1.00	-1.0
207	1400	19.4917	86.4271	4.12	27.5	5.95	297.5	6.00	357.5	-1.00	-1.0
207	1415	19.4977	86.4283	4.20	27.5	6.00	299.5	6.15	358.0	-1.00	-1.0
207	1430	19.5045	86.4320	4.25	26.5	6.05	301.0	6.20	358.0	-1.00	-1.0
207	1444S	19.5004	86.4434	4.40	26.0	6.10	301.0	6.38	356.5	-1.00	-1.0
207	1445	19.5045	86.4320	4.41	26.0	6.10	301.5	6.40	358.5	-1.00	-1.0
207	1500	19.5012	86.4433	4.50	24.0	6.25	303.0	6.55	358.0	-1.00	-1.0
207	1515	19.5047	86.4451	4.60	23.0	6.39	305.0	6.80	357.8	-1.00	-1.0
207	1530	19.5039	86.4511	4.80	23.0	6.45	305.5	6.95	358.0	-1.00	-1.0
207	1545	19.4997	86.4598	4.92	23.5	6.40	307.2	7.05	359.8	-1.00	-1.0
207	1550S	19.5070	86.4607	4.92	23.5	6.40	307.2	7.50	359.8	-1.00	-1.0
207	1600	19.5074	86.4618	5.00	24.5	6.30	310.0	7.17	1.0	-1.00	-1.0
207	1615	19.5075	86.4706	5.00	25.0	6.30	308.7	7.00	1.0	-1.00	-1.0
207	1630	19.5252	86.4608	4.40	21.0	6.60	303.5	6.80	356.0	-1.00	-1.0
207	1645	19.5395	86.4536	3.90	13.8	7.00	299.0	6.50	351.0	-1.00	-1.0

207 1700	19.5285	86.4583	3.70	7.5	7.25	295.5	6.40	347.0	-1.00	-1.0
207 1715	19.5422	86.4571	3.85	8.0	7.30	297.0	6.60	347.5	-1.00	-1.0
207 1730	19.5389	86.4640	3.90	10.0	7.28	298.0	6.70	350.0	-1.00	-1.0
207 1745	19.5499	86.4636	4.05	9.5	7.35	299.5	6.85	350.0	-1.00	-1.0
207 1800	19.5525	86.4671	4.22	9.0	7.50	301.0	7.06	350.0	7.60	350.0
207 1815	19.5465	86.4705	4.48	7.8	7.65	302.0	7.40	350.0	-1.00	-1.0
207 1830	19.5467	86.4791	4.60	7.5	7.75	304.0	7.50	351.0	-1.00	-1.0
207 1845	19.5552	86.4795	4.70	9.0	7.80	305.0	7.60	352.0	-1.00	-1.0
207 1900	19.5552	86.4795	4.80	11.0	7.70	307.0	7.70	354.0	-1.00	-1.0
207 1915	19.5510	86.4925	5.00	12.0	7.70	308.0	7.90	355.0	-1.00	-1.0
207 1930	19.5715	86.4906	5.10	13.0	7.75	309.0	8.00	355.0	-1.00	-1.0
207 1945	19.5917	86.4845	5.15	13.6	7.80	311.0	8.06	356.4	-1.00	-1.0
207 2000	19.5565	86.5126	5.26	15.1	7.71	313.7	8.14	357.8	-1.00	-1.0
207 2015	19.5624	86.5095	5.50	13.8	7.92	313.2	8.92	357.2	-1.00	-1.0
207 2030	19.5699	86.5028	5.56	13.8	8.40	314.1	8.57	357.2	-1.00	-1.0
207 2045	19.6012	86.4961	5.42	14.0	8.00	313.5	8.41	358.1	-1.00	-1.0
207 2100	19.5837	86.5103	4.82	17.2	7.60	312.8	7.90	359.0	-1.00	-1.0
207 2115	19.5954	86.5038	4.80	16.0	7.72	312.0	7.92	359.7	-1.00	-1.0
207 2130	19.5929	86.5090	4.90	17.0	7.80	313.3	8.00	.2	-1.00	-1.0
*207 2145	19.5804	86.5260	5.06	16.6	7.94	314.6	8.30	1.3	-1.00	-1.0
207 2200	19.6132	86.5028	5.23	15.1	8.12	314.5	8.46	.6	-1.00	-1.0
207 2215	19.5802	86.5041	5.40	13.3	8.41	315.2	8.72	359.3	-1.00	-1.0
207 2230	19.6082	86.5043	5.57	13.0	8.49	316.8	8.91	0.0	-1.00	-1.0
*207 2245	19.5270	86.5420	5.59	14.9	8.48	317.7	8.91	1.7	-1.00	-1.0
207 2300	19.6194	86.5170	5.61	16.7	8.40	319.3	8.91	2.3	-1.00	-1.0
207 2315	19.6059	86.5183	5.31	20.5	7.95	319.5	8.56	4.6	-1.00	-1.0
*207 2330	19.6595	86.5370	4.92	24.2	7.42	317.2	8.04	6.3	-1.00	-1.0
207 2345	19.6452	86.5355	4.50	30.0	6.90	316.0	7.58	8.5	-1.00	-1.0
208 0	19.6985	86.5281	4.25	35.5	6.48	316.5	7.22	12.5	-1.00	-1.0
208 15	19.7265	86.5370	4.20	40.0	6.30	316.0	7.20	15.0	-1.00	-1.0
*208 305	19.6903	86.5494	3.99	47.5	5.85	314.0	6.70	17.8	-1.00	-1.0
208 45	19.7429	86.5481	3.70	58.0	5.30	310.5	6.15	22.0	-1.00	-1.0
208 100	19.7572	86.5453	3.60	58.5	5.20	308.6	6.00	22.5	-1.00	-1.0
208 115	19.7412	86.5516	3.66	60.6	5.70	309.5	6.00	23.9	-1.00	-1.0
208 130	19.7345	86.5521	3.68	59.5	5.10	311.1	6.10	24.0	-1.00	-1.0
208 145	19.7134	86.5556	3.79	57.0	5.28	312.5	6.31	23.1	-1.00	-1.0
208 200	19.7470	86.5483	3.80	55.0	5.35	313.7	6.42	23.4	-1.00	-1.0
208 215	19.7597	86.5401	3.90	52.9	5.42	315.5	6.60	22.8	-1.00	-1.0
208 230	19.7765	86.5320	3.90	52.5	5.44	315.9	6.60	23.0	-1.00	-1.0
208 245	19.7562	86.5381	3.89	51.0	5.51	316.0	6.68	23.0	-1.00	-1.0
208 300	19.7225	86.5500	3.90	50.0	5.60	317.0	6.71	22.0	-1.00	-1.0
208 315	19.7184	86.5541	3.85	49.6	5.62	317.9	6.79	22.5	-1.00	-1.0
208 330	19.7520	86.5425	3.60	53.3	5.41	315.0	6.52	22.8	-1.00	-1.0
208 3385	19.7606	86.5517	3.42	56.1	5.30	313.0	6.25	23.1	-1.00	-1.0
208 345	19.7437	86.5465	3.40	58.9	5.20	312.2	6.11	24.9	-1.00	-1.0
208 400	19.7630	86.5420	3.00	59.0	5.20	309.5	6.00	24.0	-1.00	-1.0
208 415	19.7874	86.5228	2.60	53.5	5.50	307.2	5.80	20.0	-1.00	-1.0
208 430	19.7712	86.5205	2.52	48.0	5.90	305.0	5.70	17.0	-1.00	-1.0
208 445	19.7779	86.5155	2.16	38.5	6.20	301.0	5.45	11.5	-1.00	-1.0
*208 500	19.7804	86.5103	1.84	29.6	6.45	300.0	5.60	9.0	-1.00	-1.0
208 515	19.8134	86.5135	1.80	23.5	6.35	304.1	5.60	10.5	-1.00	-1.0
*208 530	19.6539	86.5533	1.86	27.2	6.40	304.4	5.80	11.1	-1.00	-1.0
208 545	19.7880	86.5125	2.08	27.8	5.75	314.8	5.95	11.6	-1.00	-1.0
208 600	19.7997	86.5058	2.27	26.0	6.43	308.9	6.32	12.5	-1.00	-1.0
208 615	19.8132	86.5003	1.52	24.0	6.80	306.0	2.70	21.0	-1.00	-1.0
208 630	19.8037	86.4930	1.79	14.0	7.10	306.0	6.20	7.0	-1.00	-1.0
208 645	19.8013	86.4981	2.06	4.0	7.00	305.0	6.20	8.5	-1.00	-1.0
208 700	19.8257	86.4876	2.34	353.5	7.60	305.0	6.40	2.5	-1.00	-1.0
208 715	19.8180	86.4900	2.73	352.0	7.75	307.0	6.60	2.0	-1.00	-1.0
208 730	19.8247	86.4806	2.78	353.0	7.65	306.0	6.60	3.0	-1.00	-1.0
208 745	19.8145	86.4838	2.80	354.0	7.60	307.0	6.70	3.5	-1.00	-1.0
208 800	19.7735	86.5066	2.64	354.0	7.60	308.0	6.75	4.1	-1.00	-1.0
*208 815	19.7474	86.5116	2.93	357.3	7.59	309.2	6.78	6.1	-1.00	-1.0
208 830	19.8392	86.4908	2.92	356.3	7.50	311.0	6.82	6.3	-1.00	-1.0
208 845	19.8374	86.4855	2.58	356.1	7.45	310.3	6.80	5.8	-1.00	-1.0

208	900	19.8390	86.4821	2.80	352.7	7.61	309.6	6.85	5.3	-1.00	-1.0
208	915	19.8400	86.4891	2.70	351.7	7.68	310.0	6.91	4.8	-1.00	-1.0
208	930	19.8654	86.4901	2.90	354.2	7.75	312.5	7.20	6.0	-1.00	-1.0
208	945	19.8605	86.5048	3.30	356.0	7.89	314.0	7.39	6.8	-1.00	-1.0
208	1000	19.8697	86.4946	3.54	356.8	7.90	316.1	7.65	7.1	-1.00	-1.0
208	1015	19.8813	86.4837	3.65	357.7	8.08	316.7	7.80	7.4	-1.00	-1.0
208	1030	19.8915	86.4893	3.75	359.3	8.10	318.2	7.92	8.3	-1.00	-1.0
208	1045	19.8807	86.4941	3.82	359.2	8.11	319.5	8.02	9.7	-1.00	-1.0
208	1100	19.8857	86.4926	3.99	1.1	8.11	320.3	8.20	10.9	-1.00	-1.0
208	1115	19.8840	86.4916	4.18	2.2	8.20	322.0	8.27	10.2	-1.00	-1.0
208	1130	19.9177	86.4886	4.25	3.1	8.18	322.9	8.44	12.3	-1.00	-1.0
*208	1145	19.8864	86.4865	4.38	5.3	8.22	323.5	8.54	13.5	-1.00	-1.0
208	1200	19.9269	86.4828	4.50	6.4	8.29	325.8	8.70	13.1	-1.00	-1.0
208	1215	19.9152	86.4938	4.54	7.3	8.24	326.6	8.76	14.0	-1.00	-1.0
208	1230	19.9345	86.4893	4.55	8.0	8.25	327.4	8.75	14.2	-1.00	-1.0
208	1245	19.9144	86.4955	4.62	8.0	8.40	327.3	8.89	14.5	-1.00	-1.0
208	1300	19.9360	86.4770	4.73	7.2	8.50	328.0	8.96	14.1	-1.00	-1.0
208	1315	19.9035	86.4960	4.88	7.0	8.68	328.9	9.20	13.8	-1.00	-1.0
208	1330	19.9212	86.4948	5.09	6.0	8.88	328.9	9.31	13.9	-1.00	-1.0
208	1345	19.9245	86.4966	5.26	6.5	9.00	330.9	9.51	13.8	-1.00	-1.0
208	1350S	19.9117	86.5061	5.30	7.0	9.02	331.1	9.55	14.4	0.00	0.0
208	1400	19.9154	86.4981	5.35	8.9	9.02	332.0	9.62	15.0	-1.00	-1.0
208	1415	19.9180	86.5061	5.21	10.6	8.93	333.9	9.69	16.9	-1.00	-1.0
208	1430	19.9374	86.5060	5.45	13.3	8.99	335.7	9.81	17.8	-1.00	-1.0
208	1445	19.9267	86.5151	5.69	14.3	9.08	336.8	11.00	18.9	-1.00	-1.0
208	1500	19.9325	86.5163	5.80	15.0	9.26	337.0	10.16	19.4	-1.00	-1.0
208	1515	19.9367	86.5165	6.06	14.4	9.55	338.0	10.50	19.0	-1.00	-1.0
208	1530	19.9427	86.5131	6.35	14.6	9.73	339.5	10.73	18.5	-1.00	-1.0
208	1532S	19.9432	86.4994	6.35	14.6	9.73	339.5	10.73	18.5	-1.00	-1.0
208	1545	19.9275	86.5221	6.40	15.2	9.78	341.0	10.81	17.5	-1.00	-1.0
208	1600	19.9639	86.5183	5.45	18.5	8.80	338.0	9.90	22.0	-1.00	-1.0
208	1615	20.0024	86.5093	4.60	22.0	8.00	336.0	9.05	24.0	-1.00	-1.0
208	1630	20.0252	86.5110	2.64	28.0	6.70	325.0	7.20	25.0	-1.00	-1.0
208	1645	20.0442	86.4978	1.75	14.0	6.60	315.0	6.70	23.0	-1.00	-1.0
208	1700	20.0716	86.4760	1.64	282.0	7.05	299.0	4.70	12.5	-1.00	-1.0
208	1715	20.0782	86.4710	1.40	282.5	7.05	301.0	4.80	13.0	-1.00	-1.0
208	1730	20.0815	86.4728	1.54	295.0	7.10	301.0	5.00	13.6	-1.00	-1.0
208	1745	20.0917	86.4741	1.58	303.0	7.15	304.0	5.25	17.0	-1.00	-1.0
208	1800	20.0834	86.4738	1.48	316.0	7.30	304.5	5.60	15.0	-1.00	-1.0
208	1815	20.0825	86.4755	1.46	316.0	7.35	309.0	5.60	15.0	-1.00	-1.0
208	1830	20.0925	86.4725	1.54	327.0	7.50	308.5	6.15	17.0	-1.00	-1.0
208	1845	20.0867	86.4756	1.66	342.5	7.05	310.5	6.03	17.2	20.00	0.0
208	1900	20.0884	86.4766	2.15	351.0	7.75	315.5	7.00	19.5	-1.00	-1.0
208	1915	20.1054	86.4816	2.40	0.0	7.65	316.0	7.22	21.5	-1.00	-1.0
208	1930	20.1105	86.4888	2.35	6.0	7.50	319.0	7.35	23.0	-1.00	-1.0
208	1945	20.0965	86.5005	2.40	11.8	7.41	320.6	7.41	25.5	-1.00	-1.0
208	1954S	20.1166	86.4850	2.46	15.5	7.32	321.8	7.58	27.5	-1.00	-1.0
208	2000	20.1389	86.4785	2.21	17.6	7.35	320.7	7.62	28.3	-1.00	-1.0
208	2015	20.1209	86.4988	2.29	23.8	7.22	321.9	7.75	30.3	-1.00	-1.0
208	2030	20.1327	86.5010	2.63	31.1	7.12	324.0	7.91	33.0	-1.00	-1.0
208	2045	20.1303	86.5062	2.50	35.8	7.00	325.5	8.03	33.4	-1.00	-1.0
208	2100	20.1552	86.4940	2.69	40.0	6.94	327.3	8.12	35.1	-1.00	-1.0
208	2115	20.1404	86.5075	2.72	43.6	6.85	328.8	8.28	36.7	-1.00	-1.0
208	2124S	20.1565	86.4930	2.81	44.5	6.81	329.2	8.35	37.0	-1.00	-1.0
208	2130	20.1730	86.5016	2.79	43.3	6.90	329.9	8.45	36.8	-1.00	-1.0
208	2145	20.1820	86.4958	2.89	43.7	6.90	330.6	8.51	37.3	-1.00	-1.0
208	2200	20.1797	86.5010	3.29	46.0	6.88	332.4	8.60	38.6	-1.00	-1.0
208	2215	20.1863	86.4960	3.21	47.0	6.83	333.3	8.60	39.2	-1.00	-1.0
*208	2230	20.2640	86.4848	2.93	53.2	6.51	333.2	8.50	42.2	-1.00	-1.0
208	2245	20.2082	86.4993	2.91	60.3	6.10	334.0	8.42	44.5	-1.00	-1.0
208	2300	20.1877	86.5161	2.93	68.3	5.79	334.6	8.35	47.4	-1.00	-1.0
208	2312S	20.2239	86.5005	3.00	74.0	5.51	335.8	8.30	49.7	-1.00	-1.0
208	2315	20.2427	86.5033	3.20	75.2	5.41	335.5	8.32	50.8	-1.00	-1.0
208	2330	20.2559	86.4931	3.43	83.6	5.00	335.2	8.35	54.0	-1.00	-1.0
208	2345	20.2502	86.5010	3.63	91.1	4.58	337.2	8.27	56.7	-1.00	-1.0
209	0	20.2705	86.5121	3.93	97.8	4.19	339.5	8.30	60.6	-1.00	-1.0
209	15	20.2939	86.5076	4.10	104.4	3.79	339.4	8.34	64.1	-1.00	-1.0
209	30	20.3015	86.5098	4.40	108.5	3.35	341.5	8.25	67.0	-1.00	-1.0

209	45	20.3297	86.4993	4.60	117.0	2.75	336.1	8.01	70.2	-1.00	-1.0
*207	100	20.3464	86.4955	4.70	119.1	2.66	334.0	7.82	71.2	-1.00	-1.0
209	115	20.3460	86.4825	4.72	119.2	2.65	336.0	7.92	72.0	-1.00	-1.0
209	130	20.3625	86.4741	4.62	116.6	2.81	337.7	8.00	70.3	-1.00	-1.0
209	145	20.3520	86.4878	4.63	114.5	2.93	341.0	8.10	69.3	-1.00	-1.0
209	200	20.3634	86.4725	4.76	117.5	2.77	341.7	8.00	71.6	-1.00	-1.0
209	215	20.3515	86.4703	4.65	126.0	2.59	332.0	7.60	73.0	-1.00	-1.0
209	230	20.3780	86.4590	4.65	132.5	2.50	321.0	7.10	75.8	-1.00	-1.0
209	245	20.3947	86.4551	4.55	137.0	2.60	311.0	6.75	76.0	-1.00	-1.0
209	300	20.4025	86.4335	4.50	139.0	2.70	309.0	6.60	77.5	-1.00	-1.0
209	315	20.4122	86.4216	4.40	142.0	2.72	307.5	6.42	76.5	-1.00	-1.0
209	330	20.3949	86.4271	4.25	142.5	2.82	308.0	6.30	76.0	-1.00	-1.0
209	345	20.3965	86.4281	4.25	143.0	2.85	308.0	6.35	77.0	-1.00	-1.0
*209	350S	19.1356	86.7392	2.60	216.0	2.02	97.0	2.60	323.0	-1.00	-1.0
209	400	20.4337	86.4118	4.30	144.5	2.78	307.5	6.70	78.0	-1.00	-1.0
209	415	20.4414	86.4181	4.30	144.0	3.10	307.5	6.40	79.0	-1.00	-1.0
209	430	20.4320	86.4153	4.35	144.5	2.96	307.5	6.40	79.5	-1.00	-1.0
209	436S	20.4295	86.4204	4.40	143.0	2.95	311.5	6.50	80.0	-1.00	-1.0
209	445	20.4455	86.4183	4.30	142.5	3.10	313.0	6.50	79.0	-1.00	-1.0
209	500	20.4500	86.4036	4.22	141.0	3.20	317.0	6.60	78.0	-1.00	-1.0
209	515	20.4510	86.4106	4.15	140.5	3.25	319.5	6.60	77.0	-1.00	-1.0
*209	530	20.4047	86.3915	4.10	137.5	3.10	323.0	6.70	77.0	-1.00	-1.0
209	545	20.4804	86.3835	4.00	136.0	3.05	325.0	6.75	75.0	-1.00	-1.0
209	600	20.4514	86.3870	3.85	143.5	3.40	318.0	6.25	75.0	-1.00	-1.0
209	615	20.4477	86.3763	3.60	150.0	3.70	311.5	5.70	74.5	-1.00	-1.0
209	630	20.4650	86.3663	3.40	160.0	4.00	306.0	5.10	75.0	-1.00	-1.0
209	645	20.4705	86.3543	3.40	170.0	4.40	301.0	4.50	74.5	-1.00	-1.0
209	700	20.5002	86.3446	3.00	172.5	4.50	301.0	4.50	73.0	-1.00	-1.0
209	715	20.5025	86.3351	3.30	171.0	4.50	302.0	4.60	73.0	-1.00	-1.0
209	730	20.5144	86.3416	3.30	168.0	4.50	305.0	4.70	72.6	-1.00	-1.0
209	732S	20.5002	86.3422	3.30	168.0	4.50	305.0	4.70	72.6	-1.00	-1.0
209	745	20.5284	86.3386	3.30	167.0	4.40	307.0	4.70	73.0	-1.00	-1.0
209	800	20.5190	86.3313	3.40	166.5	4.45	307.2	4.80	71.5	-1.00	-1.0
209	815	20.5462	86.3225	3.54	166.1	4.32	306.9	4.88	73.7	-1.00	-1.0
209	830	20.5399	86.3320	3.67	163.2	4.21	307.0	4.99	74.9	-1.00	-1.0
209	845	20.5349	86.3336	3.58	162.7	4.29	311.7	5.02	73.8	-1.00	-1.0
209	900	20.5404	86.3215	3.38	163.1	4.45	309.5	5.00	71.3	-1.00	-1.0
209	912S	20.5398	86.3261	3.30	162.5	4.49	311.0	5.09	71.8	-1.00	-1.0
209	915	20.5497	86.3288	3.32	162.8	4.50	311.9	5.01	71.0	-1.00	-1.0
209	930	20.5405	86.3258	3.30	162.1	4.60	312.0	5.12	70.9	-1.00	-1.0
209	945	20.5572	86.3308	2.94	161.2	4.57	313.4	5.09	70.2	-1.00	-1.0
209	1000	20.5590	86.3036	2.64	160.4	4.88	315.1	5.04	66.8	-1.00	-1.0
209	1015	20.5630	86.2950	2.17	158.8	5.15	317.0	5.20	61.6	-1.00	-1.0
209	1030	20.5580	86.2966	1.90	154.4	5.49	319.6	5.40	58.0	-1.00	-1.0
209	1045	20.5545	86.2903	1.68	149.1	5.86	321.6	5.60	54.9	-1.00	-1.0
209	1100	20.5677	86.2846	1.37	141.1	6.28	322.0	5.78	51.2	-1.00	-1.0
*209	1115	20.5400	86.2758	1.18	123.8	6.68	324.4	5.97	47.7	-1.00	-1.0
209	1130	20.5714	86.2628	-1.00	-1.0	7.01	325.2	6.12	45.0	-1.00	-1.0
209	1145	20.5762	86.2611	-1.00	-1.0	7.23	323.8	5.96	42.8	-1.00	-1.0
209	1200	20.5770	86.2595	-1.00	-1.0	7.50	323.1	5.90	42.1	-1.00	-1.0

210	245	19.1322	86.7235	2.34	234.6	1.89	70.2	3.40	326.0	-1.00	-1.0
210	300	19.1330	86.7088	2.50	230.4	1.80	77.0	2.93	322.7	-1.00	-1.0
210	315	19.1417	86.7179	2.64	225.9	1.74	86.9	2.93	321.0	-1.00	-1.0
210	330	19.1580	86.7246	2.68	223.0	1.82	91.5	2.79	318.9	-1.00	-1.0
210	345	19.1702	86.7356	2.63	218.3	1.90	95.3	2.60	322.7	-1.00	-1.0
210	350S	19.1356	86.7392	2.60	216.0	2.02	97.0	2.60	323.0	0.00	0.0
210	400	19.1557	86.7385	2.56	213.0	2.16	97.0	2.47	325.0	-1.00	-1.0
210	415	19.1729	86.7436	2.48	209.0	2.28	97.0	2.38	328.0	-1.00	-1.0
210	430	19.1745	86.7401	2.44	205.0	2.43	97.0	2.50	331.0	-1.00	-1.0
210	445	19.1832	86.7361	2.62	206.5	2.37	102.0	2.23	326.0	-1.00	-1.0
210	500	19.1594	86.7578	2.64	204.5	2.48	105.5	2.04	324.5	-1.00	-1.0
210	515	19.1730	86.7523	2.96	201.5	2.86	107.0	2.16	328.2	-1.00	-1.0
210	530	19.1720	86.7453	2.86	199.0	2.90	105.0	2.16	332.0	-1.00	-1.0
210	536S	19.1663	86.7567	2.79	200.0	2.88	103.0	2.20	332.0	-1.00	-1.0
210	545	19.1834	86.7493	2.68	200.0	2.88	100.5	2.27	335.5	-1.00	-1.0
210	600	19.1809	86.7543	2.34	200.0	2.64	98.4	2.10	338.5	-1.00	-1.0
210	615	19.1757	86.7646	2.45	200.5	2.94	94.5	2.45	340.5	-1.00	-1.0
210	630	19.1870	86.7685	2.37	196.0	3.10	95.0	2.42	346.5	-1.00	-1.0
210	645	19.1794	86.7751	2.36	190.5	3.00	95.0	2.32	351.0	-1.00	-1.0
210	700	19.1794	86.7795	2.20	190.0	2.93	97.5	2.00	347.0	-1.00	-1.0
210	715	19.2009	86.7761	2.50	196.0	2.85	103.2	1.82	349.0	-1.00	-1.0
210	730	19.2069	86.7816	2.71	187.0	3.60	104.0	1.90	352.0	-1.00	-1.0
210	745	19.2070	86.7860	2.90	183.0	3.35	110.0	1.67	355.0	-1.00	-1.0
210	800	19.2234	86.7885	2.84	180.2	3.65	112.9	1.23	358.3	-1.00	-1.0
210	815	19.2302	86.7878	3.00	179.7	3.70	115.5	1.21	6.0	-1.00	-1.0
210	830	19.2312	86.7948	3.30	177.0	3.90	117.2	1.14	16.5	-1.00	-1.0
210	845	19.2399	86.7953	2.95	175.1	3.80	115.0	1.26	11.0	-1.00	-1.0
210	900	19.2434	86.8015	3.20	175.7	3.79	114.1	1.38	5.8	-1.00	-1.0
210	915	19.2467	86.8033	3.12	175.0	3.80	113.3	1.45	4.8	-1.00	-1.0
210	930	19.2330	86.8088	2.91	175.0	3.76	112.0	1.57	3.2	-1.00	-1.0
210	945	19.2475	86.8016	2.49	173.2	3.73	108.0	1.56	1.5	-1.00	-1.0
210	1000	19.2415	86.8005	2.33	172.8	3.69	105.9	1.76	.9	-1.00	-1.0
210	1015	19.2364	86.8020	2.20	171.8	3.62	102.7	1.89	1.3	-1.00	-1.0
210	1030	19.2415	86.7961	2.38	166.2	3.71	102.6	2.13	7.0	-1.00	-1.0
210	1045	19.2579	86.8030	2.11	162.4	3.80	102.9	1.79	11.7	-1.00	-1.0
210	1100	19.2467	86.8033	2.52	158.3	4.00	103.2	2.14	17.2	-1.00	-1.0
210	1115	19.2717	86.8018	2.54	155.5	4.12	102.9	2.24	20.4	-1.00	-1.0
210	1130	19.2750	86.7995	2.62	151.0	4.30	103.2	2.24	24.6	-1.00	-1.0
210	1145	19.2787	86.8100	2.38	146.4	4.38	102.8	1.99	28.9	-1.00	-1.0
210	1200	19.2880	86.8086	2.49	144.4	4.50	102.8	1.93	31.8	-1.00	-1.0
210	1215	19.2781	86.8291	2.56	141.2	4.61	103.2	2.17	36.4	-1.00	-1.0
210	1230	19.2799	86.8343	2.62	137.8	4.82	101.3	2.40	35.0	-1.00	-1.0
210	1245	19.3090	86.8330	4.20	135.0	5.80	109.0	2.58	67.0	-1.00	-1.0
210	1300	19.3145	86.8533	4.52	135.6	6.40	110.9	2.75	76.0	-1.00	-1.0
210	1315	19.3237	86.8301	4.86	164.7	5.30	129.9	3.23	154.3	2.46	249.5
210	1330	19.3524	86.8028	3.80	177.0	4.20	133.3	3.71	232.6	2.90	261.7
210	1345	19.3012	86.7640	2.76	243.1	3.42	102.6	4.20	310.9	6.22	289.1
210	1400	19.2929	86.7811	-1.00	-1.0	2.64	71.9	4.40	346.2	5.10	311.5
210	1415	19.3022	86.8336	2.38	113.0	4.88	92.5	3.42	26.5	2.70	332.5
210	1430	19.3117	86.8323	2.46	110.2	4.90	92.0	3.49	27.0	2.75	333.1
210	1445	19.3084	86.8391	2.45	111.4	4.89	92.1	3.50	27.5	2.70	333.8
210	1500	19.3262	86.8338	2.37	111.3	4.73	92.0	3.49	25.8	2.85	332.6
210	1515	19.3450	86.8311	2.36	110.8	4.70	92.1	3.45	25.5	2.81	333.0
210	1530	19.3255	86.8441	2.53	111.1	4.90	93.9	3.50	27.0	2.85	333.9
210	1545	19.3470	86.8408	2.66	112.3	5.00	94.5	3.50	28.5	2.66	337.0
210	1600	19.3342	86.8490	2.80	111.0	5.10	95.0	3.50	33.0	2.52	339.0
210	1615	19.3352	86.8560	3.00	111.5	5.30	96.5	3.55	35.0	2.40	342.5
210	1630	19.3559	86.8586	3.45	112.0	5.65	97.0	3.60	39.5	2.24	347.5
210	1645	19.3594	86.8648	3.60	112.0	5.75	98.0	3.60	43.0	2.15	350.0
210	1656S	19.3589	86.8713	3.70	113.0	5.85	99.0	3.60	44.0	2.32	354.0
210	1700	19.3655	86.8703	3.80	112.3	5.90	99.3	3.63	44.0	2.40	356.0
210	1715	19.3759	86.8716	4.00	112.0	6.15	101.0	3.70	48.0	2.36	0.0
210	1730	19.3819	86.8728	4.00	110.0	6.10	99.5	3.85	46.0	2.39	0.0
*210	1745	19.4204	86.8656	4.00	108.0	6.10	97.3	3.92	44.0	2.52	359.5

211	9165	19.6893	86.8938	4.00	110.9	5.40	106.8	4.36	32.8	4.31	343.8
211	930	19.6944	86.8860	3.91	108.5	5.30	105.0	4.56	31.4	4.52	343.7
211	945	19.6955	86.8930	3.84	105.0	5.29	103.7	4.70	30.2	4.70	345.3
211	1000	19.6953	86.8843	3.84	102.4	5.27	101.8	4.90	29.9	4.98	344.9
211	1015	19.7031	86.8907	3.97	101.7	5.39	101.8	5.11	30.2	5.00	347.6
211	1030	19.7099	86.8902	4.11	101.3	5.52	101.1	5.09	32.2	4.98	349.8
211	1045	19.7144	86.8990	4.22	101.2	5.62	101.0	5.10	33.9	4.98	351.9
211	1100	19.7284	86.8787	4.39	101.8	5.79	100.9	5.21	35.7	4.95	353.5
211	1115S	19.7285	86.8831	4.58	100.8	5.91	100.7	5.28	37.3	4.95	355.7
211	1130	19.7472	86.8848	4.70	101.2	6.08	101.0	5.32	38.6	4.94	357.0
211	1145	19.7439	86.8828	4.85	101.0	6.20	101.0	5.45	40.4	4.95	359.8
211	1200	19.7544	86.8928	5.12	101.0	6.50	101.0	5.68	42.0	5.10	.5
211	1215	19.7485	86.9005	5.30	100.1	6.63	99.8	5.79	43.0	5.12	1.9
211	1230	19.7554	86.8998	5.30	96.5	6.65	97.5	6.08	41.0	5.39	3.1
211	1245	19.7620	86.8993	5.48	95.9	6.88	97.0	6.30	42.1	5.46	5.2
211	1258S	19.7581	86.9333	5.64	96.0	7.01	96.1	6.35	43.3	5.51	6.2
211	1300	19.7632	86.9063	5.63	95.9	6.99	96.9	6.35	43.2	5.57	7.0
211	1315	19.7674	86.9065	5.71	94.3	7.05	96.1	6.54	43.0	5.63	7.0
211	1330	19.7717	86.9110	5.81	91.8	7.09	94.2	6.78	42.2	5.99	7.9
211	1345	19.7700	86.9100	5.82	90.8	7.10	92.8	6.90	40.9	6.10	7.8
211	1400	19.7737	86.9163	5.99	91.5	7.25	93.6	6.85	43.0	6.00	8.9
211	1415	19.8144	86.8761	3.99	123.3	5.13	118.1	3.79	33.2	4.90	335.1
211	1430	19.8175	86.8650	3.75	123.0	5.00	118.6	3.66	31.0	4.70	334.2
211	1445	19.8277	86.8663	3.70	121.0	4.96	116.6	3.90	30.0	4.81	334.4
211	1446S	19.8211	86.8788	3.70	121.0	4.96	116.6	3.90	30.0	4.81	334.4
211	1500	19.8420	86.8633	3.69	118.7	5.00	115.8	4.05	30.1	5.00	335.0
211	1515	19.8312	86.8725	3.55	115.0	4.85	113.0	4.25	28.5	5.23	337.5
211	1530	19.8237	86.8748	3.52	112.2	4.80	117.6	4.45	28.1	5.39	338.5
211	1545	19.8484	86.8731	3.70	112.3	4.94	111.2	4.45	29.9	5.35	339.4
211	1600	19.8457	86.8740	3.65	120.5	4.88	118.1	3.92	30.5	5.08	334.0
211	1615	19.8550	86.8683	3.30	124.0	4.50	120.0	3.80	26.0	5.35	330.0
211	1630	19.8534	86.8716	3.25	122.0	4.50	118.5	3.90	24.0	5.50	331.0
211	1645	19.8685	86.8670	3.00	120.0	4.45	118.0	4.00	24.0	5.60	331.0
211	1700	19.8720	86.8690	3.10	117.0	4.58	117.0	4.20	25.0	5.68	333.2
211	1715	19.8687	86.8758	3.38	115.2	4.60	115.3	4.26	26.5	5.71	335.0
211	1730	19.8807	86.8780	3.40	111.5	4.65	112.8	4.45	27.5	5.82	337.5
211	1745	19.8839	86.8816	3.50	108.5	4.70	110.0	4.65	29.8	5.90	339.2
211	1800	19.8647	86.8843	3.50	103.8	4.70	108.5	4.82	27.2	6.10	339.5
211	1815	19.8900	86.8766	3.50	99.8	4.68	106.0	5.02	26.8	6.32	341.0
211	1830	19.8799	86.8796	3.58	96.0	4.70	103.2	5.22	28.3	6.52	341.6
211	1845	19.8910	86.8793	3.50	103.5	4.70	108.0	4.80	28.5	6.20	340.0
211	1900	19.9054	86.8763	3.59	117.0	4.80	118.5	4.10	31.0	5.60	335.5
211	1915	19.9255	86.8701	3.80	120.0	5.00	121.0	3.95	35.0	5.40	336.0
211	1930	19.9317	86.8756	4.00	119.5	5.30	120.5	4.00	39.0	5.20	337.5
211	1945	19.9437	86.8821	4.25	119.0	5.50	120.0	4.05	43.0	5.00	340.0
211	2000	19.9445	86.8848	4.50	118.3	5.75	120.1	4.12	47.1	4.87	342.0
211	2015	19.9582	86.8836	4.72	118.3	6.00	120.1	4.18	49.5	4.77	344.3
211	2030	19.9650	86.8875	4.99	118.9	6.23	120.9	4.30	53.3	4.68	347.1
211	2045	19.9542	86.8966	5.18	119.5	6.46	120.9	4.41	56.6	4.58	348.4
211	2100	19.9670	86.8971	5.43	119.8	6.66	121.2	4.50	58.9	4.46	350.9
211	2115	19.9997	86.8826	5.57	119.4	6.78	121.4	4.61	60.7	4.47	352.3
*211	2130	19.9579	86.9028	5.46	117.2	6.78	120.2	4.61	60.0	4.45	352.6
211	2145	19.9925	86.8981	5.47	115.4	6.71	119.3	4.89	58.7	4.70	355.9
211	2200	19.9925	86.8945	5.43	113.1	6.70	117.1	5.05	57.5	4.95	357.4
211	2215	19.9745	86.8905	5.40	111.5	6.65	115.6	5.15	56.0	5.12	357.0
211	2230	20.0052	86.8943	5.58	110.0	6.77	115.1	5.39	56.7	5.21	.1
211	2232S	20.0092	86.8879	5.58	110.0	6.77	115.1	5.39	56.7	5.21	.1
211	2245	19.9969	86.9026	5.81	109.0	7.00	114.6	5.66	58.0	5.30	2.3
*211	2300	20.0430	86.8870	6.00	108.2	7.20	114.2	5.89	59.5	5.39	4.2
*211	2315	20.0709	86.8828	6.14	106.6	7.31	113.2	6.02	59.6	5.45	7.1
211	2330	20.0282	86.9003	6.31	106.4	7.43	112.0	6.30	60.1	5.60	9.1
211	2345	20.0399	86.8938	6.41	105.6	7.60	112.5	6.50	61.2	5.55	10.8
212	0	20.0700	86.8801	6.14	108.8	7.42	115.6	6.20	61.9	5.10	7.4
212	15	20.0829	86.8850	5.89	114.0	7.20	119.9	5.52	63.0	4.90	3.1
212	30	20.1104	86.8721	5.73	119.9	7.01	124.9	5.00	65.3	4.43	358.3
212	45	20.1120	86.8731	5.40	125.2	6.76	130.1	4.40	67.1	4.30	351.8
212	48S	20.0909	86.8601	5.40	125.2	6.76	130.1	4.40	67.1	4.30	351.8

212	100	20.1174	86.8525	5.30	130.5	6.60	134.5	3.95	68.2	4.14	346.2
212	115	20.1122	86.8496	5.26	130.8	6.53	134.2	3.96	69.0	4.13	346.8
212	130	20.1365	86.8435	5.24	128.8	6.50	132.9	4.04	68.0	4.21	348.3
212	145	20.1150	86.8575	5.20	126.0	6.46	131.6	4.25	66.6	4.40	352.0
212	200	20.1355	86.8365	5.20	124.8	6.45	130.5	4.41	66.2	4.49	353.9
212	204S	20.1230	86.8295	5.25	127.1	6.50	132.6	4.27	68.0	4.30	353.0
212	215	20.1604	86.8200	5.23	128.8	6.50	134.0	4.14	69.7	4.26	351.5
212	230	20.1485	86.8178	5.29	134.4	6.50	138.7	3.77	73.2	4.02	347.2
212	245	20.1742	86.8040	5.34	140.0	6.59	143.6	3.39	77.8	3.71	343.0
212	300	20.1642	86.8071	5.45	145.8	6.69	147.9	2.84	84.2	3.61	335.5
212	315	20.1977	86.7953	5.70	151.2	6.96	153.0	2.60	91.3	3.45	329.3
212	330	20.1924	86.7881	5.80	153.1	7.06	154.1	2.61	96.8	3.35	328.5
212	345	20.2165	86.7776	6.10	153.0	7.38	154.0	2.74	100.2	2.89	330.2
212	400	20.2099	86.7826	6.40	154.0	7.70	155.0	3.10	104.0	3.00	330.0
212	415	20.2240	86.7753	6.75	153.0	8.00	156.0	3.40	109.0	2.86	332.0
212	430	20.2242	86.7796	6.80	154.0	8.10	157.0	3.40	109.0	2.89	332.0
212	445	20.2330	86.7651	6.25	158.0	7.50	159.0	2.96	103.0	3.36	330.0
212	500	20.2244	86.7561	5.60	159.0	6.90	160.0	2.70	90.5	4.10	331.0
212	515	20.2282	86.7475	5.40	159.0	6.70	161.5	2.60	87.0	4.22	332.0
212	530	20.2375	86.7461	5.48	159.0	6.78	160.0	2.71	89.0	4.22	334.0
212	545	20.2442	86.7455	5.41	157.8	6.78	159.2	2.83	85.0	4.25	337.0
212	600	20.2437	86.7560	5.40	155.0	6.70	157.2	3.15	82.0	4.40	342.0
212	615	20.2469	86.7491	5.35	154.0	6.70	157.0	2.90	80.0	4.45	346.5
212	630	20.2365	86.7435	5.30	152.5	6.65	157.0	3.00	78.0	4.60	348.2
212	638S	20.2535	86.7272	5.25	152.0	6.70	157.0	3.00	77.0	4.70	349.0
212	645	20.2522	86.7326	5.20	153.0	6.50	157.5	2.90	76.0	4.80	348.0
212	700	20.2539	86.7293	5.20	157.0	6.60	160.0	3.00	76.0	4.70	347.0
212	715	20.2779	86.7188	5.40	157.0	6.80	160.0	2.90	80.0	4.60	349.0
212	730	20.2895	86.7121	5.60	157.0	7.05	161.0	3.00	84.0	4.35	349.0
212	745	20.2904	86.7105	5.85	159.0	7.30	161.0	3.00	88.0	4.20	350.0
212	800	20.2910	86.7045	6.07	158.7	7.50	161.6	2.96	91.5	4.10	352.2
212	815	20.3129	86.7035	6.20	159.8	7.66	162.3	2.85	94.9	3.88	354.0
212	830	20.3035	86.7048	6.35	160.0	7.84	162.8	2.94	97.5	3.80	355.2
212	838S	20.3293	86.6960	6.50	160.1	7.90	163.0	2.99	99.0	3.70	356.0
212	845	20.3200	86.6923	6.56	160.0	8.00	163.0	3.00	100.6	3.72	356.6
212	900	20.3142	86.6956	6.78	160.0	8.30	163.2	3.31	103.2	3.60	358.7
212	915	20.3494	86.6890	6.90	160.3	8.38	163.0	3.43	104.8	3.60	1.6
212	930	20.3800	86.6778	6.90	159.4	8.41	163.6	3.50	104.0	3.80	2.6
212	945	20.3475	86.6836	6.71	158.3	8.20	162.2	3.52	99.7	4.19	5.8
212	1000	20.3680	86.6713	6.57	157.5	8.07	161.2	3.68	95.9	4.49	6.8
212	1015	20.3489	86.6760	6.42	155.9	8.00	160.0	3.78	92.3	4.91	8.3
212	1030	20.3340	86.6850	6.33	154.3	7.88	159.1	3.90	89.0	5.31	10.4
212	1045	20.3489	86.6760	6.20	152.7	7.78	158.6	4.09	86.8	5.65	11.4
*212	1100	20.4037	86.6543	6.09	152.7	7.69	158.8	4.09	85.2	5.93	12.8
212	1115	20.3969	86.6505	6.11	152.1	7.78	158.7	4.12	84.2	6.15	13.2
212	1130	20.4099	86.6405	6.14	152.2	7.78	158.3	4.28	83.8	6.49	13.3
212	1145	20.4175	86.6425	6.19	150.9	7.89	156.0	4.37	83.2	6.62	14.8
212	1200	20.4099	86.6405	6.20	151.5	7.92	157.5	4.45	82.0	6.80	16.0
212	1210S	20.4163	86.6504	6.27	151.0	7.95	157.9	4.59	82.2	6.85	16.1
212	1215	20.4224	86.6365	6.29	149.9	7.93	157.1	4.58	82.0	6.94	16.2
212	1230	20.4429	86.6198	6.50	150.2	8.13	158.2	4.72	83.4	6.90	17.1
212	1245	20.4444	86.6163	6.50	150.8	8.21	158.9	4.71	82.5	7.05	17.3
212	1300	20.4382	86.6345	6.32	149.1	8.00	158.0	4.80	76.8	7.61	16.2
212	1315	20.4472	86.6243	6.40	151.0	8.20	159.0	4.69	79.9	7.25	16.0
212	1330	20.4527	86.6166	6.23	148.1	7.99	157.9	4.95	75.0	7.90	16.9
212	1345	20.4577	86.6150	6.19	147.3	7.90	157.1	5.01	73.0	8.15	17.1
212	1400	20.4510	86.6156	6.33	145.1	7.99	157.2	5.25	73.0	8.38	17.0
212	1415	20.4742	86.6068	6.30	145.9	8.03	156.6	5.21	72.9	8.60	17.3
212	1430	20.4742	86.6068	6.25	144.8	7.96	156.7	5.33	71.2	8.81	17.8
212	1445	20.4940	86.6005	6.15	142.3	7.75	155.4	5.48	69.7	9.20	17.2
212	1500	20.4932	86.5978	6.14	140.1	7.21	155.0	5.63	67.7	9.45	17.0
212	1515	20.5054	86.5851	5.95	144.5	7.68	158.0	5.25	66.0	9.40	15.0
212	1518S	20.5053	86.5917	5.95	144.5	7.68	158.0	5.25	66.0	9.40	15.0
212	1530	20.5229	86.5840	6.09	145.1	7.83	158.7	5.19	68.0	9.29	14.1
212	1545	20.5122	86.5888	6.30	147.5	8.10	159.4	5.05	70.0	9.18	14.0
212	1600	20.5419	86.5750	6.60	146.5	8.35	159.0	5.25	71.0	9.30	14.5

212 1615	20.5412	86.5811	6.75	146.0	8.55	158.0	5.35	72.0	9.30	15.0
212 1630	20.5337	86.5835	6.90	145.0	8.70	158.5	5.40	72.5	9.30	16.0
212 1645	20.5602	86.5765	7.10	146.0	8.90	158.0	5.55	74.0	9.25	16.0
212 1700	20.5570	86.5835	7.22	144.0	9.00	159.2	5.54	74.4	9.28	18.0
212 1715	20.5894	86.5731	7.40	143.2	9.20	157.2	5.70	75.0	9.30	17.5
212 1730	20.5950	86.5698	7.52	144.0	9.32	156.7	5.80	76.2	9.26	18.8
212 1745	20.5960	86.5725	7.70	142.2	9.48	156.0	5.95	76.0	9.30	19.0
212 1800	20.6142	86.5696	7.80	141.0	9.60	155.2	6.10	76.0	9.30	19.5
212 1815	20.6299	86.5631	8.00	144.0	9.75	153.5	6.25	76.0	9.30	20.0
212 1830	20.6012	86.5560	6.60	136.0	8.40	153.0	6.20	61.0	10.50	13.0
212 1845	20.5744	86.5218	5.10	153.0	3.60	118.6	7.10	33.0	13.25	4.0
212 1900	20.5090	86.5116	2.66	57.0	2.36	140.0	9.30	7.0	22.80	359.0
212 1915	20.4970	86.4726	2.90	3.0	-1.00	-1.0	10.40	8.0	19.20	9.0
212 1930	20.5112	86.4740	2.86	11.0	-1.00	-1.0	10.50	7.0	20.40	7.0
212 1940S	20.5317	86.4511	2.67	34.4	-1.00	-1.0	9.73	12.8	18.20	14.0
212 1945	20.5512	86.4745	2.27	46.0	-1.00	-1.0	9.20	15.5	17.80	15.2
*212 2000	20.4874	86.5126	2.90	146.2	-1.00	-1.0	5.95	26.2	12.58	357.5
212 2015	20.6454	86.4486	4.29	192.8	-1.00	-1.0	3.20	.6	10.85	342.1
212 2030	20.7075	86.3901	7.31	208.6	-1.00	-1.0	3.00	293.5	10.12	325.1
*212 2045	20.7539	86.3810	10.80	202.5	-1.00	-1.0	4.25	231.9	8.15	305.5
212 2100	20.8234	86.3806	11.72	200.0	-1.00	-1.0	4.71	221.7	7.61	298.4
*212 2115	20.7852	86.3768	11.82	199.2	-1.00	-1.0	4.82	220.1	7.59	296.7
212 2126S	20.8238	86.3639	11.79	198.3	-1.00	-1.0	4.75	219.0	-1.00	-1.0
*212 2130	20.7804	86.3828	11.77	198.5	-1.00	-1.0	4.78	218.9	7.59	296.0
212 2145	20.8500	86.3586	11.78	197.8	-1.00	-1.0	4.70	219.0	7.50	294.8
212 2200	20.8452	86.3646	11.48	198.1	-1.00	-1.0	4.37	219.2	7.62	295.9
212 2215	20.8549	86.3570	11.48	198.4	-1.00	-1.0	4.43	218.8	7.61	294.9
212 2230	20.8490	86.3560	11.50	198.7	-1.00	-1.0	4.42	218.8	7.70	293.7
212 2245	20.8692	86.3626	11.50	198.6	-1.00	-1.0	4.41	218.9	7.82	292.8
212 2300	20.8709	86.3398	11.50	198.8	-1.00	-1.0	4.41	219.8	7.88	291.2
212 2315	20.8815	86.3393	11.53	199.2	-1.00	-1.0	4.50	220.1	8.03	290.7
212 2330	20.8983	86.3442	11.58	199.3	-1.00	-1.0	4.51	220.1	8.20	288.8
212 2345	20.9142	86.3271	11.60	200.1	-1.00	-1.0	4.62	221.4	8.34	288.0
*213 0	20.9789	86.2850	11.65	199.5	-1.00	-1.0	4.60	222.0	8.53	287.0
213 15	20.9527	86.3160	11.71	200.0	-1.00	-1.0	4.68	222.5	8.72	285.0
213 30	20.9714	86.3068	11.74	201.4	-1.00	-1.0	4.70	222.9	8.96	285.2
213 45	20.9757	86.3113	11.79	201.1	-1.00	-1.0	4.81	222.6	9.22	282.9
213 100	20.9717	86.2918	11.85	201.8	-1.00	-1.0	4.88	222.5	9.55	281.8
213 115	20.9739	86.2823	11.95	201.9	-1.00	-1.0	4.91	221.7	9.88	281.5
213 130	21.0117	86.2816	12.12	201.7	-1.00	-1.0	5.08	221.4	10.11	279.5
213 145	21.0199	86.2775	12.30	202.0	-1.00	-1.0	5.30	219.0	10.80	278.5
213 146S	20.9905	86.2760	12.30	202.0	-1.00	-1.0	5.30	219.0	10.80	278.5
213 200	21.0245	86.2715	12.35	202.0	-1.00	-1.0	5.40	219.5	10.65	280.5
213 215	21.0074	86.2726	12.15	202.0	-1.00	-1.0	5.10	218.5	10.80	282.0
213 230	21.0152	86.2596	11.82	201.5	-1.00	-1.0	4.81	219.6	10.95	284.3
213 245	21.0145	86.2658	11.90	202.0	-1.00	-1.0	4.80	220.0	11.20	285.5
213 300	21.0502	86.2510	12.29	201.8	-1.00	-1.0	5.08	216.8	11.45	284.5
213 315	21.0612	86.2355	12.75	201.0	-1.00	-1.0	5.40	214.0	11.45	283.5
213 330	21.0694	86.2313	13.00	200.1	-1.00	-1.0	5.51	212.2	11.29	283.9
213 345	21.0922	86.2266	13.25	201.5	-1.00	-1.0	5.70	212.6	11.25	284.0
213 400	21.1102	86.2236	13.50	200.0	-1.00	-1.0	5.70	210.0	11.20	285.0
213 415	21.1150	86.2220	13.70	199.0	-1.00	-1.0	5.90	207.0	11.05	283.5
213 430	21.1367	86.2058	13.90	199.0	-1.00	-1.0	5.80	207.0	10.90	286.0
213 445	21.1532	86.2106	13.90	198.0	-1.00	-1.0	5.80	205.0	10.80	286.0
213 452S	21.1306	86.2196	13.80	198.0	-1.00	-1.0	5.70	204.0	10.80	288.0
213 500	21.1380	86.1980	13.80	198.0	-1.00	-1.0	5.50	207.0	10.80	289.0
213 515	21.1609	86.1933	13.75	198.0	-1.00	-1.0	5.50	205.0	10.55	290.0
213 530	21.1579	86.2003	13.75	196.5	-1.00	-1.0	5.35	205.0	10.55	292.0
213 545	21.1815	86.1983	13.85	195.0	-1.00	-1.0	5.30	203.0	10.45	293.5
213 600	21.1889	86.1958	13.45	195.0	-1.00	-1.0	4.90	202.5	10.65	294.0
213 615	21.1904	86.1923	13.25	196.0	-1.00	1.0	4.55	204.5	10.80	296.0
213 630	21.2072	86.1821	13.43	196.0	-1.00	-1.0	4.70	208.5	11.22	295.6
213 645	21.2030	86.1821	13.50	195.5	-1.00	-1.0	4.55	206.5	11.20	295.5
213 700	21.2164	86.1851	13.65	195.0	-1.00	1.0	4.50	205.5	11.25	295.0
213 715	21.2480	86.1790	13.70	195.0	-1.00	-1.0	4.50	205.0	11.40	297.0
213 724S	21.2284	86.1816	13.80	194.5	-1.00	-1.0	4.40	204.0	11.30	296.0
213 730	21.2522	86.1790	13.80	193.4	-1.00	-1.0	4.40	204.0	11.30	296.5

213	745	21.2787	86.1656	13.90	193.0	-1.00	-1.0	4.30	203.0	11.40	295.5
213	800	21.2452	86.1650	14.00	191.6	-1.00	-1.0	4.40	200.4	11.43	296.5
213	815	21.2875	86.1641	14.08	191.0	-1.00	-1.0	4.30	199.5	11.64	296.2
213	830	21.3014	86.1610	14.28	189.8	-1.00	-1.0	4.30	198.0	11.58	297.0
213	845	21.3110	86.1576	14.28	189.5	-1.00	-1.0	4.25	196.9	11.72	296.8
213	900	21.3239	86.1473	14.24	188.7	-1.00	-1.0	4.15	197.0	11.90	294.4
213	9105	21.3064	86.1566	14.00	188.0	-1.00	-1.0	3.99	196.0	12.09	299.1
213	915	21.3288	86.1347	14.02	188.0	-1.00	-1.0	4.00	195.4	12.18	299.8
213	930	21.3353	86.1340	13.76	188.0	-1.00	-1.0	3.66	198.6	12.56	301.0
213	945	21.3382	86.1227	13.57	196.9	-1.00	-1.0	3.41	198.6	12.92	303.0
213	1000	21.3437	86.1148	13.32	186.3	-1.00	-1.0	2.96	196.6	13.20	304.0
213	1015	21.3420	86.1293	13.22	186.2	-1.00	-1.0	2.88	197.7	13.56	304.8
213	1030	21.3583	86.1143	13.30	186.1	-1.00	-1.0	2.80	199.1	13.89	306.5
213	1045	21.3868	86.1107	13.27	184.4	-1.00	-1.0	2.88	197.8	14.00	307.1
213	1100	21.3692	86.1182	12.75	183.3	-1.00	-1.0	2.36	193.0	14.30	310.1
213	1115	21.3835	86.1088	12.43	182.4	-1.00	-1.0	2.20	192.1	14.91	314.0
213	1130	21.3408	86.1023	9.33	180.9	-1.00	-1.0	-1.00	-1.0	-1.00	-1.0
213	1145	21.2452	86.1073	5.55	179.5	-1.00	-1.0	5.41	359.3	-1.00	-1.0
213	1200	21.2378	86.1058	1.60	170.0	-1.00	-1.0	9.70	359.7	-1.00	-1.0
213	1215	21.2195	86.0957	-1.00	-1.0	-1.00	-1.0	10.50	358.4	-1.00	-1.0
213	1230	21.2325	86.0898	-1.00	-1.0	-1.00	-1.0	11.20	357.1	-1.00	-1.0
213	1245	21.2375	86.0925	-1.00	-1.0	-1.00	-1.0	11.28	358.0	-1.00	-1.0
213	1300	21.2528	86.0858	-1.00	-1.0	-1.00	-1.0	11.28	358.5	-1.00	-1.0
213	1315	21.2527	86.0815	-1.00	-1.0	-1.00	-1.0	11.46	358.2	-1.00	-1.0
213	1330	21.2788	86.0830	-1.00	-1.0	-1.00	-1.0	9.60	358.0	-1.00	-1.0
213	1345	21.3630	86.0843	-1.00	-1.0	-1.00	-1.0	5.99	358.6	-1.00	-1.0
213	1400	21.4332	86.0843	-1.00	-1.0	-1.00	-1.0	2.31	4.0	-1.00	-1.0
213	1415	21.4845	86.0848	-1.00	-1.0	-1.00	-1.0	-1.00	-1.0	-1.00	-1.0
213	1430	21.4960	86.0868	-1.00	-1.0	-1.00	-1.0	-1.00	-1.0	17.70	327.0
213	1445	21.5650	86.1230	-1.00	-1.0	-1.00	-1.0	-1.00	-1.0	15.25	327.9
213	1500	21.6273	86.1750	-1.00	-1.0	-1.00	-1.0	-1.00	-1.0	11.49	330.0
213	1515	21.6917	86.2173	-1.00	-1.0	-1.00	-1.0	-1.00	-1.0	7.91	336.3
213	1530	21.7518	86.2700	-1.00	-1.0	-1.00	-1.0	-1.00	-1.0	3.09	356.5

228	1530	18.2055	86.3795	2.91	149.5	2.18	41.5	-1.00	-1.0	3.85	117.5
228	1545	18.2177	86.3775	2.94	154.0	2.03	87.0	-1.00	-1.0	3.80	122.0
228	1600	18.2204	86.3811	2.57	157.2	1.82	88.5	-1.00	-1.0	3.53	123.6
228	1615	18.2169	86.3835	2.84	160.0	1.69	85.5	-1.00	-1.0	3.50	126.2
228	1630	18.2210	86.3880	2.87	158.1	1.76	87.7	-1.00	-1.0	3.50	125.0
228	1645	18.2167	86.3965	2.96	156.0	1.84	91.4	-1.00	-1.0	3.74	125.0
228	1700	18.2254	86.4013	3.05	156.0	1.88	95.1	-1.00	-1.0	3.80	125.0
228	1715	18.2262	86.3996	2.98	157.5	1.81	94.2	-1.00	-1.0	3.70	127.3
228	1730	18.2244	86.4030	2.96	157.2	1.79	95.2	-1.00	-1.0	3.70	127.0
228	1745	18.2384	86.4020	2.92	158.0	1.74	95.6	-1.00	-1.0	3.52	128.0
228	1800	18.2314	86.4068	2.95	159.0	1.69	99.0	-1.00	-1.0	3.65	128.5
228	1815	18.2322	86.4095	2.96	159.0	1.70	99.5	-1.00	-1.0	3.70	129.5
228	1830	18.2374	86.4123	2.90	156.0	1.72	93.5	-1.00	-1.0	3.55	126.5
228	1845	18.2304	86.4171	2.27	143.0	1.80	65.0	-1.00	-1.0	2.94	115.0
228	1900	18.2120	86.4180	1.88	148.0	1.76	49.5	-1.00	-1.0	2.67	109.0
228	1915	18.2147	86.4130	1.96	154.0	1.56	50.0	-1.00	-1.0	2.65	115.0
228	1930	18.2340	86.4061	2.08	162.0	1.30	53.5	-1.00	-1.0	2.60	122.0
228	1945	18.2252	86.4186	1.88	152.0	1.62	46.7	.20	351.0	2.58	111.0
228	2000	18.2094	86.4231	1.45	121.0	2.29	33.5	1.40	9.0	2.63	92.0
228	2015	18.1945	86.4301	1.64	102.8	2.58	27.5	1.62	2.0	2.64	85.0
228	2030	18.2059	86.4298	.91	102.2	2.49	22.7	1.63	355.2	2.44	83.1
228	2045	18.2120	86.4223	.72	99.0	2.47	18.0	1.72	347.4	2.26	81.6
228	2100	18.2304	86.4215	.64	99.0	2.44	16.5	1.72	347.4	2.22	82.0
228	2115	18.2120	86.4266	.72	89.0	2.51	17.0	1.80	349.5	2.28	80.0
228	2130	18.2262	86.4040	.52	68.0	2.17	12.0	2.05	347.5	2.25	72.0
228	2145	18.1970	86.4293	1.09	22.0	3.28	5.0	2.73	345.0	2.38	55.0
*228	2200	18.1577	86.4316	1.15	21.8	3.30	6.0	2.80	345.6	2.39	54.5
228	2215	18.1884	86.4290	1.26	16.5	3.48	5.0	2.90	345.3	2.40	51.5
228	2230	18.1919	86.4265	1.37	8.0	3.60	2.0	3.15	343.0	2.38	46.0
228	2245	18.1927	86.4248	1.45	358.8	3.68	358.2	3.31	333.5	2.29	40.7
228	2300	18.2032	86.4263	1.50	355.7	3.73	357.1	3.34	338.7	2.31	38.7
228	2315	18.2049	86.4358	1.76	356.1	3.96	356.1	3.49	338.5	2.35	38.1
228	2330	18.2084	86.4291	1.62	356.8	3.86	356.8	3.48	338.5	2.39	37.0
228	2345	18.2250	86.4273	1.68	359.0	3.95	356.4	3.55	339.6	2.49	37.9
229	0	18.2232	86.4350	1.76	358.9	4.00	356.0	3.60	339.8	2.54	37.0
229	45	18.2032	86.4240	1.76	358.9	4.00	356.0	3.60	339.8	2.54	37.0
*229	15	18.2644	86.4163	1.78	357.7	4.05	356.0	3.66	339.3	2.54	36.8
229	30	18.2215	86.4341	1.83	357.1	4.10	355.0	3.74	339.2	2.60	35.0
229	45	18.2014	86.4340	1.94	356.0	4.20	355.0	3.83	339.3	2.61	34.4
229	100	18.2092	86.4361	2.05	355.0	4.25	354.0	3.90	338.7	2.63	32.3
229	115	18.1997	86.4373	2.12	350.9	4.26	352.1	3.99	335.9	2.54	30.0
229	124.5	18.2151	86.4152	2.20	346.0	4.23	349.5	4.00	333.6	2.43	27.1
229	130	18.2277	86.4266	2.00	345.1	4.23	349.0	4.00	333.0	2.39	27.4
229	145	18.1979	86.4320	1.93	344.3	4.20	348.0	3.95	333.0	2.30	27.9
229	150.5	18.2191	86.4210	1.93	344.3	4.20	348.0	3.95	333.0	2.30	27.9
229	200	18.2075	86.4308	1.86	343.0	4.10	347.3	3.91	331.0	2.22	28.5
229	215	18.1892	86.4360	1.79	342.9	4.02	346.9	3.85	330.5	2.14	29.9
229	230	18.2129	86.4293	1.68	342.3	3.98	346.9	3.80	329.3	2.21	31.2
229	232.5	18.2251	86.4330	1.68	342.3	3.98	346.9	3.80	329.3	2.21	31.2
229	245	18.2207	86.4271	1.62	342.0	3.90	346.0	3.77	328.8	1.97	32.0
229	300	18.2094	86.4275	1.52	341.2	3.81	345.4	3.70	327.6	1.90	33.0
229	315	18.2059	86.4255	1.44	339.8	3.74	344.5	3.65	326.7	1.82	35.1
229	330	18.1919	86.4351	1.35	340.9	3.70	344.0	3.61	325.9	1.80	37.4
229	345	18.2242	86.4203	1.32	344.9	3.70	345.2	3.60	327.5	1.88	39.6
229	400	18.2285	86.4336	1.44	350.0	3.72	347.2	3.60	328.7	1.97	44.5
229	415	18.2160	86.4616	1.54	354.5	3.80	348.5	3.65	330.7	2.04	42.3
229	418.5	18.2388	86.4524	1.54	355.5	3.80	348.5	3.65	330.7	2.90	42.3
229	430	18.2179	86.4408	1.54	359.3	3.90	349.6	3.67	332.0	2.20	43.2
229	445	18.2224	86.4411	1.58	4.0	3.97	351.2	3.70	333.9	2.28	45.0
229	500	18.2345	86.4435	1.61	7.4	3.99	352.1	3.68	333.7	2.35	46.5
229	515	18.2292	86.4450	1.59	5.5	3.90	351.1	3.70	333.5	2.32	45.3
229	530	18.2240	86.4463	1.49	3.2	3.93	348.8	3.70	331.0	2.23	45.5
229	545	18.2125	86.4510	1.46	0.0	3.85	348.0	3.65	329.2	2.14	45.0
229	600	18.2230	86.4525	1.36	355.0	3.80	346.0	3.70	327.5	2.05	45.0
229	615	18.2344	86.4565	1.30	353.5	3.80	344.5	3.70	325.5	1.96	44.0
229	630	18.2352	86.4678	1.20	348.5	3.70	343.0	3.60	323.0	1.82	45.0

229	645	18.2282	86.4640	1.28	352.0	3.80	343.0	3.70	325.0	1.90	42.5
229	700	18.2317	86.4615	1.34	357.5	3.90	346.5	3.75	328.0	2.04	46.0
229	715	18.2327	86.4425	1.46	1.5	4.10	345.5	3.85	328.0	2.18	43.0
229	730	18.2177	86.4670	1.62	3.5	4.25	348.5	4.00	330.5	2.32	43.0
229	745	18.2134	86.4666	1.72	5.0	4.35	350.0	4.10	332.0	2.42	40.5
229	800	18.2115	86.4656	1.90	5.9	4.60	350.0	4.30	334.0	2.56	37.0
229	815	18.2195	86.4548	2.06	5.8	4.75	350.0	4.50	334.0	2.68	36.0
229	830	18.2054	86.4731	2.21	4.1	4.90	348.0	4.60	336.0	2.81	33.0
229	845	18.2132	86.4753	2.37	3.0	5.10	348.8	4.80	334.0	2.92	30.8
229	8465	18.2307	86.4940	2.37	3.0	5.10	348.8	4.80	334.0	2.92	30.8
229	900	18.1957	86.4788	2.46	2.1	5.15	348.0	4.82	334.0	2.95	28.8
*229	9065	18.2330	86.4924	2.44	1.0	5.20	347.8	4.90	333.0	3.10	29.0
229	915	18.2009	86.4860	2.42	0.0	5.15	347.0	4.81	333.0	3.00	28.8
229	930	18.1922	86.4811	2.39	0.0	5.13	346.2	4.82	332.5	2.94	28.8
*229	945	18.1825	86.4825	2.41	0.0	5.22	346.5	4.82	332.2	2.96	29.4
229	1000	18.2262	86.4976	2.40	358.8	5.12	345.0	4.83	331.0	2.88	28.2
229	1015	18.2042	86.5096	2.38	355.8	5.15	343.1	4.90	329.2	2.78	26.0
229	1030	18.2384	86.5000	2.38	357.6	5.13	344.0	4.86	330.2	2.83	27.8
229	1045	18.2602	86.5055	1.97	8.8	4.62	347.6	4.30	331.0	2.68	40.8
229	10585	18.2586	86.5166	1.66	23.9	4.19	350.9	3.80	333.2	2.67	52.2
229	1100	18.2820	86.5066	1.63	26.8	4.00	352.4	3.72	333.1	2.68	53.9
229	1115	18.2845	86.5101	1.53	51.4	3.61	357.1	3.20	334.9	2.81	68.7
229	1130	18.2915	86.5140	1.59	66.8	3.70	.2	2.86	336.5	2.95	75.7
229	1145	18.2819	86.5283	1.60	69.7	3.29	.5	2.80	336.0	2.96	76.6
229	1200	18.2617	86.5411	1.60	65.5	3.36	359.2	2.90	335.0	2.94	74.9
229	1215	18.2782	86.5395	1.56	64.6	3.40	358.4	2.96	333.5	2.86	74.7
229	1230	18.2712	86.5443	1.50	58.2	3.48	356.0	3.00	331.9	2.77	72.5
229	1245	18.2860	86.5415	1.34	61.0	3.34	353.9	3.10	328.6	2.63	74.9
229	12465	18.2824	86.5471	1.34	61.0	3.34	353.9	3.10	328.6	2.63	74.9
229	1300	18.2905	86.5375	1.25	66.1	3.20	352.2	2.94	326.3	2.58	77.9
229	1315	18.2879	86.5425	1.26	68.2	3.20	353.0	2.90	326.0	2.62	78.9
229	1330	18.2947	86.5463	1.26	68.9	3.40	351.9	2.91	324.5	2.58	79.0
229	1345	18.2982	86.5438	1.08	63.7	3.20	348.0	3.10	321.0	2.37	77.6
229	1400	18.2922	86.5470	.90	56.6	3.20	343.3	3.15	317.1	2.20	77.0
229	1415	18.3052	86.5433	.83	65.4	3.20	342.6	3.20	315.8	2.18	81.0
229	1430	18.3017	86.5545	.98	74.8	2.97	344.9	2.92	316.9	2.36	84.0
229	1445	18.3017	86.5545	1.47	53.0	3.48	350.8	3.26	328.6	2.72	71.5
229	1500	18.2964	86.5603	1.48	39.2	3.70	347.9	3.50	325.9	2.59	66.0
229	1515	18.2939	86.5610	1.49	32.0	3.82	345.0	3.70	324.0	2.52	62.5
229	1530	18.3009	86.5605	1.54	27.0	3.90	344.1	3.82	323.6	2.48	60.0
229	1545	18.2947	86.5636	1.44	24.0	3.86	341.9	3.81	322.0	2.36	61.0
229	1600	18.2947	86.5680	1.41	27.8	3.81	341.3	3.78	321.5	2.38	63.3
229	1615	18.2945	86.5766	1.60	31.3	3.83	341.6	3.80	322.0	2.44	66.0
229	1630	18.3024	86.5788	1.63	31.7	3.85	341.9	3.81	322.2	2.46	64.3
229	1645	18.2997	86.5838	1.64	30.2	3.90	341.2	3.85	322.4	2.48	63.7
229	1700	18.2989	86.5855	1.70	26.7	4.00	340.0	3.95	322.5	2.48	62.5
229	1715	18.3007	86.5865	1.66	23.8	4.05	340.0	4.03	322.8	2.44	61.9
229	1730	18.2972	86.5890	1.65	20.5	4.10	337.5	4.10	320.0	2.37	61.2
229	1745	18.2954	86.5923	1.66	18.7	4.12	336.8	4.12	320.9	2.34	60.0
229	1800	18.2997	86.5925	1.63	15.2	4.20	336.0	4.22	318.8	2.29	59.3
229	1815	18.3007	86.5908	1.70	10.0	4.40	334.4	4.42	318.3	2.24	55.1
229	18185	18.2998	86.5896	1.70	10.0	4.40	334.4	4.42	318.3	2.24	55.1
229	1830	18.2954	86.6010	1.81	3.0	4.60	333.3	4.65	318.5	2.20	50.4
*229	1845	18.2187	86.7045	1.82	0.0	4.62	332.0	4.77	317.3	2.10	48.8
*229	1900	18.2204	86.7358	1.68	358.5	4.60	331.3	4.70	316.4	2.02	57.6
*229	1915	18.1789	86.7760	1.60	357.3	4.55	330.7	4.70	314.1	1.97	54.8
229	1930	18.2760	86.6121	1.58	355.6	4.54	330.0	4.70	313.0	1.90	55.5
229	1945	18.3215	86.6023	1.57	354.0	4.55	329.8	4.80	312.0	1.84	55.0
229	2000	18.3005	86.6081	1.62	350.6	4.68	329.0	4.88	311.0	1.80	53.5
229	20045	18.3130	86.5946	1.62	350.6	4.68	329.0	4.88	311.0	1.80	53.5
229	2015	18.3137	86.6088	1.65	349.6	4.75	329.0	5.00	311.5	1.79	52.4
229	2030	18.3162	86.6168	1.62	346.7	4.79	328.1	5.03	310.2	1.68	50.5
229	2045	18.2855	86.6238	1.60	343.2	4.80	326.9	5.10	309.0	1.74	49.9
229	2100	18.2952	86.6140	1.58	337.0	4.80	325.0	5.30	307.2	1.44	50.0
229	2115	18.3049	86.6171	1.54	335.5	4.70	323.8	5.20	306.0	1.41	56.5
229	2130	18.3224	86.6050	1.44	330.5	4.60	322.6	5.00	303.7	1.32	65.0
229	2145	18.3259	86.6111	1.34	327.9	4.45	321.0	5.00	302.6	1.30	73.9

229	2200	18.3520	86.6081	1.07	326.0	4.30	320.6	4.80	301.0	1.18	84.5
229	2214S	18.3334	86.6139	1.11	352.8	4.12	325.5	4.55	305.0	1.63	78.6
229	2215	18.3485	86.6106	1.11	352.8	4.12	325.5	4.55	305.0	1.63	78.6
*229	2230	18.3144	86.6375	1.73	25.0	4.21	338.9	4.32	317.2	2.54	69.8
229	2245	18.3440	86.6581	2.48	34.3	4.48	350.0	4.28	330.1	3.25	66.0
229	2300	18.3379	86.6568	3.31	40.2	4.83	.1	4.42	340.1	4.13	63.9
229	2315	18.3395	86.6708	3.42	38.7	5.00	.5	4.58	341.7	4.21	63.0
229	2330	18.3080	86.6926	3.40	39.0	4.90	.3	4.50	341.5	4.22	63.8
229	2345	18.3220	86.6873	3.33	39.8	4.82	.2	4.42	340.9	4.17	64.8
230	0	18.3361	86.6776	3.34	37.5	4.90	358.7	4.55	339.7	4.18	63.0
230	15	18.3317	86.6773	3.49	35.0	5.05	359.0	4.71	340.0	4.21	61.2
230	30	18.3299	86.6808	3.59	33.9	5.05	357.6	4.79	342.2	4.33	61.0
230	45	18.3160	86.6818	3.70	31.0	5.30	358.8	5.00	341.0	4.33	58.0
230	100S	18.3164	86.6732	3.75	26.0	5.45	355.0	5.25	338.0	4.25	55.0
230	115	18.3115	86.6771	3.81	23.3	5.50	355.0	5.40	338.1	4.22	53.0
230	130	18.3177	86.6785	3.81	22.5	5.50	354.5	5.38	337.1	4.15	53.8
230	145	18.3037	86.6751	3.81	22.0	5.48	354.3	5.39	337.1	4.13	53.9
230	200	18.3212	86.6846	3.80	22.0	5.44	353.9	5.35	336.7	4.10	53.9
230	215	18.3204	86.6776	3.80	22.0	5.40	353.9	5.33	336.7	4.11	55.0
230	230	18.3204	86.6690	3.81	21.9	5.39	353.9	5.35	336.2	4.09	54.4
230	244S	18.3289	86.6792	3.76	20.5	5.30	353.3	5.36	335.6	4.00	54.0
230	245	18.3107	86.6790	3.76	20.5	5.30	353.3	5.36	335.6	4.00	54.0
230	300	18.3265	86.6745	3.75	18.0	5.35	350.9	5.48	333.5	3.84	53.2
230	315	18.3177	86.6785	3.60	17.7	5.20	350.0	5.40	332.7	3.66	54.1
230	328S	18.3350	86.6789	3.50	15.7	5.60	347.8	5.31	330.4	3.55	55.1
230	330	18.3204	86.6820	3.50	15.4	5.05	347.4	5.31	330.0	3.55	55.1
230	345	18.3255	86.6805	3.40	15.0	4.94	347.5	5.24	329.0	3.45	57.0
230	400	18.3414	86.6805	3.30	15.0	4.80	347.5	5.20	328.0	3.45	59.0
230	415	18.3309	86.6835	3.00	16.0	4.70	346.5	5.10	326.5	3.35	61.0
230	430	18.3414	86.6891	2.88	16.0	4.50	346.0	5.00	325.0	3.00	63.0
230	445	18.3404	86.6865	2.56	15.0	4.20	342.0	4.80	320.0	2.76	70.0
230	500	18.3517	86.6905	2.34	14.0	4.00	339.5	4.65	317.5	2.65	75.5
230	515	18.3544	86.6855	2.34	13.5	3.90	339.5	4.60	316.0	2.68	75.5
230	530	18.3614	86.6893	2.30	12.0	3.90	337.5	4.60	314.0	2.57	75.0
230	545	18.3675	86.6861	2.32	9.5	3.90	336.5	4.70	314.5	2.54	77.0
230	600	18.3614	86.6850	2.33	7.0	3.90	335.0	4.80	312.0	2.38	77.0
230	606S	18.3743	86.6897	2.24	6.5	3.80	333.5	4.80	311.5	2.34	79.0
230	615	18.3640	86.6841	2.16	4.0	3.75	331.5	4.75	310.0	2.30	80.0
230	630	18.3692	86.6871	2.08	5.5	3.50	330.0	4.60	309.0	2.27	84.0
230	645	18.3692	86.6958	2.13	7.0	3.55	332.0	4.60	309.5	2.31	84.0
230	700	18.3780	86.6961	2.16	9.5	3.55	332.5	4.60	310.0	2.35	84.5
230	715	18.3885	86.6976	2.20	10.5	3.50	333.5	4.55	310.0	2.42	85.0
230	730	18.3762	86.7040	2.24	12.5	3.55	335.0	4.50	310.5	2.44	85.5
230	745	18.3754	86.7100	2.24	15.0	3.40	337.0	4.40	311.0	2.48	85.0
230	754S	18.3847	86.7122	2.29	14.8	3.42	337.0	4.42	312.0	2.52	86.0
230	800	18.3875	86.7166	2.34	16.0	3.40	338.0	4.40	312.0	2.54	86.1
230	815	18.4024	86.7095	2.36	17.6	3.10	338.8	4.39	312.0	2.60	86.2
230	816S	18.3861	86.7142	2.36	17.6	3.10	338.8	4.39	312.0	2.60	86.2
230	830	18.3684	86.7191	2.40	19.0	3.10	339.2	4.35	311.6	2.68	86.6
230	845	18.3719	86.7123	2.43	20.3	3.15	340.5	4.40	312.4	2.72	86.0
230	900	18.3684	86.7191	2.52	22.8	3.15	341.5	4.30	312.8	2.80	85.2
230	915	18.3832	86.7250	2.57	24.0	3.10	343.2	4.25	314.0	2.88	86.3
230	930	18.3824	86.7311	2.59	24.8	3.00	343.2	4.25	313.0	2.90	86.4
230	945	18.3902	86.7461	2.62	24.5	3.08	343.8	4.32	313.1	2.93	85.3
230	1000S	18.3943	86.7338	2.55	23.0	2.99	340.6	4.40	310.8	2.81	88.0
230	1015	18.4024	86.7441	2.60	23.0	3.00	341.0	4.40	311.0	2.84	87.9
230	1030	18.4059	86.7375	2.66	25.8	2.96	343.0	4.35	311.1	2.96	86.6
230	1045	18.3989	86.7423	2.76	25.5	3.10	344.0	4.40	315.2	3.00	85.0
230	1100	18.4050	86.7348	2.78	26.0	3.12	344.0	4.45	313.2	3.00	86.0
230	1115	18.3980	86.7353	2.78	26.2	3.31	344.4	4.45	313.0	3.21	86.0
230	1130	18.4250	86.7263	2.72	27.1	3.05	344.0	4.40	312.0	2.98	87.3
230	1145	18.4199	86.7365	2.70	26.2	3.20	342.5	4.44	303.5	2.98	88.2
230	1156S	18.4083	86.7417	2.67	24.3	3.20	338.9	4.50	307.0	2.97	90.0
230	1200	18.4129	86.7370	2.67	24.3	3.20	338.9	4.50	307.0	2.97	90.0
230	1215	18.4215	86.7373	2.54	20.4	3.27	335.5	4.70	305.0	2.77	92.1
230	1230	18.4155	86.7405	2.41	16.6	3.30	331.4	4.81	302.7	2.57	94.1
230	1244S	18.4139	86.7463	2.32	13.1	3.38	328.8	4.96	300.9	2.40	95.3
230	1245	18.4207	86.7348	2.32	13.1	3.38	328.8	4.96	300.9	2.40	95.3

230	1300	18.4234	86.7340	2.23	10.0	3.40	326.0	5.05	299.5	2.21	98.0
230	1315	18.4172	86.7371	2.17	5.0	3.50	324.0	5.25	298.5	2.08	99.0
230	1330	18.4304	86.7335	2.09	2.5	3.55	321.0	5.30	296.5	1.98	102.0
230	1345	18.4155	86.7578	2.06	0.0	3.55	320.0	5.40	295.5	1.91	104.0
230	1400	18.4225	86.7443	2.02	338.5	3.60	320.0	5.50	294.5	1.85	105.0
230	1415	18.4364	86.7390	1.97	335.0	3.61	319.0	5.50	294.0	1.78	108.0
230	1430	18.4390	86.7426	1.93	353.5	3.60	318.0	5.50	294.0	1.75	110.0
230	14325	18.4281	86.7522	1.93	353.5	3.60	318.0	5.50	294.0	1.75	110.0
230	1445	18.4399	86.7453	1.79	352.0	3.50	315.5	5.50	292.0	1.77	114.0
230	14525	18.4333	86.7571	1.73	351.0	3.50	315.0	5.50	291.0	1.76	118.5
230	1500	18.4452	86.7481	1.66	348.5	3.50	314.0	5.52	291.0	1.77	121.0
230	1515	18.4530	86.7503	1.59	347.0	3.35	311.5	5.45	289.5	1.97	127.0
230	1530	18.4409	86.7565	1.30	341.0	3.05	308.5	5.40	286.5	1.96	132.0
230	1545	18.4479	86.7646	1.20	356.5	3.20	306.5	5.45	285.5	2.10	137.5
230	1600	18.4539	86.7658	1.05	332.3	3.10	304.0	5.40	284.4	2.20	140.9
230	1615	18.4565	86.7738	1.10	354.5	2.72	307.0	5.00	284.0	2.40	133.0
230	1630	18.4609	86.7913	1.27	43.2	2.19	319.3	4.35	287.0	2.88	125.5
230	1645	18.4654	86.8045	1.84	58.0	2.17	342.3	3.75	293.0	3.51	115.1
230	1700	18.4487	86.8150	1.83	55.0	2.10	339.5	3.89	292.8	3.40	115.0
230	1715	18.4584	86.8138	1.69	56.8	2.05	335.2	4.25	291.0	3.40	117.0
230	1730	18.4514	86.8186	1.60	57.3	2.02	333.0	3.90	290.7	3.45	119.0
230	1745	18.4575	86.8155	1.56	55.2	2.06	331.1	4.04	290.3	3.30	119.3
230	1800	18.4522	86.8168	1.55	53.8	2.06	331.0	4.00	290.6	3.18	118.1
230	1815	18.4619	86.8156	1.62	45.0	2.28	333.5	4.25	293.0	2.94	114.0
230	1830	18.4425	86.8181	2.10	27.0	2.81	338.0	4.60	301.0	2.70	100.5
230	1845	18.4260	86.8241	2.62	18.5	3.70	342.0	5.10	307.5	2.60	84.0
230	1900	18.4304	86.8245	2.69	13.5	3.85	339.0	5.25	309.5	2.47	80.0
230	19105	18.4371	86.8201	2.74	12.0	3.95	339.0	5.30	308.0	2.48	78.0
230	1915	18.4304	86.8245	2.73	11.0	4.00	340.0	5.35	309.0	2.48	77.0
230	1930	18.4382	86.8180	2.79	10.0	4.10	338.0	5.45	309.5	2.39	75.0
230	19365	18.4355	86.8141	2.80	8.0	4.10	338.0	5.55	308.5	2.40	74.0
230	1945	18.4234	86.8250	2.82	7.0	4.10	338.0	5.55	308.5	2.36	73.0
230	2000	18.4277	86.8208	2.70	6.0	4.02	335.5	5.50	306.8	2.27	76.2
230	2015	18.4347	86.8246	2.64	2.3	4.05	332.3	5.55	305.1	2.12	75.6
230	2030	18.4242	86.8320	2.56	358.0	4.00	329.0	5.60	303.4	1.96	78.0
230	2045	18.4565	86.8215	2.38	355.0	4.00	327.0	5.60	301.0	1.88	84.5
230	2100	18.4462	86.8243	2.25	352.5	3.78	323.8	5.50	299.3	1.80	90.1
230	2115	18.4427	86.8355	2.07	351.0	3.65	322.4	5.38	297.1	1.79	96.6
230	21225	18.4597	86.8158	2.70	352.2	3.70	323.0	5.38	297.2	1.85	96.8
230	2130	18.4487	86.8323	2.10	353.2	3.60	322.8	5.30	298.0	1.89	95.8
230	2145	18.4557	86.8405	2.70	355.7	3.60	324.0	5.16	297.8	1.97	94.0
230	2200	18.4584	86.8396	1.99	350.6	3.54	321.0	5.20	296.0	1.86	98.0
230	2215	18.4845	86.8323	2.00	353.0	3.50	322.0	5.14	296.4	1.94	96.3
230	2230	18.4514	86.8316	2.04	355.5	3.49	324.3	5.08	297.7	1.99	93.1
230	2245	18.4444	86.8493	2.09	357.7	3.40	326.0	5.00	298.6	2.04	89.9
230	2300	18.4462	86.8460	2.15	.3	3.42	327.8	4.95	299.4	2.17	87.8
230	2315	18.4715	86.8533	2.15	.3	3.32	329.0	4.85	299.9	2.19	85.8
230	2330	18.4785	86.8571	2.23	3.9	3.30	330.2	4.82	301.1	2.24	83.8
230	2345	18.4697	86.8525	2.34	6.0	3.32	333.0	4.82	300.1	2.42	82.2
231	0	18.4769	86.8908	2.48	7.2	3.34	334.6	4.79	302.7	2.60	80.1
231	15	18.5084	86.8776	2.52	9.0	3.30	335.9	4.71	303.2	2.51	80.0
231	30	18.4742	86.8873	2.52	12.0	3.18	338.0	4.59	303.4	2.81	81.3
231	45	18.4777	86.8848	2.48	14.0	3.00	338.9	4.46	303.6	2.93	82.4
231	100	18.4750	86.8813	2.55	15.0	3.00	340.5	4.45	304.1	3.00	81.0
231	115	18.4855	86.8740	2.53	14.2	3.00	339.6	4.45	303.8	2.93	81.0
231	130	18.4785	86.8745	2.31	12.2	2.90	337.0	4.40	300.2	2.81	84.0
231	145	18.4672	86.8748	2.20	10.8	2.85	334.4	4.40	297.9	2.74	85.7
231	2005	18.4839	86.8648	2.20	5.6	2.75	330.9	4.55	296.0	2.56	85.1
231	215	18.4610	86.8693	2.16	4.0	2.92	329.8	4.45	294.2	2.53	85.9
231	230	18.4680	86.8645	2.12	.9	2.93	328.2	4.60	294.7	2.44	87.7
231	245	18.4750	86.8640	2.37	356.5	2.95	325.0	4.70	293.7	2.32	87.0
231	300	18.4707	86.8593	2.04	352.0	2.96	322.0	4.77	291.5	2.18	89.1
231	315	18.4794	86.8555	1.88	350.0	2.83	320.0	4.77	290.9	2.20	93.5
231	330	18.4680	86.8645	1.77	350.6	2.69	319.0	4.60	288.5	2.28	97.5
231	345	18.4820	86.8591	1.71	351.2	2.45	318.2	4.52	287.2	2.30	100.0
231	400	18.4699	86.8696	1.64	353.5	2.35	316.4	4.44	285.6	2.43	104.0

231	1900	18.5950	87.0413	2.86	65.0	2.29	66.4	1.75	295.9	4.28	94.4
231	1915	18.5879	87.0331	2.46	56.5	1.89	54.0	2.20	293.6	3.70	91.1
231	1930	18.5930	87.0230	2.33	41.3	1.83	32.4	2.75	296.3	3.27	86.0
231	1945	18.5792	87.0283	2.33	33.6	1.86	24.0	2.90	298.4	2.43	81.0
231	2000	18.5714	87.0391	2.90	36.7	2.46	35.4	2.54	303.3	3.71	83.8
231	2015	18.6014	87.0683	4.20	84.6	3.55	88.8	-1.00	-1.0	5.87	100.0
231	2030	18.5900	87.0773	3.60	75.2	3.60	78.8	-1.00	-1.0	5.20	95.0
231	2045	18.5704	87.0280	2.30	37.3	1.47	30.2	-1.00	-1.0	3.30	84.5
231	2100	18.5749	87.0368	3.99	34.0	1.90	34.2	-1.00	-1.0	3.42	85.0
231	2115	18.5794	87.0500	-1.00	-1.0	1.97	40.0	-1.00	-1.0	3.52	86.1
231	2130	18.5637	87.0587	-1.00	-1.0	1.97	46.0	-1.00	-1.0	3.70	86.9
231	2145	18.5530	87.0486	-1.00	-1.0	2.00	44.1	-1.00	-1.0	3.80	88.9
231	2200	18.5785	87.0516	-1.00	-1.0	2.01	50.1	-1.00	-1.0	3.78	88.3
231	2215	18.5804	87.0743	-1.00	-1.0	2.08	48.0	-1.00	-1.0	3.79	86.0
231	2225	18.5986	87.0364	-1.00	-1.0	2.30	48.2	-1.00	-1.0	3.73	87.1
231	2230	18.5829	87.0475	-1.00	-1.0	2.08	48.7	-1.00	-1.0	3.72	87.0
231	2245	18.5775	87.0533	2.42	43.8	2.08	47.5	-1.00	-1.0	3.73	85.6
231	2300	18.5987	87.0561	2.50	42.0	2.09	46.8	-1.00	-1.0	3.68	84.1
231	2315	18.6029	87.0477	2.56	43.0	2.16	48.0	-1.00	-1.0	3.78	84.2
231	2330	18.5907	87.0583	2.63	44.6	2.24	49.3	-1.00	-1.0	3.84	84.5
231	2345	18.6249	87.0618	2.58	46.0	2.25	51.4	-1.00	-1.0	4.00	84.1
232	0	18.6336	87.0579	2.74	46.0	2.43	52.5	-1.00	-1.0	4.30	84.0
232	15	18.6059	87.0773	2.82	48.1	2.54	54.5	-1.00	-1.0	4.25	83.9
232	30	18.6137	87.0706	2.92	48.9	2.62	55.2	-1.00	-1.0	4.39	84.9
232	445	18.6016	87.0632	3.00	48.9	2.72	56.9	-1.00	-1.0	4.50	83.4
232	45	18.6154	87.0716	3.00	48.9	2.72	56.9	-1.00	-1.0	4.50	83.4
232	100	18.6294	87.0706	3.20	49.7	2.74	57.0	-1.00	-1.0	4.55	84.0
232	1025	18.6041	87.0662	3.20	49.7	2.74	57.0	-1.00	-1.0	4.55	84.0
232	115	18.6155	87.0803	3.30	48.5	2.84	58.0	-1.00	-1.0	4.70	82.5
232	130	18.5989	87.0821	3.40	49.0	2.95	58.0	-1.00	-1.0	4.80	82.0
232	145	18.6075	87.0825	3.50	50.5	2.95	58.0	-1.00	-1.0	4.90	83.0
232	1505	18.6068	87.0710	3.50	50.5	2.95	58.0	-1.00	-1.0	4.90	83.0
232	200	18.6145	87.0733	3.60	49.6	3.00	58.0	-1.00	-1.0	4.90	81.3
232	215	18.5919	87.0826	3.60	47.5	3.20	56.0	-1.00	-1.0	4.90	81.0
232	230	18.6040	87.0720	3.60	46.0	3.20	53.0	-1.00	-1.0	4.80	80.0
232	245	18.5997	87.0718	3.70	45.4	3.20	53.0	-1.00	-1.0	4.90	78.0
232	300	18.5935	87.0748	3.80	45.4	3.50	54.0	-1.00	-1.0	5.00	79.0
232	315	18.6205	87.0701	3.90	45.0	3.54	52.6	-1.00	-1.0	5.10	79.0
232	330	18.6094	87.0791	3.90	46.0	3.60	53.0	-1.00	-1.0	5.15	78.0
232	3385	18.6080	87.0897	4.00	45.3	3.67	52.6	-1.00	-1.0	5.20	77.0
232	345	18.6042	87.0850	4.01	45.7	3.70	53.0	-1.00	-1.0	5.21	77.2
232	400	18.6059	87.0773	3.95	44.2	3.62	52.0	-1.00	-1.0	5.10	77.4
232	415	18.6154	87.0716	3.80	42.5	3.43	49.8	-1.00	-1.0	4.89	77.1
232	430	18.6180	87.0710	3.65	41.7	3.34	48.9	-1.00	-1.0	4.80	77.9
232	445	18.6129	87.0853	3.53	41.0	3.05	48.8	-1.00	-1.0	4.66	78.0
232	500	18.6162	87.0700	3.05	34.0	2.70	41.0	-1.00	-1.0	4.15	76.5
232	515	18.6180	87.0666	2.92	30.0	2.59	38.8	-1.00	-1.0	3.94	76.0
232	530	18.6154	87.0673	2.94	29.0	2.59	36.4	-1.00	-1.0	3.92	76.0
232	545	18.6127	87.0725	2.87	29.0	2.53	37.7	-1.00	-1.0	3.94	76.5
232	6005	18.6266	87.0788	2.85	30.0	2.51	38.0	-1.00	-1.0	3.90	78.0
232	615	18.6092	87.0705	2.80	29.0	2.46	37.5	-1.00	-1.0	3.85	77.0
232	630	18.6205	87.0701	2.87	28.5	2.48	37.0	-1.00	-1.0	3.90	76.0
232	645	18.6170	87.0683	2.90	26.0	2.48	32.5	-1.00	-1.0	3.80	75.0
232	700	18.6187	87.0606	2.94	13.0	2.50	16.5	-1.00	-1.0	3.35	67.0
232	715	18.6220	87.0365	3.00	2.5	2.63	2.0	-1.00	-1.0	2.78	58.0
232	730	18.6072	87.0436	3.65	352.0	2.88	350.0	-1.00	-1.0	2.55	45.5
232	745	18.5959	87.0353	4.00	344.0	3.40	340.5	-1.00	-1.0	2.42	30.5
232	800	18.5887	87.0271	-1.00	-1.0	3.90	332.4	-1.00	-1.0	2.50	12.0
232	815	18.5895	87.0211	-1.00	-1.0	4.40	327.1	-1.00	-1.0	2.68	358.1
232	8205	18.6099	87.0216	-1.00	-1.0	4.40	327.1	-1.00	-1.0	2.68	358.1
232	830	18.5904	87.0151	-1.00	-1.0	5.02	323.2	-1.00	-1.0	3.28	345.2
232	845	18.6044	87.0135	-1.00	-1.0	5.50	320.7	-1.00	-1.0	3.61	338.0
232	900	18.6174	86.9973	-1.00	-1.0	5.48	315.1	-1.00	-1.0	3.45	329.8
232	915	18.6314	87.0050	-1.00	-1.0	5.49	314.1	-1.00	-1.0	3.60	333.9
232	930	18.6384	87.0135	-1.00	-1.0	5.49	314.7	-1.00	-1.0	3.70	333.0
232	945	18.6289	87.0135	-1.00	-1.0	5.56	319.4	-1.00	-1.0	3.89	332.0

232 1000	18.6235	87.0135	-1.00	-1.0	5.68	319.1	-1.00	-1.0	3.99	334.1
232 1010S	18.6091	87.0093	-1.00	-1.0	5.68	319.2	-1.00	-1.0	4.20	331.8
232 1015	18.6165	87.0135	-1.00	-1.0	5.72	320.0	-1.00	-1.0	4.02	332.4
232 1030	18.6009	87.0135	-1.00	-1.0	5.60	319.7	-1.00	-1.0	4.02	331.1
232 1045	18.5957	87.0136	-1.00	-1.0	5.82	316.7	-1.00	-1.0	4.22	326.2
232 1100	18.6044	87.0135	-1.00	-1.0	5.96	312.7	-1.00	-1.0	4.35	320.6
232 1115	18.6427	86.9916	-1.00	-1.0	5.90	312.0	-1.00	-1.0	4.31	319.7
232 1130	18.6390	86.9855	-1.00	-1.0	5.60	312.1	-1.00	-1.0	4.10	321.0
232 1145	18.6382	86.9915	-1.00	-1.0	5.48	319.9	-1.00	-1.0	4.30	321.2
232 1200	18.6392	87.0135	-1.00	-1.0	5.20	312.8	-1.00	-1.0	3.25	320.5
232 1212S	18.6413	87.0240	-1.00	-1.0	3.62	310.0	-1.00	-1.0	2.14	322.9
232 1215	18.6612	87.0211	-1.00	-1.0	3.62	310.0	-1.00	-1.0	2.14	322.9

232	22305	19.7967	86.8000	-1.00	-1.0	4.32	310.6	2.30	330.8	4.43	340.6
232	2245	19.8682	86.7851	-1.00	-1.0	4.20	311.0	2.20	331.1	4.34	341.6
232	2300	19.8502	86.7775	-1.00	-1.0	4.03	310.0	2.04	331.8	4.12	342.7
232	2315	19.8625	86.7971	-1.00	-1.0	3.89	309.7	1.88	334.0	4.00	343.6
232	2330	19.8787	86.7951	-1.00	-1.0	3.74	309.4	1.69	337.1	3.82	345.8
232	2345	19.8675	86.7956	-1.00	-1.0	3.96	311.2	1.99	339.5	4.09	346.4
233	0	19.9089	86.7858	-1.00	-1.0	4.21	315.0	2.52	341.6	4.33	347.2
233	125	19.8722	86.7786	-1.00	-1.0	4.10	317.0	1.96	346.0	4.20	349.2
233	15	19.8895	86.7903	-1.00	-1.0	4.00	316.1	1.91	345.9	4.15	350.8
233	30	19.9055	86.7883	-1.00	-1.0	4.25	318.8	2.21	348.8	4.50	350.8
233	45	19.8779	86.8011	-1.00	-1.0	4.59	320.8	2.29	348.1	4.68	350.3
233	100	19.8962	86.7853	-1.00	-1.0	4.40	321.8	2.42	353.0	4.76	352.2
233	1045	19.8852	86.7924	-1.00	-1.0	4.40	321.8	2.42	353.0	4.76	352.2
233	115	19.8964	86.7898	-1.00	-1.0	4.40	324.0	2.46	357.2	4.86	355.3
233	130	19.8860	86.7841	-1.00	-1.0	4.35	327.7	2.50	1.0	4.82	357.6
233	145	19.8979	86.7863	-1.00	-1.0	4.40	328.0	2.57	1.5	4.90	358.5
233	2005	19.8943	86.7841	-1.00	-1.0	4.60	329.9	2.72	1.9	5.14	358.5
233	215	19.8910	86.7826	-1.00	-1.0	4.71	332.0	2.84	2.5	5.30	359.6
233	230	19.8900	86.7755	-1.00	-1.0	4.70	334.3	2.92	4.0	5.36	1.0
233	245	19.8884	86.7790	-1.00	-1.0	4.90	334.7	3.31	5.2	5.61	2.0
233	2465	19.9007	86.7806	-1.00	-1.0	4.90	334.7	3.31	5.2	5.61	2.0
233	300	19.8942	86.7756	-1.00	-1.0	4.76	336.2	3.22	6.0	5.20	3.4
233	315	19.9145	86.7740	-1.00	-1.0	5.10	338.9	3.60	8.2	5.92	3.7
233	330	19.9202	86.7620	-1.00	-1.0	5.25	340.3	3.83	9.8	6.18	5.0
*233	345	20.1079	86.7848	-1.00	-1.0	5.48	342.0	4.10	9.8	6.40	6.0
*233	400	20.0869	86.7283	-1.00	-1.0	5.70	344.2	4.38	10.2	6.70	6.9
*233	415	19.9287	87.0670	-1.00	-1.0	5.95	346.4	4.64	12.0	7.02	8.0
*233	430	20.1232	87.1808	-1.00	-1.0	6.05	348.7	4.84	13.5	7.25	8.5
*233	445	19.8872	86.7998	-1.00	-1.0	6.35	350.5	5.12	14.5	7.55	10.0
*233	500	19.9225	86.7846	-1.00	-1.0	6.56	351.6	5.35	15.5	7.77	10.3
*233	515	19.7755	86.8528	-1.00	-1.0	6.71	350.5	5.49	14.3	7.95	9.9
233	530	19.9215	86.7776	-1.00	-1.0	6.84	350.0	5.65	13.5	8.10	9.4
233	545	19.9087	86.7771	-1.00	-1.0	7.01	352.4	5.87	13.6	8.30	10.0
233	600	19.9149	86.7826	-1.00	-1.0	7.15	355.0	6.01	16.0	8.49	11.8
233	615	19.9214	86.7733	-1.00	-1.0	7.30	356.7	6.22	17.5	8.63	13.8
233	630	19.9239	86.7725	-1.00	-1.0	7.50	357.0	6.30	18.5	8.75	14.0
233	645	19.9187	86.7696	-1.00	-1.0	7.70	357.5	6.60	18.0	9.10	13.5
233	6505	19.9314	86.7792	-1.00	-1.0	7.70	357.5	6.60	18.0	9.10	13.5
233	700	19.9442	86.7751	-1.00	-1.0	7.85	359.0	6.80	19.0	9.25	14.5
233	715	19.9589	86.7853	-1.00	-1.0	7.80	358.5	6.80	19.5	9.20	15.0
*233	730	20.1194	86.6491	-1.00	-1.0	7.20	0.0	6.30	23.0	8.60	17.0
233	7365	19.9599	86.7857	-1.00	-1.0	6.80	1.0	5.85	25.0	8.20	19.0
233	745	19.9213	86.7367	-1.00	-1.0	6.60	2.0	5.75	27.0	8.10	20.0
233	800	19.9255	86.7368	-1.00	-1.0	5.90	2.9	5.21	30.0	7.52	22.3
233	815	19.9180	86.7391	-1.00	-1.0	5.18	3.3	4.63	35.8	6.91	25.7
233	830	19.9507	86.7291	-1.00	-1.0	4.41	5.4	4.05	41.9	6.28	28.7
*233	8405	20.0297	86.7602	-1.00	-1.0	3.98	5.5	3.84	47.0	5.92	31.3
233	845	19.9644	86.7323	-1.00	-1.0	3.68	7.9	3.67	51.3	5.68	33.2
233	900	19.9767	86.7196	-1.00	-1.0	3.60	9.4	3.67	52.3	5.71	34.3
233	915	19.9745	86.7335	-1.00	-1.0	3.68	13.3	3.84	55.0	5.86	37.4
233	930	19.9797	86.7363	-1.00	-1.0	3.81	14.1	4.03	54.0	6.06	37.0
*233	945	20.1312	86.7438	-1.00	-1.0	3.90	13.1	4.14	51.7	6.21	35.9
*233	1000	20.0922	86.7676	-1.00	-1.0	4.08	11.0	4.25	48.8	6.40	33.2
233	1015	20.0639	86.7500	-1.00	-1.0	4.28	11.8	4.46	46.1	6.60	31.8
233	1030	20.0429	86.7580	-1.00	-1.0	4.50	11.8	4.66	45.0	6.85	31.6
233	1045	20.0462	86.7555	-1.00	-1.0	4.62	12.9	4.81	44.6	7.06	31.6
233	1100	20.0705	86.7495	-1.00	-1.0	4.80	14.4	5.05	44.1	7.28	32.4
233	1115	20.0879	86.7353	-1.00	-1.0	4.34	15.9	4.73	47.3	6.88	34.5
233	11245	20.0821	86.7497	-1.00	-1.0	3.81	16.2	4.37	50.7	6.42	36.0
233	1130	20.1089	86.7316	-1.00	-1.0	3.81	16.2	4.38	51.0	6.48	35.4
233	1145	20.1124	86.7336	-1.00	-1.0	3.32	18.2	4.09	56.3	6.02	39.0
*233	11585	20.1277	86.7579	-1.00	-1.0	2.72	20.8	3.70	63.3	5.57	41.6
233	1200	20.1482	86.7055	-1.00	-1.0	2.72	20.8	3.70	63.3	5.57	41.6
233	1215	20.1283	86.7248	-1.00	-1.0	2.62	25.6	3.84	66.5	5.66	44.9

APPENDIX 3. GULF OF MEXICO DRIFTING DATA

Column 1	* = Questionable fix		
Column 2	Julian Day		
Column 3	Greenwich time		
Column 4	S = satellite fix		
	Blank = dead-reckoning position		
Column 5	Ship's latitude		
Column 6	Ship's longitude		
Columns 7	Range in n. mi. from ship to buoy 1		
	9		2
	11		3
	13		4
Columns 8	True bearing of buoy 1 from ship		
	10		2
	12		3
	14		4

238 2045	23.8147	86.1153	-1.00	-1.0	5.56	89.7	3.35	36.7	2.82	143.2
238 2100	23.8131	86.1067	-1.00	-1.0	5.37	90.0	3.50	33.5	2.60	147.0
238 2115	23.8078	86.1011	-1.00	-1.0	5.15	89.5	2.91	25.5	2.42	151.3
238 2130	23.8025	86.0958	-1.00	-1.0	5.00	88.0	2.86	25.8	2.33	152.0
238 2145	23.7983	86.0922	-1.00	-1.0	4.92	89.0	2.79	24.1	2.27	155.0
238 2200	23.7942	86.0883	-1.00	-1.0	4.88	88.1	2.71	21.5	2.26	156.5
238 2215	23.7925	86.0833	-1.00	-1.0	4.80	90.5	2.62	20.7	2.23	158.5
238 2230	23.7908	86.0783	-1.00	-1.0	4.80	83.5	2.45	21.0	2.28	161.0
238 2242S	23.7808	86.0897	-1.00	-1.0	4.78	97.0	2.46	24.0	2.25	168.0
238 2245	23.7814	86.0906	-1.00	-1.0	5.20	106.5	2.34	26.5	2.54	168.0
238 2300	23.7847	86.0942	-1.00	-1.0	5.50	100.2	2.18	42.2	2.88	158.0
238 2315	23.7822	86.0964	-1.00	-1.0	5.80	100.5	2.14	51.3	3.38	157.5
238 2330	23.7800	86.0983	-1.00	-1.0	5.92	104.0	2.60	52.9	3.55	157.0
238 2345	23.7761	86.0939	-1.00	-1.0	5.90	96.5	1.87	55.5	3.60	159.5
239 0	23.7719	86.0894	-1.00	-1.0	5.82	101.9	1.90	52.0	3.51	159.9
239 15	23.7717	86.0864	-1.00	-1.0	5.72	99.1	1.86	51.3	3.53	161.6
239 30	23.7686	86.0767	-1.00	-1.0	5.75	99.0	1.82	42.6	3.40	162.0
239 45	23.7644	86.0728	-1.00	-1.0	5.49	98.3	1.84	41.4	3.50	164.5
239 100	23.7606	86.0689	-1.00	-1.0	5.36	100.0	1.70	38.0	2.96	170.1
239 115	23.7564	86.0650	-1.00	-1.0	5.39	97.7	1.72	33.4	2.92	170.5
239 130S	23.7522	86.0611	-1.00	-1.0	-1.00	-1.0	-1.00	-1.0	-1.00	-1.0
239 145	23.7497	86.0583	-1.00	-1.0	5.65	95.0	1.74	35.9	2.81	168.0
239 200	23.7475	86.0558	-1.00	-1.0	5.88	94.9	1.76	40.0	2.92	176.0
239 215	23.7442	86.0528	-1.00	-1.0	6.10	96.7	1.71	45.1	2.87	172.9
239 230	23.7397	86.0494	-1.00	-1.0	6.10	92.0	1.70	45.0	2.89	168.0
239 245	23.7356	86.0458	-1.00	-1.0	6.20	85.4	1.79	34.4	2.76	167.9
239 300	23.7311	86.0425	-1.00	-1.0	6.20	93.0	1.84	42.0	2.67	165.0
239 315	23.7269	86.0392	-1.00	-1.0	6.30	90.5	1.86	49.5	2.54	165.0
239 330	23.7233	86.0333	-1.00	-1.0	6.26	88.9	1.97	36.4	2.39	166.1
239 345	23.7200	86.0269	-1.00	-1.0	6.30	89.0	1.92	35.0	2.23	168.0
239 400	23.7167	86.0206	-1.00	-1.0	6.30	84.0	1.94	30.0	2.12	167.0
239 415	23.7131	86.0142	-1.00	-1.0	6.40	89.0	1.86	34.0	2.10	171.0
239 430	23.7097	86.0078	-1.00	-1.0	6.40	88.0	1.72	33.0	2.10	174.0
239 445	23.7064	86.0011	-1.00	-1.0	6.30	88.0	1.57	32.0	2.12	180.0
239 500	23.7031	85.9947	-1.00	-1.0	6.00	90.5	1.44	32.0	2.40	189.0
239 515	23.6997	85.9883	-1.00	-1.0	5.90	87.0	1.46	28.0	1.96	193.0
239 530	23.6964	85.9819	-1.00	-1.0	6.00	88.0	1.52	25.0	1.98	199.0
239 545	23.6931	85.9756	-1.00	-1.0	6.20	82.0	1.44	33.0	2.20	198.0
239 600	23.6894	85.9692	-1.00	-1.0	6.30	86.0	1.36	35.0	2.10	191.0
239 615	23.6861	85.9628	-1.00	-1.0	6.50	87.0	1.34	29.0	2.20	186.0
239 630	23.6828	85.9564	-1.00	-1.0	6.60	89.0	1.24	29.0	2.24	189.0
239 645	23.6794	85.9500	-1.00	-1.0	6.50	90.5	1.18	23.5	2.31	195.0
239 700	23.6769	85.9425	-1.00	-1.0	6.40	86.0	1.13	20.0	2.24	197.0
239 715	23.6747	85.9350	-1.00	-1.0	6.40	85.0	1.20	18.0	2.26	201.0
239 730	23.6722	85.9278	-1.00	-1.0	6.40	85.5	-1.00	-1.0	2.30	206.5
239 745	23.6697	85.9203	-1.00	-1.0	6.40	83.0	-1.00	-1.0	2.36	210.0
239 800	23.6675	85.9128	-1.00	-1.0	6.33	81.9	1.30	352.3	2.36	212.3
239 815	23.6650	85.9053	-1.00	-1.0	6.30	83.0	1.32	343.5	2.42	217.5
239 830	23.6625	85.8981	-1.00	-1.0	6.40	81.2	1.39	339.1	2.52	221.2
239 845	23.6600	85.8906	-1.00	-1.0	6.12	80.3	1.41	332.7	2.52	225.7
239 900	23.6578	85.8831	-1.00	-1.0	6.18	80.8	1.49	336.2	2.63	232.7
239 915	23.6553	85.8756	-1.00	-1.0	6.30	75.8	1.59	329.5	2.72	231.4
239 930	23.6528	85.8683	-1.00	-1.0	6.50	82.5	1.58	341.5	-1.00	-1.0
239 945	23.6503	85.8608	-1.00	-1.0	6.67	75.7	1.57	341.5	2.74	233.7
239 1000	23.6481	85.8533	-1.00	-1.0	6.72	77.6	1.45	335.5	2.71	233.0
239 1015	23.6456	85.8458	-1.00	-1.0	6.66	73.7	1.50	332.0	-1.00	-1.0
239 1030	23.6431	85.8383	-1.00	-1.0	6.59	72.0	1.69	331.1	2.87	237.5
239 1045	23.6406	85.8311	-1.00	-1.0	6.50	73.3	1.77	325.9	3.26	240.3
239 1100	23.6383	85.8236	-1.00	-1.0	6.43	72.3	1.82	321.8	3.49	242.0
239 1115	23.6358	85.8161	-1.00	-1.0	6.38	72.4	1.86	316.5	3.67	244.6
239 1130	23.6333	85.8086	-1.00	-1.0	6.49	72.5	1.94	313.4	4.00	244.8
239 1145	23.6308	85.8014	-1.00	-1.0	6.21	70.9	2.80	307.7	4.14	249.2
239 1200	23.6286	85.7939	-1.00	-1.0	6.30	71.0	2.19	305.5	4.40	251.5
239 1215	23.6264	85.7867	-1.00	-1.0	6.35	69.5	2.22	305.5	4.60	253.0

239	1230	23.6256	85.7808	-1.00	-1.0	6.35	67.5	2.10	248.5	4.62	246.5
239	1245	23.6247	85.7747	-1.00	-1.0	6.50	71.5	2.40	300.5	4.61	247.5
239	1300	23.6236	85.7689	-1.00	-1.0	6.70	69.0	1.90	297.0	4.60	245.0
239	1315	23.6228	85.7628	-1.00	-1.0	7.00	69.0	1.68	300.0	4.52	245.0
239	1330	23.6219	85.7569	-1.00	-1.0	7.35	70.5	1.46	302.5	4.32	245.5
239	1345	23.6211	85.7508	-1.00	-1.0	-1.00	-1.0	-1.00	-1.0	-1.00	-1.0
239	1402S	23.6203	85.7442	-1.00	-1.0	7.88	67.0	1.37	306.0	4.40	243.0
239	1415	23.6200	85.7400	-1.00	-1.0	8.00	69.5	1.29	307.5	4.35	242.5
239	1430	23.6197	85.7353	-1.00	-1.0	8.23	75.0	1.18	320.0	4.22	246.0
239	1436S	23.6197	85.7333	-1.00	-1.0	8.50	68.0	.96	311.0	4.15	241.0
239	1445	23.6197	85.7283	-1.00	-1.0	8.50	68.5	.88	326.5	4.00	246.5
239	1500	23.6194	85.7200	-1.00	-1.0	8.90	67.5	.96	350.5	3.90	244.5
239	1515	23.6181	85.7106	-1.00	-1.0	9.20	66.0	.89	349.0	3.90	243.0
239	1530	23.6147	85.6992	-1.00	-1.0	8.95	62.0	1.33	335.0	-1.00	-1.0
239	1545	23.6117	85.6875	-1.00	-1.0	8.90	60.5	1.72	322.5	4.50	216.5
239	1600	23.6083	85.6761	-1.00	-1.0	8.85	54.5	2.10	319.5	4.90	257.0
239	1615	23.6061	85.6664	-1.00	-1.0	8.75	55.0	3.21	315.0	5.20	259.0
239	1630	23.6053	85.6586	-1.00	-1.0	8.85	54.0	2.29	315.0	5.40	259.0
239	1645	23.6053	85.6678	-1.00	-1.0	9.40	54.0	2.14	305.0	4.90	256.5
239	1700	23.6044	85.6692	-1.00	-1.0	10.20	58.0	1.20	350.0	4.40	259.0
239	1715	23.6047	85.6572	-1.00	-1.0	10.20	59.0	1.80	348.5	4.40	257.0
239	1730	23.6047	85.6453	-1.00	-1.0	10.25	58.5	1.75	347.5	4.50	255.5
239	1745	23.6047	85.6333	-1.00	-1.0	10.50	59.0	1.66	353.5	4.50	254.0
239	1800S	23.6050	85.6217	-1.00	-1.0	10.72	61.0	1.14	359.0	4.30	252.0
239	1815	23.6061	85.6097	-1.00	-1.0	11.10	60.5	1.73	12.5	4.15	251.5
239	1830	23.6072	85.5978	-1.00	-1.0	11.40	61.0	1.81	22.5	3.97	250.0
239	1845	23.6086	85.5861	-1.00	-1.0	11.80	58.5	1.96	27.0	3.90	246.5
239	1900	23.6097	85.5742	-1.00	-1.0	12.00	55.0	2.40	22.0	4.00	250.0
239	1945	23.5875	85.6178	-1.00	-1.0	16.70	57.0	6.25	50.0	-1.00	-1.0
239	2000	23.6156	85.5858	-1.00	-1.0	14.30	60.0	3.92	57.0	-1.00	-1.0
239	2015	23.6675	85.5367	-1.00	-1.0	10.50	68.7	3.35	167.0	-1.00	-1.0
239	2030	23.6867	85.5056	-1.00	-1.0	8.90	75.0	2.44	204.5	1.54	261.5
239	2045	23.6889	85.4422	-1.00	-1.0	6.20	64.0	4.75	245.5	4.60	271.5
239	2100	23.6911	85.3789	-1.00	-1.0	3.62	26.5	7.92	250.5	7.95	263.5
239	2115	23.6931	85.3653	-1.00	-1.0	3.60	34.0	8.10	252.0	7.92	266.0
239	2130	23.6958	85.3553	-1.00	-1.0	3.72	34.0	7.90	251.0	7.80	265.0
239	2145	23.6989	85.3453	-1.00	-1.0	3.90	34.1	7.75	250.5	7.68	264.0
239	2200	23.7017	85.3350	-1.00	-1.0	4.10	38.5	7.48	251.5	7.30	266.5
239	2215	23.7047	85.3250	-1.00	-1.0	4.41	49.0	7.12	254.0	6.98	267.0
239	2230	23.7075	85.3147	-1.00	-1.0	4.65	42.2	6.90	249.2	6.70	267.0
239	2245	23.7106	85.3047	-1.00	-1.0	4.70	43.5	6.90	250.5	6.60	267.5
239	2300	23.7214	85.2967	-1.00	-1.0	4.91	44.5	6.58	244.3	6.25	263.5
239	2315	23.7789	85.3044	-1.00	-1.0	3.80	91.5	8.56	222.5	7.35	234.2
239	2330	23.8244	85.3094	-1.00	-1.0	5.00	130.5	10.80	211.5	9.20	220.3
239	2336S	23.8256	85.3067	-1.00	-1.0	5.20	129.5	10.90	210.0	9.20	215.3
240	30	23.7556	85.3317	4.90	34.5	6.65	84.5	6.00	213.5	4.35	227.5
240	45	23.7678	85.3186	-1.00	-1.0	6.70	80.5	6.10	207.5	4.40	221.5
240	100	23.7800	85.3053	4.61	31.5	6.65	81.5	6.30	204.5	4.51	218.5
240	118S	23.7947	85.2894	4.65	31.0	6.87	82.0	6.38	202.0	4.50	215.0
240	130	23.7969	85.2814	4.70	33.0	7.00	81.0	6.41	199.0	4.50	212.0
240	145	23.7997	85.2711	4.75	34.0	7.00	83.0	6.40	201.5	4.40	210.5
240	200	23.8028	85.2611	5.00	34.0	7.20	82.0	6.30	199.0	4.20	209.0
240	215	23.8058	85.2511	5.30	35.0	7.40	80.0	6.10	198.5	4.00	208.5
240	230	23.8086	85.2414	5.60	37.0	7.55	79.0	5.90	197.0	3.85	206.5
240	245	23.8103	85.2339	5.85	39.5	7.75	78.5	5.70	198.5	3.62	205.5
240	300	23.8122	85.2261	6.00	40.0	7.85	79.0	5.80	195.0	3.70	204.0
240	315	23.8156	85.2175	5.80	36.5	7.80	75.5	6.00	191.0	3.80	199.5
240	330	23.8222	85.2067	5.60	39.5	7.60	79.5	6.15	194.5	4.00	202.5
240	345	23.8289	85.1956	5.40	38.5	7.41	80.5	6.30	195.5	4.50	204.5
240	400	23.8356	85.1847	5.20	38.5	7.30	82.0	6.50	198.0	4.20	205.5
240	415	23.8425	85.1736	5.00	37.0	7.15	82.5	6.60	195.8	4.30	203.0
240	430	23.8492	85.1628	4.86	37.0	7.10	82.5	6.80	197.0	4.45	206.0
240	445	23.8558	85.1517	4.80	38.0	6.95	85.6	6.95	196.5	4.60	206.3
240	500	23.8625	85.1408	4.70	38.0	6.85	85.5	7.50	197.5	4.70	206.5
240	515	23.8719	85.1292	4.56	39.5	6.75	86.5	7.20	196.5	4.80	207.0
240	530	23.8819	85.1172	4.50	39.5	6.70	89.5	7.30	197.5	4.90	205.0
240	545	23.8922	85.1050	4.62	39.5	6.90	87.5	7.14	195.3	4.74	204.0

240	600	23.8961	85.0983	4.90	42.0	7.10	86.0	7.00	194.0	4.60	202.0
240	615	23.8994	85.0922	-1.00	-1.0	7.40	87.5	6.70	192.5	4.25	198.5
240	630	23.9031	85.0858	5.50	44.0	7.80	84.0	6.50	190.0	4.00	194.0
240	645	23.9064	85.0797	5.80	42.5	8.00	82.5	6.40	186.5	3.80	191.5
240	700	23.9097	85.0733	5.65	44.0	8.00	83.0	6.20	187.0	3.60	191.0
240	715	23.9133	85.0669	5.80	41.5	8.10	81.5	6.10	186.5	3.50	191.5
240	730	23.9186	85.0575	5.90	41.5	8.10	80.5	6.00	186.5	3.30	190.5
240	734S	23.9200	85.0547	5.80	41.5	8.20	79.5	6.00	185.5	3.40	189.5
240	745	23.9267	85.0472	5.90	40.0	8.20	79.0	5.90	185.0	3.25	189.0
240	800	23.9317	85.0397	6.22	39.3	8.30	77.9	5.85	183.6	2.99	188.3
240	815	23.9367	85.0319	6.20	39.8	8.21	78.3	5.69	181.9	2.83	185.0
240	830	23.9428	85.0222	6.10	39.3	8.21	78.3	5.63	181.5	2.73	185.3
240	845	23.9489	85.0122	5.98	40.9	8.40	79.0	5.70	182.0	2.80	186.0
240	900	23.9550	85.0025	5.88	41.0	8.20	78.9	5.78	182.8	2.92	185.9
240	904S	23.9567	84.9997	5.97	40.3	8.80	77.2	5.88	179.4	2.99	182.8
240	915	23.9633	84.9908	-1.00	-1.0	8.10	81.8	5.70	185.0	3.40	188.0
240	930	23.9725	84.9789	-1.00	-1.0	8.40	80.8	6.10	180.4	3.50	179.7
240	945	23.9819	84.9669	-1.00	-1.0	8.60	82.0	5.80	180.0	3.10	180.0
240	1000	23.9911	84.9547	6.40	48.0	8.90	79.0	5.54	173.8	2.81	169.0
240	1015	24.0003	84.9428	-1.00	-1.0	9.15	78.1	5.49	171.5	2.77	161.8
240	1030	24.0097	84.9306	6.62	46.7	9.12	78.3	5.30	171.2	2.72	160.4
240	1045	24.0189	84.9186	6.53	51.0	9.80	83.2	5.33	175.0	2.75	159.8
240	1100	24.0281	84.9067	5.70	50.7	8.53	84.3	5.62	176.5	3.19	169.8
240	1115	24.0372	84.8944	4.83	47.0	7.88	85.3	6.21	178.3	3.72	174.9
240	1130	24.0467	84.8847	4.23	51.0	7.52	90.2	6.61	183.9	4.31	184.0
240	1145	24.0561	84.8775	3.50	42.0	7.20	88.8	7.20	188.8	4.80	190.8
240	1200	24.0656	84.8703	2.80	55.0	6.60	99.0	7.60	191.8	5.30	196.0
240	1215	24.0725	84.8633	2.25	51.5	6.20	101.5	7.75	193.7	5.50	199.5
240	1230	24.0794	84.8564	2.59	53.5	6.60	100.5	7.50	198.5	-1.00	-1.0
240	1245	24.0861	84.8494	-1.00	-1.0	6.80	100.5	7.20	191.8	5.00	142.5
240	1300	24.0858	84.8472	3.45	56.0	7.30	96.0	6.90	190.0	4.70	191.5
240	1304S	24.0858	84.8467	3.52	55.2	7.30	93.5	6.80	189.2	4.63	189.5
240	1315	24.0908	84.8394	3.82	53.0	7.60	94.0	6.60	187.0	4.40	181.0
240	1330	24.0978	84.8292	3.90	52.4	7.78	92.5	-1.00	-1.0	4.30	187.0
240	1345	24.1050	84.8192	3.90	60.0	7.90	95.0	6.40	184.0	4.50	187.5
240	1400	24.1119	84.8089	4.00	53.5	6.10	89.5	6.10	178.5	4.30	178.5
240	1415	24.1192	84.7986	4.25	55.5	8.35	89.5	5.90	177.5	4.10	179.5
240	1430	24.1261	84.7886	4.60	51.0	8.60	87.0	5.90	173.0	3.80	171.0
240	1445	24.1331	84.7783	4.70	58.5	-1.00	-1.0	5.80	177.5	3.80	175.5
240	1500	24.1400	84.7681	4.60	63.0	8.85	93.0	6.00	175.0	3.95	175.0
240	1515	24.1419	84.7533	4.30	60.0	8.70	92.0	6.00	175.5	4.00	175.0
240	1530	24.1442	84.7386	4.00	57.0	8.40	91.0	5.90	179.0	3.90	180.0
240	1545	24.1461	84.7239	3.66	55.5	8.00	93.0	5.75	184.7	3.85	189.0
240	1600	24.1481	84.7092	3.30	46.0	7.42	90.8	5.66	190.3	3.80	190.7
240	1615	24.1500	84.6944	2.78	32.0	6.75	89.8	5.65	199.0	3.90	212.8
240	1715	24.1375	84.6931	6.40	32.5	9.34	69.4	2.12	172.5	-1.00	-1.0
240	1730	24.1447	84.6828	5.75	29.0	8.90	71.8	2.29	185.1	-1.00	-1.0
240	1745	24.1942	84.6494	2.60	27.5	6.50	95.2	4.15	211.5	-1.00	-1.0
240	1800	24.2233	84.6278	-1.00	-1.0	6.21	117.0	4.75	223.5	-1.00	-1.0
240	1815	24.2631	84.5817	4.40	230.5	5.90	151.8	11.19	212.5	-1.00	-1.0
240	1830	24.3039	84.5342	7.60	232.0	7.38	178.5	14.85	216.0	-1.00	-1.0
240	1845	24.2944	84.5311	6.20	237.0	6.30	176.0	13.60	220.0	1.47	14.0
240	1900	24.2519	84.5481	3.60	257.0	3.85	142.0	9.60	223.0	6.90	28.0
240	1915	24.2222	84.5553	2.82	311.0	3.80	98.0	7.30	233.0	7.50	27.0
240	1930	24.2303	84.5431	2.92	312.0	3.80	96.5	7.20	228.5	7.50	27.0
240	2000	24.2464	84.5189	2.86	319.5	3.99	94.5	7.00	239.5	7.35	28.5
240	2015	24.2544	84.5069	2.85	309.7	4.00	96.0	7.00	230.0	7.30	22.7
240	2022S	24.2581	84.5011	2.80	310.5	4.00	95.0	6.95	231.5	7.30	29.0
240	2030	24.2608	84.4956	-1.00	-1.0	4.00	95.0	6.85	231.0	7.30	27.5
240	2045	24.2667	84.4867	2.79	309.0	3.95	110.0	6.95	238.5	7.10	37.5
240	2100	24.2761	84.4867	2.55	301.0	4.25	105.0	7.15	229.0	6.75	34.5
240	2115	24.2856	84.4867	2.10	291.0	4.60	115.0	7.30	225.0	6.30	38.0
240	2130	24.2950	84.4867	1.78	275.0	5.10	119.0	7.50	223.0	6.00	44.0
240	2145	24.3008	84.4772	1.74	280.5	5.20	120.0	7.30	221.0	6.50	43.2
240	2200	24.3061	84.4669	1.56	284.5	5.50	112.5	6.90	210.5	6.25	45.0
240	2215	24.3114	84.4567	1.25	284.0	5.85	108.0	6.52	219.5	6.60	46.0

240	2230	24.3167	84.4461	.78	302.8	6.22	113.5	6.20	221.5	6.90	53.0
240	2245	24.3219	84.4358	1.56	314.5	6.55	103.0	5.80	213.0	7.28	50.2
240	22485	24.3231	84.4336	1.50	318.5	6.58	108.5	5.70	219.5	7.32	55.5
240	2300	24.3250	84.4253	.70	333.0	6.60	103.0	5.50	216.0	7.40	48.5
240	2315	24.3192	84.4167	1.34	341.0	6.32	96.5	4.90	224.5	7.78	41.5
240	2330	24.3111	84.4086	2.50	340.0	6.20	87.0	4.50	244.0	8.30	38.0
240	2345	24.3139	84.3981	2.25	341.2	6.20	88.0	4.50	237.0	8.10	40.0
241	0	24.3164	84.3875	2.22	340.5	6.32	87.5	4.50	236.5	8.15	41.5
241	15	24.3192	84.3769	2.10	342.0	6.45	90.0	4.35	233.5	8.10	42.5
241	245	24.3208	84.3706	2.50	343.0	6.60	90.0	4.30	233.0	8.20	42.0
241	30	24.3222	84.3658	2.30	345.0	6.70	90.0	4.30	237.0	8.20	44.0
241	45	24.3292	84.3586	1.82	343.5	6.85	90.5	4.25	232.5	8.10	43.1
241	100	24.3381	84.3553	1.29	344.5	7.10	94.5	4.32	236.5	7.85	48.0
241	145	24.3533	84.3342	.90	322.3	7.55	98.5	4.20	225.8	7.95	53.5
241	200	24.3564	84.3239	1.00	2.5	7.84	96.0	4.00	228.0	8.20	53.0
241	215	24.3597	84.3144	1.60	13.0	8.20	94.5	3.70	222.5	8.47	51.5
241	230	24.3633	84.3089	1.36	23.5	8.55	94.0	3.48	220.0	8.80	51.7
241	245	24.3669	84.3033	1.58	32.5	8.95	90.5	2.92	213.5	9.20	52.0
241	300	24.3706	84.2978	1.68	40.0	9.20	93.0	2.89	214.0	9.30	54.5
241	315	24.3742	84.2922	1.73	48.0	9.40	92.7	2.79	213.2	9.45	56.5
241	3285	24.3775	84.2875	1.96	46.5	9.73	92.0	2.72	209.5	9.70	55.0
241	345	24.3775	84.2822	2.24	49.5	10.00	93.0	2.62	204.6	9.96	56.5
241	400	24.3775	84.2775	2.46	51.5	10.30	94.0	2.50	202.0	10.20	58.5
241	415	24.3792	84.2708	2.61	56.0	10.61	93.0	2.42	198.5	10.40	60.0
241	430	24.3814	84.2633	2.73	59.0	10.90	93.0	2.36	193.7	10.57	60.5
241	445	24.3833	84.2561	2.96	60.0	11.17	92.6	2.31	188.2	10.75	61.0
241	4545	24.3847	84.2514	3.40	62.0	11.32	90.4	2.26	184.0	10.85	59.9
241	500	24.3858	84.2492	3.35	66.0	11.40	91.0	2.30	183.9	10.86	61.0
241	515	24.3883	84.2433	3.55	63.0	11.66	92.3	2.35	179.4	11.50	62.5
241	530	24.3911	84.2372	3.60	64.5	11.80	92.5	2.28	177.5	11.10	63.5
241	545	24.3936	84.2314	4.00	64.0	12.25	91.0	2.25	166.0	11.40	63.0
241	600	24.3961	84.2253	4.45	66.4	12.75	91.0	2.32	158.0	11.71	63.4
241	615	24.3989	84.2194	4.70	69.5	12.90	93.5	2.38	149.5	12.10	65.5
241	630	24.4022	84.2122	5.00	73.0	13.40	92.0	2.54	139.0	12.50	64.0
241	645	24.4094	84.1956	5.50	71.5	14.00	92.5	2.74	134.5	12.80	66.5
241	700	24.4164	84.1792	5.25	71.0	14.00	92.0	2.72	132.0	12.70	65.0
241	715	24.4211	84.1642	4.90	73.0	13.60	94.0	2.60	145.0	12.10	66.0
241	800	24.4358	84.1192	3.38	80.2	12.60	98.6	2.79	176.0	10.71	66.5
241	815	24.4408	84.1042	2.64	83.9	12.15	99.8	2.91	185.9	10.16	67.8
241	830	24.4428	84.0956	2.15	87.3	11.78	103.8	3.45	196.0	9.59	67.6
241	845	24.4461	84.0861	1.94	91.9	11.64	104.0	3.66	199.0	9.37	69.0
241	900	24.4494	84.0759	1.99	92.9	11.70	104.8	3.69	201.1	9.32	69.7
241	915	24.4525	84.0675	2.17	89.7	11.92	103.1	3.42	198.1	9.71	67.0
241	930	24.4558	84.0583	-1.00	-1.0	12.20	105.3	3.30	199.5	9.92	68.5
241	945	24.4592	84.0489	2.76	93.0	12.50	105.0	3.28	194.5	10.20	60.0
241	1000	24.4622	84.0397	2.88	89.0	12.80	104.0	3.25	180.5	10.45	70.0
241	10105	24.4644	84.0333	3.32	87.0	13.10	108.0	3.20	173.0	10.75	73.0
241	1015	24.4661	84.0294	3.65	87.6	13.31	106.0	3.20	178.6	10.80	71.0
241	1030	24.4711	84.0178	3.80	93.0	13.62	105.5	3.21	172.6	11.80	72.6
241	1045	24.4761	84.0061	3.94	95.1	13.80	106.7	3.39	170.0	11.12	74.4
241	1100	24.4786	83.9947	4.10	96.6	13.89	115.3	3.51	168.5	11.20	73.7
241	1115	24.4814	83.9836	-1.00	-1.0	14.34	107.0	3.73	165.8	11.30	75.7
241	1130	24.4839	83.9725	-1.00	-1.0	14.26	107.6	3.98	166.5	11.58	77.3
241	1145	24.4869	83.9614	-1.00	-1.0	14.59	108.0	4.70	161.3	11.53	78.5
241	1200	24.4906	83.9508	4.92	104.0	14.95	110.0	4.25	161.0	11.80	79.5
241	1215	24.4933	83.9397	-1.00	-1.0	14.90	110.0	4.30	161.0	11.55	80.0
241	1230	24.4933	83.9261	4.30	105.0	14.38	111.0	4.00	169.0	11.50	79.0
241	1245	24.4933	83.9125	-1.00	-1.0	13.95	111.0	3.80	173.0	10.60	78.0
241	12585	24.4936	83.9008	3.67	110.0	13.87	112.0	3.85	179.0	10.45	79.0
241	1315	24.4942	83.8936	3.75	110.0	13.90	111.0	3.90	177.0	10.40	79.0
241	1330	24.4953	83.8881	4.20	110.0	14.30	112.0	3.90	173.0	10.70	80.0
241	1345	24.4964	83.8822	4.60	107.5	14.80	110.5	4.50	165.5	11.20	80.5
241	1400	24.4975	83.8764	5.20	106.5	15.40	111.5	4.30	159.5	11.83	78.5
241	1415	24.4986	83.8706	-1.00	-1.0	15.60	112.5	4.40	155.5	12.10	83.5
241	1430	24.4997	83.8650	-1.00	-1.0	15.92	113.0	4.40	150.0	12.50	82.0
241	1445	24.5008	83.8586	6.50	99.5	16.40	110.5	4.80	146.5	12.80	81.5

241	1500	24.5014	83.8439	-1.00	-1.0	16.90	110.5	5.00	142.5	13.30	88.5
241	1515	24.5017	83.8294	6.70	94.5	17.30	111.5	5.30	137.5	13.80	84.5
241	1530	24.5022	83.8147	-1.00	-1.0	17.90	111.0	5.70	135.0	14.25	86.0
241	1545	24.4967	83.8031	-1.00	-1.0	17.90	112.0	5.70	133.0	14.20	88.0
241	1600	24.4817	83.7925	-1.00	-1.0	17.23	112.5	5.20	137.0	13.67	86.0
241	1615	24.4747	83.7669	-1.00	-1.0	16.49	111.7	4.43	140.5	12.85	86.5
241	1630	24.4742	83.7503	-1.00	-1.0	16.30	112.5	4.30	141.2	12.77	84.9
241	1645	24.4678	83.7197	-1.00	-1.0	15.13	112.5	3.10	152.5	11.32	83.0
241	1700	24.4483	83.6578	-1.00	-1.0	11.30	114.5	2.60	236.7	8.10	70.5
241	1715	24.4333	83.6036	2.44	308.0	8.10	117.0	5.47	266.0	5.92	52.5
241	1730	24.4339	83.5889	2.59	307.0	7.92	117.0	5.60	267.0	5.81	52.0
241	1745	24.4344	83.5744	2.64	308.0	7.90	117.3	5.63	267.5	5.78	51.5
241	1800	24.4342	83.5622	2.63	310.5	8.00	120.5	5.50	269.6	5.70	55.0
241	1815	24.4331	83.5525	2.28	313.5	8.10	118.5	5.20	278.5	5.70	55.5
241	1830	24.4319	83.5425	2.26	312.0	8.35	118.0	5.10	267.0	5.75	57.0
241	1845	24.4308	83.5328	2.20	305.5	8.45	118.5	5.10	266.0	5.60	57.5
241	1900	24.4300	83.5228	2.23	312.0	8.20	119.0	5.00	273.5	5.60	55.0
241	1915	24.4289	83.5128	2.38	312.0	8.20	119.0	5.10	269.5	5.55	54.0
241	1930	24.4278	83.5031	2.51	313.0	8.10	120.0	5.20	270.5	5.50	52.5
241	1945	24.4267	83.4931	2.64	310.0	7.90	119.0	5.25	272.0	5.40	50.0
241	2000	24.4256	83.4833	2.77	311.0	7.83	119.0	5.40	273.8	5.40	49.0
241	2015	24.4244	83.4733	2.93	310.5	7.70	111.0	5.50	275.0	5.35	45.0
241	2030	24.4236	83.4633	-1.00	-1.0	7.65	116.5	5.36	274.5	5.51	45.5
241	2045	24.4225	83.4536	2.76	326.0	7.68	118.0	5.18	279.0	5.61	45.0
241	2100	24.4214	83.4436	3.15	322.2	7.80	117.0	5.20	280.0	5.82	45.0
241	2115	24.4175	83.4306	2.94	327.0	7.85	115.0	5.00	279.8	5.90	43.5
241	2130	24.4094	83.4169	2.92	329.3	7.85	114.7	5.10	282.5	5.96	41.8
241	2145	24.4017	83.4031	2.81	334.6	8.50	117.5	4.96	281.0	6.00	42.6
241	2200	24.3936	83.3894	2.76	334.5	8.25	115.7	4.80	280.5	6.10	44.5
241	22025	24.3925	83.3875	2.76	334.5	8.25	115.7	4.80	280.5	6.10	44.5
241	2215	24.3906	83.3769	2.73	329.0	9.50	113.5	4.70	279.2	6.00	44.7
241	2230	24.3881	83.3647	2.66	342.0	8.50	116.1	4.57	291.4	6.10	49.5
241	2245	24.3861	83.3525	2.49	337.2	8.60	115.1	4.60	283.0	6.10	45.5
241	2300	24.3858	83.3417	2.58	334.0	8.70	117.0	4.50	276.5	6.10	48.0
241	2315	24.3856	83.3311	2.44	334.0	8.90	118.0	4.40	280.0	6.80	50.7
241	2330	24.3856	83.3203	2.30	333.5	9.10	117.2	4.30	278.1	6.00	51.0
241	23345	24.3856	83.3172	2.21	334.1	9.17	118.2	4.23	277.7	5.90	50.5
241	2345	24.3847	83.3103	2.14	333.5	9.25	119.5	4.20	277.5	5.88	52.5
242	0	24.3844	83.2986	2.00	334.5	9.45	119.5	4.18	276.5	5.80	54.5
242	15	24.3844	83.2861	1.86	331.0	9.53	120.0	4.15	274.0	5.64	54.0
242	30	24.3844	83.2733	1.78	329.0	9.60	121.0	4.20	273.0	5.55	56.0
242	45	24.3844	83.2608	1.66	326.0	9.60	120.0	4.14	270.0	5.42	54.0
242	100	24.3817	83.2483	1.64	324.0	9.75	121.0	4.25	271.0	5.35	56.0
242	115	24.3781	83.2350	1.63	325.0	-1.00	-1.0	4.25	271.0	5.40	55.0
242	130	24.3739	83.2228	1.68	327.0	9.80	121.0	4.25	273.0	5.40	57.0
242	145	24.3689	83.2122	1.70	329.0	9.80	120.0	4.20	275.0	5.40	54.0
242	200	24.3636	83.2019	1.56	333.0	9.95	120.0	4.10	270.0	5.40	58.0
242	215	24.3589	83.1903	1.58	332.0	10.00	115.0	4.50	274.0	5.50	54.0
242	230	24.3550	83.1761	1.62	336.0	9.90	120.0	4.10	280.0	5.45	56.0
242	245	24.3467	83.1578	1.96	328.0	9.60	117.0	4.50	279.0	5.25	49.0
242	300	24.3361	83.1350	2.31	324.0	9.10	119.0	4.80	283.0	5.50	46.0
242	315	24.3256	83.1119	2.68	318.0	8.50	116.0	5.40	284.0	4.90	38.0
242	330	24.3203	83.0922	2.84	318.0	8.40	119.0	5.60	285.0	4.70	39.0
242	345	24.3167	83.0731	2.97	316.0	8.25	120.0	5.75	286.0	4.50	36.0
242	400	24.3128	83.0539	3.35	315.6	8.20	121.0	6.00	287.5	4.55	34.0
242	415	24.3089	83.0369	3.54	314.7	8.40	121.8	6.19	286.9	4.50	30.0
242	430	24.3050	83.0225	3.65	305.1	7.90	120.0	6.40	285.5	4.41	28.0
242	445	24.3011	83.0078	3.83	310.1	7.80	121.6	6.60	285.1	4.35	26.5
242	500	24.2972	82.9933	4.00	308.0	7.69	121.0	6.80	285.0	4.30	22.0
242	515	24.2933	82.9789	4.18	306.5	7.52	122.0	6.95	285.5	4.25	19.1
242	530	24.2894	82.9642	4.32	305.0	7.40	122.5	7.15	285.0	4.20	15.6
242	545	24.2853	82.9497	4.50	305.7	7.60	124.9	6.90	284.5	4.16	19.5
242	600	24.2808	82.9333	3.80	305.5	7.80	123.0	6.60	284.5	4.00	23.5
242	615	24.2758	82.9169	3.85	304.5	7.80	124.5	6.70	283.5	4.00	20.0
242	630	24.2711	82.9006	-1.00	-1.0	7.70	126.0	6.90	287.0	4.00	17.0
242	645	24.2664	82.8839	4.10	302.0	7.60	122.0	7.00	284.0	4.00	15.5

242	700	24.2617	82.8675	4.25	301.0	7.45	123.0	7.20	280.0	4.10	12.5
242	715	24.2569	82.8511	4.35	300.0	7.35	123.0	7.25	279.5	4.50	9.0
242	7265	24.2536	82.8389	4.40	298.5	7.20	123.5	7.35	281.5	4.50	8.0
242	730	24.2536	82.8369	4.45	298.0	7.15	124.5	7.43	282.0	4.00	7.0
242	745	24.2536	82.8294	4.60	298.0	7.00	124.0	7.60	282.0	4.00	4.0
242	800	24.2497	82.8136	4.72	296.2	6.89	125.2	7.69	281.0	4.10	3.0
242	815	24.2461	82.7981	4.82	295.2	6.76	124.2	7.82	280.1	4.20	358.0
242	830	24.2422	82.7822	4.96	281.3	-1.00	-1.0	6.67	273.4	4.20	346.2
242	845	24.2383	82.7664	5.20	291.5	6.60	124.3	8.12	275.6	4.50	353.2
242	900	24.2344	82.7506	-1.00	-1.0	-1.00	-1.0	8.21	277.8	4.20	353.8
242	915	24.2308	82.7350	4.85	300.5	6.45	128.0	8.35	286.0	4.16	357.0
242	930	24.2269	82.7192	-1.00	-1.0	7.25	124.7	8.22	274.0	4.10	354.6
242	945	24.2231	82.7033	-1.00	-1.0	6.80	129.0	8.20	277.5	4.00	0.0
242	1015	24.2153	82.6719	-1.00	-1.0	7.12	123.4	7.90	271.9	3.94	2.5
242	1030	24.2114	82.6561	4.41	289.9	7.19	126.4	7.86	275.2	3.79	2.3
242	1045	24.2075	82.6406	4.40	288.3	7.19	127.5	7.91	273.5	3.68	2.5
242	1100	24.2036	82.6247	4.40	287.6	7.18	126.8	8.00	274.6	3.54	1.1
242	1115	24.2006	82.6086	4.50	284.7	7.14	130.0	8.20	271.0	3.41	1.2
242	1130	24.1983	82.5925	4.50	282.8	7.26	125.5	8.35	270.1	3.32	358.7
242	1200	24.1942	82.5597	-1.00	-1.0	7.40	134.0	8.65	269.0	2.95	359.0
242	1215	24.1919	82.5436	4.62	281.0	7.48	135.0	9.74	267.0	2.86	359.0
242	1245	24.1878	82.5111	4.40	288.0	7.58	144.0	8.61	267.0	2.73	16.0
242	1300	24.1856	82.4947	4.20	273.0	8.10	134.0	8.20	264.0	2.68	15.0
242	13145	24.1833	82.4794	3.50	274.0	8.45	134.0	7.96	265.0	2.68	23.0
242	1315	24.1831	82.4786	3.50	274.0	8.45	134.0	7.96	265.0	2.68	23.0
242	1330	24.1794	82.4667	2.84	270.0	8.90	132.0	7.57	261.0	2.68	32.0
242	1345	24.1769	82.4561	2.65	268.0	9.20	129.0	7.35	260.0	2.89	41.0
242	14005	24.1767	82.4483	2.71	269.0	9.30	129.0	7.17	260.0	2.94	42.0
242	1415	24.1742	82.4331	2.24	265.0	9.50	126.0	7.00	259.0	3.15	45.0
242	1430	24.1714	82.4175	2.00	265.5	9.65	129.5	6.80	260.5	3.50	52.5
242	1445	24.1689	82.4019	1.51	260.5	10.00	128.5	6.32	257.5	3.80	58.5
242	1500	24.1664	82.3864	1.36	254.0	10.10	127.0	6.31	256.0	3.80	60.0
242	1515	24.1636	82.3711	1.50	247.0	10.20	128.0	6.50	255.0	3.70	62.0
242	1530	24.1639	82.3486	2.60	250.0	9.80	132.0	7.10	255.0	2.98	59.0
242	1545	24.1642	82.3264	2.69	253.8	9.30	137.0	7.80	257.1	2.45	55.1
242	1600	24.1614	82.3108	2.53	244.4	9.19	137.0	8.12	256.0	2.27	55.0
242	1615	24.1589	82.2953	2.85	248.2	9.18	140.5	8.28	245.0	2.17	59.0
242	1630	24.1564	82.2800	3.25	244.3	9.21	137.5	8.40	251.1	1.94	64.0
242	1645	24.1536	82.2644	2.69	244.5	9.46	139.3	8.47	249.7	2.00	68.4
242	1700	24.1511	82.2489	2.48	240.5	9.21	138.5	8.12	249.5	2.15	76.5
242	1715	24.1486	82.2336	2.42	247.5	9.21	134.8	8.50	254.0	3.26	71.0
242	1730	24.1442	82.2175	2.68	250.5	8.90	140.5	8.46	255.0	1.78	66.5
242	1745	24.1417	82.2022	2.43	246.0	9.16	139.0	8.15	254.0	1.90	71.5
242	1800	24.1389	82.1867	2.16	242.0	9.50	139.0	7.75	252.0	2.10	77.5
242	1815	24.1364	82.1711	1.80	228.5	9.70	135.5	7.30	250.0	2.39	82.5
242	1830	24.1336	82.1558	1.77	225.5	9.80	134.5	7.15	248.5	2.57	82.5
242	18465	24.1311	82.1394	1.60	219.3	10.00	133.5	7.50	249.5	2.66	83.5
242	1900	24.1300	82.1247	1.68	218.0	10.00	135.0	7.00	250.5	2.62	86.0
242	1915	24.1308	82.1153	2.70	228.0	9.80	139.0	7.50	250.5	2.11	87.0
242	1930	24.1294	82.0994	2.20	229.5	9.55	137.5	7.65	251.5	1.99	86.5
242	1945	24.1275	82.0811	2.15	226.0	9.80	138.5	7.50	251.0	2.80	89.0
242	2000	24.1256	82.0631	1.94	217.0	9.96	136.6	7.40	249.0	2.24	93.0
242	2015	24.1233	82.0447	2.12	210.0	10.20	136.7	7.20	251.6	2.44	95.0
242	20325	24.1211	82.0242	2.10	200.0	10.38	136.0	7.00	247.0	2.69	95.0
242	2045	24.1208	82.0100	2.40	197.0	10.55	135.0	6.70	246.0	2.94	97.0
242	2100	24.1206	81.9933	2.18	185.8	10.78	134.2	6.50	243.5	3.40	97.2
242	2115	24.1206	81.9769	2.38	177.0	11.00	133.1	6.15	243.0	3.71	97.2
242	2130	24.1206	81.9603	2.15	172.0	11.18	132.0	6.60	242.2	3.91	96.0
242	2145	24.1222	81.9425	2.16	170.0	11.20	134.0	5.95	243.5	4.00	97.0
242	2200	24.1236	81.9250	-1.00	-1.0	11.50	133.3	5.50	241.7	4.40	98.1
242	2215	24.1253	81.9072	-1.00	-1.0	12.40	132.8	5.11	237.8	4.92	97.8
242	2230	24.1267	81.8897	-1.00	-1.0	12.30	131.7	5.80	231.7	5.52	97.3
242	2245	24.1181	81.8789	-1.00	-1.0	12.80	130.0	4.55	231.0	5.62	94.2
242	2300	24.1092	81.8683	-1.00	-1.0	11.42	150.0	4.30	236.7	5.38	86.4
242	2315	24.1003	81.8578	-1.00	-1.0	11.00	125.0	4.28	246.0	5.32	80.8
242	2330	24.0914	81.8472	-1.00	-1.0	10.70	124.2	4.30	252.0	5.28	78.5

242	2345	24.0825	81.8367	-1.00	-1.0	10.25	122.5	4.37	249.5	5.40	72.5
243	0	24.0736	81.8264	-1.00	-1.0	9.89	121.5	4.35	262.5	5.41	68.5
243	15	24.0647	81.8158	-1.00	-1.0	10.00	120.0	4.25	263.0	5.78	69.0
243	30	24.0561	81.8050	-1.00	-1.0	10.18	119.5	4.40	263.5	6.50	69.5
243	45	24.0567	81.7883	-1.00	-1.0	10.30	118.5	3.81	265.5	6.31	70.5
243	100	24.0572	81.7719	-1.00	-1.0	10.40	118.5	3.70	259.5	6.40	72.5
243	115	24.0483	81.7581	-1.00	-1.0	10.52	118.5	3.70	256.0	6.52	82.0
243	130	24.0347	81.7447	-1.00	-1.0	10.56	119.0	3.55	260.0	6.79	77.0
243	145	24.0208	81.7314	-1.00	-1.0	10.45	115.0	3.27	266.0	7.19	70.0
243	200	24.0036	81.7200	-1.00	-1.0	10.38	111.0	3.10	275.0	7.60	67.0
243	215	23.9864	81.7086	-1.00	-1.0	10.30	111.0	2.86	287.0	8.10	55.0
243	230	23.9733	81.6958	-1.00	-1.0	10.24	106.0	2.90	291.0	8.30	61.0
243	245	23.9711	81.6811	-1.00	-1.0	10.10	17.0	3.15	294.0	8.40	61.0
243	300	23.9692	81.6661	-1.00	-1.0	10.16	103.0	3.00	291.0	8.50	61.0
243	315	23.9669	81.6514	-1.00	-1.0	10.45	103.0	2.59	296.0	8.90	63.0
243	330	23.9650	81.6364	-1.00	-1.0	10.80	105.0	2.23	299.0	9.27	65.0
243	345	23.9628	81.6217	-1.00	-1.0	11.26	-10.0	-1.00	-1.0	-1.00	-1.0
243	400	23.9606	81.6069	-1.00	-1.0	11.35	105.0	1.72	305.1	10.70	65.5
243	415	23.9586	81.5919	-1.00	-1.0	11.42	106.0	1.60	216.0	10.35	70.0
243	430	23.9564	81.5772	-1.00	-1.0	11.50	98.5	1.52	321.6	10.61	66.5
243	445	23.9553	81.5622	-1.00	-1.0	11.68	102.6	1.41	329.5	10.90	64.5
243	500	23.9544	81.5475	-1.00	-1.0	11.85	97.0	1.33	339.0	11.30	66.0
243	515	23.9539	81.5325	-1.00	-1.0	11.80	96.0	1.33	349.0	11.50	67.0
243	530	23.9533	81.5178	-1.00	-1.0	11.75	97.0	1.37	0.0	11.60	67.0
243	545	23.9525	81.5028	-1.00	-1.0	12.00	96.0	1.32	9.0	12.00	66.0
243	600	23.9519	81.4881	-1.00	-1.0	12.30	96.5	1.38	35.5	12.30	68.5
243	615	23.9511	81.4731	-1.00	-1.0	12.50	97.5	1.54	44.5	12.60	67.5
243	630	23.9506	81.4583	-1.00	-1.0	12.60	93.5	-1.00	-1.0	12.94	66.0
243	700	23.9444	81.4386	-1.00	-1.0	12.50	93.0	4.50	47.0	13.40	65.0
243	715	23.9369	81.4347	-1.00	-1.0	12.50	87.0	2.60	38.0	13.90	60.0
243	730	23.9372	81.4217	-1.00	-1.0	12.65	87.0	2.70	40.0	14.10	60.0
243	745	23.9378	81.4086	-1.00	-1.0	12.75	86.0	2.86	42.5	14.60	59.0

243	800	23.9381	81.3956	-1.00	-1.0	13.00	85.3	3.29	43.5	14.90	58.6
243	815	23.9383	81.3828	-1.00	-1.0	13.20	83.4	3.44	44.7	15.11	60.1
243	8225	23.9386	81.3767	-1.00	-1.0	13.11	82.3	3.54	47.7	15.38	60.0
243	830	23.9386	81.3667	-1.00	-1.0	13.30	80.0	3.69	46.2	15.50	58.0
243	845	23.9389	81.3481	-1.00	-1.0	13.30	81.8	3.81	48.8	15.80	59.1
243	900	23.9389	81.3297	-1.00	-1.0	13.40	83.6	3.91	50.7	16.00	60.8
243	915	23.9392	81.3111	-1.00	-1.0	13.70	81.5	4.28	53.7	16.41	58.5
243	930	23.9394	81.2925	-1.00	-1.0	13.88	82.0	4.50	55.9	16.85	59.9
243	945	23.9397	81.2739	-1.00	-1.0	13.91	80.3	4.70	57.7	17.20	58.9
243	1000	23.9397	81.2553	-1.00	-1.0	-1.00	-1.0	5.20	61.3	-1.00	-1.0
243	1015	23.9411	81.2372	-1.00	-1.0	-1.00	-1.0	5.48	59.0	-1.00	-1.0
243	1030	23.9500	81.2217	-1.00	-1.0	-1.00	-1.0	4.00	56.5	-1.00	-1.0
243	1045	23.9703	81.1803	-1.00	-1.0	-1.00	-1.0	2.86	56.5	-1.00	-1.0
243	1100	23.9975	81.1244	-1.00	-1.0	-1.00	-1.0	1.38	10.5	-1.00	-1.0
243	1115	24.0247	81.0686	-1.00	-1.0	6.60	93.5	3.50	246.5	9.68	40.5
243	1130	24.0517	81.0142	-1.00	-1.0	3.85	125.5	6.60	243.2	6.68	41.5
243	1145	24.0606	80.9986	-1.00	-1.0	3.64	130.5	6.60	243.5	6.70	40.5
243	1200	24.0694	80.9831	1.40	40.0	3.60	127.0	6.44	242.0	7.20	40.0
243	12085	24.0742	80.9747	1.46	40.0	3.50	126.0	6.32	242.0	7.18	38.0
243	1215	24.0764	80.9700	-1.00	-1.0	3.42	120.5	6.25	242.5	7.34	36.5
243	1230	24.0806	80.9597	1.72	36.0	3.25	123.0	6.20	244.0	7.60	37.0
243	1245	24.0850	80.9494	1.96	35.5	3.24	119.5	5.98	243.5	7.99	34.5
243	1300	24.0894	80.9392	2.16	34.5	3.15	116.5	5.72	244.5	8.29	34.5
243	13105	24.0922	80.9322	2.31	35.0	3.19	115.0	5.60	243.0	8.59	33.0
243	1315	24.0992	80.9236	2.39	37.0	3.20	113.0	5.54	244.0	8.62	35.0
243	1330	24.1203	80.8978	-1.00	-1.0	3.15	110.5	5.37	242.5	8.41	32.5
243	1345	24.1522	80.8642	2.18	31.0	2.84	117.0	5.74	240.0	8.77	31.0
243	1400	24.1797	80.8367	-1.00	-1.0	3.41	153.0	7.30	234.0	7.15	32.0
243	1430	24.2169	80.8006	-1.00	-1.0	3.75	161.0	7.90	229.0	6.98	30.0
243	1445	24.2347	80.7853	-1.00	-1.0	4.00	161.5	7.68	226.5	7.20	32.5
243	1500	24.2122	80.8092	-1.00	-1.0	4.12	115.5	4.79	223.5	10.40	35.5
243	1515	24.1883	80.8322	-1.00	-1.0	6.00	83.5	1.27	202.5	13.95	38.5
243	1530	24.1839	80.8344	-1.00	-1.0	6.67	1.0	-1.00	-1.0	-1.00	-1.0
243	1545	24.1897	80.8256	-1.00	-1.0	6.45	75.0	-1.00	-1.0	14.72	39.0
243	1600	24.1956	80.8164	-1.00	-1.0	-1.00	-1.0	-1.00	-1.0	-1.00	-1.0
243	1615	24.2011	80.8108	-1.00	-1.0	-1.00	-1.0	-1.00	-1.0	-1.00	-1.0
243	1630	24.2281	80.7650	-1.00	-1.0	5.50	79.0	-1.00	-1.0	14.40	33.0
243	1645	24.2494	80.6936	-1.00	-1.0	1.78	79.0	-1.00	-1.0	12.25	20.0
243	1700	24.2703	80.6219	-1.00	-1.0	-1.00	-1.0	-1.00	-1.0	11.59	13.0
243	1715	24.3208	80.5797	-1.00	-1.0	-1.00	-1.0	-1.00	-1.0	9.00	9.4
243	1730	24.3844	80.5519	-1.00	-1.0	-1.00	-1.0	-1.00	-1.0	5.42	11.0
243	1745	24.4469	80.5283	-1.00	-1.0	-1.00	-1.0	-1.00	-1.0	16.70	16.0

APPENDIX 4. NANSEN CAST AND CTD CAST DEPTH, TEMPERATURE,
AND SALINITY LISTINGS*

*Only temperature data are listed for CTD casts with bad salinity values.

CTD STATION NUMBER 1
JULY 21, 1971 0112Z
LATITUDE 17 46
LONGITUDE 83 53
DEPTH TO BOTTOM 5305 M
BUCKET TEMPERATURE 27.8
BUCKET SALINITY 36.15

CTD STATION NUMBER 2
JULY 21, 1971 0500Z
LATITUDE 17 47
LONGITUDE 84 2
DEPTH TO BOTTOM 5212 M
BUCKET TEMPERATURE 27.6
BUCKET SALINITY 36.01

CTD STATION NUMBER 3
JULY 21, 1971 0854Z
LATITUDE 17 49
LONGITUDE 84 5
DEPTH TO BOTTOM 4786 M
BUCKET TEMPERATURE 27.4
BUCKET SALINITY 36.01

DEPTH	TEMPERATURE	SALINITY
0.0	28.03	
20.0	27.87	
40.0	27.57	
60.0	27.28	
80.0	27.05	
100.0	26.51	
120.0	25.44	
140.0	24.61	
160.0	23.25	
180.0	21.94	
200.0	20.28	
220.0	18.66	
240.0	17.74	
260.0	17.18	
280.0	16.83	
300.0	16.30	
340.0	15.40	
380.0	14.04	
420.0	12.93	
460.0	11.26	
500.0	10.58	
540.0	9.44	
580.0	8.61	
620.0	8.03	
660.0	7.63	
700.0	7.01	
740.0	6.55	
780.0	6.19	
820.0	5.86	
860.0	5.60	
900.0	5.45	
940.0	5.22	
980.0	5.05	
1020.0	4.93	

DEPTH	TEMPERATURE	SALINITY
0.0	27.53	
20.0	27.51	
40.0	27.60	
60.0	27.26	
80.0	26.79	
100.0	26.27	
120.0	25.25	
140.0	24.33	
160.0	23.27	
180.0	21.67	
200.0	19.57	
220.0	18.14	
240.0	17.67	
260.0	17.22	
280.0	16.91	
300.0	16.45	
340.0	15.06	
380.0	14.06	
420.0	12.53	
460.0	11.62	
500.0	10.49	
540.0	9.56	
580.0	8.93	
620.0	8.15	
660.0	7.53	
700.0	6.91	
740.0	6.62	
780.0	6.25	
820.0	6.03	
860.0	5.73	
900.0	5.40	
940.0	5.09	
980.0	5.00	
1020.0	4.87	

DEPTH	TEMPERATURE	SALINITY
0.0	27.48	
20.0	27.44	
40.0	27.46	
60.0	27.30	
80.0	26.84	
100.0	26.20	
120.0	25.21	
140.0	24.51	
160.0	23.36	
180.0	21.58	
200.0	20.05	
220.0	18.61	
240.0	17.71	
260.0	17.21	
280.0	16.82	
300.0	16.41	
340.0	15.31	
380.0	14.03	
420.0	12.37	
430.0	11.99	

CTD STATION NUMBER 4
JULY 21, 1971 1318Z
LATITUDE 17 52
LONGITUDE 84 10
DEPTH TO BOTTOM 5003 M
BUCKET TEMPERATURE 27.4
BUCKET SALINITY 36.04

CTD STATION NUMBER 6
JULY 21, 1971 1900Z
LATITUDE 17 55
LONGITUDE 84 20
DEPTH TO BOTTOM 4930 M
BUCKET TEMPERATURE 27.6
BUCKET SALINITY

CTD STATION NUMBER 7
JULY 22, 1971 0054Z
LATITUDE 18 1
LONGITUDE 84 24
DEPTH TO BOTTOM 4873 M
BUCKET TEMPERATURE 27.0
BUCKET SALINITY

DEPTH	TEMPERATURE	SALINITY
0.0	27.55	
20.0	27.48	
40.0	27.44	
60.0	27.19	
80.0	26.75	
100.0	26.16	
120.0	25.05	
140.0	24.35	
160.0	23.38	
180.0	21.89	
200.0	20.16	
220.0	18.50	
240.0	17.73	
260.0	17.41	
280.0	17.15	
300.0	16.73	
340.0	15.53	
380.0	13.67	
420.0	12.42	
460.0	11.46	
500.0	10.78	
540.0	9.64	
580.0	8.79	
620.0	7.98	
660.0	7.14	
700.0	6.84	
740.0	6.57	
780.0	6.41	
820.0	6.28	
860.0	5.93	
900.0	5.56	
940.0	5.21	
980.0	5.04	
1020.0	4.86	
1030.0	4.83	

DEPTH	TEMPERATURE	SALINITY
0.0	27.55	
20.0	27.57	
40.0	27.51	
60.0	27.20	
80.0	26.80	
100.0	26.18	
120.0	25.14	
140.0	24.33	
160.0	23.08	
180.0	21.75	
200.0	20.13	
220.0	18.83	
240.0	18.23	
260.0	17.79	
280.0	17.49	
300.0	17.13	
340.0	15.91	
380.0	14.36	
420.0	12.95	
460.0	12.07	
500.0	10.99	
540.0	9.85	
580.0	8.65	
620.0	8.01	
660.0	7.47	
700.0	7.07	
740.0	6.71	
780.0	6.46	
820.0	6.22	
860.0	6.02	
900.0	5.78	
940.0	5.44	
980.0	5.23	
1020.0	4.96	

DEPTH	TEMPERATURE	SALINITY
0.0	27.57	
20.0	27.51	
40.0	27.48	
60.0	27.33	
80.0	27.02	
100.0	26.41	
120.0	25.53	
140.0	24.48	
160.0	23.26	
180.0	21.54	
200.0	20.33	
220.0	19.29	
240.0	18.49	
260.0	18.02	
280.0	17.61	
300.0	17.19	
340.0	15.93	
380.0	14.50	
420.0	13.16	
460.0	12.14	
500.0	11.57	
540.0	10.35	
580.0	9.13	
620.0	8.35	
660.0	7.52	
700.0	7.04	
740.0	6.74	
780.0	6.44	
820.0	6.11	
860.0	5.89	
900.0	5.62	
940.0	5.34	
980.0	5.10	
1020.0	4.91	

CTD STATION NUMBER 8
JULY 22, 1971 0512Z
LATITUDE 18 3
LONGITUDE 84 27
DEPTH TO BOTTOM 4844 M
BUCKET TEMPERATURE 27.6
BUCKET SALINITY 35.97

CTD STATION NUMBER 9
JULY 22, 1971 0906Z
LATITUDE 18 5
LONGITUDE 84 36
DEPTH TO BOTTOM 4497 M
BUCKET TEMPERATURE 27.6
BUCKET SALINITY 36.06

CTD STATION NUMBER 10
JULY 22, 1971 1306Z
LATITUDE 18 9
LONGITUDE 84 41
DEPTH TO BOTTOM 4572 M
BUCKET TEMPERATURE 27.5
BUCKET SALINITY 36.06

DEPTH	TEMPERATURE	SALINITY
0.0	27.59	
20.0	27.55	
40.0	27.51	
60.0	27.32	
80.0	27.03	
100.0	26.46	
120.0	25.45	
140.0	24.42	
160.0	23.06	
180.0	21.60	
200.0	20.60	
220.0	19.45	
240.0	18.60	
260.0	18.08	
280.0	17.55	
300.0	17.17	
340.0	15.85	
380.0	14.09	
420.0	12.45	
460.0	12.21	
500.0	11.44	
540.0	10.71	
580.0	9.39	
620.0	8.33	
660.0	7.55	
700.0	6.99	
740.0	6.78	
780.0	6.45	
820.0	6.23	
860.0	5.88	
900.0	5.56	
940.0	5.25	
980.0	5.05	
1010.0	4.92	

DEPTH	TEMPERATURE	SALINITY
0.0	27.59	
20.0	27.55	
40.0	27.50	
60.0	27.15	
80.0	26.89	
100.0	26.37	
120.0	25.58	
140.0	24.36	
160.0	23.17	
180.0	21.56	
200.0	20.16	
220.0	19.70	
240.0	18.12	
260.0	17.79	
280.0	17.56	
300.0	17.04	
340.0	15.84	
380.0	14.43	
420.0	13.27	
460.0	11.96	
500.0	11.21	
540.0	10.37	
580.0	8.99	
620.0	8.23	
660.0	7.58	
700.0	7.05	
740.0	6.58	
780.0	6.23	
820.0	5.99	
860.0	5.85	
900.0	5.60	
940.0	5.33	
980.0	5.08	
1020.0	4.99	

DEPTH	TEMPERATURE	SALINITY
0.0	27.59	
20.0	27.54	
40.0	27.43	
60.0	27.02	
80.0	26.74	
100.0	26.31	
120.0	25.49	
140.0	24.19	
160.0	23.28	
180.0	21.74	
200.0	20.31	
220.0	19.96	
240.0	19.27	
260.0	17.87	
280.0	17.51	
300.0	16.92	
340.0	15.80	
380.0	14.33	
420.0	13.32	
460.0	12.12	
500.0	11.34	
540.0	10.01	
580.0	8.81	
620.0	8.28	
660.0	7.65	
700.0	7.04	
740.0	6.58	
780.0	6.32	
820.0	6.09	
860.0	5.94	
900.0	5.78	
940.0	5.60	
980.0	5.35	
1020.0	5.13	
1030.0	5.09	

CTD STATION NUMBER 11
JULY 22, 1971 2112Z
LATITUDE 18 16
LONGITUDE 84 52
DEPTH TO BOTTOM 28.1
BUCKET TEMPERATURE 28.1
BUCKET SALINITY 36.06

CTD STATION NUMBER 12
JULY 23, 1971 0054Z
LATITUDE 18 20
LONGITUDE 84 54
DEPTH TO BOTTOM 2377 M
BUCKET TEMPERATURE 27.9
BUCKET SALINITY 36.07

CTD STATION NUMBER 13
JULY 23, 1971 0500Z
LATITUDE 18 24
LONGITUDE 84 59
DEPTH TO BOTTOM 3649 M
BUCKET TEMPERATURE 27.8
BUCKET SALINITY 36.07

DEPTH	TEMPERATURE	SALINITY
0.0	28.00	
20.0	27.64	
40.0	27.25	
60.0	27.04	
80.0	26.80	
100.0	26.39	
120.0	25.72	
140.0	24.65	
160.0	23.38	
180.0	21.77	
200.0	20.51	
220.0	19.17	
240.0	18.19	
260.0	17.50	
280.0	16.97	
300.0	16.30	
340.0	14.70	
380.0	13.99	
420.0	13.43	
460.0	12.84	
500.0	11.68	
540.0	9.77	
580.0	9.19	
620.0	8.28	
660.0	7.37	
700.0	6.98	
740.0	6.78	
780.0	6.61	
820.0	6.46	
860.0	6.15	
900.0	5.93	

DEPTH	TEMPERATURE	SALINITY
0.0	27.81	
20.0	27.67	
40.0	27.41	
60.0	27.19	
80.0	26.87	
100.0	26.51	
120.0	25.75	
140.0	24.58	
160.0	22.72	
180.0	21.59	
200.0	20.44	
220.0	19.16	
240.0	18.25	
260.0	17.67	
280.0	17.01	
300.0	16.33	
340.0	14.68	
380.0	13.94	
420.0	13.67	
460.0	12.93	
500.0	11.77	
540.0	10.59	
580.0	9.33	
620.0	8.22	
660.0	7.35	
700.0	7.10	
740.0	6.89	
780.0	6.71	
820.0	6.48	
860.0	6.29	
900.0	6.08	
940.0	5.60	
980.0	5.31	
1020.0	4.95	
1030.0	4.88	

DEPTH	TEMPERATURE	SALINITY
0.0	27.92	
20.0	27.70	
40.0	27.44	
60.0	27.47	
80.0	26.92	
100.0	26.57	
120.0	25.91	
140.0	24.56	
160.0	23.00	
180.0	21.98	
200.0	20.92	
220.0	19.41	
240.0	18.51	
260.0	17.83	
280.0	17.16	
300.0	16.70	
340.0	14.74	
380.0	13.86	
420.0	13.21	
460.0	12.71	
500.0	11.93	
540.0	10.11	
580.0	9.00	
620.0	8.06	
660.0	7.46	
700.0	7.09	
740.0	6.90	
780.0	6.63	
820.0	6.33	
860.0	6.04	
900.0	5.80	

CTD STATION NUMBER 14
JULY 23, 1971 0854Z
LATITUDE 18 27
LONGITUDE 85 4
DEPTH TO BOTTOM 2452 M
BUCKET TEMPERATURE 27.7
BUCKET SALINITY 36.10

CTD STATION NUMBER 15
JULY 23, 1971 1318Z
LATITUDE 14 30
LONGITUDE 85 11
DEPTH TO BOTTOM 3332 M
BUCKET TEMPERATURE 27.3
BUCKET SALINITY 36.13

CTD STATION NUMBER 16
JULY 24, 1971 2112Z
LATITUDE 19 6
LONGITUDE 85 46
DEPTH TO BOTTOM 4419 M
BUCKET TEMPERATURE 28.3
BUCKET SALINITY 36.09

DEPTH	TEMPERATURE	SALINITY
0.0	27.79	
20.0	27.67	
40.0	27.25	
60.0	27.07	
80.0	26.84	
100.0	26.54	
120.0	25.92	
140.0	24.72	
160.0	23.40	
180.0	22.18	
200.0	20.97	
220.0	19.96	
240.0	18.84	
260.0	17.91	
280.0	17.22	
300.0	16.76	
340.0	14.96	
380.0	13.81	
420.0	13.19	
460.0	12.53	
500.0	11.48	
540.0	9.85	
580.0	9.09	
620.0	8.22	
660.0	7.54	
700.0	7.29	
740.0	6.97	
780.0	6.68	
820.0	6.36	
860.0	5.97	
900.0	5.60	
940.0	5.38	
980.0	5.11	
1020.0	4.92	

DEPTH	TEMPERATURE	SALINITY
0.0	27.76	
20.0	27.71	
40.0	27.43	
60.0	27.39	
80.0	26.84	
100.0	26.37	
120.0	25.68	
140.0	24.65	
160.0	23.13	
180.0	21.71	
200.0	20.83	
220.0	19.70	
240.0	18.75	
260.0	17.84	
280.0	17.15	
300.0	16.48	
340.0	14.92	
380.0	13.59	
420.0	12.73	
460.0	12.23	
500.0	11.00	
540.0	9.93	
580.0	8.92	
620.0	8.29	
660.0	7.70	
700.0	7.34	
740.0	6.91	
780.0	6.59	
820.0	6.25	
860.0	5.92	
900.0	5.55	

DEPTH	TEMPERATURE	SALINITY
0.0	28.25	
20.0	28.01	
40.0	27.72	
60.0	27.68	
80.0	27.09	
100.0	26.45	
120.0	25.65	
140.0	24.92	
160.0	24.09	
180.0	22.72	
200.0	21.33	
220.0	20.30	
240.0	19.62	
260.0	19.84	
280.0	17.71	
300.0	16.93	
340.0	15.52	
380.0	14.43	
420.0	13.41	
460.0	12.35	
500.0	11.40	
540.0	10.77	
580.0	10.15	
620.0	9.21	
660.0	8.54	
700.0	7.89	
740.0	7.38	
780.0	6.68	
820.0	6.42	
860.0	6.11	
900.0	5.77	
940.0	5.46	
980.0	5.23	
1020.0	4.92	

CTD STATION NUMBER 17
JULY 25, 1971 0100Z
LATITUDE 19 9
LONGITUDE 85 49
DEPTH TO BOTTOM 4401 M
BUCKET TEMPERATURE 28.0
BUCKET SALINITY 36.04

CTD STATION NUMBER 18
JULY 25, 1971 0506Z
LATITUDE 19 10
LONGITUDE 85 53
DEPTH TO BOTTOM 4420 M
BUCKET TEMPERATURE 27.8
BUCKET SALINITY

CTD STATION NUMBER 19
JULY 22, 1971 0900Z
LATITUDE 19 10
LONGITUDE 85 58
DEPTH TO BOTTOM 4420 M
BUCKET TEMPERATURE 28.0
BUCKET SALINITY

DEPTH	TEMPERATURE	SALINITY
0.0	28.01	
20.0	27.94	
40.0	27.76	
60.0	27.52	
80.0	27.06	
100.0	26.64	
120.0	25.59	
140.0	24.73	
160.0	23.89	
180.0	22.34	
200.0	21.07	
220.0	20.20	
240.0	19.62	
260.0	18.77	
280.0	17.56	
300.0	16.94	
340.0	15.39	
380.0	14.61	
420.0	13.36	
460.0	12.41	
500.0	11.48	
540.0	10.86	
580.0	10.12	
620.0	9.16	
660.0	8.49	
700.0	8.01	
740.0	7.36	
780.0	6.82	
820.0	6.37	
860.0	6.15	
900.0	5.78	

DEPTH	TEMPERATURE	SALINITY
0.0	27.79	
20.0	27.61	
40.0	27.55	
60.0	27.35	
80.0	27.08	
100.0	26.80	
120.0	25.65	
140.0	24.85	
160.0	23.80	
180.0	22.14	
200.0	20.87	
220.0	20.25	
240.0	19.57	
260.0	18.32	
280.0	17.47	
300.0	16.85	
340.0	15.79	
380.0	14.68	
420.0	13.61	
460.0	12.57	
500.0	11.83	
540.0	11.14	
580.0	9.99	
620.0	9.30	
660.0	8.48	
700.0	8.00	
740.0	7.41	
780.0	6.95	
820.0	6.60	
860.0	6.17	
900.0	5.87	
940.0	5.62	
980.0	5.32	
1010.0	5.13	

DEPTH	TEMPERATURE	SALINITY
0.0	27.83	36.04
20.0	27.80	36.10
40.0	27.63	36.14
60.0	27.23	36.13
80.0	27.00	36.24
100.0	26.59	36.34
120.0	25.56	36.45
140.0	24.74	36.62
160.0	23.44	36.75
180.0	21.57	36.79
200.0	20.71	36.74
220.0	19.85	36.65
240.0	18.84	36.55
260.0	18.14	36.48
280.0	17.45	36.36
300.0	16.71	36.26
340.0	15.61	36.05
380.0	14.45	35.87
420.0	13.42	35.70
460.0	12.54	35.56
500.0	11.64	35.41
540.0	10.80	35.28
580.0	10.14	35.19
620.0	9.31	35.08
660.0	8.66	34.99
700.0	7.77	34.90
740.0	7.31	34.88
780.0	6.94	34.86
820.0	6.58	34.84
860.0	6.19	34.85
900.0	5.87	34.84
940.0	5.57	34.84
980.0	5.24	34.88
1020.0	5.00	34.88

CTD STATION NUMBER 20
JULY 25, 1971 1706Z
LATITUDE 19 14
LONGITUDE 86 5
DEPTH TO BOTTOM 4420 M
BUCKET TEMPERATURE 27.8
BUCKET SALINITY 36.33

CTD STATION NUMBER 21
JULY 25, 1971 1836Z
LATITUDE 19 14
LONGITUDE 86 8
DEPTH TO BOTTOM 4194 M

CTD STATION NUMBER 22
JULY 25, 1971 2106Z
LATITUDE 19 16
LONGITUDE 86 11
DEPTH TO BOTTOM 4417 M
BUCKET TEMPERATURE 27.8
BUCKET SALINITY

DEPTH	TEMPERATURE	SALINITY
0.0	27.87	
20.0	27.81	
40.0	27.52	
60.0	27.22	
80.0	26.91	
100.0	26.56	
120.0	25.81	
140.0	24.64	
160.0	23.21	
180.0	21.80	
200.0	20.73	
220.0	19.57	
240.0	18.34	
260.0	17.68	
280.0	17.27	
300.0	16.84	
340.0	15.77	
380.0	14.62	
420.0	13.44	
460.0	12.23	
500.0	11.40	
540.0	10.50	
580.0	9.80	
620.0	9.17	
660.0	8.50	
700.0	7.82	
740.0	7.28	
780.0	6.86	
820.0	6.39	
860.0	5.96	
900.0	5.61	
940.0	5.36	
980.0	5.10	
1020.0	4.91	
1060.0	4.80	
1070.0	4.77	

DEPTH	TEMPERATURE	SALINITY
0.0	28.20	
10.0	27.84	36.066
20.0	27.63	36.067
40.0	27.31	36.072
74.0	27.06	36.176
146.0	24.12	36.715
243.0	18.43	36.497
388.0	14.29	35.851

DEPTH	TEMPERATURE	SALINITY
0.0	27.86	36.07
20.0	27.80	36.08
40.0	27.46	36.09
60.0	27.15	36.14
80.0	26.84	36.29
100.0	26.30	36.37
120.0	25.26	36.50
140.0	24.03	36.71
160.0	22.72	36.81
180.0	21.48	36.79
200.0	20.30	36.69
220.0	19.09	36.59
240.0	18.26	36.50
260.0	17.71	36.44
280.0	17.31	36.38
300.0	16.87	36.31
340.0	15.82	36.14
380.0	14.60	35.92
420.0	13.37	35.71
460.0	12.25	35.54
500.0	11.26	35.37
540.0	10.51	35.26
580.0	9.82	35.17
620.0	9.30	35.10
660.0	8.66	35.02
700.0	8.09	34.96
740.0	7.49	34.90
780.0	7.09	34.88
820.0	6.59	34.85
860.0	6.09	34.87
900.0	5.78	34.88
940.0	5.37	34.89
980.0	5.12	34.91
1020.0	4.92	34.90

CTD STATION NUMBER 23
JULY 26, 1971 0112Z
LATITUDE 19 18
LONGITUDE 86 16
DEPTH TO BOTTOM 4415 M
BUCKET TEMPERATURE 27.9
BUCKET SALINITY

CTD STATION NUMBER 24
JULY 26, 1971 0500Z
LATITUDE 19 22
LONGITUDE 86 19
DEPTH TO BOTTOM 4418 M
BUCKET TEMPERATURE 27.8
BUCKET SALINITY 36.05

CTD STATION NUMBER 25
JULY 26, 1971 0900Z
LATITUDE 19 25
LONGITUDE 86 25
DEPTH TO BOTTOM 4416 M
BUCKET TEMPERATURE 27.8
BUCKET SALINITY 36.12

DEPTH	TEMPERATURE	SALINITY
0.0	27.88	36.13
20.0	27.84	36.10
40.0	27.55	36.09
60.0	27.09	36.09
80.0	26.81	36.31
100.0	26.03	36.38
120.0	25.00	36.55
140.0	23.88	36.72
160.0	22.27	36.79
180.0	21.17	36.76
200.0	19.64	36.63
220.0	18.77	36.55
240.0	18.07	36.48
260.0	17.63	36.42
280.0	17.25	36.36
300.0	16.78	36.29
340.0	15.88	36.12
380.0	14.58	35.88
420.0	13.44	35.71
460.0	12.43	35.52
500.0	11.44	35.35
540.0	10.52	35.24
580.0	9.84	35.15
620.0	9.27	35.09
660.0	8.70	35.01
700.0	8.11	34.94
740.0	7.59	34.89
780.0	7.20	34.88
820.0	6.72	34.86
860.0	6.26	34.84
900.0	5.87	34.87
940.0	5.56	34.88
980.0	5.23	34.90
1020.0	4.99	34.91
1030.0	4.96	34.91

DEPTH	TEMPERATURE	SALINITY
0.0	27.81	36.07
20.0	27.77	36.09
40.0	27.65	36.15
60.0	27.23	36.13
80.0	26.78	36.32
100.0	25.90	36.42
120.0	24.81	36.58
140.0	23.89	36.73
160.0	22.43	36.84
180.0	20.88	36.75
200.0	19.68	36.68
220.0	18.85	36.58
240.0	18.30	36.54
260.0	17.69	36.44
280.0	17.01	36.35
300.0	16.37	36.22
340.0	15.49	36.06
380.0	14.57	35.91
420.0	13.51	35.72
460.0	12.24	35.51
500.0	11.38	35.37
540.0	10.77	35.29
580.0	10.10	35.20
620.0	9.38	35.04
660.0	8.70	35.01
700.0	8.13	34.95
740.0	7.76	34.92
780.0	7.27	34.88
820.0	6.70	34.85
860.0	6.30	34.85
900.0	5.86	34.87
940.0	5.56	34.88
980.0	5.22	34.90
1010.0	5.07	34.90

DEPTH	TEMPERATURE	SALINITY
0.0	27.86	36.12
20.0	27.78	36.10
40.0	27.54	36.12
60.0	26.99	36.16
80.0	26.76	36.36
100.0	25.90	36.39
120.0	24.90	36.59
140.0	23.77	36.77
160.0	22.38	36.81
180.0	20.69	36.73
200.0	19.57	36.65
220.0	18.76	36.58
240.0	18.03	36.49
260.0	17.45	36.41
280.0	16.99	36.31
300.0	16.46	36.23
340.0	15.71	36.12
380.0	14.71	35.94
420.0	13.37	35.73
460.0	12.40	35.56
500.0	11.50	35.41
540.0	10.80	35.32
580.0	9.95	35.18
620.0	9.39	35.12
660.0	8.65	35.02
700.0	8.05	34.94
740.0	7.63	34.92
780.0	7.07	34.89
820.0	6.70	34.87
860.0	6.17	34.87
900.0	5.73	34.89
940.0	5.44	34.90
980.0	5.14	34.91
1020.0	4.94	34.91

NANSSEN STATION NUMBER 26
 JULY 26, 1971 1230Z
 LATITUDE 19 28
 LONGITUDE 06 25
 DEPTH TO BOTTOM 4431 M

CTD STATION NUMBER 27
 JULY 26, 1971 1400Z
 LATITUDE 19 29
 LONGITUDE 06 25
 DEPTH TO BOTTOM 4422 M
 BUCKET TEMPERATURE 27.9
 BUCKET SALINITY 36.18

CTD STATION NUMBER 28
 JULY 26, 1971 1706Z
 LATITUDE 19 32
 LONGITUDE 06 27
 DEPTH TO BOTTOM 4420 M
 BUCKET TEMPERATURE 28.1
 BUCKET SALINITY 36.09

DEPTH	TEMPERATURE	SALINITY
0.0	27.80	36.152
10.0	27.74	36.075
30.0	27.71	36.119
50.0	27.30	36.078
75.0	26.86	36.311
149.0	22.60	36.859
248.0	17.45	36.347
396.0	14.36	35.859
595.0	10.07	35.175
788.0	7.02	34.871
985.0	5.21	34.860

DEPTH	TEMPERATURE	SALINITY
0.0	27.77	36.11
10.0	27.69	36.11
40.0	27.57	36.17
60.0	27.07	36.16
80.0	26.80	36.33
100.0	25.83	36.34
120.0	24.70	36.58
140.0	23.47	36.76
160.0	22.05	36.81
180.0	20.39	36.72
200.0	19.32	36.62
220.0	18.45	36.52
240.0	17.68	36.41
260.0	17.15	36.34
280.0	16.84	36.32
300.0	16.64	36.28
340.0	15.79	36.13
380.0	14.86	35.98
420.0	13.76	35.79
460.0	12.56	35.59
500.0	11.74	35.45
540.0	10.79	35.31
580.0	10.25	35.23
620.0	9.79	35.17
660.0	9.05	35.07
700.0	8.28	34.98
740.0	7.71	34.93
780.0	7.13	34.88
820.0	6.65	34.86
860.0	6.24	34.86
900.0	5.80	34.88
940.0	5.48	34.90
980.0	5.23	34.91
1020.0	5.05	34.93

DEPTH	TEMPERATURE	SALINITY
0.0	24.06	36.10
20.0	27.75	36.10
40.0	27.51	36.12
60.0	27.06	36.18
80.0	26.75	36.32
100.0	25.65	36.33
120.0	24.55	36.60
140.0	23.44	36.70
160.0	21.89	36.77
180.0	20.42	36.67
200.0	19.37	36.54
220.0	18.52	36.51
240.0	18.00	36.46
260.0	17.56	36.41
280.0	17.15	36.33
300.0	16.80	36.32
340.0	16.07	36.14
380.0	14.88	35.95
420.0	13.75	35.74
460.0	12.67	35.54
500.0	11.76	35.45
540.0	10.96	35.32
580.0	10.16	35.19
620.0	9.91	35.18
660.0	9.15	35.04
700.0	8.32	34.98
740.0	7.62	34.92
780.0	7.04	34.88
820.0	6.66	34.87
860.0	6.14	34.87
900.0	5.75	34.88
940.0	5.47	34.89
980.0	5.29	34.91
1020.0	4.98	34.92

CTD STATION NUMBER 29
 JULY 26, 1971 2106Z
 LATITUDE 19 35
 LONGITUDE 06 30
 DEPTH TO BOTTOM 4160 M
 BUCKET TEMPERATURE 28.6
 BUCKET SALINITY 36.11

CTD STATION NUMBER 30
 JULY 27, 1971 0106Z
 LATITUDE 19 44
 LONGITUDE 06 33
 DEPTH TO BOTTOM 1810 M
 BUCKET TEMPERATURE 27.9
 BUCKET SALINITY 36.12

CTD STATION NUMBER 31
 JULY 27, 1971 0500Z
 LATITUDE 19 46
 LONGITUDE 06 30
 DEPTH TO BOTTOM 2315 M
 BUCKET TEMPERATURE 28.1
 BUCKET SALINITY 36.11

DEPTH	TEMPERATURE	SALINITY
0.0	28.51	36.14
20.0	27.80	36.11
40.0	27.44	36.16
60.0	27.06	36.28
80.0	26.64	36.33
100.0	25.32	36.47
120.0	24.30	36.68
140.0	23.01	36.83
160.0	21.40	36.81
180.0	20.13	36.73
200.0	19.03	36.56
220.0	18.46	36.51
240.0	17.76	36.44
260.0	17.27	36.36
280.0	16.89	36.31
300.0	16.49	36.22
340.0	15.80	36.11
380.0	14.85	35.94
420.0	13.67	35.75
460.0	12.54	35.55
500.0	11.52	35.40
540.0	10.76	35.29
580.0	10.04	35.19
620.0	9.52	35.13
660.0	9.00	35.06
700.0	8.32	34.97
740.0	7.60	34.91
780.0	6.95	34.88
820.0	6.45	34.86
860.0	6.08	34.87
900.0	5.65	34.88
940.0	5.35	34.89
980.0	5.15	34.91
1020.0	4.97	34.91

DEPTH	TEMPERATURE	SALINITY
0.0	28.17	36.08
20.0	27.77	36.13
40.0	27.46	36.15
60.0	27.09	36.19
80.0	26.61	36.31
100.0	25.62	36.39
120.0	24.35	36.63
140.0	22.97	36.74
160.0	20.99	36.69
180.0	19.52	36.57
200.0	18.75	36.54
220.0	18.10	36.47
240.0	17.69	36.43
260.0	17.33	36.37
280.0	16.95	36.32
300.0	16.50	36.23
340.0	15.69	36.11
380.0	14.94	35.97
420.0	14.30	35.88
460.0	13.35	35.72
500.0	12.61	35.60
540.0	12.24	35.54
580.0	11.11	35.37
620.0	10.58	34.99
660.0	9.14	34.95
700.0	7.70	34.93
740.0	7.24	34.90
780.0	6.64	34.87
820.0	6.45	34.87
860.0	5.82	34.89
900.0	5.65	34.89
940.0	5.44	34.89
980.0	5.19	34.92
1020.0	4.95	34.92

DEPTH	TEMPERATURE	SALINITY
0.0	28.04	36.12
20.0	27.82	36.13
40.0	27.52	36.15
60.0	27.13	36.18
80.0	26.70	36.30
100.0	25.67	36.38
120.0	24.38	36.65
140.0	23.24	36.80
160.0	21.46	36.76
180.0	19.84	36.67
200.0	18.92	36.59
220.0	18.36	36.55
240.0	17.89	36.46
260.0	17.49	36.41
280.0	17.19	36.37
300.0	16.85	36.31
340.0	16.12	36.19
380.0	15.34	36.04
420.0	14.46	35.89
460.0	13.40	35.72
500.0	12.75	35.61
540.0	12.11	35.51
580.0	11.16	35.36
620.0	9.25	35.08
660.0	8.50	34.99
700.0	7.92	34.95
740.0	7.37	34.91
780.0	6.78	34.88
820.0	6.36	34.87
860.0	5.88	34.87
900.0	5.62	34.89
940.0	5.33	34.91
980.0	5.06	34.93
1020.0	4.98	34.92

CTD STATION NUMBER 32
JULY 27, 1971 0854Z
LATITUDE 19 50
LONGITUDE 86 28
DEPTH TO BOTTOM 2487 M
BUCKET TEMPERATURE 28.0
BUCKET SALINITY 36.13

CTD STATION NUMBER 34
JULY 27, 1971 1430Z
LATITUDE 19 56
LONGITUDE 86 30
DEPTH TO BOTTOM 2290 M
BUCKET TEMPERATURE 27.9
BUCKET SALINITY 36.09

CTD STATION NUMBER 35
JULY 27, 1971 1718Z
LATITUDE 20 4
LONGITUDE 86 28
DEPTH TO BOTTOM 1591 M
BUCKET TEMPERATURE 28.2
BUCKET SALINITY 36.16

DEPTH	TEMPERATURE	SALINITY
0.0	28.00	36.05
20.0	27.76	36.06
40.0	27.55	36.12
60.0	27.13	36.14
80.0	26.57	36.14
100.0	25.36	36.32
120.0	24.09	36.65
140.0	22.68	36.74
160.0	20.77	36.73
180.0	19.38	36.64
200.0	18.82	36.60
220.0	18.33	36.53
240.0	17.94	36.46
260.0	17.55	36.45
280.0	17.21	36.36
300.0	16.89	36.35
340.0	16.25	36.18
380.0	15.37	36.04
420.0	14.78	35.97
460.0	13.74	35.80
500.0	12.59	35.61
540.0	11.65	35.46
580.0	10.68	35.33
620.0	9.54	35.15
660.0	8.73	35.06
700.0	7.93	34.95
740.0	7.17	34.91
780.0	6.56	34.88
820.0	6.12	34.88
860.0	5.83	34.88
900.0	5.46	34.90
940.0	5.21	34.92
980.0	5.04	34.93
1020.0	4.90	34.93

DEPTH	TEMPERATURE	SALINITY
0.0	28.01	36.08
20.0	27.86	36.11
40.0	27.46	36.11
60.0	27.15	36.19
80.0	26.59	36.31
100.0	25.26	36.42
120.0	24.10	36.70
140.0	22.58	36.80
160.0	20.82	36.74
180.0	19.34	36.60
200.0	18.73	36.55
220.0	18.22	36.49
240.0	17.81	36.44
260.0	17.44	36.41
280.0	17.10	36.36
300.0	16.76	36.30
340.0	16.15	36.19
380.0	15.11	36.00
420.0	14.46	35.89
460.0	13.82	35.78
500.0	12.45	35.54
540.0	11.41	35.42
580.0	10.95	35.34
620.0	9.78	35.17
660.0	8.71	35.07
700.0	8.07	34.98
740.0	7.05	34.89
780.0	6.54	34.88
820.0	6.13	34.88
860.0	5.91	34.89
900.0	5.54	34.92
940.0	5.20	34.93
980.0	4.98	34.94
1020.0	4.86	34.93

DEPTH	TEMPERATURE	SALINITY
0.0	28.07	36.11
20.0	27.85	36.12
40.0	27.68	36.17
60.0	27.42	36.22
80.0	26.63	36.25
100.0	25.55	36.39
120.0	24.50	36.54
140.0	23.07	36.76
160.0	21.26	36.74
180.0	19.67	36.61
200.0	18.77	36.55
220.0	18.26	36.49
240.0	17.78	36.44
260.0	17.42	36.37
280.0	17.11	36.33
300.0	16.79	36.28
340.0	16.21	36.19
380.0	15.53	36.08
420.0	15.03	35.99
460.0	12.62	35.56
500.0	11.50	35.39
540.0	11.03	35.33
580.0	10.01	35.17
620.0	9.24	35.10
660.0	8.68	35.02
700.0	7.53	34.92
740.0	7.26	34.89
780.0	6.89	34.88
820.0	6.36	34.87
860.0	5.88	34.88
900.0	5.47	34.90
940.0	5.29	34.91
980.0	5.14	34.92
1020.0	5.04	34.92

CTD STATION NUMBER 36
JULY 27, 1971 2106Z
LATITUDE 20 8
LONGITUDE 86 30
DEPTH TO BOTTOM 969 M
BUCKET TEMPERATURE 28.2
BUCKET SALINITY 36.15

HANSEN STATION NUMBER 37
JULY 28, 1971 0048Z
LATITUDE 20 20
LONGITUDE 86 30
DEPTH TO BOTTOM 982 M

HANSEN STATION NUMBER 38
JULY 28, 1971 0800Z
LATITUDE 20 31
LONGITUDE 86 20
DEPTH TO BOTTOM 1213 M

DEPTH	TEMPERATURE	SALINITY
0.0	29.27	36.13
20.0	28.01	36.13
40.0	27.61	36.17
60.0	26.99	36.24
80.0	26.61	36.33
100.0	25.54	36.47
120.0	24.20	36.71
140.0	22.35	36.83

DEPTH	TEMPERATURE	SALINITY
0.0	27.90	36.159
9.0	28.09	36.036
29.0	27.48	36.022
48.0	27.16	36.177
73.0	26.17	36.307
97.0	25.08	36.514
286.0	16.43	36.126
647.0	7.87	34.891

DEPTH	TEMPERATURE	SALINITY
0.0	28.00	36.120
10.0	28.01	36.082
28.0	27.74	36.079
47.0	27.37	36.133
71.0	26.74	36.233
139.0	22.67	36.786
365.0	14.92	35.923
527.0	10.13	35.151
695.0	7.52	34.939
880.0	5.53	

CTD STATION NUMBER 39			CTD STATION NUMBER 40			CTD STATION NUMBER 42		
JULY 29, 1971 0506Z			JULY 29, 1971 0900Z			JULY 29, 1971 1848Z		
LATITUDE 19 10			LATITUDE 19 14			LATITUDE 19 22		
LONGITUDE 86 45			LONGITUDE 86 48			LONGITUDE 86 53		
DEPTH TO BOTTOM 4369 M			DEPTH TO BOTTOM 3402 M			DEPTH TO BOTTOM 28.0		
BUCKET TEMPERATURE 28.1			BUCKET TEMPERATURE 36.04			BUCKET TEMPERATURE		
BUCKET SALINITY 35.93			BUCKET SALINITY			BUCKET SALINITY		
DEPTH	TEMPERATURE	SALINITY	DEPTH	TEMPERATURE	SALINITY	DEPTH	TEMPERATURE	SALINITY
0.0	28.08	35.82	0.0	28.02	35.95	0.0	28.07	36.01
20.0	28.03	35.95	20.0	28.00	36.00	20.0	28.04	36.09
40.0	27.86	36.09	40.0	27.82	36.08	40.0	27.86	36.13
60.0	27.65	36.14	60.0	27.48	36.11	60.0	27.65	36.14
80.0	26.79	36.20	80.0	26.59	36.25	80.0	26.37	36.21
100.0	25.84	36.38	100.0	25.64	36.46	100.0	25.50	36.46
120.0	24.94	36.54	120.0	24.41	36.65	120.0	24.18	36.63
140.0	23.41	36.73	140.0	22.77	36.72	140.0	22.38	36.74
160.0	21.51	36.71	160.0	20.81	36.71	160.0	20.68	36.73
180.0	19.70	36.60	180.0	19.46	36.63	180.0	19.15	36.60
200.0	18.50	36.44	200.0	18.26	36.52	200.0	18.08	36.46
220.0	17.66	36.38	220.0	17.36	36.37	220.0	17.12	36.33
240.0	16.69	36.20	240.0	16.51	36.23	240.0	16.58	36.26
260.0	15.86	36.09	260.0	16.00	36.15	260.0	15.97	36.15
280.0	15.34	36.02	280.0	15.38	36.04	280.0	15.20	36.01
300.0	14.70	35.92	300.0	14.82	35.94	300.0	14.56	35.90
340.0	13.47	35.73	340.0	13.57	35.73	340.0	13.36	35.71
380.0	12.49	35.56	380.0	12.38	35.56	380.0	12.16	35.53
420.0	11.26	35.38	420.0	11.32	35.39	420.0	11.43	35.40
460.0	10.27	35.21	460.0	10.63	35.27	460.0	10.62	35.29
500.0	9.65	35.13	500.0	9.95	35.18	500.0	10.04	35.19
540.0	9.05	35.06	540.0	9.36	35.09	540.0	10.04	35.12
580.0	8.66	35.02	580.0	8.66	35.02	580.0	9.54	35.12
620.0	8.02	34.94	620.0	8.11	34.95	580.0	9.13	35.09
660.0	7.62	34.91	660.0	7.66	34.92	620.0	8.60	35.02
700.0	6.98	34.87	700.0	7.13	34.88	660.0	7.90	34.95
740.0	6.59	34.86	740.0	6.69	34.87	700.0	7.19	34.88
780.0	6.01	34.87	780.0	6.28	34.86	740.0	6.62	34.85
820.0	5.62	34.88	820.0	5.81	34.88	780.0	6.19	34.87
860.0	5.44	34.90	860.0	5.47	34.89	820.0	5.80	34.88
900.0	5.20	34.92	900.0	5.21	34.92	860.0	5.48	34.89
940.0	4.93	34.93	940.0	5.04	34.93	900.0	5.21	34.91
980.0	4.79	34.92	980.0	4.85	34.94	940.0	5.06	34.93
			1020.0	4.68	34.94	980.0	4.90	34.94
						1020.0	4.78	34.94

CTD STATION NUMBER 43			CTD STATION NUMBER 44			CTD STATION NUMBER 45		
JULY 29, 1971 2106Z			JULY 30, 1971 0100Z			JULY 30, 1971 0518Z		
LATITUDE 19 23			LATITUDE 19 33			LATITUDE 19 38		
LONGITUDE 86 55			LONGITUDE 86 55			LONGITUDE 86 52		
DEPTH TO BOTTOM 2030 M			DEPTH TO BOTTOM			DEPTH TO BOTTOM 1035 M		
BUCKET TEMPERATURE 28.0			BUCKET TEMPERATURE			BUCKET TEMPERATURE		
BUCKET SALINITY 36.11			BUCKET SALINITY			BUCKET SALINITY		
DEPTH	TEMPERATURE	SALINITY	DEPTH	TEMPERATURE	SALINITY	DEPTH	TEMPERATURE	SALINITY
0.0	28.05	35.94	0.0	28.01	35.97	0.0	28.03	36.04
20.0	28.00	36.02	20.0	27.98	36.03	20.0	27.96	36.08
40.0	27.83	36.12	40.0	27.84	36.09	40.0	27.81	36.12
60.0	27.35	36.14	60.0	27.34	36.14	60.0	27.49	36.13
80.0	26.07	36.24	80.0	26.23	36.22	80.0	26.29	36.22
100.0	25.30	36.52	100.0	25.41	36.52	100.0	25.33	36.47
120.0	23.65	36.70	120.0	24.11	36.71	120.0	23.78	36.67
140.0	21.78	36.80	140.0	22.16	36.80	140.0	21.26	36.66
160.0	20.16	36.70	160.0	20.42	36.74	160.0	19.45	36.55
180.0	18.88	36.60	180.0	19.26	36.65	180.0	18.60	36.52
200.0	18.13	36.47	200.0	18.31	36.50	200.0	17.62	36.37
220.0	17.24	36.38	220.0	17.30	36.36	220.0	16.94	36.27
240.0	16.61	36.29	240.0	16.56	36.25	240.0	16.27	36.16
260.0	15.89	36.16	260.0	15.71	36.09	260.0	15.57	36.04
280.0	15.02	36.00	280.0	15.04	35.99	280.0	14.91	35.93
300.0	14.40	35.89	300.0	14.32	35.86	300.0	14.33	35.84
340.0	12.49	35.62	340.0	13.10	35.66	340.0	13.19	35.66
380.0	11.99	35.49	380.0	12.06	35.49	380.0	12.11	35.46
420.0	11.13	35.36	420.0	11.12	35.33	420.0	11.29	35.35
460.0	10.35	35.25	460.0	10.45	35.24	460.0	10.69	35.27
500.0	9.40	35.17	500.0	9.92	35.19	500.0	10.26	35.21
540.0	9.36	35.12	540.0	9.51	35.11	540.0	9.67	35.12
580.0	8.90	35.07	540.0	9.07	35.06	580.0	9.09	35.05
620.0	8.34	34.99	580.0	8.51	35.06	620.0	8.43	34.97
660.0	7.81	34.94	620.0	8.44	34.98	660.0	7.62	34.91
700.0	7.18	34.89	660.0	7.86	34.93	700.0	6.96	34.86
740.0	6.46	34.86	700.0	6.44	34.86	740.0	6.45	34.85
780.0	6.07	34.87	740.0	6.50	34.85	780.0	6.06	34.86
820.0	5.76	34.90	780.0	6.14	34.86	820.0	5.73	34.88
860.0	5.51	34.89	820.0	5.85	34.88	860.0	5.36	34.90
900.0	5.29	34.90	860.0	5.66	34.87			
940.0	5.01	34.92	900.0	5.38	34.88			
980.0	4.45	34.94	940.0	5.08	34.91			
1010.0	4.75	34.93	980.0	4.96	34.92			
			1010.0	4.33	34.93			

CTD STATION NUMBER 46
JULY 30, 1971 0854Z
LATITUDE 19 41
LONGITUDE 86 53
DEPTH TO BOTTOM 1244 M
BUCKET TEMPERATURE 28.0
BUCKET SALINITY 36.12

CTD STATION NUMBER 49
JULY 30, 1971 1718Z
LATITUDE 19 52
LONGITUDE 86 52
DEPTH TO BOTTOM 1240 M
BUCKET TEMPERATURE 28.1
BUCKET SALINITY 36.07

CTD STATION NUMBER 50
JULY 30, 1971 2106Z
LATITUDE 19 58
LONGITUDE 86 53
DEPTH TO BOTTOM 1170 M
BUCKET TEMPERATURE 28.2
BUCKET SALINITY 36.07

DEPTH	TEMPERATURE	SALINITY
0.0	28.00	35.98
20.0	27.96	36.03
40.0	27.82	36.06
60.0	27.49	36.08
80.0	26.50	36.21
100.0	25.33	36.46
120.0	23.64	36.73
140.0	21.41	36.69
160.0	19.64	36.60
180.0	18.70	36.49
200.0	17.70	36.40
220.0	17.02	36.33
240.0	16.31	36.20
260.0	15.63	36.09
280.0	14.87	35.98
300.0	14.30	35.89
340.0	13.23	35.70
380.0	12.14	35.52
420.0	11.48	35.45
460.0	10.91	35.35
500.0	10.37	35.27
540.0	9.88	35.20
580.0	9.29	35.12
620.0	8.70	35.03
660.0	7.80	34.95
700.0	7.17	34.89
740.0	6.68	34.87
780.0	6.23	34.88
820.0	5.89	34.89
860.0	5.70	34.90
900.0	5.43	34.91
940.0	5.12	34.94
980.0	4.87	34.94
1010.0	4.75	34.95

DEPTH	TEMPERATURE	SALINITY
0.0	28.14	36.07
20.0	27.99	36.07
40.0	27.85	36.10
60.0	27.53	36.12
80.0	26.30	36.26
100.0	25.40	36.45
120.0	23.90	36.59
140.0	20.94	36.67
160.0	19.48	36.57
180.0	18.40	36.48
200.0	17.64	36.40
220.0	17.09	36.30
240.0	16.35	36.18
260.0	15.73	36.08
280.0	15.16	36.00
300.0	14.52	35.87
340.0	13.37	35.70
380.0	12.60	35.58
420.0	11.90	35.48
460.0	11.06	35.33
500.0	10.46	35.24
540.0	9.97	35.19
580.0	9.22	35.06
620.0	8.08	34.93
660.0	7.62	34.92
700.0	7.19	34.88
740.0	6.66	34.86
780.0	6.23	34.85
820.0	5.84	34.88
860.0	5.48	34.85
900.0	5.27	34.89
940.0	5.06	34.90
980.0	4.95	34.91
1020.0	4.87	34.92

DEPTH	TEMPERATURE	SALINITY
0.0	28.28	36.06
20.0	28.06	36.05
40.0	27.82	36.07
60.0	27.30	36.17
80.0	26.10	36.32
100.0	25.27	36.51
120.0	23.75	36.67
140.0	21.59	36.67
160.0	19.66	36.60
180.0	18.51	36.49
200.0	17.84	36.41
220.0	17.15	36.31
240.0	16.58	36.23
260.0	15.90	36.12
280.0	15.38	36.03
300.0	14.57	35.88
340.0	13.52	35.71
380.0	12.53	35.55
420.0	11.69	35.42
460.0	11.04	35.32
500.0	10.43	35.22
540.0	9.80	35.14
580.0	9.02	35.05
620.0	8.26	34.96
660.0	7.65	34.89
700.0	7.09	34.86
740.0	6.63	34.86
780.0	6.22	34.85
820.0	5.80	34.86
860.0	5.53	34.87
900.0	5.27	34.89
940.0	5.08	34.90
980.0	4.93	34.90
1000.0	4.87	34.91

CTD STATION NUMBER 51
JULY 31, 1971 0054Z
LATITUDE 20 7
LONGITUDE 86 51
DEPTH TO BOTTOM
BUCKET TEMPERATURE
BUCKET SALINITY

CTD STATION NUMBER 52
JULY 31, 1971 0506Z
LATITUDE 20 13
LONGITUDE 86 44
DEPTH TO BOTTOM 1174 M
BUCKET TEMPERATURE 28.0
BUCKET SALINITY 35.97

CTD STATION NUMBER 53
JULY 31, 1971 0900Z
LATITUDE 20 18
LONGITUDE 86 41
DEPTH TO BOTTOM 1181 M
BUCKET TEMPERATURE 28.0
BUCKET SALINITY 36.09

DEPTH	TEMPERATURE	SALINITY
0.0	28.18	35.96
20.0	28.04	35.98
40.0	27.83	36.07
60.0	27.18	36.15
80.0	26.10	36.34
100.0	25.25	36.42
120.0	23.33	36.69
140.0	21.46	36.73
160.0	20.05	36.68
180.0	18.96	36.59
200.0	17.85	36.45
220.0	17.16	36.34
240.0	16.44	36.20
260.0	15.77	36.10
280.0	15.33	36.01
300.0	14.71	35.91
340.0	13.47	35.71
380.0	12.30	35.53
420.0	11.69	35.42
460.0	11.06	35.33
500.0	10.39	35.23
540.0	9.77	35.15
580.0	8.74	35.02
620.0	7.92	34.93
660.0	7.43	34.88
700.0	6.96	34.86
740.0	6.44	34.85
780.0	6.17	34.85
820.0	5.86	34.86
860.0	5.55	34.88
900.0	5.35	34.88
940.0	5.15	34.89
980.0	5.04	34.90
990.0	5.02	34.91

DEPTH	TEMPERATURE	SALINITY
0.0	28.09	35.94
20.0	28.00	36.01
40.0	27.77	36.08
60.0	26.89	36.17
80.0	25.85	36.38
100.0	24.88	36.56
120.0	21.07	36.75
140.0	21.05	36.66
160.0	19.71	36.61
180.0	18.66	36.54
200.0	17.71	36.43
220.0	17.14	36.33
240.0	16.40	36.23
260.0	15.84	36.12
280.0	15.19	36.00
300.0	14.43	35.88
340.0	13.11	35.64
380.0	12.23	35.50
420.0	11.79	35.44
460.0	11.13	35.34
500.0	10.33	35.22
540.0	9.84	35.15
580.0	8.74	35.01
620.0	7.98	34.91
660.0	7.33	34.88
700.0	6.91	34.86
740.0	6.49	34.85
780.0	6.11	34.85
820.0	5.84	34.86
860.0	5.55	34.88
900.0	5.32	34.88
940.0	5.11	34.90
980.0	4.97	34.90
1020.0	4.87	34.92

DEPTH	TEMPERATURE	SALINITY
0.0	28.02	35.95
20.0	27.99	35.98
40.0	27.70	36.07
60.0	26.68	36.14
80.0	25.74	36.39
100.0	23.84	36.69
120.0	22.09	36.76
140.0	20.11	36.65
160.0	18.76	36.47
180.0	17.80	36.44
200.0	17.30	36.35
220.0	16.68	36.26
240.0	16.08	36.15
260.0	15.51	36.05
280.0	14.78	35.94
300.0	14.38	35.86
340.0	13.28	35.69
380.0	12.38	35.54
420.0	11.53	35.40
460.0	10.48	35.23
500.0	9.96	35.17
540.0	9.34	35.07
580.0	8.24	34.94
620.0	7.62	34.90
660.0	7.12	34.87
700.0	6.91	34.87
740.0	6.44	34.84
780.0	5.91	34.85
820.0	5.69	34.88
860.0	5.41	34.88
900.0	5.20	34.90
940.0	5.03	34.91
980.0	4.91	34.92

NANSEN STATION NUMBER 54 JULY 31, 1971 1230Z LATITUDE 20 27 LONGITUDE 86 37 DEPTH TO BOTTOM 1143 M			CTD STATION NUMBER 55 JULY 31, 1971 1400Z LATITUDE 20 27 LONGITUDE 86 37 DEPTH TO BOTTOM 1116 M BUCKET TEMPERATURE 29.0 BUCKET SALINITY 36.02			CTD STATION NUMBER 55 A AUGUST 31, 1971 2118Z LATITUDE 20 47 LONGITUDE 86 22 DEPTH TO BOTTOM 1120 M BUCKET TEMPERATURE 28.1 BUCKET SALINITY 35.87		
DEPTH	TEMPERATURE	SALINITY	DEPTH	TEMPERATURE	SALINITY	DEPTH	TEMPERATURE	SALINITY
0.0	28.00	36.022	0.0	28.06	35.92	0.0	28.17	35.88
9.0	28.02	36.002	20.0	27.99	35.97	20.0	28.06	36.00
29.0	27.70	36.042	40.0	27.50	36.03	42.0	27.78	36.10
48.0	27.06	36.148	60.0	26.30	36.17	60.0	26.54	36.15
73.0	25.77	36.438	80.0	25.32	36.46	80.0	25.36	36.44
142.0	19.50	36.649	100.0	23.33	36.73	100.0	23.72	36.69
233.0	16.51	36.236	120.0	21.62	36.75	120.0	22.04	36.69
532.0	9.38	35.106	140.0	19.66	36.65	140.0	20.43	36.62
696.0	6.61		160.0	18.59	36.50	160.0	18.39	36.47
887.0	5.24		180.0	17.65	36.37	180.0	17.54	36.38
			200.0	17.21	36.33	200.0	17.08	36.30
			220.0	16.52	36.22			
			240.0	15.91	36.12			
			260.0	15.41	36.02			
			280.0	14.68	35.90			
			300.0	14.19	35.81			
			340.0	13.46	35.70			
			380.0	12.73	35.58			
			420.0	11.82	35.44			
			460.0	10.47	35.21			
			500.0	9.58	35.11			
			540.0	9.16	35.06			
			580.0	8.41	34.95			
			620.0	7.66	34.90			
			660.0	7.02	34.86			
			700.0	6.62	34.84			
			740.0	6.17	34.85			
			780.0	5.72	34.86			
			820.0	5.50	34.88			
			860.0	5.36	34.88			
			890.0	5.14	34.91			
NANSEN STATION NUMBER 56 AUGUST 1, 1971 0142Z LATITUDE 21 1 LONGITUDE 86 17 DEPTH TO BOTTOM 1302 M			NANSEN STATION NUMBER 57 AUGUST 1, 1971 0418Z LATITUDE 21 7 LONGITUDE 86 13 DEPTH TO BOTTOM 1258 M			NANSEN STATION NUMBER 58 AUGUST 1, 1971 0818Z LATITUDE 21 17 LONGITUDE 86 10 DEPTH TO BOTTOM 1373 M		
DEPTH	TEMPERATURE	SALINITY	DEPTH	TEMPERATURE	SALINITY	DEPTH	TEMPERATURE	SALINITY
0.0	28.00		0.0	28.00	35.969	0.0	28.00	35.990
10.0	28.07	35.914	10.0	28.17	35.939	9.0	28.02	35.952
29.0	27.97	36.066	30.0	27.82	36.099	27.0	27.99	36.020
49.0	27.45	36.127	50.0	27.41	36.148	45.0	27.66	36.116
73.0	26.09	36.299	74.0	26.04	36.350	68.0	26.29	36.141
146.0	20.20	36.693	142.0	20.37	36.750	132.0	21.03	36.765
241.0	17.20	36.340	228.0	17.05	36.327	214.0	17.46	36.884
377.0	13.34	35.678	356.0	13.80	35.786	328.0	14.69	35.920
549.0	8.46	34.990	535.0	9.17	35.110	490.0	10.15	35.199
			726.0	6.79				
			824.0	5.42				
NANSEN STATION NUMBER 59 AUGUST 17, 1971 0118Z LATITUDE 18 12 LONGITUDE 86 26 DEPTH TO BOTTOM 4142 M			NANSEN STATION NUMBER 60 AUGUST 17, 1971 0506Z LATITUDE 18 14 LONGITUDE 86 27 DEPTH TO BOTTOM 2265 M			NANSEN STATION NUMBER 61 AUGUST 17, 1971 0906Z LATITUDE 18 12 LONGITUDE 86 29 DEPTH TO BOTTOM 4142 M		
DEPTH	TEMPERATURE	SALINITY	DEPTH	TEMPERATURE	SALINITY	DEPTH	TEMPERATURE	SALINITY
0.0	24.00		0.0	24.90		0.0	24.70	36.144
10.0	24.75	36.102	10.0	24.84	36.117	9.0	24.70	36.123
10.0	27.62	35.998	10.0	27.93	36.026	29.0	27.92	36.025
40.0	27.33	36.009	40.0	27.55	35.992	19.0	27.34	36.015
50.0	27.12	36.055	50.0	27.27	36.029	49.0	27.18	36.038
75.0	26.88	36.072	75.0	27.02	36.068	74.0	27.03	36.074
149.0	22.89	36.742	149.0	23.14	36.731	148.0	23.48	36.745
198.0	19.54	36.497	198.0	20.04	36.602	197.0	19.66	36.563
248.0	16.65	36.190	246.0	16.99	36.255	244.0	17.06	36.256
398.0	11.28	35.312	395.0	11.26	35.318	389.0	11.41	35.348
549.0	7.91	34.882	595.0	7.87	34.870	584.0	8.03	34.890
799.0	5.80	34.834	794.0	5.79	34.840	783.0	5.86	34.831
988.0	4.69	34.908	994.0	4.70	34.911	982.0	4.73	34.896
NANSEN STATION NUMBER 62 AUGUST 17, 1971 1224Z LATITUDE 18 16 LONGITUDE 86 32 DEPTH TO BOTTOM 4151 M			NANSEN STATION NUMBER 63 AUGUST 17, 1971 1706Z LATITUDE 18 18 LONGITUDE 86 35 DEPTH TO BOTTOM 4161 M			NANSEN STATION NUMBER 64 AUGUST 18, 1971 0118Z LATITUDE 18 19 LONGITUDE 86 41 DEPTH TO BOTTOM 4179 M		
DEPTH	TEMPERATURE	SALINITY	DEPTH	TEMPERATURE	SALINITY	DEPTH	TEMPERATURE	SALINITY
0.0	24.60	36.130	0.0	24.10	36.155	0.0	24.90	36.157
9.0	24.22	36.047	10.0	24.59	36.129	10.0	24.99	36.158
29.0	24.04	36.078	20.0	24.45	36.104	30.0	24.56	36.111
39.0	27.50	36.062	40.0	27.55	36.026	40.0	24.11	36.085
49.0	27.21	36.066	60.0	27.14	36.076	50.0	27.10	36.023
74.0	26.49	36.037	85.0	26.16	36.101	75.0	26.43	36.063
147.0	23.09	36.777	155.0	22.66	36.762	148.0	22.78	36.760
196.0	19.54	36.564	203.0	19.24	36.543	196.0	14.94	36.508
246.0	16.54	36.188	253.0	16.80	36.248	246.0	15.97	36.103
393.0	11.14	35.318	401.0	10.95	35.291	395.0	10.95	35.297
583.0	8.04	34.919	600.0	7.82	34.896	592.0	7.65	34.883
783.0	5.76	34.853	800.0	5.78	34.857	791.0	5.77	34.861
983.0	4.76	34.920	1000.0	4.70	34.926	990.0	4.77	34.933

NANSEN STATION NUMBER 65
AUGUST 18, 1971 0500Z
LATITUDE 18 21
LONGITUDE 86 41
DEPTH TO BOTTOM 4190 M

NANSEN STATION NUMBER 66
AUGUST 18, 1971 0906Z
LATITUDE 18 22
LONGITUDE 86 43
DEPTH TO BOTTOM 4157 M

NANSEN STATION NUMBER 67
AUGUST 18, 1971 1312Z
LATITUDE 18 25
LONGITUDE 86 44
DEPTH TO BOTTOM 4217 M

DEPTH	TEMPERATURE	SALINITY
0.0	28.90	36.140
10.0	28.82	36.156
30.0	28.11	36.077
40.0	27.71	36.040
50.0	27.29	36.064
75.0	26.70	
147.0	21.28	36.622
192.0	19.26	36.568
242.0	18.50	36.126
349.0	11.29	35.249
549.0	7.68	34.908
749.0	5.79	34.819
949.0	4.70	34.950

DEPTH	TEMPERATURE	SALINITY
0.0	28.70	36.137
10.0	28.73	36.135
30.0	28.05	36.082
40.0	27.65	36.047
50.0	27.24	36.050
75.0	26.49	36.065
149.0	22.51	36.773
198.0	18.82	36.532
247.0	16.03	36.131
396.0	10.81	35.286
592.0	7.61	34.883
790.0	5.74	34.882
990.0	4.77	34.943

DEPTH	TEMPERATURE	SALINITY
0.0	28.50	36.135
10.0	28.58	36.130
30.0	27.88	36.062
40.0	27.39	36.047
50.0	27.18	36.089
75.0	26.57	36.193
150.0	22.81	36.753
199.0	19.01	36.555
249.0	16.28	36.178
398.0	10.97	35.302
593.0	7.61	
792.0	5.78	34.877
991.0	4.78	34.930

NANSEN STATION NUMBER 68
AUGUST 19, 1971 1700Z
LATITUDE 18 27
LONGITUDE 86 49
DEPTH TO BOTTOM 4226 M

NANSEN STATION NUMBER 69
AUGUST 19, 1971 2106Z
LATITUDE 18 27
LONGITUDE 86 50
DEPTH TO BOTTOM 4225 M

NANSEN STATION NUMBER 70
AUGUST 19, 1971 0118Z
LATITUDE 18 29
LONGITUDE 86 53
DEPTH TO BOTTOM 4199 M

DEPTH	TEMPERATURE	SALINITY
0.0	28.80	36.157
10.0	28.72	36.119
25.0	28.35	36.083
40.0	27.89	36.040
75.0	26.92	36.109
99.0	25.93	36.162
149.0	21.25	36.710
194.0	19.00	36.443
247.0	16.62	36.204
345.0	10.40	35.244
540.0	7.84	34.898
744.0	5.84	34.856
945.0	4.82	34.923

DEPTH	TEMPERATURE	SALINITY
0.0	28.00	36.141
10.0	28.97	36.149
24.0	28.50	36.105
39.0	27.88	36.056
73.0	26.80	36.087
96.0	26.23	36.264
148.0	23.40	36.708
192.0	20.28	36.685
240.0	16.44	36.256
379.0	11.05	35.306
571.0	8.04	34.918
770.0	5.98	34.840
969.0	4.85	34.895

DEPTH	TEMPERATURE	SALINITY
0.0	28.90	36.090
10.0	28.62	36.151
25.0	28.12	36.076
40.0	27.72	36.030
75.0	26.38	36.097
99.0	25.59	36.216
148.0	22.57	36.766
196.0	19.53	36.593
247.0	16.30	36.161
393.0	10.80	35.268
586.0	7.77	34.899
784.0	5.85	34.860
982.0	4.81	34.925

MANSEN STATION NUMBER 71
AUGUST 19, 1971 0506Z
LATITUDE 18 29
LONGITUDE 86 53
DEPTH TO BOTTOM 2754 M

MANSEN STATION NUMBER 72
AUGUST 19, 1971 0918Z
LATITUDE 18 31
LONGITUDE 86 57
DEPTH TO BOTTOM 759 M

MANSEN STATION NUMBER 73
AUGUST 19, 1971 1315Z
LATITUDE 18 33
LONGITUDE 86 54
DEPTH TO BOTTOM 324 M

DEPTH	TEMPERATURE	SALINITY
0.0	28.80	36.138
10.0	28.46	36.145
25.0	28.08	36.093
40.0	27.79	36.083
75.0	26.59	36.085
100.0	25.87	36.205
148.0	22.90	36.742
196.0	19.61	36.613
244.0	16.37	36.171
391.0	10.86	35.264
590.0	7.74	34.908
790.0	5.69	34.870
990.0	4.74	34.933

DEPTH	TEMPERATURE	SALINITY
0.0	28.50	35.919
10.0	28.40	35.931
25.0	28.23	36.098
39.0	27.98	36.089
48.0	27.58	36.050
72.0	26.76	36.218
287.0	14.52	35.861
481.0	9.98	35.025
676.0	6.63	34.845

DEPTH	TEMPERATURE	SALINITY
0.0	28.50	35.971
10.0	28.38	35.952
25.0	28.12	36.090
50.0	27.30	36.030
75.0	26.45	36.083
100.0	25.79	36.237
150.0	22.52	36.774
175.0	20.85	36.734
200.0	19.17	36.581
250.0	16.03	36.123
300.0	13.75	35.728

MANSEN STATION NUMBER 74
AUGUST 19, 1971 1712Z
LATITUDE 18 34
LONGITUDE 87 3
DEPTH TO BOTTOM 585 M

CTD STATION NUMBER 75
AUGUST 19, 1971 2124Z
LATITUDE 18 36
LONGITUDE 87 04
DEPTH TO BOTTOM 28.7
BUCKET TEMPERATURE 35.98
BUCKET SALINITY 35.98

CTD STATION NUMBER 76
AUGUST 20, 1971 0124Z
LATITUDE 18 35
LONGITUDE 87 4
DEPTH TO BOTTOM 28.0
BUCKET TEMPERATURE 35.97
BUCKET SALINITY 35.97

DEPTH	TEMPERATURE	SALINITY
0.0	28.30	35.955
10.0	28.45	35.917
25.0	28.45	35.945
35.0	28.00	36.069
60.0	27.30	36.030
109.0	25.72	36.376
159.0	22.18	36.769
207.0	18.91	36.536
254.0	15.99	36.106
302.0	13.82	35.742
451.0	9.36	35.062

DEPTH	TEMPERATURE	SALINITY
0.0	28.76	
20.0	28.42	
40.0	28.00	
60.0	27.05	
80.0	26.47	
100.0	25.80	
120.0	24.94	
140.0	23.36	
160.0	21.63	
180.0	20.46	
200.0	19.90	
220.0	18.16	
240.0	16.78	
260.0	15.75	
280.0	14.53	
300.0	13.97	
340.0	11.56	
380.0	10.82	
420.0	10.10	
460.0	9.37	
500.0	8.71	
540.0	8.30	
580.0	7.58	
620.0	7.12	
660.0	6.71	
700.0	6.32	
740.0	5.96	
780.0	5.69	
820.0	5.45	
860.0	5.20	
900.0	5.00	
940.0	4.83	
980.0	4.72	
990.0	4.70	

DEPTH	TEMPERATURE	SALINITY
0.0	28.55	35.84
20.0	28.35	36.02
40.0	27.93	36.04
60.0	26.96	36.05
80.0	26.39	36.25
100.0	25.74	36.40
120.0	24.62	36.59
140.0	23.26	36.73
160.0	21.69	36.74
180.0	20.34	36.66
200.0	19.10	36.54
220.0	17.97	36.42
240.0	16.64	36.19
260.0	15.49	36.01
280.0	14.79	35.89
300.0	13.81	35.72
340.0	11.65	35.40
380.0	11.11	35.32
420.0	10.21	35.17
460.0	9.58	35.10
500.0	8.83	35.01
540.0	8.52	34.97
580.0	7.87	34.91
620.0	7.19	34.86
660.0	6.84	34.85
700.0	6.41	34.83
740.0	6.16	34.84
780.0	5.79	34.86
820.0	5.44	34.88
860.0	5.32	34.84
900.0	5.08	34.90
940.0	4.98	34.92
980.0	4.84	34.92
1000.0	4.75	34.92

NANSEN STATION NUMBER 65
AUGUST 18, 1971 0500Z
LATITUDE 18 21
LONGITUDE 86 41
DEPTH TO BOTTOM 4190 M

NANSEN STATION NUMBER 66
AUGUST 18, 1971 0906Z
LATITUDE 18 22
LONGITUDE 86 43
DEPTH TO BOTTOM 4157 M

NANSEN STATION NUMBER 67
AUGUST 18, 1971 1312Z
LATITUDE 18 25
LONGITUDE 86 44
DEPTH TO BOTTOM 4217 M

DEPTH	TEMPERATURE	SALINITY
0.0	28.90	36.140
10.0	28.82	36.156
30.0	28.11	36.077
40.0	27.71	36.040
50.0	27.29	36.064
75.0	26.70	
147.0	23.28	36.622
192.0	19.26	36.568
242.0	16.50	36.126
389.0	11.29	35.249
589.0	7.68	34.908
789.0	5.79	34.819
989.0	4.70	34.950

DEPTH	TEMPERATURE	SALINITY
0.0	28.70	36.137
10.0	28.73	36.135
30.0	28.05	36.082
40.0	27.65	36.047
50.0	27.24	36.050
75.0	26.49	36.065
149.0	22.51	36.773
198.0	18.82	36.532
247.0	16.03	36.131
396.0	10.81	35.286
592.0	7.61	34.883
790.0	5.74	34.882
990.0	4.77	34.943

DEPTH	TEMPERATURE	SALINITY
0.0	28.50	36.135
10.0	28.58	36.130
30.0	27.88	36.062
40.0	27.39	36.047
50.0	27.18	36.089
75.0	26.57	36.193
150.0	22.81	36.753
199.0	19.01	36.555
249.0	16.28	36.178
398.0	10.97	35.302
593.0	7.61	
792.0	5.78	34.877
991.0	4.78	34.939

NANSEN STATION NUMBER 68
AUGUST 18, 1971 1700Z
LATITUDE 18 27
LONGITUDE 86 49
DEPTH TO BOTTOM 4226 M

NANSEN STATION NUMBER 69
AUGUST 18, 1971 2106Z
LATITUDE 18 27
LONGITUDE 86 50
DEPTH TO BOTTOM 4225 M

NANSEN STATION NUMBER 70
AUGUST 19, 1971 0118Z
LATITUDE 18 29
LONGITUDE 86 53
DEPTH TO BOTTOM 4199 M

DEPTH	TEMPERATURE	SALINITY
0.0	28.80	36.157
10.0	28.72	36.119
25.0	28.35	36.083
40.0	27.89	36.040
75.0	26.92	36.109
99.0	25.93	36.162
149.0	23.25	36.710
194.0	19.80	36.643
247.0	16.62	36.204
335.0	10.90	35.284
590.0	7.88	34.898
786.0	5.84	34.856
985.0	4.82	34.923

DEPTH	TEMPERATURE	SALINITY
0.0	28.00	36.141
10.0	28.97	36.149
24.0	28.50	36.105
39.0	27.88	36.056
73.0	26.80	36.087
96.0	26.23	36.264
146.0	23.40	36.708
192.0	20.28	36.685
240.0	16.94	36.256
379.0	11.05	35.306
571.0	8.09	34.918
770.0	5.98	34.840
969.0	4.85	34.895

DEPTH	TEMPERATURE	SALINITY
0.0	28.90	36.090
10.0	28.62	36.151
25.0	28.12	36.076
40.0	27.72	36.030
75.0	26.38	36.097
99.0	25.59	36.216
148.0	22.57	36.766
196.0	19.53	36.593
247.0	16.30	36.161
393.0	10.80	35.268
586.0	7.77	34.899
784.0	5.85	34.860
982.0	4.81	34.925

NANSSEN STATION NUMBER 71
 AUGUST 19, 1971 0506Z
 LATITUDE 18 29
 LONGITUDE 86 53
 DEPTH TO BOTTOM 2754 M

NANSSEN STATION NUMBER 72
 AUGUST 19, 1971 0918Z
 LATITUDE 18 31
 LONGITUDE 86 57
 DEPTH TO BOTTOM 759 M

NANSSEN STATION NUMBER 73
 AUGUST 19, 1971 1315Z
 LATITUDE 18 33
 LONGITUDE 86 54
 DEPTH TO BOTTOM 324 M

DEPTH	TEMPERATURE	SALINITY
0.0	28.80	36.138
10.0	28.46	36.145
25.0	28.08	36.093
40.0	27.79	36.083
75.0	26.59	36.085
100.0	25.87	36.205
148.0	22.90	36.742
196.0	19.61	36.613
244.0	16.37	36.171
391.0	10.86	35.264
590.0	7.74	34.908
790.0	5.69	34.870
990.0	4.74	34.933

DEPTH	TEMPERATURE	SALINITY
0.0	28.50	35.919
10.0	28.40	35.931
25.0	28.23	36.098
39.0	27.98	36.089
48.0	27.58	36.050
72.0	26.76	36.218
287.0	14.52	35.861
481.0	4.98	35.025
676.0	6.63	34.845

DEPTH	TEMPERATURE	SALINITY
0.0	28.50	35.971
10.0	28.38	35.952
25.0	28.12	36.090
50.0	27.30	36.030
75.0	26.45	36.083
100.0	25.79	36.237
150.0	22.52	36.774
175.0	20.85	36.734
200.0	19.17	36.581
250.0	16.03	36.123
300.0	13.75	35.728

NANSSEN STATION NUMBER 74
 AUGUST 19, 1971 1712Z
 LATITUDE 18 34
 LONGITUDE 87 3
 DEPTH TO BOTTOM 585 M

CTD STATION NUMBER 75
 AUGUST 19, 1971 2124Z
 LATITUDE 18 36
 LONGITUDE 87 04
 DEPTH TO BOTTOM 28.7
 BUCKET TEMPERATURE 35.98
 BUCKET SALINITY 35.98

CTD STATION NUMBER 76
 AUGUST 20, 1971 0124Z
 LATITUDE 18 35
 LONGITUDE 87 4
 DEPTH TO BOTTOM 28.0
 BUCKET TEMPERATURE 35.97
 BUCKET SALINITY 35.97

DEPTH	TEMPERATURE	SALINITY
0.0	28.30	35.955
10.0	28.45	35.917
25.0	28.45	35.945
35.0	28.00	36.069
60.0	27.30	36.030
109.0	25.72	36.376
159.0	22.18	36.769
207.0	18.91	36.536
254.0	15.99	36.106
302.0	13.82	35.742
451.0	9.36	35.062

DEPTH	TEMPERATURE	SALINITY
0.0	28.76	
20.0	28.42	
40.0	28.00	
60.0	27.05	
80.0	26.47	
100.0	25.80	
120.0	24.94	
140.0	23.36	
160.0	21.63	
180.0	20.46	
200.0	19.90	
220.0	18.16	
240.0	16.78	
260.0	15.75	
280.0	14.53	
300.0	13.97	
340.0	11.56	
380.0	10.82	
420.0	10.10	
460.0	9.37	
500.0	8.71	
540.0	8.30	
580.0	7.58	
620.0	7.12	
660.0	6.71	
700.0	6.32	
740.0	5.96	
780.0	5.69	
820.0	5.45	
860.0	5.20	
900.0	5.00	
940.0	4.83	
980.0	4.72	
990.0	4.70	

DEPTH	TEMPERATURE	SALINITY
0.0	28.55	35.844
20.0	28.35	36.02
40.0	27.93	36.04
60.0	26.96	36.05
80.0	26.39	36.25
100.0	25.74	36.40
120.0	24.62	36.59
140.0	23.26	36.73
160.0	21.69	36.74
180.0	20.34	36.66
200.0	19.10	36.54
220.0	17.97	36.42
240.0	16.64	36.19
260.0	15.49	36.01
280.0	14.79	35.89
300.0	13.81	35.72
340.0	11.65	35.40
380.0	11.11	35.32
420.0	10.21	35.17
460.0	9.58	35.10
500.0	8.83	35.01
540.0	8.52	34.97
580.0	7.87	34.91
620.0	7.19	34.86
660.0	6.84	34.85
700.0	6.41	34.83
740.0	6.16	34.84
780.0	5.79	34.86
820.0	5.44	34.88
860.0	5.32	34.89
900.0	5.08	34.90
940.0	4.98	34.92
980.0	4.84	34.92
1000.0	4.75	34.92

NANSSEN STATION NUMBER 77
 AUGUST 20, 1971 0500Z
 LATITUDE 18 37
 LONGITUDE 87 4
 DEPTH TO BOTTOM 1085 M

CTD STATION NUMBER 78
 AUGUST 20, 1971 0906Z
 LATITUDE 18 37
 LONGITUDE 87 0
 DEPTH TO BOTTOM 1346 M
 BUCKET TEMPERATURE 28.2
 BUCKET SALINITY 35.88

CTD STATION NUMBER 79
 AUGUST 21, 1971 0124Z
 LATITUDE 19 53
 LONGITUDE 86 47
 DEPTH TO BOTTOM 1311 M
 BUCKET TEMPERATURE 28.9
 BUCKET SALINITY 35.92

DEPTH	TEMPERATURE	SALINITY
0.0	28.60	35.956
10.0	28.45	35.942
25.0	28.31	36.059
39.0	28.11	36.042
73.0	26.82	36.189
97.0	25.73	36.327
146.0	22.36	36.760
194.0	18.96	36.528
243.0	16.10	36.118
390.0	10.55	35.223
586.0	7.64	34.885
781.0	5.73	34.856
980.0	4.84	34.909

DEPTH	TEMPERATURE	SALINITY
0.0	28.37	
20.0	28.30	
40.0	28.29	
60.0	28.10	
80.0	27.54	
100.0	26.89	
120.0	26.15	
140.0	25.19	
160.0	23.97	
180.0	22.74	
200.0	19.96	
220.0	18.57	
240.0	18.04	
260.0	17.24	
280.0	16.44	
300.0	15.62	
340.0	13.57	
380.0	12.05	
420.0	10.54	
460.0	9.86	
500.0	9.23	
540.0	8.64	
580.0	8.12	
620.0	7.68	
660.0	7.27	
700.0	6.84	
740.0	6.47	
780.0	6.14	
820.0	5.81	
860.0	5.55	
900.0	5.32	
940.0	5.09	
980.0	4.83	
1000.0	4.80	

DEPTH	TEMPERATURE	SALINITY
0.0	28.63	35.71
20.0	28.64	35.90
40.0	28.20	36.08
60.0	27.47	36.05
80.0	26.06	36.11
100.0	25.40	36.35
120.0	24.31	36.67
140.0	22.55	36.82
160.0	20.99	36.79
180.0	19.80	36.71
200.0	18.61	36.58
220.0	17.86	36.47
240.0	17.45	36.40
260.0	17.08	36.33
280.0	16.75	36.28
300.0	16.56	36.29
340.0	15.22	36.04
380.0	14.23	35.87
420.0	11.82	35.47
460.0	10.39	35.25
500.0	9.65	35.15
540.0	9.13	35.10
580.0	8.51	35.02
620.0	8.05	34.97

CTD STATION NUMBER 80
 AUGUST 21, 1971 0512Z
 LATITUDE 19 55
 LONGITUDE 86 46
 DEPTH TO BOTTOM 1085 M
 BUCKET TEMPERATURE 28.5
 BUCKET SALINITY 35.68

CTD STATION NUMBER 81
 AUGUST 21, 1971 0912Z
 LATITUDE 19 58
 LONGITUDE 86 44
 DEPTH TO BOTTOM 1198 M
 BUCKET TEMPERATURE 28.6
 BUCKET SALINITY 35.79

CTD STATION NUMBER 82
 AUGUST 27, 1971 0106Z
 LATITUDE 23 45
 LONGITUDE 86 3
 DEPTH TO BOTTOM 3392 M
 BUCKET TEMPERATURE 29.9
 BUCKET SALINITY 36.16

DEPTH	TEMPERATURE	SALINITY
0.0	28.74	
20.0	28.88	
40.0	28.15	
60.0	27.53	
80.0	26.13	
100.0	25.41	
120.0	24.48	
140.0	22.63	
160.0	21.07	
180.0	19.78	
200.0	18.69	
220.0	17.93	
240.0	17.50	
260.0	17.14	
280.0	16.93	
300.0	16.50	
340.0	15.17	
380.0	14.47	
420.0	12.36	
460.0	10.89	
500.0	9.96	
540.0	9.48	
580.0	8.81	
620.0	8.05	
660.0	7.46	
700.0	6.92	
740.0	6.57	
780.0	6.36	
820.0	5.84	
860.0	5.58	
900.0	5.49	
940.0	5.16	
980.0	4.96	
1000.0	4.89	

DEPTH	TEMPERATURE	SALINITY
0.0	28.66	35.71
20.0	28.63	35.98
40.0	28.09	36.05
60.0	26.97	36.00
80.0	25.97	36.10
100.0	25.32	36.36
120.0	24.48	36.59
140.0	22.72	36.71
160.0	21.03	36.70
180.0	19.59	36.61
200.0	18.56	36.54
220.0	17.83	36.43
240.0	17.37	36.35
260.0	17.02	36.30
280.0	16.80	36.29
300.0	15.90	36.12
340.0	14.99	35.98
380.0	13.62	35.74
420.0	11.94	35.47
460.0	10.54	35.25
500.0	9.86	35.15
540.0	9.26	35.08
580.0	8.58	34.97
620.0	8.16	34.93
660.0	7.61	34.89
700.0	7.00	34.86
740.0	6.67	34.84
780.0	6.23	34.83
820.0	5.97	34.85
860.0	5.74	34.87
900.0	5.41	34.88
940.0	5.22	34.90
980.0	4.98	34.92
1000.0	4.92	34.88

DEPTH	TEMPERATURE	SALINITY
0.0	29.59	
20.0	29.29	
40.0	28.34	
60.0	27.69	
80.0	26.88	
100.0	26.35	
120.0	25.35	
140.0	24.00	
160.0	22.73	
180.0	21.38	
200.0	19.10	
220.0	18.34	
240.0	17.85	
260.0	17.19	
280.0	16.76	
300.0	16.35	
340.0	14.49	
380.0	13.30	
420.0	11.85	
460.0	11.11	
500.0	9.78	
540.0	8.95	
580.0	8.27	
620.0	7.71	
660.0	7.24	
700.0	6.73	
740.0	6.31	
780.0	5.99	
820.0	5.68	
860.0	5.48	
900.0	5.18	
940.0	4.97	
980.0	4.88	

CTD STATION NUMBER 83
AUGUST 27, 1971
LATITUDE 23 41
LONGITUDE 85 59
DEPTH TO BOTTOM 3381 M
BUCKET TEMPERATURE 29.6
BUCKET SALINITY 36.06

CTD STATION NUMBER 84
AUGUST 27, 1971
LATITUDE 23 39
LONGITUDE 85 52
DEPTH TO BOTTOM 3374 M
BUCKET TEMPERATURE 29.4
BUCKET SALINITY 36.07

WANSSEN STATION NUMBER 85
AUGUST 27, 1971
LATITUDE 23 38
LONGITUDE 85 48
DEPTH TO BOTTOM 2036 M

DEPTH	TEMPERATURE	SALINITY
0.0	29.50	
20.0	29.46	
40.0	29.32	
60.0	28.95	
80.0	28.26	
100.0	27.39	
120.0	26.30	
140.0	25.12	
160.0	23.96	
180.0	22.47	
200.0	20.26	
220.0	19.37	
240.0	18.87	
260.0	18.36	
280.0	17.94	
300.0	17.42	
340.0	15.52	
380.0	13.92	
420.0	12.47	
460.0	11.75	
500.0	10.74	
540.0	9.89	
580.0	9.02	
620.0	8.23	
660.0	7.58	
700.0	7.14	
740.0	6.69	
780.0	6.24	
820.0	5.87	
860.0	5.63	
900.0	5.42	
940.0	5.16	
980.0	4.94	
1000.0	4.85	

DEPTH	TEMPERATURE	SALINITY
0.0	29.41	36.05
20.0	29.05	36.03
40.0	28.25	36.04
60.0	27.38	36.07
80.0	26.94	36.24
100.0	26.03	36.35
120.0	24.46	36.61
140.0	22.74	36.72
160.0	21.64	36.71
180.0	20.40	36.64
200.0	19.24	36.57
220.0	18.31	36.48
240.0	17.61	36.35
260.0	16.98	36.28
280.0	16.30	36.16
300.0	15.42	36.01
340.0	13.92	35.76
380.0	12.60	35.56
420.0	11.73	35.40
460.0	10.61	35.26
500.0	9.81	35.14
540.0	9.01	35.05
580.0	8.21	34.95
620.0	7.56	34.90
660.0	7.01	34.89
700.0	6.66	34.88
740.0	6.30	34.89
780.0	5.93	34.89
820.0	5.68	34.90
860.0	5.43	34.90
900.0	5.21	34.92
940.0	5.08	34.92
980.0	4.79	34.93
990.0	4.73	34.93

DEPTH	TEMPERATURE	SALINITY
0.0	29.30	36.153
10.0	29.30	36.089
25.0	28.71	36.062
40.0	28.01	36.101
75.0	26.60	36.238
99.0	25.83	36.362
149.0	22.58	36.734
198.0	19.36	36.591
246.0	17.47	36.356
330.0	11.44	35.464
577.0	7.47	34.973
767.0	6.01	
963.0	4.77	34.922

CTD STATION NUMBER 86
AUGUST 27, 1971
LATITUDE 23 37
LONGITUDE 85 44
DEPTH TO BOTTOM 3343 M
BUCKET TEMPERATURE
BUCKET SALINITY

CTD STATION NUMBER 87
AUGUST 27, 1971
LATITUDE 23 36
LONGITUDE 85 39
DEPTH TO BOTTOM 2995 M
BUCKET TEMPERATURE
BUCKET SALINITY 36.11

CTD STATION NUMBER 88
AUGUST 27, 1971
LATITUDE 23 41
LONGITUDE 85 21
DEPTH TO BOTTOM 3396 M
BUCKET TEMPERATURE
BUCKET SALINITY 36.14

DEPTH	TEMPERATURE	SALINITY
0.0	29.45	36.03
20.0	29.78	36.14
40.0	27.44	36.06
60.0	27.11	36.01
80.0	26.41	36.24
100.0	25.74	36.37
120.0	24.24	36.64
140.0	22.67	36.74
160.0	21.20	36.70
180.0	19.42	36.63
200.0	19.00	36.59
220.0	18.18	36.51
240.0	17.47	36.39
260.0	16.62	36.24
280.0	15.87	36.10
300.0	14.76	35.90
340.0	13.11	35.63
380.0	12.17	35.49
420.0	11.06	35.33
460.0	10.14	35.19
500.0	9.31	35.06
540.0	8.61	34.99
580.0	7.93	34.93
620.0	7.31	34.88
660.0	6.98	34.87
700.0	6.48	34.86
740.0	6.15	34.86
780.0	5.90	34.87
820.0	5.70	34.88
860.0	5.23	34.89
900.0	5.01	34.92
940.0	4.77	34.93
980.0	4.59	34.96

DEPTH	TEMPERATURE	SALINITY
0.0	29.87	
20.0	29.82	
40.0	29.59	
60.0	29.20	
80.0	28.58	
100.0	27.24	
120.0	25.50	
140.0	24.20	
160.0	22.97	
180.0	21.51	
200.0	19.81	
220.0	18.64	
240.0	18.24	
260.0	17.71	
280.0	17.05	
300.0	16.20	
340.0	14.79	
380.0	13.38	
420.0	11.22	
460.0	10.62	
500.0	9.95	
540.0	9.30	
580.0	8.59	
620.0	7.86	
660.0	7.32	
700.0	6.83	
740.0	6.45	
780.0	6.12	
820.0	5.76	
860.0	5.47	
900.0	5.20	
940.0	4.94	
980.0	4.60	
990.0	4.53	

DEPTH	TEMPERATURE	SALINITY
0.0	29.87	36.11
20.0	29.02	36.04
40.0	28.13	36.05
60.0	27.05	36.18
80.0	25.95	36.39
100.0	24.82	36.61
120.0	23.30	36.70
140.0	22.31	36.74
160.0	20.11	36.45
180.0	18.15	36.37
200.0	17.32	36.31
220.0	16.91	36.29
240.0	16.56	36.22
260.0	15.30	35.97
280.0	14.32	35.83
300.0	13.71	35.72
340.0	12.29	35.53
380.0	11.32	35.36
420.0	10.20	35.19
460.0	9.21	35.06
500.0	8.38	34.97
540.0	7.82	34.93
580.0	7.28	34.89
620.0	6.74	34.88
660.0	6.33	34.87
700.0	6.06	34.87
740.0	5.76	34.89
780.0	5.48	
820.0	5.23	
860.0	5.09	
900.0	4.78	
940.0	4.61	
980.0	4.48	
1000.0	4.41	

CTD STATION NUMBER 89
AUGUST 28, 1971 01122
LATITUDE 23 47
LONGITUDE 85 17
DEPTH TO BOTTOM 3387 M
BUCKET TEMPERATURE 29.6
BUCKET SALINITY 36.15

CTD STATION NUMBER 90
AUGUST 28, 1971 05062
LATITUDE 23 52
LONGITUDE 85 7
DEPTH TO BOTTOM 3060 M
BUCKET TEMPERATURE 29.5
BUCKET SALINITY 36.06

CTD STATION NUMBER 91
AUGUST 28, 1971 09062
LATITUDE 23 57
LONGITUDE 84 59
DEPTH TO BOTTOM 3374 M
BUCKET TEMPERATURE 29.3
BUCKET SALINITY 36.06

DEPTH	TEMPERATURE	SALINITY
0.0	29.84	35.95
20.0	28.89	35.94
40.0	28.01	36.02
60.0	26.72	36.18
80.0	25.69	36.36
100.0	24.15	36.55
120.0	22.52	36.61
140.0	20.02	36.32
160.0	18.84	36.38
180.0	17.58	36.31
200.0	16.26	36.16
220.0	15.32	36.01
240.0	14.61	35.89
260.0	13.90	35.79
280.0	13.21	35.66
300.0	12.38	35.50
340.0	10.89	35.32
380.0	9.81	35.16
420.0	9.16	35.08
460.0	8.72	35.02
500.0	8.33	34.97
540.0	7.58	34.91
580.0	7.19	34.88
620.0	6.68	34.85
660.0	6.27	34.86
700.0	6.05	34.88
740.0	5.71	34.88
780.0	5.41	34.89
820.0	5.21	34.91
860.0	5.07	34.91
900.0	4.91	34.92
940.0	4.74	34.93
970.0	4.64	34.94

DEPTH	TEMPERATURE	SALINITY
0.0	29.62	35.93
20.0	28.89	36.04
40.0	27.84	36.09
60.0	26.39	36.26
80.0	25.49	36.40
100.0	24.17	36.48
120.0	22.04	36.46
140.0	19.55	36.36
160.0	18.53	36.38
180.0	16.72	36.25
200.0	15.81	36.09
220.0	14.98	35.94
240.0	14.34	35.95
260.0	13.55	35.71
280.0	12.93	35.62
300.0	12.44	35.55
340.0	11.18	35.34
380.0	10.18	
420.0	9.62	
460.0	8.57	
500.0	8.11	
540.0	7.42	
580.0	7.01	
620.0	6.58	
660.0	6.20	
700.0	5.84	
740.0	5.60	
780.0	5.39	
820.0	5.20	
860.0	5.10	
900.0	4.97	
940.0	4.88	
980.0	4.81	
990.0	4.78	

DEPTH	TEMPERATURE	SALINITY
0.0	29.43	36.11
20.0	28.74	36.06
40.0	27.62	36.13
60.0	26.21	36.35
80.0	25.03	36.44
100.0	23.18	36.57
120.0	20.17	36.45
140.0	18.54	36.44
160.0	17.30	36.34
180.0	16.49	36.26
200.0	16.16	36.19
220.0	15.33	36.03
240.0	14.52	35.91
260.0	13.83	35.81
280.0	13.24	35.74
300.0	12.84	35.69
340.0	11.64	35.45
380.0	10.53	35.29
420.0	9.66	35.20
460.0	8.90	35.07
500.0	8.32	35.00
540.0	7.78	34.98
580.0	7.23	34.93
620.0	6.82	34.92
660.0	6.23	34.89
700.0	5.96	34.91
740.0	5.66	34.91
780.0	5.44	34.91
820.0	5.32	34.92
860.0	5.18	34.93
900.0	5.04	34.93
940.0	4.95	34.94
980.0	4.84	34.93
1000.0	4.77	34.95

NANSEN STATION NUMBER 92
AUGUST 28, 1971 12122
LATITUDE 24 4
LONGITUDE 84 52
DEPTH TO BOTTOM 3367 M

CTD STATION NUMBER 93
AUGUST 28, 1971 13362
LATITUDE 24 5
LONGITUDE 84 49
DEPTH TO BOTTOM 3363 M
BUCKET TEMPERATURE
BUCKET SALINITY

CTD STATION NUMBER 94
AUGUST 28, 1971 21302
LATITUDE 24 17
LONGITUDE 84 29
DEPTH TO BOTTOM 3359 M
BUCKET TEMPERATURE 29.8
BUCKET SALINITY 36.08

DEPTH	TEMPERATURE	SALINITY
0.0	29.40	36.059
10.0	29.28	36.055
50.0	26.89	36.192
100.0	22.73	36.449
150.0	18.44	36.392
240.0	14.52	35.903
396.0	10.26	35.233
589.0	7.26	34.909
787.0	5.51	34.919
985.0	4.79	34.922

DEPTH	TEMPERATURE	SALINITY
0.0	29.58	35.83
20.0	28.91	36.04
40.0	27.61	36.12
60.0	26.30	36.26
80.0	25.23	36.41
100.0	23.11	36.40
120.0	20.74	36.38
140.0	19.55	36.52
160.0	18.52	36.45
180.0	17.32	36.28
200.0	16.31	36.16
220.0	15.12	35.92
240.0	14.41	35.84
260.0	13.73	35.72
280.0	12.68	35.53
300.0	11.86	35.40
340.0	10.93	35.29
380.0	10.25	35.18
420.0	4.19	35.07
460.0	4.73	35.02
500.0	4.28	34.96
540.0	7.79	34.93
580.0	7.29	34.91
620.0	6.88	
660.0	6.54	
700.0	6.05	
740.0	5.66	
780.0	5.50	
820.0	5.31	
860.0	5.23	
900.0	5.14	
940.0	5.05	
980.0	4.91	

DEPTH	TEMPERATURE	SALINITY
0.0	29.73	35.92
20.0	28.97	35.96
40.0	28.08	36.02
60.0	26.65	36.20
80.0	25.21	36.36
100.0	22.18	36.25
120.0	20.31	36.37
140.0	19.08	36.39
160.0	17.58	36.29
180.0	16.68	36.21
200.0	15.97	36.11
220.0	15.44	36.01
240.0	14.65	35.84
260.0	14.16	35.83
280.0	13.43	35.69
300.0	12.70	35.57
340.0	11.15	35.32
380.0	9.86	35.16
420.0	8.97	35.06
460.0	8.42	34.98
500.0	7.99	34.95
540.0	7.33	34.91
580.0	6.88	34.89
620.0	6.46	34.87
660.0	6.20	34.88
700.0	5.86	
740.0	5.59	
780.0	5.41	
820.0	5.23	
860.0	5.10	
900.0	4.99	
940.0	4.79	
980.0	4.63	
1010.0	4.56	

CTD STATION NUMBER 95
AUGUST 29, 1971
LATITUDE 24 21
LONGITUDE 84 20
DEPTH TO BOTTOM 3358 M
BUCKET TEMPERATURE 29.5
BUCKET SALINITY 36.08

CTD STATION NUMBER 96
AUGUST 29, 1971
LATITUDE 24 23
LONGITUDE 84 14
DEPTH TO BOTTOM 3318 M
BUCKET TEMPERATURE 29.5
BUCKET SALINITY 36.00

CTD STATION NUMBER 97
AUGUST 29, 1971
LATITUDE 24 27
LONGITUDE 84 3
DEPTH TO BOTTOM 2406 M
BUCKET TEMPERATURE 29.4
BUCKET SALINITY 35.97

DEPTH	TEMPERATURE	SALINITY
0.0	29.66	36.02
20.0	29.87	36.05
40.0	27.97	36.10
60.0	25.86	36.21
80.0	25.67	36.35
100.0	23.43	36.40
120.0	20.26	36.42
140.0	18.10	36.40
160.0	17.03	36.31
180.0	16.03	36.15
200.0	15.36	36.05
220.0	14.70	35.91
240.0	13.81	35.78
260.0	13.24	35.69
280.0	12.64	35.60
300.0	11.98	35.51
340.0	10.95	35.31
380.0	9.94	35.21
420.0	9.58	35.14
460.0	8.97	35.06
500.0	8.18	34.97
540.0	7.54	34.93
580.0	7.00	34.88
620.0	6.58	34.89
660.0	6.20	34.89
700.0	5.99	34.88
740.0	5.77	34.87
780.0	5.53	34.87
820.0	5.28	34.90
860.0	5.10	34.91
900.0	4.92	34.93
940.0	4.84	34.93
980.0	4.71	34.93

DEPTH	TEMPERATURE	SALINITY
0.0	29.64	36.07
20.0	29.77	36.05
40.0	27.54	36.10
60.0	26.15	36.33
80.0	25.05	36.50
100.0	22.42	36.44
120.0	19.78	36.46
140.0	18.42	36.43
160.0	17.39	36.36
180.0	16.63	36.29
200.0	15.79	36.10
220.0	14.81	35.92
240.0	14.16	35.83
260.0	13.46	35.73
280.0	12.82	35.63
300.0	12.29	35.55
340.0	11.21	35.40
380.0	10.25	35.24
420.0	9.56	35.13
460.0	8.84	35.03
500.0	8.07	34.95
540.0	7.61	34.91
580.0	7.04	34.89
620.0	6.57	34.87
660.0	6.17	34.88
700.0	5.91	34.89
740.0	5.76	34.89
780.0	5.57	34.89
820.0	5.32	34.90
860.0	5.09	34.91
900.0	4.93	34.92
940.0	4.78	34.93
980.0	4.68	34.94
1000.0	4.66	34.91

DEPTH	TEMPERATURE	SALINITY
0.0	29.45	35.96
20.0	29.93	36.00
40.0	27.66	36.10
60.0	26.11	36.24
80.0	23.84	36.26
100.0	21.27	36.35
120.0	19.61	36.44
140.0	18.35	36.42
160.0	17.27	36.30
180.0	16.13	
200.0	15.58	
220.0	14.80	
240.0	13.99	
260.0	13.38	
280.0	12.77	
300.0	12.29	
340.0	11.16	
380.0	10.34	
420.0	9.57	
460.0	8.86	
500.0	8.23	
540.0	7.65	
580.0	7.11	
620.0	5.63	
660.0	6.33	
700.0	6.06	
740.0	5.81	
780.0	5.59	
820.0	5.37	
860.0	5.20	
900.0	4.99	
940.0	4.85	
970.0	4.75	

MANSEN STATION NUMBER 98
AUGUST 29, 1971
LATITUDE 24 30
LONGITUDE 83 50
DEPTH TO BOTTOM 1297 M

CTD STATION NUMBER 99
AUGUST 29, 1971
LATITUDE 24 26
LONGITUDE 83 34
DEPTH TO BOTTOM 884 M
BUCKET TEMPERATURE 29.4
BUCKET SALINITY 36.11

CTD STATION NUMBER 100
AUGUST 29, 1971
LATITUDE 24 24
LONGITUDE 83 25
DEPTH TO BOTTOM 472 M
BUCKET TEMPERATURE 29.6
BUCKET SALINITY 36.12

DEPTH	TEMPERATURE	SALINITY
0.0	29.30	36.050
10.0	29.39	35.911
50.0	26.71	36.213
100.0	20.85	36.372
199.0	15.82	36.079
243.0	14.31	35.833
383.0	10.24	35.204
763.0	5.57	34.884
962.0	5.09	34.928

DEPTH	TEMPERATURE	SALINITY
0.0	29.50	35.92
20.0	28.99	35.92
40.0	27.81	35.98
60.0	26.53	36.24
80.0	25.00	36.43
100.0	22.62	36.35
120.0	20.51	36.34
140.0	18.65	36.35
160.0	18.07	36.42
180.0	17.57	36.41
200.0	16.86	36.28
220.0	16.24	36.17
240.0	15.42	36.02
260.0	14.55	35.89
280.0	13.78	35.76
300.0	13.07	35.67
340.0	11.75	35.44
380.0	10.54	35.27
420.0	9.71	35.15
450.0	9.11	35.06

DEPTH	TEMPERATURE	SALINITY
0.0	29.62	36.02
20.0	29.21	36.01
40.0	27.99	35.98
60.0	26.91	36.09
80.0	25.56	36.26
100.0	23.36	36.38
120.0	20.51	36.32
140.0	18.62	36.31
160.0	18.40	36.39
180.0	17.74	36.34
200.0	17.13	36.35
220.0	16.25	36.18
240.0	15.28	36.00
260.0	14.10	35.81
280.0	13.38	35.72
300.0	12.70	35.63
340.0	11.83	35.51
380.0	10.69	35.27
390.0	10.31	35.22

CTD STATION NUMBER 101
AUGUST 30, 1971 0110Z
LATITUDE 24 22
LONGITUDE 83 14
DEPTH TO BOTTOM 305 M
BUCKET TEMPERATURE 29.4
BUCKET SALINITY 36.16

DEPTH	TEMPERATURE	SALINITY
0.0	29.58	36.11
20.0	29.10	36.07
40.0	27.81	36.12
60.0	26.66	36.22
80.0	25.41	36.41
100.0	23.34	36.44
120.0	21.15	36.37
140.0	19.29	36.43
160.0	18.07	36.48
180.0	17.16	36.33
190.0	16.94	36.30

CTD STATION NUMBER 102
AUGUST 30, 1971 0518Z
LATITUDE 24 17
LONGITUDE 82 58
DEPTH TO BOTTOM 433 M
BUCKET TEMPERATURE 29.3
BUCKET SALINITY 36.11

DEPTH	TEMPERATURE	SALINITY
0.0	29.45	36.14
20.0	29.26	36.12
40.0	28.19	36.12
60.0	27.21	36.19
80.0	25.92	36.39
100.0	23.56	36.49
120.0	20.46	36.47
140.0	18.52	36.51
160.0	17.20	36.39
180.0	16.33	36.26
200.0	15.14	36.06
220.0	13.60	35.82
240.0	12.40	35.66
260.0	11.28	35.47
280.0	10.37	35.31
300.0	9.70	35.21

CTD STATION NUMBER 103
AUGUST 30, 1971 0906Z
LATITUDE 24 13
LONGITUDE 82 44
DEPTH TO BOTTOM 553 M
BUCKET TEMPERATURE 29.5
BUCKET SALINITY 36.09

DEPTH	TEMPERATURE	SALINITY
0.0	29.46	36.12
20.0	29.18	36.11
40.0	28.00	36.10
60.0	26.86	36.21
80.0	25.44	36.42
100.0	22.24	36.37
120.0	19.43	36.41
140.0	18.25	36.49
160.0	17.11	36.33
180.0	15.99	36.17
200.0	14.48	35.92
220.0	12.90	35.66
240.0	11.27	35.39
260.0	10.70	35.34
280.0	10.28	35.27
300.0	9.60	35.18
340.0	8.96	35.08
370.0	8.68	35.01

MANSEN STATION NUMBER 104
AUGUST 30, 1971 1210Z
LATITUDE 24 11
LONGITUDE 82 30
DEPTH TO BOTTOM 604 M

DEPTH	TEMPERATURE	SALINITY
0.0	29.30	36.077
10.0	29.35	36.073
50.0	26.67	36.248
97.0	20.89	36.374
185.0	13.72	35.745
229.0	11.14	35.353
270.0	9.92	35.172
314.0	9.04	35.103
360.0	8.82	35.039
400.0	8.30	34.979

CTD STATION NUMBER 105
AUGUST 30, 1971 1354Z
LATITUDE 24 10
LONGITUDE 82 26
DEPTH TO BOTTOM 618 M
BUCKET TEMPERATURE 29.3
BUCKET SALINITY 36.09

DEPTH	TEMPERATURE	SALINITY
0.0	29.40	35.93
20.0	28.81	35.92
40.0	27.50	35.98
60.0	25.77	36.20
80.0	23.46	36.35
100.0	19.99	36.33
120.0	18.15	36.37
140.0	16.77	36.16
160.0	15.78	36.09
180.0	14.30	35.85
200.0	12.87	35.65
220.0	11.87	35.48
240.0	10.76	35.29
260.0	10.28	35.25
280.0	9.76	35.15
300.0	9.35	35.11
340.0	8.94	35.06
370.0	8.82	35.04

CTD STATION NUMBER 106
AUGUST 30, 1971 1718Z
LATITUDE 24 8
LONGITUDE 82 14
DEPTH TO BOTTOM 664 M
BUCKET TEMPERATURE 29.3
BUCKET SALINITY 36.07

DEPTH	TEMPERATURE	SALINITY
0.0	29.57	35.88
20.0	28.98	35.90
40.0	27.51	36.01
60.0	25.77	36.36
80.0	23.57	36.29
100.0	20.47	36.23
120.0	18.06	36.16
140.0	16.65	36.14
160.0	15.21	35.98
180.0	13.86	35.82
200.0	12.29	35.59
220.0	11.22	35.44
240.0	10.42	35.31
260.0	10.01	35.24
280.0	9.58	35.16
300.0	9.27	35.12
340.0	8.94	35.08
380.0	8.52	35.02
420.0	8.14	34.98
460.0	7.67	34.93
490.0	7.56	34.90

CTD STATION NUMBER 107
AUGUST 30, 1971 2118Z
LATITUDE 24 7
LONGITUDE 81 58
DEPTH TO BOTTOM 754 M
BUCKET TEMPERATURE 29.6
BUCKET SALINITY 36.05

DEPTH	TEMPERATURE	SALINITY
0.0	29.78	
20.0	29.51	
40.0	29.08	
60.0	26.30	
80.0	22.86	
100.0	19.38	
120.0	17.53	
140.0	16.14	
160.0	14.20	
180.0	12.49	
200.0	11.19	
220.0	10.23	
240.0	9.89	
260.0	9.55	
280.0	9.36	
300.0	9.15	
320.0	8.77	
340.0	8.34	
360.0	8.20	
380.0	7.43	

CTD STATION NUMBER 108
AUGUST 31, 1971 0236Z
LATITUDE 23 58
LONGITUDE 81 40
DEPTH TO BOTTOM 1083 M
BUCKET TEMPERATURE 29.1
BUCKET SALINITY 36.11

DEPTH	TEMPERATURE	SALINITY
0.0	29.44	35.90
20.0	29.12	35.94
40.0	27.86	35.93
60.0	26.61	36.10
80.0	24.79	36.26
100.0	21.19	36.34
120.0	19.31	36.45
140.0	18.46	36.48
160.0	17.43	36.37
180.0	16.27	36.20
200.0	15.09	36.00
220.0	14.12	35.75
240.0	13.14	35.58
260.0	12.39	35.48
280.0	11.66	35.43
300.0	10.99	35.31
320.0	10.16	35.21
340.0	9.36	35.13
360.0	8.74	35.05
380.0	8.26	35.00
400.0	7.76	34.96
420.0	7.37	34.95
440.0	6.89	34.92
460.0	6.61	34.90
480.0	6.54	34.86

CTD STATION NUMBER 109
AUGUST 31, 1971 0518Z
LATITUDE 23 57
LONGITUDE 81 31
DEPTH TO BOTTOM 978 M
BUCKET TEMPERATURE 29.1
BUCKET SALINITY 36.06

DEPTH	TEMPERATURE	SALINITY
0.0	29.25	35.95
20.0	29.18	36.06
40.0	29.13	36.04
60.0	26.83	36.14
80.0	25.31	36.37
100.0	22.46	36.43
120.0	20.31	36.58
140.0	19.04	36.57
160.0	17.67	36.45
180.0	16.54	36.28
200.0	15.48	36.08
220.0	14.41	35.94
240.0	13.16	35.72
260.0	12.44	35.62
280.0	11.51	35.45
300.0	10.83	35.35
320.0	9.82	35.21
340.0	9.38	35.13
360.0	8.69	35.05
380.0	8.13	35.01
400.0	7.71	34.97
420.0	7.23	34.93
440.0	7.02	34.92
460.0	6.57	34.89
480.0	6.52	34.86

CTD STATION NUMBER 110
AUGUST 31, 1971 0906Z
LATITUDE 23 56
LONGITUDE 81 18
DEPTH TO BOTTOM 1120 M
BUCKET TEMPERATURE 29.1
BUCKET SALINITY 36.10

DEPTH	TEMPERATURE	SALINITY
0.0	29.15	
20.0	29.14	
40.0	28.37	
60.0	27.17	
80.0	25.82	
100.0	23.74	
120.0	21.45	
140.0	20.22	
160.0	18.71	
180.0	17.62	
200.0	16.48	
220.0	15.60	
240.0	14.43	
260.0	13.18	
280.0	12.38	
300.0	11.60	
320.0	10.41	
340.0	9.70	
360.0	9.18	
380.0	8.72	
400.0	7.89	
420.0	7.39	
440.0	6.96	
460.0	6.57	
480.0	6.31	
500.0	6.07	
520.0	5.80	
540.0	5.64	
560.0	5.44	
580.0	5.35	

CTD STATION NUMBER 111
AUGUST 31, 1971 2254Z
LATITUDE 24 20
LONGITUDE 80 50
DEPTH TO BOTTOM
BUCKET TEMPERATURE 29.3
BUCKET SALINITY 35.99

DEPTH	TEMPERATURE	SALINITY
0.0	29.42	
20.0	29.38	
40.0	27.85	
60.0	26.01	
80.0	14.84	
100.0	11.94	
120.0	10.85	
140.0	10.08	
160.0	9.65	
180.0	9.31	
200.0	9.03	
220.0	8.68	
240.0	8.39	
260.0	8.05	
270.0	7.98	

CTD STATION NUMBER 112
SEPTEMBER 1, 1971 0148Z
LATITUDE 24 16
LONGITUDE 80 44
DEPTH TO BOTTOM
BUCKET TEMPERATURE 29.3
BUCKET SALINITY 35.50

DEPTH	TEMPERATURE	SALINITY
0.0	29.34	35.93
20.0	29.25	36.02
40.0	29.23	36.05
60.0	26.49	36.24
80.0	23.67	36.32
100.0	19.96	36.38
120.0	16.07	36.09
140.0	13.75	35.77
160.0	12.58	35.49
180.0	11.74	35.37
200.0	10.98	35.27
220.0	10.58	35.22
240.0	10.08	35.13
260.0	9.53	35.07
280.0	9.21	35.02
300.0	8.96	35.08
320.0	8.55	35.05
340.0	8.10	35.02
360.0	7.68	34.97
380.0	7.27	34.91

CTD STATION NUMBER 113
 SEPTEMBER 1, 1971 0100Z
 LATITUDE 24 11
 LONGITUDE 80 38
 DEPTH TO BOTTOM
 BUCKET TEMPERATURE 28.6
 BUCKET SALINITY 36.05

CTD STATION NUMBER 114
 SEPTEMBER 1, 1971 0306Z
 LATITUDE 24 1
 LONGITUDE 80 32
 DEPTH TO BOTTOM
 BUCKET TEMPERATURE 29.2
 BUCKET SALINITY 36.04

DEPTH	TEMPERATURE	SALINITY
0.0	29.17	36.15
20.0	29.13	36.18
40.0	27.97	36.16
60.0	26.91	36.18
80.0	25.88	36.42
100.0	24.23	36.69
120.0	22.24	36.77
140.0	20.35	36.79
160.0	19.07	36.66
180.0	18.39	36.62
200.0	17.12	36.42
220.0	15.63	36.17
240.0	15.02	36.07
260.0	14.12	35.86
280.0	12.08	35.47
300.0	12.03	35.47
340.0	10.58	35.23
380.0	9.73	35.14
420.0	9.11	35.07
460.0	8.64	35.01
500.0	8.21	34.96
540.0	7.75	34.92
580.0	7.20	34.90
620.0	6.74	34.86
660.0	6.40	34.87
700.0	6.08	34.88

DEPTH	TEMPERATURE	SALINITY
0.0	29.38	36.05
20.0	29.34	36.07
40.0	28.19	35.99
60.0	27.08	36.01
80.0	26.07	36.09
100.0	25.47	36.18
120.0	24.84	36.48
140.0	23.89	36.66
160.0	22.05	36.74
180.0	20.60	36.64
200.0	19.86	36.67
220.0	19.23	36.61
240.0	18.26	36.53
260.0	17.65	36.45
280.0	16.88	36.36
300.0	16.20	36.22
340.0	14.95	36.00
380.0	13.53	35.77
420.0	11.94	35.51
460.0	10.90	35.38
500.0	9.85	35.22
540.0	9.43	35.17
580.0	8.93	35.12
620.0	8.19	35.03
660.0	7.59	34.98
700.0	7.19	34.96
740.0	6.67	34.94
780.0	6.37	34.93
820.0	6.08	34.92

FORMULATION OF DRIFTING LIMITED CAPABILITY
BUOY PLACEMENT AND RETRIEVAL CONCEPTS

Robert L. Molinari

Donald V. Hansen

This report is submitted in response to the National Data Buoy Center's requirement for a "Formulation of Drifting Limited Capability Buoy Placement and Retrieval Concepts". The search and rescue methodologies of the agencies engaged in finding lost objects at sea are summarized, and a method for predicting the drift of a buoy subject to surface current stresses is suggested. Finally, a test program for the Drifting Limited Capability Buoy is offered.

1. INTRODUCTION

The "Formulation of Drifting Limited Capability Buoy (DLCB) Placement and Retrieval Concepts" as delineated in National Data Buoy Center (NDBC) Statement of Work 0134EC, consists of two tasks. The first task requires a "summary of buoy location prediction models" and the second "recommendations for future NDBC direction". The requirements have short term aspects related to the field testing of the buoys during the R and D phase of the program and long term operational aspects. Primary emphasis in this report is given to drift prediction and buoy retrieval concepts as placement concepts are determined by the experiment being conducted, and will require detailed individual analysis. However, some suggestions concerning deployment during initial DLCB tests will be presented.

The procedures of the United States Coast Guard and the United States Navy's Fleet Numerical Weather Central (FNWC) at Monterey, California, are summarized, as both groups are actively engaged in finding lost objects at sea. The Coast Guard Search and Rescue (SAR) plan, given in Coast Guard Manual CG-308, is operationally oriented and strives for an

engineering handbook solution to the problem. Each step of the SAR procedure is presented with accompanying charts and figures to facilitate the computations.

The FNWC has developed a computer program in support of the Coast Guard SAR operations. The program uses sea surface current and wind forecasts generated at the FNWC to determine the probable drift of a SAR object. The Coast Guard is presently instituting an operational SAR computer program which is more sophisticated than the FNWC model.

The problems encountered in balloon location are similar to those found in buoy location. The work of Quinlan and Hoxit (1968) is summarized as an example of the meteorologist's approach to balloon location. Other reports were reviewed which discussed short-term tracking of balloons and rockets (Young 1962, Rachelett and Armendary 1967, for example) but their procedure is too specialized for application to the buoy problem.

Recommendations for future NDBC action are given in a following section. A procedure for predicting drift and retrieving non-functioning buoys, as well as a test program for the DLCB are offered. The specialized nature of the DLCB's and the methods employed by various SAR agencies are considered in these recommendations.

2. SUMMARY OF PREDICTION MODELS

2.1 Coast Guard Search and Rescue Plan CG 308 Procedure

Chapter 6 of CG-308 pertains to the "Determination of Search Areas". Relevant sections of this chapter discuss the means of estimating the probable position of a SAR object, and determining the search area. The position of the lost craft is based on a probable drift from the initial location of the SAR incident.

The object's drift is computed as a function of three variables, the average sea current, the local wind current, and the wind's effect on the object (leeway). All variables are tabulated on maps, charts, or figures. For instance, the average sea current is obtained from one of three sources,

which in order of preference are U.S. Naval Oceanographic Office Atlases, Oceanographic Office Atlas of Surface Currents, and Pilot Charts.

Section I of the Oceanographic Atlas of the North Atlantic (Publ. No. 700) is an example of the first publication, and contains tides and currents of the region. Two surface flow charts are presented, one combining data taken in the summer months of July, August, and September and the other for the winter months of January, February, and March. Current directions are given by arrows. The color of the arrow indicates the variability of the flow, with only the prevailing currents to be used in the computations. Isotachs are plotted on overlays to the direction charts, permitting determination of the velocity vector at any point.

The Atlas of Surface Currents, such as Publ. No. 576, are being replaced by Publ. No. 700-type publications, and are used only in areas where these publications do not exist. Monthly current representations are given for the region of the particular atlas. Pilot charts, which also give monthly currents, are mentioned as a last resort and only in regions where no other information is available. Technical reports of NOAA, the Naval Oceanographic Office, and interested research groups are recommended as a source of supplementary data.

The wind induced current is obtained from figure 1, which is taken from James (1966). James considered the effect of wave transport as well as pure wind drift to arrive at the functional dependence of the current on the wind speed, the fetch over which the wind acts, and the duration of the wind. Although James considers the deviation of the drift from the wind to be 20° to the right in the Northern Hemisphere, the Coast Guard tabulates the drift as a function of latitude.

Both wind speed and the "sail" characteristics of the lost object are used to determine leeway. The larger the sail presented to the wind, the greater the drift caused by the wind. Figure 2 is given to aid in leeway determinations, the curves representing the leeway of a liferaft with and without drogue. Small objects other than liferafts are assumed to have leeway curves falling between the two presented. Although most boats will tend to drift off the downwind line, the direction of the leeway vector is considered downwind.

The three terms are combined vectorially to give the drift, and thus probable position, of the SAR object. Computations are continued to arrive at an estimate of the error

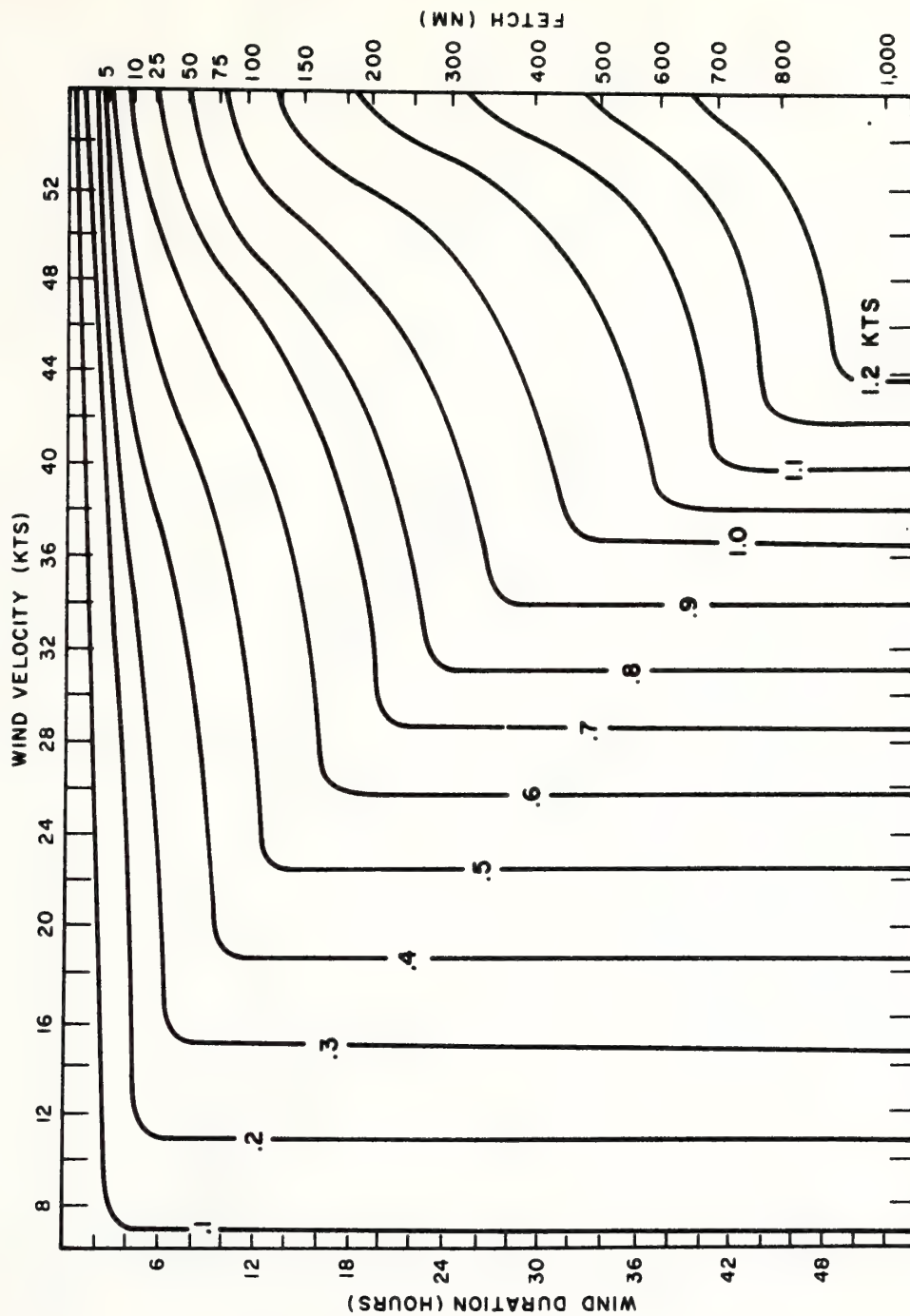


Figure 1. The wind-induced surface current component as deduced by James (1966).

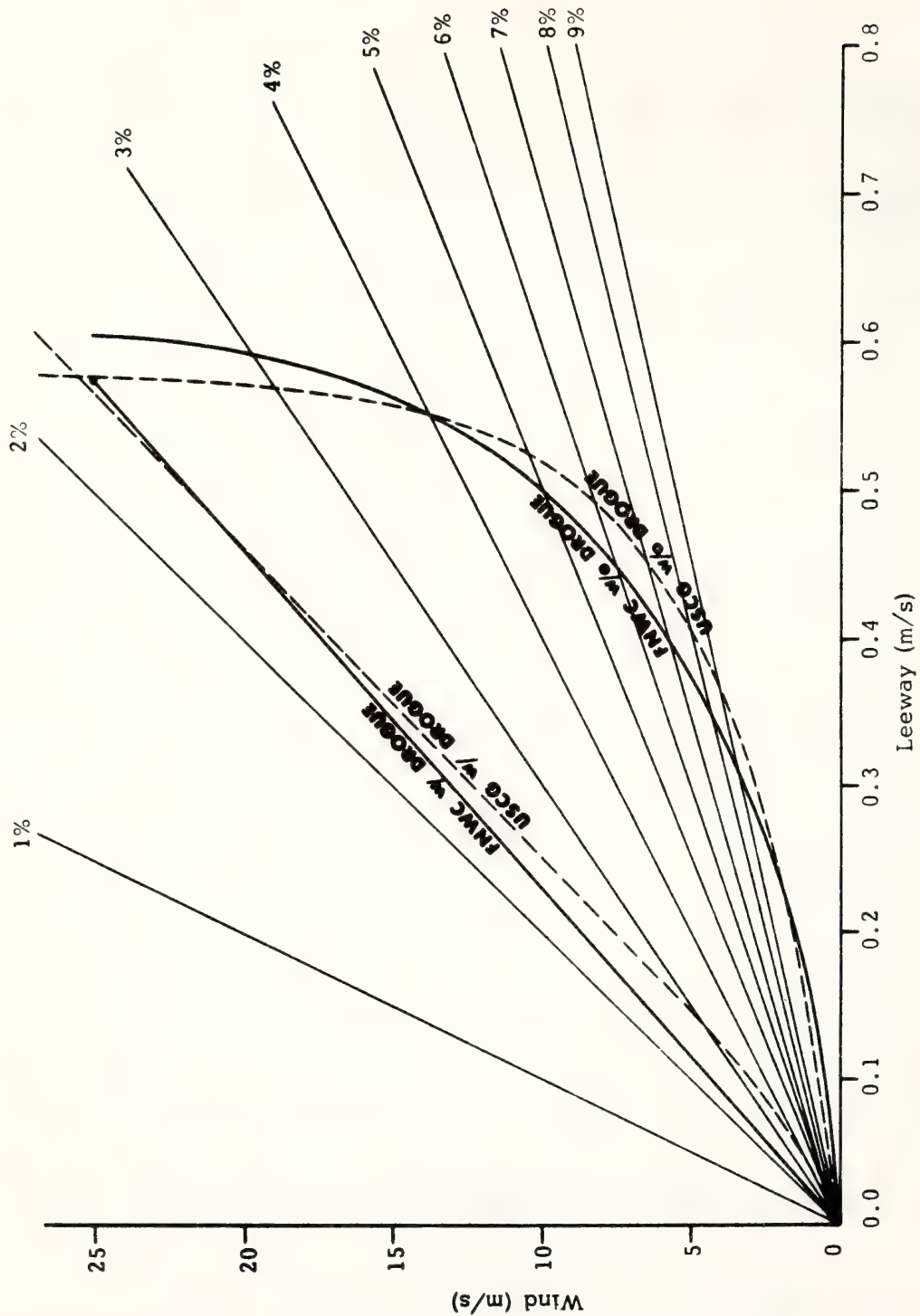


Figure 2. Leeway for liferafts with and without drogue used by the FNNC and USCG. Linear curves for percentage of wind contribution to leeway component are also shown.

in the computations. This quantity is a function of the error in the last known position of the object, the navigational errors of the search vessel and the drift error. This last error is taken as the total drift divided by eight, that is a 12% error is automatically assumed to exist in the drift computations.

An important part of Coast Guard SAR strategy is a measurement of the drift at the last known position (datum point) of the object. The effectiveness of this strategy is expected to be a strong function of the promptness of search vehicles on the scene. Ideally, a datum marker buoy, an air-droppable floating beacon which transmits on UHF frequencies, is deployed at the datum point. Listed as less desirable methods of determining the datum drift are dye markers and/or drifting ships.

2.2 SAR Center, Seventh Coast Guard District Procedure

In discussions at the SAR Center of the Seventh Coast Guard District, modifications to the CG-308 procedures were outlined. These modifications are attempts to cope with the diverse current regimes found in the large area of responsibility of this District. The particular SAR procedure applied is dependent on the current regime present and the data available.

The majority of SAR incidents in this district occur off the Florida East Coast in the area of the Florida Current. The SAR Center, in conjunction with oceanographers of the University of Miami, has developed a climatological chart of the Florida Current. The chart encompasses the entire Florida Strait. Geostrophic and direct current measurements taken by the University are averaged to give contours of average surface velocity.

When the last position of the lost object is known, its drift speed and direction are determined from the nearest isotach. If an exact position cannot be ascertained the object is put in "maximum peril", for which the core velocity of the current is used in the drift computation to delineate the search area.

In regions other than the Florida Strait, monthly charts such as Publ. No. 576 and Pilot Charts are used, rather than Publ. No. 700. A comparison of the Pilot Chart and Publ. No. 576 velocities is made; and if differences exist, they are subjectively averaged to obtain the current velocity.

The leeway component is tabulated as a function of the

lost object. A percentage of the wind speed, dependent on the sail area, is used as the velocity of the leeway. The deviation from downwind direction is also given in a table. For instance, the maximum deviation of a sailboat has been empirically determined as 60° , either to the right or to the left of the wind direction. The search area must be enlarged accordingly to compensate for this unknown drift direction component.

This Center is compiling a store of observational current measurements as datum marker buoys are deployed during most search operations. The use of these buoys follows the procedures set down in CG-308. One difficulty encountered in applying this technique is obtaining accurate positions when the plane cannot sight land.

The Center personnel do not use the Monterey Search and Rescue program operationally. They indicate that the area prescribed by this program is often prohibitively large to launch a successful search because of the poor spatial resolution afforded by this model relative to the SAR problems most frequently encountered at the Center. Occasionally they do use the program to verify their calculations.

2.3 FNWC Search and Rescue Computer Program

Hubert, Hinman, and Mendenhall (1970) describe the computer program developed at the FNWC to predict the position of an object lost at sea. The program uses in-house generated forecasts of surface current and wind to compute the probable drift of a craft. SAR missions are initiated upon request from a user who must provide the details of the SAR incident.

Larson and Laevastu (1971) describe the procedure for forecasting surface currents from local temperature structure and wind stress. The density field is approximated by the average temperature of the upper 600 feet of the water column in the calculations to determine "the permanent flow component". The average temperature is a weighted mean of the sea-surface temperature and 600-foot temperatures which are both computed twice daily from ship reports. Horizontal temperature gradients are then substituted into the following simplified version of the thermal wind equation to arrive at the velocity,

$$u = (-gz/fT) (\partial T/\partial y)$$

$$v = (gz/fT) (\partial T/\partial x)$$

where,
 (x,y) = (east, north) directions
 (u,v) = (east, north) components of velocity
 g = acceleration of gravity
 z = 600 feet
 T = average temperature
 f = Coriolis parameter.

Witting's formula is used to determine the wind-induced current. Empirically derived in the early 1900's from lightship observations (Defant, 1961), the induced flow is proportional to the wind speed. The deviation of this current, D, from the wind direction, W, is given by

$$D = 40.0 - 8.0W^{\frac{1}{2}} \quad W \leq 25\text{m/sec}$$

$$D = 0 \quad W \geq 25\text{m/sec}$$

where the deviation is to the right in the northern hemisphere.

The FNWC approximations to the liferaft leeway curves determined by the Coast Guard are given on figure 2. Options are available for calculating the leeway of craft other than liferafts. A linear percentage of the speed, depending on the sail area of the object, is applied as the leeway component. Figure 2 also contains some percentage drift lines used in the FNWC program.

Drift components are computed on a grid with 200-mile space increments. To obtain the drift at non-grid points, a non-linear interpolation is used. Drift forecasts are made every 12 hours at present, but it is planned to reduce the time interval to 6, then to 3 hours.

2.4 Coast Guard SARP Computer Program

The Operations Analysis Branch of the Coast Guard's Atlantic Area Command has developed a search and rescue computer program called SARP (Operations Analysis Branch, personal communication 1972). This program was initiated in response to the need for an automated SAR program, to the evolution of SAR methodology, and to the problems encountered during the applications of the FNWC model. SARP has been tested at Third Coast Guard District, New York, and due to its success will become operational in the near future. The present model adheres strictly to the SAR methodology of CG-308. Future models will include the newer techniques.

SARP has a surface current file based on the climatological data of Publ. No. 700. Only currents with a steadiness

of greater than 55% are on file. Supplementary information, such as the Florida Strait surface current chart constructed for the Miami SAR Center also will be input on the data file.

An updated version of the SARP current file is being developed in conjunction with the Naval Oceanographic Office. Historical data are being recompiled to arrive at new monthly climatological charts. The computations also will result in a determination of the error bounds of the current means. The present method of applying a constant 12% drift error is probably optimistic in regions of poorly known or highly variable currents.

The option to override the Publ. No. 700 current file is available in the SARP program. If the user has knowledge of the current field in the region of the SAR incident, these data can be input to the SARP program.

The local wind drift is determined from the chart of James (fig. 1). The program models the effect of wind shifts by considering the degradation of the previous wind drift as well as the onset of the new current. The technique described by James (1966) is used in these computations.

The leeway component is computed by the CG-308 method. The user option to specify the percentage of wind to apply to the leeway speed also exists.

The 200-nautical mile spacing between grid points of the Monterey program is too large for an operational SAR tool. The Coast Guard program, however, will have a space increment of approximately 30 nautical miles, with a 6-mile space in regions of numerous data such as the Florida Strait. The time increment of SARP is one hour.

The Coast Guard, through a contract to a consulting firm, is developing another SAR computer program to be called CASP. This model will be more statistical in nature producing probability maps of the search area. Environmental data, search plans and other possible factors will be assigned uncertainty values to arrive at these maps. The program will be tested operationally at the Third Coast Guard District, and if successful will become available to all the Coast Guard SAR Centers within two years.

2.5 Balloon Location

Quinlan and Hoxit (1968) describe a technique developed to determine the trajectories of high altitude balloons. A "climatology of balloon positions" for packages launched

from Chico, California, to float for up to twenty hours at 90,000 feet was needed to plan recovery operations. The climatologies were computed for seven 2-week periods to arrive at the optimum launch time.

The first step was to compute trajectories from winds aloft data stored at the National Weather Records Center Asheville, North Carolina. Displacement vectors at 5, 10, 15, and 20 hours after launch were computed from three consecutive twelve-hourly observations. Between 30 and 38 randomly selected sets of data were chosen for each two-week period.

Target ellipses (climatologies) were then constructed to outline the probable area of impact. The two-dimensional displacement vectors were assumed to have a bivariate normal distribution with a probability density which falls off exponentially in all directions from a mean value. When the standard deviations of the east and north components are equal, the distribution is circular, otherwise it is elliptical.

The computational procedure involves determining the major and minor axes of the ellipses as well as the angle of orientation. The .90 and .99 probability ellipses are then drawn on a base map for use by the retrieval personnel. Examples of these ellipses for a typical two-week period are given on figure 3. The optimum launch period has the smallest target area.

To facilitate the retrieval operation, the probability that the balloon package will be within a circle of given radius centered at the mean position of the probability ellipse can also be calculated. This computation results in a probability curve such as shown in figure 4. Although conceptually appropriate also for the drifting buoys, this technique is presently inapplicable because insufficient data on ocean current condition exist at present and, in any case, is likely to involve an impractically large search area.

3. RECOMMENDATIONS FOR FUTURE DIRECTION

3.1 Introduction

In contrast to the meteorologist's one-parameter problem, the SAR techniques of the Coast Guard and FNWC emphasize the importance of considering two variables, current and leeway,

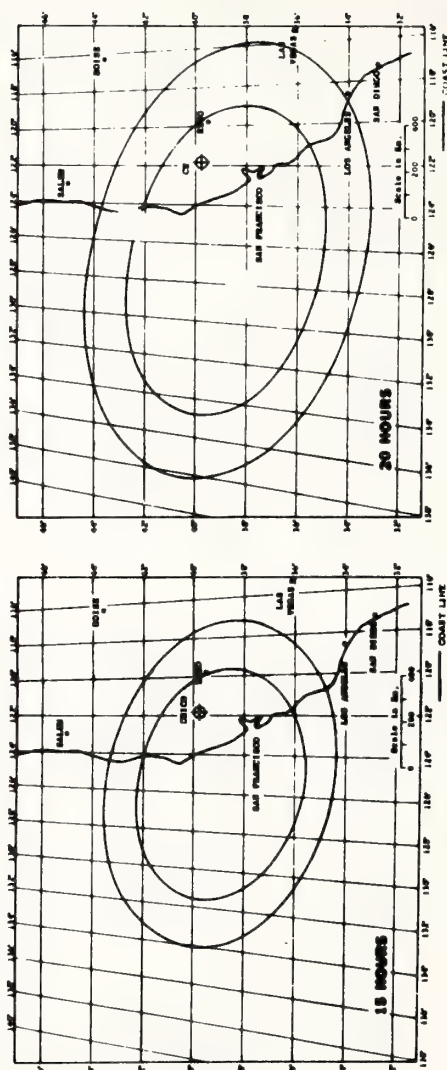
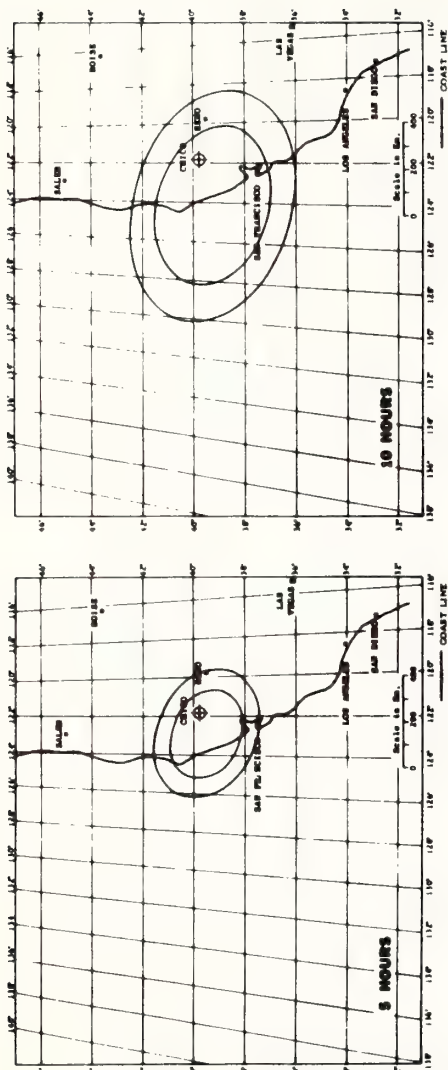


Figure 3. The 0.90 and 0.99 probability ellipses for balloon positions after 5, 10, 15, and 20 hours, at 90,000 feet.

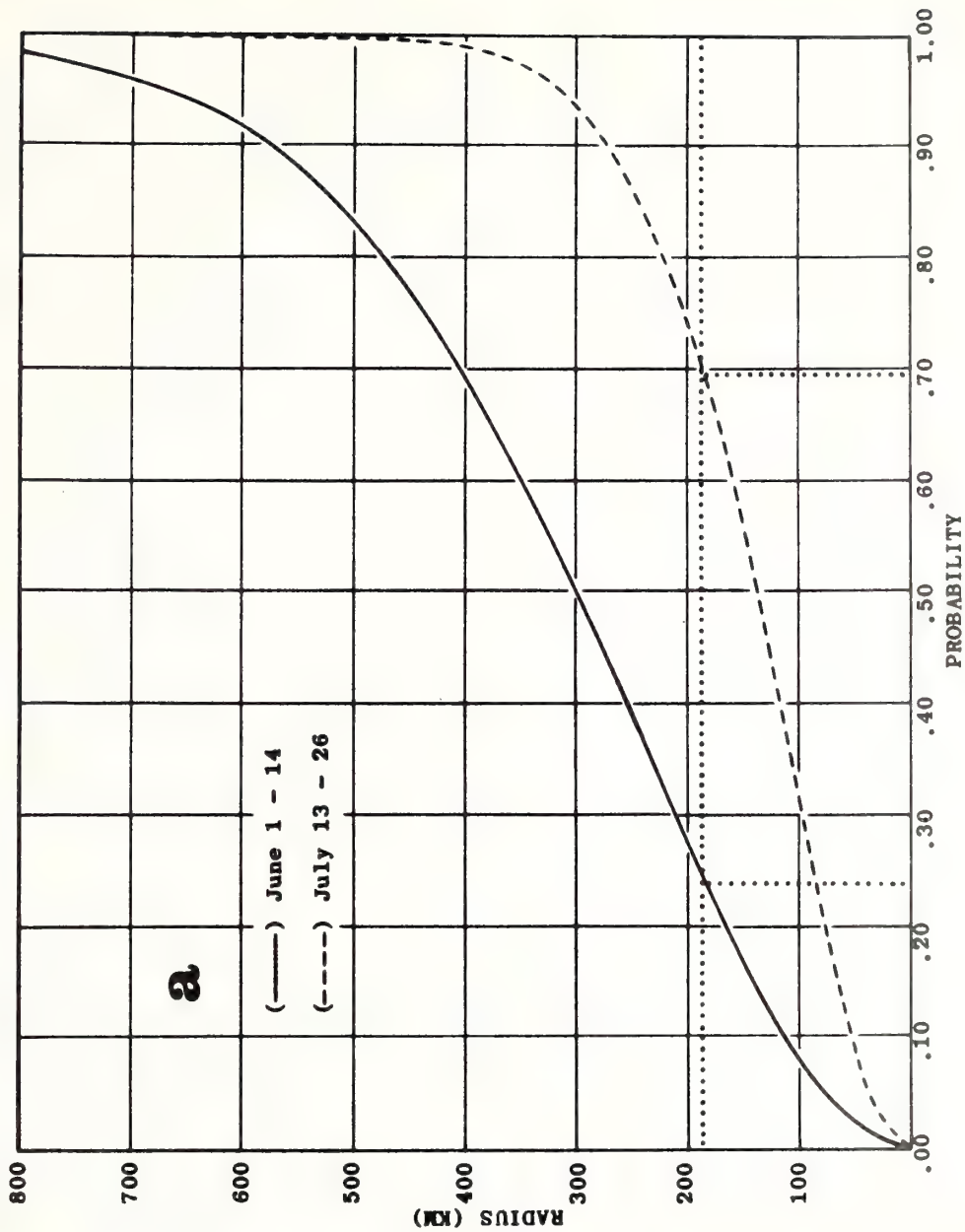


Figure 4. The probability of a balloon being within a circle centered at the mean of the respective distribution for two, two-week periods.

in the drift computations. Intuition dictates that an object will drift at the velocity of the current in which it is floating, but it is not as clear as to how a buoy will sail in the wind. Thus, an example of the magnitude of the sail component under typical oceanic conditions is presented.

Consider a 1 m/sec current flowing to the north and a 10 m/sec wind acting in the same direction. If the duration of this wind is two hours, an insignificant wind induced current will result. Assuming the DLCB approximates a liferaft with drogue, the 10 m/sec wind will produce a leeway of $\frac{1}{2}$ knot. This is a 25% and 10 mile per day increase in the resultant drift.

If this component is not considered in the drift computations, the probability of failing to locate the drifter increases. If included, the additional mileage would shift the center of the search area. Furthermore, the search area would have to be enlarged to compensate for the possibility of non-downwind drift if the sail characteristics of the object are not known.

The sailing characteristics of the DLCB are a function of the shape of the drifter, its height above and below the water, whether it is drogued or not, and other variables. These factors will have to be determined during the DLCB Test Program, and thus the leeway component of the drift cannot be realistically considered in this report. Therefore, the following sections include recommendations for determining only the current components of drift and for conducting a test program for the DLCB. Specific examples, taken from studies conducted by AOML personnel, are used to argue for various procedures.

3.2 Current Determinations

The knowledge of precisely where and when the DLCB failed and what the previous drift was greatly facilitate the task of locating the buoy. This section considers the DLCB drift as a function of only the current and offers a drift prediction plan consisting of pre-launch, launch, drift, and failure procedures. Some of these procedures are more easily applied during the test program than for operations, but may be operationally applicable in the context of large-scale geophysical experiments from which extensive supporting observations are available.

3.2.1 Pre-launch Stage

Knowledge of the initial DLCB deployment area should be

used to predict the probable drift of the DLCB, and to develop the recovery plan for a non-functioning buoy. It is recommended that all possible sources of information be considered to satisfy the prediction and recovery requirements. While describing these data sources, the limitations and advantages of various procedures given in Chapter II also are discussed.

The ideal data source for the prediction and recovery operations is a research project taking observations in conjunction with the DLCB experiment. For instance, if a DLCB is to be launched during a MODE or GATE type experiment, all the information necessary to predict the drift of the buoy is being collected. However, if such an experiment does not exist, it is recommended that the NDBC ascertain if any groups are actively engaged in other descriptive studies of the area. Some examples of such data sources follow.

Dr. W. D. Nowlin, (Personal communication) of Texas A&M University, in conjunction with the NDBC and the Environmental Data Service (EDS), is attempting to develop a seven-day analysis program for the Gulf of Mexico. Temperature data collected from the Buoy Center's EEP buoys and from ships operating in the region would be forwarded to Dr. Nowlin from the EDS and NDBC. Computer programs have been developed which will produce contours of the depth of selected isotherms. Since the temperature field closely parallels the density field in the Gulf, the flow pattern is approximated, at least in the region of the major currents.

Continuing projects of the U.S. Naval Oceanographic Office and the Coast Guard produce maps of surface temperature which, although not as valuable as the previous type of study, could be used to predict the surface flow. The Gulf Stream series of the Oceanographic Office presents monthly charts of the Gulf Stream Axis and mean surface temperature in the northwestern Atlantic Ocean. Also included are descriptions of any anomalous circulation features which were recently investigated. The Coast Guard disseminates the results of their monthly aircraft infrared thermometer measurements of the waters off the eastern seaboard. By means of such observations, the changing position of major currents can be detected and a semi-quantitative measure of current speeds can be obtained from figure 5. This figure was compiled by James (1966) from data relating sea surface temperature gradients to current speed.

Less desirable data must be obtained if these types of projects do not exist. The Coast Guard manual recommends the use of Atlases such as Publ. Nos. 576 and 700 to determine

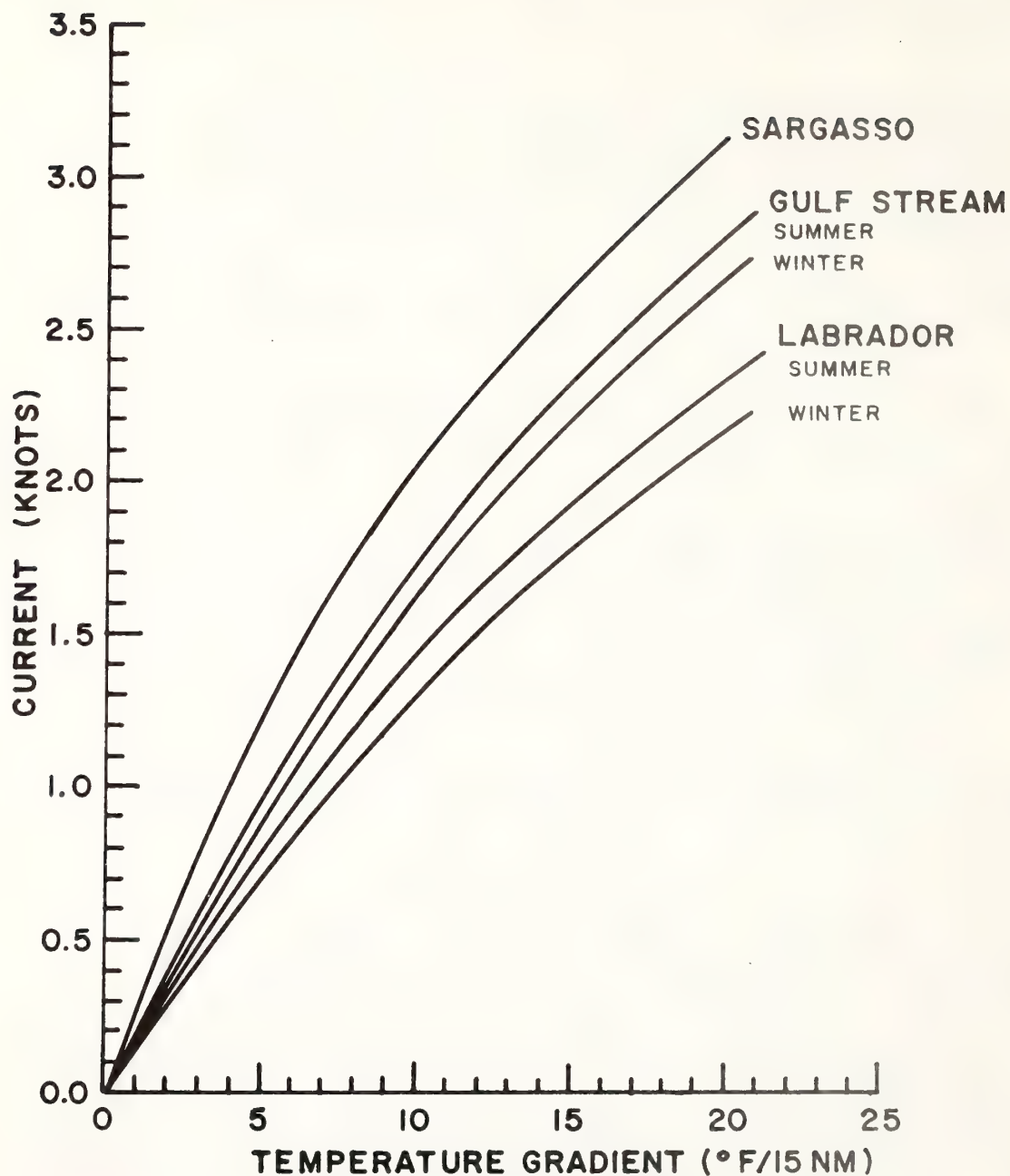


Figure 5. Estimation of geostrophic current from surface temperature gradients as given by James (1966).

the permanent current component. However, this type of data compilation filters out all temporal variations with time scales less than the averaging period. Thus, the atlas picture is seldom duplicated by an instantaneous snapshot of the circulation field. As an example of the type of differences that can occur, two AOML experiments are considered.

The first of these examples is taken from a region of intense boundary currents. Approximate tracklines of buoys drogued at 40 m to minimize leeway are shown as figures 6 and 7. The average currents given on figure 8 are taken from Publ. No. 700 and Pilot Charts. The drift, particularly the speed components, predicted by these charts is quite different from the drift experienced by the buoys. A search based on these current representations would not have a high probability of finding the drifter.

The second example is taken from a drift buoy experiment still in progress as this report is being written. Five drifting buoys using the EOLE satellite positioning system were deployed in the southern Sargasso Sea, the same mid-ocean area wherein the MODE-I experiment is to be conducted in 1973. Figure 9 shows the regional current field as given by the Pilot Chart for October in comparison to that experienced by these drifting buoys which also have parachute drogues attached to minimize leeway. Again it is clear that the mean currents shown by such charts are not a good index to individual drift experiences.

Therefore, it is recommended that historic oceanographic data from the drift area be acquired to determine the representativeness of the atlas current fields and to obtain snapshots of various flow patterns. The National Oceanographic Data Center (NODC) and research groups working in the area are possible data sources. Upon request, the NODC provides a listing of cruises made in a particular area. Most research groups compile reports giving the cruise tracks and types of data collected. Dynamic height computations relative to a deep dynamic surface are the preferred type of data. Both the speed and direction of the current can be determined from contoured dynamic height fields.

However, if this type of data is not plentiful, the use of a characteristic indicator to define the current regime should be considered. For instance, Leipper (1970) uses the depth of the 22°C isotherm to illustrate the circulation pattern in the Gulf of Mexico, while Hansen (1970) uses the 15°C isotherm at 200 m to depict the Gulf Stream axis. In areas other than the North Atlantic, it may also be possible to calibrate the temperature data to obtain current speeds as well as direction.

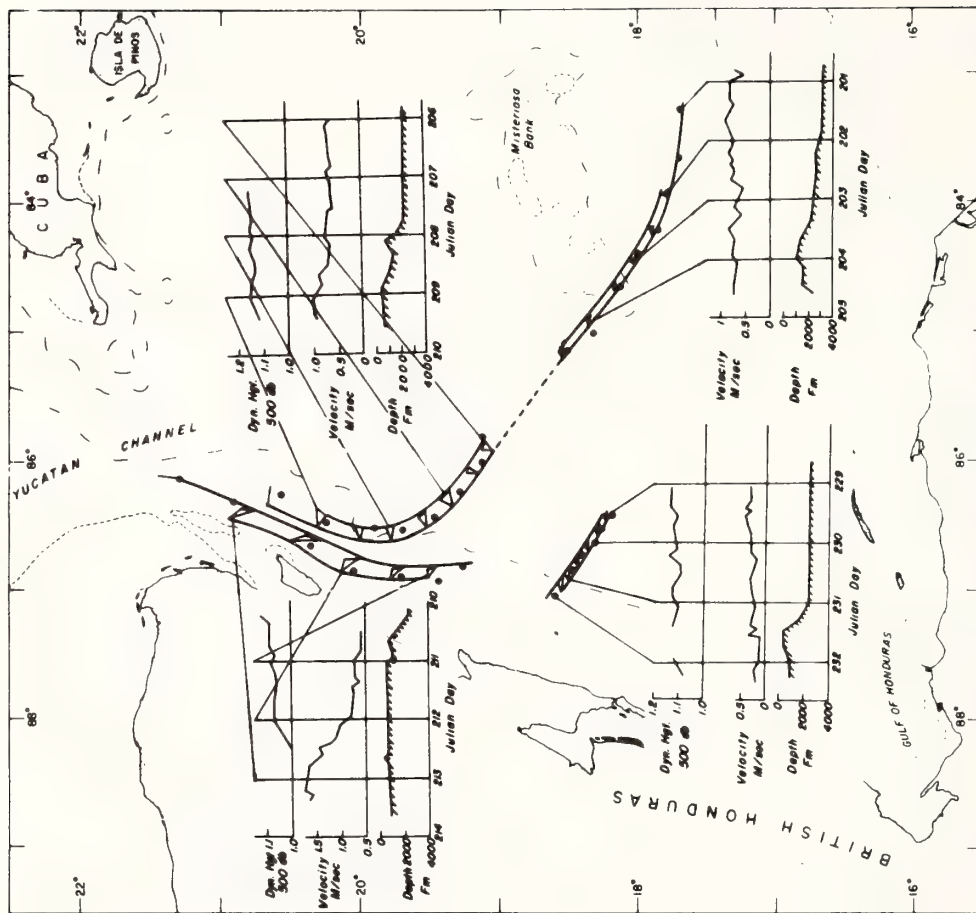


Figure 6. Approximate drogue tracks for the AOML July 1971 Caribbean Sea drifter experiment.

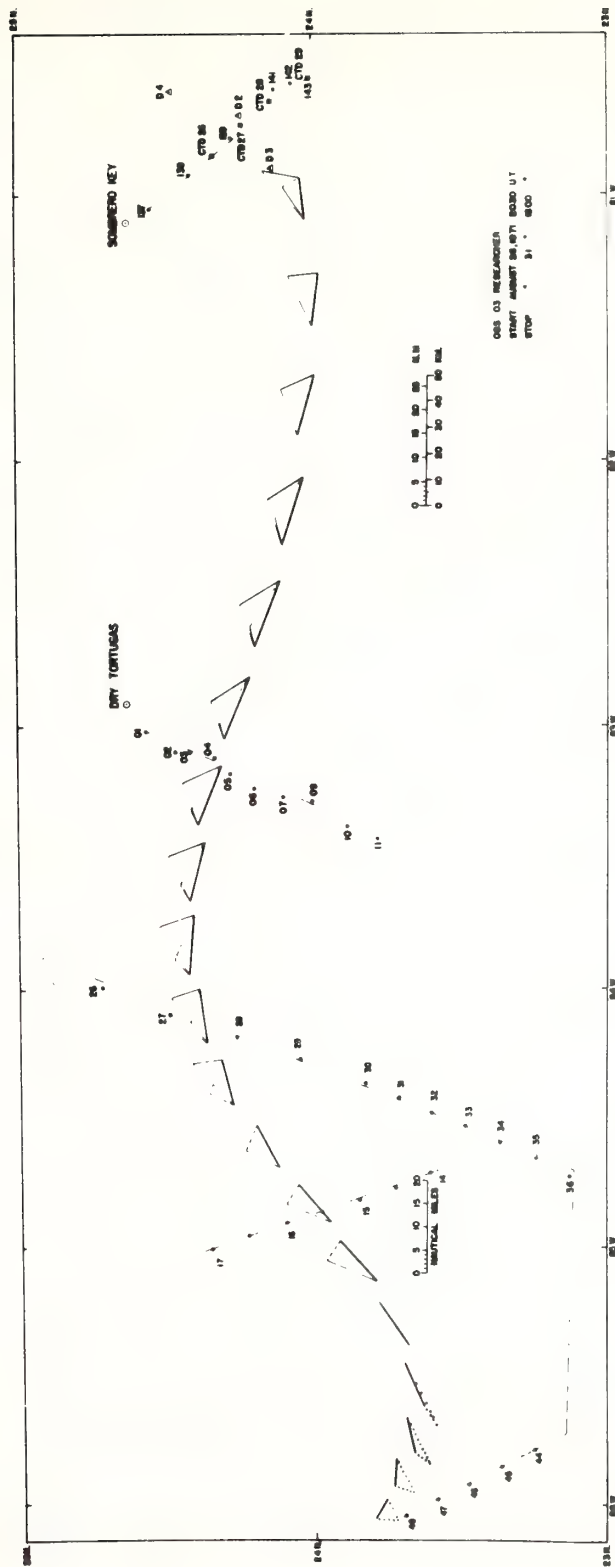
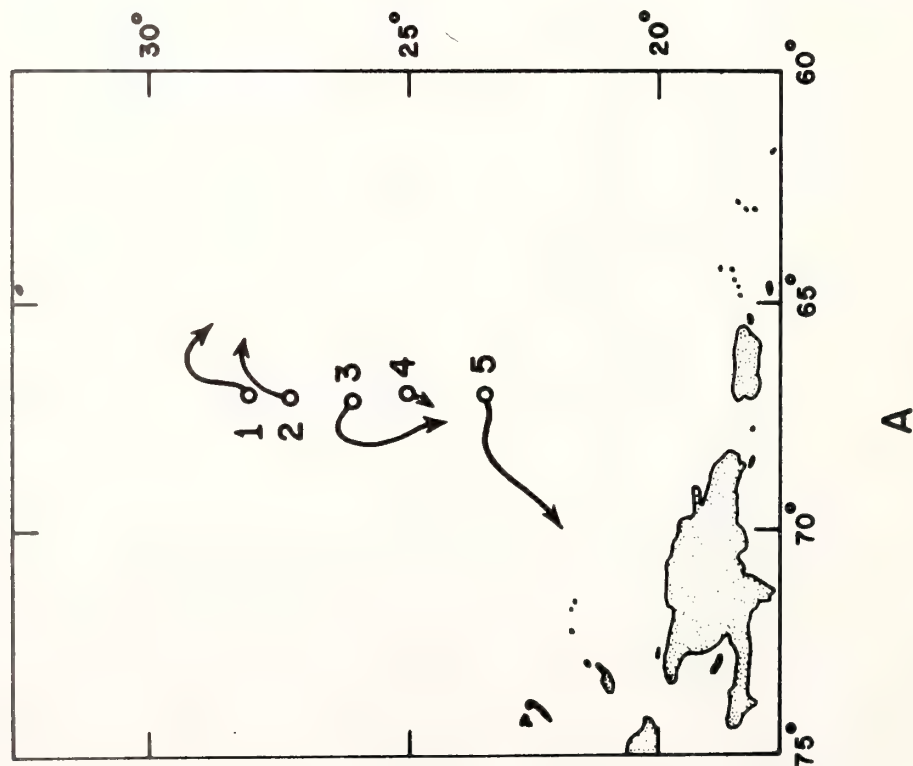
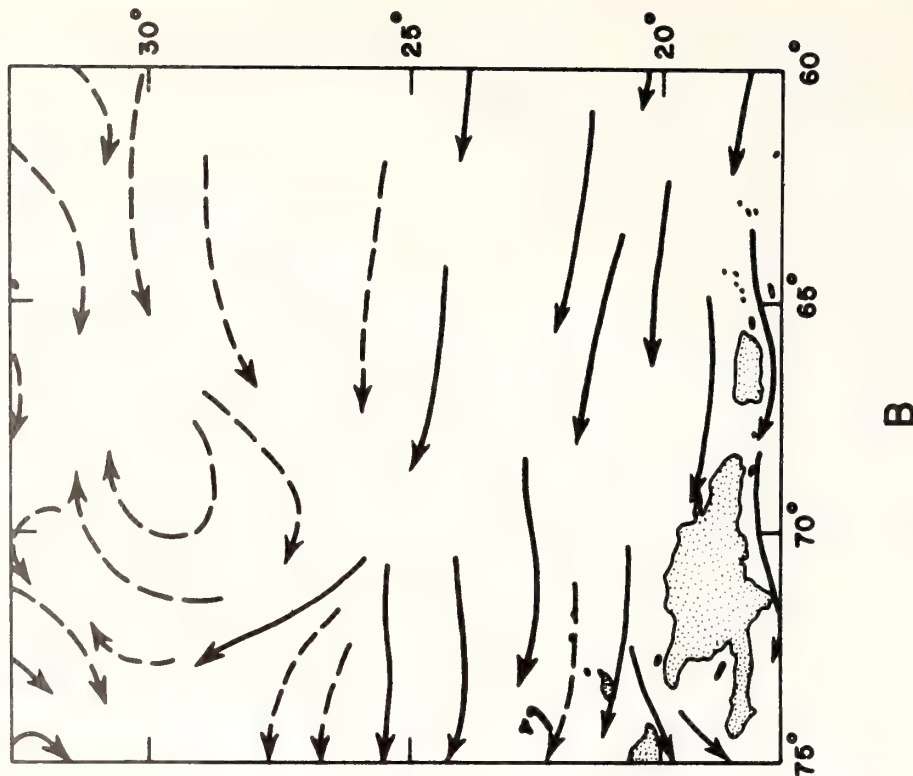


Figure 7. Approximate drogue tracks, given by the triangle apexes, for the AOML August 1971 Gulf of Mexico drifter experiment.

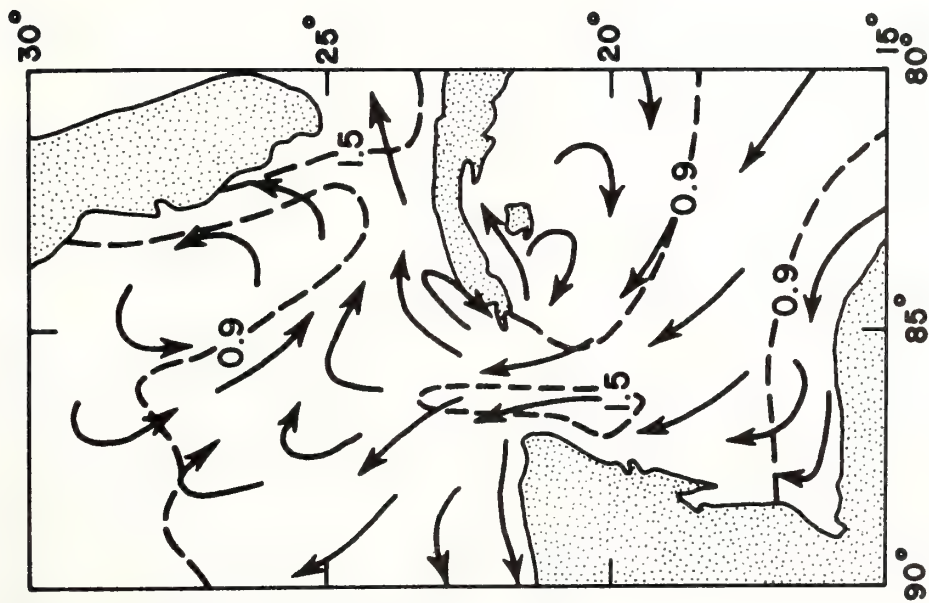


A

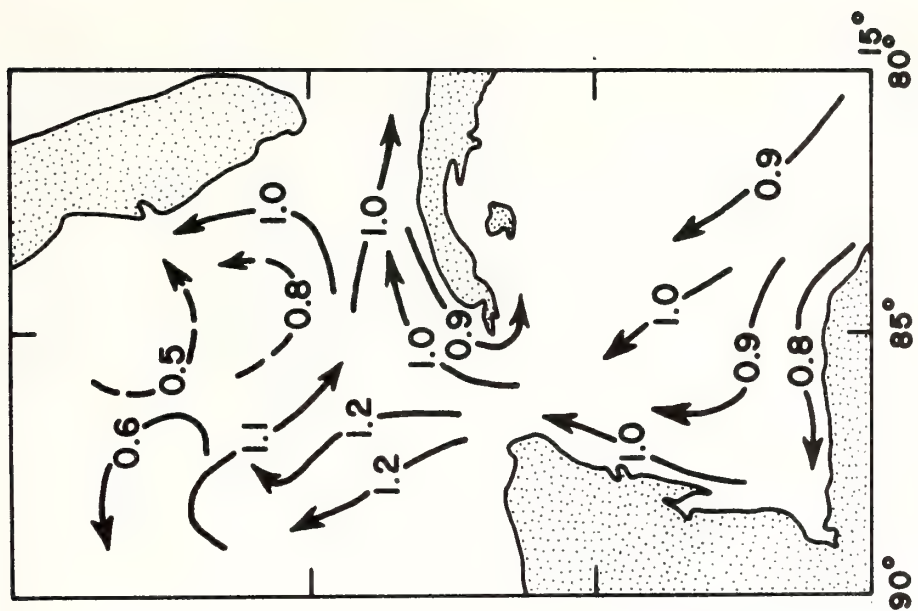


B

Figure 8. Mean surface currents for the western Caribbean Sea and Gulf of Mexico taken from Publ. No. 700, A (dashed lines represent isotachs in knots), and the August Pilot Chart (current speed in knots).



A



B

Figure 9. Preliminary drogue tracks of the five buoys deployed in September 1972, A, and the mean surface currents as given by the October Pilot Chart, B.

Since little is known about long-term cycles in the ocean, it is advised that all pertinent data be considered, not just those taken during the month of the launch. The importance of this procedure will be illustrated later.

If little or no data exist in the drift region, it will be necessary to use atlases to predict the probable DLCD drift. Supplementary information can be obtained from the FNWC temperature forecasts. As mentioned, the 200-nautical mile grid spacing of the FNWC program can define only large scale phenomena such as the Gulf Stream of Kuroshio. However, the program does use the latest ship injection and bathythermograph reports to arrive at these features. A more accurate updated representation of the current field could result from a comparison of the two circulation patterns. Over a period of years, records of drift buoy movements can be expected to improve upon the present state of knowledge of the current systems.

3.2.2 Launch Stage

The late August 1971, AOML drifter studies in the Gulf of Mexico included an XBT survey just prior to the launch of the buoys. An early October 1970 cruise and Publ. No. 700 depict a well defined Loop Current, extending deep into the Gulf of Mexico (figs. 8 and 10). Based on these data, it was decided to plant the drogues at the northern boundary of the Loop, at approximately $26^{\circ}40'N$ and $87^{\circ}30'W$.

However, midway through the survey it was obvious that the historical and snapshot picture did not exist at that time, but rather that an eddy had detached from the flow and the axis of the Yucatan Current remained at $24^{\circ}N$ (fig. 7). This circulation pattern had been observed before (Nowlin, 1972) but at earlier times of the year. A search plan based on either the previous or atlas data would have had little success in recovering a non-functioning buoy. Therefore, it is recommended that a pre-launch survey be conducted to determine the flow pattern in the drift area.

It is recommended that buoys be launched in pairs during the test program. This procedure will be of scientific as well as practical value. Practically, two buoys insure the representativeness of the measurements. For instance, the rapid separation of two drogued buoys probably indicates a parachute failure. Drogue studies (Molinari and Starr, 1972) suggest that in many current regimes the rate of separation of neighboring buoys is not great. In case of buoy failure, the trackline of the other drifter would be a valuable tool

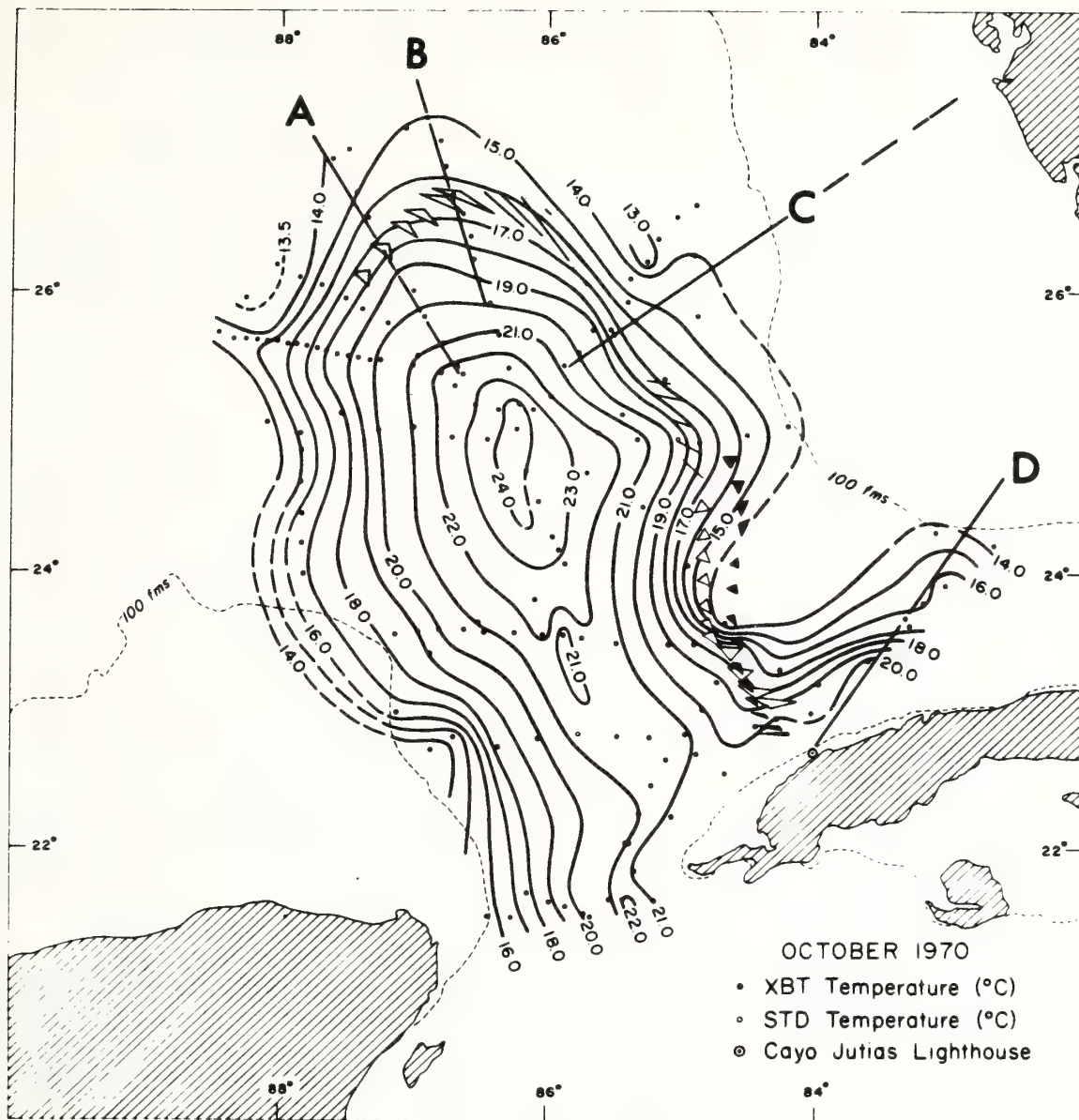


Figure 10. Approximate drogue tracks, given by the triangle apexes and the temperature field at 200 m for the AOML October 1970 Gulf of Mexico drifter experiment.

in the recovery operation. The rate of separation of properly functioning buoys will produce data on diffusive processes in the ocean.

3.2.3 Drift Stage

An attempt to correlate the DLCB drift with the available data should be made. If the correlation is good, the prediction and recovery operations are simplified. If the correlation is not good, an attempt to explain the discrepancy should be made in order to predict future drift.

The drift data should be input both to the FNWC and to the Coast Guard SAR computer programs. If either or both of these programs are successful in predicting the future drift of the DLCB, the models can be used in case of a buoy transmission failure.

3.2.4 Failure Stage

It is recommended that arrangements be made with the responsible Coast Guard District to consider the transmission failure of a DLCB as a SAR incident. In particular, the immediate deployment of a Coast Guard aircraft would increase the probability of locating the drifter. If a plane is dispatched within a day or two, under most oceanic conditions, a simple extrapolation of the buoy path would suffice to locate the DLCB.

However, if more than three days are required to initiate a search, and a plane cannot be used, other methods to drift determination must be considered. The longer time period would require a study of all the variables considered by the FNWC and Coast Guard. The procedures applied by these agencies during a SAR incident, as well as possible modifications, are considered next.

As described in the pre-launch procedures, the ideal data source for surface current determination is a simultaneously conducted experiment. The resulting data would eliminate any guesswork in determining both the wind-induced and permanent current components. As long as the buoys remained in the experiment area, which can be ascertained by current velocity computations, the time required to launch a recovery mission is not critical.

If the buoys leave the study region, or if no experiment exists, the data compiled during the pre-launch, launch, and drift state must be reviewed to predict the probable trackline.

If correlation is good between the observed drift and the compiled data, an extrapolation based on the compilation would suffice to locate the DLCB. If the correlation is bad, factors that can cause differences must be considered.

For instance, changes in the surface current forcing functions would produce different flow patterns. Large-scale wind shifts can alter the circulation. The exact form of the alteration cannot be predicted with the present knowledge of ocean dynamics. In such cases predictions of the drift would be based on a subjective choice of a theoretical or observational study.

Both the Coast Guard and FNWC deduce the wind-induced current from empirically derived relationships. The Coast Guard method considers wind duration, fetch, and wind velocity, while the FNWC program considers only the wind velocity for the prior 36-hour period. Figure 11 from James (1966) shows the results of some wind drift current formulas indicating the range of results possible. Again, the choice of a relationship is dependent on the biases of the user.

If a drogue is not used, and the sail characteristics of the buoy have not been defined, the leeway effect also has to be determined subjectively. The Coast Guard solution to the problem appears satisfactory.

Many of the choices just mentioned would not have to be made if two buoys were deployed together. If the rate of separation of the buoys were determined during the drift stage, and if no dramatic changes occurred in the drift of the functioning buoy, an extrapolation assuming a constant separation rate could determine the DLCB position. If a significant change occurred in the functioning buoy's drift, the rate of separation probably also changed (Molinari and Starr, 1972).

It most probably is not feasible to use the buoys in pairs operationally. An operational counterpart of the pairing procedure is to infer movement of nonresponding buoys from that of adjacent buoys in an array. Successful use of this idea, however, requires much greater knowledge of the horizontal coherence of ocean currents than is presently available outside major currents such as the Gulf Stream. The present EOLE buoy experiment will provide initial data of this sort, and investigators associated with MODE-I are developing new techniques for use of Lagrangian correlation data, but further drift experiments must be conducted in a variety of ocean environments to provide data needed for implementation of such techniques.

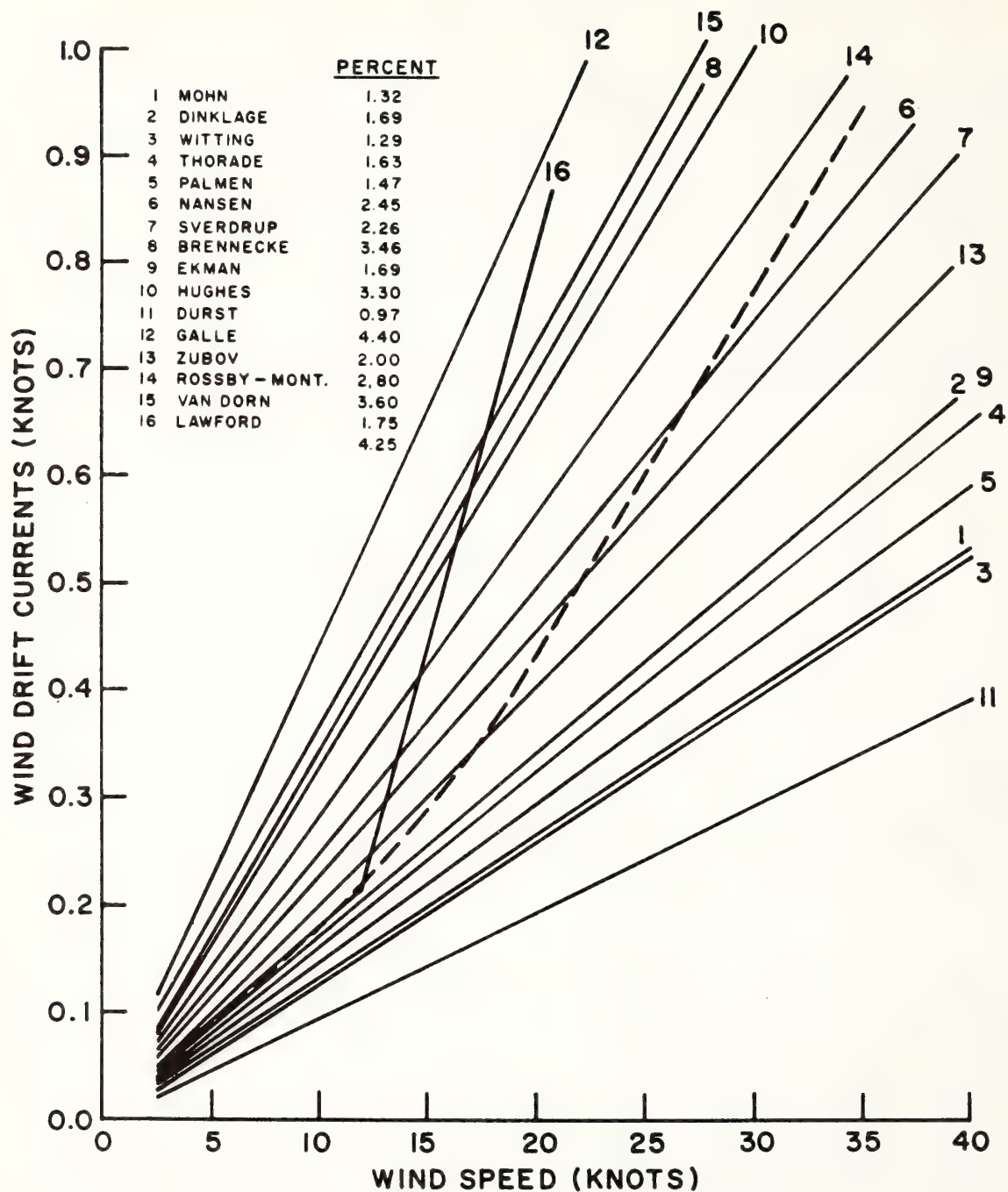


Figure 11. Results of several wind drift studies as presented by James (1966).

3.3 Recommendations for the DLCB Test Program

The five DLCB scenarios describing the possible uses of the drifter implicitly specify different modes of buoy drift. For instance, if the buoy is used in an experiment such as GATE or MODE, the participating oceanographers would require the buoy to be directly coupled to the ocean current, rather than have it actively respond to wind changes. However, in the hurricane experiment where the buoy is to be used as a floating weather station, the constraint of having the DLCB remain in the same parcel of water is not as severe. In either case, the response characteristics of the DLCB to wind, current, and wave action are required to evaluate the data received from the drifter.

Computer simulation and tank studies can not duplicate the numerous combinations of wind, wave, and current situations that are possible in the ocean. Therefore, it is recommended that the determination of the DLCB's drifting and sailing characteristics be the first priority of the test program. Furthermore, an efficient mechanism to couple the buoy and current will be required, and various drogue configurations should be tested to evaluate their effect on the drift.

An oceanographic research vessel, or at least a ship capable of taking over-the-side measurements, is necessary to conduct a comprehensive DLCB test. The vessel should have a complete suite of meteorological instruments; in particular, equipment to obtain accurate wind speed and direction is essential. An independent method of obtaining current velocity is necessary to verify the drift obtained from the buoys. The continuous current profiler, developed by Duing of the University of Miami (Duing and Johnson, 1972), can fulfill this requirement.

Accurate navigational control is an obvious necessity for the test vessel. Ship positions are needed to verify the DLCB's navigational system and to obtain the ship's drift during the current meter observations. This last measurement is necessary to eliminate the effect of ship motion from the current meter results.

One method of obtaining the floating and sailing characteristics of the DLCB's is to launch two closely spaced buoys, one drogued and the other not. Since the depth of the drogue will be determined by the requirements of the particular experiment being conducted, various drogue depths should be used during the test. Simultaneous direct current and wind measurements should be taken regularly along the buoy's tracklines.

The rate of separation of the drogued and non-drogued buoys is a function of the buoy's response to the wind. The greater the sail area, the more rapidly will the DLCB's separate in a wind. The deviation from downwind drift, if any, should be determined at this time.

The response of the drogued buoy to the current can be ascertained by a direct current measurement at the nominal depth of the drogue. Duing (personal communication) has used the continuous current profiler while in the drift mode, and he reports that the current measurements are representative of the flow if the ship's drift is accurately known. The differences between the drogue and current meter velocities are an indication of how the DLCB's react to a current.

The DLCB's response curves to wind and current are probably non-linear necessitating a series of tests in different oceanic and atmospheric situations. The optimum logistical area would be one where various wind and current regimes exist in a small region. The drifter studies of Molinari and Starr (1972) suggest that the western Caribbean Sea and Gulf of Mexico is such a region.

Figure 7 summarizes the preliminary results of a July-August 1971 drifter study in the Caribbean Sea. The current speeds vary from 1.5 knots in the basin to over 3 knots at the Yucatan Strait, and the current directions range from due west to northeast. The current also accelerates dramatically near Cozumel Island.

Testing the drifters in this area would subject them to both constant and accelerating currents, without extensive deploying redeploying of the DLCB's. For instance, the drogued buoy could be left in the water while only the non-drogued buoy was moved. This region has the logistical advantage of currents flowing towards the staging area in Mississippi.

The Gulf of Mexico also contains many dissimilar current regions. These range from the intense but usually slowly varying Loop Current in the Eastern Gulf to the weaker currents in the Western Gulf. If the test is conducted in the winter, the Gulf has the advantage of having a more variable wind pattern than the Caribbean Sea. The occurrences of "northers" and other weather systems cause frequent shifts in the wind pattern over the Gulf of Mexico. This wind variability will permit a more comprehensive study of the sail characteristics of the DLCB's.

The drift prediction procedures outlined previously

should be tested during this time to verify their usefulness. A pre-launch survey is essential during the test to assure the most efficient deployment of the DLCB's in the short time available. The validity of the Coast Guard and FNWC drift predictions should be ascertained during the test.

Finally, because the importance of ancillary data on the currents in the vicinity of the buoy test has appeared throughout our investigation of the problem, and present knowledge and predictability of instantaneous currents in most parts of the ocean are still very weak, it is advisable to associate the buoy tests with other ocean observation projects to the greatest extent possible. This will maximize the amount of current data available to those who may have to make estimates of buoy movement.

4. ACKNOWLEDGMENTS

The authors would like to express their appreciation to Lt. Cdr. A. Shirvinski (USCG), Director, Operations Analysis Branch, Atlantic Area Coast Guard, and Lt. P. Hill (USCG), Seventh Coast Guard District, for their time. The Coast Guard's SARP computer program and the Seventh District search and rescue procedures were described to the authors by these officers. This work was funded through the National Data Buoy Center's Statement of Work 0134EC.

5. REFERENCES

- Atlas of Pilot Charts, Central American Waters and South Atlantic Ocean, United States Naval Oceanographic Office (1955), HO Publ. No. 576, Supt. of Documents, Washington, D. C. 20402.
- Defant, A. (1961), *Physical Oceanography*, Vol. I, Pergamon Press, 729 pp.
- Duing, W. and D. Johnson (1972), High resolution current profiling in the Straits of Florida, *Deep-Sea Res.* 19: 259-274.
- Hansen, D. V. (1970), Correlation of movements in the Western North Atlantic, *Deep-Sea Res.* 17: 495-511.
- Hubert, W. E. K. G. Hinman, and B. R. Minderhall (1970), The NFWC search and rescue planning program (NSAR), Tech. Note 60: 217 pp., Fleet Numerical Weather Central, Monterey, California.
- James, R. W. (1966), Ocean thermal structure forecasting, SP-105: 217 pp., U. S. Naval Oceanographic Office, Washington, D. C.
- Larson, S. and F. Laevastu (1971), Numerical analysis of ocean surface currents, Tech. Note No. 71-1: 21 pp., Fleet Numerical Weather Central, Monterey, California.
- Leipper, D. F. (1970), A sequence of current patterns in the Gulf of Mexico, *J. Geophys. Res.* 75: 637-657.
- Molinari, R. L. and R. B. Starr (1972), Lagrangian current and hydrographic measurements in the Western Caribbean Sea, abstract in: *Trans. Am. Geophys. Union* 53: 392.
- National Search and Rescue Plan, United States Coast Guard, CG-308, Supt. of Documents, Washington, D. C. 20402.
- Oceanographic Atlas of the North Atlantic Ocean, United States Naval Oceanographic Office (1965), Section I, Tides and Currents, Publ. No. 700, Supt. of Documents, Washington, D. C. 20402.
- Quinlan, F. T. and L. R. Hoxit (1968), A technique for determination of a climatology of high altitude balloon trajectories, Tech. Memo EDSTM 6: 18 pp., Environmental Data Service, Silver Spring, Maryland.
- Rachelett, J. and M. Armendariz (1967), Surface wind sampling for unguided rocket impact prediction, *J. Appl. Meteorol.* 6: 516-518.
- Young, M. J. (1962), Comparison of methods for determining probable impact areas in planning short range instrumented balloon flights, *J. Appl. Meteorol.* 1: 531-536.

USE OF OCEAN TEMPERATURE WHILE COASTING BETWEEN THE STRAITS OF FLORIDA AND CAPE HATTERAS

David J. Pashinski
and
George A. Maul
Environmental Research Laboratories, NOAA
Miami, Fla.

Throughout history seafarers have had a need for familiarity with ocean currents. Beyond exploration, a knowledge of the currents is vital to the safe and expedient transport of the mariner's cargo. An early official recognition of the importance of knowing

the currents came in 1769 when Benjamin Franklin commissioned the printing of the first chart, with the location of the Gulf Stream, to assist the mail packets sailing between England and the Americas (fig. 1). A. D. Bache in 1860, when superintendent of the



Figure 1.--Chart of the Gulf Stream commissioned by Benjamin Franklin when Postmaster General of the American Colonies. The current's existence was noted by Ponce de Leon in 1513 and charts of the feature date back to 1678. English seafarers during colonial times were not aware of the Stream and refused to listen to the advice of American fishermen who took pains to avoid it. This chart confirms the layman's view that the Gulf Stream is a warm river in the sea. Physically, it is a flow along an inclined front separating cold and warm water masses. (See figure 2.)

Coast Survey (which was charged with delimiting all hydrographic features influencing the safety and efficiency of maritime operations) set the tone of future federal investigations of the Stream. He stated, "The Gulf Stream is the great hydrographic feature of the United States coast, and no survey of the coast for the purposes of navigation would be complete without it."

Numerous investigations into the nature of the Gulf Stream have been undertaken by National Oceanic and Atmospheric Administration (NOAA) components and their predecessors, as well as other federal and private groups. Early studies of the Gulf Stream revealed the complexity in the variation of its trajectory. A mean axis, the location of the maximum surface current, was decided upon by 1900 and is still found today on many of the charts of our Atlantic coast. This mean axis is based on the observations of Bartlett in 1880-81 and of Pillsbury from 1885 to 1891. These pioneering and painstaking scientists measured the velocity from anchored vessels. These ships occupied nine transects of the Gulf Stream between the Straits of Florida and Cape Hatteras. In view of modern knowledge about the short-term variability in the location and velocity of the Gulf Stream, the published axis must be accepted for the crude estimate that it is.

A recurring dream of mariners has been that a simple method might be found for identifying and utilizing the maximum surface current of the Gulf Stream to speed their northbound shipping. Con-

versely, southbound vessels need to know the inshore and offshore limits of the current to economize on their passage. Because the Gulf Stream carries the warm waters of the tropical Atlantic northward, the temperature of the sea water has been sought as the answer to this problem since Benjamin Franklin first suggested its use.

The favor of using temperature as an indicator has waxed and waned many times over the years as our knowledge of the nature of the Gulf Stream has grown. The original suggestion of using surface water temperature has been found to be inadequate to locate the desired main current because, in its meandering, the Stream sheds pockets of warm water from its edges and entrains pockets of cold water. Many of these pockets can exist at any one time and so confuse the seaman hoping to find the heart of the current. Because of these problems the use of surface temperature to locate the Gulf Stream has lain dormant for many years.

In 1965, scientists recognized that the Gulf Stream could be reliably located using temperature, not at the surface, but at 200 m. below the surface. Pathlines of Gulf Stream trajectories between Cape Hatteras and the Grand Banks were made from research ships by towing an electric thermometer at a depth of 200 m. and steering along the 15°C isotherm. The 15°C isotherm at 200 m. was chosen because the maximum surface current tends to be centered above it. Thus these pathlines were surface velocity maximum trajectories. The surface maximum velocity

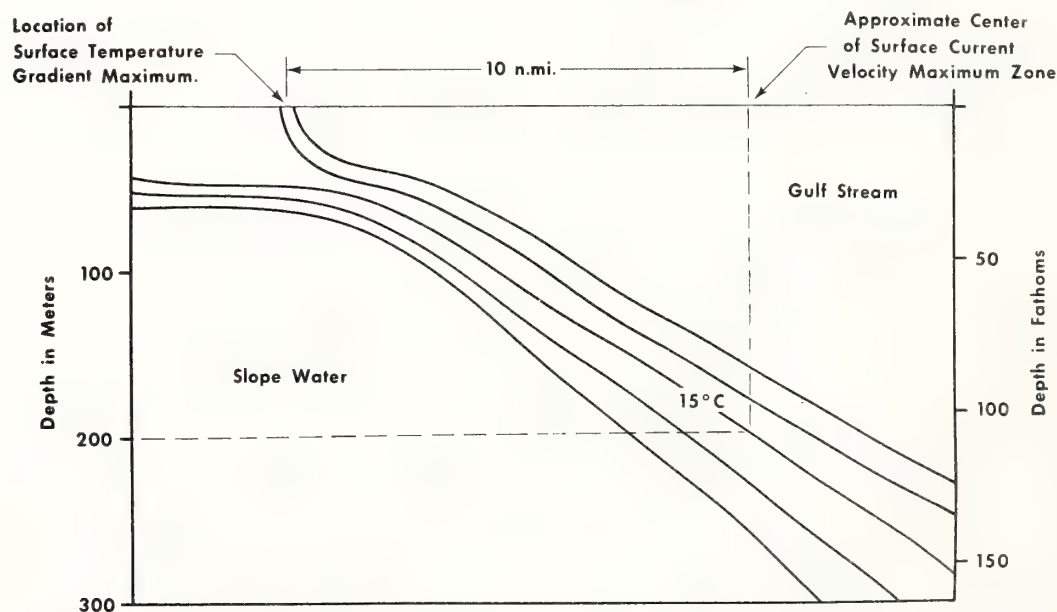


Figure 2. --Schematic temperature cross section of the Gulf Stream; the view is looking downstream, warm water to the right, cool to the left. Other than the 15°C (59°F) isotherm, the values of the lines of constant temperature are arbitrary. The temperature difference at the surface between the Gulf Stream and the slope water ranges from less than 2°C in August to as much as 10°C in March. The horizontal distance between the surface front and the center of the current maximum zone remains fairly constant and appears to be more affected by wind direction than curvature of the stream. The surface temperature change maximum is the boundary feature seen from earth orbiting satellites. (See figure 3.)

zone is about 10 mi wide. Surface current velocities in excess of 2 kt, however, are found over a much broader region which extends approximately 30 to 40 mi seaward from a point several miles on the warm side of the surface temperature change.

Following the indicated isotherm is made easy near the edge of the Gulf Stream because the isotherms are inclined almost 1° , which is very steep oceanographically (fig. 2). The vessel steering along the isotherm will very quickly get an increase in temperature if she should wander too far toward the Sargasso Sea side of the Stream, or a rapid decrease if toward the East Coast.

At first glance, it seems as if the problem of locating or avoiding the Gulf Stream has been solved since relatively economical methods exist for measuring water temperatures at these depths. In fact, attempts to utilize the deep structure in navigating the Gulf Stream were undertaken in 1969. Once again, the complexity of the Gulf Stream was revealed when a large, fairly frequently occurring meander was found between 31.5°N and 33.0°N . On one occasion, the Stream flowed essentially east along latitude 32.5°N to longitude 76.5°W before turning northward to return to the coast. This feature can be understood in light of current theories that take into account the rotation of the earth and the depth of the water.

In these days of rapid ocean commerce, a mariner cannot afford to sail additional miles without a compensating reduction in total transit time. He must know the path and magnitude of the currents that lie before him, so he can best judge the most efficient and safe course for his particular ship with its own speed and handling characteristics. Enough is known about the Gulf Stream to predict a current of at least 3 kt in the surface maximum zone which can represent a boost up to 30 percent for many ships.

Aid in solving this modern statement of an ocean oriented problem is coming from an unlikely source--space. Many meteorological satellites carry infrared scanning devices which yield an image of the heat of the underlying earth. The warm waters of the Gulf Stream stand out nicely in these images (fig. 3), in contrast to the cool shelf waters. This image of the Gulf Stream also shows the meander that frequently occurs off the Carolinas and reveals the value such an image would have to the navigator about to pass through this area. Though the maximum current lies approximately 10 mi offshore of the sharp change from cold to warm water, the resolution of the present infrared scanners is insufficient to reliably locate the surface temperature gradient maximum accurately enough for the mariner. Further, daily coverage is not usually possible because clouds frequently obscure the view of the sea surface. Additional information gained from the deep thermal structure pinpointing



Figure 3. --Infrared image of the East Coast obtained by the NOAA-1 satellite in Feb. 1971. The cold land masses and cloud tops are white, the warmer coastal waters and slope water are grey, and the warm Gulf Stream is black. Note the eastward flow in the offing of Charleston, S.C. This appears to be a quasi-permanent feature of the stream. The inset shows the surface front (dashed) from this image plotted at the same scale as the mean axis (dotted) determined by Bartlett in the 1880's which still appears on modern charts.

the current is required to complement the satellite image.

The future holds much promise. Modest equipment now exists to receive Automatic Picture Transmissions (APT) from meteorological satellites by ships at sea. Likewise, similarly modest equipment is available to get temperature at depth. Ships at sea with APT equipment will be able to obtain infrared images, similar to those in figure 3, from the NOAA-2 meteorological satellite launched in October 1972. Thus, there is the prospect that after nearly 200 yr, Benjamin Franklin's ideas of using ocean temperature to guide and assist ships in commerce will have come to full fruition.

Palaeotemperature and Cohesion in Globigerina Ooze Sediment Cores from the Caribbean Sea

OXYGEN isotope research has provided a means for measuring temperatures of ancient seas, substantially increasing understanding of the broad climatic trends over the past several million years of Earth history. Shear strength measurements of submarine sediments, over the past decade, have given the marine geologist and engineer a clearer understanding of some of the mass physical properties of these sedimentary deposits¹⁻⁴.

I have evaluated the influence of palaeotemperature variations on sediment characteristics related to cohesion. Two sediment cores of Globigerina ooze from the Caribbean were selected (No. P-6304-8, 14° 59' N, 69° 20' W, and 6304-9, 14° 57' N, 68° 55' W). The two cores have been preserved since their retrieval (1963) in the core repository of the Rosenstiel School of Marine and Atmospheric Sciences, University of Miami. Ambient temperature and humidity were, respectively, 4° C and 100%. A total of 81 vane shear measurements were performed at selected depths corresponding as closely as possible to depths at which oxygen isotope analyses of pelagic tests had been determined previously⁵. Shear strengths were measured with a vane shear apparatus using a 12 mm × 12 mm vane, using methods described by Richards². Equations expressing strength as a function of vane size and spring strength have been published by Cadling and Oderstad⁶. Shear strength and cohesion relationships are governed by the equation

$$S = c + \bar{\sigma} \tan \Phi$$

where c is cohesion, $\bar{\sigma}$ is effective stress and Φ is the angle of internal friction. Fine-grained saturated sediments which are stressed without loss of pore water respond with respect to the applied load as if they were cohesive materials with an angle of internal friction equal to zero ($\Phi = 0$). This is a special case in which shear strength is equal to cohesion. Detailed discussion of shear strength may be found elsewhere^{7,8}.

Testing was performed in a refrigerated core storage room to maintain uniform ambient conditions and to prevent excessive

evaporation from the sediment. Each core was cut into sections and each section was split longitudinally, and half of each section used for testing. Measurement of cohesion was made by inserting the vane directly into the core normal to the core axis. Cohesion measured vertically in a core (the usual testing procedure) may differ in absolute value from measurement made normal to the core axis; however, relative rather than absolute values throughout the cores were of paramount importance in this study.

Megascopic examination of both cores revealed an over-all homogeneous, Globigerina-ooze lithology, and average grain specific gravity values determined at three depths in core P-6304-8 ranged from 2.76 to 2.79 showing little variation with depth. Two measurements in the upper section of core P-6304-8 at 6 cm and 13.5 cm gave cohesion values much higher than any other measurement in the core. This was due to some desiccation of the sample, as borne out by visual examination, apparently caused by considerable previous sampling. Consequently, these values have not been included in Fig. 1, set B. Water contents were determined at seven depths in the core below the desiccated area. Values, expressed as % dry weight, ranged from 72–93% indicating negligible water loss throughout the remainder of the core.

In Figs. 1 and 2 the A curves show weight percentages of the sediment fraction larger than 62 μm with core depth. Curves C depict $^{18}\text{O}/^{16}\text{O}$ ratios of the pelagic foraminiferal species *Globigerinoides sacculifera* reported by Emiliani (δ ‰ with respect to the Chicago Standard PDB-1)⁵. The oxygen isotopic ratios are a function of temperature and indicate palaeotemperature variations. Extensive treatment of the analytical methods and interpretation of data are given by various researchers^{5,9–12}. Warm cycles are indicated by 0.0 to –1.0 values and cold cycles by 0.0 to +1.0 values. A marked correlation exists between oxygen isotopic ratios and sediment grain size. Warm periods are characterized by a greater relative abundance of particles (almost exclusively foraminiferal tests) greater than 62 μm in size; cold periods are characterized by a greater abundance of small carbonate particles (mainly coccoliths) and of silt and clay.

The relative values for cohesion throughout the cores are shown in Figs. 1 and 2, sets B. A few high values are found in the upper 300 cm of core P-6304-8 but most values range between 30 and 100 g cm^{-2} . In core P-6304-9 the cohesion ranges between 28 and 78 g cm^{-2} . Despite this large range of values, the relative variation in cohesion with depth for both cores shows a strong relationship to sediment texture and a correlation with palaeotemperature variations. In general, cohesion is higher in sediment deposited during warm periods

and lower in deposits representative of cold periods. Cohesion is not a function of palaeotemperature but rather is influenced significantly by the size of the carbonate tests which are responsive to temperature. These relationships appear to be valid for the depositional environment in the area from which these cores were collected. Similar relationships may not exist for other deep-sea environments.

Correlation coefficients were determined between grain size and cohesion for the two *Globigerina* ooze sediment cores

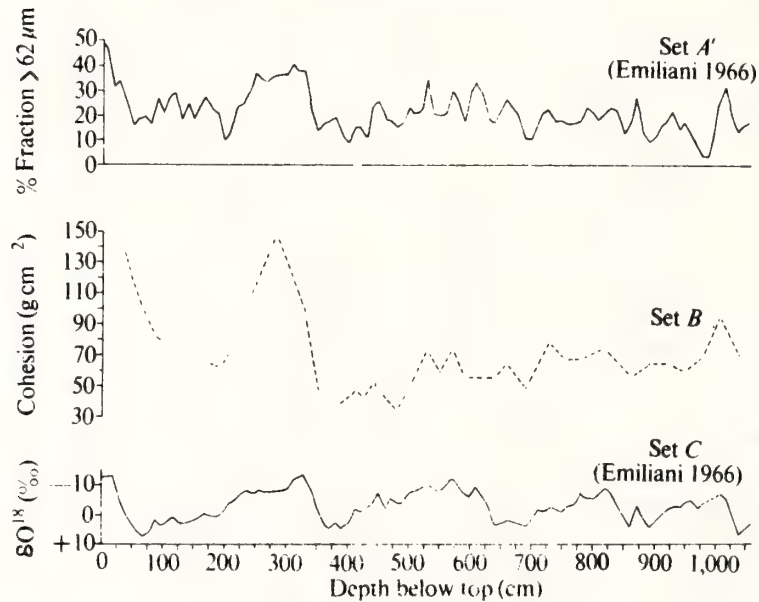


Fig. 1 Core P-6304-8.

using data from the lower portions of the cores to obviate possible effects of desiccation as observed in some areas. Grain size was read directly from the curves in Figs. 1 and 2 corresponding to intervals measured for cohesion. The linear trend of cohesion versus depth was removed before testing for correlation. Unfortunately, the actual grain size analyses ($\% > 62 \mu\text{m}$) did not in every case correspond to the same intervals tested for cohesion; thus the grain size values read from the curves can be considered as approximations only. With this limitation in mind, a correlation coefficient of 0.70 was determined for core 6304-8 indicating a rather strong relationship between grain size and cohesion for this core. In contrast, however, the correlation coefficient for the data of core 6304-9 was 0.10 indicating a rather poor correlation between the two properties. The discrepancy between the two correlation values may reflect erroneous grain size data for the

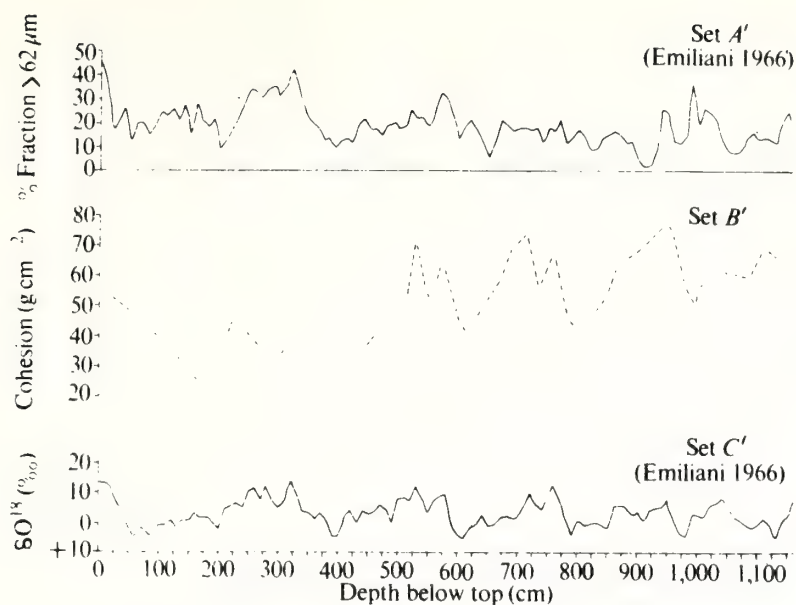


Fig. 2 Core P-6304-9.

selected intervals. Visual assessment of the major fluctuations in cohesion and oxygen isotopic curves indicates, however, an apparent correlation between both sets of data (Figs. 1 and 2). These data indicate a strong requirement for precise grain size analyses corresponding to intervals measured for cohesion.

Other studies^{13,14}, concerning the effect of clay content and grain size on strength of soil mixtures, showed an increase in strength with decrease in grain size and increase in clay content. The results published by Trask and Close¹³ contrast sharply with the present study; however, sediment types used in their investigations were significantly different being composed of clay minerals and sand. An earlier study by Bennett *et al.*¹⁵ of carbonate sediment and the present study indicate a strong influence of sediment texture on cohesion.

In conclusion, relative values of cohesion throughout the cores suggest a strong relationship to variation in texture (% > 62 μ m) and a correlation with palaeotemperature variations. In general, high and low values of cohesion correspond to warm and cold periods of palaeotemperature, respectively. Further research of cohesion versus oxygen isotopic ratios from selected sedimentary environments would substantially increase our understanding of these two important variables.

I thank Cesare Emiliani for the samples and for encouragement and suggestions, and George H. Keller and Kelvin

Rodolfo, for helpful criticism. I also thank Sue O'Brien for drafting the figures.

R. H. BENNETT

NOAA,
Atlantic Oceanographic and Meteorological Laboratories,
Miami, Florida 33149

Received November 10, 1971.

- ¹ Hamilton, E. L., *Geol. Soc. Amer. Bull.*, **70**, 405 (1959).
- ² Richards, A. F., *US Hydrographic Office Tech. Rept.*, 63 (1961).
- ³ Richards, A. F., *US Hydrographic Office Rept.* 106 (1962).
- ⁴ Moore, D. G., *Geol. Soc. Amer. Bull.*, **73**, 1163 (1962).
- ⁵ Emiliani, C., *J. Geol.*, **74**, 109 (1966).
- ⁶ Cadling, L., and Oderstad, S., *Roy. Swed. Geotech. Inst. Proc.*, **2** (1950).
- ⁷ Terzaghi, K., and Peck, R. B., *Soil Mechanics in Engineering Practice*, second edition (Wiley, New York, 1967).
- ⁸ Taylor, D. W., *Fundamentals of Soil Mechanics*, 700 (Wiley, New York, 1948).
- ⁹ Emiliani, C., *Aspects of Deep Sea Research*, NAS-NRC Publication, 473 (1957).
- ¹⁰ Emiliani, C., *Scient. Amer.*, February (1958).
- ¹¹ Emiliani, C., *Science*, **154**, 851 (1966).
- ¹² Bowen, R., *Palaetemperature Analysis*, 265 (Elsevier, Amsterdam, 1966).
- ¹³ Trask, P. D., and Close, J. E. H., *Proc. Sixth Conf. Coastal Engineering*, 827 (1958).
- ¹⁴ Trask, P. D., *Bull. Geol. Soc. Amer.*, **70**, 569 (1959).
- ¹⁵ Bennett, R. H., Keller, G. H., and Busby, R., *J. Sed. Pet.*, **40**, 1038 (1970).

13. PHYSICAL PROPERTIES EVALUATION

Richard H. Bennett and George H. Keller, National Oceanic and Atmospheric Administration, Atlantic Oceanographic and Meteorological Laboratories, Marine Geology and Geophysics Laboratory, Miami, Florida.

INTRODUCTION

The field of soil mechanics has firmly established the importance of sediment mass physical properties as applied primarily to foundation design and problems of sediment bearing capacity and slope stability. In recent years marine geologists have employed a number of soil mechanics principles and tests to study the depositional processes and history of the ocean basins. These studies have dealt mainly with the regional distribution of the physical properties, their relationships to sediment acoustical properties, and the consolidation characteristics of deep-sea deposits (Hamilton, 1959; Richards, 1961, 1962; Keller and Bennett, 1968). Most of the sediment samples and related analyses to date have been restricted to the upper 10 meters of the sea floor due to the limited capability of coring devices. With the advent of the experimental Mohole program and later the Deep Sea Drilling Project (DSDP) came the first opportunity to study sediment physical properties to great depths below the sea floor. The DSDP samples have proved, and are still proving a unique opportunity to study the tectonics, lithology, biostratigraphy, and depositional history of the ocean basins, and particularly the processes of diagenesis which are directly related to changes in mass physical properties.

The measurement of water content, wet bulk density, porosity, relative strength, natural gamma radiation, and acoustical properties has been a standard shipboard practice in the DSDP. The importance of obtaining reliable mass properties data prompted a critical review of the testing procedures and analytical techniques used during DSDP Leg 16. This evaluation uncovered a number of problem areas and the purpose of this discussion is to review not only these areas so that researchers using the information are cognizant of its limitations, but also to offer suggestions for further improvement of physical properties data acquisition, systems, and techniques.

CORE HANDLING AND DISTURBANCE

Sediment cores are recovered in plastic liners within steel core barrels. After a core barrel is removed from the drill string it is cradled in a horizontal position to withdraw the plastic liner. The liner is removed from the core barrel after unscrewing two barrel sections, 20 cm and 27 cm in length, from the lower end of the barrel. The 20-cm section extends below the liner and contains two core catchers and a plastic sock used to prevent the loss of extremely soft sediment. The sock interferes with the sediment in the catcher area and occasionally pieces of the plastic are torn loose and moved well up in the sediment core. Elimination of the plastic sock alleviates some of this disturbance; however, its use is best left to the discretion of the chief scientists.

A steel sleeve 7.6 cm in length is pressed into the lower end of the plastic liner to prevent damage and collapse of the plastic during coring. The steel sleeve and liner are retained in position by the two end sections of the core barrel. The sediment in the core catcher section and in the steel sleeve is usually the least disturbed material of the entire 9 meters of core. Generally, the lower portion of core Section 6 is considerably less disturbed than the other sections. The zero section and Section 1, however, contain sediment that has passed through the entire length of the barrel. This is a length of over 9 meters in the case of the zero section. The greater the distance from the lower end of the core barrel, the higher the degree of disturbance. Some sediment core sections are nothing more than slurries that can be poured easily from the liner.

After the plastic liner is withdrawn from the barrel, six 1.5-meter sections are cut and the zero section is removed (that which is in excess of 9 m). The liner is cut first with a special knife blade and then the sediment is sheared and separated by hand. A recommended method would be to carefully slice the 1.5-meter sediment core with a wire knife or sharp blade after the liner is cut. Shearing and tearing the sediment by hand with the ends of the liner sections disturbs the core section ends excessively and unnecessarily.

Quite often, large pockets of water occur between sediment core segments when sediment does not fill the plastic liner completely. In such cases, the common practice for draining the water is to punch holes in the liner by means of a hammer and a nail. After the water is removed, the separated core segments are pushed together by inserting a cloth-wrapped broom handle into the lower end of the liner. This procedure, of course, is carried out before cutting the 1.5-meter sections. Usually the core segments between the water pockets are not measured, and after they are pressed together at the upper end of the tube, the original segment lengths are unknown. Breaks in the sediment core can yield erroneous GRAPE data in these areas; this is discussed later. The procedure of pushing the sediment core segments together obviously increases sediment disturbance. The original breaks in the core may be undetectable by megascopic examination at the time of lithologic description and subsampling. In cases where liners are not completely filled, a recommended procedure would be to log in all core segments by length, noting areas of water pockets and breaks in their original spatial distribution when collected, and using a specially designed tool compatible with the inside diameter of the plastic liner to carefully place all core segments together.

Ends of selected sediment core sections are sampled for interstitial water chemistry after the liner is cut into 1.5-meter lengths. The sediment is removed with a spatula or large syringe, leaving a sizable void at the end of the

1.5-meter section. These large voids result in core disturbance due to collapse, and the voids contribute to erroneous GRAPE data owing to the removal of sediment.

Core handling on the drilling floor during sectioning and later in the sediment laboratory was observed to be quite rough, with seemingly little concern about core disturbance. Treatment such as hammering holes in the plastic liner to remove water, pushing sediment together in the core liner to eliminate voids, bending the 9-meter core during removal from the core barrel and during its transport on deck all increase the likelihood of core disturbance. This can result in changes in sediment strength, composition, migration of water within the liner, and possible sediment flow. Although truly undisturbed sediment cores can not be obtained with the present coring techniques, sediment disturbance could be minimized substantially by careful core handling.

An extended core head was employed at DSDP 157A in an effort to obtain sediment cores with minimal disturbance. The extended core head passes through the hole in the bit and may extend to the bottom of the bit or further as desired. At Site 157A the core head extended 10 cm below the bit and recovery showed that one out of three cores was in somewhat better condition than when the extension was not used. The technique, however, did not prove as satisfactory as anticipated. Apparently more refinement of engineering design and testing is necessary before an optimum technique is achieved to recover sediment cores showing minimal disturbance.

The type and physical characteristics of the sediment, as well as drilling technique and sea state, are all important to the ultimate condition of the cores. Highly plastic sediment appears to reflect less disturbance than low-cohesion material of high water content. Well-indurated sediment of high strength sometimes shows undisturbed "biscuits" surrounded by an homogenized disturbed matrix. Varying degrees of disturbance are observed, from the undisturbed "biscuit" pieces of sediment to slurries. In general, shearing and flow features can be observed in various types of cored sediment. In the final analysis of the DSDP physical properties data, scrutiny and careful examination of sediment core photographs is strongly recommended.

DISCUSSION OF SYSTEMS AND TECHNIQUES

GRAPE

Wet bulk density and porosity of the 1.5-meter core sections are measured with the Gamma Ray Attenuation Porosity Evaluator (GRAPE), and data are recorded in the form of continuous analog graphs. GRAPE testing is made on a routine basis aboard the *Glomar Challenger* and discussions of the instrument and procedures are given by Peterson, Edgar, et al. (1970). Various aspects of this technique for measuring bulk density have been reported by Richards and Baumgartner (1967), Preiss (1968), Brier et al. (1969), and Bader, Gerard, et al. (1970). A recent study of wet bulk density determination by gamma-ray attenuation was made by Whitmarsh (1971), comparing the DSDP GRAPE data with bulk densities obtained by weighing 1.5-meter core sections aboard the *Glomar Challenger*.

During Leg 16, numerous problems were encountered with the GRAPE and are reviewed in this discussion. In addition, data are presented from a detailed study comparing GRAPE results with shore-based laboratory wet bulk density and porosity values of carefully selected subsamples from Leg 16.

The calibration of the GRAPE is routinely checked using a water-filled plastic tube and an aluminum standard. The two to three minute scans were found to be inadequate in establishing a well-defined curve for each standard. In some instances, a straight-line trace was hardly discernable on the analog. Obviously, if the curves for the standards are not clearly established, the calibration is questionable, resulting in the use of inadequate scales to determine the actual GRAPE values. Furthermore, a poorly defined standard does little to indicate if the instrument is functioning normally prior to measurement of the cores.

Calibration of the GRAPE is usually made before testing each 9-meter core. In many cases, the scales obtained from the standards were considerably different for various tests. These calibration differences resulted in density variations of as much as 0.2 g/cc. In an effort to test for possible drift in the system, standards were run in a stationary position for over one hour but no drift was recorded. Further testing revealed that minor adjustment of the sensitivity of the GRAPE's analog recorder resulted in changes of the density and porosity scale by different magnitudes. Although the cause of the calibration changes was not firmly established, inadvertent movement of the sensitivity adjustment is suggested.

The calibration runs for the aluminum and water standards were checked in detail and found to show considerable variation ranging up to 0.11 g/cc for density and as high as 7 percentage points for porosity. At present, the extreme variability in the GRAPE calibration curves appears to be totally unpredictable. This condition may be due to an inherent characteristic of gamma-ray emission and/or instrumentation. In any case, point values of sediment bulk density and porosity by GRAPE scanning are highly suspect. Average GRAPE values determined over a several-centimeter scan or the 1.5-meter section scan appear to be more reliable and representative than point values.

The occasional occurrence of large pyrite nodules in the sediment tended to reduce porosity values considerably, in some cases to below zero. The presence of small nodules which may not be readily detected megascopically may result in erroneous values.

An effort was made to limit GRAPE measurements only to completely filled, undamaged sections. Warped and damaged core liners have a geometry between the source and sensor abnormal enough to produce error in the GRAPE readings. Section ends are highly suspect and commonly show erroneously high porosities and low bulk densities due to the removal of sediment for analyses of interstitial water chemistry. Breaks in the sediment cores which may not be detected prior to testing, and separations due to water pockets may result in excessively high GRAPE porosities and low bulk densities.

Considerable variation in the wall thickness of the plastic core liners was observed. The possible influence of

these variations on bulk density and porosity measurements was not determined but is undoubtedly a contributing variable affecting GRAPE measurements.

GRAPE Values Versus Shore-Based Laboratory Data

Carefully selected subsamples were collected for shore-based laboratory determination of wet bulk density, porosity, water content, and average grain density from each DSDP site during Leg 16. The methods for determining bulk density and porosity followed procedures described by Bennett and Lambert (1971) and are considered reliable and reproducible to better than ± 0.02 g/cc and ± 1 per cent for wet bulk density and porosity, respectively. GRAPE bulk density and porosity data were determined using the measured values of average grain density from laboratory tests. This gives more reliable GRAPE values than applying an assumed grain density to the calculations (Boyce, R.E. and Woodbury, P., personal communication). Direct comparison of the two techniques was made for wet bulk density and porosity using only the reliable GRAPE and laboratory measurements from the same intervals in the core sections. A relatively high degree of scatter is observed in sediments of higher density, although considerably more measurements were made in this material than in the lower density samples (Figure 1). Bader, Gerard, et al. (1970) pointed out that for wet bulk densities greater than 1.80 g/cc, the error in the GRAPE measurements becomes increasingly large, as high as 10 to 15 per cent for aluminum. The error should be minimized, however, by applying correct grain densities to the calculations, as were applied to the GRAPE data reported here.

These data (Figure 1) indicate clearly that 29 to 30 per cent of the bulk density comparisons differ by more than 0.05 g/cc, and only 36 per cent of the values agree within 0.02 g/cc. Comparison of GRAPE porosity versus laboratory porosity shows that 10 to 11 per cent of the values differ by greater than 5 per cent, and only 56 per cent of these data agree within 2 per cent (Figure 2). The scatter diagrams for wet bulk density and porosity, as well as the statistics, reveal a considerably larger disagreement than is desirable. Certainly, agreement to within 0.02 to 0.03 g/cc for bulk density and 2 to 3 per cent for porosity is not an unreasonable demand for reliable data. These comparisons indicate random scatter which appears at the present time to be unpredictable.

GRAPE Bulk Density Versus Bulk Density by Section Weight

A routine shipboard procedure for measuring wet bulk density is carried out by weighing the 1.5-meter core sections and assuming a constant volume based on core length and inside diameter of the plastic liner. Inherent in this procedure are a few easily recognized difficulties. First is the problem of weighing the 1.5-meter core with the ship in constant motion. The balance is a triple beam type and the method is rather gross. Secondly, any changes in the geometry of the plastic core liner, such as changes in the radius, increase the error in measurement of sediment volume (any error in the radius is squared). Finally, and of equal concern, is the fact that the core sections must be completely filled prior to weighing; this is not always the

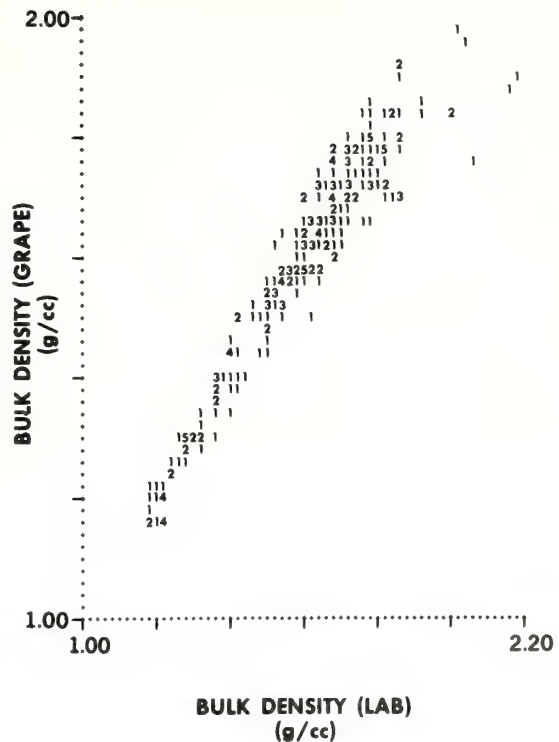


Figure 1. Comparison of GRAPE bulk density with that measured in the laboratory ashore.

case. The technique of weighing the sediment cores to determine wet bulk density, referred to here as bulk density by section weight, is considered only a rough approximation owing to these various problems. For the sake of comparison, however, GRAPE bulk density averages per core section versus bulk density by section weights are plotted in a scatter diagram (Figure 3). These data, as expected, show a relatively high degree of scatter and disagreement between the respective techniques. This scatter is due not only to the inherent limitations of the GRAPE, but also to the rather crude method in determining bulk density by section weighing. Scatter occurs in both high-density as well as low-density sediment, and these data indicate overall higher values as determined by the GRAPE than by the section weight method. This, of course, would be expected when either the core section volumes are less than the assumed values and/or the liners are not completely filled with sediment. An average GRAPE bulk density value determined by scanning the 1.5-meter core sections would tend to average out erroneously high and low values and would be likely to be the more representative than the section weight value.

Subsampling of 15 to 20 grams of sediment from carefully selected portions of the cores complement the

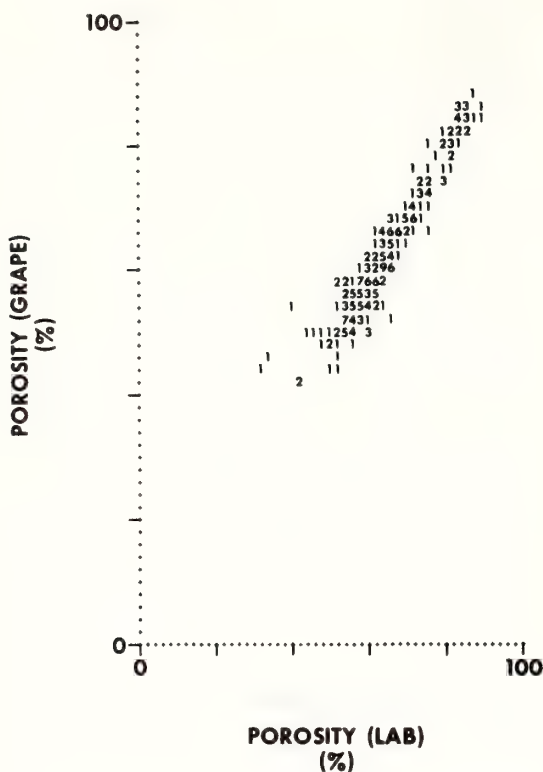


Figure 2. Comparison of GRAPE porosity with that measured in the laboratory ashore.

GRAPE data (average values per 1.5-m section) and ensure that the most reliable sediment mass physical properties data are obtained. When lithologic boundaries occur in a given core section, GRAPE values may be averaged for each lithology.

Syringe Technique

Wet bulk density, porosity, and water content are determined by a routine shipboard technique using a very small (1 to 2 cc) syringe sample, withdrawn from the split core. The open end of the syringe is taped and the samples are stored in an open container in the laboratory, usually for several hours prior to analysis. The sample is examined for possible voids and separations before extruding a given amount of sediment from the syringe. The usual practice is to press the sample against a Kimwipe or a paper towel with the plunger to eliminate voids. This results in an unknown amount of moisture loss into the towel and an unknown change in sediment volume. After this treatment, approximately 0.5 to 1.0 cc of sediment is extruded for weighing and then oven dried for determination of moisture content. The oven-dried samples remain in the

laboratory out of the desiccator for periods of one-half to one hour prior to weighing. The effect of water absorption by the dry sediment is obvious.

Numerous syringes were checked for volume calibration and found to be in error by approximately 0.022 cc. This is a 4.4 per cent error in volume for a 0.5 cc sample.

A comparison was made between shore-based laboratory and shipboard syringe wet bulk densities and porosities using corrected syringe volumes. These data show that 41 per cent of the bulk density comparisons did not agree closer than ± 0.05 g/cc. Most of the 41 per cent fell well outside this range. Only 13 per cent of the porosity values did not agree within ± 5 per cent.

Water content is obtained from the syringe sample by weighing, oven drying, and reweighing to determine moisture loss. Oven temperatures were checked prior to shipboard laboratory analysis of Leg 16 samples and found to range from 106°C to 157°C for different areas in the oven. This was a result of two shelves being completely covered

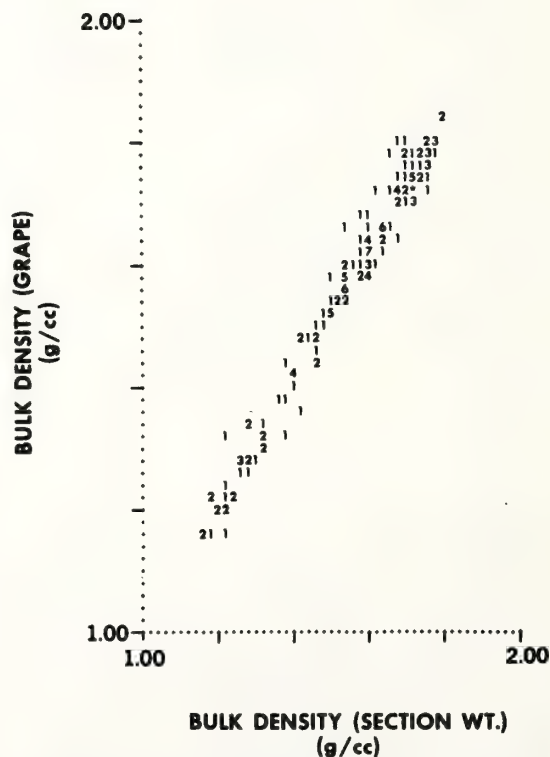


Figure 3. Comparison of GRAPE bulk density with that obtained by weighing of full core sections.

with aluminum foil which drastically affected air circulation. Personal communication with shipboard technicians revealed that the foil had been placed in the oven several months prior to Leg 16 and perhaps as much as one year earlier. The foil was removed and the temperature conditions rechecked. An even temperature was then maintained throughout the oven for Leg 16 analysis (1967, ASTM standard for water content measurements, 110°C). All water contents and porosities previously determined when the shelves were covered with foil are highly suspect. The combined difficulties in determining wet bulk density, porosity, and water content using the syringe technique include not only volume determination and weighing accuracy, but also water loss due to pressing the sediment on a towel, compaction of the sample, and the use of extremely small samples (500 to 800 mg). Shipboard weighing errors appear to be minimal, usually less than 1 per cent of the observed value for samples of 500 to 800 mg (checked during Leg 16). Tests with 20, 10, 5, and 1 mg standards were found to have percentages of error of 0.5, 2, 4, and 10 per cent, respectively. Obviously, the use of very small samples poses problems by magnifying any error that occurs during preparation of the sample and while testing.

Bulk densities and porosities were consistently low as compared with GRAPE measurements before volume corrections were applied to the syringe values. Bader, Gerard, et al. (1970) found that GRAPE porosities were generally 10 per cent higher than water-content-volume data. They also estimated weighing errors of approximately ± 1 per cent and error in syringe volume of less than 5 per cent. This agrees well with the present study, indicating that problems with the syringe technique existed for quite some time. The entire technique is plagued with problems and should be abandoned. As a recommended procedure, the shipboard geologist should carefully select 10 to 20 gram subsamples in the least disturbed areas of the cores and place them in vials which can be sealed against moisture loss. The vials should be completely filled to prevent condensation and kept under refrigeration while aboard ship. Samples can be analyzed at a shore-based laboratory following standard techniques for measuring water content and average grain density (Lambe, 1951) and the techniques described by Bennett and Lambert (1971) for determining wet bulk density and porosity.

Natural Gamma Radiation

Natural gamma activity is measured on a routine basis aboard the *Glomar Challenger*. The 1.5-meter core sections are scanned in 7.6-cm intervals, each for a period of 75 sec, measuring total counts of activity. Shipboard handbooks indicate that the total volume of core scanned for 75-sec intervals is greater than the volume of the 7.6-cm core segment. Apparently the actual volume of sediment scanned per interval never has been assessed. At present only a relative measure of activity is obtained from the raw data. If the volume of sediment scanned per unit time were known and wet bulk density, water content, and average grain density were obtained from other tests, the volume of the dry sediment scanned could be determined

easily, resulting in more useful data. From these parameters a "radiation index" could be derived, relating the total number of gamma counts (activity) per unit time per unit volume of dry sediment. Natural gamma activity could be compared directly with depth throughout the lithologic sections and an assessment of the degree of correlation among different lithologies and their gamma activity characteristics would then be realized.

Due to the high degree of sediment disturbance in many cores, the natural gamma activity data is not necessarily representative of in situ conditions. However, if vertical mixing within a given lithology is limited, the values are probably fairly representative since the activity is not dependent upon the undisturbed physical properties of the sediment. Measurements are time-consuming, requiring approximately 25 minutes per 1.5-meter core section, and testing should be limited to carefully selected, completely filled plastic liners. Separations in the sediment and incompletely filled liners such as the ends of certain sections show abnormally low activity values. Usually data from the middle portion of 1.5-meter sections are the most reliable.

Sonic Velocity

Numerous sonic velocity measurements of selected sediment samples and of prepared samples of basalt were carried out during Leg 16 using the Hamilton Frame with the compatible electronic gear. The instrumentation and techniques are thoroughly discussed by Boyce (in preparation). The instrumentation is considered reliable; however, a number of problems were encountered which require attention in order to obtain useful data. Sonic velocities were measured on sediment samples removed from the core liners and also on sediment retained in the split core liners. Repeated measurements were made on the same sample whenever possible in order to obtain an approximation of the reproducibility of the method and an indication of operator technique. Velocities were remeasured on the same sample immediately following the initial test. Operator technique was found to be extremely erratic, and occasionally sonic velocities obtained by different technicians resulted in variations as great as 0.25 km/sec on the same sample. Velocity variations obtained from reruns by the same operator resulted in differences as high as 0.19 km/sec. Of the 472 reruns, 72 per cent of the values showed a variation of ± 0.01 km/sec or less. Although considerably higher variations were observed in 28 per cent of the cases, this method for determining sonic velocities appears to be generally reliable. Based on these data and tests made by Boyce (personal communication) measurements are reproducible to ± 1 per cent, provided operator technique is consistent. These findings reveal a strong requirement for a consistent technique in order to minimize operator error.

Sonic measurements of sediment retained in split core liners are routinely corrected for travel time through the liner and for liner thickness, using values of 1.18 microseconds and 2.56 mm respectively. Several checks of liner thickness revealed considerable variation ranging from 0.47 to 3.91 mm. Assuming the sonic velocity through plastic liners is constant, which implies uniform

properties of the plastic from core to core, and then adjusting the travel time to correspond to the different liner thicknesses found, the sediment sonic velocities differ by as much as 30 m/sec as compared to velocities determined using the routine corrections. A few measurements indicated that the sonic velocity through the liners may not be constant for different liners. Testing must include measurement of liner thickness and travel time through the liner in order to apply corrections to the data.

A further complication of in-liner velocity measurement is the unknown thickness and effect of the disturbed sediment in contact with the plastic liner. Most cored sediment exhibits this disturbed zone and the effect on the sonic velocity measurement is usually ignored. The most reliable sonic measurements are made on sediment that can be removed from the liners and placed directly in the Hamilton Frame. This direct method should be employed whenever possible.

Velocity tests should be made as rapidly as possible and the sediment sampled immediately following testing to minimize water loss due to evaporation. A few sonic tests were made on basaltic samples, and in one case a variation of 1.00 km/sec was observed for the same sample. Other samples, however, revealed a considerably lower degree of variation between reruns. This high degree of variation is considered to be a result of operator technique. The reader is referred to a study by Christensen (this volume) of velocities in basaltic rocks from Leg 16. Leg 16 samples were tested after they had reached ambient temperature and no corrections were applied to the data for in situ temperature and pressure because most of the velocity measurements did not warrant such refinement.

Sediment Shear Strength

Prior to Leg 16, testing of sediment strength with an asphalt (AP-210) penetrometer was a routine procedure. The instrument was designed for use on asphalt and has not proven to be suitable for use on sediments. These tests have provided no quantitative strength data and only rough approximations of relative strength in a limited number of cases. Use of the asphalt penetrometer aboard the *Glomar Challenger* should be terminated.

Vane shear testing holds much more promise of providing strength data and the technique was first employed on Leg 16. Vane shear tests were made on sediment retained in the core catchers and steel sleeve by inserting a standard four-bladed vane (2.54-cm high \times 1.27-cm diameter) parallel to the core axis. These core samples proved to be the least disturbed and usually the most amenable to vane testing. Testing is commonly made on both the "undisturbed" and remolded sediment which provides a measure of the sensitivity (ratio of undisturbed strength to remolded strength) of the sediment and an indication of possible core disturbance.

After vane testing in the catcher and/or sleeve sample, the sediment was extruded and split open for assessment of coring disturbance. Sediment samples were collected for later physical properties measurements at a shore-based laboratory. A detailed discussion of vane shear testing of submarine sediments is given by Richards (1961).

Valuable and reliable data can be obtained by making vane shear tests on high quality, relatively undisturbed

Glomar Challenger sediment samples, but only if tests are made on relatively undisturbed sediment. Close inspection for disturbance must be made before accepting the data as significant.

During Leg 16 the Swedish Fall Cone penetrometer was tested in carefully selected cores showing minimal disturbance. The fall cone must be calibrated with vane shear measurements in order to obtain reliable quantitative shear strength data. Calibration depends on sediment type and the degree of disturbance, which is a function of sampler design. The fall cone values obtained during Leg 16, therefore, are most useful as a measure of relative strength because the instrument can not be accurately calibrated due to the variable degree of sediment disturbance. Other problems occasionally encountered were ship vibrations causing premature triggering of the instrument and artificial penetration of the fall cone. This required immediate readings to obviate the settling effect due to vibration. The reader is referred to a detailed study by Hansbo (1957) of the Swedish Fall Cone penetrometer.

SUMMARY

The DSDP Leg 16 evaluation of techniques and systems used in the shipboard determination of physical properties, as well as detailed shore-based analyses, has clearly revealed the urgent need for (a) high quality sediment cores; (b) the elimination of poor techniques and instruments; (c) the use of reliable methods and instruments; and (d) precise measurements by well-trained technicians who are cognizant of the basic care necessary to obtain reliable physical properties data. Instruments and techniques used aboard ship need to be checked by shipboard scientists and technicians on a regular basis. Frequent communication among geologists and technicians is of paramount importance, not only in maintaining high quality performance, but also in detecting instrument failures and related problems.

A high quality physical properties program demands that only carefully selected sediment cores showing minimal disturbance be used for testing and sampling rather than making routine measurements at some specified interval. For an effective study of mass physical properties, subsamples must be collected and carefully sealed in vials for shore-based analyses of wet bulk density, porosity, water content, and grain density. Average values from GRAPE scanning are more reliable than discrete point values. Determining bulk density by weighing core sections aboard ship contributes neither useful nor reliable data. The syringe technique for determining water content, wet bulk density, and porosity should be terminated. The technique is not reliable and is plagued with many problems.

Strength tests with the asphalt penetrometer have not provided useful data and should be discontinued and replaced with vane shear measurements performed in carefully selected cores. Vane measurements in the core catchers and steel sleeves usually provide the most reliable data owing to the lower degree of sediment disturbance commonly observed in these intervals as compared to most core sections. Vane shears of the undisturbed and remolded sediment are important for estimating sediment sensitivity and possible sampling disturbance.

Sonic velocities measured by a single technician for an entire cruise are highly desirable in order to minimize variations due to operator technique. Tests made on samples removed from the core liners are more reliable than in-liner measurements. When in-liner tests are made, however, liner thickness and travel time through the liner must be determined. Reruns and frequent calibration are important to ensure the reliability of the velocity data.

Natural gamma activity measurements are considered reliable on a relative basis provided vertical mixing is limited. More useful data could be realized, however, if the total volume of sediment counted were known. A "radiation index" could relate the number of counts (activity) per unit time to the unit volume of dry sediment and direct comparisons could be made both vertically and horizontally.

REFERENCES

- American Society for Testing and Materials, 1967. 1967 Book of A.S.T.M. Standards, Part II. Philadelphia (A.S.T.M.). 669.
- Bader, R.G., Gerard, R.D. et al., 1970. Initial Reports of the Deep Sea Drilling Project, Volume IV. Washington (U.S. Government Printing Office). 753 p.
- Bennett, R.H. and Lambert, D.N., 1971. Rapid and reliable technique for determining unit weight and porosity of deep-sea sediments. *Marine Geol.* **11**, 201.
- Boyce, R.E. (in preparation). Initial Reports of the Deep Sea Drilling Project, Volume XV. Washington (U.S. Government Printing Office).
- Brier, C., Bennin, R. and Rona, P.A., 1969. Preliminary evaluation of a core scintillation counter for bulk density measurement in marine sediment cores. *J. Sediment. Petrol.* **39**, 1509.
- Hamilton, E.L., 1959. Thickness and consolidation of deep-sea sediment. *Bull. Geol. Soc. Am.* **70**, 1399.
- Hansbo, S., 1957. A new approach to the determination of the shear strength of clay by the fall-cone test. *Proc. Roy. Swedish Geotech. Inst.* **8**, 1.
- Keller, G.H. and Bennett, R.H., 1968. Mass physical properties of submarine sediments in the Atlantic and Pacific Basins. *Proc. Intern. Geol. Congr.*, 23rd, **8**, 33.
- Lambe, T.W., 1951. *Soil Testing for Engineers*. New York (John Wiley & Sons, Inc.), 165.
- Peterson, M.N.A., Edgar, N.T. et al., 1970. Initial Reports of the Deep Sea Drilling Project, Volume II. Washington (U.S. Government Printing Office).
- Preiss, K., 1968. Non-destructive laboratory measurement of marine sediment density in a core barrel using gamma radiation. *Deep-Sea Res.* **15**, 401.
- Richards, A.F., 1961. Investigations of deep-sea sediment cores, I. Shear strength, bearing capacity and consolidation. U.S. Navy Hydrographic Office, Tech. Rept. **63**.
- Richards, A.F., 1962. Investigations of deep-sea sediment cores, II. Mass physical properties. U.S. Navy Hydrographic Office, Tech. Rept. 106.
- Richards, A.F. and Baumgartner, T., 1967. Continuous nondestructive measurement of bulk density by gamma ray transmission through sediment inside core barrels (abstract). *Proc. 7th Intern. Sediment. Cong.*
- Whitmarsh, R.B., 1971. Precise sediment density determination by gamma-ray attenuation alone. *J. Sediment. Petrol.* **41**, 882.

CARBONATE SEDIMENTS AND THEIR DIAGENESIS

By Robin Bathurst

Published by Elsevier, New York; 1971; 620 pp.

Reviewed by Robert S. Dietz, NOAA, Atlantic Oceanographic and Meteorological Laboratories, Miami, Fla. 33130

This monograph, volume no. 12 in Elsevier's series on *Developments in Sedimentology*, is a welcome addition to the science of modern carbonate sedimentation. The book is a high-quality production of excellent format, style, and balance. However, the endless summaries of recent results make for difficult reading. It is well illustrated and contains a list of 1200 references, making it useful either as a text or source book. While some students are likely to falsely equate oceanography with scuba diving, carbonate sedimentology is perhaps the one branch of marine geology where diving scientists have made a major contribution.

Subjects covered in this text are: the petrography of carbonate skeletal structures; the nature of oolites, pisolites, pellets and various micritic fabrics; the regions of active carbonate deposition (the Bahamas seem to have become the mecca of the carbonate geologist. End-on-end field trips sponsored by oil companies, universities, NSF and others now trek across these banks); algal stromatolites, which are characteristic of the Precambrian but have counterparts being deposited in shallow carbonate environments today; the chemistry of carbonate deposition and relationships between aragonite, calcite and dolomite; considerations concerning the growth of oolites, pisolites and graptolites; diagenesis in the subaerial fresh-water environment and in the marine environment; the process of cementation and lithification; pressure-solution phenomena, for example, the formation of stylolites; neomorphic processes in diagenesis (neomorphism is defined as a "comprehensive term of ignorance to embrace all transformation between one mineral and itself or a polymorph..."); recent dolomites, the deposition of primary dolomite and the diagenetic transformation of limestone into dolostone. The last is one of the great problems of carbonate sedimentology and is of special interest to oil geologists, as it develops the porosity necessary for the accumulation of petroleum.

It is a telling comment on the present environmental problems that a Coke can rather than the geologist's hammer is frequently used for indicating scale in underwater photos.

In summary, Dr. Robin Bathurst (Univ. of Liverpool) has prepared a handsome and authoritative volume which can be recommended to marine scientists generally. However, the new language of carbonate geology leaves one longing for easily readable texts like Twenhofel's *Treatise on Sedimentation* and the old times when science was simpler.

The Bahamas Enigma

By ROBERT S. DIETZ

*NOAA Atlantic Oceanographic and Meteorological Laboratories
Miami, Florida*

THE BAHAMAS long have been a geologic enigma. Although a realm of water where only an occasional island or cay breaks the surface, the entire Bahama platform hugs sea level so closely that from the air one can clearly see the coral bottom everywhere. If just a few fathoms of water were removed, the platform would appear like a giant crescent, half the size of Texas, plastered against southeastern North America, Cuba and Hispaniola. The Bahamas belong to the continent because this platform is separated from the abyssal Atlantic by a 3-mile-high continental slope which is the world's most precipitous.

Because of this near-vertical slope, University of Miami oceanographers a few years ago suggested that it might be feasible to drill a Mohole, a drill hole to the earth's mantle beneath the ocean crust, from the island of San Salvador at the edge of the Bahama platform. Such a drill hole, of course, would have to be whipstocked or curved towards the ocean so as to end up in the mantle beneath the seafloor, but it would have the advantage of be-

ing drilled from dry land rather than from a ship, which would be more complicated and costly.

A Blanket of Limestone

Unlike Australia's Great Barrier Reef where the coral reefs are only skin deep, those of the Bahamas extend to depths of 3 to 4 miles so that it probably is the world's largest deposit of modern (Cretaceous to Recent) limestone. Ultradeep drill holes in the search for oil reveal only flat-lying, structureless coral-algal limestone, all of which was deposited in shallow water not more than a few fathoms deep. In the driller's lingo, the Bahamas are "all vanilla." The shallow-water character of the limestones means, of course, that they had a remarkable history of steady sinking over the past 150 million years, with continuous addition of fresh shallow deposits over the sinking mass.

One might at first suppose that the Bahama platform is sort of a giant atoll. As Charles Darwin correctly surmised, the atolls of the Pacific are the "gravestones" of departed volcanoes.



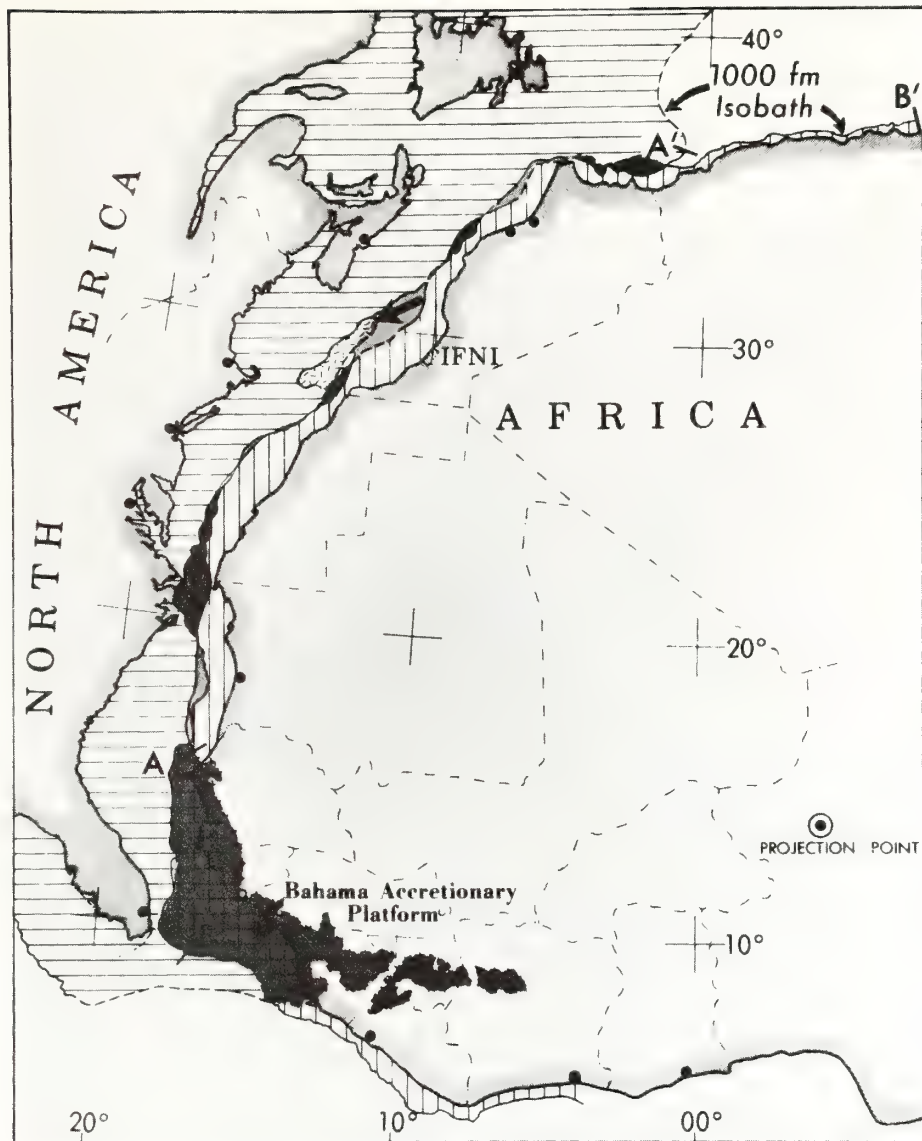
NASA

THE GREAT BAHAMA BANKS and the Tongue of the Ocean (looking north). Running diagonally across the middle from upper left to lower right is the Exuma chain of islands. Above these to the right is Cat Island, with Exuma Sound lying between. To the left of the Exumas is the Tongue of the Ocean, over 1 mile deep, while depths on the Bank vary from 6 to 30 feet. The lower left shows the bottom topography (sand gullies) at the head of the Tongue of the Ocean.

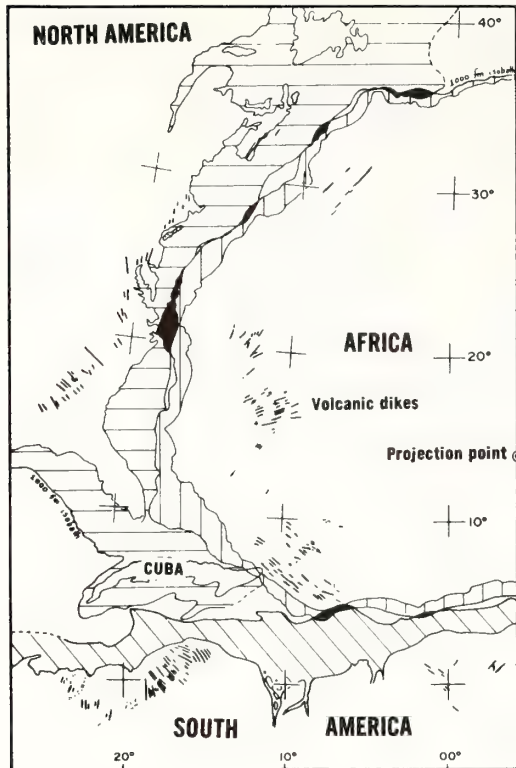
As volcanic islands are eroded into banks and then slowly sink beneath the sea, coral reefs attach themselves and, by growing upward, offset the subsidence and so maintain a sea-level freeboard. Such limestone upbuilding doubtlessly applies to the Bahamas as well, but in other respects their similarity to atoll formation ceases. The

Bahamas probably are larger than all of the Pacific atolls combined and the limestone blanket is much thicker—thicker than the ocean is deep, a situation never found on atolls.

A second mystery concerning the Bahamas may be termed the continental-drift overlap problem. The reality of continental drift has been



THE FIT OF AFRICA against North America 200 million years ago, before the two continents drifted apart. This is a computerized fit between the points A to A' on the North American continental slope and B to B' on the African margin which matches the 6,000-foot depth curve (isobath), so as to minimize the total misfit—that is, the gaps (blue) plus the overlaps (red and orange). The Bahama platform created a large overlap (orange) onto Africa. This suggests that this platform is “new ground” entirely created subsequent to the drift of North America away from Africa. The stippled area off Ifni is the West Canary Islands block, which is thought to have slipped out of the Ifni gap (black arrow).

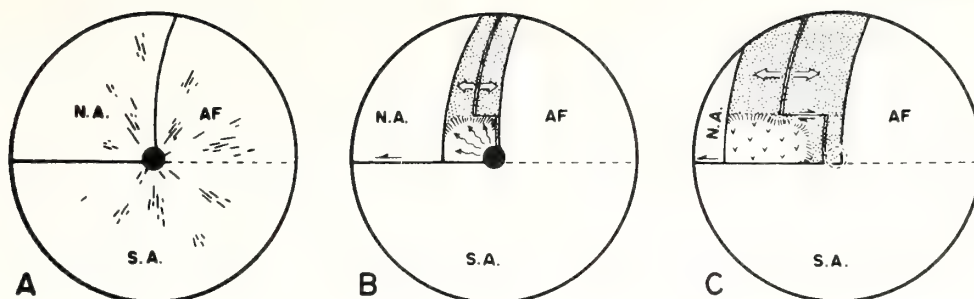


DIKE SWARMS. *The pre-drift fit of Africa/North America/South America is shown with the Bahama overlap removed. The short black lines are Triassic and Lower Jurassic volcanic dikes simultaneously injected into all three continents 180 to 190 million years ago. The strike of these dikes converges toward the region of the Bahama platform, suggesting that this was the site of a "hot spot," a giant plume of volcanic magma which rose from deep within the earth's mantle. These volcanic effusions probably form the basement upon which the Bahamian limestones were subsequently deposited. This plume also may have provided the force that rifted North America away from Africa/South America. The solid black areas are overlaps in the fit.*

virtually established in the past few years. Geologists now believe that all of the continents were joined into the universal continent of Pangaea 200 million years ago. This, in turn, means that the Atlantic Ocean did not exist, the bulge of Africa being in close contact with eastern North America. If we push the continents as they now are back into this original position, we find the fit to be a snug one *except* that the Bahamas would form a large overlap onto the continent of Africa. Since two pieces of continent, of course, could not have occupied the same space, the Bahamas could not have existed in pre-drift time. The most likely explanation is that they are "new ground." (Certain other solutions are possible, such as rotating the Bahamas into the Gulf of Mexico gap, but are highly unlikely.) Therefore, the Bahamas cannot be underlain by the same kind of ancient rock as that which underlies the rest of North America, a basement complex or shield of ancient folded and metamorphosed Precambrian rocks. An acceptable theory must account for the origin of the entire Bahama platform at a much later date, during the last few percent of geologic time, since the post-Triassic.

Hot Lava Plumes

In terms of the recently acquired new understanding of the ocean floor, the concept of plate tectonics, it is, however, possible to offer a reasonable geologic history of the Bahama platform. It seems likely that a giant plume or "hot spot" of lava from deep within the mantle arose at the Bahama site. Such plumes may be likened to thunderheads in the atmosphere which rise



ORIGIN OF A BASEMENT. *In the midst of the Pangaea universal continent, a hot spot (black dot) was born 190 million years ago (A). Dikes, injections of lava, extended out from the hot spot—and these remain today as the only unburied evidence for it. North America was blocked out by fracturing associated with the intrusion of the hot spot. As shown in diagram B, the hot spot rose from the fixed deep mantle of the earth, while Africa/South America remained fixed with respect to the earth's spin axis. North America drifted westward. A new ocean basin, the proto-Atlantic, was created, paved by the process of sea-floor spreading. Since sea-floor spreading involves the symmetrical splitting of dikes ("crack-fillings") at the mid-ocean ridge, this ridge migrated westward at one-half the rate of North America, thus maintaining its mid-ocean position. Lavas from the hot spot spilled westward into the oceanic void, creating the Bahama platform basement. The hot spot died about 170 million years ago, and a new southern segment of the mid-ocean ridge commenced to migrate westward (C). It was earlier held adjacent to Africa by the magmas of the hot spot which "overprinted" and prevented migration of this ridge by sea-floor spreading. The Bahama platform basement (v symbols) was created on the North American plate. Corals subsequently grew on the platform and maintained a sea-level freeboard by upbuilding as the platform subsided. This history accounts for the construction of the Bahama platform in a remarkably short time; the absence of a mirror-image platform on the Africa margin, a normal expectation under generation of ocean basins by sea-floor spreading; and the asymmetrical position of the "mid-ocean" ridge in the southern sector of the North Atlantic Ocean.*

by the upward convection of a cylindrical tube of warm moist air which then spreads out into the observable mushroom cloud. This lava plume even may have provided the driving force which split North America away from Africa and opened up the proto-

North Atlantic Ocean 190 million years ago.

With the drifting away of North America from Africa, a giant volcanic center developed at the Bahamas like the island of Iceland today whose volcanoes currently spew out about one-

third of the world's molten rock. Today we have no observable record of this outpouring in the Bahamas. Such rocks presumably are deeply buried beneath limestone beyond the reach of drilling. This suggestion is not gratuitous, however, as similar rocks in the world's most extensive dike swarms (solidified lava intrusions) of the appropriate age (180 to 195 million years old) exist on three continents—North America, South America, and Africa—peripheral to where the Bahamas region would have been before continental drift. The Palisades sill along the Hudson River is, for example, a remnant of this massive and far-reaching extrusion of basaltic lavas. Significantly, these dikes converge towards the Bahamas, when the continents are placed together under a predrift reconstruction, indicating that this must have been a giant volcanic center.

Giant Crack-Filler

The drifting of continents apart involves relative motions. It is usually impossible to tell which continent has moved in an absolute sense—that is, relative to the earth's spin axis. Hot spots, however, may provide an answer as these plumes rise from the deep mantle which seems to be fixed in the absolute sense. In addition, hot spots interfere with or "overprint" sea-floor spreading, which is the process by which a new ocean floor is generated.

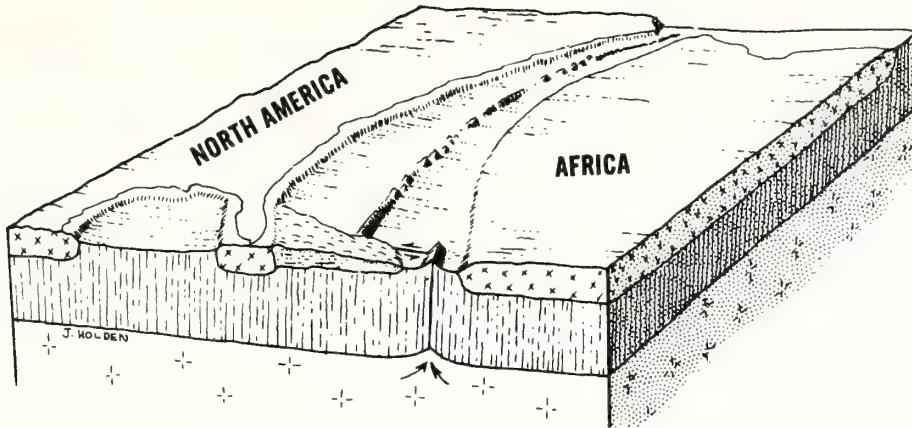
Normally new ocean crust is generated at a mid-ocean ridge, a rift in the 60-mile-thick lithosphere which is slowly opening. Dikes of lava intrude this spreading rift as a giant crack-

filler constantly healing this wound. As a new dike solidifies and the opening continues, the dike is symmetrically split apart so that equal accretion occurs on each wall of the rift pull-apart. It may be likened to inserting a new card into a card deck placed on end and then splitting this new card in half. Thus, new ocean floor is created and paved like the back-to-back unrolling of two window shades. This process is remarkably symmetrical and explains why the rift, as the mid-ocean ridge axis, remains almost precisely in mid-ocean, equidistant between Africa and North America.

Precise symmetry usually results, but, when the Bahamas were blocked out in the early opening of the Atlantic Ocean, this process met with interference. We know this because the mid-ocean rift is not now in the mid-ocean position between Florida and Portuguese Guinea, the points which were originally juxtaposed before continental breakup. Actually the rift along this continental-drift flow line is about 650 miles closer to Africa than to America. In contrast, the mid-ocean position of the axial rift *is* maintained farther north between Africa and North America north of the Kane fracture zone.

Unbalanced Sea-Floor Spreading

The following explanation seems to be appropriate. During the early opening of the Atlantic, Africa remained fixed and so did the hot spot. This hot plume then apparently thermally dominated or "overprinted" the usually symmetrical sea-floor spreading, causing asymmetrical sea-floor spreading as North America drifted away. In



THE ABNORMAL OUTGROWTH. *The Bahama platform was attached as an excrescence of "new ground" off North America shortly after the death of the hot spot. Within the proto-Atlantic, a transform fault connected the two segments of the Mid-Atlantic Ridge, and dikes of lava acted as a crack-filler. As the African and North American plates moved apart, one-half of the dike upon cooling was accreted to each plate while a new hot dike was injected. The process may be likened to a deck of cards on end into which a new card is repeatedly inserted in mid-deck. It then splits into two equal halves.*

other words, the dikes injected at the mid-ocean rift did not split in two but accreted entirely to the North America plate. The rift therefore remained positioned along the African margin while an oceanic void was created on the American plate into which the volcanic effusions poured, building the Bahama platform. Eventually, after about 20 million years, the hot spot died. With this extraneous heat source turned off, normal symmetrical seafloor spreading commenced so that the

mid-ocean rift moved away from the African margin. This history would account for modern asymmetry of the mid-ocean rift (at the Dolphin fracture zone) between Florida and Portuguese Guinea on the African margin. It would also explain why the Bahama platform is attached to North America and not to Africa. There is only a small mirror-image excrescence on the African margin, the Guinea marginal plateau indicating minor deposition of volcanics on the African plate.

8.3

ROBERT S. DIETZ

*NOAA, Atlantic Oceanographic &
Meteorological Laboratories
15 Rickenbacker Causeway
Miami, Florida 33149, USA*

Morphologic Fits of North America/ Africa and Gondwana: A Review

Introduction

The purpose of this paper is to review morphologic fits as applied to continental drift reconstructions and especially the reconstruction of Gondwana. The appearance of a fit between continents has, of course, been the classic inspiration for drifters since the time of Wegener and even before.

Morphologic fits should be based upon the matching 2000 m or 1000 fm isobaths, as this contour is approximately equal to one half of the isostatic freeboard of continents (Carey 1958). It is understandable, however, that Bullard *et al.* (1965) obtained a better fit by matching the 500 fm (~1000 m) isobaths, as the 2000 m isobath is more apt to be displaced by sedimentary and volcano-tectonic excrescences. In those cases where the 2000 m isobath falls beyond the continental slope, my method has been to use an extrapolated or inferred former position of the 2000 m isobath by projection of the slope of the continental slope.

One can surmise many possible reasons for misfits in continental drift reconstructions. A few are indicated here, but the list is not intended to be complete. It is remarkable that the continents did break apart rather cleanly as evidenced by the close congruency between Africa and South America. Both Wegener and du Toit were satisfied with the mere semblance of a fit between these two continents and did not bother to test the fit precisely. They argued that the exigencies of geologic history were such that the margins did undergo major changes of outline. Wegener also supposed that the Mid-Atlantic Ridge and certain island groups such as the Cape Verde Islands were sialic. If this were true, they would need to be incorporated into the jigsaw-puzzle fit.

Gaps or underlaps generally are more difficult to account for than overlaps. Possibly there is some logic for making computerized fits based on some criterion which minimizes gaps at the expense of permitting considerable overlap. Basaltification or 'oceanization,' whereby the sialic craton is engulfed, foundered, and converted to sima, is a commonly offered explanation for such things as the disappearance of hypothetical Appalachia. While basins such as the North Sea basin and the Michigan basin commonly form within cratons, I doubt that the complete assimilation and disappearance of a craton is a real geologic process.

Tectonic translation by strike slip, but without detachment of the shifted block from the craton, may be one explanation for a gap. In this case the gap should be compen-

sated by an equal area of overlap nearby. Tectonic detachment of a marginal sialic block through sea floor spreading associated with continental drift is another possible way of producing gaps. In this case the microcontinental block should be preserved in the new ocean basin. The Seychelles Islands are presumably an example.

So far as overlaps are concerned, sedimentation on the continental slope causes a post-rift accretion. This is especially true if a delta pile is imposed. The Niger delta may be regarded as the type example, for it forms a large overlap in the fit between Africa and South America. The continental slope off Louisiana and Texas offers another example. There the continental margin has been extensively built outward by the emplacement of a series of depocenters, creating a smeared deltaic pile which has migrated eastward along Texas to the present debouchment of the Mississippi River off Louisiana. Even in the absence of deltas, some sediment may be carried across the shelf and prograde the margin over oceanic crust, but such accretionary elements must be of small scale causing only minor irregularities in the fit.

Special problems and complexities are associated with Y-junctions, or triple points. The development of the Afar triangle in the Red Sea at a Y-junction between three crustal plates is a case in point. A large area of new ground apparently has been created with a complex volcano-tectonic history. It seems likely that ancient equivalents of such regions are now preserved as marginal plateaus. The Naturaliste Plateau off the southwest point of Australia may be an example, and many others could be cited.

Africa to North America Fit

The Africa to North America fit is critical to drift reconstructions, as it forms the principal join between Gondwana and Laurasia. The failure of this fit would mean (to drifters) that the continents were once configured into the supercontinents of Laurasia and Gondwana, but not into a Pangaea. The congruency as, for example, achieved by the Bullard fit at first was unconvincing to many drifters, including myself, but a re-examination of this fit supports its validity.

Our fit (Dietz *et al.* 1970), as shown in Fig. 1, is similar to the Bullard fit, but with less total mismatch; also it is somewhat looser in that the Guinea Nose (near the southern end) is placed about 200 km west of the Bullard position which overlaps about one third of Florida. Also unlike the Bullard fit, a snug congruency is attained between Morocco and North America which argues that this portion of the African craton has remained rigid and has not been appreciably crumpled or translated by Cenozoic orogeny in the Atlas mountains. A gap in the fit appears off the Ifni enclave, but this may be accounted for by the displacement of eastern Canaries island group (Lanzarote, Fuerteventura, and Concepcion Bank) of the Canary Islands as a micro-continental fragment (Dietz & Sproll 1970a). Unlike the fully volcanic western Canaries, this island group may well have a sialic foundation (e.g., Dash & Bosshard 1968). A more detailed analysis of the overlaps and underlaps in the Africa-North America fit has been presented elsewhere (Dietz & Sproll 1970b).

Bahama Platform Overlap

The major region of misfit of Fig. 1 is the Bahama platform overlap, an enormous area half the size of Texas, which must be accounted for as 'new ground' if the North

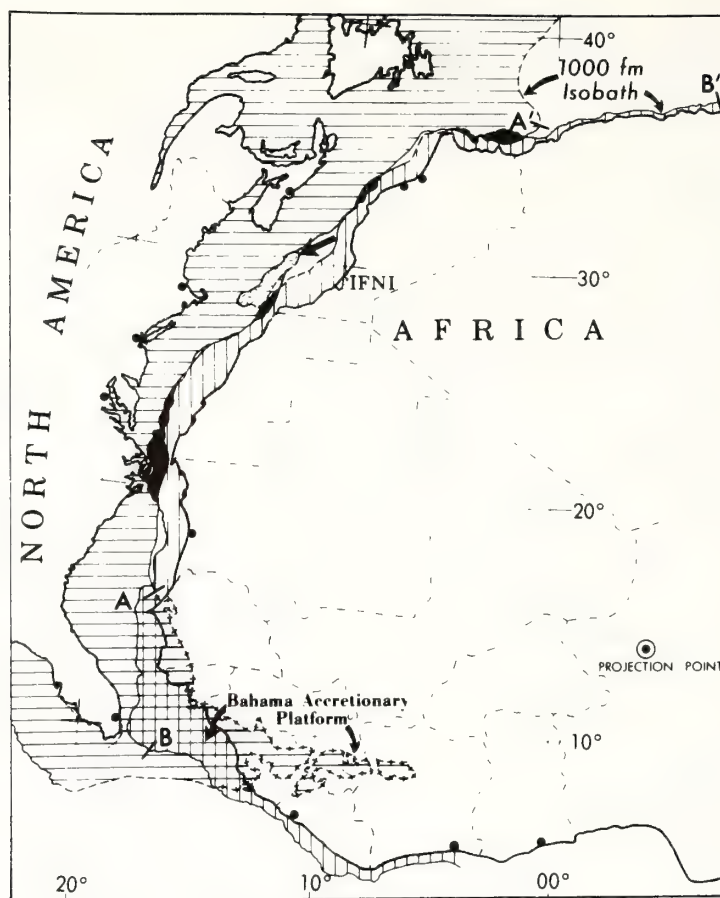


FIGURE 1 A computerized continental drift reconstruction fit between Africa and North America matching the 1000 fm isobaths and based on the criterion of smallest average misfit. The match was made by comparing the North American margin between points A to A' with the African margin between points B to B'. The North American shelf is shown by horizontally ruled lines and the African shelf by vertically ruled lines. The overlaps are shown as opaque areas except for the Bahama platform which is cross-hatched. The clear areas are gaps or underlaps in the fit. The West Canaries block, which may have fitted into the Ifni gap, is shown in random dash pattern. (From Dietz *et al.*, 1970.)

America–Africa fit is valid. A 5 km thick section of Cretaceous and Cenozoic shallow water carbonates caps the platform, implying a history of great subsidence. Dietz *et al.* (1970) have suggested that this platform is not underlain by the usual sialic basement complex, but by a thick layer of Jurassic clastics beneath the carbonate which rests directly on oceanic crust. We supposed that a small ocean basin was filled with these clastics when North America initially split away from Africa about 190 m.y. Reef corals then attached themselves and flourished, creating upbuilding sufficient to offset subsidence so that the platform has maintained a sea level freeboard. This interpretation obviates the overlap problem.

A modification of this evolution now seems in order whereby it is proposed that an Iceland-like 'hot spot' rose 195 m.y. as a lava plume from the deep mantle at the Bahamas

site. It served to initially drive North America away from Africa, a type of motive force for plate tectonics suggested by Morgan (1971). Thus, a large pile of alkalic basalts as well as sedimentary detritus would underlie the Bahama carbonates. This hot spot is inferred by the strike of lower Jurassic dike swarms (180 to 193 m.y.) in North America which converge toward the Bahama platform (May 1971). In North Africa similar dike swarms converge toward the Guinea Nose, the conjugate point under drift reconstruction. This would nicely account for the asymmetrical spreading early in the opening history of the Atlantic Ocean. A hot spot apparently has the effect of 'overprinting' the symmetrical splitting of injected dikes as occurs with normal sea-floor spreading. Thus, the mid-ocean rift is not permitted to migrate. This effect can be observed today for Iceland and for the Galapagos rift (Holden & Dietz, 1972). When the North Atlantic first opened, North America moved away from an almost fixed Africa so that the hot spot held the rift fixed near Africa. Nearly all of the lava was spilled on the North American plate and but little on the African plate. Thus the Bahama platform is much larger than the Guinea Nose, its conjugate area of new ground. This history also would account for the very rapid filling up of the Bahama basin to sea level, permitting the early attachment of coral reefs where up-growth would offset subsequent subsidence.

Closing of the Caribbean and Gulf of Mexico

Another difficulty of the Bullard fit is the large overlap of southern Mexico and Central America onto South America. A solution has been offered by Freeland & Dietz (1971), whereby this overlap is obviated by using plate tectonic rotations of the overlapping areas so as to close the Gulf of Mexico. We suggest that the Gulf of Mexico was rather quickly blocked out in the early Jurassic with the Luanne salt being the basal formation as a deep-water salt. The Caribbean region would then have been blocked out in the lower Cretaceous. Our analysis must be regarded as preliminary and highly speculative; however, it may offer the proper type of scenario to explain the geotectonic evolution of the region. The Caribbean and Gulf of Mexico would then be new ocean basins created after the breakup of Pangaea.

South America/Africa Fit

This fit remains the most convincing of all fits and it is supported, for example, by the matching of Precambrian provinces of similar radiometric age (Hurley 1971). Overlaps caused by the Niger delta and volcanic excrescences off the Walvis and Rio Grande ridges serve only to support the fit, as these are clearly areas of new ground. Local areas of salt domes along both Africa and South America are presumably also strips of new ground so that future studies of the fit should probably subtract these areas. The Benue Trough, trending northeast through Nigeria, was presumably an incipient, but abortive, rift which opened in the Lower Cretaceous and closed in the Upper Cretaceous. About 5 km of closure is indicated by the folding within the trough which is much less than the initial spreading. It would seem, therefore, that some small eastward rotation of the stem of Africa may have occurred with respect to the congruent margin of South America.

Reconstructing the Indian Ocean

Unlike the Atlantic, almost a pure rift ocean, the Indian Ocean is a mixed ocean basin—both a rift ocean and a subduction ocean. And, rather than being created by simply splitting a craton, the re-arrangement of Tethys is involved. The reconstruction, or ‘closing,’ of the Indian Ocean remains far from being solved. However, Smith and Hallam (1970) have made an admirable attempt, and a similar solution has been offered by Dietz & Holden (1970). Dietz & Sproll (1970c) have presented a fit of Antarctica against Africa which avoids the problem of positioning the horn of Antarctica (the Antarctic peninsula) under the assumption that it did not exist in the Triassic, at least not in its present position. The fit achieved is good in the sense that the total mismatch is small, but uncritical in that the congruent margins are both nearly straight. It also assumes that Madagascar was initially located in the Tanzania position, while apparently there was growing geologic evidence that it should be placed in the Mozambique position. From a morphologic viewpoint, Madagascar fits poorly in both positions. The adoption of the 2000 m isobath solves a major problem in the Smith & Hallam reconstruction, as it reveals that the Weddell Sea, which they show as

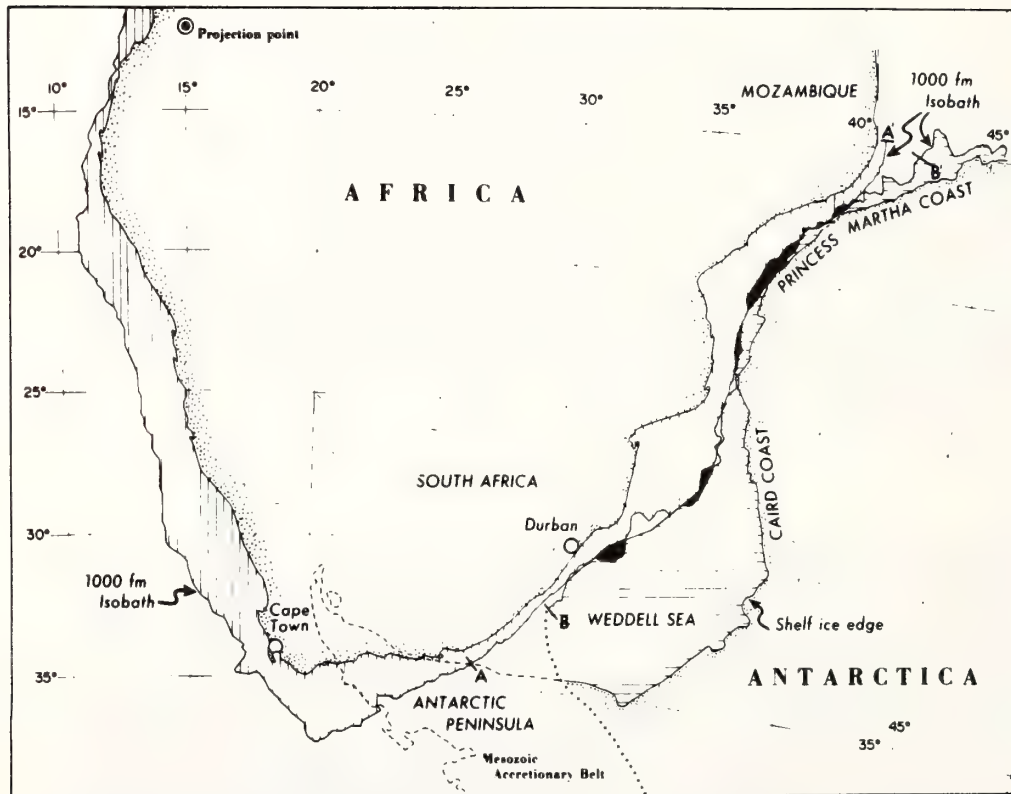


FIGURE 2 The best fit position between Antarctica and Africa, a continental drift reconstruction. Departures from congruency are shown as overlaps (opaque areas) or as underlaps (clear areas). (From Dietz & Sproll, 1970c.)

a 'gap', can be considered to be a deep shelf-sea and therefore part of the Antarctica cratonic block.

India fits equally badly in several positions (Dietz, in press) against Antarctica, Australia or Madagascar, but all of these fits can be accommodated by 'major surgery', e.g., removing the Exmouth Rise for the fit of Australia and India or moving Ceylon for the fit of Antarctica against India. My view is that the east coast of India belongs against Antarctica, but this is based upon interpreting the strike of major tectonic features on the ocean floor as flow lines for the drift of India. The idea (Dietz & Holden, 1971) that the Wharton Basin may be a remnant of Sinus Australia (a southern bay in ancient Tethys) and hence remnant Paleozoic ocean crust must now be abandoned, as it is not supported by the recent JOIDES drilling which suggests that this ocean floor is Cretaceous.

Australia/Antarctica and New Zealand

There has always been a general agreement on the fit of Australia with respect to Antarctica which can be assigned almost by inspection. This, however, has been given more precision by Sproll & Dietz (1969), who found that the best fit position is also blocked in the three marginal plateaus, the Iselin, Bruce and Naturaliste plateaus, which suggests that effusion of lavas over hot spots like today in the Afar triangle of the Red Sea may have played a role in the creation of triple junctions and subsequent breakup (Fig. 3).

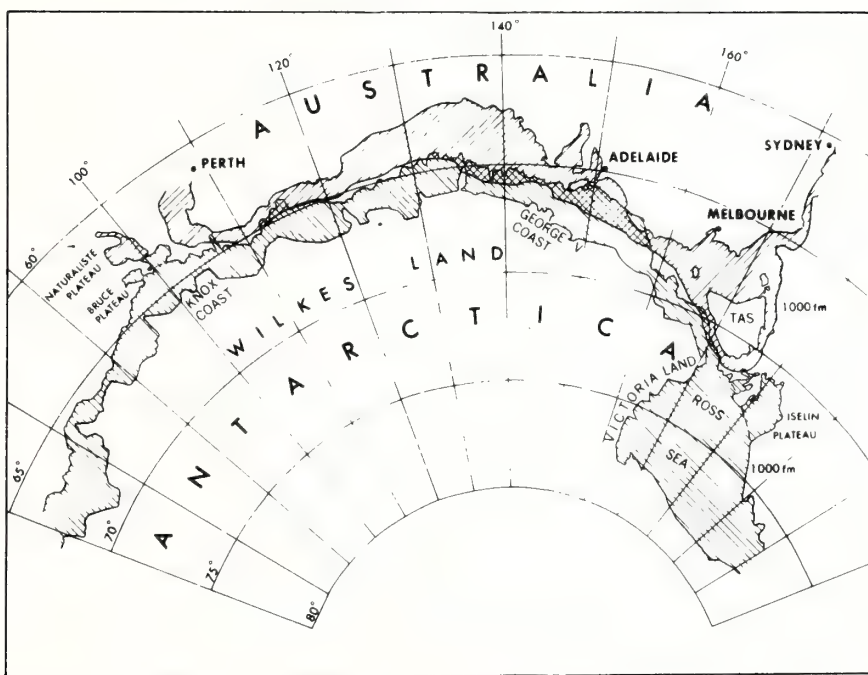


FIGURE 3 The best fit of Australia with respect to Antarctica by computerized matching of the 1000 fm isobaths. Ruled line pattern indicates continental shelf and slope from shoreline (inner contour) to the 1000 fm isobath (outer contour). Overlap areas are cross-ruled and underlap areas are blank. (From Sproll & Dietz, 1969.)

The New Zealand plateau appears to have been positioned against eastern Australia and West Antarctica. The Tasman Sea opened up first, commencing 85 m.y. and ending 60 m.y. The cessation of opening was caused by the rifting of Australia away from stationary Antarctica beginning 60 m.y. and continuing to the present day at about 5.4 cm/yr (Griffiths, 1971, Griffiths & Varne, 1972, and Weissel & Hayes, 1971).

It is interesting to note that, if the Tasman Sea continued to open while Australia moved away from Antarctica, a quadruple junction would have been involved. It would seem that in plate tectonics such junctions are prohibited and only triple junctions are permitted. It appears as if the Earth adjusts itself to maintain only six main spreading axes and six *major* plates with eight triple junctions at any one time—and thus to adopt the symmetry of a 'cube' or, more accurately, a spherical hexahedron.

References

- Bullard, E. C., Everett, J. E., and Smith, A. G., 1965. The fit of the continents around the Atlantic. *In* Symposium on continental drift, *Phil. Trans., R. Soc. A*, **258**, (1088), 41–51.
- Carey, S. W., 1958. A tectonic approach to continental drift. *In* Continental Drift, a Symposium, S. W. Carey, ed., Univ. of Tasmania Press, Hobart, 177–355.
- Dash, B. P., and Bosshard, E., 1968. Crustal studies around the Canary Islands, Rep. 23rd Int. Geol. Congr., Prague, **1**, 249–260.
- Dietz, R. S. (in press). Antarctica and continental drift; *In* Proc. SCAR Symposium on Antarctica Geology and Solid Earth Geophysics, Oslo 1970.
- Dietz, R. S., and Holden, J. C., 1970. Reconstruction of Pangaea: Breakup and dispersion of continents, Permian to Present, *J. Geophys. Res.*, **75**, (26), 4939–4956.
- Dietz, R. S., and Holden, J. C., 1971. Pre-Mesozoic oceanic crust in the eastern Indian Ocean (Wharton Basin)? *Nature*, **229**, (5283), 309–313.
- Dietz, R. S., Holden, J. C., and Sproll, W. P., 1970. Geotectonic evolution and subsidence of Bahama platform, *Bull. Geol. Soc. Amer.*, **81**, (7) 1915–1928.
- Dietz, R. S., and Sproll, W. P., 1970a. East Canary Islands as a microcontinent within Africa–North America continental drift fit, *Nature*, **226**, 1043–1045.
- Dietz, R. S., and Sproll, W. P., 1970b. Overlaps and underlaps in North America to Africa continental drift fit. *In* vol. 1 Geology of Atlantic Continental Margins, 143–151, H. M. Stationery Office, London.
- Dietz, R. and Sproll, W., 1970c. Fit between Africa and Antarctica: a continental drift reconstruction, *Science*, **197**, 1612–1614.
- Freeland, G. L., and Dietz, R. S., 1971. Plate tectonic evolution of Caribbean-Gulf of Mexico region, *Nature*, **232**, 20–23.
- Griffiths, J., 1971. Reconstruction of the south-west Pacific margin of Gondwana, *Nature*, **234**, 203–207.
- Griffiths, J., and Varne, R., 1972. Plate tectonic model for evolution of Tasman Sea, Macquarie Ridge and Alpine fault, *Nature*, **235**, 83–86.
- Holden, J. C., and Dietz, R. S., 1972. Galapagos gore, NazCoPac triple junction and Carnegie/Cocos ridges, *Nature*, **235**, 266–269.
- Hurley, P., 1971. The confirmation of continental drift. *In* Continents Adrift, 57–67, Freeman and Co., San Francisco.
- May, P. R., 1971. Pattern of Triassic-Jurassic diabase dikes around the North Atlantic in the context of pre-drift position of the continents, *Geol. Soc. Amer. Bull.*, **82** (5), 1285–1291.
- Morgan, J., 1971. Convection plumes in the lower mantle, *Nature*, **230**, 42–43.
- Smith, A., and Hallam, A., 1970. The fit of the southern continents, *Nature*, **235**, (5228), 139–144.
- Sproll, W. P., and Dietz, R. S., 1969. Morphological continental drift fit of Australia and Antarctica, *Nature*, **222**, 345–348.
- Weissel, J., and Hayes, D., 1971. Asymmetric sea floor spreading south of Australia, *Nature*, **231**, 513–521.

Comment

J. V. AVIAS

*Laboratoire de Geologie
Université de Montpellier, France*

I would like to point out the close agreement of palaeofaunal evidence with Dietz's reconstruction of land and sea for the Caribbean and Mexican areas in early Mesozoic times.

(1) Liassic ammonoids (family Psiloceratidae) are well known in Pacific side of both North and South America but are unknown in early Jurassic times (Hettangian) showing that this fauna, coming from the west, had not yet reached the Caribbean region, because of the existence of a 'Panamean' barrier (Avias 1966).

(2) In Sinemurian times (Avias 1966, Freneix 1956, Guerin-Franiatte 1966) Arietitidae faunas are known only on the east side, not on the Pacific side, of the same region. This, together with the close affinities with European faunas, shows that:

(a) the sea communication and faunal migration was from the proto-Atlantic ocean sea to the east.

(b) the same 'Panamean' barrier was still in existence.

(3) Pacific-Atlantic sea communication (2-3) occurred in this area in post Lower Liassic times.

References

- Avias, J. V., 1966. Sur le probleme des relations entre les faunes du Lias inferieur de Nouvelle-Caledonie, d'Amerique et d'Europe. *C. R. XX° Congr. Geol. Intern. Mexico 1957*, 1-5 1966.
- Freneix, S., 1956. Contribution a l'etude des Lamellibranches du Cretace de Nouvelle-Caledonie. *Sc. de la Terre. T. IV*, 153-208.
- Guerin-Franiatte, S., 1966. Ammonites du Lias inferieur de France. *Psilocerataceae: Arietitidae*. C. N. R. S. Paris 1966.

New Global Tectonics and "The New Geometry": Discussion¹

ROBERT S. DIETZ²

Miami, Florida 33149

INTRODUCTION

This discussion is an answer to Mantura's (1972) somewhat anthropomorphic geologic note, in which he finds the "new global tectonics" totally at odds with the real earth. I will attempt to reply to the arguments Mantura raised in the order he presented them by using his own major headings to insure a parallel format.

Plate tectonics ("the new global tectonics") with its corollary of continental drift, although still imperfectly understood, seems to be a proper geotectonic model for the earth. The geometric contradictions suggested by Mantura are largely illusory. A lithospheric plate is bounded typically by a spreading rift along which accretion of oceanic crust occurs, subduction zones of lithospheric descent and consumption, lithosphere-piercing strike-slip transform faults. In this scheme, there is usually no geometric need for a plate to interact with any other—i.e., the plates (except for the Antarctic plate which lacks a subduction zone and the Americas plate which "shares" a subduction zone) are not interlocked but can move more or less freely on their own. Because the spreading, midocean rifts are accreting boundaries, they also may migrate in a variety of ways. Confusion (to easy understanding) also is added because plate rotations measured are only relative to the adjacent plate across a rift. This applies to (1) closing cratons against conjugate margins (jigsaw method); (2) measuring the strike of fracture zones; and (3) closing against matched magnetic anomalies. There is some evidence that the approximate

absolute drift of crustal plates with respect to the earth's spin axis can be achieved by using the strike of nematoliths laid down by mantle plumes (hot spots). In brief, the plate motions proposed for Africa, various midocean ridges, *etc.*, although not easy to visualize, can be modeled and are permissible.

PINPOINT DOCKING AND PRECISION TIMING

Mantura asks, "How can South America rotate about the Gibraltar pole of rotation, which is itself moving first west, then east, and finally north? Such a 'pole' hardly could provide firm pivotal support for the alleged rotation. Moreover, the so-called Gibraltar pole is in a plate which is separate from that of South America."

The answer to all of this is: no problem. Mantura appears not to understand the basic geometrics involved in moving a rigid plate on the surface of a sphere. Although there are other mathematical schemes for describing the movement of a plate across the globe, Euler's theorem is the simplest for the mind's eye to comprehend. It states that the motion of a rigid plate from one position to another position can be described in terms of three parameters, the latitude and longitude of a pole of rotation whose axis passes through the center of the earth (which insures that the plate stays on the

© 1973. The American Association of Petroleum Geologists. All rights reserved.

¹ Discussion received, March 28, 1973; accepted, May 9, 1973.

² National Oceanic and Atmospheric Administration, Atlantic Oceanographic and Meteorological Laboratories.

surface of the sphere) and by a suitable angular rotation about that pole. There is nothing here which states that a pole of rotation must provide a "firm pivotal support" from which the moving plate is controlled by, say, a stout metal bar. There is no geometric reason why North America, in drifting away from Africa, could not have undergone a random walk involving a migrating pole of rotation (using an infinite number of poles) or one which has jumped from position to position. The Bullard pole for opening the north-central Atlantic is simply an average pole which best merges the congruencies of the North American margin with those of Africa. By fitting together the magnetic-anomalies pattern of the North Atlantic, Dewey *et al.* (in prep.) have utilized six poles of rotation. Doubtless, these will be refined further and others added to the list, although the anomaly patterns seem to reveal that there is considerable "inertia" in drift rotations. Drifters commonly speak of drift in terms of compass directions, but this is (or should be) simply a descriptive manner of speaking to assist the mind's eye, for it is geometrically impossible for the motion of a plate on a sphere to be other than a rotation. It is possible in plane geometry to translate plates, according to the fixed-point theorem, and this is a special case when the common fixed point is at infinity; on a sphere the common fixed point (the pole) can never be at infinity.

We agree with Mantura that our (Freeland and Dietz, 1971) plate-tectonic evolution of the Gulf of Mexico and Caribbean is "highly imaginative"—but it is not imaginary. We make no claim to having found the correct answer, but we suppose it is the proper type of solution, as it abides by the rules of plate tectonics. It is a solution that others, of the plate tectonic persuasion, can conveniently criticize, discard piece by piece, or eventually build upon. The cratons we move about (Yucatan, Honduras, *etc.*) never precisely fill the gap between North and South America. We surmised that Panama and much of Costa Rica are "new ground" born along a subduction zone. In brief, the gap between North and South America could have been of any length and the gap still would have been filled by a Panamanian "island arc" so long as the Cocos plate had its subduction boundary common to both North and South America. This is hardly "so mind-boggling that it defies the imagination."

Mantura cites many examples of "pinpoint docking," inferring that geologic matching can

be carried across geosutures where cratons have been welded together along fossil subduction zones. This problem is too complex to pursue here in any detail, especially for the complex Mediterranean region. Many subplates are involved along the Tethyan belt from the Azores to the Himalayas (*e.g.*, Udias and Lopez Arroyo, 1972). It can be mentioned, however, that it is not correct simply to equate the entire Mediterranean Sea with a suture. For example, drifters commonly suppose that Italy is a part of Africa with the suture being located in the Alps. Of course, if Mantura clearly can demonstrate geologic continuity across an obvious suture, one where oceanic crust and mantle rocks have been squeezed up into ophiolite zones, then plate tectonics is in deep trouble. Such correlations, however, are not easy. For example, the attempts to establish the amount of slip along the San Andreas fault has been fraught with difficulties in establishing stratigraphic correlations along the fault zone; and this history includes those who have argued for no offset.

It is not at all surprising that geologic units can be carried across the Persian Gulf at the Gulf of Oman. This body of water is a shallow epeiric sea flooding a unified cratonic block. The western boundary of the Arabian subplate runs along the Zagros Mountains of central Iran and not down the Persian Gulf.

It is difficult to understand how Mantura regards the various cratons and foldbelts in the world today as having "arrived 'on time'." Plate tectonics predicts that the circum-Pacific mountain belt will persist millions of years into the future, as it also has into the past. The same can be said for the Tethyan mountain belt. There is nothing geologically unique about the present.

AFRICA'S BELLY DANCE

Over the past 200 million years Africa appears to have drifted generally north while rotating counterclockwise (*e.g.*, Dietz and Holden, 1970b). Quite possibly this drift motion largely was halted about 25 million years ago by the collision of Africa with Europe (Burke and Wilson, 1972). Africa has moved toward a subduction zone which now is marked generally by the Mediterranean Sea. However, there are midocean rifts on both the east and west which must have moved relatively out from the African margin. It seems likely, however, that the Southwest Indian Ocean rift is largely a transform fault—at least it has acted as such

during the Cenozoic. A point of absolute reference for the motion of Africa possibly is the Walvis hot spot, which suggests that mantle plumes play some role in moving the lithospheric plates. But even that part of the mid-ocean ridge probably has migrated westward for the past 25 million years.

The drift motions described above and probably also the "belly dance" described by Mantura are both geometrically permissible in terms of the rules of plate tectonics. In fact, the freedom of motion offered by plate tectonics usually makes a unique solution impossible, especially when beyond the limits of guidance by magnetic-reversal anomaly patterns.

Mantura appears to have a confused version of the drift history of the Canary Islands. Our (Dietz and Sproll, 1970) version is that the eastern Canary Islands (Fuertaventura, Lanzarote, and Concepcion Bank), but not the western Canary Islands which are oceanic volcanoes, may be a sialic microcontinent detached from Africa in the early stage of the North America/Africa breakup. The North America/Africa fit reveals a prominent gap (Ifni gap) into which this presumed microcontinent would fit nicely, assuming it has drifted about 200 km southwest. There is nothing "difficult" about such a geotectonic history. We need only to assume that this segment of sial was split off of Africa by a rift and soon was abandoned on the African plate as this rift died, or jumped, to a new position west of this microcontinent. By referring to the Canaries and Madagascar "swimming against the current," Mantura takes us back to Alfred Wegener and his continents, which plowed like ships through the sima. The beauty of plate tectonics is that it does provide a mechanism for continental drift which physically is permissible.

INDIA'S JOURNEY

Drifters do not believe that India has "re-joined" Asia, but rather simply that India joined it in a mid-Cenozoic cratonic collision. Most drifters believe that India formerly was joined with Antarctica and Africa, possibly via Madagascar. No pinpoint docking is needed to fit India neatly into the "Himalayan oro-framework," as this collision is believed to have created this framework. If a man is kicked by a horse, it will surely leave the imprint of the shoe—pinpoint docking into a previous crescentic indentation is unnecessary.

Much more documentation is needed than

Mantura presented to demonstrate that "India never shifted from its original and authentic place in the Asian landmass." We should remember that, long before drift achieved any adherence, early geologists, like Blanford and Suess, recognized that India had geologic affinities with the southern continents. In fact, India is the type locality for Gondwanaland, which was named by Suess after the Permo-Carboniferous Gondwana tillites of central India.

AUSTRALIA AND ANTARCTICA

The usually proposed drift history of Australia-Antarctica is not as haphazard as Mantura suggests. The initial fit of Australia into Antarctica has been determined with considerable accuracy, as the congruency of the continental slopes is about as convincing as the Africa-South America fit (Sproll and Dietz, 1969). The best fit hooks Tasmania into the Ross Sea, and the western tip of Australia lies against Antarctica's Bruce marginal plateau. The northward rotation of Australia from Antarctica is achieved nicely with respect to a pre-Eocene and post-Eocene pole of rotation with central Africa (Le Pichon and Heirtzler, 1968). The Tasmantid seamounts, in terms of the concept that hot spots are fixed, suggests that Antarctica has remained virtually stationary while Australia has moved northward at a rate of 5.6 cm/yr (Vogt and Conolly, 1971).

It is not necessary to suppose that the lineup of the foldbelt on the Antarctic peninsula with the Andes is another example of "pinpoint docking." As both the Andean orogeny and that of the Antarctic peninsula are postdrift events, we only need to believe that the orogenic compression was of intercontinental dimensions.

Mantura mentions the zigzag form of the midocean rift surrounding Antarctica. A midocean rift does not have a zigzag form. If the zigs are midocean rifts, then the zags are ridge/ridge transform faults. He further states that zigzag periphery means that a mantle convection cell of this exact shape is required to drift the Antarctic plate. This is by no means necessary, as the motion may be the vector sum of many cells. Probably most plate tectonicists today, in fact, doubt the reality of convection cells. All we know is that the lithospheric plates seem to move.

In a sense, the Antarctic plate is a nonplate—a cicatrix from which other plates have migrated. It is surrounded entirely by a rift-transform fault system and has no trench boundary.

It does not even "share" a trench like the Americas plate. Thus, the Antarctic plate is locked in by its surrounding plates and can drift only when these plates provide space. There is a considerable difference of opinion as to how much Antarctica has drifted in the past 200 million years, because paleopole-position measurements are very limited and somewhat doubtful. Because of its locked-in aspect, it very likely has been the most fixed of all the continents. In worldwide relative-drift reconstruction it has been a common practice arbitrarily to hold Africa fixed. Probably more appropriate would be to use Antarctica as point of relative reference.

MIDOCEAN, WORLDWIDE RIDGE SYSTEM

That the rifts, in rift oceans where cratons have been split asunder, maintain a midocean position is, of course, remarkable. However, the passive injection of dikes and their symmetric splitting and accretion afford a most reasonable concept of how this can happen.

Contra Mantura, the plates need not depart symmetrically either in direction or velocity; for example, the absolute motion of one plate may be at 45° with respect to the rift, and its adjacent plate may remain absolutely fixed with respect to the earth's spin axis. But even in this event the midocean rift remains medianized, and the newly created ocean displays magnetic lineations which parallel and are symmetric with respect to the rift—but this reveals a record of *relative motion* only. The plate "dies" by being wholly consumed as the rift is swallowed by the trench, which cancels both of these boundaries and leaves only a suture. The swallowing of a rift by a trench (as has occurred to the Kula plate) would be an impossibility under any simple convection-current model, and it would require both up and down mantle flow along the identical line.

Perhaps the best model for a crustal plate is that of a "rigid" towel with some sinkers at one end resting in a swimming pool. As the towel becomes wet and grows heavier, it plunges (subducts) along the boundary with the added sinkers. In addition, we can visualize the opposing boundary of the towel as a rift along which new toweling is accreted at one half of the subduction velocity which then provides a migrating ridge moving at this velocity and remaining medianized with respect to its original position. To make this model clearer, we can surround the towel with a free-floating framework of wood. This rigid framework in no way affects

the performance of the towel, as there is no interaction between the two. Note also that this towel motion (plate motion) is the result of body forces and has nothing to do with convection cells of any size, shape, or velocity within the water. Note also that the "plate" does not conserve its size or shape; in fact, in this model the area of plate is doubled by the time it is wholly consumed.

CONCLUSIONS

In his summary, Mantura finds continental drift philosophically distasteful—leading to continental destruction by disunification and dismemberment of cratons into a disharmonious earth. May I point out that a plate-tectonic earth has attributes which are philosophically equally satisfying to those of a fixed, nondrifting earth.

First, plate-tectonic continental drift does not lead to cratonic dismemberment and geologic chaos. The plate tectonic process is such that the sialic cratons move toward trenches and, once reached, remain adjacent to trenches. The overall effect of this is that the Pacific Ocean is a collapsing ocean, the Atlantic Ocean an opening ocean, and the Indian Ocean a mixed ocean. The end effect of modern drift-plate motion, if no new plates are formed, is that all the continents, with the exception of Antarctica, eventually will suture up in a new Pangea (which apparently happened earlier in the late Paleozoic), with the Indo-Atlantic Ocean becoming Panthalassa. We (Dietz and Holden, 1970a) already have prepared a map of the world 50 million years hence which reveals that another Pangea is in the pattern of the future.

Second, let us consider some aspects of permanency which classicists always have regarded an intrinsic attribute of the earth. With continental fixity, geologists require "elevator tectonics" which modifies the configuration of the continents, the volume of ocean basin, and the continental "freeboard" with respect to the position of sea level. Drifters ask that ocean basins expand and collapse, but at the same time they retain their overall volume and hence the freeboard of continents. Also, the continents approximately maintain their size and shape, although they may suture together. The continents remain as the permanent features of the earth. In brief, continental drift is really no more catastrophic than fixity; with drift, many types of permanency are retained, although different from those envisioned by the classicists.

If one is searching within geology for geometric harmony, an ordered plan or hand of the Creator (I do not happen to be), plate tectonics and continental drift constitute a subject worthy of contemplation.

REFERENCES CITED

- Burke, K., and J. T. Wilson, 1972, Is the African plate stationary?: *Nature*, v. 239, no. 5372, p. 387-390.
- Dewey, J., W. Pitman, W. Ryan, and J. Bonnin, in prep., Plate tectonics and the evolution of Tethys.
- Dietz, R. S., and J. C. Holden, 1970a, The breakup of Pangaea: *Sci. American*, v. 223, no. 4, p. 30-41.
- and ——— 1970b, Reconstruction of Pangaea: breakup and dispersion of continents, Permian to present: *Jour. Geophys. Research*, v. 75, no. 26, p. 4939-4956.
- and W. P. Sproll, 1970, East Canary Islands as a microcontinent with the Africa-North America continental drift fit: *Nature*, v. 226, no. 5250, p. 1043-1045.
- Freeland, G. L., and R. S. Dietz, 1971, Plate tectonic evolution of the Caribbean-Gulf of Mexico region: *Nature*, v. 232, no. 5305, p. 20-23.
- Le Pichon, X., and J. R. Heirtzler, 1968, Magnetic anomalies in the Indian Ocean and sea-floor spreading: *Jour. Geophys. Research*, v. 73, p. 2101-2117.
- Mantura, A. J., 1972, New global tectonics and "the new geometry": *Am. Assoc. Petroleum Geologists Bull.*, v. 56, no. 12, p. 2451-2455.
- Sproll, W. P., and R. S. Dietz, 1969, Morphological continental drift fit of Australia and Antarctica: *Nature*, v. 222, p. 345-348.
- Udias, A., and A. Arroyo Lopez, 1972, Plate tectonics of the Azores-Gibraltar region: *Nature Phys. Sci.*, v. 237, no. 74, p. 67-69.
- Vogt, P. R., and J. R. Conolly, 1971, Tasmanid guyots, the age of the Tasman basin, and motion between the Australia plate and the mantle: *Geol. Soc. America Bull.*, v. 82, p. 2577-2584.

Two Probable Astroblemes in Brazil

MORE than forty structures have now been identified as astroblemes, ancient geological scars produced by the impacts of large cosmic bodies on the Earth¹. We report here some preliminary results on the study of two new astroblemes in Brazil, the Araguainha Dome and the Serra da Canghala structure. Although relatively young meteorite impact craters have been identified in Argentina² and Chile³, these two Brazilian structures are the first ancient astroblemes to be reported from South America. The impact origin of the Araguainha Dome has been established by the discovery of diagnostic shock-metamorphic effects⁴ in its rocks. No shock effects have yet been identified in rocks from the Serra da Canghala structure.

The Araguainha Dome, centred at 16° 46' S, 52° 59' W, is located near the town of Araguainha in the state of Mato Grosso, Brazil. The structure has been regarded as an alkaline intrusive, of which there are many examples in Brazil. It consists of a central uplift about 10 km across, in which cataclastically deformed Devonian Furnas Sandstone is exposed. Around this uplift is an annular ring syncline in which Permo-Carboniferous sediments, chiefly sandstones, are exposed in a series of downdropped grabens. The diameter of the structure estimated from ground studies is about 20 km. But a photograph of the structure taken from the ERTS-1 satellite (ERTS-1 photograph 1089-13005; October 20, 1972) shows that the circular pattern extends across a diameter of about 40 km (Fig. 1). If this pattern represents the true size of the structure, then the Araguainha Dome is one of the larger known astroblemes.

The central part of the central uplift is occupied by an unusual igneous breccia which contains inclusions of buried quartzofeldspathic Precambrian crystalline rocks in an igneous matrix. Thin sections of this breccia and the inclusions, made available to us by officials of *Petróleo Brasileiro SA* (Petrobras), contain a wide variety of distinctive shock-metamorphic effects, which are diagnostic of the intense shock pressures (≥ 100 kbar) produced by meteorite impact. The inclusions show extensive development of planar features (shock lamellae) in quartz, often as many as six to eight distinct sets of lamellae per grain, with orientations corresponding to the distinctive $\{10\bar{1}3\}$, $\{10\bar{1}2\}$, $\{11\bar{2}2\}$, and $\{11\bar{2}1\}$ planes^{5,6}. The igneous matrix of the breccia



Fig. 2 Aerial photograph of Serra da Canghala structure, showing high wall of uplifted Poti Sandstone around the central uplift. Part of the downdropped ring syncline is in the foreground. White streak at left is an aircraft landing strip.

exhibits a heterogeneous texture and contains numerous shocked and partly melted rock and mineral inclusions. The breccia from the Araguainha Dome is identical in appearance to impact produced breccias observed at other astroblemes.

The Serra da Canghala structure ("Pack-Saddle Mountain") is located in the remote northern corner of the state of Goiás (8° 05' S, 46° 52' W) in north-eastern Brazil, on the southern limb of the Amazon basin. The structure (diameter 12 km) has a damped-wave form with a central uplift of diameter 5 km surrounded by a downdropped annulus at least 3.5 km across. Serra da Canghala is a remarkably impressive feature of the region. In the central uplift, a circular wall, 250 m high, of steeply dipping Poti (Carboniferous) Sandstone surrounds a central basin of uplifted Longa (Devonian) Shale (Fig. 2). The central part of the structure thus has a crater-like appearance resulting from the preferential erosion of the Longa Shale by streams which flow through a breach in the Poti Sandstone wall.

In 1971 the Company for Research on Mineral Resources (CRPM) drilled three diamond drill holes, each 200 m deep, within the centre of the structure to test the possibility that the structure might be a kimberlite intrusion. No igneous rocks were found, and the drilling encountered only highly deformed and steeply dipping Longa Shale. The drilling results and the surface outcrop pattern indicate that the central uplift becomes progressively more disturbed towards the centre of the structure and displays the forms of an eviscerated dome. The intensely disturbed central area, the down thrown peripheral annulus, and the ratio of the central uplift diameter to total diameter are consistent with the structural features found in astroblemes. The overall structural pattern and geomorphology are strongly similar to those at the Gosses Bluff astrobleme in central Australia^{7,8}.

The rock units underlying the Serra da Canghala structure down to the Precambrian basement are entirely clastic and do not contain significant carbonate or salt units; the structure cannot be a salt diapir. Igneous rocks are entirely absent from the structure, and large cross-cutting sandstone dikes are the only anomalous features.

One of us (R. S. D.) made a three-day reconnaissance and collection at the Serra da Canghala structure in October 1972. Shatter coning, a useful field criterion for meteorite impact⁹, was not observed. The rocks collected were almost entirely fine-grained siltstones which did not show any shock-metamorphic effects. One specimen of coarser grained quartzite, collected as a cobble in a conglomeratic unit of the Poti Sandstone in the central part of the structure, showed small areas characterized by unusual fracturing of the quartz grains. Similar fracturing in quartz has been reported in mildly-shocked rocks from known meteorite impact craters^{10,11}, but the features observed in the Poti Sandstone are not distinctive enough to be considered diagnostic for meteorite impact. At present, the structural deformation in the Serra da Canghala structure, combined with the apparent

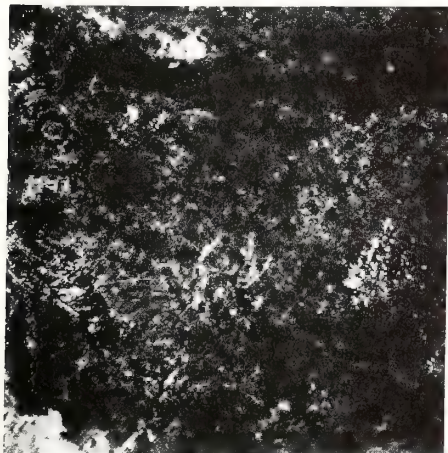


Fig. 1 ERTS-1 photograph of the Araguainha Dome. The structure appears at upper left as a dark inner ring and an outer circular pattern about 40 km across. NASA photograph, courtesy N. M. Short.

absence of igneous activity, favours the theory that the structure is an astrobleme. But definite proof will require the identification of unquestionable shock-metamorphic effects in its rocks.

We thank the Company for Research on Mineral Resources (CRPM) for making possible the field work at Serra da Canhala and for providing the assistance of J.-M. Coehlo in the field. M. Antonio M. de Oliveira of Petróleo Brasileiro SA (Petrobras) provided the thin sections and information on the Araguinha Dome. Petrographic studies were carried out at NASA, Goddard Space Flight Center, courtesy of C. C. Schnetzler. N. M. Short, also of NASA, Goddard, provided information and ERTS photographs of the Araguinha Dome. Partial support for R. S. D.'s travel to South America was provided by the Barringer Crater Co., Philadelphia, Pennsylvania.

ROBERT S. DIETZ

NOAA, Atlantic Oceanographic and
Meteorological Laboratories,
15 Rickenbacker Causeway,
Miami, Florida 33149

BEVAN M. FRENCH

7408 Wyndale Lane,
Chevy Chase,
Maryland 20015

Received July 24, 1973.

- ¹ Dence, M. R., *Rep. Twenty-fourth Int. geol. Cong., Montreal, Canada*, part 15, 77 (1972).
- ² Cassidy, W. A., Villar, L. M., Bunch, T. E., Kohman, T. P., and Milton, D. J., *Science, N.Y.*, **149**, 1055 (1965).
- ³ Sanchez, J., and Cassidy, W., *J. geophys. Res.*, **71**, 4891 (1966).
- ⁴ *Shock Metamorphism of Natural Materials* (edit. by French, B. M., and Short, N. M.) (Mono Book Corp., 1968).
- ⁵ Robertson, P. B., Dence, M. R., and Fos, M. A., in *Shock Metamorphism of Natural Materials* (edit. by French, B. M., and Short, N. M.), 433 (Mono Book Corp., 1968).
- ⁶ Engelhardt, W. v., and Bertsch, W., *Contrib. Mineral. Petrol.*, **20**, 203 (1969).
- ⁷ Dietz, R. S., *Nature*, **216**, 1082 (1967).
- ⁸ Milton, D. J., Barlow, B. C., Brett, R., Brown, A. R., Glikson, A. Y., Mainwaring, E. A., Moss, F. J., Sedmik, E. C. E., Van Son, J., and Young, G. A., *Science, N.Y.*, **175**, 1199 (1971).
- ⁹ Dietz, R. S., *Rep. Twenty-fourth Int. geol. Cong., Montreal, Canada*, Part 15, 112 (1972).
- ¹⁰ Bunch, T. E., in *Shock Metamorphism of Natural Materials* (edit. by French, B. M., and Short, N. M.), 413 (Mono Book Corp., 1968).
- ¹¹ Kieffer, S. W., *J. geophys. Res.*, **76**, 5449 (1971).

R. S. DIETZ and J. C. HOLDEN

*National Oceanic and Atmospheric
Administration, Atlantic Oceanographic
and Meteorological Laboratories,
901 South Miami Ave., Miami,
Florida 33130*

Continents Adrift: New Orthodoxy or Persuasive Joker?

The modern rebirth of interest in continental drift commenced, we believe, in the mid-1950s when it was shown by a certain British geophysicist (who will remain nameless) from studies of rock magnetism that the polar-wander curves of North America and Europe, congruent in earlier times, diverged by about 30° in the Cretaceous and Cenozoic. This was widely, or perhaps wildly, hailed as proving the opening of the North Atlantic by continental drift.

This enthusiasm proved premature, because geologists rather carelessly handle their rocks, as Sir Harold Jeffries (1970) recently pointed out in his book, *The Earth*. He writes:

'When I last did a magnetic experiment (about 1909), we were warned against careless handling of permanent magnets, and the magnetism was liable to change without much carelessness. In studying the magnetism of rock the specimen has to be broken off with a geological hammer . . . It is supposed that, in the process, its magnetism does not change of any important extent, and, though I have often asked how this comes to be the case; I have never received any answer.'

For this, and other reasons, Jeffries dismisses Wegener's drift as being 'quantitatively insufficient and qualitatively inapplicable. It is an explanation which explains nothing which we wish to explain.' It would seem, therefore, that rocks collected for paleomagnetic measurements by hammers (and how else does a geologist collect his rocks) would have their magnetic memory scrambled. This being obviously so, rock magnetic studies must be regarded as worthless. The first law of geology, we suppose, is: The rocks remember, while liquids and gases forget. But it can hardly apply to rocks which have been hit on the head.

On the authority of Belousov (1962) we have it that, 'the hypotheses suggesting horizontal drift of the continents, among them the hypothesis of Wegener, which was once famous, must be regarded as fantastic and having nothing to do with science . . . It is a source of profound amazement that such a hypothesis—based as it is on an overtly formalistic approach to the major problems and on a total and consistent disregard of the basic geotectonic data and, as already stated, explaining nothing of what must be explained in the first place—was not only seriously discussed in scientific literature but achieved considerable success and attracted some of the leading

authorities into the ranks of its adherents. These men were apparently hypnotized by the boldness of Wegener's ideas and by his brilliant style of writing.'

This was a traumatic revelation to the zealots of continental drift and they fell into disarray. Like all true scientists, the drifters would 'rather be right than President,' but obviously they were neither.

The Animals Remember

All was not lost, however, for new evidence came in from an entirely unexpected quarter—the animal kingdom. Animals have some remarkably developed instincts, which sometimes recapitulate their evolutionary history. Witness the so-called loud bats with their FM sonar chirps by which they can search out and classify a moving target—usually moths, their favourite meal. But it remained for a bird, by its remarkable migratory path, to first demonstrate that the New World really has drifted away from the Old World.

This doughty bird, the sooty hoodwink, *Puffinus oceanicus*, winters in the Atlantic sector of Antarctica; then each spring it heads north, determined to nest in far away Spitzbergen. As if flying to this remote island is not a sufficient demonstration of fortitude, this bird chooses a zigzag path. First it touches down in Southwest Africa where, because of its confused and dazed habit of stumbling about (apparently searching for fresh bearings), it is locally termed the random walkabout. Then this bird executes further zigs and zags across the ocean as it threads its way north. On April 1st, the frayed remnants of the flock touch down on the British Isles at Lands End. (Remarkable as it is, their navigation sometimes goes awry. An errant flock was seen in 1967 far off course in the spaghetti fields of the Po valley.) Toward the end of April the sooty hoodwink finally reaches its destination, Spitzbergen.



FIGURE 1
... bat sonar

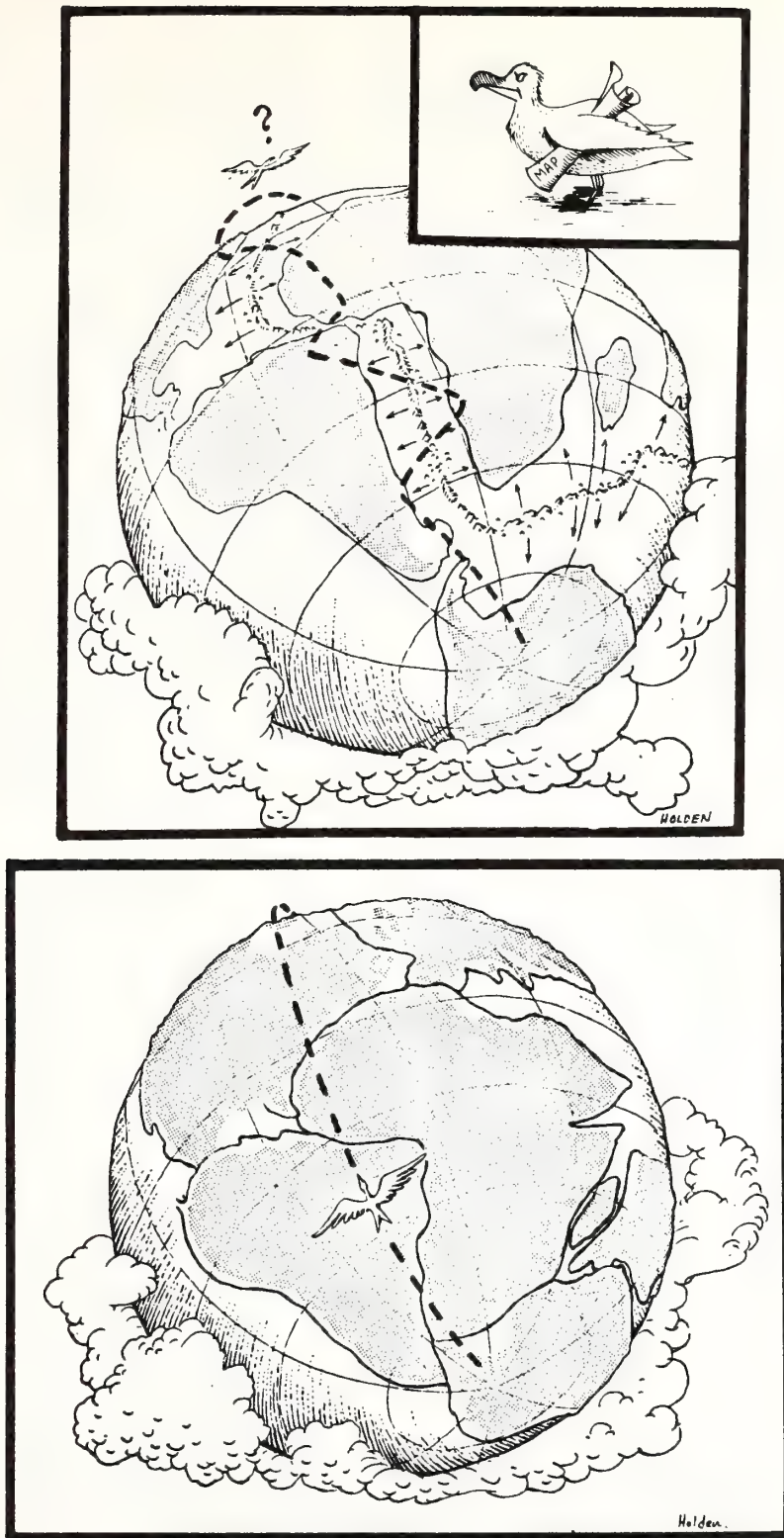


FIGURE 2 . . . a doughty bird

This curious migration path finds ready explanation once we recognize that continental drift has occurred. If we close the Atlantic Ocean, we find that the zigzag path becomes a straight line, a great circle route, or the shortest distance between Antarctica and Spitzbergen.

Another animal, albeit extinct, fills in still another facet of the continental drift puzzle. We refer here to *Glossopstempodon loathifoliata*, whose bleached remains are found in the Permian red beds of the Sahara. Critics of drift have argued that there never could have been a universal continent of Pangaea in the late Paleozoic, because, if this were true, the *Glossopoteris* flora on Gondwana would certainly have invaded the northern continents of Laurasia. These critics, however, failed to reckon with the tempestuous temper and unremitting phobia of *Glossopstempodon* for glossopterids. By setting up a rampaging patrol along the equator and trampling any young glossopterids sprouts, this reptile established a successful barrier against the northward migration of this flora. (We are reminded here in passing of the acceptance speech by a young English geophysicist when receiving a medal for his contribution to plate tectonics. If I recall correctly, he said with characteristic British modesty, 'If I have seen farther than others, it is because I have stomped on heads of giants.')

A somewhat similar explanation applies to the curious swimming behavior of the deep sea squid, *Architeuthis solenoides*. Nearly all squid swim backwards through life, apparently preferring not to look where they are going, but to see where they have been. By swimming forward, *A. solenoides* is exceptional, but apparently he has not always swum in this manner. Experiments show that he may be programmed to swim either forward or backward within an aquarium surrounded by a coil simply by



FIGURE 3
... *Glossostempodon loathifoliata*



FIGURE 4
... *Architeuthis solenoides*

reversing the magnetic field. It would seem, then, that *A. solenoides* became a forward swimmer only 700,000 years ago when the earth's field switched from reversed to normal at the Matsuyama–Brunhes boundary.

We have learned of late from the paleomagicians that, although 'east is east and west is west, and never the twain shall meet,' this adage does not apply to north and south. Every so often, and quicker than you can say Willem Jean Marie van Waterschoot van der Gracht, north may become south and, we hope, vice versa. We have learned this from the 'fossil compasses' frozen in basalts and other rocks. Actually, animals which are sensitive to the magnetic field of force have known this all along. It has been known for many years that, upon molting, crabs place a grain of sand in their inner ear, which then becomes a sensor for geotropism or, more simply, balance. Some crabs carelessly choose a grain of magnetite—a ferromagnetic mineral. Then, if a strong magnet is above their aquarium, they will forever crawl along the roof of their home. This much is evident by direct experimentation. But why do crabs crawl sideways? This mystery is solved when we recall the frequent flips in the earth dipole field. The crab becomes confused as to whether he should walk forwards or backwards, so, adapting to compromise, he instead walks sideways.

Yet another animal may be cited as proving continents drift. This is the common European eel, *Anguila*. After a few years in the streams of Europe, the eel heads for the Sargasso Sea on the far side of the mid-ocean spreading rift to spawn and then die. Then the newborn eel, the *Leptocephalus* stage, swims back to Europe—this instinct inherited from its parents. But by this time Europe is not where it was supposed to be,

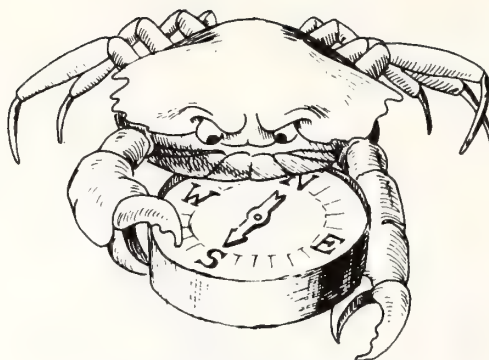


FIGURE 5
... and never the twain shall meet (?)

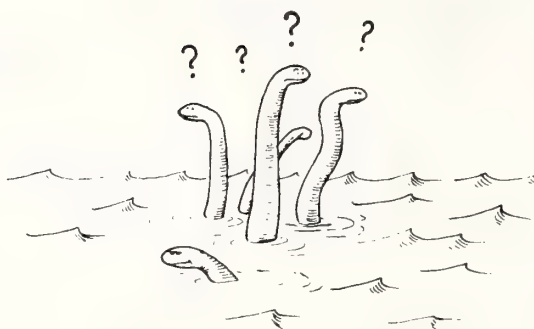


FIGURE 6
... one more last step

as this continent has drifted several centimeters eastward. No one knows for sure just what crosses the mind of a young eel in the face of this predicament. All we know for sure is that all eels go through life with a quizzical look. A Chinese proverb runs that, in a journey of a thousand miles, the last step is no more important than any other. But suppose that every year someone adds *one more* last step. For eels, it would seem that one more step beyond the last step is needed for survival of the species.

A final animal which adds credence to drift is none other than the famous Loch Ness monster. Photos and descriptions of this elusive monster show its long neck and small, reptilian head, so that it is a swimming 'dinosaur' or pleisiosaur, a living fossil from the Jurassic. It also has been noted by boats plying the loch that Nessie yields to the right, thus obeying Napoleonic (or North American) rather than Caesarian (or British) rule-of-the-road. Clearly, then, Nessie is a beast of the New World now stranded in the Old World by the break away of Europe from North America in the Cretaceous. There seems now to be a new urgency for somehow corralling Nessie and, while treating her with the tender loving care that befits an endangered species, making such measurements as would permit identification as to species—for example, counting her teeth.

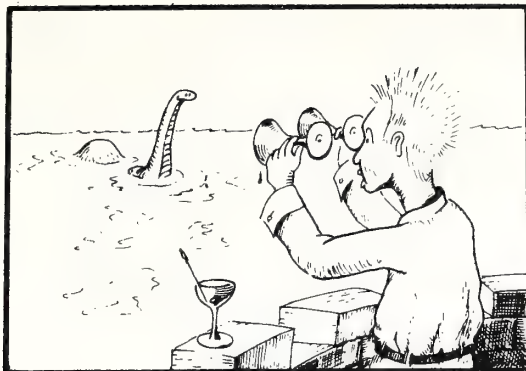


FIGURE 7
... over the loch from Urquhart castle

Historical Beginnings

Before proceeding further, we would like to pay homage to the originators of continental drift. There seems little doubt that the concept is originally ascribable to Frank Bacon (Blackett, *et al.* 1965), who, in his *Novum Organum* of 1620, wrote: 'The very configuration of the world itself in its greater part presents Conformable Instances which are not to be neglected. Take, for example, Africa and the region of Peru with the continent stretching to the Straits of Magellan, in each of which tracts there are similar isthmuses and similar promontories, which can hardly be by accident.' Bacon undoubtedly thought that, given this hint, the reader would have sufficient intelligence to see that the South Atlantic Ocean can be closed in a continental drift reconstruction. This, of course, is simply a matter of flipping South America upside down, north for south, and then sliding this continent eastward such that the bulge of Peru fits beneath the bulge of Africa. (We should mention in passing that there is no truth to the rumor that Bacon wrote the Shakespearean plays. For that matter, Bill Shakespeare didn't either. They were written by another man of the same name—and that should be an object lesson in general semantics.)

Let us also set the record straight as to the first symposium on continental drift, because A. Meyerhoff (1972) accorded that niche in history to the American Association of Petroleum Geologists 1926 symposium on continental drift organized by W. J. M. van Waterschoot van der Gracht. This is incorrect. The distinction clearly belongs to Samuel Pepys, FRS.

Pepys' diary for 23 May 1661 reads:

'To the Rhenish wine-house in Crooked Lane, and there Mr. Jonas Moore, to us, and there he did by discourse make us fully believe that *England and France were once the same continent* (italics added), by very good arguments, and spoke very many things not so much to prove the Scripture false, as that the time therein is not well computed nor understood. In my black silksuit (the first day I have put it on this year) to my Lord Mayor's by coach, with a great deal of honourable company, and great entertainment. At table I had very good discourse with Mr. Ashmore, wherein he did assure me that frogs and many insects do often fall from the sky, ready formed.'

From the above, it is clear that Pepys accepted the view that England had drifted away from Europe. A symposium in the purest sense of that word, and, as its Greek roots reveal, is a wine-drinking party. To Samuel Pepys, Cheers!, or Drink Hail!—for convening the first symposium on continental drift.

Humpty Dumpty had a Great Fall

Piecing together all of the continents has been described as a jigsaw puzzle. This is hardly correct, because solving a jigsaw puzzle is child's play. In contrast, piecing the continents together would seem to be a Humpty Dumpty problem, for, as you will recall, all the king's horses and all the king's men could not put Humpty Dumpty together again. Similarly, all the world's eggheads have been unable to reconstruct Pangaea.

The congruency of the margins of Africa and South America has always been the inspiration for drift. Alfred Wegener (1922) opened his classical book on drift with: 'He who examines the opposite coasts of the South Atlantic Ocean must be somewhat struck by the similarity of the shapes of the coast line of Brazil and Africa This phenomenon was the starting point of a new conception . . . called displacement of continents.' Wegener apparently did not realize that many decades ago A. Snider (1859) had already quantitized this fit with nice precision. This is presented in his remarkable book—'The Creation and its Mysteries Revealed: A Work which Clearly Explains Everything Including the Origin of the Primitive Inhabitants of America, etc., etc.' Snider illustrated by lithograph the fit of the New World against the Old World (see cut). It will be noted that, in his closing of the Atlantic Ocean, the match is

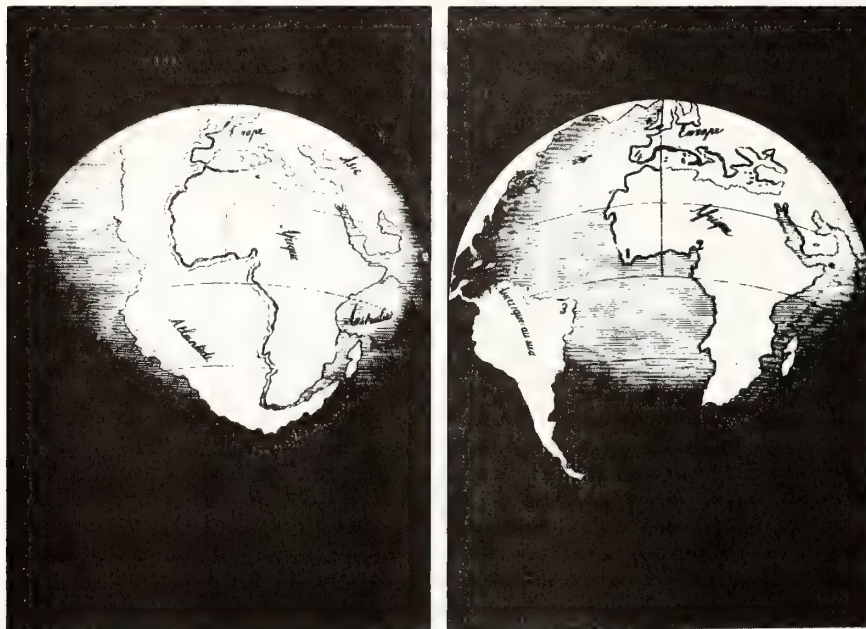


FIGURE 8
... Snider's fit of 1858 BC

perfect with neither overlaps nor underlaps. This fit is far superior to those attained by recent workers—for example, the Bullard *et al.* fit (1965). And Snider's fit was obtained in 1859 BC—yes, BC, Before Computers.

Subsequently, Carey (1958) has redone the Snider fit with cartographic precision, juxtaposing the 1000 fm isobaths on a common stereographic projection. This shows that the knee of South America fits snugly into the groin of Africa, that broad swales match broad re-entrant, bumps fit into bays, and even bumps on the bumps fit into bights in the bays. Of Carey's fit, Chester Longwell (1958) remarked, 'If the fit between South America and Africa (is not a gigantic rift), surely it is a device of Satan for our frustration.' Unlike the zealous drifters, Longwell at least has given us a choice. In view of this dilemma, we suppose we must resort to higher authority. In this respect, we can hardly do better than the eminent Sir Harold Jeffries (1970), who writes: 'On a moment's examination, the alleged fit of South America into the angle of Africa is seen to be really a misfit by about 12°.' It would seem that this supposed fit is no more than a persuasive joker.

Perhaps no one has shown better than Meyerhoff & Meyerhoff (1972) the folly of attempting to shoehorn continents together. In a diagram showing a family of squiggles said to represent the outline of Japan he has shown that Japan may be fitted almost anywhere in the world. Another masterwork of meyerhoffiana reveals that the eastern margin of North America, when turned upside down, fits nicely against the eastern coast of Australia. There has been much argumentation over the years about the position of Madagascar when the Indian Ocean is closed—whether this microcontinent fits against Tanzania or against Mozambique. In point of fact, both positions are morphologically poor. A proper fit is achieved only when Madagascar is leapfrogged over Asia and inserted into the Caspian Sea.

Wheels Within Wheels Within Wheels

It has been widely proposed that the continents can be piggybacked about by convection of the mantle. With convection one can do almost anything as the entire process is wonderfully amenable to mathematic manipulation. And there are many modes of convections—toroids, plumes with thunder-heads, helixes, etc.—all of which can be readily explained by arm waving which conjures up explicit models. Furthermore, simple but ingenious experiments can be performed at which the British scientists excel. The result has been a new third school of experimentalists (the earlier schools being the 'baling wire and sealing wax school' and the 'negative experiment school') which may be termed the 'kitchen experiment school'. But in all fairness it should be pointed out that this last-named school was anticipated in America by those early workers who successfully modeled lunar craters by dropping marbles into porridge. And we must mention here the important contribution by an early selenologist on the American frontier who discovered nearly a century ago that, regardless of the obliquity of the angle at which he shot a buffalo, the hole, like a lunar crater, was always round.

In defense of convection, a dimensionless formula is presented (see cut) for oboe and flute. Ideas that are too bizarre to record in writing may yet be sung with perfect propriety. The equation has no particular relevance to the present discussion, but it does add a touch of elegance. In this particular equation, it will be noted that all of



FIGURE 9
... a proper fit

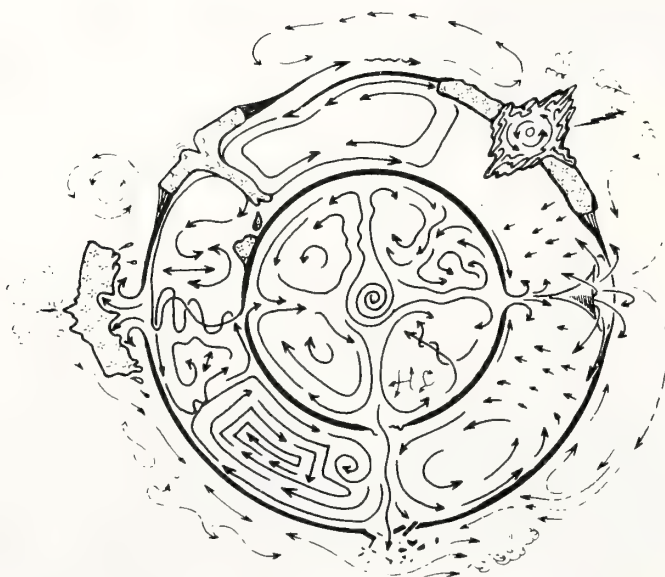


FIGURE 10
... wheels within wheels within wheels

the terms are either negligible or trivial; hence the entire equation is inconsequential. If we are ever to deal successfully mathematically with convection in the mantle, we must first establish some simplifying boundary conditions. For example, the rings around Saturn remained beyond understanding until a certain German mathematician cracked the problem by assuming just two simplifying conditions, the first being that the rings are square and the second being that the rings are at an infinite distance from Saturn.

The dimensionless form of the problem becomes

$$\frac{d^3 V}{d\eta^3} = \left\{ \left(-\langle \tau_0 \rangle + \left\langle \frac{\partial p}{\partial x} \right\rangle \eta \right) \left[\exp \frac{c}{T_0} \right. \right. \right. \\ \left. \left. \left. - \frac{(c/T_0)[1 + (bL/c)\eta]}{\left[1 - \left(-\langle \tau_0 \rangle + \left\langle \frac{\partial p}{\partial x} \right\rangle \eta \right) \frac{dV}{d\eta} + 2 \left\langle \frac{\partial p}{\partial x} \right\rangle V \right]} \right] \right\} \\ \cdot \left[\langle \mu_0 \rangle \left(1 - \frac{dV}{d\eta} \left(-\langle \tau_0 \rangle + \left\langle \frac{\partial p}{\partial x} \right\rangle \eta \right) \right. \right. \\ \left. \left. + 2 \left\langle \frac{\partial p}{\partial x} \right\rangle V \right) \right]^{-1} \quad (20)$$

$$K = \frac{2}{3}P - \frac{1}{3a_x} \sum_{x \text{ face}} x_{ii} \frac{\partial f_{ii}}{\partial r_{ii}}$$

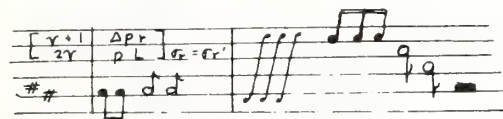
$$c_{11} = \frac{1}{a_x} \sum_{x \text{ face}} f_{ii} \frac{x_{ii}}{r_{ii}} \left(\frac{x_{ii}^2}{r_{ii}^2} - 1 \right)$$


FIGURE 11
... dimensionless formula for oboe and flute

Continents on the Move

We are told that the earth's crust is a mosaic of six large, 100 km thick plates in relative motion and that the continents are embedded in these plates as passive passengers. The plates never impinge, for they subduct instead, but the continents do, for they are composed of sial which is not geo-degradable. And it is these continental collisions which cause orogenies—linear mountain belts thrown up along the margins of continents. The Miocene collision of the Indian subcontinent with the soft underbelly of Asia is the type example. The three-mile-high Himalayan rampart overlooking the Gangetic plain resulted and India received a bashed-up nose in the process. We may liken this to the English bulldog, renowned for his remarkable tenacity, and some say, but I am sure it cannot be true, stupidity. Anyway, the comparison holds, because the abrupt profile of the English bulldog comes from chasing after parked cars.

A tenet of plate tectonics is that the ocean basins are ephemeral features—they are either opening or closing, but the continents exist forever—suturing up, unsuturing and generally being shunted about. The Pacific plate is moving fast enough to

entirely circumnavigate the globe during the Phanerozoic alone. Africa collided with North America in the Devonian 400 m.y. ago, triggering the abrupt Acadian orogeny. This collision must have stored elastic stresses, for 180 m.y. ago Africa took off again in the opposite direction, breaking apart generally along the earlier suture. In view of this historical scenario, we can expect Africa's return at any time, as the Atlantic Ocean cannot grow forever larger and larger. Surely a new plate boundary will form along the American shore and, first of all, a massive slab of the upper mantle will be obducted or thrust across the eastern seaboard, sweeping away the cities like some giant glacier. The implications are catastrophic; time is of the essence and we need now to establish a Continental Drift Early Warning System.



FIGURE 12
... Continents adrift

A New Twist

It is now well known that the Sea of Tethys, a vast arm off the former universal ocean of Panthalassa and lying between Gondwana and Laurasia, was the site of a subduction zone or trench along which there was also considerable transform slippage which has been termed the *Tethyan twist* (van Hilton, 1964). This slippage apparently was sinistral in the early opening phases of the North Atlantic Ocean, but became dextral during the Cenozoic, carrying Spain back from the open Atlantic to its present point of contact against Africa.

The Tethyan twist was one of the major scenarios of drift, but perhaps an even more important one, undiscovered until now, was the sinistral *Equatorial twist*. The proof that this twist has occurred lies in the remarkable symmetries achieved. The transformation may be performed using a suitable globe (e.g., the National Geographic 16" Physiographic Globe) by slipping the northern hemisphere of the earth along the equator dextrally for precisely one quadrant of earth (90°). The result is an

entirely new distribution pattern of land and oceans, but one which is entirely realistic. Indonesia is found to be exactly on register with the northern half of Africa, producing the new continent of Afrodesia. The mid-ocean rift of the North Atlantic lines up precisely with that of the southern Indian Ocean, producing an Indo-Atlantic rift. The southern half of Africa falls on register with the northern half of South America, producing an Amerafrica. Farther west, the North Pacific ridge can be connected to the South Atlantic ridge by imposing only a short segment of ridge-ridge transform fault, forming the Paclantic ridge. Proceeding even farther west, one finds the southern portion of South America standing alone in the central Pacific. The skeptic may pounce upon this as an oddity which vitiates entirely our Equatorial twist. But the reverse is true, for this is the lost continent of Mu whose former existence was adduced many years ago by James Churchward. This gentleman found the history of Mu written on secret tablets of stone amongst the archeological ruins of Mexico. He erred in just one respect: Mu did not sink beneath the waves of the Pacific, but instead it suddenly was wrenched eastward to become the southern portion of South America. It seems that some eons ago an errant asteroid, a cosmic cannonball, zeroed in on the earth, and . . . Bang!

The equatorial twist provides no answers, but it poses many questions.

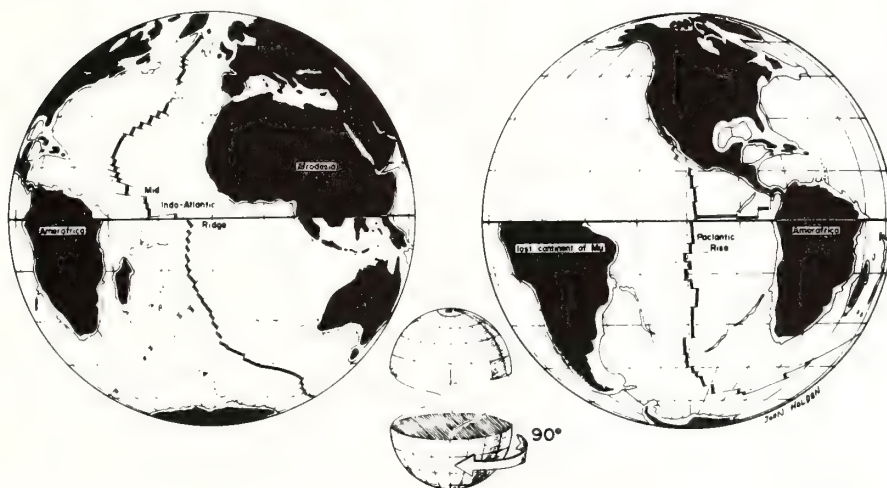


FIGURE 13
... the Equatorial Twist

Expansive Thoughts

There is a school of natural philosophy, prominent in the topsy-turvy world of Down Under, that our planet was once much smaller than it is now—and that it expanded to its present size only in the past 200 m.y. A common version of this concept is that the continents were all once joined and even the Pacific was closed, so that the world was without ocean basins. Continents, to the 1000 fm isobath, cover 40% of the earth, so that this earth would have only two-fifths the area of the modern world ($510 \times 10^6 \text{ km}^2$). The 'drifting' of continents could then be explained in a manner somewhat similar to the dispersion of points on the surface of an expanding

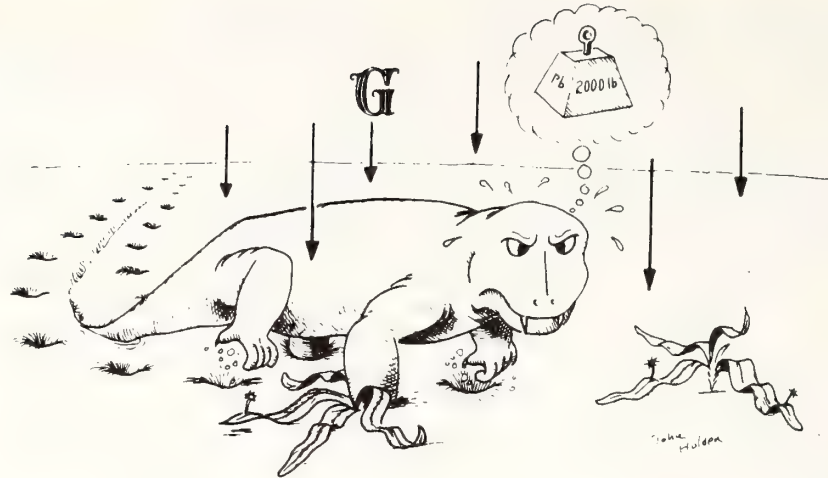


FIGURE 14
... small world of the Triassic

balloon—or like the stars in our expanding universe. However, only the oceans would grow while the continents maintained their original dimensions. The continents then would separate by displacement rather than drift.

Animals once again provide a key and appear to demonstrate that the earth may have been smaller in the Triassic than now. Assuming no change in Big *G* and accomplishing this miniaturization by phase change, the world of the early Triassic would have had a density of 22 and animals roaming the surface would have weighed $2\frac{1}{2}$ times as much as now. But this is not too unreasonable. Witness the squatty robust morphology of the fossil tetrapod, *Lystrosaurus*, with his belly scraping the ground. Does this stance not suggest that this sheep-sized reptile weighed not 100 pounds (scaled to the modern-sized earth), but actually 250 pounds in the *Triassic*? And why do you suppose all of those deep tracks and trails are found impressed on Triassic red beds. Their greater weight on a smaller earth would seem to provide the answer.

Many other things would happen on a 40% earth. Lazy rivers would become torrents. The nearly tripling of the Coriolis force would cause animals unconsciously to roam in circles of ever increasing concentricity, finally chasing their own tails. The high gravity field probably explains why plants of the Triassic such as the horsetail (*Equisetum*) were stiffened with stems high in silica. Conservation of the moment of inertia would increase the rate of the earth's spin, so that the Triassic day would have been a mere ten hours long. This may explain why the modern descendants of the Triassic reptiles remain today as the sleepest of all God's creatures.

Admittedly, for all its advantages there are some aspects of the expanding earth concept which need a bit of tidying up. For example, what to do with all that water if there were no ocean basins to contain that stuff— 1300×10^6 km². One solution would be to assume that it was all locked up as fresh water in enormous ice caps on the continents and, of course, there was a great Permo-Carboniferous glaciation. But then what about all that residual salt. . . .

'I have discovered the length of the sea serpent, the price of the priceless and the square of the hippopotamus . . . and how many birds you can catch with the salt in the ocean—187,796,132 if it would interest you to know,' said the Royal Mathematician. 'There aren't that many birds,' said the King. 'I didn't say there were,' said the Royal Mathematician.

(Thurber/*Many Moons*)

Considering sodium chloride alone, the only type useful for taming birds, at 85% of total ocean salts we derive a figure of 43×10^{25} tons. Rounding the number of birds to be tamed to 188×10^6 provides us with 230×10^6 tons per bird. With due regard for the Royal Mathematician's wisdom, this does seem a bit much to pour on the tail of each bird.

Carey (1970) would configure the world into eight primitive (Paleozoic) polygons—one for each continent plus an Eo-Pacific polygon, all of which would have moved away from each other over the past 200 m.y., causing a 75% increase ($220 \times 10^6 \text{ km}^2$) in the earth's surface area. This is a story of separating polygons, beginning with a roughly 60% earth, motivated by six convecting mantle toroids plus a jet stream. The old moribund passivity is replaced by a kaleidoscopic crust with gross churnings of the earth's interior. This may seem bizarre, but, as Carey points out, so was Wegener's drift a few years ago when 'the American bandwagon chanted *Ein Marchen*, a pipe dream, and beautiful fantasy.'

Carey adheres to the Egyed principle that the continents have dried off as the ocean was slowly withdrawn into the growing ocean basins. The ultimate cause, according to Egyed, was an expanding atom. The collapsed atoms of the inner core, he supposed, eventually evolved into outer-core substance with constrained electron shells and then into normal mantle rock. In other words, the core evolved into the mantle rather than the core being differentiated from the mantle as is usually supposed.

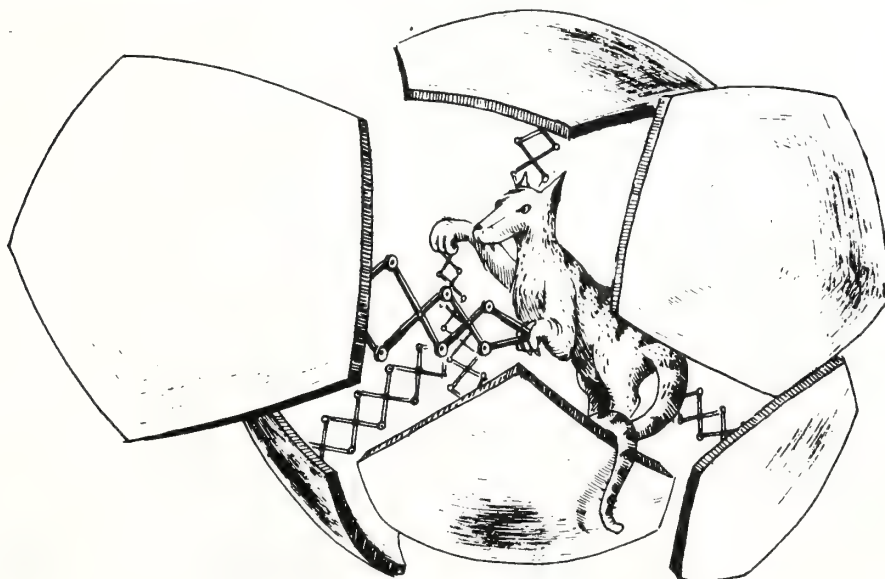


FIGURE 15
... Hungarian atom and the Tasmanian tessellated earth

Possibly Egyed of Budapest has provided ultimate key with which to unsuture Carey's zipped-up, tessellated earth of the Paleozoic. A Hungarian expanding atom would force apart the Tasmanian polygonal shells, causing the earth to grow and grow . . .

In short, an expanding earth remains an exhilarating concept worthy of philosophic contemplation. It seems rather unkind that some unimaginative persons call it 'balloonus balonus.'

Drifters are Alive, . . . and Well

We drifters are now being pushed around, even as we push the continents around. There is a need to be more assertive—and to make some more flat-out bold statements. We need a return to the faith of Galileo Galilei, who, when forced under duress to recant his theory that the Earth rotates on its axis and revolves around the Sun, muttered aloud as he left the Inquisition, 'Eppur si muove' ('but still it moves'). Earlier, in his *Sidereus Nuntius* of 1610, Galileo wrote, 'The Moon is not perfectly smooth . . . but, on the contrary, it is full of inequities, uneven, full of hollows and protruberances just like the Earth itself.' The philosophers scoffed at this bizarre notion, for it was at variance with the writings of Aristotle. And even if the Moon did have irregularities, it must still be covered with a thick, smooth crystalline layer. Otherwise, how would the Moon so clearly reflect the map of the Earth on its face, with the dark region being our oceans and the light regions being our continents? Galileo retorted with an answer precisely suited to the merit of this argument. 'Let them be careful, for, if they provoke me too far, I will erect, on their crystalline shell, invisible crystalline mountains ten times as high as any I have yet described.'

So, let those fulminous forecasters of fixity take warning. If we devious disciples of drift are not permitted to move our continents a paltry few centimeters each year, then we will drift them several meters each day!

The Geotectonics Creed

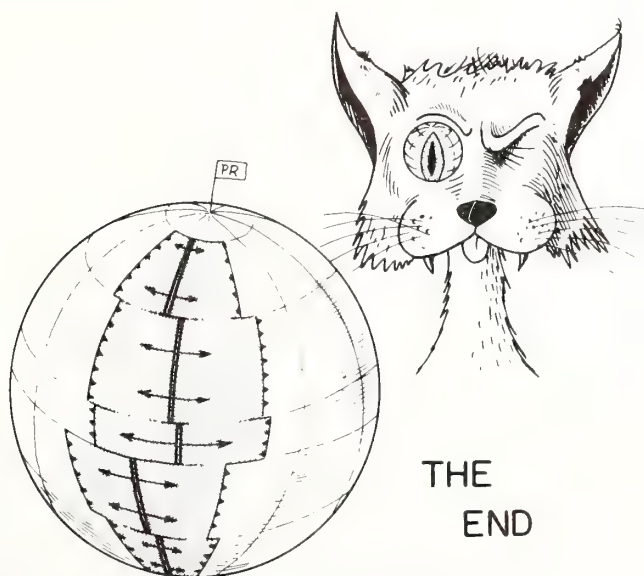
In closing, it would seem that continental drift, as derived from sea floor spreading, transform faulting, and plate tectonics, is the new orthodoxy. As statement of faith, the oath of office for the modern global tectonicist seems in order as is provided by the new Geotectonics Creed (Scharnberger & Kern, 1972), with apologies to the Council of Nicea.

'I believe in Plate Tectonics Almighty, Unifier of the Earth Sciences, and explanation of all things geological and geophysical; and in our Xavier LaPichon, revealer of relative motion, deduced from spreading rates about all ridges; Hypothesis of Hypothesis, Theory of Theory, Very Fact of Very Fact; deduced not assumed; Continents being of one unit with the Oceans, from which all plates spread; Which, when they encounter another plate and are subducted, go down in Benioff Zones, and are resorbed into the Aesthenosphere, and are made Mantle; and cause earthquakes foci also under Island Arcs; They soften and can flow; and at the Ridges magma rises again according to Vine and Matthews; and ascends into the Crust, and maketh symmetrical magnetic anomalies; and the sea floor shall spread again, with continents, to make both mountains and faults, Whose evolution shall have no end.

And I believe in Continental Drift, the Controller of the evolution of Life, Which proceedeth from Plate Tectonics and Sea-Floor Spreading; Which with Plate Tectonics and Sea-Floor Spreading together is worshipped and glorified; Which was spake of by Wegener; And I believe in one Seismic and Volcanistic pattern; I acknowledge one Cause for the deformation of rocks; And I patiently look for the eruption of new Ridges and the subduction of the Plates to come. Amen.'

References

- Belousov, V. V., 1962. Basic Problems in Geotectonics. McGraw-Hill, London, 465 pp.
 Blackett, P. M. S., Bullard, E. and Runcorn, S. K., 1965. A Symposium on Continental Drift. The Royal Society, London, 323 pp.
 Bullard, E. C., Everett, J. and Smith, A. G., 1965. The fit of the continents around the Atlantic. *In: Symposium on Continental Drift, Phil. Soc.* 1066, *Roy. Soc.*, **258A**, 41-51.
 Carey, S. W., 1958. Tectonic approach to continental drift. *In: Continental Drift, A Symposium*, pp. 177-358. Univ. Tasmania Press.
 Carey, S. W., 1970. Australian, New Guinea and Melanesia in the current revolution in concept of the evolution of the earth, *Search*, **1**, No. 5, 178-89.
 Jeffreys, H., 1970. The Earth: 5th edition. Cambridge Univ. Press, 525 pp.
 Longwell, C. R., 1958. My estimate of the continental drift concept. *In: Continental Drift, A Symposium*, pp. 1-12. Univ. Tasmania Press.
 Meyerhoff, A., 1972. Continental drift, *Geotimes*, **17**, No. 4, 34-6 (rev. of book by D. and M. Tarling).
 Meyerhoff, A. A. and Meyerhoff, H. A., 1972. The new global tectonics: major inconsistencies, *Amer. Assoc. Petrol. Geol.*, **56**, 269-336.
 Scharnberger, R. and Kern, E., 1972. Geotectonics creed, *Geotimes*, **17**, No. 1, 9-10.
 Snider, A., 1859. La Creation et ses Mysteres dévoiles. A. Franck and E. Dentu, Paris, 487 pp.
 van Hilton, D., 1964. Evaluation of some geotectonic hypotheses by palaeomagnetism, *Tectonophysics*, **1**, 3-71.
 Wegener, A., 1924. Origin of Continents and Oceans (English trans. 3rd edition by J. Skerl), 212 pp. Dutton and Co.



... hypotheses, like cats, have nine lives

Geophysical Illusions of Continental Drift: A Discussion¹

ROBERT S. DIETZ² and JOHN C. HOLDEN²

Miami, Florida 33149

Abstract The "illusions of continental drift," as envisioned by Mantura, are not illusions. Continental drift is a necessary consequence of plate tectonics according to which the continents are embedded in a mosaic of even larger rigid lithospheric plates which drift in relative rotation on the earth's spherical surface. The plates are bounded by spreading rifts, subduction zones, and transform faults. Our reply is an attempt to answer the 20 questions posed by Mantura in his open letter to plate tectonicists. Many problems remain unresolved, but plate tectonics remains a strong, viable, and persuasive concept.

In a recent Geological Note, "Geophysical Illusions of Continental Drift," A. J. Mantura

(1972) posed 20 questions in the form of an open letter and asks that they be answered. He concluded that "the proofs against continental drift . . . are overwhelming . . ." We will attempt to answer briefly the questions one by one so far as we understand them, but some-

© 1973. The American Association of Petroleum Geologists. All rights reserved.

¹ Discussion received, November 27, 1973; accepted, April 2, 1973.

² Marine Geology and Geophysics Laboratory, National Oceanic and Atmospheric Administration, Atlantic Oceanographic and Meteorological Laboratories.

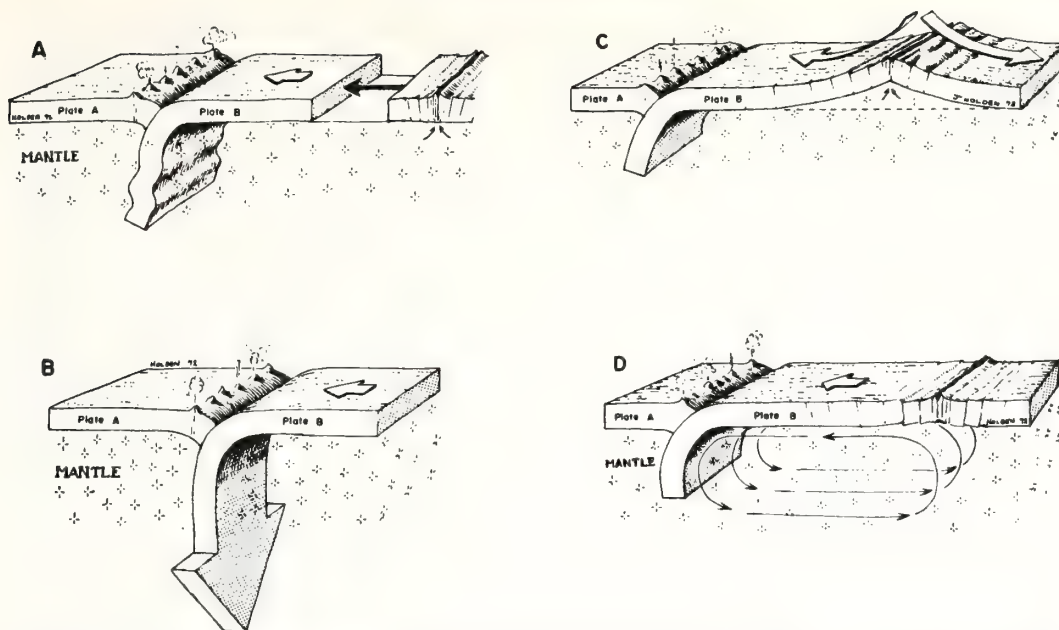


FIG. 1—Some possible, highly diagrammatic, mechanisms of plate motion. **A.** The plate is *pushed* by the insertion of dikes into the midocean rift. **B.** The plate is *pulled* into the subduction zone as the downgoing slab becomes heavier by cooling, by addition of eclogite "sinkers," or by phase changes in olivine. **C.** The plate moves by *sliding* downhill—i.e., down a gravity slope. **D.** The plate is *carried* on the back of a convection cell by stress coupling. For the purpose of this illustration, a symmetrical cell is shown but many other convection cell types and configurations are possible—for example, the plate motion being the vector sum of many small cells. Model **A** is certainly *incorrect* but models **B**, **C**, and **D**, plus other forces, may account for plate motion.

times paraphrased. Following his format, we also will keep the discussion general and minimize references to the voluminous literature of plate tectonics. Our views must not be construed necessarily to be the orthodox opinions of plate tectonists. Mobilists are under no more obligation to agree than are fixists. The new horizontal motion or drift dimension of plate tectonics adds an additional degree of freedom to geology. This increases the number of possible solutions to any problem. Two easily readable recent articles on plate tectonics are Dewey (1972) and McKenzie (1972).

Convection cells, and their doubtful validity, are a recurrent theme throughout Mantura's critique. How can convection cells follow ridges which are migrating? How can these cells conform to the various and curious shapes of the crustal plates? How can a ridge be consumed within a trench, as, by convection theory, this implies upward and downward flow at the same place? We agree (as most plate tectonists do) that the concept of drifting crustal plates on the backs of mantle cells leads to highly unlikely cell geometries and kinematics.

But many other possible mechanisms for driving plates remain (Lliboutry, 1969). Some of these are: (1) sliding of the plates downhill from the high ridge to the low trenches by gravity (Hales, 1969); or drift by other body forces—e.g., tidal pull. (2) The cold and thick part of the plate may pull the remainder into a trench. (3) The plates may be pushed by the emplacement of new dikes at the midocean rift (a highly unlikely model). (4) The mantle plumes, which create the hot spots, may entrain the plates (Morgan, 1971), a modified type of convection. (5) Various other motions of the mantle, such as transvection, may entrain the plates. In defense of those who believe in mantle convection cells, however, we must emphasize that there need not be any exact matching between cells and crustal plates. The drift of any plate easily could represent the vector sum of the stresses imposed by two or more mantle cells. It is of course true that plate tectonics enjoys something less than theory status until a full understanding of the drift mechanism is understood and this remains today far from being achieved. In the interim, we still can ob-

serve and study plate motion even though we don't know what is inside the "black box."

1. *Congruency of midocean ridges and continental margins*—Midocean ridges never "mirror" continental margins, as Mantura states, for there is no left-right inversion; rather, they are roughly congruent with these margins. This is apparent especially in the Atlantic Ocean, which is wholly a rift ocean; it is partly true for the Indian Ocean, a complex ocean basin with both a rift and subduction crust, and not at all true for the Pacific (north of the Eltanin fracture zone) as this is a trench (closing) ocean where the initial rift did not split a continent. Obviously this congruency can apply only to an oceanic basin between cratons which have been sundered. The congruency can be explained by the mechanism of sea-floor spreading, by which dikes are intruded into the midocean rift as the plates *passively* move apart. The dikes are hot and therefore weak, especially down their central axes away from their chilled side walls. They split apart symmetrically with one-half of each dike being accreted to each plate. Hence the shape of the original continental break is preserved. It should be noted, however, that the fit of Africa to North America is somewhat better than the fit of either craton to the midocean rift. The rift is never "subjected to intensive and repeated episodes of convective movement." The plates remain rigid, a basic tenet of plate tectonics.

2. and 3. *Shapes of ridge and convection cells*—These questions largely are answered in our opening statement about convection cells. In addition, Mantura fails to recognize the importance of transform faults, plate margins which are lines of shear so that there is conservation of crust. The sinuous form of the Mid-Atlantic Ridge is explainable by offsets of the rift along roughly east-west transform faults; the spreading ridge segments are roughly north-south. Much of the worldwide midocean ridge system is composed of transform fault segments (*e.g.*, Southwest Indian Ocean ridge). A transform fault can be defined as a major strike-slip fault which is also a plate boundary. This means in turn that it is a megashear which terminates at either a trench or a spreading ridge; hence, it transforms into another type of plate boundary. If plates are rigid, a transform fault, in order to conserve crust, necessarily must lie along a small circle of earth with respect to the relative pole of rotation of the two plates for which it is a boundary—*e.g.*, the San Andreas fault for the Americas/Pacific plates.

This also means that, if the amount of slip or creep is 6 cm/year along one point on the San Andreas fault, it must be the same along all parts of that fault. Transform faulting implies continental drift. Before this model was invoked, it was necessary to suppose that the entire Pacific basin was rotating counterclockwise (rigid lithosphere model) or that the fault gradually died out (nonrigid model).

4. *Latitudinal control of spreading rates*—In stating that convection models suggest that spreading rates should be maximal at the equator and minimal at the rotational pole, Mantura presumably has in mind models with longitudinal toroids (*e.g.*, Runcorn, 1962). Such models almost certainly are incorrect as probably are also all models involving idealized mantle convection cells. Spreading in the North Atlantic can be measured in terms of the Eurasia/America rotation and the Africa/America rotation (south of the Azores ridge/ridge/fault triple point). It happens, for reasons not yet understood, that both of these poles of rotation fall in high latitudes near the earth's rotational pole. The spreading rate varies at the cosine of the latitude with respect to the pole of rotation. Hence the spreading rates in the equatorial Atlantic are relatively large, not small as Mantura states. Poles for some of the crustal plates around the Indian Ocean (*e.g.*, Indian-Australian plate) lie at low latitudes.

5. *"S" shape of Mid-Atlantic Ridge*—The shape of the Mid-Atlantic Ridge need not, and almost certainly does not, have anything to do with a convection cell of that shape. The rift segments, in fact, strike generally north-south. These spreading axes in turn are offset by transform faults (Charlie, Azores, Romanche, *etc.*), which are the real cause of the so-called "S" shape. The irregularity of the Atlantic basin is due largely to the split being staggered in time, with North America/Africa (180 m.y. ago) separating first, then South America/Africa (135 m.y. ago), and finally North America/Eurasia (65 m.y. ago).

6. *Subsidence of ridges*—Mantura asks why the topography of the Mid-Atlantic Ridge becomes increasingly subdued away from the ridge crests. According to the sea-floor-spreading concept, both the ridges and their central rift (the axis of spreading) are steady-state features. The central rift, commonly about 10 km wide, had this same width 10 m.y. ago and will have the same width 10 m.y. from now. Although new ocean crust is being accreted constantly to the plate edge, the rift is not growing

wider. Clearly a process of "unfaulting" (reverse faulting) is taking place whereby the rift is healed and uplifted into a broken arch (Deffeyes, 1970). As further spreading occurs, any point on the arch is carried away from the rift, and this is accompanied by cooling and, hence, subsidence of the lithospheric plate (Menard, 1969). Some tectonic smoothing of the topography also may occur, but most of the smoothing is due to covering by a sedimentary blanket.

7. *Trenches as subduction zones*—In plate tectonics, trenches are regarded as the marking lines of lithospheric descent and of oceanic crustal consumption. This subduction is occurring today, a steady-state condition, which explains why the trenches remain open even though they are sediment traps. The unconsolidated sediments within trench axes are weak; hence, they are not thrown into compressive "rug folds" away from the landward wall of a trench. The absence of large thicknesses of deformed sediments in oceanic trenches is due to these deposits having been converted into thickened sedimentary and metamorphic rocks underlying the continental slope following deformation along the Benioff zone. The beds within the accreted nose are dipping too steeply and are too highly faulted to provide coherent acoustic reflectors (Seyfert, 1969).

8. *Jurassic sediments*—Spreading rates derived from the magnetic anomaly patterns indicate that about 2.5 sq km of new ocean floor is born each year (Deffeyes, 1970). At this rate the entire ocean floor is renewed, on an average, every 120 million years. We therefore should expect to find (and do find according to the Joides deep sea drilling results) Cretaceous and Jurassic sediments commonly overlying the oceanic crust in those regions at some distance away from a spreading axis. Joides findings in the South Atlantic apparently confirm the rift opening of that basin since the early Cretaceous (110 m.y. ago; Maxwell *et al.*, 1970). This does not preclude the possible existence of even Paleozoic sediments on the ocean floor at some unusual site, but none older than middle Jurassic have been found to date. We (Dietz and Holden, 1970) suggested the Wharton basin might contain late Paleozoic strata, but Joides results appear to disprove our model. Plate tectonics has been highly successful in explaining the youth of the ocean floor. It is clearly not a Precambrian terrane as the fixists had proposed.

9. *Persistence of ridges*—The lithosphere (when defined in terms of mechanical

strength) is thinnest and weakest at the rift axis and hot rock is weak. The "eternal" supply of dike rock is explainable by the upper mantle being composed of ilerzomite (pyrolite), which is incompletely differentiated into refractory ultramafic rock like dunite. Hence, its partial melting constantly can supply fresh tholeiitic basalt to the spreading axis. New plate boundaries have formed in the past and can form again. Sykes (1970) has suggested that a new plate boundary now is forming in the west-central Indian Ocean and that this is related to the impaction of India against Eurasia.

10. *Explanations for Cape Verdes, Canaries, Madeiras, Jan Mayen, Chile Rise, Seychelles, Faeroes, and Rockall*—Plate tectonicists are under no obligation to explain all features of the ocean floor, but, it is true, we rarely are left wordless. The Cape Verdes, Madeiras, and Canaries (far offshore) are alkaline basalt, volcanic island edifices of the central eruption type probably associated with hot spots. They were created mostly in the past 25 million years since the position of Africa has become almost fixed; hence, they are not strung out (Burke and Wilson, 1972). The nearshore Canaries (Lanzarote, Fuerteventura, and Concepcion Bank) probably are a microcontinental fragment associated with the early phase of breakup of Africa/North America (Dietz and Sproll, 1970). The Seychelles are clearly part of a microcontinent (sialic cratonic fragment), as is also Rockall, at least in large part. The Faeroes are a volcanic excrescence on the Eurasian plate, the eastward anchor of the Faeroes-Iceland-Greenland ridge—a volcanic nematath laid down over a mantle hot spot as the overlying plates drifted. The Chile Rise is the boundary between the Nasca plate and the Antarctica plate; it is composed of segments of spreading rift and transform faults.

11. *Iceland*—Mantura emphasized that Iceland is anomalous in many respects and, he argued, disproves sea-floor spreading. We believe that Iceland fits nicely into plate tectonics once we recognize that this mass of subalkaline volcanics was formed above a mantle hot spot—a plume of magma rising from the deep mantle. Although Iceland lies athwart the midocean ridge and appears to be in fact rifting apart at a full spreading rate of about 1.60 cm/year, a hot-spot plume dominates its tectonic style. Iceland is the only place where the midocean ridge breaches the ocean surface, making the ridge available to subaerial study, but we must bear in mind that Iceland is anomalous. Iceland is

not a proper "type locality" for sea-floor spreading as is the Reykjanes ridge, the South Atlantic, and the southeast Pacific. The Atlantic rift is offset by transform faults 200 km to the east where it crosses Iceland. The usually symmetric sea-floor spreading has been asymmetric in Iceland, this asymmetry probably being imposed by the hot spot "overprinting." It is reasonable to suppose that the symmetric pull-apart of dikes (sea-floor spreading) could be affected by the injection of additional magma from a deep-mantle, extraneous source. A fixed hot spot then would tend to keep a ridge from migrating. The "tape recording" of magnetic reversal anomalies also might be expected to find interference at Iceland, not only because of the hot spot, but also because the subaerial injection of magma into the rift precludes the formation of pillow lavas. All in all, Iceland tends to confirm plate tectonics rather than disprove it (Ward, 1971; Johnson *et al.*, 1972).

12. *India-Eurasia collision*—In plate tectonics, plates never collide; instead one plate is subducted beneath the other along a trench. Cratons collide, giving rise to collision tectonics, obduction, and "flake tectonics" (Oxburgh, 1972). The suture zone generally is marked by oceanic crustal rocks (ophiolites) and upper mantle rocks (ultramafics). Such a suture zone can be identified clearly between the India and the Eurasia plates (Coleman, 1971). Plate tectonicists accept the collision of India with Eurasia, but the exact nature of the tectonic style involved remains much debated. Suffice it to say, the simplistic picture objected to by Mantura of the India craton being subducted *in toto* and without breakup beneath Eurasia is doubtful. It is interesting to note, however, that the southward facing Himalayan rampart is nearly 5,000 m high, so that it is the only escarpment on land which equals the relief of a continental slope. It would seem, therefore, if isostasy prevails, that this part of the Himalayan plateau is supported by a double thickness of sialic crust.

13. *Alaska-Siberia suture*—In placing the geologic joining of the North America plate to the Eurasia plate through the Bering Strait, Mantura appears to be accepting geographic or political boundaries as proper geologic boundaries. Neither the Siberian nor the Alaskan cratons are "pointed," even though the shorelines are. The narrowest waist of the American-Eurasian juncture lies along the Alaska-Yukon boundary and not through the Bering Strait when continental-shelf widths are taken into

consideration. It is true that most continental-drift sequences (*e.g.*, Dietz and Holden, 1970) require at least a minor collision between the North America plate and the Eurasian plate, but the suture is not placed through the Bering Strait, for Alaskan tectonic patterns appear to continue into Siberia. The correct suture most probably runs from the Alpha Ridge in the Arctic Ocean through the Verhojansk foldbelt and then strikes southeasterly across the Siberian craton to intersect the flexure between the Kurile and Kamchatka trenches. This line is coincident with Mesozoic-Cenozoic foldbelts and some modern seismicity.

14. *Africa as a pivot*—Africa is not the heartland of continental drift. Antarctica possibly can be so regarded, as the Antarctica plate has no subduction zones and hence "no place to go," at least on its own. Any drift must be accommodated by that of other surrounding plates. It is in a sense a "non-plate" and a cicatrix. Mantura appears to have confused Africa and Antarctica with respect to our paper on the breakup of Pangaea (Dietz and Holden, 1970). It is the latter from which the various fragments of Gondwana departed radially. We recognized two general drift motions for the continents relative to the earth's spin axis, a western drift for the New World and a northward drift for those surrounding the Indian Ocean. Paraphrasing Wegener, one can term these a *Westwanderung* and a *Sudpolarfluchtkraft*. The reason remains unknown.

15. *Drift of India*—There is nothing within plate theory which suggests that continents move toward "voids" (ocean basins), as Mantura remarks. Africa, India, and Arabia have collided with Eurasia. If the present plates persist, North America eventually will collide with Asia. In reality, continents, as well as the plates themselves, move toward subduction zones (usually expressed as trenches) and away from rifts. Trenches, consuming plate margins, however, can form only in ocean basins. Only ocean floor can be subducted and consumed down Benioff zones. Ocean basins expand and collapse whereas continents persist through geologic time.

16. *Are ridges stationary or migratory?*—Ridges generally migrate and there is every reason within the scheme of plate tectonics to expect them to migrate. The new dike which is inserted into passively separating plates along a spreading axis and later is symmetrically split apart has no knowledge of which plate has moved in an absolute sense. In some special in-

stances they may be stationary or approximately so, especially when they coincide with hot spots. It seems likely that the South Atlantic ridge near Tristan da Cunha Island remained stationary for much of its history (Dietz and Holden, 1970), but then commenced to migrate westward 25 m.y. ago (Burke and Wilson, 1972).

17. *What can we hold still?*—Probably the earth's spin axis and hot spots, but certainly nothing else. All continents, all plates, and all plate boundaries have moved in varying amounts. The migrations which Mantura terms absurd are in fact plausible. Our reconstructions (Dietz and Holden, 1970), by way of example, were accomplished graphically and in model on a globe. They may not be correct, but they certainly are geometrically permissible on the spherical earth and under the rules of plate tectonics.

18. *More about convection cells*—Mantura confuses convection-cell geometries with plate configurations. There is no need for a 1:1 correspondence between the two. In fact, there is no need for convection cells at all as a mechanism for moving the crustal plates. There is some evidence that streaming of substance within the upper mantle away from a hot spot is a factor in plate motion (Morgan, 1971). Plate tectonics remains today in the descriptive stage, but it is not necessary to know the causal mechanism to observe that crustal plates exist and rotate as rigid spherical shells on the earth.

19. *Drift of Madagascar*—Madagascar is a microcontinent or better, a subcontinent, for its size places it on a par with Greenland, India, and the New Zealand plateau. All are sialic continental fragments associated with the breakup of Pangaea, commencing about 180 m.y. ago. The exact derivation of Madagascar remains unsettled. Recently the Angola position has been gaining in favor over the Tanzania position. Which way did it drift? We can only reply: relative to what? We think (Dietz and Holden, 1970) that its drift was generally northward in an absolute sense (with respect to the earth's rotational axis), but this would be southward (a falling behind) with respect to Africa. We must remember, also, that a drifting plate almost never follows a fixed compass direction, in the general case, for it is impossible to translate a rigid shell on a sphere; it can be rotated only in accordance with Euler's theorem.

20. *Western North America*—Plate tectonics do not hold that the North American

plate was thrust onto the Pacific plate, except possibly for that sliver west of the San Andreas fault. The usual version is that North America drifted westward; a trench was encountered, which was at first displaced westward and then "flipped." The Farallon plate (of which the Riviera and Gorda plates are now remnants) then was subducted into the trench. Eventually the spreading ridge of the Farallon plate was swallowed by the trench. The conjunction of a ridge with a trench destroys both, leaving a suture behind. If it remains as an active plate boundary, it is a transform fault—in this case the San Andreas fault.

CONCLUSION

Plate tectonics envisions that the earth's outer shell or lithosphere is divided into a mosaic of rigid spherical shells bounded by subduction zones (trenches) where oceanic crust largely is consumed, ridges (midoceanic rifts) along which new ocean crust is accreted symmetrically (sea-floor spreading), and transform faults (great strike-slip faults) usually connecting the other two boundaries. Continental drift is a necessary corollary of plate tectonics, as the cratons are rafted across the face of the earth embedded into the even larger crustal plates. Although much remains to be understood, especially as to mechanisms, plate tectonics is a viable and correct concept which will continue to revolutionize earth science.

REFERENCES CITED

- Burke, K., and J. T. Wilson, 1972, Is the African plate "stationary"? *Nature (Phys. Sci.)*, v. 239, no. 5372, p. 387-390.
- Coleman, R. G., 1971, Plate tectonics emplacement of upper mantle peridotites along continental edges: *Jour. Geophys. Research*, v. 76, no. 5, p. 1212-1222.
- Deffeyes, K. S., 1970, The axial valley: a steady-state feature of the terrain, in H. Johnson and B. L. Smith, eds., *The megatectonics of continents and oceans*: New Brunswick, New Jersey, Rutgers Univ. Press, p. 194-222.
- Dewey, J. F., 1972, Plate tectonics: *Sci. American*, v. 226, no. 5, p. 56-68.
- Dietz, R. S., and J. C. Holden, 1970, Reconstruction of Pangaea: breakup and dispersion of continents, Permian to present: *Jour. Geophys. Research*, v. 75, no. 26, p. 4939-4956.
- , and —, 1971, Pre-Mesozoic oceanic crust in the eastern Indian Ocean (Wharton Basin): *Nature*, v. 229, no. 5283, p. 309-312.
- , and W. P. Spill, 1970, East Canary Islands as a microcontinent within the Africa-North America continental drift fit: *Nature*, v. 226, no. 5250, p. 1043-1045.
- Hales, A. L., 1969, Gravitational sliding and continental drift: *Earth and Planetary Sci. Letters*, v. 6, p. 31-34.

2296

Discussions and Replies

- Johnson, G. L., J. R. Southall, P. W. Young, and P. R. Vogt, 1972, Origin and structure of the Iceland plateau and Kolbeinsey Ridge: *Jour. Geophys. Research*, v. 77, no. 29, p. 5688-5696.
- Lliboutry, L., 1969, Sea floor spreading, continental drift and lithosphere sinking with an asthenosphere at melting point: *Jour. Geophys. Research*, v. 74, no. 27, p. 6525-6540.
- Mantura, A. J., 1972, Geophysical illusions of continental drift: *Am. Assoc. Petroleum Geologists Bull.*, v. 56, no. 8, p. 1552-1556.
- Maxwell, A. R., R. P. von Herzen, K. J. Hsü, J. E. Andrews, S. F. Saito, E. D. Percival, E. D. Millow, and R. E. Boyce, 1970, Deep-sea drilling in the South Atlantic: *Science*, v. 168, p. 1047-1059.
- McKenzie, D. P., 1972, Plate tectonics and sea-floor spreading: *Amer. Scientist*, v. 60, no. 4, p. 425-435.
- Menard, H. W., 1969, Elevation and subsidence of

- oceanic crust: *Earth and Planetary Sci. Letters*, v. 6, p. 275-284.
- Morgan, W. J., 1971, Convection plumes in the lower mantle: *Nature (Phys. Sci.)*, v. 230, no. 5288, p. 42-43.
- Oxburgh, E. R., 1972, Flake tectonics and continental collision: *Nature (Phys. Sci.)*, v. 239, p. 202-204.
- Runcorn, S. K., 1962, Towards a theory of continental drift: *Nature*, v. 193, no. 4613, p. 311-314.
- Seyfert, C. K., 1969, Undeformed sediments in oceanic trenches with sea-floor spreading: *Nature*, v. 222, p. 70.
- Sykes, L., 1970, Seismicity of the Indian Ocean and a possible nascent island arc between Ceylon and Australia: *Jour. Geophys. Research*, v. 75, no. 26, p. 5041-5055.
- Ward, P. L., 1971, New interpretation of the geology of Iceland: *Geol. Soc. America Bull.*, v. 82, p. 2991-3012.

ROBERT S. DIETZ } *National Oceanic and Atmospheric Administration, Atlantic Oceanographic and*
JOHN C. HOLDEN } *Meteorological Laboratories, 15 Rickenbacker Causeway, Miami, Florida 33149*

Geotectonic Evolution and Subsidence of Bahama Platform: Reply

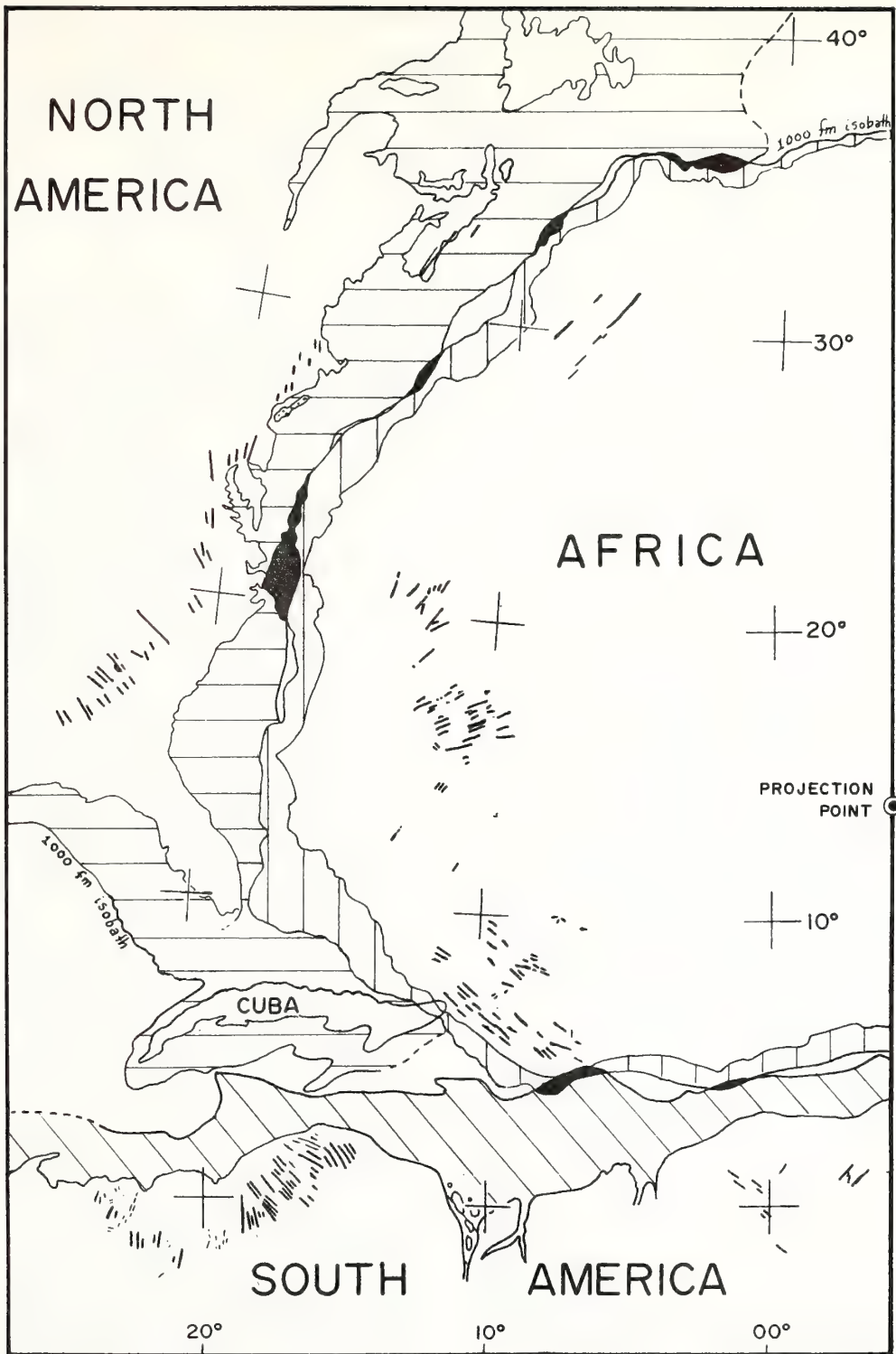
We agree with Glockhoff (1973) that a Triassic-Jurassic volcanic foundation probably underlies the Bahama carbonate platform, at least partially. We suggest that a mantle plume (hot spot) in that region initiated the rifting of North America from Africa, resulting in asymmetrical spreading and causing the volcanic rocks to build up as a marginal plateau on the American plate only. In contrast to Glockhoff, we suggest that a small ocean basin, rather than a topographic high above sea level, also was created which was the site of deposits of taphrogenic Jurassic clastic material and deep-water salt.

Glockhoff (1973) and we agree that the Bahama carbonate platform was laid down on a subsiding Mesozoic ocean crust and thus is a neo-craton, not one underlain by a Precambrian basement complex. We are also in accord in accepting a plate tectonic-continental drift solution (Dietz and others, 1970). We agree, furthermore, that the Bahama platform may have a volcanic foundation, but we suggest that there is an extensive clastic basin as well, underlying the carbonate rocks. In fact, we have recently modified our model for the geotectonic evolution of the Bahama platform, which brings us into somewhat closer accord with Glockhoff's views (Dietz and Holden, 1973; Dietz, 1973). This also brings us closer to the modification of Uchupi and others (1971), who regard the Bahama escarpment as a buried fracture zone.

We have proposed that the Bahama platform was originally the site of a hot spot (deep-mantle magma plume) which may have been part of the driving force that initiated the rifting of North America from the remainder of Pangaea. This hot spot laid down an Iceland-

like (or Afar trianglelike) bolus of alkalic volcanic rocks of which the Late Triassic-Early Jurassic dikes (about 200 to 180 m.y. ago) of North America-South America-Africa would be the now-unburied remnants. Significantly, these dike swarms, under drift reconstruction, converge toward the Bahama platform (May, 1971) suggesting to us a former eruptive center there (Fig. 1).

We suggest that the North American plate, upon breakup, drifted northwest while the African plate remained essentially fixed with respect to the Earth's spin axis. The magma plume, also remaining fixed, thermally "overprinted" the symmetrical splitting of dikes involved in the sea-floor spreading process, so that the ridge axis within the proto-Bahama basin also remained fixed and adjacent to Africa, causing *asymmetrical* sea-floor spreading. Magmas were selectively poured onto the North American plate as this was the site of the small ocean void. A ridge-to-ridge transform fault connected this nonmigrating ridge with the normally spreading mid-ocean ridge farther north. The position of this former transform fault would now be marked by the northern escarpment (continental slope) of the Bahamas (Figs. 2, 3). This "fixing" of the spreading ridge by a hot spot seems intuitively reasonable and may explain, as well, why the ridge through Iceland is offset 175 km eastward with respect to the Rekjanes ridge. A similar "ridge fixing" appears to have occurred on the Galápagos rift (Holden and Dietz, 1972). The radiometric ages of the dikes suggest that the magma plume existed between about 200 to 180 m.y. ago (May, 1971) or over a span of 20 m.y. With the death of the hot spot, symmetrical sea-floor spreading



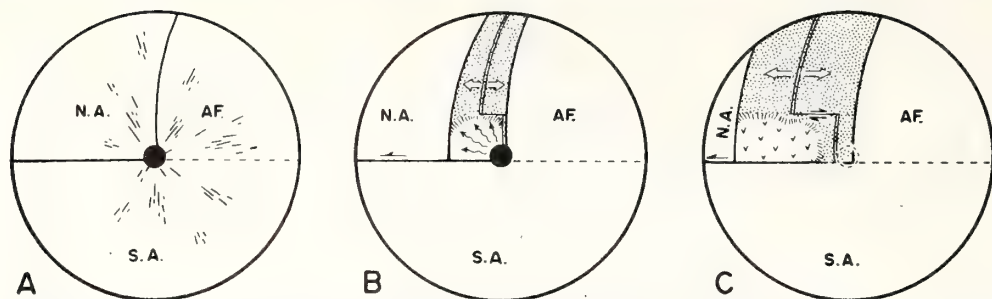


Figure 2. Schematic drawing of the generation of the Bahama plateau by a mantle-plume hot spot and associated asymmetrical spreading. A. Birth of the hot spot about 195 m.y. ago, with associated injection of a dike swarm; B. Initial rift of North America from Africa-South America about 185 m.y. ago. The hot spot and Africa-South America remained fixed while North America drifted away. The hot spot "overprinted" spreading and held the rift stationary

would commence. This history would account for the lack of deposition of a mirror-image excrescence on the African margin. The Guinea Nose marginal plateau, however, might be a small counterpart excrescence. This would also explain why the mid-ocean ridge (at $11^{\circ}00' \text{ N.}$, $43^{\circ}30' \text{ E.}$), at the Vema fracture zone, is not mid-oceanic with respect to the pertinent conjugate points (the southern tip of Florida, at $25^{\circ}45' \text{ N.}$, $80^{\circ}00' \text{ W.}$, and the Guinea Nose, at $8^{\circ}50' \text{ N.}$, $15^{\circ}30' \text{ E.}$). The leg between the African margin and the "mid-ocean" rift is 3,200 km long, while that between the rift and Florida is 4,300 km long. This difference in length of 1,100 km approximates the length of the Bahama platform. (It may be that the Dolphin fracture zone, about 1° farther south, is actually the correct mid-ocean conjugate point and, in this case, the asymmetry is greater.) The formation of Bahamian basement as a volcanic and sedimentary marginal plateau led to its quick creation. This seems a valid conclusion because JOIDES hole no. 4 of the Deep Sea Drilling Project in the deep Atlantic immediately to the west of the Bahamas revealed a probable oceanic-crust age of about 160 m.y. (Peterson and Edgar, 1969). The Bahama platform base-

while symmetrical spreading created a median rift farther north. The Bahama platform was selectively laid down on the North American plate and not on the African plate as a volcanic marginal plateau; C. The hot spot died about 175 m.y. ago, so that the associated rift commenced symmetrical spreading, migrating westward. For simplicity of presentation, this time-sequence diagram takes no account of concomitant sedimentation in the Bahamas region.

ment necessarily would have to have been completely formed shortly prior to that time.

A basic disagreement between Glockhoff and us is that Glockhoff suggested that a volcanic high above sea level initially occupied the Bahama region, but we inferred the presence of a basin. Central to her argument are the probable diapiric structures reported by Ball and others (1968) which may well be salt diapirs. This salt, she suggested, was deposited in shallow water. We disagree; salt diapirs require at least a 300- to 400-m-thick bed of mother salt (Gera, 1972), and such large deposits of salt are probably laid down not in sabkhas but in a deep basin cut off by a shallow sill from the open ocean (Schmaltz, 1969).

Glockhoff (1973) suggested that the salt associated with the Cayetano formation in northern Cuba (Furrazola-Bermúdez and others, 1964) is related to the probable salt under Exuma Sound. We have already suggested (Dietz and others, 1970) that this formation may be an outcrop of the clastic section underlying the Bahama platform. This presumably taphrogenic clastic and salt sequence is extremely thick (about 6,000 m), which suggests deposition in a small ocean basin rather than in shallow water.

Glockhoff also inferred that the purity of a salt formation means deposition in a basin starved for clastics. In contrast, we believe that such purity usually implies that, when conditions are correct, thick salt can be laid down in a remarkably short time. Evaporite salts appear to accumulate at rates of 1 to 20

Figure 1. Late Jurassic-Early Triassic dike swarms point generally toward the Bahama platform, suggesting that this area was the locus of a mantle magma plume which may have initiated the rifting of North America from the remainder of Pangea. (Dike swarms are redrawn from May, 1971.) The Africa-North America fit is from Dietz and others (1970).

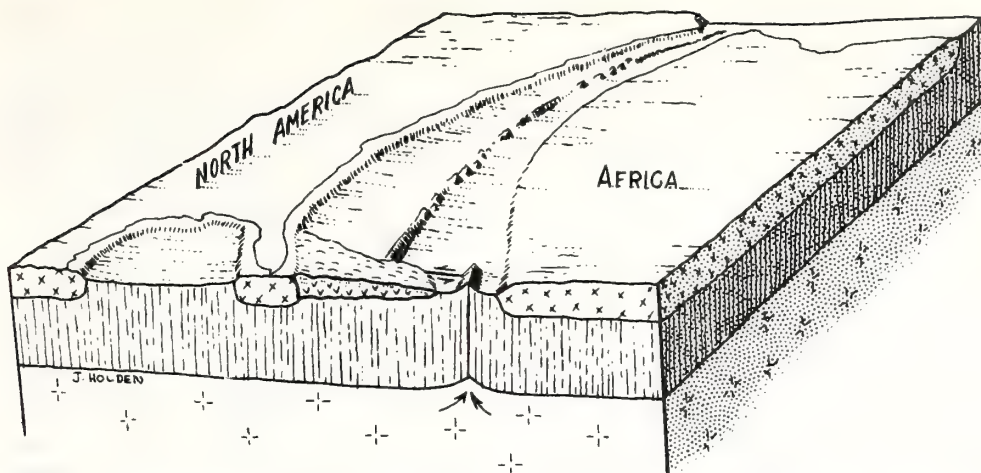


Figure 3. Block diagram of the evolution of the Bahama platform as a marginal plateau shortly after the death of the hot spot about 180 m.y. ago. For simplicity, only one fracture-zone offset is shown. Actually, asymmetry of the mid-ocean ridge commences at the Kane fracture zone, considerably to the north of the Vema fracture zone, so that the total asymmetry is caused by the summation of a number

of left-lateral offsets of the ridge axis. This suggests that hot-spot magma flowed north along the ridge, "overprinting" symmetrical sea-floor spreading for a considerable distance to the north of the Bahama platform. An effect of this type has been proposed by Vogt (1971) to account for V-shaped ridges south of Iceland.

cm per year, or 100 to 10,000 times faster than carbonates and clastic sediments (Schmaltz, 1969). A shallow sill separating the deep ocean from a new rift basin could easily be largely dammed by reef deposits which, if evaporation exceeded the inflow, would create a one-way flow of ocean water across the sill and into the new basin. A rapid deposition of deep-water salt would result.

We are reluctant to believe that the great re-entrants (for example, Tongue-of-the-Ocean, New Providence Channel, and Exuma Sound) reflect basement grabens (Ball, 1967). The gravity minima over these re-entrants can be variously interpreted based upon the density-layering model chosen. The modern Bahama cays and atolls of the Pacific show remarkable environmental adaption—for example, for formation of surge channels in a reef front to dampen the onslaught of waves. We believe that these re-entrants most likely serve to greatly increase the perimeter of the platform and place the interior portions near deep water. Oceanic water interchange is vital to reef growth. Hence, we suggest that basement topography, especially in the northern Bahamas, may have had little control on the development of the re-entrants, which have been constructed by differential carbonate build-up.

Glockhoff assumed that the high ground would surround the initial Bahama rift. Sea-floor spreading appears to result from passive injection and symmetrical splitting of dikes. This mechanism per se causes no uparching of the sialic crust, only thermal uplift of the new oceanic crust. However, uparching is observed in High Africa and along the margins of the Red Sea and the Gulf of California, indicating some mantle bulging, perhaps associated with a hot-spot plume, which exerts some control on the locus of rifting. We do not know with any certainty that uparching of the sialic crust (for example, in the absence of a hot spot) is always necessarily associated with the rifting of a continent.

We doubt Glockhoff's assumption that a rift basin surrounded by uparched sialic margin would necessarily be starved for clastic sedimentation. This is analogous to stating that rivers cannot reach the Gulf of California; the Colorado River gets to the gulf in spite of extensive Neogene uplifts. The hypothetical Bahama small ocean basin would be a large depression near the center of the Pangean supercontinent. Major rivers would certainly flow to this basin regardless of any mountainous barriers, probably entering one end of the elongate depression. Starved basins in the geologic record are usually related to ultra-

penplanation of the hinterland and not to surrounding mountainous barriers.

Glockhoff inferred a triple junction. Although it is possible, there is no absolute need for a triple junction in the history of the Bahama platform. The rifting of North America from Pangaea required no triple junction at the proto-Bahamas, because South America and Africa remained joined. Similarly, the rifting of South America from Africa about 120 m.y. B.P. required no triple junction, if South America and North America were both part of a single American plate. Of course, there could have been one similar to the abortive Cretaceous triple junction, which temporarily opened and then closed the Benue Trough as South America rifted from Africa. Or there may even be a triple junction today at the Mid-Atlantic Ridge with a ridge-to-trench transform fault extending to the Antilles Trench; but this is not evident from the locations of modern earthquake epicenters.

Glockhoff's Figure 1 (1973) is not entirely clear and, we believe, contains a few errors. A mid-ocean ridge never breaches the ocean surface unless, like Iceland, it is also a hot spot. In reference to her Figure 1, stage I, a mid-ocean ridge is a steady-state rift and does not grow wider with time; also, the mid-ocean axial dikes create only ocean crust, not volcanoes (central edifice cones of alkali basalt).

In summary, we agree with Glockhoff regarding a volcanic foundation for the Bahama platform, but, in our view, there are thick Jurassic sediments as well. We also believe that initially there was also a small ocean basin and not a mountain massif above sea level.

REFERENCES CITED

- Ball, M. M., 1967, Tectonic control of the configuration of the Bahama Banks: *Gulf Coast Assoc. Geol. Soc. Trans.*, v. XVII, p. 265-267.
- Ball, M., Gaudet, R., and Leist, E., 1968, Sparker reflection seismic reflections in Exuma Sound, Bahamas: *Am. Geophys. Union Trans.*, v. 49, p. 196-197.
- Dietz, R. S., 1973, Morphologic fits of North America/Africa and Gondwana, in *NATO symposium on continental drift at Newcastle, England, Proc.*: New York, Academic Press (in press).
- Dietz, R. S., and Holden, J. C., 1973, Plate tectonic evolution of the Bahama platform [abs.]: *EOS (Am. Geophys. Union Trans.)*, v. 54, no. 4, p. 417.
- Dietz, R. S., Holden, J. C., and Sproll, W. P., 1970, Geotectonic evolution and subsidence of Bahama platform: *Geol. Soc. America Bull.*, v. 81, p. 1915-1928.
- Furrazola-Bermúdez, G., and others, 1964, *Geología de Cuba*: Havana, Instituto Cubano de recursos minérales, Editora del Consejo Nacional de Universidades, 239 p.
- Gera, F., 1972, Review of salt tectonics in relation to disposal of radioactive wastes in salt formations: *Geol. Soc. America Bull.*, v. 82, p. 3551-3574.
- Glockhoff, C., 1973, Geotectonic evolution and subsidence of the Bahama platform: Discussion: *Geol. Soc. America Bull.*, v. 84, p. 3473-3476.
- Holden, J. C., and Dietz, R. S., 1972, Galapagos gore, NazCoPac triple junction, and Carnegie/Cocos ridges: *Nature*, v. 235, p. 266-269.
- May, P. R., 1971, Pattern of Triassic-Jurassic dikes around the North Atlantic in the context of pre-drift position of the continents: *Geol. Soc. America Bull.*, v. 82, p. 1285-1292.
- Peterson, M., and Edgar, N., 1969, Deep ocean drilling with *Glomar Challenger*: *Oceans*, v. 1, no. 5, p. 17-32.
- Schmaltz, R. F., 1969, Deep-water evaporate deposition: *Am. Assoc. Petroleum Geologists Bull.*, v. 53, p. 798-823.
- Uchupi, E., Milliman, J., Luyendyk, B., Bowin, C., and Emery, K. O., 1971, Structure and origin of the southeastern Bahamas: *Am. Assoc. Petroleum Geologists Bull.*, v. 55, p. 687-704.
- Vogt, P., 1971, Asthenosphere motion recorded by the ocean floor south of Iceland: *Earth and Planetary Sci. Letters*, v. 13, p. 153-160.

MANUSCRIPT RECEIVED BY THE SOCIETY MARCH 28, 1973

Antarctica and Continental Drift

ROBERT S. DIETZ, JOHN C. HOLDEN and WALTER P. SPROLL
NOAA, Atlantic Oceanographic and Meteorological
Laboratories, Miami, Florida 33130, U.S.A.

Abstract. Continental drift reconstructions by computerized matching of the 1,000 fm isobaths are presented for Africa/Antarctica, Australia/Antarctica and India/Antarctica. Sufficiently good congruency is obtained for the first two to suggest that they are probably correct but the India fit remains puzzling. A set of five maps is presented showing the original position of Antarctica within the framework of Gondwana and the subsequent continental drift break-up and dispersion through space and time. We suggest that, while the Antarctic plate offers only modest prospect as the site of stranded areas of pre-Mesozoic ocean crust, the Wharton basin (defined as that sector of the Australian plate delimited by Ninetyeast Ridge, Java trench, western Australia and the Diamantina fracture zone) is underlain by old oceanic crust. We associate the circular outline of east Antarctica with the passive tensional scar left by fast-drifting plates moving northward from relatively fixed Antarctica.

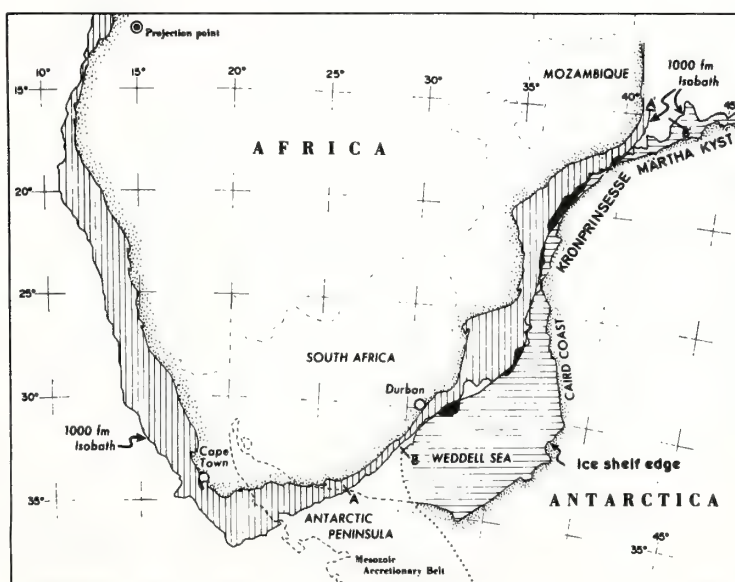
We propose in this paper to discuss the geometric position of Antarctica within Gondwana, especially with respect to Africa, India and Australia. We will also discuss the break-up and continental drift dispersion of these continents northward from Antarctica – a *Südpolarfluchtkraft*, to paraphrase Wegener's *Polarfluchtkraft*. Some comments are included about the circularity of east Antarctica and the possible location of old (pre-Mesozoic) ocean floor. This analysis is based upon the concept of sea-floor spreading and plate tec-

tonics. An interesting previous synthesis has been made by Heirtzler (in press).

Africa/Antarctica fit

As Fig. 1 shows, a close morphological fit (on the criterion of smallest average misfit) can be obtained by a computerized comparison of the 1,000 fm isobath of Africa and Antarctica. This reconstruction places the margin of south-eastern Africa against the region of the

Fig. 1. The best-fit position between Antarctica and Africa, a continental drift reconstruction in stereographic projection. Departures from congruency are shown as overlaps (opaque areas) or as underlaps (clear areas). The Antarctic Peninsula is shown in ghost outline on the presumption that it was non-existent (at least in its present position) prior to continental drift break-up.



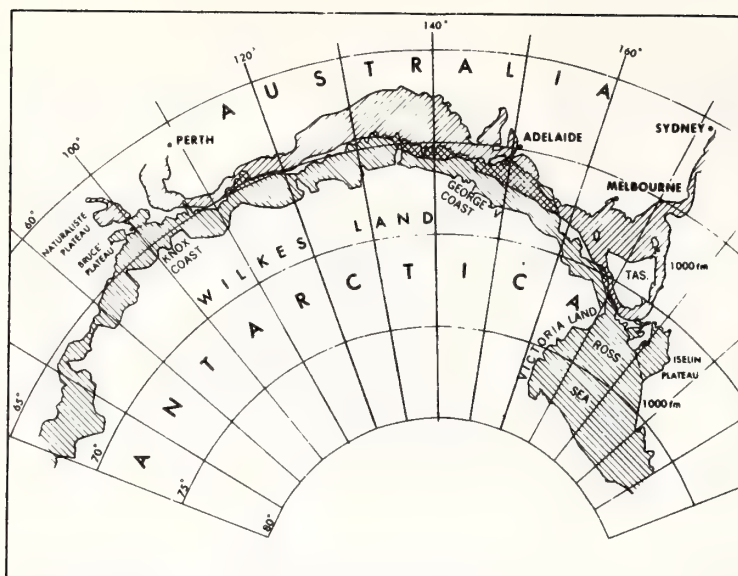


Fig. 2. The best-fit position of Australia relative to Antarctica, a continental drift reconstruction. Ruled lines indicate shelf and upper continental slope areas to the 1,000 fm isobath. Overlap areas are thus cross-ruled and underlap areas are blank.

Weddell Sea, Caird Coast and Kronprinsesse Märtha Kyst of east Antarctica. S-shaped parts of each continental margin then become congruent, with a total mismatch of only 60,000 km² (an area about the size of Denmark). The overlap is 36,000 km² and the underlap is 24,000 km². The average misfit along the join is 28 km (Dietz and Sproll, 1970).

This satisfying fit can only be obtained once the Antarctic Peninsula is omitted from consideration, on the rationale that the tip of this horn is a post-break-up accretionary fold belt and/or a sector of considerable geotectonic displacement. Hence, in our reconstruction the outer part of this horn is permitted to overlap, in ghost outline on Fig. 1, onto the Africa craton. We, of course, agree that this fold belt is properly regarded as an extension of the Andean orogen but we assume that it was developed subsequent to the initial continental drift break-up and probably during Antarctica's westward (counter-clockwise) rotation and probable slight southward drift. Based on the radiometric age of the Stormberg lavas and related extrusions, this rifting commenced in the mid-Triassic about 200 m yr ago (McDougall, 1963; Manton, 1968). It is noteworthy that the South America/Africa continental drift reconstruction has an underlap at its southern end. This gap originally may have been occupied by a cratonic block which was later incorporated by drift into the modern Antarctic Peninsula, as it seems to be a mix of old and new rock.

Smith and Hallam (1970) proposed a fit almost identical to ours. However, they placed Antarctica slightly westward, based upon the desire to close the Indian Ocean continents of Antarctica, India and Madagascar against Africa, so as to eliminate a small ocean basin

within the framework of Gondwana. By using the 500 fm isobath for fitting, their fit still results in a meriterranean sea occupying much of the Weddell Sea region within Gondwana. This inland sea is totally eliminated in our reconstruction because we use the 1,000 fm isobath for fitting. This isobath, in fact, seems to better delimit the true margin of a continent (Carey, 1958).

Antarctica/Australia fit

As Fig. 2 shows, a good fit can also be obtained along the 1,000 fm isobath between the Great Bight of Australia and the margin of Antarctica extending from the Ross Sea to the Knox Coast (Sproll and Dietz, 1969). The total mismatch of this fit is 150,000 km², with an overlap of 95,000 km² and an underlap of 55,000 km².

Although this fit is a purely geometric solution, it is geologically permissible as well. The Adelaide Precambrian-Cambrian miogeosyncline, characterized by Archaeocyatha, becomes contiguous to a similar geosyncline in Antarctica. Dolerite dykes of Tasmania also become adjacent to dykes of similar age and orientation in Victoria Land. The intrusion of these dykes, which are about 160 m yr old (Sunderland, 1966), probably seems not to be related to the 'lift off' of Australia from Antarctica, as the magnetic reversal anomalies suggest that this occurred as late as early Cenozoic (Le Pichon and Heirtzler, 1968). Their intrusion possibly could be synchronous with the break-away of New Zealand from the Antarctica-Australia supercraton, as this event apparently occurred earlier.

A satisfying aspect of this join is that three marginal plateaux form toe ends which nicely box in an con-

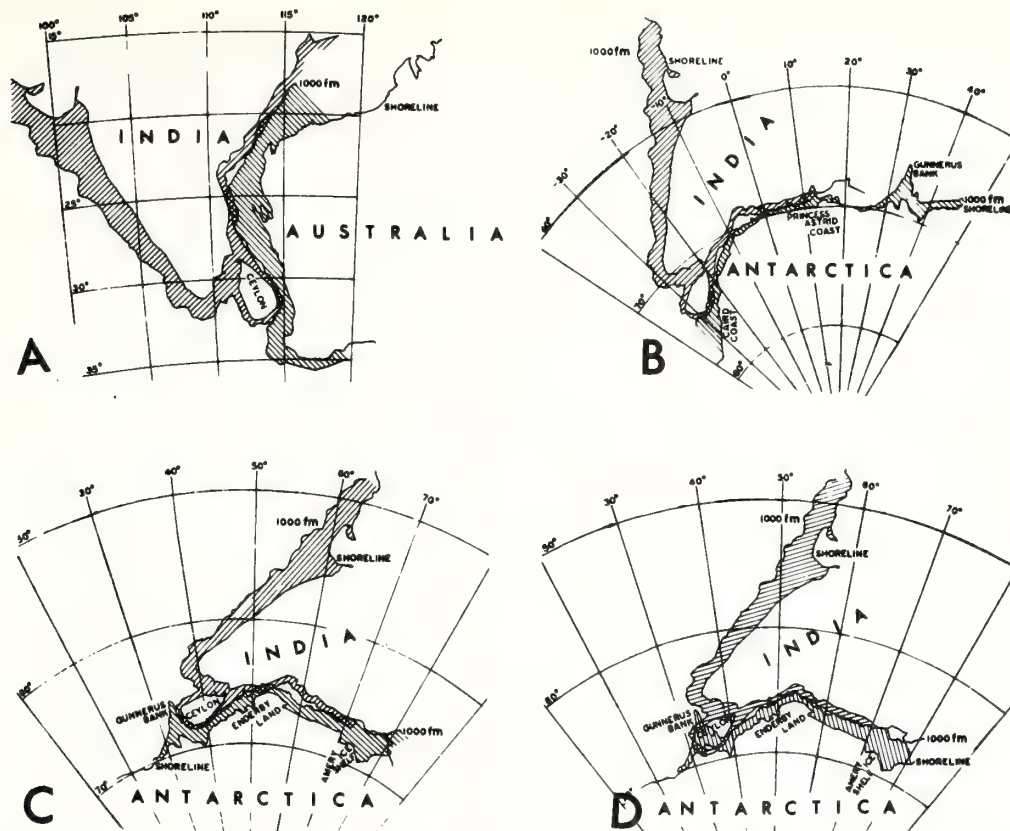


Fig. 3. Possible continental drift reconstruction for India which places this continent either against Australia or Antarctica. None of the fits are regarded as good but that shown in D is our preference. The apparently good fit of A is achieved by omitting the Exmouth Plateau as an integral part of Australia, a doubtful assumption.

strain the reconstruction. These are the Iselen and Bruce Plateaux off Antarctica and the Naturaliste Plateau of south-western Australia. These mid-depth salients were omitted from the fit solution shown in Fig. 2 on the basis that they might not be cratonic and because they would introduce too much bias in achieving the fit. In other words, the fit achieved would be virtually a foregone conclusion by simple inspection. The development of such marginal plateaux seems to be somehow related to former Y-junctions or triple-points (points of intersection between three crustal plates). The Afar triangle in the Red Sea is a modern example.

India/Antarctica fit

Unlike the reconstructions described above, the fit of India against Antarctica finds no really satisfying morphological solution, so it remains puzzling. Fig. 3 shows four possible pre-drift positions of India within Gondwana. The first of these versions (Fig. 3A) shows India as fitting against western Australia rather than Antarc-

ca. This appears to be a reasonably good fit in that Ceylon is nicely accommodated into a bight within the Australian margin. To achieve this fit, however, we eliminated the large Exmouth Plateau off north-western Australia as being an integral part of the Australian craton. This assumption, however, is doubtful. More importantly, considerations of plate tectonics seem to void this reconstruction as there is no mid-ocean ridge (rift) between India and Australia. (It is conceivable that the Ninetyeast Ridge is a fossil rift which once inserted new ocean crust between India and Australia. We prefer, however, to believe that this is a megashear boundary between the Indian and Australian plates which has conserved crust.) The fracture zones within the Indian Ocean, which provide useful 'dead-reckoning tracks' for continents, rather strongly suggest that the east coast of India was once juxtaposed against Antarctica (Dietz and Holden, 1970).

Fig. 3B shows a second option but, aside from the fit being rather poor, this position is unlikely as India overlaps Africa once Africa is fitted against Antarctica as

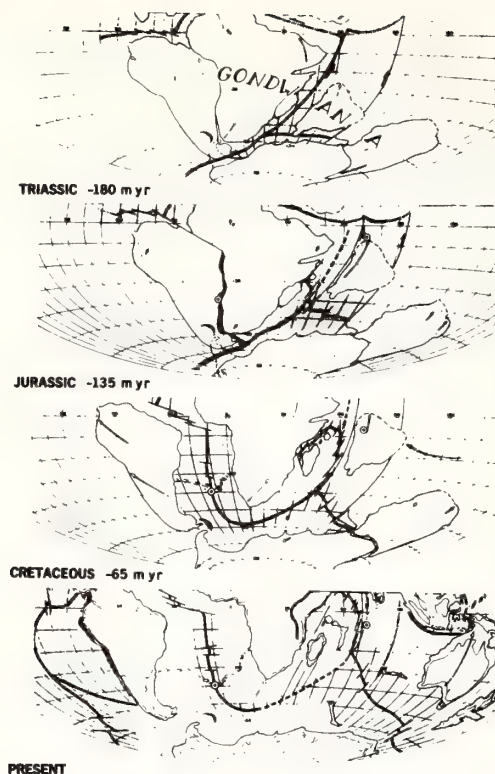


Fig. 4. Dispersion of the Gondwana continents from Antarctica by the opening up of the Atlantic and Indian oceans on an Aitoff projection. Antarctica remains relatively fixed while the other continents move north or west. Initial positions are adjusted to fit magnetic palaeolatitudes and orientations with the later dispersion fixed in geographical coordinates by regarding the Walvis thermal centre as fixed (Wilson, 1965). Explanation: Double lines are rifts and crossed lines are trenches. The stipple shows new ocean floor generated by sea-floor spreading for each geological period. Solid line is transform fault megashears. Open arrows are vectors showing the total drift rotation during each geological period. The hatched arc is the Scotia arc to give the reader an arbitrary geographical fix. Circles with central dots are the Walvis and Maldives thermal centres from which nemataths (basaltic thread ridges) have developed.

described above. Fig. 3C shows a third version in which Ceylon is accommodated against Gunnerus Bank, but in doing so a poor congruency results between the first-order curvature of both continents in that the convexity of Enderby Land does not fit into the concavity of the east margin of India.

Fig. 3D shows our preferred solution. In this fitting test, Ceylon is omitted from the computation, so that it is permitted to overlap Gunnerus Bank. This, of course, is somewhat arbitrary but perhaps Gunnerus Bank is a post-rift excretion on the margin of Antarctica. Smith and Hallam (1970) showed a similar position for India

against Antarctica and, in turn, have arbitrarily detached Ceylon from India and inserted it against the west side of Gunnerus Bank. This is an interesting optional solution but so far as we are aware there is no geological evidence that Ceylon was ever separated from India.

Break-up and dispersion of continents from Antarctica

The probable history of the break-up and dispersion of the continents once attached to Antarctica is depicted in Fig. 4. The positions of the continents are shown as of the end of each geological period from the Triassic to the Present. The need for brevity prohibits any description of this dispersion here. Our basis for this map has been presented elsewhere (Dietz and Holden, 1970).

We emphasize here that Antarctica apparently is the most fixed of continents. The Antarctic plate is unique in that it is entirely margined by a rift system (the Pan-antarctic rift). There is no associated trench into which this plate is subducted. This rift system must have migrated outward from the margin of east Antarctica (Fig. 5). As rift-system zones commonly accommodate shear, Antarctica probably has undergone some 'tight' rotation westward with the pole of rotation being within the Antarctic continent. If Antarctica has drifted southward, as some palaeomagnetic results suggest, the plate must have moved as a unit.

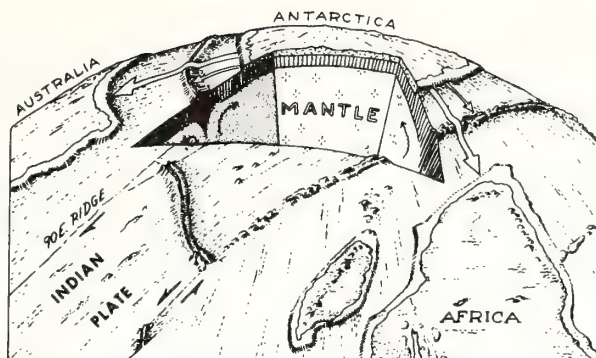
In some previous drift reconstructions, Africa has been considered as fixed as it is the heartland continent of Pangaea and is also largely surrounded by a rift. However, the African plate is bounded on the north by the Tethyan trench or subduction zone toward which this plate has moved.

Pre-Mesozoic ocean crust

The sea-floor spreading rates inferred from magnetic reversal anomalies of from 1 to 6 cm/yr suggest that about one-half of the ocean floor has been 'repared' with new crust during the Cenozoic (Vine, 1968). By extrapolation, nearly all the remainder is probably younger than the -200 m yr (mid-Triassic) commencement of the modern drift event associated with the break-up of Pangaea. The oldest sea floor known to date, of -160 m yr, was drilled on Joides leg 11 just west of the Bahama platform (preliminary communication from J. Ewing and C. Hollister). The search for ancient oceanic crust (pre-Mesozoic) has become an interesting quest. The small ocean basins behind trenches, which could represent crustal sub-plates protected from subduction, offer a possibility. In fact, they appear to be neo-oceanic (e.g. Japan Sea, as this arc seems to have slowly migrated outward from Asia) or no older than Mesozoic (e.g. Caribbean).

At first thought, the Antarctic plate would seem to offer a bright prospect for preserving regions of ancient ocean floor, as this plate contains no subduction zones.

Fig. 5. A physiographic diagram showing the outward (northward) migration of the Panantarctic rift relative to Antarctica. New oceanic crust is emplaced along this northerly migrating axis of sea-floor spreading while Antarctica has remained essentially fixed in position. Africa, India and Australia have all drifted northward at twice the half-spreading rate as measured by the emplacement of new oceanic crust on one limb of the mid-oceanic rift. The southern part of the Indian plate is also depicted as bounded by a rift and two mega-shears.



If the Panantarctic rift has migrated only outward, as suggested above, those marginal regions of Antarctica, which were not originally defined or blocked out as rift edges (where other continents formerly fitted under drift reconstruction), should contain stranded areas of pre-Mesozoic ocean floor. The Pacific sector of west Antarctica fits this description but it is margined by a young fold belt which suggests that a 'fossil' sub-plate was consumed along this margin. So ancient sea floor is unlikely here.

Perhaps a more likely possibility is a marginal area about present-day long. 90° E. as this is a region of gap in our proposed reconstruction between the former joins of India and Australia, as, in other words, a southern arm of Tethys. However, it may be that the margin of Antarctica along this sector is a rift scar, too, with the Broken Ridge micro-continent (Francis and Raitt, 1967) being the congruent jig-saw piece. (This region of ocean crust would also have been consumed if the Ninetyeast Ridge is a fossil-spreading rift which originally opened up the longitudinal distance between India and Australia. This prospect seems unlikely to us.)

The former Antarctica/Australia supercraton and crustal plate is, however, another matter. The Australian plate probably separated from Antarctica only in the early Cenozoic and has drifted northward, along with its associated rift, in a regime of fast spreading, as Le Pichon and Heirtzler (1968) have shown. Unlike these authors, we suppose that the Australian plate must have had a quite separate history and is independent of the Indian plate. In this context, the Wharton Sea basin (as bounded by Ninetyeast Ridge, Java trench, western Australia and Diamantina fracture zone) may be pre-Mesozoic ocean crust which has not as yet been subducted into the Java trench (Fig. 6). Here, then, is an extensive area of probable pre-Mesozoic ocean floor, perhaps the only large such region in the world.

Circularity of east Antarctica

East Antarctica is remarkably circular in outline; it is a margin that was established by rifting. We offer the following speculation to account for this circularity. By the

usual version of the plate-tectonics concept, the rifts are passive tensional breaks resulting from the active descent of the crustal plate into a subduction zone (Isacks and others, 1968). The shape of the leading edge of a plate is unknown as these are everywhere now subducted into

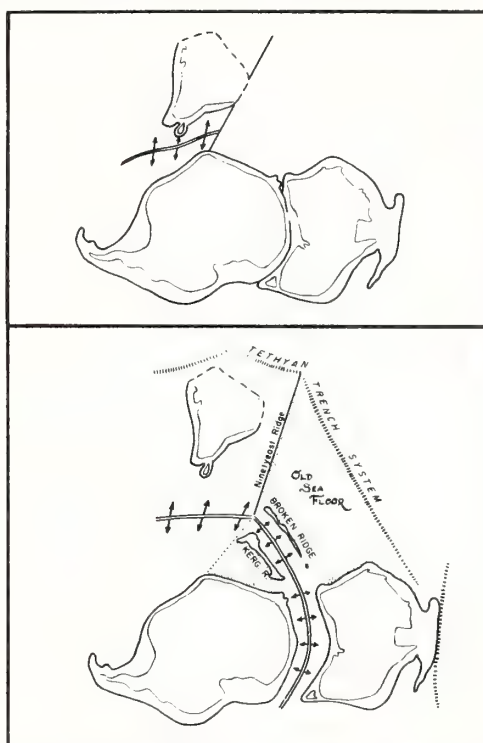


Fig. 6. The Wharton Sea basin offers a good prospect for being underlain by pre-Mesozoic ocean crust. The subduction of this western part of the Australian crustal plate into the Java trench commenced only about 40 m yr ago with the separation of Australia from Antarctica. Another small area of ancient ocean floor might be present near the Antarctic margin. Probably, any old crust along west Antarctica has been subducted into a fossil trench with the development of the young west Antarctic fold belt.

trenches. We suggest, however, that they may tend to be convex outward or in opposition to the shape of island arcs which mark the surface trace of the subduction zone. In turn, the associated or paired rift may tend to parallel this curvature and so be convex into the active plate. When a plate is created and moves actively away from a relatively passive craton, a convex margin is impressed upon this craton. At least we seem to observe this result for the bight of north America which complements the bulge of Africa which may be regarded as the type example: The same relationship of an active plate moving away from a relatively fixed craton seems to apply for the margins of Antarctica–Australia and for India (eastern margin)–Antarctica. The resultant effect impressed a circular outline on east Antarctica.

Concluding note

To further investigate the main points raised in this paper, precise bathymetric and geophysical surveys are urgently needed along the margin of Antarctica by ice-reinforced survey ships equipped with satellite navigation. For example, is the Iselen Plateau really a marginal plateau or merely a group of seamounts? Is the Gunnerus salient really a cratonic projection which must be accommodated in a continental drift reconstruction or is it 'new ground'? Palaeomagnetic studies should help unravel any history of tectonic rotation of the Antarctic Peninsula. These and many other questions remain to be answered.

REFERENCES

- Carey, S. W. 1958. The tectonic approach to continental drift. (In Carey, S. W., ed. *Continental drift: a symposium*. Hobart. University of Tasmania, 177–355.)
- Dietz, R. S. and J. C. Holden. 1970. Reconstruction of Pangaea; its breakup and dispersion of continents — Permian to Present. *J. geophys. Res.* 75, No. 26, 4939–56.
- Dietz, R. S. and W. P. Sproll. 1970. Fit between Africa and Antarctica: a continental drift reconstruction. *Science*, 167, No. 3925, 1612–14.
- Francis, T. and R. Raitt. 1967. Seismic refraction measurements in the southern Indian Ocean. *J. geophys. Res.*, 72, No. 12, 3015–41.
- Heirtzler, J. R. In press. Evolution of the southern oceans. (In *proceedings of the Symposium on Antarctica*. Washington, D.C., American Association for the Advancement of Science.)
- Isacks, B., Oliver, J. and L. R. Sykes. 1958. Seismology and the new global tectonics. *J. geophys. Res.*, 73, No. 18, 5855–99.
- Le Pichon, X. and J. R. Heirtzler. 1968. Magnetic anomalies in the Indian Ocean and sea-floor spreading. *J. geophys. Res.*, 73, No. 6, 2101–17.
- McDougall, I. 1953. Potassium-argon age measurements on dolerites from Antarctica and South Africa. *J. geophys. Res.*, 68, No. 5, 1535–45.
- Manton, W. I. 1968. The origin of associated basic and acid rocks in the Lebombo–Nuanetsi igneous province, southern Africa, as implied by strontium isotopes. *J. Petrology*, 9, Pt. 1, 23–39.
- Smith, A. G. and A. Hallam. 1970. The fit of the southern continents. *Nature, Lond.*, 225, No. 5228, 139–44.
- Sproll, W. and R. Dietz. 1959. Morphological continental drift fit of Australia and Antarctica. *Nature, Lond.*, 222, No. 5191, 345–48.
- Sunderland, F. L. 1966. Considerations on the emplacement of the Jurassic dolerites of Tasmania. *Pap. Proc. R. Soc. Tasm.*, 100, 133–45.
- Vine, F. 1968. Evidence from submarine geology. (In *Symposium on Gondwanaland revisited: new evidence for continental drift*. *Proc. Am. phil. Soc.*, 112, No. 5, 325–34.)
- Wilson, J. T. 1965. Submarine fracture zones, aseismic ridges and the International Council of Scientific Unions line: proposed western margin of the East Pacific Ridge. *Nature, Lond.*, 207, No. 5000, 907–11.

Experimental Isostasy

3. Inversion of the Isostatic Green Function and Lateral Density Changes

LEROY M. DORMAN¹

*Department of Terrestrial Magnetism, Carnegie Institution of Washington
Washington, D.C. 20015*

BRIAN T. R. LEWIS

University of Washington, Seattle, Washington 98105

We have applied the Backus-Gilbert inversion technique to the isostatic Green function for the continental United States, which we measured earlier. A two-level compensation mechanism (overcompensation beneath the crust with the resulting mass deficiency compensated deeper in the mantle) is indicated at about the 80% confidence level. This model is consistent with seismic refraction and surface-wave data.

Advances in geophysical instruments and analytical methods have led to the demonstration that the lateral variations in the physical properties apparent on the earth's surface extend to great depths. The surface-wave results of *Dorman et al.* [1960] indicated differences to depths of several hundred kilometers between continent and ocean. These differences were taken by *MacDonald* [1963] as supporting continental formation by vertical segregation. More recently *Toksöz and Anderson* [1966], *Kanamori* [1970], and *Dziewonski* [1971] have shown differences in mantle surface-wave velocities between tectonic and shield regions. *Lewis and Meyer* [1968] and *Green and Hales* [1968] have given examples of the variation in upper-mantle structure from seismic refraction experiments.

In terms of genesis and evolution the differences in the earth's physical properties underlying various types of physiography are probably more important than the average structure. We attempt to illuminate these differences in this paper.

In all studies the resolution of the analytical method is of central interest, for this alone tells

us how seriously we should take our results. It is easier but less constructive to show models whose details are unrestrained by the data.

Our present approach to this problem is to use as few parameters as possible and to associate lateral variation of density at depth with the overlying topography. In this manner we will attempt to describe the differences in structure between the stable and the tectonic areas of the North American continent.

The observational fact that free-air gravity anomalies are small and uncorrelated with topography at long wavelengths shows that near-surface mass variations of large areal extent are effectively compensated [see *Kaula*, 1967]. That the free-air gravity anomalies are highly correlated with topography at short wavelengths means that the mass compensating small features is either spread out by the strength of the earth or is so far away that its gravity field is smoothed by upward continuation. We can use this dependence on wavelength of the correlation between gravity anomaly and topography to solve the isostatic problem, which is, briefly, What are the differences in density within the earth between areas of different surface elevation that bring about the approximate equality of mass per unit surface area?

The use of gravity data to determine the density distribution is hampered by the lack of uniqueness in solutions of the inverse potential problem. There is simply not enough

¹ Now at Atlantic Oceanographic and Meteorological Laboratories, National Oceanic and Atmospheric Administration, Miami, Florida 33130.

information contained in the potential field external to a body to define completely the density distribution within it. With isostasy, however, we have an additional constraint. We know that the density changes associated with isostasy must be systematically related to the topographic load or, more precisely, to the stresses within the earth that support the topography. The addition of the information about the arrangement of the topography allows us to obtain a unique solution for the density variations within the earth that are systematically associated with the topographic load. In two earlier papers [Dorman and Lewis, 1970; Lewis and Dorman, 1970; hereafter referred to as papers 1 and 2, respectively], to develop a constructive solution of this problem, we made use of the statistical theory of communication [see Lee, 1960] that has been developed over the past 30 years. We applied this analysis to gravity and topographic data from the continental United States and extracted the Green function, i.e., the gravity anomaly due to a concentrated load on the earth's surface. The shape of the Green function implied compensation at more than one depth (under the assumption of local compensation), but we were unable to treat satisfactorily the inversion problem of finding the function of density change versus depth that characterizes the isostatic process. In this paper we present a heuristic treatment of the theory that, although lacking in rigor, should serve to show the physical principles involved without requiring the reader to be conversant with the communication theory. The inversion problem has been admirably dealt with by several workers since the publication of our original works, and we will use their results to show what constraints are placed on earth models.

Harold Jeffreys (personal communication, 1972) pointed out to us that Love [1911, section 14] obtained a compensating density distribution that produces overcompensation at small depths. Love started with the assumptions that the external field is undisturbed and that a state of hydrostatic stress exists at the internal boundary of what is now called the lithosphere. Love's calculation, however, provides no way of determining the distribution of compensating density as a function of depth, as our calculation does, and requires the assumption of hydrostatic

stress at some depth, whereas our calculation does not.

A SIMPLER, LESS GENERAL TREATMENT OF THE ANALYSIS

The earth and its gravity field are approximately elliptically symmetric. To refine this approximation further, we add a perturbation term; thus the density at any point within the earth is linearly related to the topographic load (the elevation of the earth's surface above the point).

The perturbation term is the product of the elevation $h(\theta, \varphi)$ and a density contrast function $\Delta\rho(r)$, which varies with distance from the center of the earth. (We will use spherical geometry for the perturbation term and elliptical geometry only through the use of the international gravity formula for the removal of the symmetric main gravity field.)

We define the product $\Delta\rho(r) \cdot h(\theta, \varphi)$ to be the compensating density at radius r , colatitude θ , and longitude φ . The integral of the compensating density over a column from the center of the earth to sea level must equal the mass in column above sea level in order for the column to be compensated.

We now show how to extract the density contrast function from the observables $ba(\theta, \varphi)$ (the Bouguer anomaly) and the topography $h(\theta, \varphi)$. The Bouguer gravity anomaly is the gravity field from the compensating mass (plus that from other inhomogeneities, which we ignore for the moment). It turns out that the complex harmonic expansion coefficients of these two functions, BA_{nm} and H_{nm} , respectively, are of more immediate use, however, because the expression of the effect of upward continuation is much simpler in terms of harmonic expansion coefficients.

The harmonic expansion coefficients of the compensating density in a shell at radius r , are from the definition above $\Delta\rho(r_s) \cdot H_{nm}$. From Jeffreys and Jeffreys [1966, section 24.111] the harmonic expansion coefficients of the gravity field at the earth's surface (radius = a) from an internal spherical shell with this density distribution are

$$BA_{nm} = 4\pi\Gamma \frac{n+1}{2n+1} \left(\frac{r_s}{a}\right)^{n+2} \Delta\rho(r_s) H_{nm} \quad (1)$$

The gravitational constant is Γ .

The gravity field due to the sum of all shells constituting the compensating mass is the integral of this equation over r :

$$BA_{nm} = 4\pi\Gamma \frac{n+1}{2n+1} H_{nm} \cdot \int_0^a \left(\frac{r}{a}\right)^{n+2} \Delta\rho(r) dr$$

We can define R_n as

$$R_n = \int_0^a \left(\frac{r}{a}\right)^{n+2} \rho\Delta(r) dr = \frac{BA_{nm}}{H_{nm}} \left(\frac{2n+1}{n+1}\right) \frac{1}{4\pi\Gamma} \quad (2)$$

The far right-hand side of the equation contains only observables; thus we can use (2) to obtain a set of integral relations that determine $\Delta\rho(r)$. These R_n are also the spherical harmonic expansion coefficients of the isostatic Green function, the gravity anomaly associated with a concentrated load on the earth's surface.

We have taken the Green function to be independent of azimuth; thus its harmonic expansion is dependent only on the degree n . The harmonic expansion of the data, however, contains nonzero terms for $m \neq 0$; thus for $n \neq 0$ (2) is overdetermined. The averaging resulting from this overdetermination serves to reduce the effect of uncorrelated density variations, as was explained more fully in paper 1.

INVERSION

Theory. For each degree n we have a number that represents an average of $\Delta\rho$ over depth weighted by $(r/a)^{n+2}$. We now ask, what constraints does this average place on $\Delta\rho$? In paper 2 we showed several functions of $\Delta\rho$ that satisfied the observational data from the continental United States, but we were not able to say on the basis of these data alone which function was better. The problem of the inversion of integral relations such as the one above is a general one and has recently been treated by *Backus and Gilbert* [1967, 1968, 1970], *Der et al.* [1970], *Dziewonski* [1970], and *Gilbert and Backus* [1968].

We have followed the elegant development given by *Backus and Gilbert* [1970]. In their terminology each number R_n is a 'gross earth

datum' and the set of known R_n is a set of gross earth data that can be used to form localized averages of $\Delta\rho(r)$. These localized averages (averages over some depth interval) are the best (in a least-squares sense) we can obtain under the restrictions that the mathematical relationship between the density distributions and the observable, the gravity field, is inherently a smoothing one [*Gilbert and Backus*, 1968]. Moreover, the observations that we must work with are subject to experimental uncertainty, further reducing the resolution obtainable [*Backus and Gilbert*, 1970]. Backus and Gilbert showed how to determine the accuracy of each localized average from the covariance matrix associated with the R_n and how to evaluate the trade off of accuracy versus resolving power. The covariance matrix of the R_n is composed of the elements $\langle R_i R_j \rangle$.

The inversion scheme makes use of the fact that our observables, in this case the R_n , are weighted averages of the earth's physical properties and that the weighting functions G_n , called data kernels, vary with n . From (1) the G_n for this problem are $(r/a)^{n+2}$ and are shown in Figure 1. In the linear problem, which this is, the localized average near radius r_0 is given by some linear combination of R_n :

$$\int_0^a A(r) \Delta\rho(r) dr = \sum_n a_n R_n \quad (3)$$

where the a_n are chosen so that $A(r) = \sum_n a_n G_n(r)$ is sharply peaked near $r = r_0$. Backus and Gilbert call $A(r)$ an averaging kernel and define the spread of $A(r)$ as being small when the peak of $A(r)$ is narrow and centered on r_0 .

The variance of the localized average defined in (3) is found by propagating the covariance matrix of the R_n through the right-hand side of (3). The optimum set of a_n for a given variance is the one for which the spread is smallest.

The curve of spread versus variance is called the trade off curve and shows how much depth resolution we can obtain for an answer with a given variance.

Estimation of the accuracy of R_n . For the analysis in paper 2 we used data from a rectangle about 4000 km E-W by 2000 km N-S covering the continental United States. The Bouguer anomalies came from the Bouguer anomaly map of the United States [*Woollard and Joesting*, 1964]. The elevation data were

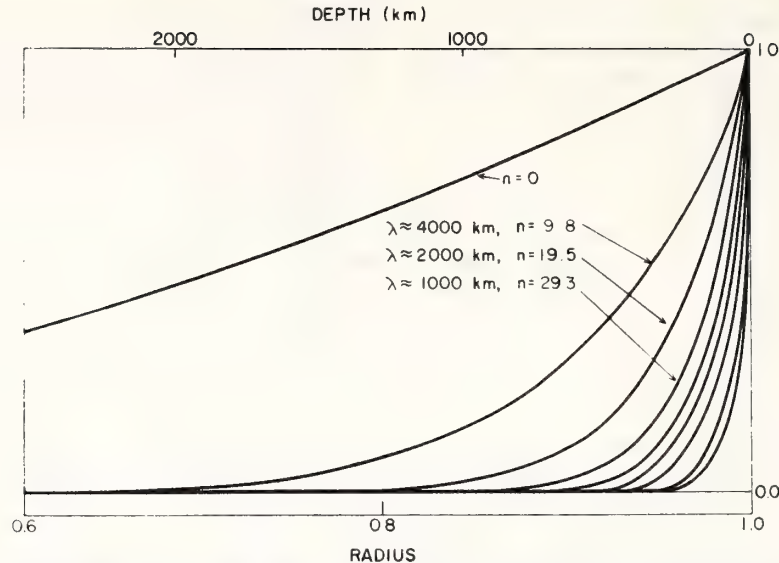


Fig. 1. The data kernels representing the relative sensitivity of the components of the harmonic expansion of the isostatic Green function to the density changes in the earth associated with isostasy. The data kernels shown are for the first nine R_n . The n are the nonintegral values associated with a data block of 4000-km size.

those accompanying about 80,000 of the gravity observations used in making the map. For the elevations we computed values on the 32-km grid by using the arithmetic mean of all data in a 32-km square centered on the grid point.

We then performed harmonic analysis of these gridded data by using the two-dimensional Fourier transform instead of a spherical harmonic expansion, since the plane approximation for surface distances is sufficiently accurate within a block of this size.

The conversion from the plane Bouguer anomaly to the spherical earth equivalent is done in the wave-number domain, where the conversion amounts to a simple multiplication.

We are not certain of the best way to estimate the quotient $\langle BA_{nm}/H_{nm} \rangle$ averaged over m . In paper 2 we formed the average by linear regression of $BA_{ij} \cos \theta_{ij}$ against H_{ij} and by forcing the regression line through the origin. The i and j values in each set were those representing approximately the same value of wave-number modulus, $|\vec{k}|$. (θ is the angle between BA_{ij} and H_{ij} .) This is averaging the estimate around an annulus $1/64 \text{ km}^{-1}$ wide in wave-number space.

We forced the Green function to be symmetric about the loaded point by constraining the quotient above to be real.

Random errors. Bartlett [1966] showed that the harmonic expansion coefficients obtained from analysis of the result of a linear operation on random data are independent. This result implies that the contributions from random density variation to the computed R_n will take the form of irregular 'grass.' The smoothing character of the integral transform in (2) shows us that, on the other hand, the contribution from $\Delta\rho$ to the computed R_n will be very smooth as a function of n .

Bearing this fact in mind, we drew a smooth envelope containing about 68% of the values of R_n and took the half-width of the envelope to be the standard deviation of R_n . This standard deviation is of course a function of n . We used the square of the standard deviation obtained in this manner for the diagonal elements of the covariance matrix.

Correlated errors. The map from which we took the gravity data contained topographic corrections in only part of the mountainous area. Since this correction is always positive, an insufficient terrain correction produces Bouguer anomalies and hence R_n that are too negative.

We can obtain a crude estimate of the uncertainty involved in the estimates of the long-wavelength terms by comparing -0.117 mgal/

m_n the R_n we obtained, with -0.1119 mgal/m, the value we obtained by direct calculation of the plate correction. The difference between these values must be the sum of the mean free-air anomaly, the terrain correction, and any errors of interpolation. In our study this difference amounted to 5%; thus we used 5% as the minimum fractional standard deviation for the error estimates made in the section on random errors.

Since the terrain correction is highest in areas of high elevation, an incomplete terrain correction will produce an erroneous correlation of Bouguer anomaly with topography. The nonlinear relationship will produce false correlation between R_i and R_j where $i \neq j$. If we knew more about errors of this kind we could estimate the covariances $\langle R_i R_j \rangle$ for $i \neq j$, but we do not, and we have set these off-diagonal terms of the covariance matrix equal to 0.

INVERSION RESULTS

Figure 2 shows the data set and the assigned standard deviations. In paper 2 we used the 64 R_n obtained by averaging the 4096 pairs of B_{ij} and H_{ij} around annuli. The information

about $\Delta\rho(r)$, however, is not uniformly distributed with order n but is more nearly distributed with wavelength.

We discovered how independent the G_n are of each other and hence how much more information each additional G_n added by considering them to be basis vectors with which we must describe the solution vector $\Delta\rho$ in the space $r = 0, a$. We want each additional element in the data set to contribute approximately the same amount of information. We chose to average the R_n into blocks centered on values $n = n_k$ such that

$$\int_0^a G_{n_k} G_{n_{k+1}} dr / \left(\int_0^a G_{n_k}^2 dr \int_0^a G_{n_{k+1}}^2 dr \right)^{1/2} \simeq \text{const} \quad \forall k$$

This relation means that we seek basis vectors in which each one differs in angle from the preceding one by approximately an equal amount. We found this condition to be satisfied by averaging by fractions of an octave and used one-third octave averages as a compromise between analytical rigor and numerical tractability. When the constant is very near 1, the basis vectors are very nearly parallel. Thus

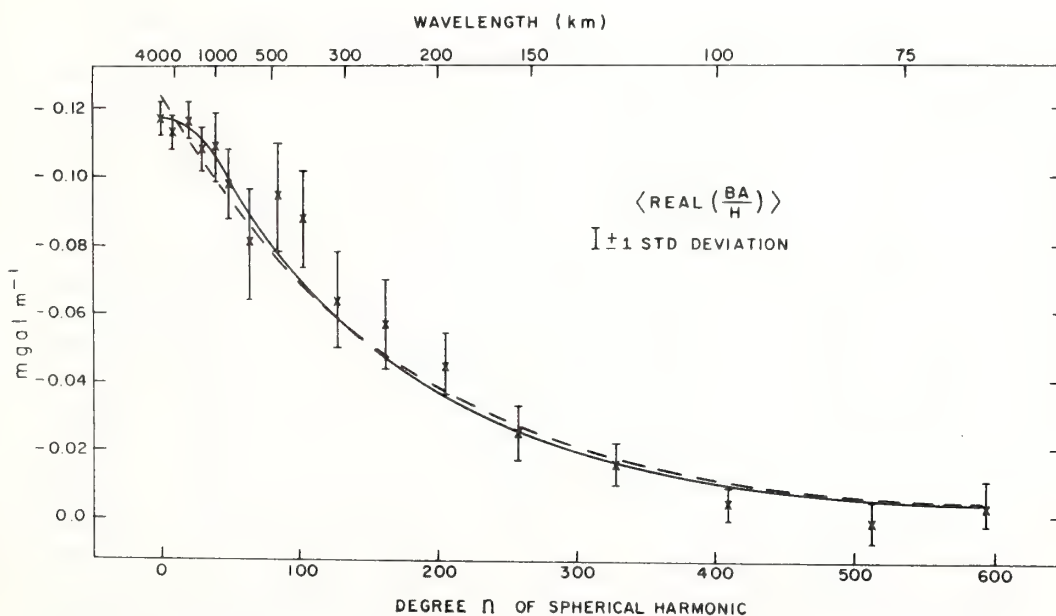


Fig. 2. The harmonic expansion of the isostatic Green function for the continental United States. Filtering the topography with this function produces the gravity field due to the compensation of the topography.

each basis vector adds very little more information, and we are forced to attempt to invert matrices that are very nearly singular. The curves in the figure will be discussed later.

The trade off curves for a number of depths are shown in Figure 3. We plotted the width w of the averaging kernel versus e , the standard deviation of the estimate of $\Delta\rho$ at several depths. Figure 4 shows the averaging kernels we used. The vertical line marked C represents the center, and the horizontal line denotes the w , the width of the kernel, all as defined by *Backus and Gilbert* [1970]. These kernels correspond to the circles in Figure 3.

Curve D in Figure 5 shows the resulting localized averages of the function $\Delta\rho(r)$ compared with some other physical properties. The center of each cross marks the center of the kernel and the average value of $\Delta\rho$. The length of the vertical line is the width, and the length of the horizontal line is 2 standard deviations. To restrict the uncertainty, we had to sacrifice depth resolution; hence the estimate for $r = 0.85$, which is positive at about the 80% confidence level, is hardly localized at all.

COMPARISON AND COMBINATION WITH SEISMIC DATA

Refraction. Because of the linear relationship between the topography and the density perturbation term, the difference between the density beneath the mountainous area of the western United States and the density beneath the lowlands of the central United States must be a constant times $\Delta\rho(r)$. Figure 5 compares $\Delta\rho(r)$ with the differences between tectonic and lowland values of two other physical properties, the compressional and shear seismic velocities. Curves A and C in Figure 5 show the P velocity difference and the $\Delta\rho$ model given in paper 2. Curve D in Figure 5 shows the estimates from the inversion in this paper, and curve B in Figure 5 shows the difference in S velocity between 'tectonic' and 'shield' pure-path models. The preceding inversion treatment is useful for our gravity data and for seismic surface-wave analyses but has not yet been extended to seismic body waves. In paper 2 we compared our $\Delta\rho$ models with the difference between two seismic compressional-wave velocity models from regions with different mean elevations, with the

purpose of attributing the differences between the two models principally to the isostatic compensation of their different elevations. Figure 5 shows this difference. The refraction method yields the only data we have that have appreciable depth resolution away from the surface; hence we have used the refraction results, in particular the positive 'bump' in the difference at 400–450 km, to constrain the depth of the $\Delta\rho$ increase.

To use this constraint, we will examine models in which $\Delta\rho$ is 0 except for one or two depths. A one-depth, two-parameter solution calculated by the method of nonlinear least squares is shown as the dashed line in Figure 2. This solution corresponds very nearly to Airy compensation. We did not force isostasy, and the model ends up overcompensated by about 5%. If we had forced isostasy by making the 0-degree end of the curve go through the data, the entire curve would have been moved downward, and the fit would have been much worse. The solution depth is 38 km.

Adding a compensating layer at 400 km but not specifying its density give the two-depth, three-parameter solution shown as the solid line in Figure 2. The mechanism for this solution involves a layer at 43 km that overcompensates the topography by about 20% and a layer at about 400 km that cancels out the extra 20%. We prefer this latter solution since it best satisfies the gravity and refraction data. The improvement in the variance of residuals over the two-parameter fit is significant at the 90% confidence level.

Velocity-density relations. Using the data on P velocity and crustal thickness tabulated by *Arkani-Hamed and Toksöz* [1968], *Toksöz et al.* [1969] computed for harmonics of degree 2–6 the gravity field due to the seismically predicted density variations. This predicted field was about 30 times greater than that observed, and they concluded that these density variations must be compensated elsewhere in the mantle.

When we examine quantitatively the relief of the discontinuity at ~ 400 km, assuming that it is the olivine-spinel phase transition [*Fujisawa*, 1968] and that this transition corresponds to the positive part of the dipole in the two-layer solution, we compute that for a change in mean elevation of topography of

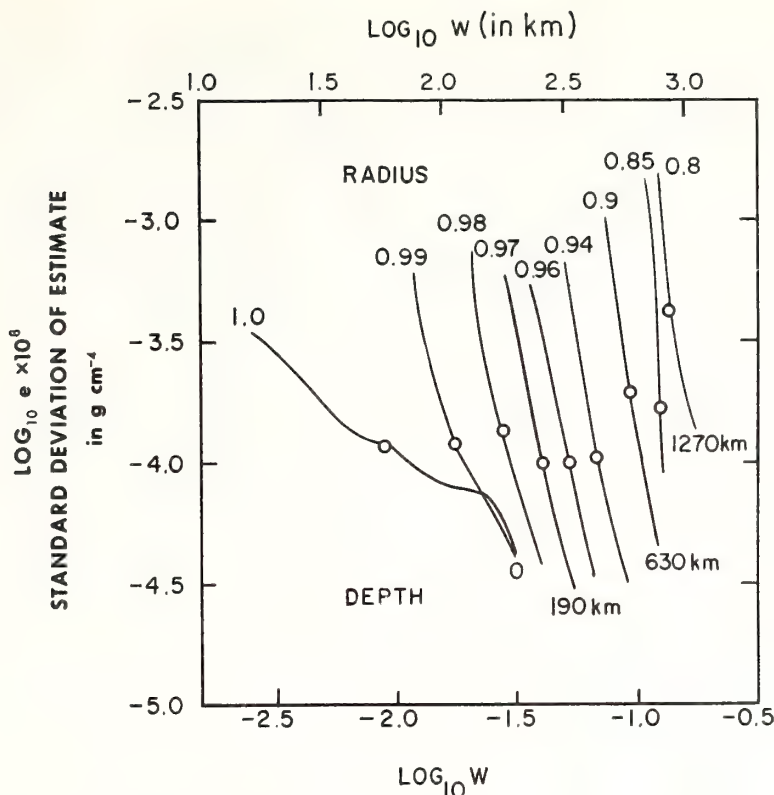


Fig. 3. The trade off curves for various depths. These curves show the relationship between the width of the averaging kernel and the standard deviation of the associated estimate of $\Delta\rho(r)$. The width of averaging kernel versus error (in earth radii) is indicated by w .

1 km about 1.5 km of relief on the discontinuity should be found. From curve A in Figure 5 we see from the seismic refraction results that the depth of the presumed olivine-spinel phase change is some 50 km less under the western United States than under the mid-continent area. Although it is difficult to estimate the resolution of the refraction results, it seems likely that the relief of this discontinuity is something like 30 times the value necessary to satisfy the gravity data. A possible answer to this dilemma lies in the fact that the two-layer solution on which this calculation is based is the simplest solution that will satisfy the gravity data. The preferred model in the 1970 solution (Figure 5, curve C) has density changes that are larger than the present inversion results by an order of magnitude, but it fits the gravity data equally well. The larger density changes would seem to be supported by the refraction results.

Surface waves. We can compare seismic surface-wave observations and models by looking at differences as we did with the refraction results. Dziewonski [1971] applied the Backus and Gilbert inversion technique to pure-path Love-wave dispersion data to obtain shear velocity models for oceanic, tectonic, and shield regions. His models contain the least number of parameters required to satisfy the data.

In curve B of Figure 5 we show the difference in shear velocity between Dziewonski's tectonic and shield models. There is general agreement between the shear velocity and the other differences, when the resolution of the respective methods is considered.

CONCLUSIONS

Compensation occurs to depths of at least 400 km. The relationship between the topography and the earth's gravity field indicates that isostatic adjustment extends into the mantle

to depths of 400 km or so. Associated with a surface load, we find a density decrease near the crust-mantle boundary and a lesser density increase at a greater depth.

A two-depth model provides a significantly better fit to the data than a model in which compensation takes place in one depth (or thin layer). The best fitting model in which compensation occurs at two depths (or thin layers) requires about 20% overcompensation near the crust-mantle boundary. The resulting mass deficiency is made up deeper in the mantle. That is, a surface load of 1 unit of mass is associated with a mass deficiency of 1.2 units near the crust-mantle boundary and with a mass excess near a depth of 400 km.

Seismic data indicate greater density variations than those required to satisfy the gravity data. When differences in seismic velocity are used to predict mantle density differences between tectonic and stable regions, we find that the predicted density variations are higher by an order of magnitude than those required to satisfy the gravity data. A model with large density differences can satisfy both the gravity and the seismic data, however, by possessing oscillations with depth that are not resolved by the gravity analysis.

Acknowledgments. We thank Professor Charles R. Bentley of the University of Wisconsin and Dr. David E. James for critically reading the manuscript. We are also indebted to Dr. John R.

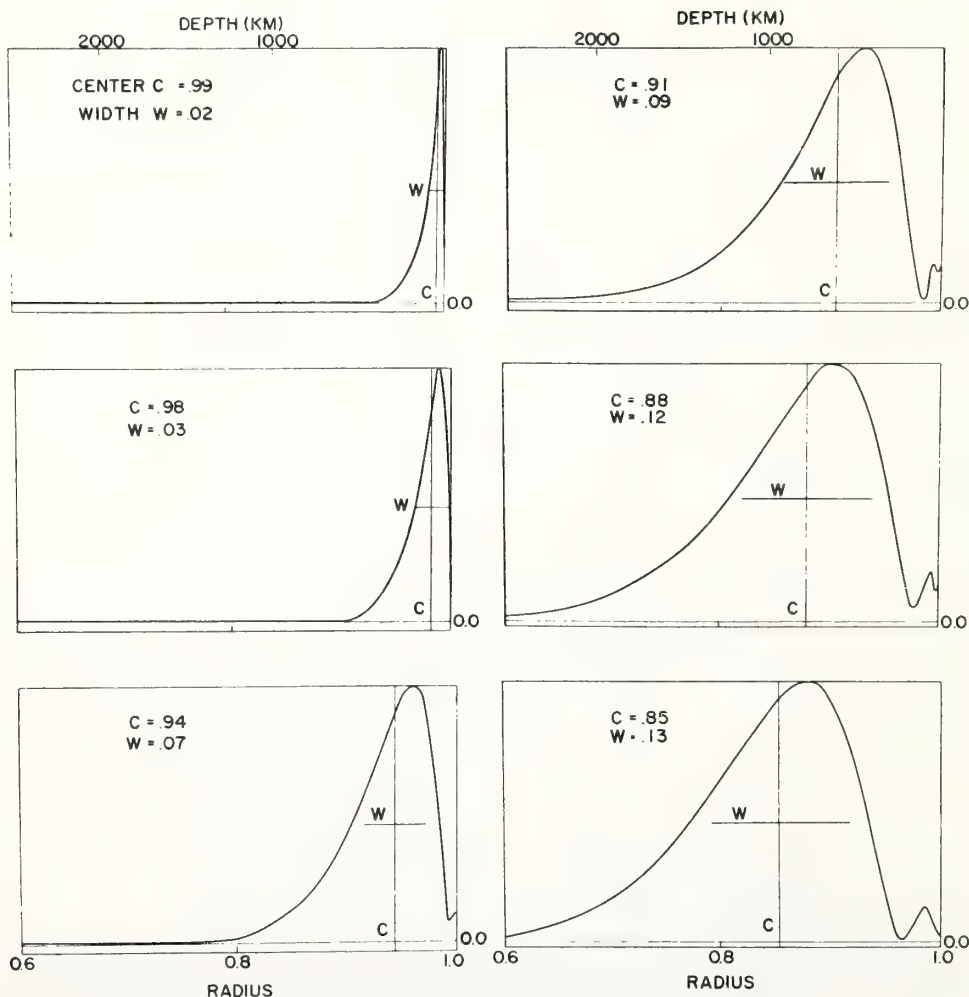


Fig. 4. The averaging kernels associated with six of the circles in Figure 3.

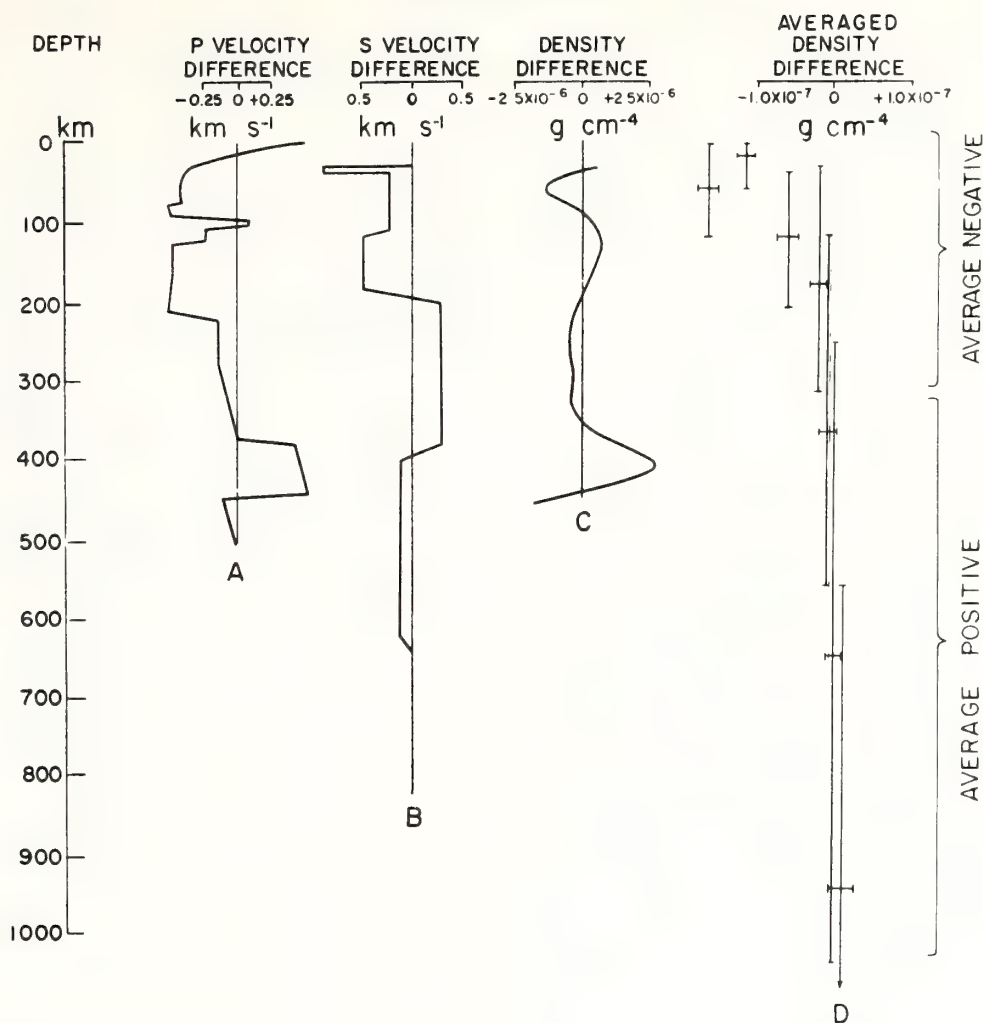


Fig. 5. Differences in P velocity, S velocity, and density between tectonic and continental stable regions. A, Nevada N3 [Green and Hales, 1968] minus midcontinental United States [Lewis and Meyer, 1968] from seismic refraction; B, tectonic minus shield [Dziewonski, 1971] from seismic surface waves; C, from gravity and topography [Lewis and Dorman, 1970]. A comparison of the differences shows a dipolar character, i.e., negative at the top of the mantle and positive somewhere beneath. The density difference curve is that given in paper 2 and contains oscillations that are not really resolved by the data. Note that the maximum excursions of density are larger by an order of magnitude than those indicated by the Backus and Gilbert inversion shown as 'averaged density difference.'

Booker for pointing out an error in the mathematics.

REFERENCES

- Arkani-Hamed, J., and M. N. Toksöz, Analysis and correlation of geophysical data, *Nuovo Cimento Suppl.*, **6**, 22-66, 1968.
- Backus, G. E., and J. F. Gilbert, Numerical applications of a formalism for a geophysical inversion problem, *Geophys. J. Roy. Astron. Soc.*, **13**, 247-276, 1967.
- Backus, G. E., and F. Gilbert, The resolving power of gross earth data, *Geophys. J. Roy. Astron. Soc.*, **16**, 169-205, 1968.
- Backus, G. E., and F. Gilbert, Uniqueness in the inversion of gross earth data, *Phil. Trans. Roy. Soc. London, Ser. A*, **266**, 123-192, 1970.
- Bartlett, M. S., *Stochastic Processes*, p. 304-314, Cambridge University Press, London, 1966.

- Der, Z., R. Masse, and M. Landisman, Effects of observational errors on the resolution of surface waves at intermediate distances, *J. Geophys. Res.*, **75**, 3399-3409, 1970.
- Dorman, J., M. Ewing, and J. Oliver, Study of shear-velocity distribution in the upper mantle by mantle Rayleigh waves, *Bull. Seismol. Soc. Amer.*, **60**, 87-115, 1960.
- Dorman, L. M., and B. T. R. Lewis, Experimental isostasy, 1, Theory of the determination of the earth's isostatic response to a concentrated load, *J. Geophys. Res.*, **75**, 3357-3365, 1970.
- Dziewonski, A. M., Correlation properties of free period partial derivatives and their relation to the resolution of gross earth data, *Bull. Seismol. Soc. Amer.*, **60**, 741-768, 1970.
- Dziewonski, A. M., Upper mantle models from 'pure-path' dispersion data, *J. Geophys. Res.*, **76**, 2587-2601, 1971.
- Fujisawa, H., Temperature and discontinuities in the transition layer within the earth's mantle: Geophysical application of the olivine-spinel transition in the $\text{Mg}_2\text{SiO}_4\text{-Fe}_2\text{SiO}_4$ system, *J. Geophys. Res.*, **73**, 3281-3294, 1968.
- Gilbert, F., and G. E. Backus, Approximate solutions to the inverse normal mode problem, *Bull. Seismol. Soc. Amer.*, **58**, 103-131, 1968.
- Green, R. W. E., and A. L. Hales, The travel times of *P* waves to 30° in the central United States and upper mantle structure, *Bull. Seismol. Soc. Amer.*, **58**, 267-289, 1968.
- Jeffreys, H., and B. S. Jeffreys, *Methods of Mathematical Physics*, p. 641-642, Cambridge University Press, London, 1966.
- Kanamori, H., Velocity and *Q* of mantle waves, *Phys. Earth Planet. Interiors*, **2**, 259-275, 1970.
- Kaula, W. M., Geophysical implications of satellite determinations of the earth's gravitational field, *Space Sci. Rev.*, **7**, 769-794, 1967.
- Lee, Y. W., *Statistical Theory of Communication*, John Wiley, New York, 1960.
- Lewis, B. T. R., and L. M. Dorman, Experimental isostasy, 2, An isostatic model for the U.S.A. derived from gravity and topographic data, *J. Geophys. Res.*, **75**, 3367-3386, 1970.
- Lewis, B. T. R., and R. P. Meyer, A seismic investigation of the upper mantle to the west of Lake Superior, *Bull. Seismol. Soc. Amer.*, **58**, 565-596, 1968.
- Love, A. E. H., *Some Problems of Geodynamics*, pp. 6-11, Cambridge University Press, London, 1911. (Also published by Dover, New York, 1967.)
- MacDonald, G. J. F., The deep structure of continents, *Rev. Geophys. Space Phys.*, **1**, 587-605, 1963.
- Toksöz, M. N., and D. L. Anderson, Phase velocities of long period surface waves and structure of the earth's upper mantle, 1, Great-circle Love and Rayleigh wave data, *J. Geophys. Res.*, **71**, 1649-1958, 1966.
- Toksöz, M. N., J. Arkani-Hamed, and C. H. Knight, Geophysical data and long-wave heterogeneities of the earth's mantle, *J. Geophys. Res.*, **74**, 3751-3770, 1969.
- Woollard, G. P., and H. R. Joesting, Bouguer gravity anomaly map of the United States, *U. S. Geol. Surv. Spec. Map* **1**, 1964.

(Received April 23, 1971;
revised January 7, 1972.)

The Isostatic Green's Function and the Inverse Potential Problem

L. M. Dorman and B. T. R. Lewis

Although the Earth's gravity field is simply and directly related to the Earth's density, the usefulness of gravity for examination of the density variations within the Earth is limited by the inherent non-uniqueness of solutions to the inverse potential problem. When we are studying isostasy, however, we have the additional constraint that the density variations we are interested in must be systematically related to the variations in elevation of the Earth's surface. This additional constraint is sufficient to allow us to extract the isostatic Green's function from observational data (gravity and surface elevation).

The Green's function thus computed can be used to calculate isostatic anomalies which are not based on any specific model. It is, however, of more use to us than that. By remembering that the Green's function relates the forcing function of our problem (the topography) to the observable (the gravity anomaly). We can see that the Green's function must represent the gravity anomaly associated with a concentrated load on the Earth's surface. If we have knowledge of, or make assumptions about, the mechanical properties of the Earth's crust, we can invert this Green's function and find the density changes as a function of depth which are associated with this concentrated load.

For the assumption of local compensation (compensation occurring directly beneath the load), this inversion requires us to invert an integral transform similar to the Laplace transform where the function to be inverted is derived from observations and hence contains errors.

Using gravity and elevation from the continental U.S., we have extracted the Green's function and, using the elegant techniques of Backus and Gilbert, inverted it.

These calculations show that compensation occurs at at least two depths. Near the base of the crust, there is over compensation by about 20 per cent. This extra 20 per cent is cancelled out deeper in the mantle, at about 450 km depth.

Comparison of the density differences between the Earth beneath low-lying regions and that beneath elevated regions with the differences in seismic *P* and *S* wave velocities between these regions gives support for a two-depth compensation mechanism.

L. M. Dorman:

*NOAA Atlantic Oceanographic
and Meteorological Laboratory,
Miami, Florida 33149, USA*

B. T. R. Lewis:

*University of Washington,
Seattle, Washington 98105, USA*

References

- Dorman, LeRoy M. & Lewis, Brian T. R., 1970. Experimental Isostasy: 1, The theory of the determination of the isostatic response of the Earth to a concentrated load, *J. geophys. Res.*, **75**, 3357–3365.
- Dorman, LeRoy M. & Lewis, Brian T. R., 1972. Experimental Isostasy: 3, Inversion of the isostatic Green's function and lateral density changes, *J. geophys. Res.*, **77**, 3068–3077.
- Lewis, Brian T. R. & Dorman, LeRoy M., 1970. Experimental Isostasy: 2, An isostatic model for the U.S.A. derived from gravity and topographic data, *J. geophys. Res.*, **75**, 3367–3386.

CARIBBEAN ATLANTIC GEOTRAVERSE,
NOAA-IDOE 1971,
REPORT NO. 3, GRAVITY

LeRoy M. Dorman,¹ B. G. Bassinger,¹ E. Bernard,² S. A. Bush,¹
O. E. DeWald,¹ L. A. Lapine,² R. K. Lattimore,¹ and G. Peter¹

This report describes the collection and reduction of about 30,000 km of gravity data that were acquired during 1971 by the NOAA ship *Researcher* as part of the NOAA-IDOE program. Data are presented as a free-air anomaly map and as profiles of free-air anomaly, accompanied by a track chart. The data, in processed and original form, are available through the NOAA National Geophysical and Solar-Terrestrial Data Center, Boulder, Colo., under NGSDC file number 00102.

INTRODUCTION

As part of a 2-year program funded in part by the Office for the International Decade of Ocean Exploration of the National Science Foundation, the NOAA ship *Researcher* collected gravity, magnetic, and bathymetric data along tracklines shown in figure 1. The collection and reduction of the gravity data are described in this report.

INSTRUMENTATION AND DATA ACQUISITION

The gravimeter used was the La Coste and Romberg gyrostabilized sea gravimeter serial number S-52. The calibration table used was dated 1/12/70. Observations were made every minute and recorded on digital magnetic tape (the raw-data tape). The parameters measured were the

¹ NOAA Atlantic Oceanographic and Meteorological Laboratories, Miami, Fla.

² NOAA Corps, NOAA Ship *Researcher* (OSS-03).

corrected gravity, spring tension, total correction, averaged-beam position, and cross-coupling correction. The beam position may have been recorded improperly because it was not recoverable from the tape.

DATA REDUCTION

The data reduction process divides naturally into two parts: (1) correction for ship motion, and (2) removal of the earth's main field as represented by the international gravity formula of 1930.

The first correction (the Eötvös correction) is by far the most difficult and, at present, is the factor limiting the accuracy of the data. This Eötvös effect represents the vertical component of the centripetal acceleration resulting from the east-west (E-W) component of the ship velocity. The magnitude of this effect requires knowledge of the E-W velocity to about 0.1 kt to achieve an accuracy of 1 mgal. The navigation control during this field season consisted of the SRN-9 satellite navigation system (Guier, 1966; Talwani et al., 1966) and the Loran C. Fixes from satellites were available, on the average, about every 2 hours. Because most of the survey area is at such a distance from the Loran station on the east coast of the United States, the accuracy of the Loran fixes is questionable; therefore, the Loran was used principally to validate the dead-reckoning (DR) interpolation which was used to generate the track between satellite fixes. The DR track between fixes was generated by integrating the velocity and heading and by adding a correction velocity vector (a constant for each fix pair) to make the DR track coincide with the position of the second fix of each pair (Talwani, 1970; Bowin et al., 1972).

The frequency standard used in the satellite navigation receiver failed on Julian Day (JD) 295 and was replaced on JD 302. The gravimeter failed on JD 300 at 0611 and was repaired at JD 301 at 0000.

One of the navigation files covering the period from JD 292/0700 to JD 294/0805 was lost so that data could not be processed in the same manner as the remainder. The basic data are available, however, so that these data can be recovered.

The shipboard data-acquisition system provides real-time correction of gravity data using DR from the last available fix. These provisionally corrected data are written on another digital magnetic tape (the processed-data tape). The fundamental observable—the meter gravity—however, is not preserved on this tape nor on the printout of the results of the real-time reduction so that the processing results are of evanescent value only.

At the first still reading at Barbados (JD 281), a zero meter gravity (ZMG) value, approximately 102 mgal too low, was obtained. This value was not repeated at the still reading upon departure on JD 285 nor were any data found to be in error by this value. It is probable that the reading resulted from a dial-reading error of 100 dial divisions.

ACCURACY

From the values of ZMG in table 1, we see that the meter drift over the experiment is less than 1 mgal and that the gravity values for the bases are consistent to within 1 mgal.

From 71 track crossings made, the root-mean-square crossing error is 3.7 mgal.

Table 1. Researcher base ties 1971

Location	Base gravity	Meter gravity	ZMG	JD
Miami	979045.55		972893.00	
Barbados	978294.19	5401.38	972892.81	285
Guadeloupe	978559.27	5666.25	972893.02	302
Miami	979045.55	6152.27	972892.28	327

The base stations used were:

Miami, Fla.; NOAA Ship Base

Barbados; Deep Water Pier
(Naval Oceanographic Office NO 0045.21)

Guadeloupe; Pointe-à-Pitre Airport
(Naval Oceanographic Office NO 0045.14).

DATA DISPLAY

Tracklines for which data have been reduced are shown in figure 1. Figure 2 shows the primary survey area and the profile number for each line segment. Table 2 tells the times of the beginnings and ends of each profile in the Appendix. The profiles themselves, designated by number, are also shown in the Appendix. The East-West profiles, beginning with the most northerly, are shown first and are approximately alined by longitude. The North-South profiles, beginning with the most westerly, follow next and are alined approximately by latitude. Finally, the remaining short profiles are shown in numerical order. The caption on each page lists the profile numbers, reading from left to right and then top to bottom.

Figures 3 and 4 are contour maps of the free-air anomaly for the region of densest coverage. The contours on these maps are derived from a grid representation of the data, with the grid interval set at about 17 km. Grid values were obtained from the data by taking a weighted average of values near the grid point. Gravity data from *Chain* cruise 75 (Bowin et al., 1969) are included in the data set from which the contour map was made.

Table 2. Profile start and stop times
RP-12-RE-71

Profile number	Start		Stop	
	JD	Time	JD	Time
1	261	0800	262	0130
2	262	0405	263	1515
3	263	2330	264	1740
4	264	1835	265	1230
5	265	1420	266	0600
6	266	1010	266	1620
7	266	1625	267	0740
8	267	0745	267	1610
9	267	1615	268	2200

Table 2. Profile start and stop times RP-12-RE-71—continued.

Profile number	Start		Stop	
	JD	Time	JD	Time
10	268	2205	269	1330
11	269	2125	270	1240
12	270	1245	271	0420
13	271	0425	271	1920
14	271	1925	272	0310
15	272	0315	272	1320
16	272	1325	274	1005
17	274	1010	274	1535
18	274	1540	274	2240
19	274	2245	275	1730
20	275	1835	276	2240
21	276	2245	277	0815
22	277	0820	277	1400
23	277	1405	279	1710
24	279	1725	279	2200
25	279	2205	280	1230
26	280	1505	280	1910
27	280	1915	281	0055
28	286	0100	286	0830
29	286	0905	290	2040
30	290	2300	294	1505
31	294	1717.5	299	0100
32	299	0240	302	0555
33	306	2115	309	2240
34	310	0015	312	1645
35	312	2230	315	1835
36	315	2005	318	1710
37	318	1715	320	1830
38	320	2000	322	1650

ACKNOWLEDGMENTS

We appreciate the cooperative spirit shown by CAPT Steven L. Hollis and the crew of the NOAA ship *Researcher*. We are especially grateful to LCDR T. Wyzewski for his zealous supervision of all phases of the navigation. This work was funded in part by NSF-IDOE Grant No. AG-253.

REFERENCES

- Bowin, C. O., T. C. Aldrich, and A. Wertheimer (1969): "Gravity data obtained during *Chain* cruise 75," Woods Hole Oceanographic Institution unpublished manuscript. (Available from the National Technical Information Service under accession number AD 698 791.)
- Bowin, C. O., T. C. Aldrich, and R. A. Folinsbee (1972): VSA gravity meter system: tests and recent developments, *J. Geophys. Res.* 77: 2018-2033.
- Guier, W. H. (1966): Satellite navigation using integral Doppler data—the AN/SRN-9 equipment, *J. Geophys. Res.* 71: 5903-5910.
- Talwani, M. (1970): Developments in navigation and measurement of gravity at sea, *Geoexploration* 8: 151-183.
- Talwani, M., J. Dorman, J. L. Worzel, and G. M. Bryan (1966): Navigation at sea by satellite, *J. Geophys. Res.* 71: 5891-5902.

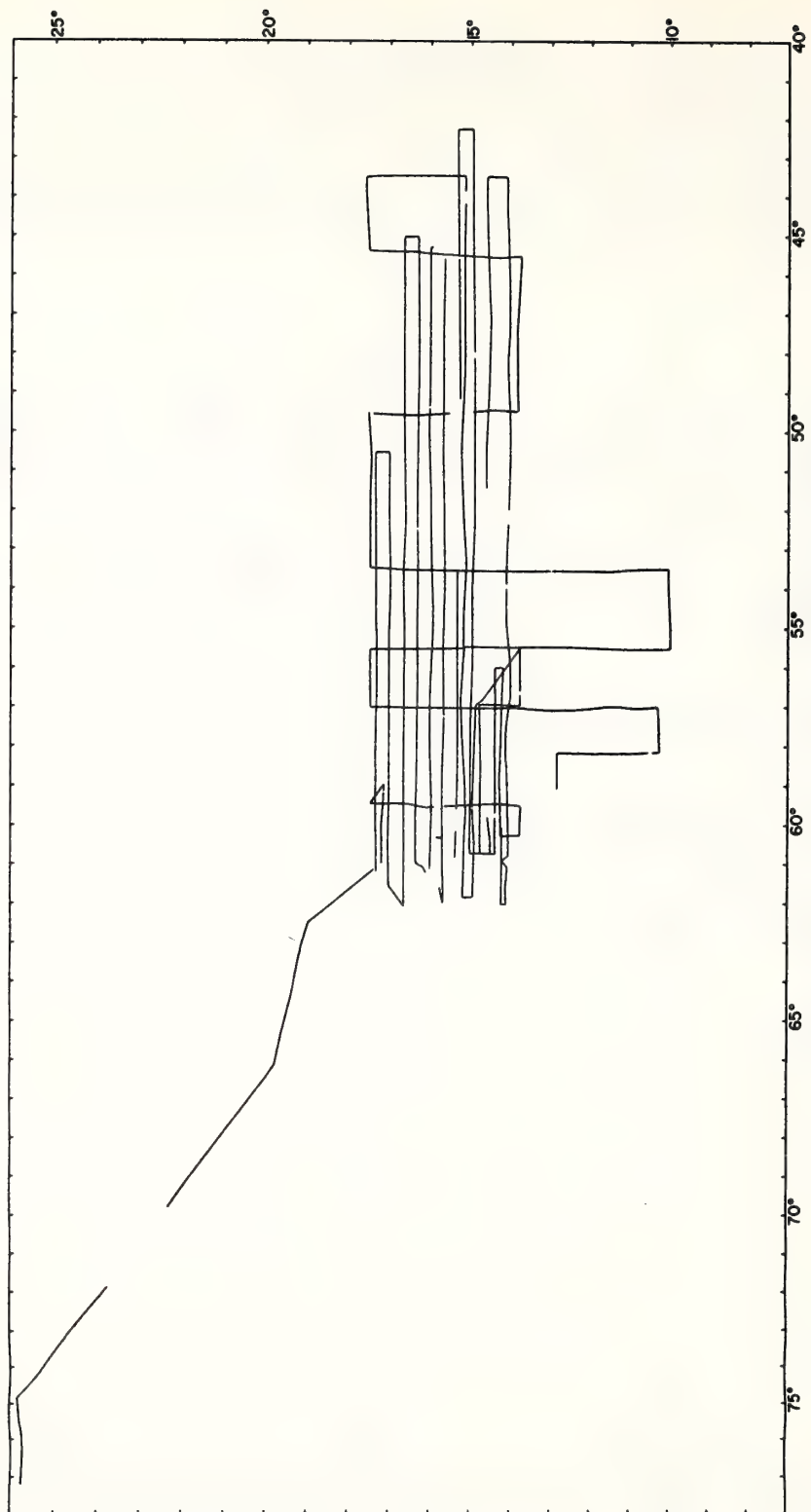


Figure 1. Trackline coverage for gravity data covered by the NOAA ship Researcher in 1971.

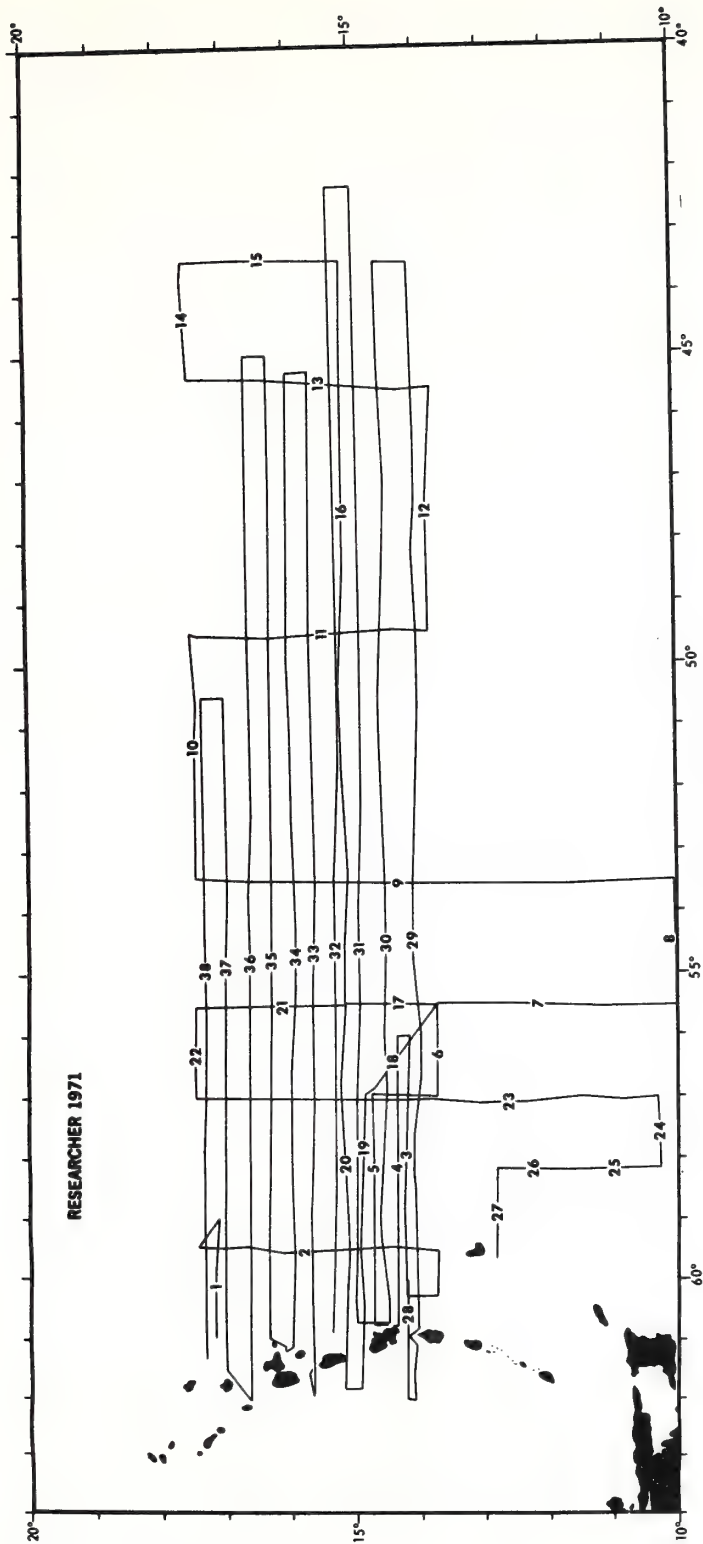


Figure 2. Key to profiles.

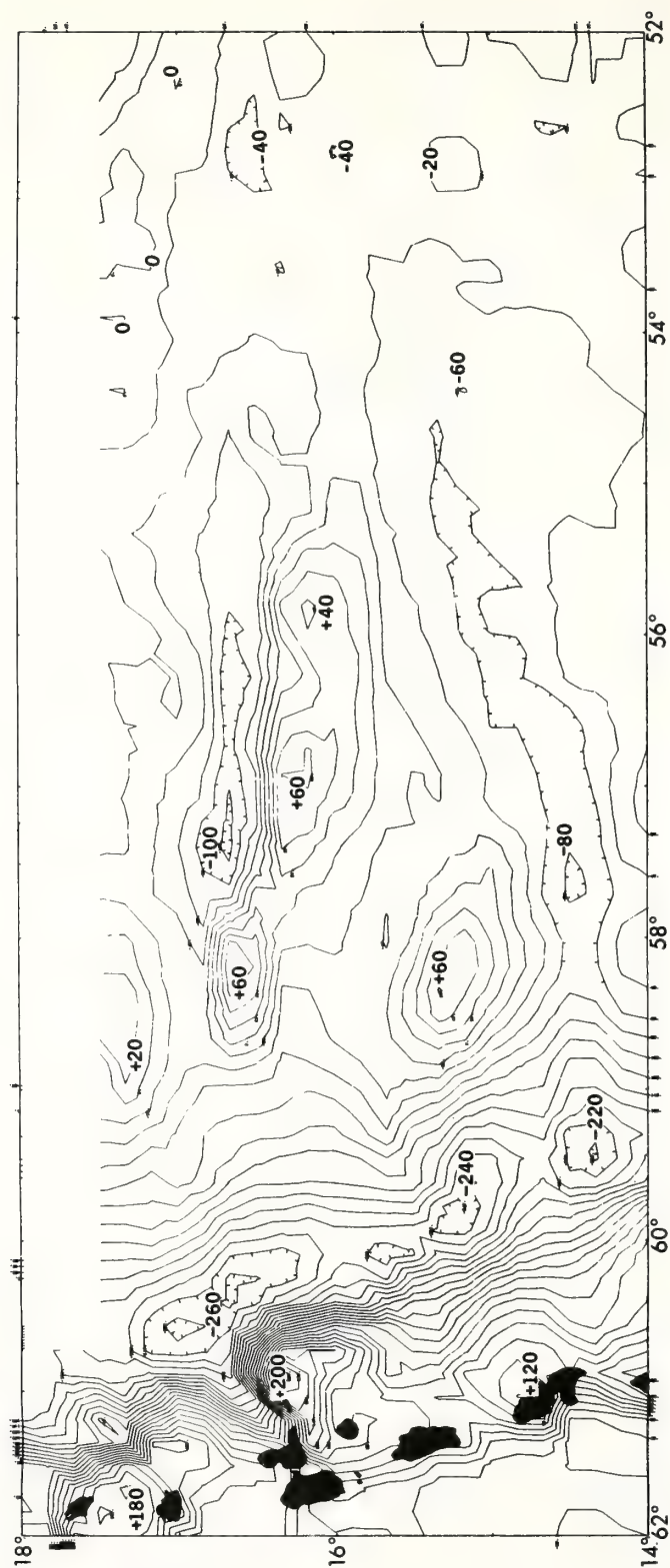


Figure 3. Free-air gravity anomaly map, western portion.

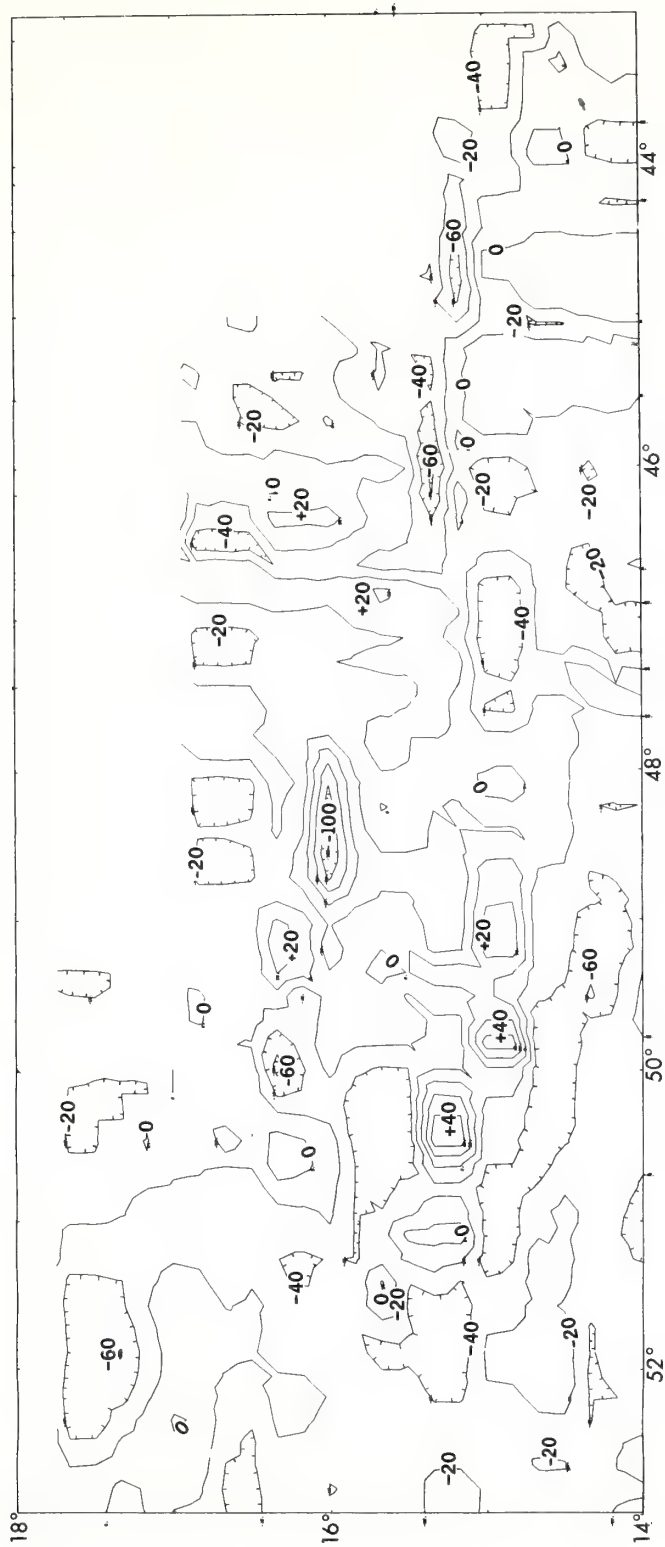
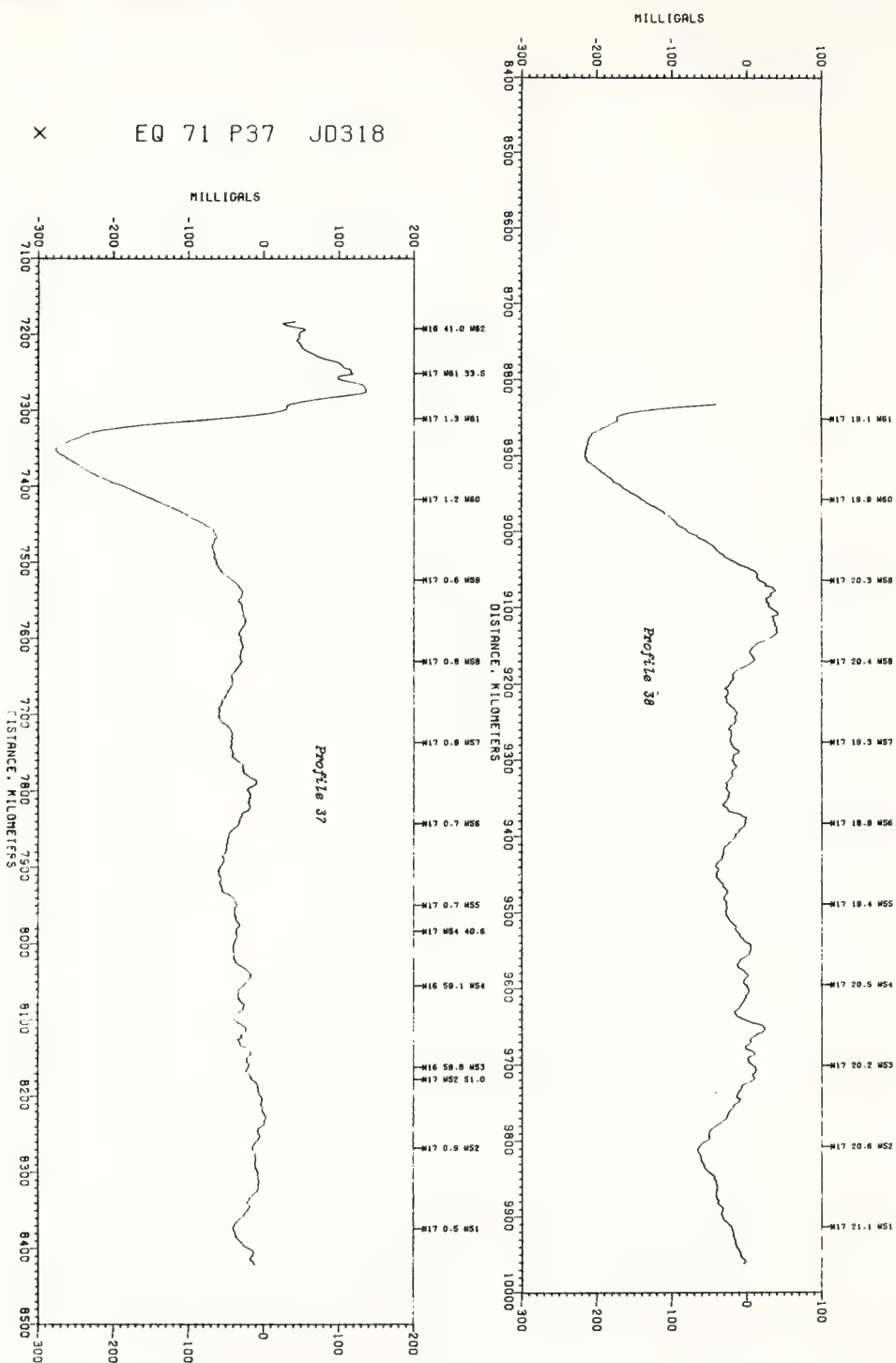


Figure 4. Free-air gravity anomaly map, eastern portion.

APPENDIX. PROFILES

* EQ 71 P38 JD320

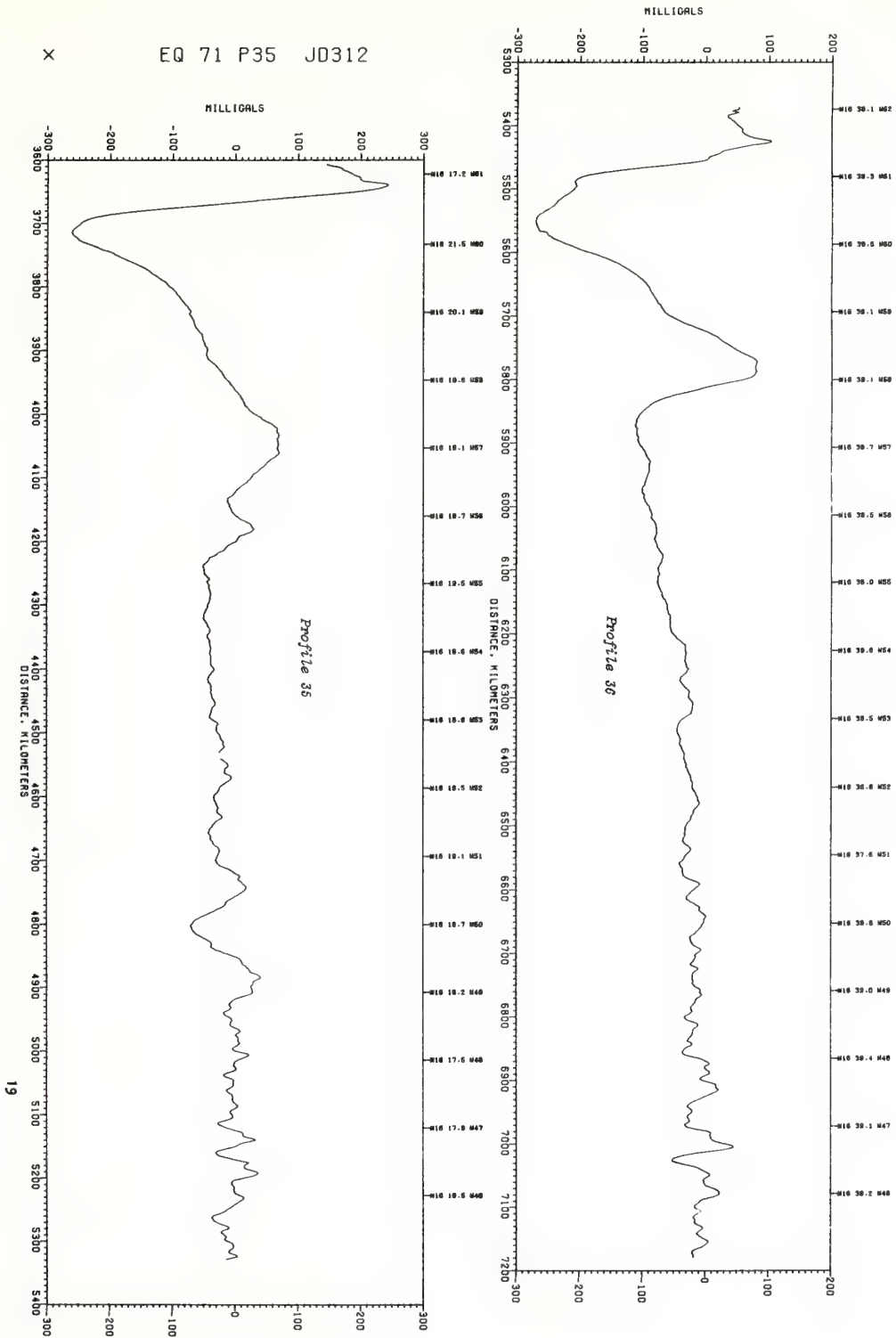


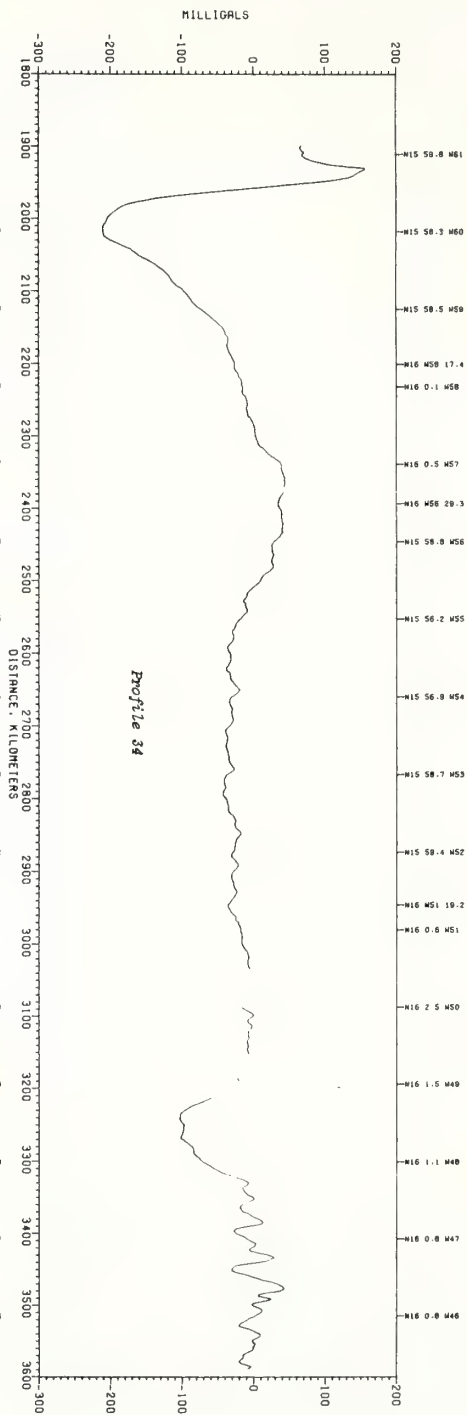
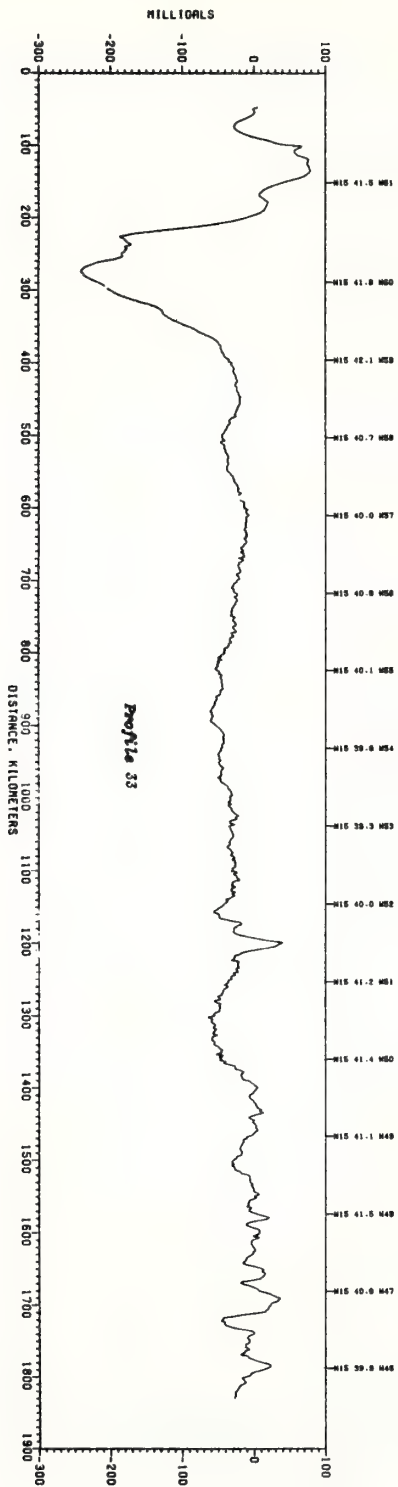
*

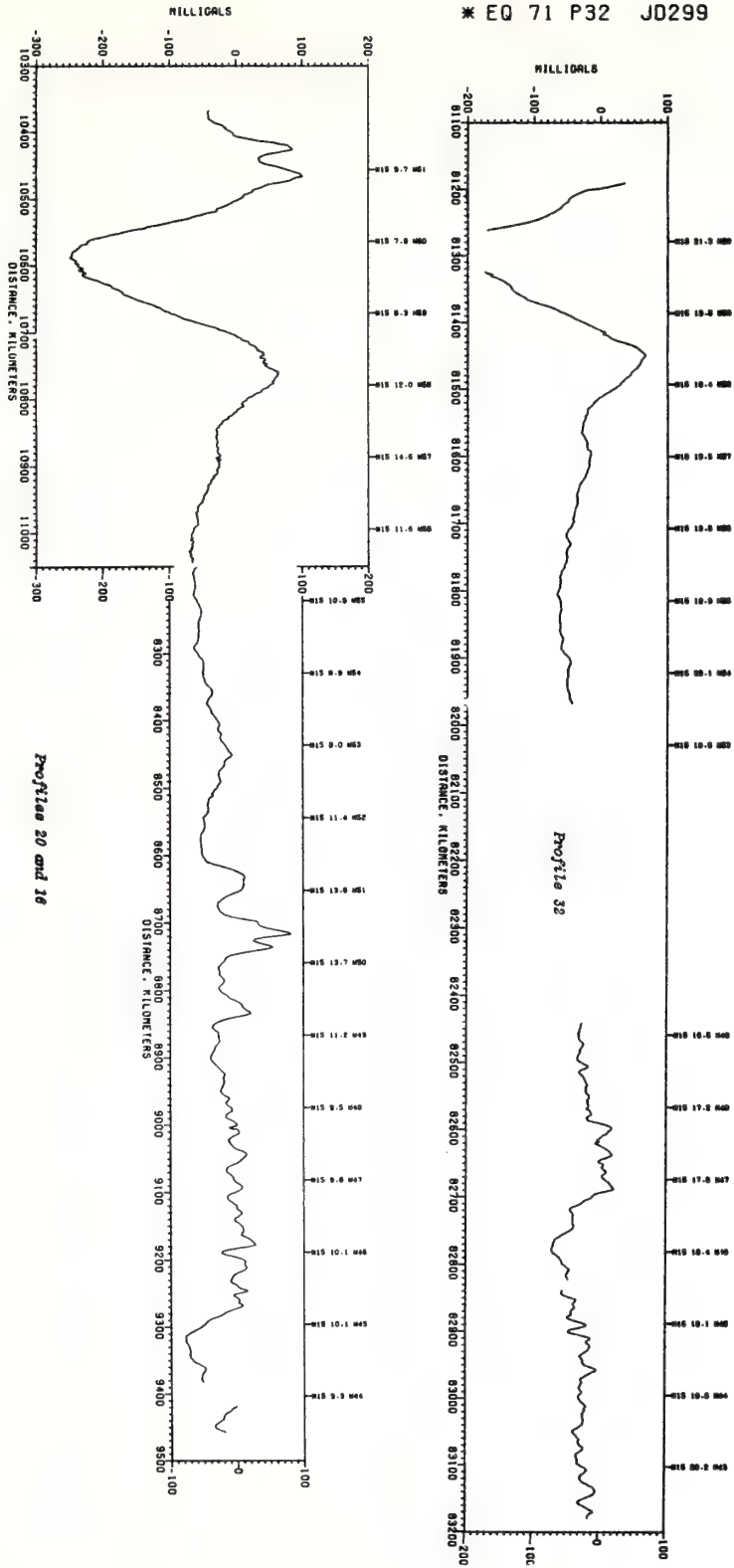
EQ 71 P36 JD315

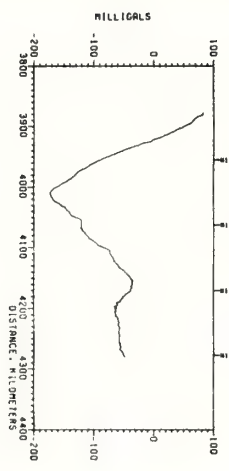
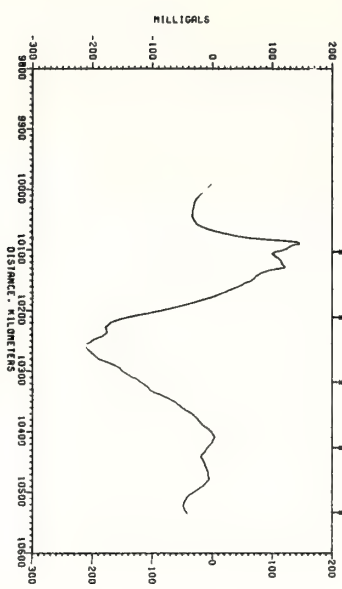
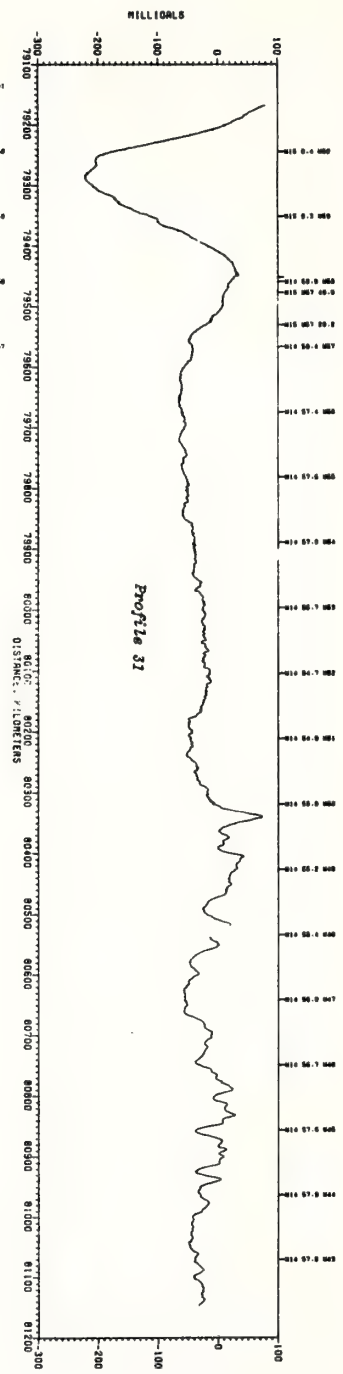
X

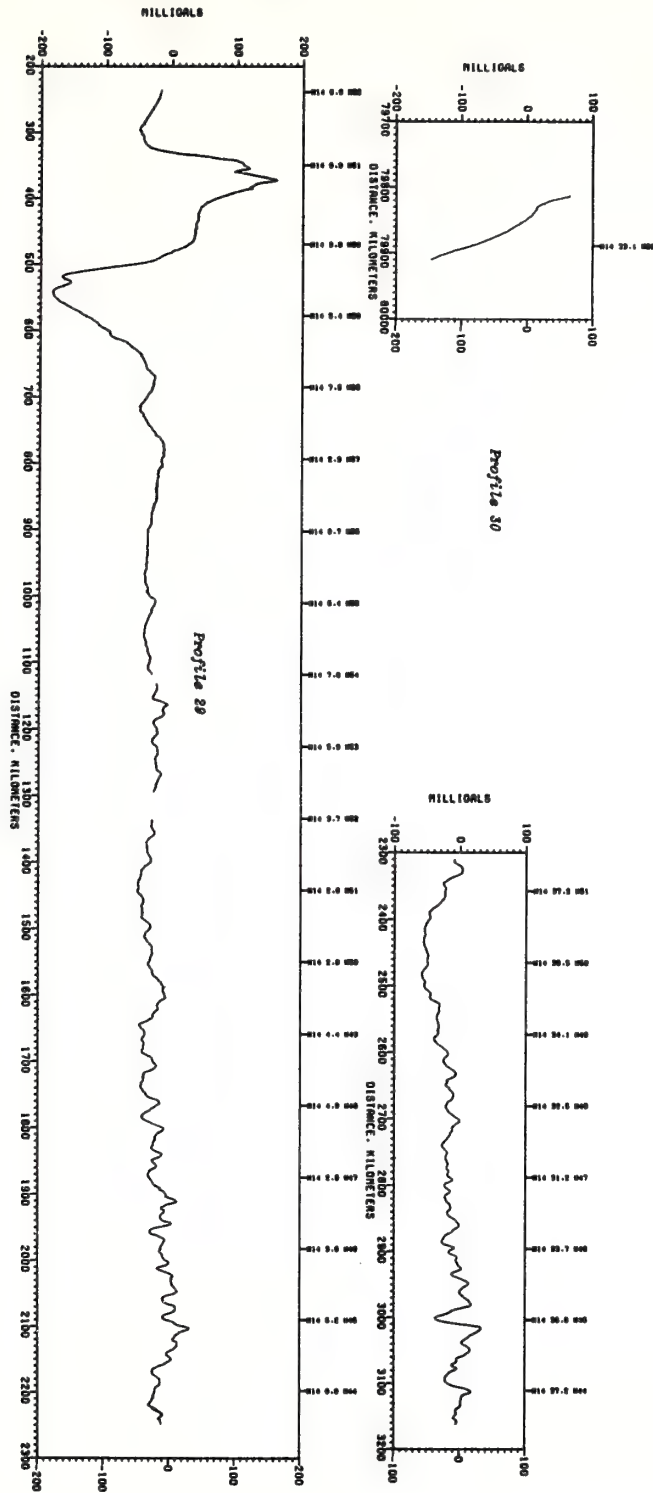
EQ 71 P35 JD312

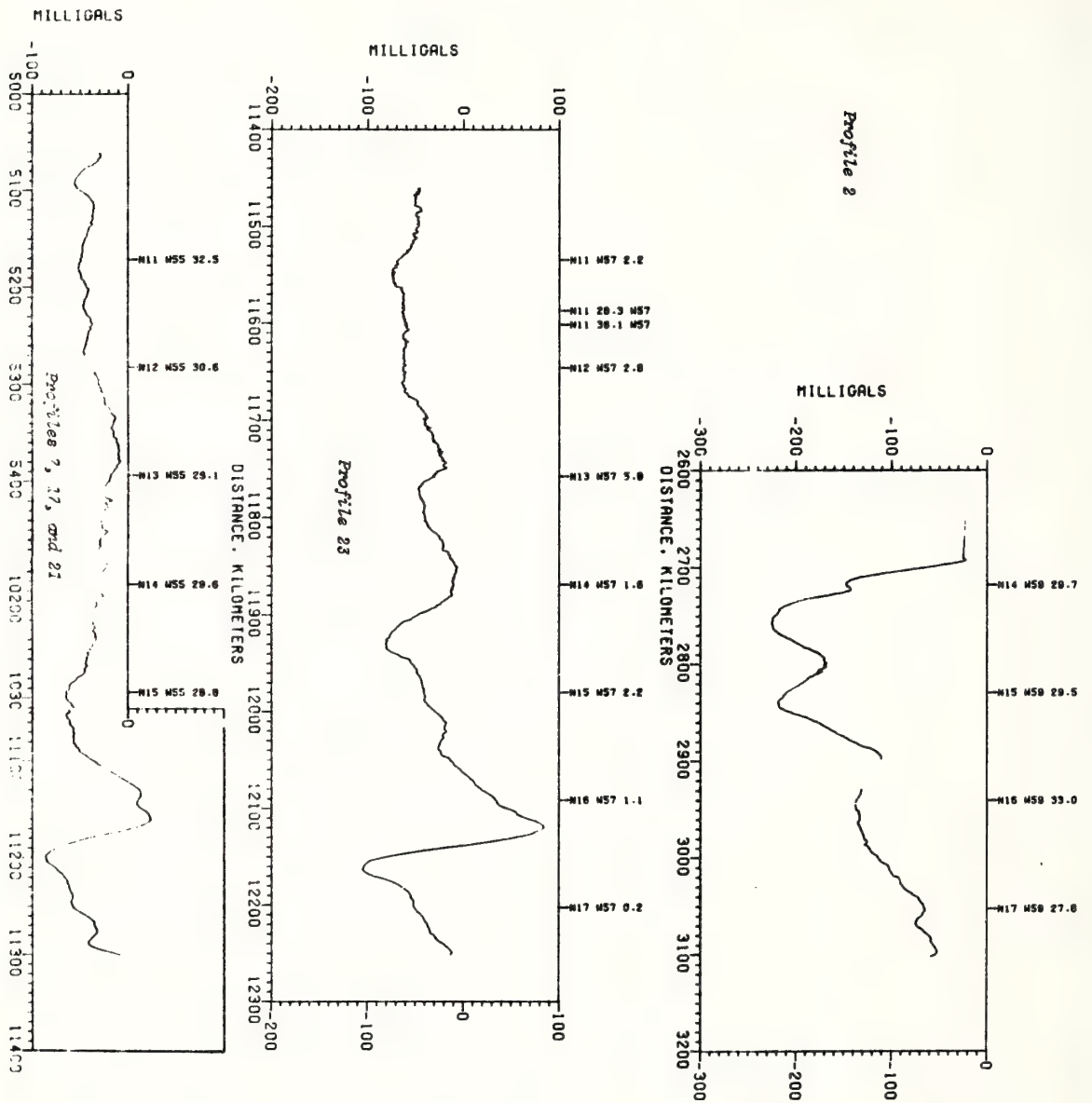


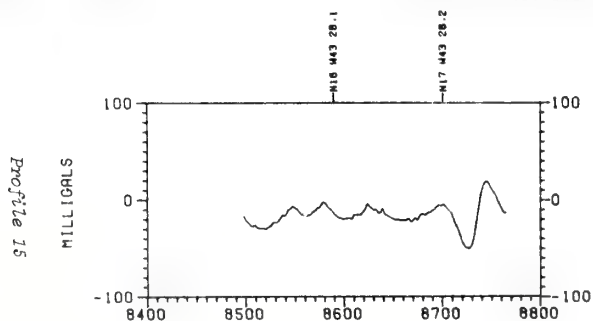
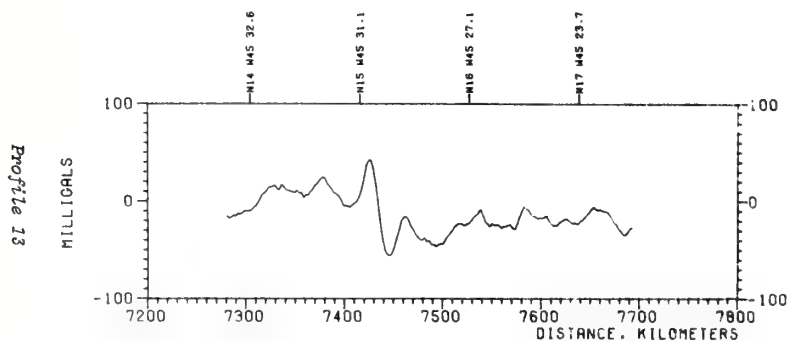
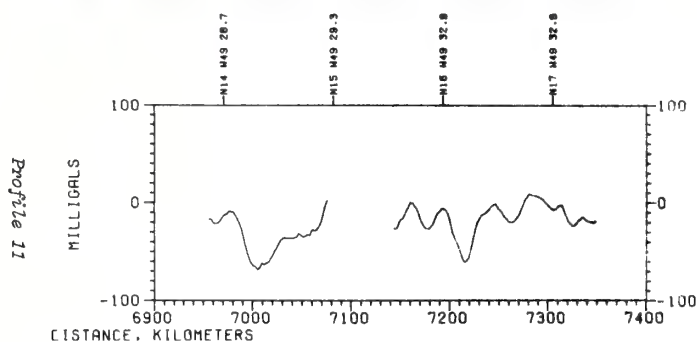
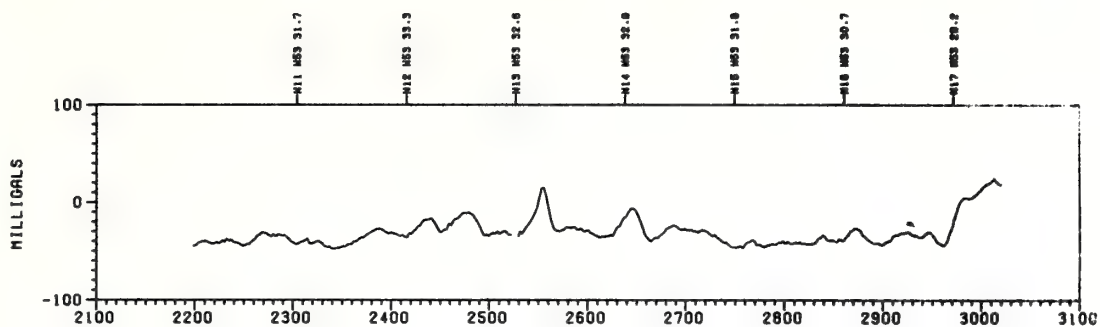


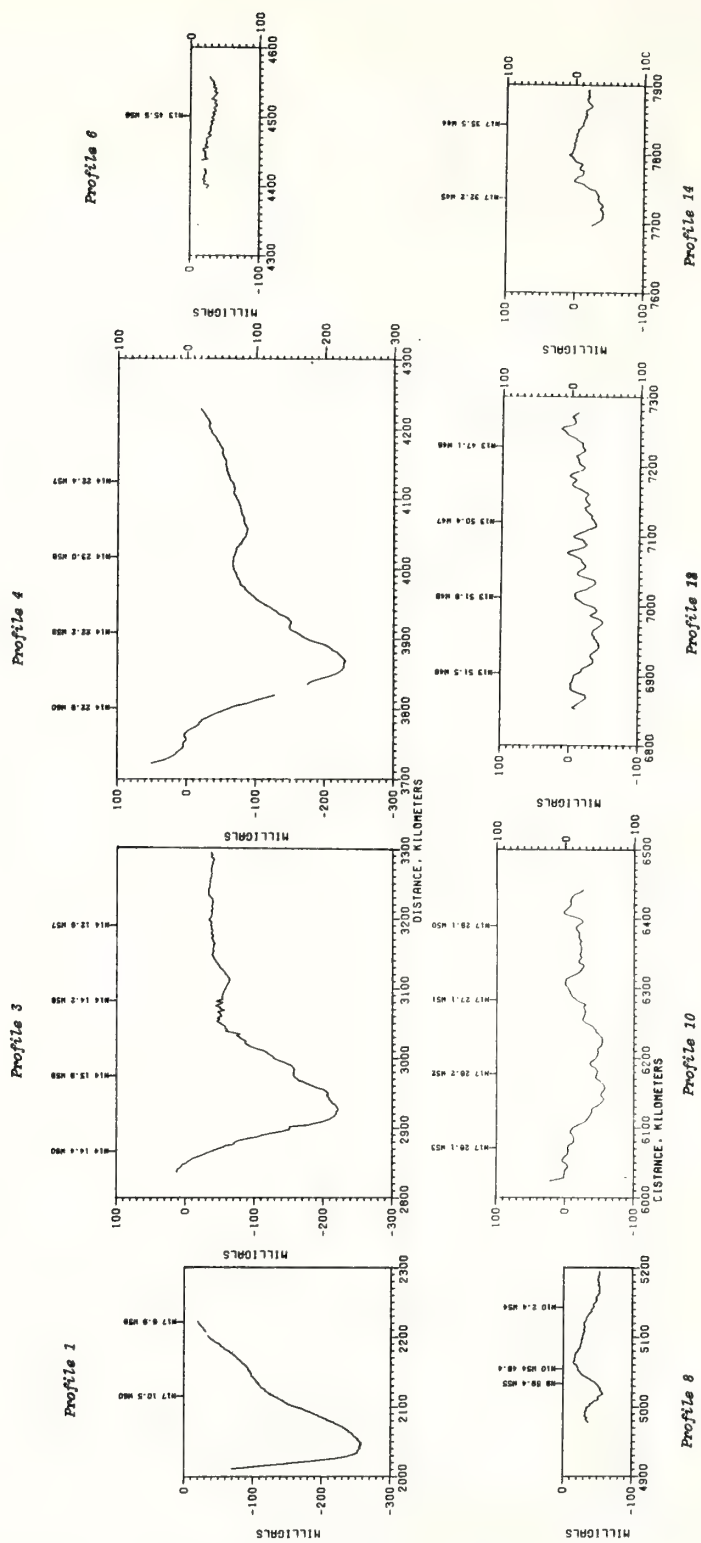


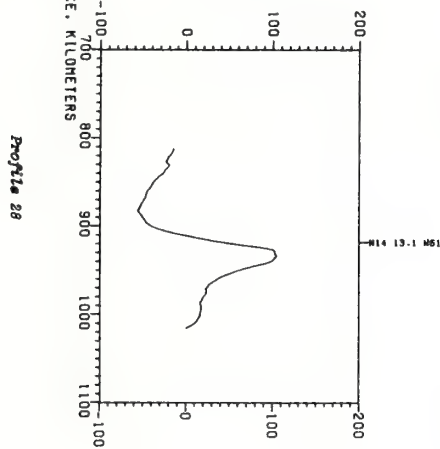
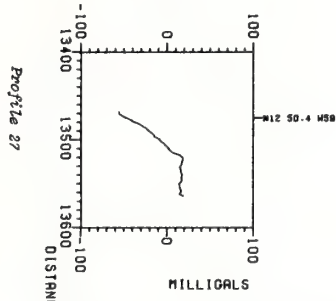
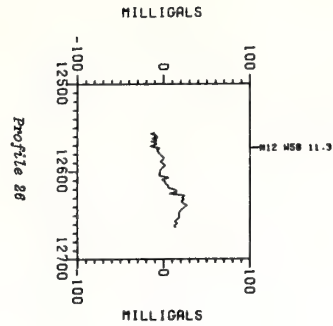
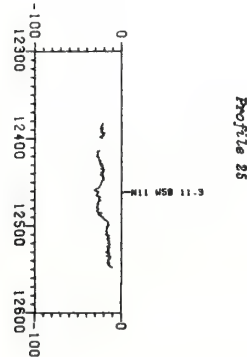
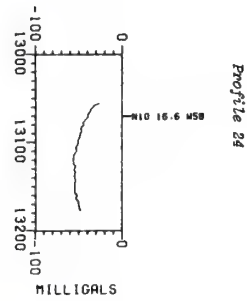
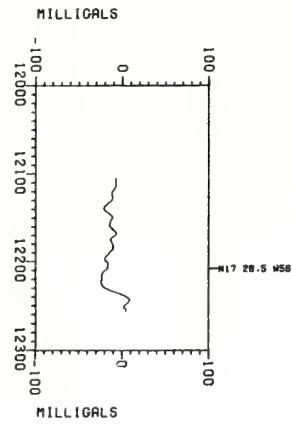
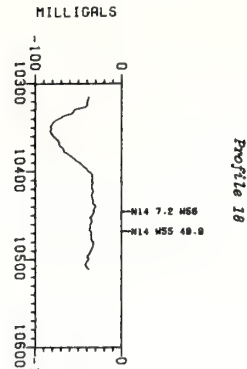












ROTATION HISTORY OF ALASKAN TECTONIC BLOCKS

GEORGE L. FREELAND and ROBERT S. DIETZ

NOAA, Atlantic Oceanographic and Meteorological Laboratories, Miami, Fla. (U.S.A.)

(Accepted for publication March 12, 1973)

ABSTRACT

Freeland, G.L. and Dietz, R.S., 1973. Rotation history of Alaskan tectonic blocks. *Tectonophysics*, 18: 379-389.

Alaska is considered to be tectonically comprised of five elongate blocks separated by transcurrent faults formed prior to rotation which enter the state from the southeast and continue westward to the edge of the Bering Sea continental shelf. We propose an additional, inactive fault, indicated by gravity and magnetic data and other observations, to extend between the Bering Strait and the Arctic Ocean continental shelf east of the Northwind escarpment, separating northern Alaska from northeast Siberia. Near the center of the state the faults are bent, concave to the south, about the north-south axis of the so-called Alaska orocline. In our reconstruction the blocks have rotated from a position whereby the north slope was adjacent to Banks Island of the Canadian basin. During the rotation the northernmost, or Brooks block, was squeezed, up to 15% in the western end, to its present width. After rotation, when the three southern blocks were in their present position, the Brooks block and the next block to the south were pushed eastward by North America moving against Siberia, forming the bend in the British-Richardson-Ogilvie Mountains we call the Ogilvie orocline.

INTRODUCTION

The great bend of the Alaskan foldbelt and associated tear faults has provoked several attempts at explanation (Carey, 1958; Grantz, 1966; Tailleux, 1969). Carey proposed a simple tension rift parallel to the Lomonosov Ridge whereby North America rotated clockwise from Asia, opening both the Arctic and North Atlantic Ocean and forming the Alaskan orocline. We now know that magnetic lineations in the Arctic Ocean, as well as most of the Alpha Cordillera, are parallel to the Lomonosov Ridge (Vogt and Ostenso, 1970; Hall, 1970); therefore, the pole of rotation for the opening must be about 90° west of Carey's pole at the apex of the Alaskan orocline, as the opening direction has to be perpendicular to these ridges. Grantz (1966) outlined the rotation of Alaskan continental slabs, but did not close the oceanic Canada Basin. Tailleux (1969) proposed the rotation, parallel to the Alpha Cordillera, of Alaska and the eastern part of northeastern Siberia as a unit against the Canadian archipelago. This too violates the data indicating the spreading direction in the vicinity of the Alpha Cordillera. In subsequent work (Tailleux, 1970a; Tailleux and Brosge, 1970) he accepts the separation of Alaska from Siberia and describes

the enlarged portion of northern Alaska closing the Canada Basin. Packer and Stone (1972) have examined the paleomagnetic data relevant to the rotation of the orocline and conclude that counterclockwise bending of the orocline is contrary to their data. However, because of data scatter and lack of consistency of North America data west of the Sierra Nevada Mountains, they do not consider their data to be a test of the oroclinal model.

RECONSTRUCTION

We propose a variation of these reconstruction themes whereby Alaska, comprised of five elongate continental blocks not part of northeastern Siberia, has rotated counterclockwise from a position whereby the Alaskan north slope was initially adjacent to Banks Island, western Canadian archipelago. The Alaskan movement occurred as the result of opening in the Arctic Ocean along the Alpha Cordillera when northeastern Siberia, rotating about a pole near the continental margin offshore from the Lena River delta, moved southward against Alaska, a spur of the North American continent. A secondary spreading center in the southern Canada Basin developed concurrently with spreading in the central Arctic and caused the rotation of the Alaskan blocks along pre-existing lines of weakness. Therefore, Alaskan drift opened only the southern part of the Canada Basin. The reconstruction, based on a model study, is related to relative motions of adjacent lithospheric plates: (1) the North American plate, assumed to be attached to Europe until the Late Cretaceous (Pitman and Talwani, 1972); (2) the northeast Siberian plate, assumed to have closed the Arctic Ocean (Freeland and Dietz, 1972); and (3) the Mesozoic Pacific plates (central, north, and northeast Pacific plates) (Hayes and Pitman, 1970), which play a passive role in the rotation, but which affect tectonism on the continental blocks. Western Canada and Alaska are orogenic belts which have been partly created and considerably deformed by marginal interactions of these plates. Although the orogenic belt from southern British Columbia to western Alaska at first glance appears to have had a similar tectonic history along its whole length because of similar geological terrain, the arcuate bend of the great faults and mountain ranges of Alaska indicates a somewhat different history for Alaska.

ALASKAN TECTONICS

In this paper Alaska includes the continental shelves of the North Slope, the Gulf of Alaska, the Bering Sea, and the eastern part of the Chukchi Sea as defined below (Fig. 1). We divide Alaska into five elongate blocks separated by the four major transcurrent faults crossing the state (King, 1969; Lathram, 1972). From north to south these are: (1) the *Brooks block*, including the Brooks Range and the North Slope, north of the Kobuk–Tintina fault system; (2) the *Koyukuk block*, between the Kobuk and Kaltag faults, which wedges out to the east where these faults join the Tintina fault; (3) the *Kuskokwim block*, which lies between the Kaltag–Tintina and the Denali fault systems; (4) the *Susitna block*, lying between the Denali system and the Castle Mountain fault and its probable southeast-

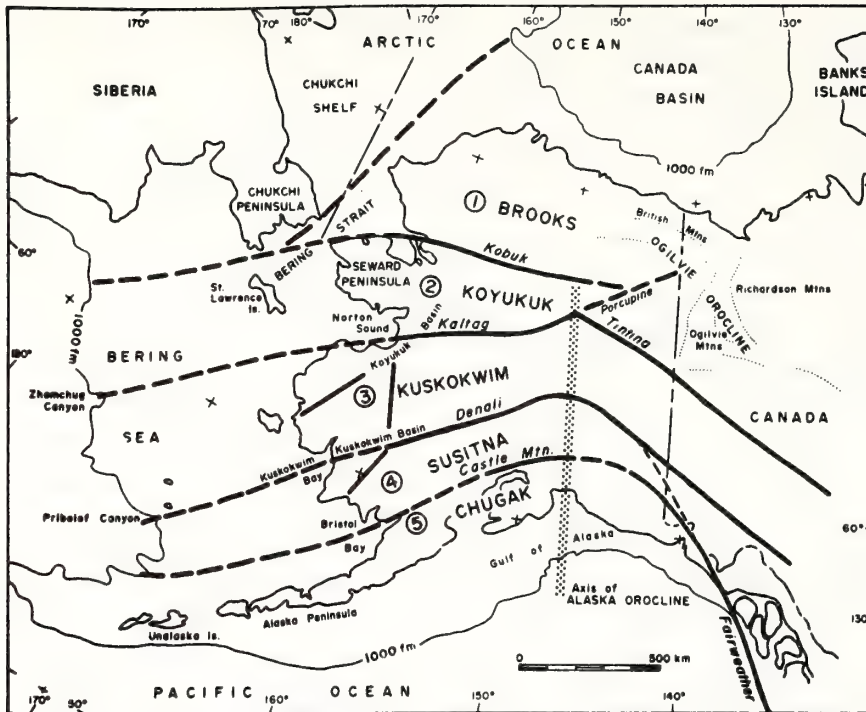


Fig. 1. Index map showing the tectonic blocks of Alaska (numbered from 1 to 5 and named), separated by the major transcurrent faults (heavy lines with slanted names). Dashed portions show extensions proposed in this paper. The present positions of the Kaltag and Denali faults near the western Alaska coastline are shown west of numbers 3 and 4. Between number 3 and "K" of Kuskokwim is the sinistral fault mentioned in text. Azimuthal equidistant projection centered on the North Pole.

ward extension connecting to the Fairweather fault; and (5) the *Chugak block*, bordering the Pacific Ocean. We have named the blocks after prominent mountain ranges and rivers within them. They were largely created in pre-Mesozoic times (Brosge, 1970; Churkin, 1970; Sainsbury et al., 1970; Jones et al., 1972), although they are extensively intruded by Mesozoic plutons (King, 1969; Reed and Lanphere, 1970). The lack of regional thrusting and folding in blocks 2, 3 and 4 (to the extent in blocks 1 and 5) precludes major crustal shortening within them; we assume these blocks have remained at about their present width, although some compression is related to vertical emplacement of plutons. Compression in block 5 is probably related to subduction of the Pacific plate.

The major faults are assumed to have been transcurrent dextral fault zones which allowed the blocks to slide past one another during rotation. Assumed to have been formed during Paleozoic continental accretion (Churkin, 1970; Forbes et al., 1971; Jones, 1971), they are presently bent in a great arc, concave to the south, that is known as the Alaskan orocline (Carey, 1958). The center of curvature of the faults is aligned on the north-south oroclinal axis. Curvature of the bends increases from about 20° in the north to about 50° in the south. The faults are also assumed to have extended southwestward

to the Bering Sea continental slope, most of which was formerly a subduction zone, the plate boundary between Alaska (North America) and the Pacific Ocean (Anon, 1972; Moore, 1972). We suppose that the submarine canyons there (King, 1969) are related to the intersection of these faults with the slope, presumably having formed by submarine erosion along fault zone lines of weakness. The westward extension of the Kobuk graben is assumed to have passed north of the Seward Peninsula, then trended southwestward through the Bering Strait between St. Lawrence Island and the Chukchi Peninsula, terminating in the submarine canyon at 61°N , 180° . Southwest of the Bering Strait this fault marks the western edge of continental Alaska.

Similarly, the Kaltag fault originally extended seaward through the southern part of Norton Sound to Zhemchug Canyon at 58°N , 175°W . The southwestward extension of the Denali (Farewell) fault probably passed through Kuskokwim Bay to Pribilof Canyon

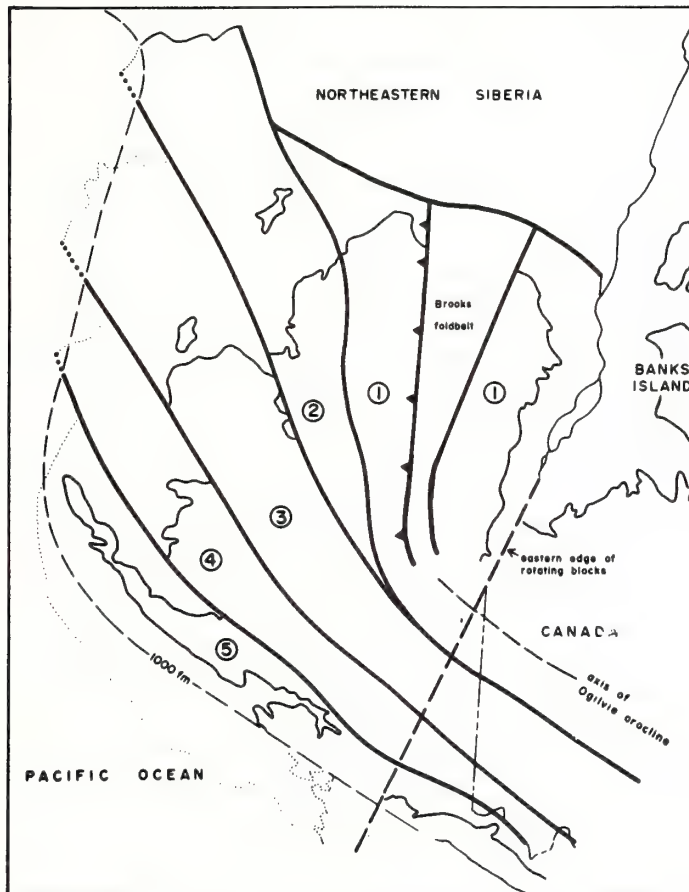


Fig. 2. Detail of Alaskan reconstruction. Heavy lines indicate transcurrent faults except those delineating the Brooks foldbelt. 1000-fathom dashed line is approximate location of original continental margin. Light dotted and solid lines are present 1000-fathom line from Fig. 1. The Brooks foldbelt and the Ogilvie orocline have been expanded to their pre-drift positions.

at 56°N, 169°W, and the Castle Mountain fault extended to Bristol Bay and thence seaward parallel to the Alaskan Peninsula to the submarine canyon north of Unalaska Island at 45°N, 167°W. The Aleutian Islands to the west of Unimak Island originated after the tectonic movements of Alaska proposed here and are not considered.

We suggest that the Brooks block (block 1) was bordered on the west by a now inactive fault extending from the Bering Strait across the Chukchi shelf to the eastern edge of the Northwind plateau. Indications of this junction are the lack of continuity of mountain ranges from Alaska into northeastern Siberia, the extreme difference in shelf widths north of the Alaskan and Siberian mainlands, and the steepness, straightness, and direction of the eastern scarp of the Northwind plateau. Additional evidence is a band of north-northeast-trending positive gravity and magnetic anomalies almost coincident with the proposed fault from the Bering Strait to the Canada Basin (Ostenso and Parks, 1964; Bassinger, 1968).

The Alaskan reconstruction closes the southern portion of the Canada Basin by rotation of the blocks to their palinspastic positions (Fig. 2). Blocks 3, 4 and 5 are in positions immediate-

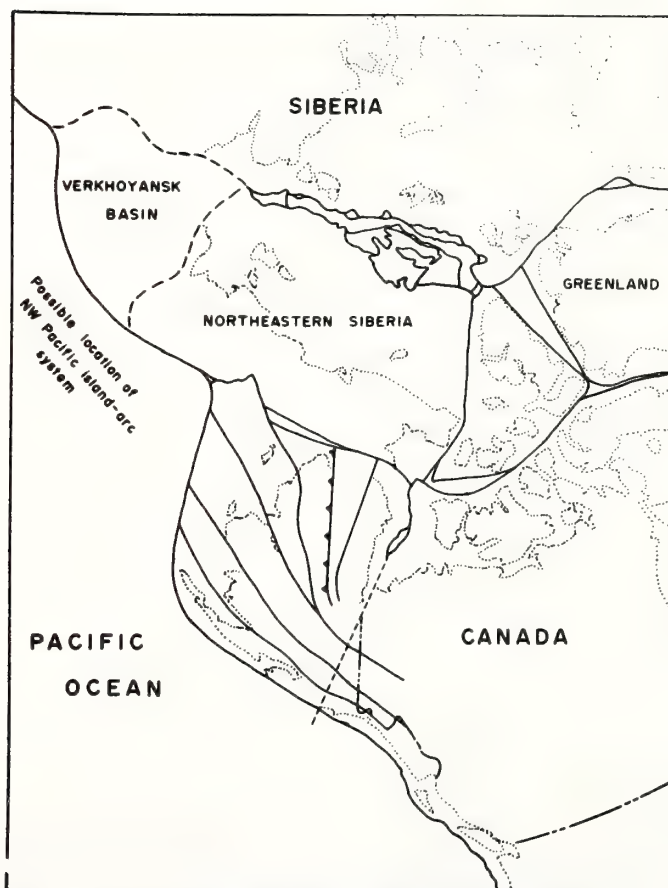


Fig. 3. Palinspastic map of the Arctic Ocean tectonic reconstruction.

ly prior to the Arctic opening, after any earlier transcurrent movements which may have moved these blocks from positions to the southeast (Churkin, 1970; Forbes et al., 1971; Jones, 1971). The eastern edge of the rotating blocks is drawn from the intersection of the axis of the Alaskan orocline with the 1000-fathom contour in the Gulf of Alaska through eastern Alaska, crossing the transcurrent faults at the eastern ends of their curvature. This line is also aligned with the trend line of the Canada—Greenland continental margin and the Nansen fracture zone. Within block 1 the belt of folded Mesozoic miogeosynclinal rocks, lying north of the Paleozoic core of the Brooks Range, has been reconstructed to its original width, nearly twice its present width in the western part (Tailleur, 1969, 1970b). The enlarged Brooks Block occupied the area which is now the southern part of the Canada Basin. The Devonian, Permian, and Triassic terrigenous sedimentary rocks of the North Slope, interpreted to have had a “northerly” source (relative to their present position) (Churkin, 1969; Brosge, 1970; Detterman, 1970), were probably derived from the Banks Islands area.

To the east of the Brooks Range lies the area of the Ogilvie orocline, encompassing the S-shaped bend of the British, Richardson, and Ogilvie mountains (Fig. 1). In the reconstruction the bends have been straightened, resulting in westward extension of the Brooks block of about 300 km. Although the Brooks Range is only part of a regional compression zone extending through western Canada into the United States, the amount of compression near the apex of the Brooks block wedge, between the Yukon Flats basin and MacKenzie Bay, appears to be considerably less than to the west or southeast (King, 1969).

Thus, with the blocks in their palimpsestic positions (Fig. 3), the northwest trend of the axes of the Paleozoic and Mesozoic orogenic belts of British Columbia and the Yukon continue through Alaska with a slight northward curvature. The northwest trend of the coastline of British Columbia and southeast Alaska was also maintained to the western end of the Alaskan peninsula. Block 5 is drawn thinner than at present in anticipation of continental accretion along the seaward edge.

ROTATION SEQUENCE

The reconstruction conforms with the concept that the continental margin of northeastern North America was the site of Paleozoic accretion and deformation (Churkin, 1970; Forbes et al., 1971; Jones, 1971) due to the subduction of one or more Pacific paleoplates when the northeast Pacific triple junction existed (Hayes and Pitman, 1970). Although the position of the triple junction with respect to North America prior to the split-up of Pangaea has not been determined, it does appear that there probably were northward-, northwestward-, and northeastward-moving oceanic plates seaward of this continental margin at various times to account for both subduction (compression) and translation (strikeslip) of the mobile belts before the rotation of Alaska. It seems unlikely that major translational movements of the more southerly blocks occurred after oroclinal bending.

Fig. 4 shows the initial opening of the southern part of the Canada Basin and the beginning of the Alaskan rotation. Relative to North America, movement was counterclockwise

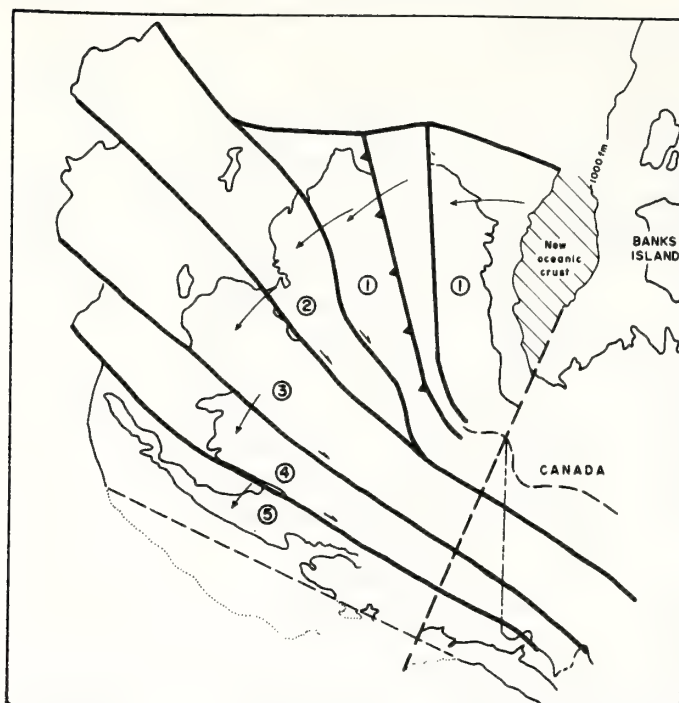


Fig. 4. Initial rotation of Alaskan blocks. Arrows show the amount of rotation of each block and dextral strikeslip along each fault since closure. New oceanic crust forming west of Banks Island is part of the southern Canada Basin. Compression in block 1 has started to fold the Brooks Range.

rotation of the five blocks about poles near their eastern ends. As the blocks rotated, each moved to the right with respect to the next block south. Within block 1, compression, accompanying rotation, caused the initial folding in the Brooks Range. Along the western and southern edges of the blocks Pacific oceanic crust was subducted prior to the existence of the Aleutian trench-island arc system (Anon., 1972; Moore, 1972). Compression and continental-margin accretion occurred in block 5 (Burk, 1965).

Rotation continued until blocks 3, 4 and 5 reached approximately their present positions (Fig. 5). Then relative movement between blocks 1 and 2 also stopped, perhaps because at this stage they had moved into their present position relative to northeastern Siberia and became attached to that block (Freeland and Dietz, 1972). At this time, or slightly later, the compression in the Brooks Range and to the southeast in Canada (the Laramide foldbelt) was completed. The North American plate, however, continued to move somewhat closer to Siberia (Pitman and Talwani, 1972), resulting in the eastward shift of blocks 1 and 2 relative to the rest of Alaska and Canada. Movement occurred along the Kaltag fault and a northeastern spur which developed across the Tintina fault. The spur, lying north of and parallel to the Porcupine River, offsets the Kobuk-Tintina system and dies out in the bend of the British-Richardson mountains. This last stage of major transcurrent movement formed the S-shaped bend of the Ogilvie orocline. Compres-

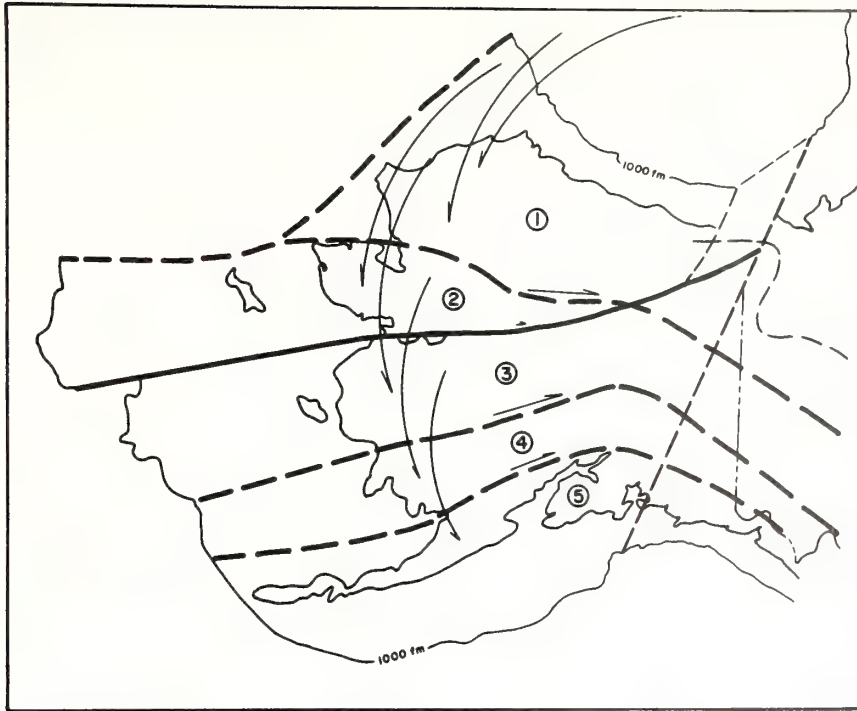


Fig. 5. Post-Laramide stage prior to final movement along Kaltag-Porcupine fault. Arrows indicate rotational and dextral strikeslip movement since the time of Fig. 4. Blocks 3, 4, and 5 are in their present positions. Folding in the Brooks Range and the Canadian cordillera is mostly completed at this time. The final movement between this stage and the present (Fig. 1) is along the Kaltag fault and its newly-developed Porcupine extension to the north-east (heavy solid line between blocks 2 and 3). Blocks 1 and 2, pushed between North America and Siberia, moved eastward relative to block 3 and completed formation of the Ogilvie orocline (light dashed line).

sion in the Koyukuk and Kuskokwim basins of blocks 2 and 3 (Fig. 1) was probably also related to the push against Siberia. The western ends of the subaerially exposed portions of the Kaltag and Denali faults were shifted to the south by compression and a left-lateral fault connecting the two basins.

TIMING OF EVENTS

The timing of the movements proposed here can only be approximated. While our maps have been drawn on a continuous-motion basis, the movements could have occurred in pulses, possibly coinciding with the major Alaskan plutonic episodes. Most plutonic rocks in Alaska are Mesozoic in age, although there are occasional small Paleozoic plutons and many small, widely scattered Tertiary plutons (King, 1969). In the central and southern Alaska Range (located in the central part of block 4 and extending southwestward into block 5), no plutonic bodies older than Jurassic have been found (Reed and

Lanphere, 1970). The three major plutonic episodes there are Early Jurassic (180–155 m.y.B.P.), Late Cretaceous to middle Tertiary (85–41 m.y.B.P.), and late Tertiary (30–25 m.y.B.P.). High sedimentation rates in the Alaskan peninsula area correspond closely to these times (Burk, 1965, p. 143). The first episode is possibly an early stage of the Nevadan orogeny. The start of the second episode roughly corresponds to the time of the initial opening of the North Atlantic north of the Azores triple junction (Pitman and Talwani, 1972). Possibly this caused a new subduction regime along the western margin of North America which triggered another plutonic episode.

Near the middle of the second episode, from 70 to 65 m.y.B.P., the Laramide orogenic movements started on the North American plate. Not yet deduced are the reasons why this tectonism occurred along the inland edge of the Mesozoic orogenic zone instead of along the continental margin. It is readily apparent that there is an abrupt change in the tectonic style of the two orogenic belts if one compares the folding and faulting of the Brooks Range and the Canadian Rocky Mountains with the intruded character of the more seaward Mesozoic orogenic belts. Thus, we have drawn blocks 2, 3 and 4 of more or less constant width while block 1 has been compressed and block 5 has been accreted to.

The late Tertiary plutonic episode (30–25 m.y.B.P.) possibly corresponds to the time of right lateral movement along the Kaltag–Porcupine fault and left lateral movement between the Koyukuk and Kuskokwim basins. The Kaltag–Porcupine movement, at least, must be post-Laramide as it offsets Laramide-age folds.

In northwestern Alaska a somewhat different timing sequence has been proposed based on studies in the western Brooks Range and the DeLong Mountains (Martin, 1970). Here the main periods of movement are Late Jurassic to Early Cretaceous, mid-Cretaceous, and Late Cretaceous to early Tertiary (Laramide).

On St. Lawrence Island six major plutonic bodies which intrude folded but unmetamorphosed Paleozoic and Mesozoic sediments and volcanics have been dated as mid-Cretaceous (100 m.y.B.P.) (Patton and Miller, 1971).

Since we tie the rotation of Alaska directly to the opening of the Arctic Ocean, alternative timing sequences based on the Arctic Ocean chronology are possibly preferable. Vogt and Ostenso (1970) proposed initial opening along the Alpha Cordillera starting at 60 m.y.B.P., switching to spreading along the Nansen Ridge at 40 m.y.B.P. Pitman and Talwani (1972), from their study of opening in the North Atlantic, propose opening times of 81–63 m.y.B.P. and 63–0 m.y.B.P. for the Alpha Cordillera and Nansen ridges, respectively. The Vogt timing sequence allows part of the Laramide folding to occur before the formation of the Alaskan orocline while the tectonic trends were still straight. None of the earlier Mesozoic tectonism in Alaska need be related to rotation of the blocks; similar geology exists to the southeast in Canada.

Recent tectonic movements include additional transcurrent motion in southeastern Alaska along the Fairweather (Page, 1969) and other faults and along parts of the Denali system (Page and Lahr, 1971). The former are in response to northwestward motion of the Pacific plate (Morgan, 1972, Jackson et al., 1972). We believe central Alaskan (Denali) faulting is due to adjustments within the continental block to subduction-related compression.

sion; seismic evidence indicates the subduction zone remains at the continental margin in the Gulf of Alaska (Anon., 1970). The former subduction zone along the western continental margin in the Bering Sea has shifted southward to the Aleutian trench, forming the Aleutian arc starting in the Tertiary (Burk, 1965, p. 155).

SUMMARY

Alaska and western Canada are Paleozoic and Mesozoic belts of continental-margin accretion along the North American–Pacific plate boundary. Transcurrent movement of elongate continental slabs parallel to the plate boundary seems to have occurred during subduction-related orogenesis, indicating oblique relative motion between the plates. The Arctic Ocean is assumed to have closed partly by Alaska occupying the southern part of the Canada Basin. The remaining area was occupied by northeastern Siberia. This would eliminate the need for a “Sinus Borealis”, or paleo-Arctic Ocean, in the reconstruction of Pangaea. Rotation of the Alaskan ends of the continental slabs was caused by drift of northeastern Siberia, opening the Arctic Ocean, and concurrent spreading in the southern Canada Basin. Reactivation of transcurrent faults allowed the slabs to move past one another during bending, with little internal deformation. Upon reaching nearly their present positions, additional compression between North America and Siberia caused renewed transcurrent movement of the northern Alaska blocks, forming the Ogilvie orocline. Recent tectonic activity is related to the subduction of the Pacific plate along the southern Alaska continental margin and related adjustments within the continental blocks.

REFERENCES

- Anon., 1970. *World Seismicity 1961–1969*. N.O.A.A., N.E.I.C., Chart 3005, Washington, D.C.
- Anon., 1972. Old North Pacific Trench. *Nature*, 236: 261–262.
- Bassinger, B.G., 1968. Marine magnetic study in the northeast Chukchi Sea. *J. Geophys. Res.*, 73: 683–687.
- Brosge, W.P., 1970. Paleozoic of northern and central Alaska. *Bull. Am. Assoc. Pet. Geol.*, 54: 2473 (abstract).
- Burk, C.A., 1965. Geology of the Alaska peninsula-island arc and continental margin. *Geol. Soc. Am. Mem.* 99: 250 pp.
- Carey, S.W., 1958. A tectonic approach to continental drift. In: S.W. Carey (Convenor), *Continental Drift, A Symposium*. Univ. Tasmania, pp. 177–355.
- Churkin, Jr., M., 1969. Paleozoic tectonic history of the Arctic Basin north of Alaska. *Science*, 165: 549–555.
- Churkin, Jr., M., 1970. Paleozoic and Precambrian rocks of Alaska and their role in its structural evolution. *Open File Rep. No. 448, U.S. Geol. Surv.*, Menlo Park, Calif., 131 pp.
- Detterman, R.L., 1970. Mesozoic sequence in Arctic Alaska. *Bull. Am. Assoc. Pet. Geol.*, 54: 2477.
- Forbes, R.B., Hamilton, T., TAILLEUR, I., MILLER, T.P., and PATTON, W.W., 1971. Tectonic implications of blueschist facies metamorphic terraces in Alaska. *Nature*, 234: 106–108.
- Freeland, G.L. and Dietz, R.S., 1972. Geotectonic reconstruction of the Arctic Ocean. *Trans. Am. Geophys. Union*, 53 (11): 1122 (abstract).
- Grantz, A., 1966. Strike-slip faults in Alaska. *Open File Rep. No. 267, U.S. Geol. Surv.*, Menlo Park, Calif., 82 pp.

- Hall, J.K., 1970. Geophysical evidence for ancient sea-floor spreading from Alpha Cordillera and Mendeleev Ridge. *Bull. Am. Assoc. Pet. Geol.*, 54: 2483 (abstract).
- Hayes, D.E. and Pitman, III, W.C., 1970. In: J. D. Hays (Editor), *Geological Investigations of the North Pacific*. *Geol. Soc. Am. Mem.* 126: 291–314.
- Jackson, E.D., Silver, E.A. and Dalrymple, G.B., 1972. Hawaiian-Emperor chain and its relation to Cenozoic circum-Pacific tectonics. *Geol. Soc. Am. Bull.*, 83: 601–618.
- Jones, D.L., 1971. In: *U.S. Geol. Surv., Prof. Pap.* 750-A, p. A54.
- Jones, D.L., Irwin, W.P. and Owenshine, A.T., 1972. Southeastern Alaska – a displaced continental fragment? *U.S. Geol. Surv., Prof. Pap.* 800-B: B213–B219.
- King, P.B., 1969. Tectonic map of North America, 1 : 5,000,000. *U.S. Geol. Surv., Prof. Pap.* 628: 94 pp. (text).
- Lathram, E.H., 1972. Nimbus IV view of the major structural features of Alaska. *Science*, 175: 1423–1427.
- Martin, A.J., 1970. Structure and tectonic history of the western Brooks Range, DeLong Mountains, and Lisburne Hills, northern Alaska. *Geol. Soc. Am. Bull.*, 81: 3605–3622.
- Moore, J., 1972. Uplifted trench sediments: southwestern Alaska–Bering shelf edge. *Science*, 175: 1103–1105.
- Morgan, W.J., 1972. Deep mantle convection plumes and plate motions. *Bull. Am. Assoc. Pet. Geol.*, 56: 203–213.
- Ostenso, N.A. and Parks, Jr., P.E., 1964. Seaborne magnetic measurements in the Chukchi Sea. *Geophys. Polar Res. Cent., Dep. Geol., Univ. Wis. Res. Rep.*, 64–5.
- Packer, D.R. and Stone, D.B., 1972. An Alaskan Jurassic palaeomagnetic pole and the Alaskan orocline. *Nature (Phys. Sci.)*, 237: 25–26.
- Page, R., 1969. Late Cenozoic movement on the Fairweather fault in southeastern Alaska. *Geol. Soc. Am. Bull.*, 80: 1873–1878.
- Page, R. and Lahr, J., 1971. Measurements for fault slip on the Denali, Fairweather, and Castle Mountain faults, Alaska. *J. Geophys. Res.*, 76: 8534–8543.
- Patton, Jr., W.W. and Miller, T.P., 1971. In: *U.S. Geol. Surv., Prof. Pap.* 750A: A51–A52.
- Pitman, III, W.C. and Talwani, M., 1972. Sea-floor spreading in the North Atlantic. *Geol. Soc. Am. Bull.*, 83: 619–646.
- Reed, B.L. and Lanphere, M.A., 1970. Plutonic belts of central and southern Alaska range and Alaska peninsula. *Bull. Am. Assoc. Pet. Geol.*, 54: 2502 (abstract).
- Sainsbury, C.L., Hedge, C.E. and Bunker, C.M., 1970. Structure, stratigraphy, and isotopic composition of rocks of Seward peninsula, Alaska. *Bull. Am. Assoc. Pet. Geol.*, 54: 2502 (abstract).
- Tailleur, I. L., 1969. Speculations on North Slope geology. *Oil Gas J.*, 9/22: 215–226; 9/29: 128–130.
- Tailleur, I. L., 1970a. Probable rift origin of Canada Basin, Arctic Ocean. *Bull. Am. Assoc. Pet. Geol.*, 54: 2508 (abstract).
- Tailleur, I.L., 1970b. Structure and stratigraphy of western Arctic Alaska. *Bull. Am. Assoc. Pet. Geol.*, 54: 2508 (abstract).
- Tailleur, I.L. and Brosge, W.P., 1970. Tectonic history of northern Alaska. In: *Proceedings of the Geological Seminar on the North Slope of Alaska, Pacific Section, Am. Assoc. Pet. Geol.*, E1–E20.
- Vogt, P.R. and Ostenso, N.A., 1970. Magnetic and gravity profiles across the Alpha Cordillera and their relation to Arctic sea-floor spreading. *J. Geophys. Res.*, 75: 4925–4937.

Marine Geophysical Study off Western India

R. N. HARBISON AND B. G. BASSINGER

*National Oceanic and Atmospheric Administration
Atlantic Oceanographic and Meteorological Laboratories
Miami, Florida 33149*

Seismic reflection and total magnetic field intensity observations were made off the western coast of India as part of the 1967 global scientific expedition of the USS *Oceanographer*. Linear fault block fragments appear to form the base of the northern segment of the platform that comprises the Laccadive-Maldives-Chagos trend. The NW continuation of these linear fault block fragments creates a basement ridge that extends to at least 20°N and is interpreted to be the NW continuation of the main Laccadive structural trend. This basement ridge may be a relict margin of the Indian continent. No obvious magnetic lineations were found in the study area. Short-wavelength variations of the magnetic field along the Laccadive trend suggest a relatively shallow source. Long-wavelength high-amplitude magnetic anomalies suggest the presence of a broad ridge composed of relatively high magnetic material near the western shelf edge of the Indian peninsula.

Seismic reflection, magnetic, and bathymetric observations were made off western India as part of the 1967 global expedition conducted from the USS *Oceanographer* (Figure 1). The reconnaissance study was designed to investigate structural characteristics of the Maldives-Laccadive platform and its relationship to the Indian continent. A proton precession magnetometer was used to measure the total magnetic field intensity along all the ship's tracks. On all east-west traverses, seismic reflection profiles were made utilizing a 10-in.³ air gun as a sound source. A narrow-beam echo sounder was used for bathymetry, and position was determined mainly by the satellite navigation system.

In this article, basement means acoustical basement, or those rocks that give a comparatively strong reflected return but that cannot be penetrated by the seismic technique used.

GENERAL GEOLOGY AND INTERPRETATIONS

The Laccadive and Maldives islands, along with the Chagos Archipelago, form a common ridge that is partly outlined by the 1830- and 3660-meter contours (Figure 2). Coral atolls and banks form the islands on this ridge; no outcrops of other rock types have been reported [Wilson, 1963].

Davis [1928] interpreted the Maldives Islands to have a foundation of a double-crested mass formed by a pair of long narrow fault block fragments. He assumed that subsidence of these fault blocks, formerly part of the Indian continent, caused drowning of the coral at lower levels and growth of new reefs at the crest of the blocks to form the Maldives Islands.

The Indian craton is considered to have extended further west, but has been partially faulted down into the Arabian Sea [Davis, 1928; Krishnan, 1968; Pepper and Everhardt, 1963; Harbison and Bassinger, 1970].

More recently, with the advent of the theories of sea floor spreading and plate tectonics, many authors have postulated that India has moved to the north. Dietz and Holden [1970] have theorized that the Indian plate moved north, bordered on the west by a large shear zone along the Chagos-Maldives-Laccadive trend. They suggest the presence, at latitude 7°S and longitude 72°E, of a mantle thermal center that poured out basalt as the Indian plate moved north, forming the Chagos-Laccadive platform. Fisher *et al.* [1971] interpret the Chagos-Laccadive platform to be a former large fracture zone, the Indian plate moving toward the north adjacent to it.

On the basis of continental geology, Meyerhoff and Meyerhoff [1972] interpret India as having been part of Asia since Proterozoic.

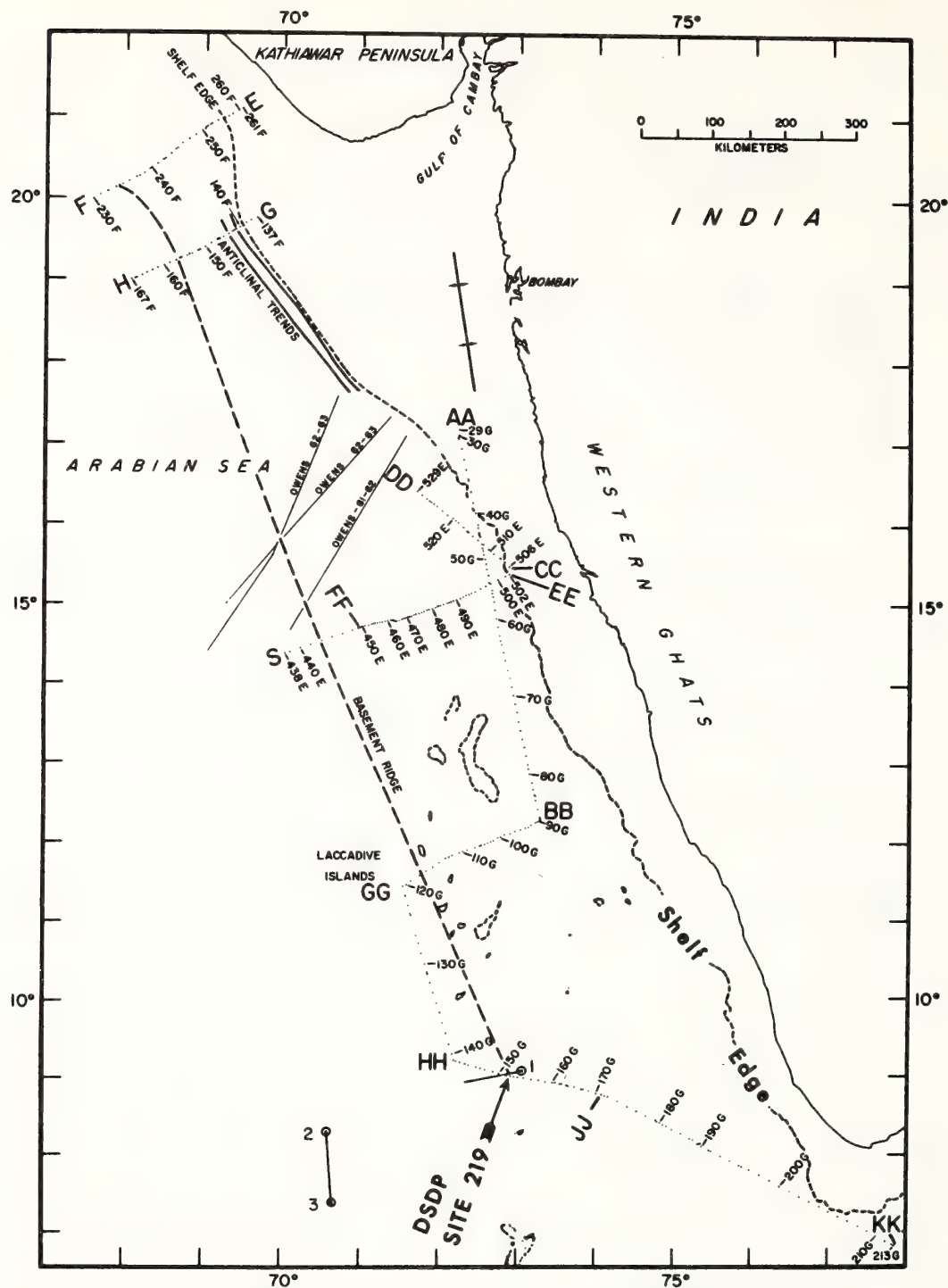


Fig. 1. Track line chart of survey area and location of refraction stations 1, 2, and 3 from Francis and Shor [1966] and track lines of HMS Owen [London Hydrographic Department, 1963, 1966].

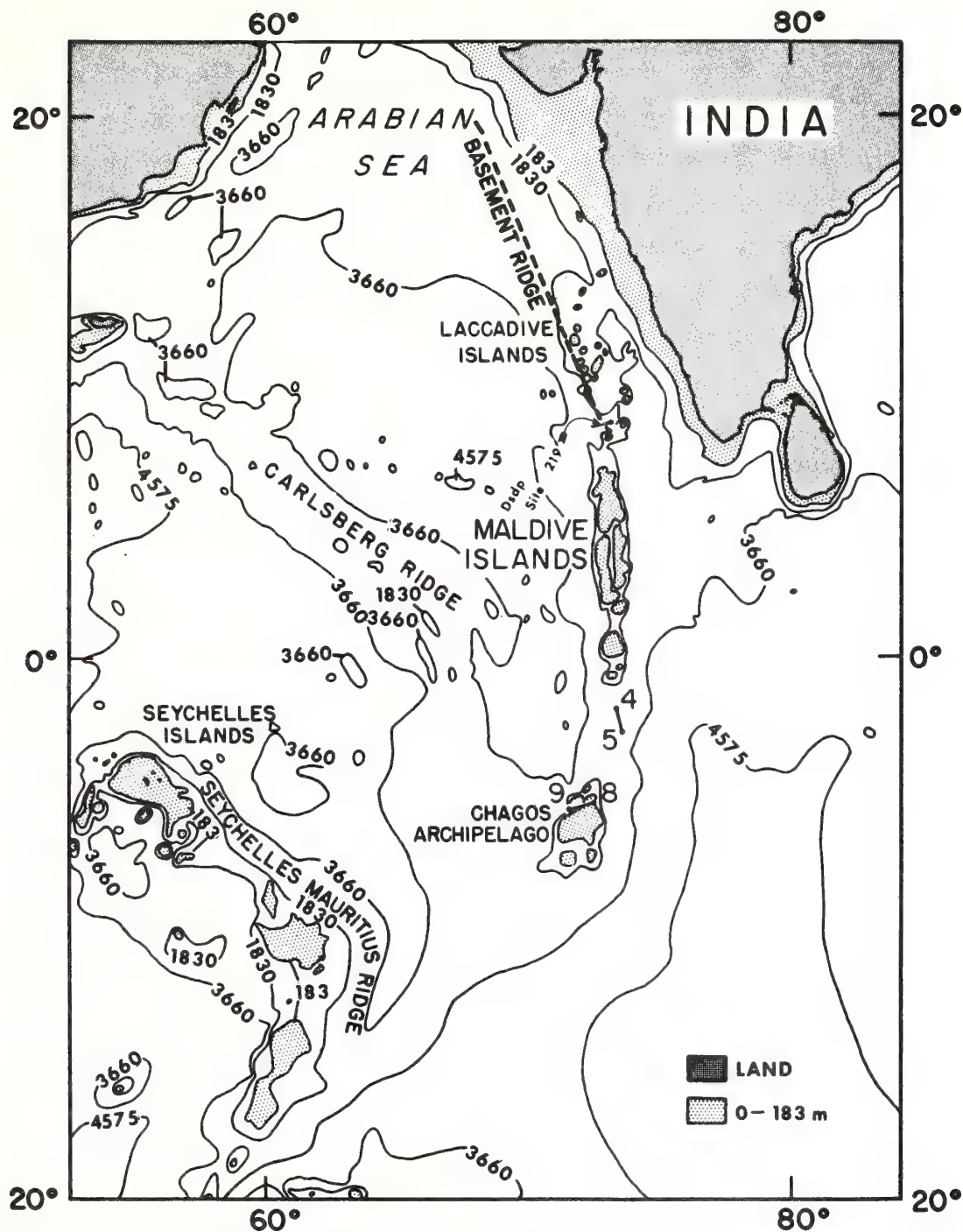


Fig. 2. Regional map of NW Indian Ocean showing location of refraction stations 1, 4, 5, 8, and 9 from Francis and Shor [1966]. Bathymetry and land forms based on chart I-380, U.S. Department of Interior.



INTERPRETATION OF SEISMIC REFLECTION PROFILES

In Figure 3, the broad bathymetric and structural features between 102G and 120G on profile *GG-BB* are strikingly similar to those present between 149G and 169G on profile *HH-JJ* and have been aligned to show this correlation. This alignment indicates a major north-west structural trend between the Laccadive and Maldivé islands. A prominent basement high near the western ends of profiles *GG-BB* and *HH-JJ* (Figures 3 and 4) appears to be the result of major faulting.

Deep Sea Drilling Project (DSDP), leg 23, drilled to 411 meters at site 219, near (within 1 km) profile *HH-JJ* (Figures 1, 3, and 4). According to the *Scientific Staff* [1972], there is 219 meters of pelagic nannofossil ooze and chalk (Pleistocene to middle Eocene). This sequence is probably represented by the acoustically transparent layer near the sea floor (Figure 4). In addition, these scientists reported that an 89-meter sequence of semilithified chalk, limestone, and chert (middle Eocene to middle Paleocene) is underlain by 103 meters of terrigenous glauconitic calcareous sandstone and

siltstone (early Paleocene). Part of the 89-meter sequence of limestone and chert may be represented on the seismic profile by the first stratified sequence beneath the acoustically transparent layer at DSDP site 219, assuming a velocity of 2 km/sec (Figures 3 and 4). Because of velocity uncertainties and because the exact location of the DSDP site 219 cannot be determined within less than 1 km on the reflection profile (Figure 4), the terrigenous glauconitic sandstone cannot be identified, but it probably lies close to the acoustic basement. The deepest reflector reported for DSDP site 219 was chert, and the site survey indicated normal north-south faults were active after middle Eocene.

Structural features from profile *GG-BB* northward to profile *FF-EE* cannot be easily correlated on the basis of seismic data alone. In the area of this last profile, the sea floor is much deeper, perhaps as a result of rapid subsidence of the sea floor, which terminated the main northwestward extension of the reef growth of the Laccadive Islands.

Three small structural highs (Figure 3) between 480E and 490E, profile *FF-EE*, may correlate with three similar highs between 521E

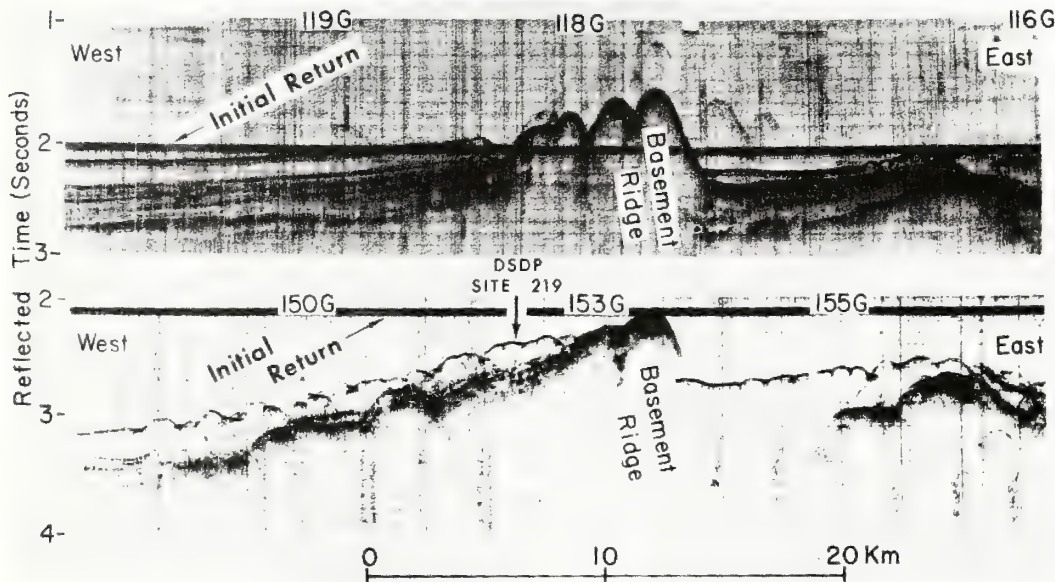


Fig. 4. Photographs of seismic reflection profiles showing basement ridge on seismic profile *GG-BB* (top) and *HH-JJ* (bottom). See Figure 1 for location. 'Initial return' refers to dark horizontal line caused by the arrival of the outgoing signal through the water to the hydrophone.

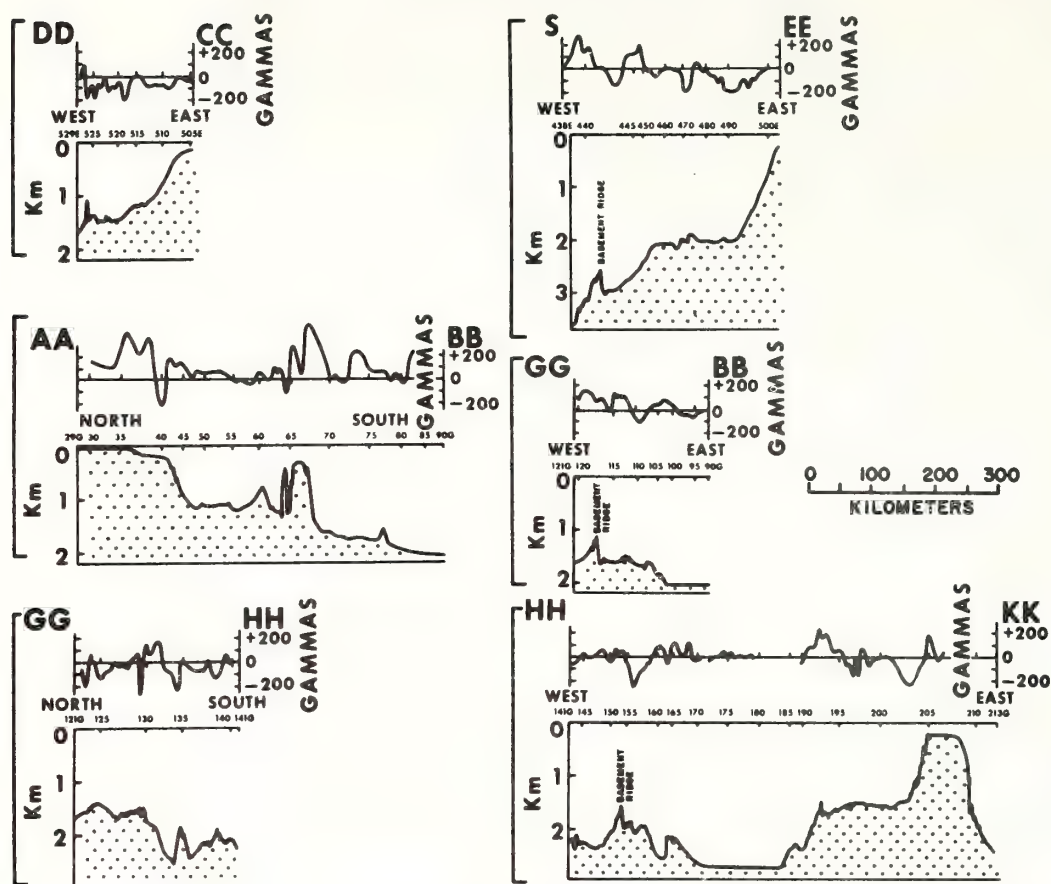


Fig. 5. Bathymetric and residual magnetic profiles (regional magnetic gradient removed by inspection). For location see Figure 1.

and 528E, profile DD-CC (Figure 3), suggesting possible secondary trends aligned in a northerly direction. This northerly trend is weak and does not support postulations by *Krishnan* [1968] that the Laccadive structural trend continues through the Gulf of Cambay into the Indian continent.

MAGNETIC AND BATHYMETRIC PROFILES

Residual magnetic profiles are shown, along with bathymetric profiles in Figure 5. No significant magnetic trend can be found along the Laccadive-Maldives area. Generally, the short-wavelength variations of the magnetic field near the structural high within the Laccadive trend (profile GG-BB) suggest that the magnetic source may be near the surface. These short-wavelength variations grade into higher-

amplitude longer-wavelength anomalies to the north and east.

A broad regional slope of the sea floor to the east, similar to that of peninsular India, is present between 152G and 170G, profile HH-KK (Figure 5). A shallow plateau between 205G and 208G and a deeper plateau between 193G and 204G dip toward the east approximately $0^{\circ}5'$ as measured on the relatively flat undisturbed parts of the sea floor. These tilted plateaus are similar to the eastward-tilting fault blocks postulated by *Davis* [1928] to be present along the SE coast of India near the Maldives Islands.

Profile AA-BB, subparallel to the coast, shows rather long wavelength, high-amplitude magnetic anomalies near the shelf edge (35G-40G, Figure 5). A similar magnetic anomaly near a

flat-topped bathymetric high (65G-67G) may be an anomalous westward extension of the Indian shelf. Also a magnetic anomaly of comparable magnitude is present along the west Indian coast at 13°N latitude [Narain *et al.*, 1968]. These anomalies suggest the existence of a broad ridge composed of material of relatively high magnetization near the shelf edge and parallel to it.

A terrace between 455E and 493E, profile S-EE, has a topographic expression similar to the terrace previously discussed between 193G and 204G, profile HH-KK, although the latter is approximately 0.5 km shallower. Magnetic lows on the eastern margin and in the center are common to both terraces. Topographically, these terraces resemble the Blake Plateau [Sheridan, 1969, Figure 1] and, like the Blake Plateau, appear to be portions of a subsiding continental margin.

BASEMENT RIDGE

What is believed to be a continuous NW-SE-trending basement ridge (Figure 1) can be traced from seismic reflection profile HH-JJ to profile GG-BB (Figures 3 and 4), and (on the basis of bathymetric information) along a straight line projection northwestward to profile S-EE (Figure 5). Further to the NW, the ridge can be recognized by bathymetric profiles from the HMS *Owen* [London Hydrographic Department, 1963, 1966] and in seismic reflection profiles F-E and H-G (Figures 1 and 3). In the latter profiles, the ridge is predominantly a subsurface feature. A more westerly trend of the basement ridge between profiles F-E and H-G may be due to intersection of major SW- and NW-trending faults [Harbison and Bassinger, 1970].

To the south, the basement ridge is apparently composed of elongated fault block fragments, which appear as fault scarps in the western part of profiles HH-JJ and GG-BB (Figures 3 and 4). The ridge here is apparently composed of 3.85-km/sec rock about 1.5 km thick near 153G, profile HH-GG, as revealed by a refraction profile shot from station 1 (Figure 2) [Francis and Shor, 1966]. Francis and Shor, on the basis of comparison with areas in the Pacific, suggest that this 3.85 rock may be vesicular basalt. This velocity range, however, includes many lithologic types, including car-

bonates. Since the basement ridge is apparently a fault block and has subsided, it is likely that at least part of this 3.85-km/sec zone may be reef material. This interpretation is based on the presence of reefs growing to the north and south on the same structural trend and on a comparison with a similar geological setting of the Blake-Bahama area which has limestones with comparable velocities of 3.8 to 4.8 km/sec in an area of known subsidence [Sheridan *et al.*, 1966; Sheridan, 1969]. Since the basement ridge in Figures 1 and 2 is primarily a structural feature, the lithology may vary to the north and south of profile HH-KK.

COMPARISON OF THE LACCADIVE PLATFORM-BASEMENT RIDGE OFF INDIA WITH NORTH BRAZILIAN RIDGE

Along the continental margin of northern Brazil, a basement ridge was found by reconnaissance geological and geophysical methods [Hayes and Ewing, 1970]. There is an unusual similarity between the Laccadive platform-basement ridge off India and this North Brazilian ridge. They are both approximately parallel to the continental margin and about the same distance offshore. Both are associated with magnetic anomalies of comparable magnitude with randomly varying signatures. In most places the North Brazilian ridge is in deeper water and is greater in topographic relief than the Laccadive platform-basement ridge complex, but their morphological expression is similar, including a double ridge in some places. Since middle Miocene to late Eocene, the North Brazilian ridge has apparently subsided about 2 km at the locality of the Joides site 25-25A. Here, beneath a shallow acoustically transparent layer, sonobuoy reflection-refraction data indicate the presence of a 2-km-thick layer with a velocity of 3.8 km/sec apparently overlying 4.8-km/sec material [Hayes and Ewing, 1970]. These layers are comparable in depth, thickness, and velocity to those across the basement ridge which the authors of this paper consider to be part of the Laccadive structural platform [Francis and Shor, 1966, refraction station 1, Figure 2]. Like the North Brazilian ridge, the basement ridge at the DSDP site 219 (Figures 1, 3, and 4) has subsided about 2 km, mostly in late Paleocene to early Eocene, as indicated by faunal

and lithologic evidence [*Scientific Staff*, 1972].

Investigations of the Brazilian ridge suggest that it is not a fracture zone. The Laccadive platform and its structural continuation to the north as a basement ridge, like the Brazilian ridge, is not interpreted to be a fracture zone (in the sense that a fracture zone is either a transform or a transcurrent fault). This interpretation is preferred because of normal faulting within the sediment column on seismic sections. Also, continuing reef development on the Laccadive-Maldives platform is a monument to subsidence within an area where the climate has been favorable for coral growth since late Paleocene to early Eocene. Further evidence is the presence of the 17-km-deep Mohorovicic discontinuity near 9°N latitude along the basement ridge, where refraction profile 1 and DSDP site 219 are located, suggesting that the crust here is transitional and may be a remnant of the Indian continental shelf.

Hayes and Ewing interpret the North Brazilian ridge to be formed by volcanism shortly after separation of Africa and South America. However, the basement ridge off India is interpreted to be a downfaulted part of the Indian continental margin.

RELATIONSHIP OF TECTONIC TRENDS

Alignment, physiographic similarities, and correlated seismic reflection profiles previously discussed link the platform created by the Chagos, Maldives, and Laccadives with the basement ridge to form a large arcuate structural feature (Feature 2). The basement ridge is interpreted to be the main northwestern extension of the Laccadive platform. On the basis mostly of refraction information, *Narain et al.* [1968] prefer a northwestern extension of the Chagos-Maldives-Laccadive trend along the shelf break of western India and Pakistan instead of the more easterly trend through the Gulf of Cambay as proposed by *Krishnan* [1968]. Their northwestern extension is east of the basement ridge and appears to be associated with the anticlinal trends along the shelf break off Bombay [*Harbison and Bassinger*, 1970]. These anticlinal trends were interpreted to be formed by block faulting and may be part of a structural zone that includes the elongated fault block fragments that form the basement ridge.

SUMMARY

The Chagos-Maldives-Laccadive platform is interpreted to continue structurally to the NW as a basement ridge to the northern limits of the study area near 20°N latitude. This basement ridge is interpreted to be composed of linear fault blocks. Between the Maldives and Laccadive platforms the basement ridge has subsided at least 2 km as indicated by information from DSDP site 219 information and at this same point, the Mohorovicic discontinuity is 17 km deep. The basement ridge is interpreted to be a relict fragment of the Indian continent.

Refraction profiles across the central and southern areas of the arcuate Chagos-Maldives-Laccadive basement ridge feature suggest that it is underlain by transitional oceanic-continental crust. The Seychelles-Mauritius ridge is comprised of partly continental crust. As a median ridge, the Carlsberg ridge appears to be structurally interrelated to these partly continental masses that it separates. The true nature of this interrelationship is difficult to explain with the data presently available. Fisher et al., with data south of 0°30'N latitude in the northwestern Indian Ocean, interpret a structural relationship in their study area according to the plate tectonics theory.

No obvious magnetic lineations were detected in the study area. Long-wavelength, high-amplitude magnetic anomalies suggest the existence of a broad, deep-seated ridge composed of material with a relatively high magnetization characteristic near the western shelf edge of the Indian peninsula.

Acknowledgments. The authors wish to thank the officers and crew of the USS *Oceanographer* and Dr. Robert Burns of the Pacific Oceanographic Laboratory. The cartographic assistance of Sue O'Brien, George Merrill, and Christopher Widaski is also gratefully acknowledged. Review of this manuscript by L. Butler, G. Keller, R. Lattimore, and G. Peter is greatly appreciated.

REFERENCES

- Davies, D., and T. J. G. Francis, The crustal structure of the Seychelles bank, *Deep-Sea Res.*, 11, 921-927, 1964.
- Davis, M. D., The coral reef problem, *Spec. Publ.* 9, pp. 524-534, American Geographical Society, New York, 1928.
- Dietz, R. S., and J. C. Holden, Reconstruction of Pangea: Breakup and dispersion of continents,

- Permian to present, *J. Geophys. Res.*, **75**, 4939-4966, 1970.
- Fisher, R. L., J. G. Sclater, and D. P. McKenzie, Evolution of the Central Indian Ridge, Western Indian Ocean, *Bull. Geol. Soc. Amer.*, **82**, 553-562, 1971.
- Francis, T. J. G., and G. G. Shor, Jr., Seismic refraction measurements in the northwest Indian Ocean, *J. Geophys. Res.*, **71**, 427-449, 1966.
- Harbison, R., and B. Bassinger, Seismic reflection and magnetic study off Bombay, India, *Geophysics*, **35**, 603-612, 1970.
- Hayes, D. E., and M. Ewing, North Brazilian ridge and margin, *Bull. Amer. Assoc. Petrol. Geol.*, **54**, 2120-2150, 1970.
- Krishnan, M. S., *Geology of India and Burma*, 5th ed., 536 pp., Higginbothams, Madras, 1968.
- London Hydrographic Department, Bathymetric, magnetic and gravity investigations, HMS *Owen*, 1961-1962, International Indian Ocean Expeditions, *Admiralty Marine Sci. Publ.* **4**, part 1, 19 pp., 1963.
- London Hydrographic Department, Bathymetric, magnetic and gravity investigations, HMS *Owen*, 1962-1963, International Indian Ocean Expedition, *Admiralty Marine Sci. Publ.* **9**, part 1, 26 pp., 1966.
- Meyerhoff, A. A., and H. A. Meyerhoff, The new global tectonics: Major inconsistencies, *Bull. Amer. Assoc. Petrol. Geol.*, **56**, 269-336, 1972.
- Narain, H., K. L. Kaila, and R. K. Verma, Continental margin of India, *Can. J. Earth Sci.*, **5**, 1051-1065, 1968.
- Pepper, J. F., and G. M. Everhart, The Indian Ocean: The geology of its bordering lands and the configuration of its floor, *Misc. Geol. Invest.* **1**, p. 380, U.S. Dep. of Interior, Washington, D.C., 1963.
- Scientific Staff, Deep Sea Drilling Project: Leg 23, *Geotimes*, **17**(7), 22-26, 1972.
- Sheridan, R. E., Subsidence of continental margins, *Tectonophysics*, **7**, 219-229, 1969.
- Sheridan, R. E., C. L. Drake, J. E. Nafe, and J. Hennion, Seismic refraction study of continental margin of Florida, *Bull. Amer. Assoc. Petrol. Geol.*, **50**, 1972-1991, 1966.
- Wilson, J. T., A résumé of the geology of islands in the main ocean basin, Atlantic and Indian oceans, *Sci. Rep.* **4**, vol. 1, chap. 3, pp. 50-75, Univ. of Toronto, Toronto, Ont., Canada, 1963.

(Received January 31, 1972;
revised October 6, 1972.)

STRUCTURAL LINEATIONS IN THE CANARY BASIN, EASTERN CENTRAL NORTH ATLANTIC

R. N. HARBISON, R. K. LATTIMORE and PETER A. RONA

National Oceanic and Atmospheric Administration, Atlantic Oceanographic and Meteorological Laboratories, Miami, Fla. (U.S.A.)

(Accepted for publication February 1, 1973)

ABSTRACT

Harbison, R. N., Lattimore, R. K. and Rona, P. A., 1973. Structural lineations in the Canary basin, eastern central North Atlantic. *Mar. Geol.*, 14: 269-275.

A corridor 315 km wide centered along the southeast projection of the Atlantis fracture zone between 21° W and 29° W was investigated with seismic reflection, bathymetric, gravity, and magnetic profiles. Six sub-parallel, sediment-filled troughs in acoustic basement trend about 106° across the abyssal hills and lower continental rise off northwest Africa. Where the southernmost structural lineations cross the abyssal plain, they are interrupted by a ridge trending 080° surmounted by volcanic peaks.

The structural lineations become less distinct landward of the western margin of the abyssal plain coincident with a decrease in topographic relief on acoustic basement and increasing sediment thickness. This transition is coincident with a reduction in the amplitude of gravity and magnetic anomalies.

INTRODUCTION

The N.O.A.A. "Discoverer" conducted a marine geophysical investigation in 1970 to delineate primarily the major east-west oriented structural trends across the basin between the abyssal hills and the lower continental rise (Fig.1). Narrow-beam bathymetric, gravimetric, and magnetic measurements were recorded along ten lines oriented generally north-south in a zigzag pattern. Seismic reflection (40 in³ - 655 cm³ - air gun) and 3.5-kHz profiles were obtained on alternate lines. Primary position control was by satellite navigation.

Free-air gravity anomalies measure within 10 mgal of unpublished U.S. Navy gravity data in this area.

DESCRIPTION OF STRUCTURAL LINEATIONS

Primary evidence for the azimuths of trends were derived from geophysical profiles along the apices of the tracklines (Fig.1). Constrained by these azimuths, more distant

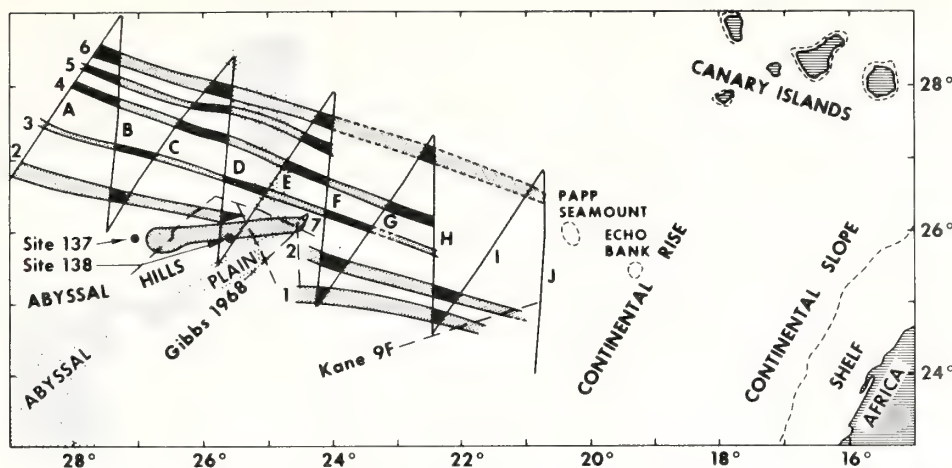


Fig.1. Map indexing ships tracks along profiles *A–J* across structural lineations *1–7*. Heavy lines along lineations *1–6* indicate zones with closer trackline control. Deep-Sea Drill sites 137 and 138 are shown.

and more tenuous correlations were made between adjacent apices. In the center of the tracklines, only the most distinct trends were picked, owing to the uncertainty caused by the greater average separation of tracklines. From 29°W to 24°W sediment-filled troughs were correlated between profiles on the basis of distinctive topography. The correlations become more tenuous where the sedimentary layer thickens beyond the penetration of our seismic system east of 24°W . The troughs in this eastern area were identified primarily by gentle synclinal trends within overlying strata and, to a lesser extent, from the regional free-air gravity and residual magnetic signature. Along the southeast margin of the study area, between 20°W and 22°W , Lowrie and Escowitz (1969) show as much as 2 km of sediments overlying basement.

Structural lineation *1* is a basement trough about 30 km wide which trends about 106° along the southern boundary of the area investigated (Fig.1, 2). Basement relief of about 0.5 km (0.5 sec) is associated with a broad, negative, free-air gravity anomaly, and a positive magnetic anomaly. This structural lineation is distinct in profiles *F* and *H* (Fig.2), where it appears as a broad, gentle syncline in stratified sediments. Lineation *1* extends eastward to the Kane profile 9F where it appears as a low in the acoustic basement beneath about 2 km of sediment.

Structural lineation *2* was traced from $26^{\circ}55'\text{N}$, $28^{\circ}50'\text{W}$ to $26^{\circ}10'\text{N}$, $25^{\circ}40'\text{W}$ as a southeast-trending trough 25 km in width bounded by basement highs (Fig.2; profiles *A*, *B*, *C*, *D*). The trough is filled with about 0.5 km (0.5 sec) of nearly horizontal sedimentary layers, unconformably overlying acoustically transparent sediment which mantles many of the adjacent basement highs. Structural lineation *2* is interrupted by a 080° -trending ridge at $25^{\circ}30'\text{W}$ but continues landward on profiles *F*, *G*, *H*, *I* and *J* (Fig.2), and also on the Kane profile 9F (Fig.1). A gravity minimum is associated with this structural lineation (Fig.2; profiles *B*, *C*, *D*, *F*).

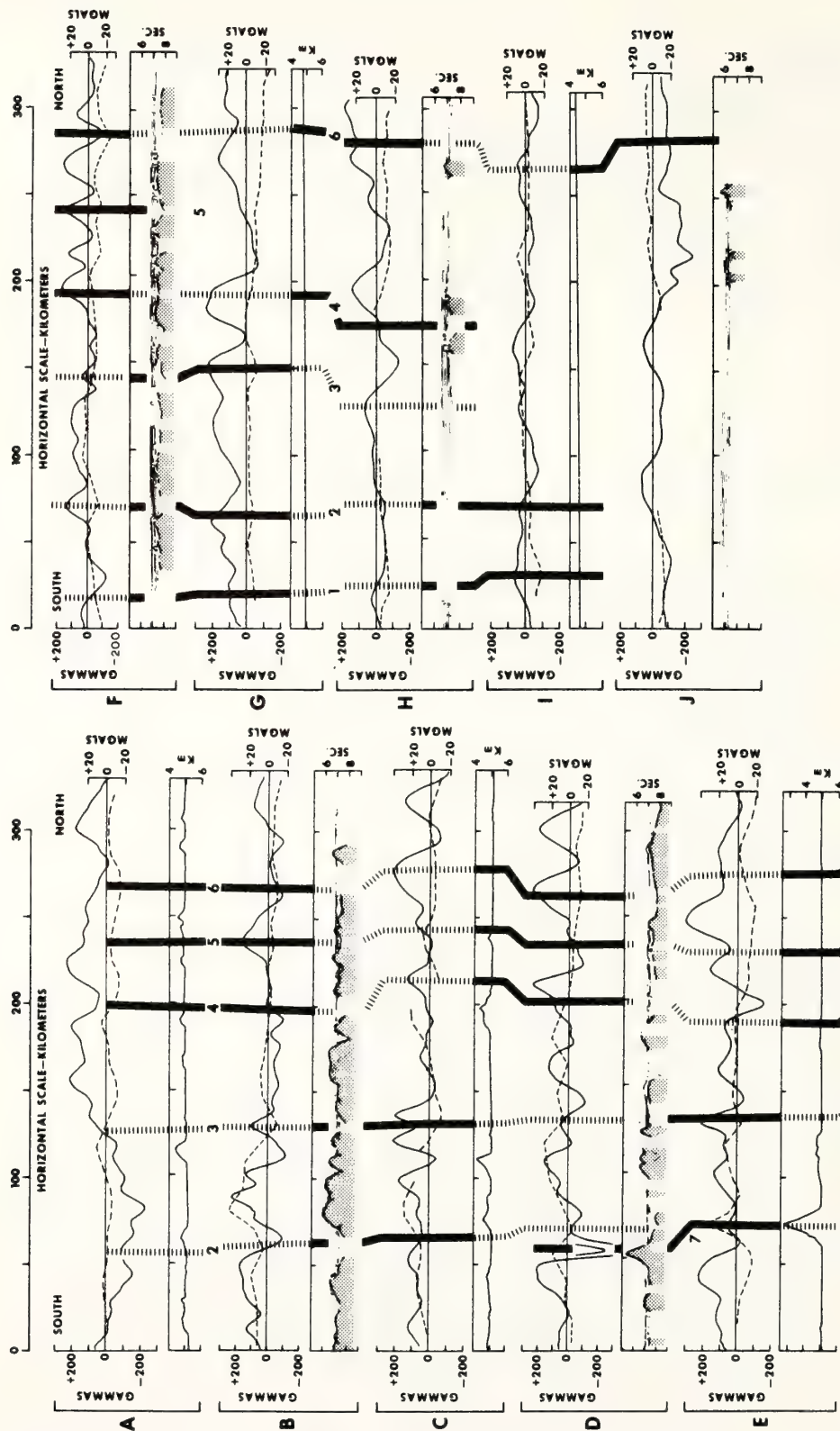


Fig. 2. Seismic reflection profiles *B*, *D*, *F*, *H* and *J* and narrow-beam bathymetric profiles *A*, *C*, *E*, *G* and *I* with concurrent free-air gravity (dashed curves) and residual magnetic (solid curves) profiles. Acoustic basement is shaded on the seismic reflection profiles. Heavy lines along lineations 1–6 indicate zones controlled by closer trackline spacing.

Structural lineation 3 is the most distinct trough in the study area. On profiles west of 24°W , lineation 3 appears as a half-graben tilted to the south (Fig.2, 3; profiles *B*, *D*, *F*). Overlying sedimentary layers thicken and dip southward. The dip increases with depth beneath the bottom suggesting a normal fault along the southern margin of the half-graben. On profiles east of 24°W the structural lineation is manifested as a gentle syncline in subbottom sedimentary layers (Fig.2; profile *H*). A pronounced minimum in the free-air gravity is associated with the axis of lineation 3 (Fig.2; profiles *B*, *C*, *D*, *E*). A free-air gravity anomaly ranging between +20 and +40 mgal is associated with a basement ridge along the southern boundary of lineation 3. A positive magnetic anomaly is associated with the axis of the trough of lineation 3 where it can most clearly be defined in seismic reflection profiles *B*, *D*, *F* and *H*.

Structural lineation 4 is a shallow trough filled with sediment in profiles *B*, *D* and *F* (Fig.2). The sedimentary layers are relatively flat in profiles *D* and *F*, although in profile *D* the flat strata appear to have been locally disrupted by what appear to be small intrusive bodies (Fig.3, 4).

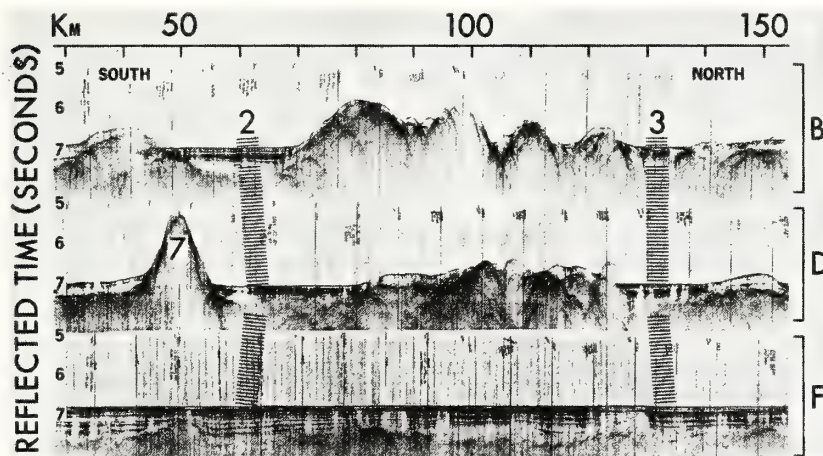


Fig.3. Photographs of eastern portions of seismic reflection profiles *B*, *D* and *F*.

Structural lineation 5 is a shallow, sediment-filled trough about 15 km wide, bounded by gentle basement highs. This trough can be followed landward to 24°W (Fig.2).

Structural lineation 6 is about 30 km wide (Fig.2; profiles *A–J*). A basement high along the southern margin of lineation 6 projects landward to include Papp seamount and Echo bank (Lowrie and Escowitz, 1969).

Structural lineation 7 is a topographic ridge rising from acoustic basement. The ridge is about 30 km wide and about 150 km long as delineated from this and previous work (Rona, 1971). This ridge trends 080° , oblique to all the other structural lineations described. It is surmounted by volcanic peaks which attain 2,500 m of relief at the intersection with structural lineation 2 (Fig.2; profiles *D*, *E*). Basalt encrusted with manganese was dredged from the ridge (Scott et al., 1972). The largest residual magnetic anomaly in the study area (–495 gammas) is associated with this ridge on profile *D* (Fig.2).

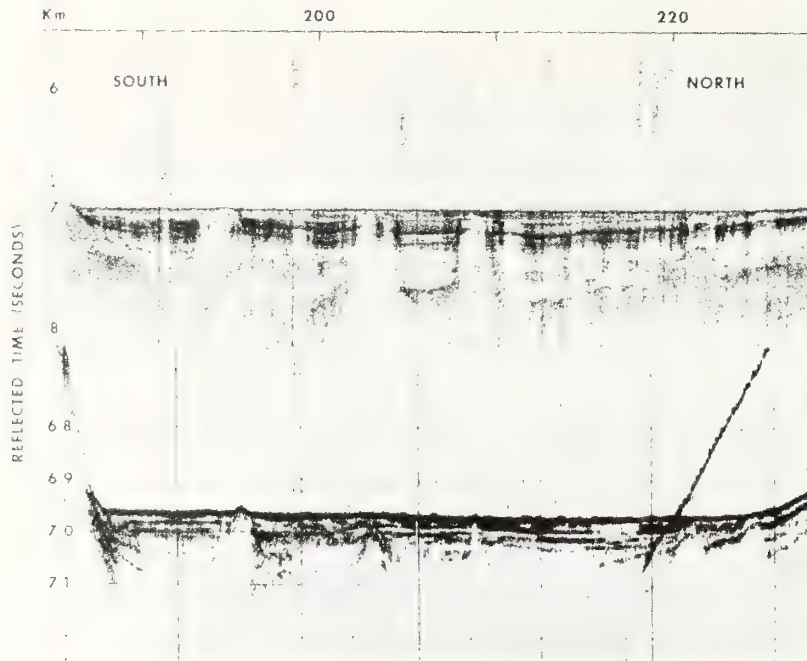


Fig.4. Seismic reflection (air gun) (upper profile) and 3.5 kHz (lower profile) records from profile *D* showing small intrusive bodies beneath the abyssal plain.

DISCUSSION

Consideration of the results of a detailed 18.5-km grid survey of a 185-km square area of the abyssal hills (Harbison and Rona, 1972), centered at $23^{\circ}30'N$ latitude, $31^{\circ}00'W$ longitude about 230 km south of profile *A* (Fig.1), is helpful interpreting structural trends within the reconnaissance area of the present investigation. Two intersecting linear topographic trends, each paralleled by a free-air gravity (-20 to $+20$ mgal) and residual magnetic (-50 to $+200$ gammas) anomalies were delineated in the detailed abyssal hills as follows: (1) elongate ridges and troughs trending 050° with an average topographic wavelength of 13 km and 0.6 km amplitude; (2) two fracture zones about 80 km apart trending 112° which resemble grabens about 10 km wide. The smaller of these fracture zones extends 165 km and the larger extends for more than 185 km to limits of the study area. A free-air gravity low and a positive magnetic anomaly are generally associated with the lows in acoustic basement fracture zones. The larger of these fracture zones appears as a half-graben tilted to the south with a ridge up to 1 km high and over 110 km long forming its south wall. This longer fracture zone also has a stronger positive magnetic anomaly than is present over the smaller fracture zone.

If trends similar to those in the detailed study are present 280 km to the northeast in the reconnaissance area, only the east-west lineations could be determined because of the configuration of tracklines.

In common with the fracture zones identified in the detailed study (Harbison and Rona, 1972), structural lineation 3 appears as a 10-km wide half graben tilted to the south, is generally associated with a free-air gravity minimum and a positive residual magnetic anomaly, and has a south footwall about 1 km high (Fig. 2, 3). According to Van Andel et al. (1971), major fracture zones of the Atlantic are characteristically graben-like and have transverse asymmetry and bordering ridges. Since structural lineation 3 has these characteristics and is also similar to the best developed fracture zone in the detailed study area, it is interpreted to be a fracture zone. As the best developed structural lineation in the reconnaissance area, lineation 3 may be the extension of one of the major fracture zones which transect the adjacent Mid-Atlantic Ridge. Utilizing the same criteria, lineation 2 also appears to be a fracture zone. Lineations 1, 4, 5 and 6 are not as well developed as lineations 2 and 3 and their nature is less clear.

Information obtained from the Deep-Sea Drilling Project at sites 137 and 138 Hayes et al. (1972) suggests that the acoustically transparent sediment penetrated in seismic reflection profiles *B*, *D*, and *F* (Fig. 2, 4) may be Upper Cretaceous marls, oozes, silty clays, shales, and mudstones overlain by Tertiary clays, silts, and sandstones; part of the Early to Middle Tertiary section is believed to be absent, which may account for the unconformity noted in the description of lineation 2. Basalt at 400–500 m below the sea floor at both sites forms acoustic basement.

Small (0.2–2 km wide), steep-sided, apparently intrusive bodies were observed on three of the seismic reflection profiles which cross the abyssal hills, the abyssal plain, and the lowermost continental rise (Fig. 2, 3, 4; profiles *B*, *D*, *F*). Since these relatively narrow bodies reach a comparatively uniform height with none of them extending more than 10 m above the sea floor, they are interpreted to be diapirs, as distinct from buried topography associated with differential compaction. However, differential compaction probably accounts for the slight (less than 10 m) perturbation of the sea floor above some of these features (Fig. 4). Profile *F*, which has more diapiric features than the other profiles, also has a higher frequency magnetic signature, suggesting volcanic intrusives (Fig. 2). The presence of basalt layers within the dolomite clay sequences at D.S.D.P. site 138 is also suggestive of intrusives (Fig. 1). Also, a basalt diapir similar to those noted was drilled at D.S.D.P. site 141, 700 km south of our study area (Hayes et al., 1972). We interpret the apparent diapirs in our study area also to be igneous in origin on the basis of their shapes, reflection characteristics, and association with igneous basement.

The structural lineations become progressively more difficult to follow in a landward direction, owing to an increase in sediment thickness and reduction in relief of the acoustic basement. The landward thickening of the sedimentary layer is apparent as both an increasing depth relative to sea level of acoustic basement and a decreasing depth of sea floor landward (Fig. 2). Relief on the acoustic basement decreases in a landward direction (Fig. 2; profiles *B*, *D*, *F*), so that the transition from abyssal hills to abyssal plain is due to this reduction in basement relief as well as to the increase in sediment thickness.

SUMMARY

A tectonic grain of 106° was established in the northern Canary basin by correlating basement troughs and adjacent highs revealed on northerly trending geophysical profiles. One of these basement troughs, lineation 3, is interpreted as a fracture zone by analogy with recognized Atlantic fracture zones. In the companion paper (Rona and Fleming, 1973), the delineation of structural lineation 2 is continued landward up to the outer continental shelf off northwest Africa, and the structural lineations described are used to deduce motions relative to the African lithospheric plate during the Mesozoic.

ACKNOWLEDGEMENTS

We thank Captain H. W. Keith Jr., the officers and crew of the N.O.A.A. "Discoverer" for their exceptional cooperation and S. O'Brien for cartographic assistance. Dr. L. W. Butler helped to collect the data.

The preparation of this report was partially supported by funding from the National Science Foundation, International Decade of Ocean Exploration, for the N.O.A.A. Trans-Atlantic Geotraverse (TAG).

REFERENCES

- Harbison, R. N. and Rona, P. A., 1972. Abyssal hills in the eastern central North Atlantic. *Trans. Am. Geophys. Union*, 53(4): 408.
- Hayes, D. E., Pimm, A. C., Beckmann, J. P., Benson, W. E., Berger, W., Roth, P. H., Supko, P. R. and Von Rad, V., 1972. *Initial Reports of the Deep Sea Drilling Project, XIV*. U.S. Government Printing Office, Washington, D.C., pp. 1-975.
- Heezen, B. C. and Tharp, M., 1965. Tectonic fabric of the Atlantic and Indian oceans and continental drift. *Phil. Trans. R. Soc. Lond. - Symp Continental Drift, Ser. A*, 258: 90-106.
- Lowrie, A. and Escowitz, E. (Editors), 1969. Kane 9. In: *Global Ocean Floor Analysis and Research Data Series, I*. U.S. Naval Oceanographic Office, Washington, D. C., pp. 1-973.
- Rona, P. A., 1971. Bathymetry off central northwest Africa. *Deep-Sea Res.*, 18: 321-327.
- Rona, P. A. and Fleming, H. S., 1973. Mesozoic plate motions, in the eastern central North Atlantic. *Mar. Geol.*, 14: 239-252.
- Scott, R. B., Rona, P. A., Butler, L. W., Nalwalk, A. J. and Scott, M. R., 1972. Manganese crusts of the Atlantic fracture zone. *Nat. Phys. Sci.*, 239(92): 77-79.
- Van Andel, T. H., Von Herzen, R. P. and Phillips, J. D., 1971. The Vema fracture zone and the tectonics of transverse shear zones in oceanic crustal plates. *Mar. Geophys. Res.*, 1: 261-283.

1. INTRODUCTION

G. Ross Heath, Department of Oceanography, Oregon State University, Corvallis, Oregon
 Richard H. Bennett, NOAA Atlantic Oceanographic and Meteorological Labs, Miami, Florida
 and

Kelvin S. Rodolfo, University of Illinois at Chicago Circle, Chicago, Illinois

OBJECTIVES

The main objectives of Leg 16, between the Panama Canal and Hawaii, were: (a) to examine the ages of volcanic basement, the stratigraphic sections, and the depositional histories of the ridges surrounding the Panama Basin; (b) to supplement the series of holes begun on Legs 5, 7, 8, and 9 to examine the depositional and tectonic histories of the eastern equatorial Pacific; (c) to study the metalliferous sediments reported above basalt basement on Legs 5, 7, and 9; and (d) to critically evaluate the physical properties measurements made on board the *Glomar Challenger*.

Panama Basin Ridges

Recent work by van Andel et al. (1971) suggests that the ridges surrounding the Panama Basin formed by fragmentation of a single ancestral ridge of which the present Carnegie Ridge is the largest remnant. This hypothesis is based on the acoustic character of the sediment cover of the various ridges and on the seismicity and morphology of the area. Sites DSDP 155, 157, and 158 of Leg 18 (Figure 1-in pocket at back of volume) were designed to test the hypothesis by comparing the lithologies, microfossil assemblages, and basement ages at the three sites.

Eastern Equatorial Pacific

Legs 8 and 9 of DSDP drilled a north-south series of sites along 140°E and an east-west series near the equator south of the Clipperton Fracture Zone. Sites DSDP 159 through 163 of Leg 16 (Figure 1) were designed to complement the earlier array of Leg 8 by filling gaps in the 140°W profile, and to sample the sedimentary record between the Clarion and Clipperton fracture zones, providing an east-west section parallel to the equatorial section of Leg 9. Because of the improved bits available on Leg 16 compared to those used on Leg 8, we expected to penetrate the Middle Eocene cherts that terminated most of the earlier 140°W holes.

Metalliferous Sediments

Sites DSDP 37 through 39 of Leg 5 and DSDP 77, 78, and 80 through 83 of Leg 9 encountered high concentrations of brown, finely divided "amorphous" iron oxides in the sediments directly above basalt basement. These deposits, now scattered over the west flank of the East Pacific Rise, are thought to have formed at the crest of the rise by processes associated with the formation of new oceanic crust (Boström and Peterson, 1966). If so, the metalliferous deposits have been carried to their present positions by sea floor spreading.

DSDP 159 and 160 of Leg 16 were located between the Leg 5 and 9 site clusters listed above. DSDP 159 and 160 were designed to test the continuity of the band of metalliferous sediments, as well as to provide more data on the nature of these deposits.

Physical Properties

As the sediment cores come on board, a number of physical properties such as gamma-ray attenuation, compressional sound wave velocity, and porosity have routinely been determined by the shipboard technicians. Despite the almost ubiquitous core disturbance reported by all scientific parties, the appropriateness and scientific value of the shipboard measurements have not been fully evaluated. The mass physical properties program of Leg 16 was focused on two basic objectives: critical evaluation of analytical techniques, instrumentation, and sediment core quality as they influence the mass physical properties, and measurement of sediment shear strength using a vane shear apparatus and Swedish Fall Cone over selected intervals of the cores. As an integral part of the evaluation study, approximately 400 ten- to fifteen-gram subsamples were taken from the least disturbed portions of the cores, as well as from zones of significant lithologic change, for analysis in a shore-based laboratory.

Standard shipboard techniques and procedures of previous legs were employed (Peterson, Edgar et al., 1970), with the exception of the AP-210 penetrometer and the velocimeter. A decision was made to abandon the penetrometer for shear strength tests and to use a vane shear apparatus with complementary measurements made with a Swedish Fall Cone penetrometer. The AP-210 penetrometer has provided no quantitative or definitive strength measurements but only very rough approximations of relative sediment strength, and, in some instances, even these have been questioned. Vane shear measurements on the unconsolidated sediments with the least apparent disturbance are the most reliable strength tests. Vane shear measurements can be related to sediment shear strength and are particularly useful in determining cohesion of high-porosity unconsolidated clays. Shear strength can be converted to cohesion in the case of fine-grained cohesive sediments by

$$S = c + \bar{\sigma} \tan \phi$$

where c is the cohesion, $\bar{\sigma}$ is the effective stress normal to the shear plane, and ϕ is the angle of internal friction. The Swedish Fall Cone was used for comparison with vane shear

tests on a number of samples. Fall cone determinations can be related to undrained shear strength by

$$S = K Q/h$$

where Q is the weight of the cone, K is a constant which depends on the cone angle and the sampler type, which in turn determines the degree of disturbance. The factor h is the depth of penetration of the cone (Hansbo, 1957). For the purpose of this study, K is considered as unity, and thus the values reported here may be easily converted by choice of the reader. Commonly, the fall cone is calibrated with the vane shear in order to determine the correct K value for a particular type of coring device and sediment type. A number of vane shears were measured normal to the split core sections in close proximity to fall cone tests. In some cases the K values proved to be very close to unity, and in other instances the values deviated significantly from unity. This undoubtedly results from varying degrees of disturbance. Fall cone measurements are most useful as a relative measure of sediment strength and care must be exercised in the interpretation of the values. The sediment closest to the drill bit proved to be the least disturbed; therefore, most vane shear tests were made in sediment trapped between the core catchers or at the lower end of the core barrel. These areas were particularly suitable for vane shear testing, inasmuch as the vane could be inserted normal to bedding and the test performed prior to removal of sediment from the retaining sleeve or catchers. The sediment was extruded after shearing, examined for coring disturbance, and sampled for other physical properties.

Bulk density and porosity were determined by three techniques, two of which were standard shipboard procedures—Gamma-Ray Attenuation Porosity Evaluator (GRAPE) and syringe techniques. The third technique, developed by Bennett and Lambert (1971), was used for all the shore-based measurements. Bulk density (γ) and porosity (n) by the latter method are found by determining the water content (per cent dry weight) and the average grain density and are related by

$$\gamma = \frac{w_d D_g}{w_d + w_w D_g}$$

$$n = \frac{w_w}{\frac{w_d}{D_g} + w_w} \times 100 \text{ (uncorrected for salt)}$$

or

$$n = \frac{w_w + V_{ss}}{\frac{w_d}{D_g} + w_w} \times 100 \text{ (corrected for salt)}$$

where w_t is the total weight of the sample; w_w is the weight of the water, determined by oven drying at 100°C for 24 hours; w_d is the weight of dry solids; D_g is the average grain density; and V_{ss} is the volume of the salts in solution. The technique for determining average grain density can be found in Lambe (1951). The syringe technique was found

to be unreliable and the GRAPE system was plagued with various problems, rendering bulk density and porosity determinations at selected intervals unreliable. These problems and others are discussed in detail in Chapter 13 of this volume, which gives a detailed analytical treatment and evaluation of the techniques used aboard the *Glomar Challenger*. In addition to the methods noted above, a very rough approximation of bulk density was determined for an entire core section (1.5 m) by weighing it and assuming a constant volume for the plastic liner (Peterson, Edgar et al., 1970).

Considerable core disturbance was apparent throughout the majority of barrels (9 m) at each drilling site. Consequently, GRAPE porosity and bulk density values may be in error by varying degrees depending upon the amount of vertical mixing, disturbance (such as core separation), and changes in water content of the sediment during periods of pumping while drilling. Comparison of GRAPE porosity and bulk density values with values obtained for carefully selected samples by the onshore laboratory technique, has shown that approximately 30 per cent of the bulk density measurements do not agree within ± 0.05 g/cc and 10 per cent of the porosity measurements do not agree within ± 5 per cent. The onshore technique is considered reliable and reproducible to ± 0.01 g/cc for bulk density and ± 0.42 per cent for porosity (Bennett and Lambert, 1971). Furthermore, the extreme deviations of the GRAPE data from the laboratory values appear to be unpredictable. A similar discrepancy has also been found by Brier et al. (1969) and is apparently an inherent characteristic of the GRAPE unit.

Erroneous GRAPE values were sometimes due to incomplete filling of the core liner and to separations in the sediment. Low bulk densities and high porosities were common at the ends of many sections because of removal of subsamples for interstitial water analysis. Abnormally low densities and high porosities also reflect areas of possible core separation. Close examination of the core photographs should be considered by the reader in the final interpretation of physical properties data. GRAPE measurements are clearly not necessarily representative of in situ properties nor even of many of the sediment core characteristics in the disturbed state. The GRAPE section averages appear to be more reliable than any particular point value obtained from the GRAPE plot.

For consistency with previous DSDP volumes, water contents are reported as per cent total weight of sample rather than per cent dry weight as commonly used by engineering geologists.

Acoustic velocities were measured using the Hamilton Frame in combination with an oscilloscope as described in DSDP Volume 15 (in preparation). The system is reliable. In extreme cases, however, variations as high as 0.19 km/sec for the sediments and 1.0 km/sec for the basalts were found when measurements were repeated on the same sample. This variation was due primarily to technique and operator error and secondarily to variable core liner thickness. Numerous velocities were measured with the sediment retained in the split core liner. The standard correction factor for the liner thickness in the velocity equation (see Volume 15 for discussion) is therefore not always correct,

especially in extreme cases of thickness variation. Corrections for temperature were not made since the quality of the data does not warrant such refinements. All the cores were stored for several hours in the lab prior to testing to ensure ambient temperature conditions.

Most of the measured velocity values are plotted; consequently, discretion should be exercised in the interpretation of these data. General trends are probably representative of the acoustic properties through a given lithologic sequence.

Natural gamma radiation counts are considered reliable on a relative basis provided vertical mixing within a given lithology is limited. Minor variation may not be representative of in situ conditions due to varying degrees of disturbance throughout the core barrel lengths. Wide ranges of radiation counts within a given core section may reflect variations in the relative concentrations of radionuclides, sediment disturbance, or argillaceous/nonargillaceous ratios. Calibration of the instrument in terms of counts per unit volume apparently has never been assessed.

Detailed treatment of the analytical aspects of the mass physical properties studies during Leg 16 is presented in Chapter 12 of this volume.

OPERATIONAL SUMMARY

Glomar Challenger left Cristobal, Panama, on February 2 and arrived in Honolulu, Hawaii, on March 30, 1971 (Figure 1). During the fifty-six-day leg, the vessel traveled about 6400 nautical miles and drilled twelve holes at nine sites. The drilling statistics are summarized in Table 1.

While under way, 12 kHz echograms, magnetometer readings, and continuous reflection profiles were recorded in analogue form. The original records are on open file at the Scripps Institution of Oceanography. Digitized versions of the navigation, and 12 kHz and magnetometer records are also available from the Scripps Institution.

Coring techniques on Leg 16 were basically the same as those of earlier legs. We experimented with an extended core barrel designed to reduce disturbance of soft sediments by coring ahead of the bit face. Although Leg 15 had some success with this barrel, we could not detect any consistent

improvement in core quality as compared to the conventional barrels. Our experience at DSDP 157 and 158, where the sediments above chert were similar, but the sea state varied from flat calm to 4-foot swell, suggests that vertical movement of the ship far outweighs core-barrel design in influencing the degree of disturbance of soft cores.

Coring in all lithologies was greatly aided by the use of button bits with shaped inserts. These bits, developed since the earlier Pacific campaign, readily penetrated the lower Tertiary cherts that troubled Leg 8. In addition, they drilled soft and semi-consolidated sediments more rapidly than conventional button bits and withstood the drilling conditions well enough to allow adequate sampling of basalt basement. The combination of longer insert buttons and sealed bearings in the new bits eliminated the need for reentry that we had anticipated at Sites DSDP 161 through 163. An experimental reentry attempt at DSDP 163 was unsuccessful due to malfunction of the EDO sonar scanning transceiver while being lowered into the hole. The drilling operations at each site are summarized in the individual site reports.

EXPLANATORY NOTES

Identification System for Sites, Holes, and Samples within Holes

Each drilling site has a number, for example, DSDP 163. The number of the first hole at each site has the site number, for example, Hole 163. Subsequent holes at a site have a following letter, for example, Hole 163A is the second hole at Site DSDP 163.

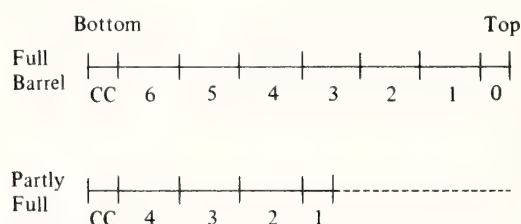
The cores recovered from each hole are numbered successively in the order in which they were taken: Core 1, Core 2, and so forth. The core barrels used on Leg 16 were 9.4-meters long. Drilling was carried out in 9-meter steps. Because of the many uncertainties in determining depths in the drill holes, the depth from which cores were taken is generally given only to the nearest meter.

When the core barrel is recovered on the deck of the drilling vessel, the core catcher is removed from the core barrel, and any material in the catcher (as much as 25 cm in

TABLE 1
Drilling and Coring Summary

Hole	Position		Drilling Dates Of	Water Depth (corr m)	Penetration (m)	No. Cores Cut	Total Cored (m)	Total Core Recovered (m)	Per Cent Recovery
	Latitude	Longitude							
155	06°07.38'N	81°02.62'W	6-8 Feb 1971	2752	536	15	102	57.0	55.8
156	01°40.80'S	85°24.06'W	11-12 Feb 1971	2369	4	2	7	0.5	7.0
157	01°45.70'S	85°54.17'W	12-15 Feb 1971	2591	437	49	427	273.6	64.1
157A	01°45.70'S	85°54.17'W	15-16 Feb 1971	2591	27	3	27	19.3	71.5
158	06°37.36'N	85°14.16'W	18-20 Feb 1971	1953	323	36	323	249.9	77.4
159	12°19.92'N	122°17.27'W	1-3 Mar 1971	4484	109	14	109	96.8	88.8
160	11°42.27'N	130°52.81'W	5-7 Mar 1971	4940	114	14	114	95.8	84.0
161	10°50.25'N	139°57.21'W	9-11 Mar 1971	4939	126	14	126	94.5	75.0
161A	10°40.27'N	139°57.27'W	11-13 Mar 1971	4939	245	15	126	87.8	69.7
162	14°52.19'N	140°02.61'W	15-17 Mar 1971	4854	153	17	153	131.6	86.0
163	11°14.66'N	150°17.52'W	20-25 Mar 1971	5320	294	29	243	155.7	64.1
163A	11°14.66'N	150°17.52'W	25-26 Mar 1971	5320	151	2	5	5.0	99.0
Total:					2519	210	1762 (5781 ft)	1267.5 (4159 ft)	71.9

length in some cores) is labeled core catcher, or CC. The plastic core liner is withdrawn from the core barrel and cut into 150-cm lengths called Sections, beginning at the lower end of the barrel. A 9.4-meter liner can be cut into six such sections, with a short section—about 40 cm in length—at the top end. The sections are numbered according to the amount of material recovered. In a full barrel, the short uppermost section is called the zero section, and the first 150-cm section below that is Section 1, the next Section 2 and so forth. When the barrel is only partly filled with core material, the cutting of the liner into 150-cm sections proceeds as usual, starting from the bottom of the liner. The labeling, however, begins with the uppermost 150-cm section in which there is core material; that section, even if only partly full, is Section 1, the next section below is Section 2, etc. The following diagram illustrates this convention.



Within each section individual samples or observations are located by measuring in centimeters down from the top of the section. This is true even when a section is not full of material, either because of original lack of recovered material (a short Section 1, for example), or because of voids produced by compaction or shrinkage.

In the following chapters, samples are identified by abbreviated notations such as 163-5-1(147). This example denotes a depth of 147 cm in Section 1 of Core 5 of Hole 163.

In using the Visual Core Description as a guide to ordering samples, the reader is cautioned that the core material, especially if it is unconsolidated or watery, has a tendency to shift up or down within the core liner, and that a feature located at, say, 43 cm on the description may be shifted to 46 cm by compaction during handling of the core.

Disturbance

In unconsolidated or semi-consolidated sediments, the bumper subs of the bottom-hole assembly are fully extended. Consequently, any vertical movement of the ship is transmitted directly to the face of the bit. Under the sea conditions encountered on Leg 16, vertical movement of the *Glomar Challenger* due to the long-period swell was as much as several feet. The effect on the cores ranged from complete homogenization of radiolarian oozes, through complex diapiric deformation of somewhat plastic calcareous oozes and clays, to alternations of deformed and relatively undeformed material in the most indurated clays and oozes. In the third case, the alternation of disturbed and undisturbed intervals may recur several times per meter.

Additional disturbance is induced by the large ratio of the area of the bit face to the core area. When the drill is punching ahead in soft sediment, only 5 per cent of the displaced sediment should directly enter the core barrel. The remaining 95 per cent is pushed aside by the face of the bit. Most of this material moves outward, but some is forced into the core barrel. Consequently, the first part of the 9-meter cored section tends to fill the barrel in such deposits, whereas the final few meters may not be sampled at all. This phenomenon explains the disproportionate number of lithologic and biostratigraphic boundaries that fall between cores.

Finally, in semi-indurated sediment, drilling fluid (seawater in most cases) is injected several times per core to prevent the drill from binding. Each such injection removes a section of sediment and also tends to mix with the cored material to produce what look like less indurated beds. True alternations of unconsolidated and semi-indurated sediment (for example, in calcareous sequences) can be distinguished with certainty only by the presence of sedimentary structures in both soft and hard intervals.

Core Processing

After recovery, cores were cut into 1.5-meter lengths and capped. One 50-cc sample per core was normally removed at this stage from the end of one of the lower sections for geochemical studies. The core sections were weighed, the gamma-ray attenuation measured (for saturated bulk density and porosity), and the natural gamma radiation measured. During continuous coring in soft sediment, when cores were arriving on deck every ninety minutes or less, only two sections per core were subjected to natural gamma radiation measurements because of the slowness of this procedure.

With the exception of a few very fluid cores, sections were then split longitudinally by sawing through the plastic liner and slicing the sediment with a wire (if soft) or band saw (if hard). One-half of the core was described by a lithologist (who made smear slides as necessary to aid in the description) and lightly scraped with a spatula to remove markings produced by the splitting technique. This half was then photographed in black and white and color before being sealed in a D-shaped tube as the archive portion of the core.

The other (working) half of the core was first checked for degree of disturbance. If it included intervals that appeared undisturbed, the compressional sound velocity of such intervals was measured by means of the Hamilton Frame and, in a few cases, vane shear strength was also measured (see Bennett and Keller, Chapter 12). The working half was then sampled for carbonate and X-ray diffraction measurements to be performed ashore, as well as for the various investigations reported by the shipboard lithologists in this volume. This half of the core was then sent to the paleontology laboratory where it was sampled for shipboard and shore-based biostratigraphic studies before being sealed in a D-tube. Both archive and working halves of cores are permanently stored at about 4°C to minimize deterioration.

In the course of the coring program, R. Bennett observed that the sediment recovered in the core catcher

assembly at the bottom of the core is often less disturbed than the sediment in the plastic liner. Where possible, such core catcher samples were used for vane shear measurements.

Detailed descriptions of the theory and operation of the gamma-ray attenuation porosity evaluator (GRAPE) and natural gamma activity measuring system can be found in the Initial Reports of the Deep Sea Drilling Project, Volume II, Appendix II (Peterson, Edgar et al., 1970).

Lithologic Nomenclature

Classification of the unconsolidated sediment is shown in Table 1. Generally it follows Olausson (1960). However, pelagic clay, brown clay, or pelagic brown clay are used in lieu of red clay where the color or the origin is obvious. Nannofossil is commonly used rather than Olausson's term nannoplankton, especially for the pre-Pleistocene oozes and chalks.

Most of the consolidated rocks recovered on Leg 16 are carbonates and cherts; their classification is discussed below. For volcanic rocks, details of texture and composition generally are given in the visual core descriptions, thin section and smear slide descriptions, and shore laboratory reports on carbonate and X-ray mineralogy. They enable the reader to name the rock according to the classification he prefers.

The following descriptive terms are used for the degree of lithification of carbonate rocks. Oozes have little strength and are readily deformed under the finger or the broad blade of a spatula. Chalks are partly indurated oozes; they are friable limestones that are readily deformed under the fingernail or the edge of a spatula blade. Chalks more indurated than that are simply termed limestones. During the coring process, chalk ooze is commonly folded but remains coherent, whereas chalk fractures. Generally the chalk in cores is badly shattered, and most of the fragments have irregular tabular shapes normal to the core axis. Fragments of chalk as thick as 2 or 3 cm are rare; most chips are but a few millimeters thick. Portions of cores with these lithologies (chalk or limestone) commonly alternate with portions of mud or slurry of the same color and grain composition but which are ground up and mixed with water and injected into the core barrel during periodic motions that affect the bit on bottom, such as the ship's motion or letting out on the draw works brake. The mud so formed differs from ooze in being wetter, in showing near-vertical flow-folding and diapir-like structure, and in grading to or containing less homogenized portions that retain recognizable pieces of ooze or chalk.

The cherty rocks are subdivided on the basis of their degree of silicification. Porcelanites (porcellanites) are waxy

and dull in luster and commonly show abundant pores under a hand lens. Where cored specimens are allowed to dry out, their surfaces dry to a matte or checked appearance. Thin section and X-ray analyses show that the silica in porcelanite is largely cristobalite and that much of the rock consists of montmorillonite or other nonsilica minerals. On the other hand, the name chert is more appropriately applied to the dense, glassy rocks. Cherts are markedly purer than porcelanites, and their silica is present as chalcedony or microcrystalline quartz. Both porcelanite and chert have conchoidal fracture and both can scratch steel. In contrast, only the more porous and impure porcelanites commonly can be scratched by knife point.

Color symbols are from the Munsell system. Both the soil color charts (Munsell Color Company, 1954) and the rock color charts (Goddard et al., 1948) were used for comparing with the cores. For the reds, yellows, and browns, the soil color charts had more color chips and so were used more frequently. However, the terminology in the rock color chart was always used, whether the symbol was obtained by matching to the soil chart or to the rock chart.

Terminology of sedimentary structures is generally that of the Pettijohn and Potter (1964) atlas and glossary. Grain size terminology is that of Wentworth (1922). For carbonate-rich deposits a more useful boundary would have been at 20 microns because it separates most microfossils from nannofossils.

Both optical and X-ray diffraction methods were used for mineralogical determinations. Terminology of minerals identified optically is that of Deer et al. (1962). The method of mutual standards and the degree of development of recognition criteria in the programs to interpret the digital X-ray diffraction patterns are discussed by Rex (1970).

Biostratigraphic Framework

Because a large number of paleontologists with different views are participating in the work leading to the initial core descriptions, the JOIDES Advisory Panel on Paleontology and Biostratigraphy recommended a scheme of period/system, epoch/series, age/stage classifications for uniform application in this work. It is probable that no worker will be happy with all of the details of this scheme—indeed, there was not unanimity among the members of the panel that formulated it. But it has been necessary to apply such a scheme uniformly in order that the contributions of diverse authors can be integrated into a coherent whole.

TIME-STRATIGRAPHIC FRAMEWORK

			Stage	Bibliographic reference to the concept of the stratotype being applied for the purposes of this manual.
CENOZOIC	QUATERNARY	PLEISTOCENE-RECENT	Calabrian	Gignoux, M., 1910. <i>Compt. Rend. Acad. Sci. Paris.</i> 150 , 841. Gignoux, M., 1913. <i>Ann. Univ. Lyon.</i> 36 . Gignoux, M., 1948. <i>Intern. Geol. Congr. 18th</i> (Report published 1950). Gignoux, M., 1952. <i>Congr. Geol. Intern. Compt. Rend. 19th</i> (Report published 1954). Gignoux, M., 1954. <i>Congr. Geol. Intern. Compt. Rend. 19th.</i> p. 249. Selli, R., 1962. <i>Quaternaria.</i> 6 , 391.
	TERTIARY	PLIOCENE	Astian	Astian: de Rouville, P. G., 1853. <i>Description geologique des environs de Montpellier.</i> Boehm (Montpellier), 185.
			Piacenzian	Piacenzian: Mayer-Eymar, C., 1858. <i>Verhandl. Schweiz. Naturforsch. Ges.</i> 17-19 Aug., 1857. Pareto, L., 1865. <i>Bull. Soc. Geol. France.</i> (2) 22 , 209. Gignoux, M., 1915. <i>Bull. Soc. Geol. France.</i> (4) 14 , 338. Gignoux, M., 1924. <i>Boll. Soc. Geol. Ital.</i> 42 , 368. di Napoli-Alliata, 1954. <i>Congr. Geol. Intern. Compt. Rend. 19th.</i> p. 229-234.
		Lower	Zanclean (A)*	Seguenza, G., 1868. <i>Bull. Soc. Geol. France.</i> (2) 25 , 465. Baldacci, L., 1886. <i>Mem. Descrit. Carta Geol. Ital.</i> 1 , 1. Ogniben, L., 1954. <i>Mem. 1st Geol. Mineral. Univ. Padova.</i> 18 . Wezel, F. C., 1964. <i>Riv. Ital. Pal. Strat.</i> 70 , 307.
	MIOCENE	Upper	Messinian	Mayer-Eymar, C., 1867. <i>Catologue systématique et descriptif des fossiles des terrains tertiaries qui se trouvent au musée fédéral de Zurich.</i> (Zurich) 2 , 13. Selli, R., 1960. <i>Giorn. Geol. Ann. Museo. Geol. Bologna.</i> (2) 28 , 1. d'Onofrio, S., 1964. <i>Giorn. Geol. Ann. Museo. Geol. Bologna.</i> (2) 32 , 409.
			Tortonian (B)	Mayer-Eymar, C., 1858. <i>Verhandl. Schweiz. Naturforsch. Ges.</i> 17-19 Aug., 1857. Gino, G. F. et al., 1953. <i>Riv. Ital. Paleont., Mem.</i> 6 , 7. Giannotti, A., 1953. <i>Riv. Ital. Pal. Strat. Mem.</i> VI , 168. Cita, M. B. et al., 1965. <i>Riv. Ital. Pal. Strat.</i> 71 , 217.

*Capital letters in parentheses refer to "Notes on Concepts of Stages and Other Boundaries"

CENOZOIC			
TERTIARY			
MIOCENE	Middle	Serravallian	Pareto, M. F., 1865. <i>Bull. Soc. Geol. France</i> , ser. 2, vol. 22, p. 232. Vervloet, C. C., 1966. <i>Stratigraphical and micropaleontological data on the Tertiary of southern Piedmont (Northern Italy)</i> , p. 11-49, Schotanus and Jens, Utrecht. Cita, M. B. and Premoli-Silva, I., 1968. <i>Gior. Geol.</i> , vol. 35 (1967), fasc. 3, p. 1-23.
		Langhian (C)	Pareto, L., 1865. <i>Bull. Soc. Geol. France</i> . (2) 22 , 229. Cita, M. B. and Silva, I. P., 1960. <i>Intern. Geol. Congr. 21st, Copenhagen, 1960, Rep. Session, Norden</i> . 22 , 39. Cita, M. B. and Elter, G., 1960. <i>Acad. Nazl. dei Lincei. Ser. 8(5)</i> , 29 , 360.
	Lower	Burdigalian	Burdigalian: Depéret, C., 1892. <i>Compt. Rend. Soc. Geol. France</i> . (11), 145. Depéret, C., 1893. <i>Bull. Soc. Géol. France</i> . (3) 21 , 263. Dollfus, 1909. <i>Bull. Serv. Carte Géol. France</i> . (124) 19 , 380. Drooger, C. et al., 1955. <i>Koninkl. Ned. Akad. Wetenschap. Verslag Gewone Vergader. Afdel. Nat. Ser. 1 (2)</i> , 21 , 1.
		Aquitanian	Aquitanian: Mayer-Eymar, C., 1858. <i>Verhandl. Schweiz. Naturforsch. Ges.</i> 17-19 Aug., 1857, p. 188. Tournouer, R., 1862. <i>Bull. Soc. Geol. France. Ser. 2</i> , 19 , 1035. Drooger, C. W. et al., 1955. <i>Koninkl. Ned. Akad. Wetenschap. Verslag Gewone Vergader. Afdel. Nat.</i> Szots, E., 1965. <i>Bull. Soc. Geol. France</i> . (7) 7 , 743.
OLIGOCENE	(E)		Girondian: Vigneaux, M., Magne, A., Veillon, M. and Moyes, J., 1954. <i>Compt. Rend. Acad. Sci. Paris</i> . 239 , 818. Caralp, M. and Vigneaux, M., 1961. <i>Compt. Rend. Soc. Geol. France</i> . 140 . Drooger, C. W., 1958. <i>83rd Congr. Soc. Sav., Sect. Sci.</i> p. 171.
	Chattian		Fuchs, T., 1894. <i>Jahresber. Ungar. Geol. Anstalt</i> . 10 , 172. Gorgès, J., 1952. <i>Abhandl. Hess. Landesametes Bodenforsch.</i> 4 , 1. Hinsch, W., 1958. <i>Lexique Strat. Intern.</i> 1 5hl. Anderson, H. J., 1961. <i>Meyniana</i> . 10 , 118. Hubach, H., 1957. <i>Ber. Naturhist. Ges. Hannover</i> . 103 .
	Rupelian		Dumont, A., 1849. <i>Bull. Acad. Roy. Med. Belg.</i> (1) 16 , 370. Batjes, A., 1958. <i>Inst. Roy. Sci. Nat. Belg. Bull. Mém.</i> 143.
	Lattorfian		Mayer-Eymar, C., 1893. <i>Bull. Soc. Geol. France</i> . (3) 21 , 8. Munier-Chalmas, E. and de Lapparent, A., 1893. <i>Bull. Soc. Geol. France</i> . 21 , 478. von Koenen, A., 1893-1894. <i>Abhandl. Geol. Spec. Preussen</i> . 10 , 1005. cf. Krutzsch, W. and Lotsch, D., 1957. <i>Geologie</i> . 6 , 476. Krutzsch, W. and Lotsch, D., 1958. <i>Ber. Deut. Geol. Ges.</i> 3 , 99.
EOCENE	Upper	Priabonian	Priabonian: Munier-Chalmas, E. P. and de Lapparent, A., 1893. <i>Bull. Soc. Geol. France</i> . (3) 21 , 471. Roveda, V., 1961. <i>Riv. Ital. Pal. Strat.</i> 67 , 153.
		Bartonian	Fabiani, R., 1915. <i>Mem. 1st Geol. Mineral Univ. Padova</i> . 3 , 1.

CENOZOIC	TERTIARY	EOCENE	UPPER	Priabonian	Bartonian Mayer-Eymar, C., 1858. <i>Verhandl. Schweiz. Naturforsch. Ges.</i> 178. Prestwich, J., 1847. <i>Quart. J. Geol. Soc., London.</i> 3, 354. Prestwich, J., 1857. <i>Quart. J. Geol. Soc., London.</i> 13, 108. Curry, D., 1958. <i>Lexique Strat. Intern.</i> I 3a 12.		
				(F)			
			Middle	Lutetian	de Lapparent, A., 1883. <i>Traite de Geologie.</i> 1st Ed., p. 989. Blondeau, A. and Curry, D., 1964. <i>Bull. Soc. Geol. France.</i> (7) 5, 275. Blondeau, A. et al., 1966. <i>Bull. Soc. Geol. France.</i> (7) 7, 200. Blondeau, A., 1964. <i>Mem. Bur. Rech. Geol. Min.</i> No. 28. 21.		
		Lower	Ypresian	Dumont, A., 1849. <i>Bull. Acad. Roy. Med. Belg.</i> (1) 16, 368. Kaasschieter, J. P. H., 1961. <i>Inst. Roy. Sci. Nat. Belg. Bull. Mem.</i> 147.			
		PALEOCENE	UPPER	Thanetian	Renèvier, E., 1873. <i>Tableau des terrains sédimentaires (in 4°) et un texte explicatif.</i> Lausanne (G. Bridel). Renèvier, E., 1897. <i>Chronogr. Geol.</i> Prestwich, J., 1852. <i>Quart. J. Geol. Soc., London.</i> 8, 235. Barr, F. T. and Berggren, W. A., 1965. <i>Stockholm Contrib. Geol.</i> (2) 13, 9.		
			LOWER	Montian	Dewalque, G., 1868. <i>Prodrome d'une description geologique de la Belgique.</i> p. 185. Cornet and Briart, 1866. <i>Bull. Acad. Roy. Med. Belg.</i> (2) 20, 757. Briart and Cornet, 1880. <i>Ann. Soc. Geol. Belg.</i> 7, 139. Rutot, A. and von den Broeck, E., 1885. <i>Ann. Soc. Roy. Malac. Belg.</i> 20, 108. Rutot, A. and von den Broeck, E., 1886. <i>Ann. Soc. Geol. Belg.</i> 13, 94. Rutot, A. and von den Broeck, E., 1887. <i>Bull. Soc. Geol. France.</i> (3) 15, 157. Marlière, R., 1955. <i>Ann. Soc. Geol. Belg.</i> 78, 297. Berggren, W. A., 1964. <i>Stockholm Contrib. Geol.</i> (5) 11, 135.		
	Tertiary		Danian	Tertiary: de Grossouvre, A., 1897. <i>Bull. Soc. Geol. France.</i> Ser. 3, 25, 57. Loeblich, A. R., Jr. and Tappan, H., 1957. <i>U. S. Nat. Museum Bull.</i> 215, 173. Troelsen, J., 1957. <i>U. S. Nat. Museum Bull.</i> 125. Berggren, W. A., 1962. <i>Stockholm Contrib. Geol.</i> (2) 9, 103. Berggren, W. A., 1964. <i>Stockholm Contrib. Geol.</i> (5) 11, 103. Cretaceous: Eames, F. E. (in press), 1968. <i>J. Geol. Soc. India.</i> Desor, E., 1847. <i>Bull. Soc. Geol. France.</i> Ser. 2, 4, 179. Brotzen, F., 1959. <i>Sveriges Geol. Undersokn. Arsbok, Ser. C.</i> (571), 81 pp. Rasmussen, H. W., 1965. <i>Mededel. Geol. Sticht. N. S.</i> , (17), 33. (Supplemented by M. Meijer, <i>loc. cit.</i> , pp. 21-25).			
		Cretaceous		Campanian (G)	Coquand, H., 1857. <i>Bull. Soc. Geol. France.</i> 749. Van Hinte, J., 1965. <i>Koninkl. Ned. Akad. Wetenschap. Proc., Ser. B.</i> (1) 68, 14. Marie, P., 1941. <i>Mem. Museum Nat. Hist. Nat. (Paris).</i> 12, 1.		
					Upper	Maestrichtian	Dumont, A., 1849. <i>Bull. Acad. Roy. Sci. Lettres, Beaux-Arts, Belgique.</i> 351. Hofker, J., 1966. <i>Paleontographica.</i> Supplement-Band 10, Atlas of Foraminifera, 5. Jeletzsky, J., 1951. <i>Beih. Geol. Jahrb.</i> (1), 1.

M E S O Z O I C	C R E T A C E O U S	U P P E R	Santonian S.S. (H)	Coquand, H., 1857. <i>Bull. Soc. Geol. France</i> , 749. Seronie-Vivien, M., 1959. <i>Colloque sur le Crétacé Supérieur Français rendus de Congrès des Sociétés Savantes de Paris et des Départements, Comité des Travaux historiques et scientifiques, section des sciences, sous-section de géologie, tenu à Dijon</i> . Paris (Gauthier-Villars). 581.
			Lower Santonian – Coniacian (I)	Coquand, H., 1857. <i>Bull. Soc. Geol. France</i> . 748. Seronie-Vivien, M., 1959. <i>Colloque sur le Crétacé Supérieur Français rendus de Congrès des Sociétés Savantes de Paris et des Départements, Comité des Travaux historiques et scientifiques, section des sciences sous-section de géologie, tenu à Dijon</i> . Paris (Gauthier-Villars). p. 581. Schijfsma, E., 1946. <i>Mededel. Geol. Sticht. Ser. C-V</i> (7), 1.
			Turonian	D'Orbigny, 1842. <i>Les Cephalopodes</i> . (Published by author) 622 pp. D'Orbigny, 1842. <i>Les Animaux Mollusques et Rarones</i> . (Published by author) 456 pp. Lacointre, 1959. <i>Colloque sur le Crétacé Supérieur Français rendus de Congrès des Sociétés Savantes de Paris et des Départements, Comité des Travaux historiques et scientifiques, section des sciences, sous-section de géologie, tenu à Dijon</i> . Paris (Gauthier-Villars). 415. Butt, A. A., 1966. <i>Micropaleontology</i> . (2) 12, 168.
			Cenomanian	D'Orbigny, 1842. <i>Les Cephalopodes</i> . (Published by author) 622 pp. D'Orbigny, 1842. <i>Les Animaux Mollusques et Rarones</i> . (Published by author) 456 pp. Marks, P., 1967. <i>Koninkl. Ned. Akad. Wetenschap., Proc., Ser. B</i> (3), 70, 264.
		L O W E R	Albian	Collignon, 1965. Rapport sur L'Etage Albian. In <i>Colloque sur le Crétacé Inférieur</i> , Lyon. <i>Mem. Bur. Rech. Geol. Min.</i> (34) (Lyon), 313. Casey, 1961. The stratigraphical paleontology of the Lower Greensand. <i>Paleontology</i> . 3, 487.
			Aptian	Fabre-Taxy, S., Moullade, M. and Thomel, G., 1965. A-Les stratotypes de l'Aptien. In <i>Colloque sur le Crétacé Inférieur</i> , Lyon. <i>Mem. Bur. Rech. Geol. Min.</i> (34), 173. Casey, R., 1961. The stratigraphical paleontology of the Lower Greensand. <i>Paleontology</i> . 3, 487.
			Barremian	Busnardo, R. 1965. Le stratotype de Barremien. In <i>Colloque sur le Crétacé Inférieur</i> , Lyon. <i>Mem. Bur. Rech. Geol. Min.</i> (34) (Lyon), 101.
			Hauterivian	Debelmas, J. and Thieuloy, J., 1965. E'tage Hauterivien. In <i>Colloque sur le Crétacé Inférieur</i> , Lyon. <i>Mem. Bur. Rech. Geol. Min.</i> (34), 85.
			Valanginian	Barbier, R. and Thieuloy, J., 1965. E'tage Valanginien. In <i>Colloque sur le Crétacé Inférieur</i> , Lyon. <i>Mem. Bur. Rech. Geol. Min.</i> (34), 79.
			Berriasian	Busnardo, R., Hegaret, G. L. and Magne, J., 1965. Le stratotype du Berriasien. In <i>Colloque sur le Crétacé Inférieur</i> , Lyon. <i>Mem. Bur. Rech. Geol. Min.</i> (34) (Lyon), 5.

MESOZOIC	JURASSIC	UPPER	Tithonian	Enay, R., 1964. L'étage Tithonique. In <i>Colloq. du Jurassique</i> (Luxembourg, 1962). <i>Compt. Rend. Mem., Luxembourg</i> . 355.
			Kimmeridgian	Ziegler, B., 1964. Das Untere Kimeridgien in Europa. In <i>Colloque du Jurassique</i> (Luxembourg, 1962). <i>Compt. Rend. Mem., Luxembourg</i> . 345.
			Oxfordian	Callomon, J. H., 1964. Notes on the Callovian and Oxfordian Stages. In <i>Colloque du Jurassique</i> (Luxembourg, 1962). <i>Compt. Rend. Mem., Luxembourg</i> . 269. Enay, R. <i>et al.</i> (in press). Les Faunes Oxfordiennes d'Europe Meridionale. Essai de Zonation. In <i>Colloque International du Jurassique</i> (Luxembourg, 1967).
		MIDDLE	Callovian	Callomon, J. H., 1964. Notes on the Callovian and Oxfordian Stages. In <i>Colloque du Jurassique</i> (Luxembourg, 1962). <i>Compt. Rend. Mem., Luxembourg</i> . 269.
			Bathonian	Cox, L. R. 1964. The type Bathonian. In <i>Colloque du Jurassique</i> (Luxembourg, 1962). <i>Compt. Rend. Mem., Luxembourg</i> . 265. Torrens, H. S. (in press). Standard zones of the Bathonian. In <i>Colloque International de Jurassique</i> (Luxembourg, 1967). Elmi, S., 1964. Précisions stratigraphiques sur la Bathonien supérieur du nord de l'Ardèche. In <i>Colloque du Jurassique</i> (Luxembourg, 1962). <i>Compt. Rend. Mem., Luxembourg</i> . 535.
			Bajocian	Elmi, S., Enay, R. and Mangold, C., 1964. La stratigraphie et les variations de faciès du Bajocien de l'île Crémieu (Jura meridional tabulaire). In <i>Colloque du Jurassique</i> (Luxembourg, 1962). <i>Compt. Rend. Mem., Luxembourg</i> . 539.
		LOWER	Aalénien	Enay, R. and Elmi, S., 1964. Précision sur la stratigraphie de l'Aalénien dans le Bugey occidental. In <i>Colloque du Jurassique</i> (Luxembourg, 1962). <i>Compt. Rend. Mem., Luxembourg</i> . 559. Maubeuge, P. L., 1963. La position stratigraphique du gisement Ferrifère Lorrain (Le problème de l'Aalénien). <i>Bull. Tech. Chambre Syndicale Min. Fer France</i> . (72).
			Toarcian	Elmi, S. <i>et al.</i> (in press). L'étage Toarcien. Zones et Sous-Zones d'Ammonites. In <i>Colloque International de Jurassique</i> (Luxembourg, 1967). Howarth, M. K., 1964. Whilbian and Yeovilian Substages. In <i>Colloque du Jurassique</i> (Luxembourg, 1962). <i>Compt. Rend. Mem., Luxembourg</i> . 189.
			Pleinsbachian	Geyer, O. F., 1964. Die typuslokalität des Pleinsbachian in Württemberg (Südwestdeutschland). In <i>Colloque du Jurassique</i> (Luxembourg, 1962). <i>Compt. Rend. Mem., Luxembourg</i> . 161.
			Sinemurian	Maubeuge, P. L., 1964. Quelques remarques a propos de l'Hettangien du Sinemurien et du Lotharingien. In <i>Colloque du Jurassique</i> (Luxembourg, 1962). <i>Compt. Rend. Mem., Luxembourg</i> . 127.
			Hettangian	Elmi, S. <i>et al.</i> (in press). Les Subdivisions biostratigraphiques de l'Hettangien en France. In <i>Colloque International du Jurassique</i> (Luxembourg, 1967).

NOTES ON CONCEPTS OF STAGE— AND OTHER BOUNDARIES

- (A) Zancian is used in preference to Tabianian because the former has been shown to contain a better and more diverse marine fauna which can be used in regional stratigraphic correlation.

- (B) Tortonian is placed in the Upper Miocene because:
1) This was its original placement.
2) Although subsequently placed in Middle Miocene, it has now been returned to its original position because the Langhian has been moved up from the top of the Lower Miocene into the Middle Miocene. The type Tortonian is subsequent to beds called "Elveziano" or "Tortonian of Vienna basin", from which many species of Mollusca, especially, have been described as typical of the Middle Miocene. These "Vienna beds" are within the same stratigraphic interval as the beds of the Langhian (=Serravallian of Vervloet, 1966).

- (C) The Langhian is restricted, for the purposes of this Manual, to the beds included in the Cessole Formation, and excludes the older horizons included in the Langhian by Cita and Elter.

This essentially follows the usage of Pareto (1865), who directly referred only to the section north of Cessole, which commences with the Cessole Formation. This is in accordance with the results of the work carried out by Drooger and colleagues, who recommended that the first evolutionary appearance of the genus *Orbulina* occurs from the base of the Middle Miocene, which is a few meters above the base of the exposed Cessole Formation at Cessole.

This is supported by the fact that the base of the French stage Sallomacian (which falls within the Langhian Stage) has always been regarded by the French as the commencement of the Middle Miocene. (The name "Sallomacina" has two years' priority over the term "Vindobonian".) The beds included in the Langhian and Sallomacian Stages are also equivalent to the Badenian Stage of Reiss and Gvirtzman, which covers beds included in the Vindobonian from which virtually all the typical Middle Miocene molluscs were obtained.

- (D) The Girondian Stage (Vigneaux *et al.*, 1954) is coextensive with the Aquitanian and Burdigalian, and forms a stratigraphic unit well defined in terms of larger Foraminifera and Mollusca.
- (E) Regarding the position of the Oligocene-Miocene boundary, for the purposes of this Manual, the panel has accepted (by majority opinion) the base of the stratotype Aquitanian to represent the base

of the Neogene (Oligocene-Miocene boundary), as recommended by the Comité du Néogène Méditerranéen in 1959 (published 1960), 1961 (published 1964), 1964 (published 1966) and 1967 (in press), but not yet formally approved by the IUGS.

There is a radical dichotomy of opinion represented among the panel members, and the two viewpoints are explained below, labelled 1 and 2.

1. It has been recommended that the base of the stratotype Aquitanian should be taken as the base of the Miocene (and, therefore, the base of the Neogene). The following points apply:
 - (1) When originally proposed, the Bormidian was regarded as Miocene, and one of the latest publications (Lorenz, 1964), also regarded it as Miocene.
 - (2) The Bormidian is highly conglomeratic and rests directly upon the Triassic; normally it would not be considered suitable for a stratotype for a standard stage. There has been no indication whether any of the fossils recorded are derived or not (the pebbles of phyllites, schists, etc. obviously are derived). Some fossils were believed later to be Oligocene, but some have been found elsewhere *only* in beds of Miocene age. To the east of the area the Bormidian is cut out, and the overlying Aquitanian rests directly on nummulitic Oligocene (not present to the west) so that there is an unconformity at the base of the Bormidian—the Triassic underlying it in one area, and nummulitic Oligocene underlying it in another area.
 - (3) The European stage names on the Tertiary Chart prepared by this panel were all based upon marine megafossil faunas such as Mollusca, Echinoidea, larger Foraminifera, etc. (except for the Paleocene, which originally was based upon plant evidence). The evidence of planktonic foraminifera, however important an asset it may be in the refinement of zonation within and correlation of these stages, did *not* enter into the primary definitions. It seems quite wrong *arbitrarily* to select one level of planktonic foraminiferal zonation to define the Miocene-Oligocene boundary; it remains but one part of a much larger field for synthesis. In any case, terms such as "Miocene" and "Oligocene" are time-stratigraphic units, and cannot be stratotyped. Consequently, the evidence of megafossils should be considered when

- attempting to find a suitable position for the Miocene-Oligocene boundary.
- (4) In the Marnes Blanches de Bernachon, which immediately and conformably underlie the stratotype Aquitanian, there are 7 species of Gastropoda, 9 species of bivalvia, and 20 species and 1 subspecies of Ostracoda, all of which occurred in the overlying Miocene faunas, but have not been found anywhere else in beds regarded as being of Oligocene age. There were a few Ostracoda having known long ranges, but *not a single* mollusc or ostracod previously known only from the Oligocene or from Oligocene and older beds. This fauna is to be regarded as Neogene and Miocene. In the same beds are found Miogypsina at a more advanced stage of evolution than those of the Eochattian of Bunde. These beds rest unconformably upon nummulitic Middle Oligocene.
 - (5) In the Nordic Province of Northwestern Europe, the fauna of the Vierlander Stage, although originally regarded as Aquitanian, was later regarded by Kautsky (1925) as being of Burdigalian or even younger age. Consequently, in this Nordic province, there are *no* basal Miocene megafossil faunas at all available for comparison with the megafossil faunas of the stratotypes of the Chattian, Eochattian and Neochattian. Furthermore, it is evident that the top ends of the ranges of the megafossils in the stratotype Chattian are completely unknown since some of them may well (and probably do) range up into basal Miocene age of much of the Eochattian-Neochattian succession were not realized, such extensions of ranges would never come to light.
 - (6) With regard to the Eochattian-Neochattian succession it is perhaps significant that: (a) there are several common molluscan species in the Neochattian of which there is no sign in the Eochattian, and (b) there are three levels in the Eochattian at which derived Liassic ammonites occur.
 - (7) The fauna of the Escornebéou beds as published by Butt (1966) was regarded by him (and Drooger) as late Oligocene ("Chattian"). Not only does this material contain derived material from at least two older levels, and not only do the beds in the area rest unconformably on the Cretaceous, but the faunas include good *Globigerinoides* which correlate the material with material *within* the type Aquitanian at the *oldest*. This material is therefore *younger* than the Neochattian.
 - (8) Conclusions: The terms "Miocene" and "Oligocene" are time-stratigraphic units and cannot be stratotyped. Miocene faunas occur *beneath* the stratotype Aquitanian, and at Escornebéou (where they were called Oligocene). Much of the Eochattian-Neochattian succession can reasonably be regarded as basal Miocene. Useful levels of changes in planktonic foraminiferal faunas are certainly to be used to refine the time-limits within which successions of megafossil faunas occur, but any single one of these *alone* should *not* be taken to define a boundary such as "Miocene-Oligocene" without synthesizing the planktonic foraminiferal faunal evidence with that of the megafossils. Any attempt to take the "Miocene-Oligocene" boundary at the incoming of *Globigerinoides* (i.e., base of stratotype Aquitanian) would result in a large number of molluscan, echinoid, larger foraminiferal, etc. faunas having their ranges extended a very short distance down into the "Oligocene" (*sic*), at which level there is not only a very noticeable faunal change in many groups of fossils (justifiably taken as the Neogene-Palaeogene boundary) but very often evidence of unconformity in the Alpine-Himalayan region (used in a broad sense). It seems to be highly undesirable to have a major faunal change occurring a short distance below one of relatively minor significance, and to use the latter rather than the former as a "Miocene-Oligocene" boundary.
2. The stratigraphic extent of the Bormidian can be shown in terms of planktonic foraminiferal zones to include much of the interval ascribed to the Eochattian and Neochattian of Northern Germany. The uppermost part of the Bormidian is approximately at the same level as the middle part of the Neochattian, and both are prior to the *Globigerinoides* datum which can be recognized at the base of the stratotype Aquitanian. This *Globigerinoides* datum, as expressed in the stratotype Aquitanian, was recommended in 1959 and reaffirmed in 1963 and 1967, by the Neogene Commission on Mediterranean Neogene as the horizon to be taken to mark the base of the Miocene. The base of the Bormidian falls within the upper part of the Eochattian succession, while the lower part of Eochattian succession, has been correlated, Hubach

(1957), and Anderson (1961) with the type Kassel Sands representing the type Chattian. Therefore, there is a *prima facie* case for regarding the Bormidian as post-Chattian, but pre-Aquitainian. German workers have long regarded the successions seen at Kassel, Doberg and Astrup as being a single major lithological unit, and have considered them as Oligocene. However, where Beyrich (1854 and 1858) did not discuss the present exposure at Astrup, he did discuss the beds at Doberg which include both Eochattian and Neochattian. Therefore, in Beyrich's terminology, the term "Oligocene" should be applied, not only to the Kassel Sands, but also to the succession at Doberg. *Miogypsina septentrionalis* occurs from near the exposed base of the succession at Doberg (Bed Number 10 of Hubach). This horizon is referable to Zone P.19 of Blow, and also was correlated by Hubach and Anderson to be within the interval of the type Kassel Sands. Furthermore, the latest horizon recognized within the Boom Clay of Belgium (type Rupelian) is also within Zone P. 19. Thus, in agreement with the work of Batjes (1958), there is a reasonable case for considering the Chattian as part equivalent, at least, of the later parts of the Rupelian. The range of *Miogypsina* ss. must include a part of the Oligocene, and, therefore, cannot be used to decide Neogene or Paleogene affinities.

- (F) The Biarritzian Stage has been shown to be partly upper Lutetian and partly lower Auversian. Curry (1967) has suggested that the term "Auversian" covers a recognizable and useful sequence, although it is not quite as extensive stratigraphically as suggested by its usage by some previous French workers. Since the terms Biarritzian and Auversian are provincial in nature they are not used in this manual.
- (G) Van Hinte (1965) erected a neostratotype for the Campanian which contains planktonic foraminiferal faunas in the lower part and orbitoids in the higher part. The Campanian planktonic foraminiferal faunas are, from analysis of Van Hinte's figured forms (by Pessagno and Blow), an assemblage which is long-ranging in the broad concept of Campanian, but is not likely to be that which occurs in immediately pre-Maestrichtian horizons. There is no justification for accepting Van Hinte's supposition that *G. calcarata* bearing beds (his Unit G), immediately overlie the neostratotype G of Van Hinte. In support of this, Blow (unpublished) has observed a single broken specimen of *G. calcarata* presumably from the same Unit G from which Van Hinte recorded his planktonic faunas. In view of the fact that the occurrence of *G. calcarata* is sporadic and the fauna from the neostratotype is very much restricted in diversity and in number of species, it

appears that Van Hinte's Unit G is in part, at least, representative of the *G. calcarata* zone. However, there is an interval between the top of Unit G and the first horizon of occurrence of undoubted orbitoids (e.g. *Orbitoides media*) which have been accepted by many authors as characteristic of Maestrichtian.

It should be noted that many small "*Orbitoides*" occur in the interval between the first occurrence of *O. media* and the top of the planktonic foraminiferal fauna of Bed G. These forms (e.g. *Schlumbergeria*) have been accepted as Campanian forms by many authors; therefore, at least the lower half of Van Hinte's Unit F must be considered as Campanian, whereas the upper half of Unit F and the younger horizons should be ascribed to Maestrichtian. Because of this, this manual shows *G. calcarata* disappearing just prior to the Campanian-Maestrichtian boundary and *G. ventricosa* disappearing at or very near the Campanian-Maestrichtian boundary.

- (H) Santonian s.s. is that part of the Santonian represented by the stratotype.
- (I) Beneath the exposed beds of the stratotype Santonian is an interval, part of which is undoubtedly Coniacian as represented in its "stratotype", but between the two there are both beds and faunas which have not been unambiguously differentiated.
- (J) The Vraconian of certain Continental authors is here arbitrarily included as low Cenomanian.

Basis for Age Determinations

Based on earlier legs of the Deep Sea Drilling Project and on observations made during Leg 16, the correlation of microfossil zones shown in Table 2 is used throughout this volume. The absolute ages of the major boundaries shown in Table 2 are from Laughton, Berggren et al. (1972). The uncertainty of any of the values shown is probably less than 4 my, based on the various compilations published during the past four years.

Data Presentation

As far as possible, raw data are presented in the various site reports and specialized studies included in this volume. Because of space limitations, however, the core descriptions represent a condensation of the detailed section and smear slide descriptions made on the ship. The original descriptions are on open file at DSDP headquarters in La Jolla. Limitations on the accuracy and precision of the various types of data are mentioned in this chapter and in the various integrated reports of the shore laboratory studies of Part II of this volume (particularly those on physical properties and biostratigraphy). They should be consulted before attempting to synthesize data from the site chapters.

362

* • Brinvaginata and C. tuberosa

ACKNOWLEDGMENTS

The material presented in this chapter, particularly the Explanatory Notes, draws heavily on comments and suggestions of our colleagues on Leg 16 and on earlier introductory sections of Initial Reports of the Deep Sea Drilling Project (particularly those of the Leg 7 report). We gratefully acknowledge the assistance provided by these various sources.

REFERENCES

- Anderson, H. J. 1961. *Meyniana*, **10**, 118.
- Batjes, D. A. J., 1958. Foraminifera of the Oligocene of Belgium. *Inst. Roy. Sci. Nat. Belg., Mem.* 143.
- Bennett, R. H. and Lambert, D. N., 1971. Rapid and reliable technique for determining unit weight and porosity of deep-sea sediments. *Marine Geol.* **11**, 201.
- Beyrich, E., 1854. Über die Stellung der Hessischen Tertiärbildung. *Verhandl. Preussen Akad. Wiss. Berlin*. 640.
- , 1858. Über die Abgrenzung der Oligocänen Tertiärzeit. *Monatsber. Preussen Akad. Wiss. Berlin*. **54**.
- Boström, K. and Peterson, M. N. A., 1966. Precipitates from hydrothermal exhalations on the East Pacific Rise. *Econ. Geol.* **61** 1258.
- Brier, C., Bennin, R. and Rono, P. A., 1969. Preliminary evaluation of a core scintillation counter for bulk density measurement in marine sediment cores. *J. Sediment. Petrol.* **39**, 1509.
- Butt, A. A., 1966. Late Oligocene Foraminifera from Escornebéou, S. W. France. Utrecht (Schotanus & Jens).
- Curry, D. 1966. Correlations within the Anglo-Paris-Belgian Palaeogene Basin. *Proc. Geologists' Assoc. London*. **77**, 437.
- Deer, W. A., Howie, R. A. and Zussman, J., 1962. *Rock-Forming Minerals*. Vol. 1-5. London (Longmans, Green and Co., Ltd.).
- Goddard, E. N. et al., 1948. Rock color charts. Natl. Res. Council. Washington, D.C. (republished by Geol. Soc. Am.), 8 p.
- Hansbo, S., 1957. A new approach to the determination of the shear strength of clay by the fall-cone test. *Royal Swedish Geotech. Inst. Proc.* **8**, 1.
- Hubach, H., 1957. Das Oberoligocän des Doberges bei Bunde in Westf. *Ber. Naturhist. Gesell. Hannover*. **103**, 1.
- Kautsky, 1925. *Abhandl. Geol. Landesamst. Ber. N.F.*, **97**, 1.
- Lambe, T.W., 1951. *Soil Testing for Engineers*. New York (John Wiley and Sons), 165 p.
- Laughton, A.S. and Berggren, W.A. et al., 1972. Initial Reports of the Deep Sea Drilling Project, Volume XII. Washington (U.S. Government Printing Office), 15.
- Lorenz, L., 1964. *Bull. Soc. Geol. France, Ser. 7*, **6**, 192.
- Munsell Color Company, 1954. *Munsell Soil Color Charts*. Baltimore (Munsell Color Co., Inc.), 23 p.
- Olausson, E., 1960. Descriptions of sediment cores from the central and western Pacific with adjacent Indonesian region. *Rept. Swedish Deep-Sea Exped., 1947-1948*. **6(5)**, 161.
- Pareto, L., 1865. *Bull. Soc. Geol. France*. **2(22)**, 229.
- Peterson, M.N.A., Edgar, N.T. et al., 1970. Shipboard scientific procedures, *In* Initial Reports of the Deep Sea Drilling Project, Volume II. Washington. (U.S. Government Printing Office). 452.
- Pettijohn, F.J. and Potter, P.E., 1964. *Atlas and Glossary of Primary Sedimentary Structures*. New York (Springer-Verlag). 305 p.
- Rex, R.W., 1970. Shore-based laboratory procedures (X-ray mineralogy). *In* Bader, R.G., Gerard, R.D. et al., 1970. Initial Reports of the Deep Sea Drilling Project, Volume IV. Washington (U.S. Government Printing Office). 748.
- van Andel, Tj. H., Heath, G.R., Malfait, B.T., Heinrichs, D.F. and Ewing, J.I., 1971. Tectonics of the Panama Basin, eastern equatorial Pacific. *Bull. Geol. Soc. Am.* **82**, 1489.
- Van Hinte, J.E., 1965. The type Campanian and its planktonic Foraminifera. *Koninkl. Ned. Akad. Wetenschap. Proc. Ser. B*, **68** (1), 8.
- Vervloet, C.C., 1966. Stratigraphical and Micropaleontological Data on the Tertiary of Southern Piedmont (Northern Italy). Thesis, Univ. Utrecht. Utrecht (Schotanus & Jens).
- Vigneaux, M., Magne, A., Veillon, M. and Moyes, J., 1954. *Compt. Rend. Acad. Sci. Paris*, **239**, 818.
- Wentworth, C.K., 1922. A scale of grade and class terms of clastic sediments. *J. Geol.* **30**, 377.

12. SEDIMENT MASS PHYSICAL PROPERTIES — PANAMA BASIN AND NORTHEASTERN EQUATORIAL PACIFIC¹

George H. Keller and Richard H. Bennett, National Oceanic and Atmospheric Administration, Atlantic Oceanographic and Meteorological Laboratories, Miami, Florida

ABSTRACT

Leg 16 provided a rare opportunity to conduct a detailed study of the sediment mass physical properties from depths greater than a few meters. Data presented here, with the exception of shear strength, are derived from shore-based laboratory analyses rather than the shipboard tests which have normally been reported for previous legs. This study indicates that there is no apparent relationship between variation of mass physical properties and the age of the sediment or the rate of sedimentation. The greatest single factor influencing the physical properties appears to be the depth of burial. Based on this study it is possible to delineate the characteristic physical properties of the six prominent sediment types encountered on Leg 16. In all but one test the samples were found to be overconsolidated. It is felt that these sediments are not overconsolidated in the sense that the term is used in soil mechanics but display this characteristic as a result of some form of diagenetic bonding developed during deposition. At only one of the eight sites of Leg 16 was porosity found not to decrease appreciably with depth. This condition may, in some way, correlate with the increased content of clay-size material relative to the other sites.

INTRODUCTION

Diagenetic changes from a soft deep-sea sediment to a marine sedimentary rock have been of utmost interest for many years. In recent years, a relatively new approach, the detailed analysis of the mass physical properties of deep-sea sediment cores, has received limited use in the study of these changes (Arrhenius, 1952; Richards, 1961, 1962). These early attempts have been hindered by the relatively short sediment cores (3 to 10 m) taken from oceanographic vessels. It was not until 1961, with the experimental Mohole drilling off Guadalupe Island, that deep-sea deposits were sampled below a depth of about 25 meters. This project provided Rittenberg et al. (1963), Hamilton (1964), and Moore (1964) with the opportunity to study selected mass physical and chemical properties of the 170 meters of sediment overlying basaltic basement. With the advent of the Deep Sea Drilling Project (DSDP) in 1968, continuous sampling to depths of 700 to 800 meters below the sea floor became a reality. Although many significant data have been collected by DSDP, only gross descriptions of the samples and their mass properties have been published in the respective cruise reports.

During Leg 16 specific attention was given to the examination of sediment mass physical properties as well as to the various shipboard test procedures used in the determination of these properties. Evaluation of these procedures is the subject of a separate section in this volume (Chapter 13). In conjunction with the "standard" shipboard tests, e.g., GRAPE density and porosity, and water

content, approximately 295 shear strength tests were made. In addition, 410 ten- to fifteen-gram subsamples were collected from the least disturbed sections of the cores and returned to a shore laboratory (N.O.A.A., Atlantic Oceanographic Laboratory, Miami) for bulk density, porosity, water content, and grain density determinations. An additional thirteen whole core samples (7 cm in length) were taken for later study of consolidation characteristics.

Leg 16 has provided the opportunity for making one of the most thorough studies of sediment mass physical properties of DSDP cores to date. Not only can we report on samples from depths as great as 500 meters and as old as late Cretaceous, but the study has yielded data on specific sedimentary deposits, e.g., zeolitic clays, radiolarian and diatom oozes, and chalks. These deeper samples have provided the opportunity to examine an important part of the diagenetic processes at a number of sites in the eastern Pacific.

The determination and understanding of mass physical properties of deep-sea sediments are as important to any study of diagenesis as they are in foundation engineering. As has been demonstrated by Hamilton (1959, 1964) and Moore (1964), if the depositional history of the ocean basins is to be unraveled, an understanding of sediment mass properties, particularly consolidation characteristics, must be attained.

This discussion is based on those data which have been determined in a shore laboratory, e.g., wet bulk density, water content, porosity, Atterberg limits, average grain density (specific gravity), and consolidation characteristics. The only exception is the shear strength measurements which were made aboard the *Glomar Challenger*.

¹The original data will be compiled in a NOAA-AOML Technical Report to be published in 1973 and available through the authors.

Shipboard measurements of bulk density and porosity have been reported in the site chapters but have not been included here because of the questionable nature of some of these results (Bennett and Keller, Chapter 13).

ANALYTICAL TECHNIQUES

There is no such thing as an undisturbed sediment core, and the cores taken by the Deep Sea Drilling Project are much more disturbed than standard piston or gravity cores. A concerted effort was made to sample only those portions of the core where disturbance was observed to be minimal.

Shore-based measurements of wet bulk density, water content, porosity, and average grain density were made on 10- to 15-gram subsamples taken from the cores immediately after they were split aboard the *Glomar Challenger*. Each subsample was placed in a polyethylene vial (completely filling it) which was sealed with electrical tape and in turn was placed in a small plastic bag and sealed in a larger plastic bag containing a damp paper towel in order to maintain high humidity within the bag. The sealed bag was kept under refrigeration to further reduce any chances of moisture loss.

A brief explanation of analytical procedures used for the laboratory determination of bulk density, water content, porosity, and grain density was presented as part of the initial discussion of sediment mass physical properties of DSDP 155 (Chapter 2) and will only be touched on briefly in a few instances.

Thirteen 7-centimeter lengths of core were removed prior to splitting of the core aboard ship for later consolidation tests at the shore laboratory. These samples were primarily taken from the core catcher sleeve portion of the core barrel because of the relatively undisturbed condition of this portion. Samples were carefully packaged to insure against disturbance and moisture loss and then hand-transported to the laboratory.

All consolidation tests were made with an Anteus Back Pressure Consolidometer. A description of this apparatus, and the testing procedures employed, have been thoroughly discussed by Lowe et al (1964). The unique aspect of the back pressure technique is that as hydrostatic pressure is applied to the sample, any gas bubbles entrapped in the pore water as a result of removing the sample from its original hydrostatic pressure are redissolved. For samples taken from environments of high hydrostatic pressure, the in situ pressure cannot be attained, but a maximum back pressure of 150 psi probably insures that all gas is redissolved.

Shear strength measurements were made on board the *Glomar Challenger* using two techniques new to the Deep Sea Drilling Project, the laboratory vane shear and Swedish Fall Cone. The vane shear test consists of inserting a small four-bladed vane into the sample and applying an increasing torque until a shear occurs (Evans and Sherratt, 1948). This particular instrument and its use with submarine sediments have been more fully discussed by Richards (1961). Vane rotation for all tests was six degrees per minute. A laboratory vane shear test in clays and clayey sediment is equivalent to an undrained shear test,

e.g., the unconfined compression test. In this case, vane shear strength is considered equal to the cohesion or one-half the compressive strength. A more complete discussion of the vane shear test is presented by Evans and Sherratt (1948) and The American Society for Testing and Materials (1957).

Swedish Fall Cone measurement of shear strength is widely used in Europe, where it has been adequately calibrated for the soils as well as the commonly used samplers. Although this test is not frequently used in the United States, its simplicity made it appealing for use on the Leg 16 cores. The test is basically one of dropping a weighted cone from a specific height and measuring the depth of its penetration into the sample. Penetration is then related to shear strength (S) by

$$S = K Q/h$$

where K is a constant which depends on the cone angle and the sampler design (as the latter influences sample disturbance), Q is the cone weight, and h the penetration depth of the cone (Hansbo, 1957). A K value of unity was used in determining the shear strength results presented here. In the few instances where results from the fall cone could be compared with the vane shear, the fall cone was always found to give higher values by a factor ranging from 1.1 to 3.0. It must be pointed out that the Swedish Fall Cone (Geonor model G-200) was not calibrated for the sampler used aboard the *Glomar Challenger* and caution must be exercised in the interpretation of these data. All but twenty fall cone measurements were made with the 400 g, 30° cone. The 100 g, 30° cone was used with the others. Owing to the manner in which the cores were processed aboard the *Glomar Challenger*, it was necessary to make most fall cone tests on the cores after they were split in half. All such tests were made in a plane parallel to the bedding rather than perpendicular to it as in the normal testing procedure. The effect of this procedural change is unknown and undoubtedly would vary with the degree of sample disturbance and sediment type.

The majority of the vane shear tests were made at right angles to the bedding in the lower section of each barrel between the core catcher and the steel sleeve. Not only was this usually the least disturbed section of the barrel, but it also allowed the vane to be inserted into the core and the sample tested before the sediment was removed from the barrel.

TEST RESULTS

For the purpose of this discussion, the eight sites from Leg 16 have been placed in two groups, the Panama Basin (DSDP 155, 157, and 158) and the northeastern equatorial Pacific (DSDP 159-163). Although distinct differences are seen in the mass physical properties between the sites, a certain degree of similarity exists within each grouping.

Panama Basin

The three Panama Basin sites are located on the major ridges (Coiba, Cocos, and Carnegie) which border the basin. Lithologies at the three sites are relatively similar with an upper section of nannofossil chalk ooze rich in calcareous and siliceous microfossils and volcanic glass

overlying a chalk ooze which grades down to a chalk with some chert stringers at a depth of about 430 meters. Only DSDP 155 was sampled below this depth and here interbedded claystone and moderately indurated nannofossil marl and marly clay predominate to a depth of 485 meters. A nannofossil chalk, locally dolomitized and rich in altered volcanic debris, constitutes the remainder of the sedimentary section above basalt which occurs at a depth of 519 meters.

DSDP 155

Unfortunately only the lowermost portion of the hole was cored (434–536 m); however, bulk density and porosity data are available for the upper interval from DSDP 84, 176 kilometers to the west, which is probably reasonably similar to DSDP 155. In order to present a more complete discussion of the physical properties at this site, we have taken the liberty of using the section bulk densities (average bulk density per 150-cm section) and GRAPE porosities from DSDP 84 for the interval from 0 to 250 meters. Although the reliability of these data is not believed to be as good as that of our laboratory measurements (for the section from 434–500 m at DSDP 155), it is felt that they do provide some indication of the characteristics of the overlying deposits in this area.

Wet bulk density increases gradually to a depth of about 444 meters where a noticeable offset in the density profile occurs (Figure 1). Here, in conjunction with the occurrence of a claystone-marl sequence, densities are on the order of 1.65 to 1.80 g/cc versus 1.80 to 1.92 g/cc for the immediately overlying sediment. Although prominent local variations occur, bulk density tends to increase slightly with depth within this sequence (444–480 m). These variations reflect the layered nature of the sequence, with the claystone intervals commonly displaying lower densities than the adjacent marl. The occurrence of chalk in the lower 16 meters of the section is reflected in the density profile, where values suddenly increase, ranging from 2.00 to 2.18 g/cc.

The porosity profile tends to be a mirror image of the density profile. In the uppermost part of the section, porosities are high (85 %) and slowly decrease with depth to 50 per cent at 444 meters. Here the porosity increases sharply to 65 per cent, reflecting the claystone-marl sequence. Little change in porosity occurs within the next 20 meters, but below 464 meters the marly claystone sediments display a slight decrease in porosity with depth. Locally, higher porosities are usually found to be associated with the claystone layers. The underlying chalk is quite distinct, with porosity values as low as 32 per cent. In viewing the entire sediment section (DSDP 84 and 155 data), porosities are seen to decrease on the order of 62 per cent within the 521-meter interval.

Water content at this site, defined as per cent of the sediment by dry weight, varies with depth in much the same way as does porosity. Where the claystone-marl interval is encountered, a distinct offset in the profile reflects a relative increase in water content, on the order of 70 per cent. Towards the lower part of the sequence, a gradual decline in water content occurs until the chalk zone is reached (480 m), where a pronounced decrease of about

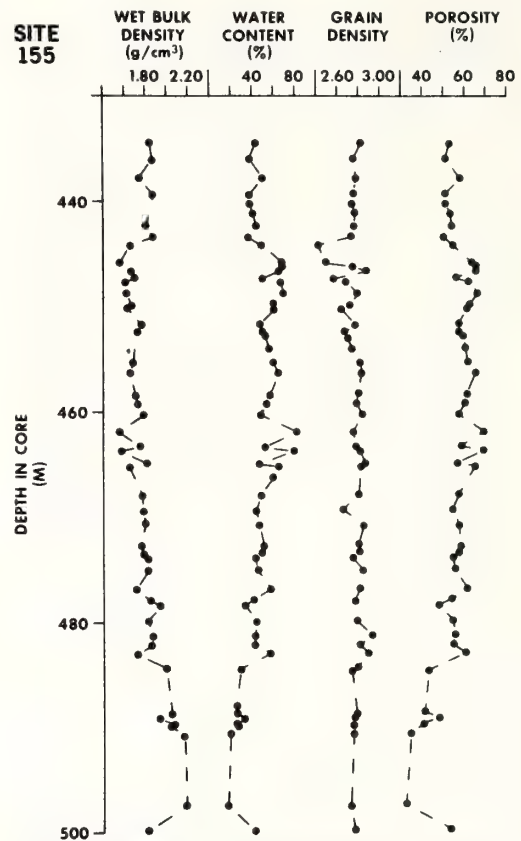


Figure 1. Variation of physical properties with depth, DSDP 155.

50 per cent is observed. Local anomalies between 444 and 480 meters reflect the relatively high water content associated with the claystone layers.

Grain density normally varies relatively little with depth except when major lithology changes are encountered. At DSDP 155 the overall variation is minimal, but the claystone-marl sequence can be seen to possess a slightly higher grain density (ranging from 2.76 to 2.82) than either the overlying marl or the underlying chalk. Minor variations along the profile are attributed to the claystone layers which commonly have lower grain densities (2.49 to 2.54).

The degree of symmetry and the similarity of the profiles is quite distinct and appears to be more pronounced here than at the other sites. This possibly may be attributed to the greater burial depth to which these samples have been subjected. Within the interval cored at this site, there is a gradual increase in bulk density and a decrease in porosity and water content with depth; changes in these properties over the 86-meter interval are on the order of 21 per cent, 40 per cent, and 50 per cent respectively. Although local variations in grain density occur, there is

basically little change from top to bottom of the sampled section.

DSDP 157

Severe disturbance and mixing of the upper 198 meters of the core made mass physical properties analyses impractical throughout much of this interval. Only a very few measurements were possible in the upper 70 meters. Below 333 meters, core disturbance again precluded any laboratory measurements of physical properties. As a result, DSDP 157 provides relatively little data on these properties (Figure 2), and only broad generalizations are possible.

Bulk density varies only slightly (1.38 to 1.60 g/cc), increasing gradually with depth in the chalk ooze (0-240 m). Within this interval, the data indicate the occurrence of interlayering of finer grained sediment possessing lower densities. In the underlying sequence of semi-indurated chalk ooze, the distinct zone of low bulk density (252 m) probably corresponds to an interval of finer grained, less indurated sediment. Densities in the chalk (284-333m) appear to be more uniform and increase slowly with depth.

Local variations from the gradual decrease in porosity with depth are minor with only three anomalous zones of any significance evident from the profile (Figure 2). The relatively high values at 60 and 252 meters are probably associated with finer sediments as mentioned earlier, whereas the occurrence of burrows at 220 meters is believed to have resulted in the local increase in porosity and decrease in bulk density in that interval. The burrows serve to concentrate finer, less dense material.

Variations in water content with depth are usually much more pronounced than those of the other physical parameters. Thus, water content often serves as an indicator for variations in the sediment section that may not be readily apparent from other physical measurements. At DSDP 157, even with the limited data, there does not appear to be any major variation in the overall trend of decreasing water content with depth except for the anomalies at 60 and 252 meters. These two zones of relatively high water content are believed to be associated with intervals of finer grained sediment.

Except for the anomalous character of the grain density profile at 252 meters, relatively little change in density is seen throughout the sediment section. This interval of low

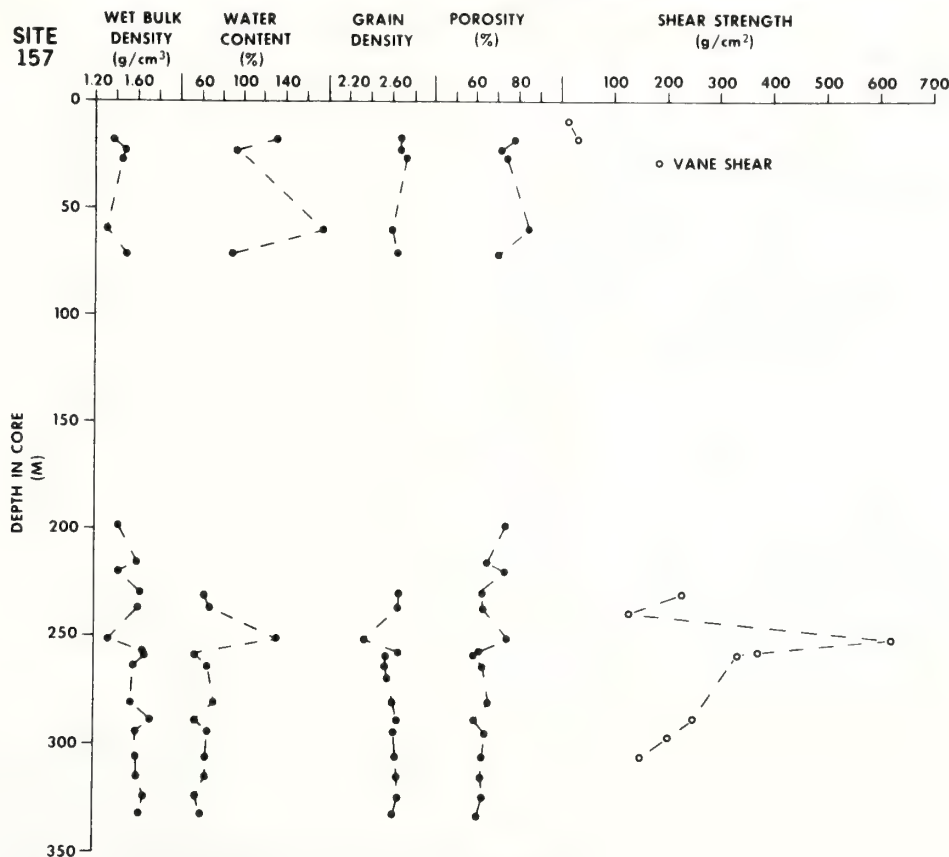


Figure 2. Variation of physical properties with depth, DSDP 157.

grain density may possibly be due to a relative increase in the occurrence of microfossils, but without a detailed examination of the sediment composition, an explanation is not readily available.

Unfortunately, core disturbance severely limited the number of vane shear tests that could be made at this site. Shear strengths in the lower section (230-300 m) were commonly on the order of 200 g/cm² except in the interval of 240 to 255 meters where values of 350 and 620 g/cm² were recorded. The anomalous nature of this 15-meter interval is clearly reflected in all the physical properties. The high shear strength observed in this zone is unusual in that relatively low strengths are commonly found in association with sediments of low density and high water content. An explanation for this higher strength is not apparent, but it possibly could be explained if a concentration of microfossils were found in this interval along with some degree of cementation.

The mass physical properties observed at this site indicate a gross uniformity of the sedimentary sequence sampled. The recorded variations are basically attributable to depth of burial. Wet bulk density is seen to increase while porosity decreases 18 and 22 per cent respectively from the top to the bottom of the sampled section. The absence of any sharp changes in bulk density and porosity with depth indicates that induration of the chalk sequence (240-335 m) is apparently a gradual process.

DSDP 158

The largest change in the mass physical properties with depth occurs within the upper 64 meters of the cored section. Here porosity and water content decrease on the order of 21 and 59 per cent respectively, while bulk density increases approximately 28 per cent. Overall, these same properties tend to be more or less uniform throughout the remainder of the section. Exceptions to this are three sections which display distinct changes in lithology. A sharp decrease in bulk density, with a correspondingly rapid increase in porosity and water content, occurs at 141 to 168 meters in association with a nannofossil ooze rich in Radiolaria, as well as large numbers of diatoms and foraminifera. Such a concentration of microfossils could explain the anomaly displayed by the respective profiles. These microfossils often contain a relatively large internal cavity which in turn is water-filled. These forms generally possess a much larger volume per unit of weight than rock particles of comparable size. Such unique properties could account for the low bulk density and the higher water content and porosity. However, a similar behavior of these properties would also be seen if a concentration of clay-size material occupied this interval. A more definitive explanation for these rapid changes is not feasible without closer examination of the sediment composition.

The marked increase in density and decrease of water content and porosity in the underlying interval (170-182 m) appear to reflect the occurrence of an increased concentration of volcanic ash. The associated increase in grain size would result in the higher densities and relatively low water content.

The most distinct offset of the respective profiles occurs at 209 meters where the lowest bulk density and some of

the highest water content and porosity values were recorded. Although the reason for this severe change in the properties must await further analysis, indications are that these values reflect the presence of a great abundance of Radiolaria and diatoms. The extremely low grain densities recorded for this interval lend support to this assumption. Grain densities of 2.30 reflect the concentration of low specific gravity material such as Radiolaria and diatoms, which are primarily composed of opaline silica with a specific gravity of 2.10.

Grain density varies relatively little with depth and only at 160 and 208 meters are any significant changes recorded. These relatively low values undoubtedly reflect the increased abundance of a low specific gravity mineral such as opaline silica, as noted above.

Vane shear measurements reveal a rapid increase in shear strength to a depth of about 60 meters. Below this horizon the increase is gradual until the anomalous interval at 141 to 158 meters, where a sharp increase in strength is recorded. This increase, in a zone of relatively low bulk density and high water content, presents a problem similar to that noted for DSDP 157. No apparent explanation is available for this association, unless there was a possible concentration of microfossils, as suggested earlier, which would cause these increased strengths.

Although the Panama Basin sites are some distance apart, generalizations about the mass physical properties appear possible. Indications are that the physical properties undergo their most rapid change with depth within the uppermost sedimentary sequence (0-70 m). Below depths of about 70 to 100 meters, changes in bulk density, porosity, and water content tend to be rather gradual except in zones associated with local variations in lithology. In some cases it appears there may be large intervals of the section where there are no changes in these properties, such as in the lowermost parts of the cores from DSDP 157 and 158 (Figures 2 and 3). Examining the deeper section cored at DSDP 155, it can be seen that the respective parameters are gradually changing with depth.

Porosities are seen to decline from about 80 to 64 per cent in the upper 300 meters. If this were extrapolated to 500 meters based on DSDP 155 data, porosity is found to reach a low of 32 per cent, or an overall decrease of 63 per cent through the 500-meter interval. This is in considerable contrast to the very small (5 %) decrease Hamilton (1964) found in the 136-meter interval sampled by the experimental Mohole at the Guadalupe site.

Similarly, using the recorded values from the three sites, water contents are found to decrease on the order of 86 per cent through the 500-meter interval, whereas bulk density increases about 61 per cent. Viewing the mass physical properties, the transition from nannoplankton chalk ooze to chalk is quite gradual, as might be anticipated.

Northeastern Equatorial Pacific

The stratigraphic section sampled at the five sites in the northeastern equatorial Pacific is basically similar. A relatively thin layer (10-30 m) of zeolitic brown clay blankets the area. Underlying this clay, a gradation is seen from a calcareous clay to a nannofossil chalk ooze down to the

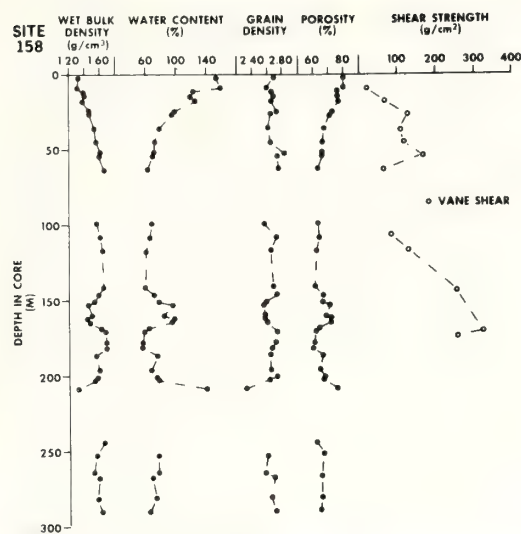


Figure 3. Variation of physical properties with depth, DSDP 158.

top of the basalt. Alternating sequences of clay and marl are common as are thin chert stringers in the lower part of the cored interval. Local zones of ferruginous clay rich in Radiolaria occur at various depths throughout the section. Of particular note at a number of the sites is the occurrence of ferruginous microaggregates in a clay matrix in a relatively thin zone just above the basalt.

DSDP 159

Sediments at DSDP 159 consist of Radiolarian clay overlying a sequence of alternating layers of calcareous clay and marl which grades to a nannofossil chalk ooze in the lowermost section.

Bulk densities are relatively low throughout the sampled interval, ranging from 1.29 g/cc at 10 meters to 1.54 g/cc at 88 meters. Little change in density is observed in the upper 30 meters of the section. A somewhat anomalous profile is seen for the interval of 30 to 58 meters, where densities are lower than those of the overlying material. Commonly, bulk density increases with depth owing to the effect of overburden; however, in this instance it appears that the abundance of clay in this sequence has strongly influenced the observed density profile. At 58 meters bulk density increases markedly and continues to increase gradually to the base of the section at 88 meters (Figure 4). This pronounced change clearly reflects the combined effects of less clay-size material and the increasing degree of consolidation found at depth.

As shown at this site, water content seems to amplify the lithologic changes. The high peaks (water contents of 180 % or higher) clearly reflect the presence of clay layers, whereas the lower values are indicative of the interlayered marls. A similar relationship is displayed by porosity, but to a lesser degree.

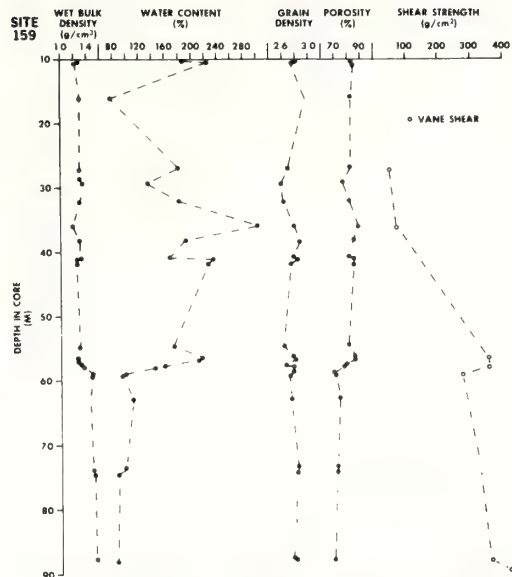


Figure 4. Variation of physical properties with depth, DSDP 159.

Remarkably little variation is seen in both wet bulk density and porosity throughout the sampled interval. An overall density increase of 16 per cent and a 6 per cent decrease in porosity are relatively minor. Hamilton (1964), in reporting a similar observation, attributed these small changes to low rates of deposition, the great age of the sediment, and interparticle bonds behaving as a chemical cement. Similar porosity characteristics with depth are found at other sites and are mentioned later.

Owing to the high overall degree of disturbance at this site, the shear strengths (Figure 4) have only a limited value and caution must be exercised in the use of these data. Strengths increase gradually with depth to about 59 meters where the base of the interlayering clay-marl sequence occurs. Below this interval the section consists primarily of a marl ooze which appears, based on the bulk density and water content profiles (Figure 4), to be increasing in degree of consolidation with depth.

Vane shear strengths recorded at 59 and 88 meters are questionable due to the development of cracks around the sample during the shear test. The low vane value at 59 meters is particularly suspect since in the same interval bulk density and water content markedly increase and decrease respectively; shear strength would normally be expected to increase in this case. Fall cone measurements in the same interval give considerably higher strengths than the vane value and appear to more adequately reflect the relative properties of the denser marl sequence. The vane value at 88 meters, although probably a bit low, agrees reasonably well with the fall cone measurements at 89.5 meters. However, both of these values appear much lower than might be anticipated considering that bulk density and water content are essentially at their highest

and lowest respective limits in the sampled section. At best, the data presented here can only serve as a crude generalization of the anticipated shear strengths at this site.

DSDP 160

Variation with depth of lithology and physical properties is relatively minor at this site in comparison to the others from Leg 16. The sediment column consists primarily of 27 meters of zeolitic clay overlying 81 meters of nannofossil chalk ooze, with a thin (1 m) layer of calcareous clay, rich in ferruginous aggregate, above the basalt in which the site bottomed.

As shown in the respective profiles (Figure 5), the zeolitic clay and the underlying nannofossil chalk ooze display distinctly different mass physical properties. The zeolitic clay possesses relatively low bulk densities (1.30 to 1.33 g/cc and distinctly high water contents (170 to 290 %) and porosities (82 to 89 %). Grain densities are also found to be relatively higher (2.70 to 2.84) in the clay.

Aside from two slightly anomalous zones in the chalk ooze sequence, the section appears to be homogenous. Within this sequence (27-106 m), bulk densities increase gradually with depth from 1.47 g/cc at 35 meters to 1.64

g/cc at 106 meters. Similarly, water content and porosity display an overall decrease with depth through the same interval. These overall trends are considered characteristic of a relatively homogenous sequence which is undergoing increasing consolidation with depth of burial.

The explanation for the anomalous behavior of the bulk density, water content, and porosity profiles at a depth of 58 meters is not entirely clear. However, the increased abundance of ferruginous microneules and a slightly higher calcium carbonate content may have been responsible for the observed properties. The slightly smaller offset in the profiles at 87.5 meters may reflect the higher degree of consolidation of the chalk ooze as reported in the lithologic log.

The slight decrease in bulk density and grain density with the corresponding increase in water content and porosity at the base of the hole reflects the presence of the thin calcareous clay zone overlying the basalt.

A look at the respective profiles (Figure 5) indicates that over the entire interval (106 m) of the sampled section, bulk densities increase approximately 26 per cent, whereas porosity decreases about 23 per cent. Water content on the other hand displays a much more pronounced decrease (66 %) over the same interval. Examining only

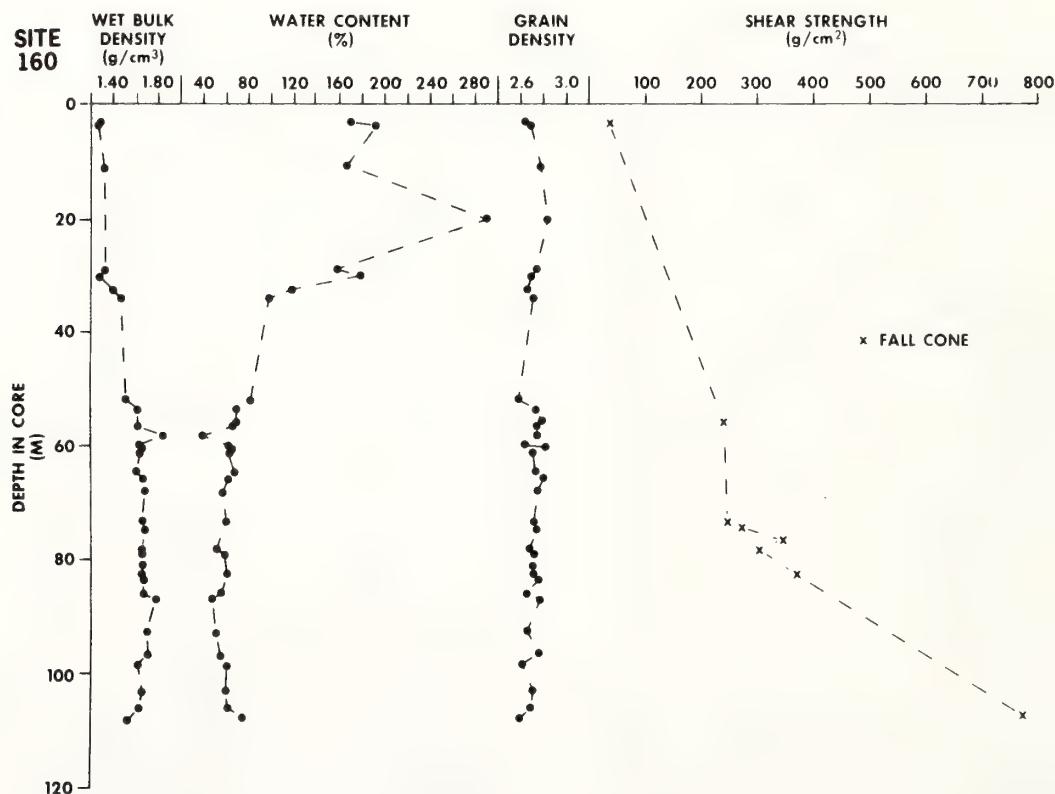


Figure 5. Variation of physical properties with depth, DSDP 160.

the interval from 27 to 106 meters (the chalk ooze), bulk densities are seen to increase 12 per cent as porosities and water contents decrease 15 and 38 per cent respectively.

Unfortunately, only limited shear strength data are available for this site. It is equally unfortunate that the available data are not from intervals which would provide a valid comparison between the strength characteristics of the zeolitic clay and the underlying chalk ooze. Based on the other physical properties, it could be expected that a noticeable contrast would exist between the shear strengths of these two distinct units. Although the strength of zeolitic clay can be quite high as reported at DSDP 163, it would probably be lower than that of the denser and drier chalk ooze. The few observations reveal only that the overall profile is indicative of the anticipated increase in shear strength with depth in a relatively homogenous unit (Figure 5).

DSDP 161

Four major lithologic units comprise the stratigraphic section at DSDP 161. The uppermost is a thin veneer (2 m) of zeolitic clay which blankets a 155-meter section of relatively homogenous nannofossil marl-chalk ooze. Below this unit a nannofossil chalk with less marl occupies the 155- to 200-meter interval. The lowermost sedimentary unit (200-245 m) is a clayey radiolarian ooze with an abundance of ferruginous microaggregates.

Of the eight sites studied on Leg 16, DSDP 161 provided the best series of subsamples for the measurement of mass physical properties. Although sample disturbance was still a problem, there were fewer zones of severely disturbed material than usual.

Except for minor local variations, bulk densities increase gradually from 1.47 g/cc in the zeolitic clay to 1.67 g/cc at a depth of 140 meters in the nannofossil chalk ooze. A corresponding decrease in water content and porosity occurs in this same interval. A reversal in these general trends is noted in the 140- to 155-meter interval, although no major change in lithology was recorded. Here bulk density actually decreases about 11 per cent relative to that of the overlying material. A somewhat comparable increase in water content and porosity is associated with this section.

The change from a chalk ooze to a chalk at 155 meters is clearly reflected in the physical properties (Figure 6). At this contact, bulk density increases sharply and, although it tends to decrease with depth to 200 meters, it is relatively higher than that of the immediately overlying material. The general slope of the water content, porosity, and bulk density profiles associated with the chalk are somewhat anomalous in that just the opposite slopes would be anticipated because of the increasing degree of consolidation with depth.

The radiolarite in the lower 45 meters of the core is distinctly characterized by its mass physical properties. Bulk densities are the lowest (1.36 g/cc, recorded throughout the sampled interval, whereas water contents and porosities are the highest measured in the core. These extreme values are not readily explained by the available data; however, the combination of intense burrowing and the abundance of ferruginous aggregates, clay, Radiolaria, and diatoms may well account for the observed properties.

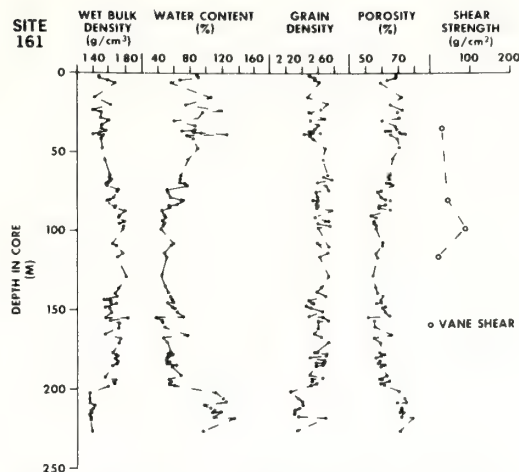


Figure 6. Variation of physical properties with depth, DSDP 161.

The radiolarite is also distinguished by very low grain densities, owing to the high opaline silica content of the Radiolaria.

Although a limited number of shear strength measurements were made at this site, it was determined that sample disturbance in these intervals was so great that the measured values were essentially that of the remolded strength. These remolded strengths for the chalk ooze were on the order of 20 to 40 g/cm².

Despite the distinct lithologic changes encountered in the cored section, the variation of physical properties with depth appeared to be somewhat unusual. Although distinct changes are expected to reflect different lithologies, an overall trend of increasing bulk density and decreasing water content and porosity would normally be anticipated with increasing depth. No such trend is observed at this site; in fact, higher water contents and porosities occur in the lower part of the section than in the upper few meters of the core. The lower portion of the core did not appear to be excessively disturbed, certainly not more than other intervals.

DSDP 162

The sedimentary section consists of about 26 meters of interlayered chalk ooze, clayey radiolarian marl ooze, and ferruginous radiolarian clay overlying a 37-meter thickness of relatively homogenous clayey radiolarian ooze. The remainder of the 150-meter section is primarily a clayey radiolarian marl ooze with some ferruginous clayey radiolarian ooze and an occasional chert layer. Only the lowermost 6 meters of this section differs in that it is a ferruginous zeolitic clay.

The clay intervals within the interlayering sequence (0-26 m) display considerably higher water contents (100 % higher) and porosities (24 % higher) than the adjacent chalk ooze. Similarly, the wet bulk densities of the clay are approximately 21 per cent lower than those of the chalk ooze. Bulk density and porosity are remarkably uniform within the clayey radiolarian ooze sequence (26-63 m),

varying little from 1.20 g/cc and 85 per cent respectively. An examination of grain densities indicates that the section is not quite as homogenous as bulk density and porosity values might suggest. Although there is some variation in water content, it is relatively minor, and the entire sequence is found to possess a water content on the order of 245 per cent.

Insofar as bulk density and porosity are concerned, the remainder of the section (63-140 m) is similar to that of the overlying clayey radiolarian ooze. Variations in either parameter are only on the order of 5 to 6 per cent throughout the 87-meter interval. Water contents and grain densities appear to vary slightly more.

DSDP 162 displays a rather unusual variation of physical properties with depth. Not only are the bulk densities and porosities remarkably uniform throughout the lower 123 meters of section, but lower densities as well as higher porosities and water contents are found at depth than in the uppermost portion of the section (Figure 7). Bulk density decreases about 20 per cent, whereas water content and porosity increase 116 per cent and 12 per cent respectively within the cored interval. These variations are anomalous in that they are just opposite to those commonly reported in a depth profile. Exceptions have been reported, however, such as Hamilton's (1964) finding of relatively little change in porosity (5 %) through a 136-meter interval of deep-sea deposits off Guadalupe Island and Meade's (1963) reporting of an increase in porosity with depth in fine-grained sediments in the San Joaquin Valley of California. Meade attributed the anomalous condition to variations in grain size, high diatom content, and the type of exchangeable cation adsorbed on the clay minerals. A detailed analysis of the DSDP 162 core has not been completed, so a definite explanation for the observed variation cannot be given. There is good reason to believe,

however, that the very high concentration of Radiolaria at this site may have strongly influenced these physical properties. Evidence for this is suggested by the findings of other studies where it has been shown that a similar relationship of these three properties often occurs in zones relatively rich in the skeletal remains of microorganisms (A.F. Richards, 1962, personal communication). This relationship is attributed to the unique shape and internal structure of these forms.

Unfortunately, only a small number of shear strength measurements were made at this site. In one of the upper clay zones, a shear strength of 88 g/cm² was recorded at a depth of 9 meters. Lower in the section (84-95 m) a series of fall cone tests showed strengths from 224 to 264 g/cm² for the clayey radiolarian marl ooze and the ferruginous clayey radiolarian ooze sequence. Because of so few measurements, little more than a presentation of the observed values is feasible (Figure 7).

DSDP 163

Lithologically, the sample sequence at this site can be divided into four major units. The uppermost consists of 28 meters of ferruginous radiolarian zeolitic clay which, in turn, overlies 112 meters of clayey radiolarian ooze with thin porcelaneous chert beds scattered throughout the section. Underlying this interval is a relatively thin zone (22 m) of ferruginous zeolitic clay with a few chert beds. The lowermost part of the sedimentary section (162-276 m) is a nannofossil chalk with some flinty cherts.

Both the zeolitic clay and the clayey radiolarian ooze are characterized by very low bulk densities as well as high water contents and porosities. Although the wet bulk densities are basically similar (1.22 g/cc), there is a decided contrast among the other physical properties of these two units (Figure 8). Water contents, grain densities, and porosities are notably greater in the zeolitic clay than in the radiolarian ooze. Water contents of 200 to 260 per cent and porosities of 85 to 90 per cent as are found at this site characterize the zeolitic clays blanketing much of the Pacific basin (Keller and Bennett, 1968). The underlying clayey radiolarian ooze displays a remarkably low grain density of 2.00, which undoubtedly reflects the high concentration of Radiolaria and diatoms found in this section.

The overall trend with depth of the various properties is interrupted by a zone of ferruginous zeolitic clay (140-162 m). Here, in respect to the established trend, the zeolitic clay displays a slight decrease in bulk density along with increases in water content and porosity. Such a relationship is indicative of zeolitic clays, just as it is in the surface deposits, but in this instance the water contents and porosities are slightly lower and the bulk densities higher owing to the effective overburden pressure.

The nannofossil chalk which comprises the lowermost sedimentary unit, contrasts sharply with the overlying material. Bulk densities are much higher, ranging from 1.72 to 1.90 g/cc, while water contents and porosities are considerably lower, varying from 54 to 35 per cent and 60 to 49 per cent respectively.

At DSDP 163 the "normal" trend of increasing bulk density and decreasing water content and porosity with depth is clearly displayed. Within the sampled section,

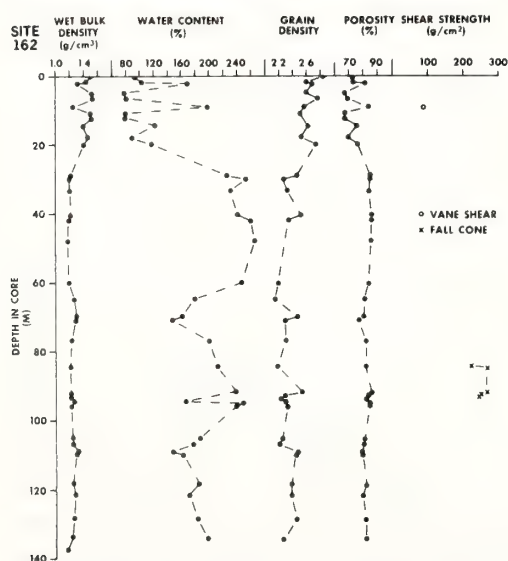


Figure 7. Variation of physical properties with depth, DSDP 162.

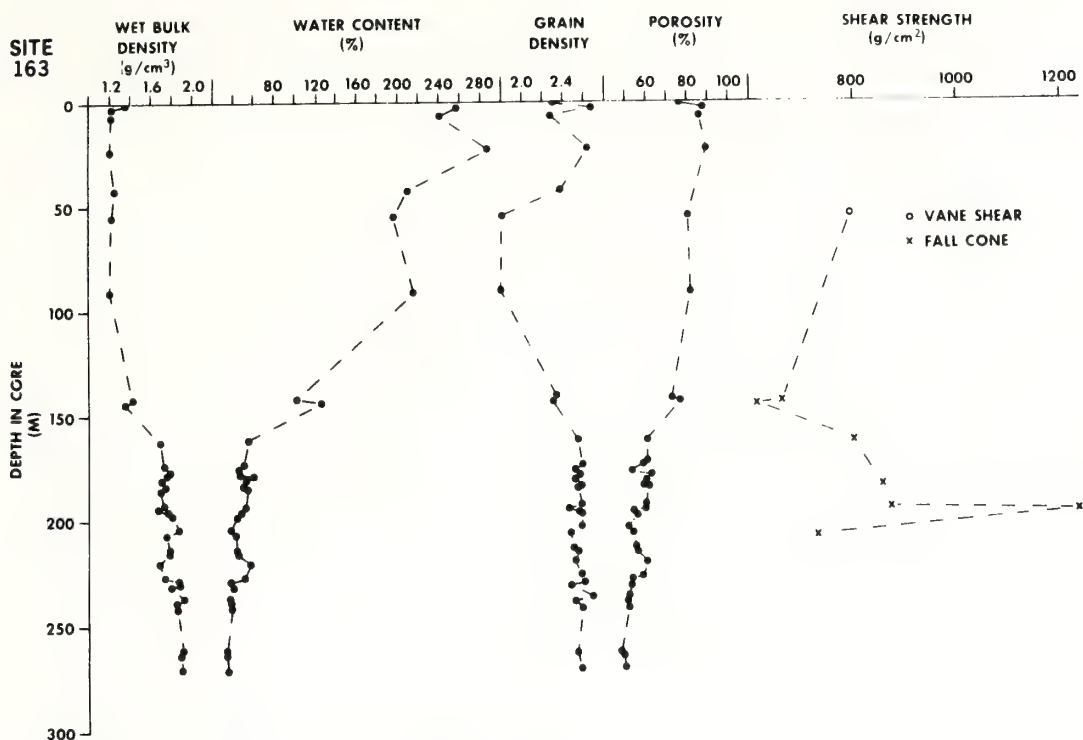


Figure 8. Variation of physical properties with depth, DSDP 163.

density is found to increase from 1.36 to 1.90 g/cc (41 %), whereas water content decreases about 73 per cent and porosity by about 36 per cent.

Shear strength measurements were made in all the lithologic units except the uppermost zeolitic clay. Based on only a few measurements, a broad generalization can be made in regard to the overall strength characteristics of the sediment section. The clayey radiolarian ooze sequence appears to have a relatively high shear strength, on the order of 800 g/cm², whereas the ferruginous zeolitic clay (140-162 m) possesses a notably lower strength (610-660 g/cm²). As might be anticipated, the underlying denser chalk displays much higher values. The sharp decrease in shear strength at 208 meters is associated with a zone of mottling and may possibly reflect the slight increase in water content and decrease in bulk density.

Consolidation Characteristics

Consolidation is used here in the soil mechanics sense, meaning the reduction of volume due to an imposed load. The consolidation test is commonly employed by the foundation engineer to determine the rate and amount of settlement of a structure, but here it is used basically to assist in understanding the depositional behavior of deep-sea sediments.

The consolidation test, in the very simplest of terms, consists of loading a small free-draining, confined, cylindrical sample of sediment with increasingly larger normal

loads, while recording the rate and amount of volume decrease under each load. Results of this test are usually displayed in a plot of void ratio (volume of voids divided by the volume of solids) versus the log of normal pressure, commonly referred to as an e -log p curve. It is this curve that serves as the basis for settlement calculations as well as determining the preconsolidation pressure (the greatest load to which a sediment sample has been subjected). A thorough discussion of the consolidation theory as well as testing procedures can be found in most soil mechanics texts and only a limited discussion is presented here.

Consolidation tests normally provide a means whereby the depositional history of a deposit can be determined. In soil mechanics terminology a deposit is said to be *normally consolidated* if the effective overburden pressure is equal to the preconsolidation pressure. The effective overburden pressure acting on the sample in place is the combined wet bulk density of the overlying sediment minus the bulk density of water, which, in this case, is an assumed average of 1.026 g/cc. If the overburden pressure is greater than the preconsolidation pressure, the sediment is said to be *underconsolidated* (the sediment has not yet consolidated under its present load), and, if the overburden pressure is less than the preconsolidated pressure, the deposit is considered to be *overconsolidated*. Underconsolidated sediments commonly occur in areas of rapid deposition such as deltas, owing to insufficient time for the drainage of pore water (Moore, 1961). On the other hand, overcon-

solidated sediments are found where considerable erosion has removed much of the overburden or in deposits which have been desiccated to some degree.

As noted earlier, the degree of sample disturbance of the *Glomer Challenger* cores is considerable and subsampling had to be done very selectively. Unfortunately, even with the great care in subsample selection and later transport to the laboratory, only four of the thirteen samples collected provided usable results from the consolidation tests.

To date, consolidation tests have been made on approximately twenty-five deep-sea samples from depths greater than 9 meters below the sea floor. The first such tests were those by Hamilton (1964) on the Mohole (Guadalupe site) samples and more recently by W. Bryant (1972, personal communication) on samples collected in the Gulf of Mexico during Leg 10 of the Deep Sea Drilling Project.

The four samples discussed here are from the northeastern equatorial Pacific (DSDP 160, 161, and 163) and represent depth intervals of 9, 63, 81, and 142 meters respectively. At DSDP 160 two subsamples from depths of 9 and 63 meters were tested and found to possess a considerable degree of overconsolidation (Figures 9 and 10). Although sample disturbance pressure from the e -log p curves to within more than 20 or 25 per cent based on the graphical method of Casagrande (1936), the overconsolidated nature of these sediments is clearly evident by the contrasting low overburden pressures. The zeolitic clay at 9 meters (DSDP 160) appears to be considerably more overconsolidated than the nannofossil chalk ooze sampled at 63 meters. In a chalk ooze at a depth of 81 meters (DSDP 161) a similar, but less pronounced overconsolidated condition is observed (Figure 11). At a depth of 142 meters (DSDP 163A), a zeolitic clay displays an essentially normally consolidated characteristic (Figure 12).

The predominant overconsolidated characteristics found here were also reported by Hamilton (1964) in his study of Mohole (Guadalupe site) cores to a depth of 136 meters. It is obvious that these deep-sea sediments have not been stripped of a significant amount of overburden by

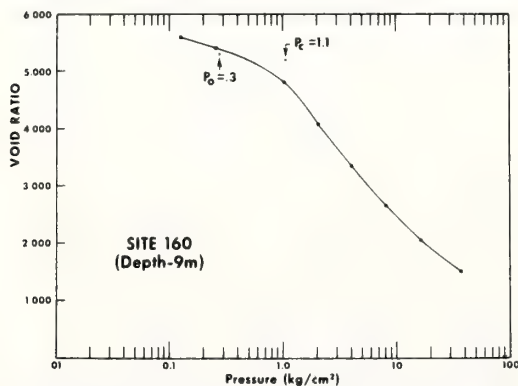


Figure 9. Void ratio versus log pressure curve. P_c = pre-consolidation pressure, P_o = overburden pressure. DSDP 160, 9 meter depth.

erosion nor have they been subjected to desiccation, the two usual causes of overconsolidation. Although not yet

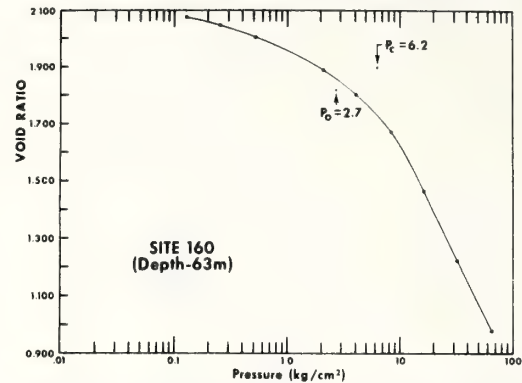


Figure 10. Void ratio versus log pressure curve. P_c = pre-consolidation pressure, P_o = overburden pressure. DSDP 160, 63 meter depth.

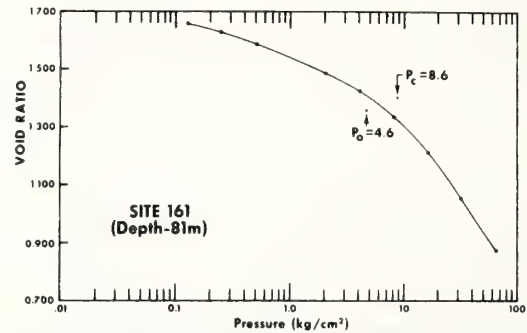


Figure 11. Void ratio versus log pressure curve. P_c = pre-consolidation pressure, P_o = overburden pressure. DSDP 161, 81 meter depth.

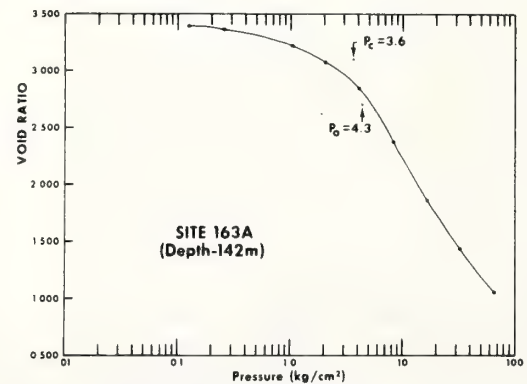


Figure 12. Void ratio versus log pressure curve. P_c = pre-consolidation pressure, P_o = overburden pressure. DSDP 163, 142 meter depth.

proven, it appears that the extremely slow rate of deposition and the great age of deep-sea sediments may be responsible for this apparent overconsolidated state. Earlier investigators have postulated that the slow deposition rate is responsible for the development of "rigid bonds" as the result of adsorbed water around clay particles or inter-grain bonds attributed to incipient lithification from the solution and redeposition of various minerals (Terzaghi, 1941; Hamilton, 1964). Bjerrum (1967) attributes this phenomenon to diagenetic bonds and goes further to say that, where diagenesis has affected a clay, the preconsolidation pressure cannot be determined from a consolidation test. If this assumption is followed, then none of the preconsolidation pressures reported here are valid and the degree of overconsolidation cannot be accurately determined. It can only be stated that these samples display consolidation characteristics similar to that of an overconsolidated sediment.

The 142-meter sample from DSDP 163A differs in that it is the only sample not found to be overconsolidated. Unfortunately, this was the only sample from this site, and the overall consolidation characteristics with depth for this site are not known. It is unusual that the deepest sample tested should be normally consolidated. Owing to the limited data available, and explanation for this phenomena has not been attempted.

Plasticity

Atterberg limits provide the basis for a very simple yet effective classification system. These limits, liquid and plastic, are basically the water contents at which a sediment changes from the liquid to the plastic state. A detailed discussion of these limits can be found in almost any soil mechanics text. Owing to the relatively large amount of sediment needed for the Atterberg limit determinations, only nine of the Leg 16 samples were classified by this test.

Studies of short sediment cores by Richards (1962) and Keller (1970) indicated that the majority of deep-sea sediments can be classified as inorganic clays of medium to high plasticity using the classification of Casagrande (1948). The samples from Leg 16, which are from greater depths below the sea floor, appear to be slightly more organic clays of high compressibility (Figures 12 and 13). As shown in Figure 13, chalk and chalk oozes commonly display much lower liquid limits and degrees of plasticity than the zeolitic clays which have exceptionally high liquid limits and plasticity indices.

Sensitivity

Sensitivity determinations (the ratio of undisturbed strength to remolded strength) were made on only nine samples at DSDP 157, 158, and 159 owing to the lack of time needed to make additional shear strength tests. These nannofossil chalk oozes, with varying concentrations of Radiolaria, diatoms, and foraminifera, ranged in sensitivity from 2 to 7, slightly insensitive to very sensitive based on the classification of Rosenquist (1953). These values agree with those reported by Keller and Bennett (1970) for a large number of short cores from the Pacific. Within the depth ranges of the Leg 16 samples tested (9-117 m), no apparent correlation was found between sensitivity and depth of burial.

SUMMARY

As has been shown in the depth profiles of the various physical properties, not only is there considerable variation with depth, but from site to site as well. Even between the two closest sites (DSDP 161 and 162), a distance of 450 km, a major difference exists among the physical properties. However, making the assumption that the samples collected during Leg 16 represent the 0- to 300-meter interval, a number of generalizations can be made concerning the sediments from the sampled area.

There is no apparent relationship between variation of mass physical properties and the age of the sediment or the rate of sedimentation for the respective stratigraphic sequences. It has been reported elsewhere, however, that, in the areas of extreme rates of sedimentation, such as in deltaic deposits, the physical properties are influenced by the deposition rates (Moore, 1961). In the case of the abyssal plain deposits encountered on this leg, the greatest single factor influencing the physical properties appears to be the depth of burial. Lithologic changes are also major factors responsible for many of the variations noted here.

Excluding DSDP 155, since the samples were only taken from below 300 meters, it is possible to delineate the characteristic mass physical properties of a number of the sediment types encountered during Leg 16 (Table 1). Table 1 presents average values for the various parameters based on the laboratory rather than the shipboard analyses. Of particular interest is the radiolarite found at 200 meters at DSDP 161. This material displays a remarkably low wet bulk density yet high water content and porosity for its depth of burial. This can probably be attributed to the unique packing of the individual Radiolaria.

A number of the samples display properties similar to that of an overconsolidated sediment as determined from a consolidation test. This characteristic is not truly due to overconsolidation as the term is employed in soil mechanics, but appears to be a diagenetic property of deep-sea sediments. Hamilton (1964) and others have postulated that this property results from a bonding of the grains such that the fabric of the sediment is altered little by an

TABLE 1
Sediment Types and Selected Physical Properties

	Wet Bulk Density (g/cc)	Water Content (% dry wt.)	(%) Porosity	Grain Density
Radiolarian brown clay	1.25	200	85	2.30
Brown zeolitic clay with Radio- laria	1.25	250	85	2.67
Nannofossil chalk ooze	1.53	83	72	2.61
Nannofossil chalk	1.67	53	58	2.65
Brown clay with Radiolaria and ferruginous aggregate	1.60	65	65	2.60
Radiolarite	1.38	105	73	2.40

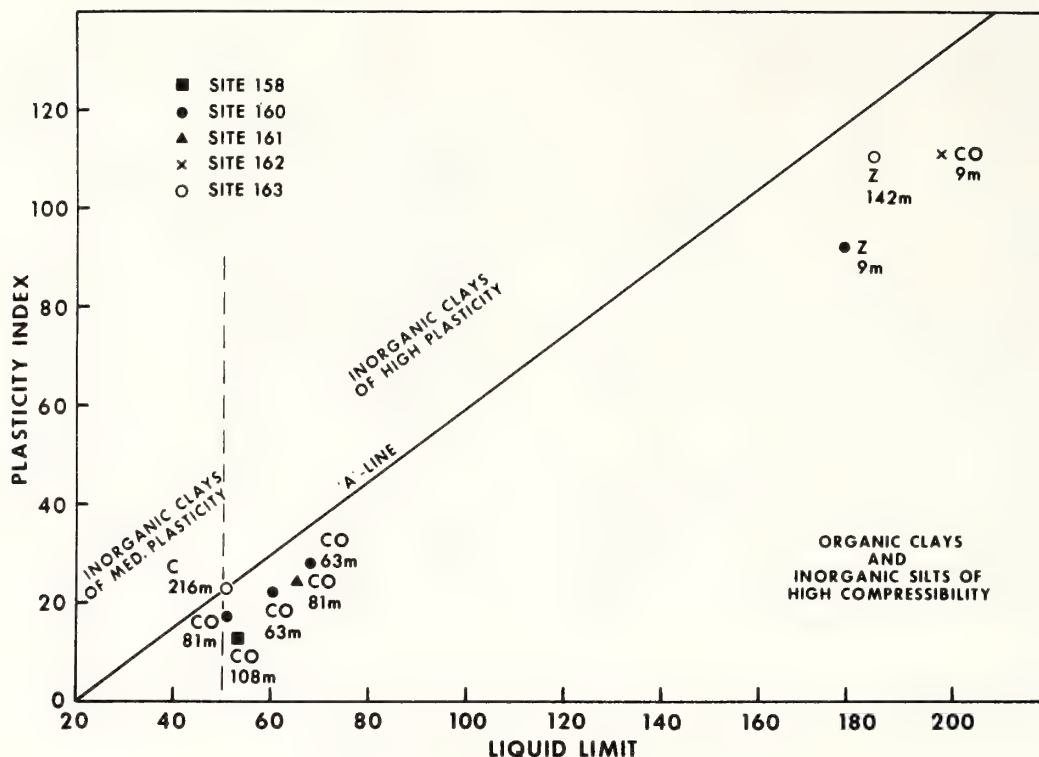


Figure 13. Plasticity chart; letters indicate sediment type C = chalk, CO = chalk ooze, Z = zeolite clay; numbers are the depth in hole of the subsample.

overburden pressure. In his study of the Mohole core (Guadalupe site), Hamilton (1964) found little change in porosity with depth and attributed this to the bonding and stabilization of the sediment fabric. This appears to be a logical finding in view of the assumptions made above. Leg 16 data, however, present a slightly different finding. Although most of the samples tested give the appearance of an overconsolidated sediment, porosities are found to decrease considerably with depth at all but one site. This would appear to be an anomalous situation if the sediments are indeed overconsolidated as the tests indicate. There may be, however, an explanation for this phenomenon in the fact that these porosity decreases occur primarily in sediments consisting largely of chalks abundant in Radiolaria, diatoms, and coccoliths. These may, in turn, contribute significantly to resolution and the reduction of voids. If this is the case, evidence should readily be seen from a close examination of these microfossils. DSDP 162, which displays little or no change in porosity with depth, possesses much more clay throughout its section. There is an indication from sections of the various cores that, in clay sequences, the porosity change with depth is minor. The clay at DSDP 162 may therefore serve to balance out the effect of the chalk ooze.

REFERENCES

- American Society for Testing and Materials, 1957. Proceedings, Symposium on Vane Shear Testing of Soils. Spec. Tech. Pub. 193.
- Arrhenius, G., 1952. Sediment cores from the East Pacific. Rept. Swedish Deep-Sea Expedition 1947-1948. 5, 227.
- Bjerrum, L., 1967. Progressive failure in slopes of overconsolidated plastic clay and clay shales. J. Soil Mech. and Found. Div., Am. Soc. Civil Engrs. 93 (SM5), 1.
- Casagrande, A., 1936. The determination of the preconsolidation load and its practical significance. Proc. Intern. Conf. Soil Mech. Foundation Engineering, 1st. Cambridge. 3, 60.
- , 1948. Classification and identification of soils. Trans. Am. Soc. Civil Engrs. 113, 901.
- Evans, I. and Sherratt, G.G., 1948. A simple and convenient instrument for measuring the shear resistance of clay soils. J. Sci. Inst. and Physics in Industry. 25, 411.
- Hamilton, E.L., 1959. Thickness and consolidation of deep-sea sediments. Bull. Geol. Soc. Am. 70, 1399.
- , 1964. Consolidation characteristics and related properties of sediments from experimental Mohole (Guadalupe site). J. Geophys. Res. 69, 4257.
- Hansbo, S., 1957. A new approach to the determination of the shear strength of clay by the fall-cone test. Proc. Roy. Swedish Geotech. Inst. 14, 47.

- Keller, G.H., 1970. Engineering properties of North Atlantic deep-sea sediments. *Proc. Intern Congr. for Ocean Research and Ocean Exploitation*. Dusseldorf. **2**, 65.
- Keller, G.H. and Bennett, R.H., 1968. Mass physical properties of submarine sediments in the Atlantic and Pacific Basins. *Proc. Intern. Geol. Congr.*, 23rd. **8**, 33.
- , 1970. Variation in the mass physical properties of selected submarine sediments. *Marine Geol.* **9**, 215.
- Lowe, J. III, Zaccheo, P.F. and Feldman, H.S., 1964. Consolidation testing with back pressure. *J. Soil. Mech. and Found. Div.*, Am. Soc. Civil Engrs. **90**, 69.
- Meade, R.H., 1963. Factors influencing the pore volume of fine-grained sediments under low-to-moderate overburden loads. *Sedimentology*. **2**, 235.
- Moore, D.G., 1961. Submarine slumps. *J. Sediment Petrol.* **31**, 343.
- , 1964. Shear strength and related properties of sediments from experimental Mohole (Guadalupe site). *J. Geophys. Res.* **69**, 4271.
- Richards, A.F., 1961. Investigations of Deep-Sea Sediment Cores, I. Shear Strength Bearing Capacity, and Consolidation. U.S. Navy Hydrographic Office, Tech. Rept. 63.
- , 1962. Investigations of Deep-Sea Sediment Cores, II. Mass Physical Properties. U.S. Navy Hydrographic Office, Tech. Rept. 106.
- Rittenberg, S.C., Emery, K.O., Hulseman, J., Degens, E.T., Fay, R.C., Reuter, J.H., Grady, J.R., Richardson, S.H. and Bray, E.E., 1963. Biogeochemistry of sediments in experimental Mohole. *J. Sediment. Petrol.* **33**, 140.
- Rosenquist, I.Th., 1953. Considerations on the sensitivity of Norwegian quick-clays. *Geotechnique*. **3**, 195.
- Terzaghi, K., 1941. Undisturbed clay samples and undisturbed clays. *J. Boston Soc. Civil Engrs.* **28**, 211.

Geotechnical Properties of Submarine Sediments, Mediterranean Sea

George H. Keller and Douglas N. Lambert

*National Oceanic and Atmospheric Administration,
Miami, Florida*

ABSTRACT

Investigation of the mass physical properties (sediment type, shear strength, water content, unit weight, and porosity) of sediment cores from 27 sites in the Mediterranean Sea provides an insight into the general distribution of these properties within the surficial deposits. Deposits of the western portion of the basin, with an abundance of turbidites, tend to possess higher shear strengths and unit weights than do those sediments blanketing the eastern Mediterranean. Much of the easternmost Mediterranean is strongly influenced by the deposition of the Nile-contributed sediments which are fine grained and display very low shear strengths (less than 50 g/cm²) and unit weights (1.40–1.47 g/cc), but relatively high water contents (103 to 124 percent) and porosities (73 to 77 percent).

A study of the vertical variation of selected mass properties clearly reveals the unique characteristics of both the turbidites and sapropelic mud layers found in the Mediterranean. Turbidite sequences commonly possess relatively high shear strengths and unit weights as well as low water contents and porosities. Sapropelic muds exhibit just the opposite characteristics. Using plasticity as a means of delineating sediments, the easternmost Mediterranean deposits are readily distinguished by their high plasticity indices in contrast to the much lower values observed in sediments from the central and western parts of the basin. Four samples tested for degree of consolidation possess characteristics similar to those of overconsolidated material. This is attributed to some form of cementation or "ionic bonding" and not to previous overburden pressures.

INTRODUCTION

Marine geotechnique is a relatively young field, but one which is receiving considerable attention today. It is the area of study which deals with the investigation of the engineering and geological aspects of the

RESUME

L'examen des propriétés de masse (types de sédiments, shear, teneur en eau, poids spécifique et porosité) de carottes prélevées dans des bassins de la Mer Méditerranée donnent un aperçu de la distribution générale de ces propriétés dans les dépôts supérieurs. Les dépôts du Bassin Occidental, avec un grand nombre de turbidites, ont une résistance à la rupture par cisaillement plus haute et un poids spécifique plus élevé que ceux du Bassin Oriental. Une grande partie, à l'Est de ce bassin, est fortement influencée par le dépôt des sédiments d'apport du Nil, avec grains fins, shear (moins que 50 g/cm²) et poids spécifique (1.40 à 1.47 g/cc) faibles, mais avec teneur en eau (103 à 124 pour cent) et porosité (73 à 77 pour cent) relativement élevées.

Une étude de la variation verticale des propriétés de masse dégage nettement les caractéristiques des turbidites et couches de boue sapropélique rencontrées dans la Méditerranée. Les successions des turbidites présentent généralement shear et poids spécifique relativement élevés, et une teneur en eau et porosité faibles. Les boues sapropéliques présentent des caractéristiques renversées. En utilisant la plasticité, les couches des sédiments de la partie Est de la Méditerranée se distinguent par leurs indices de plasticité élevés en comparaison des valeurs bien inférieures observées dans les sédiments des parties centrale et occidentale du bassin. Quatre échantillons dont on a étudié le degré de consolidation présentent des traits similaires à ceux des matériaux surconsolidés. On peut attribuer ce fait à un type de cimentation ou "ionic bonding," et non à la compression exercée par les terrains de couverture.

sediments and rocks comprising the sea floor. Specifically, it is more commonly used to denote the study of the mass chemical and physical properties of the electrolyte-gas-solid system of the sea floor and the response of this sedimentary system to applied static and dynamic loading.

One of the earliest studies in marine geotechnique was that of Arrhenius (1952) in which relative strength measurements were made on sediment cores collected from the Pacific during the Swedish Deep-Sea Expedition 1947–1948. Shortly thereafter, a number of U. S. Navy scientists commenced a research program into the mass physical properties of deep-sea sediments. These early efforts of Hamilton and Menard (1956), Hamilton (1959), Richards (1961, 1962), and Moore (1962), along with the offshore foundation studies by Fisk and McClelland (1959) for drilling platforms, have served as an impetus for the increased interest in marine geotechnique of both marine geologists and civil engineers.

Recent studies have provided an insight into the areal distribution of various mass physical properties in the North Pacific and North Atlantic basins (Keller and Bennett, 1968), the stability of submarine deposits (Morgenstern, 1967; Bryant and Wallin, 1968; and Morelock, 1969), and the consolidation characteristics of submarine sediments (Hamilton, 1964; Richards and Hamilton, 1967; and Bryant *et al.*, 1967).

Studies of the mass physical properties of deep-sea sediments in the Mediterranean basin have been limited. To our knowledge only six such studies have been published. Richards (1961, 1962), in his initial reports on the mass properties of deep-sea sediment cores, provided data from three sites in the vicinity of the Strait of Gibraltar. Einsele's (1967) study of eight sediment cores from just north of the Nile Delta made available the first detailed information on the mass properties of surficial deposits off the Nile River. Off the coast of Tel-Aviv, Israel, Almagor (1967) investigated the shear strength, water content, and consolidation characteristics of nine sediment cores collected from water depths ranging from 35 to 1100 meters. Studies attempting to correlate the acoustical and mass physical properties of Mediterranean sediments on a regional scale have been reported by Horn *et al.* (1968), and on a more local basis by Ryan *et al.* (1965) and Kermabon *et al.* (1969) in the Tyrrhenian Sea.

The present study has assembled all the available data, published and unpublished, relating to sediment distribution, shear strength, water content, unit weight, and porosity in the Mediterranean basin (Table 1). It is based on data obtained from 96 sediment cores representing 27 areas in the Mediterranean. The majority of the cores were collected and analysed by, or on contract for, the U. S. Naval Oceanographic Office and, as yet, the data are mainly unpublished. Included in the 96 cores are four collected by the OCEANOGRAPHER in 1967 and analyzed by the authors.

Because of the nature of the measurements made on the cored sediment, disturbance of the sediment

fabric during sampling is of utmost concern. Even under ideal sampling conditions with the best available sampler, truly undisturbed samples cannot be obtained from the sea floor. Since the data presented here are from several sources representing different types of samplers (both piston and gravity corers) and sampling techniques, it is clear that some degree of variation in measured properties is inevitable, based solely on sampling disturbance. The degree to which these properties have been affected by sampling cannot now be ascertained and, for the purpose of this discussion, no attempt has been made to adjust these data for disturbance. Obviously disturbed samples, *e.g.*, displaying distorted bedding due to piston sucking, were discarded.

Cores used in this study vary in length from 0.18 m to 9.4 m with an average of about 3.5 m. Considering the short core lengths relative to the scale of the Mediterranean basin, it was decided to average the respective parameter values, except for sediment type, over the entire length of each core. For example, if ten shear strength measurements were made on a core, the average of these values was used to derive the areal distribution of the respective properties shown in later figures. Subsample values from each core were critically evaluated to exclude any which were obviously in error as a result of sampling or testing procedures.

GENERAL SEDIMENTATION PATTERNS IN THE MEDITERRANEAN

The Mediterranean Sea occupies a zone of considerable crustal activity, lying along one of the major earthquake belts of the world. Consequently, tectonism and volcanic activity have played a major role in determining the morphological characteristics of the present sea floor. In conjunction with tectonism, detritus from the surrounding land mass has contributed much to modify or smooth out the basin floor irregularities.

Morphologically, the Mediterranean basin is divided distinctly into western and eastern sectors (Figure 1). The western portion is by far the simpler of the two with regard to structure and topography. It consists primarily of the Balearic Abyssal Plain (largest in the Mediterranean), the Tyrrhenian Abyssal Plain and their adjacent continental margins. Another prominent feature is the Rhône Fan which covers an extensive area of the northwestern portion of the Mediterranean basin. There appears to be little doubt that the River Rhône has provided the sediments needed to build this feature (Menard *et al.*, 1965).

With its median ridge, trenches, continental border-

Table 1. Sources and total number of measurements of geotechnical properties used in this study.

Source	Area	no. Cores	Ave. Core Length (cm)	Shear Strength	Unit Weight	Water Content	Porosity	Atterberg Limits	Type of Corer
Horn <i>et al.</i> (1967)	Entire Med.	14	748	954	338	338	338	—	Ewing
Kermabon <i>et al.</i> (1968)	Tyrrhenian Sea	21	807	—	3255	3255	3255	—	Sphincter
*P. Blavier, C. Gehin, & F. Kögler	Tyrrhenian Sea	3	792	166	238	238	238	—	Sphincter
Richards (1962)	Strait of Gibraltar	3	180	30	33	33	33	23	Kullenberg
Gehin & Blavier (1969)	Alboran Sea	7	510	—	681	681	681	—	Sphincter
Einsele (1967)	Nile Cone	8	200	53	14	36	14	13	Kastenlot
Almagor (1964)	Israel Margin	9	280	170	219	219	219	93	Hydroplastic (modified)
†*NAVOCEANO	Off Palomares, Spain	24	66	81	57	59	4	—	Hydroplastic
†*NAVOCEANO	Strait of Gibraltar	3	82	6	6	24	6	—	Kullenberg
OCEANOGRAPHER (this study)	Eastern & Western Mediterranean	4	167	14	17	48	11	14	Hydroplastic

†U.S. Naval Oceanographic Office.

*Unpublished data.

land, limited abyssal plains, and numerous volcanoes and seamounts, the eastern sector of the Mediterranean presents a relatively complex area of bottom morphology. The most prominent feature of the eastern Mediterranean is a broad median ridge (Mediterranean Ridge) extending from the continental margin of Italy to the island of Cyprus. Although the median line is not denoted by an axial rift valley, the general relief and steep local slopes indicate a tectonic origin for the ridge (Emery *et al.*, 1966). A number of basinal enclosures such as the Sicilia, Herodotus and Ionia Basins are not entirely smooth-floored and have not been designated as abyssal plains (Watson and Johnson, 1969). The Nile and Messina Cones are deposits resulting from rapid sedimentation and slumping. The source for the former is obvious, but the same cannot be said for the Messina Cone. Indications are that northerly currents concentrate sediment in the vicinity of the strait between Italy and Sicily. Numerous slumps and turbid flows resulting from periodic seismic shocks of this sediment accumulation have amassed the deposits now comprising the Messina Cone (Ryan and Heezen, 1965). For a more detailed discussion of the morphology of the Mediterranean basin, the reader is referred to the studies of Pfannenstiel (1960), Goncharov and Mikhailov (1964), Hersey (1965), Emery *et al.*, (1966), and Watson and Johnson (1969).

The Mediterranean Sea is one of relatively active and diverse sedimentation as might be anticipated in

an essentially land-locked basin. Average sedimentation rates for the Quaternary have been estimated at 10 to 30 cm/1000 years by Mellis (1954) with an overall average rate of 0.5 cm/1000 years since Cretaceous time (Wong and Zarudzki, 1969).

In addition to the widespread occurrence of calcareous oozes and terrigenous lutites, there appears to have been a long history of turbidity currents, slumping, and ash falls in the Mediterranean. A unique aspect of Mediterranean deposits is the occurrence of numerous sapropelic mud layers in the eastern sector of the basin. These Pleistocene muds are indicative of an anoxic depositional environment brought on by stagnant bottom water, a condition not found presently in the Mediterranean Sea.

The Adriatic and Aegean Seas have been purposely omitted from this discussion owing to the lack of any mass physical properties data in these areas. Only in the section pertaining to surface sediment have these two seas been included.

SURFACE SEDIMENT TYPES

Sediment distribution (Figure 2) is based mainly on a compilation of published data from the U. S. Naval Oceanographic Office (1965) and the Interdepartmental Geophysical Committee of the Academy of Science, USSR (1969). Additional data have been obtained from the files of the U. S. Naval Oceano-

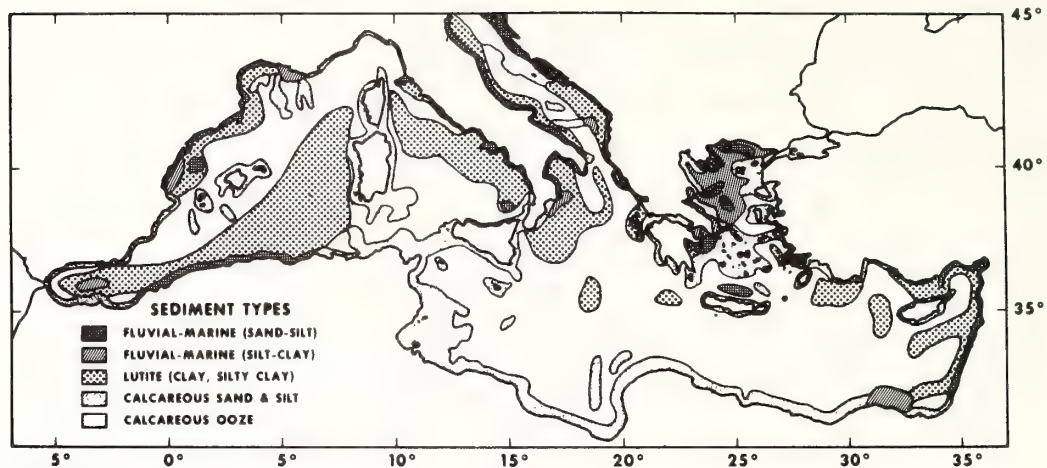


Figure 2. Surface sediment distribution.

graphic Office, U. S. Navy contract reports from Texas Instruments Incorporated (1967), and such published studies as the Swedish Deep-Sea Expedition 1947–1948 (Olausson, 1960, 1961), Ninkovich and Heezen (1965), and Emery *et al.* (1966).

Lack of a common sediment classification system among the various sources noted above has made the task of collating these data difficult and, at best, the results can only be considered as a broad generalization. An effort has been made here to use a simple classification of five sediment types which tends to unite the majority of the systems previously used: (1) fluvial marine (sand-silt), representing the coarse fraction (larger than 0.062 mm); (2) fluvial-marine (silt, clayey silt), the finer fraction (0.062 to 0.002 mm); (3) lutite (silty clay, clay), the finest fraction (smaller than 0.002 mm) of material primarily of terrigenous origin and containing less than 30 percent calcium carbonate; (4) calcareous sand and silt, consisting mainly of shell fragments and coralline debris of sand and silt-size particles; (5) calcareous ooze, used here to denote sediment composed of at least 30 percent calcium carbonate which is in the form of skeletal material from various planktonic animals and plants. *Globigerina* and pteropod oozes are those most commonly found in the Mediterranean. Volcanic ash, which is widespread in the eastern Mediterranean, does not readily fit into the classification used here. However, to maintain this system, ash is classed as fluvial-marine for the purpose of this discussion.

It is readily apparent (Figure 2) that much of the Mediterranean basin is blanketed by either lutite or calcareous oozes. The latter constitute the predominant sediment type and occur primarily in those areas

not strongly influenced by high current energies, turbidity currents, major rivers, strong volcanic activity, or reefs. Lutite is present in areas influenced by terrestrial drainage such as the far eastern Mediterranean, off the coast of Spain and France, in the Adriatic Sea, and on those continental rises and abyssal plains where turbidity currents are most common. The largest lutite deposits are those covering the Balearic Abyssal Plain which receives much of its sediment from turbidity currents originating on the Rhône Fan (Menard *et al.*, 1965) and from portions of the African margin (Heezen and Ewing, 1955).

The relatively large lutite deposit in the Tyrrhenian Sea extends across both the continental rise and abyssal plain provinces. This distribution may possibly be attributed to the northwestern flow of intermediate water carrying terrigenous fines away from Italy. Another area of extensive lutite is that of the Messina Cone and Messina Abyssal Plain where Ryan and Heezen (1965) report active slumping and flow of turbidity currents.

Coarse-grained calcareous deposits are prominent along the southern margin of the Mediterranean where large shell and coralline concentrations occur. Similar occurrences are common in the vicinity of the Balearic islands, Corsica, Sardinia and Sicily as well as among many of the islands in the Aegean Sea. Surprisingly, few areas of fluvial-marine (silt, clayey silt) material are reported among the deposits of the Mediterranean.

The surface sediment distribution map (Figure 2) is deceiving in that it delimits only the surface deposits and may not adequately present the true sedimentological setting. It is particularly misleading in an area such as the Nile Cone where great quantities of

sediment (Wong and Zarudzki, 1969, reported 120 million tons; Holeman, 1968, reported 57 million tons) enter the basin annually. Only after examining seismic reflection records and core samples is it obvious that Nile-contributed sediments extend over a much greater portion of the eastern Mediterranean than is revealed by the map. To a lesser extent, a similar corollary can be drawn from the Rhône River deposits in the northwestern portion of the Mediterranean.

Of particular interest to the sedimentologist, but not obvious from the map, is the influence of volcanism on the sedimentary regime, especially in the eastern Mediterranean. Numerous ash layers have been noted throughout the province (Ninkovich and Heezen, 1965), but only in a few areas, such as north of Crete, has ash been reported in the surface deposits (Horn *et al.*, 1968).

SHEAR STRENGTH

Sediment cores used in this study consisted primarily of fine-grained cohesive material with a few laminae of fine sand occurring in a number of the samples. Laboratory shear strength measurements of relatively weak, saturated sediments are commonly accomplished by one of three tests: vane shear, unconfined compression, or fall cone. A vane shear test consists of inserting a small four-bladed vane into the sample and applying an increasing torque until shear occurs (Evans and Sherratt, 1948). The unconfined compression test basically involves loading a vertically oriented cylindrical sample, unconfined in all lateral directions, at a constant rate until failure. A more detailed discussion of these two tests as applied to submarine sediments has been presented by Richards (1961).

The fall cone test was developed in Sweden and has received wide usage in the study of various Scandinavian clays. This test is quite simple and consists of relating the penetration of a falling metal cone into a sediment to the strength of the material. A complete description of this test has been presented by Hansbo (1957).

Depending on the type and strength of the sediment, it is sometimes difficult to compare shear strength measurements made by these three techniques. There does, however, seem to be a better correlation between the vane shear and unconfined compression tests than between either of these two and the fall cone measurements, particularly at lower shear strength values (Flaate, 1965, and Einsele, 1967).

Shear strength measurements on 14 of the 96 cores used in this study were made with the fall cone and can be identified by the prefix "A" in Figure 1. These values do appear to be slightly higher in some cases

than shear strengths determined by the other testing techniques. Caution is in order when referring to the shear strength distribution pattern (Figure 3).

Even with the difficulty of comparing these various test data, some generalizations can be drawn from the available shear strength values. In viewing the overall shear strength distribution, a distinct difference is noticed between the eastern and western sectors of the Mediterranean basin. In the western Mediterranean, the Balearic Abyssal Plain appears to be blanketed with sediments of relatively high shear strength ($> 200 \text{ g/cm}^2$). These are the highest average values yet observed in the Mediterranean. As pointed out by others (Heezen and Ewing, 1955; and Menard *et al.*, 1965), the Rhône Fan and the Balearic Abyssal Plain are largely composed of turbidites. Turbidite layers within any core display distinctly different values (*e.g.*, higher shear strength and unit weight) than are found associated with the matrix of the core as a whole thus, when averaged into the entire core, generally resulting in higher shear strengths for the overall abyssal plain and outer fan deposits. This contrast is further discussed in a later section dealing with vertical variations of mass properties at a select number of sites. Westward towards the Strait of Gibraltar, few if any turbidites are reported and shear strengths are commonly lower than those observed for the Balearic Abyssal Plain.

The influence of the Nile in the eastern Mediterranean is clearly apparent from the distribution pattern of the various mass physical properties. Our study indicates that the Nile-contributed sediments possess shear strengths lower than most others yet reported for the Mediterranean basin. A marked contrast in shear strength values is noted between the offshore areas of the rivers Nile and Rhône. Although turbidites are common to both areas, they appear to occur in greater abundance in the vicinity of the Rhône and may be responsible for the associated higher shear strengths found there. Calcium carbonate and organic carbon analyses from both these areas indicated a notable contrast between the respective deposits. Nile sediments are relatively high in organic carbon, as high as 1.194 percent, in comparison to values of the order of 0.180 percent for the general area of the Rhône Fan. Calcium carbonate content is slightly higher in the Rhône Fan deposits than was observed on the Nile Cone. The combination of lower calcium carbonate and higher organic carbon may well have contributed to the lower shear strengths occurring in the eastern Mediterranean. Variations in mineralogy and grain size between the two areas undoubtedly are also a contributing factor to the observed strength differences. Relatively low shear strengths are also found in the Messina Cone and Messina Abyssal

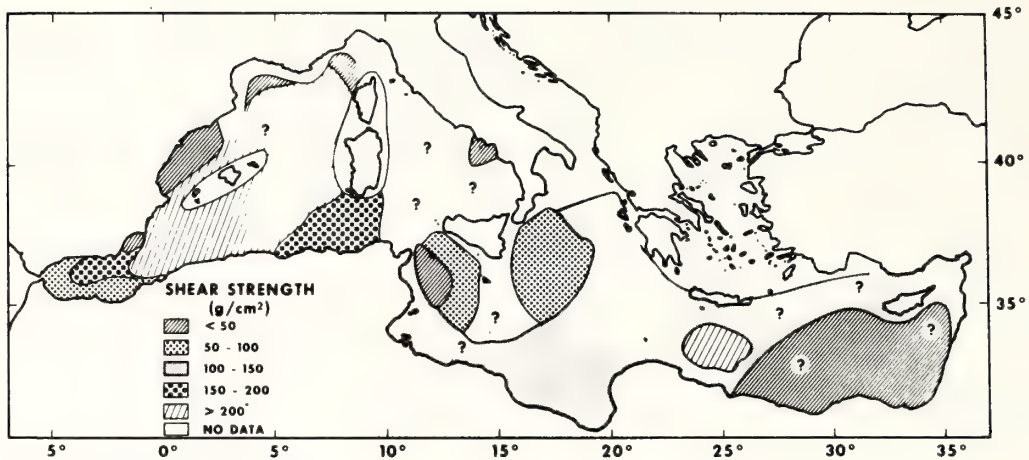


Figure 3. Average shear strength distribution.

Plain sediments which are areas of slumping and sediment disturbance (Ryan and Heezen, 1965).

WATER CONTENT

Water content is used here as the ratio, in percent, of the weight of water to the weight of oven dried (110°C) solids in a given sediment mass. It is determined by weighing a representative fraction of the sample, oven-drying at least over night, cooling in a desiccator and reweighing.

Overall water content variation in the Mediterranean basin appears to be rather moderate (Figure 4). The major portion of the abyssal plain and rise sediments have water contents ranging from 50 to 100

percent, much the same as has been reported for Atlantic sediments (Keller and Bennett, 1968). This relatively moderate amount of variability compared to Atlantic and Pacific deposits, may possibly reflect the strong influence turbidity currents have over much of the basin and thereby lead to some degree of lateral uniformity among the submarine sediments. Marginal deposits in the western and central Mediterranean Sea are characterized by relatively low water contents (< 50 percent) as are commonly found in association with coarser material. North of the island of Crete, the low water content reflects the unusually high volcanic ash content of these deposits.

Distribution of the Nile lutites, with their characteristic high water content, is clearly evident from Figure 4. The highest values yet observed in the

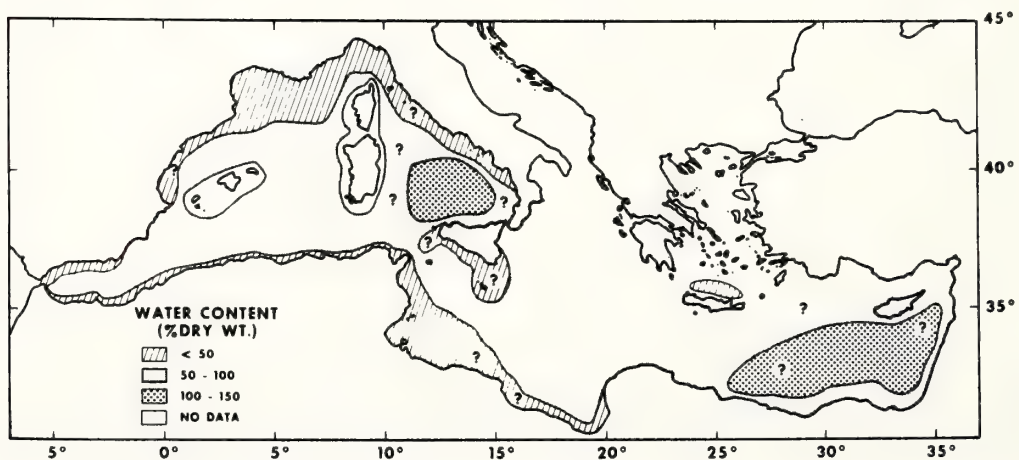


Figure 4. Average water content distribution.

Mediterranean are those associated with the Nile sediments. Influence of these deposits on the normally lower water content sediments of the coastal margins is plainly evident off Israel where higher than expected values are found. The Tyrrhenian Abyssal Plain is the only other locale in the Mediterranean reported to have average water contents greater than 100 percent. In contrast to the Nile Cone, the outer Rhône Fan deposits possess rather low water contents. This may be possibly ascribed to a greater concentration of coarse-grained turbidites in the Rhône-contributed sediments. The relatively low water contents of the Balearic Abyssal Plain are not surprising when it is recalled that a prominent portion of these deposits is attributed to turbidity currents from both the Rhône Fan and Algerian areas.

UNIT WEIGHT

Unit weight, or wet bulk density as referred to by some investigators, is the weight per unit of total volume of a sediment mass. Submarine sediments are usually 100 percent saturated or are sufficiently close to 100 percent to allow the term saturated unit weight (the in-place unit weight) to be substituted for unit weight. It is that value which is presented here.

Unit weights ranging from 1.50 to 1.75 g/cc tend to characterize a large portion of the eastern Mediterranean basin deposits, whereas values between 1.75 to 2.00 g/cc predominate over much of the western portion of the basin (Figure 5). Nile-derived lutites possess some of the lowest unit weights found in the Mediterranean. These unit weights, as do the other

mass physical properties, clearly identify these Nile sediments.

Low unit weight (1.35 g/cc) in the Tyrrhenian basin are attributed to the concentration of lutite found there. Unit weights from the Rhône Fan and Balearic Abyssal Plain are the highest yet reported from the Mediterranean. These high values undoubtedly are related to the great abundance of turbidites and the mineralogy associated with these sequences. High unit weights also occur along the southern margin of Spain and in the Strait of Gibraltar. The relatively low unit weights found off the northern margin of Morocco may possibly reflect the characteristics of material entering the basin from Morocco and northwestern Algeria. Prevailing westerly surface currents may have contributed to the observed distribution pattern.

POROSITY

Porosity is the ratio, expressed as a percent, of the volume of voids in a given mass to the total volume of the sediment mass. It was determined from calculations based on the measured water content, unit weight, and grain specific gravity values.

The lutites of the Nile-contributed sediments as well as those of the Tyrrhenian Abyssal Plain clearly stand out as those deposits possessing the highest average porosities yet found in the Mediterranean basin (Figure 6). Porosities of 60 to 70 percent tend to predominate throughout most of the basin. A relatively low average porosity appears to characterize the Rhône Fan as might be anticipated in this depositional environment of numerous coarse-grained turbidites.

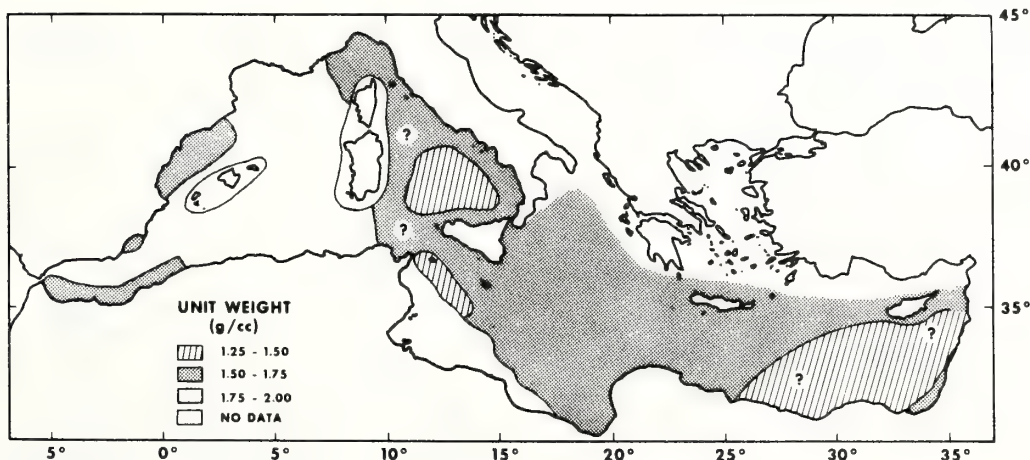


Figure 5. Average unit weight distribution.

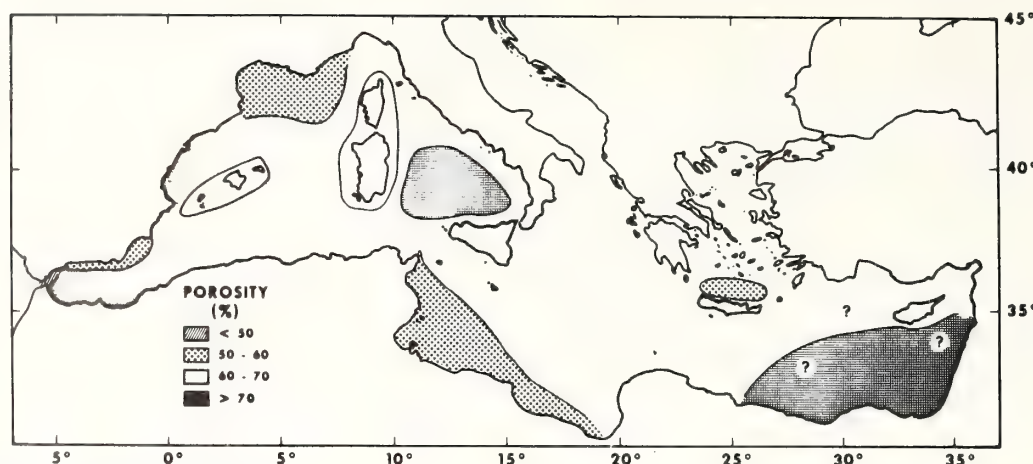


Figure 6. Average porosity distribution.

Similar low porosities are displayed by the fine grained ash and pumice deposits occurring north of the island of Crete. Average porosities of less than 50 percent are found in association with relatively coarse-grained sediments such as in the Strait of Gibraltar, and off the east coast of Tunisia.

VERTICAL VARIATION OF MASS PROPERTIES

The diverse sediments and depositional conditions in the Mediterranean are strongly reflected in the mass properties of the respective deposits. A series of profiles from various parts of the Mediterranean is presented in Figures 7 and 8 to show the variation of selected mass properties with depth as well as the interrelationship of these properties. Two cores from Horn *et al.* (1967) were selected from the Balearic Abyssal Plain, one just off the Rhône Fan (Core A-1) and the other from the southwest sector of the abyssal plain (Core A-2). As noted earlier, the Balearic Abyssal Plain deposits are largely composed of turbidites originating from the Rhône Fan and the continental margin of northern Africa. This depositional environment is clearly shown in cores A-1 and A-2, each of which display a number of sandy layers (turbidites) within a matrix of calcareous ooze. Although not distinct in the profile, core A-1 possesses 14 turbidite sequences and core A-2 has 5 such layers (Horn *et al.*, 1967). The influence of these layers on the overall properties of the deposits is obvious from the profiles. In contrast to the calcareous ooze, the turbidites exhibit higher percentages of sand, high shear strength, low water content and porosity, and high unit weight.

Calcium carbonate content is often higher in the turbidite zone, but not in all cases, owing to probable differences in the source areas for the respective turbidites.

Core A-3 (Figure 8) was collected from the Messina Abyssal Plain, approximately 275 km southeast of Italy (Horn *et al.*, 1967). There is little doubt, based on the study by Ryan and Heezen (1965), that much of the sediment reaching this plain results from turbidity currents and slumping on the Messina Cone. Variation of the mass properties with depth appears to be strongly influenced by the silt concentration. The presence of a turbidite between 100 cm and 110 cm is noted by distinct changes in the mass properties. An overall increase in silt content from 110 cm to 680 cm is associated only with a gradual decrease in water content and porosity and a slight increase in unit weight. In the presence of relatively large silt percentages, only shear strength appears to be significantly affected by minor changes in sand content.

The lower 200 cm of the core presents an interesting number of relationships. Increased sand contents at intervals 770 cm, 850 cm, and 885 cm indicates possible turbidites although none were reported (Horn *et al.*, 1967). The unusual aspect of these three zones is the relative increase in water content and porosity with a decrease in unit weight. This is in contrast to that observed in turbidites from the Balearic Abyssal Plain. Although a reason for this relationship is not clear, the increased percentage of calcium carbonate found in these same intervals may indicate a concentration of Foraminifera in the sand layers. This in turn could explain the lower unit weights (forams being filled with water) and possibly the higher water contents.

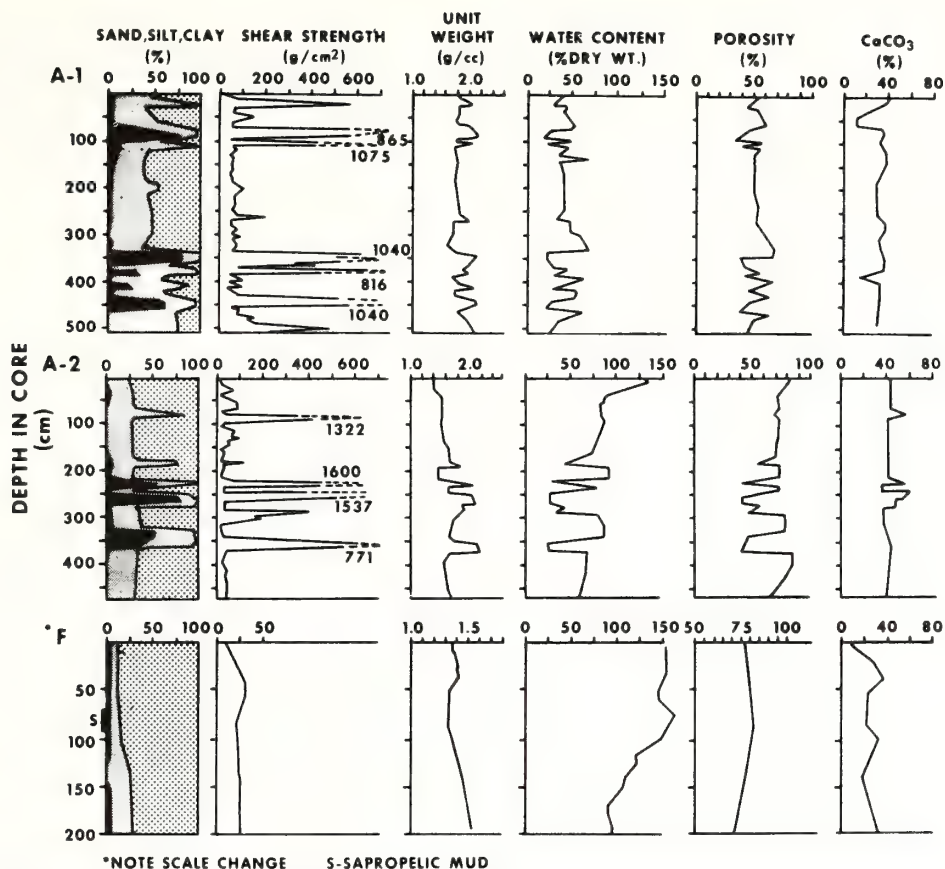


Figure 7. Vertical variation of selected mass properties from cored turbidite sequences (A-1, A-2) and the Nile Cone (F). See Figure 1 for core locations.

Core A-4 from the Mediterranean Ridge, southwest of the island of Crete (Horn *et al.*, 1967) represents a calcareous ooze sequence with minor variation in silt and sand content throughout the sampled interval. Of particular interest are the three sapropelic mud layers that occur at 145 cm, 190 cm, and 225 cm below the top of the core. These sediments are characterized by significant increases in water content and porosity, along with a notable decrease in unit weight. Porosities as high as 83 percent are found in association with the sapropelic muds. Shear strength of these muds appears to be slightly less than that found in the adjacent sediment. The marked increase of shear strength at the 325 cm depth reflects the notable increase in calcium carbonate content.

In contrast to the other areas of the Mediterranean basin, sediments comprising the upper portion of the Nile Cone display only a slight variation in their mass properties to a depth of at least 200 cm, as seen in a

core collected by the OCEANOGRAPHER (Core F). Within this interval, the sediments consist primarily of clay-size material (73 to 89 percent), minor amounts of silt (9 to 25 percent), and traces of sand (1 to 3 percent). Water content and porosity are considerably higher than those observed elsewhere in the Mediterranean, having values of 150 to 162 percent and 77 to 82 percent respectively in the upper 100 cm of the sampled interval. Below 100 cm a general decrease in these values takes place. Except for the weaker surficial layers, shear strength is almost uniform with depth. Examination of the unit weight and calcium carbonate content profiles from core F indicates a somewhat parallel pattern of distribution with depth. The low calcium carbonate and unit weight noted at a depth of approximately 80 cm corresponds to the occurrence of a layer of sapropelic mud. The influence of this layer is also clearly noted in the water content profile.

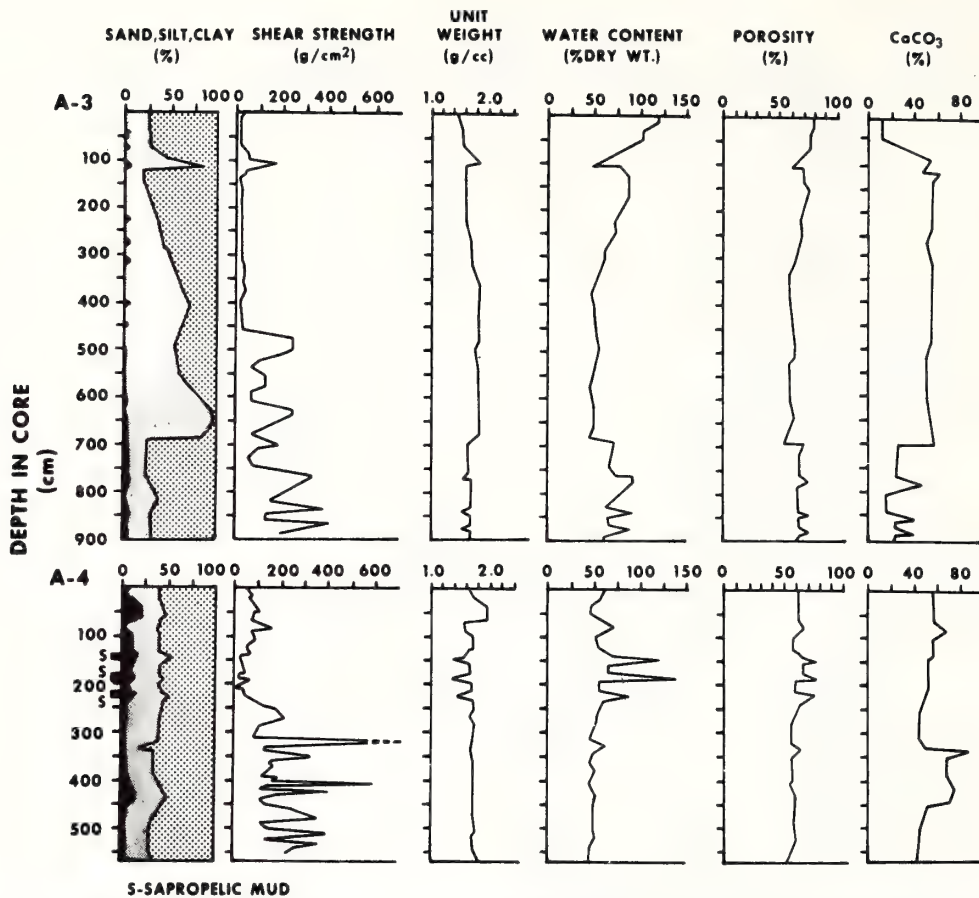


Figure 8. Vertical variation of selected mass properties in cores from the Messina Cone (A-3) and the Mediterranean Ridge (A-4). See Figure 1 for core locations.

PLASTICITY CHARACTERISTICS

Based on a sediment's plasticity, Casagrande (1948) devised a method for classifying fine-grained deposits. This technique employs a plasticity chart, the ordinate being the plasticity index and the abscissa the corresponding liquid limit. On the chart an "A"-line is drawn to represent an empirical boundary between inorganic clays, commonly above the line, and organic clays along with inorganic silts below it. Although this is a relatively simple classification and easily determined, it serves to quickly characterize sedimentary deposits not only as to their plastic properties, but as to their source as well. A detailed discussion of this classification can be found in most soil mechanics text books.

In an attempt to classify the Mediterranean sedi-

ments, a comparison of subsamples from a number of cores was made using the method proposed by Casagrande. A distinction is readily made between those samples collected in the eastern Mediterranean and those from the central (south of Sicily) and western portions of the basin (Figure 9). Sediments influenced by the Nile River are either highly organic or highly plastic and generally plot above the "A"-line or very close to it. Although primarily derived from the Nile River, sediments from off Israel possess a distinct characteristic of their own and are easily identified from the chart. Plasticity is generally higher and organic carbon content frequently lower than is found in the Nile Cone deposits. In contrast, sediments from the central and western Mediterranean display lower plasticity indices which agree reasonably well with those reported for open Atlantic deposits (Richards, 1962).

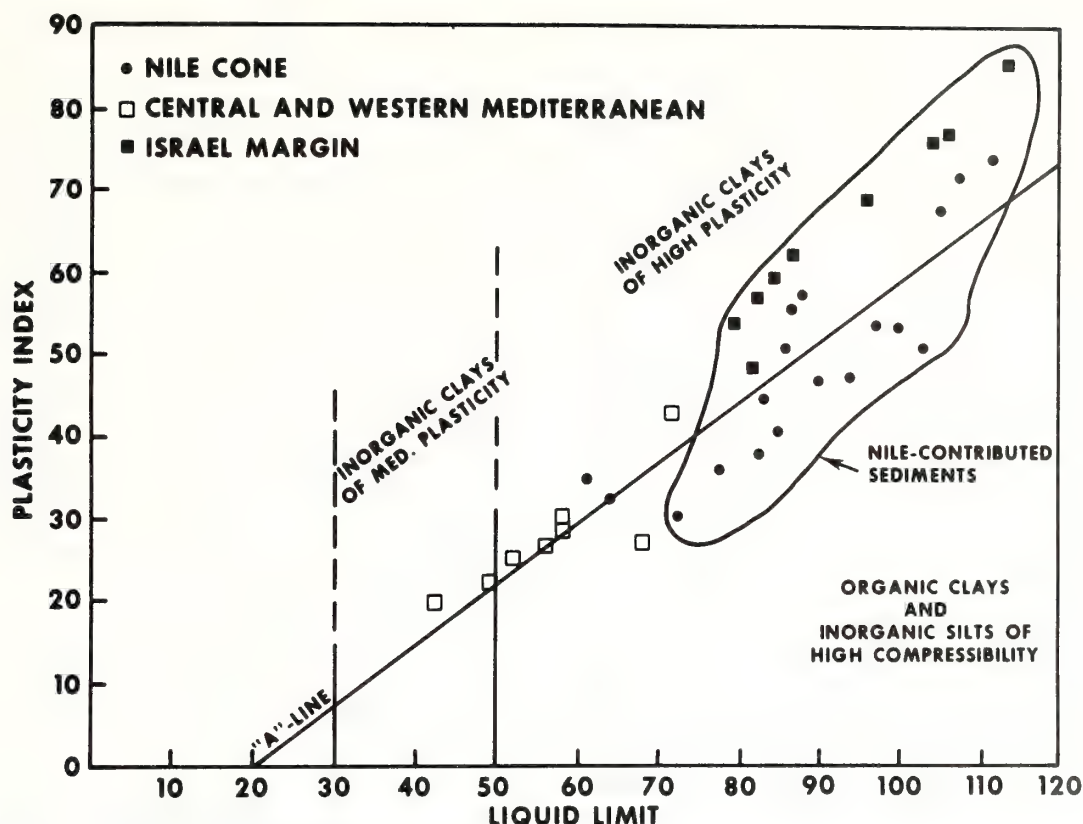


Figure 9. Plasticity chart and the classification of Mediterranean sediments.

CONSOLIDATION CHARACTERISTICS

In an effort to investigate the consolidation or compaction (as used by geologists) characteristics of the Mediterranean sediments, four samples were selected for consolidation tests. Consolidation, as used here, refers to the reduction of the volume of a sediment under an imposed load. In the case of a saturated sediment, this can only result when there is a loss of pore water. This load can be man-made (e.g., installation of a structure) or result from pressure exerted by the overlying sediment. The consolidation test is commonly used in the field of soil mechanics to determine the amount of settlement from any given load. It also is used to provide an insight into the depositional history of the particular deposit by indicating the loading conditions that have affected the deposit. For a detailed discussion of this test, the reader is referred to a basic text of soil mechanics as well as to the study by Richards and Hamilton

(1967) dealing with consolidation characteristics of submarine sediments.

Each of the four samples tested revealed that they were overconsolidated. Normally (in the soil mechanics sense) this would indicate that the sediment has been subjected to a greater load than is presently exerted by the overlying material. On land this is usually explained by erosion of previously deposited material. Erosion is known to take place on the sea floor, but it is highly unlikely in the case of the samples studied here. Core F, for example, was collected from the Nile Cone where deposition rather than erosion is currently taking place. A subsample of this core from a depth of one meter displayed a preconsolidation pressure, P_c , (pressure under which sediment has been previously loaded as defined in soil mechanics) of 0.072 kg/cm^2 and an overburden pressure, P_o , (present field load on the sampled interval) of 0.035 kg/cm^2 clearly indicating a state of overconsolidation. The void ratio (ratio of the volume of voids to the volume

of solids) versus log of pressure curve shown in Figure 10 is basically similar to those of the other tested samples. Similar studies of submarine sediments from the Atlantic and Pacific (Richards and Hamilton, 1967) and the Gulf of Mexico (Bryant *et al.*, 1967) have also reported "over-consolidated" sediments. Since it is highly improbable that these deposits are "overconsolidated" (as the term is used in soil mechanics) there must be some unique aspect or property of submarine sediments that results in this increased strength. It has been suggested that cementation or unusually strong interparticle forces are responsible for this increased strength (Rittenberg *et al.*, 1963; Richards and Hamilton, 1967). As yet, little is known about this phenomenon, but there seems to be little doubt that such factors as ionic bonding and/or solution and redeposition within the sediment of various cations, (e.g., silicon, iron, calcium or phosphorus) tend to alter the structural strength of the mass.

The finding of "overconsolidated" sediments in the Mediterranean basin is not surprising in light of similar observations reported elsewhere. It was somewhat surprising, however, to find that core F also displayed "overconsolidated" characteristics. This core was collected from the upper portion of the Nile Cone which is an area of relatively rapid deposition. In areas of rapid sedimentation, such as off the Mississippi River, which is admittedly an extreme case, sediments are commonly found to be underconsolidated owing to insufficient time for consolidation (dissipation of pore water pressure) to take place (Fisk and McClellan, 1959). For the type of sediment involved, it is apparent that the deposition rate on the upper Nile Cone is not so rapid that the pore water pressure cannot dissipate.

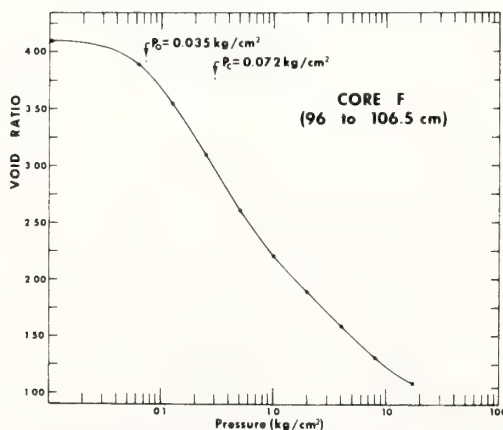


Figure 10. Consolidation test, void ratio-pressure curve.

SUMMARY

A total of 96 sediment cores from 27 different sites in the Mediterranean Sea were examined for their mass physical properties. Although these relatively few cores cannot possibly represent all the unconsolidated deposits occurring in the basin, some generalizations can be made regarding the distribution of selected mass physical properties and the range of these values can be anticipated for the surficial layers of the sea floor.

Morphologically, the Mediterranean basin can be divided into eastern and western sectors. The western Mediterranean consists largely of the Balearic and Tyrrhenian Abyssal Plains and the Rhône Fan. To the east, the basin becomes complex with a median ridge, continental borderland, few abyssal plains, and the Nile and Messina Cones. The contrast between the eastern and western portions of the Mediterranean is also evident in the sediments associated with each of the two provinces.

1. Submarine sediments west of Italy are mainly composed of terrigenous lutites derived from the River Rhône and the margins of Africa and Italy. Turbidity currents appear to be the major mechanism by which these lutites as well as fine sands are deposited in this portion of the Mediterranean. *Globigerina* and pteropod oozes are the predominant surficial deposits in the eastern Mediterranean. Although the Nile River is a major source of lutite, its influence on the sediment distribution in the eastern part of the basin is deceiving when only the surface deposits are considered. It is obvious from an examination of various mass properties with depth, even in relatively short sediment cores, that the unique characteristics of Nile-contributed sediment are rather extensive. Also, not revealed in the surface deposits, but of major importance to the overall sedimentary properties in the eastern Mediterranean, are the numerous tephra and sapropelic mud layers.

2. Average shear strengths vary from 16 to 227 g/cm²; the lower values commonly being associated with the Nile-contributed lutites and higher values with the turbidite deposits off the Rhône Fan. The western Mediterranean, with its greater abundance of turbidites, displays higher average shear strengths overall than do those sediments in the eastern sector of the basin.

3. Water content varies from 30 to 124 percent, but commonly occurs in the range of 50 to 100 percent throughout the most of the Mediterranean basin. Only in the Tyrrhenian basin and in those areas influenced by the Nile do water contents greater than 100 percent occur. Continental margin deposits tend to be coarser-grained and possess relatively low water contents. Fine-

grained ash and pumice deposits in the vicinity of the island of Crete also display low water contents.

4. Unit weight values are found to range from 1.35 to 1.90 g/cc throughout the Mediterranean. The western Mediterranean is blanketed primarily by sediments displaying unit weights of 1.75 to 1.90 g/cc. This same property in the eastern Mediterranean commonly varies from 1.65 to 1.70 g/cc except in the easternmost areas where Nile-contributed sediments display unit weights of 1.40 to 1.47 g/cc.

5. Average porosities vary only slightly (60 to 68 percent) throughout most of the Mediterranean basin. The highest observed values occur in the Tyrrhenian basin and in the extreme eastern Mediterranean where Nile-derived lutites predominate. Low porosities (50 percent) are found to characterize sediments from the outer Rhône Fan, the fine-grained ash and pumice occurring north of Crete, and those deposits along the eastern margin of Tunisia which are composed largely of relatively coarse-grained calcareous material.

Variation of the selected mass physical properties within the upper 3 to 4 m of the sea floor is mainly controlled by changes in sediment texture. Turbidites in the western Mediterranean are clearly distinguished from the surrounding sediments by their high shear strengths and unit weights as well as low water contents and porosities. Just the reverse is observed in the case of the numerous sapropelic mud layers occurring in the eastern Mediterranean. Nile-contributed lutites, which cover much of the eastern Mediterranean display decidedly different plasticity characteristics than those sediments from the central and western portions of the basin. The lutites are highly plastic whereas those from other parts of the Mediterranean possess distinctly lower plasticity indices.

Examination of the consolidation or compaction (as commonly used in geology) characteristics of sediments from both the eastern and western Mediterranean indicates that they are similar to those of "overconsolidated" deposits. There is little doubt that these sediments are not "overconsolidated" (as defined in soil mechanics), but have increased in strength by means of ionic bonding or some form of "cementation" so as to behave in a manner indicating an "overconsolidated" state.

ACKNOWLEDGMENTS

Thanks are due to David R. Horn of the Lamont-Doherty Geological Observatory and John Bethell of the SACLANT ASW Research Centre, La Spezia, Italy, for providing us with data on sediment mass properties. We are indebted to P. Blavier and C. Gehin of the SACLANT Centre and F. Kögler of

Kiel University for allowing us to use some of their unpublished data in this study. We are most grateful for the assistance provided us by the officers and crew of the NOAA OCEANOGRAPHER during the collection of sediment cores for this study. We acknowledge with many thanks the critical review of this paper by Louis Butler, Harris B. Stewart, Jr., Adrian F. Richards, and Richard Bennett.

REFERENCES

- Almagor, G. 1964. Studies of sediments in core samples collected from the shelf and slope off Tel-Aviv-Palmakhim coast. *Geological Survey of Israel Report*. QGR/2/64:80p. (unpublished).
- Almagor, G. 1967. Interpretation of strength and consolidation data from some bottom cores off Tel Aviv-Palmakhim coast, Israel. In: *Marine Geotechnique*, ed. Richards, A. F., University of Illinois Press, Urbana, 131-153.
- Arrhenius, G. 1952. Sediment cores from the East Pacific. *Reports of the Swedish Deep-Sea Expedition 1947-1948*, 5(1): 227 p.
- Bryant, W. R., P. Cernock and J. Morelock, Jr. 1967. Shear strength and consolidation characteristics of marine sediments from the Western Gulf of Mexico. In: *Marine Geotechnique*, ed. Richards, A. F., University of Illinois Press, Urbana: 41-62.
- Bryant, W. R., and C. S. Wallin 1968. Stability and geotechnical characteristics of marine sediments, Gulf of Mexico. *Transactions, Gulf Coast Association of Geological Societies*, 18:334-356.
- Casagrande, A. 1948. Classification and identification of soils. *American Society of Civil Engineers, Transactions*, 113:901-931.
- Einsele, G. 1967. Sedimentary processes and physical properties of cores from the Red Sea, Gulf of Aden and off the Nile Delta. In: *Marine Geotechnique*, ed. Richards, A. F., University of Illinois Press, Urbana, 154-169.
- Emery, K. O., B. C. Heezen and T. P. Allan 1966. Bathymetry of the Eastern Mediterranean Sea. *Deep-Sea Research*, 13:173-192.
- Evans, I. and G. G. Sherratt 1948. A simple and convenient instrument for measuring the shear resistance of clay soils. *Journal of Scientific Instruments and Physics in Industry*, 25:411-414.
- Fisk, H. N. and B. McClelland 1959. Geology of continental shelf off Louisiana: its influence on offshore foundation design. *Geological Society of America Bulletin*, 70:1369-1394.
- Flaate, K. 1965. A statistical analysis of some methods of shear strength determination in soil mechanics. *Norwegian Geotechnical Institute Publication*, 62:8p.
- Gehin, C. and P. Blavier 1969. Numerical results of the analysis of sea-bottom cores, Vol. 2 Alboran Sea. *NATO SACLANT ASW Research Centre, La Spezia, Special Report* (unpublished), M-52:30p.
- Goncharov, V. P. and O. V. Mikhailov 1964. New data on the bottom relief of the Mediterranean. *Deep-Sea Research*, 11:625-628.
- Hamilton, E. L. 1959. Thickness and consolidation of deep-sea sediments. *Geological Society of America Bulletin*, 70:1399-1424.
- Hamilton, E. L. 1964. Consolidation characteristics and related properties of sediments from experimental MOHOLE (Guadalupe site). *Journal of Geophysical Research*, 69:4257-4269.
- Hamilton, E. L., and H. W. Menard 1956. Density and porosity of sea-floor surface sediments off San Diego, California. *Bulletin of the American Association of Petroleum Geologists*, 40:754-761.
- Hansbo, S. 1957. A new approach to the determination of the shear strength of clay by the fall-cone test. *Royal Swedish Geotechnical Institute Proceedings*, 14:47p.
- Heezen, B. C. and M. Ewing 1955. Orleansville Earthquake and turbidity currents. *Bulletin of the American Association of Petroleum Geologists*, 39:2505-2514.

- Hersey, J. B. 1965. Sedimentary basins of the Mediterranean Sea. In: *Submarine Geology and Geophysics*, eds. Whittard, W. F. and R. Bradshaw, Butterworths, London, 75-89.
- Holeman, J. N. 1968. The sediment yield of major rivers of the world. *Water Resources Research*, 4(4):737-741.
- Horn, D. R., B. M. Horn and M. N. Delach 1967. Correlation between acoustical and other physical properties of Mediterranean deep-sea cores. *Texas Instruments, Inc., Technical Report*, 2: 152p.
- Horn, D. R., B. M. Horn and M. N. Delach 1968. Correlation between acoustical and other physical properties of deep-sea cores. *Journal of Geophysical Research*, 73:1939-1957.
- Interdepartmental Geophysical Committee of the Academy of Sciences, USSR. 1969. *Bottom Sediment Chart*. Main Administration for Geodesy and Cartography, Moscow, USSR.
- Keller, G. H., and R. H. Bennett 1968. Mass physical properties of submarine sediments in the Atlantic and Pacific basins. *Proceedings, 23rd International Geological Congress*, 8:33-50.
- Kermabon, A., C. Gehin and P. Blavier 1968. Numerical results of the analysis of sea-bottom cores, Vol. I, Naples and Ajaccio zones. *NATO SACLANT ASW Research Centre, La Spezia, Special Report* (unpublished), M-46:14p.
- Kermabon, A., C. Gehin, P. Blavier and B. Tonarelli 1969. Acoustic and other physical properties of deep-sea sediments in the Tyrrhenian Abyssal Plain. *Marine Geology*, 7:129-145.
- Mellis, O. 1954. Volcanic ash-horizons in deep-sea sediments from the Eastern Mediterranean. *Deep-Sea Research*, 2:89-92.
- Menard, H. W., S. M. Smith and R. M. Pratt 1965. The Rhône deep-sea fan. In: *Submarine Geology and Geophysics*, eds. Whittard, W. F. and R. Bradshaw, Butterworths, London, 271-284.
- Moore, D. G. 1962. Bear strength and other physical properties of some shallow and deep-sea sediments from the North Pacific. *Geological Society of America Bulletin*, 73:1163-1166.
- Morelock, Jr., J. 1969. Shear strength and stability of continental slope deposits, Western Gulf of Mexico. *Journal of Geophysical Research*, 74:465-482.
- Morgenstern, N. R. 1967. Submarine slumping and the initiation of turbidity currents. In: *Marine Geotechnique*, ed. Richards, A. F., University of Illinois Press, Urbana, 189-220.
- Ninkovich, D., and B. C. Heezen 1965. Santorini Tephra. In: *Submarine Geology and Geophysics*, eds. Whittard W. F. and R. Bradshaw, Butterworths, London, 413-452.
- Olausson, E. 1960. Description of sediment cores from the Mediterranean and Red Sea. *Reports of the Swedish Deep-Sea Expedition 1947-1948*, 8(3):287-334.
- Olausson, E. 1961. Studies of deep-sea cores. *Reports of the Swedish Deep-Sea Expedition 1947-1948*, 8(4):337-391.
- Pfannenstiel, M. 1960. Erläuterungen zu den Bathymetrischen Karten des Östlichen Mittelmeeres. *Bulletin de l'Institut Océanographique*, Monaco, 1192:60p.
- Richards, A. F. 1961. Investigations of deep-sea sediment cores, I. Shear strength, bearing capacity, and consolidation. *U. S. Navy Hydrographic Office, Technical Report*, 63:70p.
- Richards, A. F. 1962. Investigations of deep-sea sediment cores, II. Mass physical properties. *U. S. Navy Hydrographic Office, Technical Report*, 106:146p.
- Richards, A. F., and E. L. Hamilton 1967. Investigations of deep sea sediment cores, III. Consolidation. In: *Marine Geotechnique*, ed. Richards, A. F., University of Illinois Press, Urbana, 93-112.
- Rittenberg, S. C., K. O. Emery, J. Hulseman, E. T. Degens, R. C. Fay, J. H. Reuter, J. R. Grady, S. H. Richardson and E. E. Bray 1963. Biogeochemistry of sediments in experimental MOHOLE. *Journal of Sedimentary Petrology*, 33:140-172.
- Ryan, W. B. F. and B. C. Heezen 1965. Ionian Sea submarine canyons and the 1908 Messina Turbidity Current. *Geological Society of America Bulletin*, 76:915-932.
- Ryan, W. B. F., F. Workum, Jr. and J. B. Hersey 1965. Sediments of the Tyrrhenian Abyssal Plain. *Geological Society of America Bulletin*, 76:1261-1282.
- Texas Instruments Incorporated 1967. 1965-67 North Atlantic Ocean, Norwegian Sea and Mediterranean Sea Area 6. *U. S. Naval Oceanographic Office Report*, Contract No. N62306-1687, 48p.
- U. S. Naval Oceanographic Office 1965. *Oceanographic Atlas of the North Atlantic Ocean. Section V. Marine Geology*. Washington, D. C. 700; 71p.
- Watson, J. A. and G. L. Johnson 1969. The marine geophysical survey in the Mediterranean. *International Hydrographic Review*, 46:81-107.
- Wong, H. K. and E. F. K. Zarudzki 1969. Thickness of unconsolidated sediments in the Eastern Mediterranean Sea. *Geological Society of America Bulletin*, 80:2611-2614.

Bottom Currents in the Hudson Canyon

Abstract. *In-place measurements of the bottom currents in the Hudson Canyon reveal that the current regime is characterized by a pronounced reversal of flow up and down the canyon. Velocities are commonly of the order of 8 to 15 centimeters per second, reaching 27 centimeters per second on occasion in the upper and central portion of the canyon. Although a 2.5-day recording of currents showed a net transport upcanyon, a combination of 66 current measurements from the submersible Alvin, the analysis of sediment texture and organic carbon, and the determination of the benthic fauna-nutrient relationship indicate that over the long term there is a net transport of fine material through the canyon to the outer continental rise.*

Bottom current measurements in canyons off the east coast of North America date back to the early studies of Stetson (1) in the canyons on Georges Bank. More recently, a limited number of current observations have been made in Oceanographer (2) and Corsair (3) canyons off New England, and in Wilmington Canyon (4) east of the Maryland-Delaware border. Most of these recent studies have been based on either a series of observations of very short duration (minutes) from a submersible or interpretations of bottom photographs and video tapes. Fenner *et al.* (5) obtained a limited number of short-term measurements over a 3-day period in the Wilmington Canyon

by using a free fall and return type of current meter (6). Stetson (1), although the only one to employ a bottom-mounted current meter, was held to roughly 30-minute observations at each station due to the station-keeping limitations of his ship. Bottom and near-bottom current activity has only been monitored to any extent in the canyons off southern California, where Shepard and Marshall (7, 8) recorded currents for periods up to 15 days, and in the submarine valley of the Var, off Nice, where Genesseeux *et al.* (9) observed currents over a 25-day period. This report deals with a series of in-place measurements of bottom currents along the axis of the Hudson Canyon;

the measurements were made during a 3-month period and ranged in duration from 1 minute to 2.5 days.

The Hudson Canyon, 220 km southeast of New York City, is the most pronounced of the east coast canyons, cutting from 200 to 800 m into the continental slope and extending approximately 370 km from the shelf edge to the deep sea (Fig. 1). Its axial slope is of the order of 23 m/km to a depth of 800 m, increasing to about 30 m/km out to 2000 m. Its overall appearance is that of a relatively broad (7 to 9 km wide), well-incised canyon which has been blanketed with fine-grained sediments throughout most of its length. Only in the canyon head area does erosion appear to be taking place. Within the central canyon (at depths of 400 to 1000 m) ridges of semiconsolidated silty clay trending both parallel and perpendicular to the axis rise as much as 70 m above the canyon floor. Indications are that some of the ridges crossing the canyon serve to restrict the movement of bottom water up and down the canyon. The overall physiographic aspects of the canyon and its relationship to the surrounding sea floor have already been described (10).

The present study was undertaken to investigate the bottom current condi-

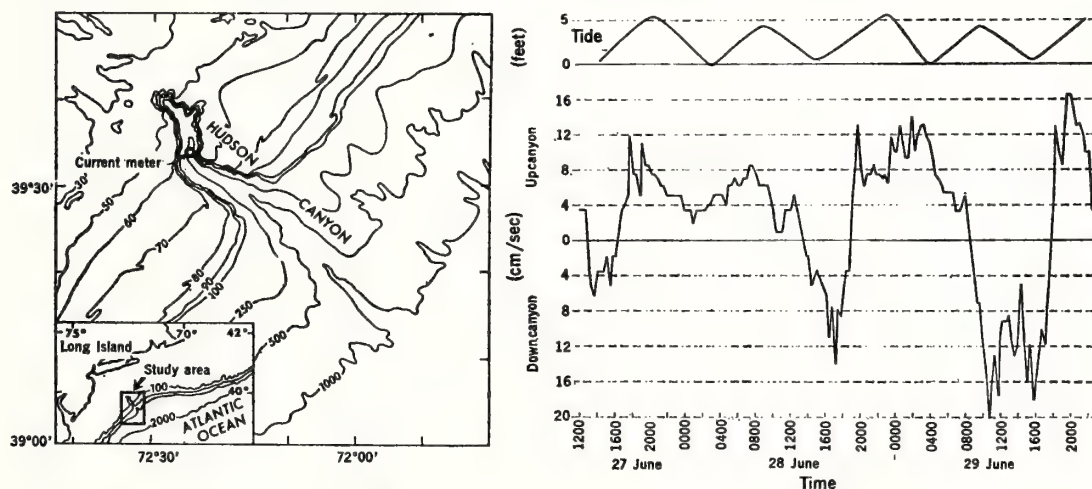


Fig. 1 (left). Generalized bathymetry and location of the Hudson Canyon. The contours are in fathoms (1 fathom \approx 1.8 m). [Data from Coast and Geodetic Survey Chart 1108] Fig. 2 (right). Comparison of upcanyon and downcanyon flows measured by a bottom-mounted meter at 471 m. The tides for the same period predicted for Sandy Hook, New Jersey, are shown at top (1 foot = 30.48 cm).

tions in the Hudson Canyon, to relate these conditions to both the mass physical properties and flux of the sediment, and to determine the influence of the currents on the benthic fauna within the canyon. This report, however, deals primarily with the observed current regime.

Much of the study was conducted from the submersible *Alvin* during a series of 15 dives in the months of June and September 1972. Basic observations during the dives consisted of measurements of bottom currents with a Savonius type meter held 12 cm above the canyon floor, collection of suspended sediments, core and grab sampling of the bottom sediment, and almost continuous photographic coverage of the dive sites. The dive sites were located from the canyon head out to depths of 1826 m, and the average time on the bottom was 4 hours per dive. In addition to observations from the submersible, 30 camera and coring stations on the bottom, both in the canyon and on its banks, were occupied remotely from a surface vessel. To define the current activity, a bottom-mounted current meter (General Oceanics, model 2010) was placed in the axis of the canyon at a depth of 471 m during the dives in June and retrieved in September. In addition, a series of reference stakes were planted from *Alvin* in the vicinity of the meter to monitor possible sediment movement.

Although relatively few bottom current measurements have been made to date, it appears that flow reversal is a characteristic common to submarine canyons (1, 7). Stetson (1) related such flow to tidal activity, but Shepard and Marshall (7), in a much more extensive study of La Jolla and Scripps canyons, could find no distinct tidal relationship.

Unfortunately, the bottom-mounted meter placed in the Hudson Canyon had a failure of its recording element after 2.5 days. Although the limitations of such a short observation period are obvious, the data obtained do serve to document the reversal of flow within the canyon (Fig. 2). During this period, upcanyon flow was of longer duration but usually at much lower velocities than downcanyon transport, for which currents as high as 22 cm/sec were recorded. Owing to the limitations of these data, it is difficult to assess the periodicity of flow reversals or any possible tidal relations. During the first 35 hours of observation, it appears that reversals occurred about every 12 to

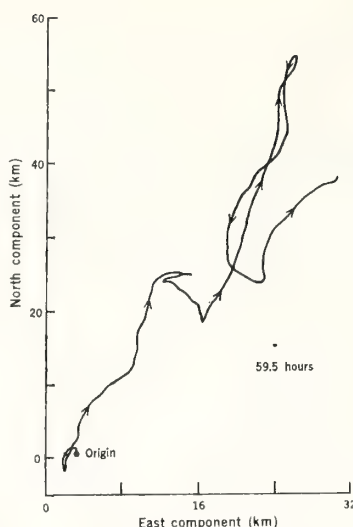


Fig. 3. Progressive vector diagram showing net transport during a 59.5-hour period, as determined from the bottom-mounted current meter at 471 m.

14 hours, closely approximating the tidal cycle recorded at Sandy Hook, New Jersey. During this time, downcanyon flow or minimum upcanyon activity appears to have coincided with periods of low tide at Sandy Hook (Fig. 2). Such a relationship, however, was not found during the last 24 hours of recording. Just how the current reversal is related to tidal activity is not evident from our observations. Internal waves generated by tidal currents impinging on the continental margin probably influence the current reversals to some extent and thus further complicate the overall relationship. A progressive vector diagram of the data from the bottom station reveals that during the 2.5 days of operation the net transport was upcanyon (Fig. 3); the canyon is oriented north-south at the current meter station. A bias in these measurements cannot be ruled out. In a relatively wide canyon like the Hudson, the tidal flow will be asymmetrically distributed at any one location between the zones of maximum flood and ebb, so that a single meter may show some degree of bias.

There are, however, strong indications that over the long term there may be a net transport downcanyon. During the two series of dives, 24 to 30 June and 7 to 14 September, approximately 66 bottom current measurements were made with a Savonius meter deployed from *Alvin*. The actual measurements

were for periods of 1 to 2 minutes, but the duration and direction of flow was monitored throughout the dive. By compiling these determinations of direction and duration for the measured velocities during all the diving days, an attempt was made to roughly approximate the net transport. For the June period it was found that 61 percent of the flow was downcanyon, whereas the September dives showed 83 percent of the transport downcanyon. These are necessarily crude estimates of the net transport, but we believe that the short-period observations from the submersible do provide an important indication of current flow.

Based on the measurements from *Alvin*, it was found that relatively high velocities (20 to 27 cm/sec) commonly occurred in the upper and central portion (150 to 1000 m) of the canyon. Beyond 800 m, velocities were considerably less, commonly of the order of 2 to 5 cm/sec. These relatively few observations are far from adequate to document the bottom current conditions, but they do appear to present the generalized current regime along the axis of the canyon.

Our study of the sediments lends further support to the concept of long-term transport downcanyon. The sediments progress in texture from sand with well-rounded pebbles in the canyon head to silt and clayey silt to depths of 400 m and silty clay to the 2000-m isobath. Some silts and fine sands do occur in the deeper portions along the margins of the canyon.

The central portion of the canyon (400 to 1000 m) appears to be a unique zone of deposition. Sediments are very soft with a fluffy surface resembling accumulated dust. Cohesion in the upper 4 cm of this sediment is of the order of 5 to 9 g/cm², the lowest recorded in the canyon. The current velocities in this section of the canyon were as high as 27 cm/sec during one dive and averaged 10 to 15 cm/sec (Fig. 2). Although the sediments are fine-grained, one might have anticipated that at least the fluffy material would have been moved by these currents. This was not the case; no movement of bottom material was recorded. Observations of the bottom in the vicinity of reference stakes for an additional 3 months further indicated that no erosion or deposition was taking place. The fluff covering the canyon floor appears to be largely biological in origin and may in some way develop cohesion from the organic makeup of its various

components. This portion of the canyon also happened to be a zone of very low visibility owing to a turbid water mass blanketing the bottom. The turbid suspension was concentrated in a zone 4 to 5 m thick, and often caused zero visibility. The suspension was largely made up of biological material of varying sizes and shapes, but a brown coloration seen from the backscatter of the *Alvin's* lights indicated that sediment also comprised a large portion of the turbid mass. A comparison of the visibility conditions found throughout the canyon indicates that the zone of high turbidity is confined to this part of the canyon. The possible damming influence of ridges trending across the canyon in this area may account for the localization of these conditions. These turbid conditions were not related to the sea state at the time of observation (state 3), but are believed to have resulted from much stormier conditions some time before the dives.

Most of the canyon consists of much finer material than the surface sediments reported for the surrounding continental margin (11). Only in the canyon head, where sands apparently enter from the surrounding continental shelf, are textures similar to those on the adjacent shelf.

A study of organic carbon in the canyon sediments indicates enrichment by a factor of 2 to 3 relative to that reported for deposits on the adjacent continental shelf, slope, and rise (11, 12). The organic carbon contents of 3.0 to 3.5 percent commonly found in the canyon are similar to those reported for areas of upwelling (13).

A study of biomass concentration in the canyon sediments and the determination of available food for these organisms indicates that concentrations of food are considerably higher in the canyon than elsewhere in the North Atlantic. Since there is no indication that surface productivity is any greater over the canyon than in adjacent waters, the nutrient-rich material apparently is moving out into the canyon from a shelfward source.

Although all the data have not yet been fully analyzed, they lend strong support to the hypothesis of long-term net transport down the canyon. The sediment and biological data reveal the presence of a tongue of fine-grained, nutrient-rich material extending out to the continental rise through the Hudson Canyon. It is suggested that these sediments are primarily carried in suspension out across the continental shelf and into the canyon, where they are further transported downcanyon. Some of this material may also be derived from resuspension of sediment eroded from the shelf break.

During lower stands of sea level the canyon displayed much higher current activity than is found today. Coring of turbidite sequences not only in the canyon but from its outer terminus reveals that the canyon served as a conduit for the transport of coarse-grained material from the continental shelf to the deep-sea floor during the Pleistocene (14). Although coarse sands and gravels are present in the canyon head and are being transported locally by bottom currents today, there is no indication that this material is carried very far down the canyon. Despite strong bottom currents, the Hudson Canyon is relatively less active in funneling coarse-grained material or large volumes of finer sediment to the abyssal plain than it was in the Pleistocene, and less active than the canyons off southern California today.

Although the 2.5 days of continuous bottom current measurements in the Hudson Canyon revealed periodic reversals of flow as well as a net transport up the canyon, a considerable amount of other evidence indicates that the long-term net transport may be down the canyon. Not only did the majority of current observations from the *Alvin* show predominant downcanyon flow, but the sediment and biological studies indicate that the flux of fine-grained, nutrient-rich sediment is directed into the canyon from the coastal zone.

Coarse sediment is transported as a traction load only in the canyon head

and does not appear to move very far down the canyon. Canyon sediments are mainly silt, clayey silt, and silty clay, which are apparently carried into the canyon in suspension. This fine-grained material is transported across the outer continental shelf, bypassing the canyon head and largely being deposited in the central part. The blanket of very turbid water plus sediments of low cohesion and density found in this portion of the canyon attest to relatively high rates of sedimentation taking place at this time. Beyond this zone, finer sediments are carried to the outer limits of the canyon.

GEORGE H. KELLER
DOUGLAS LAMBERT

National Oceanic and Atmospheric
Administration, Atlantic Oceanographic
and Meteorological Laboratories,
Miami, Florida 33149

GILBERT ROWE
NICHOLAS STARESINIC

Woods Hole Oceanographic Institution,
Woods Hole, Massachusetts 02543

References and Notes

1. H. C. Stetson, *Trans. Amer. Geophys. Union* 18, 216 (1937).
2. J. V. A. Trumbull and M. J. McCamis, *Science* 158, 370 (1967).
3. D. A. Ross, *Nature* 218, 1242 (1968).
4. D. J. Stanley and G. Kelling, *U.S. Coast Guard Oceanogr. Rep.* 22 (1968).
5. P. Fenner, G. Kelling, D. J. Stanley, *Nature* 229, 52 (1971).
6. S. J. Niskin, *Mar. Sci. Instrum.* 3, 123 (1965).
7. F. P. Shepard and N. F. Marshall, *Science* 165, 177 (1959).
8. —, *Amer. Ass. Petrol. Geol. Bull.*, in press.
9. M. Genesseeux, P. Guibout, H. Lacombe, *C.R.H. Acad. Sci. Ser. D* 273, 2456 (1971).
10. B. C. Heezen, M. Ewing, M. Tharp, *Geol. Soc. Amer. Spec. Pap. No. 65* (1959); R. M. Pratt, *Deep Sea Res.* 14, 409 (1967).
11. J. C. Hathaway, *Woods Hole Oceanogr. Inst. Ref. No. 71-15* (1971).
12. H. L. Sanders, R. R. Hessler, G. R. Hampson, *Deep Sea Res.* 12, 845 (1965).
13. G. T. Rowe, *Invest. Pesq.* 35 (No. 1), 127 (1971).
14. D. B. Ericson, M. Ewing, G. Wollin, B. C. Heezen, *Geol. Soc. Amer. Bull.* 72, 193 (1961); D. R. Horn, M. Ewing, B. M. Horn, M. N. Belach, *Mar. Geol.* 11, 287 (1971).
15. Funding for support of the submersible and surface vessel was provided by the Manned Undersea Science and Technology Office, National Oceanic and Atmospheric Administration. We acknowledge the significant contribution that the staff of the *Alvin* made to this study by their fine cooperation and unique capability.

4 December 1972; revised 19 January 1973

SEDIMENTS IN THE ATLANTIC CORNER SEAMOUNTS: CONTROL BY TOPOGRAPHY, PALEO-WINDS, AND GEOCHEMICALLY-DETECTED MODERN BOTTOM CURRENTS

BONNIE A. MCGREGOR¹*, PETER R. BETZER² and DALE C. KRAUSE¹*

¹ Graduate School of Oceanography, University of Rhode Island, Kingston, R. I. (U.S.A.)

² Marine Science Institute, University of South Florida, St. Petersburg, Fla. (U.S.A.)

(Accepted for publication January 9, 1973)

ABSTRACT

McGregor, B. A., Betzer, P. R. and Krause, D. C., 1973. Sediments in the Atlantic Corner seamounts: control by topography, paleo-winds, and geochemically-detected modern bottom currents. *Mar. Geol.*, 14: 179-190.

The topography in the Corner seamounts area in the western North Atlantic was studied to determine its relationship to the sedimentation pattern. The areas of anomalously thick sediment accumulation that are found on the north side of the seamounts are related to volcanic activity as well as paleocurrent and wind patterns. An irregular sediment surface has been formed by slump structures and actively eroding bottom currents, the latter as evidenced by high particulate iron concentrations in the bottom water.

INTRODUCTION

The Corner seamount group, originally called the Corner rise (Heezen et al., 1959), physiographically is located at the boundary of the mid-ocean ridge and deep basin (Fig.1). It is also located at a sedimentation pattern boundary, between turbidity current sediments of the Sohm abyssal plain and pelagic sediments of the mid-ocean ridge. Ewing et al. (1964) noted anomalous sediment structures and sediment thicknesses in this area and suggested that post-depositional tectonic activity had occurred. Bathymetric data and additional seismic reflection profiles were made to characterize the sediment distribution pattern and sediment thickness in the area between 34-37°N and 47-52°W in the western North Atlantic. Surface to bottom water samples from the area were filtered and analyzed for particulate iron, as a nepheloid layer indicator, to show the degree of sediment/bottom-water interaction.

* Present address: Atlantic Oceanographic and Meteorological Laboratories, National Oceanic and Atmospheric Administration, 15 Rickenbacker Causeway, Miami, Fla. (U.S.A.)

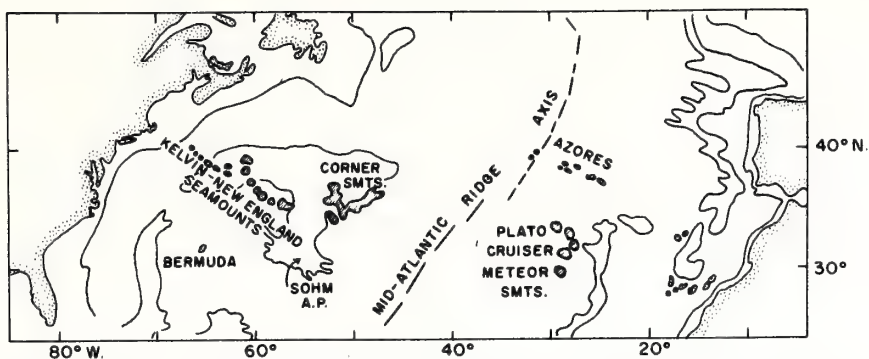


Fig.1. Index map of North Atlantic showing the location of the Corner seamounts area.

BATHYMETRY

Continuous bathymetric data were collected along the ship's tracks (Fig.2), using a metric P.E.S.R. (Precision Echo Sounding Recorder, Alpine Geophysical Associates, Inc.) with an Edo transmitter and transducer (AN/UQN-1C). Fig.3 is a bathymetric map of the area with depths in uncorrected meters and a 100 m contour interval. Contouring of the seamount at $35^{\circ}50'N$, $50^{\circ}45'W$ is based on scattered soundings from the U.S. Naval Oceanographic Office data collection sheets, and the seamount at $36^{\circ}20'N$, $51^{\circ}20'W$ was surveyed by Woods Hole Oceanographic Institution.

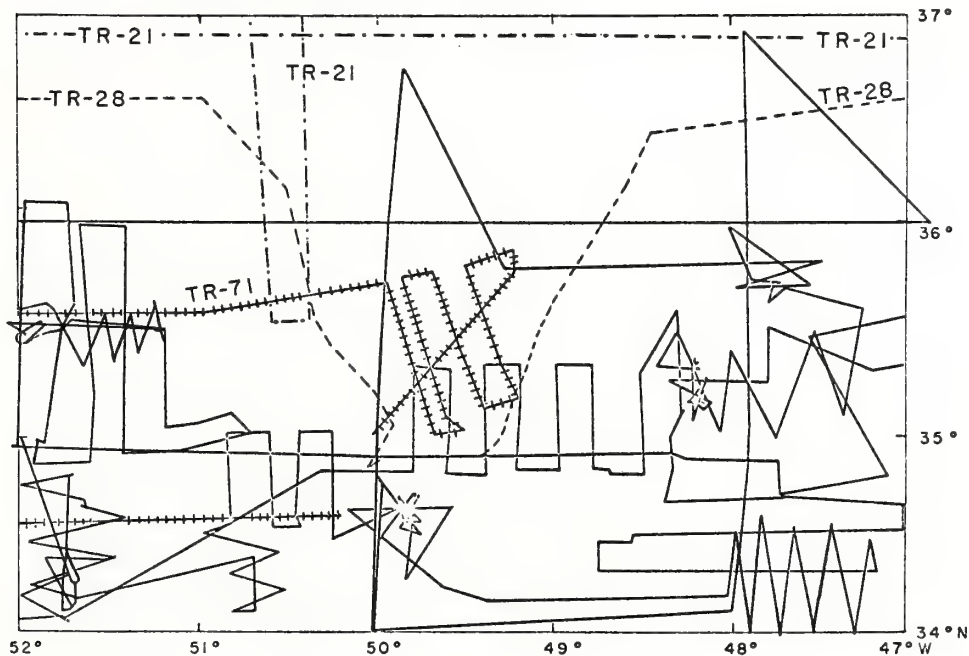


Fig.2. Track chart of R/V "Trident" cruises in the Corner seamounts area. Solid line TR-49, solid crossed TR-71, dashed TR-28, and dot dashed TR-21.



Fig. 3. Bathymetric map of Corner seamounts. Contour interval 100 m. Depths in uncorrected meters with 1500 m/sec assumed sound velocity. Shaded area depths greater than 5000 m. Circled dots are Betzer's (1971) stations (Table I).

The seamounts are aligned in two distinct trends, N25°W and N65°E. The significance of the seamount trends and their relationship to the tectonic evolution of the North Atlantic sea floor are discussed elsewhere (McGregor and Krause, 1972). Their preferred model requires that the seamounts result as volcanoes from hot spot migration (Morgan, 1971) with interaction of the hot spot and Late Cretaceous Mid-Atlantic Ridge rift so that seamount trends indicate relative North American plate motion. The topography around the seamounts consists of an abyssal plain to the west, abyssal hills to the south and undulating sea floor to the north. A sediment finger from the Sohm abyssal plain extends into the area between 35°N, 52°W and 34°20'N, 51°W and slopes slightly downward to the southeast with a gradient of 1:4600. Topography and trend indicate that this sediment finger is confined in a fracture zone. A low ridge to the north of the N65°E seamounts is outlined by the 5,000 m contour. Of the five seamounts with tops at approximately 1,000 m depth, four are guyots, with the seamount at 34°45'N, 50°25'W the exception (Fig.3). The minimum depth in the area is 650 m (655 m corrected) on the westernmost seamount and the maximum depth is 5500 m (5565 m corrected) at the end of the sediment finger.

SEISMIC REFLECTION PROFILES

Three seismic reflection profiles (Fig.4) were run across the area using three 10 cu in (160 cc) air guns (Bolt Associates Pneumatic Acoustic Repeater) with a General Oceanics "garden hose" hydrophone and a Raytheon PFR recorder. Profile 4 (Fig.4) from Ewing et al. (1964) shows an increase in sediment thickness in the general area of the Corner seamounts. The sediment and basement topography are rough in the area, giving way to the flat sediments of the Sohm abyssal plain in the north. Profile 4 also shows that the maximum sediment thickness in the area is 750 m. Acoustic basement was not reached in many places on profiles 1 to 3. A few internal reflectors are present, but much of the sediment is acoustically transparent. Two rather flat-surfaced sediment ponds are present at the western end of profile 1 with thicker sediment accumulation in the eastern pond. Proceeding eastward along the profile on the east flank of the seamount at 36°N, 51°20'W, a channel has been cut into the slumped sediments at its base. Along the remainder of the profile, the sediment surface is irregular, suggesting sculpturing by bottom currents. On profile 2 (Fig.4, 5) a considerable amount of slumped sediment is present around the base of the seamounts. A sequence of slumps is present on the north side of the seamount at 35°N, 48°W, and a channel cutting this material has been filled by acoustically transparent sediment. Other channels or zones of nondeposition are present on the northern half of this profile. Profile 3 shows that the guyot at 34°45'N, 50°W, has a transparent cap. This was the only guyot summit that was crossed. Similar transparent caps of pelagic sediment on guyots are reported by Karig et al. (1970) in the Pacific and by Emery et al. (1970) on Mytilus seamount in the Atlantic. From these four profiles and, as demonstrated by the record of profile 2 (Fig.5), the general sediment distribution can be characterized by an increase in sediment thickness north of the N65°E trending seamounts, with extensive sculpturing by bottom currents also occurring in this area.

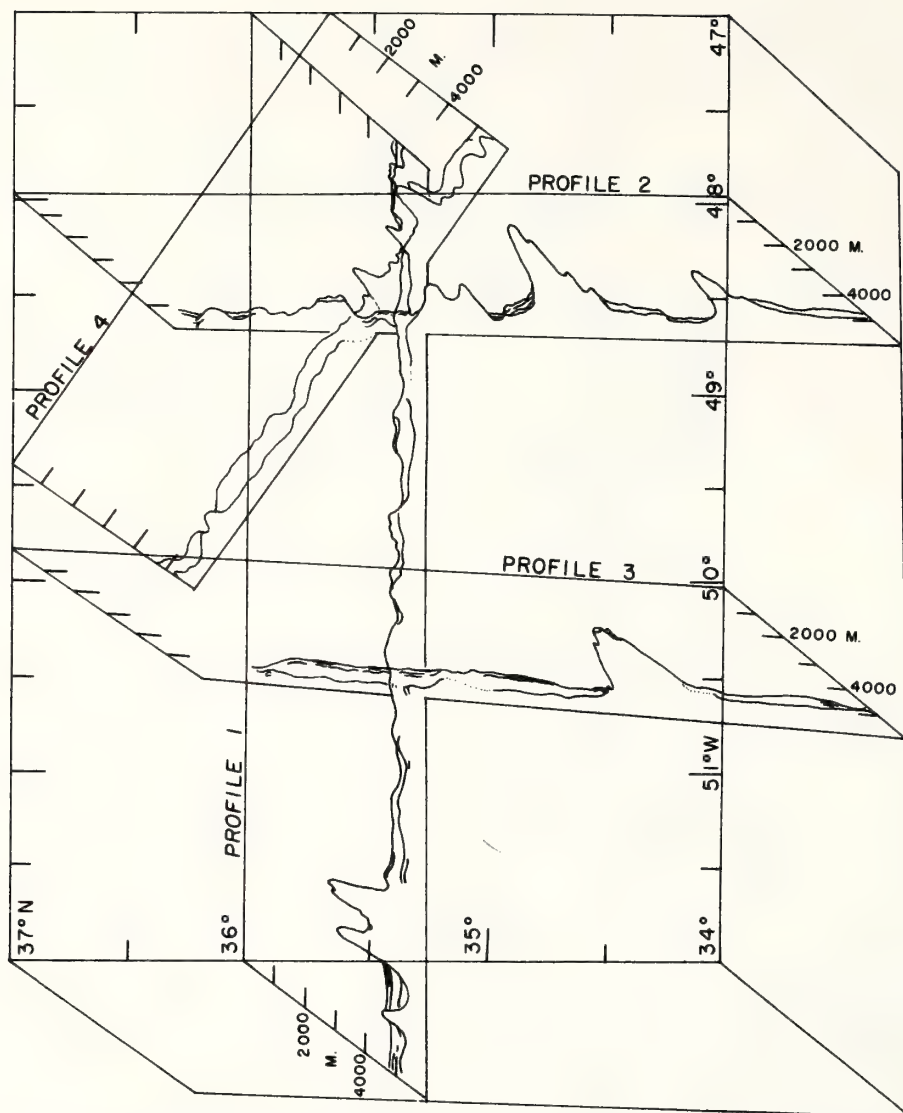


Fig.4. Sub-bottom profiles. Profiles 1–3 were run on cruise TR-49. Profile 4 is from Ewing et al. (1964).

DISCUSSION

The origin of the sediment and its distribution pattern is significant in determining the environmental and depositional history in the area. Ewing et al. (1964) show a sediment thickness in the Corner seamounts area double that to the east, with this increase primarily north of the N65°E seamounts. The pelagic sediment can be expected to give a layer

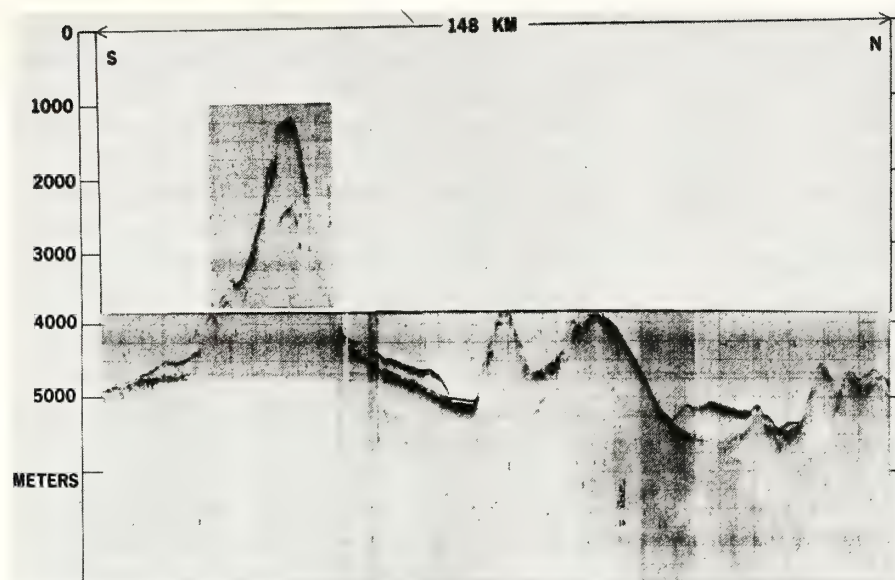


Fig. 5. Sub-bottom reflection record of profile 2 (Fig. 4), between $34^{\circ}55'N$, $47^{\circ}54'W$ and $36^{\circ}15'N$, $47^{\circ}56'W$.

of uniform thickness, except where slumped or sculptured by currents. However, the presence of the volcanic guyots themselves suggest that the older sediments in the area must be volcanic as well as pelagic. Explosive shallow-water volcanism probably occurred during the active period of the Corner seamounts, producing much ash and volcanic debris. This is supported by the presence of guyots and shallow-water reef algae associated with Eocene Foraminifera (K.N. Sachs, 1969, personal communication) dredged from the seamount at $35^{\circ}30'N$, $52^{\circ}W$. The occurrence of explosive volcanism is also supported by an increase in volcanic material in the Campanian age sediments from the JOIDES Leg II site 10 hole at $32^{\circ}52'N$, $52^{\circ}13'W$ (Peterson et al., 1970). The age of the Corner seamounts is believed to be Late Cretaceous based on a hot spot model of formation and their association with Late Cretaceous sea floor dated on the basis of the sea-floor magnetic lineation pattern from earth's field reversals (McGregor and Krause, 1972). From the JOIDES site 10 hole a slightly higher sedimentation rate is found for the interval Campanian to Upper Maastrichtian (Peterson et al., 1970), which may be attributed to the volcanic activity. Lack of a thick accumulation of volcanic material implies that the site 10 hole is up-wind or up-current from the seamounts. Also the thicker sediment accumulation north of the $N65^{\circ}E$ trending seamounts is consistent with this implied current or wind pattern.

In order to consider current and wind patterns, the location of the seamounts when active volcanically must be determined in light of plate motions. From the hot spot model of origin, the Corner seamounts would have formed on the Mid-Atlantic Ridge

crest at a latitude slightly lower than 30°N. Paleolatitude determination on sediments from JOIDES site 10 show a uniform increase in the mean latitude from Late Cretaceous to the present (Sclater and Cox, 1970). The presence of reef algae can be interpreted as support for this in that a lower latitude in the past could explain these reef algae. Assuming that paleocurrent and wind patterns are similar to those found today, the predominant surface current direction over the Corner seamounts would have been from the south-southeast (Neumann and Pierson, 1966), with a similar southerly wind pattern (*Oceanographic Atlas*, 1963). This would insure that most volcanic debris would have been swept or blown to the north side of the N65°E seamounts. Most slump features shown on the sub-bottom profiles are in this area where sediment accumulation is greater. Rapid accumulation of sediment on the volcanic slopes would contribute to sediment failure and slumping.

TABLE I

Concentrations of particulate iron in sea water samples from Tr-49 (Betzer, 1971)

Station number			Station number		
Position	Sample	Fe	Position	Sample	Fe
Date	depth (m)	($\mu\text{g/l}$)	Date	depth (m)	($\mu\text{g/l}$)
Water depth			Water depth		
7	600	0.064	9	600	0.110
35 09'N	1000	0.045	34 30'N	1000	0.132
49 32.5'W	2000	0.055	47 26.5'W	2000	0.072
23/5/68	3000	0.044	25/5/68	3000	0.068
5302 m	4000	0.132	4533 m	3002	0.085
	5000	1.110		3500	0.072
11	600	0.096	15	300	0.042
34 33'N	998	0.092	34 17'N	600	0.067
50 35'W	1000	0.069	51 42'W	900	0.095
28/5/68	2000	0.076	30/5/68	1200	0.078
4379 m	3000	0.104	2004 m	1500	0.115
	4000	0.259		1800	0.189
17	600	0.077	18	600	0.081
35 05'N	1000	0.242	35 07'N	1200	0.122
51 48'W	2000	0.108	50 40'W	2200	0.098
31/5/68	3000	0.080	1/6/68	3200	0.108
5533 m	4000	0.112	5071 m	4200	0.375
	5000	1.160		5000	2.560
19	600	0.100			
35 28'N	1000	0.098			
52 18'W	2000	0.130			
2/6/68	3000	0.131			
5456 m	4000	0.155			
	5000	1.270			

Present-day bottom currents have actively eroded channels or prevented deposition, especially where flow is restricted by the topography as shown on profile 2 (Fig.4, 5). Evidence of bottom-current/sediment interaction is shown by high concentrations of particulate iron Fe_p in the bottom water which indicates the presence of a nepheloid layer (Betzer and Pilson, 1971). The highest concentrations of Fe_p in the bottom water are north of the N65°E seamounts, stations 18 and 7 (Table I; Fig.3), where channels are located, and in the sediment finger from the Sohm abyssal plain, stations 19 and 17, where the bottom slope direction and therefore probable flow direction is from northwest to southeast. Salinity measurements on bottom water samples gathered north of the N65°E seamounts (stations 7 and 18) and over the intrusive finger of the Sohm abyssal plain (stations 17 and 19) indicate a derivation from Antarctic bottom water (Worthington and Metcalf, 1961). This interpretation would also be consistent with salinity-depth contours for this area of the western North Atlantic (Worthington and Wright, 1970). The Fe_p data for station 11 (Table I) indicate that a poorly developed near-bottom nepheloid layer exists south of the N65°E seamounts. The salinity (34.906‰) of the 4,000 meter sample from this station indicates it was derived from North Atlantic deep water. Station 15 was taken directly over a seamount and showed a slight increase in Fe_p toward its crest. It is apparent from the Fe_p data for stations 9, 11, and 15 that minimal amounts of suspended matter are swept off the topographic highs by North Atlantic Deep water. A nepheloid layer may exist in deeper waters further south of the N65°E seamounts where North Atlantic Deep and/or Antarctic Bottom water can interact with fine-grained, abyssal plain sediments. The sub-bottom profiles (Fig.4) would suggest, however, that the area directly south of the N65°E seamounts does not have as dynamic bottom water movements as the area to the north. Since no evidence of post-depositional tectonic activity was found, the undulations of the sediment surface reported by Ewing et al. (1964) in the Corner seamount area can probably be attributed to slumping and sculpturing by bottom currents.

The anomalously thick accumulation of sediments can be accounted for by volcanic activity in the formation of the seamounts themselves. Some of the topographic features can be related to slump structures and dynamic bottom currents. Thus the origin of the sediments and features can be related to volcanism, paleo-wind and current pattern, modern deep currents and the general evolution of this area of sea floor.

ACKNOWLEDGEMENTS

The authors would like to thank Capt. Barnes Collinson, the crew of the R/V "Trident" and the scientific party who participated in Cruises Tr-49 and Tr-71.

The field work was supported by Office of Naval Research contract N00014-68-A-0215-0003. The data analysis was supported by National Science Foundation grant GA-21164.

REFERENCES

- Betzer, P. R., 1971. *Particulate Iron in Sea Water*. Thesis, Univ. of Rhode Island (unpublished).
- Betzer, P. R. and Pilson, M. E. Q., 1971. Particulate iron and the nepheloid layer in the western North Atlantic, Caribbean and Gulf of Mexico, *Deep-Sea Res.*, 18: 753–761.
- Emery, K. O., Uchupi, E., Phillips, J., Bowin, C., Bunce, E. and Knott, S., 1970. Continental rise off eastern North America. *Am. Assoc. Petrol. Geol., Bull.*, 54: 44–108.
- Ewing, M., Ewing, J. and Talwani, M., 1964. Sediment distribution in the oceans: the Mid-Atlantic Ridge. *Geol. Soc. Am. Bull.*, 75: 17–36.
- Heezen, B. C., Tharp, M. and Ewing, M., 1959. The floors of the oceans, 1. North Atlantic. *Geol. Soc. Am., Spec. Pap.*, 65: 122 pp.
- Karig, D. E., Peterson, M. N. A. and Shor, G. G., 1970. Sediment-capped guyots in the Mid-Pacific mountains. *Deep-Sea Res.*, 17: 373–378.
- McGregor, B. and Krause, D. C., 1972. Evolution of the sea floor in the Corner seamounts area. *J. Geophys. Res.*, 77: 2526–2534.
- Morgan, W. J., 1971. Convection plumes in the lower mantle. *Nature*, 230: 42–43.
- Neumann, G. and Pierson, Jr., W. J., 1966. In: *Principles of Physical Oceanography*, Prentice-Hall, Englewood Cliffs, N. J., pp. 424–427.
- Oceanographic Atlas of the North Atlantic Ocean, Section IV, Sea and Swell*, 1963. U.S. Naval Oceanographic Office, Washington, D. C., Publ. 700, 227 pp.
- Peterson, M. N. A., Edgar, N. T., Von der Bosch, C., Cita, M. B., Gartner, S., Goll, R. and Nigrini, C., 1970. In: *Initial Reports of the Deep-Sea Drilling Project*, 2. U.S. Gov. Printing Office, Washington, D. C., pp. 117–225.
- Sclater, J. G. and Cox, A., 1970. Paleolatitudes from the JOIDES deep-sea sediment cores. *Nature*, 226: 934–935.
- Worthington, L. V. and Metcalf, W. G., 1961. The relationship between potential temperature and salinity in deep Atlantic water. *Rapp. Proc. Verb. Cons. Int. Expl. Mer*, 149: 122–128.
- Worthington, L. V. and Wright, W. R., 1970. *North Atlantic Ocean Atlas*, Woods Hole Oceanographic Institution Atlas Series, 2, 24 pp.

15. MARINE MAGNETIC ANOMALY LINEATIONS AND PALEOMAGNETIC RESEARCH: PRELIMINARY THOUGHTS

George Peter

Atlantic Oceanographic and Meteorological Laboratories
Marine Geology and Geophysics Laboratory

Marine magnetic anomaly lineations, associated with the formation of new crust at the center of mid-oceanic ridges under the influence of the periodically reversing magnetic field of the earth, are utilized almost exclusively for the development of theories related to global tectonism. Marine paleomagnetic research relies on sedimentary samples obtained through coring of the sea floor, on igneous rock samples dredged from the ridges and seamounts, and on magnetic model studies made on selected seamounts.

There are drawbacks with all three approaches: The sedimentary samples can usually yield information only for the last few million years, the igneous rocks obtained through dredging are unoriented and can only give information on their magnetic properties, and the model computations of seamounts may give erroneous results because the true age, composition, and magnetic property of a seamount is often difficult or impossible to ascertain.

Marine magnetic anomaly lineations, on the other hand, possess certain characteristics, which may enable their utilization in marine paleomagnetic studies. These characteristics are:

1. The marine magnetic anomaly lineations each represent a discrete, recognizable time interval in geologic history.
2. Most of the magnetic lineations are distributed throughout the global oceans.
3. As the magnetized rocks responsible for the magnetic lineations were formed through the process of plate-separation (sea floor spreading) at the center of mid-ocean ridges, they represent a rather simple geologic entity (as opposed to the structure of seamounts).
4. As (a) the remnant magnetization of the ocean crust (layers 2 and 3, and maybe part of the upper mantle, with decreasing strength and order of importance) is responsible for the magnetic lineations, and (b) the remnant to induced

magnetization (Q) ratio is 10 or greater, the strength of this remnant magnetization is directly proportional to the strength of the earth's paleofield, and the amplitudes of the magnetic anomalies produced.

It is proposed that these characteristics combined enable the marine magnetic anomaly lineations to be used for statistical studies of paleofield variations and, if the rigid crustal plate motions can be established, the magnetic lineations may provide a new approach toward the determination of the motion of the paleomagnetic pole.

Preliminary studies of the amplitude (peak-to-trough) versus latitude variations of anomalies 25 through 28 in the Northeast Pacific indicate little difference between the observed amplitude changes and the computed amplitude changes, using the parameters of the earth's present magnetic field (figure 1). The interpretation of the significance of this result, as well as the refinement of the technique, awaits further studies. An independent study by Vogt et al. (1971), reports however, that good match was obtained between the amplitude changes of the "J" anomalies in the Atlantic with the computed amplitude changes, using the Jurassic magnetic pole, taken from the North American polar wandering curve.

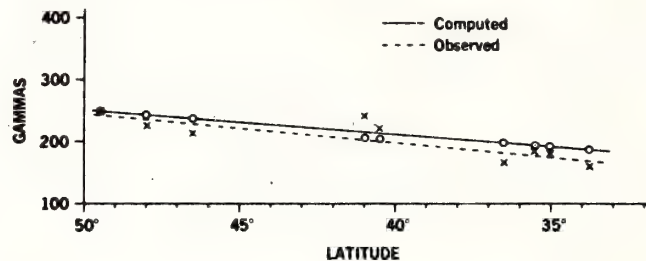


Figure 1. Averaged half amplitudes (peak-to-trough) of anomaly lineations 25 through 28, compared with the positive amplitudes of computed anomalies. For each location, the parameters (inclination, declination, field strength) of the earth's present field were used.

Reference

- Vogt, P. R., C. N. Anderson, and D. R. Bracey (1971), Mesozoic magnetic anomalies, sea floor spreading, and geomagnetic reversals in the southwestern North Atlantic, *J. Geophys. Res.*, 76, 4796-4823.

CARIBBEAN ATLANTIC GEOTRAVERSE,
NOAA-IDOE 1971,
REPORT NO. 2, MAGNETIC DATA

G. Peter, O. E. DeWald, and B. G. Bassinger

Studies of the Lesser Antilles Island Arc, the adjacent Atlantic Basin, and the Mid-Atlantic Ridge were undertaken in 1971 as part of the NOAA-IDOE-supported Caribbean Atlantic Geotraverse (CAG) project. During these investigations, approximately 30,000 km of bathymetric, magnetic, and gravity data and 1,500 km of seismic reflection data were collected in an area bordered by latitudes 14° and 17°30'N and by longitudes 42° and 62°W.

This report describes the acquisition, processing, and results of the marine magnetic data taken during the CAG project and presents a magnetic total-intensity anomaly map and a series of magnetic anomaly profiles.

Based on the magnetic data collected, the entire Cenozoic magnetic anomaly sequence has been identified east of the Lesser Antilles Island Arc to the Mid-Atlantic Ridge. From this identification, it can be concluded that the evolution of the Mid-Atlantic Ridge in the study area from the Cretaceous to the present was essentially similar to that of the rest of the North Atlantic. Possible structural control is suggested for the northern margin of the Barbados Ridge by an east-west-trending magnetic anomaly band.

INTRODUCTION

In 1971, NOAA received 1-year support from the Office for the International Decade of Ocean Exploration (IDOE) of the National Science Foundation (NSF) for geophysical studies along a 380-km wide strip extending from the Lesser Antilles Island Arc to the Mid-Atlantic Ridge (fig. 1). Studies under this project (the Caribbean Atlantic Geotraverse—CAG) were designed to test the working hypotheses which are generally proposed to explain the evolution of the Atlantic and Caribbean Basins.

Data collection commenced in 1971 aboard the NOAA ship *Researcher*. A system of east-west-oriented tracklines, spaced 38 km apart, formed the basis of the survey in the area bordered by longitudes 42° and 62°W and by latitudes 14° and 17°30'N (fig. 1). Distances between the north-south tielines varied between 200 and 360 km. Four north-south crosslines were extended southward to latitude 10°N to provide reconnaissance information for future studies.

Processed and original data collected during these investigations are available from the National Geophysical and Solar-Terrestrial Data Center (NGSDC) of NOAA in Boulder, Colo. This report in the series describes the instrumentation, acquisition, and processing of the marine total-intensity data and the major results of the magnetic studies. The reduced data are shown in the appendix in the form of stacked total-intensity anomaly profiles. Description of the overall CAG project is given in *Report No. 1* by Peter et al. (1973a).

INSTRUMENTATION AND DATA ACQUISITION

A continuous recording of the earth's total magnetic field intensity was made along the tracklines of the *Researcher*, using a Varian direct-reading proton-precession magnetometer. The sensing head of this instrument was towed approximately 215 m astern of the ship. The polarization rate was set at 6.0 seconds, and the measured field values were recorded on an analog recorder. At 1-minute intervals, the observations were also recorded on a digital magnetic (raw-data) tape. Spurious values were checked onboard and were either deleted or corrected on the tape.

DATA PROCESSING

The first phase of the data processing consisted of the merger of the navigation tape of the ship with the raw-data tape and the development of a processed data tape containing the geophysical data (depth, magnetic, and gravity) and the observation positions at 5-minute intervals. These data were available onboard ship, both in the form of digital printouts and as profiles.

The 5-minute values were adequate to describe the magnetic field in most locations. However, in the laboratory, the analog records were checked again; wherever the tracklines ran near the islands, the additional peaks and troughs of the magnetic field were read, key punched, and added to the processed data tape. The International Geomagnetic Reference Field (IGRF-1965) was computed for each data position, and the total magnetic field anomaly was obtained (Cain et al., 1967). We found the IGRF values too high in the study area; to obtain more representative anomalies, a -230 gamma correction was added to the IGRF values.

ACCURACY

The distance between the tracklines, approximately 38 km, did not warrant correction for diurnal variations. Because of its comparatively small value, the influence of the ship on the sensor was assumed to be negligible. Data accuracy is estimated to be better than ± 25 gammas from repeated observations at trackline crossings.

DATA PRESENTATION

From the final-processed magnetic data tape, listings and profiles were prepared in the laboratory. The listing contains the following columns: (1) index number; (2) Julian Day number; (3) Greenwich Mean Time—GMT (hour, minutes, and 0.1 minute); (4) latitude; (5) longitude (items (4) and (5) in degrees and decimal fractions); (6) nautical miles traveled; (7) kilometers traveled; (8) magnetic anomaly; (9) observed magnetic field; and (10) theoretical magnetic field.

In the Appendix, a presentation of the magnetic anomaly data is shown in the form of stacked profiles. The magnetic total-intensity anomaly data are plotted against latitude or longitude, depending on the heading of the profile. An index number on each profile refers to the trackline chart (fig. 1) where the location of the profiles is indicated. The time interval for each profile is given in table 1.

Table 1. Profile start and stop times for project RP-12-RE-71

Profile Number	Start		Stop	
	JD	Time	JD	Time
1	261	0800	262	0130
2	262	0405	263	1515
3	263	2330	264	1740
4	264	1835	265	1230
5	265	1420	266	0600
6	266	1010	266	1620
7	266	1625	267	0740
8	267	0745	267	1610
9	267	1615	268	2200
10	268	2205	269	1330
11	269	2125	270	1240
12	270	1245	271	0420
13	271	0425	271	1920
14	271	1925	272	0310
15	272	1315	272	1320
16	272	1325	274	1005
17	274	1010	274	1535
18	274	1540	274	2240
19	274	2245	275	1730
20	275	1835	276	2240
21	276	2245	277	0815
22	277	0820	277	1400
23	277	1405	279	1710
24	279	1725	279	2200
25	279	2205	280	1230
26	280	1505	280	1910
27	280	1915	281	0055
28	286	0100	286	0830
29	286	0905	290	2040
30	290	2300	294	1505
31	294	1717.5	299	0100
32	299	0240	302	0555
33	306	2115	309	2240
34	310	0015	312	1645
35	312	2230	315	1835
36	315	2005	318	1710
37	318	1715	320	1830
38	320	2000	322	1650

An interpretive magnetic total-intensity anomaly contour map is included in this report as figure 2. This map was prepared in two steps. First, a magnetic total-intensity map was prepared, and a regional grid was constructed over it on the basis of these observed data. This procedure allowed the determination of the true regional values, reflecting the actual magnetic field of the earth far better than even the corrected IGRF. Second, the differences between the observed and theoretical (regional) values were plotted at each crossing of the observed field and the grid lines, and these values were contoured.

DISCUSSION

Before the magnetic survey of the CAG project was made, it was not known whether a magnetic anomaly-lineation pattern, typical of mid-ocean ridges, exists east of the Lesser Antilles Island Arc. The difficulty in recognizing lineations in the existing data could have resulted from: (1) large distance and angle between tracklines; (2) small anomaly amplitudes; (3) complex fracture patterns; (4) severe topographic influences; or (5) these magnetic lineations could have been absent from the area as the Funnell-Smith (1968) hypothesis predicted. According to this hypothesis, the sea floor east of the Lesser Antilles Island Arc was formed through north-south extension, over which either east-west-oriented magnetic lineations or a completely chaotic magnetic pattern should exist. A careful correlation of the east-west magnetic anomaly profiles of this project revealed that, although the amplitude of the magnetic anomalies is small and their correction on adjacent profiles is difficult, the entire Cenozoic magnetic-lineation sequence is present in the area. The conclusion from this finding is that from the Cretaceous to the present the evolution of the Mid-Atlantic Ridge east of the Lesser Antilles Island Arc was essentially similar to that of the rest of the North Atlantic (Peter et al., 1973b). In terms of plate tectonics (Le Pichon, 1968; Morgan, 1968), the magnetic anomalies support the view that North and South American separated from Africa during this period as a single plate (minor rotations and faulting disregarded).

The identifiable magnetic lineations are located to the east of longitude 54°W. These, with the exception of the immediate area of the crest of the Mid-Atlantic Ridge, are not obvious on the magnetic anomaly map (fig. 2). A trackline system with closer than the 38-km line spacing would be needed to improve on the mapping of the magnetic lineations and on the outline of the magnetic anomalies over the topographic features and offset zones. However, one very strong east-west-trending anomaly discontinuity is outstanding on the magnetic anomaly map along latitude 15°N. Over the crest of the Mid-Atlantic Ridge, this discontinuity is associated with the 15°20'N fault zone (Collette and Rutten, 1972). The large anomalies between longitudes 48° and 51°W are over the Researcher Ridge, and the anomalies extending to longitude 54°W outline the Researcher fracture zone (Peter et al., 1973b). Large anomalies are located also over large topographic elevations at latitude 16°50'N, longitude 53°30'W; but, surprisingly, over the Barracuda Ridge, the only noticeable ridge-related anomalies are over its western and eastern edges.

The magnetic field over the Barbados Ridge is generally quiet. However, there is a group of distinct east-west-trending magnetic anomalies over the extreme northern part of the ridge (lat. 15°N). These anomalies are at the direct westward extension of similarly trending anomalies over the Atlantic Basin (discussed above) and together with topographic trends suggest that the northern terminus of the Barbados Ridge is structurally controlled.

ACKNOWLEDGMENTS

We appreciate the cooperation of CAPT Steven L. Hollis and the officers and crew of the NOAA ship *Researcher*. This work was supported in part by NSF-IDOE Grant No. AG-253.

REFERENCES

- Cain, J. C., S. J. Hendricks, R. A. Langel, and W. V. Hudson (1967): A proposed model for the International Geomagnetic Reference Field—1965, *J. Geomag. Geoelect.* 19(4):335-355.
- Collette, B. J., and K. W. Rutten (1972): Crest and fracture zone geometry of the Mid-Atlantic Ridge between 10° and 16°N, *Nature Phy. Sci.* 237(78):131-134.
- Funnell, B. M., and G. A. Smith (1968): Opening of the Atlantic Ocean, *Nature* 219(5161):1328-1333.
- Le Pichon, X. (1968): Sea-floor spreading and continental drift, *J. Geophys. Res.* 73(12):3661-3697.
- Morgan, W. J. (1968): Rises, trenches, great faults, and crustal blocks, *J. Geophys. Res.* 73(61):1959-1982.
- Peter, G., G. Merrill, and S. A. Bush (1973a): Caribbean Atlantic Geotransverse, NOAA-IDOE 1971, Report no. 1, Project introduction—Bathymetry, *NOAA Tech. Rept. ERL AOML* , pp.
- Peter, G., R. K. Lattimore, O. E. DeWald, and G. Merrill (1973b): Development of the Mid-Atlantic Ridge east of the Lesser Antilles Island Arc, *Nature Phy. Sci.* 245(148):129-131.

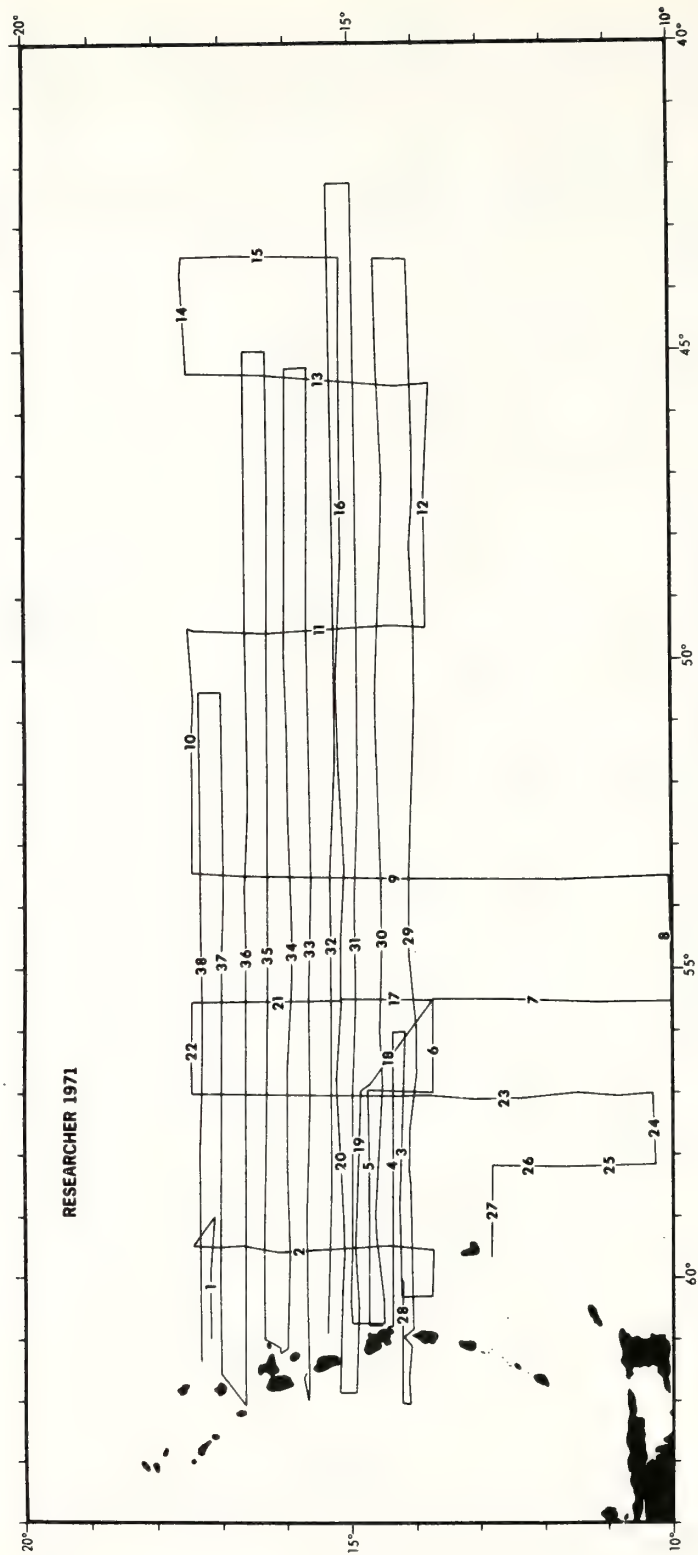


Figure 1. Trackline chart on identification of profiles.

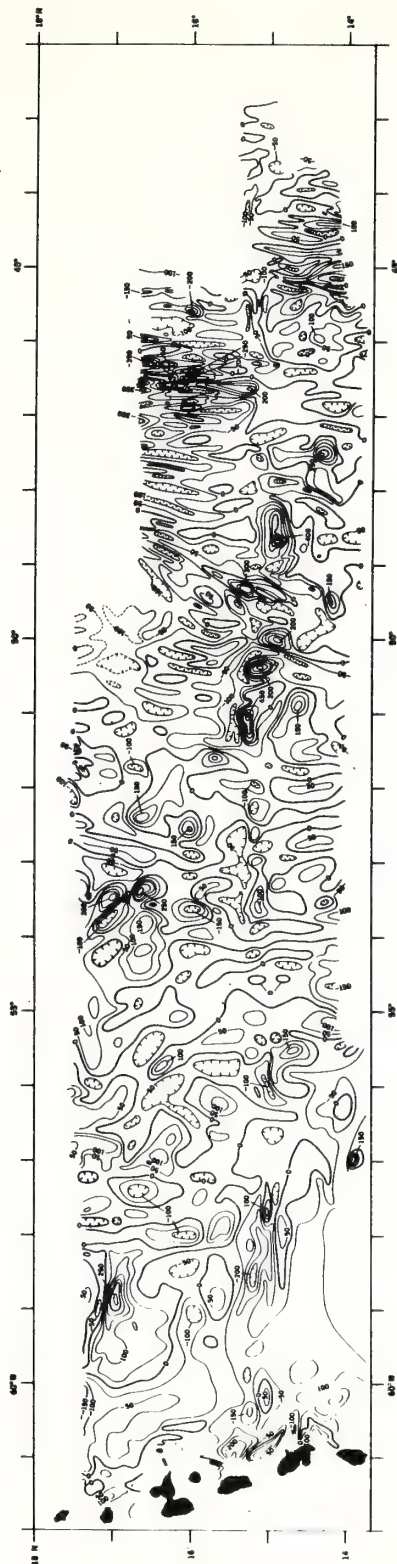
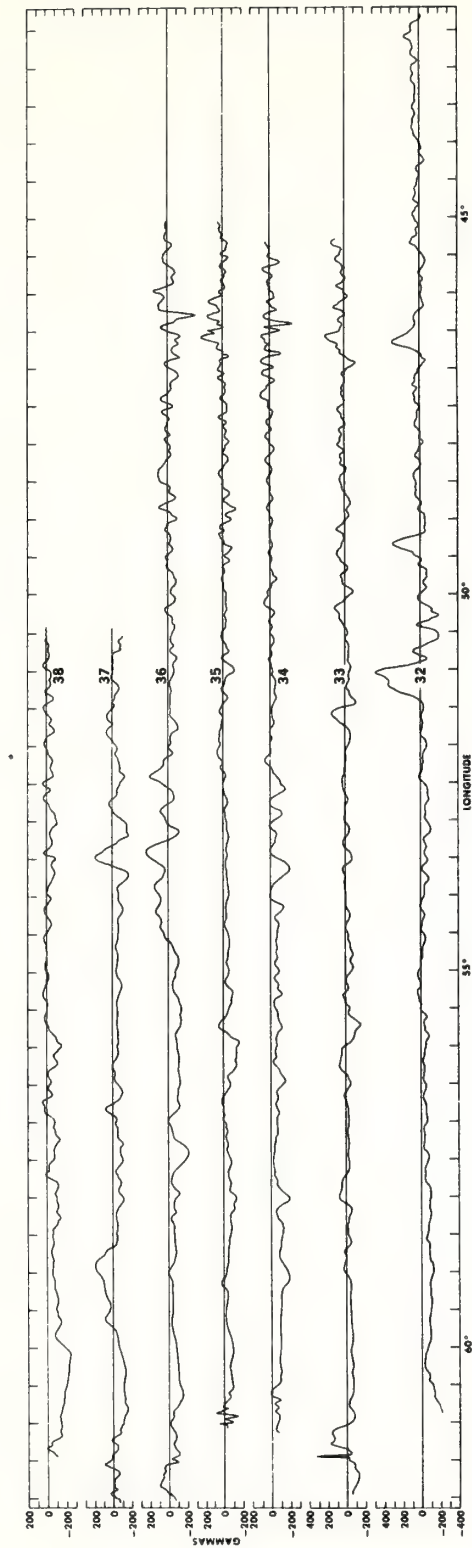
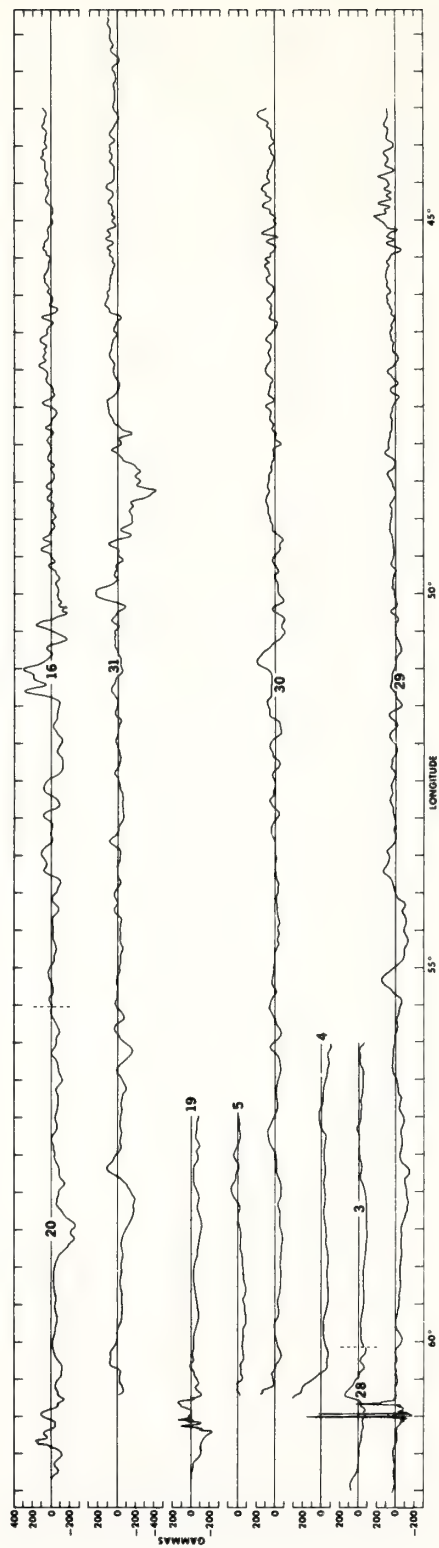


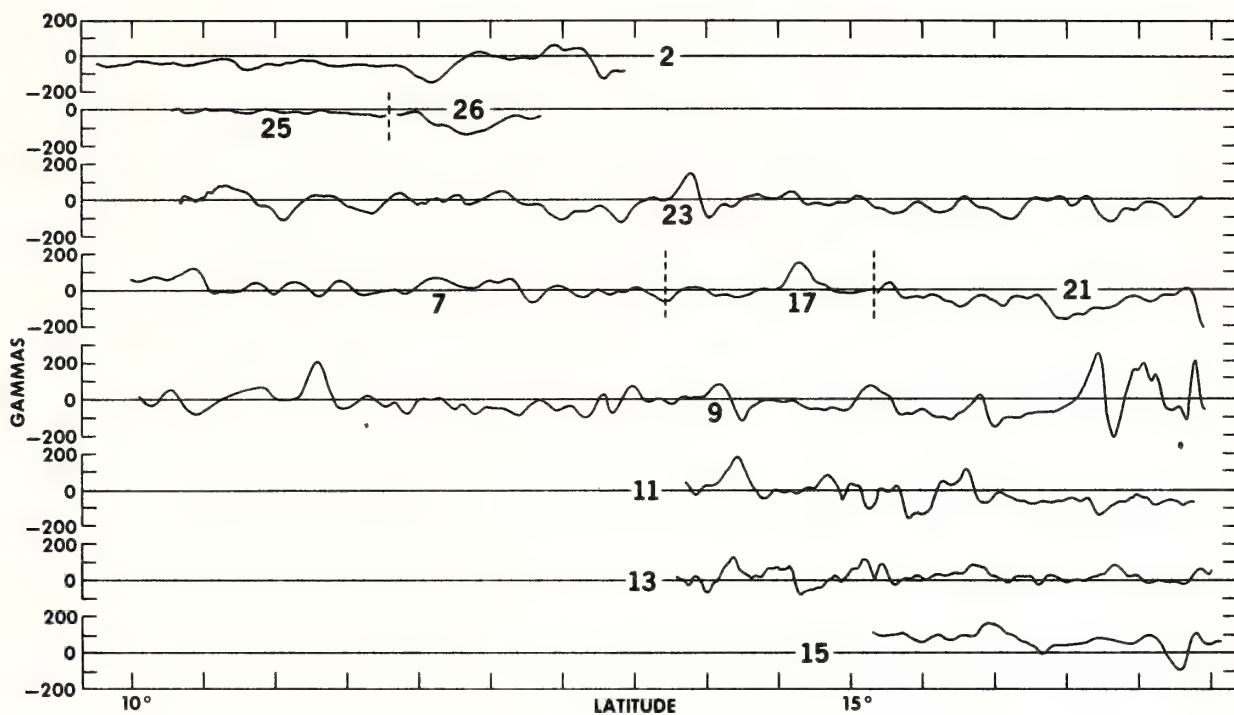
Figure 2. Magnetic field intensity anomaly contour map of study area.

APPENDIX. PROFILES

The index number on each profile is keyed to a location on the trackline chart (fig. 1).







CARIBBEAN ATLANTIC GEOTRAVERSE,
NOAA-IDOE 1971,
REPORT NO. 1, PROJECT INTRODUCTION—BATHYMETRY

G. Peter, G. Merrill, and S. Bush

Studies of the Lesser Antilles Island Arc, the adjacent Atlantic Basin, and the Mid-Atlantic Ridge were performed in 1971 as part of the NOAA-IDOE-supported Caribbean Atlantic Geotraverse (CAG) project. During these investigations, approximately 30,000 km of bathymetric, magnetic, and gravity data and 1,500 km of seismic reflection data were collected in an area bordered by latitudes 14° and 17°30'N and by longitudes 42° and 62°W.

Bathymetric investigations of this project established that: (a) the Barracuda Ridge is an isolated feature which does not extend to the Mid-Atlantic Ridge; (b) another ridge system exists east-southeast of the Barracuda Ridge which was named the Researcher Ridge after the survey ship; (c) a "typical" Mid-Atlantic Ridge topography extends from the northern Atlantic to the east of the Lesser Antilles Island Arc; and (d) east-west-trending topographic lineaments suggest faulting of the Atlantic Basin east of the Barbados Ridge.

Magnetic and gravity studies confirmed the findings above and established that, during the Tertiary, the development of the Mid-Atlantic Ridge in the study area was similar to that of the rest of the North Atlantic.

This report contains: (1) the introduction of the CAG project; (2) a summary of the major accomplishments; (3) a description of the bathymetric data; and (4) a presentation of data profiles and an interpretive bathymetric contour map. Similar treatments of the magnetic and gravity data are contained in *Caribbean Atlantic Geotraverse Report No. 2* and *Report No. 3*, respectively.

INTRODUCTION

The Caribbean Atlantic Geotraverse (CAG) project outlined a series of studies which required a systematic geophysical data coverage between the Lesser Antilles Island Arc and the Mid-Atlantic Ridge. To establish this high-density geophysical data traverse and to test the "Funnel-Smith" (1968) hypothesis, support for 3 years was requested from the National Science Foundation Office for the International Decade of Ocean Exploration (NSF-IDOE). The work was planned to provide the first phase in a series of systematic scientific investigations directly north of the equatorial Atlantic region where fracture zones and a generally complex tectonic pattern made the interpretation of existing geophysical data difficult. The proposed studies were designed to provide critical tests of working models that are generally proposed to explain the evolution of the Atlantic and Caribbean Basins.

NOAA received only 1-year support from NSF-IDOE, and the project commenced in 1971 aboard the NOAA ship *Researcher*. Because of the reduced support, a system of east-west-oriented tracklines, spaced 38 km apart, was established in an area bordered by longitudes 42° and 62°W and by latitudes 14° and 17°30'N (fig. 1). The distance between the north-south tracklines varied between 200 and 360 km. Four north-south crosslines were extended southward to about latitude 10°N to provide reconnaissance information for future investigations.

Processed and original data collected during this project are available from the NOAA National Geophysical and Solar-Terrestrial Data Center (NGSDC) in Boulder, Colo. This report contains the introduction of the project, its scientific objectives and major results, and the description of the bathymetric data acquisition and processing methods. The appendix contains a series of bathymetric profiles which provide an easy overview of the data. Introduction and presentation of the magnetic and gravity data are contained in *Report No. 2* (Peter et al., 1973a) and *Report No. 3* (Dorman et al., 1973), respectively. Copies of the seismic data are available from NGSDC. These data serve as the basis for a number of interpretive publications presently in preparation.

SCIENTIFIC OBJECTIVES

The overall objective of this study was the establishment of the regional geophysical and geological trends between the islands of the Lesser Antilles Arc and the Mid-Atlantic Ridge. Under this broad definition, the following specific objectives were sought.

(1) To establish the magnetic anomaly pattern south of the Barracuda fault to test the Funnell and Smith (1968) hypothesis and to gain insight into the evolution of the Atlantic Basin east of the Lesser Antilles Island Arc.

(2) To study the crustal structure of the Atlantic Basin east of the island arc both in terms of the evolution of the area and the proposed underthrust (Chase and Bunce, 1969) of the Atlantic floor beneath the Lesser Antilles Island Arc.

(3) To examine the Desirade fault and its possible relation to the Barracuda fault.

(4) To study the transition zone between the Puerto Rico Trench and the Barbados Ridge. The possible role of the Barracuda fault zone, forming an abrupt structural barrier of the trench as opposed to the gradual termination of the trench caused by increasing sediment fill toward the south, was to be established.

(5) To study the possible relation between the east-west faults of the Atlantic Basin and those similar faults intersecting the Lesser Antilles Island Arc.

BATHYMETRIC DATA INSTRUMENTATION AND ACQUISITION

Bathymetric data were recorded aboard the *Researcher* along approximately 30,000 km of trackline. The principal sounding system aboard consisted of 12-kHz Harris narrow-beam echo sounder with a 3°-wide single-vertical effective beam. Progressive electronic failure necessitated the use of a conventional (60° beam width) sounding system during the second half of the cruise (profile 28 onward; fig. 1).

During the use of the narrow beam system, the depths were sampled automatically and stored in the shipboard computer with other geophysical data at 1-minute intervals. When using the wide-beam sound source,

5-minute values as well as peaks and troughs were manually entered into the shipboard computer system and stored on the raw-data tape. Spurious values were later checked and edited out or corrected on a processed data tape aboard the *Researcher*.

DATA REDUCTION

Data reduction in the laboratory consisted of: (1) further editing of the processed data tape to obtain data at 5-minute intervals, plus the peaks and troughs; (2) keypunching on cards and adding to the data file the bathymetric highs, lows, and the inflection points that were missed previously; and (3) merging the smooth navigation tape with the data tape and computing the geographical coordinates for each data point.

A final data tape was provided that contained the following information: (1) index number; (2) Julian day (JD); (3) Greenwich Mean Time—GMT (hour, minute, and 0.1 minute); (4) latitude; (5) longitude (items (4) and (5) in degrees and decimal fractions); (6) nautical miles traveled; (7) kilometers traveled; (8) uncorrected fathoms; (9) correct fathoms; and (10) corrected meters.

Velocity corrections were computed from the Matthews Tables. The limits of this project fall within four echo-sounding areas: 11, 12, 16, and 19. Corrections for these areas were plotted and, because of the great similarity noted, an average velocity correction curve was drawn for the entire study area. The corrections applied are indicated in table 1. From the final processed data tapes, data listings and displays were prepared.

NAVIGATION

The position of the *Researcher* during this project was controlled by an SRN-9 satellite navigation system (Guier, 1966). Fixes from the satellites were available on the average of about every 2 hours. Between the satellite fixes, the shipboard computer interpolated dead-reckoning positions, based on the previous satellite data, on new input of course and speed information when pertinent, and on Loran-C data.

Table 1. Depth corrections applied to sounding data

Depth in fathoms	Correction
0 to 400	0 to 11
400 to 1,200	11 to 27
1,200 to 1,800	27 to 46
1,800 to 2,500	46 to 77
2,500 to 2,800	77 to 98
2,800 to 3,600	98 to 128

The satellite navigation system was inoperative between JD 295 and JD 302. During this interval, a combination of Loran-C, Omega, and star fixes provided the navigation control.

A position data tape of the ship and computer plots of the tracklines were provided by the ship at each port stop.

DATA DISPLAY

In the appendix, bathymetric profiles are shown in corrected meters. Depths are plotted against latitude or longitude, depending on the dominant heading of the profile. The scales are such that the vertical exaggeration of the bathymetry is approximately 50:1. Index numbers on the profiles refer to the trackline chart (fig. 1) where the location of each profile is indicated. Table 2 gives the time intervals for each profile that will be helpful in requesting specific data from NGSDC.

An interpretive bathymetric contour map is included in this report as figure 2. During the preparation of the map, other data available for this area were also consulted (Collette and Rutten, 1972) and were incorporated when they did not contradict *Researcher* data. Over the Mid-Atlantic Ridge, the rapidly changing topography clearly demonstrated the inadequacy of the 38-km east-west line spacing. While admittedly other interpretations are possible, the authors believe that their presentation is consistent, and that it complements other maps and data available for this area.

Table 2. Profile start and stop times for Project RP-12-RE-71

Profile number	Start		Stop	
	JD	Time	JD	Time
1	261	0800	262	0130
2	262	0405	263	1515
3	263	2330	264	1740
4	264	1835	265	1230
5	265	1420	266	0600
6	266	1010	266	1620
7	266	1625	267	0740
8	267	0745	267	1610
9	267	1615	268	2200
10	268	2205	269	1330
11	269	2125	270	1240
12	270	1245	271	0420
13	271	0425	271	1920
14	271	1925	272	0310
15	272	1315	272	1320
16	272	1325	274	1005
17	274	1010	274	1535
18	274	1540	274	2240
19	274	2245	275	1730
20	275	1835	276	2240
21	276	2245	277	0815
22	277	0820	277	1400
23	277	1405	279	1710
24	279	1725	279	2200
25	279	2205	280	1230
26	280	1505	280	1910
27	280	1915	281	0055
28	286	0100	286	0830
29	286	0905	290	2040
30	290	2300	294	1505
31	294	1717.5	299	0100
32	299	0240	302	0555
33	306	2115	309	2240
34	310	0015	312	1645
35	312	2230	315	1835
36	315	2005	318	1710
37	318	1715	320	1830
38	320	2000	322	1650

DISCUSSION OF RESULTS

The CAG project successfully accomplished the majority of the pre-set scientific objectives. Although the shorter timespan of the project did not allow for planned high-density data acquisition, sufficient data were obtained to establish the magnetic anomaly pattern in the study area. This pattern suggested that the Cenozoic evolution of the Mid-Atlantic Ridge east of the Lesser Antilles Arc was essentially similar to that of the rest of the North Atlantic (Lattimore et al., 1973; Peter et al., 1973b; and Peter et al., 1973c).

North of the Barbados Ridge, several seismic profiles show that the Atlantic basement (second layer) and the entire overlying sediment column dip below and eventually are overlain by apparent slump material from the island arc. This sediment column appears undisturbed several kilometers west of the Puerto Rico Trench (its southeastward extension) without any indication that the column is in the process of being "scraped off" due to the commonly proposed underthrust of the sea floor below the island arc.

We found that the northern boundary fault of the Barracuda Ridge can be extended west-northwestward. No connection was observed, however, between it and the Desirade fault (Schubert and Peter, 1973). The seismic reflection work was unsuccessful in providing a definitive answer to this question and to the question of the nature of the transition zone between the Puerto Rico Trench and the Barbados Ridge. The lack of success is attributable to the combination of the following: (1) The sediments covering this part of the sea floor underwent repeated slumping and became so deformed that they are devoid of reflecting horizons; (2) the sediments below the sea floor consist of uniform, dense material that quickly absorbs all acoustic energy; and (3) the basement is so deep that it is beyond the capacity of our seismic system. The topography of the sea floor does suggest, however, that the transition is structurally controlled.

Numerous faults have been observed east of the Lesser Antilles Arc both in the bathymetric and seismic data. Further careful studies

are required to establish whether these faults are related in any way to similar east-west-oriented faults noted on the Barbados Ridge.

The bathymetric map (fig. 2) clearly shows the Mid-Atlantic Ridge province, the Demerara and Barracuda abyssal plains to the west of the ridge province, and the complex topography of the Barbados Ridge. The axis of the Mid-Atlantic Ridge is indicated by heavy arrows; the offset of the ridge crest is along the 15°20'N fault zone (Collette and Rutten, 1972). North of this fault, the depression following the same trend is the Royal Deep (Collette and Rutten); to the south of the fault zone, the elongated trough is the Researcher fault zone (Lattimore et al., 1973; Peter et al., 1973b; and Peter et al., 1973c). Directly south of this fault trough, between longitudes 48° and 51°30'W, lies a complex ridge system which we have named the Research Ridge (Lattimore et al., 1973; and Peter et al., 1973b, and 1973c).

The clearest evidence of the inadequacy of the 38-km east-west trackline spacing is shown between the Royal Deep and the Researcher Ridge. We expect that the topography in this area is just as complex as the flank of the Mid-Atlantic Ridge north of the Royal Deep. Within this same area the westward extension of the Royal Deep, the 15°20'N fault zone, and the Researcher fault zone to approximately longitude 51°W is permitted by available data; however, because we had only a few north-south lines available to establish this trend, it is possible that a more detailed survey would indicate that the termination of these features is closer to the crest of the Mid-Atlantic Ridge than is indicated in figure 2.

The contours in the area between longitudes 41° and 54°W are also ambiguous because, outside of the Researcher Ridge, the relatively subdued topography can be contoured with a north-south trend (as shown) or with a trend parallel to the Researcher Ridge. The contours in figure 2 were adopted after careful studies of these alternatives and of the broader, more regional bathymetric trends.

A somewhat unexpected result of the bathymetric survey involves the Barracuda Ridge (located between long. 54° and 59°W and lat. 16°30' and 17°N). It had generally been assumed that this feature is part of a

major transform fault cutting across the Atlantic Basin. Our results indicate that the Barracuda Ridge is an isolated feature, without any obvious extension toward the east-southeast to the flank of the Mid-Atlantic Ridge. A closer look at the bathymetric contours suggests that both the Barracuda and Researcher Ridges contain east-west-trending components which are probably the results of east-west faults. Seismic as well as magnetic data support this conclusion, with correlations of the major east-west bathymetric trends either with normal faulting or with major offsets of the magnetic lineations (Lattimore et al., 1973; Peter et al., 1973b; and Peter et al., 1973c).

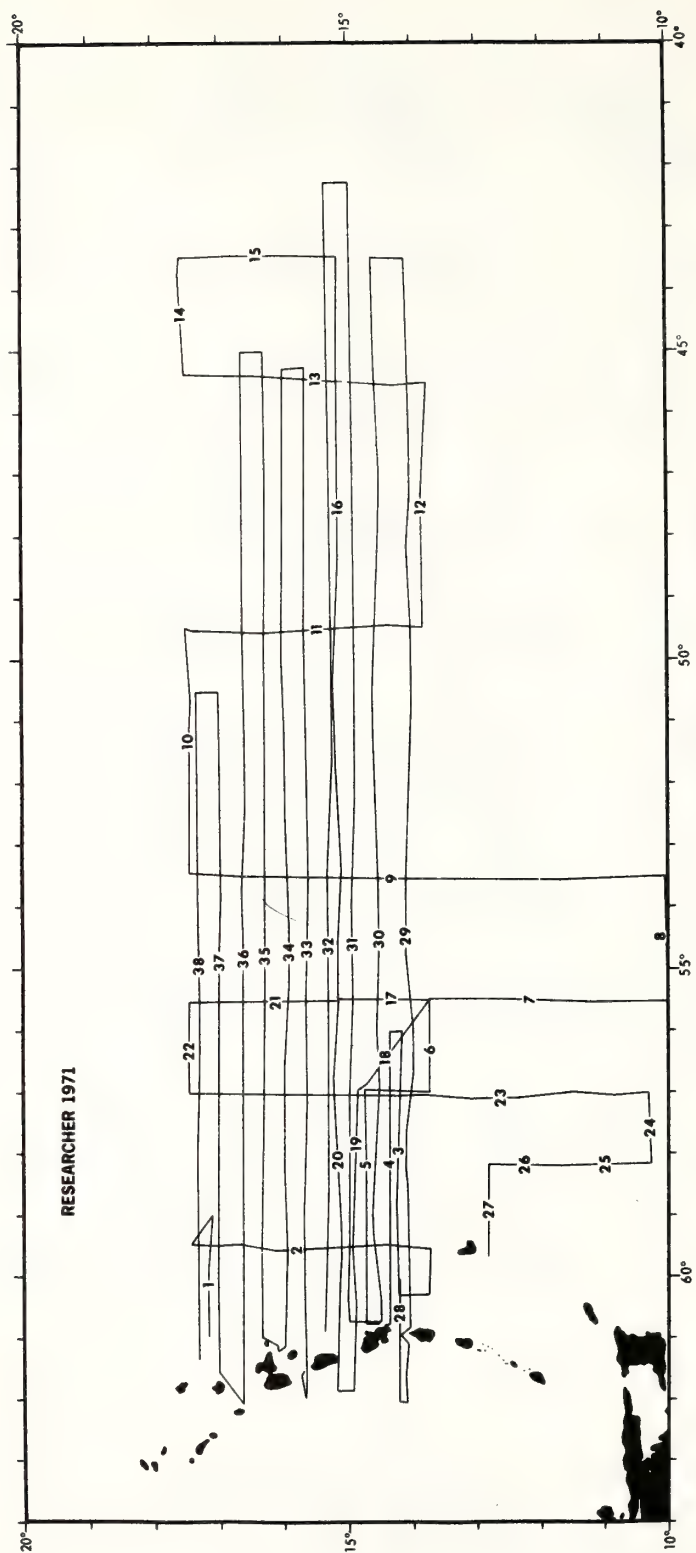
ACKNOWLEDGMENTS

The success of this project was largely due to the cooperation provided by CAPT S. Hollis and the officers and crew of the NOAA ship *Researcher*. CDR J. Grunwell and LTC T. Wyzewski were especially helpful by providing invaluable assistance to our work. For the success of the seismic investigations, we are indebted to Mr. C. Lauter of NOAA-AOML.

We gratefully acknowledge NSF-IDOE for Grant No. AG-253 which, in part, supported these studies.

REFERENCES

- Chase, R. L., and E. T. Bunce (1969): Underthrusting of the eastern margin of the Antilles by the floor of the western North Atlantic Ocean, and origin of the Barbados Ridge, *J. Geophys. Res.* 74(6): 1413-1420.
- Collette, B. J., and K. W. Rutten (1972): Crest and fracture zone geometry of the Mid-Atlantic Ridge between 10° and 16°N, *Nature Phys. Sci.* 237(78): 131-134.
- Dorman, L. M., B. G. Bassinger, E. Bernard, S. A. Bush, O. E. DeWald, L. A. Lapine, R. K. Lattimore, and G. Peter (1973): Caribbean Atlantic Geotraverse, NOAA-IDOE 1971, Report No. 3, Geodesy, *NOAA Tech. Rept.* ERL 277-AOML 11, 35 pp.
- Funnell, B. M., and A. G. Smith (1968): Opening of the Atlantic Ocean, *Nature* 219(5161): 1328-1333.
- Guier, W. H. (1966): Satellite navigation using integral Doppler data—the AN/SRN-9 equipment; *J. Geophys. Res.* 71(24): 5903-5910.
- Lattimore, R. K., O. E. DeWald, and G. Peter (1973): NOAA-IDOE equatorial Mid-Atlantic Ridge investigations (abstract), *EOS, Trans. Am. Geophys. Union* 54(4): 326.
- Peter, G., O. E. DeWald, and B. G. Bassinger (1973a): Caribbean Atlantic Geotraverse, NOAA-IDOE 1971, Report No. 2, Magnetic Data, *NOAA Tech. Rept.* ERL 288-AOML 12, 19 pp.
- Peter G., O. E. DeWald, G. Merrill, and L. M. Dorman (1973b): NOAA-IDOE equatorial Atlantic studies 1971 (abstract), *EOS, Trans. Am. Geophys. Union* 54(4): 326.
- Peter, G., R. K. Lattimore, O. E. DeWald, and G. Merrill (1973c): Development of the Mid-Atlantic Ridge east of the Lesser Antilles Island Arc, *Nature Phys. Sci.* 245(148): 129-131.
- Schubert, C., and G. Peter (1973): Sea floor tectonics west of the Barracuda Ridge (abstract), *EOS, Trans. Am. Geophys. Union* 54(4): 326.



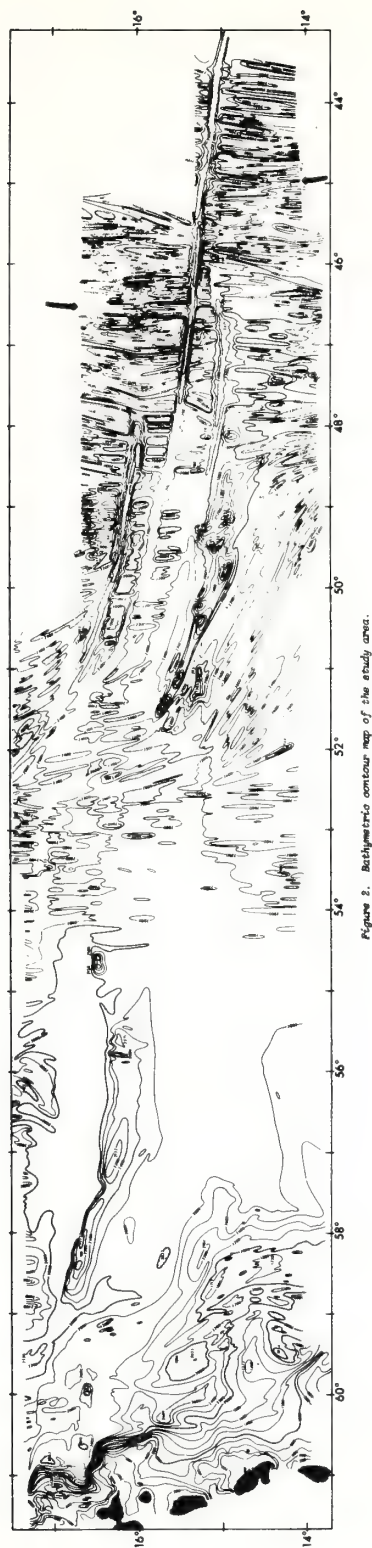
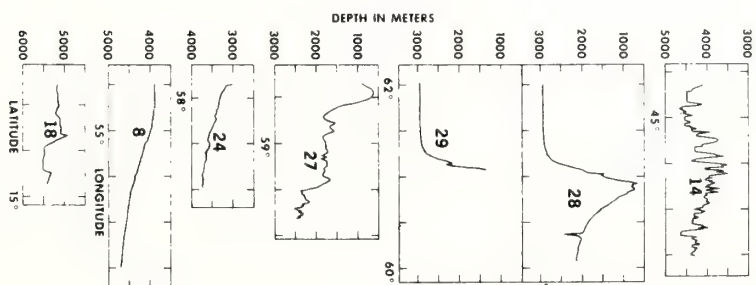
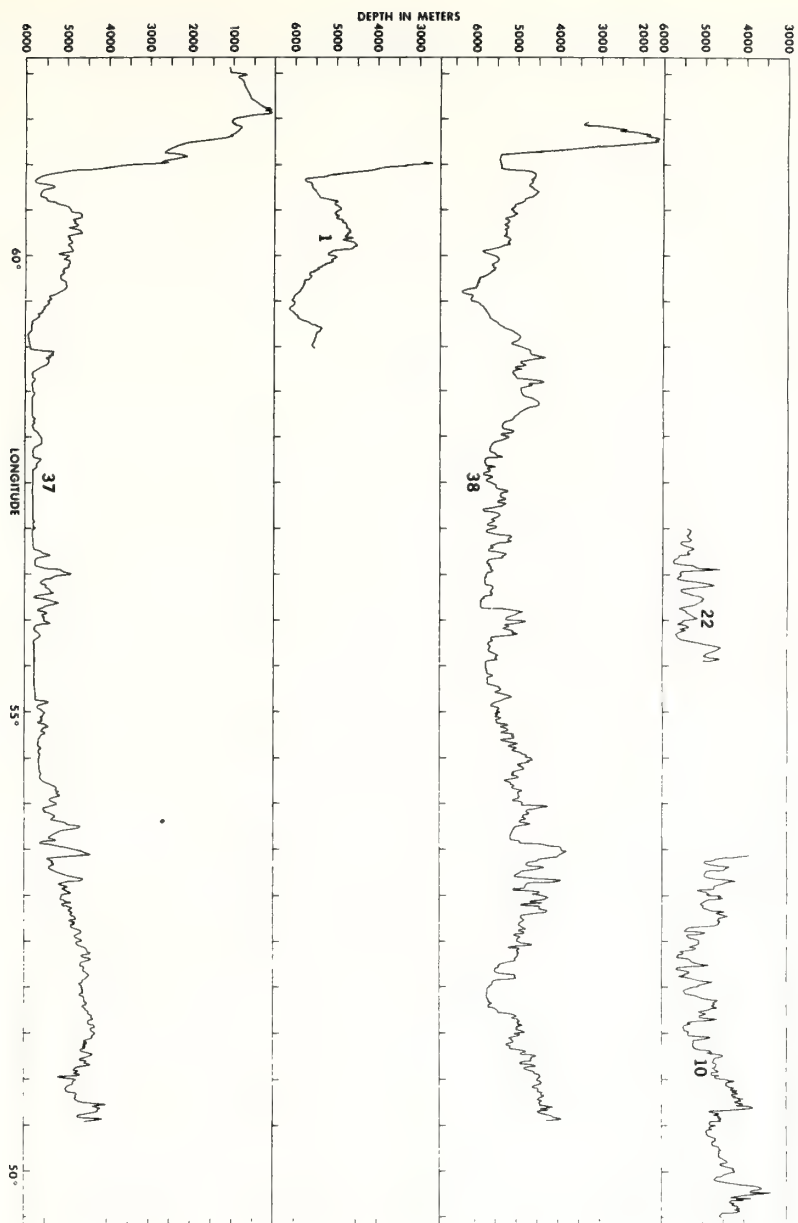
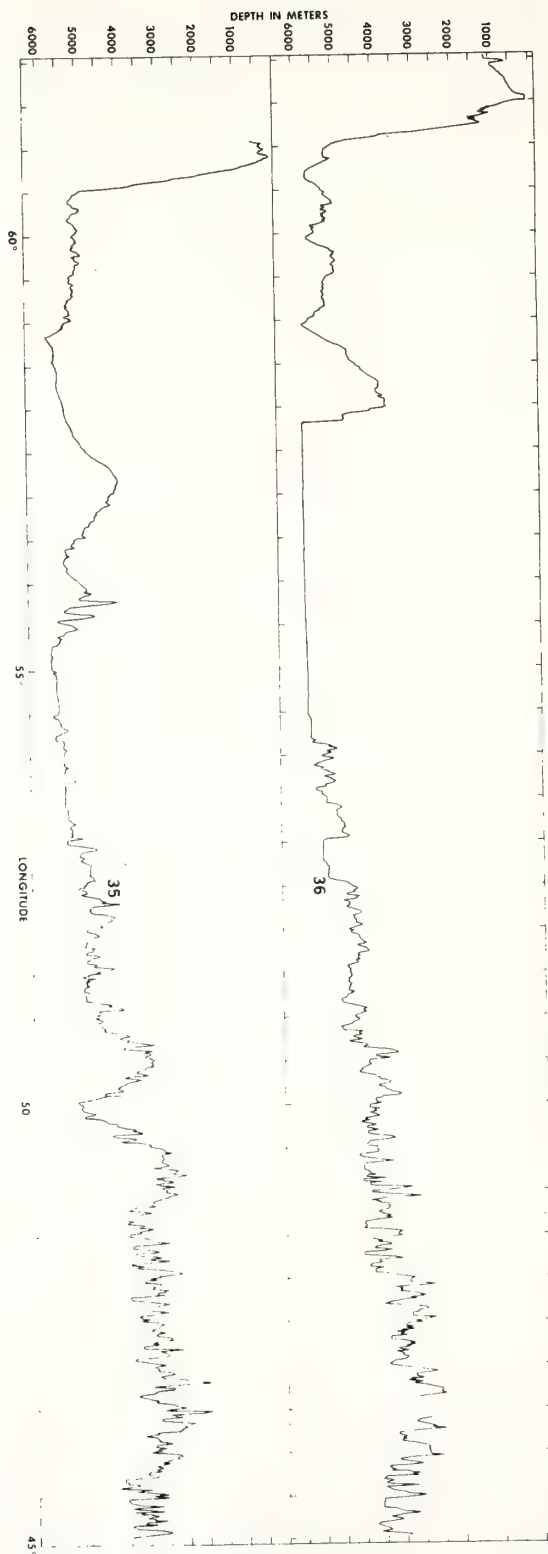


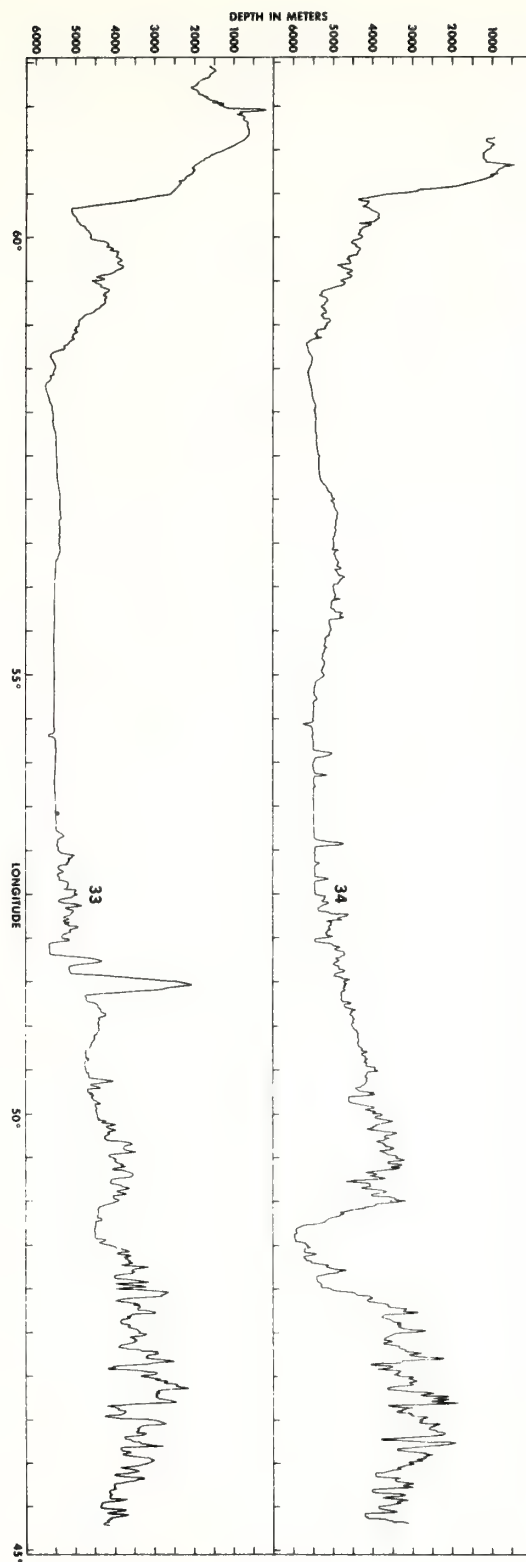
Figure 2. Bathymetric contour map of the study area.

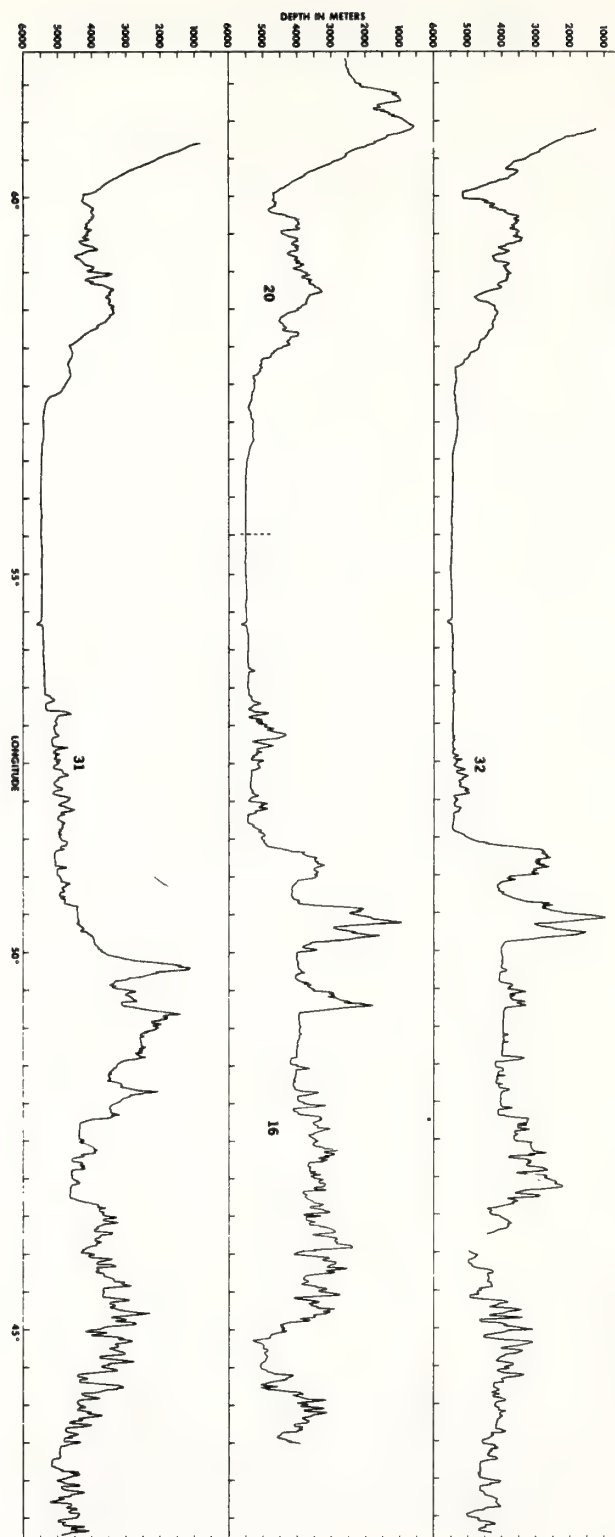
APPENDIX. PROFILES

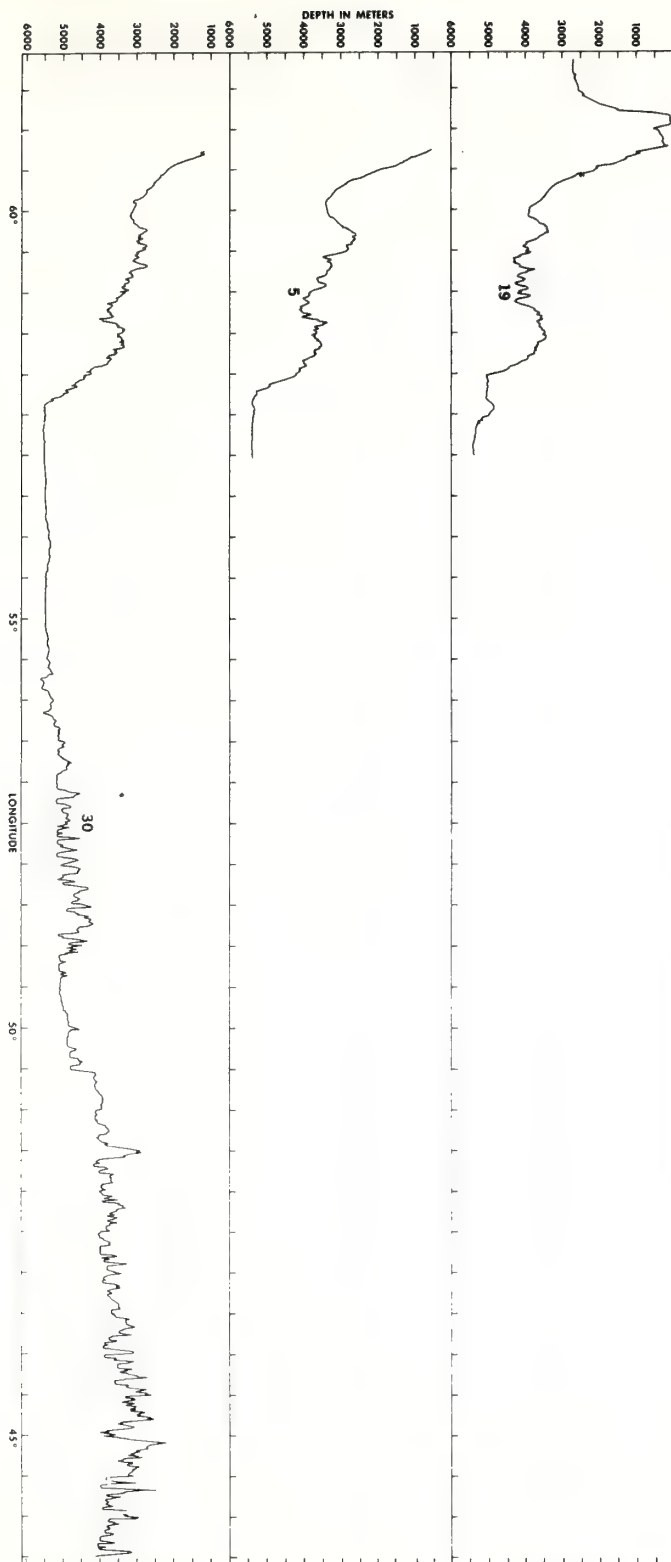
The index number on each profile is keyed to a location on the trackline chart (fig. 1).

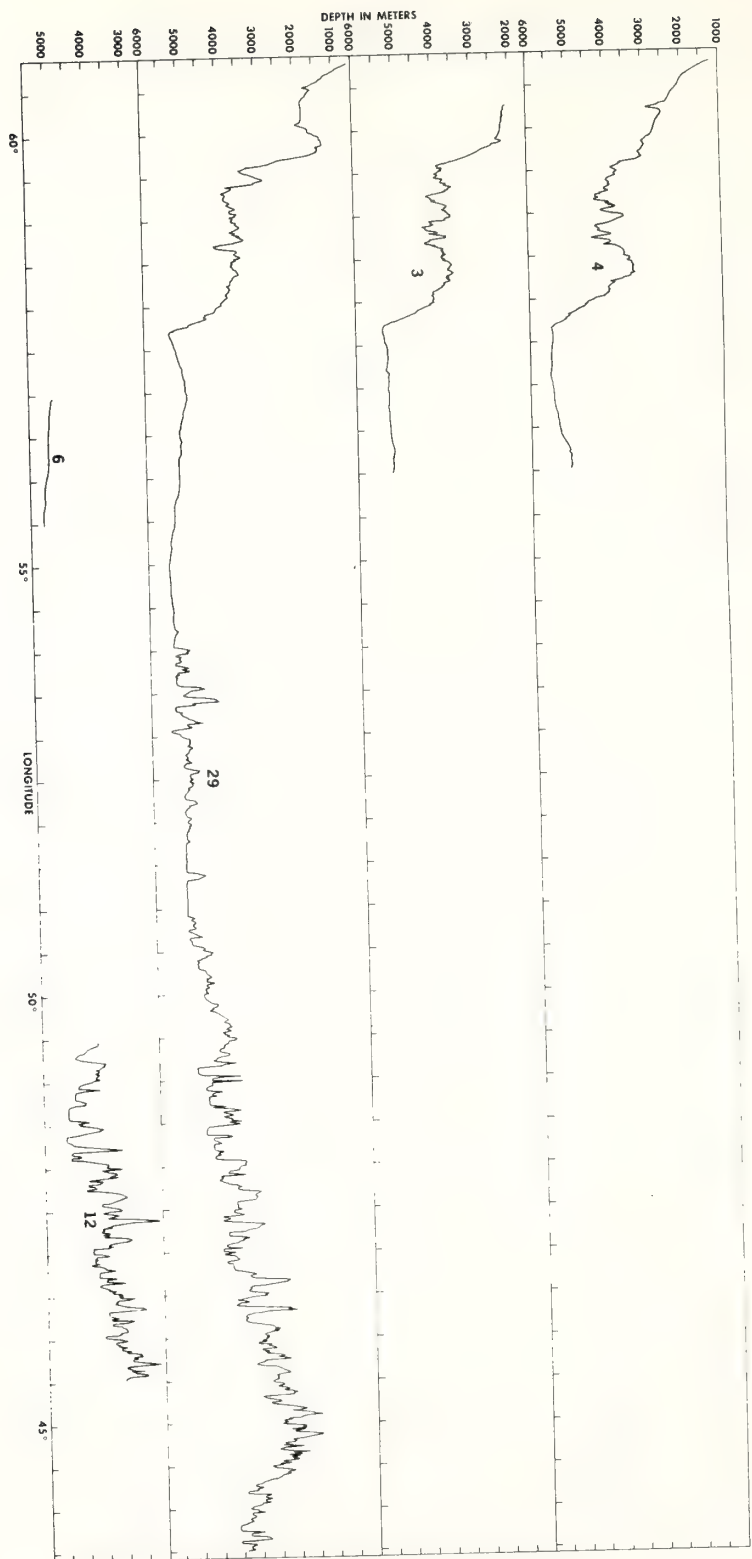


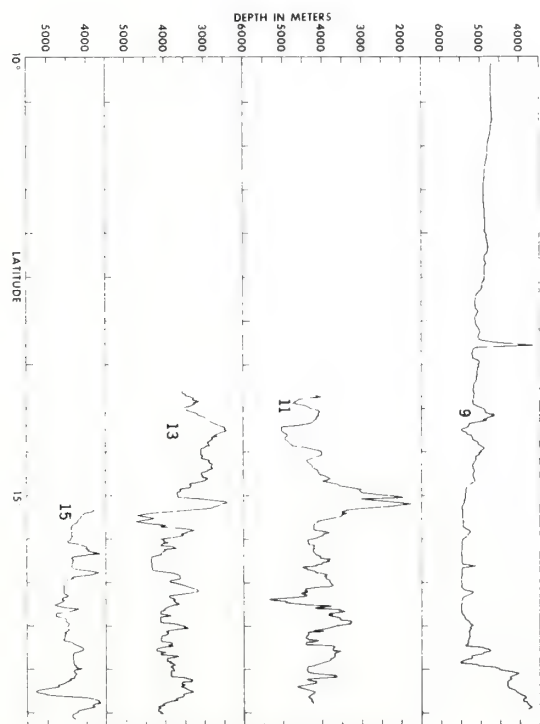
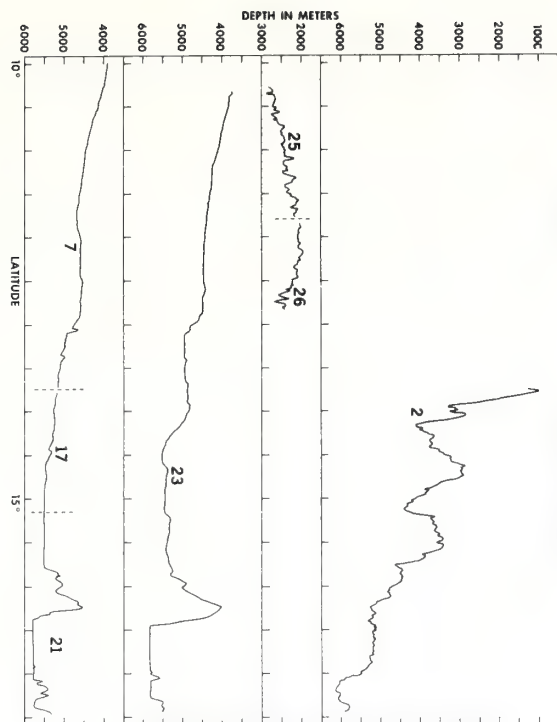












Development of the Mid-Atlantic Ridge east of the Lesser Antilles Island Arc

G. PETER, R. K. LATTIMORE, O. E. DEWALD & G. MERRILL

National Oceanic and Atmospheric Administration, Atlantic Oceanographic and Meteorological Laboratories, 15 Rickenbacker Causeway, Virginia Key, Miami, Florida 33149

The entire Cainozoic magnetic anomaly lineation sequence has been identified east of the Lesser Antilles Island Arc, indicating that the evolution of the Mid-Atlantic Ridge in the area was essentially similar to the rest of the North Atlantic.

MARINE geophysical data were collected east of the Lesser Antilles Island Arc in 1971 and 1972, as part of the International Decade of Ocean Exploration (IDOE) supported programme of the National Oceanic and Atmospheric Administration (NOAA) aboard the ships *Researcher* and *Discoverer*. Studies of the magnetic and bathymetric data collected along the track lines during this project (Fig. 1) enabled us to correlate the magnetic anomalies and the topography of the Mid-Atlantic Ridge east of the Lesser Antilles Island Arc with a 'standard' Mid-Atlantic Ridge segment, taken from the Trans-Atlantic Geotraverse corridor (located between the Atlantis and Kane fracture zones in the North Atlantic)^{1,2}. The correlation demonstrates that the ridge topography and associated magnetic anomaly sequence considered 'typical' of the North Atlantic extends southwards to the Vema fracture zone, and that the Cainozoic evolution of the ridge east of the Lesser Antilles Island Arc was contiguous with and essentially similar to that of the rest of the North Atlantic.

Difficulties of identification and correlation are encountered when describing the magnetic anomaly lineations of the

North Atlantic north of 15° N (refs 1 to 3). Further south, in the area east of the Lesser Antilles Island Arc, a much reduced anomaly amplitude makes the identification and correlation problem more difficult (compare the amplitude scales of the standard section 'S' and the numbered profiles in Fig. 2); this is generally due to the combination of slow spreading rate, offsets at fracture zones, and topographic influences.

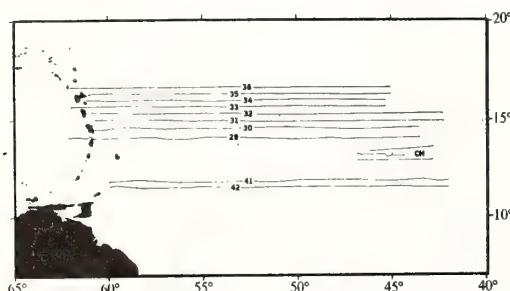


Fig. 1 Track lines extending from the Lesser Antilles Island Arc to the crest of the Mid-Atlantic Ridge.

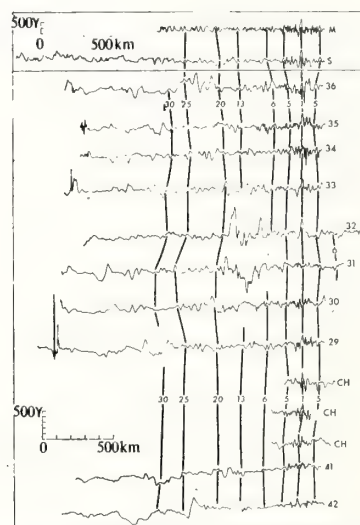


Fig. 2 Identification and correlation of the magnetic anomalies east of the Lesser Antilles Island Arc. Numbers on the right of each profile refer to the identification of profiles in Fig. 1. Profile S is 'standard section'; profile M is the syntetic anomaly (model)*.

The identification of the anomalies in our study area was based on comparisons between the magnetic anomaly sequence of the 'standard section' and the individual magnetic anomaly profiles, and on the comparisons of these profiles with theoretical magnetic spreading models^{4,5}. The correlation and identification shown in Fig. 2 represent one of several such attempts; depending on the criteria used,

the designation of the individual anomalies varied slightly in these attempts, but the overall pattern implied by the distinctive anomaly groups was the same.

Three basic criteria were used in the derivation of the identifications and correlations in Fig. 2: (1) The offset pattern of the magnetic lineations in the study area (Fig. 3) should be the simplest possible; (2) when an offset zone is established, the offsets of individual anomalies should be consistent; and (3) we assumed that the relationship between the 'ridge elevation and the age of the oceanic crust' is essentially true⁶.

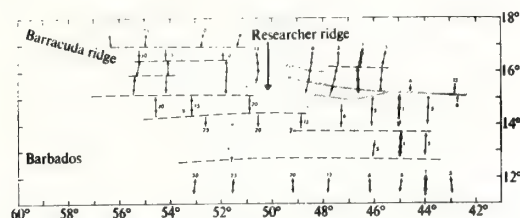


Fig. 3 Magnetic lineations and their offset pattern east of the Lesser Antilles Island Arc. ---, Magnetic offsets; // fault troughs (from north to south) of the Royal deep, 15° 20' N fracture zone, and the Researcher fracture zone, respectively; ●, control points for identification.

In applying the last criterion, first an average curve was drawn across the topography of the 'standard section', and the average depths under the well established magnetic anomalies¹⁻³ were compared with the 'Empirical Elevation-North Pacific' curve of Sclater *et al.*⁶ The overall agreement was remarkably good but, as they also noted, the heights of the crestal regions of the Mid-Atlantic Ridge fell above the empirical elevation curve of the East Pacific Rise. Next we compared this average depth curve to the east-west topographic profiles east of the Lesser Antilles Island Arc. As the samples in Fig. 4a and b demonstrate, the agreement is quite good along most of the ridge. The largest deviations are either due to oblique crossings of fracture zone topography or, as in the southernmost profiles, due to burial of the ridge flank by large accumulations of sediments¹. After confirming that the topography of the 'standard section' and the associated magnetic anomalies (which, of course, represent discrete crustal ages^{4,5}) fit a predictable pattern⁶, and that the topography of the 'standard section' closely approximates the Mid-Atlantic Ridge topography east of the Lesser Antilles Island Arc, discrete magnetic anomaly points (anomalies 1, 5, 6, 13, 20, 25 and 30), based on the average depth curve of the 'standard section', were marked off on all of our east-west profiles. These points were then allowed to 'bias' our identification of the magnetic anomalies. This method was especially useful in the region between anomalies 1 and 13, which was the area where the average depth curve best fitted the actual topography.

Table 1 Half-spreading Rates in cm per m.y. between given Anomaly Intervals North and South of 15° 20' N

Anomaly interval	North of 15° 20' N	South of 15° 20' N
1-5	1.0	1.2
5-6	1.0	1.2
6-13	1.25	1.0
13-20	1.25	1.55
20-25	1.6	1.6
25-30	1.7	1.8

An approximate breakdown of the half-spreading rates north of the 15° 20' N fracture zone⁸ and between the Vema and 15° 20' N fracture zones is given in Table 1. Although the computed spreading rates for the magnetic anomaly profiles in the North Atlantic vary in detail¹⁻³, the general tendency for a spreading rate increase at the times of anomaly 13 and anomaly 25 is also reflected in the profiles east of the Lesser Antilles Island Arc.

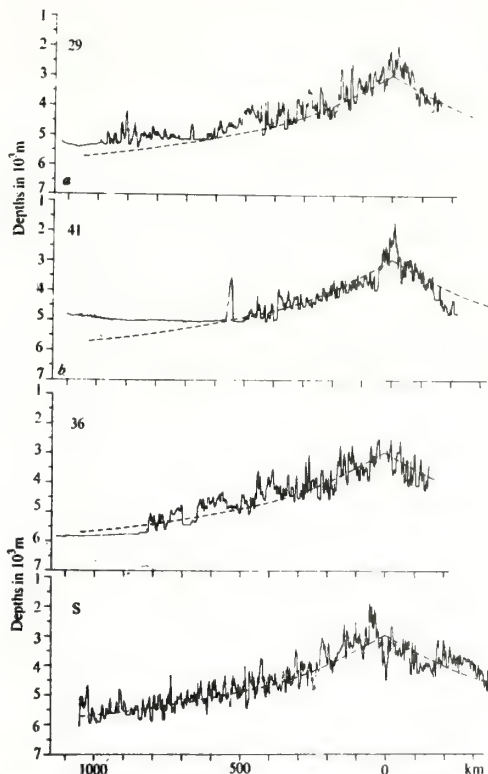


Fig. 4 a, Comparison of the Mid-Atlantic Ridge topography at the 'standard section' (S) and at profile 36. The chosen 'standard section' crosses the ridge at 25° N. b, Comparison of the average ridge elevation curve of the standard section (dashed line in each half of figure a and b) and profiles 29 and 41. Location of profiles shown in Fig. 1.

One of the unexpected results of the magnetic anomaly pattern (Fig. 3) is that with the possible exception of the area near the crest of the Mid-Atlantic Ridge, the offsets trend east-west. Bathymetric data⁹ and the continuity of the magnetic lineations across the north-west/south-east (N108°E) trend of the Barracuda Ridge indicate that instead of being part of a major transform fault, the Barracuda Ridge is only a local feature. The largest magnetic offset in the area is along 15° N. The trough of the 15° 20' N (ref. 8) fracture zone coincides roughly with the magnetic offset on the eastern flank of the Mid-Atlantic Ridge, but on the western flank the major magnetic offset seems to be related to a southern branch of this fault. This southern fault (here referred to as the Researcher fracture zone) parallels the northern edge of the Researcher Ridge (name applied for; Board on Geographic Names) to 49° W.

where it cuts across the ridge and trends due west. Provided that the identification of the magnetic lineations adopted in Fig. 2 is correct, there are no detectable magnetic offsets along the faults associated with the Royal deep⁸ and with the 15° 20' N fault zone itself on the western ridge flank. These features, together with parts of the Barracuda and Researcher ridges, are therefore probably the products of normal or reverse faulting.

A close examination of the bathymetry⁹ reveals that there are several possible east-west trending faults in the area, some of which coincide with the deduced east-west magnetic offsets. The best examples are the east-west trending scarps in the bathymetry along the western half of the Researcher fracture zone, and along the offsets north-east of the Barracuda Ridge. East-west trending faults also occur west of the identifiable magnetic pattern, between 54° W and the Barbados Ridge, and there are suggestions in the detailed bathymetry of the Barracuda and Researcher ridges that these features also contain east-west components. To the north, the transition from east-west magnetic offsets (transform faults) to north-west/south-east striking offsets most likely occurs around 19° N, where the trend of the ridge crest also changes from roughly north-south to north-east/south-west.

The Cainozoic magnetic lineations north of the Barracuda Ridge agree well with the pattern derived by Pitman and Talwani³. The continuity of the lineations from the Azores-Gibraltar Ridge to the Vema fracture zone suggests that, other than minor offsets and orthogonal normal or reverse faulting which seem to be normal phenomena in the North Atlantic¹⁰, there are no indications for major north-south extension in the area east of the Lesser Antilles Island Arc during the Cainozoic. Such a zone of extension and associated shear was predicted^{11,12} basically on the assumption that the separation of North America and South America away from Africa began at the same time.

We believe that our data support the interpretation^{13,14} that, from the Upper Cretaceous to the Present, North America and South America drifted away from Africa more or less as a single plate. We agree, in part, also with Le Pichon and Fox¹⁵ who suggested a modification of the Bullard *et al.*¹⁶ fit of North America and Africa (they moved North America southward to align fracture zones near the continental margins), and demonstrated that the Caribbean and Gulf of Mexico regions formed during the Jurassic-Lower Cretaceous opening of the Atlantic. But we prefer a modification in which North America is situated to the north in the pre-rift reconstruction of the North Atlantic.

Such modification would allow a much less severe rotational sequence for the Central American Palaeozoic blocks to avoid their overlap on South America¹⁷, and would allow for an east-west spreading of the early Mid-Atlantic Ridge (Upper Triassic-Jurassic-Lower Cretaceous) between Africa and the Central American blocks. This hypothesised east-west spreading could account for the east-west shear along the El Pilar fault of Venezuela, the east-west trend of the Puerto Rico Trench and the Greater Antilles, and it might explain the origin of some of the other east-west faults that were discussed previously. Since the Central American crustal blocks moved somewhat independently from North America¹⁷ it is possible to treat the area of the Atlantic to the east of them as an independent crustal plate. The pole of opening for this plate could then be different from the pole derived for the separation of North America and Africa. During the process of opening, the Bahamas and possibly some of the Greater Antilles islands may have developed over fracture zones which separated the North American and Central American plates during the early opening of the Atlantic, a suggestion that is similar to that derived by Pitman and Talwani³.

Received July 20, 1973.

¹ Rona, P. A., and Orlin, H., in *Proc. joint oceanographic Assembly*, 513 (1971).

² Lattimore, R. K., Rona, P. A., and DeWald, O. E., *J. geophys. Res.*, 77 (in the press).

³ Pitman, W. V., III, and Talwani, M., *Bull. geol. Soc. Am.*, **83**, 619 (1972).

⁴ Pitman, W. C., III, and Heirtzler, J. R., *Science, N.Y.*, **154**, 1164 (1966).

⁵ Heirtzler, J. R., Dickson, G. O., Herron, E. M., Pitman, W. C., III, and Le Pichon, X., *J. geophys. Res.*, **73**, 2119 (1968).

⁶ Sclater, J. G., Anderson, R. N., and Bell, M. L., *J. geophys. Res.*, **76**, 7888 (1971).

⁷ Ewing, M., Carpenter, G., Windisch, C., and Ewing, M., *Bull. geol. Soc. Am.*, **84**, 71 (1973).

⁸ Collette, J. B., Schouten, H., and Rutten, K., *EOS*, **54**, 325 (1973).

⁹ Peter, G., DeWald, O. E., Merrill, G., and Dorman, L. M., *EOS*, **54**, 326 (1973).

¹⁰ Rona, P. A., *EOS*, **54**, 243 (1973).

¹¹ Funnell, B. M., and Smith, G. A., *Nature*, **219**, 3128 (1968).

¹² Ball, M. M., Harrison, C. G. A., and Supko, P. R., *Nature*, **223**, 167 (1969).

¹³ Morgan, J. W., *J. geophys. Res.*, **73**, 1959 (1968).

¹⁴ Le Pichon, X., *J. geophys. Res.*, **73**, 3661 (1968).

¹⁵ Le Pichon, X., and Fox, P. J., *J. geophys. Res.*, **76**, 6294 (1971).

¹⁶ Bullard, E. C., Everett, J. E., and Smith, A. G., *Phil. Trans. R. Soc.*, **A258**, 41 (1965).

¹⁷ Carey, S. W., *Continental Drift: A Symposium*, 177 (Univ. Tasmania, Hobart, 1958).

¹⁸ Freeland, G. L., and Dietz, R. S., *Nature*, **232**, 20 (1971).

A. F. Richards,¹ V. J. McDonald,² R. E. Olson,³
and G. H. Keller⁴

In-Place Measurement of Deep Sea Soil Shear Strength

REFERENCE: Richards, A. F., McDonald, V. J., Olson, R. E., and Keller, G. H., "In-Place Measurement of Deep Sea Soil Shear Strength," *Underwater Soil Sampling, Testing, and Construction Control*, ASTM STP 501, American Society for Testing and Materials, 1972, pp. 55-68.

ABSTRACT: A vane shear device was developed for in-place measurement of the undrained strength of clays in the marine environment. It was designed to operate at a water depth of 4.6 km (15,000 ft) and to penetrate nearly 3 m (10 ft) below the mudline in steps of about 0.3 m (1 ft). The device contained its own power supply. Data were wire telemetered to the ship for recording and analysis. Experiments in several locations in the Atlantic Ocean and the Gulf of Mexico demonstrated the capability of the apparatus. The shear strength measured in place generally exceeded the strengths measured on soil samples collected from shallow water, where the sedimentation rate was relatively rapid. There was little difference between shear strength measured in place and on cores from the Gulf of Mexico abyssal plain site, where the sedimentation rate was slow.

KEY WORDS: underwater environments, clays, ocean bottom, underwater structures, boring, vane shear tests, shear strength, bearing strength, sediments, geophysical surveys, soil properties, electric control, strain gages.

A. F. Richards was invited by the Office of Naval Research in 1965 to initiate research on the geotechnical properties of deep sea soils. At that time, the only knowledge available on the geotechnical properties of soils from water depths over 3 km came from tests on samples that had been probably seriously disturbed by the sampling operations. The obvious next step was to attempt in-place measurements. From an engineering point of view, such tests should extend to depths on the order of 15 m (50 ft) or more below the mudline. However, because of limitations on the sizes of ships available for the work, and on both funds and

For authors' affiliations, see p. 68.

time, the decision was made to limit the prototype to soil depths of about 3 m. This distance coincided with the minimum depth required for most structures placed on the deep sea floor at the time the project was initiated. This paper is concerned only with the use of the device for shear strength measurements; it was also used for in-place measurement of bulk density using a nuclear transmission densitometer [1, 2].

In-place undrained shearing strengths can be estimated from a variety of measurements, such as the torque needed to rotate a vane or the force needed to push a cone into the soil. The cone was considered because it would give a continuous record of strength and also would lead to a mechanically simpler apparatus. However, the uncertainty involved in converting the cone resistance into strength and the widespread use of the vane in geotechnical engineering favored the use of the vane.

The mechanical and electrical design of the apparatus will be discussed in general terms. Experiences with the apparatus in sea trials will be briefly cited, and the measured soil properties will be summarized and compared with similar properties measured on samples in the laboratory.

Mechanical Equipment

A survey of the known measurements of strengths of deep sea soils in 1962 [3] suggested that the undisturbed strengths would probably range from about 0.4 to 23 kN/m² (8 to 470 lb/ft²) and the remolded strengths would probably be two to five times as small. The mechanical equipment was designed with a strength limiting of 15 kN/m² (312 lb/ft²) for a 0.076 by 0.15 m (3 by 6 in.) vane. Interchangeable larger and smaller vanes were provided should particularly weak or strong soils be encountered.

The standard rotational velocity for vane shear testing [4] is 0.002 rad/s (6 deg/min). Such slow rates are suitable for normal terrestrial applications where hourly costs are low but are unreasonable for deep sea tests where ship costs run into thousands of dollars per day. As a result, the apparatus was geared to operate at 0.02 rad/s (80 deg/min). Vane tests were performed at vertical spacings of 0.3 m (1 ft) to give a usable precise strength profile. Testing time was reduced and test locations were separated by a distance sufficient to prevent one test from influencing the next.

All components were designed for a hydrostatic pressure of 48,000 kN/m² ($1 \sim 10^6$ lb/ft²), corresponding to a seawater depth of about 4.6 km (15,000 ft). To minimize weight and provide resistance to corrosion, most of the apparatus was constructed of type 6061-T6 aluminum. A few parts, for instance the vanes, were constructed of type 316-L stainless steel to better resist abrasion and deflection.

The proportioning of the apparatus was a compromise between a series

of factors. Thus, the total height of the apparatus was limited to about 4.6 m (14 ft) by the characteristics of the boom on board the ship. This in turn limited the depth of penetration of the vane. The vane was attached to a continuous rigid rod, rather than a telescoping rod, to simplify the mechanical and electrical design, reduce weight, and reduce power requirements for this prototype apparatus. The weight of the equipment was limited by the mechanical characteristics of the ship-to-apparatus cable, which had a strength of 2700 kg (6000 lb) and a length of 3.6 km (12,000 ft). When the cable was fully unreeled, a major

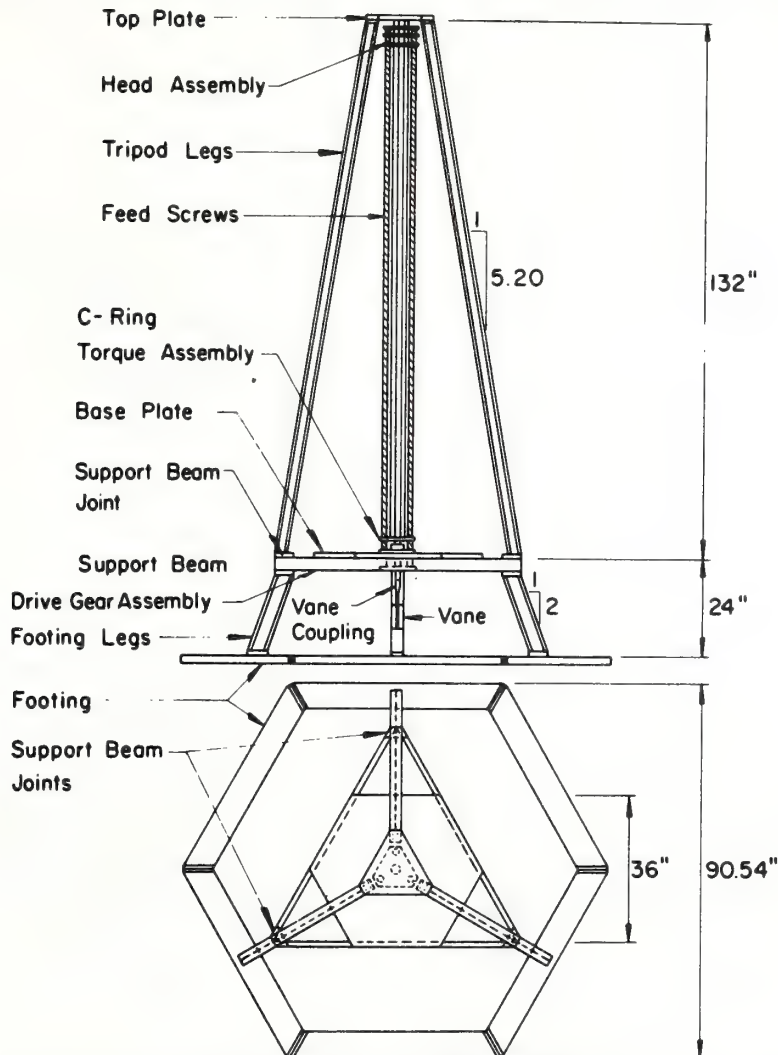


FIG. 1—Simplified drawing of the vane shear strength equipment in 1967. The footing legs later were extended 0.15 m (0.5 ft).

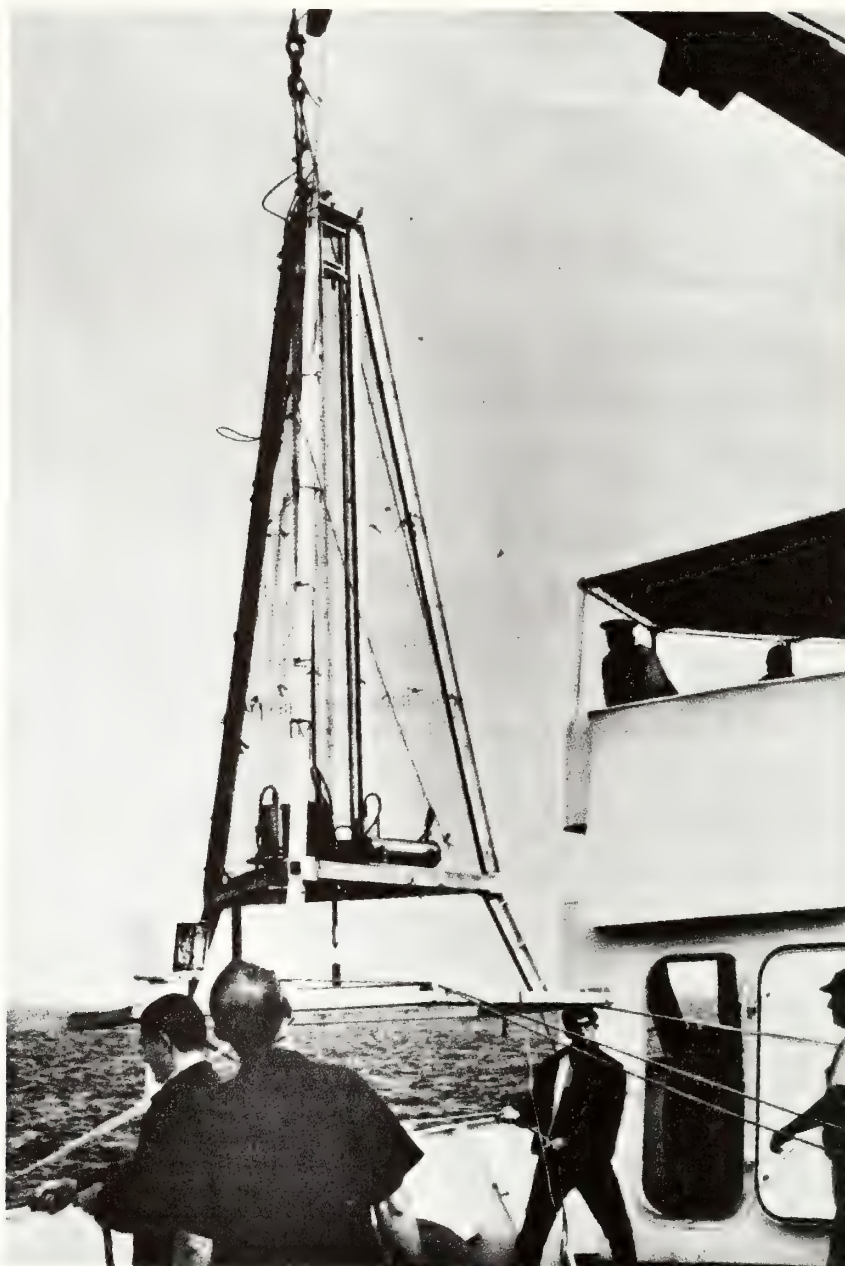


FIG. 2—*Photograph of the device at sea in 1967.*

part of the strength was needed to support its dead weight. The apparatus was designed for a submerged weight of about 135 N (600 lb).

The apparatus had to be able to withstand dragging across the bottom by a drifting ship or collision with the side of a ship. The apparatus also had to be sufficiently streamlined so that it could be lowered rapidly through the water without kiting.

A cross section showing only the mechanical equipment is presented in Fig. 1; Fig. 2 is a photograph of the apparatus. The structural members are provided with welded gusset plates. Assembly involved the bolting together of gusset plates to permit easy disassembly into small pieces for shipment.

The apparatus was self-powered, because of electrical limitations of the cable (see next section), using a pressure compensated lead-acid battery. To obtain a low shaft speed, easy control of motion, and use of minimum power, all motors were of the step-motor type. These motors produced a shaft motion of 200 steps per turn and one step per pulse of applied power. The vane was mounted on the end of a solid, square stainless steel rod (0.02 by 0.02 by 3.35 m) which was attached to a crosshead. The crosshead was moved vertically by three lead screws in a manner similar to that used on the crosshead of universal testing machines. The drive motor was totally immersed in oil in a pressure compensated housing and was geared to give a vane penetration of 0.3 m (1 ft) in about 40 s.

The square vane shaft was passed through a square hole in a turntable to provide for rotary movement. The turntable was rotated by another stepping motor, also contained in a pressure compensated housing. The torque to the turntable was measured in early tests using a transducer, called a C ring, mounted between the drive motor and the turntable. In later tests, a torque transducer was installed immediately above the vane. In both locations, electrical strain gages served as torque sensing elements. The vane was equipped with a slip clutch that allowed the shaft to rotate about 1 rad before engaging. This established the base for zero torque level. The apparatus was equipped with suitable limit switches to avoid overruns.

Electrical Equipment

The primary factors controlling the electrical design were (1) controlled power was needed for the two stepping motors, (2) measurements were required for the penetration and rotation of the vane and the applied torque, and (3) all functions were to be controllable from shipboard. Electrical communication between the ship and the vane shear apparatus was via a single conductor within the mechanical cable used in lowering or raising the apparatus. Direct current was used to transmit commands from the ship to the equipment. To avoid interaction of signals in the cable, execution of commands or transmission of data

occurred only after termination of the appropriate command signal. Data were transmitted to the ship by frequency modulated, multiplex wired telemetry.

Command System

The electrical system on board the ship was designed to give only four commands: ROTATE, STOP, PENETRATE, and REVERSE. The command signals were generated as a two-level, two-directional current (four combinations). Thus, the command PENETRATE to the motor, which was used to force the vane down into the soil, consisted of a signal current at a relative level of one and a positive direction. REVERSE was a current at a relative level of ten and a positive direction. ROTATION and STOP were signals in the reverse direction at levels one and ten, respectively. At the apparatus, the signals were decoded and delivered to a "logic unit" which produced the desired operation.

Penetration of the vane was automatically stopped every 0.3 m (1 ft) by proximity switches mounted on the tower. These switches were activated by a magnet mounted on the crosshead. A limit switch prevented excessive penetration. Rotation or penetration of the vane could be stopped with the STOP signal. Limit switches automatically stopped vane rotation at about 3 rad (180 deg). Combinations of the above commands were used to initiate other activities, such as reading the power levels and platform orientation.

Measurement System

Direct measurement of the penetration of the vane could have been accomplished, but it would have added an unnecessary complication. Instead, the number of pulses of electricity delivered to the stepping motor were counted. Since there was a direct relationship between pulses and penetration, the penetration could usually be determined relative to the initial position of the vane. Similarly, the pulses delivered to the motor that rotated the turntable were counted to determine the vane rotation. Various checks were available to ensure that the motors had not stalled.

The tilt of the base plate (Fig. 1) was measured by an electrolytic tilt gage which produced a resistance change proportional to the angle of tilt of each of two perpendicular horizontal axes. The gage was calibrated by physically tilting the gage and recording the output. In actual use the gage proved to be not as sensitive as desired and nonlinear in response but, nevertheless, provided approximate values of tilt. The gage was mainly useful in ascertaining that the tower was standing vertical after having been lowered to the sea floor.

The torque was determined with electrical resistance type strain gages mounted either on the C ring or in the load cell machined at the end

of the vane rod, which attached directly above the vane coupling. Signals from the gage circuits were fed into a telemetry oscillator that produced an alternating current with a frequency which, within a specified range, was proportional to the amplitude of the supplied signal voltage. The resulting alternating current was transmitted to the surface for recording and interpretation. Another oscillator was used to transmit data on the same wire, but in a different frequency range, to indicate either tilt of the platform or inverter voltage and pulse counts.

Electrical Calibration

The torque transducers (C ring or load cell) were initially calibrated by applying known torques, mechanically, and recording voltage changes in the measuring circuits. In actual operation, however, the output of the electrical system could be expected to vary because of purely electrical problems, so it was necessary to provide a calibration of the electrical system itself each time a torque measurement was started. This electrical calibration was achieved by automatically inserting resistors in the measuring circuit prior to each test. The resistors produced an equivalent change in circuit resistance in the same manner as a strained gage. The resistors had been calibrated at the same time as the transducers, so inserting a certain resistor into the circuit produced the same electrical effect as a certain torque. Thus, at the beginning of each torque measurement a signal equal to that produced by a known torque was recorded and used in subsequent reduction of data.

Shipboard Electronics

Signals from the vane shear apparatus were displayed on an X-Y recorder as well as recorded, in their raw form, on a magnetic tape recorder for semipermanent storage. The data in the two frequency ranges were also separated and converted back into direct current for use in operating the various meters and plotters used for monitoring and controlling the operation of the apparatus during actual operation. A typical example of the recorded torques relative to testing time is shown in Fig. 3.

Sea Trials

Gulf of Maine, 1967

The apparatus was first tested in seawater off Provincetown, Mass., and was then used for measurements in the Wilkinson and Murray Basins (Fig. 4) from the U. S. Coast and Geodetic Survey ship *Davidson* [5]. A total of eleven successful vane shear profiles at eight sites (Fig. 4) were made in water depths ranging from about 212 to about 290 m (650 to 880 ft). Tests showed that the apparatus could be towed while im-

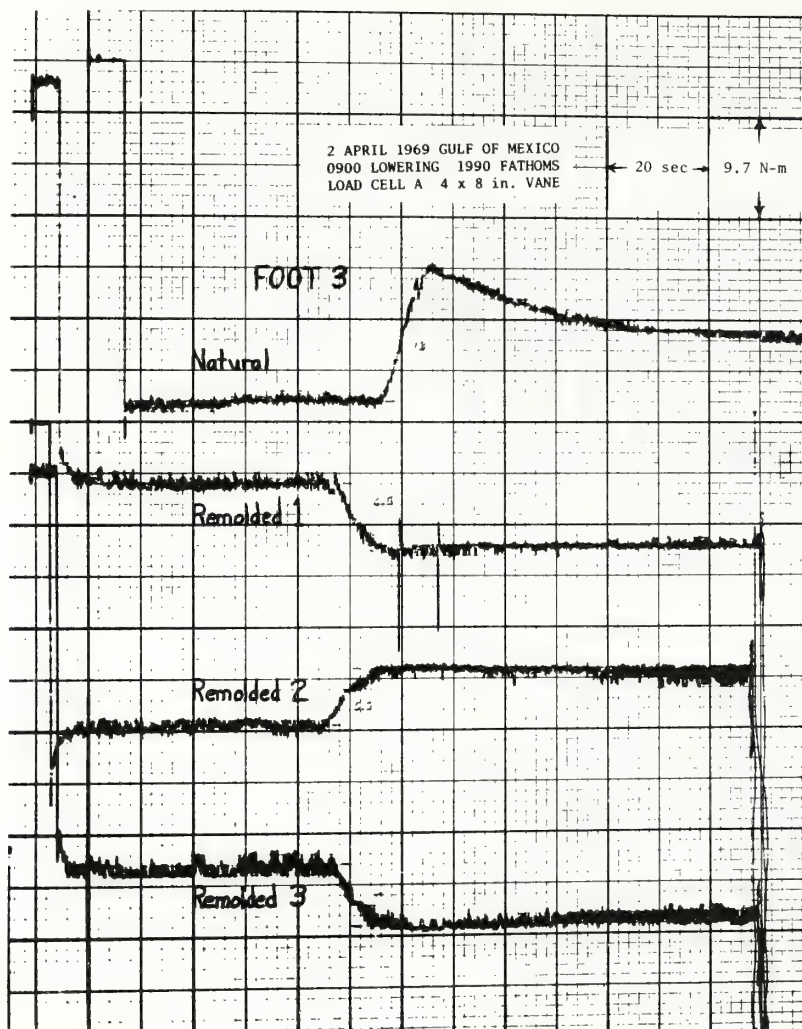


FIG. 3—Photograph of an actual record showing torque on the y axis related to time on the x axis for one natural and three successive remolded shear strength measurements; torquing at 0.02 rad/s (78 deg/min). The essentially identical torque over the first 53 s represents shaft rotation before the vane is engaged in the coupling.

mersed, thus saving considerable time; in one 7-h period, successful vane borings were made at three locations in the Murray Basin up to 4.4 km (2.4 nautical miles) apart without raising the apparatus to the surface. Actual penetration depths into the soil ranged from 2.6 m (8.6 ft) in soft clay to 0.7 m (2.3 ft) in a glacial moraine.

Difficulties were experienced with the electrical lines in the cable, which failed periodically, especially when the tension in the cable ex-

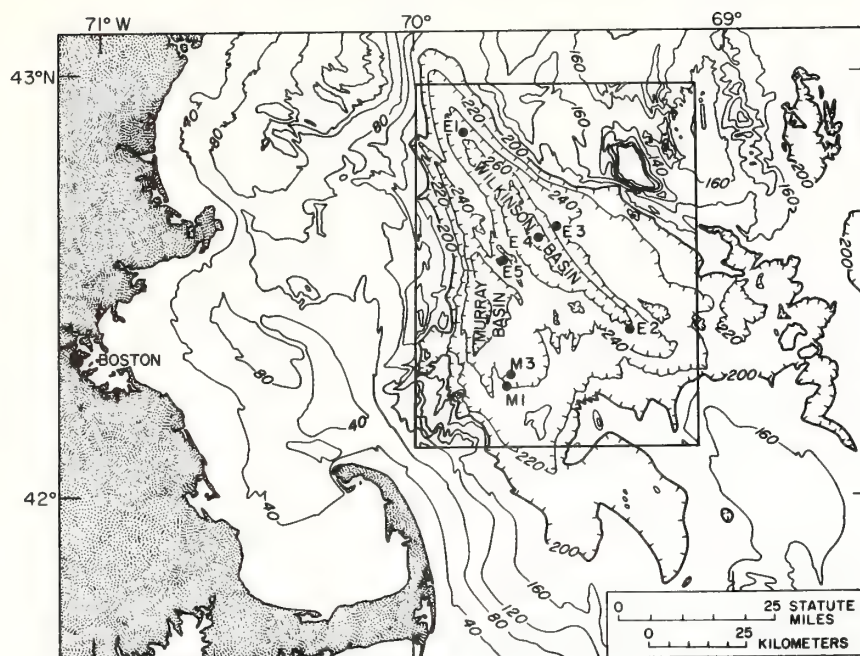


FIG. 4—Location map of the Gulf of Maine test sites in Wilkinson and Murray Basins. Depths are in meters.

ceeded about 1800 kg (4000 lb). Various changes were also required in the electrical system following these trials.

Exuma Sound, Bahamas, 1968

Tests were attempted in 1686 m (5530 ft) of water in the northern part of Exuma Sound from the U. S. Coast and Geodetic Survey ship *Whiting*. Satisfactory signals were received from the apparatus for water depths less than about 1 km, but for greater depths the noise on the receiving channel increased to such an extent that no data could be obtained. The cause of this behavior was not definitely determined, but it is believed to be associated with "ground loops." Recurrence of the malfunction was prevented during the subsequent winter by shielding the strain gage leads from the load cell to the telemetry module on the apparatus. The tests were terminated when the ship's cable became coiled around the apparatus during recovery and the apparatus was raised inverted

Gulf of Mexico, 1969

The apparatus was used for three tests in 95 m (312 ft) of water east of the South Pass of the Mississippi River, from the anchored Texas A&M University R/V *Alaminos* [6]. The soil in this area is predominant-

ly clay. Four separate lowerings of the vane shear apparatus were made to the abyssal plain in a water depth of about 3635 m (11,930 ft) from the *Alaminos* [7]. Three profiles were obtained with the 0.1 by 0.2 m (4 by 8 in.) vane and the torque transducer and one profile was obtained with the 0.076 by 0.15 m (3 by 6 in.) vane equipped with the C ring transducer. The abyssal plain soil is composed of clay and an iron-rich layer near the surface. All tests were successful although problems were encountered with ship drift. On two occasions, while the vane rod was being retracted after the test, the ship drifted sufficiently to run out all the cable and the tower was dragged across the bottom.

Results

Wilkinson Basin

Typical results of the in-place measurements in the Wilkinson Basin are shown in Fig. 5. Also shown are shear strengths measured by laboratory vane, operated at 0.006 rad/s (21 deg/min), on a gravity-type core raised from essentially the same location in 1966 by the U. S. Coast Guard cutter *Evergreen*. Unpublished studies on these cores have shown that tests with laboratory vanes operated at 0.006 and 0.02 rad/s yield comparable strengths. The lower shear strength in the cores, compared with the in-place measurements, probably indicates sampling disturbance. For depths ranging from 0.6 to 1.2 m (2 to 4 ft), the average lab strength was 2.77 kN/m² (58 lb/ft²) whereas the average in-place strength was 4.10 kN/m² (86 lb/ft²). The in-place strengths are thus about 50 percent higher than the lab strengths. These data are similar to those reported by Doyle et al [8] for field and laboratory vane tests in 29 m (94 ft) of water in the west delta region of the Mississippi River delta.

The c/p ratio (undisturbed shear strength/effective overburden pressure) is high near the surface. For the top 1 m, based on the field tests, the ratio is about 1.0. However, for depths ranging from 1 to 3 m, the slope of the strength effective stress curve is about 0.25. The soil is believed to be normally consolidated in this basin.

Generally, similar results were obtained for three other locations in the Wilkinson Basin. In the southeast location (Fig. 4), for depths ranging from 0.5 to 1.5 m, the laboratory vane strength was 2 kN/m² (40 lb/ft²) whereas the field strengths for both sizes of field vane were 4 kN/m² (80 lb/ft²). At two other locations the larger field vane yielded higher strengths than the smaller one. Thus, at the northwest location in the Wilkinson Basin, for depths of 0.5 to 1.5 m, the lab vane yielded an average strength of 2 kN/m² (40 lb/ft²), the smaller field vane gave 4 kN/m² (80 lb/ft²), and the larger field vane gave 5.5 kN/m² (110

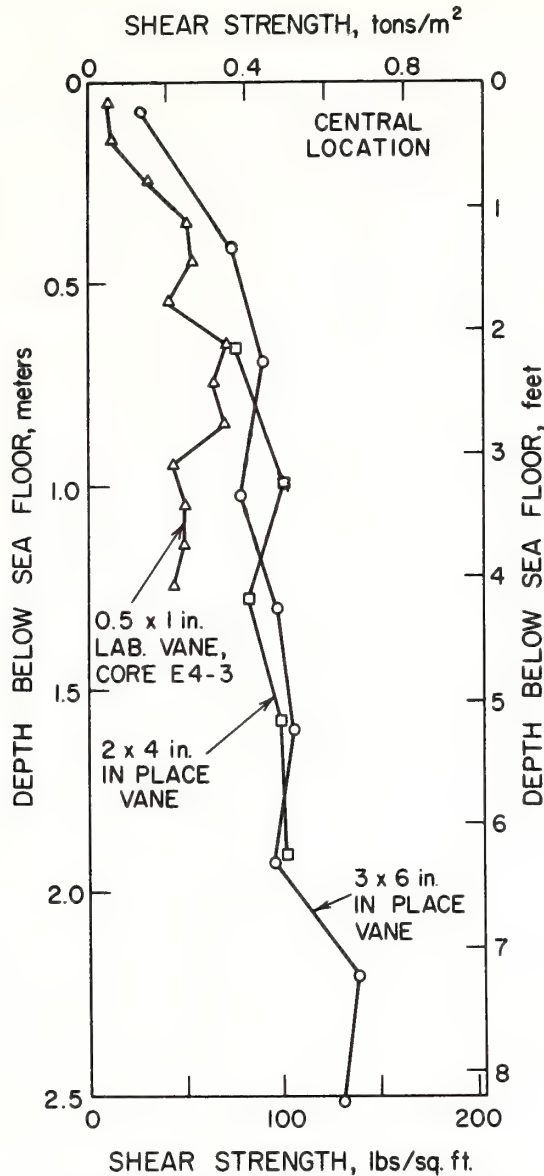


FIG. 5—Comparison of laboratory vane shear strength measurements on a core and in-place vane shear strength measured at locations differing by less than 0.5 km at site E4, Wilkinson Basin. Laboratory vane rotated 0.006 rad/s (21 deg/min) and in-place vane rotated at 0.02 rad/s (78 deg/min). One-half metric ton/m^2 equivalent to 5 kN/m^2 .

lb/ft^2). At the east central location for the same depth range and sequence of measurements, the average strengths were, respectively, 3.1,

3.6, and 4.1 kN/m². It is not known why the larger field vane yielded higher strengths in the latter two locations.

All of these strengths are too low for shallow support of typical terrestrial structural loads; a larger field vane apparatus with a telescoping vane shaft would be useful for exploring greater depths of soil. The strengths are adequate, however, to support many structures presently used in ocean engineering having low bearing loads.

Abyssal Plain, Gulf of Mexico

Typical data for tests in the Abyssal Plain of the Gulf of Mexico (latitude 24°43' North and longitude 93°49.5' West) are shown in Fig. 6. For the depth range from 0.3 to 1.5 m (1 to 5 ft), the laboratory strengths determined on gravity cores averaged about 4 kN/m² (80 lb/ft²), whereas the field vane strengths using the 0.1 by 0.2 m (4 by 8 in.) vane averaged about the same or a little higher. The sensitivities determined using the field vane were on the order of 2 to 3. For depths between 1 and 2.5 m, the *c/p* ratio was 0.53.

Summary and Conclusions

A highly portable field vane shear device was designed and constructed for use from ships. The device was designed for operation with booms and cable sizes that severely limit the height and weight of the apparatus. Further, the electrical characteristics of the cables were such that significant amounts of power could not be transmitted from the ship to the apparatus. For these reasons, and because of time and financial limitations, the prototype device was designed for testing only about the top 3 m (10 ft) of the soil. The apparatus was designed for operation in water depths up to 4.6 km (15,000 ft).

The device was successfully used for a series of vane borings in the Wilkinson and Murray Basin and in the Gulf of Mexico. The in-place vane strengths were low, as expected for normally consolidated clays, but the *c/p* ratios were high, a characteristic common to deep sea marine soils. The in-place strengths generally were about twice the strengths measured on gravity-type cores using miniature laboratory vanes.

There appears to be no reason why the device could not be redesigned for testing to depths on the order of 15 m (50 ft) or more if suitable ship facilities are available.

Acknowledgments

The mechanical design was detailed by T. G. Gavin, graduate research assistant. F. B. Claridge, graduate research assistant, finished the mechanical design, supervised construction, and aided in the Wilkinson

Basin sea trials. J. N. Sterner, who operated and successfully maintained the electronic equipment at sea, and G. Lafenhagen served as electronic technicians. P. Douglass, principal machinist, contributed many useful

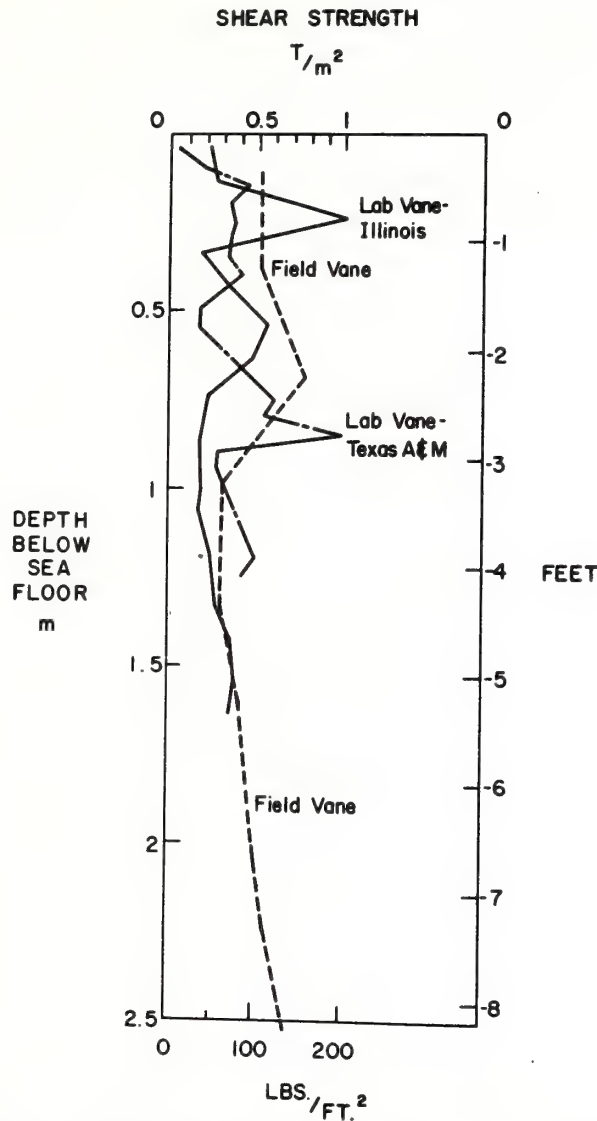


FIG. 6—Comparison of laboratory vane shear strength measurements on a core and in-place vane shear strength measured in the Gulf of Mexico Abyssal Plain at about the same location. Water depth 3.6 km. One T/m^2 equivalent to $10 \text{ kN}/m^2$. Illinois laboratory vane 0.5 by 1 in. (0.01 by 0.025), rotated at 0.02 rad/s (79 deg/min); Texas A&M laboratory vane 0.5 by 0.5 in. (0.01 by 0.01 m), rotated at about 0.009 rad/s (30 deg/min); and Illinois field or in-place vane 4 by 8 in. (0.1 by 0.2 m), rotated at 0.02 rad/s (78 deg/min).

ideas and participated in some of the sea trials. W. Bryant, Texas A&M University, kindly arranged for ship support in 1969 and permitted the use of unpublished data shown in Fig. 6.

The captains, officers, and crew of the four ships used in the investigations were helpful. We are appreciative of help from those unnamed persons who have contributed in many ways to the success of this equipment. This project was jointly supported during the first few years at the University of Illinois by the U. S. Navy Bureau of Yards and Docks and the Office of Naval Research; afterwards, until 1969, primarily by the latter organization under contract Nonr 3985(09), NR 081-260. This paper was partly written under the sponsorship of ONR contract N00014-67-A-0370-0005, NR 083-248 to Lehigh University.

References

- [1] Preiss, K., *Deep-Sea Research*, DROAA, Vol. 15, 1968, pp. 637-641.
- [2] Preiss, K. in *Proceedings of the American Nuclear Society Topical Meeting, San Juan, Puerto Rico, 4-6 May 1969*, Puerto Rico Nuclear Center—135 (TID-4500). 1969, pp. 483-493.
- [3] Richards, A. F., "Investigations of Deep-Sea Sediment Cores, II. Mass Physical Properties," U. S. Navy Hydrographic Office Tech. Report 106, 1962.
- [4] Osterberg, J. O. in *Symposium on Vane Shear Testing of Soils, ASTM STP 193*, American Society for Testing and Materials, 1957, pp. 1-7.
- [5] Richards, A. F. and Keller, G. H. in *Transactions*, American Geophysical Union, EOSTA, Vol. 49, 1968, pp. 221-222.
- [6] Bryant, W., Richards, A. F., and Keller, G. H. in *Transactions*, 19th Annual Meeting, Gulf Coast Association of Geological Societies, Miami, 1969, p. 267.
- [7] Richards, A. F., Keller, G. H., and Bryant, W. R. in *Abstracts with Programs for 1969*, Geological Society of America, Part 7, 1969, pp. 188-189.
- [8] Doyle, E. H., McClelland, B., and Ferguson, G. H. in *Preprints*, 3rd Annual Off-shore Technology Conference, Houston, Tex., Vol. 1, 1971, pp. I 21-32.

¹ Professor of oceanography and ocean engineering and director, Marine Geotechnical Laboratory, Lehigh University, Bethlehem, Pa. 18015.

² Associate professor of civil engineering and research engineer, University of Illinois, Urbana, Ill. 61801.

³ Professor of civil engineering, Engineering-Science Building, University of Texas, Austin, Tex. 78712.

⁴ Director of the Marine Geology and Geophysics Laboratory, NOAA, Atlantic Oceanographic and Meteorological Laboratories, Miami, Fla. 33130.

Marine geology

Recent results of the Trans-Atlantic Geotraverse (TAG) of the National Oceanic and Atmospheric Administration (NOAA) and complementary investigations have advanced understanding of the evolution of continental margins, sea-floor spreading, and the occurrence of oil and mineral deposits in the deep ocean basin. TAG was initiated in 1970 following a proposal by the United States Upper Mantle Committee to extend the Transcontinental Geophysical Survey of the Upper Mantle Project across the central North Atlantic basin between eastern North America at Cape Hatteras, N.C., and northwestern Africa at Cap Blanc, Mauritania (Fig. 1).

Rifted continental margins. TAG comprises a natural unit to study the evolution of rifted continental margins because the continental margins of southeastern North America and northwestern Africa, in reconstructions of the positions of the continents prior to continental drift, are considered to have been joined, with Cape Hatteras and Cap Blanc occupying nearly conjugate points. Geological and geophysical observations of the two continental margins were compiled, compared, and interpreted by P. A. Rona in light of the theory of plate tectonics.

The continental margins of southeastern North America at Cape Hatteras and northwestern Africa at Cap Blanc appear broadly symmetric with respect to (1) distribution of subaerial and submarine physiographic provinces, with the exception of the lower continental rise hills which have not been observed off northwestern Africa; (2) early and middle Paleozoic, Mesozoic, and Cenozoic (the past 570,000,000 years) stratigraphic frameworks; (3) late Precambrian, Paleozoic, and Mesozoic (70,000,000–700,000,000 years) structural frameworks, within the limit of geological resolution; and (4) certain offshore magnetic anomalies, including an anomaly associated with the continental slope and the magnetic boundary between regions of relatively smooth (landward) and rough (seaward) magnetic fields.

The two continental margins appear broadly asymmetric with respect to Cenozoic (the past 70,000,000 years) structural frameworks. Sedimentary strata underlying the coastal plain, continental terrace, and continental rise near Cape Hatteras are predominantly undeformed except by superficial gravitational displacement processes. Sedimentary strata underlying the corresponding physiographic provinces off Cap Blanc are deformed by deep structural processes, including (1) compressional folding related to Alpine mountain building movements in the Mediterranean region, (2) tensional faulting along west-northwest trending fracture zones which cross the Mid-Atlantic Ridge, and along inferred north-northeast trending fractures which regionally parallel the continental

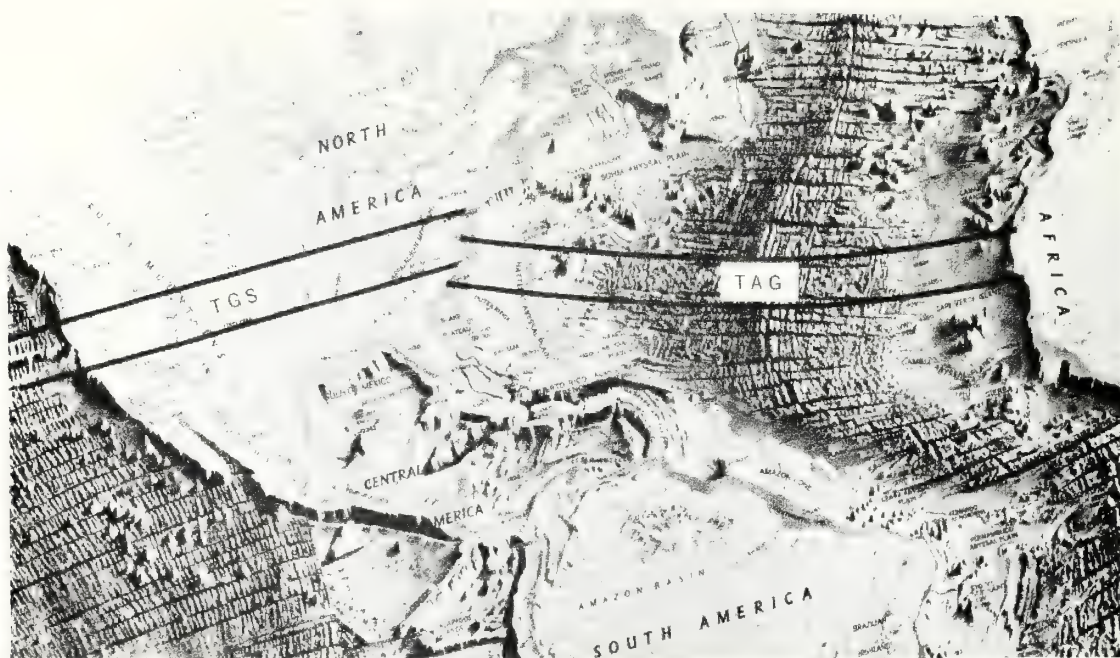


Fig. 1. Relief map showing the path of the NOAA Trans-Atlantic Geotraverse (TAG) to establish a standard crustal section across the central North Atlantic continuous

with the section already established across North America by the Transcontinental Geophysical Survey (TGS). (National Geographic Society)

margin, (3) volcanism concentrated along the fracture zones, and (4) movements of salt domes originating from salt deposits of probable Late Triassic and Early Jurassic age (160,000,000–205,000,000 years) beneath the northwest African continental shelf, slope, and continental rise.

The observations of symmetries and asymmetries in time and in space in the stratigraphy and structure of the eastern North American and northwestern African continental margins can be explained in terms of the theory of plate tectonics. The African and North American continents probably drifted toward each other across an early Atlantic ocean basin (proto-Atlantic) during the early Paleozoic (400,000,000–570,000,000 years). The two continents collided in the late Paleozoic (250,000,000–350,000,000 years), resulting in symmetrical deformation which produced the southern Appalachian fold belt of eastern North America and the Mauritanide fold belt of northwestern Africa. Africa and North America were apparently joined until tensional stresses began to rift the continents during the Triassic (195,000,000–225,000,000 years).

The African and North American continents separated as a result of growth of the intervening central North Atlantic ocean basin by sea-floor spreading, generally assumed to have begun about 180,000,000 years ago. As the two continents drifted apart, the two continental margins tilted seaward at average rates of about 2.5 cm per 1000 years, resulting in accumulation of seaward expanding wedges of sedimentary strata on the coastal plains and continental shelves; the wedges

of sediment attain thicknesses of about 5 km beneath the seaward edges of both continental shelves. B. C. Heezen and his students have stressed the role of deep ocean currents in shaping the sediment accumulations on the continental slope and continental rise of eastern North America during the past 50,000,000 years, including the lower continental rise hills. The fact that deep ocean currents are weaker and more diffuse over the continental slope and rise off northwestern Africa may account for the exceptional width of that continental rise (three times that of southeastern North America), the absence of well developed lower continental rise hills, and the activity of additional processes, particularly transport of sediment by the wind, in shaping sediment accumulation on the sea floor off northwestern Africa.

Africa and Eurasia apparently collided across the Mediterranean Sea during the Cenozoic (about 40,000,000 years ago). The collision deformed the northwestern African continental margin, resulting in folding of sedimentary strata, including development of the Atlas Mountains, and the rejuvenation of faulting and volcanism. The continental margin of eastern North America, isolated from plate interactions since separation from Africa, has remained largely quiescent. Africa and North America continue to move apart as the central North Atlantic widens at an average rate of 2.8 cm per year.

Sea-floor spreading. Africa and North America have behaved as if joined to the adjacent ocean basin since rifting apart, so that growth of the central North Atlantic by sea-floor spreading has re-

sulted in continental drift. The rate of growth of the ocean basin has been derived by determining the age of the oceanic crust at numerous points between Africa and North America. The ages are determined by the dating of rock samples recovered by the Deep Sea Drilling Project and by the identification of the sequence of remanent magnetic anomalies in the geomagnetic time scale. The remanent magnetic anomalies are interpreted as being due to normal and reversely magnetized rocks, which in turn were caused by reversals in the geomagnetic field during sea-floor spreading. The identification of magnetic anomalies sometimes gives ages greater than, but in no cases less than, ages determined from rock samples. Such discrepancies can be reconciled by considering the ages determined on rock samples as minimum ages, because it is uncertain whether the oldest rocks present have been recovered.

The oldest Atlantic sea floor is represented by magnetic smooth zones of very-low-amplitude anomalies extending seaward of the continental shelves off southeastern North America and northwestern Africa. Extrapolation of ages determined by the Deep Sea Drilling Project suggests the magnetic smooth zones were formed between 155,000,000 and 180,000,000 years ago. Rona and

others observed that the magnetic smooth zone is nearly twice as wide off Cape Hatteras (530 km) as off Cap Blanc (330 km), which they interpreted to indicate that an eastward jump or migration of the mid-ocean ridge axis occurred during the time of the magnetic smooth zone. Immediately seaward of the magnetic boundary in the western central North Atlantic, P. R. Vogt and others identified a 300-km-wide band of correlatable linear remanent magnetic anomalies (the USNS *Keathley* sequence) which they designated J anomalies because the anomalies occur in oceanic crust of Late Jurassic age (135,000,000–155,000,000 years). Coincident with the Bermuda discontinuity at the seaward end of the *Keathley* sequence, the sea floor changes from smooth to rough, fracture zones become more closely spaced, the rate of sea-floor spreading and the frequency of geomagnetic reversals apparently decrease, and the direction of sea-floor spreading changes. Vogt and G. L. Johnson recognized at least 13 positive magnetic anomalies seaward of the Bermuda discontinuity (K anomalies), which they ascribed to geomagnetic reversals in the Early and Middle Cretaceous (90,000,000–135,000,000 years). A magnetic smooth zone occurs seaward of the K anomalies in oceanic crust of Late Cretaceous age (80,000,000–90,000,000

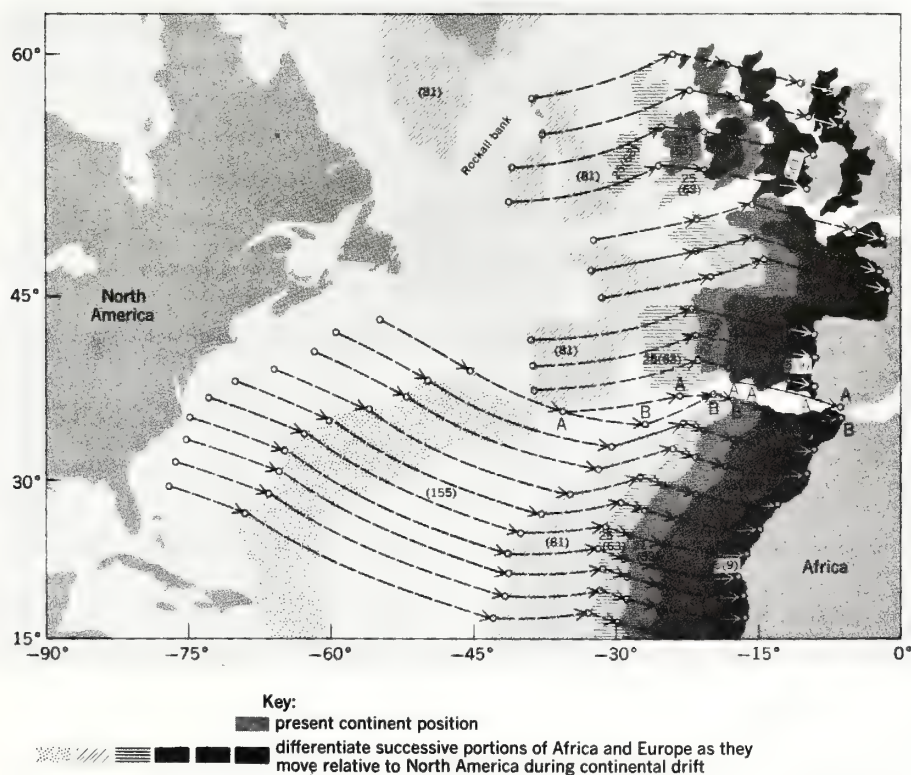


Fig. 2. Relative positions of Africa and Europe with respect to North America for specific times in millions of years determined by rotating corresponding magnetic anomalies of known ages on either side of the North Atlantic into coincidence. The arrows show the path of continental drift of Africa and Europe (with A and B as refer-

ence points), assuming that the position of North America remains fixed. Actually, both Africa and North America have moved during continental drift. (From W. C. Pitman III and M. Talwani, *Sea-floor spreading in the North Atlantic*, *Geol. Soc. Amer. Bull.*, 83:619–646, 1972)

years). Nearly the complete sequence of J and several of the K anomalies have been identified in the eastern central North Atlantic by R. K. Lattimore and others.

The direction and rate of continental drift of Africa and North America have varied with time since rifting. W. C. Pitman III and M. Talwani reconstructed the paleogeographic relations of the continents during the growth of the central North Atlantic ocean basin by fitting together corresponding remanent magnetic lineations interpreted as lines of equal crustal age (isochrons) from opposite sides of the Mid-Atlantic Ridge. The result is a sort of motion picture showing the successive positions of the continents at the time of generation of each corresponding pair of magnetic lineations (Fig. 2). In Fig. 2 numbers in brackets designate the date in millions of years ago for each successive position of Africa and of Europe relative to North America during continental drift. Numbers outside brackets designate the number of the magnetic reversal anomalies in the geomagnetic time scale corresponding to the date. The flow lines of relative movement of Africa and North America during continental drift were found to parallel the major fracture zones which cross the central North Atlantic, consistent with interpretation of these fracture zones as the physical expression of flow trajectories. Their computations (for 35°N latitude) indicate that separation of Africa and North America proceeded at average rates of 2.8 cm per year from the present to 9,000,000 years ago; 2.0 cm per year from 9,000,000 to 38,000,000 years ago; 3.4 cm per year from 63,000,000 to 81,000,000 years ago; 4 cm per year from 81,000,000 to 180,000,000 years ago.

Oil and mineral deposits. Scientific findings of TAG are contributing to the assessment of oil and mineral deposits in the deep ocean basin.

Seismic reflection and magnetic measurements, reported by Rona in 1969, across the continental rise in water depths up to 5500 m off Cap Blanc, northwestern Africa, revealed buried geological structures which resemble salt domes. Oil exploration has proved the existence of domes containing rock salt (halite) of Triassic and Early Jurassic age (170,000,000–225,000,000 years) associated with oil accumulations in sedimentary basins underlying the adjacent northwestern African coastal plain and continental shelf (with a water depth up to 100 m). At that time it was believed that these sedimentary basins, including the rock salt deposits, terminated near the seaward edge of the continental shelf.

In order to account for the possible extent of rock salt deposits as far as 1000 km seaward of the edge of the continental shelf in the deep ocean basin, Rona proposed the hypothesis of the Atlantic Sea (Fig. 3). The Atlantic was a sea with its circulation restricted by the continents in their positions during the Late Triassic to Late Jurassic (160,000,000–205,000,000 years) stage of continental drift. The Atlantic Sea created an environment in which evaporation of seawater may have exceeded inflow, favoring the deposition of thick, extensive rock salt layers and the preservation of organic matter similar to environments observed in the Dead and Red seas. As the continents continued to separate during continental drift, the cir-



Fig. 3. Interpretive sketch of the Atlantic Sea restricted by the inferred positions of the surrounding continents until the Late Jurassic (160,000,000 years) stage of continental drift. Sites 139 and 140 of the Deep Sea Drilling Project are shown.

ulation of the Atlantic changed from that of a restricted sea to that of a more open ocean, evidenced by the appearance of marine limestones in the African coastal basins during the Late Jurassic (135,000,000–160,000,000 years). The hypothesis of the Atlantic Sea has received support from 1970 results of the Deep Sea Drilling Project, which encountered marked salinity gradients in interstitial water of sediment cores recovered from the middle and lower continental rise off northwestern Africa (drilling sites 139 and 140); such gradients confirm the presence of rock salt deposits at least as far seaward as beneath the lower continental rise. The hypothesis of the Atlantic Sea should have general application in that conditions favorable for the deposition of rock salt and for preservation of organic matter should have existed at an early stage of growth of other ocean basins during the period when their circulation was restricted.

R. B. Scott and others participating in TAG reported dredging manganese crusts in 1971 with the NOAA *Discoverer* at numerous sites along a 2000-km-long section of the Atlantis fracture zone trending northwest-southeast between the Mid-Atlantic Ridge (30°N latitude) and the lower continental rise off northwestern Africa. Manganese crusts up to about 10 cm in thickness, covering basalt and limestone bedrock surfaces in the fracture zone, were sampled. Manganese crusts of similar appearance have been reported from certain other fracture zones and mid-ocean ridges. The blanket nature and areal extent of such manganese crusts

Accumulation rates of metals in Atlantis manganese crusts in grams per square centimeter per million years

Metal	Mid-Atlantic Ridge crest	2000 km east of crest
Mn	0.3	0.04
Fe	0.5	0.05
Ni	0.004	0.0006
Co	0.009	0.0008
Cu	0.003	0.0002
Cr	0.001	0.0001

suggest that they may be volumetrically more important than the better known occurrences of manganese nodules.

The manganese crusts recovered from the Atlantis fracture zone are most similar mineralogically and chemically to the type of manganese nodules which occur on volcanic seamounts. The principal mineral present is poorly crystallized delta manganite, $\delta\text{-MnO}_2$, with broad, diffuse 25- and 14-nm peaks as determined by x-ray diffraction. The Atlantis manganese crusts are relatively high in manganese content (about 15% by weight), iron (about 20% by weight), and cobalt (about 1% by weight) and low in copper and nickel (each less than 1% by weight). The accumulation rates of metals in the crusts at the Mid-Atlantic Ridge crest and 2000 km east of the crest are shown in the table. The growth rate of the Atlantis manganese crusts at the Mid-Atlantic Ridge crest is 11 mm per million years, based on the thickness of manganese accumulated over limestone containing microfossils 3,000,000 years old. The growth rate 2000 km east of the Mid-Atlantic Ridge crest is 1.2 mm per million years, based on uranium-thorium dating. The accumulation rates of metals in the Atlantis manganese crusts and the growth rates of the crusts are both an order of magnitude greater at the Mid-Atlantic Ridge crest than 2000 km east of the crest. These observations suggest that an active volcanic source may be contributing to the deposits at the ridge crest.

For background information see CONTINENT FORMATION; MARINE GEOLOGY; MARINE SEDIMENTS; OIL AND GAS, OFFSHORE in the McGraw-Hill Encyclopedia of Science and Technology.

[PETER A. RONA]

Bibliography: J. Ewing et al., *Geotimes*, 15(7): 14-16, 1970; D. E. Hayes et al., *Geotimes*, 16(2): 14-17, 1971; R. K. Lattimore, P. A. Rona, and O. E. DeWald, *Trans. Amer. Geophys. Union*, 53:407, 1972; W. C. Pitman III and M. Talwani, *Geol. Soc. Amer. Bull.*, 83:619-646, 1972; P. A. Rona, *Amer. Ass. Petrol. Geol. Bull.*, 54:129-157, 1970; P. A. Rona, *Deep-Sea Res.*, 18:321-327, 1971; P. A. Rona, J. Brakl. and J. R. Heirtzler, *J. Geophys. Res.*, 75:7412-7420, 1970; R. B. Scott et al., *Trans. Amer. Geophys. Union*, 53:529, 1972; P. R. Vogt, C. N. Anderson, and D. R. Bracey, *J. Geophys. Res.*, 76:4796-4823, 1971; P. R. Vogt and G. L. Johnson, *Nature*, 234:22-25, 1971.

New Evidence for Seabed Resources from Global Tectonics

Peter A. Rona

ABSTRACT

Patterns of mineral distribution are emerging from the conceptual framework provided by the new global tectonics. The occurrence of mineral deposits, including petroleum, is related to boundaries where plates of the Earth's lithosphere converge and diverge. Interpretation of limited evidence indicates particular potential for metallic sulphide deposits and petroleum accumulations associated with lithospheric plate boundaries at continental margins and in ocean basins. Recognition of the global patterns will accelerate discovery of mineral resources of the seabed as well as of the continent.

INTRODUCTION

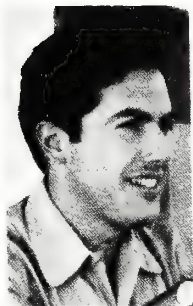
A scientific revolution is in progress, which over the past five years has already changed our understanding of the Earth as profoundly as the Copernican revolution changed our understanding of the solar system. The Copernican revolution entailed a fundamental change in man's understanding from an Earth-centered to a Sun-centered solar system leading to the development of modern astronomy and the space age. The present scientific revolution entails a fundamental change in our understanding from a static Earth to a dynamic Earth, and presages benefits that man will derive from his new knowledge (Wilson, 1968a,b, 1972). The implications of "the new global tectonics", as this dynamic Earth view is called, for the mineral potential of the seabed are only now emerging.

SAMPLING THE SEABED

The only seabed minerals that certainly have economic potential are oil and gas beneath many continental margins, gravel, sand, shells, and placer deposits, various other minerals beneath the continental shelves specifically related to adjacent continental deposits (McKelvey and Wang, 1969; McKel-

vey et al., 1969) and manganese deposits which blanket areas of the deep sea floor (Horn et al., 1972). Consider how much we would know about mineral deposits of the continents if our sampling procedure were limited to flying in a balloon at an altitude of up to ten kilometers (six miles) and suspending a bucket on the end of a cable to scrape up loose rocks from the surface of the land. What are the chances that we would find the major known ore bodies which generally underlie areas of less than a few square kilometers (a square mile)? This describes our capacity of sampling the sediments and rocks of the ocean bottom utilizing coring, drilling, and dredging devices lowered from ships through the water column over an area twice as large as that of the continents. Averaged over the world's oceans, the distribution of ocean-floor rocks that have been sampled is about three dredge hauls per million square kilometers (Cann and Simkin, 1971). As James (1968) qualified his review of seabed minerals. "This appraisal of the resource potential of the deep ocean is based almost entirely on inferences drawn from existing knowledge and theory. These inferences seem reasonable—but it must be remembered that the area of the oceans is enormous and that the amount of specific information on the underlying rocks is minute in comparison".

Dr. Peter A. Rona is presently Senior Research Geophysicist with the NOAA, Atlantic Oceanographic and Meteorological Laboratories in Miami, Florida. He is Chief Scientist of the Trans-Atlantic Geotraverse (TAG), an international cooperative project to investigate the Earth's crust along a corridor across the Atlantic between southeastern North America and northwestern Africa to gain an understanding of continental drift, sea-floor spreading, and the occurrence of seabed minerals. He generally spends several months of the year at sea leading explorations of the seabed.



Prior to joining NOAA in 1969 he was Exploration Geologist with Standard Oil Company (N.J.) between 1957 and 1959. From 1960 to 1969 he was with Columbia University, Hudson Laboratories where he developed and became Head of Marine Geophysics. He received the degree of Ph.D. in 1967 from the Department of Geology and Geophysics at Yale University. He has published about 50 scientific papers and is a member of 12 professional societies.

GLOBAL TECTONICS

An idea anticipates every discovery of a hidden mineral resource. For example, once scientists realized that a definite association existed between the type of geological structure termed an "anticline" and accumulations of oil, they knew where to drill and the rate of discovery accelerated. In the same way, the right conceptual framework can be used to extend our limited direct knowledge of resources of the ocean basin toward a realistic appraisal of potential. The test of the value of a conceptual framework is how well it explains what we see and predicts what we do not see. The conceptual framework of a static Earth held that the continents and ocean basins were permanent features which had existed in their present configurations since early in the 4,500-million-year history of the Earth. Only the most accessible continental mineral deposits were discovered, largely by trial and error, with little understanding of why and where they occurred. The recent change to a conceptual framework based on a dynamic Earth, upon which continents are constantly moving and ocean basins are opening and closing, is leading toward a global understanding of the distribution of mineral deposits in space and in time.

The basis of the new conceptual framework is the theory of plate tectonics, the essentials of which are widely accepted (Isacks et al., 1968; Morgan, 1968; Alexander, 1969; Dickinson, 1970; McKenzie, 1972; Matthews, 1973), although much work remains to be done and differences of opinion exist (Meyerhoff and Meyerhoff, 1972). "Tectonics" is a geological term pertaining to Earth movements. The movements involve the rigid outer shell of the Earth termed "lithosphere," which is of the order of 100 km thick, including the Earth's crust. The lithosphere behaves as if floating on underlying plastic material called the "asthenosphere." The lithosphere is segmented into about six primary slabs or plates (Fig.1), each of which may encompass a continent and part of an adjacent ocean basin, as well as numerous sub-plates. The boundaries of the plates are delineated by linear zones of earthquakes where the plates are moving relative to one another. Three types of boundaries are recognized which account for the movements of the plates (Fig.2).

(1) Convergent plate boundary where two adjacent plates move together and collide or one plate plunges downward beneath the other plate and is resorbed into the interior of the Earth.

(2) Divergent plate boundary where two adjacent plates move apart because new lithosphere is added to each by the process of "sea-floor spreading." The new lithosphere spreading more-or-less symmetrically to either side of the divergent plate boundary acts like a conveyor belt which carries the

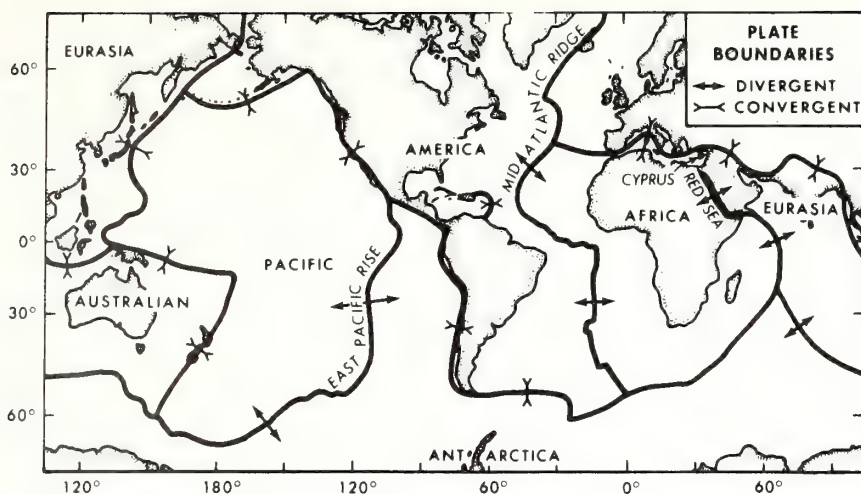


Fig. 1. Boundaries of six principal lithospheric plates (after Le Pichon, 1968). Convergent and divergent plate boundaries are indicated (after Isacks et al., 1968).

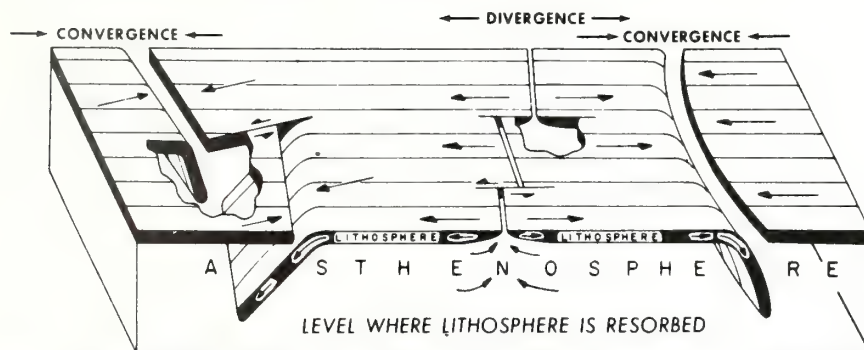


Fig. 2. Block diagram illustrating schematically how convergent and divergent lithospheric plate boundaries work (after Isacks et al., 1968). One-hundred-kilometer-(60-mile)-thick lithospheric plates move like conveyor belts from mid-ocean ridges (divergent plate boundaries) and plunge downward beneath deep-sea trenches (convergent plate boundaries).

continents apart in the motion of "continental drift." The existence of both convergent boundaries where lithosphere is destroyed and divergent boundaries where lithosphere is created implies that the diameter of the Earth is not changing.

(3) Parallel plate boundary where two adjacent plates move edge-to-edge along their common interface.

METALLIC MINERALS OF CONTINENTAL MARGINS AND VOLCANIC ISLAND CHAINS (CONVERGENT PLATE BOUNDARIES)

Hydrothermal mineral deposits, those mineral deposits which form by precipitation from solutions, constitute a major part of our useful metallic ores on the continents. The most economically important type of hydrothermal deposits is the sulphides, in which various metals combine with sulphur to precipitate from the hydrothermal solution. Sawkins (1972) has pointed out that a major portion of the sulphide deposits of the world are situated along present or former convergent plate boundaries, where an oceanic lithospheric plate plunges beneath the margin of a continent (including the continental shelf) or beneath a chain of volcanic islands such as Japan (Fig.2). The processes which concentrate the sulphide deposits along convergent plate boundaries, only partially understood, are related to mineralizing solutions emanating from the downgoing lithospheric plate which melts as it is re-absorbed into the interior of the Earth. Metallic sulphide deposits along convergent plate boundaries include the Kuroko deposits of Japan, sulphide ore bodies of the Philippines, and belts of deposits which extend along the western cordillera of North and South America (Sillitoe, 1972) and from the eastern Mediterranean to Pakistan (Ridge, 1972). Gold deposits are not sulphides but often accompany sulphide minerals. The majority of gold deposits in Alaska, Canada, southeastern United States, California, Venezuela, Brazil, West Africa, Rhodesia, southern India and southeastern and western Australia, occur in rocks interpreted to be related to former convergent plate boundaries.

METALLIC MINERALS OF THE OCEAN BASIN (DIVERGENT PLATE BOUNDARIES)

Divergent plate boundaries are formed by oceanic ridges which occur at the sites of divergence of spreading lithospheric plates in the central portions of ocean basins. The Red Sea and the island of Cyprus in the Mediterranean Sea provide important clues to the potential of metallic sulphide deposits at divergent plate boundaries.

The Red Sea

The Red Sea is interpreted as a divergent plate boundary developing between the African and Eurasian plates (Fig.1) (Drake and Girdler, 1964;

Hutchinson and Engels, 1972; Lowell and Genik, 1972), thus providing a natural laboratory to study mineral processes associated with such boundaries. About five years ago the richest known submarine metallic sulphide deposits were found in three basins with a total area of 70 km² (27 sq. miles) situated along the center of the Red Sea at a depth of about 2,000 m (6,600 ft.) below sea level (Degens and Ross, 1969). The sulphide minerals are disseminated in sediments that fill the basins to a thickness estimated between 20 and 100 m (65 and 330 ft). The top 10 m (33 ft.) of sediment that have been explored by coring the largest of the basins totals about 80 million tons (dry weight) with average metal contents of 29% iron, 3.4% zinc, 1.3% copper, 0.1% lead, 0.005% silver, and 0.00005% gold (Bischoff and Manheim, 1969). The deposits are saturated with, and overlain by, salty brines carrying the same metals in solution as are present in the sulphide deposits (Backer and Schoell, 1972). The salty brines are considered to be the hydrothermal solutions from which the sulphide minerals are precipitated. It remains controversial whether the brines are being charged with minerals from volcanic sources beneath the Red Sea or by transit through sediments with high copper, vanadium, and zinc contents adjacent to the basins where the metallic sulphide deposits occur (Ross et al., 1972).

Mid-Ocean Ridges

The Red Sea represents the earliest stage in the growth of an ocean basin when a divergent plate boundary rifts a continent in two. The most advanced growth stage of a divergent plate boundary is the mid-ocean ridge system, an 87,000-km-(47,000-mile)-long undersea mountain chain that extends through all the major ocean basins and girdles the globe (Fig.1). The mid-ocean ridge system has not been adequately sampled to determine whether concentrations of metallic sulphides comparable to the Red Sea are present at sites along its crest or in basins on its flanks. Measurements of the distribution of heat emanating from mid-ocean ridges (Lister, 1972) and of the chemical alteration of ridge rocks (Muelenbachs and Clayton, 1971a,b) indicate that sea water forms a hydrothermal solution which penetrates fissures, dissolves minerals from rocks underlying the ridges, and precipitates these minerals in concentrated deposits.

A limited amount of sampling indicates that hydrothermal processes are actively concentrating metals from volcanic sources underlying mid-ocean ridges. Sediments on active mid-ocean ridges are generally enriched; typical values in parts per million on a carbonate-free basis are iron 100,000, manganese 80,000, copper 1,000, nickel 800, lead 150, chromium 200, cobalt 350, uranium 10, mercury 0.4, and trace amounts of vanadium, cadmium and

bismuth (Bostrom and Peterson, 1966, 1969; Bostrom et al., 1969; Fisher and Bostrom, 1969; Bender et al., 1970; Bostrom, 1970; Bostrom and Fisher, 1969, 1971; UST Soundings, 1972). The concentrations cited are typical of sediments covering widespread areas on mid-ocean ridges and are not economic; much higher concentrations exist locally.

Metallic sulphides occur in rocks dredged from the Indian Ocean Ridge (Baturin, 1971). Small veins of pure copper have been recovered by the Deep Sea Drilling Project at several sites. At the crest of the Ninety East Ridge (Deep Sea Drilling Project Site 216), near the equator in the Indian Ocean, veins of copper occur in volcanic rocks (basalt) overlain by 437 m (1440 ft.) of sediment in water depth of 2,237 m (7,380 ft.) (Von der Borch et al., 1972). A small vein of pure copper and clusters of copper crystals are present in sediment about 20 m (65 ft.) above volcanic rocks (basalt) beneath the lower continental rise in water depth of 5,245 m (17,150 ft.) about 650 km (350 miles) southeast of New York (Site 105). A sample of manganese oxide 4.2 cm (1.7 inches) thick recently dredged from a water depth of about 3,635 m (12,000 ft.) in the axial valley of the Mid-Atlantic Ridge (26°N latitude) by the Trans-Atlantic Geotraverse of the National Oceanic and Atmospheric Administration (NOAA) (Rona and Orlin, 1971), has particular significance. The composition, form and thickness of this sample, which accumulated at a rate at least 100 times faster than manganese nodules, indicates a hydrothermal origin and demonstrates that hydrothermal mineral deposits are actively accumulating at certain divergent plate boundaries in ocean basins (Scott et al., 1973). Because the sea floor is supposed to originate by spreading from mid-ocean ridges, a mineral deposit on a mid-ocean ridge would be expected to extend in a linear zone from the ridge, across the ocean basin, to the adjacent continental margin if the depositional process is continuous.

At this stage in our exploration of the oceans it would seem beyond expectation to be able to make detailed observations on an economically important metallic sulphide deposit that originated at a divergent plate boundary on a submerged mid-ocean ridge. Yet, such a deposit is known and has been extensively studied. The Troodos Massif on the island of Cyprus is interpreted to be a slice of oceanic lithosphere that was formed by processes of sea-floor spreading about a mid-ocean ridge and subsequently was thrust upward to its present position (Gass and Masson-Smith, 1963; Moores and Vine, 1971; Khan et al., 1972, Gass and Smewing, 1973). The composition and layered sequence of rocks that constitute the Troodos Massif are the same as are known to underlie the seabed.

Since classical times, Cyprus has been famous for its mineral wealth. The mining of copper was an important industry in pre-Roman times. The bril-

liant green stains of copper sulphides on ancient mine tailings attracted modern prospectors (Lavender, 1962). Between 1965 and 1970 the average annual exports amounted to about one million tons each of iron pyrites, chromite, and gypsum, about 150,000 tons of cupreous pyrites, and 100,000 tons of cupreous concentrates. The estimated value of mineral products exported from Cyprus in 1970 amounted to 30 million dollars (Petropoulos, 1971).

The principal ore bodies occur in the uppermost volcanic (basaltic) layers of the Troodos Massif. Uncertainty has existed whether the Troodos sulphide ore bodies originated before or after the upthrust of the Troodos Massif. In the first case the ore bodies would be representative of the seabed. In the second case, the ore bodies would be attributed to special conditions unrelated to the seabed. The sulphide deposits are clearly genetically related to the volcanic rocks in which they occur (Hutchinson, 1965; Govett and Pantazis, 1971). Recent studies reveal that iron- and manganese-rich sediments interlayered with the volcanic rocks and associated with the ore bodies of the Troodos Massif are chemically identical to those metal-enriched sediments found on active mid-ocean ridges, indicating that both the sediments and the ore bodies were formed in situ on the sea floor by hydrothermal processes (Corliss, 1972).

The Troodos ore bodies (Wilson and Ingham, 1959) may provide the first actual indication of the nature of metallic sulphide deposits in ocean basins. The Skouriotissa ore body is roughly elliptical in map-view, measures approximately 600 m (2,000 ft.) long and 180 m (600 ft.) wide, and is lens-shaped in cross-section. Its estimated weight is six million tons. The average composition of the ore is 2.25% copper (ranging to greater than 5%), 48% sulphur, and 43% iron. The Mavrovouni ore body is also roughly elliptical in map-view, measures approximately 300 m (1,000 ft.) long and 180 m (600 ft.) wide, and forms a lens which attains a thickness of 240 m (800 ft.) in cross-section. Its estimated weight is greater than 15 million tons. The average composition of the ore is 4.2% copper, 48% sulphur, 43% iron, 0.4% zinc, 0.25 oz. per ton gold, and 0.25 oz. per ton silver. Sediments underlying the Skouriotissa ore body, supposed to be a disintegration product of the pyrite in the ore body, contain 2.12 oz. per ton gold and 12.96 oz. per ton silver. Exposed patches of metallic oxides indicate the presence of the ore bodies beneath the mountainous surface of the Troodos Massif. Exploitation of the Skouriotissa ore body is by underground shafts and that of the Mavrovouni ore body is by strip mining.

What kind of a target for exploration would a Troodos ore body make if the body were submerged beneath hundreds to thousands of meters of water on the crest or flank of a mid-ocean ridge? It is unlikely that any of the

present exploration methods are capable of detecting the body (Rona, 1972). Both the engineering development involved to improve present methods and the exploration-at-sea will be costly.

SEABED PETROLEUM AND THE NEW GLOBAL TECTONICS

The prerequisites for petroleum accumulation consist of a source of organic matter to generate the petroleum, a natural reservoir to contain the petroleum, and a trap to concentrate the fluid and gas. Petroleum is a hydrocarbon derived from organic matter consisting of the remains of plants and animals themselves constituted of hydrocarbons. The organic matter must accumulate in an environment where it is preserved. This is favored by an environment that is toxic to life, so that the organic matter is not consumed as food, and deficient in oxygen, so that the hydrocarbon is not decomposed. How do conditions which favor the accumulation of petroleum relate to convergent and divergent plate boundaries?

PETROLEUM OF CONTINENTAL MARGINS (CONVERGENT PLATE BOUNDARIES)

Convergent plate boundaries where the oceanic portion of a lithospheric plate plunges downward beneath the margin of a continent are characterized by the presence of a deep-sea trench which runs along their length (Fig.2). A system of deep-sea trenches runs along the entire western margin of North and South America, where the Pacific lithosphere is plunging beneath the continents. In addition to a deep-sea trench, arcuate chains of volcanic islands are present along some convergent plate boundaries between the trench and the continent. The western margin of the Pacific exhibits such chains of volcanic islands, including the Aleutian, Kuril, Japanese, Ryukyu, Philippine, and Indonesian; other island chains include the Mariana, South Sandwich, and Lesser Antilles. The chains partially enclose smaller basins between the islands and the adjacent continent such as the Bering Sea, the seas of Okhotsk and Japan, the Yellow Sea, and the East and South China seas (Emery et al., 1969; Parke et al., 1971; Emery and Ben-Avraham, 1972). Both the marginal trenches and the volcanic island chains create a habitat favorable for the accumulation of petroleum in several ways:

- (1) The trenches and island chains act as barriers which catch sediment and organic matter from the continent and ocean basin.
- (2) The shape of the trenches and small ocean basins acts to restrict the

circulation of the ocean so that oxygen is not replenished in the sea water and organic matter is preserved.

(3) The accumulation of sediments and the geological structures which develop owing to deformation of the sediments by earth forces, provide reservoirs and traps for the accumulation of petroleum. According to Hedberg (1970), "these marginal semi-enclosed basins constitute some of the most promising areas in the world for petroleum accumulation".

PETROLEUM OF THE OCEAN BASIN (DIVERGENT PLATE BOUNDARIES)

The development of divergent plate boundaries may create a habitat favorable for the accumulation of oil and opens immense possibilities for petroleum resources in the deep ocean basin (Rona, 1969, 1970). When a divergent plate boundary develops beneath a continent, the continent is rifted in two and the continental fragments are carried apart on a conveyor belt of new lithosphere generated at the divergent plate boundary. As the two continental fragments move apart, a sea surrounded by the adjacent continents forms between them. The surrounding continents act as barriers to restrict the circulation of the sea. Consequently, organic matter is preserved and, if evaporation of sea water exceeds replenishment, then layers of rock salt are deposited along with the organic matter. As the continental fragments continue to move apart and to subside along with the adjacent sea floor, the restricted sea becomes an open ocean. The layers of organic matter and salt are buried beneath sediments. The organic matter subsequently develops into petroleum by processes that are only partially understood and the salt forms dome-shaped masses which act to trap the petroleum.

The Red Sea is an example of a restricted sea formed at an early stage of development of the divergent plate boundary about which Arabia is drifting from Africa; layers of rock-salt up to 5 km (17,000 ft.) thick and organic muds are present beneath the Red Sea (Friedman, 1972; Hutchinson and Engels, 1972; Lowell and Genik, 1972). Along both east and west margins of the North and South Atlantic apparent salt domes have been discovered extending seaward from continental shelves to continental rises in water depths up to 5 km (16,500 ft.) (Rona, 1969; Butler, 1970; Pautot et al., 1970; Watson and Johnson, 1970; Baumgartner and Van Andel, 1971; Templeton, 1971; Emery, 1972; Leyden et al., 1972). The occurrence of these salt domes in the deep Atlantic indicates that, at an early stage of continental drift, the Atlantic was a sea with its circulation restricted by the surrounding continents in their positions at that time (Rona, 1969, 1970).

Like the present Red Sea, conditions in the Atlantic Sea favored the preservation of organic matter and the deposition of rock salt. As the Atlantic widened in response to the symmetric creation of new lithosphere by sea-floor spreading about the Mid-Atlantic Ridge, the Atlantic Sea became an ocean and the organic matter and salt were buried under sediments which form the present margins of the Atlantic. It is reasonable to expect that petroleum accumulations will extend seaward beneath the continental shelf, continental slope, and the continental rise to water depths of about 5.5 km (18,000 ft.) along large portions of both the eastern and western margins of the North and South Atlantic. Petroleum may likewise be found in other ocean basins that have grown through the stage of a restricted sea by sea-floor spreading about a divergent plate boundary.

CONCLUSIONS: PATTERNS OF MINERAL DISTRIBUTION

Patterns of mineral distribution are emerging from the conceptual framework provided by the new global tectonics which will guide our search for mineral deposits. Hydrothermal processes have concentrated the majority of known metallic sulphide ore bodies along convergent lithospheric plate boundaries originally at continental margins (Fig. 1, 2). Hydrothermal processes are also active at divergent plate boundaries from initial stages, represented by the metallic sulphide deposits accumulating in the Red Sea, to advanced stages represented by metal concentration in sediments on mid-ocean ridges and by possible Troodos-type metallic sulphide deposits. The Troodos metallic sulphide ore bodies (copper, zinc, other metals including gold and silver) provide an actual example of the type of deposits that may be expected in sea floor generated from mid-ocean ridges. Confirmation and economic evaluation of Troodos-type metallic sulphide deposits in ocean basins await technological advances in marine exploration methods. With regard to petroleum, convergent plate boundaries create conditions which form accumulations in small ocean basins and deep-sea trenches marginal to continents. Divergent plate boundaries create conditions which favor the development of oil accumulations extending from the continental shelf into the deep ocean basin beneath the continental rise.

The global patterns of mineral distribution that are emerging will accelerate discovery of mineral resources of the seabed as well as of the continent.

ACKNOWLEDGEMENTS

This paper was prepared for the United Nations. I thank V. Baum, J.P. Lévy and G. Matthews of the Ocean Economics and Technology Branch of the United Nations for their encouragement and both the National Oceanic and Atmospheric Administration and the United Nations for support. Communications with F.G. Blake, formerly of the U.S. Office of Science and Technology, F. Nagle Jr. of the University of Miami, R.B. Scott of Texas A and M University, and J.S. Tooms of the United Nations were helpful.

REFERENCES

- Alexander, T., 1969. The secret of the spreading ocean floor. *Fortune Mag.*, February: 112-117.
- Backer, H. and Schoell, M., 1972. New deeps with brines and metalliferous sediments in the Red Sea. *Nature Phys. Sci.*, 240: 153-158.
- Baturin, G.N., 1971. In: L.A. Zenkevitch (Editor), *History of the World Oceans*. Nauka, Moscow, p. 259.
- Baumgartner, T.R. and Van Andel, T.H., 1971. Diapirs of the continental margin of Angola, Africa. *Geol. Soc. Am. Bull.*, 82: 793-802.
- Bender, M., Broecker, W., Gornitz, V. and Middel, U., 1970. Accumulation rate of manganese and related elements in sediments from the East Pacific Rise. *Am. Geophys. Union Trans.*, 51: 327.
- Bischoff, J.L. and Manhein, F.T., 1969. Economic potential of the Red Sea heavy metal deposits. In: E.T. Degens and D.A. Ross (Editors), 1969. *Hot Brines and Recent Heavy Metal Deposits in the Red Sea*. Springer, New York, N.Y., 600 pp.
- Bostrom, K., 1970. Submarine volcanism as a source for iron. *Earth Planet. Sci. Lett.*, 9: 348-354.
- Bostrom, K. and Fischer, D.E., 1969. Distribution of mercury in East Pacific sediments. *Geochim. Cosmochim. Acta*, 33: 743-745.
- Bostrom, K. and Fisher, D.E., 1971. Volcanogenic U, V and Fe in Indian Ocean sediments. *Earth Planet. Sci. Lett.*, 11 (2): 95-98.
- Bostrom, K. and Peterson, M.N.A., 1966. Precipitates from hydrothermal exhalations on the East Pacific Rise. *Econ. Geol.*, 61: 1258-1265.
- Bostrom, K. and Peterson, M.N.A., 1969. Origin of aluminum-poor ferromanganoan sediments in areas of high heat flow on the East Pacific Rise. *Mar. Geol.*, 7: 427-477.
- Bostrom, K., Peterson, M.N.A., Joensuu, O. and Fisher, D.E., 1969. Aluminum-poor ferromanganoan sediments on active oceanic ridges. *J. Geophys. Res.*, 74: 3261-3270.
- Butler, L.W., 1970. Shallow structure of the continental margin, South Brazil and Uruguay. *Geol. Soc. Am. Bull.*, 81: 1079-1096.
- Cann, J.R. and Simkin, T., 1971. A bibliography of ocean-floor rocks. *Philos. Trans. R. Soc. Lond., Ser. A*, 268: 737-743.
- Corliss, J.B., 1972. Rare earth data for iron- and manganese-rich sediments associated with sulfide ore bodies of the Troodos Massif, Cyprus. *Geol. Soc. Am., 1972 Ann. Meet., Abstracts with Programs*, pp. 476-477.
- Degens, E.T. and Ross, D.A. (Editors), 1969. *Hot Brines and Recent Heavy Metal Deposits in the Red Sea*. Springer, New York, N.Y., 600 pp.
- Dickinson, W.R., 1970. Global tectonics. *Science*, 168: 1250-1259.

- Drake, C.L. and Girdler, R.W., 1964. A geophysical study of the Red Sea. *Geophys. J.*, 8 (5): 473-495.
- Emery, K.O., 1972. Eastern Atlantic continental margin: some results of the 1972 cruise of the R.V. Atlantis II. *Science*, 178: 298-300.
- Emery, K.O. and Ben-Avraham, Z., 1972. Structure and stratigraphy of China Basin. *Bull. Am. Assoc. Pet. Geologists*, 56: 839-859.
- Emery, K.O., Hayashi, Y., Hilde, T.W.C., Kobayashi, K., Koo, J.H., Meng, C.Y., Niino, H., Osterhagen, J.H., Reynolds, L.M., Wageman, J.M., Wang, C.S. and Yang, S.J., 1969. Geological structure and some water characteristics of the East China Sea and the Yellow Sea. *Econ. Comm. Asia Far East, Comm. Coordination of Joint Prospecting for Mineral Resources in Asian Offshore Areas, Tech. Bull.*, 2: 3-43.
- Fisher, D.E. and Bostrom, K., 1969. Uranium-rich sediments on the East Pacific Rise. *Nature*, 224: 64-65.
- Friedman, G.M., 1972. Significance of Red Sea in problem of evaporites and basinal limestones. *Bull. Am. Assoc. Pet. Geologists*, 56 (6): 1072-1086.
- Gass, I.G. and Masson-Smith, D., 1963. The geology and gravity anomalies of the Troodos Massif, Cyprus. *Philos. Trans. R. Soc. Lond., Ser. A*, 255: 417-467.
- Gass, I.G. and Smewing, J.D., 1973. Intrusion, extrusion and metamorphism at constructive margins: evidence from the Troodos Massif, Cyprus. *Nature*, 242: 26-29.
- Govett, G.J.S. and Pantazis, Th.M., 1971. Distribution of Cu, Zn, Ni and Co in the Troodos Pillow Lava Series: Cyprus. *Trans. Inst. Mining Metallurgy*, 80: B27-46.
- Hedberg, H.D., 1970. Continental margins from viewpoint of the petroleum geologists. *Bull. Am. Assoc. Pet. Geologists*, 54: 3-43.
- Hollister, C.D., Ewing, J.I., Habib, D., Hathaway, J.C., Lancelot, Y., Luterbacher, H., Paulus, F.J., Paag, C.W., Wilcoxon, J.A. and Worstell, P., 1972. *Initial Reports of the Deep Sea Drilling Project, XI*. U.S. Gov. Printing Office, Washington, D.C., 1077 pp.
- Horn, D.R., Horn, B.M. and Delach, M.N., 1972a. Metal content of ferromanganese deposits of the oceans. *Lamont-Doherty IDOE/NSF GX33616 Tech. Rep.*, 3. Office for Int. Decade of Ocean Exploration, Nat. Sci. Found., Washington, D.C., 51 pp.
- Horn, D.R., Ewing, M., Horn, B.M. and Delach, M.N., 1972b. Worldwide distribution of manganese nodules. *Ocean Industry Mag.*, January: 26-29.
- Hutchinson, R.W., 1965. Genesis of Canadian massive sulfides reconsidered by comparison to Cyprus deposits: *Trans. Can. Inst. Mining Metallurgy*, 68: 286-300.
- Hutchinson, R.W. and Engels, G.G., 1972. Tectonic evolution in the southern Red Sea and its possible significance to older rifted continental margins. *Geol. Soc. Am. Bull.*, 83: 2989-3002.
- Isacks, B., Oliver, J. and Sykes, L.R., 1968. Seismology and the new global tectonics. *J. Geophys. Res.*, 73: 5855-5899.
- James, H.L., 1968. Mineral resource potential of the deep ocean. In: *Proc. Symp. Miner. Resour. World Ocean: Rhode Island Univ. Grad. School Oceanography Occas. Publ.*, 4: 39-44.
- Khan, M.A., Summers, C., Bamford, S.A.D., Chroston, P.N., Poster, C.K. and Vine, F.J., 1972. Reversed seismic refraction line on the Troodos Massif, Cyprus. *Nature*, 238: 134-136.
- Lavender, D., 1962. *The Story of Cyprus Mines Corporation*. Huntington Library, San Marino, Calif., 387 pp.
- Le Pichon, X., 1968. Sea-floor spreading and continental drift. *J. Geophys. Res.*, 73: 3661-3697.
- Leydon, R., Bryan, G. and Ewing, M., 1972. Geophysical reconnaissance on African Shelf: 2. Margin sediments from Gulf of Guinea to Walvis Ridge. *Bull. Am. Assoc. Pet. Geologists*, 56 (4): 682-693.
- Lister, C.R.B., 1972. On the thermal balance of a mid-ocean ridge. *Geophys. J.*, 26: 515-535.
- Lowell, J.D. and Genik, G.J., 1972. Sea-floor spreading and structural evolution of southern Red Sea. *Bull. Am. Assoc. Pet. Geologists*, 56: 247-259.

- Matthews, S.W., 1973. This changing earth. *Natl. Geogr. Mag.*, 143 (1): 1—37.
- McKelvey, V.E. and Wang, F.F.H., 1969. Preliminary maps, world subsea mineral resources. *U.S. Geol. Surv., Misc. Geol. Investig.*, Map 1—632.
- McKelvey, V.E., Tracey Jr. J.I., Stoertz, G.E. and Vedder, J.G., 1969. Subsea mineral resources and problems related to their development. *U.S. Geol. Surv. Circ.*, 619: 26 pp.
- McKenzie, D.P., 1972. Plate tectonics and sea-floor spreading. *Am. Scientist*, 60 (4): 425—435.
- Meyerhoff, A.A. and Meyerhoff, H.A., 1972. "The new global tectonics": major inconsistencies. *Bull. Am. Assoc. Pet. Geologists*, 56: 269—336.
- Moores, E.M. and Vine, F.J., 1971. The Troodos Massif, Cyprus, and other ophiolites as oceanic crust: evaluation and implications. *Philos. Trans. R. Soc. Lond., Ser. A*, 268: 443—466.
- Morgan, W.J., 1968. Rises, trenches, great faults, and crustal blocks. *J. Geophys. Res.*, 73: 1959—1982.
- Muelenbachs, K. and Clayton, R.N., 1971a. Oxygen isotope ratios in submarine diorites and their constituent minerals. *Can. J. Earth Sci.*, 8: 1591—1595.
- Muelenbachs, K. and Clayton, R.N., 1971b. Oxygen isotope studies of fresh and weathered submarine basalt. *Can. J. Earth Sci.*, 9: 172—173.
- Parke, Jr., M.L., Emery, K.O., Szymankiewicz, R. and Reynolds, L.M., 1971. Structural framework of the continental margin in the South China Sea. *Econ. Comm. Asia Far East, Comm. Coordination of Joint Prospecting for Mineral Resources in Asia Offshore Areas, Tech. Bull.*, 4: 103—142.
- Pautot, G., Cuzende, J. and Le Pichon, X., 1970. Continuous deep salt layer along North Atlantic margins related to early phase of rifting. *Nature*, 227: 351—354.
- Petropoulos, P.G., 1971. *Annual Report of the Senior Mines Officer for the Year 1970*. Nicosia, 33 pp.
- Ridge, J.D., 1972. Annotated bibliographies of mineral deposits in the western hemisphere. *Geol. Soc. Am. Mem.*, 131: 681 pp.
- Rona, P.A., 1969. Possible salt domes in the deep Atlantic off northwest Africa. *Nature*, 224: 141—143.
- Rona, P.A., 1970. Comparison of continental margins of eastern North America at Cape Hatteras and northwestern Africa at Cap Blanc. *Bull. Am. Assoc. Pet. Geologists*, 54: 129—157.
- Rona, P.A., 1972. Exploration methods for the continental shelf: geology, geophysics, geochemistry. *NOAA Tech. ERL 238-AOML*, 8: 47 pp.
- Rona, P.A. and Orlin, H., 1971. NOAA Trans-Atlantic Geotraverse (TAG). *Japan Soc. Promotion of Sci., Proc. Joint Oceanog. Assembly IAPSO, IABO, CMG, SCOR*, Sept. 1970: 513—514.
- Ross, D.A., Whitmarsh, R.B., Ali, S., Boudreaux, J.E., Fleischer, R.L., Malter, A., Nigrini, C., Stoffers, P., Cofman, R., Girdler, R., Manheim, F. and Supko, P., 1972. Deep Sea Drilling Project in the Red Sea. *Geotimes*, 17 (7): 24—26.
- Sawkins, F., 1972. Sulfide ore deposits in relation to plate tectonics. *J. Geol.*, 80: 377—397.
- Scott, M.R., Scott, R.B., Nalwalk, A.J., Rona, P.A. and Butler, L.W., 1973. Hydrothermal manganese in the median valley of the Mid-Atlantic Ridge. *Eos, Am. Geophys. Union, Trans.*, 54 (4): 244.
- Sillitoe, R.H., 1972. Relation of metal provinces in western America to subduction of oceanic lithosphere. *Geol. Soc. Am. Bull.*, 83: 813—818.
- Templeton, R.S.M., 1971. Geology of the continental margin between Dakar and Cape Palmas. In: F.M. Delany (Editor), *ICSU/SCOR Working Party 31 Symp., Cambridge 1970: The Geology of the East Atlantic Continental Margin. 2. Africa. Inst. Geol. Sci. Rep.*, 70/16: 47—60.
- UST Soundings, 1972. Metal deposits found in South Pacific. *Undersea Technol.*, 13 (9): 11.

- Von der Borch, C.C., Sclater, J.G., Gartner Jr., S., Hekinian, R., Johnson, D.A., McGowran, B., Pimm, A.C., Thompson, R.W. and Veevers, J.J., 1972. Deep Sea Drilling Project Leg 22. *Geotimes*, 17 (6): 15-17.
- Watson, J.A. and Johnson, G.L., 1970. Seismic studies in the region adjacent to the Grand Banks of Newfoundland. *Can. J. Earth Sci.*, 7: 306-316.
- Wilson, J.T., 1968a. A revolution in earth science. *Geotimes Mag.* 13 (10): 10-16.
- Wilson, J.T., 1968b. Static or mobile earth; the current scientific revolution, in Gondwanaland revisited. *Am. Philos. Soc. Proc.*, 112 (5): 309-320.
- Wilson, J.T., 1972. *Continents Adrift*. Freeman, San Francisco, Calif., 172 pp.
- Wilson, R.A.M. and Ingham, F.T., 1959. The geology of the Xeros-Troodos area, with an account of the mineral resources. *Cyprus Geol. Surv. Dep. Mem.*, 1: 1-177.

Plate Tectonics and Mineral Resources

The concepts of continental drift and sea-floor spreading provide clues to the location of economically important minerals such as oil and metals. These clues have already led to promising deposits

by Peter A. Rona

A scientific revolution is in progress that over the past five years has already changed our understanding of the earth as profoundly as the Copernican revolution changed medieval man's understanding of the solar system. The Copernican revolution entailed a fundamental change in man's world view from an earth-centered planetary system to a sun-centered one and led to the development of modern astronomy and the exploration of space. The current scientific revolution entails a fundamental change in man's world view from a static earth to a dynamic one and presages comparable benefits. Some of the benefits may even be economic. The implications of the new global tectonics for mineral resources, particularly the mineral resources of the ocean floor, are only now beginning to emerge.

At present the only undersea mineral resources that certainly have economic value are the vast oil and gas reserves found under many continental shelves and continental slopes, gravel, sand, shells and placer deposits on the continental shelves, various other minerals buried under the continental shelves in specific relation to adjacent continental deposits, and fields of manganese nodules that blanket large areas of the deep-sea floor. Even this limited knowledge is remarkable in the light of the difficulty that was encountered in obtaining it. Consider how much we would know about the mineral deposits of the continents if our sampling procedure were limited to flying in a balloon at an altitude of up to six miles and suspending a bucket at the end of a cable to scrape up loose rocks from the surface of the land. What are the chances that we would find the major known ore bodies, which generally underlie areas of less than a square mile?

Yet this farfetched analogy accurately describes man's present capacity for sampling the sediments and rocks of the ocean bottom, utilizing a variety of coring, drilling and dredging devices lowered from ships through the water column over an area twice as large as that of the continents. Averaged over the world's oceans, the distribution of ocean-floor rocks that have been sampled to date is only about three dredge hauls per million square kilometers!

In recent years every major discovery of a hidden mineral resource has been anticipated by a theoretical vision. For example, once field geologists realized that there was a definite association between the type of sedimentary structure termed an anticline and accumulations of oil, they knew where to drill and the rate of discovery of oil deposits accelerated accordingly. In the same way the right conceptual framework can be used to extend man's limited direct knowledge of resources of the ocean basin toward a realistic appraisal of their potential. The test of the value of such a conceptual framework is how well it explains what one sees and predicts what one does not see.

The old conceptual framework of a static earth held that the continents and ocean basins were permanent features that had existed in their present form since early in the 4.5-billion-year history

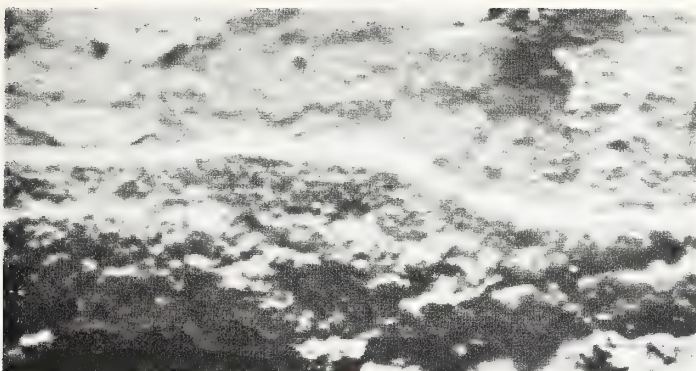
of the earth. Only the most accessible continental mineral deposits were discovered, largely by trial and error, with little understanding of why or where they existed. The recent change to a conceptual framework based on a dynamic-earth model, in which continents are constantly moving and ocean basins are opening and closing, is leading toward a better understanding of the global distribution of mineral deposits in both space and time.

The basis of the new conceptual framework is the theory of plate tectonics, the essentials of which have already been reported in *SCIENTIFIC AMERICAN* [see "Plate Tectonics," by John F. Dewey; May, 1972]. "Tectonics" is a geological term pertaining to earth movements. The movements in question involve the lithosphere, the rigid outer shell of the earth, which is of the order of 60 miles thick. The lithosphere, which behaves as if it were floating on an underlying plastic layer, the asthenosphere, is segmented into about six primary slabs, or plates, each of which may encompass a continent and part of an adjacent ocean basin [see top illustration on page 5].

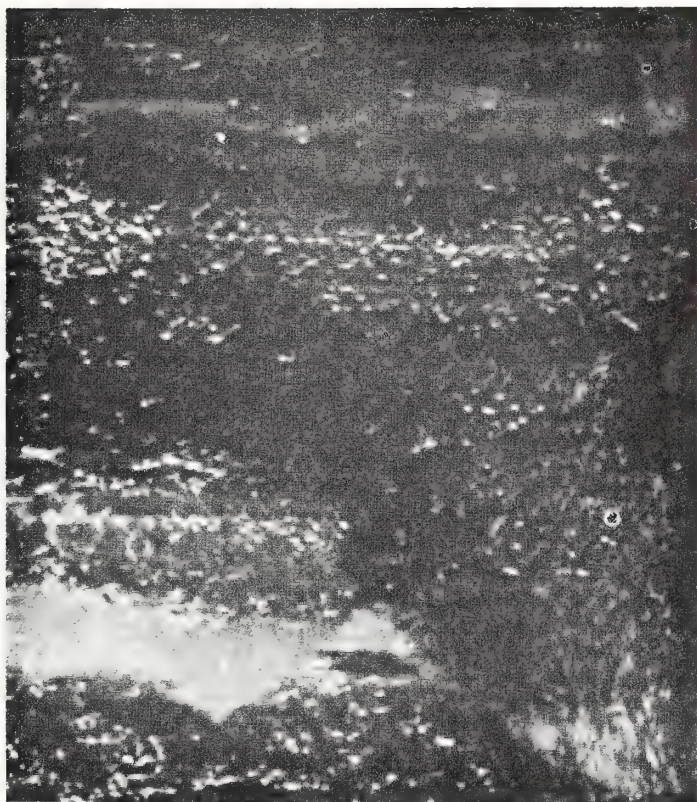
The boundaries of the lithospheric plates are delineated by narrow earthquake zones where the plates are moving with respect to each other. Three types of boundary are recognized. One type, called a convergent plate boundary, is where two adjacent plates move

TROODOS MASSIF on the island of Cyprus, the site of economically important mineral deposits that originated at a divergent tectonic-plate boundary, stands out clearly as the dark-colored mountainous region in the middle of the satellite photograph on the opposite page. The photograph was made recently from an altitude of nearly 600 miles by a multispectral camera system on board the first Earth Resources Technology Satellite (ERTS 1). Region is believed to be a slice of oceanic lithosphere that was formed by the process of sea-floor spreading from a submerged mid-oceanic ridge and was subsequently thrust upward.





SMALL VEIN OF PURE COPPER was discovered in a core sample of sedimentary rock obtained by the Deep Sea Drilling Project some 350 miles southeast of New York City. The copper vein, the horizontal reddish structure in this longitudinal section of a piece of the original core, is about half an inch long. It was found in sediment about 65 feet above the volcanic basement rocks under the lower continental rise at a water depth of 17,000 feet.



METAL-RICH CORE, collected from the Atlantis II Deep, one of the hot-brine pools located along the axial valley of the Red Sea at a depth of about 6,600 feet below sea level, represents the most concentrated submarine metallic sulfide deposits known. The muddy sediments containing the sulfide minerals fill the Red Sea basins to a thickness estimated at between 65 and 330 feet. The deposits are saturated with (and overlain by) salty brines considered to be the hydrothermal solutions from which the sulfide minerals were precipitated. The photograph was made by David A. Ross of the Woods Hole Oceanographic Institution.

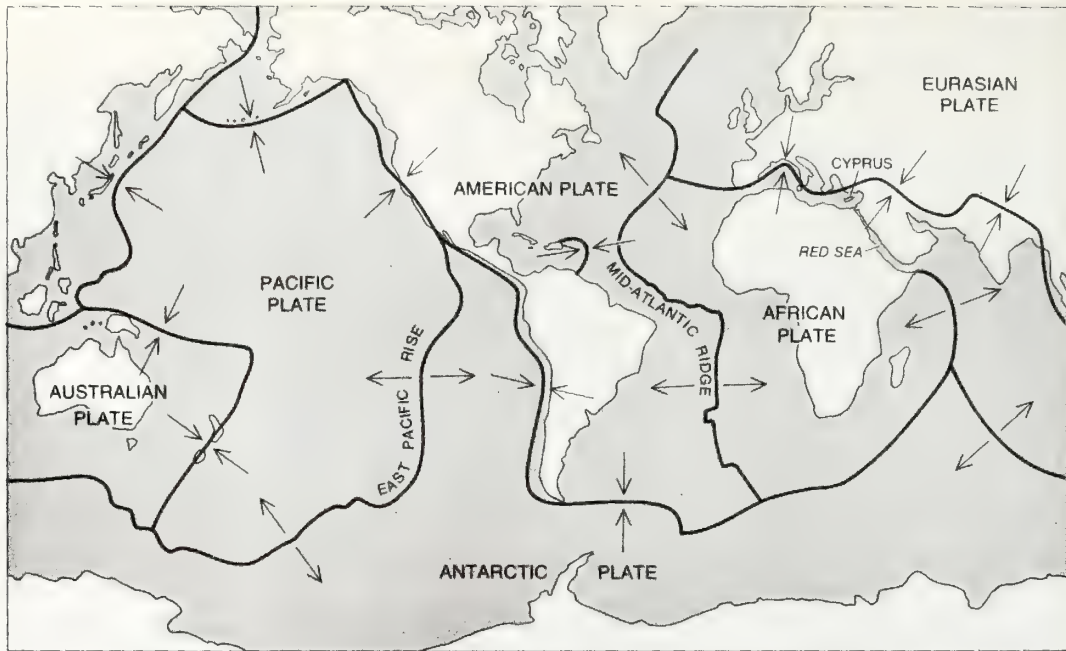
together and collide or where one plate plunges downward under the other plate and is absorbed into the interior of the earth.

The second type of boundary, called a divergent plate boundary, is where two adjacent plates move apart because new lithosphere is added to each plate by the process of sea-floor spreading. The new lithosphere, which moves more or less symmetrically to each side of the divergent plate boundary, acts like a conveyor belt, carrying the continents apart in the motion that has become known as continental drift. The dual existence of convergent boundaries where lithosphere is destroyed and divergent boundaries where lithosphere is created implies that the diameter of the earth is not changing radically.

The third type of tectonic-plate boundary is the parallel plate boundary, where two adjacent plates move edge to edge along their common interface.

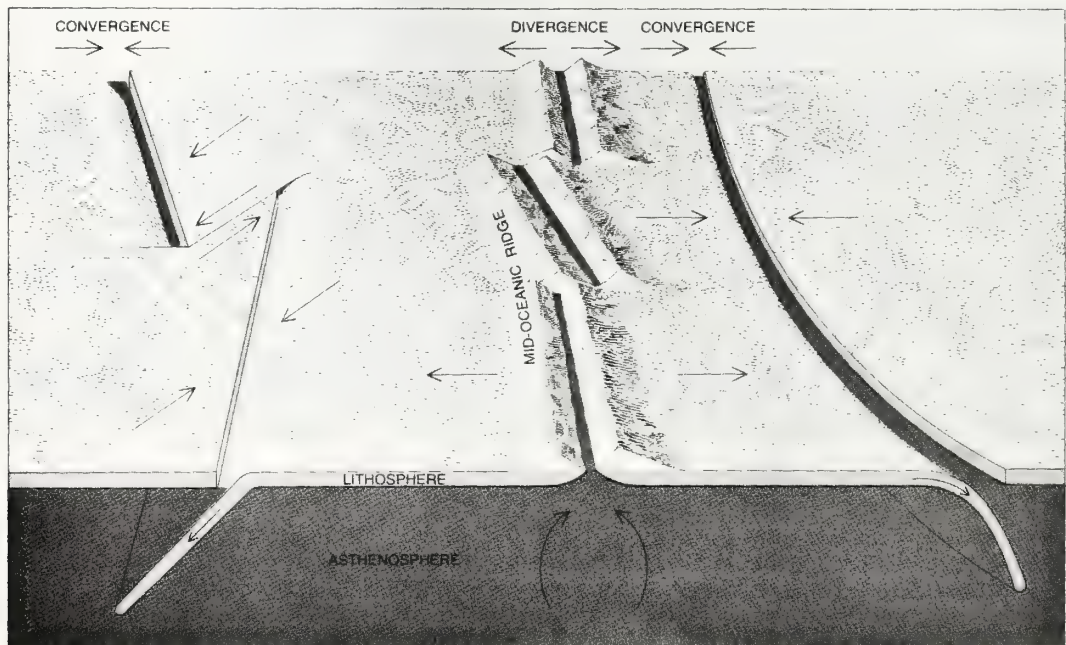
Hydrothermal mineral deposits, that is, mineral deposits formed by precipitation from solutions, constitute a major part of our useful metallic ores on the continents. Economically the most important types of hydrothermal deposit are the sulfides, in which various metals combine with sulfur to precipitate from the hydrothermal solution. About a year ago Frederick Sawkins, a geologist at the University of Minnesota, pointed out that most of the sulfide deposits of the world are located along present or former convergent plate boundaries where an oceanic lithospheric plate plunges under the margin of a continent (including the continental shelf) or under a chain of volcanic islands. The processes that concentrate the sulfide deposits along convergent plate boundaries, which are at present only partly understood, involve mineralizing solutions that emanate from the plunging lithospheric plate, which melts as it is absorbed into the interior of the earth.

Metallic sulfide deposits along convergent plate boundaries include the Kuroko deposits of Japan, the sulfide ore bodies of the Philippines and the deposits extending along the mountain belts of western North America and South America (the Coast Ranges, the Rockies and the Andes) and from the eastern Mediterranean region to Pakistan. Gold-bearing deposits are not sulfides but often accompany sulfide minerals. The majority of gold deposits in Alaska, Canada, the southeastern U.S., California, Venezuela, Brazil, West Africa, Rhodesia, southern India and



SIX PRINCIPAL TECTONIC PLATES of the lithosphere, the rigid outer shell of the earth, are delineated by the heavy color

lines on this world map. The paired arrows indicate whether a plate boundary is convergent or divergent (see illustration below).



TWO TYPES OF PLATE BOUNDARY are illustrated schematically in this block diagram. The 60-mile-thick lithospheric plates move outward like conveyor belts from the mid-oceanic ridges (diver-

gent plate boundaries) and plunge downward under the deep-sea trenches (convergent plate boundaries). The third major type of plate boundary, not shown here, is the parallel plate boundary.

southeastern and western Australia occur in rocks that can be associated with former convergent plate boundaries.

Divergent plate boundaries are formed by the spreading of lithospheric plates in the central portions of ocean basins. The Red Sea and the island of Cyprus in the Mediterranean Sea provide important clues to the potential of metallic sulfide deposits at divergent plate boundaries.

The Red Sea, the product of a divergent plate boundary developing between the African plate and the Eurasian plate, provides an accessible natural laboratory for the study of mineral processes associated with divergent plate boundaries. About five years ago the richest submarine metallic sulfide deposits known were found in three rather small basins along the center of the Red Sea at a depth of about 6,600 feet below sea level. The sulfide minerals are disseminated in sediments that fill the basins to a thickness estimated at between 65 and 330 feet. The top 30 feet or so of sediment, which has been explored by coring the largest of the basins, has a total dry weight of about 80 million tons, with average metal contents of 29 percent iron, 3.4 percent zinc, 1.3 per-

cent copper, .1 percent lead, .005 percent silver and .00005 percent gold. The deposits are saturated with (and overlain by) salty brines carrying the same metals in solution as those present in the sulfide deposits. The salty brines are considered to be the hydrothermal solutions from which the sulfide minerals are precipitated. It remains controversial whether the brines are being charged with minerals from volcanic sources under the Red Sea or from sediments with high copper, vanadium and zinc contents adjacent to the basins where the metallic sulfide deposits are found [see "The Red Sea Hot Brines," by Egon T. Degens and David A. Ross; SCIENTIFIC AMERICAN, April, 1970].

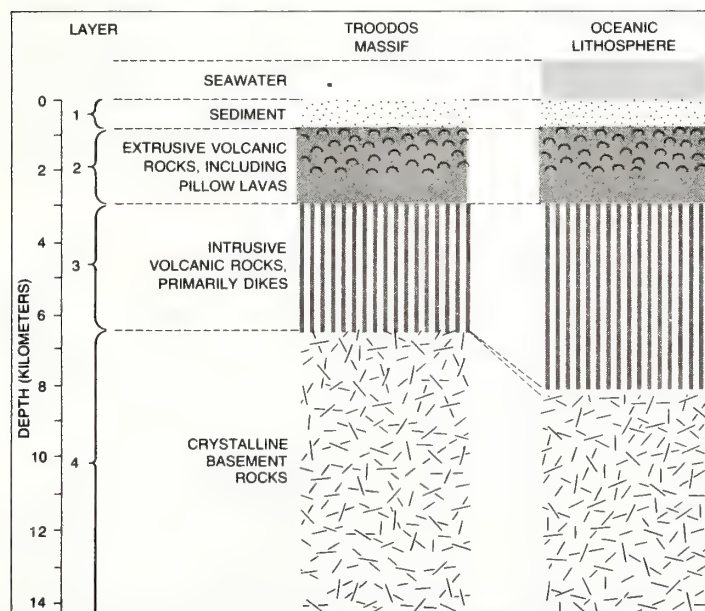
The Red Sea represents the earliest stage in the growth of an ocean basin: the stage where a divergent plate boundary rifts a continent in two. The most advanced growth stage of a divergent plate boundary is the mid-oceanic-ridge system, a 47,000-mile undersea mountain chain that extends through all the major ocean basins and girdles the globe. The mid-oceanic-ridge system has not been adequately sampled to determine whether or not concentrations of

metallic sulfides comparable to the Red Sea deposits are present at sites along its crest or in basins in its flanks. Measurements of the distribution of heat emanating from mid-oceanic ridges and of the chemical alteration of ridge rocks indicate that seawater forms a hydrothermal solution by penetrating fissures, dissolving minerals from rocks underlying the ridges and precipitating those minerals in concentrated deposits.

A limited amount of sampling indicates that hydrothermal processes are actively concentrating metals from volcanic sources underlying mid-oceanic ridges. Sediments on active mid-oceanic ridges are generally enriched in iron, manganese, copper, nickel, lead, chromium, cobalt, uranium and mercury, with trace amounts of vanadium, cadmium and bismuth. The concentrations typical of sediments covering widespread areas on mid-oceanic ridges are not economic, but much higher concentrations exist locally.

Metallic sulfides are found in rocks dredged from the Indian Ocean Ridge. In addition small veins of pure copper have been recovered by the Deep Sea Drilling Project at several sites. At the crest of the Ninety East Ridge near the Equator in the Indian Ocean, for example, veins of copper are found in volcanic rocks overlain by 1,440 feet of sediment at a water depth of 7,380 feet. Some 350 miles southeast of New York City a small vein of pure copper and clusters of copper crystals have been discovered in sediment about 65 feet above the volcanic basement rocks under the lower continental rise at a water depth of 17,000 feet [see top illustration on page 4].

A specimen of manganese 1.7 inches thick recently dredged from a water depth of about 12,000 feet in the median valley of the Mid-Atlantic Ridge by the Trans-Atlantic Geotraverse of the National Oceanic and Atmospheric Administration has particular significance. The composition, form and thickness of this manganese sample, which accumulated at a rate about 100 times faster than the manganese in nodules, indicates a hydrothermal origin and demonstrates that hydrothermal mineral deposits are actively accumulating at certain divergent plate boundaries in ocean basins. Because the sea floor is supposed to originate by spreading from mid-oceanic ridges, a mineral deposit on a mid-oceanic ridge would be expected to extend in a linear zone from the ridge across the ocean basin to the adjacent continental margin if the depositional process is a



CLOSE CORRESPONDENCE between the layered sequence of rocks in the Troodos Massif (left) and that of the oceanic lithosphere (right) is evident from this comparison. The geological structure of the Troodos Massif was determined directly from rock outcrops; the structure of the oceanic lithosphere was determined indirectly by seismic-refraction techniques. The sulfide ore bodies of the Troodos Massif are in the upper portion of layer made up of extrusive volcanic rocks. Pillow shapes form when volcanic lava cools on the sea floor.

continuous one [see illustration on next page].

At this point in man's exploration of the oceans it would seem to be too much to expect that it would be possible to make detailed observations on an eco-

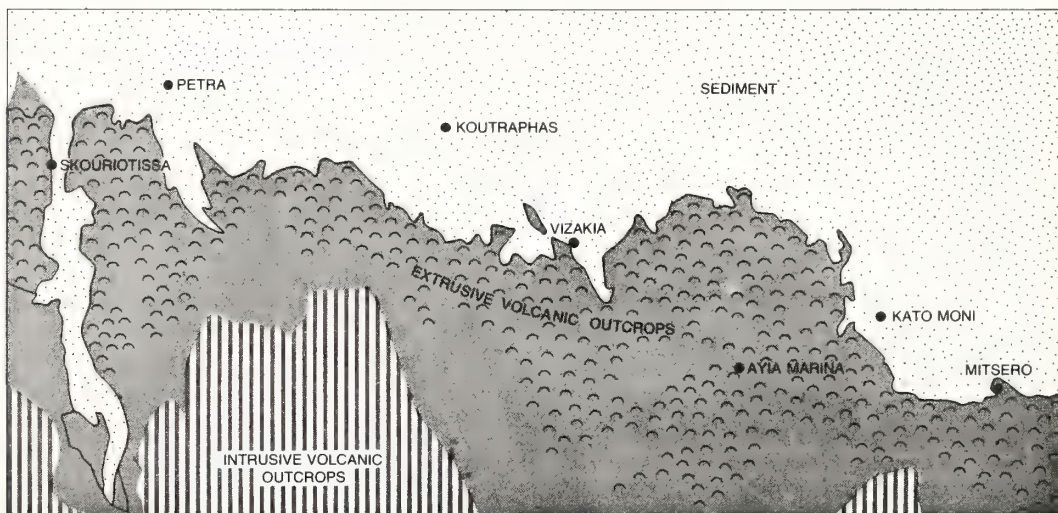
nomically important metallic sulfide deposit that originated at a divergent plate boundary on a submerged mid-oceanic ridge. Yet such a deposit is known and has been extensively studied. The Troodos Massif on the island of Cyprus is interpreted as being a slice of oceanic

lithosphere that was formed by the process of sea-floor spreading from a mid-oceanic ridge and was subsequently thrust upward to its present position [see illustration on page 3]. The composition and layered sequence of rocks that constitute the Troodos Massif are the



ISLAND OF CYPRUS has been famous for its mineral wealth since Phoenician times. The principal ore bodies are in the uppermost volcanic layers of the Troodos Massif, the total extent of which

is indicated by the dark-colored area. The hatched area represents sediments, including alluvium. A geological map of a portion of the Troodos igneous complex (small rectangle) is shown below.



GEOLOGICAL MAP of a region that lies along the northern fringe of the Troodos Massif is based on studies that were undertaken by

the Geological Survey of Cyprus. The map shows outcrops of extrusive volcanic rock that incorporate bodies of metallic sulfide ore.

same as those known to underlie the seabed.

Cyprus has long been famous for its mineral wealth. The mining of copper (for which the island is named) was an important industry in Roman and even in Phoenician times. The brilliant green stains of copper sulfides on ancient mine tailings have attracted modern prospectors. Between 1965 and 1970 the average annual exports amounted to about a million tons each of iron pyrites, chromite and gypsum, about 150,000 tons of

copper pyrites and 100,000 tons of copper concentrates. The estimated value of the mineral products exported from Cyprus in 1970 amounted to \$30 million.

The principal ore bodies are in the uppermost volcanic layers of the Troodos Massif. It has been uncertain whether the Troodos sulfide-ore bodies originated before the upthrust of the Troodos Massif or afterward. In the first instance the ore bodies would be representative of the seabed. In the second the ore bodies would be attributed to special condi-

tions unrelated to the seabed. The sulfide deposits are clearly related to the volcanic rocks in which they occur. Recent studies reveal that iron-rich and manganese-rich sediments interlayered with the volcanic rocks and associated with the ore bodies of the Troodos Massif are chemically identical with those metal-enriched sediments found on active mid-oceanic ridges, indicating that both the sediments and the ore bodies were formed on the sea floor by hydrothermal processes.

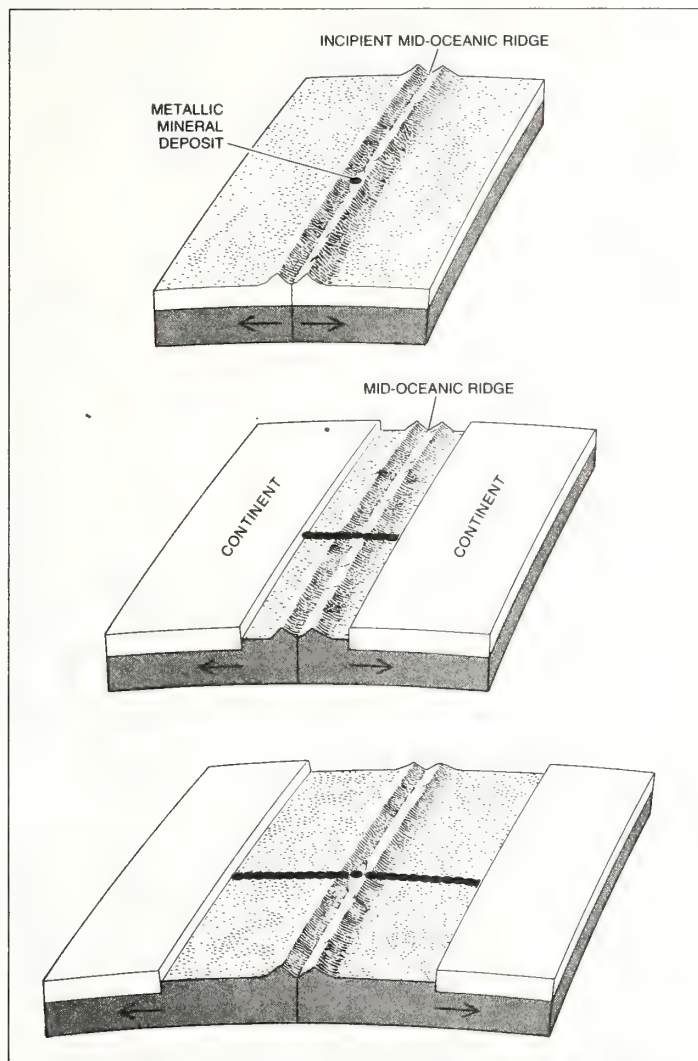
The Troodos ore bodies may provide the first firm evidence on the nature of metallic sulfide deposits in ocean basins. The Skouriotissa ore body, for example, is roughly elliptical in plan view, measures approximately 2,000 feet long by 600 feet wide and is lens-shaped in cross section. Its estimated mass is six million tons. The average composition of the ore is 2.25 percent copper (ranging to greater than 5 percent), 48 percent sulfur and 43 percent iron.

The Mavrovouni ore body is also roughly elliptical in plan view, measures approximately 1,000 feet long by 600 feet wide and forms a lens that attains a thickness of 800 feet in cross section. Its estimated mass is greater than 15 million tons. The average composition of the ore is 4.2 percent copper, 48 percent sulfur, 43 percent iron, .4 percent zinc, .25 ounce per ton gold and .25 ounce per ton silver.

Sediments underlying the Skouriotissa ore body, presumably a disintegration product of the pyrite in the ore body, contain 2.12 ounces of gold per ton and 12.96 ounces of silver per ton. Exposed patches of metallic oxides indicate the presence of the ore bodies under the mountainous surface of the Troodos Massif. The Skouriotissa ore body is exploited by underground shafts and the Mavrovouni ore body by strip-mining.

What kind of target for exploration would a Troodos ore body make if it were submerged under thousands of feet of water on the crest or flank of a mid-oceanic ridge? It is unlikely that any of the present exploration methods would be capable of detecting the ore body. The resolution of present geophysical exploration methods will have to be improved in order to detect such an ore body under the sea. Both the exploration methods and the engineering development involved will be costly.

The prerequisites for the accumulation of petroleum consist of a source of organic matter to generate the petroleum, a natural reservoir to contain it



HYDROTHERMAL MINERAL DEPOSIT (color) formed in a hot-brine pool on the axis of a mid-oceanic ridge would be expected to extend in a linear zone from the ridge across the ocean basin to the adjacent continental margins as the ocean basin progressively widens (from top to bottom) as a consequence of sea-floor spreading from the mid-oceanic ridge.

and a trap to concentrate its fluid and gas constituents. Petroleum is hydrocarbons derived from the remains of plants and animals. As the progenitor of the petroleum, the organic matter must accumulate in an environment where it is preserved. The preservation of organic matter is favored by an environment that is toxic to life (so that the organic matter is not consumed as food) and deficient in oxygen (so that the hydrocarbon is not decomposed). How do conditions favorable to the accumulation of petroleum relate to convergent and divergent plate boundaries?

Convergent plate boundaries where the oceanic portion of a lithospheric plate plunges under the margin of a continent are characterized by the presence of a deep-sea trench running along their length. A system of deep-sea trenches runs along the entire western margin of North America and South America where the Pacific lithosphere is plunging under the continents. In addition to a deep-sea trench, chains of volcanic islands are present along some convergent plate boundaries; they are located between the trench and the continent. There are many such chains of volcanic islands at the western margin of the Pacific, including the Aleutians, the Kuriles, Japan, the Ryukyus, the Philippines and Indonesia. Other such chains are the Marianas, the South Sandwich Islands and the West Indies. The island chains divide an ocean basin into smaller basins partially enclosed between the islands and the adjacent continent; such basins include the Bering Sea, the Sea of Okhotsk, the Sea of Japan, the Yellow Sea, the East China Sea and the South China Sea.

Both the marginal trenches and the volcanic-island chains create a habitat that is favorable for the accumulation of petroleum in several respects. First, the trenches and island chains act as barriers that catch sediment and organic matter from the continent and the ocean basin. Second, the shape of the trenches and the small ocean basins acts to restrict the circulation of the ocean, so that oxygen is not replenished in the seawater and organic matter is preserved. Third, the accumulation of sediments and the geological structures that develop as a result of the deformation of the sediments by tectonic forces provide reservoirs and traps for the accumulation of petroleum. According to Hollis D. Hedberg of Princeton University, "these marginal semienclosed basins constitute some of the most promising areas in the world for petroleum accumulation."



AT AN EARLY STAGE of continental drift the Atlantic was a sea with its circulation restricted by the surrounding continents. As in the present Red Sea, conditions in the Atlantic Sea favored the preservation of organic matter and the deposition of rock salt, leading to the formation of petroleum accumulations under the present continental margins.

The development of divergent plate boundaries may also create a habitat favorable for the accumulation of oil, a finding that would open immense possibilities for petroleum resources in the deep ocean basin. When a divergent plate boundary develops under a continent, the continent is rifted in two and the continental fragments are carried apart on a conveyor belt of new lithosphere generated at the divergent plate boundary. As the two continental fragments move apart, a sea forms between them. The surrounding continents act

as barriers to restrict the circulation of the sea. As a result organic matter is preserved and, if the evaporation of the seawater exceeds its replenishment, layers of rock salt are deposited along with the organic matter. As the continental fragments continue to move apart and to subside along with the adjacent sea floor, the restricted sea becomes an open ocean. The layers of organic matter and salt are buried under sediments. The organic matter subsequently develops into petroleum (the processes that are only partly understood) and the salt

forms into dome-shaped masses that act to trap the petroleum.

The Red Sea is an example of a restricted sea formed at an early stage of development of the divergent plate boundary along which Arabia is rifting from Africa. Layers of rock salt up to 17,000 feet thick and organic muds have been found under it. Along both the eastern and western margins of the North Atlantic and the South Atlantic apparent salt domes have been discovered extending seaward from continental shelves to continental rises in water depths of up to 16,500 feet. The occurrence of these salt domes in the deep Atlantic indicates that at an early stage of continental drift the Atlantic was a sea with its circulation restricted by the surrounding continents in their positions at that time [see illustration on preceding page].

Like the present Red Sea, conditions in the Atlantic Sea favored the preservation of organic matter and the deposition of rock salt. As the Atlantic widened in response to the symmetric creation of new lithosphere by sea-floor spreading from the Mid-Atlantic Ridge, the Atlantic Sea became an ocean and the organic matter and salt were buried under sediments, forming the present margins of the Atlantic Ocean. It is reasonable to expect that petroleum accumulations will extend seaward under the conti-

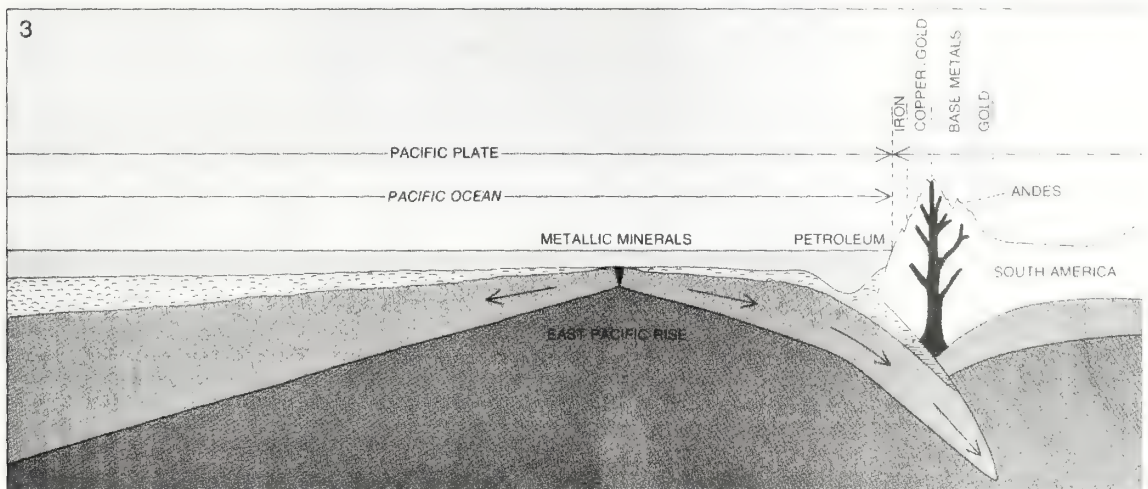
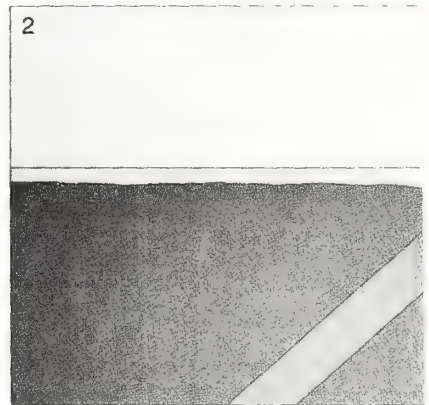
ental shelf, the continental slope and the continental rise to water depths of about 18,000 feet along large portions of both the eastern and western margins of the North Atlantic and South Atlantic. Petroleum may likewise be found in other ocean basins that have grown through the stage of a restricted sea by sea-floor spreading.

In short, the patterns of mineral distribution that are emerging from the conceptual framework provided by the new global tectonics will clearly help to guide man's search for new mineral deposits. Hydrothermal processes have concentrated the majority of known metallic sulfide ore bodies along convergent lithospheric plate boundaries originally at continental margins. Hydrothermal processes are also active at divergent plate boundaries from initial stages (represented by the metallic sulfide deposits accumulating in the Red Sea) to advanced stages (represented by the metal concentration in sediments on mid-oceanic ridges and by possible metallic sulfide deposits of the Troodos Massif type). The Troodos Massif metallic sulfide ore bodies provide an actual example of the type of deposits that can be expected in sea-floor rock generated by mid-oceanic ridges. The confirmation and economic evaluation of metallic sulfide deposits of the Troodos Massif

type in ocean basins await technological advances in marine exploration methods.

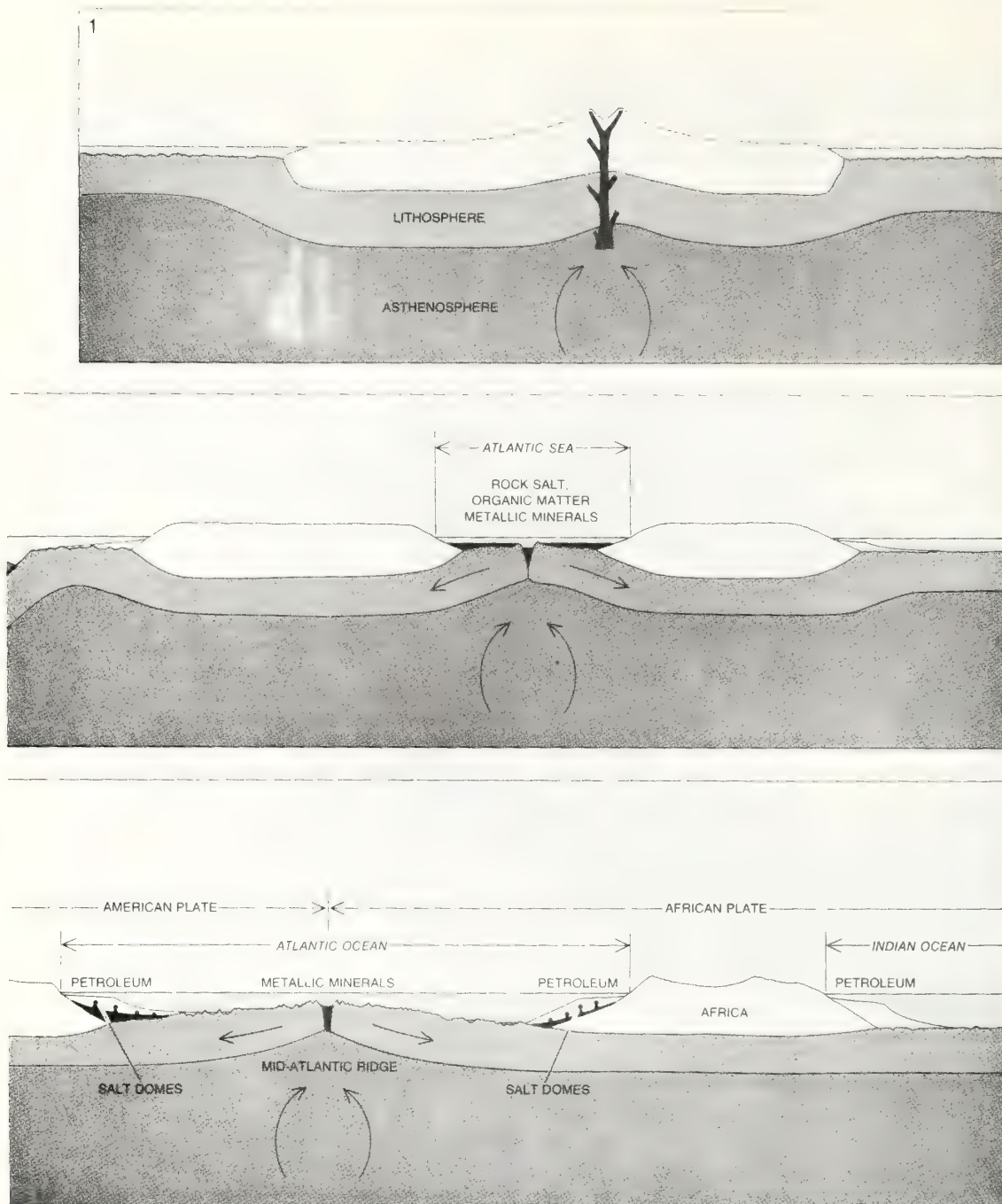
With regard to petroleum, convergent plate boundaries create conditions that form accumulations in small ocean basins and deep-sea trenches marginal to continents. Divergent plate boundaries, on the other hand, create conditions that favor the development of oil accumulations extending from the continental shelf into the deep ocean basin under the continental rise.

The global patterns of mineral distribution that are emerging from such models can be expected to accelerate the discovery of resources not only on the seabed but also on the continents.



ROLE OF PLATE BOUNDARIES in the accumulation of mineral deposits is exemplified in this sequence of cross-sectional views of the development of the South Atlantic Ocean. The position of Africa is assumed to be stationary throughout the sequence of cross sections. In stage 1 a single ancestral continent, called Pangaea, is rifted into two continents (South America and Africa) about a divergent plate boundary. In stage 2 the oceanic crust created by the

process of sea-floor spreading from the divergent plate boundary (a precursor of the Mid-Atlantic Ridge) rafts South America westward and is compensated for by the consumption of oceanic crust at a trench (a convergent plate boundary) that develops to the west of South America. Thick layers of rock salt, organic matter and metallic minerals accumulate in the Atlantic Sea during this early stage of continental drift. In stage 3 continued sea-floor spreading



from the Mid-Atlantic Ridge widens the Atlantic into an ocean, rafts South America westward over the trench, reversing the inclination of the trench and producing the Andes mountain chain as a consequence of the deformation that develops at the convergent plate boundary along the western margin of South America. Metallic minerals that are melted from the Pacific plate as it plunges under South America ascend through the overlying crustal layers and

are deposited in them to form the metal-bearing provinces of the Andes. Meanwhile in the Atlantic Ocean metallic minerals continue to accumulate about the Mid-Atlantic Ridge. Salt originating in the thick layers of rock salt that have been buried under the sediments of the continental margins rises in large, dome-shaped masses that act to trap the oil and gas that are generated from the organic matter that was preserved in the former Atlantic Sea.

Relations between Rates of Sediment Accumulation on Continental Shelves, Sea-Floor Spreading, and Eustacy Inferred from the Central North Atlantic

ABSTRACT

Rates of sediment accumulation were derived from Upper Jurassic to Holocene stratigraphic columns encountered in seven deep wells penetrating the coastal plains and continental shelves of southeastern North America and northwestern Africa. Three intervals with relatively fast average rates (maxima) and two intervening intervals with relatively slow average rates (minima) were determined on both continental margins as follows: maximum 1, Cretaceous (136-65 m.y. B.P.); minimum 1, Paleocene (65-53.5 m.y. B.P.); maximum 2, early through middle Eocene (53.5-45 m.y. B.P.); minimum 2, late Eocene through Oligocene (45-22.5 m.y. B.P.); maximum 3, Miocene (22.5-5.5 m.y. B.P.). Each maximum lasted 10 to 70 m.y. and correlated with a worldwide epicontinental marine transgression or with the reversal between a transgression and a regression. Each minimum lasted 10 to 20 m.y. and correlated with a worldwide marine regression or with the reversal between a regression and a transgression. To a first approximation, the sedimentary maxima and minima are directly proportional to rates of sea-floor spreading in the intervening ocean basin.

The successive maxima and minima in average rates of sediment accumulation on continental shelves are controlled by eustatic sea-level changes. Major eustatic changes in sea level, other than glacio-eustatic, result from changes in the cubic capacity of ocean basins primarily caused by changes in the volume of the worldwide mid-oceanic ridge system and by orogenic compression of continental crust. These two factors are related in a cycle manifested in the stratigraphic record of epicontinental

marine transgression and regression:

- (1) Volume increase of the worldwide mid-oceanic ridge system associated with relatively fast sea-floor spreading and *net* orogenic quiescence of continents results in transgression.
- (2) Volume decrease of the worldwide mid-oceanic ridge system associated with relatively slow sea-floor spreading and *net* orogenic activity of continents results in regression.

INTRODUCTION

Vertical movements involving uplift and subsidence of lithospheric plates (epeirogeny) and worldwide changes in sea level (eustacy) are established phenomena. The extent of horizontal movements of lithospheric plates has more recently been recognized. I attempt to deduce relations between these vertical and horizontal movements from the stratigraphic record of the continental margin and from the growth record of the ocean basin.

The study area encompasses the continental margin of southeastern North America (centered at Cape Hatteras) and of northwestern Africa (centered at Cap Blanc, Mauritania) and the intervening central North Atlantic Ocean Basin (Figs. 1, 2). This area is a controlled natural unit. Cape Hatteras and Cap Blanc occupy nearly conjugate points in precontinental drift reconstructions of North America and Africa (Bullard and others, 1965, Fig. 8; Dietz and Spröll, 1970, Fig. 1), and their locations within the relatively stable interiors of the North American and African plates are isolated from interference effects associated with unstable plate boundaries. After continental rifting, the intervening ocean basin is inferred to have grown horizontally by sea-floor spreading. The stratigraphy of the continental margins, as revealed in deep wells,

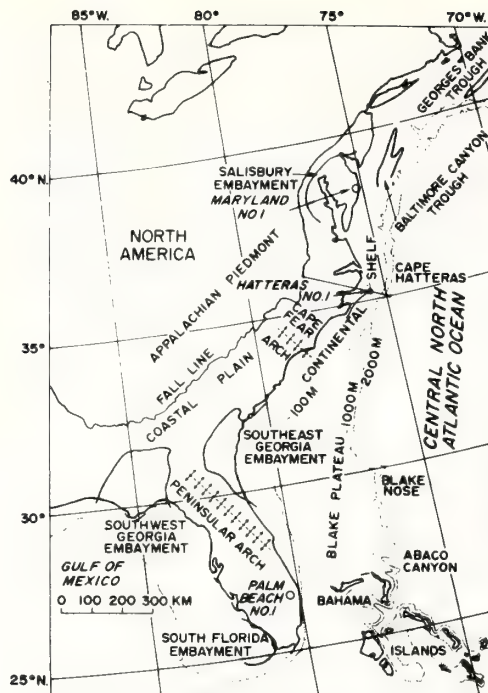


Figure 1. Map of eastern North America with locations of three wells used to obtain stratigraphic information. Structurally positive and negative regions (arches and basins) are delineated (after Maher, 1965, Fig. 1).

records Mesozoic through Cenozoic epeirogenic and eustatic movements. Remanent magnetic anomalies, fracture zones, and deep-sea stratigraphy record the history of horizontal movements involving the oceanic crust. The evidence reveals that sediment-accumulation rates, averaged over intervals of the duration of geologic periods, varied synchronously on the two continental shelves. The intervals of maximum and minimum rates correlate with events in the intervening ocean basin (Rona, 1972).

STRATIGRAPHY OF CENTRAL NORTH ATLANTIC CONTINENTAL MARGINS

Measurements

Mesozoic and Cenozoic sequences of strata on the continental margins of southeastern North America and northwestern Africa progressively thicken seaward from zero thickness at the landward margin of the coastal plain to greater than 5 km at the seaward edge

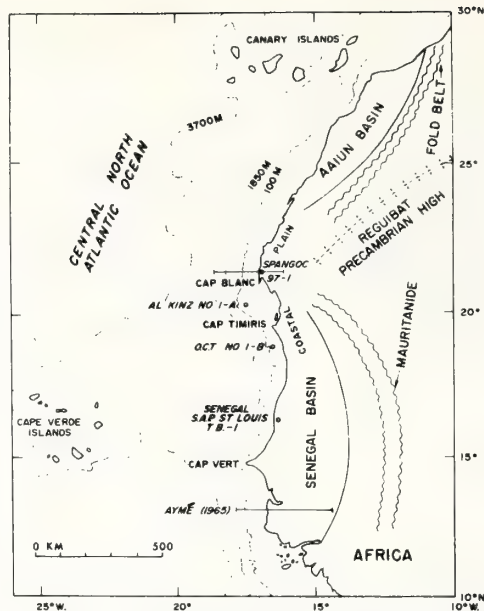


Figure 2. Map of northwestern Africa with locations of four wells and one cross section (Aymé, 1965) used to obtain stratigraphic information. Structurally positive and negative regions (highs and basins) are delineated.

of the continental shelf. The inclination of successively older units increases also (Fig. 3). From these sequences, the following three parameters, indicative of vertical movements of land and sea, were measured:

1. The average vertical rate of sediment accumulation (cm per 10^3 yr) is derived from the thickness of sediment accumulated in a vertical column within a given time interval. The effect of compaction is not considered. The rates of sediment accumulation so derived increase seaward in the direction of thickening of the stratigraphic column (Fig. 3). For this reason, comparison of graphs showing thicknesses of strata, encountered in a vertical column and plotted against age, is deceptive. However, the ratios of rates of sediment accumulation within corresponding stratigraphic intervals remain constant downdip if the seaward-thickening units are time-stratigraphic, that is, are bounded by isochrons.

2. The vertical angle subtended by the column of sediment that accumulated within a given time interval is measured. To normalize these values, the two sides of the angle are projected to a common apex at the point of zero sediment thickness which generally cor-

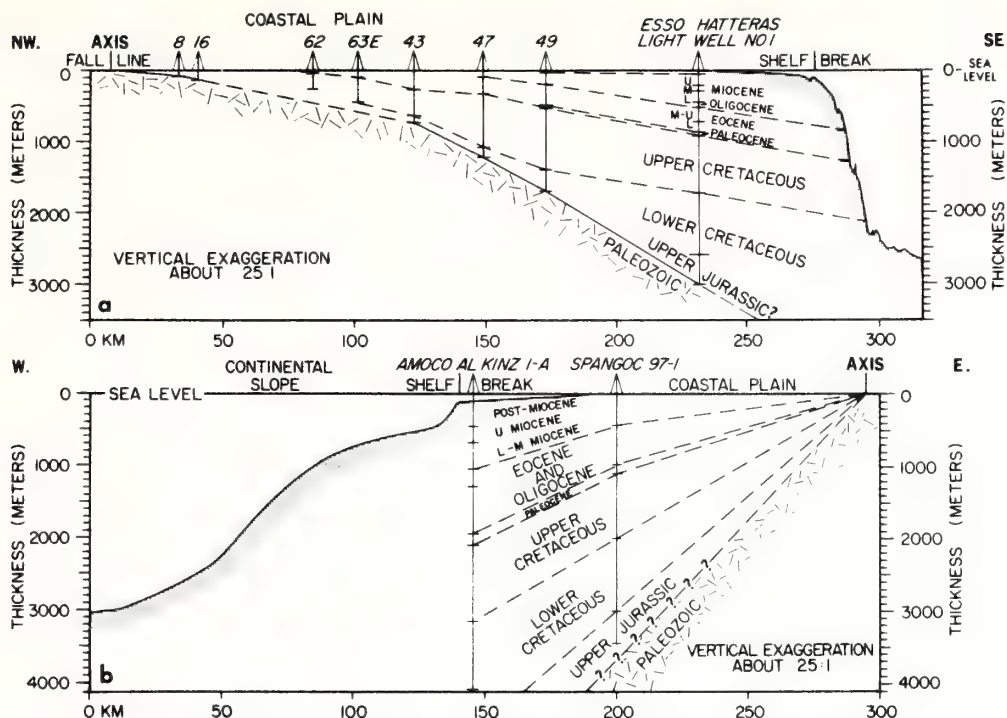


Figure 3. (a) Stratigraphic section across the coastal plain, continental shelf, and continental slope at Cape Hatteras, U.S.A. (see Fig. 1; after Maher, 1965, Pl. 5). The apparent inclination of Paleozoic basement underlying the coastal plain and continental shelf increases from about $0^{\circ}27'$ between the Fall Line and a prominent

break in slope 130 km seaward of the Fall Line, to about $1^{\circ}38'$ seaward of the break in slope. (b) Stratigraphic section across the coastal plain, continental shelf, and continental slope at Cap Blanc, Mauritania (see Fig. 2). The Al Kinz well has been projected about 100 km north to the section that intersects the Spangoc well.

responds to the landward margin of the coastal plain in the sections measured (Fig. 3).

3. The average angular rate of sediment accumulation ($\times 10^{-7}$ deg per yr) is derived from the angle subtended by the vertical column of sediment accumulated within a given time interval. Unlike the vertical rate of sediment accumulation, the angular rate is independent of the absolute thickness of sediment accumulated. Figures 4 through 11 are plots of these three parameters versus time for eight locations around the central North Atlantic. The time scale of Berggren (1969) is used for the Cenozoic and that of the Geological Society of London (1964) for the Mesozoic and Paleozoic.

Southeastern North America

The stratigraphy of the southeastern continental margin of North America along the 1,400-km span between Maryland and Florida has been well documented in published sections

(Swain, 1952a, 1952b; Maher, 1965, Pls. 2, 3, 5; Maher and Applin, 1971). The Esso Hatteras Light well No. 1 at Cape Hatteras, the Esso No. 1 Maryland well (350 km north of Cape Hatteras), and the Humble Tucson Palm Beach well No. 1 (1,050 km south of Cape Hatteras) were chosen for analysis on the basis of their distribution along the continental margin and their locations in structurally negative regions favoring the presence of relatively complete sections (Fig. 1).

The average vertical and angular rates of sediment accumulation derived from the post-Jurassic portion of the stratigraphic column underlying Cape Hatteras (Fig. 4) exhibited three intervals of relatively fast rates (maxima), each followed by an interval of relatively slow rates (minima). The maximum and minimum sediment-accumulation rates were recognized in the other wells analyzed (Figs. 5, 6) and correlated with respect to time as follows:

Maximum 1. Sediment-accumulation rates

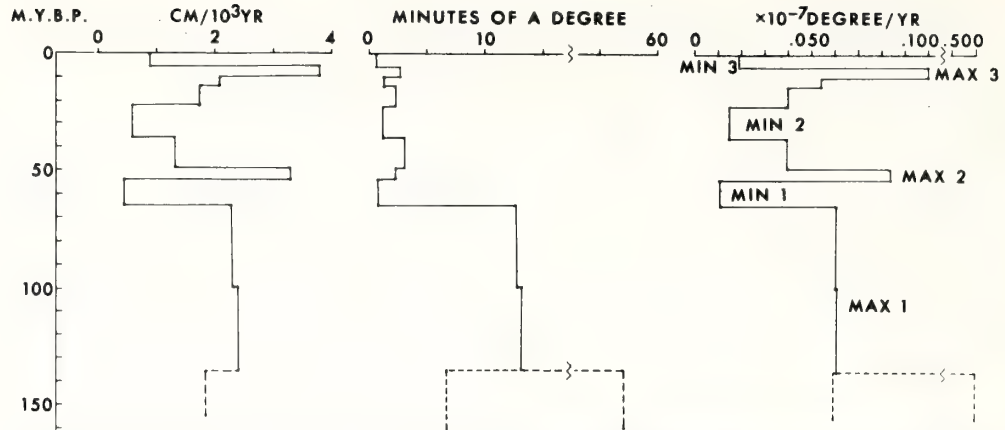


Figure 4. Sediment-accumulation rates derived from the stratigraphic column of the Hatteras well (Swain, 1952a, 1952b; Maher, 1965, Pl. 5). Sediment accumulation is presented as an average rate (cm per 10^3 yr), as the vertical angle defined by the projection of two time-stratigraphic horizons to a common apex (for example, axis in Fig. 3), and as an average angular rate ($\times 10^{-7}$ deg per yr). Points on the curve indicate age determinations. Intervals of relatively fast (maximum)

and slow (minimum) sediment-accumulation rates are labeled.

Two average angular sediment-accumulation rates are given for the Upper Jurassic(?) sequence; the slower rate was calculated about the Fall Line; and the faster rate was calculated about the prominent break in Paleozoic basement slope 130 km seaward of the Fall Line (Fig. 3a), which is the landward limit of Upper Jurassic (?) strata.

during the Cretaceous Period (136–65 m.y. B.P.) were relatively fast at all the well sites considered (range, 1.9–4.0 cm per 10^3 yr; 0.029 – 0.069×10^{-7} deg per yr). Early Cretaceous (136–100 m.y. B.P.) rates were generally 5–25 percent greater than Late Cretaceous (100–65 m.y. B.P.) rates. The initiation of sediment accumulation on the original surface of the continental shelf is indicated by Upper Jurassic (?) strata overlying an erosional surface developed on Paleozoic rocks encountered in the Hatteras, Maryland, and Palm Beach wells. The Upper Jurassic (?) strata are probably at least as old as Oxfordian (155 m.y. B.P.), because Oxfordian is the age of the oldest sediments that overlie basaltic acoustic basement with a baked contact recovered in the adjacent ocean basin (Hollister and others, 1972, Site 105, located at lat $34^{\circ}54'$ N., long $69^{\circ}10'$ W.). Assuming 155 m.y. as the age of the oldest sediment overlying Paleozoic basement, the average rate of sediment accumulation was slower during the Late Jurassic than during the Cretaceous. The rate during this interval shows a marked increase in the Hatteras well (Fig. 4), however, if the angular rate of sediment accumulation is calculated about the landward limit of Upper Jurassic strata at the prominent break in basement slope 130 km seaward of the

Fall Line in the Hatteras section (Fig. 3a).

Minimum 1. Sediment-accumulation rates abruptly decreased (range, 0.4–2.6 cm per 10^3 yr; 0.011 – 0.013×10^{-7} deg per yr) in the Paleocene Epoch (65–53.5 m.y. B.P.) to about 15 percent of their Cretaceous values. The Paleocene minimum represents the slowest rates recorded during the Mesozoic and Cenozoic.

Maximum 2. An abrupt increase in sediment-accumulation rates (3.3 cm per 10^3 yr; 0.084×10^{-7} deg per yr) occurred in the early and middle Eocene (53.5–45 m.y. B.P.). This increase, up to 125 percent of Cretaceous values, is resolved in the Hatteras well.

Minimum 2. Sediment-accumulation rates decreased abruptly during the early Eocene (45–36 m.y. B.P.) to 5–50 percent of their Cretaceous values in Oligocene time (36–22.5 m.y. B.P.; range, 0.3–0.6 cm per 10^3 yr; 0.005 – 0.015×10^{-7} deg per yr). Minimum 2 is unresolved in the Maryland well where Oligocene and Miocene strata are undifferentiated.

Maximum 3. Sediment-accumulation rates gradually increased (range, 1.3–3.8 cm per 10^3 yr; 0.027 – 0.100×10^{-7} deg per yr) during the early and middle Miocene (22.5–10 m.y. B.P.) to 165 percent of Cretaceous values in the late

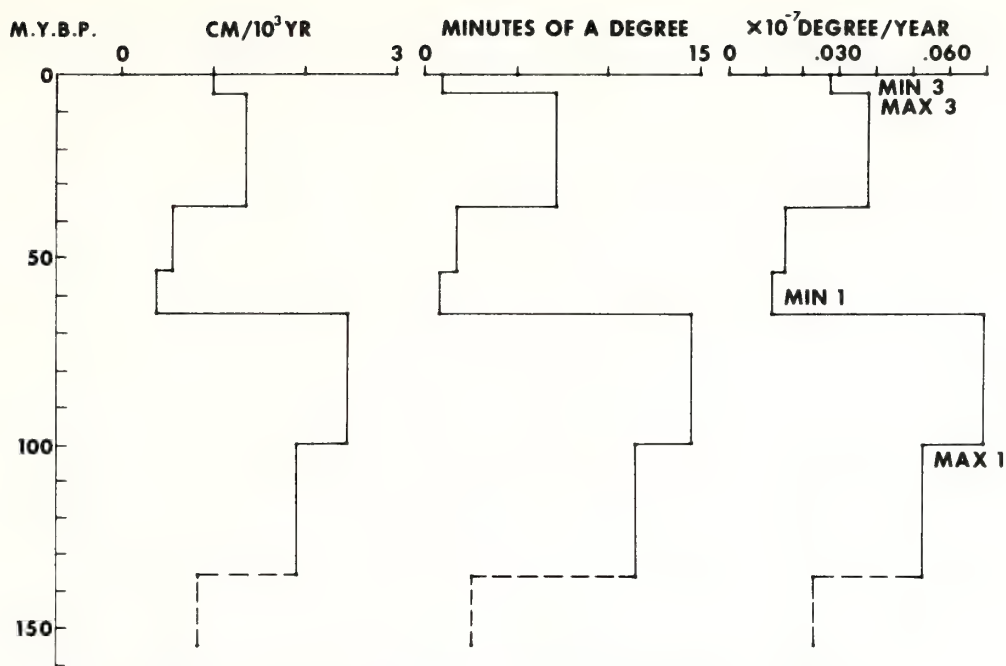


Figure 5. Sediment-accumulation rates derived from 1965, Pl. 4). Presentation as in Figure 4. the stratigraphic column of the Maryland well (Maher,

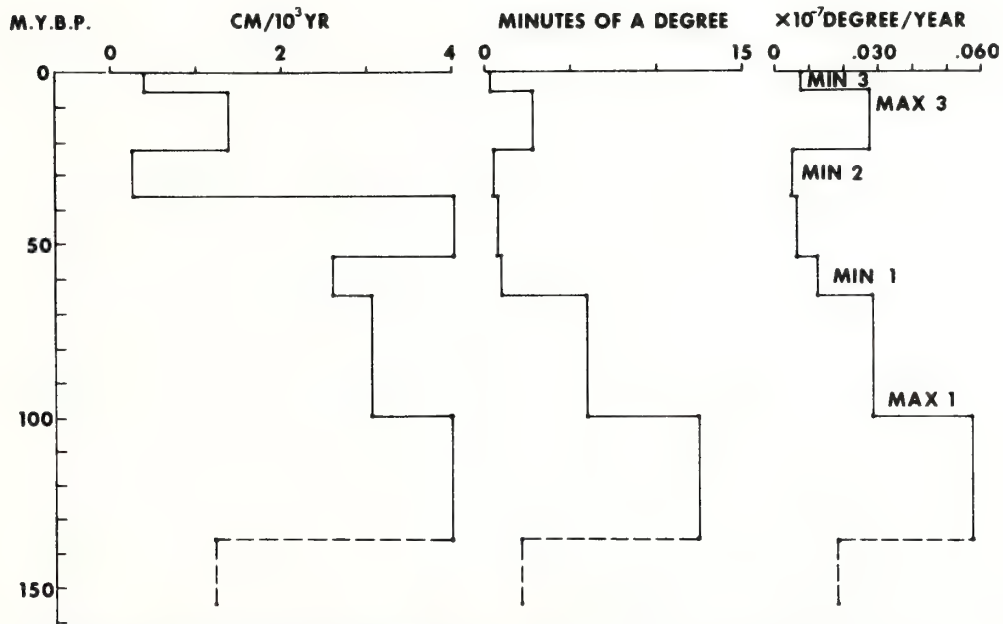


Figure 6. Sediment-accumulation rates derived from (Maher, 1965, Pl. 2). Presentation as in Figure 4. the stratigraphic column of the Palm Beach well

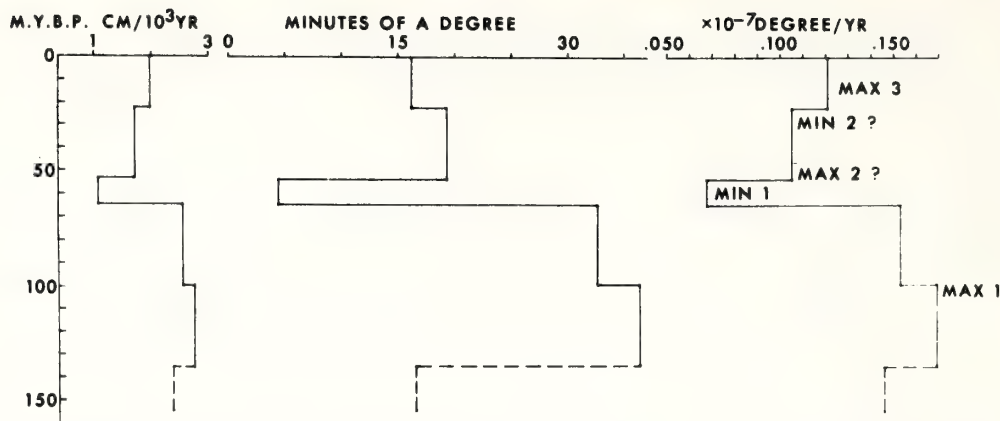


Figure 7. Sediment-accumulation rates derived from the Spangoc well. Presentation as in Figure 4. See Table 1 for stratigraphy.

Miocene (10–5.5 m.y. B.P.), as resolved in the Hatteras well. The rates abruptly increased during the same time interval in the Maryland and Palm Beach wells.

Minimum 3. Post-Miocene (5.5–0 m.y. B.P.) sediment-accumulation rates decreased (range, 0.4–1.0 cm per 10^3 yr; 0.008 – 0.028×10^{-7} deg per yr) to 10–40 percent of Cretaceous values in the three wells considered.

Northwestern Africa

Four deep wells and one section provide stratigraphic information along the 950-km span from Cap Blanc to the southern end of the Senegal basin (Fig. 2). The Spanish Gulf Oil Company (Spangoc) 97–1 well is situated at Cap Blanc; the Amoco Al Kinz No. 1–A, the Amoco Offshore Cap Timiris (O.C.T.) No. 1–B, the Senegal S.A.P. St. Louis Permit

Toundou Besset 1 (T.B.–1; Monciardini, 1966) wells, and a stratigraphic section across the southern Senegal basin (Aymé, 1965) are situated, respectively, about 100, 275, 600, and 950 km south of Cap Blanc. The four wells penetrate Cenozoic through Lower Cretaceous or Upper Jurassic strata; the stratigraphic section shows lower Mesozoic strata unconformably overlying Paleozoic rocks. Three intervals of relatively fast rates of sediment accumulation (maxima) and two intervals of relatively slow rates (minima) are generally recognized as follows (Figs. 7–11, Tables 1–4):

Maximum 1. Sediment-accumulation rates during the Cretaceous Period (136–65 m.y. B.P.) were relatively fast (range, 2.4–6.0 cm per 10^3 yr; 0.072 – 0.169×10^{-7} deg per yr). Early Cretaceous (136–100 m.y. B.P.) rates were 10–25 percent greater than Late Cre-

TABLE 1. STRATIGRAPHY OF SPANGOC WELL, LAT $21^{\circ}25'10''$ N., LONG $16^{\circ}55'34''$ W.

Given depth below sea level (m)	Given age*	Adjusted depth below sea level (m)	Adjusted age*
0	Oligocene or younger	0	Post-Oligocene
351	Upper and middle Eocene	445	Eocene and Oligocene
1,098	Upper Cretaceous and middle Eocene	978	Paleocene
1,998	Lower Upper Cretaceous	1,107	Upper Cretaceous
2,640	Upper Jurassic and Lower Cretaceous	2,000	Lower Cretaceous
3,455		3,000	Upper Jurassic
		3,455	

*The given age designations (1963) are adjusted to subsequent stratigraphic information from the Al Kinz and O.C.T. 1–B wells which place the top of the Jurassic above the first distinct sequence of marine limestone, retain the boundary between Lower and Upper Cretaceous, distinguish the Paleocene both by the predominance of shale (64 percent of interval by volume) and by the appearance of chert beds extending into the lower Eocene, and differentiate the post-Oligocene strata.

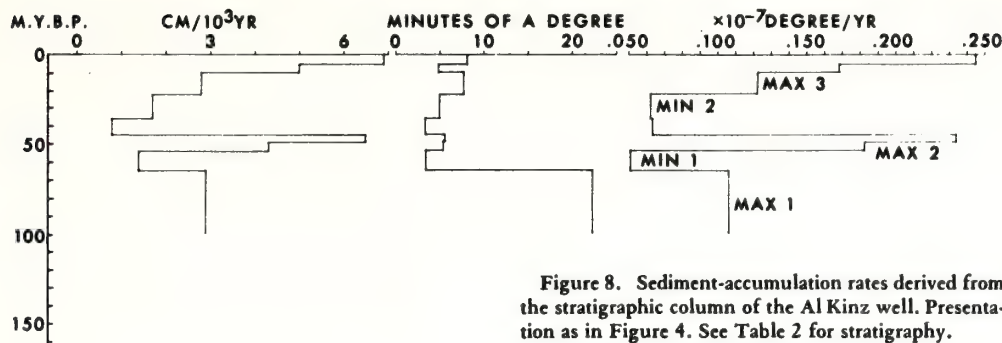


Figure 8. Sediment-accumulation rates derived from the stratigraphic column of the Al Kinz well. Presentation as in Figure 4. See Table 2 for stratigraphy.

taceous (100–65 m.y. B.P.) rates.

Minimum 1. Sediment-accumulation rates abruptly decreased (range, 0.4–2.0 cm per 10^3 yr; 0.005 – 0.068×10^{-7} deg per yr) to 5–40 percent of their Cretaceous values during the Paleocene (65–53.5 m.y. B.P.).

Maximum 2. Sediment-accumulation rates abruptly increased (range, 1.0–6.5 cm per 10^3 yr; 0.037 – 0.233×10^{-7} deg per yr) in the early and middle Eocene (53.5–45 m.y. B.P.), as resolved in the Al Kinz, O.C.T. 1-B, and Senegal T.B.-1 wells; this increase is unresolved in the Spangoc well or in the stratigraphic section across the southern Senegal basin.

Minimum 2. Sediment-accumulation rates decreased (range, 1.4–1.7 cm per 10^3 yr; 0.015 – 0.062×10^{-7} deg per yr) in the late Eocene and Oligocene (45–22.5 m.y. B.P.), as resolved in the Al Kinz, O.C.T. 1-B, and Senegal T.B.-1

wells; the rate decrease is unresolved in the Spangoc well or in the stratigraphic section across the southern Senegal basin.

Maximum 3. A post-Oligocene (22.5–0 m.y. B.P.) increase in sediment-accumulation rate (range, 0.7–2.0 cm per 10^3 yr; 0.020 – 0.168×10^{-7} deg per yr) occurred in the Spangoc, Al Kinz, and O.C.T. 1-B wells, but the increase did not occur in either the Senegal T.B.-1 well or in the southern Senegal basin stratigraphic section.

Three maxima and two intervening minima in rates of sediment accumulation are observed both on the coastal plains and continental shelves of northwest Africa and southeastern North America. Each of the three maxima and each of the two intervening minima occurred synchronously on the two continental margins. The average vertical rates of sediment accumulation are similar on both sets of coastal plains and continental shelves in the wells analyzed; the average angular rates of sediment accumulation are consistently greater on the northwest African continental margin owing to the shorter distance to the line of zero sediment thickness (Fig. 3).

TABLE 2. STRATIGRAPHY OF AL KINZ WELL, LAT $20^{\circ}17'35''$ N., LONG $17^{\circ}32'03''$ W.

Depth below sea level (m)	Age
0	(Water column)
67	Post-Miocene
447	Upper Miocene
674	Lower and middle Miocene
1,033	Oligocene
1,266	Upper Eocene
1,427	Middle Eocene
1,687	Lower Eocene
1,946	Paleocene
2,101	Upper Cretaceous
3,141	Lower Cretaceous (Neocomian)
4,113	

LITHOSPHERIC PLATE MOVEMENTS IN THE CENTRAL NORTH ATLANTIC

Rates and Directions of Sea-Floor Spreading

The history of relative horizontal movements of the North American and African lithospheric plates in the central North Atlantic is recorded as rates and directions of sea-floor spreading. The rates of sea-floor spreading are averaged over intervals between points on the ocean bottom dated (1) by the identification of remanent magnetic anomalies (Vine and Matthews, 1963) in the geomagnetic polarity time scale, which extends from 0 to about 78 m.y.

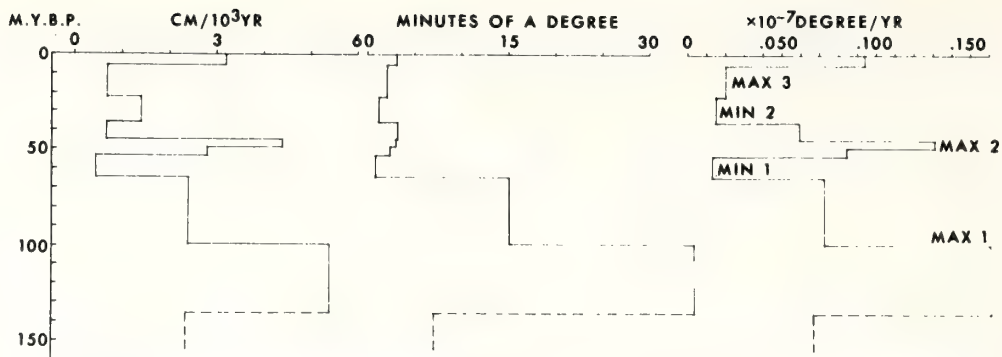


Figure 9. Sediment-accumulation rates derived from the stratigraphic column of the O.C.T. 1-B well. Presentation as in Figure 4. See Table 3 for stratigraphy.

B.P. (Heirtzler and others, 1968), and (2) by age determinations on samples of oceanic crust recovered by deep-sea drilling (Peterson and others, 1970; Hollister and others, 1972; Hayes and others, 1972). Evidence from the ages of crustal samples, remanent magnetic anomalies, discontinuities in topography, sediment thickness (Ewing and Ewing, 1967), and heat flow (Langseth and others, 1966) about the Mid-Atlantic Ridge indicates that episodic variations in the rate of sea-floor spreading have occurred through most of the history of the central North Atlantic (Schneider and Vogt, 1968). Pitman and Talwani (1972) recognized at least four rate changes, and Larson and Pitman (1972) recognized at least eight intervals of significantly different, average spreading rates from Jurassic to Holocene; Lattimore and others (1973) resolve at least six such intervals within the Cenozoic Era alone, based on the identification of remanent magnetic anomalies in the central North Atlantic (Fig. 12). The intervals are determined by the availability of dated points on the oceanic crust and so do not necessarily represent natural intervals or resolve all significant changes in spreading rate. Flow lines show that the direction of relative movement of Africa and North America, determined from the trends of magnetic isochrons and fracture zones, changed during continental drift (Pitman and Talwani, 1972, Fig. 2); the flow lines are consistent with pre-continental drift reconstructions that join the two continents near Cape Hatteras and Cap Blanc (Bullard and others, 1965; Dietz and Sproll, 1970). Evidence, as yet limited, suggests that major changes in rate and direction of sea-floor spreading may occur simultaneously on a worldwide basis as part of an intercom-

municating system (Vine, 1966; Larson and Pitman, 1972).

CENTRAL NORTH ATLANTIC SEA-FLOOR SPREADING AND SEDIMENT ACCUMULATION ON THE CONTINENTAL SHELVES

Relation of Rates

The Hatteras well (Fig. 4) and the Al Kinz well (Fig. 8) are considered representative because they each resolve the major maxima and minima in average sediment-accumulation rates and occupy nearly conjugate structural positions on their respective continental margins. The following compares average rates of sediment accumulation on the continental shelves and sea-floor spreading (Figs. 13, 14):

1. Cretaceous (136–65 m.y. B.P.): Average rates of sediment accumulation (range, 2.3–

TABLE 3. STRATIGRAPHY OF O.C.T. 1 - B WELL,
LAT 18°50'57" N., LONG 16°29'48" W.

Depth below sea level (m)	Age
0	(Water column)
84	Post-Miocene
259	Miocene
375	Oligocene
561	Upper Eocene
620	Middle Eocene
796	Lower Eocene
923	Paleocene
974	Upper Cretaceous
1,816	Lower Cretaceous
3,755	Upper Jurassic
4,180	

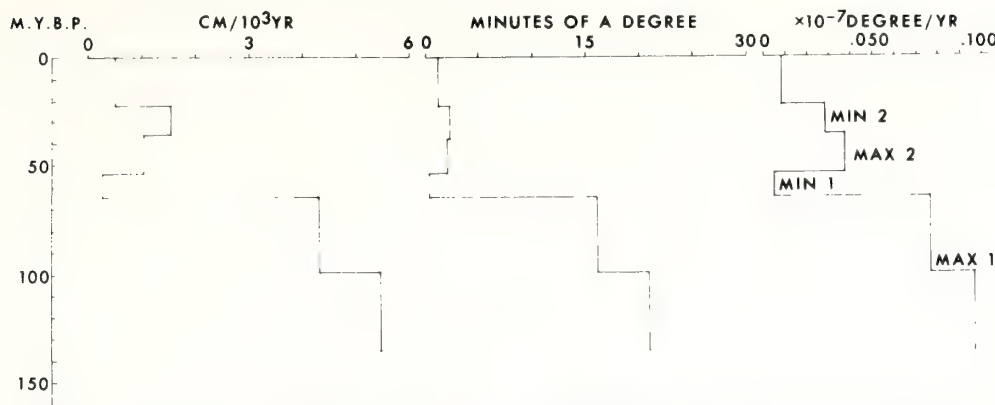


Figure 10. Sediment-accumulation rates derived from the stratigraphic column of the Senegal T.B.-1

well (Monciardini, 1966). Presentation as in Figure 4. See Table 4 for stratigraphy.

2.9 cm per 10^3 yr; 0.060 – 0.106×10^{-7} deg per yr) and of sea-floor spreading (range, 1.7 – 2.0 cm per yr; 5.0 – 8.4×10^{-7} deg per yr) were simultaneously relatively fast.

2. Paleocene (65–53.5 m.y. B.P.): Sediment accumulation (range, 0.4 – 1.4 cm per 10^3 yr; 0.111 – 0.051×10^{-7} deg per yr) and sea-floor spreading (1.3 cm per yr; 2.8×10^{-7} deg per yr) had relatively slow average rates.

3. Early through middle Eocene (53.5–45 m.y. B.P.): Sediment accumulation (range, 1.5 – 6.5 cm per 10^3 yr; 0.040 – 0.233×10^{-7} deg per yr) and sea-floor spreading (2.0 cm per yr; 4.5×10^{-7} deg per yr) attained relatively fast average rates.

4. Late Eocene through Oligocene (45–22.5 m.y. B.P.): Sediment accumulation (range, 0.6 – 1.7 cm per 10^3 yr; 0.015 – 0.063×10^{-7} deg per yr) and sea-floor spreading (0.9 cm per yr; 1.8×10^{-7} deg per yr) had relatively slow average rates.

5. Early Miocene (22.5–14 m.y. B.P.): Sediment accumulation (range, 1.7 – 2.9 cm per 10^3 yr; 0.044 – 0.102×10^{-7} deg per yr) and

sea-floor spreading (1.3 cm per yr; 2.5×10^{-7} deg per yr) attained relatively fast average rates. Average rates of sediment accumulation continued to increase during middle and late Miocene (14–5.5 m.y. B.P.). Average rates of sea-floor spreading decreased during the middle Miocene (14–10 m.y. B.P.) and increased during the late Miocene (10–5.5 m.y. B.P.).

The intervals of relatively fast and slow average rates of sediment accumulation and of sea-floor spreading overlap but do not correlate precisely in time. The lack of precise correlation may result from (1) actual differences in timing of the expression of various processes or (2) apparent differences attributable to problems of dating resolution and of averaging techniques for rates of sediment accumulation and sea-floor spreading. These data support the following relations between the rates of sediment accumulation on the continental shelves at Cape Hatteras and at Cap Blanc and of spreading of the intervening sea floor during each of the five intervals distinguished, with the exception of a short interval in the middle Miocene (Figs. 13, 14):

1. To a first approximation, the average rates of sediment accumulation on the continental shelves are directly proportional to the rates of spreading of the intervening sea floor. If rates of sea-floor spreading are shown to vary in unison on a worldwide basis, then this statement may be generalized to proportionality between rates of sediment accumulation on subsiding continental shelves and rates of sea-floor spreading in the ocean basin.

2. The average vertical rates of sediment accumulation on the continental shelves (cm per

TABLE 4. STRATIGRAPHY OF SENEGAL T.B.-1 WELL, LAT $16^{\circ}19'30''$ N., LONG $16^{\circ}18'30''$ W.

Depth below sea level (m)	Age
0	Post-Oligocene
110	Approximately Oligocene
320	Approximately Eocene
506	Paleocene
537	Upper Cretaceous
2,045	Lower Cretaceous
4,002	

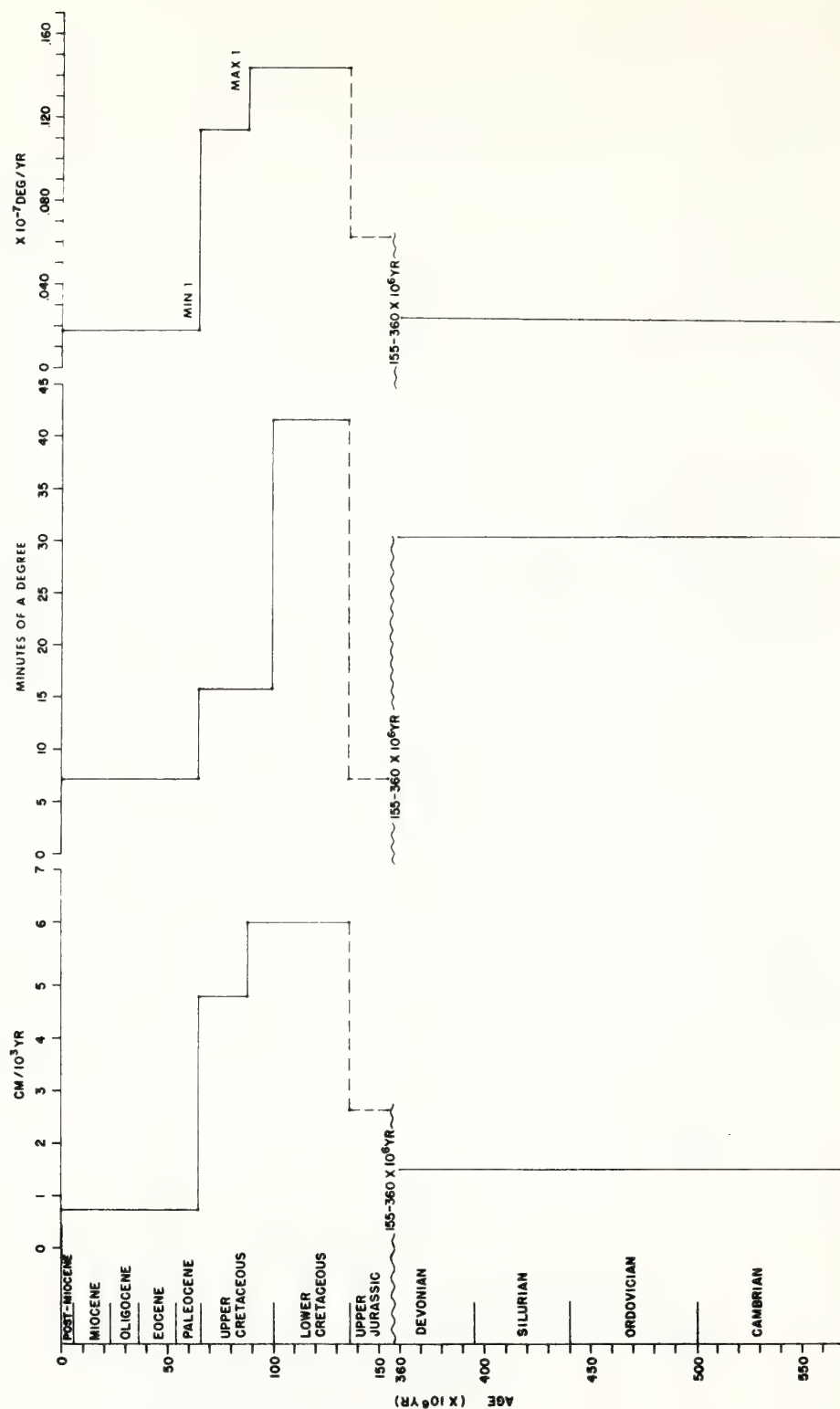


Figure 11. Sediment-accumulation rates derived from a schematic stratigraphic section across the southern Senegal basin (Aymé, 1965, Fig. 3). The Jurassic and Devonian strata. Presentation as in Figure 4.

10^3 yr) are approximately 10^{-3} the average half-rates of sea-floor spreading (cm per yr).

3. The average angular rates of sediment accumulation on the continental shelves ($\times 10^{-7}$ deg per yr) are approximately 10^{-2} the average angular rates of sea-floor spreading ($\times 10^{-7}$ deg per yr).

DISCUSSION

Epirogenic Subsidence of Continental Shelves of Southeastern North America and Northwestern Africa

That certain rifted, aseismic continental margins have undergone a history of epirogenic subsidence has long been recognized (Lawson, 1932; Bourcart, 1938; Veatch and Smith, 1939; Jessen, 1943). The best documented case is the eastern continental margin of North America where a history of seaward subsidence is inferred from the progressive seaward increase in thickness and successive downward increase in inclination of Mesozoic and Cenozoic strata which underlie the coastal plain and continental shelf (Fig. 3). The same inference pertains to the northwestern African continental margin (Fig. 3).

The history of subsidence of the southeastern North American and northwestern African continental shelves can be interpreted with qualifications from the sediment-accumulation rates derived from stratigraphic columns encountered in deep wells penetrating the coastal plain and continental shelf. The only actual shelf-subsidence rate that can be determined is the average Late Jurassic to Holocene subsidence rate derived from the present vertical distance below sea level of the original shelf surface, which is 2.0 cm per 10^3 yr (0.051×10^{-7} deg per yr seaward tilting) at Cape Hatteras and estimated as 2.4 cm per 10^3 yr (0.136×10^{-7} deg per yr seaward tilting) at Cap Blanc. Other subsidence rates pertaining to intervals between the Late Jurassic and Holocene are qualified as "apparent," rather than as actual, because three assumptions are made in equating sediment accumulation with epirogenic subsidence rates:

1. The rate of vertical sediment accumulation is controlled by the rate of subsidence. Underlying this assumption is the concept that deposition on the continental shelf is controlled by a profile of equilibrium such that sediment is deposited up to a base level of aggradation and is eroded above that level (Barrall, 1917; Dunbar and Rodgers, 1957, p. 128–

131; Krumbein and Sloss, 1963, p. 391–395). Once the continental shelf approaches a graded state in equilibrium with the prevalent range of hydraulic and sedimentary conditions, then subsidence is necessary to permit further up-building, although the sediment may continue to build seaward or prograde (Curry, 1964).

2. The available sediment supply is equal to or greater than that required to maintain a profile of equilibrium during subsidence.

3. Sea level remains constant. A change in sea level would change the profile of equilibrium, altering the balance between rates of sediment accumulation and subsidence.

Development of the characteristic seaward-thickening wedge of Mesozoic and Cenozoic sedimentary strata beneath the coastal plains and continental shelves of southeastern North America and northwestern Africa (Fig. 3) is controlled by seaward tilting involving epirogenic subsidence of the original, pre-Late Jurassic shelf surfaces about nearly horizontal axes located at the landward margins of sediment accumulation. Vogt and Ostenso (1967) incorporated the subsidence of continental shelves of rifted continental margins into the hypothesis of mid-oceanic ridge formation by postulating that the shelves originate when a continental plate rifts over a preoceanic uplift. An implication of this hypothesis is that seaward tilting of the continental shelf would be controlled by subsidence of the adjacent ocean basin. The rate of subsidence of oceanic crust, spreading about a mid-oceanic ridge,

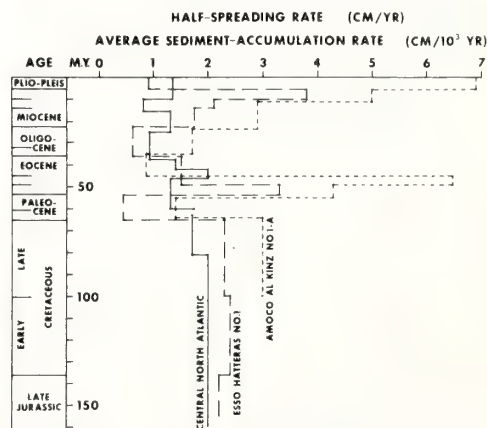


Figure 13. Comparison of average half-spreading rates of the central North Atlantic sea floor (lat 26° N.; see Fig. 12) with average vertical sediment-accumulation rates on the continental shelves at Cape Hatteras (Hatteras well; see Fig. 4) and at Cap Blanc, Mauritania (Al Kinz well; see Fig. 8).

decreases with time after generation at the ridge crest as a function of age of the oceanic crust and reaches an apparent equilibrium of about 2.0 cm per 10^3 yr about 40 m.y. after generation (Menard, 1969; Sclater and others, 1971). Coupled subsidence with the ocean basin may at least partially account for the average Late Jurassic to Holocene subsidence rates of the continental shelves at Cape Hatteras and Cap Blanc but cannot account for the synchronous, transatlantic maxima and minima of average accumulation rates of shelf sediment (Figs. 4–11). The assumption that sea level has remained constant, made in interpreting accumulation rates of shelf sediment as apparent subsidence rates, is examined next.

Relation between Rates of Sediment Accumulation on Continental Shelves and Epicontinental Marine Transgressions and Regressions

Continental margins are subject to local tectonic activity; therefore, the least ambigu-

ous record of eustatic sea-level changes is provided by the stratigraphy of cratonic interiors. Marine transgressions are inferred where continental sediments grade up into marine sediments or where the latter overlie older continental deposits with a notable stratigraphic gap. Marine regressions are inferred where marine sediments grade up into continental sediments or, more equivocally, where unconformities occur. Synthesizing the upper Precambrian to Holocene stratigraphy of the entire cratonic interior of North America, Sloss (1963) identified six craton-wide, rock-stratigraphic units, designated with geographic names from representative localities, separated by six craton-wide unconformities (Fig. 15). Each unit represents deposition during a major marine transgression and overlap beginning at the continental margins and spreading to the cratonic interior and includes offlap from the cratonic interior to the continental margin during a succeeding marine regression; each unconformity represents nondeposition and (or) erosion during the regressional maximum. Although numerous local unconformities occur, only these six are craton-wide. The approximate dates of the regressional maxima represented are (1) very late Precambrian, (2) early Middle Ordovician, (3) early Middle Devonian, (4) "post-Elvira" Mississippian, (5) early Middle Jurassic, and (6) late Paleocene. A seventh unconformity presently developing is interpreted to represent a seventh major regression in progress, of which the Holocene transgression represents a perturbation (Sloss, 1963). The stratigraphic information available from other continents is less comprehensive than from North America. Six major post-late Precambrian rock-stratigraphic units separated by six major unconformities may be identified in Africa and appear broadly synchronous with those present in North America (Fig. 15; Dearnley, 1966, Fig. 21; Haughton, 1963). Like their North American counterparts, the African sequences and unconformities represent major marine transgressions and regressions (Reyre, 1966; Querol, 1966; Templeton, 1971).

Each of the three successive maxima in sediment-accumulation rates observed to have occurred synchronously on the coastal plains and continental shelves of southeastern North America and of northwestern Africa correlates in time to the limit of resolution with an epicontinental marine transgression or the interval of reversal between a transgression and re-

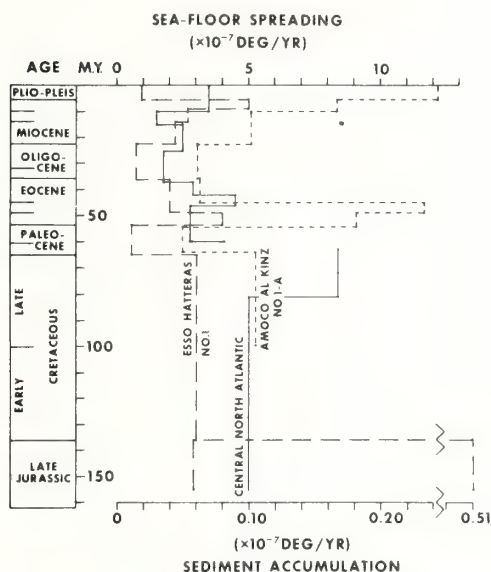


Figure 14. Comparison of average angular velocities of spreading in the central North Atlantic (lat 26° N.; see Figs. 12, 13) with average angular rates of sediment accumulation at Cape Hatteras (Hatteras well; see Fig. 4) and at Cap Blanc, Mauritania (Al Kinz well; see Fig. 8). The spreading rates of Latimore and others (1973) between 0 and 60 m.y. B.P. were converted to angular velocities using the poles of plate rotation of Pitman and Talwani (1972, Table 4); angular velocities of spreading between 63 and 155 m.y. B.P. are from Pitman and Talwani (1972, Table 4).

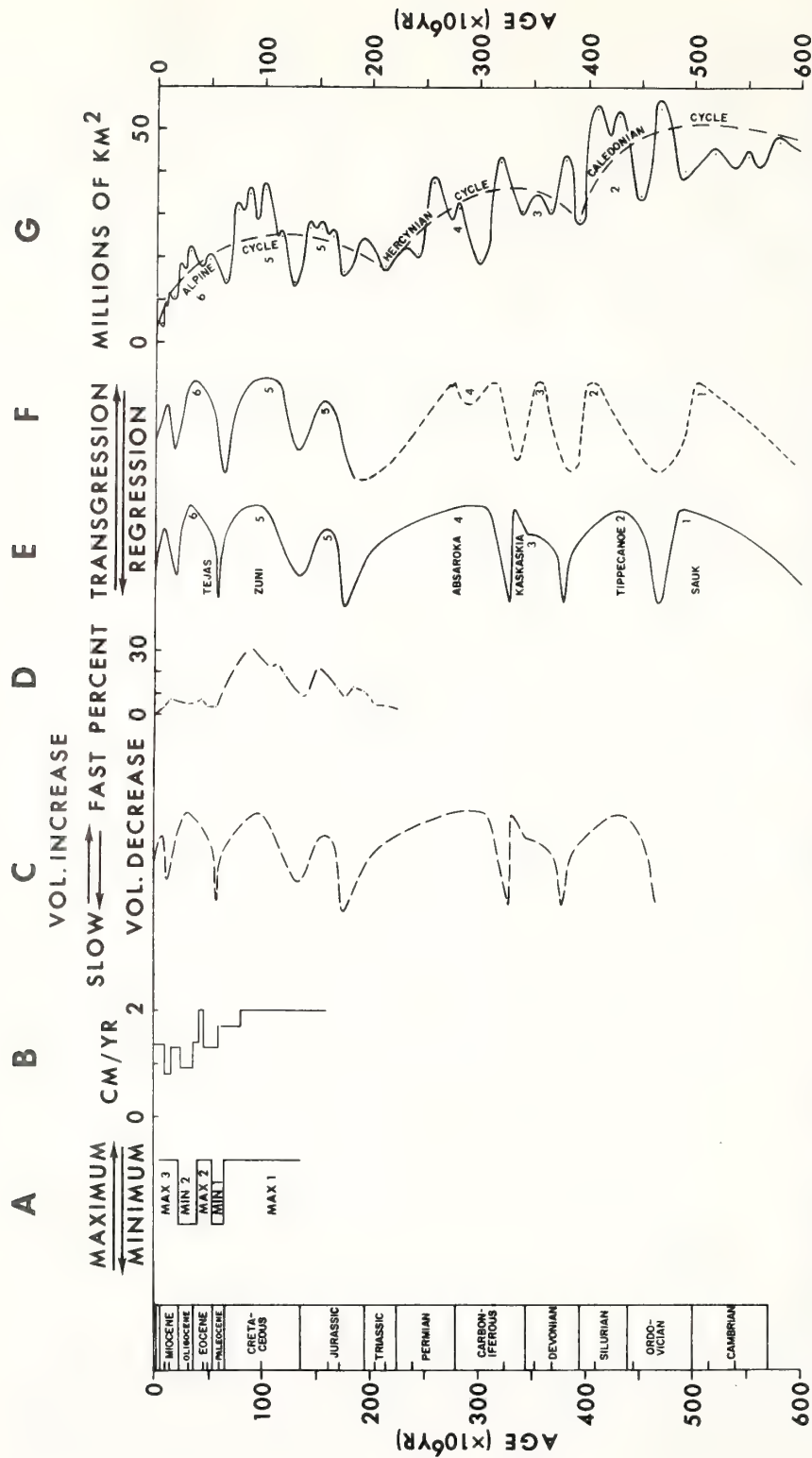


Figure 15. Relations through time between rates of sediment accumulation on continental shelves, sea-floor spreading, and eustasy. A. Average rates of sediment accumulation (Figs. 4 to 11). B. Half-rates of sea-floor spreading, central North Atlantic (Lattimore and others, 1972, 1973; Pitman and Talwani, 1972). C. Inferred worldwide rate of sea-floor spreading (relatively slow or fast) and inferred state of mid-oceanic ridge system (volume change); these are considered to vary in unison. D. Area of North America covered by sea, from stratigraphic record (Schuchert, 1955; Damon and Mauger, 1966, Fig. 4). E. North American marine transgressions and regressions, from stratigraphic record (Sloss, 1963). F. African marine transgressions and regressions, from stratigraphic record (Dearnley, 1966, Fig. 21; Haughton, 1963; Reyre, 1966). G. World continental area covered by sea, from stratigraphic record (Egyed, 1956; Holmes, 1965, Fig. 719).

gression when a relatively large area of North America and other continents was covered by the sea (Fig. 15). Each of the three intervening minima in sediment-accumulation rates correlates in time to the limit of resolution with an epicontinental marine regression or the interval of reversal between a regression and a transgression when a relatively small area of North America and other continents was covered by the sea (Fig. 15). The correlations are as follows:

Maximum 1. Cretaceous (136–65 m.y. B.P.); transgression in Early through middle Cretaceous (136–90 m.y. B.P.), followed by a gradual transition to relatively rapid regression in Late Cretaceous (90–65 m.y. B.P.).

Minimum 1. Paleocene (65–53.5 m.y. B.P.); interval of reversal between relatively rapid regression in Late Cretaceous to middle Paleocene (75–60 m.y. B.P.), and transgression in middle to late Paleocene (60–53.5 m.y. B.P.).

Maximum 2. Early through middle Eocene (53.5–45 m.y. B.P.); transgression in early Eocene through late Eocene (53.5–36 m.y. B.P.).

Minimum 2. Late Eocene through Oligocene (45–22.5 m.y. B.P.); regression in early Oligocene to Miocene (36–22.5 m.y. B.P.).

Maximum 3. Miocene (22.5–5.5 m.y. B.P.) for southeastern North America, Miocene to Holocene (22.5–0 m.y. B.P.) for northwestern Africa; transgression in Miocene (22.5–5.5 m.y. B.P.).

Minimum 3. Pliocene to Holocene (5.5–0 m.y. B.P.) for southeastern North America only; glacio-eustatic transgressions and regressions in Pliocene to Holocene (5.5–0 m.y. B.P.). The absence of minimum 3 in northwest Africa may be due to peculiar late Cenozoic structural conditions (Rona, 1970).

Two alternative explanations may account for the observed association of marine transgressions with maximum values and of marine regressions with minimum values in average rates of sediment accumulation on the continental shelf: (1) A higher ratio of nondeposition-to-deposition and (or) erosion-to-deposition may prevail during regression than during transgression. (2) If rates of sediment accumulation on the continental shelf are nearly equal during both transgression and regression, as would be expected, then conditions favoring nondeposition, including bypassing of sediments and (or) erosion, would occur during the interval of reversal between regression and

transgression when the shoalest water depths would prevail and the largest area of the continental shelf would be exposed subaerially (Fig. 16). As a result, an unconformity would develop on the sedimentary sequence deposited on the continental shelf during the regression; therefore, the rate of sediment accumulation, averaged over that entire regressional sequence, would be lowered. The unconformity would persist through the initial stage of the succeeding transgression, and its effect would depend on whether the hiatus was averaged with the sediment-accumulation rates of the overlying transgressive or underlying regressive deposits. Conversely, the continental shelf would be less vulnerable to nondeposition and (or) erosion at the time of reversal between transgression and regression, resulting in higher average sediment-accumulation rates based on the apparent completeness of the transgressional sequence.

Causes of the Marine Transgressions and Regressions

Two types of alternation of sea level are recognized: local and worldwide. The former is due to warping or faulting of parts of a continent, with resultant local retreat or advance of the sea. The latter affects the entire surface of the ocean and is due to eustatic processes. Those marine transgressions and regressions inferred to be worldwide and synchronous from the stratigraphic record (numbered 2, 3, 4, 5, and 6 in Fig. 15) are best explained by eustatic processes. Irreversible processes of sea-level rise, such as addition of sedimentary and volcanic materials and juvenile water to ocean basins, add to the extent of transgressions, reduce the extent of regressions, but do not explain oscillations of sea level. Glacio-eustasy, a reversible process, is supposed to be too limited in occurrence to apply during the Mesozoic and Cenozoic prior to the Pliocene, although its importance may be underestimated. Geodetic changes, such as shift of the Earth's rotational pole or adjustment of the figure of the Earth, may contribute to the sea-level changes; however, because geodetic changes generally result in differential response of the hydrosphere, they do not explain synchronous worldwide changes (Fairbridge, 1961, Fig. 3; Olson and Bryan, 1972).

Reversible tectono-eustatic processes affecting the capacity of the combined ocean basins have been recognized as capable of the primary control of worldwide transgressions

and regressions at times other than ice ages (Darwin, 1842; Chambers, 1848; Suess, 1906; Grabau, 1924, 1936; Stille, 1924; Bucher, 1933; Umbgrove, 1947; Kuenen, 1950). Three situations are as follows:

1. State of the Mid-Oceanic Ridge System.

Volume increase of the mid-oceanic ridge system would produce a eustatic rise in sea level resulting in worldwide epicontinental transgression; conversely, volume decrease of the ridge system would produce a eustatic lowering of sea level resulting in worldwide regression (Hallam, 1963, 1971; Menard, 1964; Damon and Mauger, 1966; Russell, 1968; Rona, 1970, p. 151). The volume of existing ridges is roughly $1.6 \times 10^8 \text{ km}^3$, which is equivalent to a eustatic rise of sea level of 300 m after isostatic compensation (Menard, 1964, Table 11.2; Menard and Smith, 1966). An increase or decrease in the relief and (or) length of the mid-oceanic ridge system would produce positive or negative changes in the capacity of the ocean basins and would result in transgression or regression. It follows that the Phanerozoic history of volumetric changes of the worldwide mid-oceanic ridge system can be inferred from the stratigraphic record of worldwide non-glacio-eustatic marine transgressions and regressions (Fig. 15).

2. Orogenic State of the Continents. It has

been observed that major orogenic episodes (compressional phase of mountain development) tend to correlate in time with worldwide regressions (Fig. 15; Grabau, 1936, Fig. 1; Damon and Mauger, 1966; Hallam, 1969), although the distribution and resolution of data are presently inadequate to unambiguously demonstrate such a correlation. A possible mechanism to explain this tentative correlation is the net increase in oceanic area (volume) that would result from orogenic compression of continental crust (decrease in area but not volume of continental crust) (Grasty, 1967). An increase of 1 percent in oceanic area would lower mean sea level by about 40 m, assuming an average depth for the oceans of 4 km, which is the magnitude of the effect computed for the main Himalayan orogeny about 70–60 m.y. B.P. (Grasty, 1967). Conversely, destruction of continental crust by erosion and deposition of the eroded material in the ocean basin would result in a corresponding decrease in oceanic volume and rise in sea level.

3. Volumetric Relation Between Crust Created and Crust Consumed.

According to Dietz (1961), the volumetric capacity of the oceans is fully conserved during sea-floor spreading, assuming a constant diameter earth. If the volume of crust created during expansion of an ocean basin is equal to the volume of crust

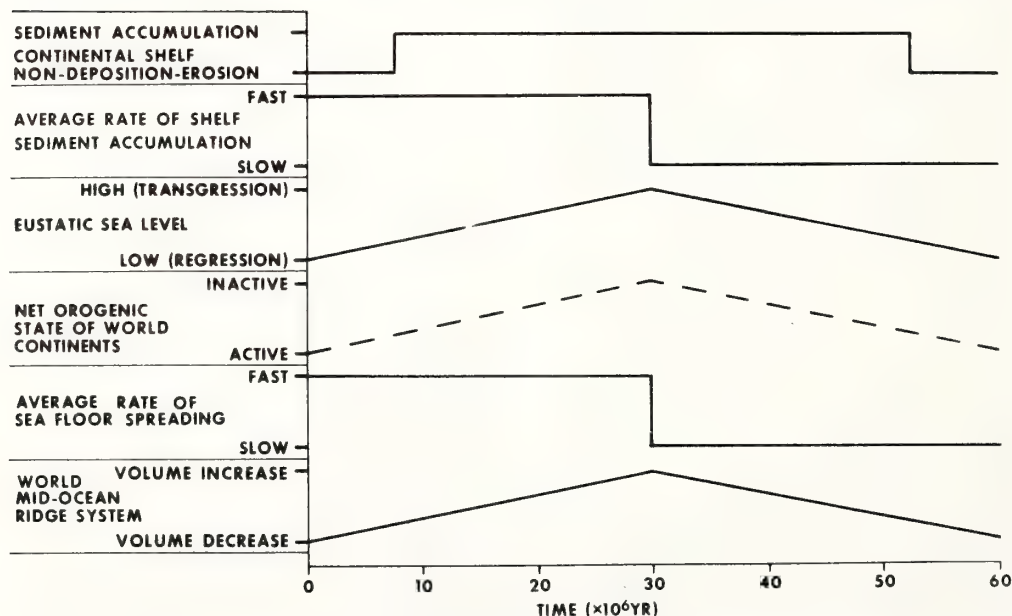


Figure 16. A model cycle showing inferred relations between the phenomena discussed.

consumed during the related contraction of another ocean basin, then the combined capacity of the ocean basins would be conserved. However, volumetrically unequal creation and consumption of crust would result in a change in combined capacity of the ocean basins involved. For example, where North and South America override the East Pacific Rise, crustal creation in the Atlantic would be compensated by consumption of a larger volume of crust in the Pacific, resulting in an increase in combined oceanic capacity. Conversely, overriding of a subduction zone expressed as an oceanic trench by the leading edge of a plate would result in a decrease in capacity of the ocean basins. The increase in capacity of ocean basins caused by the development of subduction zones expressed as trenches would be partially cancelled by sedimentary infilling, whereas the decrease caused by concurrent uplift of mid-oceanic ridges would be fully realized.

The contribution of various component factors to the combined capacity of the ocean basins depends on the magnitude of each factor and the relation in time between the individual factors. Volume changes of the mid-oceanic ridge system and continental orogenies reflect cyclic processes. The relation in time between the cycles determines to what degree the volumetric effects of the cycles will add coherently (in phase) to reinforce each other or add incoherently (out-of-phase) to cancel each other. The behavior of the mid-oceanic ridge system is insufficiently known to determine the degree to which different segments of the system respond coherently, but a reasonable degree of coherence is suspected. For example, the breakup and dispersion of "Pangaea" in the Mesozoic probably entailed a marked increase in the volume of the mid-oceanic ridge system (Dietz and Holden, 1970).

Continental orogeny has been described as either a globally more-or-less continuous process (Gilluly, 1949) or a random-walk process (Rodgers, 1971) with episodic peaks (King, 1955). The migration in space and in time of orogenic activity, rather than its occurrence as a sharp, synchronous, worldwide event, appears consistent with the principle of plate tectonics that orogenies occur where plates impinge (Morgan, 1968; Isacks and others, 1968, Fig. 2; Dewey and Horsfield, 1970). Since orogeny may be globally more-or-less continuous, it is not surprising that orogeny has been correlated both with world-

wide epicontinental marine regression (evidence cited in this paper; Fig. 15) as well as with transgressions ("Antler" or "Haug Effect" of Johnson, 1971, 1972). Correlation of a single orogeny with eustatic sea level is not meaningful unless considered in terms of the combined global effect of all orogenies and other factors affecting volume of ocean basins at the time of the sea-level change.

Like orogeny, the volumetric relation between crustal creation and consumption is a function of the spatial distribution of lithospheric plates and the vectors of plate motion. Because states ranging from orogeny to quiescence and from crustal creation to consumption may be globally coeval and change continuously with time, it is the *net* global effect of each factor at a given time that counts. The total effect on the capacity of the combined ocean basins at a given time is the summation of the *net* global effect of each contributing component factor at that time.

The states of mid-oceanic ridges and of continental orogeny are related within the framework of plate tectonics. Field measurements (Heirtzler and others, 1968; Menard, 1969; van Andel and Heath, 1970) indicate and models (Langseth and others, 1966; Oxburgh and Turcotte, 1968; Le Pichon and Langseth, 1969; McKenzie and Sclater, 1969; Sclater and Francheteau, 1970; Sclater and others, 1971, Fig. 4) suggest that, when mid-oceanic ridges are inferred to be loci of active sea-floor spreading, they are in an expanded state and that, when inactive, they contract. According to the rates of subsidence determined for oceanic crust as a function of time (Menard, 1969; Sclater and others, 1971) a typical mid-oceanic ridge would subside about 1,000 m in the initial 10 m.y. after cessation of sea-floor spreading; the result would be roughly a one-third reduction in cross-sectional area and a one-half reduction in volume. It follows that changes in ocean-basin capacity contributing to epicontinental marine transgression are associated with active sea-floor spreading and changes contributing to regression are associated with a spreading slowdown or lapse (Rona, 1970, p. 151).

Sea-floor spreading, like orogeny, appears to be episodic (Ewing and Ewing, 1967; Schneider and Vogt, 1968). Mounting evidence suggests that slowdowns or lapses in spreading tend to be associated with peak phases of continental orogenies (Le Pichon, 1968; Van Houten,

1969; Rona, 1970; Coney, 1971), as if the plate collisions producing the orogenies impose an added load upon the forces driving the plates. This inferred feedback between drifting lithospheric plates and the forces which drive the plates may contribute to the slowdown or lapse in sea-floor spreading until plate motion is reorganized into a pattern of less resistance. Whatever the mechanism, the suspected coincidence in time between orogenic compression and a slowdown or lapse in sea-floor spreading would mean that the effects of mid-oceanic ridge contraction and areal increase of the ocean basin would reinforce each other and contribute to epicontinental marine regression. Epeirogenic uplift of the continent by isostatic adjustment of the continent in response to the orogenically thickened crust would further reinforce the marine regression.

CONCLUSIONS

The relations discussed between eustatic sea-level changes and plate tectonics provide a basis for interpretation of the maxima and minima observed in Mesozoic and Cenozoic rates of sediment accumulation, which were established from the stratigraphy of the continental shelves of southeastern North America (Figs. 4-6) and northwestern Africa (Figs. 7-11); the relations also explain the direct proportionality of these rates to rates of sea-floor spreading in the central North Atlantic (Figs. 13, 14). The maxima and minima in sediment-accumulation rates were controlled by eustatic changes of sea level. The oscillatory sea-level changes required to produce the transgressions and regressions may be explained as the product of reversible changes in the capacity of the combined ocean basins primarily caused by changes in the volume of the mid-oceanic ridge system. Since fast spreading is associated with an expanded mid-oceanic ridge state and slow spreading with a contracted ridge state, the correlation of marine transgression with sedimentary maxima and with intervals of relatively fast sea-floor spreading (Fig. 15) indicates that volume increase of the mid-oceanic ridge system was a major factor in contributing to the transgression. Likewise, the correlation of marine regression with sedimentary minima and with intervals of relatively slow sea-floor spreading indicates that volume decrease of the mid-oceanic ridge system was a major factor in contributing to the regression. The Late Cretaceous to middle Paleocene and the Oligocene regressions may have been reinforced by in-

crease of ocean-basin capacity that was due to the compression of continental crust during the Andean, Himalayan, Laramide, Alpine, and Atlas orogenies.

A model cycle shows the inferred relations between the phenomena discussed (Fig. 16). Rates of sediment accumulation on continental shelves are averaged over alternating intervals of accumulation and of nondeposition and (or) erosion which are influenced by eustatic height of sea level. Eustatic sea-level fluctuations result largely from changes in the capacity of the combined ocean basins, which are determined by the states of continental orogeny and of the mid-oceanic ridge system. These, in turn, are determined by the forces which drive the lithospheric plates. Actually, the cycle tends to be asymmetric with respect to time: the regressive portion generally has a shorter duration than the transgressive portion (Fig. 15).

The worldwide nature of the cycle implies that a sequence of maxima and minima in average sediment-accumulation rates similar to that established for southeastern North America and northwestern Africa should be recognizable in the stratigraphy of other continental shelves which have undergone more-or-less continuous subsidence during Mesozoic and Cenozoic time. Continental and oceanic stratigraphy may record events correlatable with the shelf maxima and minima, because the controlling changes in sea level would have affected both continental erosion and oceanic circulation (Rona, 1973; Wise, 1973).

ACKNOWLEDGMENTS

I thank M. J. Hill of the Gulf Oil Company and both the Spanish Gulf Oil Company and Compania Española de Petróleos, S.A., for providing the stratigraphic section of their Spangoc well. I thank G. E. Abbey of Amoco Mauritania Petroleum Company, W. E. Humphrey of Amoco International Oil Company, and R. O. Mitchell of Planet Oil and Mineral Corporation for providing the data presented on the Al Kinz well and O.C.T. 1-B well. I thank Tj. H. van Andel, E. Uchupi, J. S. Schlee, K. O. Emery, R. L. Larson and K. K. Turekian for helpful critical reviews. The paper benefited from discussion at the 1972 Penrose Conference on Continental Margins. This work was partially supported by the National Science Foundation International Decade of Ocean Exploration funding for the NOAA Trans-Atlantic Geotraverse (TAG).

REFERENCES CITED

- Aymé, J. M., 1965, The Senegal salt basin, *in* Salt basins around Africa: London, Inst. Petroleum, p. 83-90.
- Barrell, J., 1917, Rhythms and the measurements of geologic time: *Geol. Soc. America Bull.*, v. 28, p. 745-904.
- Berggren, W. A., 1969, Cenozoic chronostratigraphy, planktonic foraminiferal zonation and the radiometric time scale: *Nature*, v. 224, p. 1072-1075.
- Bourcart, J., 1938, La marge continentale: essai sur les régressions et transgressions marines: *Soc. Géol. France Bull.*, sér. 5, v. 8, p. 393-474.
- Bucher, W. H., 1933, The deformation of the Earth's crust: Princeton, N.J., Princeton Univ. Press, 518 p.
- Bullard, E., Everett, J. E., and Smith, A. G., 1965, The fit of the continents around the Atlantic, *in* A symposium on continental drift: Royal Soc. London Philos. Trans., ser. A, v. 258, p. 41-51.
- Chambers, R., 1848, Ancient sea-margins, as memorials of changes in the relative level of sea and land: Edinburgh and London, Chambers, Orr and Co., 388 p.
- Coney, P. J., 1971, Cordilleran tectonic transitions and motion of the North American plate: *Nature*, v. 233, p. 462-465.
- Curry, J. R., 1964, Transgressions and regressions, *in* Miller, R. L., ed., Papers in marine geology (Shepard volume): New York, The Macmillan Company, p. 175-203.
- Damon, P. E., and Mauger, R. L., 1966, Epeirogeny-orogeny viewed from the Basin and Range Province: *Soc. Mining Engineers Trans.*, v. 235, March, p. 99-112.
- Darwin, C. R., 1842, The structure and distribution of coral reefs: London, Smith, Elder and Co.
- Dearnley, R., 1966, Orogenic fold-belts and a hypothesis of Earth evolution, *in* Ahrens, L. H., Press, F., Runcorn, S. K., and Urey, H. C., eds., Physics and chemistry of the Earth: London, Pergamon Press, v. 7, p. 1-114.
- Dewey, J. F., and Horsfield, B., 1970, Plate tectonics, orogeny, and continental growth: *Nature*, v. 225, p. 521-525.
- Dietz, R. S., 1961, Continent and ocean basin evolution by spreading of the sea floor: *Nature*, v. 190, p. 854-857.
- Dietz, R. S., and Holden, J. C., 1970, Reconstruction of Pangaea: Breakup and dispersion of continents, Permian to Present: *Jour. Geophys. Research*, v. 75, p. 4939-4956.
- Dietz, R. S., and Sproll, W. P., 1970, East Canary Islands as a microcontinent within Africa-North America drift fit: *Nature*, v. 226, p. 1043-1045.
- Dunbar, C. O., and Rodgers, J., 1957, Principles of stratigraphy: New York, John Wiley & Sons, Inc., 356 p.
- Egyed, L., 1956, The change of the Earth's dimensions determined from paleogeographical data: *Geofisica Pura e Applicata* (Milano, Italy), v. 33, p. 42-48.
- Ewing, J., and Ewing, M., 1967, Sediment distribution on the mid-ocean ridges with respect to spreading of the sea floor: *Science*, v. 156, p. 1590-1592.
- Fairbridge, R. W., 1961, Eustatic changes in sea level, *in* Ahrens, L. H., Press, F., Rankama, K., Runcorn, S. K., eds., Physics and chemistry of the Earth: London, Pergamon Press, v. 4, p. 99-185.
- Geological Society of London, 1964, Geological Society Phanerozoic time-scale 1964: *Geol. Soc. London Quart. Jour.*, v. 120, p. 260-262.
- Gilluly, J., 1949, Distribution of mountain building in geologic time: *Geol. Soc. America Bull.*, v. 60, p. 561-590.
- Grabau, A. W., 1924, Principles of stratigraphy; 1960 Dover edition of the last revised edition as published in 1924 by A. G. Seiler, 581 p.
- 1936, Oscillation or pulsation?: *Internat. Geol. Cong.*, 16th, Washington, D.C. 1933, v. 1, p. 539-552.
- Grasty, R. L., 1967, Orogeny, a cause of worldwide regression of the seas: *Nature*, v. 216, p. 779-780.
- Hallam, A., 1963, Major epeirogenic and eustatic changes since the Cretaceous and their possible relationship to crustal structure: *Am. Jour. Sci.*, v. 261, p. 397-423.
- 1969, Tectonism and eustasy in the Jurassic: *Earth-Sci. Rev.*, v. 5, no. 1, p. 45-68.
- 1971, Mesozoic geology and the opening of the North Atlantic: *Jour. Geology*, v. 79, p. 129-157.
- Haughton, S. H., 1963, The stratigraphic history of Africa south of the Sahara: Edinburgh and London, Oliver & Boyd, 365 p.
- Hayes, D. E., Pimm, A. C., Beckman, J. P., Benson, W. E., Berger, W. H., Roth, P. H., Supko, P. R., and von Rad, U., 1972, Initial reports of the Deep Sea Drilling Project, Vol. 14: Washington, D.C., U.S. Govt. Printing Office, 975 p.
- Heirtzler, J. R., Dickson, G. O., Herron, E. M., Pitman, W. C., III, and Le Pichon, X., 1968, Marine magnetic anomalies, geomagnetic field reversals, and motions of the ocean floor and continents: *Jour. Geophys. Research*, v. 73, p. 2119-2136.
- Hollister, C. D., Ewing, J. I., Habib, D., Hathaway, J. C., Lancelot, Y., Luterbacher, H., Paulus, F. J., Poag, C. W., Wilcoxon, J. A., and Worstell, P., 1972, Initial reports of the Deep Sea Drilling Project, Vol. 11: Washington, D.C., U.S. Govt. Printing Office, 1077 p.
- Holmes, A., 1965, Principles of physical geology: New York, Ronald Press, 1288 p.
- Isacks, B., Oliver, J., and Sykes, L. R., 1968, Seismology and the new global tectonics: *Jour.*

- Geophys. Research, v. 73, p. 5855-5899.
- Jessen, O., 1943, Die Randschwellen der Kontinente: *Petermanns Geogr. Mitt., Erg. no.* 241.
- Johnson, J. G., 1971, Timing and coordination of orogenic, epeirogenic, and eustatic events: *Geol. Soc. America Bull.*, v. 82, p. 3263-3298.
- 1972, Antler effect equals Hang effect: *Geol. Soc. America Bull.*, v. 83, p. 2497-2498.
- King, P. B., 1955, Orogeny and epeirogeny through time: *Geol. Soc. America Spec. Paper* 62, p. 723-739.
- Krumbein, W. C., and Sloss, L. L., 1963, *Stratigraphy and sedimentation* (2d ed.): San Francisco, W. H. Freeman and Company Publishers, 660 p.
- Kuenen, P. H., 1950, *Marine geology*: New York, John Wiley & Sons, Inc., 568 p.
- Langseth, M. G., Le Pichon, X., and Ewing, M., 1966, Crustal structure of the mid-ocean ridges. 5. Heat flow through the Atlantic Ocean floor and convection currents: *Jour. Geophys. Research*, v. 71, p. 5321-5355.
- Larson, R. L., and Pitman, W. C., III, 1972, Worldwide correlation of Mesozoic magnetic anomalies and its implications: *Geol. Soc. America Bull.*, v. 83, p. 3645-3662.
- Lattimore, R. K., Rona, P. A., and DeWald, O. E., 1972, Magnetic anomaly sequence, central North Atlantic Ocean: *EOS (Am. Geophys. Union Trans.)*, v. 53, p. 407.
- 1973, Magnetic anomaly sequence in the central North Atlantic: *Jour. Geophys. Research* (in press).
- Lawson, A. C., 1932, Insular arcs, foredeeps, and geosynclinal seas of the Asiatic coast: *Geol. Soc. America Bull.*, v. 43, p. 353-381.
- Le Pichon, X., 1968, Sea-floor spreading and continental drift: *Jour. Geophys. Research*, v. 73, p. 3661-3697.
- Le Pichon, X., and Langseth, M. G., Jr., 1969, Heat flow from the mid-ocean ridges and sea-floor spreading: *Tectonophysics*, v. 8, p. 319-344.
- Maher, J. C., 1965, Correlations of subsurface Mesozoic and Cenozoic rocks along the Atlantic Coast: Tulsa, Am. Assoc. Petroleum Geologists, 18 p., 9 pls.
- Maher, J. C., and Applin, E. R., 1971, *Geologic framework and petroleum potential of the Atlantic coastal plain and continental shelf*: U.S. Geol. Survey Prof. Paper 659, 98 p.
- McKenzie, D. P., and Sclater, J. G., 1969, Heat flow in the eastern Pacific and sea floor spreading: *Bull. Volcanol.*, v. 33, no. 1, p. 101-118.
- Menard, H. W., 1964, *Marine geology of the Pacific*: New York, McGraw-Hill Book Co., 271 p.
- 1969, Elevation and subsidence of oceanic crust: *Earth and Planetary Sci. Letters*, v. 6, p. 275-284.
- Menard, H. W., and Smith, S. M., 1966, Hypsometry of ocean basin provinces: *Jour. Geophys. Research*, v. 71, p. 4305-4324.
- Monciardini, C., 1966, La sédimentation éocène au Sénégal: [Paris] *Bur. de Recherches Géol. et Minières Mém. No.* 43, 65 p., 14 charts.
- Morgan, W. J., 1968, Rises, trenches, great faults, and crustal blocks: *Jour. Geophys. Research*, v. 73, p. 1959-1982.
- Olson, W. S., and Bryan, G. M., 1972, A dynamic model for epicontinental marine transgression: *Geol. Soc. America, Abs. with Programs (Ann. Mtg.)*, v. 4, no. 7, p. 618.
- Oxburgh, E. R., and Turcotte, D. L., 1968, Mid-ocean ridges and geotherm distribution during mantle convection: *Jour. Geophys. Research*, v. 73, p. 2643-2661.
- Peterson, M. N. A., Edgar, N. T., Cita, M., Gartner, S., Jr., Goll, R., Nigrini, C., and von der Borch, C., 1970, Initial reports of the Deep Sea Drilling Project, Vol. 2: Washington, U.S. Govt. Printing Office, 501 p.
- Pitman, W. C., III, and Talwani, M., 1972, Sea-floor spreading in the North Atlantic: *Geol. Soc. America Bull.*, v. 83, p. 619-649.
- Querol, R., 1966, Regional geology of the Spanish Sahara, in Reyre, D., ed., *Sedimentary basins of the African coasts*, Pt. 1 Atlantic Coast: Paris, Assoc. African Geol. Surveys, p. 27-38.
- Reyre, D., ed., 1966, *Sedimentary basins of the African coasts*. Pt. 1 Atlantic Coast: Paris, Assoc. African Geol. Surveys, 304 p.
- Rodgers, J., 1971, The Taconic orogeny: *Geol. Soc. America Bull.*, v. 82, p. 1141-1178.
- Rona, P. A., 1970, Comparison of continental margins of eastern North America at Cape Hatteras and northwestern Africa at Cap Blanc: *Am. Assoc. Petroleum Geologists Bull.*, v. 54, p. 129-157.
- 1972, Relation between rates of sediment accumulation on continental shelves and sea floor spreading in the central North Atlantic: *Geol. Soc. America, Abs. with Programs (Ann. Mtg.)*, v. 4, no. 7, p. 644.
- 1973, Worldwide unconformities in marine sediments related to eustatic changes of sea level: *Nature* (in press).
- Russell, K. L., 1968, Oceanic ridges and eustatic changes in sea level: *Nature*, v. 218, p. 861-862.
- Schneider, E. D., and Vogt, P. R., 1968, Discontinuities in the history of sea-floor spreading: *Nature*, v. 217, p. 1212-1222.
- Schuchert, C., 1955, *Atlas of paleogeographic maps of North America*: New York, John Wiley & Sons, Inc., 177 p.
- Sclater, J. G., and Francheteau, J., 1970, The implications of terrestrial heat flow observations on current tectonic and geochemical models of the crust and upper mantle of the earth: *Royal Astron. Soc. Geophys. Jour.*, v. 20, p. 509-542.

- Sclater, J. G., Anderson, R. N., and Bell, M. L., 1971, Elevation of ridges and evolution of the central eastern Pacific: *Jour. Geophys. Research*, v. 76, p. 7888-7915.
- Sloss, L. L., 1963, Sequences in the cratonic interior of North America: *Geol. Soc. America Bull.*, v. 74, p. 93-114.
- Stille, H., 1924, *Grundfragen der vergleichenden Tectonik*: Berlin, Borntraeger, 443 p.
- Suess, E., 1906, *The face of the earth*: Oxford, Clarendon Press, v. 2, 556 p.
- Swain, F. M., 1952a, Ostracoda from wells in North Carolina. Pt. 1. Cenozoic Ostracoda: U.S. Geol. Survey Prof. Paper 234-A, p. 1-58.
- 1952b, Ostracoda from wells in North Carolina. Pt. 2. Mesozoic Ostracoda: U.S. Geol. Survey Prof. Paper 234-B, p. 59-152.
- Templeton, R.S.M., 1971, The geology of the continental margin between Dakar and Cape Palmas, in Delany, F. M., ed., *The geology of the east Atlantic continental margin. 4. Africa*: Inst. Geol. Sci. Rept. no. 70/16, p. 42-60.
- Umbgrove, J.H.F., 1947, *The pulse of the earth*: The Hague, Martinus Nijhoff, 358 p.
- van Andel, Tj. H., and Heath, G. R., 1970, Tectonics of the Mid-Atlantic Ridge, 6°-8° south latitude: *Marine Geophys. Researches*, v. 1, p. 5-36.
- Van Houten, F. B., 1969, Molasse facies: Records of worldwide crustal stress: *Science*, v. 166, p. 1506-1508.
- Veatch, A. C., and Smith, P. A., 1939, Atlantic submarine valleys of the United States and the Congo submarine valley: *Geol. Soc. America Spec. Paper* 7, 101 p.
- Vine, F. J., 1966, Spreading of the ocean floor: New evidence: *Science*, v. 154, p. 1405-1415.
- Vine, F. J., and Matthews, D. H., 1963, Magnetic anomalies over oceanic ridges: *Nature*, v. 199, p. 947-949.
- Vogt, P. R., and Ostenso, N. A., 1967, Steady state crustal spreading: *Nature*, v. 215, p. 810-817.
- Wise, D. U., 1973, Freeboard of continents through time, in Shagam, R., and others, eds., *Studies in earth and space sciences (Hess volume)*: *Geol. Soc. America Mem.* 132, p. 87-96.

MANUSCRIPT RECEIVED BY THE SOCIETY DECEMBER 4, 1972

REVISED MANUSCRIPT RECEIVED MARCH 26, 1973

MESOZOIC PLATE MOTIONS IN THE EASTERN CENTRAL NORTH ATLANTIC

PETER A. RONA and HENRY S. FLEMING

National Oceanic and Atmospheric Administration, Atlantic Oceanographic and Meteorological Laboratories, Miami, Fla. (U.S.A.)

Naval Research Laboratory, Washington, D.C. (U.S.A.)

(Accepted for publication February 1, 1973)

ABSTRACT

Rona, P. A. and Fleming, H. S., 1973. Mesozoic plate motions in the eastern central North Atlantic. *Mar. Geol.*, 14: 239-252.

A 1500 km long segment of a fracture zone exhibiting continuity of trend and offset with the Atlantis fracture zone (30° N) was mapped with bathymetric, seismic reflection, and magnetic profiles between the outer continental shelf and the abyssal hills off northwest Africa. The fracture zone segment occurs in crust of Mesozoic age dated tentatively by the identification of remanent magnetic anomalies.

Lithospheric plate motions in a frame of reference fixed with respect to Africa are deduced along the fracture zone. During the Early and Middle Jurassic (≤ 180 to > 155 my) the plate motion was east-west described by a rotation of 10° about a pole located at $36^\circ \pm 2^\circ$ N, $17.5 \pm 1^\circ$ W with respect to Africa. The location of this pole indicates that the opening of the Atlantic between North America and Africa was independent of the opening between North America and Europe with an intervening plate boundary in the position of the present Azores-Gibraltar ridge. The rotation changed to northwest-southeast during the Late Jurassic (> 155 to about 150 my), when the azimuth to the pole of plate rotation jumped about 20° of arc eastward from the azimuth to the prior pole. The northwest-southeast relative rotation continued during the Late Jurassic and Early Cretaceous (about 150 to about 100 my). The azimuth to the rotational pole appears to have migrated progressively westward toward the Cenozoic pole.

INTRODUCTION

This investigation is part of a concerted effort to derive the history of relative motions of lithospheric plates in the central North Atlantic by delineating the Atlantis fracture-zone system from the Mid-Atlantic Ridge (Phillips and Luyendyk, 1970), across the Canary basin (Harbison et al., 1973), up to the northwest African continental shelf (Fig.1). According to the geometry of plate tectonics (McKenzie and Parker, 1967; Morgan, 1968), transform faults (Wilson, 1965) follow small circles analogous to lines of latitude about a pole of plate rotation. Rotation about this pole describes the relative motion between a diverging pair of rigid lithospheric plates. Numerous fracture zones

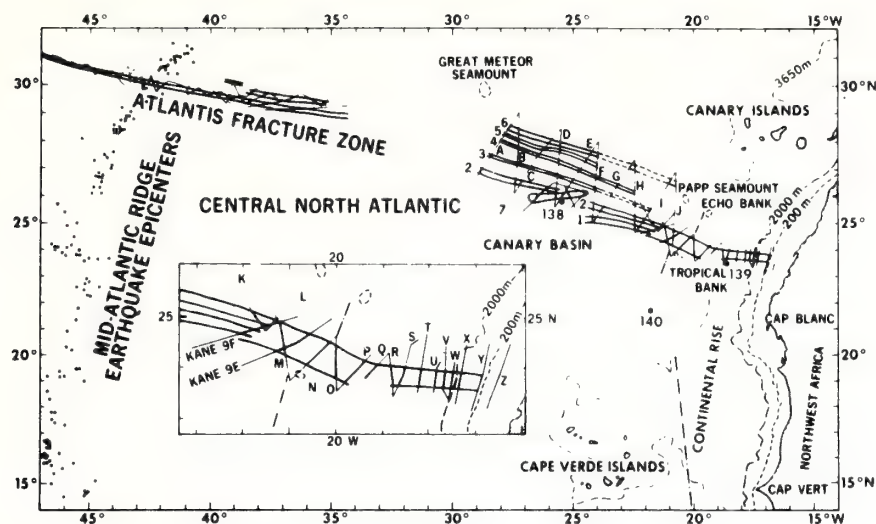


Fig.1. Index map of ship's tracks across the Atlantis fracture-zone system in the eastern central North Atlantic (Phillips and Luyendyk, 1970; Harbison et al., 1973). The inset enlarges the structural lineations described. The dashed-dotted line is the magnetic boundary between relatively smooth (landward) and rough (seaward) remanent magnetic fields (Heirtzler and Hayes, 1967) situated near the middle of the continental rise (Rona et al., 1970). The points labeled 138, 139 and 140 are Deep-Sea Drilling sites (Hayes et al., 1972).

crossing the central North Atlantic, including the Atlantis, have been interpreted as transform faults which are the physical expression of trajectories of the North American and African plates during their divergence over the past approximately 180 my. These fracture zones are best exposed in the middle one-third of the central North Atlantic (Heezen and Tharp, 1968), where certain of them have been mapped with sufficient accuracy to deduce Cenozoic relative motion vectors and poles of plate rotation (Le Pichon, 1968; Morgan, 1968; Fox et al., 1969; Phillips and Luyendyk, 1970; Phillips et al., 1971; Pitman and Talwani, 1972). Fracture zones are less completely known in the landward two-thirds of the central North Atlantic where they are obscured due to sediment cover. The segment of the fracture zone investigated occurs in oceanic crust tentatively dated as Early Jurassic to Middle Cretaceous by the identification of remanent magnetic anomalies (Fig.2).

A fracture zone comprises a system of generally parallel structural lineations, so that delineation of a single included structural lineation may suffice to establish the trend of the zone. The degree of certainty with which a structural lineation can be identified and followed depends on the distinctness and continuity of the particular lineation and the sampling interval of the survey. In 1970 the U.S.N.S. "J. W. Gibbs" was used to delineate structural lineations within a 550 km long segment of a fracture zone between the lower continental rise and the continental shelf off northwest Africa (Fig.1). This segment of the fracture zone had been recognized on a 1968-"Gibbs" cruise (Rona, 1970). Concurrent

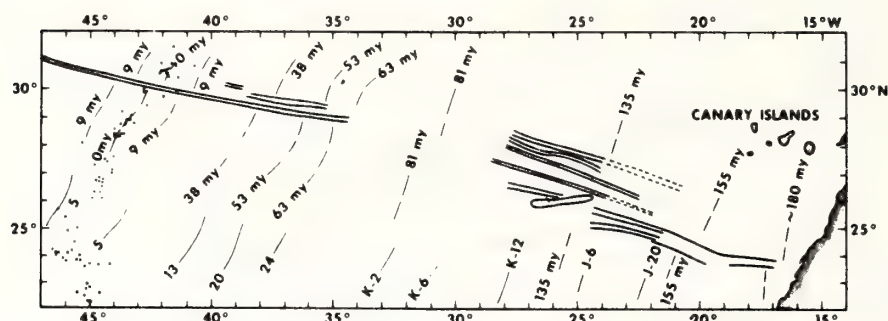


Fig. 2. Tentative ages of oceanic crust along the Atlantis fracture-zone system. Ages are assigned to the oceanic crust assuming datums of about 180 my for initiation of Mesozoic sea-floor spreading off northwest Africa, 155 my for the age of the magnetic quiet zone boundary, and 155–135 my for the age of the "J" series of magnetic anomalies (Vogt et al., 1971) identified off northwest Africa (Rona et al., 1970), by analogy with counterparts off eastern North America (Peterson et al., 1970; Hollister, et al., 1972), and magnetic reversal chronology between 81 and 0 my (Pitman and Talwani, 1972). The locations of identified remanent magnetic anomalies (Lattimore et al., 1973) labeled according to the geomagnetic time scale (Heirtzler et al., 1968) and current usage (Vogt et al., 1971; Vogt and Johnson, 1971) are shown south of the fracture zone.

bathymetric, magnetic, and continuous seismic reflection ($30 \text{ in}^3 - 500 \text{ cm}^3 - \text{air gun}$) profiles were obtained along sixteen crossings of the fracture zone (Fig. 3–6). Primary control of position was by satellite navigation.

Where oceanic crustal layer 2 is exposed with little sediment cover on the Mid-Atlantic Ridge, fracture-zone morphology is characterized by continuous linear valleys generally bounded by steep walls which transect the ridge. Because layer 2 lies deeper than the penetration of the seismic reflection profiles in the area investigated adjacent to the continent, structural lineations were identified from associated topography, deformation of subbottom sedimentary layers, and, in certain cases, magnetic signature. The linearity of trend established from twenty-five crossings (Fig. 1) and the fact that no similar features were observed in reconnaissance of the continental slope and rise between the Canary and Cape Verde islands (Rona, 1970, 1971), indicate that the features investigated are the expression of a fracture zone rather than the result of random superficial slumping of the sedimentary layer.

DESCRIPTION OF STRUCTURAL LINEATIONS

Within the segment of the fracture investigated the most distinct and continuous structural lineations observed resemble a graben. Profiles which cross the graben-like structure between the lower and upper continental rise reveal a topographic depression about 40 km wide underlain by deformed sedimentary layers and bounded by normal faults which form inward-facing scarps with 50–150 m relief (Fig. 4, 5, 7; profiles *Q*, *R*, *S*, *T*). The surface expression of the boundaries of the graben-like structure changes from fault scarps to opposing topographic slopes between the upper continental rise and the

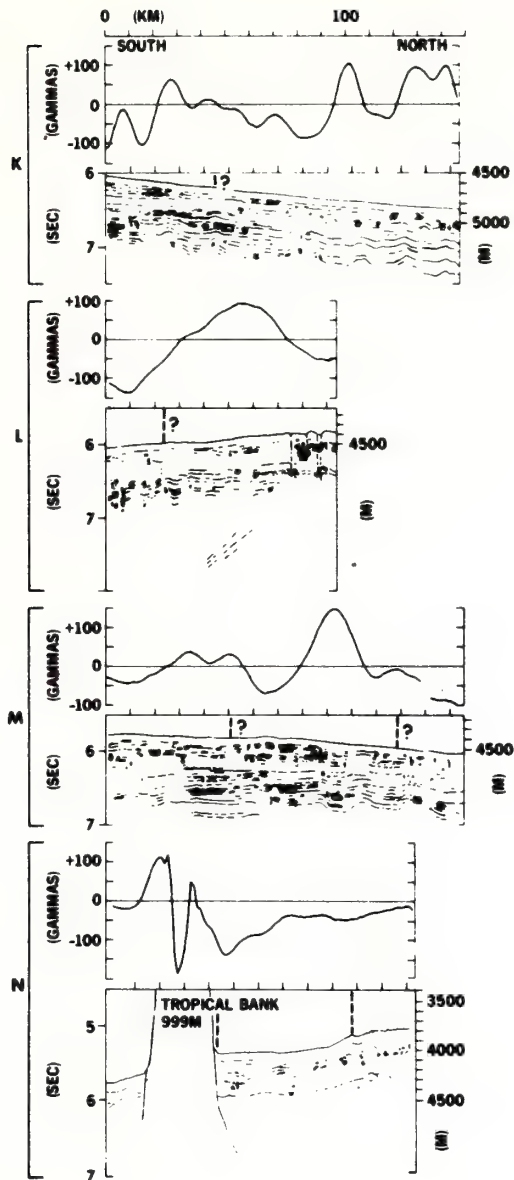


Fig.3. Line drawings of continuous seismic reflection and residual magnetic profiles (Cain et al., 1967) K through N located on Fig.1. The vertical dashed lines above the seismic profiles mark the northern and southern boundaries of a graben-like structure which was followed from the lower continental rise to the outer continental shelf off northwest Africa (Fig.3-6). Vertical exaggeration of the seismic profiles is about 40:1.

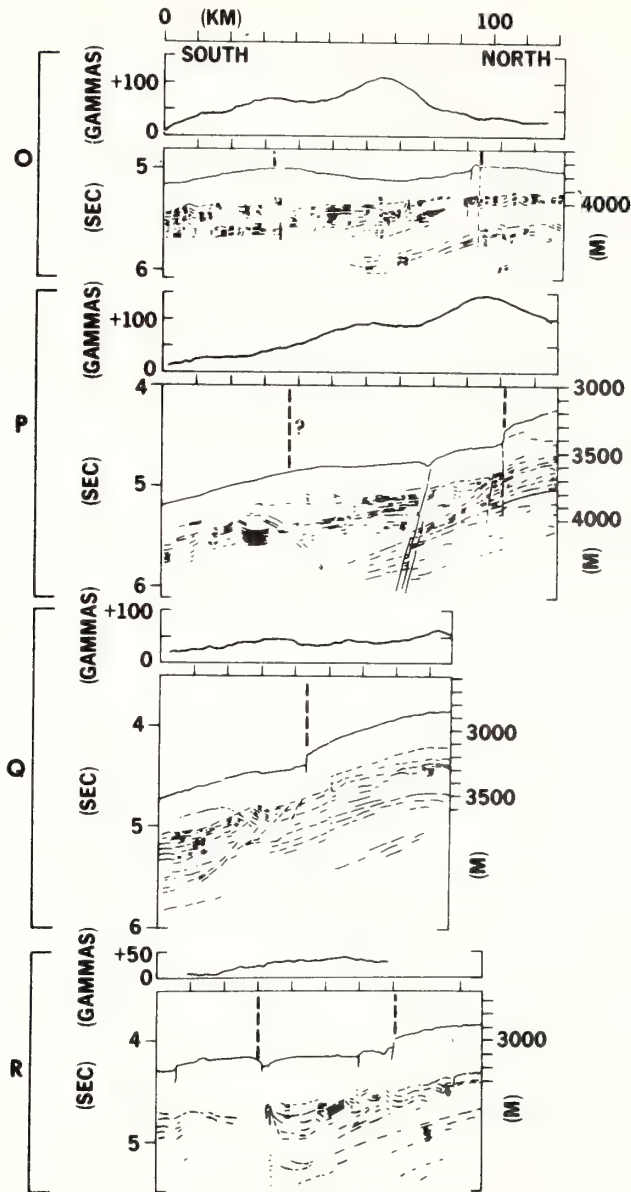


Fig.4. Line drawings of continuous seismic reflection and residual magnetic profiles *O* through *R*, as in Fig.3.

middle of the continental slope (Fig.5, 6, 7; profiles *U*, *V*, *W*). Increased seismic penetration beneath acoustically transparent sediment of the upper continental slope (Fig.6; profile *X*) reveals a sequence of inclined, parallel planar reflection interfaces occurring between 1 and 2 km (1–2 sec) beneath the bottom which resemble the upper surfaces of

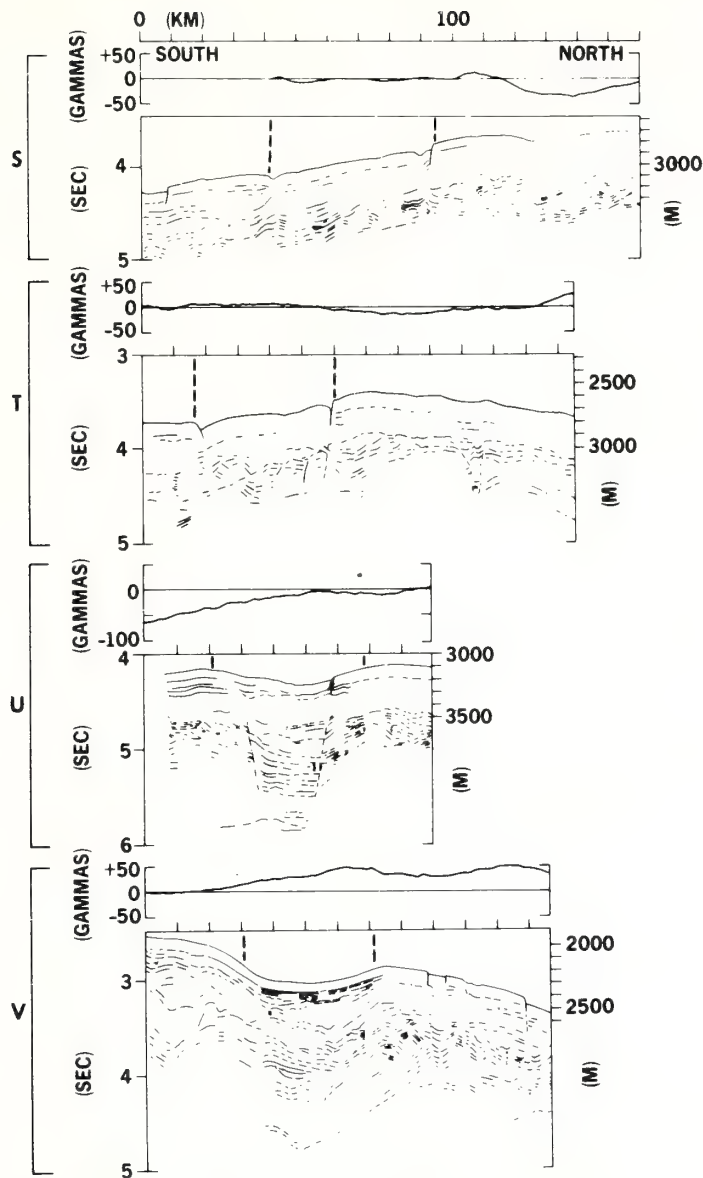


Fig.5. Line drawings of continuous seismic reflection and residual magnetic profiles *S* through *V*, as in Fig.3.

tilted fault blocks, each several tens of kilometers wide in the direction of the profile along the continental margin; the associated residual magnetic field remains relatively smooth. The attitude of overlying sedimentary layers appears to be controlled by the attitudes of the presumed fault blocks. The graben-like structure continues beneath the upper continental slope as a sediment-filled trough within a wider zone that coincides

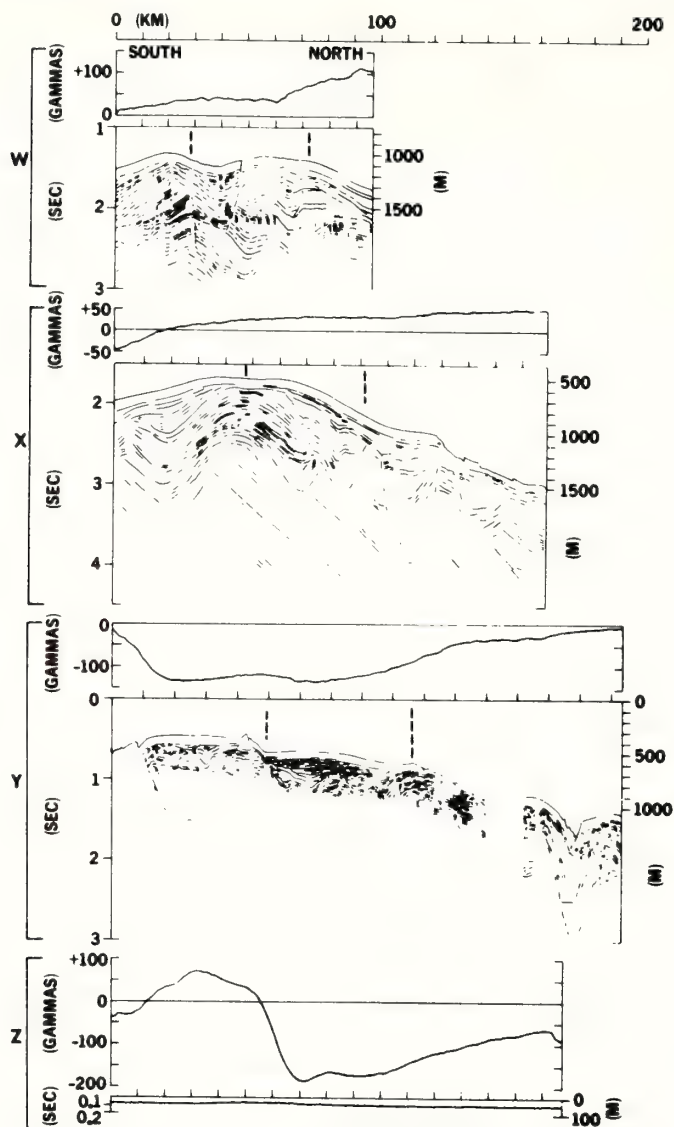


Fig.6. Line drawings of continuous seismic reflection and residual magnetic profiles *W* through *Z*, as in Fig.3.

with a marked 100-gamma decrease in residual magnetic intensity (Fig.6; profile *Y*). A similar magnetic anomaly is recorded on a profile along the outer continental shelf in the projected position of the trough, suggesting that the trough may continue landward at least as far as the outer continental shelf (Fig.6; profile *Z*). The landward projection of the fracture zone intersects a right-lateral offset of 40–80 km in the Paleozoic rocks of the Mauritanide fold belt and associated Precambrian crystalline basement along the northern

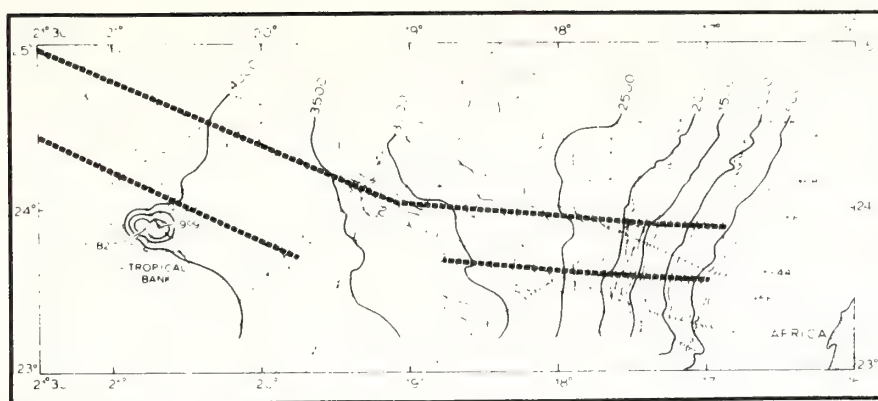


Fig. 7. Bathymetric map of the area investigated between the continental shelf and the lower continental rise off northwest Africa. The northern and southern boundaries of the graben-like structure are indicated by heavy dashed lines. Sounding tracks are indicated by light dotted-dashed lines (U.S.N.S. "Gibbs", 1970) and dashed lines (U.S.N.S. "Gibbs", 1968). Contour interval is 100 m. A vertical sounding velocity of 1500 m/sec was used.

flank of the Reguibat structural high between $23^{\circ}40'N$ and $24^{\circ}30'N$ (Choubert et al., 1968), indicating a possible relationship between the fracture zone and continental structure.

The graben-like structure can be traced seaward between the middle and lower continental rise where it appears to widen to about 65 km and its boundaries become less distinct (Fig. 3, 4, 7; profiles *P, O, N, M, L, K*). Tropical Bank, a two-peaked seamount (Rona, 1971), is situated at its southern boundary (Fig. 3; Profile *N*). The structural lineations become indeterminate for a distance of about 150 km on the lower continental rise (Fig. 3; profiles *L, K*, and Kane 9E in Lowrie and Escowitz, 1969, pp. 340–341, 14 August 1968, 1000–1600). The graben-like structure continues beneath the lower continental rise as a trough in rough acoustic basement overlain by 1.5–2.0 km (1.5–2.0 sec) of deformed sedimentary layers (Kane 9F in Lowrie and Escowitz, 1969, p. 521, 23 August 1968, 0600–1300). At the seaward limit of investigation on the lower continental rise the graben-like structure appears continuous with structural lineations described in the companion paper (Harbison et al., 1973, Fig. 1, lineations 1 and 2).

DETERMINATION OF PLATE MOTIONS

To qualify for determination of plate motions, the segment of the fracture zone investigated must have been formed by a transform fault. Structural lineations within the fracture zone segment may be eastward continuations of the Atlantis fracture zone (Fig. 1). The Atlantis fracture zone offsets the Mid-Atlantic Ridge crest about 65 km in a right lateral direction (Heezen and Tharp, 1965). The fracture zone segment offsets the magnetic quiet zone boundary (Heirtzler and Hayes, 1967) situated near the middle of the northwest African continental rise about 65 km in a right lateral direction (Fig. 1) (Rona et al., 1970).

TABLE I

Crossings of the northern boundary of the graben-like structure (Fig.1)

Ship's track	Latitude (N)	Longitude (W)	Azimuth of perpendicular to mid-point of line segment between crossings	Identification (Fig.3-6)
K				indeterminate
Kane 9F	24° 51'	21° 15'	021.8°	distinct
Kane 9E				indeterminate
L				indeterminate
M	24° 50'	21° 12'	022.1°	indistinct
N	24° 27'	20° 10'	024.0°	distinct
O	24° 23'	20° 00'	022.2°	distinct
P	24° 08'	19° 18'	019.2°	distinct
Q	24° 04'	19° 06'	005.0°	distinct
R	24° 02'	18° 47'		distinct
S*	24° 03'	18° 32'	003.3°	distinct
T	24° 00'	18° 10'	002.9°	distinct
U	23° 59'	17° 50'	000.0°	distinct
V	23° 59'	17° 39'	000.0°	distinct
W	23° 59'	17° 29'	000.0°	indistinct
X	23° 59'	17° 18'	000.0°	indistinct
Y	24° 00'	16° 50'	358.2°	distinct
Z				indeterminate

*Crossing not used for pole determination (Fig.8).

TABLE II

Crossings of the axis of structural lineation 3 (Fig.1)

Ship's track	Latitude (N)	Longitude (W)	Azimuth of perpendicular to mid-point of line segment between crossings	Identification (Harbison et al., 1973)
A	27° 29'	28° 27'		distinct
B	27° 10'	27° 22'	018.0°	distinct
C	27° 02'	26° 46'	013.0°	distinct
D	26° 44'	25° 40'	017.7°	distinct
E	26° 33'	25° 02'	017.1°	distinct
F	26° 14'	24° 07'	021.8°	distinct
G	26° 02'	23° 26'	018.0°	distinct
H	25° 44'	22° 27'	018.5°	distinct
I	25° 30'	21° 47'	022.0°	indistinct

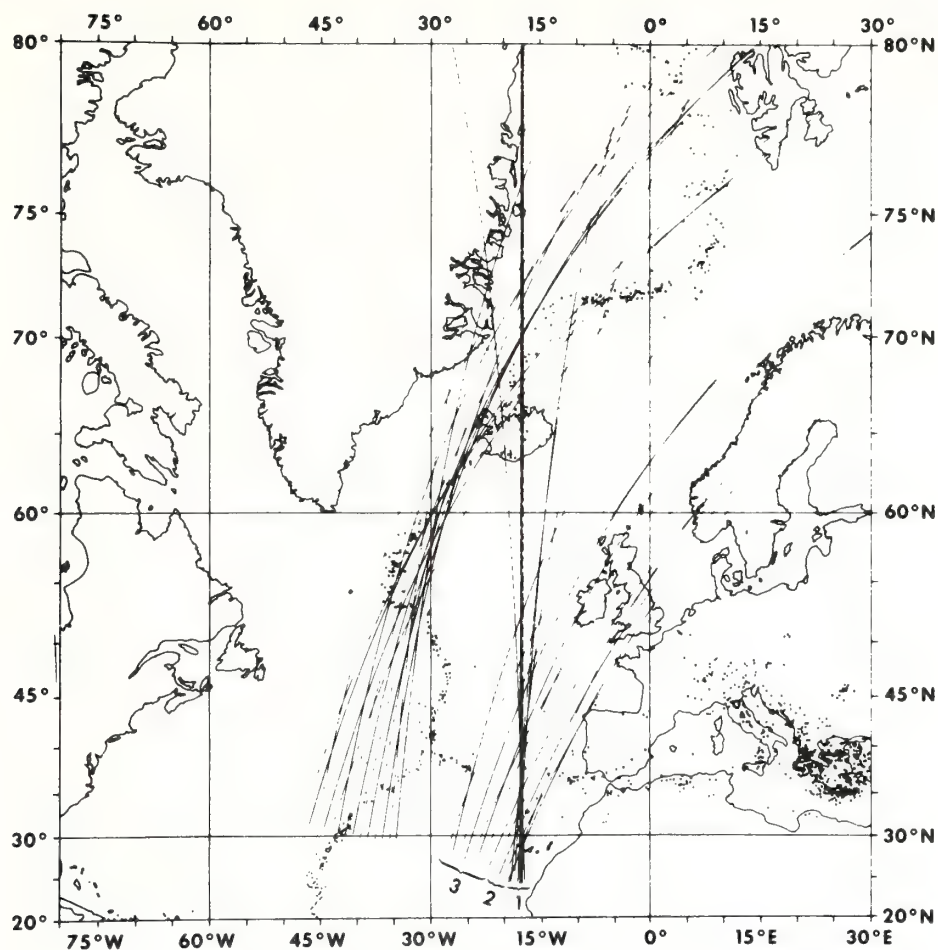


Fig.8. Great circles projected perpendicular to segments of structural lineations within the Atlantis fracture-zone system. Proceeding westward from Africa seven great circles of set 1 intersect at $36 \pm 2^\circ\text{N}$, $17.5 \pm 1^\circ\text{W}$; the azimuths of five great circles of set 2 jump about 20° to the east; eight great circles of set 3 progressively move westward. The set of great circles centered over the Mid-Atlantic Ridge intersect at $57.9 \pm 5^\circ\text{N}$, $31.4 \pm 5^\circ\text{W}$ (Phillips et al., 1971). The dots mark earthquake epicenters which delineate the crests of the Mid-Atlantic Ridge and the Azores-Gibraltar ridge (National Earthquake Information Center, 1970).

The projected lateral continuity and constant horizontal displacement suggest that the Atlantis fracture zone at the Mid-Atlantic Ridge and the fracture zone segment on the northwest African continental rise belong to the same transform fault system.

The faulted northern boundary of the graben-like structure establishes the trend of the transform fault between the outer continental shelf and the lower continental rise (Table I). The structural lineation designated 3 (Fig.1) (Harbison et al., 1973) establishes the trend of the transform fault between the lower continental rise and the abyssal hills (Table II). Plate movement occurred along these structural lineations. Azimuth to

the relative pole of plate rotation was determined by making a forward geographic position computation to project a great circle (Morgan, 1968; Bomford, 1971) perpendicular to the mid-point of each line segment between points at ship's crossings of a given structural lineation. The line segments range from 20 to 150 km in length corresponding to a time interval of 1–10 my. Each line segment so defined approximates a tangent to a small circle about a pole of plate rotation (Fig.8). The pole of plate rotation is located at the intersection of the great circles. This method, in which each line segment between known points on a structural lineation is treated independently, as opposed to the practice of fitting small circles to sets of points, facilitates observation of violations of the assumption of a fixed pole (Harrison, 1972).

MESOZOIC PLATE MOTIONS

The Early Jurassic through Middle Cretaceous directions of plate movement along the structural lineations described (Fig.2, 8) are given assuming that the position of Africa has remained fixed and North America has moved away from Africa in a westerly direction. The dating is subject to change as more direct knowledge of the age of the ocean bottom is obtained, but the fundamental motions determined should remain valid.

(1) The earliest relative direction of motion of the North American plate in a reference frame fixed with respect to the African plate progressively changed from 268 to 275° along a distance of 230 km from the outer edge of the northwest African continental shelf (24°00'N, 16°50'W) to the middle of the continental rise (24°04'N, 19°06'W) during the Early and Middle Jurassic (≤ 180 to > 155 my). The associated earliest pole of plate rotation was located at $36 \pm 2^\circ\text{N}$, $17.5 \pm 1^\circ\text{W}$ with respect to the present position of Africa, based on the intersections of seven great circles with errors estimated equal to the lengths of the major (longitudinal) and minor (latitudinal) axes of an ellipse which encompasses all of the intersections (Fig.8). The total rotation of the North American plate about this pole was 10°. The plate motion deduced differs from that of Le Pichon and Fox (1971) who predicted a rotation of 45.6° about a pole at 58.3°N, 1.0°W with respect to Africa between about 180 and 80 myB.P. based on the assumption that the early opening of the North Atlantic was controlled by the offset of the North American continental margin along the Newfoundland fracture zone. The plate motion deduced also differs from that of Pitman and Talwani (1972) who determined a rotation of 8.93° about a pole at 72.7°N, 165.7°W with respect to Africa between 180 and 155 myB.P. based on the juxtaposition of magnetic isochrons from opposite sides of the Mid-Atlantic Ridge.

The earliest pole of plate rotation with respect to the present position of Africa lies on the Azores–Gibraltar ridge (Fig.8). The location of this pole indicates that the opening of the Atlantic between North America and Africa was independent of the opening between North America and Eurasia with an intervening plate boundary in the position of the present Azores–Gibraltar ridge. Other lines of evidence suggest that the opening between North America and Africa preceded that between North America and Eurasia

(Pitman and Talwani, 1972). The apparent block faulting beneath the northwest African continental slope (Fig.6; profile *X*) may have developed in response to a tensional stress field associated with this early phase of rifting; a prominent magnetic anomaly occurs at this continental slope (Rona et al., 1970) and it has not been determined whether or not the underlying crust is continental.

(2) The relative direction of motion of the North American plate with respect to the African plate varied between 289 and 292° along a distance of 285 km from the middle ($24^\circ 04'N$, $19^\circ 06'W$) to the lower continental rise ($25^\circ 02'N$, $21^\circ 43'W$) off northwest Africa during the Late Jurassic (> 155 to about 150 my). The azimuth to the associated pole of plate rotation jumped about 20° of arc eastward from the prior pole based on the projections of five great circles and moved an unknown amount northward. These five great circles do not converge. The absence of convergent intersections indicates either small errors in determinations of azimuth, non-rigid plate behavior resulting in secondary alteration of trend, or sufficiently rapid change in the position of the pole of plate rotation to preclude convergence. The eastward jump in azimuth of the pole of plate rotation implies that a major reorganization of plate motion occurred.

The change in the surrounding configuration of continents resulting from horizontal plate motion (sea-floor spreading), and the eustatic change in sea level related to vertical plate motion (ocean-basin subsidence and development of a world mid-ocean ridge and marginal trench system), caused the circulation of the Atlantic to change (Rona, 1970, 1972). The Atlantic circulation changed during the Late Jurassic from that of a restricted sea, a condition which had prevailed since the Late Triassic evidenced by the extent of salt deposits of probable Late Triassic through Middle Jurassic age as far seaward as beneath the lower continental rise off northwest Africa (Rona, 1969; Hayes et al., 1972; Waterman et al., 1972) (Fig.1; Deep-Sea Drilling Project sites 139, 140), to that of a more open ocean.

(3) The relative direction of motion of the North American plate with respect to the African plate varied between 283 and 292° along a distance of 850 km from the lower continental rise ($25^\circ 30'N$, $21^\circ 47'W$) to the abyssal hills ($27^\circ 29'N$, $28^\circ 27'W$) off northwest Africa during the Late Jurassic and Early Cretaceous (about 150–100 my). Eight great circles projected normal to the structural lineation designated 3 (Fig.1, 8) do not converge, indicating either small errors in azimuth determination, non-rigid plate behavior, or sufficiently rapid change in the pole position to preclude convergence. Interpretation of evidence from the western central North Atlantic suggests the existence of a stationary pole in the vicinity of $67^\circ N$, $10^\circ W$ with respect to North America during the Late Jurassic (155–135 my) (Vogt et al., 1971) and the absence of a unique pole during the Cretaceous (Vogt and Johnson, 1971). Further work is required to resolve whether the pole position was changing or stationary during the Late Jurassic. However, the evidence from both sides of the central North Atlantic indicates that the position of the pole was changing during the Cretaceous. The nature of this change is evident in the eastern central North Atlantic where the direction to the pole of rotation with respect to Africa appears to migrate progressively westward toward the Cenozoic relative motion pole (Fig.8).

ACKNOWLEDGEMENTS

R. K. Perry and N. Z. Cherkis of N.R.L. helped to collect and reduce the data. C. Brier assisted by R. Nabor of N.R.L. was responsible for the electronics at sea. N.R.L. Code 8004 gave reliable support. P. J. Grim and A. Herman of N.O.A.A. applied their computer programs to the data processing. Captain R. E. Salman and the officers and crew of the U.S.N.S. "J. W. Gibbs" provided exceptional cooperation. The preparation of the paper was partially supported by funding from the National Science Foundation, International Decade of Ocean Exploration, as part of the N.O.A.A. Trans-Atlantic Geotraverse (T.A.G.).

REFERENCES

- Bomford, F., 1971. *Geodesy*. Oxford Univ. Press, London, 3rd ed., 731 pp.
- Cain, J. C., Hendricks, S. J., Langel, R. A. and Hudson, W. V., 1967. A proposed model for the International Geomagnetic Reference Field 1965. *Geomagn. Geoelectr.*, 19:335.
- Choubert, G., Faure-Muret, A. and Sougy, J., (Coordinators), 1968. *International Tectonic Map of Africa 1:5,000,000 Sheet 1*. Association of African Geological Surveys.
- Fox, P. J., Pitman, III, W. C. and Shepard, F., 1969. Crustal plates in the central Atlantic: evidence for at least two poles of rotation. *Science*, 165:487-489.
- Harbison, R. N., Lattimore, R. K. and Rona, P. A., 1973. Structural lineations in the Canary basin, eastern central North Atlantic. *Mar. Geol.*, 14: 269-275.
- Harrison, C. G. A., 1972. Poles of rotation. *Earth Planet. Sci. Lett.*, 14:31-38.
- Hayes, D. E., Pimm, A. C., Beckman, J. P., Benson, W. E., Berger, W. H., Roth, P. H., Supko, P. R. and Von Rad, U., 1972. *Initial Reports of the Deep-Sea Drilling Project XIV*. U.S. Government Printing Office, Washington D.C. 975 pp.
- Heezen, B. C. and Tharp, M., 1965. Tectonic fabric of the Atlantic and Indian oceans and continental drift. *Phil. Trans. R. Soc. Lond. - Symp. Continental Drift, Ser. A*, 258:90-106.
- Heezen, B. C. and Tharp, M., 1968. Physiographic diagram of the North Atlantic (revised). *Geol. Soc. Am., Spec. Pap.*, 65: 122 pp.
- Heirtzler, J. R. and Hayes, D. E., 1967. Magnetic boundaries in the North Atlantic Ocean. *Science*, 157:185-187.
- Heirtzler, J. R., Dickson, G. O., Herron, E. M., Pitman, III, W. C. and Le Pichon, X., 1968. Marine magnetic anomalies, geomagnetic field reversals and motions of the ocean floor and continents. *J. Geophys. Res.*, 73:2119-2136.
- Hollister, C., Ewing, J. I., Habib, D., Hathaway, J. C., Lancelot, Y., Luterbacher, H., Paulus, F. J., Poag, W., Wilcoxon, J. A. and Worstell, P., 1972. *Initial Reports of the Deep-Sea Drilling Project XI*. U.S. Government Printing Office, Washington, D. C., 1077 pp.
- Lattimore, R. K., Rona, P. A. and DeWald, O. E., 1973. Magnetic anomaly sequence in the central North Atlantic Ocean. *J. Geophys. Res.* (in press).
- Le Pichon, X., 1968. Sea-floor spreading and continental drift. *J. Geophys. Res.*, 73:3661-3697.
- Le Pichon, X. and Fox, P. J., 1971. Marginal offsets, fracture zones, and the early opening of the North Atlantic. *J. Geophys. Res.*, 76:6294-6308.
- Lowrie, A. and Escowitz, E. (Editors), 1969. Kane 9. In: *Global Ocean Floor Analysis and Research Data Series, I*. U.S. Naval Oceanographic Office, Washington, D.C., 971 pp.
- McKenzie, D. P. and Parker, R. L., 1967. The North Pacific: an example of tectonics on a sphere. *Nature*, 216:1276-1280.
- Morgan, W. J., 1968. Rises, trenches, great faults, and crustal blocks. *J. Geophys. Res.*, 73:1959-1982.
- National Earthquake Information Center, 1970. World Seismicity 1961-1969. *Environ. Sci. Serv. Adm.*, Chart NEIC-3005.

- Peterson, M. N. A., Edgar, N. T., Cita, M., Gartner, S., Goll, R., Nigrini, C. and Von Der Borch, C., 1970. *Initial Reports of the Deep-Sea Drilling Project II*. U.S. Government Printing Office, Washington, D.C., 501 pp.
- Phillips, J. D. and Luyendyk, B. P., 1970. Central North Atlantic plate motions over the last 40 million years. *Science*, 170:727–729.
- Phillips, J. D., Luyendyk, B. P. and Forsyth, D. W., 1971. Central North Atlantic plate motions. *Science*, 174:846.
- Pitman, III, W. C. and Talwani, M., 1972. Sea-floor spreading in the North Atlantic. *Bull. Geol. Soc. Am.*, 83:619–646.
- Rona, P. A., 1969. Possible salt domes in the deep Atlantic off northwest Africa. *Nature*, 224:141–143.
- Rona, P. A., 1970. Comparison of continental margins of eastern North America at Cape Hatteras and northwestern Africa at Cap Blanc. *Bull. Am. Assoc. Pet. Geol.*, 54:129–157.
- Rona, P. A., 1971. Bathymetry off central northwest Africa. *Deep-Sea Res.*, 18:321–327.
- Rona, P. A., 1972. Relation between rates of sediment accumulation on continental shelves and sea-floor spreading in the central North Atlantic. *Geol. Soc. Am. Bull., Programs Ann. Meetings, 1972*, 4(7):644 (Abstr.).
- Rona, P. A., Brakl, J. and Heirtzler, J. R., 1970. Magnetic anomalies in the northeast Atlantic between the Canary and Cape Verde islands. *J. Geophys. Res.*, 75: 7412–7420.
- Vogt, P. R. and Johnson, G. L., 1971. Cretaceous sea-floor spreading in the western North Atlantic. *Nature*, 234:22–25.
- Vogt, P. R., Anderson, C. N. and Bracey, D. R., 1971. Mesozoic magnetic anomalies, sea-floor spreading, and geomagnetic reversals in the southwestern North Atlantic. *J. Geophys. Res.*, 76:4796–4823.
- Wilson, J. T., 1965. A new class of faults and their bearing on continental drift. *Nature*, 207:343–347.
- Waterman, L. S., Sayles, F. L. and Manheim, F. T., 1972. Interstitial water studies on small core samples, leg 14. In: D. E. Hayes, et al. (Editors), *Initial Reports of the Deep-Sea Drilling Project, XIV*. U.S. Government Printing Office, Washington, D.C., pp. 753–759.

Development and Preliminary Test of a 1000-Hertz Pulse Compression Seismic Reflection Profiling System

PETER A. RONA,¹ ANTARES PARVULESCU,² WILLIAM LIANG,³ AND
CHARLES A. LAUTER, JR.¹

A continuous seismic reflection profiling system was developed to achieve acoustic penetration into sea floor sediments between that achieved by air guns and by 3500-Hz systems in all water depths at ship cruising speeds. The system utilizes a multiple-bit correlator to compress a 1000-Hz chirp signal of low amplitude and long duration into a signal of high amplitude and short duration, thereby significantly increasing the signal-to-noise ratio without loss of time resolution. The results of a field test demonstrate the feasibility of such a system.

Present marine seismic reflection profiling systems involve towing a sound source such as an air gun [Ewing and Zaunere, 1964] or a sparker [Hersey, 1963] and an array of receiving hydrophones from a moving ship. Deterioration of the signal-to-noise ratio with increase in ship's speed effectively limits the operation of such towed systems to speeds less than about 18 km/hour (10 knots), although concurrent bathymetric, gravimetric, and magnetic measurements can be made at faster cruising speeds.

Development of a seismic reflection profiling system was undertaken with the objective of achieving acoustic penetration beneath the ocean bottom between that obtained by a small air gun of 655 cm³ (40 in.³) capacity and a conventional 3500-Hz subbottom profiling system in water depths of about 5 km at the cruising speed of NOAA class 1 research vessels, about 28 km/hour (15 knots). The penetration would suffice to reach acoustic basement beneath most of the ocean bottom seaward of the thick sediment accumulations at continental margins. The increase in ship's speed, nearly double that presently attained, would result in a correspond-

ing increase in efficiency of ship utilization for underway concurrent bathymetric and geophysical measurements.

The system development entailed selection of an optimum acoustic signal to achieve the performance objectives, construction of an appropriate sonar transducer, and utilization of pulse compression techniques to increase the amount of acoustic energy introduced into the water. The prototype system was field tested in the deep ocean basin on a NOAA class 1 vessel, the NOAA Ship *Discoverer*. The test is considered preliminary because all performance objectives were not realized. However, sufficient data were obtained to extrapolate to the ultimate performance of the 1000-Hz pulse compression seismic reflection profiling system.

ACOUSTIC SIGNAL

A center operating frequency of 1000 Hz was selected for the acoustic signal, because this frequency is low enough for substantial improvement in subbottom penetration over the widely used 3500-Hz profiling systems and high enough to allow directivity gain from a transducer array of convenient size. The 1000-Hz signal has certain advantages and disadvantages over the lower-frequency signals (tens to hundreds of hertz) of air guns and sparkers. Flow and ship-generated noise are known to be larger at the lower than at the higher audio frequencies [Urlick, 1967], so that at least a 10-db advantage over the lower-frequency system is gained by operating at 1000 Hz. The 1000-Hz

¹Atlantic Oceanographic and Meteorological Laboratories, NOAA, Miami, Florida 33149.

²Hawaii Institute of Geophysics, University of Hawaii, Honolulu, Hawaii 96822.

³Underwater Technology Corporation, Nanuet, New York 10954.

signal of a given duration is reflected as a single pulse from each smooth reflector without the bubble pulses that complicate the signals of the lower-frequency systems. The 1000-Hz signal is equivalent to the lower-frequency signals with respect to the absorption of sound in seawater, which is essentially insignificant at all frequencies from 10 to 2000 Hz. The 1000-Hz signal undergoes greater loss by absorption in sediments and random scattering from rough interfaces than the lower-frequency signals.

The signal bandwidth available for the transducer utilized is 140 Hz. This bandwidth represents a compromise between electroacoustic conversion efficiency and resolution of reflecting interfaces and should resolve two reflecting interfaces with a time separation of 10 msec (about 10 meters).

The signal duration can be switch-selected at 0.5, 1.0, 2.0, and 4.0 sec. The transmission of the signal must cease before the first echoes are recovered from the sediment-water interface, and so use in water depths of less than about 200 meters is precluded. A simple design change to shorten the minimum signal duration could, however, extend operation to water depths

shoaler than 200 meters. The reduction in the amount of acoustic energy transmitted would be compensated by the decrease in spreading loss in shallow water.

SONAR TRANSDUCER

The sonar transducer was constructed after designs of the WT-2 series developed at Hudson Laboratories of Columbia University [Hole, 1969, pp. 224-252, Figures XVII-7, 9]. It consists of four units, each constructed of a number of barium titanate cylinders cemented together to form a single long cylinder 67.3 cm (26.5 in.) in length and 7.5 cm (3 in.) in outside diameter (Figure 1). The ceramic material is so polarized and equipped with electrodes that sinusoidal voltage applied to the electrodes will vary sinusoidally the total length of this assembly by about 25μ (1×10^{-3} in.) at full drive. The length of the active portion is sandwiched between two circular pistons 27.9 cm (11 in.) in diameter, and this entire assembly is held in compression by a steel threaded rod and two nuts. An outer cylindrical jacket of aluminum is fitted over this active assembly, and O rings are used to maintain air between the inner faces



Fig. 1. Sonar transducer consisting of four cylindrical units with eight active faces mounted on an aluminum towing structure for the test.

of the two pistons for both acoustic loading and prevention of short circuits in the electrodes. The two piston faces move physically against the water in the same phase of compression or rarefaction. The length of the assembly is such that the radiation at right angles to the cylindrical axis is in phase from both pistons, whereas the radiation in the axial direction substantially cancels out due to the geometric separation of the two pistons, which is about half the wavelength. The four cylinders that comprise the sonar transducer constitute a planar array of eight active faces configured to have a directional pattern of approximately 1 radian of beamwidth in the fore and aft direction and 1.5 radians to either side. Pressure release foam is mounted one quarter wavelength above the central plane of the array in order to reduce upward radiation and increase downward radiation. The electrostrictive ceramic active material of the transducer allows use of the same transducer for reception, with the same directivity pattern as for transmission.

The transducer gain due to directivity (directivity index) is of the order of 10 db on both transmit and receive. The overall source level in the downward-looking beam is estimated at about 109 db relative to 1 μ b at 1 meter using the design maximum rating of 3000 watts. The transducer efficiency is approximately 50% at resonance. Including the effects of the 10-db directivity index and the 50% efficiency of the transducer, the acoustic energy projected toward the sea floor is about 5000 joules. Comparable input energy levels are available from air guns and sparkers, but the conversion efficiency from thermodynamic to acoustic energy in such impulsive devices is not large.

For the preliminary test of the seismic profiling system, the transducer array was assembled on an aluminum towing structure of no particular streamline design, intended to tow stably at cruising speeds up to 15 knots (Figure 1). A lead nose and tail fins provide stabilization. Acoustic reception in the upper range of ships' speeds is undoubtedly hampered by turbulence due to the lack of streamlining. A seismic streamer 8 meters (25 ft) long containing five pairs of variable reluctance hydrophones mounted about 1 meter apart (Bolt Associates, Inc., model 1011) was used as a receiver during a portion of the test because of

the stability of the streamer array relative to the 1.5-meter (5-ft) wavelength of the acoustic signal used. The ultimate objective is to permanently hull-mount the sonar transducer. A line of cylinders could be mounted athwartships to transmit and fore-and-aft to receive, thereby achieving a narrow beamwidth according to the principle of a crossed linear array.

CORRELATOR

The use of correlation techniques for extracting a weak but expected signal from strong background noise dates back about 30 years [North, 1943; van Vleck and Middleton, 1946]. After World War II the technique was extensively utilized in sonar [Faran and Hills, 1952; Anderson, 1956; Stewart and Westerfield, 1959; Turin, 1960; Stewart et al., 1965; Allen et al., 1963], radar [Klauder et al., 1960], and communications. Application to marine seismic profiling was proposed by Clay [1959] and implemented by Clay and Liang [1962], Clay et al. [1964], and Chramiec [1969].

In principle, the correlation detector maintains a recording of the transmitted waveform (reference signal) and compares it with the received waveform (consisting of noise and possibly of echo as well) to determine a measure of similarity between these two waveforms. When the noise is reasonably random and white, the comparison procedure is successful most frequently if it uses the cross-correlation integral, which is the summation of many products consisting of the instantaneous values of the two waveforms. If the transmitted signal is chosen to be reasonably broad band and random, the similarity measure is very large, but only at or near the instant when the two complicated waveforms coincide in time. The signal-to-noise power ratio at the output of a matched filter or correlation receiver is [Turin, 1960] the energy in the transmitted signal divided by the noise power. The energy in the transmitted signal is the signal power multiplied by the signal duration. The correlation receiver compresses a signal having a long time duration into a short time interval by coherently adding successive components of the signal. The gain in signal-to-noise ratio is approximately equal to twice the time-bandwidth product.

The correlator used in the present system (A. Parvulescu, L. Kroenke, and W. Liang, un-

published manuscript, 1973) extends general principles described by *Anderson* [1956] and by *Allen and Westerfield* [1964]. It is essentially a wired program digital computer specialized to perform this one computation on-line in real time. It has a pair of memory units built from large-scale integrated microcircuits; the memories store, respectively, the transmitted reference in its entirety and the most recent corresponding duration of the received reflected signal. The correlator is arranged to accept reference and reflected signals of durations 0.5, 1.0, 2.0, and 4.0 sec corresponding to the durations selected for the coded signal generator and quantizes the two signals into 128 levels plus sign; it possesses a quasi-analog dynamic range of 42 db. Since memories are digital, the two waveforms are each sampled at 2000, 1000, and 500 samples per second, and their amplitude is quantized in 8 bits. As an example, the use of a 0.5-sec signal means that 1000 independent samples of both reference and the most recent reflected signal are stored, and that 1000 multiplications (and 1000 summations) are performed sample-by-sample every 0.005 sec, yielding a numerical value for the cross correlation

at that 0.005-sec time instant. Digital-to-analog conversion provides a signal that after further filtering can be applied to any of the widely used seismic recorders. The entire process is synchronized by trigger pulses (Figure 2). Infinitely clipped signals ('clipper,' 'polarity coincidence,' or 'zero-crossing' correlators) used in past work retain only the strongest of several overlapping signals, so that a strong reflection from the sediment-water interface effectively suppresses weaker reflections from subbottom interfaces. The multiple-bit correlator used in the present work retains amplitude information essential to the detection of subbottom reflection interfaces of lower amplitudes than the bottom reflection.

The advantage of correlation can be variously described as follows. (1) The total energy transmitted into the water by a power-limited amplifier and a power-limited transducer is greatly increased without loss of time resolution. The bandwidth of signal used determines the shortest time resolution achievable, and the long but random coded signal retains the same resolution after correlation. For example, a 1000-watt power amplifier used in the system described could transmit only 7 joules into the transducer at maximum time resolution for short (7 msec) pulses. Transmission of a 1-sec pulse occupying the same bandwidth allows transmission of 1000 joules into the water with no loss of the 7-msec resolution in the correlated signal for a power gain of about 140. (2) The time-bandwidth product of a short pulse system at 1000 watts power level would be unity. The time-bandwidth product for a signal of 1-sec duration would be 140, the same value of gain. (3) To supply the same energy of 1000 joules in a short (7 msec) pulse would require a power amplifier and transducer capable of 140,000 watts (about 200 horsepower). (4) Although the resolution of a 7-msec signal with 140-Hz bandwidth remains 7 msec after reflection, the use of a correlated signal 1 sec in duration reduces the noise interference to that associated with a 1-Hz-wide filter ($1 \text{ Hz} = 1/\text{bandwidth}$), so that the signal-to-noise ratio is improved in the ratio 140 to 1.

We selected an FM chirp for the preliminary test but contemplate digitally generated waveforms for later stages of development. The block diagram in Figure 2 shows that the waveform applied to the power amplifier undergoes several

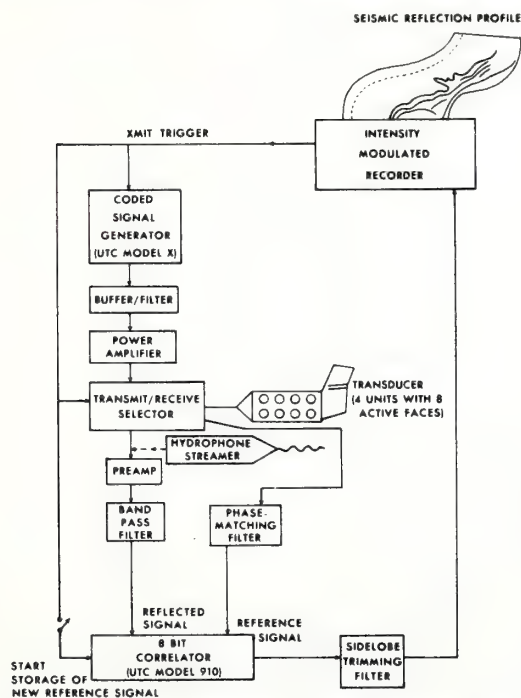


Fig. 2. Block diagram of the 1000-Hz pulse compression seismic reflection profiling system.

modifications before entering the correlator as a 'reflected signal:' the transducer resonance introduces one set of phase and amplitude changes, and the use of a narrow receiving filter further affects relative phase of the reflected chirp signal. For optimum performance, the correlator should be supplied with a reference waveform (phase-matching filter in Figure 2), which is identical to the actual transmitted signal. This is ignored in the preliminary test reported here, and the mismatch would decrease both the signal-to-noise power gain and resolution.

EXPERIMENTAL RESULTS

To test the 1000-Hz system (Figures 1 and 2), a profile was made across Abaco Canyon at the northern end of the Bahama Banks (Figure 3). The following results were obtained between the specified distances along the profile at ship's speed of 14 km/hour (7.5 knots) (Figure 4):

0-20 km

10-sec recorder sweep.
0.5-sec outgoing signal.
water depth, 1.4-1.5 sec (1050-1125 meters).
subbottom penetration, 0.25 sec (about 250 meters).
resolution, 0.05 sec (about 50 meters).

20-28 km

5-sec recorder sweep.
0.5-sec outgoing signal.

water depth, 1.6-2.5 sec (1200-1875 meters).

subbottom penetration, 0.25 sec (about 250 meters).

resolution, 0.05 sec (about 50 meters).

28-44 km

5-sec recorder sweep.

1.0-sec outgoing signal.

water depth, 2.5-2.8 sec (1875-2100 meters).

subbottom penetration, 0.50 sec (about 500 meters) at buried channel within Abaco Canyon between 32 and 37 km along the profile.

resolution, 0.10 sec (about 100 meters).

The results demonstrate that the 1000-Hz signal is capable of at least 0.50 sec (about 500 meters) of subbottom penetration under the conditions of the test. Increase in the amount of acoustic energy transmitted into the water by lengthening the duration of the outgoing signal should improve the subbottom penetration. The resolution achieved was less than that theoretically attainable with the system and is attributed to improper match of the transmitted and reference signals, as well as to the effect of rough sea floor, which increased the duration of the return signal.

The NOAA Ship *Discoverer* is equipped with a conventional hull-mounted 3500-Hz profiling system that was operated at 160 watts electric input power to stay within the steady state

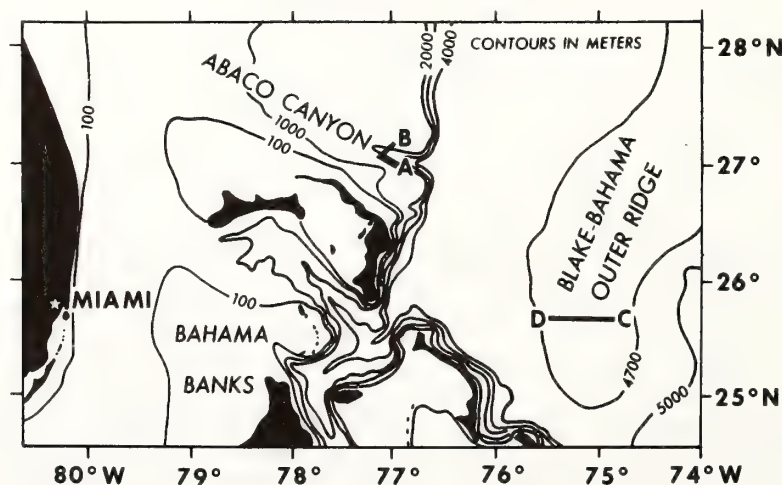


Fig. 3. Locations of 1000-Hz seismic reflection profile A-B (Figure 4) across Abaco Canyon, and of 3500-Hz profile C-D (Figure 5) across Blake-Bahama Outer Ridge.

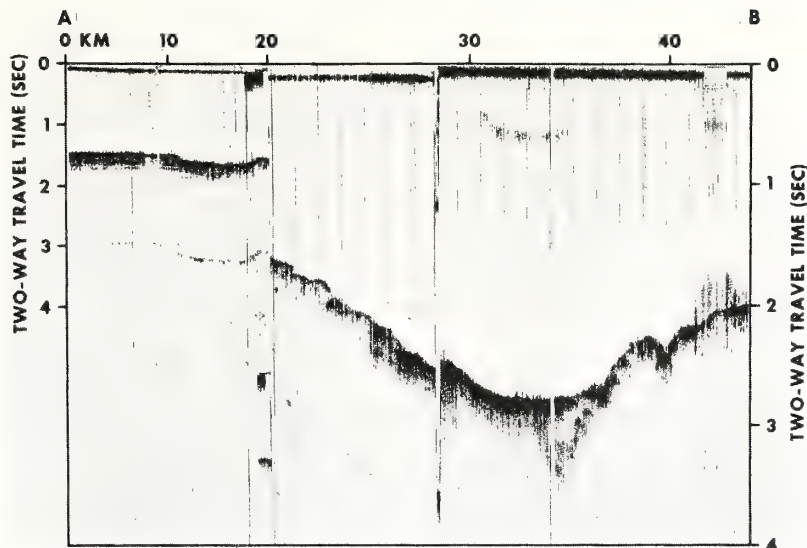


Fig. 4. Profile A-B obtained with 1000-Hz pulse compression system across Abaco Canyon by using an 8-bit correlator. Two-way travel time scale on left applies to 0-20 km along the profile; scale on right applies to 20-44 km.

rating of the transducer (Edo model 415). The 8-bit correlator was used with the 3500-Hz system to compress a transmitted pulse of 0.5-sec duration to a measured value of 0.005 sec; the signal bandwidth was 350 Hz. The profile obtained with the 3500-Hz system in about 7 sec (5250 meters) water depth (Figure 5) at cruising speed of 28 km/hour (15 knots) can be used to extrapolate the potential performance of the 1000-Hz system as follows. (1) Penetration of 0.10 to 0.15 sec (about 100 to 150 meters) was achieved with input power of 160 watts. Extrapolation of power levels indi-

cates that a power increase by a factor of 20 to the level of 3000 watts used in the 1000-Hz system would increase subbottom penetration of the 3500-Hz system by a factor in the range of $(20)^{1/2} = 4.4$ for perfect reflectors and $(20)^{1/4} = 2.1$ for imperfect reflectors resulting in about 0.21 to 0.66 sec (about 210 to 660 meters) of penetration. (2) At any given power level, operation at 1000-Hz frequency will provide better penetration than at 3500 Hz. The wavelength ratio is 3.5 to 1, but the improvement ratio cannot be specified, as it is dependent on both the Q of the solid medium through which

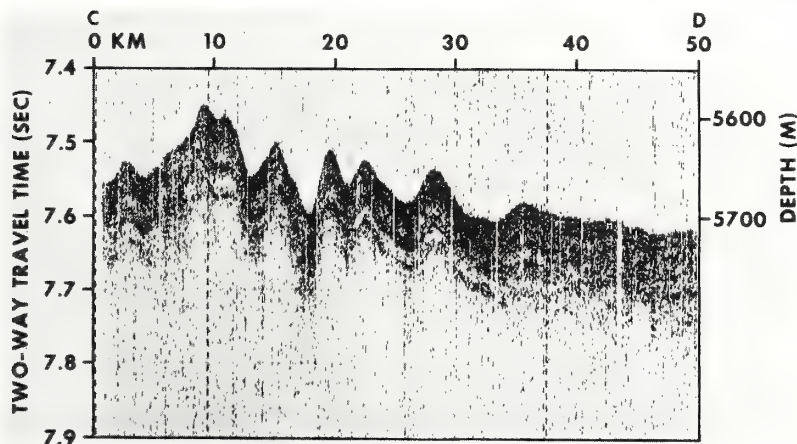


Fig. 5. Profile C-D obtained with 3500-Hz system by using an 8-bit correlator.

the sound is propagated and the roughness of the interface from which the sound is reflected (or scattered). Both Q and interface roughness will work to the advantage of the 1000 over the 3500-Hz frequency. (3) To extrapolate separately the record obtained at 1000 Hz from the power level actually used of 1200 to 3000 watts of electric input power (a factor of 2.5) assures an increase of subbottom penetration, as was discussed above, by a factor in the range of $(2.5)^{1/2} = 1.6$ for perfect reflectors to $(2.5)^{1/4} = 1.3$ for imperfect reflectors, which would result in about 1 sec of subbottom penetration. (4) The 3500-Hz system attained the theoretical resolution of about 0.005 sec (about 5 meters) (Figure 5), indicating that after careful trimming the 8-bit correlator can compress the signal and retain resolution even when the ocean bottom is relatively rough. The 1000-Hz system would obtain comparable resolution with an acoustic source having at least 200-Hz bandwidth, as resolution is proportional to the reciprocal of the bandwidth.

CONCLUSION

The preliminary test indicates that the 1000-Hz system is feasible, and it is a recommended way to make routine seismic reflection profiles in the future.

Acknowledgments. Dr. C. S. Clay of the University of Wisconsin, Dr. G. H. Keller, G. Lapiene, Dr. J. Proni, and R. Ross of NOAA provided useful advice. Dr. L. W. Butler was Chief Scientist during the field test. Captain F. J. Tucker, Jr., the officers and crew of the NOAA Ship *Discoverer* cooperated effectively.

The system was assembled by Underwater Technology Corporation under a cost-sharing agreement with NOAA. The assembly and field testing of the prototype 1000-Hz seismic profiling system was partially supported by funding from the International Decade of Ocean Exploration (IDOE), National Science Foundation, to the NOAA Trans-Atlantic Geotraverse (TAG).

Hawaii Institute of Geophysics contribution 536.

REFERENCES

- Allen, W. B., and E. C. Westerfield, Digital compressed-time correlators and matched filters for active sonar, *J. Acoust. Soc. Amer.*, **36**, 121, 1964.
- Allen, W. B., J. L. Stewart, R. M. Zarnowitz, and M. K. Brandon, Pseudorandom signal-correlation methods of underwater acoustics, 2, Instrumentation, *J. Acoust. Soc. Amer.*, **39**, 62, 1966.
- Anderson, V. C., Deltic correlator, *Tech. Memo. 37*, Harvard Univ. Acoustic Res. Lab., Cambridge, Mass., 1956.
- Chramiec, M. A., Improvements to subbottom profiling sonars through application of correlation signal processing, M.S. Thesis, 82 pp., Univ. of R. I., Kingston, 1969.
- Clay, C. S., Methods for geophysical measurements using noise or an FM source, *Tech. Rep. 72*, 45 pp., Columbia Univ., Hudson Lab., New York, 1959.
- Clay, C. S., and W. L. Liang, Continuous seismic profiling with matched filter detector, *Geophysics*, **27**, 786, 1962.
- Clay, C. S., W. L. Liang, and S. Wisotsky, Seismic profiling with a hydroacoustic transducer and correlation receiver, *J. Geophys. Res.*, **69**, 3419, 1964.
- Ewing, J., and R. Zaunere, Seismic profiling with a pneumatic sound source, *J. Geophys. Res.*, **69**, 4913, 1964.
- Faran, J. J., Jr., and R. Hills, Jr., Correlators for signal reception, *Tech. Memo. 27*, Harvard Univ. Acoustic Res. Lab., Cambridge, Mass., 1952.
- Hersey, J. B., Continuous reflection profiling, in *The Sea*, edited by M. N. Hill, vol. 3, pp. 47-72, Interscience, New York, 1963.
- Hole, W. L., Ed., Hudson Laboratories, 1951-1969 (Final Summary Report), Unclassified Technical Programs, CU-212-69-ONR-266-Phys., 349 pp., Columbia Univ., Hudson Laboratories, New York, 1969.
- Klauder, J. R., A. C. Price, S. Darlington, and W. J. Albersheim, The theory and design of chirp radars, *Bell System Tech. J.*, **39**, 745, 1960.
- North, D. O., Analysis of the factors that determine signal/noise discrimination in radar, *Rep. PTR-6C*, RCA Lab., Princeton, N. J., June 1943.
- Stewart, J. L., and E. C. Westerfield, A theory of active sonar detection, *Proc. Inst. Radio Eng.*, **47**, 872, 1959.
- Stewart, J. L., W. B. Allen, R. M. Zarnowitz, and M. K. Brandon, Pseudorandom signal correlation methods of underwater acoustics, 1, Principles, *J. Acoust. Soc. Amer.*, **37**, 1079, 1965.
- Turin, G. Z., An introduction to matched filters, *IRE Trans. Information Theory*, **IT-6**, 311, 1960.
- Urick, R. J., *Principles of Underwater Sound for Engineers*, 342 pp., McGraw-Hill, New York, 1967.
- van Vleck, J., and D. Middleton, A theoretical comparison of the visual, aural and meter reception of pulsed signals in the presence of noise, *J. Appl. Phys.*, **17**, 940, 1946.

(Received June 17, 1973;
revised July 13, 1973.)

Delaware Shelf Valley: Estuary Retreat Path, Not Drowned River Valley

ABSTRACT

The transverse shelf valleys of the North American Atlantic Shelf have generally been interpreted as relict fluvial landforms. While they were indeed initiated as such, they subsequently became estuary retreat paths, in which constructional as well as erosional topography has been formed in a shallow marine environment subsequent to transgression. The Delaware Shelf Valley is an especially informative example of such an estuary retreat path, in that the shelf valley has not been decoupled from the generative estuary mouth by the late Pleistocene reduction in the rate of sea-level rise, as many other estuary mouths have been. The transverse bar blocking the mouth of Delaware Bay is breached on the south side by a well-developed, en echelon set of ebb-dominated and flood-dominated channels. The seaward-trending flood channel, a response to the tidal regime of the bay mouth, is continuous with the Delaware Shelf Valley. This feature is only approximately superimposed on the subsurface fluvial channel and is more precisely termed a *flood-channel retreat path*. North of the conjugate set of ebb and flood channels, Delaware Bay mouth is blocked by a large shoal which is the depocenter for the littoral drift system of the New Jersey coastal compartment. It may be traced seaward into a shelf-transverse high on the north flank of the flood-channel retreat track, which is thus an *estuary shoal-retreat massif*. This set of paired morphologic retreat elements terminates in a large mid-shelf high which is interpreted as a mid-shelf delta. However, comparison with the modern Apalachicola Delta suggests that, as it was transgressed, the delta had superimposed upon it a *cape shoal-retreat massif*, deposited by the littoral drift convergence of a retreating cusped foreland.

The tide-generated ridges and swales of the

estuary-mouth shoal are normal to shore. As the shoal is traced seaward into the shoal-retreat massif, ridge-and-swale orientations rotate until they trend across the massif, parallel to shore. This change in orientation suggests that as the shoreline has retreated, the initially tidal topography has been remade in response to southwest-trending storm currents. Such a compensating response to a change in regime is the definitive characteristic of an equilibrium system. Thus, while a relict component may be observed in the topographic pattern, the descriptor "relict" is not particularly appropriate for the sand body itself.

INTRODUCTION

Since the pioneer study of Veatch and Smith (1938), the transverse shelf valleys of the North American Atlantic Shelf have been interpreted as the result of the drowning of the master streams of the Atlantic slope by the postglacial transgression, and consequently, have been considered classic examples of relict topography. While the basic premise cannot be challenged, this conceptual model is not particularly efficient in explaining component topographic elements, surficial sediment distributions, or shallow stratigraphy. The transverse shelf valleys of the Atlantic Shelf and their interfluves are becoming increasingly important as sinks for the waste of the East Coast megalopolis, a substrate for its food resources, and even as sites for its power plants and airports. If our model for their evolution cannot even predict their gross morphology, it is doubtful whether it can predict the more detailed information concerning the nature of their substrate that is required by environmental managers.

The problem becomes apparent when Uchupi's (1970) topographic compilation of the central Atlantic Shelf is examined. Here shelf valleys appear as broad to sharply defined,

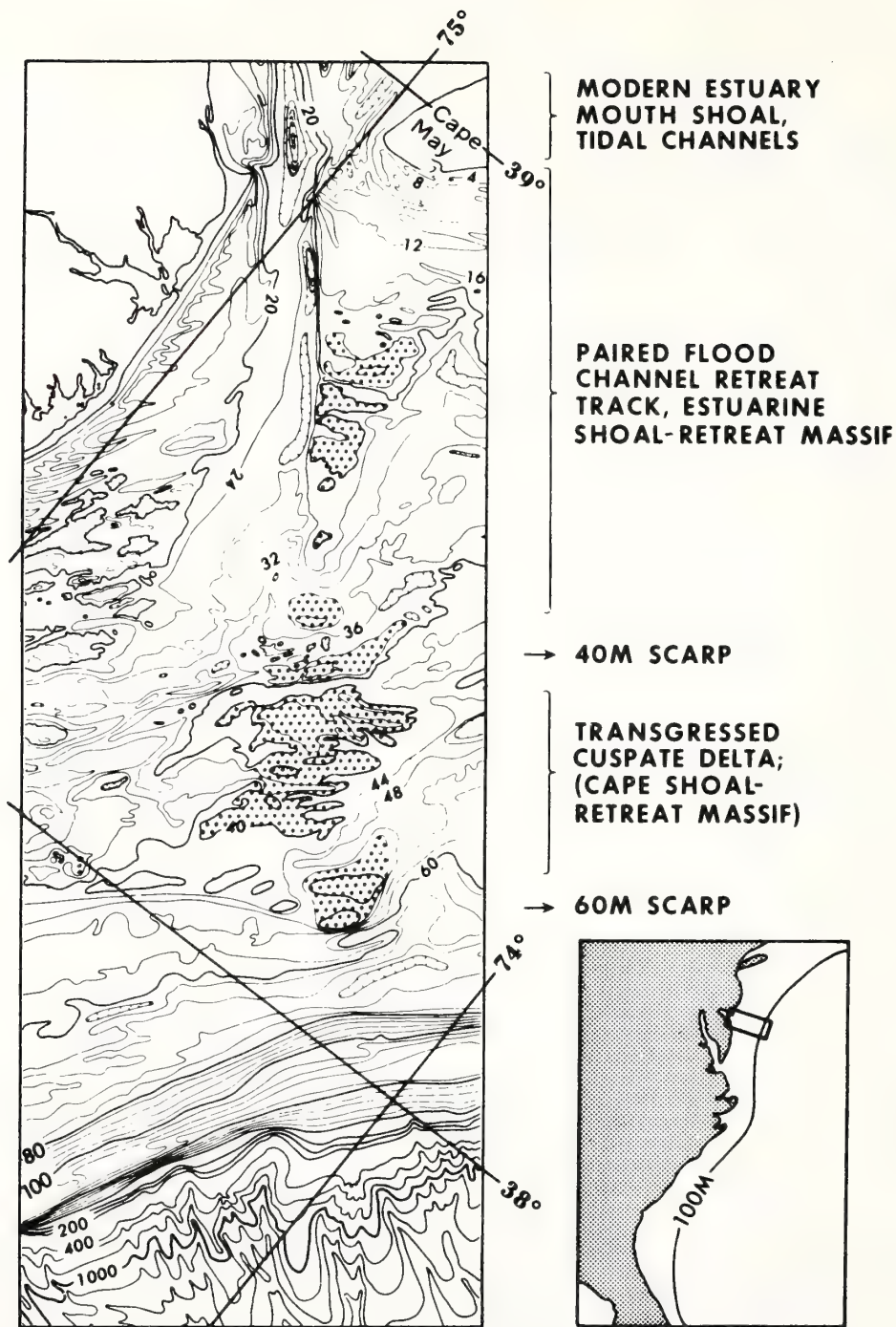


Figure 1. Delaware Bay mouth, Shelf Valley, Mid-shelf Delta, and associated topographic features (from Uchupi, 1970). Isobaths in meters.

shelf-transverse, linear lows. They are peculiarly youthful in cross section compared with their subaerial extensions, in that they are separated by broad, flat, plateaulike interfluves. The subaerial valleys, on the other hand, are mature; valley sides climb gently toward a sharply defined drainage divide where they intersect the flank of the adjacent valley. Yet more inexplicable is the tendency for shelf valleys to be bordered on their northern flanks by a rim raised above the adjacent flat interfluve.

The anomalous patterns of shelf-valley morphology begin to be understood when it is realized that the penultimate environment of the shelf valleys was not that of a subaerial river, but instead that of an estuary. The next step is to develop a conceptual model for shelf-valley evolution by comparing shelf valleys with their associated estuaries in accord with the principle of uniformitarianism.

The reduction in periglacial meltwater discharge during the early Holocene and the reduction in the rate of sea-level rise during the later Holocene have heavily modified most estuaries with respect to their earlier counterparts, with the result that shelf valleys cannot always be traced directly into estuaries. The Delaware Shelf Valley (Fig. 1) is a unique exception to this general rule (Swift and others, 1972) and is consequently the topic of this report.

DELAWARE BAY MOUTH

The Delaware Bay mouth (Fig. 2), our actualistic model for the generation of the Delaware Shelf Valley during the postglacial transgression, represents a relatively simple system of hydraulic process and substrate response. The broad sill, extending with interruptions from Cape May to Cape Henlopen, is an *estuary-mouth shoal*. It is the depocenter for the wave-driven littoral sand-drift system of the New Jersey and Delaware coasts. This shoal behaves as a sand sink because of the complex structure of the semidiurnal tidal wave at the bay mouth. The entering tidal stream preferentially seeks flood-dominated channels, in which the flood-tidal stream is more prolonged, or more intense, or both, than the ebb-tidal stream. Such channels are paired with ebb-dominated channels, and the coast-normal ridge-and-swale topography of Delaware Bay mouth, by analogy with better studied areas (Ludwick, 1970), represents the interdigitation of the two channel types. The channels char-

acteristically shoal in the flow direction of the dominant phase of the tidal cycle, and their cross-sectional area decreases. To satisfy continuity, the current must accelerate, and also diverge, moving obliquely up the channel sides. Since the adjacent channel is dominated by the other half of the tidal cycle, the bottom currents on the medial ridge that are residual to the tidal cycle can be represented by two sets of vectors, oblique to the ridge crest, which meet head on along the crest. Thus, each ridge comprises a sand circulation cell, or closed loop in the sand transport path, and the ridges are stabilized in the reversing tidal regime. Most of the tidal-water exchange takes place in a single large ebb-flood channel couplet on the southwestern side of the bay mouth.

RETREAT—ESTUARINE PHASE

A comparison of Figures 1 and 2 shows that the explanation for the peculiar configuration of the Delaware Shelf Valley and its north-flank ridge lies in this scheme of hydraulic process and substrate response. The shelf valley is continuous with the modern bay-mouth flood channel, hence it is the retreat *path* of this dynamic response feature during the postglacial transgression of the sea. Geometrically it is a shelf valley, but genetically it must be called a *flood-channel retreat path*. Similarly, the north-flank ridge may be traced directly into the estuary-mouth sand shoal (Kraft, 1971; Swift and others, 1972). The ridge therefore is an *estuarine shoal-retreat massif*, marking the retreat path of the littoral drift depocenter.

Thus the originally subaerial river valley has been filled with estuarine deposits and the gross topographic pattern of Figure 1 is largely inherited from the nearshore submarine environment. Seismic and coring studies by Sheridan, Dill, and Kraft (University of Delaware, 1973, oral commun.) have revealed that the fluvial channel beneath the fill is at least locally offset from the modern sea-floor channel and that, where examined, the two are distinct entities.

Consideration of the shoal-retreat massif suggests that at least for this feature, the descriptor "relict" is of dubious value. On a line extending from the active estuary-mouth shoal to the seaward extent of the shoal-retreat massif, the orientation of the second-order ridges (Figs. 1, 2) can be seen to change. Within the bay mouth they are parallel to the tidal flow and the crestline of the massif, but as the open

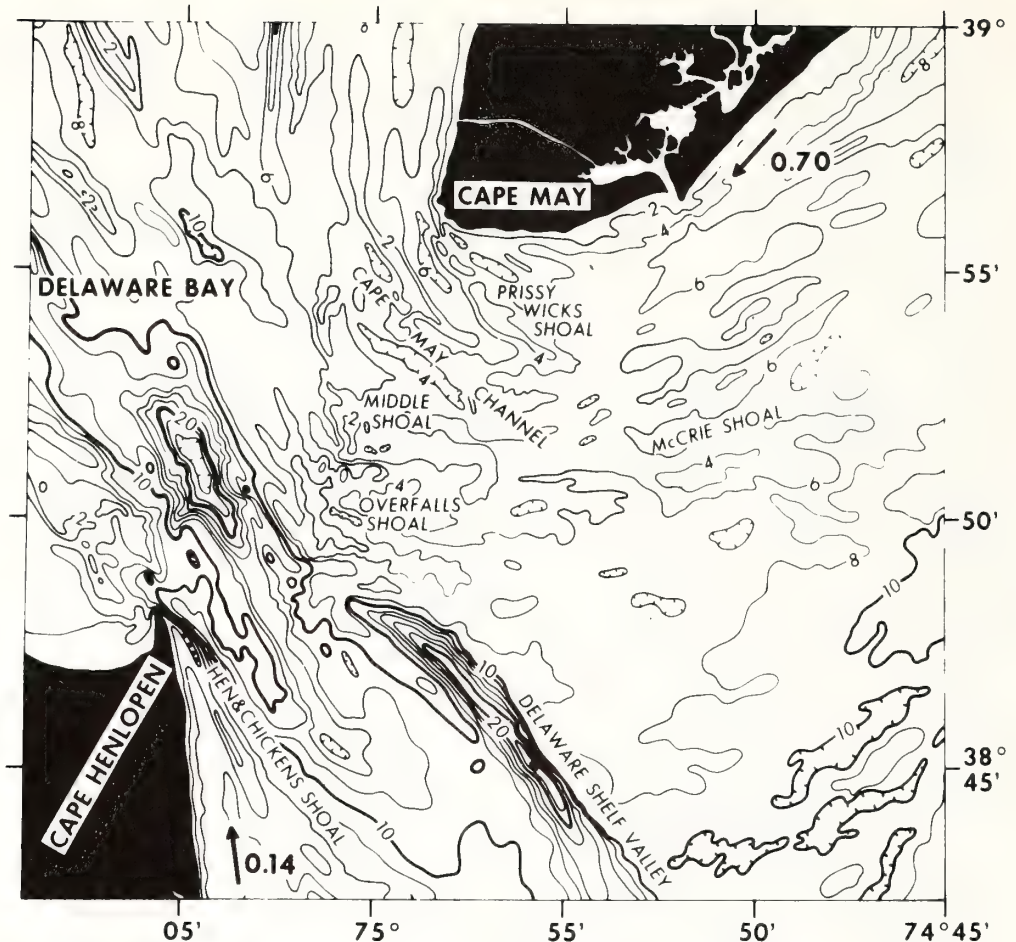


Figure 2. Delaware Bay mouth. From U.S. Coast and Geodetic Survey Bathymetric Map 6807N-57. Lit-

toral drift in million cubic yards per yr (from Caldwell, 1966, and Moody, 1964). Isobaths in fathoms.

shelf is approached they rotate rapidly to a position normal to the crestline of the massif, and parallel to the regional trend of the coastline. With one exception, contours define transverse troughs on the back of the massif close to the southeast; in other words, the trough axes rise in that direction. In this respect, the ridges and troughs on the back of the massif differ only in position from the ridge-and-swale topography of the plateaulike interflues on either side of the shelf valley. The ridge fields of the interflues are believed to have been initiated as responses not to nearshore tidal currents, but, instead, to the interaction of storm waves and storm-generated, south-trending, wind set-up currents on the shoreface of the

open coast (Swift and others, 1972; Duane and others, 1972). These open-coast ridges are believed to be detached from the retreating shore face with the continued rise of sea level and to be maintained as an offshore ridge topography by southward movements of the water column during storms.

The similarity of offshore ridges on the interflues and on the shoal-retreat massif suggests that the ridge-and-swale topography of the central shelf is the product of convergent evolution of topographies of differing shallow-water origin. Furthermore, the striking rotation of the ridges on the massif crest, as the tidal component of the hydraulic regime is subordinated to the storm-driven component,

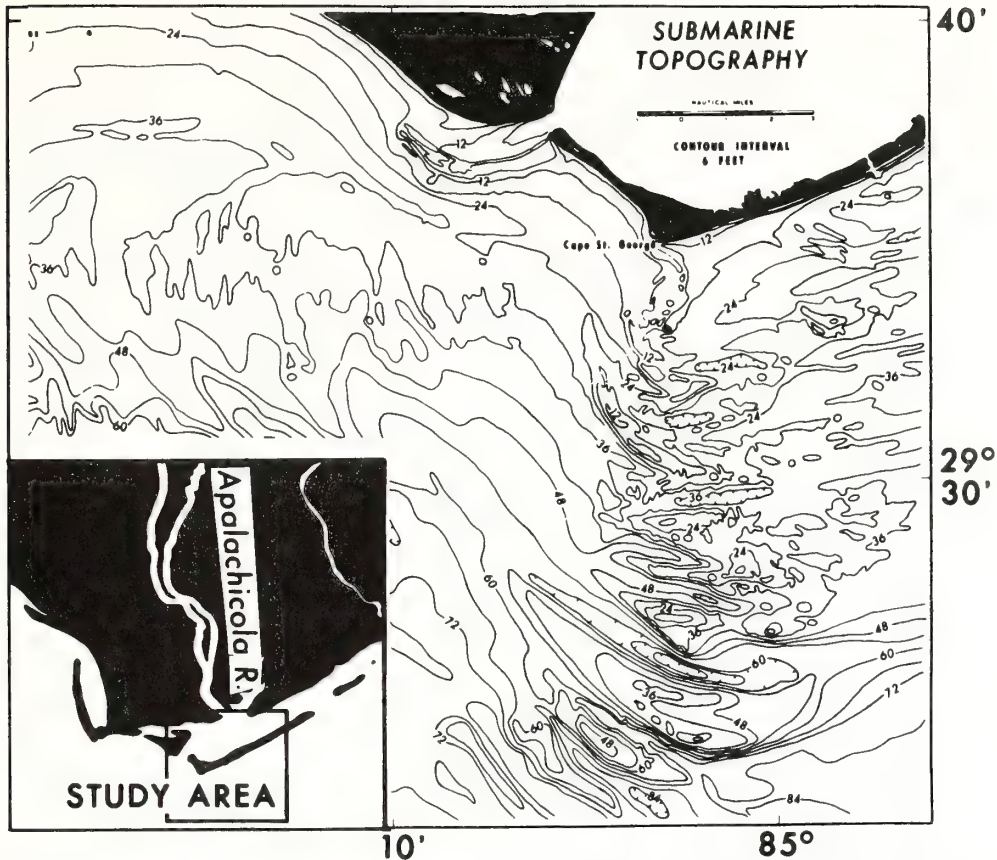


Figure 3. Cape-associated shoal and cusped foreland of the Apalachicola Delta, Panhandle Florida

(from Schnable and Goodell, 1968). Isobaths in feet.

shows that the massif fits the classical definition of an equilibrium system—one which, when stressed, responds in such a way as to relieve the stress.

RETREAT—DELTAIC PHASE

A final insight into the evolution of the shelf surface can be extracted from Figure 1. The paired retreat features are clearly defined as far seaward as a coast-parallel scarp whose toe lies at the 40-m isobath. This scarp appears to have been shoreline cut during a stillstand in the postglacial sea-level rise. It can be traced north and south of Figure 1 by topography (Swift and others, 1972) and as a concentration of dated oyster shells (Merrill and others, 1965).

A broader massif lies seaward of the scarp, with its base at the 40-m scarp and its apex defining a deeper 60-m scarp. By analogy with

other features such as the Block Delta (Garri-son and McMaster, 1966) and the Hudson Apron (Veatch and Smith, 1938), this is a mid-shelf delta, a consequence perhaps of the same 40-m stillstand that built the upper scarp. However, a more meaningful evolutionary model can be constructed by considering the penultimate environment of this ultimately fluvial landform. In the face of moderate to intense wave attack (Swift and others, 1972) and a relatively coarse sediment supply, deltas tend to adopt a cusped form. Such deltas are in some respects comparable to a tombolo differing mainly in that the shielding point and focus for wave refraction is a dynamic one, the river mouth, rather than the static rock shield of a true tombolo. As cusped deltas are overridden by intensified transgression, the hydraulic regime changes. Distributaries shift

and broaden to become estuaries or lagoons behind the original shoreline which now is a barrier chain capped by a cusate foreland (Fig. 3). As transgression continues, the submerged tip of the foreland becomes a new shielding point. This cape-associated shoal is a focus for wave energy, and the resulting wave refraction pattern drives littoral drift from the foreland flanks toward its apex, where it in turn feeds the adjacent shoal. Thus, the cape-associated shoal advances landward and the cusate foreland retreats landward as a coupled feedback system. As they do so, coastal storm surges cut spillways through the resulting *cape shoal-retreat massif* (Swift and others, 1972). Its channels shoal in the dominant flow direction (or may shoal in alternating directions if normal to storm paths), and wave refraction molds the intervening ridges into seaward-convex arcs (Tanner, 1960). Here again a ridge-and-swale topography appears to be a stable end configuration. Such a continuing substrate response to hydraulic process renders the term "relict" of dubious value for this second class of shoal-retreat massif as well.

The crenulated eastern margin of the Delaware Midshelf Delta strongly suggests that this landform was capped by a cape shoal-retreat massif as it was transgressed. When transgression resumed after the 40-m stillstand, the foreland-shoal interaction was replaced by a true estuarine regime, and the paired estuarine retreat features were substituted for the initial cape shoal-retreat massif.

CONCLUSIONS

A great deal of the transgressional history of the Atlantic Shelf, and probably many others, is illustrated by Delaware Bay, Shelf Valley, and Midshelf Delta. Three conclusions constitute a new paradigm for the shelf surface which will permit the recognition and interpretation of repeating patterns of shelf topography. (1) Shelf highs may be constructional elements outlining the retreat paths of littoral depocenters. (2) Shelf-valley topography, like other forms of shelf topography, reflects mainly its shallow marine stage of evolution, rather than the earlier subaerial stage. (3) The ridge-and-swale topography is an equilibrium response to the modern hydraulic climate, that may be elicited from diverse beginnings.

REFERENCES CITED

- Caldwell, J. M., 1966, Coastal processes and beach erosion: *Jour. Soc. Civil Eng.*, v. 53, p. 142-157.
- Duane, D. B., Field, M. E., Meisburger, F. P., Swift, D.J.P., and Williams, S. J., 1972, Linear shoals on the Atlantic Inner Continental Shelf, Florida to Long Island, in Swift, D.J.P., Duane, D. B., and Pilkey, O. H., *Shelf sediment transport: Process and pattern*: Stroudsburg, Pa., Dowden Hutchinson and Ross, p. 447-498.
- Garrison, L. E., and McMaster, R. L., 1966, Sediments and geomorphology of the Continental Shelf off southern New England: *Marine Geology*, v. 4, p. 273-289.
- Kraft, J. C., 1971, Sedimentary facies patterns and geologic history of a Holocene marine transgression: *Geol. Soc. America Bull.*, v. 82, p. 2131-2158.
- Ludwick, J. C., 1970, Sandwaves and tidal channels in the entrance to Chesapeake Bay: *Virginia Jour. Sci.*, v. 21, p. 213-248.
- Merrill, A. S., Emery, K. O., and Rubin, M., 1965, Oyster shells on the Atlantic Continental Shelf: *Science*, v. 147, p. 395-400.
- Moody, D. W., 1964, Coastal morphology and processes in relation to the development of submarine sand ridges off Bethany Beach, Delaware [Ph.D. thesis]: Baltimore, Johns Hopkins Univ., 167 p.
- Schnable, J. E., and Goodell, H. G., 1968, Pleistocene-Recent stratigraphy evolution, and development of the Appalachian Coast, Florida: *Geol. Soc. America Spec. Paper* 112, 72 p.
- Swift, D.J.P., Kofoed, J., Saulsbury, F. P., and Sears, P., 1972, Holocene evolution of the shelf surface, Central and Southern Atlantic Shelf of North America, in Swift, D.J.P., Duane, D. B., and Pilkey, O. H., eds., *Shelf sediment transport: Process and pattern*: Stroudsburg, Pa., Dowden Hutchinson and Ross, p. 499-573.
- Tanner, W. F., 1960, Expanding shoals in areas of wave refraction: *Science*, v. 132, p. 1012-1013.
- Uchupi, E., 1970, Atlantic Continental Shelf and slope of the United States—shallow structure: *U.S. Geol. Survey Prof. Paper* 519-I, 44 p.
- Veatch, A. C., and Smith, P. A., 1938, Atlantic submarine valleys of the United States and the Congo Submarine Valley: *Geol. Soc. America Spec. Paper* 7, 101 p.

MANUSCRIPT RECEIVED BY THE SOCIETY JANUARY 12, 1973

REVISED MANUSCRIPT RECEIVED MARCH 5, 1973

RIDGE AND SWALE TOPOGRAPHY OF THE MIDDLE ATLANTIC BIGHT, NORTH AMERICA: SECULAR RESPONSE TO THE HOLOCENE HYDRAULIC REGIME

DONALD J. P. SWIFT, DAVID B. DUANE and THOMAS F. MCKINNEY

Atlantic Oceanographic and Meteorological Laboratories, National Oceanic and Atmospheric Administration, Miami, Fla. (U.S.A.)

Coastal Engineering Research Center, Washington, D.C. (U.S.A.)

Department of Geology, Vassar College, Poughkeepsie, N.Y. (U.S.A.)

(Accepted for publication July 17, 1973)

ABSTRACT

Swift, D. J. P., Duane, D. B. and McKinney, T. F., 1973. Ridge and swale topography of the Middle Atlantic Bight, North America: secular response to the Holocene hydraulic regime. *Mar. Geol.*, 15: 227-247.

The ridge and swale topography of the Middle Atlantic Bight was originally interpreted as a relict strand plain whose ridges reflect stillstands of the returning Holocene sea. However, close examination indicates that the ridges appear to be instead longitudinal bed forms, responses to a regime of intermittent, south-trending storm currents. Ridges may be initiated on the shore face and detached as the coast retreats to form fields of isolated ridges, or they may be molded into the shelf-transverse sand massifs that mark the retreat paths of littoral-drift depositional centers at estuary mouths and off cusped forelands. The ridge and swale topography is thus a stable end configuration toward which a variety of near-shore constructional topographies have converged during the Holocene transgression.

Morphologic evidence for readjustment of ridge topography to the deepening shelf flow field during the Holocene transgression is discernable. However, the extent to which the offshore topography continues to respond to hydraulic regime is unclear. The role of helical flow structure in the storm flow field remains to be documented. Resolution of these problems will require more detailed information of hydraulic process and substrate response on storm-dominated shelves.

INTRODUCTION

Much of the surface of the Middle Atlantic Bight between Cape Cod and Cape Hatteras, North American Atlantic Shelf, is a vast sand plain. First-order morphologic elements consist of transverse shelf valleys (Fig. 1), often paired with shelf-transverse massifs on their north flanks (Swift et al., 1972). The term massifs is here used to connote a large-scale topographic high, which itself exhibits appreciable relief and is composed of such smaller-scale features as sand ridges. Though fundamentally drowned river valleys,

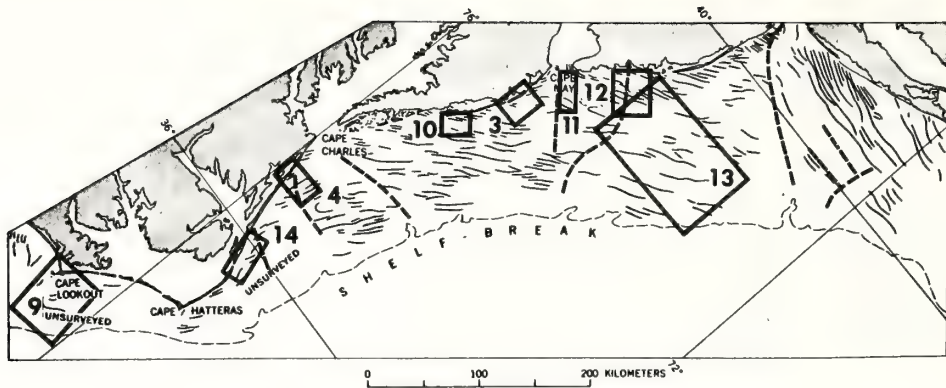


Fig.1. Crest line of the more prominent ridges of the Middle Atlantic Bight, and the courses of the major shelf-transverse valleys. Boxes indicate locations of other figures. (Modified from Uchupi, 1968.)

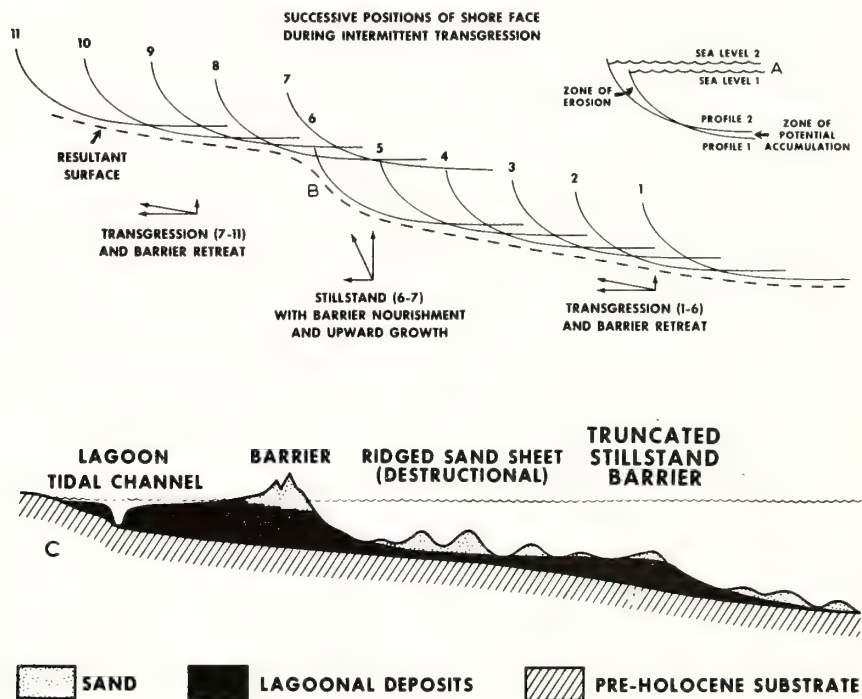


Fig.2.A. Zones of erosion and potential deposition created by the landward translation of the hydraulically induced inner-shelf profile.

B. Generation of a shelf scarp by depositional stillstand and upward profile translation during a period of general transgression and landward profile translation.

C. Schematic profile of shelf sector indicating relationship of ridge topography to terraces and scarps. Surficial sand sheet on each terrace is the debris of shore-face erosion, molded into ridge and swale topography after passage of shore face.

shelf-valley topography reflects mainly the estuary environment; the more sharply defined channels may be locally traced into tide-generated flood channels in the modern estuary; hence these are termed *flood-channel retreat paths*. Massifs on the north flanks of channels may be traced into estuary mouth shoals which are sediment sinks for south-trending littoral drift, hence are *estuary shoal-retreat massifs*. *Cape shoal-retreat massifs* are not necessarily associated with transverse shelf valleys, but occur at such cusped forelands as Cape Hatteras, Cape Lookout and Cape Fear on the Carolina coast, as a result of littoral-drift convergence at the foreland apex.

Shoal-retreat massifs and shelf valleys are transverse first-order elements which divide the shelf surface into compartments. The regional morphologic pattern is complicated by two other first-order morphologic elements. Oblique-trending "cuestas" are prominent on the north New Jersey and Long Island shelves (Swift et al., 1972). Here subaerial fluvial processes have exerted a prominent influence relative to later estuarine processes in shaping the intervening lows. The shelf surface is not a simple seaward-inclined surface; instead it consists of a series of nearly horizontal "terraces" separated by more steeply inclined scarps (Veatch and Smith, 1939; McClennen and McMaster, 1971). The terraces reflect periods of transgression when the equilibrium shore-face profile translated shore-ward (Fig. 2). During these periods, the landward component of profile translation remains of lower shore faces. They were formed during periods of near stillstand, when shore-face translation was dominantly upwards. As transgression resumed, shore-face translation returned to the horizontal mode. The barrier superstructure of the stillstand shore-face was shaved off by erosional shore-face retreat as terrace formation resumed, but the lower shore face was locally preserved (Swift et al., 1972).

Second-order morphologic elements comprise the *ridge and swale topography* (Swift et al., 1972; also referred to as linear shoal topography, Duane et al., 1972): fields of sand ridges 2–4 km apart and up to 10 m high, which extend for tens of kilometers (Fig. 1). Side slopes are a few degrees or less. Crest lines and trough axes climb obliquely southwest across the shelf (Uchupi, 1968), converging with the shoreline (Duane et al., 1972). All ridges of the study area form a small acute angle with the shoreline; almost all angles open to the north. The mean convergence angle (measured clockwise) is 22° with a standard deviation of 16° . Seismic reflection profiles and cores of the ridges show them to be plano-convex features molded into a discontinuous sheet of well-sorted sand that rests on a nearly horizontal surface. Marked compositional differences exist between the sands of ridges and the more heterogeneous sediment of the underlying substrate (Duane et al., 1972; Swift et al., 1973). On the inner shelf where data are available, the ridges are less than 11,000 years old; the substrate may consist of slightly older Holocene lagoonal deposits, or older Pleistocene strata (Meisburger and Duane, 1971; Duane et al., 1972; Field and Duane, 1973). The discontinuous sand sheet whose upper surface is molded into the ridge and swale topography appears to be the "sawdust" of the process of intermittent landward translation of the shore-face profile that created the terraces (Veatch and Smith, 1939; Swift et al., 1972). The ridge and swale topography is more apparent on most bathymetric maps than is the first-order topography on which it is superimposed.

Since first systematically described by Veatch and Smith (1939), the ridge and swale topography has generally been interpreted as a relict strand plain whose ridges were formed during stillstands of the returning Holocene sea (Shepard, 1963, p.214). A variant hypothesis has interpreted certain clusters of shoreface-connected ridges as beach-ridges relict from Pleistocene regressions (Sanders, 1962; Kraft, 1969). Uchupi (1968) observed the persistent southward convergence of the ridges with the shoreline and sardonically noted that, if the Holocene interpretation is correct, "there has been a drastic reorientation of the shoreline in recent times." He suggested a modern hydraulic origin, although he later (1970) reverted to the strand-plain hypothesis. The Pleistocene strand-plain hypothesis also creates more problems than it solves. The zone of shoaling waves is a high-energy environment in a state of equilibrium with its morphologic counterpart, the shore face. The response time of the shore face is geologically instantaneous: 20 m of beach, stripped off in a single storm, may be returned a few weeks later. It is difficult to imagine this dynamic zone migrating over an unconsolidated Pleistocene beach ridge without annihilating it. Furthermore, shelf-ridge morphology is not barrier morphology. Barriers are dune-capped scarps; they are backed by lagoons a few meters deep, but their seaward faces drop to 15 – 20 m over a few kilometers. Shelf ridges are usually nearly bilaterally symmetrical; the landward trough is rarely a meter shoaler than the seaward trough, while the ridge in between may rise 10 m. The coast-parallel scarps are probably the only true barrier remnants of the Central Atlantic Shelf; the ridge and swale topography is molded into the surficial sand sheet of the intervening terraces (Fig.2). When closely examined, the sheet appears to have formed at the trailing edge of a shore face undergoing erosional retreat (Swift et al., 1972; Stahl et al., 1973), hence its ridge topography postdates passage of the shoreline.

We present elsewhere (McKinney and Friedman, 1970; Duane et al., 1972; Swift et al., 1972; McKinney et al., 1973) extensive analyses of Atlantic Shelf morphology. As a byproduct of these analyses, we have concluded that the ridge topography is primarily of dynamic near-shore submarine origin, rather than a relict littoral subaerial feature. The ridges are judged to form as a secular or long-term substrate response to the hydraulic processes associated with the Holocene transgression.

The ridges have diverse origins and locally are erosional rather than constructional responses to the hydraulic regime (Duane et al., 1972), but in most cases are initiated in response to storm and south-trending storm currents on the shore face and adjacent shelf. The diverse origins become less apparent as the shoreline recedes, and the ridge topography becomes more homogeneous. In this paper we present a systematic analysis of available evidence relating to the evolution of the ridge topography, so that it may be compared with other shelf surfaces and perhaps may be shown as an example of a more general class of marine topography. We outline the limitations as well as the implications of our data; in particular, our severely restricted knowledge of the Atlantic Shelf's hydraulic climate. We propose a hypothesis of transgressive ridge formation on a storm-dominated shelf, and invite our colleagues to join our continuing attempts to test its validity.



Fig.3. Shoreface-connected ridge field of the Delmarva coast. Dashed lines are crest lines. (See U.S.C.G.S. map 0807N-57 for 1-fathom resolution.)

THE DELMARVA SHELF: RIDGE DETACHMENT ON AN OPEN COAST

An extremely regular ridge field occurs on the coast of the peninsula occupied by the states of Delaware, Maryland, and Virginia (Fig.3). Ridges are attached to the shore face at depths as shoal as 2 m, or are connected to the shore face by saddles more nearly normal to the shore face than the ridges themselves, or are isolated from the shore face. Close study of a similar shoreface-connected ridge system off the Virginia–North Carolina border (Fig.4; Duane et al., 1972; Swift et al., 1973) has shown that the troughs landward of such ridges are undergoing active scour and headward erosion in response to south-trending wind set-up currents associated with mid-latitude lows (northeasters). Limited current-meter work and related observations suggest that helical flow occurs in troughs landward of shoreface-connected ridges during storms (Swift et al., 1973). Southwest-advancing waves, breaking on shallower portions of the ridge crests, pump water obliquely landward over the main body of wind-driven coast-parallel trough flow (Fig.5). The resulting hydraulic head (wave set-up) induces a southeast-trending return flow near the bottom. Ridge crests experience bottom-current convergence. The return-flow bottom currents of the trough converge obliquely southward with the wave-driven (mass transport)

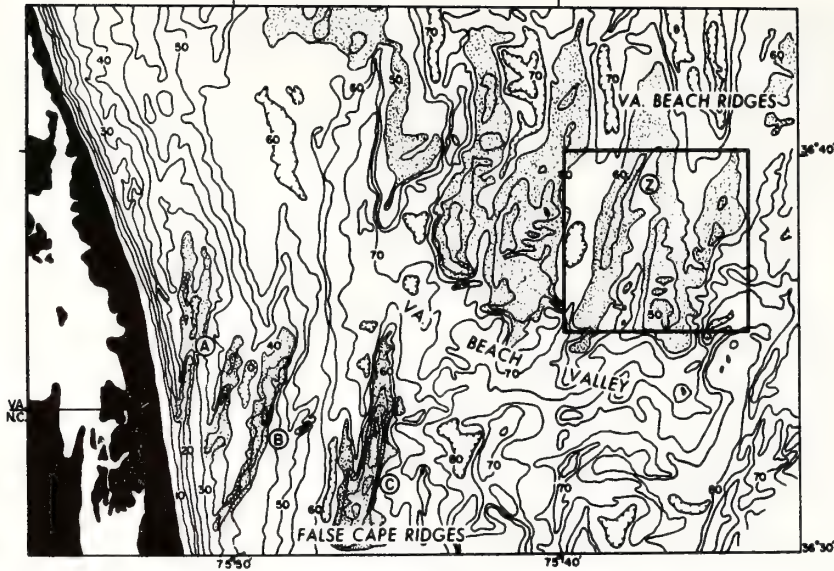


Fig. 4. Transgressed estuary mouth of the ancestral James River. Virginia Beach ridges extend through the seaward margin of the figure as an estuary shoal-retreat massif. Massif was remolded into transverse ridges subsequent to transgression and illustrates the second major mode of ridge formation. Virginia Beach Shelf Valley is here a flood-channel retreat path. False Cape ridges are presently forming by lateral detachment. Contours in feet; box shows location of Fig. 7.

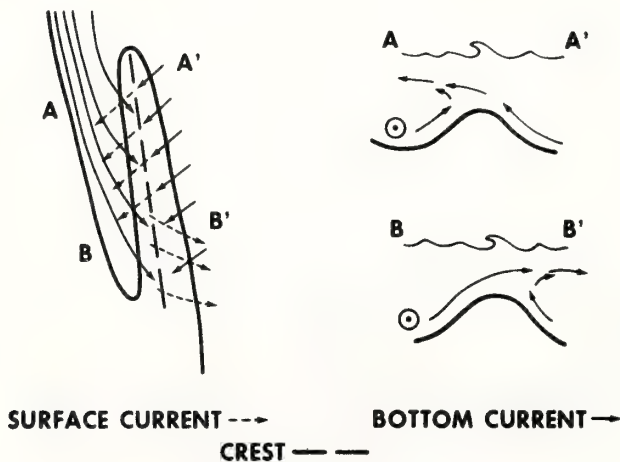


Fig. 5. Schematic hydraulic model for maintenance of shoreface-connected ridge. During northeasters, southward wind drift currents flow down landward trough and break out over ridge base. Wave-induced mass transport currents move obliquely up ridge's seaward flank. Trough current experiences helical flow structure, as waves, breaking on shallow base of ridge, pump water over coast-parallel trough flow. Resulting wave set-up induces seaward bottom flow in trough. Convergence of bottom currents aggrades ridge crest (see Swift et al., 1973).

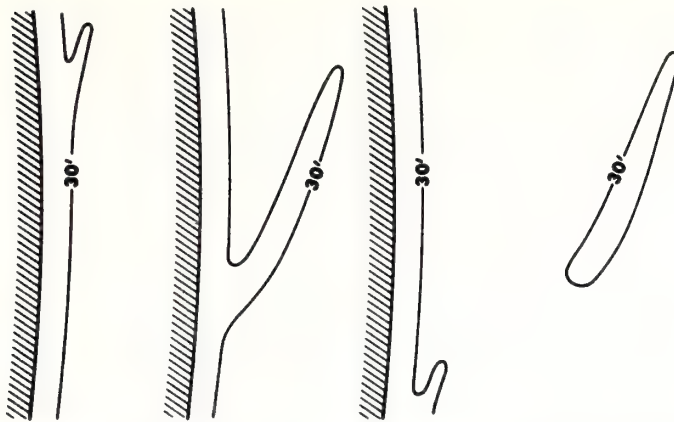


Fig.6. Schematic model for evolution of shoreface-connected ridge into isolated shelf ridge during transgression. Headward extension and axial deepening of trough intensifies rip-like current which sweeps over ridge base, cutting saddle, and eventually isolating ridge. Shoreline retreats and ridges migrate down-coast and offshore. (Compare with Fig.3.)

bottom currents on the seaward flank, and ridge crests are consequently aggraded. Large-scale rip currents break out over ridge stems and cut shifting saddles into them (Swift et al., 1973). This model should be considered tentative until further hydraulic documentation is attained.

In Fig.6, the stepwise trend of ridge crests is taken to reflect a stepwise process of ridge growth and detachment during the Holocene transgression. As troughs grow by headward erosion and axial scour, wave-amplified trough currents become more intense, and a saddle is eventually cut through the ridge base; the process then repeats further down the shore face.

THE SOUTHERN VIRGINIA SHELF: RIDGE FORMATION BY REMOLDING OF AN ESTUARY SHOAL-RETREAT MASSIF

The False Cape Ridge System (Fig.4) is judged to fit the Delmarva pattern in that an apparent evolutionary sequence of ridge formation and detachment may be discerned. However, the detachment mechanism does not serve to explain the origin of the Virginia Beach Ridge System north of the Virginia Beach Shelf Valley (Fig.4), as the valley itself separates the northern ridges from the adjacent beach. The two ridge systems and the intervening valley comprise a transgressed estuary mouth (Swift et al., 1972); and the Virginia Beach ridges extend seaward beyond the figure's margin as an estuarine shoal-retreat massif. The transverse ridges and swales of the massif do not, however, constitute a tributary pattern of relict subaerial drainage, for the master valley does not lie in a plane of bilateral symmetry. Crest lines and thalwegs do not descend to the central valley; instead they generally climb to the southwest, both north and south of the valley. Thus, the Virginia Beach Ridge System is not a mirror image of the False Cape System; instead it comprises a northward translation of it.

The Virginia Beach Ridge System is more readily explained as the result of in situ remolding of a pre-existing shoal-retreat massif, particularly as vibracores (Swift et al., 1973) reveal that the ridges consist of fine sand cores, apparently dating from the estuarine phase, mantled by coarser, post-transgression sands. The remolding process appears to have involved scour and down-cutting in the troughs, with simultaneous aggradation of the ridge crests.

The operative agent appears to be southward drift currents generated northeast by storm winds and confined by the shoreline; in deeper water a barotropic response to wind set-up may be important (Harrison et al., 1967). Evidence for such a flow occurs as flow-transverse, southward-asymmetric bed forms with amplitudes up to 2 m. These have been observed in constricted portions of the troughs (Swift et al., 1973) and are responsible for the irregularities in the contours of the Z-shaped ridge (Fig.4).

Examination of current-meter records suggests that the threshold of grain movement is regularly exceeded at least on the inner shelf during storms (Fig.7; Lavelle et al., 1973). Such activity should serve to degrade the ridge topography; however, it exists and continues to be maintained.

The initiation and survival of the ridge topography on shoal-retreat massifs may indicate a general helical flow structure in the storm flow field, analogous in some respects to the more specialized pattern associated with shoreface-connected ridges. Flow fields such as those of the inner shelf, which are much wider than deep, may be inherently unable to maintain flow continuity, so that bands of more rapidly moving water descend and diverge; intervening, slower bands would experience bottom convergence and would rise, resulting in a pattern of helical flow in which alternating cells rotate with the opposite sense. Such a helical flow structure may be the consequence of an unequal distribution of turbulent (Reynolds) shear stresses in the flow field (Allen, 1970) and may serve to stabilize the Ekman velocity (Brown, 1970). Common descending limbs of adjacent cells would scour the bottom; common ascending limbs would cause southward-trending sand streams to converge and aggrade the bottom. The resulting ridge topography would initiate and localize helical flow structure during future storm events (Fig.8). The coupling between hydraulic process and substrate response during this evolutionary process is marked. The troughs are tailored by their flow field so that they shoal in the down-current direction and become broader; thus, the high-velocity thread of trough flow, with its greater momentum, must impinge on the rising trough thalweg, and spread laterally. This geometry is ubiquitous in the ridge topography of the Middle Atlantic Bight, although it is by no means clear that helical flow is everywhere occurring at present. (See Wilson, 1972, for a discussion of analogous large-scale aeolian features arising from helical flow.)

There exists no direct evidence for helical flow during storms on the Western Atlantic Shelf as has been reported by Houbolt (1968) for the tidal regime of the North Sea ridge fields. However, the grain-size distribution of the ridge and swale topography is compatible with such a pattern of trough scour and crestal aggradation (Fig.7). The north ends of troughs are scoured out to bare Pleistocene or Early Holocene clay (Swift et al., 1973). The clay is intermittently veneered with medium to coarse sand with an admixture of

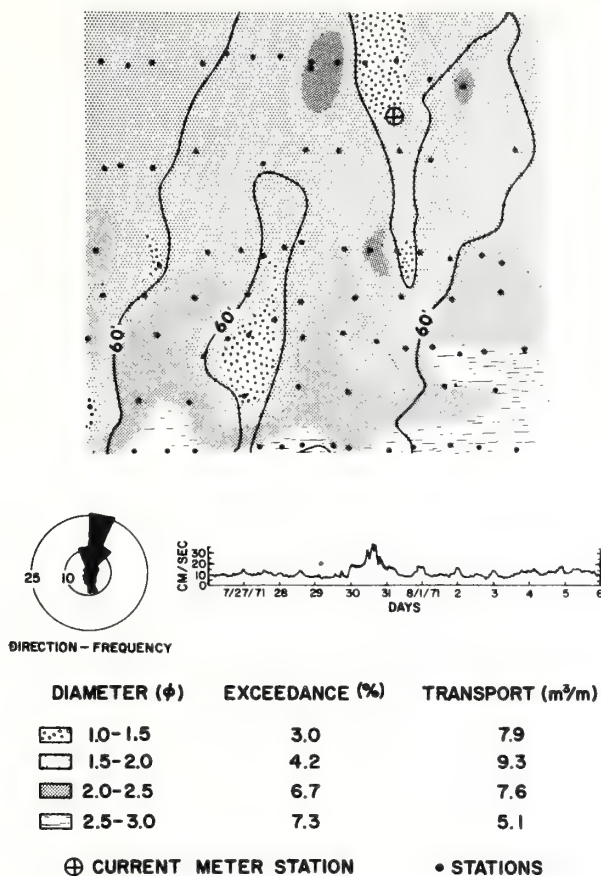


Fig.7. Distribution of mean diameters of the sand fraction as calculated by Rapid Sediment Analyzer (Sanford and Swift, 1971) on a portion of the Virginia Beach Massif. Location is indicated by box in Fig.4. Grain size varies in sympathy with north-south ridge and swale topography and also in sympathy with inherited large-scale topography elements; shoal-retreat massif (coarser sand of north) and shelf valley (finer sand of south). The coarse-sand patch at the top of the map contains clay and chert pebbles; vibracores indicate that Late Pleistocene clays occur a few decimeters beneath sand (Swift et al., 1973). Current-meter record at bottom recorded by geodyne meter, tripod-mounted with rotor center 37 cm off bottom. The record reveals semidiurnal tidal currents and a velocity pulse associated with mild summer northeaster. Horizontal band is envelope of shield's threshold velocity for grain sizes present. Percent exceedance figures are based on Shield's threshold criterion for grain movement. Net volume transport figures and vectors describe sediment discharge in m^3/m transverse to flow during entire record duration. They are based on Laursen's (1955) total load equation. Assumptions such as a value of 3×10^{-3} for the drag coefficient limit, the quantitative significance of the figures but suggest that the surface was mobile during the duration of the record. (See Lavelle et al., 1973, for discussion of methods.) Direction-frequency rose is based on half-hour samples of record. Frequency rings are in percent.

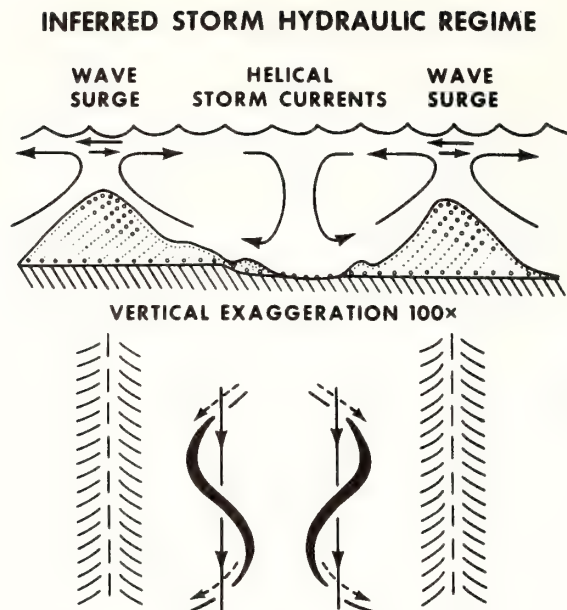


Fig. 8. Schematic diagram of secondary flow motions (helical flow structure) and storm wave surge believed to be associated with storm flow field.

chert and clay pebbles. Near-shore troughs may accumulate localized mud lenses during quiet summer months, but these are commonly flushed out during the winter. The troughs shoal towards the south and eventually are bridged over by fine to very fine sands of the ridge flanks. Crestal sands tend to be medium- to fine-grained, and are notably better sorted than trough sands (Swift et al., 1972). Dives to inner-shelf ridge crest indicate that crestal sands are visibly affected by wave surge during fair weather, and they may be secondary lags which lose their finer fraction to ridge flanks through wave winnowing during periods of waning storm activity (Swift et al., 1973). Thus, the ridge field topography controls ridge field grain-size patterns, whereby sands are differentiated into medium to fine crestal sands, fine to very fine flank sands, and (locally) coarse trough sands. Helical flow structure in the storm flow field, and the winnowing activity of storm waves are tentatively inferred to be the causative agents.

Regional grain-size gradients are superimposed on this small-scale pattern (see for instance Milliman et al., 1972; Fig. 7, this paper). The regional patterns are in part inherited, reflecting coastwide variations in the energy budget of the retreating shore face, and are partly a result of subsequent sand fractionation on a regional scale. In this regional process, sand fine enough to travel in suspension is winnowed out by southward storm currents and is deposited in shelf valleys or other areas of flow expansion and decreasing flow competence (Swift et al., 1973). Coarser sand with a significant portion traveling as bed load remains to be molded into the ridge topography. In fact, a basic requirement for a ridge topography appears to be a sandy substrate whose initial size distribution has a coarse admixture.

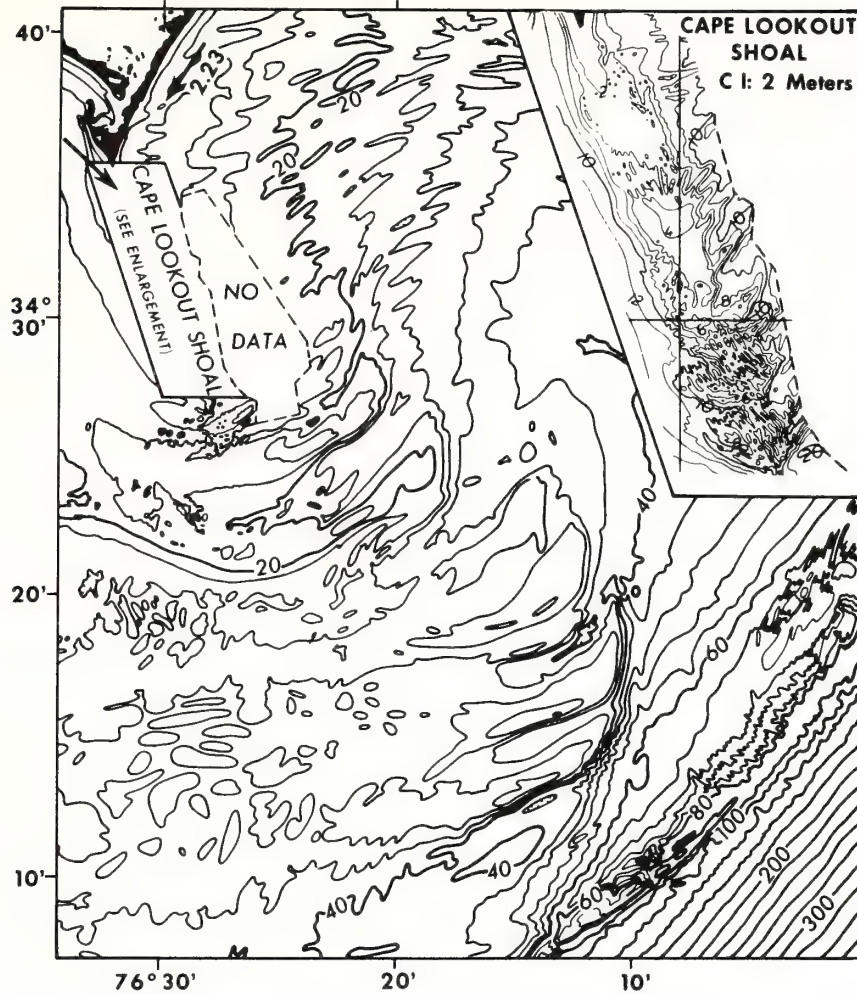


Fig.9. Cape Lookout Shoal, a cape-associated shoal and shoal-retreat massif. Massif has been molded into arcuate transverse ridges, separated by swales which serve as storm spillways. Ridges have been flexed into an arcuate shape by wave refraction. They represent the third major mode of ridge formation. Littoral drift in cu. yd/yr $\times 10^3$ from Langfelder et al., (1968). Contours in meters.

THE CAROLINA SHELF: RIDGE FORMATION BY REMOLDING OF CAPE SHOAL-RETREAT MASSIF

The Carolina coast is characterized by a series of cusped forelands, two of which appear in Fig.1. Each is associated with a cape shoal-retreat massif; Lookout Shoals are figured in Fig.9. Foreland and massif comprise a well-defined feedback system. The shoal focuses wave energy on the foreland, resulting in its double arcuate form, and generates a littoral-drift convergence at the foreland apex. The shoal is, in turn, created

by the retreat of this littoral-drift depocenter through time and is progressively modified by the regime of storm waves and south-trending storm currents (Swift et al., 1972, 1973).

Northeasterly storm winds generate a hydraulic head north of such shelf-transverse massifs, and according to the *Coastal Pilot*, the resulting currents "set across the shoals with great violence". The massifs are dissected by large, generally southward-shoaling troughs which appear to be spillways cut by the storm surges. Unpublished wave-refraction studies indicate that, during storms, wave trains are refracted into hairpin shapes over the massifs so that their distant wings collide head-on over the massif crests. The arcuate shape of the ridges on the back of the massifs must reflect adjustment of the ridge to the wave-refraction pattern, as the momentum of flow in the channels would otherwise serve to keep the channels and ridges straight. Flow through such arcuate channels must presumably constitute a single helical cell in the manner of river meanders.

Fields of southward asymmetrical current-transverse sand waves up to 4 m high develop on the shoaler portions of the shoals (inset, Fig.5); where associated with longitudinal sand ridges, they form southward-convex festoons between ridge crests. This constitutes circumstantial field evidence for helical flow, as it indicates that bottom currents are converging obliquely southward on ridge crests.

RIDGE AND SWALE TOPOGRAPHY AS A SECULAR RESPONSE TO THE HOLOCENE HYDRAULIC REGIME

The ridges appear to be the dominant elements in a bed-form hierarchy of the sort described by Allen (1968). Small-scale elements include the transverse sand waves of the North Carolina shelf and the smaller transverse bed forms of the Virginia shelf. These latter features, in 20 m of water, are commonly less than a meter high and are technically current ripples. Their heights are clearly independent of flow depth; they are presumably responses to perturbations of the boundary layer rather than of the whole flow field (Allen, 1968a). However, it is perhaps more useful to classify these bed forms in terms of response times to intermittent storm pulses. For one thing, intermediate and large-scale elements (ridges and sand waves) must represent time-integrated responses to these pulses in which ridge heights and side slopes are less than maximum, reflecting a compromise between storm aggradation and degradation by fair-weather wave surge. Secondly, the large-scale forms extend up into the wave-agitated zone; this fact as well as flow depth limits their height.

Finally, the hydraulic regime itself is not stationary, but changes through the lives of the larger bed forms as a consequence of water deepening attendant on the Holocene transgression. Inner-shelf ridges on open coasts are formed as a consequence of the interaction of storm waves and currents with each other and the substrate. With detachment they find themselves in a simpler regime for which 10 m appears to be a wave-limited crestal depth (Duane et al., 1972). Shelf ridge fields with crests accordant at deeper levels may have retained this limit from lower sea-level stands, even though their troughs are being actively scoured.

The differing geometries of the ridge systems of estuary shoal-retreat massifs, cape shoal-retreat massifs and on the intervening shelf tend to disguise their fundamental genetic relationship. All are large-scale, more or less current-parallel bed forms whose spacing tends to increase with flow depth (Swift et al., 1972). Thus, the ridge and swale topography appears to be a stable end configuration toward which a variety of erosional and depositional topographies converge.

The extent to which offshore ridge fields are actively maintained and the extent to which helical flow occurs is difficult to evaluate without far more hydraulic data than is presently available. The coast-oblique orientation of shoreface-connected ridges may locally be traced for tens of kilometers offshore. It is a response to the pattern of wave and wind currents which prevailed in the generating zone on the shore face. On the shelf floor it is a relict pattern, as coast-parallel storm currents on the shelf would presumably have an offshore rather than onshore secondary compartment, if any, in the reverse Ekman spiral of the bottom friction layer. Thus, if helical flow cells are induced in coast-converging offshore troughs, their axes would be skewed relative to the main flow



Fig.10. Chincoteague Shoals, Maryland Coast, with 1881-isobaths (dashed) and 1934-isobaths (solid), and 1934-coast. Shoals are transitional between a shoreface-connected ridge field and a cape-associated shoal. Note southeastward movement of ridges (from Duane et al., 1972; from U.S.C.G.S. Surveys.)

field. On the inner shelf, ridges at least locally respond to such a flow structure by migrating to the southeast, seaward and down-coast (Duane et al., 1972; Fig.10, this paper), behaving more nearly like current-transverse bed forms than current-parallel ones; hence a coast-converging orientation of a ridge does not necessarily imply no sediment or bed-form movement. Note that in Fig.10, ridges further offshore have moved into parallelism with the shoreline, but are still migrating in a direction more southeasterly than their axes.

Elsewhere there is more direct morphologic evidence for reorientation of near-shore topography under the impetus of the shelf hydraulic regime. On the shoal-retreat massif associated with the Delaware Shelf Valley (Swift et al., 1972), ridges near the bay mouth are oblique to the regional trend of the shoreline and their crest lines are seaward-convex, presumably following tidal flow-lines sweeping from the shelf into the mouth of Delaware Bay (Fig.11). But as the crest of the shoal-retreat massif is traced seaward, the ridge crest lines become straight and essentially coast-parallel. If the Delaware shoal-retreat massif comprises a record of the retreat of the Delaware estuary-mouth shoal under steady state conditions, then the apparent rotation of transverse crest lines with distance from shore may be inferred to reflect the diminishing significance of the tidal component of flow and the increasing significance of the storm-driven flow component as the shoreline receded through Holocene time.

Remolding of the ridge topography as response to the inner-shelf hydraulic regime may have been discontinuous rather than continuous on the Great Egg Shoal-Retreat Massif (Swift et al., 1972). At a distance of 40 km from the shoreline and in 40–50 m of water, two ridge patterns are apparent on the back of the massif (first-order feature).

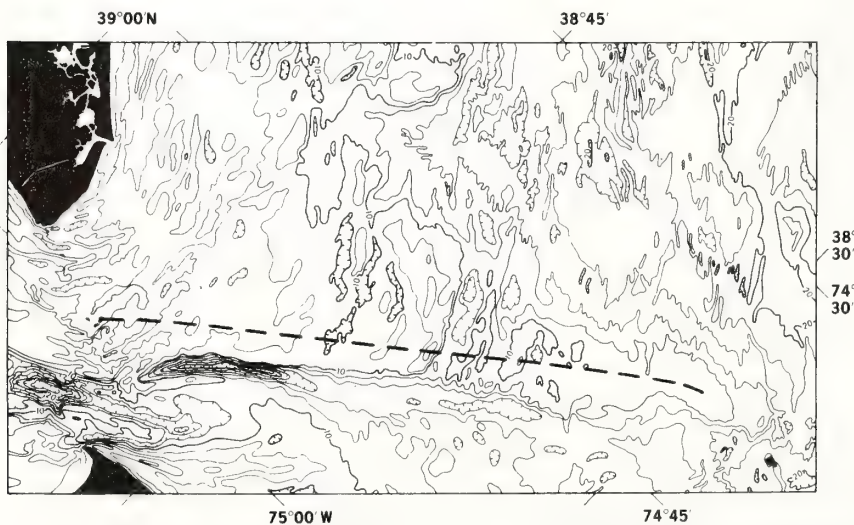


Fig.11. Delaware Bay mouth shoal and shoal-retreat massif. Note curved pattern of ridge crest lines near bay mouth. As axis of massif (dashed line) is traced seaward, ridge crestlines become coast-parallel. Contours in fathoms. (See U.S.C.G.S. map 0807N-57 for 1-fathom resolution.)

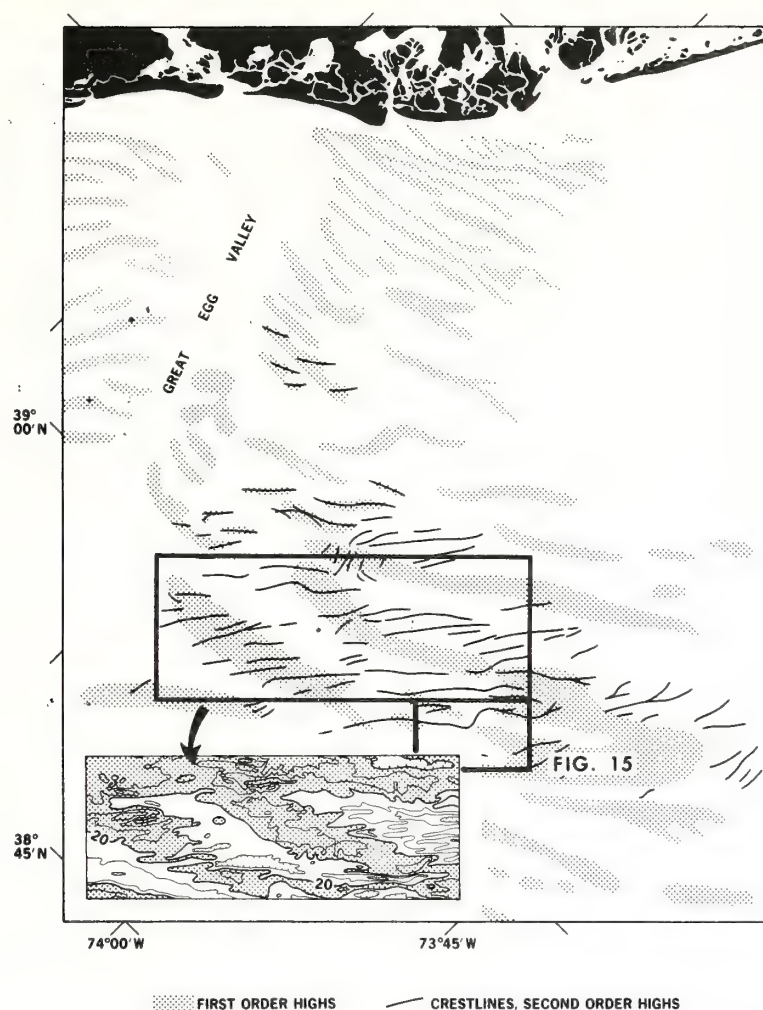


Fig.12. Great Egg Shelf valley and shoal-retreat massif. The more seaward large-scale ridges have had superimposed on them a more southerly trending, finer-scale ridge system. Inset contours in fathoms; depths shallower than 20 fathoms stippled. Based on U.S.C.G.S. map 0807N-55. (Adopted from McKinney et al., 1973.)

A large-scale pattern consists of "J"-shaped ridges which curve southward and westward toward the Great Egg Shelf valley (Fig.12). This pattern has been partly obliterated by a finer-scale pattern which trends more southerly than the first pattern. Small troughs have been incised into large ridges, which are still recognizable as en-echelon patterns of small ridges (inset, Fig.12). Apparently the initial cross ridges of the Great Egg Shoal-Retreat Massif were so large and so deeply incised during an initial stage of the transgression that they were unable to rotate in response to the more southerly flow of later stages and were instead cut into en-echelon segments.

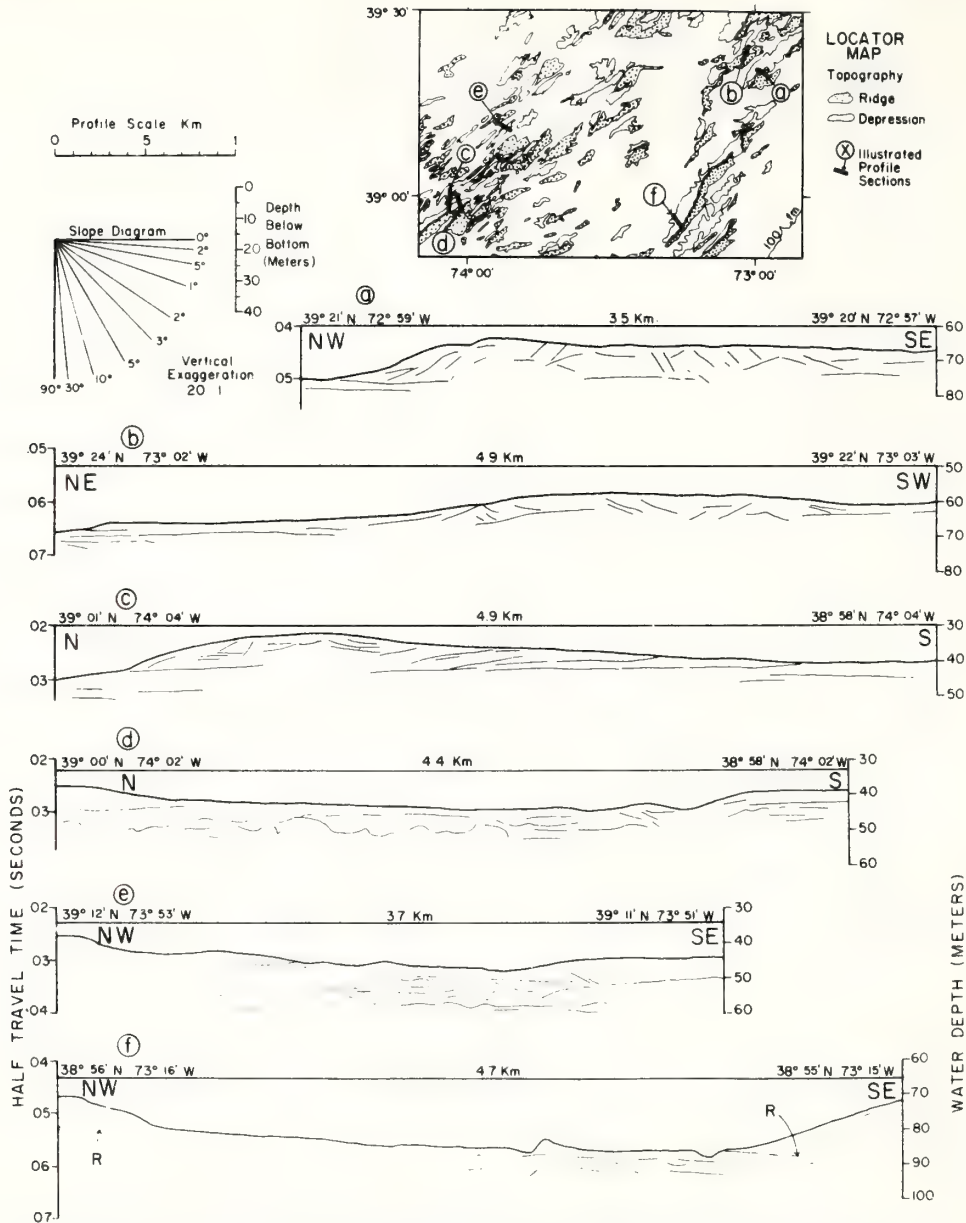


Fig.13. Line drawing from seismic records indicating internal stratification of ridges on New Jersey. (From McClennen, in press)

A final important piece of evidence concerning progressive modification of the ridges comes from seismic profiles collected by McClennen (in press) on the New Jersey Shelf (Fig.13). These records show that ridges may have one or more cores of strata dipping away from a common crest. These core strata tend to be more steeply inclined than

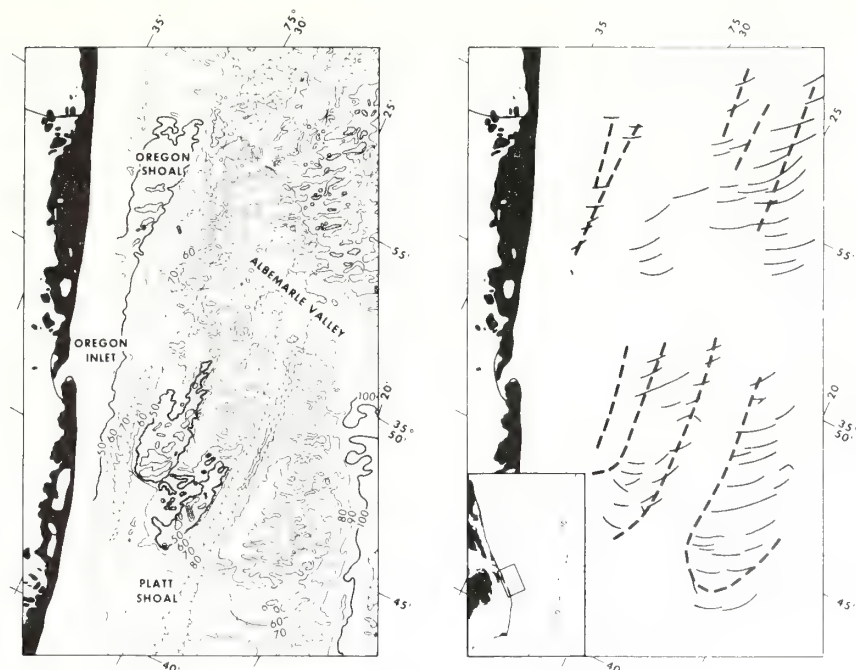


Fig.14. Bathymetry of the Platt Shoals sector, North Carolina Shelf. Contour interval 10 ft. Isolated highs are stippled. Oregon Shoal is still connected to shore face; other ridges south of Albermarle Shelf valley are largely or wholly detached. Lower ridges are double-crested. Shallow troughs between double crests contain southward-convex sand waves suggestive of divergent trough currents. (From Swift et al., 1973).

existing slopes (profiles *a* and *b*). In one case, the crest of a ridge seems to have shifted so that some strata are inclined away from a former crest sited in what now is the adjacent trough (right-hand side of profile *c*).

A comparison of ridge spacing with flow depth on the Atlantic Shelf suggests that, as noted by Allen (1968a), ridges become further apart with increasing depth (Swift et al., 1972, fig.232). The internal stratification of Fig.13 suggests that ridge spacing increases partly by the merging of several ridges and partly by lateral migration. The irregular tendency toward progressive decrease in size slope suggests that ridge-maintaining processes are not able to increase height at the same rate as spacing.

A particularly vexing problem is the role of helical flow in inducing ridge topography. Direct observations of the fine structure of the storm flow field are almost nonexistent, although instrumentation potentially capable of such observations is presently being developed. Morphologic evidence for helical flow such as oblique or herringbone patterns of sand waves on ridge flanks which are present in the North Sea (Caston, 1972) have not yet been identified with certainty on the Atlantic Shelf, although some suggestive patterns appear in recent precision surveys of the National Ocean Survey (Swift et al., 1973; Fig.14, this paper).

There is, however, a consoling aspect to the general scarcity of sand-wave fields on the Atlantic Continental Shelf, in that this lack is consonant with the general hypothesis of storm-driven sedimentation. Sandwave fields are localized in areas where the storm flow-direction is stabilized by the proximity of the shoreline (Fig.14), or by the friction of a regionally shoaling bottom, as on the crests of cape shoal-retreat massifs (Fig.9). Elsewhere, the variance in direction of successive storm-current directions may be assumed to be high (Sternberg and McManus, 1972), and currents may in fact rotate during a single storm as the wind direction rotates. As noted by McCave (1971), a variable current attack inhibits transverse bed forms, and Smith (1969) favors longitudinal ones. The dominant meso-scale bed form of the Atlantic Shelf may in fact be the sand ribbons and elongate sand patches detected by McKinney et al. (1973) on side-scan sonar records from the central New Jersey Shelf (McKinney et al., 1973; Fig.15, this paper). If large-scale helical flow structure prevails during storms, sand ribbons (from small-scale helical flow) also might be expected to form herringbone patterns. Such patterns are not apparent in Fig.15. However, bottom-current convergence angles are very small in helical flow structure (Allen, 1968b), and resulting convergent ribbon patterns would be difficult to resolve without precision navigation and close control of the lateral exaggeration (Bel-

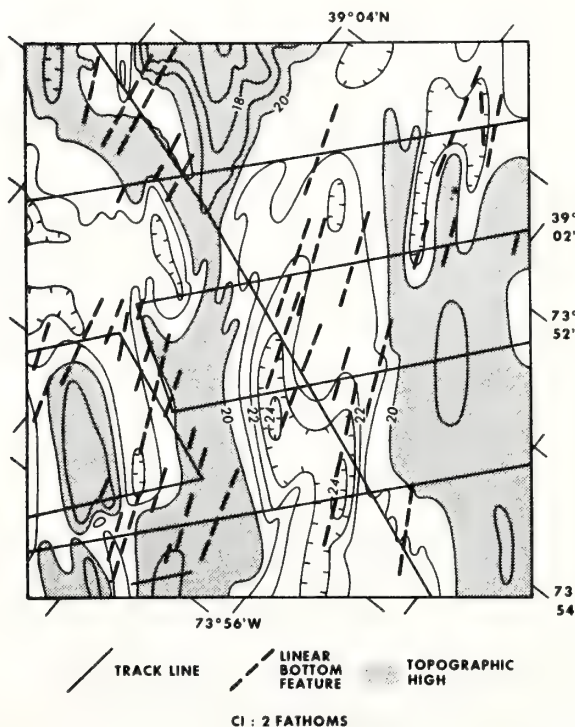


Fig.15. Detail of central New Jersey Shelf. See Fig.12 for location. Dashes indicate orientations of representative sand ribbon-like features observed by side-scan sonar. (From McKinney et al., 1973.)

derson et al., 1972) inherent in side-scan sonar records. Patterns of very slight ribbon convergence may or may not be concealed in Fig.15. In any case, the ribbons and any convergences that they might define, trend obliquely across the ridges in an independent fashion

The problem is further complicated by the variability of storm current directions mentioned above. The sand ribbon-like features mapped in Fig.15 have spacings up to 100 m, but commonly do not exhibit detectable relief. They may represent the mean current direction of the last significant storm, skewed slightly to ridge axes. Some fish-hook-shaped features (skewed barchans; Allen, 1968a) may be transverse sand waves formed during the flow maximum of a single storm and partially remade into longitudinal forms as the waning current rotated (McKinney et al., 1973). Thus, the main sand ridges, if capable of responding, may reflect a mean storm flow direction. When flow directions coincide with ridge axis, helical flow may or may not still be induced; as currents rotate and become increasingly oblique to ridge axis, helical cells skewed to the regional flow direction may persist; or flow may become uniform. Smith (1969) has argued that rotating tidal currents maintain ridges orientated parallel to mid-tide flow vectors simply by sweeping first up one side then up the other. Variable storm currents may similarly help to preserve offshore ridge fields of the Atlantic Shelf even without the helical flow mechanism.

The selected portions of the Mid-Atlantic Shelf discussed in this paper show that relict topography patterns may be discerned in offshore ridge fields. But in some cases, there is evidence for progressive morphologic change on the inner shelf during transgression. Thus, the shelf surface has at least locally fulfilled the criterion of an equilibrium system — one which, when stressed, responds in such a way as to relieve the stress. Whether the outer shelf ridge fields are capable of so responding is a moot point. As the shoreline recedes and the water depth increases, fewer storm events are sufficiently prolonged and intense for wind drift currents to propagate to the sea floor. As water depth increases, the geostrophic component of flow becomes more important. The geostrophic component, unlike the wind drift component, is driven by horizontal pressure gradients which are constant with depth. Its frequency of occurrence, however, is a function of distance from shore, since the required landward pile-up of water may require several days of onshore winds to propagate as far seaward as the outer shelf. Consequently it may not be particularly meaningful to inquire whether or not outer shelf ridge fields on storm-dominated shelves such as the North American Atlantic Shelf are purely equilibrium or relict surfaces. We should perhaps instead be concerned with the time constants associated with substrate response.

ACKNOWLEDGEMENTS

Portions of data presented in this study stem from the general research program of the corps of U.S. Army Coastal Engineering Research Center. Permission was granted by the Corps of Engineers to publish this information. Work on the Virginia coast was carried

out under contract DACW79-69-C-0016 between CERC and Old Dominion University, Norfolk, Va. Additional funding of the Virginia coast work was provided by NSF Grants GA-13831 and GA-27305 and by the office of Marine Geology, United States Geological Survey, Woods Hole, Mass. Portions of the field work were conducted aboard the Duke University R/V "Eastward", supported by NSF Grant GB-17545. Contributions by Swift and McKinney to this paper are part of the Atlantic Oceanographic and Meteorological Laboratories' contribution to NOAA's MESA project. The side-scan sonar data from the central New Jersey Shelf were gathered in the course of a submersible investigation sponsored by the Manned Undersea Science and Technology Office of NOAA.

REFERENCES

- Allen, J. R. L., 1968a. The nature and origin of bed-form hierarchies. *Sedimentology*, 10: 161–182.
- Allen, J. R. L., 1968b. *Current Ripples*. North-Holland, Amsterdam, 433 pp.
- Allen, J. R. L., 1970. *Physical Processes of Sedimentation*, American Elsevier, New York, N.Y., 248 pp.
- Belderson, R. H., Kenyon, N. H., Stride, A. H. and Stubbs, A. R., 1972. *Sonographs of the Sea Floor*. American Elsevier, New York, N.Y., 185 pp.
- Brown, R. A., 1970. Secondary flow model for the planetary boundary layer. *J. Atmos. Sci.*, 27: 742–757.
- Caston, V. N. P., 1972. Linear sand banks in the southern North Sea. *Sedimentology*, 18: 63–78.
- Duane, D. B., Field, M. E., Meisburger, E. R., Swift, D. J. P. and Williams J. S., 1972. Linear shoals on the Atlantic inner continental shelf, Florida to Long Island. In: D. J. P. Swift, D. B. Duane and O. H. Pilkey (Editors), *Shelf Sediment Transport: Process and Pattern*, Dowden, Hutchinson and Ross, Stroudsburg, Pa., pp. 477–498.
- Field, M. E. and Duane, D. B., 1973. Geomorphology and sediments of the inner continental shelf off Cape Kennedy, Florida. *U. S. Army Coastal Eng. Res. Cent., Tech. Memo.*, 39 (in press).
- Harrison, W., Norcross, J. J., Pore, N. A. and Stanley, E. M., 1967. Shelf waters off the Chesapeake Bight. *Environ. Sci. Serv. Adm., Prof. Pap.*, 3: 1–82.
- Kraft, J. C., 1969. Sedimentary facies patterns and geologic history of a Holocene marine transgression. *Geol. Soc. Am. Bull.*, 82: 2131–2158.
- Langfelder, J., Stafford, D. and Amein, M., 1968. *A Reconnaissance of Coastal Erosion in North Carolina*. Civil Engineering Dept., North Carolina State University, Raleigh, N. C., 127 pp.
- Laursen, E. M., 1958. The total sediment load of streams. *Proc. Am. Soc. Civil Eng.*, 84: 1530.
- Lavelle, W., Stubblefield, W., and Swift, D. J. P., 1973. Application of sediment transport functions to the shelf floor (in preparation).
- McCave, I. N., 1971. Sand waves in the southern bight of the North Sea. *Mar. Geol.*, 10: 199–225.
- McClennen, C. E., 1973. New Jersey continental shelf near bottom current meter records and recent sediment activity. *J. Sediment. Petrol.*, 43: 371–380.
- McClennen, C. E., in press. Nature and origin of the New Jersey continental shelf topographic ridges and depressions. *Geol. Soc. Am. Bull.*
- McClennen, C. E., and McMaster, R. L., 1971. Probable Holocene transgression effects in the geomorphic features of the continental shelf off New Jersey, United States. *Marit. Sed.*, 7: 69–72.
- McKinney, T. F., and Friedman, G. M., 1970. Continental shelf sediments of Long Island, New York. *J. Sediment. Petrol.*, 40: 213–248.
- McKinney, T. F., Stubblefield, W. and Swift, D. J. P., 1973. Large-scale current lineations on the central New Jersey shelf: Evidence from side scan sonar (in preparation).
- Meisburger, E. P. and Duane, D. B., 1971. Geomorphology and sediments of the inner continental shelf, Palm Beach to Cape Kennedy, Florida. *U. S. Army Coastal Eng. Res. Cent., Tech. Memo.*, 34: 42 pp.

- Milliman, J. D., Pilkey, O. H. and Ross, D. A., 1972. Sediments of the continental margin off the eastern United States. *Geol. Soc. Am., Bull.*, 83: 1315–1334.
- Sanders, J. E., 1962. North–south trending submarine ridge composed of coarse sand off False Cape, Virginia. *Am. Assoc. Pet. Geol., Bull.*, 46: 278 (abstract).
- Sanford, R. B. and Swift, D. J. P., 1971. Comparison of sieving and setting techniques for size analysis, using a Benthos Rapid Sediment Analyzer. *Sedimentology*, 17: 257–264.
- Shepard, F. P., 1963. *Submarine Geology*. Harper and Row, New York, N.Y., 2nd ed., 557 pp.
- Smith, J. D., 1969. Geomorphology of a sand ridge. *J. Geol.*, 72: 39–55.
- Smith, J. D. and Hopkins, T. S., 1973. Sediment transport on the continental shelf of Washington and Oregon in the light of recent current meter measurements. In: D. J. P. Swift, D. B. Duane and O. H. Pilkey (Editors), *Shelf Sediment Transport: Process and Pattern*. Dowden, Hutchinson and Ross, Stroudsburg, Pa., pp. 143–180.
- Stahl, L., Koczan, J. and Swift, D., 1973. Anatomy of a shoreface-connected ridge system on the New Jersey shelf: Implications for the genesis of the shelf surficial sand sheet. *Geol. Soc. Am., Bull.* (in press).
- Sternberg, R. W. and McManus, D. A., 1972. Implications for sediment dispersal from long term bottom current measurements on the continental shelf of Washington. In: D. J. P. Swift, D. B. Duane and O. H. Pilkey (Editors), *Shelf Sediment Transport: Process and Pattern*. Dowden, Hutchinson and Ross, Stroudsburg, Pa., pp. 143–180.
- Swift, D. J. P., Kofoed, J. W., Saulsbury, F. P. and Sears, P., 1972. Holocene evolution of the shelf surface, central and southern Atlantic shelf of North America. In: D. J. P. Swift, D. B. Duane and O. H. Pilkey (Editors), *Shelf Sediment Transport: Process and Pattern*. Dowden, Hutchinson and Ross, Stroudsburg, Pa., pp. 499–573.
- Swift, D. J. P., Shideler, G. L., Holliday, B. W., McHone, J. and Sears, P., 1973. Distribution and genesis of inner continental shelf sands, Cape Henry to Cape Hatteras. *U. S. Army Coastal Eng. Res. Cent., Tech. Memo.* (in press).
- Uchupi, E., 1968. Atlantic continental shelf and slope of the United States – Physiography. *U. S. Geol. Surv., Prof. Pap.*, 529C: 30 pp.
- Uchupi, E., 1970. Atlantic continental shelf and slope of the United States – Shallow structure. *U.S. Geol. Surv., Prof. Pap.*, 600D: 231–234.
- Veatch, A. C. and Smith, P. A., 1939. Atlantic submarine valleys of the United States, and the Congo submarine valley. *Geol. Soc. Am., Spec. Pap.*, 7: 101 pp.
- Wilson, I. G., 1972. Aeolian bed-forms, their development and origins. *Sedimentology*, 19: 173–210.

CHAPTER 23

Holocene Evolution of the Shelf Surface, Central and Southern Atlantic Shelf of North America

**Donald J. P. Swift,* John W. Kofoed,*
Francis P. Saulsbury,* and Phillip Searst†**

ABSTRACT

The floor of the central and southern Atlantic shelf is a palimpsest or multiple imprint surface. An initial pattern is an erosional one consisting of major transverse shelf valleys and plateaulike interfluvies. The dominant pattern is that of constructional topography formed at the foot of the shoreface. This constructional pattern is undergoing modification toward a third pattern in response to the modern hydraulic regime; therefore, the term "relict" does not seem an adequate descriptor. A unifying concept for the interpretation of Holocene shelf history is that of Bruun coastal retreat. This variant of the equilibrium profile hypothesis states that a rise in sea level over an unconsolidated coast results in shore-face erosion, equivalent to parallel slope retreat, and a concomitant aggradation of the adjacent sea floor. The resulting discontinuous debris mantle, the Holocene transgressive sand sheet, is only partly autochthonous with respect to the Holocene sedimentary cycle, since it incorporates Holocene fluvial deposits.

The surface of this sand sheet has been molded into a variety of morphologic elements. Where the sheet has been generated directly from the retreating shoreface, a ridge-and-swale topography has been impressed upon it. Off cusped forelands, the convergence of littoral drift has resulted

*Atlantic Oceanographic and Meteorological Laboratories, National Oceanic and Atmospheric Administration, 15 Rickenbacker Causeway, Miami, Florida, 33149.

†Institute of Oceanography, Old Dominion University, Norfolk, Virginia 23508.

in cape-associated shoals. Off estuary mouths the intersection of littoral drift with the reversing estuary tide has created inlet-associated shoals. Seaward of each of these shoal types, earlier generations of the same shoals commonly occur. The resulting shelf-transverse sand bodies, formed by the progressive landward displacement of shoreline depositional centers, are shoal-retreat massifs.

The ridge-and-swale topography is impressed on shoal-retreat massifs, as well as on other sectors of the shelf floor and appears to be a stable end-configuration toward which a variety of depositional and erosional topographies tend to converge. The asymmetry of large-scale morphological elements and also of small-scale bedforms suggests that southward sediment transport in the Middle Atlantic bight intensifies toward shore and toward the south. The southward asymmetry of ridges and shoal complexes is seen as far south as Florida.

INTRODUCTION

Scope of Paper

This paper has been written on the premise that the existing data on the morphology of the North American Atlantic shelf floor, and to a lesser extent data on petrography, shallow structure and hydraulic regime, has reached a sort of critical mass, whereby this information can be systematically appraised and conclusions concerning the Holocene evolution of the shelf surface can be drawn, which could not be inferred from examination of the facts separately.

The preceding chapter has concerned itself with a morphological element that constitutes a major key to the nature of shoreface retreat and the morphological development of the shelf surface—namely, the linear shoals that dominate the inner-shelf surface. The preceding paper has maintained that, while many aspects of the process are obscure, the shoreface-connected shoals appear to be presently forming at the foot of the shoreface, and that the shoal fields of the inner shelf comprise a record of Holocene shoreface retreat. This paper explores ramifications of this hypothesis. It considers the more general problem of Holocene shoreface retreat of the central and southern Atlantic shelf and its effect on the shelf surface. It also considers large-scale morphological elements that themselves are compounded of the linear shoals described in the previous chapters, and attempts to determine their relevance to the Holocene history of the shelf. Lastly, it attempts to draw preliminary conclusions concerning the nature of Holocene shelf sediment transport in the study area.

Nature of Data: Approach

The central and southern Atlantic coast of North America was the first to be explored and is presently the most densely populated; consequently, bathymetric data are abundant for this sector (Schopf, 1968). Much of it dates from the advent of echo sounding in the third decade of the century. Veatch and Smith (1939) were the first to utilize echo-sounding data for geologic interpretation

and prepared a detailed bathymetric map of the New Jersey shelf at a scale of 1 : 120,000, contoured at a one-fathom interval. They gave names to numerous large- and small-scale morphological features in this region.

Stearns (1967) prepared 15 bathymetric maps of the shelf between Cape Cod and the Delaware coast at a scale of 1 : 25,000, contoured at a one-fathom interval. The data points are considerably denser than those available to Veatch and Smith. The maps reveal a ridged surface with a relief of 5 to 10 m, whose complexity and variety must be seen to be believed.

Other significant maps used in this study include: "Map showing relationship of land and submarine topography, Nova Scotia to Florida," at a scale of 1 : 100,000, with a 20 m contour interval by Uchupi (1965, 1968), and "Bathymetric map of the slope, shelf, and rise between Nantucket Shoals and Chesapeake Bay," by Uchupi (1970), at a scale of 1 : 75,000 with a 4 m contour interval. Portions of this map have been presented in the previous chapter as Figs. 171 to 173.

Since some maps used in this paper use the English system of units, their values will be described in the text in both the metric and English systems. Elsewhere, distances will be reported in the metric system.

The net effect of these maps is to produce a wealth of bathymetric detail which is embarrassingly in advance of our knowledge of the shallow stratigraphy, petrography, and hydraulic regime for the same area. A full understanding of the genesis of the shelf morphology will require further acquisition and interpretation of data in all these fields. Supplementary stratigraphic, petrographic, and hydraulic data from the literature and from the author's own observations are employed in this paper wherever possible. However, the bulk of the analysis is based on unsupported bathymetric information. This procedure is employed in the hope that such a preliminary regional assessment will greatly aid the authors and readers in defining specific problems relating to evolution of the shelf surface, and water-substrate interaction at this interface, and in designating specific areas in which the substrate should be sampled and the hydraulic regime monitored.

A Topographic Inventory

The morphological elements of the central and southern Atlantic shelf can be conveniently arranged in a hierarchical array (Table XXX), in which higher-order elements tend to incorporate lower-order elements. The ridge-and-swale topography, examined on the inner shelf in the preceding paper, is the dominant first-order morphological element over many shelf sectors (Figs. 171, 172, 173, preceding chapter).

An inner shelf province consists of long, regular, subparallel ridges and swales aligned obliquely across the regional trend of the contours and converging with

Table XXX
Morphological Elements of the Central and Southern Atlantic Shelf

Small-scale elements	
Ripples and sand waves	
Large-scale elements	
First order:	Shoreface-connected ridges and swales Isolated ridges and swales
Second order:	Cape-associated shoals Inlet-associated shoals Ridge fields
Third order:	Shoal-retreat massifs Shelf-transverse valleys Cuestas Deltas Scarps

the shoreline at an angle averaging 20°. Ridge spacing averages 2.1 km (1.2 n mi); ridge amplitude ranges from 2 to 10 m (6 to 33 ft) and ridge length varies from 9 to 56 km (5 to 3 n mi). See Table XXXI. Side slopes are generally several degrees or less. Locally, clusters of ridges trend into the shoreface, generally merging with it at depths of 10 m (33 ft) or less.

A second topographic province occurs on the outer shelf. The boundary on the Long Island shelf occurs at variable depths and distances from shore, being generally coincident with the change in slope separating the relict Long Island drainage basin of the outer shelf from the ridged surface of the inner shelf (Figs. 192, 193, 194). Typical inner-shelf ridge-and-swale topography extends seaward on the promontory east of the drainage basin to depths of 76 m (225 ft) at a distance of 102 km (55 n mi) from shore. Further west, on the Long Island shelf, the boundary between the inner and outer topographic provinces coincides with the 40 m (131 ft) contour, and this isobath continues to serve as the boundary on the New Jersey shelf (Fig. 171, previous paper). To the south, however, the boundary shoals; at Cape Hatteras it lies at 30 m (100 ft). See Fig. 196 and Fig. 173, 174, previous paper. The outer shelf ridge-and-swale topography appears less complex, partly, perhaps, because bathymetric data is less dense. Ridges are subparallel to the shelf edge, but still form northward-opening angles with the regional trend of the contours and with the shelf edge. They tend to be further apart, with an average spacing of 6 km (2.8 n mi). The pattern made by the troughs suggests an incomplete trellis pattern (Figs. 194, 195). Scarps of apparent littoral origin are more abundant.

Careful examination of existing maps indicates that the ridge-and-swale topography is superimposed on a framework of higher-order morphological elements of both constructional and erosional origin. Ridges occur in groups as inner shelf ridge fields, inlet-associated shoals, and cape-associated shoals (see pre-

Table XXXI
Descriptive Statistics for Ridge-and-Swale Topography

Map	NE Corner, 15' Quadrangle	Province	Mean ridge length (km)	Mean ridge spacing (km)	Mean relief (m)	Trough line km per km ²
Long Island 0808N-54	40° 45' - 73° 00'	Shoreface	17.8	2.2	5.5	0.10
Long Island 0808N-54	40° 45' - 72° 15'	Inner shelf	30.7	2.0	3.4	0.10
Long Island 0808N-54	40° 30' - 72° 00'	Inner shelf	54.9	2.2	1.7	0.07
Long Island 0808N-54	40° 15' - 69° 45'	Inner shelf	18.5	1.7	3.8	0.10
New Jersey 0807N-55	39° 15' - 74° 15'	Shoreface	12.2	1.4	4.7	0.14
New Jersey 0807N-55	39° 15' - 74° 00'	Inner shelf	16.6	2.6	6.2	0.09
New Jersey 0807N-55	30° 00' - 73° 45'	Inner shelf	12.8	2.4	5.7	0.09
New Jersey	38° 45' - 73° 30'	Outer shelf	32.9	6.1	6.0	0.08

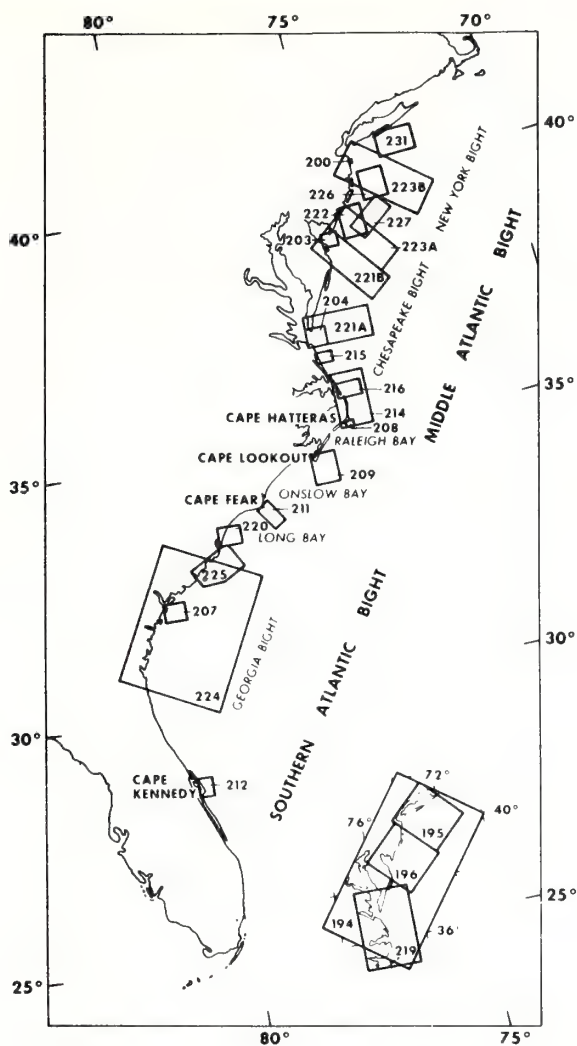


Figure 192.

Index map of topographic maps presented in this paper.

vious paper). Obvious erosional elements are the transverse shelf valleys (Fig. 193; Figs. 171, 172, 173, preceding paper), upon whose interfluvies the ridge-and-swale topography has been developed. The Hudson shelf valley (Veatch and Smith, 1938), Block shelf valley (Veatch and Smith, 1938; Garrison and McMaster, 1966), and Long Island shelf valley (Garrison and McMaster, 1966; McKinney and Friedman, 1970) are known from the literature. Other shelf

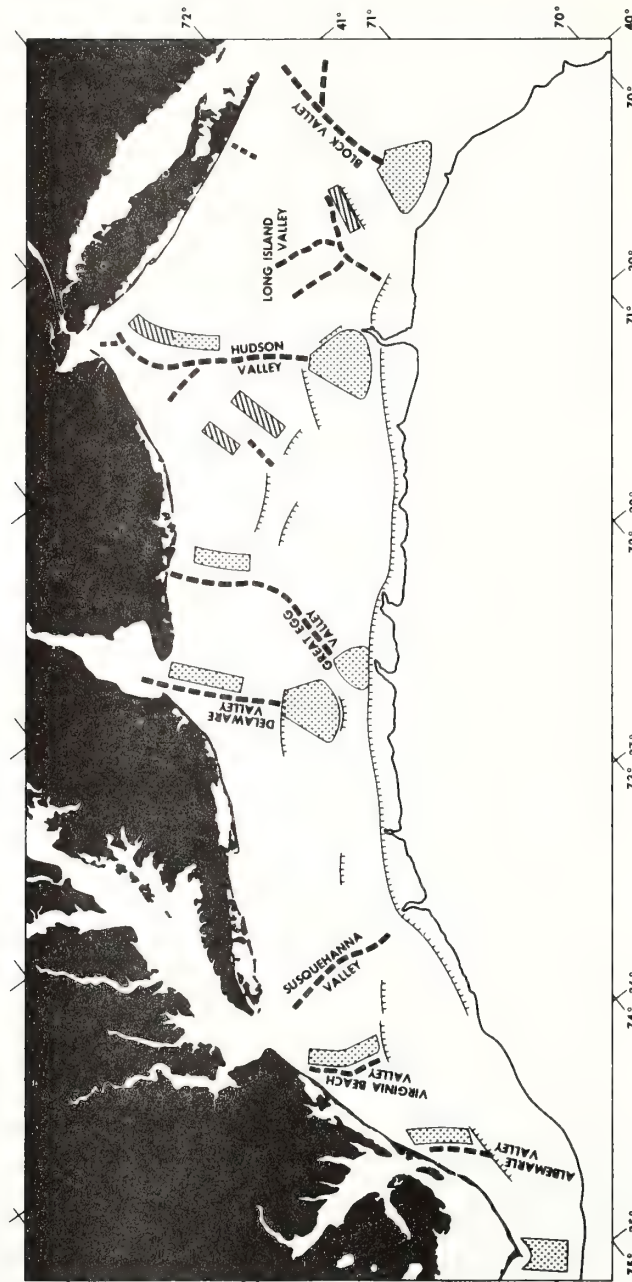


Figure 193.
Major morphological elements of the middle Atlantic bight. Dashed lines are shelf valleys. Hachured lines are scarps. Stippled areas are highs of probable constructional origin, including shoal-retreat massifs and stillstand deltas. Diagonally ruled areas are areas of probable erosional origin, including cuestas.

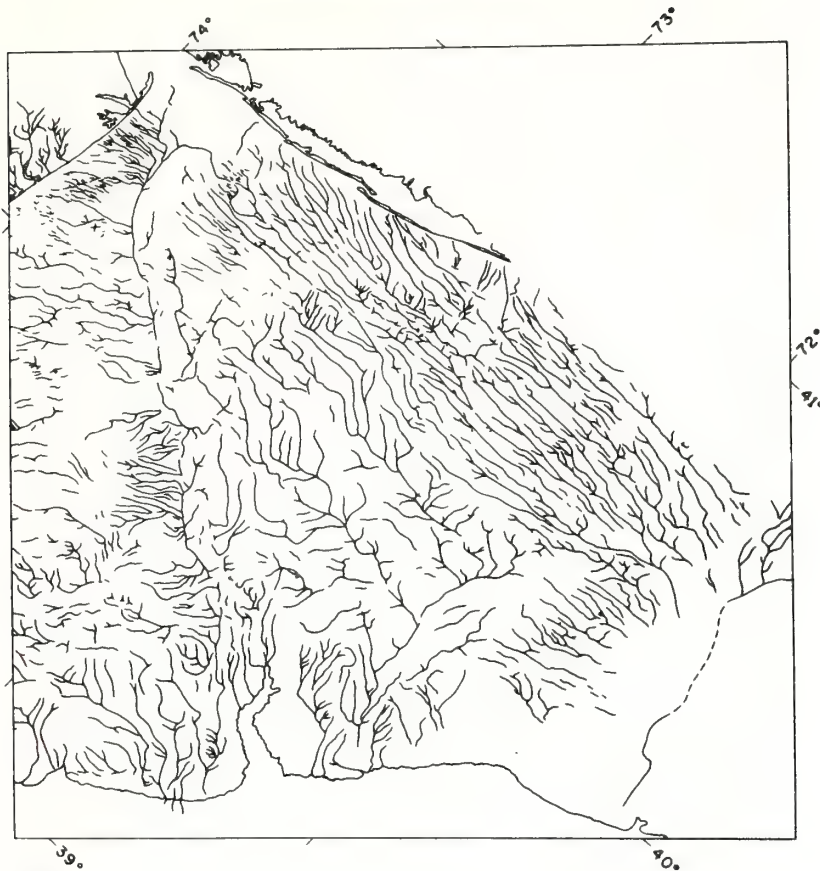


Figure 194.

Pattern of linear lows on the Long Island shelf. Based on Stearns (1967).

valleys in Fig. 193 have been designated in this paper on the basis of existing and newly prepared bathymetric maps. Low, poorly defined large-scale, shelf-transverse ridges, often with ridge-and-swale topography superimposed on them, are believed to be in part shoal-retreat massifs or constructional features resulting from the retreat of nearshore depositional centers (cape- and inlet-associated shoals) with the transgressing shoreline (Fig. 193; Figs. 171, 172, 173, preceding paper). Other shelf ridges, particularly on the northern New Jersey and Long Island shelves, are interpreted as cuestas of erosional origin.

An additional higher-order morphological element consists of subcircular shelf-edge and mid-shelf plains, which may be either ridged or smooth. Their inner margins are depressed with respect to the surrounding shelf, and the contours here bend landward. Their outer margins tend to stand above the surrounding

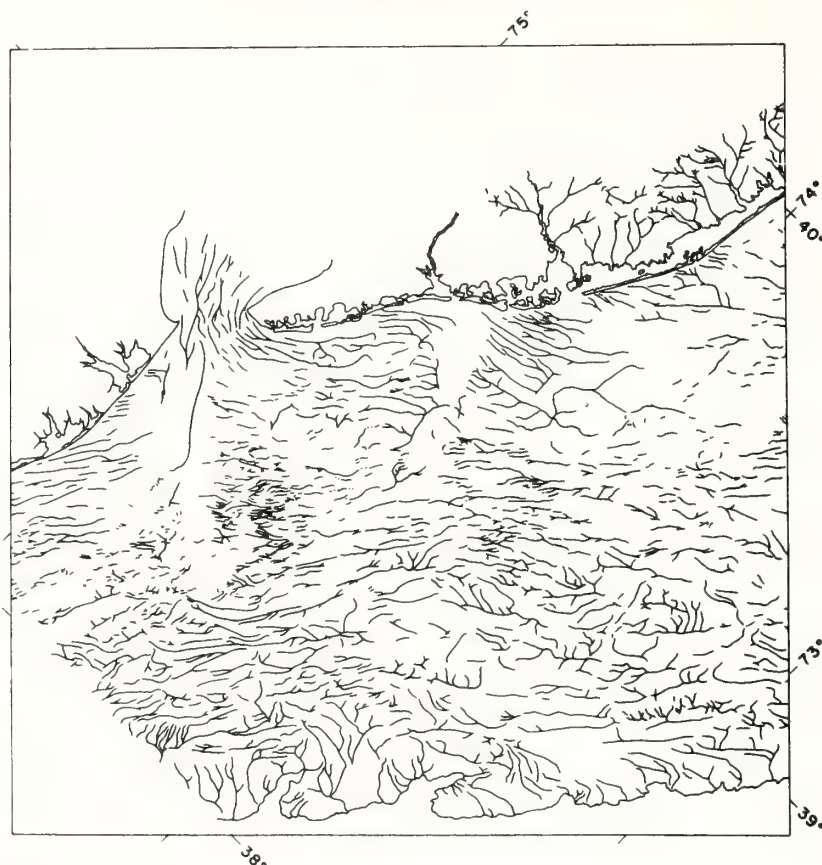


Figure 195.

Pattern of linear lows on the New Jersey shelf. Based on Stearns (1967).

shelf, and the contours here bend seaward. Proximity to transverse shelf valleys indicates that these are shelf deltas. The Block and Hudson shelf deltas have been described in the literature (Veatch and Smith, 1938; Ewing and others, 1963; Garrison and McMaster, 1966; Knott and Hoskins, 1968). The Delaware and Great Egg shelf deltas have been placed in Fig. 193 on the basis of maps by Stearns (1967) and Uchupi (1970).

A final higher-order morphological element consists of the partly constructional and partly erosional shelf-parallel scarps that are interpreted as drowned shorelines. The Nichols and Franklin shorelines have been described by Veatch and Smith (1938) and Uchupi (1968, 1970). The boundary between the inner- and outer-shelf provinces is at many localities a well-defined scarp. It is designated in this paper as the mid-shelf shore. Merrill and others (1965) have noted a

concentration of oyster shells at this depth, with dates suggesting a Holocene stillstand.

THE RETREATING SHORE FACE

Nature of the Problem

The genesis of the inner-shelf ridge systems and the evolution of the Holocene shelf surface as a whole are inextricably bound up in the problem of shore-face retreat, and it is necessary to consider this process in detail before attempting to interpret the morphological elements described in the preceding section. Three dominant hypotheses for the generation of the ridge-and-swale topography of the shelf have been presented in the previous paper. They imply three differing modes of shore-face retreat. The hypothesis that the ridges reflect stillstands of the advancing Holocene sea requires that the advancing sea deposit a blanket of littoral sand and that the terrestrial surface is preserved beneath it. The hypothesis that present submarine shelf surface is a drowned subaerial surface of relict fluvial or older marine origin requires that the advancing sea neither bury nor destroy the terrestrial surface. The hypothesis set forth by Moody (1964) requires that Holocene marine marginal deposits are consumed during retreat of the shore face and that the resulting debris is reshaped to form the ridge topography. In this case the advancing sea also deposits a blanket of sand, but it is the product of nearshore marine rather than littoral processes and the terrestrial surface has been truncated by the transgressive process itself.

Sloss (1962) and Allen (1964) have given some thought to the variables which determine the nature of shore-face retreat. They have listed them as the rate of relative sea-level rise (R), the character of the sediment (G), the rate of sediment input (S), and the energy input (E). It is convenient for expository purposes to group these variables in quasi-quantitative fashion:

$$\left(\frac{S}{E}\right)_G - R = K$$

to indicate that, for a given sediment character (for instance, grain size), the ratio between the rate of sediment input (S) and the energy available to disperse it (E) must be balanced by the relative rise in sea level (R); otherwise, the coastline will advance or retreat. Curray (1964) has described three cases of transgression involving successively larger negative values of K and corresponding to the three varieties of shore-face retreat listed above. In depositional transgression, subsidence is only slightly in excess of the rate of sediment input, but is more significant than the energy level. It corresponds to the first case, where a littoral sand blanket is deposited. In discontinuous depositional transgression, deposition is less able to keep up with the rate of sea-level rise and deposits

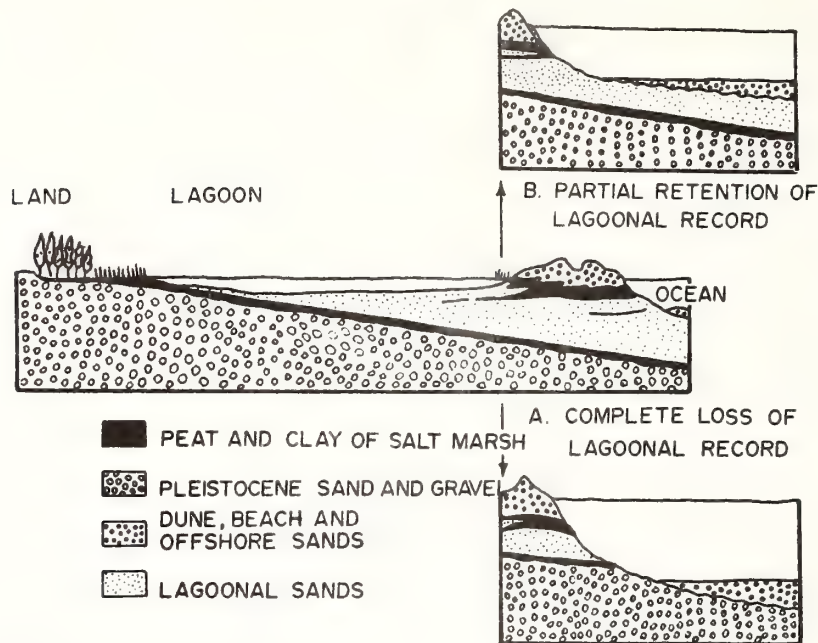


Figure 196.

Erosional (A) and depositional (B) transgressive stratigraphy, depending on the relative depth of excavation of the shore face. From Fischer, 1961.

are thin and discontinuous or lacking. In erosional transgression, the energy level is presumably also significant and the deposits formed are the consequence of shore-face erosion. See Fig. 196.

The problem of shoreface retreat has also been attacked from a geometric point of view. The concept of the equilibrium profile was the focal point of the early, deductive school of shelf geomorphology exemplified by Gulliver (1899), Fenneman (1902), and Johnson (1919). The shelf was seen as a surface curved exponentially about an axis parallel to the shore and concave up, with the steep, nearshore sector comprising the shore face. The shore face was interpreted as a response to the regime of shoaling waves, whereby the slope at any point is the most stable one for purposes of absorbing wave energy. A change in the intensity or configuration of the long-term average energy field must be met by a compensating change in the equilibrium profile, by such erosion or deposition as is necessary.

The concept of the equilibrium profile has recently been restated by Bruun (1962) in a more restricted form that is helpful in interpreting coastal evolution. Bruun's rule, as amplified by Schwartz (1965, 1967, 1968), states that, on a low, unconsolidated coast, a rise in sea level results in shore-face erosion

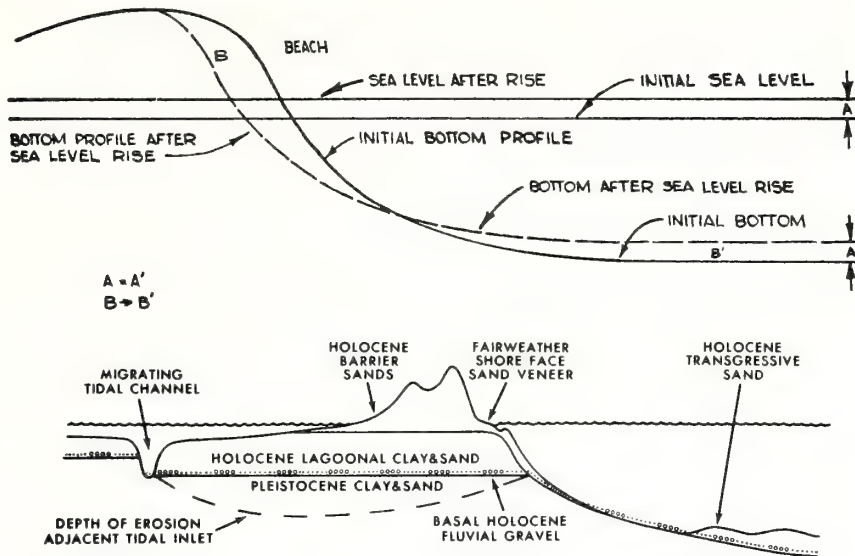


Figure 197.

(A) Schematic diagram of Bruun coastal retreat. During a rise in sea level, shore-face erosion and aggradation of the sea floor tend to balance. The resulting forward and upward translation of the shore profile results in a constant shore distance to water-depth relationship. From Schwartz, 1965. (B) Schematic stratigraphic model of North Carolina coast. Bruun coastal retreat has resulted in debris mantle (Holocene transgressive sand sheet) over resting disconformably on substrate. Size of beach greatly exaggerated. From Swift et al. (1971).

and an equal-volume aggradation on the adjacent sea floor. The result is a landward and upward translation of the equilibrium profile (Fig. 197), such that, in the immediate vicinity of the shore face, sea-level rise at a given point is balanced by deposition. The utility of the idea lies in the accretionary sediment blanket, which becomes the "relict" or transgressive sand blanket found on the present Atlantic Shelf floor, and the deposit on whose surface the ridge topography has formed. The concept emphasizes shore-normal sediment transport and, taken literally, requires that longshore transport be a steady-state process resulting no net change of sediment volume in the area under consideration. The concept as described is applicable primarily to a mainland beach or substructure of a coastal barrier. A model for barrier island retreat must be extended to include the behavior of the barrier superstructure, which tends rather to undergo retreat in cyclic, tank-tread fashion by a process of storm washover, burial, and re-emergence at the shore face (Dillon, 1970; Swift and others, 1971a, see Fig. 197, this paper). A mathematical model for shore-face erosion as a consequence of sea-level change has been presented by Scheidegger (1970, p. 324-328).

The concepts presented above will be used to examine, by means of case studies, the nature of coastal retreat along the central and southern Atlantic coast.

Erosional Transgression and Coastal Retreat in the Middle Atlantic Bight

General

The middle Atlantic Bight, between Cape Cod and Cape Hatteras, would appear to be experiencing the necessary conditions for erosional transgression. The large intracoastal water bodies of Long Island Sound, New York Harbor, and Delaware and Chesapeake Bays suggest a strongly negative solution for the equation of transgressive variables. It has been generally assumed that these water bodies are effective bedload traps (Emery, 1965); hence, cannibalization of the coastal substrate would be the only significant sediment source. The repetitive pattern of coastal morphology, noted in the preceding paper, attests to the effectiveness of storm energy input. The wave climate of the area is moderate to high (Dolan and others, 1972). Various studies (Wicker, 1951; United States Army Corps of Engineers, 1955; Langfelder, 1968; Newman and Munsart, 1968) indicate that the open coast is receding at rates commonly in excess of a foot a year. There are at least three areas where bathymetric time series suggest that an erosional transgression is occurring, with the shore-face retreat tending to be of the type defined by Bruun.

Bathymetric time series, Virginia coast

The 47-yr time series available at False Cape, Virginia (Fig. 198), shows that the sea floor, deeper than about 18 m (60 ft) has aggraded while the shore face has eroded (Swift and others, 1972). The sediment budget has been distorted by the lateral transfer; the upper shore face to the south has aggraded somewhat in response to fine sand moving south through the ridge system (see previous paper). Here shore-face erosion has penetrated to lagoonal deposits of mid-Wisconsinan and early Wisconsinan age. The results of a heavy mineral study suggest that the shelf transgressive sand blanket and the shore-face veneer of fine sand was generated by fractionation of the Pleistocene substrate (Swift and others, 1971b).

Bathymetric time series on the Delaware Coast

Moody (1964, p. 142-154) presents a time series on the bathymetry of the Bethany Beach area which affords an insight into the complex short-term changes which result in shore-face erosion. "The barrier face steepens over a period

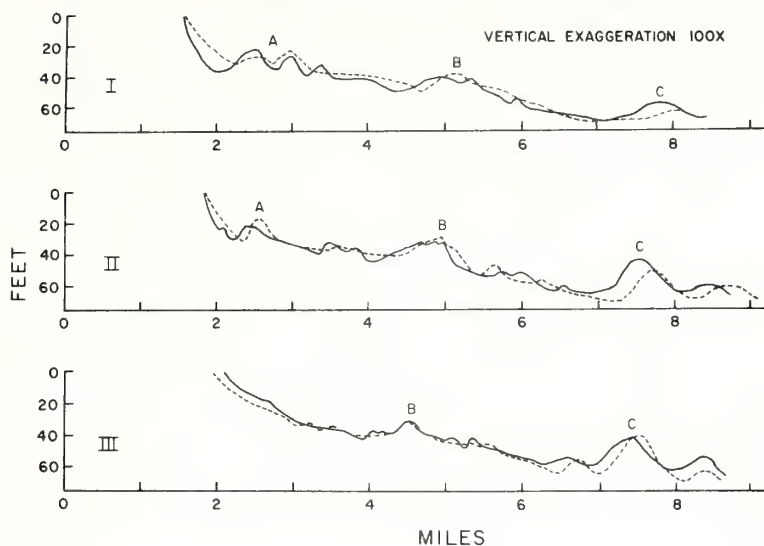


Figure 198.

Comparison of False Cape, Virginia, bathymetry from 1922 USCGS survey (dashed) and 1964 survey (Swift and others, 1972, solid lines). See Fig. 186a, previous paper, for location of lines. Bruun coastal retreat is occurring in I and II; upper shore face has aggraded in III due to coast-parallel transport.

of years to a critical slope, during which time the shoreline remains relatively stable." He notes that a groin system built in 1934-1938 "presumably trapped sand, causing the upper part of the barrier between mean low water and -3 m to build seaward. However, erosion continued offshore at depths between 6 or 7 m below mean low water." The steepening process is not continuous, but varies with the intensity and frequency of storms. "The slope of the [Bethany Beach] barrier steepened from 1:40 to 125 . . . between 1929 and 1954, but deposition on the barrier face between 1954 and 1961 regraded the slope to 1:40."

The steepening process is culminated by a major storm, during which time the gradient is reduced and a significant landward translation of the shoreline occurs. Moody (1964, p. 152) describes the Ash Wednesday storm of 1962 as having stalled for 72 hr off the central Atlantic coast. Its storm surge raised the surf 3 m above mean low water and brought the surf into the dunes of Bethany Beach for six successive high tides. The shoreline receded 18 to 75 m during the storm. While much of the sand was transported over the barrier building washover fans up to 4 m thick, much more was swept back onto the sea floor by large rip currents (revealed by aerial photographs taken during the storm; Moody, 1964, p. 114), and by the mid-depth return flow. Moody's time series shows that, over a thirty-two year period, shore-face erosion was

Table XXXII

Sediment Budget for the Barrier and Offshore areas Between Indian River Inlet and Bethany Beach, Delaware*

<i>Area</i>	<i>Period</i>	<i>Average volumetric change (m³ yr⁻¹)</i>
A. Erosion		
Shore face	1929-1961	- 148,000
Beach and dunes	1954-1961	- 100,000 (estimated)
Inner shelf floor (northwest sides of ridges)	1919-1961	- 100,000
Erosion from bay inside Indian River Inlet	-	- 69,000 [†]
		- 417,000
B. Deposition		
Tidal delta	1939-1961	+ 120,000
Barrier south of Indian River Inlet	1939-1961	+ 5,700
Offshore accretion	1919-1961	+ 256,000
		+ 381,700
C. Net Change		
Total Erosion		- 417,000
Total Accretion		+ 318,000
Net (Erosion)		- 98,300 m ³ yr ⁻¹

*Volumes of erosion (or accretion) are equal to the difference in area between 1929 and 1961 bottom contours multiplied by average change in depth. From Moody, 1964.

[†]Estimated by United States Corps of Engineers.

nearly compensated for by the growth of the ridges on the adjacent sea floor (Table XXXII), the difference here probably being accounted for partly by storm washovers and partly by the growth of the adjacent Cape Henlopen spit (Kraft, 1971b). The stratigraphic penetration of the shore face does not appear to be quite as deep in the Bethany Beach area as in the False Cape area. Coring and radiometric dating by Kraft (1971a) indicate that the Bethany Beach ridges are underlain by Holocene lagoonal deposits overridden by the retreating barrier. Moody (1964) cites heavy mineral data which leads him to conclude that the barrier and inner shelf sands are derived from the underlying substrates.

Bathymetric Time Series on the North New Jersey Coast

Harris (1954) examined the Long Branch, New Jersey, dredge dump site over a four-year period to determine whether or not the dumped sand had replenished the beach. Instead, his series of precision navigation surveys (Fig. 199) showed that the shore face was undergoing erosional retreat and that the adjacent sea floor seaward of the 9 m (30 ft) contours had undergone little net change, thus inadvertently demonstrating Bruun coastal retreat. Local aggradation seaward of 9 m (30 ft) is nearly normal to shore, following the trend of the north New Jersey ridge system (see Fig. 179, previous chapter). Harris'

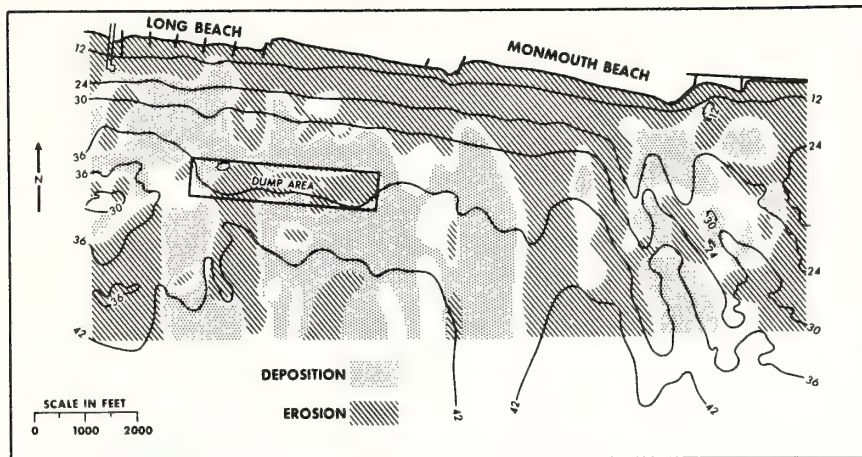


Figure 199.

Long Branch, N.J., coastal bathymetry, with erosion, deposition, or less than 0.4 ft of change indicated. Most changes were less than several feet. Dominance of erosion on shore face and near balance of sea-floor change relative to sea level is in accord with Bruun concept of coastal retreat. Modified from Harris (1954). Contour interval 6 ft.

data shows a net loss from his study area, partly because it does not extend sufficiently seaward to cover the entire system of sediment transfer, but mainly because the system is an open one with a net deficit as a consequence of littoral drift and the growth of nearby Sandy Hook spit (Caldwell, 1966). McMaster (1954) has concluded that in this area, the glauconitic heavy mineral suite has been derived from the underlying Tertiary substrate.

Evidence from the Pleistocene Record; Conclusions

The post-Pleistocene transgression of the middle Atlantic bight is one of a series of similar glacio-eustatic transgressions, and the subaerial coastal plain is veneered by a succession of deposits from previous cycles of Quaternary sedimentation. These comprise a time series of considerably greater scale and a significant test for hypotheses concerning the nature of the Holocene transgression. Coch (1963) has shown that major Pleistocene strand lines on the Virginia coastal plain are perched on the edge of steps in the underlying units cut by the respective marine transgressions, with the risers being old shore faces and the trends being marine erosional unconformities (Fig. 200). Colquhoun (1969) has mapped terrace deposits in South Carolina and notes that only such deeply incised portions of the primary terrestrial erosional surface as drowned river channels survive the beveling process of the retreating shore face (Fig. 201).

Thus, Bruun coastal retreat appears to be widespread in time and space along the central Atlantic coast. The truncation of the subaerial surface and the continu-

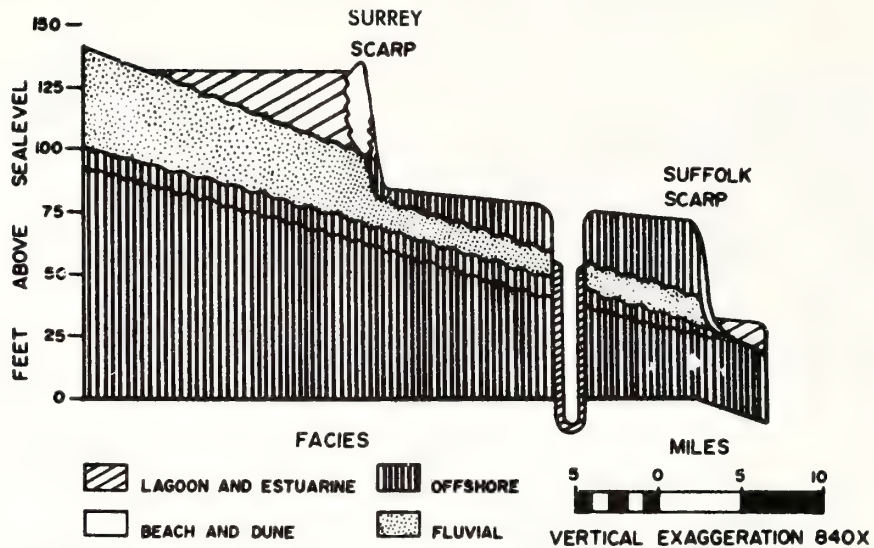


Figure 200.

Section through the Surrey and Suffolk scarps in southeastern Virginia, indicating erosional shore-face retreat. From Coch (1965).

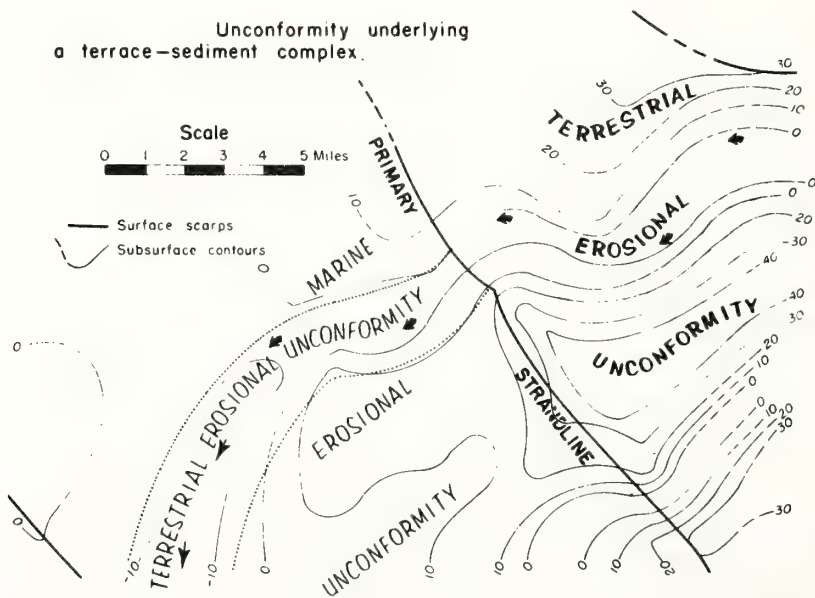


Figure 201.

Schematic diagram of the nature of marine erosional unconformities seen in raised Quaternary deposits of the South Carolina coast. From Colquhoun (1969).

ous destruction of marine marginal deposits by the advancing shoreline would preclude the survival of subaerial landforms, except under special conditions. In stratigraphic terms the result of shore-face retreat is the generation of a thin blanket of winnowed sand over a variable substrate of early Holocene and Pleistocene age. The sheet is not entirely autochthonous with respect to the Holocene sedimentary cycle, however, for it has locally incorporated Holocene fluvial deposits as they emerge at the foot of the shore face (Swift and others, 1971a).

Shore-face Retreat and Littoral Drift; Coastal Discontinuities as Sediment Sinks

General

On previous pages, shore-face retreat has been described in two-dimensional terms. However, in order to fully understand shore-face retreat and its part in shaping the shelf floor, it is necessary to examine the shore face in three dimensions, and to consider the role played by projecting capes and reentrant estuary mouths in the retreat process.

As noted earlier, the Bruun concept of coastal retreat requires that littoral drift be treated as a steady-state process that does not effect the onshore-offshore mass balance. When areas of appreciable long-shore extent are considered, departures from this balance are to be expected as a consequence of loss of sediment to adjacent sinks for littoral drift.

The term littoral drift is commonly used to refer to the coast-parallel transport of sand by a wave-generated current in and landward of the breaker. This current is believed to be most intense beneath the breaker itself (Ingle, 1966). Very little is known about the behavior of the seaward margin of current. There is some reason to believe that with onshore or alongshore wind, the water column of the entire shore face and adjacent inner shelf is set into motion during storms. Murray (1970) has noted "an unexpected seaward extension of the wave-driven longshore current," on the Louisiana coast during the onset of Hurricane Camille. The evidence presented in the preceding paper, and that presented by Harrison et al. (1965) suggests that during northeasters, wind and wave setup along the middle Atlantic bight generates in response a barotropic, southward-trending current strong enough to shape such large-scale bedforms as the inner shelf ridge fields.

Inner Shelf Ridge Fields and Littoral Drift

The relationship between littoral drift patterns and the distribution of shoreface-connected and isolated ridges is unclear. As noted in the previous paper, the ridges of the Atlantic coast open to the north regardless of the direction of littoral drift. Many shoreface-connected ridges merge with the shore face at

depths as shoal as 4 m, and it seems probable that during intervals of long-period waves out of the southwest these features serve as natural groins, diverting littoral drift seaward along their crests. If so, then this circulation pattern, taken together with the storm pattern of Figure 186, previous paper, constitutes a closed loop in the sediment transport path. The shoreface-connected ridges would thus comprise sand circulation cells (Ludwick, 1970), and a mechanism would exist for nourishing the ridges from littoral drift prior to their detachment.

Inlet-Associated Shoals and Littoral Drift

The patterns formed by the intersection of coastal littoral drift cells with the reversing tidal regimes of barrier island inlets have long been known (Bruun and Gerritsen, 1960). The stable, large-scale, bed configuration is that of an arcuate, seaward-convex, sand shoal concentric about a scour trench. The curved crest of the shoal is generally high enough so that it breaks during heavy weather, or ordinary low water, and littoral drift is able to bypass the inlet on the shoal crest. If the littoral drift input is high enough, and the inlet wide enough, the shoal is transected by an intricate pattern of interdigitating ebb and flood channel systems stabilized by tidal currents (Ludwick, 1970). In each respective channel type, the ebb of flood current is longer or more intense, and for a brief portion of the tidal cycle currents of a given ebb-flood channel pair are going in opposite directions. Partitions between the channels are thus ebb-dominated on one side and flood-dominated on the other. They become circulating sand cells or closed loops in the sediment transport path (Ludwick, 1970), and grow upward until tidal aggradation is balanced by wave scour (Ludwick, 1972; Smith, 1969).

Many small shoals occur on the central and southern Atlantic coasts, associated with the small inlets between barrier islands. They play a role in shore-face retreat in that their associated scour trenches and back-barrier channels take part in beveling Holocene lagoonal and older Pleistocene deposits (Fig. 198). However, true barrier inlets are areally unimportant on the central and southern Atlantic coast. We are concerned here with the shoals associated with large estuaries, that have left a significant imprint as they have retreated across the Atlantic shelf floor.

Inlet-Associated Shoals of the Middle Atlantic Bight

As noted in the previous paper, the four estuary mouths which define the coastal compartments of the middle Atlantic bight, namely Block Island Sound, New York Harbor, Delaware Bay, and Chesapeake Bay, are sectors of tidal sedimentation. Delaware and Chesapeake Bay (Figs. 202, 203) have large scale, flamboyantly patterned, inlet-associated shoals as a consequence of (a) the extremely large volumes of the tidal prisms of these enormous estuaries, resulting

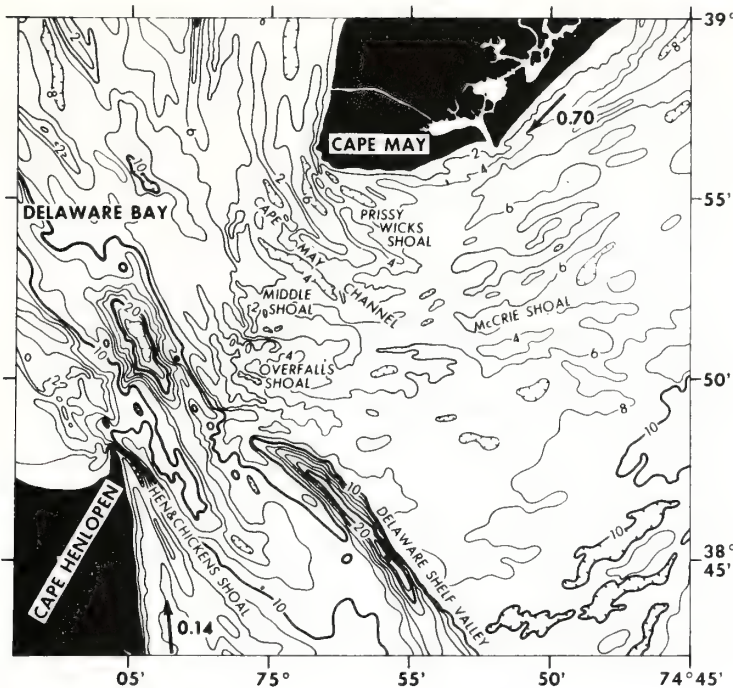


Figure 202.

Inlet associated shoal of Delaware Bay mouth. Flood-dominated channels deepen seaward, ebb-dominated channels deepen landward. Outer flood-dominated channel is continuous with Delaware shelf valley. Contour interval 2 fathoms. See USCGS Map 0807N-57 for 1 fathom resolution. Littoral drift in millions of cubic yards per year from Caldwell, 1964, and Moody, 1966.

in mid-tide surface velocities locally in excess of 200 cm sec^{-1} ; (b) the broad nature of the estuary mouths (8 km or more); and (c) the high discharge of flanking littoral drift cells (volumes given in Figs. 202 and 203). The high lateral sediment input, however, is not enough to overcome the other two factors. The shoals are skeletal with respect to the typical barrier-inlet shoal and their axes are not appreciably seaward-convex. The north sides of the bay mouths receive the dominant littoral drift input, and probably also a significant input of fine sand from the intermittent, storm-driven transport system of the inner shelf. The previous paper has noted that the shore face of the southern New Jersey and Delmarva coastal compartments consist of fine sand (Fig. 177; and text, previous paper). The material may have been winnowed from the massive ridge fields that characterize the central portions of these compartments. The subdued ridges and swales of the terminal sectors of the coastal compartments curve smoothly into large scale ridge fields of inlet-associated shoals themselves (Figs. 202 and 203), and may serve as sediment conduits.

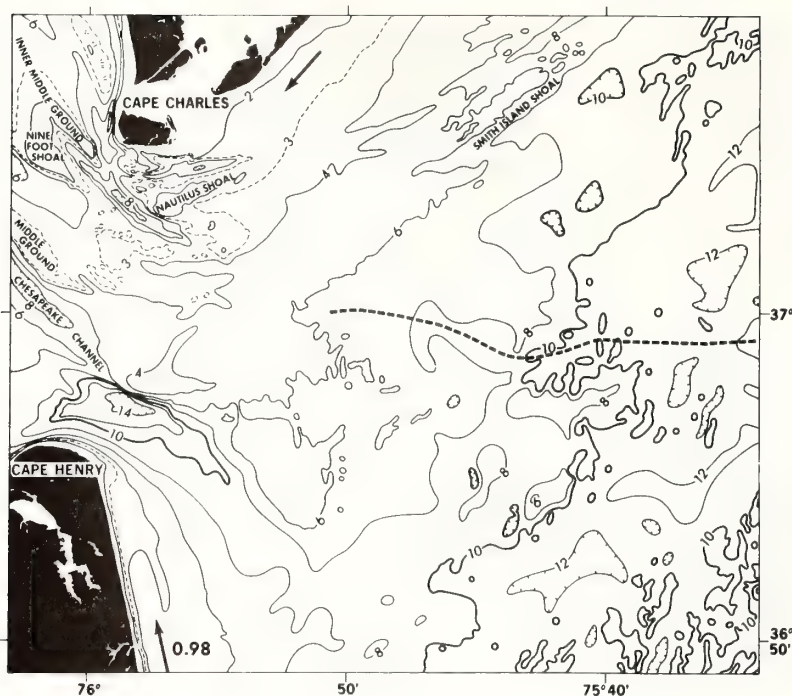


Figure 203.

Inlet-associated shoal of Chesapeake Bay mouth. Main scour channel is almost entirely contained within inlet-associated shoal. Older, relict channel is dashed. Well defined ridge and swale topography starts at 10 fathoms. From USCGS Chart 1222 contour interval 2 fathoms. Littoral drift at Virginia Beach in millions of $\text{yd}^3 \text{yr}^{-1}$ from Weinman (1971).

As a result of dominant sediment input from the north, the northern ends of the inlet-associated shoals are best developed, with intricate systems of mutually evasive ebb and flood channels, whose relief is on the order of 15 to 20 m (49 to 75 ft; see Figs. 203 and 204). The main scour channel in Chesapeake and Delaware Bays lies south of the drift-fed sand mass. In Chesapeake Bay, it sits athwart the crest of the inlet-associated shoal and its southward curving seaward terminus fades into a low smooth apron of sand referred to by Payne (1970) as a submarine "tidal delta." Typical ridge and swale topography begins seaward of the 15 m (45 ft) isobath. On the Delaware Bay Mouth's southern side, a couplet of mutually evasive ebb and flood channels comprises the main scour trench. The flood channel is the more seaward of the two, and is continuous with the Delaware shelf valley (Fig. 202).

The south sides of Delaware (Kraft, 1970b) and Chesapeake Bays (Fisher, 1967) developed cusate spits during the Holocene. Cape Henlopen became a rapidly prograding recurved spit during historic times (Kraft, 1970b). It has



Figure 204.

An hydraulic and geomorphic interpretation of the net non-tidal (residual) flow pattern at the bottom in the entrance to Chesapeake Bay. Numbers are measured flood and ebb flow durations at the bottom in hours; small arrows show measured direction of near-bottom currents. Stippled areas are shoaler than 18 ft. Ruled areas are major areas of ebb or flood flow predominance. Large arrows indicate which is predominant. Nonpatterned areas are neutral, or are too finely structured for resolution. From Ludwick (1970).

advanced to the scour trench, and is presently feeding Hen and Chicken shoals, an ebb-dominated shoal. A small scale, subdued version of this shoal is seen off Cape Henry in Chesapeake Bay.

*Shoreface Retreat on an Inlet-Dominated Coast,
Georgia Bight*

The retreating estuary mouths of the middle Atlantic bight have had left significant traces on the Atlantic shelf floor as will be indicated on following pages. In the middle Atlantic bight, these estuary tracks are anomalous features of the shelf floor. In the southern Atlantic Bight, however, the closely spaced estuaries dominate the coast. Therefore, before considering the shelf floor, it is useful to briefly consider the dissimilar nature of shore-face retreat in the southern Atlantic bight. Comparison of the shorelines of the middle Atlantic and Georgia bights reveals very different patterns (Fig. 205). The valleys of the middle Atlantic bight were deeply eroded by glacial runoff, and the returning Holocene sea has drowned them for considerable distances inland (Meade, 1969). The result is a coastline whose solution for the equilibrium equation is strongly

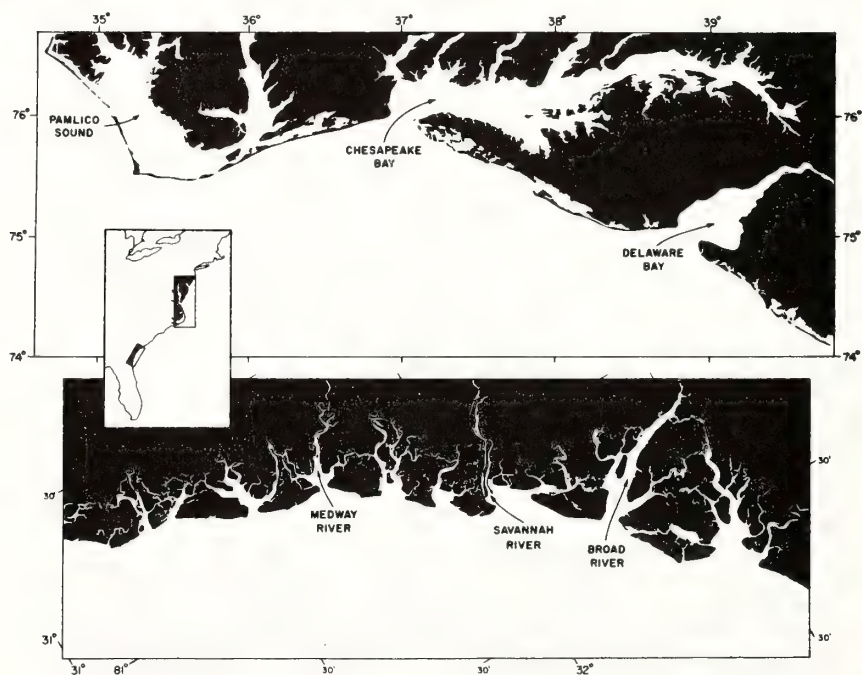


Figure 205.
Comparison of the central and southern Atlantic coasts.

negative. The large estuaries have dendritic outlines like those of recently dammed streams, indicating that the rate of sea level rise is great relative to the rate of sedimentation.

On the Georgia coast, runoff per unit area is less than it is further north due to greater evaporation, a larger growing season, and loss from aquifers directly to the sea floor (Manheim, 1967, Hidore, 1966; cited in Meade, 1969). Consequently, the southern estuaries are smaller and closer together, a fact partly masked in Figure 205 by the different scales. However, the small-scale stream net that drains the deeply weathered southern hinterland carries much more sediment than do the northern rivers, whose drainage basins are thinly veneered with compact, resistant till. The result is a nearly neutral (stillstand) coastline of estuaries whose simple, flaring mouths and meandering heads are primarily constructional rather than erosional forms (Leopold and others, 1964, p. 272). Their channels are presumably in equilibrium with their tidal prisms, a relationship of discharge to geometry which is indicated when the upstream intertidal volume of successive cross-sections forms a linear plot on log-log paper with the subtidal cross-sectional area (Weigel, 1964, p. 380). It seems probable that only a slight increase in the rate of sedimentation would be needed to reverse the sign of the solution for the equilibrium equation and cause it to prograde. Locally, as at the confluence of the Pee Dee and Santee Rivers, the coast seems as nearly a deltaic as an estuarine coast.

Unlike the disequilibrium estuaries of the middle Atlantic bight the southern estuaries are potentially capable of bypassing sediment (Meade, 1969, p. 232). The presence of phosphorite in the Georgia estuaries (Pevear and Pilkey, 1966) indicates that the salinity underflow introduces littoral drift into the estuaries, but does not necessarily mean that fluvial sand does not escape when flood conditions push the salt wedge out (Meade, 1969). The phosphorite may be of quite local origin, since the scour trenches of the estuary mouths are up to 30 m (100 ft) deep and probably cut through to the surface of the underlying Miocene.

The Georgia coast differs in energy input as well as in sediment input. Mean annual wave heights are markedly lower than in the middle Atlantic bight (Tanner, 1961; Dolan and others, 1972), because of the orientation of the coast and its shoal nature. However, the shelf tide is concentrated by the bight and the spring tide is 2 to 3 m (6 to 10 ft). The result is efficient, coast-normal dispersion and fractionation of sediment by tidal currents.

The high sediment input and complex hydraulic structure of the transition zone has resulted in a lens of paralic sediment up to 40 km wide, which attains a maximum thickness of 15 to 30 m (49 to 100 ft) along the shoreline (Henry and Hoyt, 1968). The broad band of estuaries comprises an efficient sediment filter in which sand undergoes progressive sorting (Swift and Heron, 1968, p. 226; Swift, 1970, Fig. 16). Sand released to shore-face processes is fine-

to very fine-grained. The shoreface is very broad and gentle, probably as a result of the low effective angle of repose of this material. The first 2 km offshore slope at 1.5 to 2 m per km, but this rate diminishes rapidly to 1 m per km, then 0.6 m per km in the next 4 km.

Shore-face retreat in the Georgia Bight is dominated by the scour trenches of the closely spaced estuary mouths (Fig. 206), which cut completely through the paralic lens. These commonly attain depths of 20 m (60 ft) and locally 30 m (100 ft) (Hoyt and Henry, 1965; Henry and Hoyt, 1969). A controlling element in their distribution is the Silver Bluff barrier chain, dating from a slightly higher than present stand of the sea at 25 to 30 thousand years ago (Hoyt and Hails, 1967). The modern barrier islands rest on the seaward flank of this older chain and the position of modern inlets are controlled by positions of Silver Bluff inlets. They tend to migrate southward (Henry and Hoyt, 1967), but apparently sea level has not been at its present height long enough for the inner Pleistocene barriers to be consumed and remade by migration of the modern inlets.

As the scour trenches advance landward, they erode leading-edge paralic deposits of basal fluvial sand and upper marsh sediments and probably also underlying Tertiary and Pleistocene materials. The debris of excavation together with littoral drift from the coastal compartment to the north is piled behind the scour trench as large, arcuate, inlet-associated shoals with transverse ridges and channels impressed upon them (Fig. 206). Crestal sectors of the arcuate shoals may be exposed at low water 7 to 9 km (3 to 4 n mi) offshore (Henry and Hoyt, 1969). The shallow crests of the shoals receive littoral drift from the north, and are scoured by south-trending storm currents. Hence, ramps and chutes are prominent on the north side; the central channel curves to the south, and the southeast sides are oversteepened. See Oertel and Howard, this volume, for a discussion of the hydraulic regime associated with the shoals.

If the coast is retreating more rapidly or as rapidly as the inlets are migrating, or if this relationship was true in the past, then the Pleistocene "basement" of the shelf should be deeply furrowed with closely spaced tracks of inlet scour-trench retreat. These furrows would be filled with sand from the retreating inlet shoal; the narrow interfluvies would be capped with a thinner veneer, also beveled by shoreface retreat, which might include Holocene back-barrier marsh deposits. The trough fill might stand higher on the sea floor than the adjacent interfluvie, or, if a mutually evasive ebb-flood channel pattern (Ludwick, 1970, Fig. 1) has been impressed on the shoal, the seaward channel may have partially reexcavated the trough as the shoal retreated.

Hails and Hoyt (1969, p. 63) and Henry and Hoyt (1969, p. 201) have examined the Georgia coast in detail and have concluded that, like the central Atlantic coast, it is retreating according to the Bruun scheme. It seems to differ mainly in the greater role played by estuary mouths in generating coastal strati-

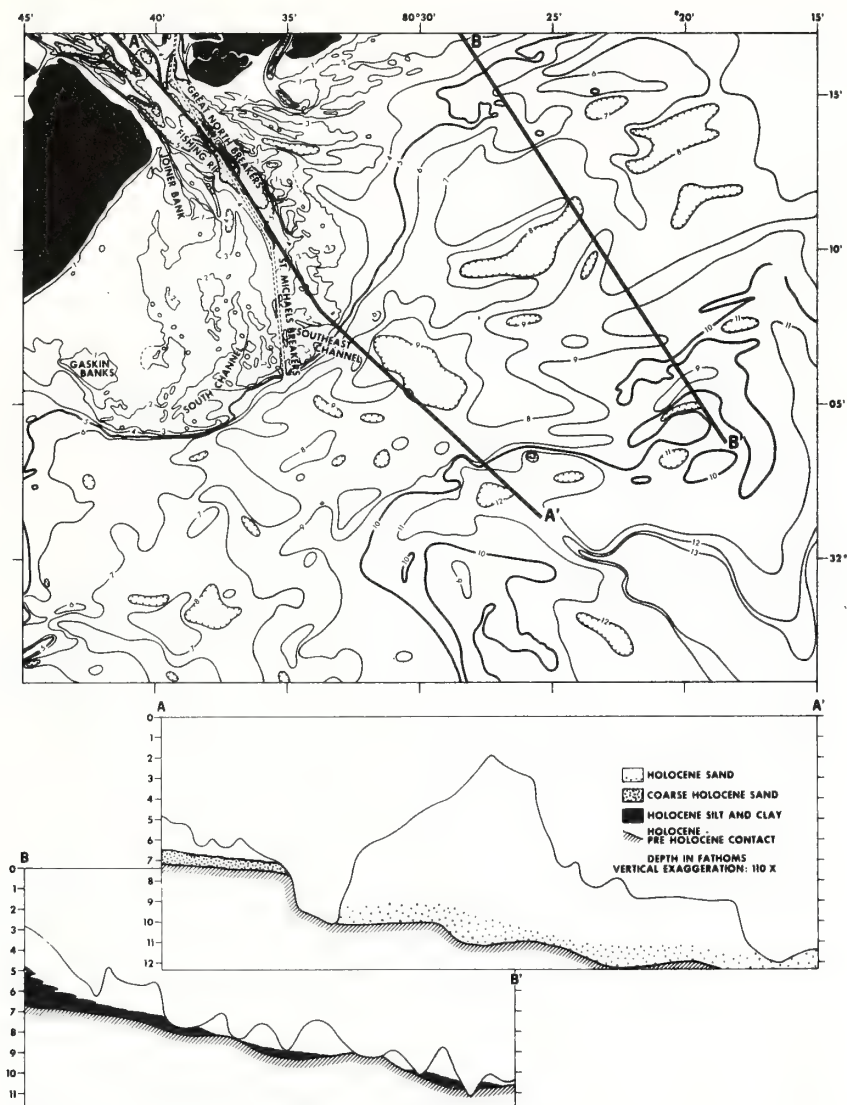


Figure 206.

Port Royal Sound, an inlet-associated shoal from the Georgia coast. Geological sections are hypothetical. From USCGS Chart 1240. Contour interval 1 fathom.

graphy, in the greater thickness of paralic deposits, and in the gentle slope of the shore face. These characteristics may result in a more nearly continuous record of paralic strata surviving shoreface retreat than is found further north; the continuous depositional transgression of Curray (1964). Ongoing studies by workers cited above will shortly test this hypothesis.

Cape-Associated Shoals and Littoral Drift

In addition to the estuary mouths, the cusped forelands and associated shoals of the central and southern Atlantic coast are significant sinks for littoral drift, and their role in shore-face retreat must be considered, before examining the consequences on the shelf floor.

The discontinuities of Middle Atlantic Bight coastal compartments (see discussion, previous paper) tend to have prominent ridge fields associated with them; however, only the southernmost (Chicoteague Shoals) has a well developed cusped foreland (Fig. 178, previous paper). The northern half of the southern Atlantic Bight has three classic, large-scale cusped forelands (Fig. 192); Capes Hatteras, Lookout, and Fear. A fourth, Cape Romain, is nearly a delta. Cape Kennedy, midway down the Florida coast, is also a cusped foreland.

Cusped forelands appear to require for their formation (a) a high rate of sediment input in the littoral drift zone, (b) a high energy input, and (c) stabilizing or shielding points around which sand can accumulate. Given these factors, a feedback process begins. The waves refract around the shielding point and the shore face (if initially straight) rotates into two arcuate segments behind the shielding point, a configuration more stable in the face of wave attack. As the shore face rotates in this manner, the pattern of wave refraction adjusts to the new bottom configuration, and the bottom to wave refraction, until stability is attained.

Cusped forelands as a class of coastal landforms are transitional with cusped deltas, described by Curray (1969) as a characteristic morphological response of deltas to a coast with a high value of wave-energy input relative to sediment supply. The formation of cusped deltas also seems to be favored by a high input ratio of bedload sediment to suspended sediment. Here the shielding point is the river mouth itself. For stability, littoral drift must trend from the apex toward the base on both sides.

While a deltaic origin has been proposed for the Carolina Capes (Hoyt and Henry, 1970) and since debated (Hopkins, 1971; Henry, 1971), close examination of the shoals seaward of the capes suggests that, if valid, it must have been so mainly at an early period in the capes' history. At present, the prevailing wave direction for the Carolina capes and Cape Kennedy, Florida, is from the northeast, oblique to the axes of the capes. The result is that littoral drift converges, rather than diverges, on the apices of the capes, since in the shadow

zone to the south, waves from the southeast dominate. The large-scale, well-defined sand shoals which extend from the Carolina and Florida capes almost to the shelf edge (Figs. 207-211) must be a consequence of drift convergence. Either the shoals must have grown seaward from the tips of the forelands (Tanner, 1960; Shepard and Wanless, 1971), or the shoals must have grown landward with the retreat of the cape-apex depositional center. Consideration of available bathymetric information plus what little is presently known concerning the hydraulic regime in the vicinity of the capes permits an evaluation of these hypotheses.

Morphology of Cape-Associated Shoals

As noted in the previous chapter, the cape-associated shoals of the Carolina and Florida capes tend to be shelf-transverse, "hammer-headed," second-order features composed of first-order, seaward-convex ridges and swales. The latter are not quite symmetrical about the shoal axis; most troughs tend to become shallower to the south or southwest and may not extend completely through the shoal (Figs. 207-211). A minority of the arcuate swales become shallower in the reverse direction, however, and locally the two types alternate as apparent ebb-flood channel couplets of the sort seen in the entrances to tidal estuaries (Ludwick, this volume). The arcuate ridges tend to extend further from the shoal crest line on the shoal's northeast side than they do on the southeast; in other words, the large-scale shoals on which the ridges and swales are superimposed tend themselves to be asymmetrical, with steeper southwestern flanks. Thus, Lookout and Southeast shoals are comb-line shelf transverse structures with toothlike ridges projecting northeastward (Figs. 208, 21). Toward the base of the shoals the sequence of arcuate ridges may continue along the northeast mainland shore as shoreface-connected ridges.

A remarkable photomosaic of Lookout Shoals (El Ashry and Wanless, 1968; Shepard and Wanless, 1971; Fig. 209, this paper) shows in addition to a tendency toward longitudinal differentiation of the shoals. It indicates that the proximal third of Lookout Shoals consists of "overlapping" sand masses, which El Ashry and Wanless (1968) reasonably suggest represent major pulses of sand emplaced during storms. The central portion is flat, however, and the distal third is furrowed by small-scale features in the form of linear sand ridges, with amplitudes up to 4 m (12 ft) parallel to the main shoal axis. These features also appear on the more detailed bathymetry available for some of the capes (Fig. 210). Their axes tend to be gently convex toward the south, and on acoustic profiles a southward asymmetry is dominant, with steeper southward flanks locally attaining the angle of repose. A 6 m (19 ft) vibrocore taken from a large feature immediately south of the Diamond Shoals Light consisted of coarse sand with southward-inclined cross-bedding at the base. The upper portion of the core was so loosely packed that it flowed within the core liner and no structures were retained.

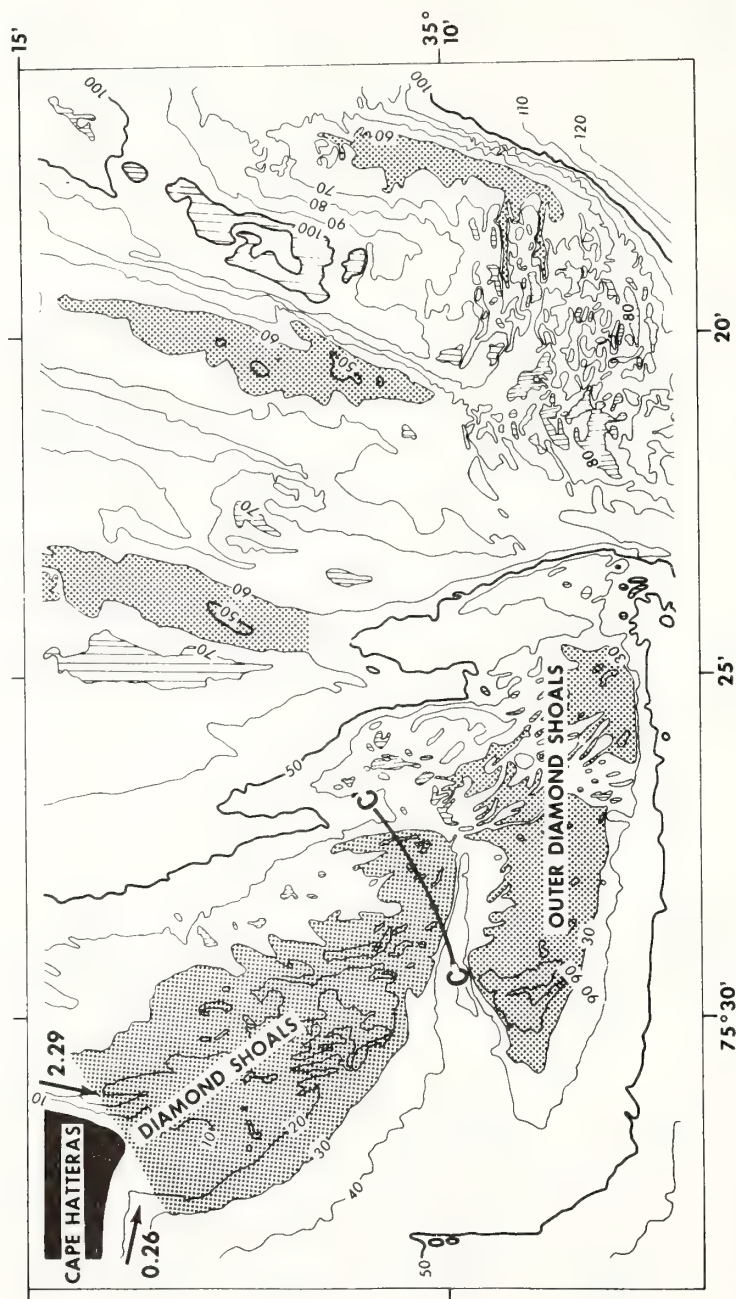


Figure 207.
Diamond Shoals, off Cape Hatteras, North Carolina. From USCGS surveys. Littoral drift in millions of cu yds/yr from Langfelder and others, 1968. Major isolated highs are stippled. Profile CC' in Fig. 231. Contour interval 10 ft.

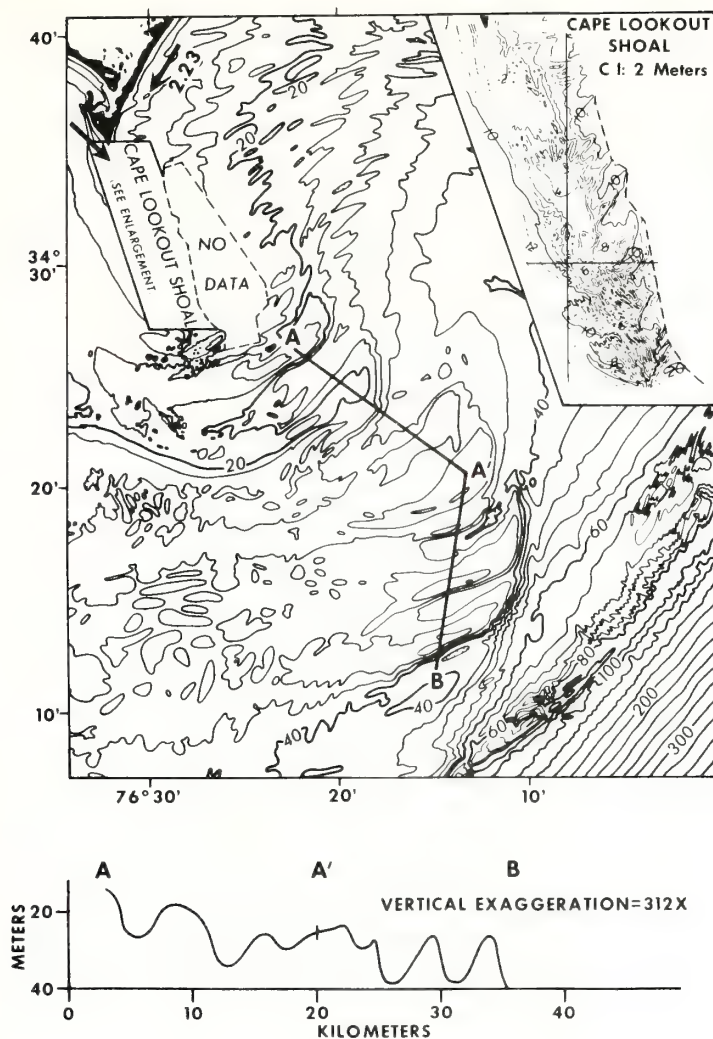


Figure 208.

Lookout Shoals, off Cape Lookout, North Carolina. From USCGS surveys. Littoral drift in millions of $\text{yd}^3 \text{ yr}^{-1}$ from Langfelder et al. (1968). Contour interval 10 m out to 100 m, then 25 m.

These characteristics led us to conclude that the small-scale features are transverse sand waves. The southward asymmetry of the shoals and of the sand waves parallel to their crests indicates that the dominant sediment transport direction is across the shoals to the south. We therefore conclude that the shoals could not have grown seaward from their present bases; rather, the bases are the only growing portion and these are growing landward by the accretion of pulses of littoral drift received from the retreating foreland apex during storms.

Thus, forelands and shoals exist in a state of homeostatic equilibrium; as



Figure 209.

Lookout Shoals, off Cape Lookout, North Carolina. From Shepard and Wanless (1971).

as

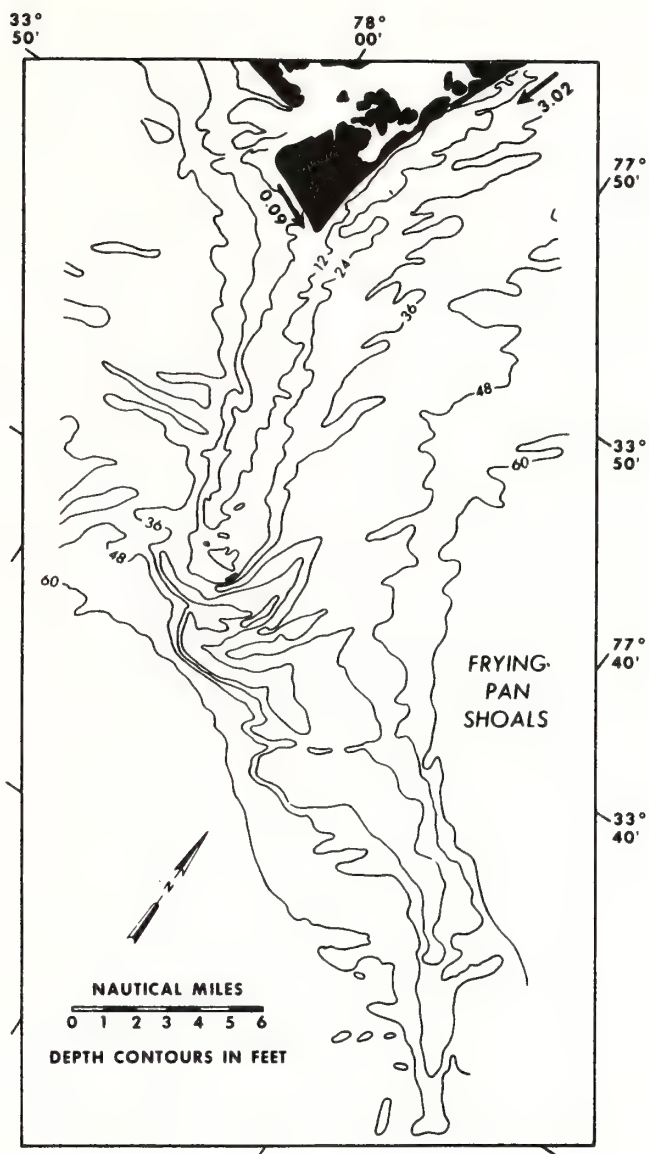


Figure 210.
Frying Pan Shoals, off Cape Fear, North Carolina. From Hopkins, 1971. Littoral drift in millions of $\text{yd}^3/\text{yr}^{-1}$ from Langfelder and others, 1968. Contour interval 12 ft.

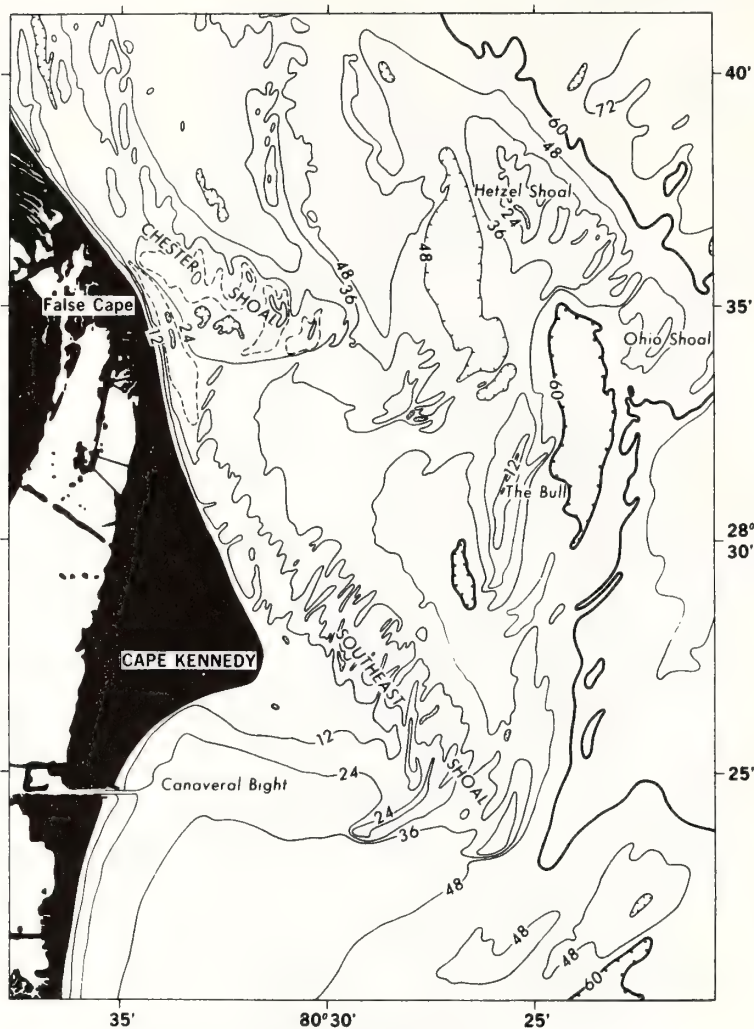


Figure 211.

Cape Kennedy and associated shoals, Florida. From USCGS bathymetric surveys. Countour interval 12 ft; dashed supplementary contours at 6 ft.

the shore face of the retreating foreland wastes away, the debris feeds the landward-prograding shoal base, so that its aggrading surface keeps pace with the rise in sea level in accord with the Bruun principle. The shoal, for its part, serves as the shield to which the foreland is anchored and a focal point for the wave energy which shapes the foreland. While the Carolina capes might have been initiated as deltaic (river-stabilized) forelands, they are at present shoal-stabilized forelands.

Hydraulic Regime of Cape-Associated Shoals

Scattered bits of hydraulic data, available in the literature, support this picture of seaward sediment transport at the shoal base and cross-shoal sediment transport over its central and distal portions. Transfer of littoral drift from foreland apices to shoal bases has been documented by the United States Army Corps of Engineers (El Ashry and Wanless, 1968, p. 360) for Cape Fear and Frying Pan shoals. At Frying Pan shoals, the eastern face of the apex has lost more sand than the western face has gained, the difference being gained by the shoal. The Corps of Engineers estimates an average shoal accretion of 24,500 yd³ a year for a 72-yr period.

Tides are weak over the shoals; surface tidal currents over Lookout Shoals average 0.07-0.18 knots (El Ashray and Wanless, 1968). However, there is evidence to indicate that south-trending, coast-parallel storm currents are a major factor in the shaping of the shoals. El Ashry and Wanless (1968) quote the United States Army Corps of Engineers to the effect that "surface-water velocities average 1.7 to 2.6 per cent of wind velocity." The Atlantic Coastal Pilot (1964) notes that, "during strong winds, currents set across the shoals with great violence." Stefansson et al. (1970) have noted surges of Virginia coastal water across inner Diamond shoals in periods of strong northeast winds during the winter. We infer that the south-shoaling arcuate troughs of the cape-associated shoals are spillways for these pulses and that the sand waves are also activated by them. The smooth surface of the inner shoals may indicate that, during storms, critical flow is attained in this shallow area. The regional asymmetry of the shoals may also be attributed to south-trending currents; a comparison of the 1953 and 1963 USCGS surveys of Diamond shoals indicates that north-facing slopes experienced up to 8 m (25 ft) of accretion, while south-facing slopes underwent an equivalent accretion (Fig. 212).

Wave refraction must be a second major force shaping the shoals and, in particular, the arcuate first-order ridges; the ridges are curved so as to be normal to wave orthogonals converging on the shoals. Tanner (1961) has noted a direct correlation between the grain size and topography on the San Blas and St. George cape-associated shoals, panhandle, Florida. Ridges are mantled with (or composed of) fine, well-sorted sands; troughs are floored with coarse, poorly sorted sands. The fine-grained sands of ridges are presumably analogs of the fine-grained sands of mainland shore faces and are the consequence of wave-winnowing, while the coarse trough sands are best understood as scour lags, generated in response to the coast-parallel, storm-generated currents. If Tanner's sampling had been more closely spaced, he might have found the secondary grain-size maxima on crests that occur as a response to wave winnowing in the False Cape ridge system (preceding chapter).

Thus the arcuate ridges and troughs of the cape-associated shoals appear to belong to the same basic class of features as the inner shelf ridge fields

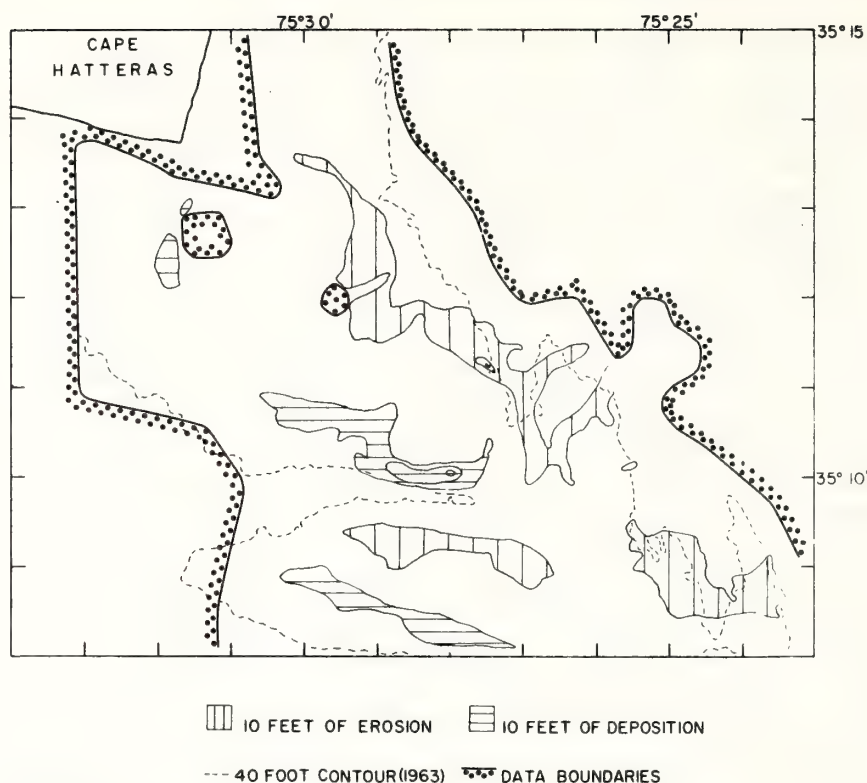


Figure 212.

Accretion and erosion at Diamond shoals between 1953 and 1963. From USCGS surveys.

with which they merge (Fig. 213); and like them are responses to south-trending storm currents and storm waves. Their arcuate nature is merely a result of the different boundary conditions under which they formed.

Shore-face Retreat and the Provenance of Coastal Sands

General

The preceding analysis of shoreface retreat on the central and southern Atlantic coast has been based primarily on stratigraphic and morphological considerations. However, petrographic studies of the provenance of Atlantic coast sands have yielded results which suggest a somewhat different model. In the southern Atlantic Bight (numerous studies summarized by Pilkey and Field, this volume) and again on the central and southern New Jersey coast (McMaster, 1954; Frank and Friedman, 1971) analysis indicates that coastal sands are petrographically dissimilar to modern river sands, and to the sands of the subaerial

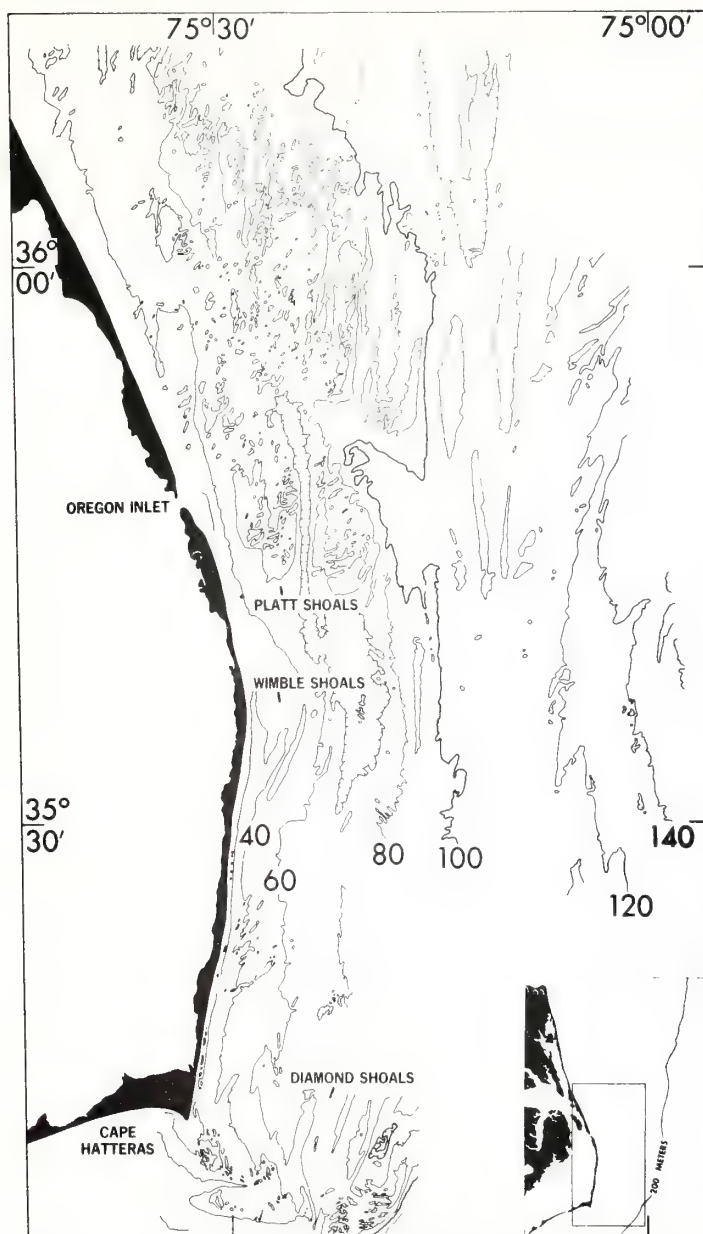


Figure 213.

Bathymetry of a portion of the North Carolina shelf. Contour interval 20 ft. From USCGS hydrographic surveys.

Pleistocene substrate, but are presumed, or are in fact similar to shelf sands. In these areas, the coastal sands have, therefore, been assumed to have moved "onshore" from a "continental shelf" source. These terms suggest a model diametrically opposed to Bruun coastal retreat, in which the response to a rising sea level is shelf floor erosion and coastal aggradation; a response difficult to visualize in dynamic terms. However, careful examination of the evidence suggests that despite the differing terminology, the Petrographic data comprises in some cases a converging line of evidence for shoreface retreat of the Bruun type, and in other cases, is at least compatible with it.

Provenance of New Jersey Coastal Sands

McMaster (1954) has investigated the provenance of New Jersey beach sands by means of detailed heavy-mineral analysis. His studies reveal a northern glauconitic province equivalent to the eroding headland sector described in the previous paper, an opaque heavy-mineral province equivalent to the proximal, seaward-convex barrier arc, and a hornblende province equivalent to the distal, seaward-concave barrier arc. He concludes that, within the glauconitic province, the beach is supplied by erosion of subjacent, glauconitic, Tertiary strata.

McMaster's study indicated that the genesis of the opaque heavy-mineral and hornblende provinces are less clear cut. The presumed source is the underlying Cape May Formation of Pleistocene age. A comparison of heavy mineral suites of the Cape May Formation versus those of the modern beach (McMaster, 1954, p. 178-185) is inconclusive. However, McMaster (1954, p. 187) notes that the Cape May mineralogy is quite variable. He surmises that the beach sands of the central and southern New Jersey shelf are derived from the offshore Cape May formation of the continental shelf rather than from the Cape May formation of the mainland. The conclusion appears to contradict the concept of beach nourishment by shore-face erosion. However, McMaster's (1954, p. 185) main argument is geographic rather than mineralogical:

Along the [New Jersey] seaboard, the possible submarine source contributors are restricted to the [Cape May Formation of the eroding headland sector] . . . , since a series of barrier bars guards the headlands . . . It is apparent that the major contribution of sediment for the beach opaque . . . and hornblende mineral zones cannot be located on the subaerial portion of the coastal plain. The only alternative must be the continental shelf.

Despite such terms as "continental shelf" and "offshore," McMaster seems nevertheless to be referring to the retreating shore face, since elsewhere (McMaster, 1954, p. 192) he comments more explicitly:

The present-day source for the beach sands in this area . . . is local. Therefore, all beach nourishment must be obtained in the vicinity of the beach itself. The beach-building material is derived from a reworking of bottom sediment in the immediate vicinity of [barriers] and [from] the sands moved by drift.

Frank and Friedman (1971) have recently compared landward lagoonal beach heavy-mineral suites with barrier beach heavy-mineral suites north of Atlantic City. They noted marked differences and concluded that the central New Jersey barrier formed from "the adjacent continental shelf." They propose that the barrier retreated slowly landward by washover and concluded that "this process would not result in massive shore-face erosion or aggradation of the adjacent sea floor, as has been proposed." Their argument is difficult to follow, since landward migration of a barrier requires "massive shore-face erosion" by definition. It is possible to envisage a variant of Bruun coastal retreat, whereby stratigraphic penetration of the shoreface is shallow as at Bethany Beach and the retrograding barrier retreats over a carpet of its own back-barrier muds (Fig. 196). Insulated from subjacent sands by the mud carpet, the barrier becomes a reservoir of relatively far-traveled and mineralogically distinctive sand, undergoing slow dilution by littoral drift during its cycle of washover, burial, and remergence. However, as noted by Pilkey (personal communication), the repeated subaerial exposure should render the heavy mineral suite more mature than that of its source. This variant model is compatible with McMaster's data, but not necessitated by it.

Provenance of Southern Coastal Sands

On the Georgia coast, the fine-grained shoreface sands extend to a feather edge 23 to 34 km (10 to 15 n mi) seaward in 12 to 15 m (40 to 49 ft) of water (Henry and Hoyt, 1969). Medium- and coarse-grained sands lie to the seaward; the contact between the two has been described as the contact between "modern" and "relict" sand by Pilkey and Frankenberg (1964). It has been suggested that the coarse sands are relict and residual sands and that the fine sand mantle of the broad, gentle shoreface is an out-winnowed fraction that has moved in with the advancing Holocene sea (Henry and Hoyt, 1969). The presence of trace amounts of phosphorite in the sand fraction of the Georgia shelf and beaches, and its absence in Georgia rivers, has been cited as evidence (Peavear and Pilkey, 1966). See also heavy mineral data of Pilkey and Field, 1972. However, it is possible to suggest an alternate hypothesis. The reversing jets at the estuary mouths must serve as efficient elutriators of sand, and the fine sand may be fractionated and spread across the shore face by such a mechanism. The leading edge of the paralic lens must consist of relatively coarse, fluvial sands at the fall line; these would be reworked by the advancing estuary mouth scours and incorporated into the bases of the arcuate shoals (hypothetical cross sections, Fig. 206). Retreat of the superstructure of the arcuate shoal with the shoreface would reexpose the coarse basal material, which thus would be allochthonous with respect to the Holocene sedimentary cycle rather than autochthonous, or "relict." The anomalous trace minerals, as noted above,

could be explained as mined from the underlying Tertiary by the estuary mouth scours.

However, it should be noted that these hypotheses are not necessarily mutually exclusive. Elsewhere in the southern Atlantic bight, notably in Onslow Bay (Filkey and Field, 1972) long distance onshore movement of shelf sand seems to be the only viable hypothesis. Here the phosphorite component of the beach sands appears to be derived from offshore exposures of the Miocene Yorktown formation at a stratigraphically higher level than exists on land (Roberts and Pierce, 1964). The submarine outcrop area lies 20 km seaward of the modern in over 20 m of water. Here the phosphorite may have moved in with the recycling beach prism during the past millenia of sea level rise; or the barrier may indeed be exchanging sand with the adjacent sea floor.

THE PALIMPSEST SHELF FLOOR

General

In the previous chapter the evolution of shoreface-connected ridges into isolated inner shelf ridges was examined. The preceding section of this chapter has considered this transformation as part of a more general process of shore-face retreat. This section will attempt to explain the shelf-floor morphology in terms of shore-face retreat. To the extent that the shelf floor can be viewed as resulting from shore-face retreat, and modified by subsequent shelf processes, it is a palimpsest surface, or surface whose original (foot of shore face) features have been partially, but not wholly, obliterated by the subsequent (shelf) processes. However, detailed examination of the shelf suggests that the simple transition of shore-face ridge system to shelf ridge-field, developed in the preceding chapter, is only one of several modes of formation of the constructional, high-order morphological elements of the shelf floor.

Shelf-Transverse Elements I: Shoal-Retreat Massifs from Inlet-Associated Shoals

The Problem

The hypothesis of detachment of shoreface-connected ridges to form isolated shelf-floor ridges, as set forth for the False Cape and Platt Shoals sector (previous chapter has internal consistency with respect to the areas discussed. It becomes less satisfactory when a relationship is sought between the ridges so isolated and the transverse shelf valleys and shelf ridge systems that lie to the north of each of the detached ridge sets. The Delmarva inner-shelf ridge field which

formed the main actualistic example in the previous paper is in fact an anomaly in that it is the only large-scale, inner-shelf ridge field of the middle Atlantic bight that is not associated with a transverse shelf valley. The other two examples, the Virginia Beach ridge field (Fig. 214) and the Platt shoals ridge field (Fig. 215), surround shelf valleys and attain their primary development on the northern sides of these shelf valleys. Any convincing model of ridge development must explain this association of shelf-floor ridge fields with transverse shelf valleys. Truncation of nearly coast-parallel inner-shelf ridges by shelf-transverse valleys seems at first glance to place constraints on the time relationships of the respective morphological elements. Payne (1970) has in fact suggested that the Virginia Beach shelf valley (Fig. 214) was cut by a pre-recent river, conceivably an ancestral Susquehanna, and that the flanking ridges which it appears to truncate may be relict Pleistocene barriers. However, close examination of flanking ridge systems raises major difficulties for this hypothesis.

Evolution of the Virginia-North Carolina Coast

The difficulties first appear when transverse profiles of the two shelf valleys are considered. These lack the bilateral symmetry to be expected if valley and ridges comprise a simple drainage basin (Fig. 216). Ridge crests and trough

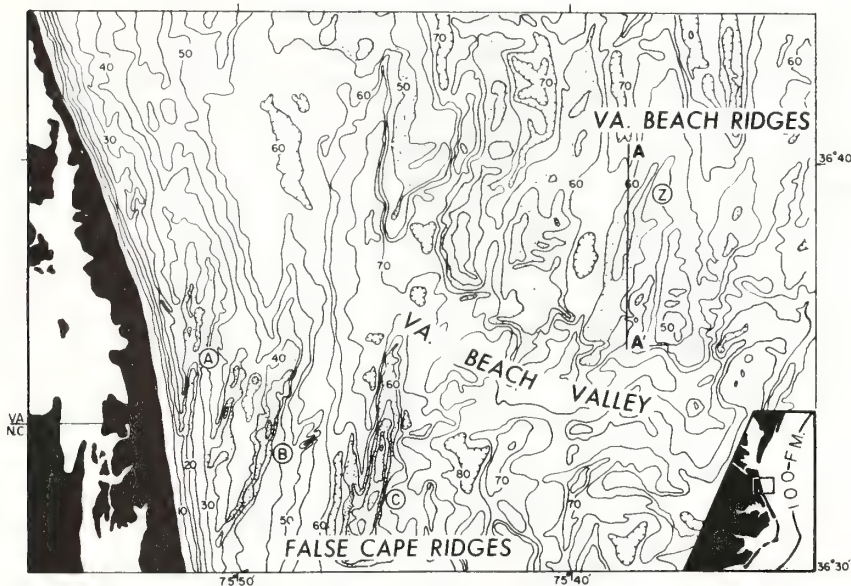


Figure 214.

Bathymetry of a portion of the Virginia shelf. Contour interval 10 ft. From Payne (1970). Profile AA' presented in Fig. 231. Dashed lines in profile are an acoustic reflector.

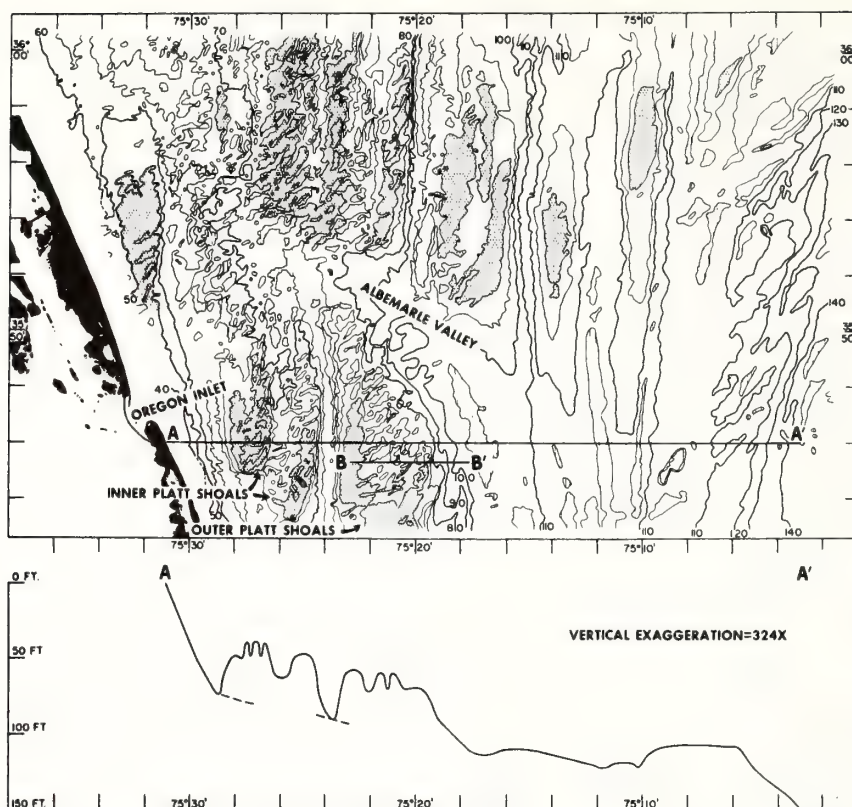


Figure 215.

Platt Shoals ridges and Albemarle shelf valley. Contour interval 10 ft. From USCGS hydrographic surveys. Profile BB' presented in Fig. 231. Dashed lines in profile are an acoustic reflector.

axes climb to the south, both north and south of the valley (Figs. 214, 215, 216). Troughs north of the two valleys are separated from the valleys by low sills; thus the ridge set north of each valley comprise in each case a complex comblike transverse sand body with "teeth" pointing north, as do the cape-extension shoals previously discussed.

The pervasive southward asymmetry of the drowned valley systems appears to be a consequence of periodic, intense, south-trending currents generated by storms, as described in the preceding paper (see also Swift et al., 1972; Shideler et al., 1972). These currents, probably structured into helicoidal flow cells, have scoured troughs down to the Pleistocene substrate, have generated small-scale transverse bedforms in them, and have swept finer sand south through the ridge systems, into the old river channels, and onto the flats south of the southern ridge sets. Thus, modern marine processes have resulted in extensive

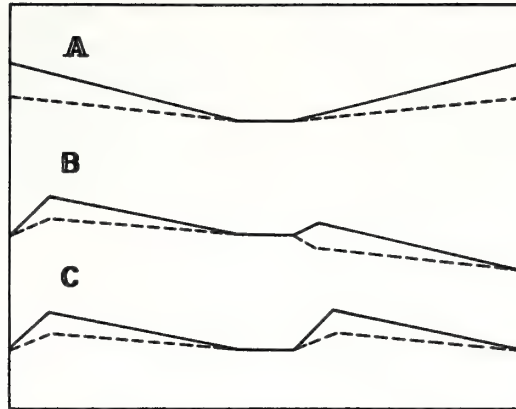


Figure 216.

Schematic coast-parallel profiles through inner shelf ridge channel complexes: (A) Bilateral symmetry of hypothetical subaerial drainage net; (B) Southward asymmetry of Great Egg shelf valley; (C) Southward asymmetry of Virginia Beach and Albemarle shelf valleys.

modification of an older, river-dominated topography. However, evolution of the ridges flanking the channels is still obscure. If the southern ridge sets are detached shore-face ridges, what are the northern sets and what is their relationship to the channels? These questions are best answered by recourse to our knowledge of late Holocene sea-level rise and its effects on continental shelf sedimentation.

Holocene sea-level rise is known to have undergone a reduction of rate between 4000 and 7000 BP, from a rapid to a gradual rise (Milliman and Emery, 1968). Presumably, the Middle Atlantic coast would have been undergoing erosional transgression (Curry, 1964, p. 200) prior to that time. As the rate of sea-level rise decreased relative to the rate of sedimentation, the coast stabilized or began to undergo depositional regression. Curry (1969) has suggested that many modern barrier systems with bases at 10 m (33 ft) began at this time, and the suggestion seems valid for the middle Atlantic coast (Newman and Munsart, 1968; Kraft, 1971b). The effective increase in the rate of sedimentation may have caused the barriers of the Carolina coast to prograde (Dolan, 1970). This coastal sector has since resumed its retreat (Langfelder and others, 1968). The resumption may have been a consequence of an increase in the rate of sea-level rise. However, even without such an increase the continued deepening of the water and upward growth of the barrier would have increased the submarine surface area of the barrier that needed nourishment (Dillon, 1970 and the concomitant widening of the lagoon would have separated it from fluvial sources of sand (Curry, 1964).

During the earlier period of rapid erosional retreat, the Virginia-northern North Carolina coast would have resembled the modern Georgia-South Carolina coast

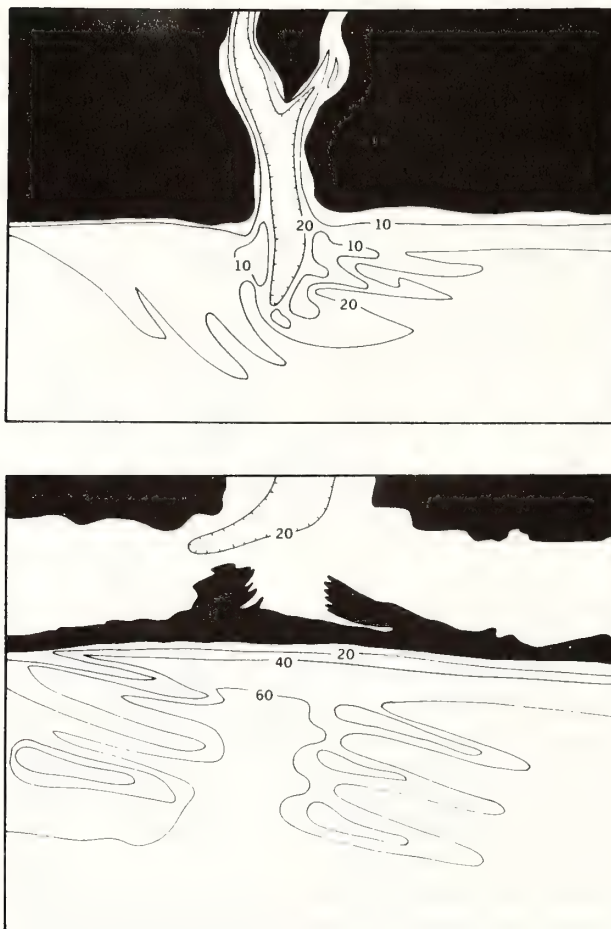


Figure 217.

Schematic model for evolution of inlet-associated shoal into an inner shelf ridge system. Above: Estuary mouth with arcuate sand body. Based on the numerous similar estuarine shoals of the Georgia-South Carolina coast; Fig. 206, this paper. Below: Inner Shelf ridge system, modified from inlet-associated shoals during coastal retreat. Based on the Oregon Inlet area, with Platt Shoals, the closed Albemarle inlet, Currituck spit, and Roanoke and Currituck sounds on the North Carolina coast. Compare with Fig. 218. Contours in ft.

as described on previous pages, in that the estuarine regime would have extended from the river mouths across narrow marsh-filled lagoons and through inlets to build large, arcuate, inlet-associated shoals in the adjacent shoreface and inner shelf (Fig. 217). We propose that the Platt shoals complex and Virginia Beach-False Cape ridge complex were built as such shoals before the Ancestral Albemarle and James (or possibly Susquehanna) Rivers during this period.

However, the ancestral Albemarle and James' drainage basins lacked the innately high fluvial sediment input of the Georgia coast and their lower valleys had become deeply incised during the pleistocene (Meade, 1969). As sea-level continued to rise behind the stabilized barrier, they were unable to retain their direct outlets to the sea. The lower valleys become flooded almost to the fall line. The zones of maximum stratification and associated turbidity maxima withdrew to the upper portions of the resulting estuaries, which were now effective sediment traps. Roanoke and Currituck Sounds grew respectively north and south of lower Albemarle Sound into the sediment-starved back-barrier marshes, thus detaching the future Currituck Spit from the mainland (Fig. 218). A closed inlet in the vicinity of Kitty Hawk may be the last vestige of the former river mouth. If so, the inlet migrated north before closing, for recent seismic work (Riggs and O'Connor, personal communication) shows that the main channel passes under Currituck Spit a little to the south. Our interpretation of North Carolina coastal evolution differs from that of Pierce and Colquhoun (1970) in that we consider Currituck spit as well as Hatteras Island to have formed as a primary barrier (detached mainland beach; Hoyt, 1967) rather than as a secondary barrier, or true, genetic (coastwise prograding) spit.

This remarkable change in coastal regime, from erosional transgression to near standstill, has resulted in a complex of large-scale, intracoastal water bodies that contains one of the largest estuaries (Chesapeake Bay) and one of the largest lagoons (Pamlico Sound) in the world. The two-step cycle, taken as a unit, is tantamount to Curry's (1964) discontinuous depositional transgression in which barriers grow up vertically, only to be overstepped. Presumably, were it not for the stability afforded by Diamond Shoals as a focus for wave energy, the Carolina-Virginia barriers would be overstepped or driven back.

The ridge fields before the North Carolina barriers would thus appear to have been initiated as inlet-associated shoals. They can hardly be called relict, however, for the great bulk of their relief most post-date their abandonment by their respective rivers; the arcuate, inlet-associated shoals of the Georgia coast have only incipient first order ridges impressed upon them (Fig. 206), and these features are mainly on the north side, facing southward littoral and shore-face storm currents. Thus, the ridge systems north of the Albemarle and Virginia Beach shelf valleys may have started as ramps and chutes, but, since abandonment, have deepened and elongated their troughs and have aggraded their crests. Preliminary examination of the vibracores from the Virginia Beach ridge system indicates that the ridges contain cores of sand finer than the medium-grained sands of the crests.

Shelf valley segments appear to be ubiquitous on the inner shelf. Another example may be seen in Long Bay on the Carolina coast between Cape Fear and Cape Romain (Fig. 219). It is apparently a former channel of the Waccamaw



Figure 218.

North-Carolina-Virginia shelf, showing Albemarle and Virginia Beach shelf valleys (dashed). Dotted subsurface extension of the Albemarle Shelf Valley has been mapped by seismic profiler (Riggs and O'Connor, East Carolina University, personal communication). Dotted lines north of Virginia Beach Channel are subsurface channels traced by seismic profiler (Meisberger, 1972; Harrison et al., 1965). Depths in ft.

River. The Waccamaw presently flows toward the coast, then is deflected southward by a raised Pleistocene barrier. The shelf valley is aligned with a wind gap in the barrier near the area of the river's deflection. This shelf valley, like those to the north, has a thalweg at the same depth as the adjacent sea floor; it is defined not by an incised thalweg, but instead by two well-defined levees. The northern levee has transverse, coast-parallel ridges on its crest close to the shore and at the seaward end.

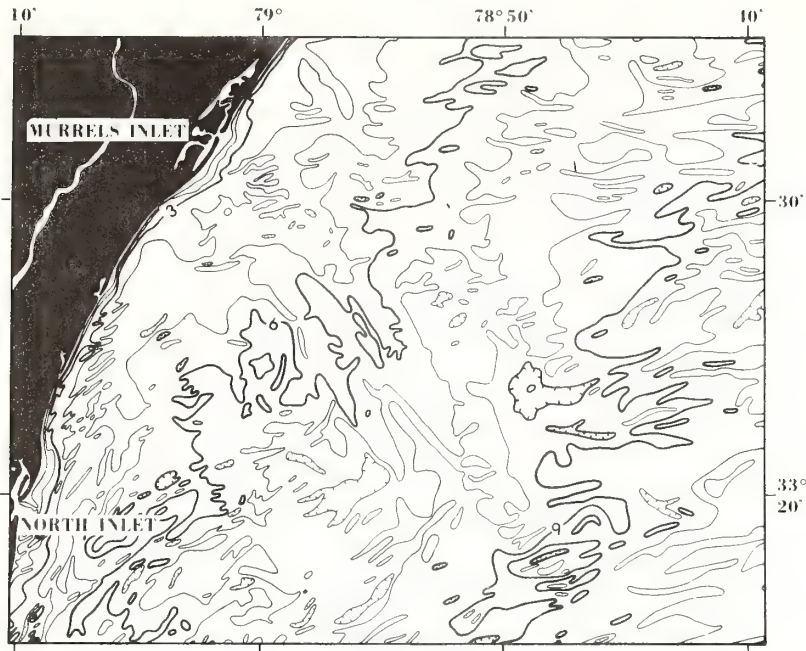


Figure 219.
Waccamaw shelf valley, Long Bay, Carolina shelf. Contour interval 1 fathom.

Shelf Valleys and Shoal Retreat Massifs

The transform of estuarine shoals into inner-shelf shoals may be most explicitly worked out for the short inner shelf channel segments. However, it also appears to explain a number of much larger-scale features. The Virginia Beach ridges extend from the area shown in Fig. 214 out to the mid-shelf shore (Fig. 218). The theory presented above would require that this entire shelf-transverse ridge, comprised of successive, nearly shore-parallel ridges, is a shoal-retreat massif left by the retreating James during a time when it occupied the Virginia Beach shelf valley.

The Susquehanna shelf valley to the north (Fig. 221a) has no such ridge in its northern flanks. Its inlet-associated shoal seems to have retreated directly up the valley, leaving it largely filled. Subdued transverse ridges interrupt the thalweg, suggesting continued post-transgression modification of the sea floor.

The Delaware shelf valley (Fig. 220b) consists of a well-defined channel paired with a well-defined shoal-retreat massif. The massif can be traced directly and without interruption into Delaware Bay-mouth shoal, as noted by Kraft (1971b). The channel can be traced directly into the seaward member of an ebb-flood channel couplet which breaches the bay-mouth shoal, and it is the

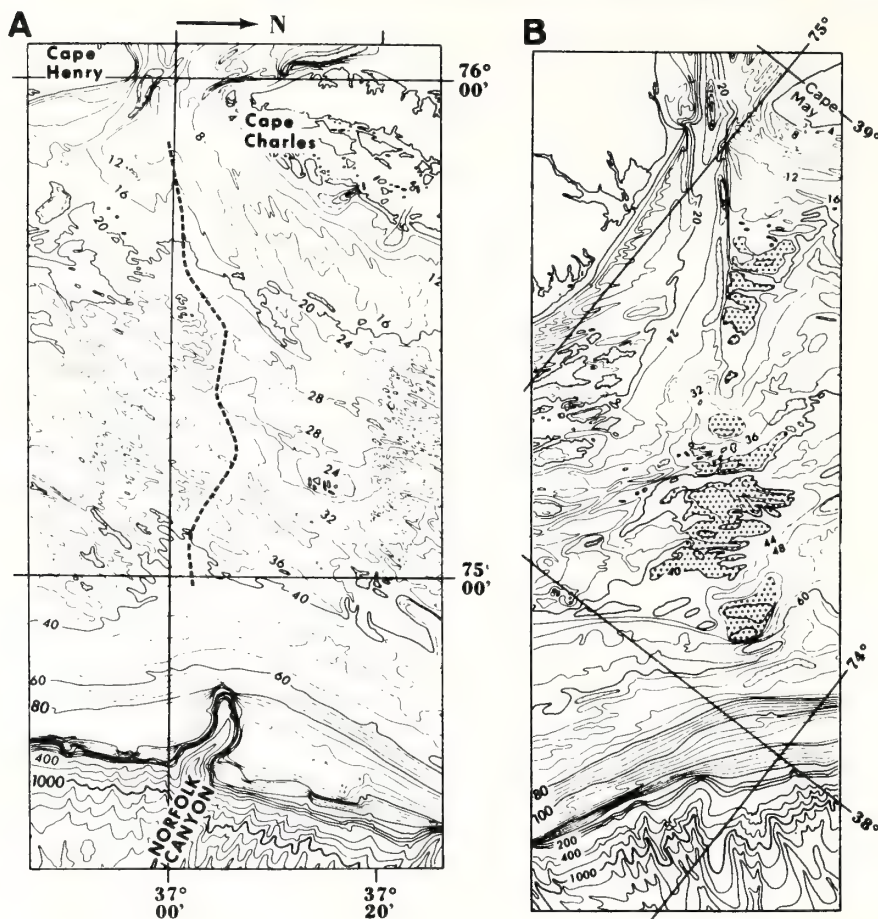


Figure 220.

Middle Atlantic bight shelf valleys. Contour interval 4 m. From Uchupi (1969). (A) Partially filled Susquehanna shelf valley. Thalweg (dashed line) locally interrupted by Post-transgression ridges or swales. (B) Delaware shelf valley. Paired estuarine scour channel and shoal retreat ridge. Isolated highs are stippled.

persistence through time of this tide-maintained channel on the retreating seaward face of the shoal that seems to have resulted in the sharply defined nature of the shelf valley (cf. Fig. 212).

The Great Egg shelf valley (Fig. 221, 222a) is the seaward extension of an insignificant modern river of that name. The headwaters of the Great Egg River are close to the right-angle bend in the Delaware, where it turns to parallel the fall line on its course toward Delaware Bay. It seems probable that at one time the Delaware River flowed without deviation across the Great Egg

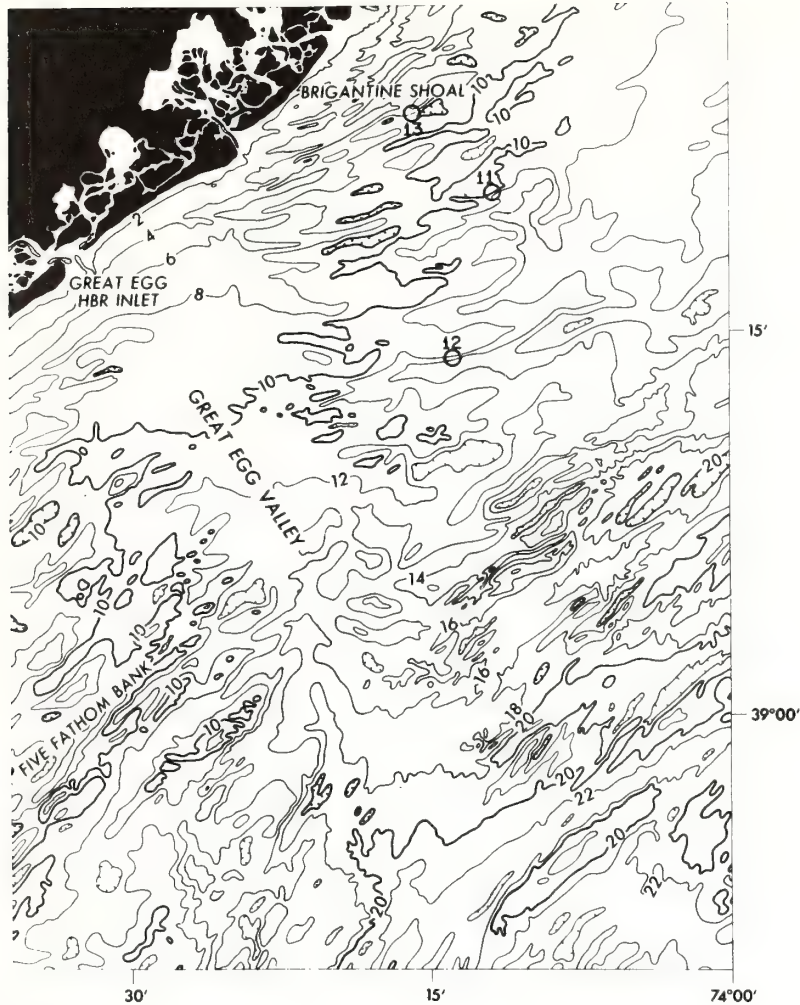


Figure 221.

Bathymetry of a portion of the New Jersey shelf. Contour interval 2 fathoms. From Stearns (1967). See source map, USCGS bathymetric map 0807N-55 for 1-fathom resolution. Numbered circles are submersible stations.

channel to the Baltimore canyon but since has been diverted by piracy (Widmer, 1964). This ancestral Delaware may have been joined by the Hudson along a fall-line valley since abandoned (Sanders, 1972, personal communication).

On the inner shelf, the Great Egg shelf valley (Figs. 221, 222a) exhibits an extreme form of southward asymmetry (Fig. 216); ridge crests to the north are little higher than the valley floor, while the northern trough axes are consider-

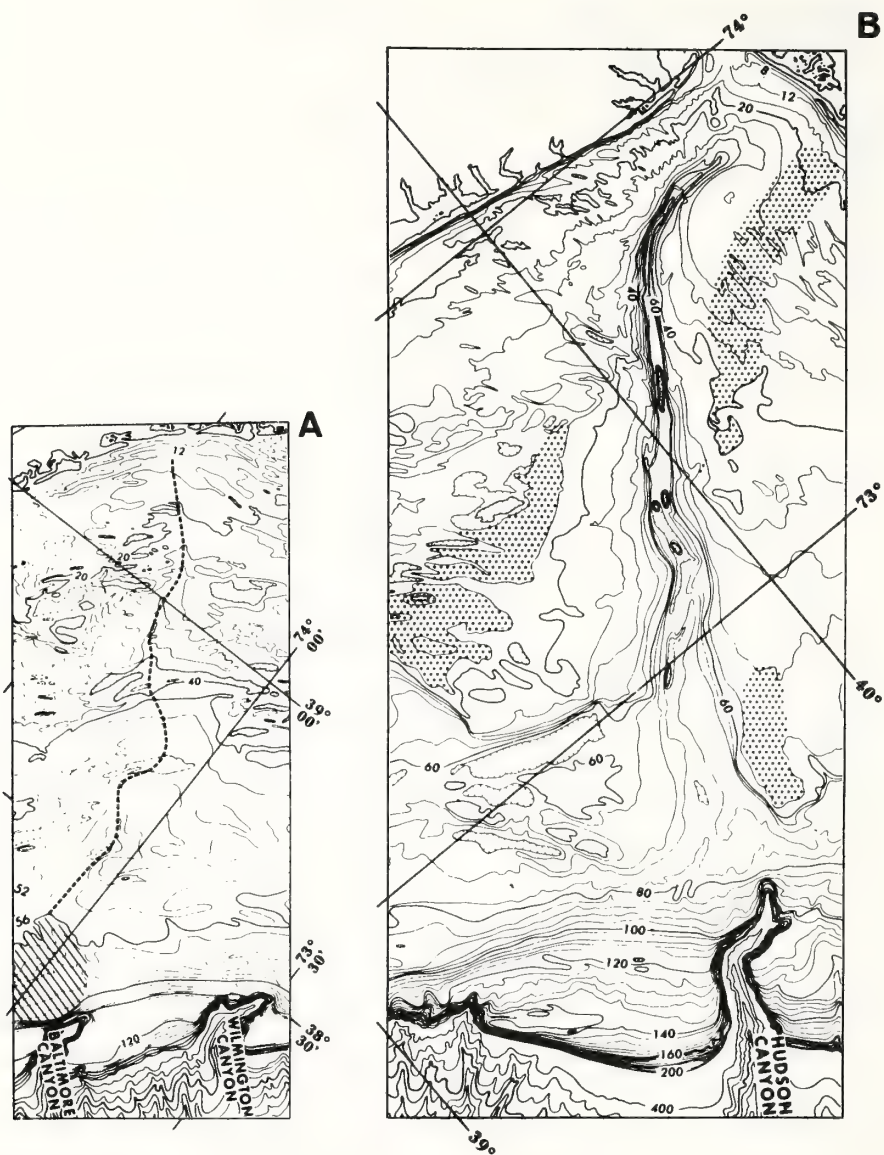


Figure 227.

Middle Atlantic bight shelf valleys. Contour interval 4 m. From Uchupi, 1969: (A) Great Egg shelf valley. Thalweg dashed; probable delta is diagonally ruled; (B) Hudson shelf valley. Highs are indicated by stippling.

ably below this level. To the south, trough axes continue at the same level as the valley floor, while the ridges rise above them. Thus, in profile, the inner valley is more nearly a complex sort of step than a true channel. This configuration is probably a result of valley fill and interfluvial scour by south trending currents, after piracy of the Delaware and during subsequent development of the modern barrier shoreface under near stillstand conditions. A little further seaward, the northeastern side becomes a poorly developed shoal-retreat massif, out as far as the mid-shelf shoreline. Complex aspects of this massif will be described in a later section. Resolution deteriorates beyond this point, but the channel may be traced through a post-transgression ridge and swale topography to a deltalike bulge immediately above the Baltimore Canyon.

The highs on the southeast flank of the Hudson shelf valley (Fig. 222b) appear to be mainly of erosional origin and will be discussed in a later section. However, the more subdued northeast lip may be at least partly of shoal-retreat origin.

The shelf-transverse grain of the inner Gorgia coast (Fig. 223) is best interpreted as a primarily constructional shoal-retreat complex, formed by the retreat of closely spaced estuaries. Much of it is associated with the ancestral Altamaha drainage system (Pilkey and Giles, 1965).

Shelf-Transverse Elements II: Shoal-Retreat Massifs from Cape-Associated Shoals

Cape-Associated Shoals and Shoal-Retreat Massifs

The frequency and dimensions of arcuate troughs on cape-associated shoals tend to increase toward their distal end, as though the water impounded on their north sides during northeasters can more easily incise spillways at points more distant from the point of sand input on the foreland apex, where such breaches are not readily repaired. Due east of outer Diamond shoals (Fig. 185) lies a zone of broken topography. Coast-parallel ridges up to 15 m high rest on a surface 15 m below the crest of Diamond shoals; the ridges terminate in a field of transverse sand waves similar to the field on top of outer Diamond shoals. This zone of broken topography appears to be an older, earlier, cape-associated shoal, which has been much dissected since formation, separated from the present Diamond shoals by a 10 m scarp.

The area between Lookout shoals proper and the shelf edge is occupied by a series of seaward-convex, arcuate ridges of much larger scale than those comprising the shoals proper (Fig. 186). Transverse asymmetry is reversed on this outer sector of Lookout shoals; the frontal scarps of the ridges curve to the east and north, causing this side of the outer shoal to be more sharply defined than the southwest. Possibly this is caused by the scour of bottom water flowing seaward around the shoal tip during storms.

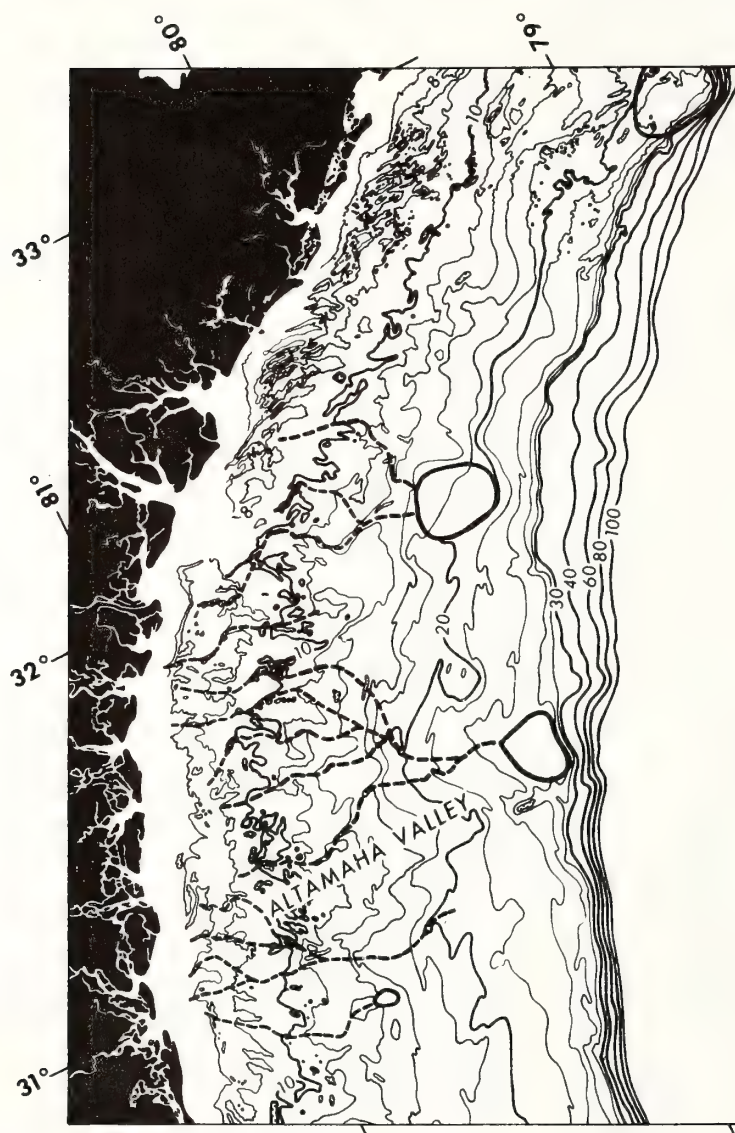


Figure 223.
Bathymetry of the Georgia shelf. From AAPG bathymetric maps of eastern continental margin. Contours in fathoms. Circled areas are probable mid-shelf deltas.

The large-scale arcuate ridges appear to represent an older shoal sequence, dissected by cross-shoal erosion. The step from the outer to inner shoal may reflect a stepwise rise of sea level, or, more probably, two periods during a continuous rise in sea level, when shoal-top accretion was able to keep pace with the sea-level rise. Taken together, the sequence comprises a shoal-retreat massif with an actively growing inner terminus and a distant portion undergoing heavy modification in response to the outer-shelf hydraulic regime.

The South Carolina Shelf as a Shoal-Retreat Complex

Facts pertaining to the nature of cape-associated shoal-retreat massifs that have been gleaned from the North Carolina shelf can profitably be applied to the South Carolina shelf. Here the coast is transitional to the estuarine coast of the Georgia bight, which, in fact, begins at Cape Romain. The Carolina capes form a continuum in terms of river dominance, in which Cape Hatteras, during an early shelf-edge stage, may have been associated with the ancestral Pamlico River and Cape Lookout with the ancestral Neuse. Cape Fear (Fig. 210) is presently associated with the Cape Fear River, but is not a true cusped delta, in that the river mouth is on the southern side and does not serve as a shielding point. Cape Romain, southernmost of the Carolina capes in the transitional zone, constitutes the near confluence of the Pee Dee and Santee Rivers and is as nearly a cusped delta as a retrograding coastal landform can be. South of Cape Romain are a series of cusped forelands of much smaller scale, each with its associated shoal (Fig. 224). The shoals are flatter and more poorly defined than those to the north, but the salient features are present; each shoal is marked by arcuate, transverse channels shallowing to the southwest and a scarp at the seaward margin. The better defined cape-associated shoals in the northwestern half of Fig. 224 are in fact shoal-retreat massifs composed of successive scarps and flats. The deeper, more seaward segments in some cases have seaward scarps that curve to the north and east, reversing the normal asymmetry, as is the case with outer Diamond and Lookout shoals. A prominent abandoned shoal segment on the northeast margin of Fig. 224 is apparently related to an ancestral Santee-Pee Dee confluence. However, like other cape-associated shoals, it is cut by arcuate channels and there is no evidence to indicate that it was ever a subaerial delta surface; true deltaic strata, if they exist, must lie beneath it. If so, the abandoned cape-associated shoal would comprise a special case of Scruton's (1960) destructional phase of delta building. Other, yet more poorly defined, shoal-retreat ridges may exist on the southwest end of Fig. 224, as suggested by the scalloped pattern of isobaths, with landward pointing cusps. However, no well-defined scarps are present to define individual segments; hence in this sector it may be more meaningful to talk in terms of a shoal-retreat sand sheet.

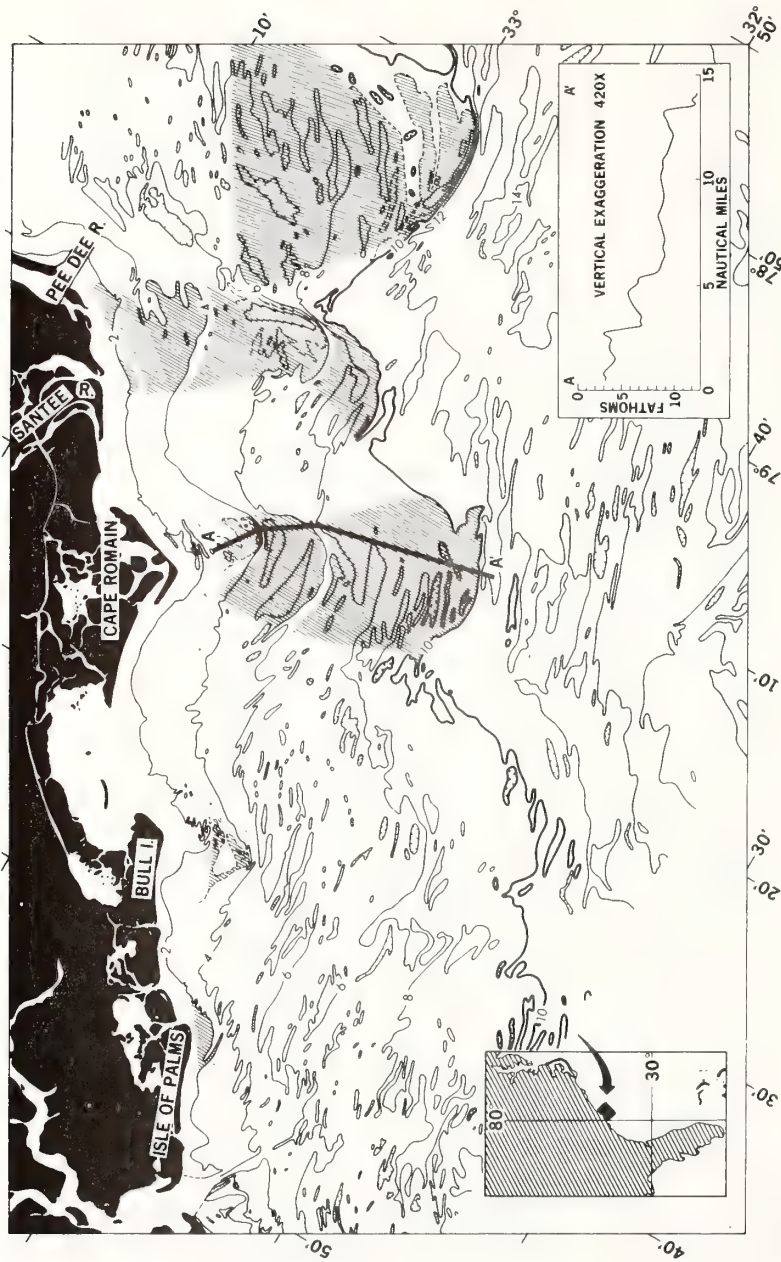


Figure 224. Bathymetry of a portion of the South Carolina coast. Contour interval is 2 fathoms. Ruled areas are cape extension shoals, presently or formerly associated with cusped forelands. Profiles were taken from original map contoured at 1 fathom. On letter map all separate ruled areas have, at least locally, seaward-facing scarps.

The mid-shelf delta of the ancestral Delaware (Fig. 220a) is traversed by arcuate, southward-shoaling troughs and, in its last phase, may have been a cape-associated shoal. After the establishment of the mid-shelf shoreline at approximately 40 m (132 ft) the coastal regime changed, such that the retreating bay mouth left not a cape shoal-retreat massif, but a scour trench paired with an inlet shoal-retreat massif.

Shelf-Transverse Elements III: Shelf Valleys and Cuestas

The Hudson shelf valley appears nearly gorgelike on maps (Fig. 222b). Although its slopes rarely exceed 10° , over 60 m (180 ft) of relief occurs along its upper portion. While the localized deeps within the Hudson shelf valley may also be relict estuarine scour trenches, something more is needed to account for the valley's remarkably deep incision. Veatch and Smith (1938) have suggested that during part of the late Wisconsinan ice retreat, the Hudson received the entire Great Lakes drainage and that the entrenchment of its shelf valley occurred then.

As a consequence of the Hudson's incisement, the flanking topography has become considerably dissected. Nearly coast-parallel highs of apparent erosional origin on the north New Jersey coast have been described in the previous paper. North-northeast trending highs also occur further seaward on the west flank of the Hudson shelf valley; the depression between them can be traced as far as the mid-shelf shore and will be referred to as the north New Jersey shelf valley (Fig. 225). The coastal and offshore highs are nearly parallel to Cholera Bank, a high on the east lip of the upper Hudson shelf valley which can be traced into the Long Island shore face. Locally there is direct evidence for an erosional origin for some of these highs. Divers have observed residual boulders at Shrewsbury Rocks on one of the north New Jersey coastal highs (personal communication, 1972, Charles Gibson, National Marine Fisheries Service, Sandy Hook Laboratory), and a submersible dive (senior author) to the Veatch and Smith scarp on the east flank of the north New Jersey shelf valley has revealed stiff, outcropping clay. It is more difficult to decide if these features are truly cuestas. The north to north-northeast trend of these highs is more northerly than the regional strike of outcropping strata on the subaerial coastal plain, but parallels isopach lines of the submarine Upper Cretaceous (Garrison, 1970, Fig. 7). Garrison's profiles suggest that at least the highs flanking the north New Jersey shelf valley are structurally controlled.

A northeast-trending high lies on the Long Island shelf between the Block and Long Island shelf valleys. A well-developed scarp on its seaward flank is a deeper northern member of the series of scarps collectively referred to in this report as the mid-shelf shore. The shielding action of this promontory during the drowning of the Long Island shelf valley was apparently responsible

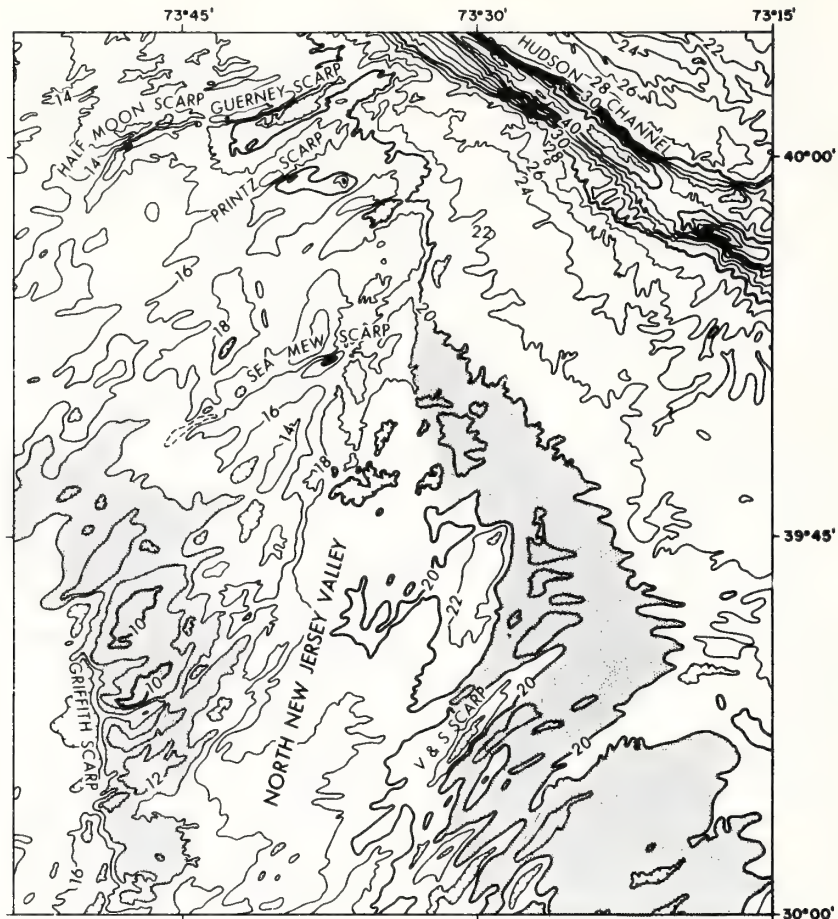


Figure 225.

South flank of the Hudson shelf valley. Contour interval is 2 fathoms. See source map, USCGS bathymetric map 0807N-54, by Stearns (1967), for 1 fathom resolution. Cuestas bracketing north New Jersey shelf valley are indicated by stipple.

for the amazing state of preservation of the valley's drainage net (Figs. 193, 194).

Shelf-Parallel Elements I: Ridge-Capped Scarps as Overstepped Barriers

As noted in the previous paper, earlier theories of the origin of the Atlantic shelf ridge-and-swale topography saw it as a relict strand plain, with successive ridges recording temporary stillstands of the Holocene transgression. However,

as previously indicated in this paper, coastal retreat of the Bruun type results in destruction of barrier deposits by shore-face erosion. Preservation of a barrier formed during a transgression requires that the barrier grow in place due to an abundant sand supply, so that its surface keeps pace with the rise of sea level. Eventually there is a reduction in the supply of river sand as the lagoons widen (Curry, 1964) or an increase in the rate of sea-level rise. These factors, or simply the increase in submarine surface area of the barrier requiring nourishment (Dillon, 1970), causes the barrier to starve and be overstepped by the sea. If the toe of the old shore face is below the effective wave base of the new sea floor, the overstep process will not completely destroy the barrier and some topographic expression of the feature should survive, although the result should be more nearly a scarp than a ridge. Gilbert (1890) has defined a morphological criterion for identifying barriers successively overstepped during a marine transgression; they should form a staircase sequence, with the crest of each barrier remnant lying at the altitude of the toe of the next barrier to the landward. Seaward flanks should be steeper than landward flanks, as is the case with active barriers. Intermittent coastal retreat by barrier overstep is a rather theoretical process and not a very actualistic one; no one has ever caught a barrier in the act of being overstepped, while coastal retreat of the Bruun type can be documented (previous section). Convincing examples of drowned barriers have been reported in the literature (Curry, 1961; McMaster and Garrison, 1966). However, the latter, a spit tied to a rock eminence on the southern New England shelf, is a special case. Such a rock-tied spit has literally nowhere to go as the shoreline retreats. Recently overstepped tombolos, rock-tied spits, and pocket beaches might indeed be sought on modern rugged coasts with a fully indurated (crystalline) substrate.

The successive scarps and terraces of the central and outer middle Atlantic shelf render this sector a reasonable place in which to seek overstepped barriers. One of the most interesting potential examples occurs on the New Jersey shelf in the area of complex, anastomosing inner-shelf ridges east of the Great Egg shelf valley (Figs. 221, 222a, 226), where it intersects scarps with toes at 40 and 46 m (131 and 150 ft). Two orders of ridges are apparent. Several large-scale ridges are 6 to 10 km (3 to 5 n mi) apart, with 10 to 20 m of relief. Their seaward flanks are generally steeper than landward flanks. Superimposed on these are ridges of smaller scale, with a spacing of 0.5 to 2.6 km (0.25 to 1.3 n mi) and a relief of 6 m (20 ft). Smaller-scale ridges are most abundant on the gentle northwest flanks of the large-scale features, where they climb toward the main crest line and tend to converge with it. Large-scale lows tend to be compartmentalized into an echelon small-scale lows, with up to 6 m (20 ft) of closure, that trend a few degrees more northerly than the main features.

It is possible to surmise that the large-scale features are barriers. Their widths of up to several miles are more comparable to the widths of raised Pleistocene

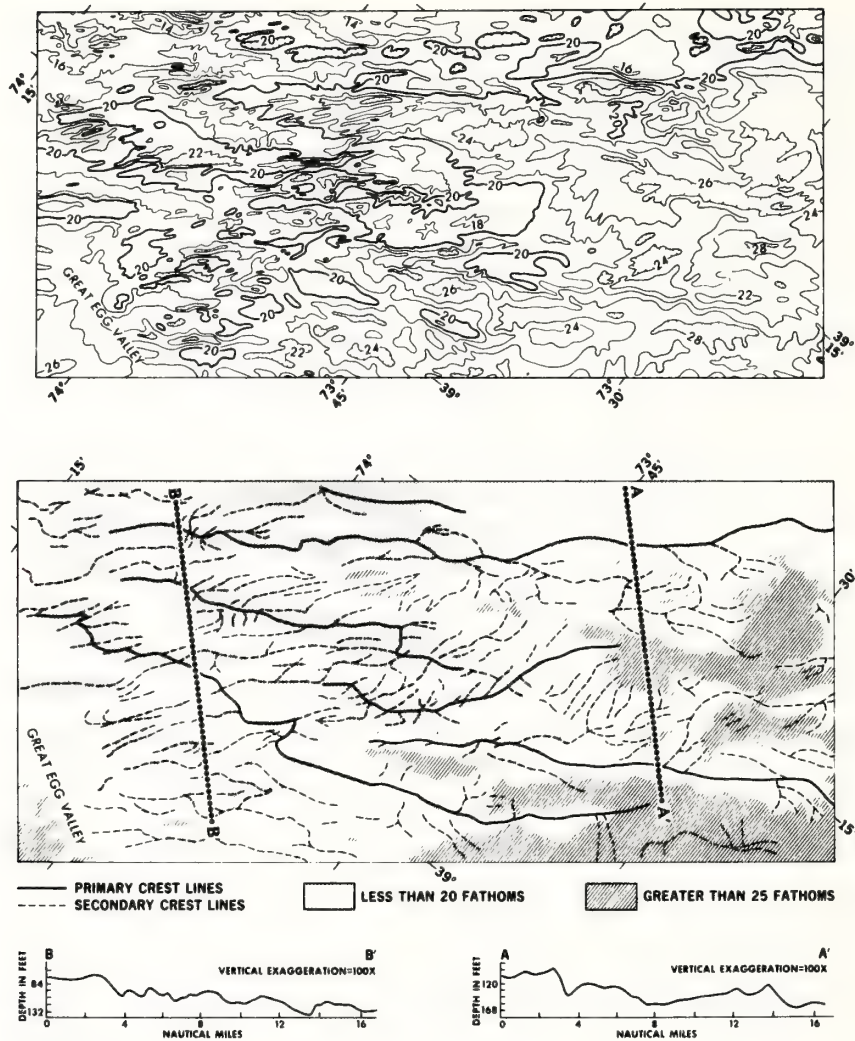


Figure 226.

Area of complex inner shelf topography off Atlantic City, New Jersey. Above: Map with 1 fathom interval. Below: Analysis. Possible overstepped barriers are outlined by 20- and 25-fathom contours. See USCGS bathymetric map 0807N-55, for 1 fathom resolution.

barriers on land (Colquhoun, 1969) and their steeper seaward faces, with 10 m (33 ft) or more of relief, are comparable to the modern shoreface. One such ridge sits squarely athwart the Little Egg shelf valley (Fig. 221); its resemblance to an estuary-mouth spit is diminished, however, by its reverse asymmetry; its landward face is steeper.

The two large-scale ridges crossed by profile AA' satisfy the stairstep criterion. However, the sequence of three large-scale ridges crossed by profile BB' does not, and simple intermittent transgression does not suffice to explain them. Perhaps sufficient sediment was available here in the vicinity of the Great Egg River mouth, so that depositional regression occurred during the 40 m stillstand of the mid-shelf shore and a northward-branching sequence of spits developed, similar to the Sandbridge spit sequence of the early Wisconsin of Virginia (Oaks, 1964; Swift et al., 1971, Fig. 3); or possibly the barriers of the 40 m Holocene stillstand were localized by a preexisting Pleistocene shoreline, much as the modern Georgia barriers were localized by the Pleistocene Silver Bluff barriers when the advancing modern shoreline impinged on it (Hoyt and Hails, 1967). At any rate, the complex of barrierlike forms here on the flat central portion of the shelf between 30 and 60 m depth is compatible with Emery's (1967; 1968, Fig. 15) interpretation of shelf history. Emery suggests that, despite the low gradient, the advancing Holocene shoreline transversed this portion of the continental shelf slowly as a consequence of the low early Holocene rate of sea-level rise, and that, as a result, a great deal of river-transported sand was deposited as barriers on the central shelf. However, a more conservative explanation might call upon Emery's hypothesis simply as a reason for the presence of an unusually thick layer of loose sand over the older Pleistocene substrate and might interpret both large- and small-scale ridges to a response of the layer to the modern hydraulic regime.

The complex superimposition of small-scale ridges and swales at small angles to the large-scale form seems to have involved both the incision of the large-scale forms and the construction of attached tails and streamers of sand. Submersible dives in this sector reveal a distribution of grain sizes similar to that observed by the authors on the Virginia shelf (Swift et al., 1971). Troughs are floored by fine-grained sand; locally, a basal layer of coarse, pebbly sand over a stiff clay substrate is exposed. Fine-grained flank sands coarsen up the sides of ridges to a well-sorted, medium-grained sand on crests (Figs. 227, 228). As previously concluded by Donohue and others (1966), this topography has been heavily modified by the post-transgression hydraulic regime. It appears to be presently maintained by strong, intermittent currents which scour out troughs and fair-weather wave surge which winnows crests.

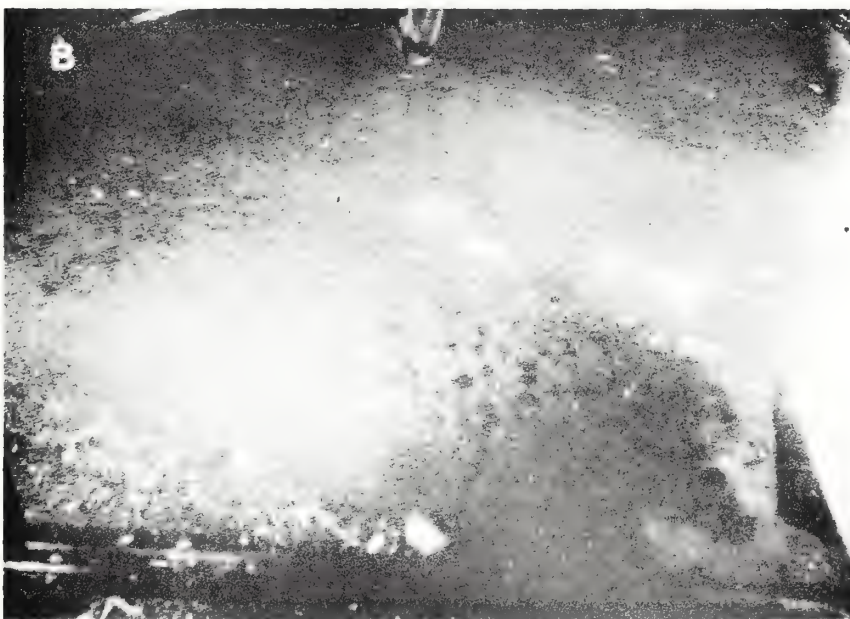
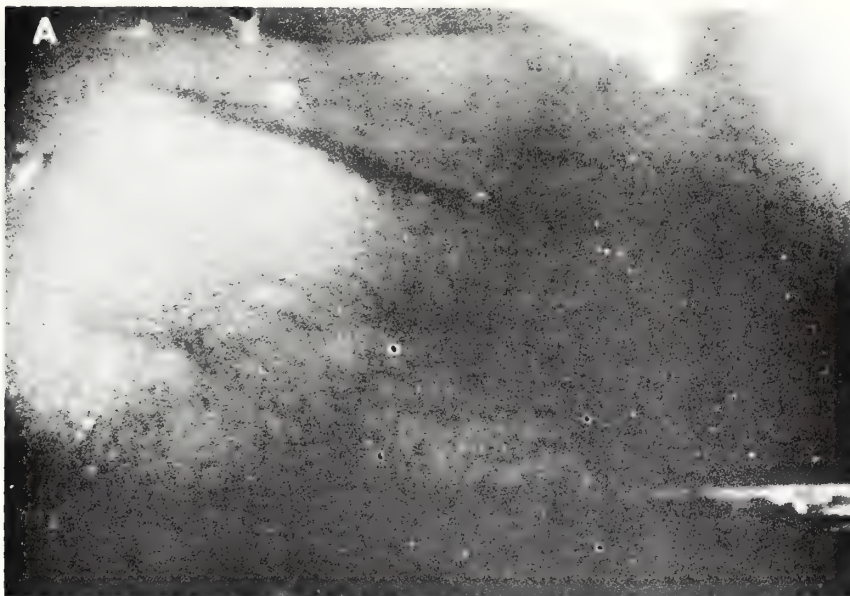
Frank (1971) has performed textural analyses on samples from this sector and concludes that relict littoral and nearshore deposits are present. His findings are compatible with our interpretation. However, the result of grain-size analyses must be used with caution, since it is not always possible to arrive at a unique solution. The hydraulic regime associated with the ridges very probably fractionates sand into types resembling those produced by the littoral hydraulic regime (Fig. 186b, preceding chapter).

Scarps of apparent littoral origin (Fig. 193) and large-scale ridges with spacings of barrier scale are common on the outer shelf, seaward of the 40 m (130 ft) isobath. The presence of orthogonal tributaries in the intervening lows, reminiscent of an incomplete dendritic drainage pattern (Figs. 194, 195), suggests a barrier topography with a superimposed subaerial drainage. However, the stairstep criterion is only locally satisfied and most profiles suggest that if these are barrier sequences, much post-transgression modification has occurred. Profiling of the North Carolina shelf (Shideler and Swift, 1972) indicates that the flanks of some large outer-shelf ridges truncate horizontal internal reflectors, indicating an erosional origin.

Within the middle Atlantic bight, the more northerly scarps tend to be found at successively deeper levels (Fig. 229). The reason for this is not clear. Veatch and Smith (1939) considered incomplete recovery of the northern sector from glacial loading, but believed that it was not entirely an adequate explanation. Fairbridge and Neuman (1967) suggest that geosynclinal subsidence may play a role. The mid-shelf shore appears to be a Holocene feature in that the shoal-retreat ridges and shelf valleys that extend to it are fresh and undissected, and oyster shells from its vicinity yield mid-Holocene dates (Merrill et al., 1965). If so, the tilting must have been fairly recent, or else the collection of scarps designated by this name is not a synchronous group.

Shelf-Parallel Elements II: Tributary Shelf Valleys and the Ridge-and-Swale Topography

Shelf-parallel notches are incised into the south flank of the Block shelf valley, into the south flank of the Hudson shelf valley, and into the *cuestas* on both sides of the north New Jersey shelf valley (Fig. 193, 225). These notches are separated by flat-topped divides and appear to be products of subaerial fluvial erosion. Notches tributary to the Hudson and northern New Jersey shelf valleys tend to have steeper northwest, seaward-facing sides. Many of these are capped by low ridges parallel to the scarps, with highest points immediately west of the steepest part of the scarp (Half Moon, Guerne, Printz, Sea Mew, and Veatch and Smith scarps, Fig. 225). It seems reasonable to interpret these seaward-facing scarps as wave-cut scarps and the ridges as remnants of barriers. However, the close correlation of ridge peak with steepest portion of scarp in Fig. 225 may indicate modification by modern currents sweeping sand west along the notches and diagonally up the north sides of the scarps. If so, the sand ridges are more nearly modern submarine levees than relict subaerial barriers. A dive by the senior author in the Perry submersible PC-8 to the Veatch and Smith scarp on the west flank of the north New Jersey shelf valley (Fig. 225) revealed bare gray clay substrate thinly veneered with coarse, rippled sand and



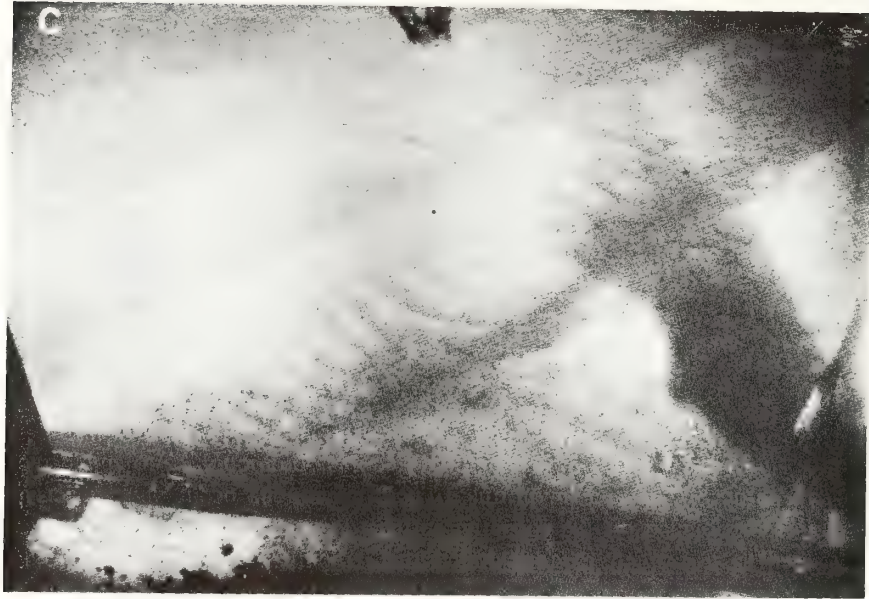


Figure 227.

Small-scale bedforms of the New Jersey shelf, photographed from the Perry submersible PC-8, on October 6 and 7, 1971. (A) Ripples, 15 cm high, in coarse sand of swale. Ripples are mantled with clay film. Station 11, Fig. 216. (B) Asymmetric ripples in medium sand on ridge crest, formed by a combination of wave surge and unidirectional flow, probably during Hurricane Ginger, 1971. Steep faces towards observer. Crests are armored with sand dollars. Station 11, Fig. 216. (C) Wave ripples in medium sand on ridge crest, 14 cm high. Small-scale current ripples at right angles are responses to tidal current.

clay pebbles from 46 to 38 m (150-125 ft), then a cap of sand, grading from fine sand at its base to medium sand at the crest at 30 m (100 ft). A dive several hours earlier to the nearby Sea Mew scarp had revealed active lingoid ripples of fine sand moving directly down the scarp in response to the rotary tidal current, then at its maximum value. But despite such intermittent movement of sand into the valleys, the sand caps have not been flattened. The valleys have not been filled, but merely veneered by coarse lag. Some sort of intermittent current has apparently been sweeping them out through the millenia since transgression.

On the Long Island shelf, valleys tributary to the Block shelf valley merge toward the west with the very regular ridge-and-swale topography of the Long Island inner shelf (Fig. 194, 230). Garrison and McMaster (1966) and McKinney

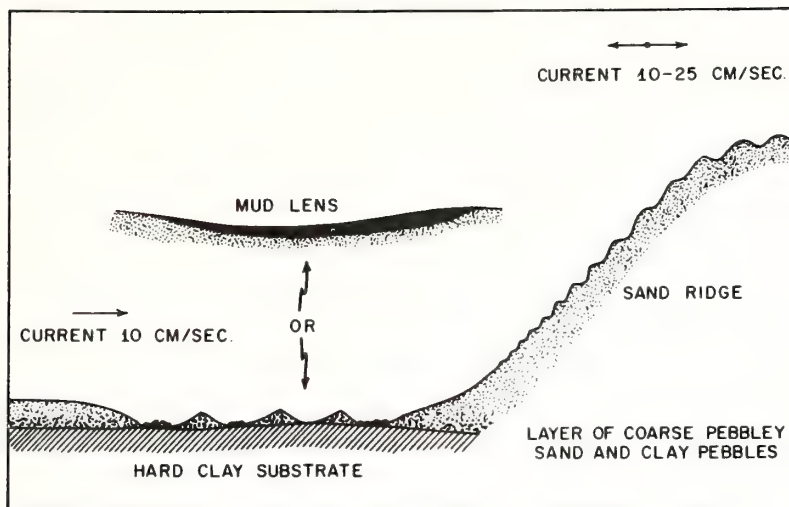


Figure 228.

Schematic model of an inner New Jersey shelf swale and adjacent ridge, based on submersible observations at stations 11-13, Fig. 216.

and Friedman (1970) have consequently deduced a fluvial origin for the topography, attributing the trend of the swales diagonally across the regional contours to subsequent tilting. However, the only subaerial "drainage" pattern that resembles this pattern of parallel ridges and troughs, with tuning-fork bifurcations (see Fig. 194) and numerous enclosed depressions (blowouts), is that of a seif dune desert (Folk, 1971a, b; Glennie, 1971). All other subaerial drainage patterns with dominantly parallel lows that were examined had at least occasional orthogonal (obsequent and resequent) first-order streams, forming an incipient trellis pattern. The inner shelf topography differs, however, from a seif dune topography in that ridge spacing is greater and side slopes are less.

Thus, the ridge-and-swale topography of the Long Island inner shelf comprises a sort of optical illusion, with a western margin of apparent relict fluvial channels, an ambiguous central sector, and an eastern margin where ridges, merging with the shoreface, are clearly of modern hydraulic origin. This surface may well have been initiated as a braided outwash plain draining eastward from the Long Island ice tongue toward the Block shelf valley. If so, its channels would have become incised during glacial rebound. We conclude that this sand deposit has been planed off by shore-face retreat and its drainage pattern partially erased, then subjected to an inner shelf hydraulic regime and partially rebuilt by it into a seiflike topography.

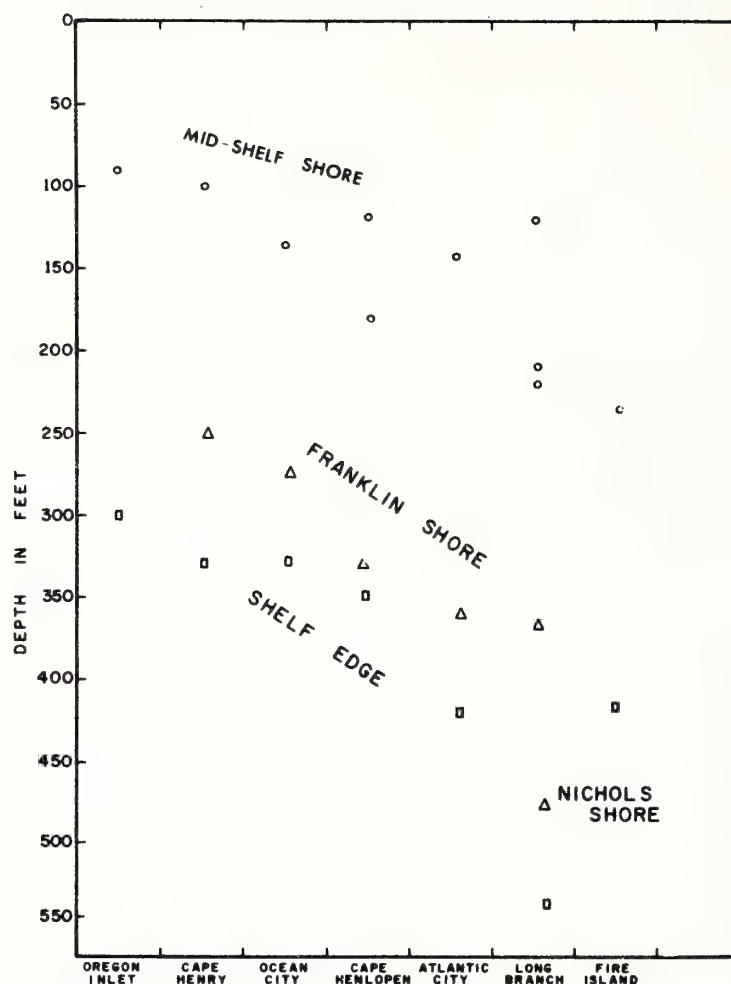


Figure 229.
Correlation of terraces, middle Atlantic bight.

SOUTHWARD SEDIMENT TRANSPORT ON THE CENTRAL AND SOUTHERN ATLANTIC SHELF

Bedform Asymmetry and Southward Transport

Throughout the preceding discussion, much evidence has been presented which suggests that sediment is moving southward along the middle Atlantic bight.

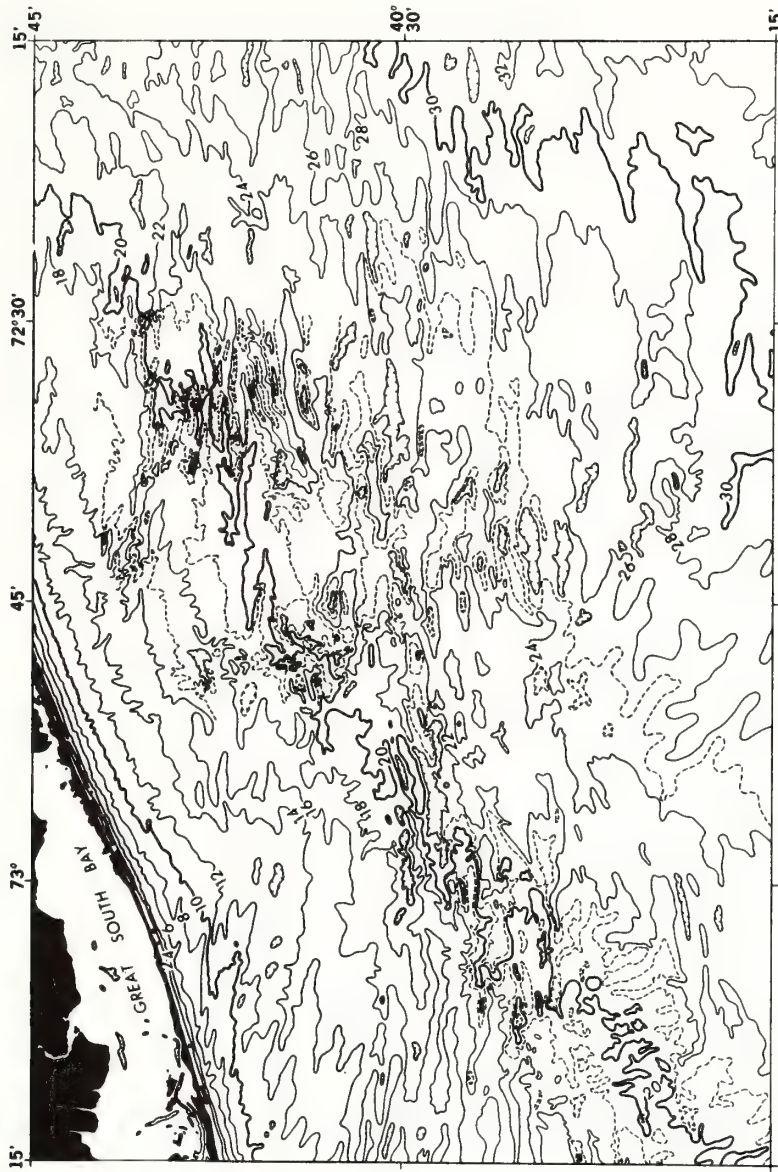


Figure 230.
Bathymetry of a portion of the Long Island shelf. Contour interval is 2 fathoms, with supplementary dashed contours at 1 fathom.
From USCGS bathymetric map 0808N-54 by Stearns, 1967. See original for 1-fathom resolution.

This section will consider the evidence systematically and will introduce new information in support of the concept.

Evidence on the northern portion of the middle Atlantic bight is tenuous. To the extent that the inner shelf ridges, with their extreme parallelism and numerous enclosed lows, are seiflike bedforms, southward transport is occurring, for the ridges gain in relief and thalwegs climb and branch in this direction, as seif troughs do in the direction of transport. Evidence is stronger on the inner shelf. The ridges of the Fire Island shore face tend to be asymmetrical, with steeper faces to the southeast, as do the shoreface ridge systems of the New Jersey shelf (Figs. 179, 191, previous paper; Figs. 221, 227). In the North Sea, sand ridges of similar geometry are interpreted as large-scale current-parallel bedforms built by helical flow (Houbolt, 1968; see previous chapter). Transverse asymmetry of the sort noted above is taken as evidence that oblique, crest-converging currents on one side are stronger than on the other; and that the ridge, as well as extending longitudinally, is also shifting laterally. Thus, the asymmetry of inner Atlantic shelf ridges is compatible with the concept of southward bed-load transport. This asymmetry is locally reversed where large ridges join the shoreface in shallow water. Judging by the analogy of the inner False Cape ridge (previous chapter), intense scour in the heads of the troughs behind the ridges sweeps fine, shoreface sand out over the ridge base. The sand is fine enough to travel in suspension for considerable distances in the ridge-base rip current, with the result that the seaward flank of the ridge, where it joins the shore face, is aggraded to the point that asymmetry is reversed.

In the ridges of the inner shelf off Atlantic City (Fig. 221), New Jersey, longitudinal asymmetry becomes apparent; crestlines of isolated ridges climb gently to the southwest, then drop abruptly. Transverse and longitudinal asymmetry is well developed in the Fenwick ridge field of the Delaware coast (Fig. 188, previous chapter). A time series of 93 years on Chincoteague Shoals (Fig. 178, previous chapter) shows that the inner-shelf ridges are growing southward. On the Virginia-North Carolina shelf crest and trough lines of the ridge systems climb to the south. The regional distribution of grain sizes suggest that fine sand has been swept out of the troughs of the Virginia Beach, False Cape, and Platt shoals ridge systems and is being deposited in low areas south of these systems (Swift and others, 1972; Shideler and others, 1972). On the Virginia-North Carolina shelf a new element appears in the form of small current-transverse bedforms that are associated with the current-parallel sand ridges. South-facing sand waves with up to a meter of relief have been observed during summer scuba dives in the Virginia Beach ridge system. Clay lenses in troughs 10 cm (4 in) thick suggest that sand waves are relict from winter storms (Holliday et al., in press). Larger south-facing transverse forms with heights up to 3 m have been observed (Fig. 231), suggesting that the wavy appearance of the flanks of the Virginia Beach ridges in Fig. 214 is only partly a mapping artifact.

At Platt shoals (Fig. 215) and on outer Diamond shoals (Fig. 207) the crests tend to wrap around to the west at the ends of the ridges, swinging into parallelism with the small-scale, obliquely or transversely oriented, southward asymmetrical ridges that overlie the large-scale ridges. Tidal currents are too weak in these areas to generate these features. Presumably they are activated only by storm currents. Profiles (Fig. 231) indicate that their steeper southward slopes were not at the angle of repose during the summer of mapping.

Clear-cut evidence for sand transport in the form of sand waves and bathymetric changes occurs predominantly within the 25 m (78 ft) isobath. However, the flamboyant ridge-and-swale topography on the central New Jersey shelf east of the Great Egg shelf valley suggests that where a sufficient thickness of loose sand occurs, it will become current-molded out to depths of 40 m (125 ft). One of the few careful studies of outer shelf microtopography (Stanley and Kelling, 1968; Stanley and others, 1972) suggests that, at least in the vicinity of the Wilmington Submarine canyon, shelf-edge sediment transport is toward the southwest.

Thus, within the middle Atlantic bight, sediment transport becomes more intense with increasing proximity to shore and with increasing proximity to the southern end of the bight. It has been suggested in the previous paper that the dominant hydraulic element molding the middle Atlantic shelf floor are the southerly wind-drift currents generated by winter storms. It seems reasonable that their velocities and bottom shear stresses would become more intense

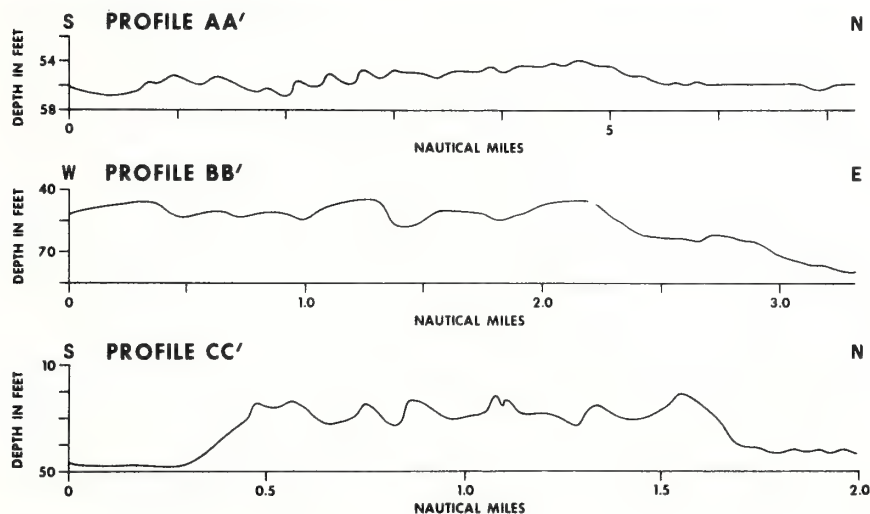


Figure 231.

Representative profiles of sand waves on the Virginia-North Carolina shelf. See Figs 204, 205, and 215 for locations. Top: Virginia Beach; middle: Platt shoals; bottom: Diamond Shoals.

as they moved toward shore and southward up the shoaling and narrowing shelf floor toward Cape Hatteras. The pattern of southward asymmetry of morphologic elements reflecting southward sediment transport continues through the series of shoal-retreat massifs which is associated with the Carolina capes. On the Georgia bight, arcuate, inlet-associated shoals are higher on the northern side and tend to have well developed ramps and chutes (Fig. 206). Southern and seaward margins are oversteepened. The channels within the shoals curve to the south, suggesting diversion by a south-trending coastal current. Southward asymmetry is clearly apparent at Cape Kennedy (Fig. 211).

Other papers in this volume indicate that this pattern of coastwise sediment transport is a common one, as indeed it must be, for reasons of hydraulic continuity. Coastwise advective transport of sediment is compatible with seaward diffusive transport; however, we are far from a point where our quantitative knowledge of the sediment budget for this coast will permit resolution of these components.

Bedform Hierarchies and the Ridge and Swale Topography

Allen (1968) has noted that several orders of bedforms tend to occur simultaneously and that such hierarchies of bedforms

arise because the quantities that determine flow are sufficiently numerous that several mutually unstable combinations can exist, each combination being expressed in terms of a bedform of a characteristic physical scale and orientation relative to flow.

Such a hierarchy appears to exist on the Atlantic shelf. Here coexisting forms include current, wave and combined flow ripples (small scale current-transverse bedforms whose scale is independent of water depth), sandwaves (intermediate scale, current-transverse bedforms with scale limited by flow depth), and sand ridges (large scale, current-parallel bedforms with scale limited by flow depth). The assemblage appears to result from Allen's *Condition 1*, in which stream power has a small or moderate value, such that the Froude number is substantially less than unity, and the sand bed is deep and continuous. Conditions on the Atlantic shelf, however, are more complex than this. For one thing, the major component of the flow field consists in most cases of storm-generated currents with durations of several days. Small-scale wave, current, and combined flow ripples (Fig. 227b) are obliterated between pulses by bioturbation or wave surge. Intermediate and large scale bedforms (sand waves and ridges) must represent time-integrated responses to these pulses, in which spacing, heights and side slopes are less than maximum, reflecting a compromise between storm aggradation and fair weather degradation. Second, the large-scale forms extend up into the wave-agitated zone. This, rather than the unidirectional flow component limits their height, and to a certain extent controls their geometry.

Finally, the hydraulic regime itself is not stationary, but changes through

the lives of the larger bedforms as a consequence of water deepening attendant on the Holocene transgression. Inner-shelf ridges are created entirely within the wave-agitated zone, as a consequence of the complex interaction of unidirectional storm currents and wave surge with each other and with the substrate (previous chapter). With detachment, they find themselves in a simpler inner shelf regime, for which 10 m appears to be the wave-limited crestal depth. Shelf ridge-fields with crests accordant at deeper depths may have retained this limit from shallower sea level stands, even though their troughs are being actively scoured.

The very different geometries of the ridge systems of cape-associated, inlet-associated, and inner shelf ridge fields tend to disguise their fundamental genetic relationship. All are large-scale, current-parallel bedforms whose spacing increases with flow depth (Fig. 232). Allen (1968) suggests that this geometry is a basic response of a mobile substrate to a flow regime with perturbations transverse to the mean current direction. The perturbations take the form of helical flow cells, in which bottom currents diverge over trough axes, and converge on crest axes. Thus the ridge and swale topography appears to be a stable end-configuration toward which a variety of erosional and depositional topographies converge.

Nature of Sediment Flux through the Ridge and Swale Topography

It is interesting to contrast the geomorphic evidence for southward sediment transport with textural evidence for sediment movement. In general, the patchy nature of sediments on the Atlantic continental shelf have led observers to assume

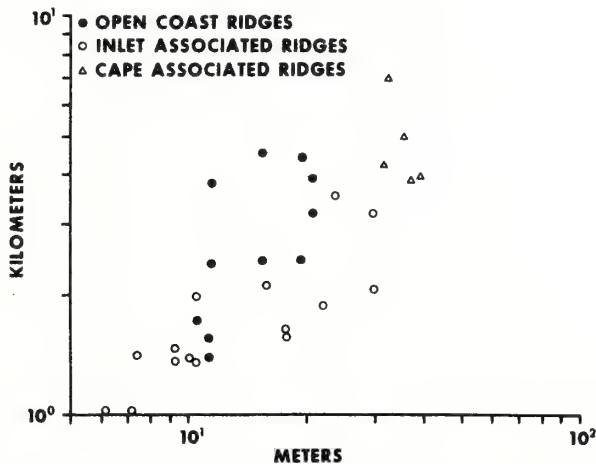


Figure 232.

Spacing against flow depth, ridge and swale topography of the central and southern Atlantic shelf.

that the surficial materials are "relict," that is, autochthonous with respect to the present sedimentary cycle. Milliman and others (1968, 1972) note that "the sharpness of assemblage boundaries and the patchy areal distribution of various carbonate parameters, both within and between (sectors of the Carolina shelf) indicate that transportation and redistribution by bottom currents has been local."

The apparent conflict of geomorphic and petrographic evidence can perhaps be resolved by the following considerations. The transgressive sand sheet of the Atlantic shelf has been molded into linear sand bodies. When careful attention is paid to the mechanics of sediment transport over their surfaces, most shallow marine sand bodies are resolved as the products of sand circulation cells, closed loops in sand transport paths (Houbolt, 1968; Ludwick, 1970, 1972; Oertel and Howard, 1972). This is certainly the case for the tide-maintained ridges of Chesapeake and Delaware Bay mouths (Ludwick, 1970). It may be true for some of the shore-face systems and may apply, or have applied at one time, to the shelf ridges. In such circulation cells the residence time of a sand grain in a loop is generally long with respect to the duration of the total excursion along the transport path. A grain trapped in such a cell stands a very high chance of being accepted for permanent deposition in the growing sand body, whose surface comprises the circulating sand cell. Thus, if the southerly transport paths of the middle Atlantic shelf have many such loops, then most bottom-sediment transport may consist merely of a sand grain migrating obliquely southward to the nearest ridge and being buried there, and long-distance transport may not be significant. However, it is worth noting that characteristic grain trajectories in sand circulation cells may vary greatly with grain size, and it is possible that long-distance transport may be occurring on the Atlantic shelf for fine- and very-fine sand classes. The observation has been made in the preceding paper that the shoreface before the distal, concave-seaward barrier arcs of the New Jersey and Delmarva coastal compartments are made of fine-grained sand. Much of this material may have been winnowed out of the ridge systems to the north. A similar coastwise segregation appears to be occurring between Cape Henry and Cape Hatteras on the Virginia-North Carolina coast (Swift and others, 1971a). This lateral fractionation by sediment size class has led to the statement that the Atlantic shelf is approaching textural equilibrium (Milliman and others, 1972) or that it is undergoing *in situ* or autochthonous grading (Swift, 1970).

EVOLUTION OF THE SHELF SURFACE

Analysis of existing bathymetric and geological information reveals a systematic distribution of morphologic elements on the central and southern Atlantic shelf and indicates the course of events which formed them. Bruun coastal

retreat, whereby a rise in sea level results in shore-face erosion and concomitant aggradation of the adjacent sea floor, serves as a unifying concept by which a variety of constructional shelf-floor features may be traced back to an origin at the foot of the retreating shore face.

The simplest case appears to be the development of shelf-floor ridge fields by detachment during shoreface retreat as exemplified by the Delmarva ridge field, described in the previous paper. Two other major evolutionary sequences are those observed in inlet-associated, shoal-retreat massifs and cape-associated, shoal-retreat massifs. In these cases littoral drift plays a significant role, transporting sand to depositional centers which retreat through time with the shoreline.

The prominent ridge and swale topography of the central and southern Atlantic shelf appears to be a stable end-configuration toward which a variety of depositional topographies tend to converge. It may form directly at the leading edge of the residual Holocene sand sheet by the detachment of shoreface-connected ridges. Inlet-associated shoals may be relatively featureless initially or may bear an intricate ridge structure controlled by their tide-dominated hydraulic regimes. However, on abandonment by the shoreline, old ridges are rotated to conform to the coast-parallel storm currents and new ones are incised. Helical flow in these channels causes ridge crests to build to heights where aggradation is balanced by wave erosion, hence the process is constructional as well as erosional. Cape-associated shoals are progressively segmented into arcuate ridges separated by deep spillways. The fluvial topographies on the western margins of the Block and Hudson shelf valleys have been modified by southwest-flowing currents to fit the regional pattern; southwest-trending lows have been kept open by scour and locally deepened, while lows at other angles have been smoothed or filled. Southwest-trending highs have developed sand caps.

While shelf-floor constructional elements are relict in the sense of having survived from an earlier, different environment, the term is not an entirely satisfactory descriptor. They have responded to the changes in the hydraulic regime that built them by corresponding changes in their morphology. Hence they fit the basic definition of an equilibrium system; one that, when stressed, responds in such a way as to relieve the stress. If we are to gain further insight into the nature of shelf-floor sand bodies, we must undertake to monitor this sequence of hydraulic process and substrate response along lines indicated by earlier chapters in this volume.

Thus, the central and southern Atlantic shelf is a palimpsest or overprinted surface whose two major patterns are both submarine. The earlier of the two was formed at the foot of the shore face. Even the major shelf valleys may be viewed as tracks left by retreating estuary mouths. Bruun coastal retreat seems to have planed off the subaerial surface and destroyed all but the most resistant or deeply incised landforms. Where exceptions occur and subaerial features survive, the probable paleogeography includes promontories to shield the

surviving features from wave attack, as in the case of the Long Island shelf valley.

Textural studies likewise stress the nearshore zone as the penultimate environment of modern shelf sands. Pilkey et al. (1969), after examining the carbonate fraction of Georgia bight sands, have concluded that "much of the present-day shelf sediment cover was deposited in the nearshore zone of the last transgressing sea, but the sediment was not derived from the beach environment itself, as indicated by particle roundness considerations." McKinney and Friedman (1970) note that, on the Long Island shelf, various sediment types can be recognized by grain-size criteria "mostly [relict] from the shallow . . . nearshore environments. Sediments relict [from] the beach swash zone environment, however, do not appear to be common. They apparently are destroyed by the advancing surf zone.

The stratigraphic consequence of this evolutionary course consists of a thin, discontinuous sand sheet of residual provenance, which might be said to result from "the destructional phase of shelf building." The sheet rests with marked disconformity on older Quaternary regressive deposits or, locally, remnants of Holocene lagoonal deposits (Kraft, 1971b; Swift and others, 1972; Shideler and Swift, 1972). The Holocene sand sheet is generally coarser, partly because its fines have been winnowed from it and partly because it has incorporated into its base Holocene fluvial sands which have passed through a resting stage in head-of-estuary sand bodies before emerging through the shoreface.

ACKNOWLEDGMENTS

This study was undertaken as a preliminary step in the NOAA-AOML Continental Margin Sedimentation project (COMSED). It incorporates data accumulated at Old Dominion University with the support of National Science Foundation Grants GA-13837 and GA-27305, and Coastal Engineering Research Center Contract DACW-72-69-C-0016. Some of the data was collected during Cruise E-21-71 of the Duke R.V. Eastward. The cooperative oceanographic program of Duke Marine Laboratory is supported by National Science Foundation Grant GB-17545. Some of the bathymetry presented in this paper was originally prepared by the late G. F. Jordan. The photographs of Fig. 227 and the data of Fig. 228 was collected from the Perry Submersible PC-8 under charter to the Manned Undersea Science and Technology Office of NOAA.

REFERENCES

- Allen, J. R. L. (1968). The nature and origin of bedform hierarchies. *Sedimentology* **10**, 161-182.
 Allen, P. (1964). Sedimentological models. *J. Sed. Petrol.* **34**, 289-293.
 Anonymous (1964). United States Coastal Pilot. Atlantic Coast, Cape Henry to Key West, Vol. 4, 7th Ed., Natl. Ocean Surv., National Oceanic and Atmospheric Admin., Rockville, Maryland.

- Bruun, P. (1962). Sea level rise as a cause of shore erosion. *J. Waterways and Harbors Div., Am. Soc. Civ. Eng. Proc.* **88**, 117-130.
- Bruun, P., and Gerritsen, F. (1960). "Stability of Coastal Inlets." 123 pp., North Holland Pub., Amsterdam.
- Caldwell, J. M. (1966). Coastal processes and beach erosion. *J. Soc. Civ. Eng.* **53**, 142-157.
- Coch, N. K. (1963). Post-Miocene Stratigraphy and Morphology, Inner Coastal Plain, Southeastern Virginia. *U.S. Office of Naval Research Tech. Rept.* **6**, 97 pp.
- Colquhoun, D. J. (1969). Geomorphology of the Lower Coastal Plain of South Carolina. *Div. Geol. State Devel. Board*, 36 pp.
- Curry, J. R. (1964). Transgressions and regressions. In "Papers in Marine Geology" (R. L. Miller, ed.) pp. 175-203. MacMillan, New York.
- Curry, J. R. (1969). Shore zone sand bodies: barriers, cheniers, and beach ridges. In "The New Concepts of Continental Margin Sedimentation" (D. J. Stanley, ed.), pp. JC-2-1 to JC-2-19. Am. Geol. Inst., Washington, D.C.
- Dillon, W. P. (1970). Submergence effects on a Rhode Island barrier and lagoon and inferences on migration of barriers. *J. Geol.* **78**, 94-106.
- Dolan, R. (1970). Dune reddening along the outer banks of North Carolina. *J. Sed. Petrol.* **40**, 765.
- Dolan, R., Hayden, B., Hornberger, G., Zeiman, G., and Vincent, M. (1972). "Classification of the Coastal Environments of the World, Part 1: The Americas." Washington, Office of Naval Research, 163 pp.
- Donohue, J. G., Allen, R. C., and Heezen, B. C. (1966). Sediment size distribution profile on the continental shelf off New Jersey. *Sedimentology* **7**, 155-159.
- El Ashry, M. T., and Wanless, H. R. (1968). Photo interpretation of shoreline changes between capes Hatteras and Fear (North Carolina). *Marine Geol.*, **6**, 347-379.
- Emery, K. O. (1965). Geology of the continental margin off eastern United States. In "Submarine Geology and Geophysics" (W. F. Whittard and R. Bradshaw, eds.), p. 1-20. Butterworths, London.
- Emery, K. O. (1967). Estuaries and lagoons in relationship to continental shelves. In "Estuaries" (G. H. Lauff, ed.), Washington Am. Assoc. Adv. Sci., 757 pp.
- Emery, K. O. (1968). Relict sediments on continental shelves of world. *Am. Assoc. Petrol. Geol. Bull.* **52**, 445-464.
- Ewing, J., Lepichon, X., and Ewing, M. (1963). Upper stratification of the Hudson Apron. *J. Geophys. Res.* **68**, 6303-6316.
- Fairbridge, R. W., and Newman, W. S. (1967). Post-glacial crustal subsidence of the New York area. *Zeitschrift für Geomorph.* **12**, 296-317.
- Fenneman, N. M. (1902). Development of the profile of equilibrium of the subaqueous shore terrace. *J. Geol.* **10**, 31-38.
- Fischer, A. G. (1961). Stratigraphic record of transgressing seas in the light of sedimentation on Atlantic coast of New Jersey. *Am. Assoc. Petrol. Geol. Bull.* **45**, 1656-1666.
- Fisher, J. J. (1967). "Development Pattern of Relict Beach Ridges, Outer Banks Barrier Chain, North Carolina." 250 pp. Ph.D. thesis. Univ. North Carolina (unpublished).
- Folk, R. L. (1971a). Genesis of longitudinal and Oghurd dunes elucidated by rolling upon grease. *Geol. Soc. Am. Bull.* **82**, 3461-3468.
- Folk, R. L. (1971b). Longitudinal dunes of the northwestern edge of Simpson Desert, Northern Territory, Australia. Pt. 1: Geomorphology and grain size relationships. *Sedimentology* **16**, 5-54.
- Frank, W. A., and Friedman, G. (1971). Barrier Island and migration: new evidence from New Jersey. In "Abstract Volume, Second National Coastal and Shallow Water Conference." 327 pp. University Press, Univ. Southern Calif., Los Angeles.
- Frank, W. M. (1971). Continental-Shelf Sediments off New Jersey. Ph.D. thesis, 84 pp. Rensselaer Polytech. Inst. (unpublished).

- Garrison, L. E. (1970). Development of the continental shelf south of New England. *Am. Assoc. Petroleum Geologists Bull.* **54**, 109-124.
- Garrison, L. E., and McMaster, R. L. (1966). Sediments and geomorphology of the continental shelf off southern New England. *Marine Geol.* **4**, 273-289.
- Gilbert, G. K. (1890). Lake Bonneville. *U.S. Geol. Surv. Mono.* **1**, 438 pp.
- Glennie, K. W. (1971). "Desert Sedimentary Environments." 222 pp. Amsterdam, Elsevier.
- Gulliver, F. (1899). Shoreline topography. *Am. Acad. Arts and Sciences Proc.* **34**, 151-258.
- Hails, J. R., and Hoyt, J. H. (1969). An appraisal of the evolution of the lower Atlantic coastal plain of Georgia, U.S.A. *Trans. Papers Inst. Brit. Geog.* **46**, 53-68.
- Harris, R. L. (1954). Restudy of Test-Shore Nourishment By Offshore Deposition of Sand, Long Branch, New Jersey. Beach Erosion Board Tech. Mem. **62**, 1-18.
- Harrison, W., Malloy, R. J., Rusnak, G. A., and Terasmae, J. (1965). Possible late Pleistocene uplift, Chesapeake Bay entrance. *J. Geol.* **73**, 201-229.
- Harrison, W., Norcross, J. J., Pore, N. A., and Stanley, E. M. (1967). Shelf waters off the Chesapeake Bight. *Environ. Sci. Services Administration Prof. Paper* **3**, 1-82.
- Henry, V. J., Jr., and Hoyt, J. H. (1968). Quaternary paralic shelf sediments of Georgia. *Southeastern Geol.* **9**, 195-214.
- Henry, V. J., Jr. (1971). Origin of capes and shoals along the southeastern coast of the United States: reply. *Geol. Soc. Am. Bull.* **82**, 3541-3542.
- Hopkins, E. M. (1971). Origin of capes and shoals along the southeastern coast of the United States: discussion. *Geol. Soc. Am. Bull.* **82**, 3537-3540.
- Houbolt, J. J. H. C. (1968). Recent sediments in the southern bight of the North Sea. *Geol. en Mijnbouw* **47**, 245-273.
- Hoyt, J. H., and Hails, T. R. (1967). Deposition and modification of Pleistocene shoreline sediments in coastal Georgia. *Science*, 1541-1543.
- Hoyt, J. H. (1967). Barrier Island Formation. *Geol. Soc. America Bull.* **78**, 1129-1136.
- Hoyt, J. H., and Henry, V. J., Jr. (1965). Significance of inlet sedimentation in the recognition of ancient barrier islands. pp. 190-194. In Wyoming Geol. Assoc. 19th Field Conf.
- Hoyt, J. H., and Henry, V. J., (1967). Influence of island migration on barrier-island sedimentation. *Geol. Soc. Am. Bull.* **76**, 77-86.
- Hoyt, J. H., and Henry, V. J. (1971). Origin of the capes and shoals along the southeastern coast of the United States. *Geol. Soc. Am. Bull.* **82**, 59-66.
- Ingle, J. C. (1966). "The Movement of Beach Sand." 221 pp. Elsevier, Amsterdam.
- Johnson, D. (1919) (1938, 2nd Ed.). "Shore Processes and Shoreline Development" Wiley, New York.
- Knott, S. T., and Hopkins, H. (1968). Evidence of Pleistocene events in the structure of the continental shelf off the southeastern United States. *Marine Geol.* **6**, 5-26.
- Kraft, J. C. (1971a). "A Guide to the Geology of Coastal Delaware." 220 pp. College of Marine Studies, Univ. Delaware, Newark.
- Kraft, J. C. (1971b). Sedimentary facies patterns and geologic history of a Holocene marine transgression. *Geol. Soc. Am. Bull.* **82**, 2131-2158.
- Langfelder, J., Stafford, D., and Amein, M. (1968). "A Reconnaissance of Coastal Erosion in North Carolina." 127 pp. Dept. Civ. Eng., North Carolina State Univ., Raleigh.
- Leopold, L. B., Wolman, M. G., and Miller, J. P. (1964). "Fluvial Processes in Geomorphology." 522 pp. Freeman, San Francisco.
- Ludwick, J. C. (1970). Sandwaves and tidal canals in the entrance to Chesapeake Bay. *Virginia J. Sci.* **21**, 178-184.
- Ludwick, J. C. (1972). Migration of tidal sand waves in Chesapeake Bay entrance. In "Shelf Sediment Transport: Process and Pattern" (D. J. P. Swift, D. B. Duane, and O. H. Pilkey, eds.). Dowden, Hutchinson & Ross, Stroudsburg, Pennsylvania.
- McKinney, T. F., and Friedman, G. M. (1970). Continental shelf sediments of Long Island, New York. *J. Sed. Petrol.* **40**, 213-248.

- McMaster, R. L. (1954). Petrography and genesis of New Jersey beach sands. *State of New Jersey Dept. Conservation and Econ. Devel., Geol. Surv. Bull.* **63**, 239 pp.
- McMaster, R. L., and Garrison, L. E. (1967). A submerged Holocene shoreline near Block Island, Rhode Island. *Marine Geol.* **75**, 335-340.
- Meade, R. H. (1969). Landward transport of bottom sediments in estuaries of Atlantic coastal plain. *J. Sed. Petrol.* **39**, 229-234.
- Meisburger, E. P. (1972). Geomorphology and Sediments of the Chesapeake Bay Entrance. *U.S. Army Corps of Engineers, Coastal Eng. Research Ctr., Tech. Memo* (in press).
- Merrill, A. S., Emery, K. O., and Rubin, M. (1965). Oyster shells on the Atlantic continental shelf. *Science* **147**, 395-400.
- Milliman, J. D., and Emery, K. O. (1968). Sea levels during the past 35,000 years. *Science* **162**, 1121-1123.
- Milliman, J. D., Pilkey, O. H., and Blackwelder, B. W. (1968). Carbonate sediments on the continental shelf, Cape Hatteras to Cape Romain. *Southeastern Geol.* **9**, 245-268.
- Milliman, J. D., Pilkey, O. H., and Ross, D. A. (1972). Sediments of the continental margin off the eastern United States. *Geol. Soc. Am. Bull.* **83**, 1315-1334.
- Moody, D. W. (1964). "Coastal Morphology and Processes in Relation to the Development of Submarine Sand Ridges off Bethany Beach, Delaware." Ph.D. thesis, 167 pp. Johns Hopkins Univ., Baltimore (unpublished.)
- Murray, S. P. (1970). Bottom currents near coast during Hurricane Camille. *J. Geophys. Res.* **75**, 4579-4582.
- Newman, W. S., and Munsart, C. A. (1968). Holocene geology of the Wachapreague Lagoon, eastern shore peninsula, Virginia. *Marine Geol.* **6**, 81-105.
- Oaks, R. Q., Jr. (1964). Post-Miocene stratigraphy and morphology, outer coastal plain, Southeastern Virginia. *Office of Naval Research, Tech. Rept.* **5**, 240 pp.
- Oertel, G. F., and Howard, J. D. (1972). Water circulation and sedimentation at estuary entrances on the Georgia coast. In "Shelf Sediment Transport: Process and Pattern" (D. J. P. Swift, D. B. Duane, and O. H. Pilkey, eds.). Dowden, Hutchinson & Ross, Stroudsburg, Pennsylvania.
- Osmond, J. K., May, J. P., and Tanner, W. F. (1970). Age of the Cape Kennedy barrier-and-lagoon complex. *J. Geophys. Res.* **75**, 469-479.
- Payne, L. H. (1970). "Sediments and Morphology of the Continental Shelf off Southeast Virginia." Ph.D. thesis, 70 pp. Columbia Univ., New York (unpublished).
- Pevear, D. R., and Pilkey, O. H. (1966). Phosphorite in Georgia continental shelf sediments. *Geol. Soc. Am. Bull.* **73**, 365-374.
- Pierce, J. W., and Colquhoun, D. J. (1970). Holocene Evolution of a portion of the North Carolina Coast. *Geol. Soc. America Bull.* **81**, 3697-3714.
- Pilkey, O. H., and Field, M. E. (1972). Onshore transportation of continental shelf sediment: Atlantic southeastern United States. In "Shelf Sediment Transport: Process and Pattern" (D. J. P. Swift, D. B. Duane, and O. H. Pilkey, eds.). Dowden, Hutchinson & Ross, Stroudsburg, Pennsylvania.
- Pilkey, O. H., and Frankenberg, J. (1940). The relict-recent sediment boundary on the Georgia continental shelf. *Georgia Acad. Sci. Bull.* **27**, 37-40.
- Pilkey, O. H., and Giles, R. T. (1965). Bottom topography of the Georgia continental shelf. *Southeastern Geol.* **7**, 15-18.
- Roberts, W. P., and Pierce, J. W. (1967). Outcrop of the Yorktown Formation (Upper Miocene) in Oslow Bay, North Carolina. *Southeastern Geology* **8**, 131-138.
- Scheidegger, A. E. (1970). "Theoretical Geomorphology," 2nd Ed. 435 pp. Springer Verlag, New York.
- Schopf, T. J. M. (1968). Atlantic continental slope and shelf of the United States—Nineteenth Century exploration. *U.S. Geol. Surv. Prof. Paper* **529-F**, 12 pp.

- Schwartz, M. L. (1965). Laboratory study of sea level rise as a cause of shore erosion. *J. Geol.* **73**, 528-534.
- Schwartz, M. L. (1967). The Bruun theory of sea level rise as a cause of shore erosion. *J. Geol.* **75**, 76-92.
- Schwartz, M. L. (1968). The scale of shore erosion. *J. Geol.* **76**, 508-517.
- Scruton, P. C. (1960). Delta building and the deltaic sequence. In "Recent Sediments, Northwest Gulf of Mexico" (F. P. Shepard and F. B. Phleger, eds.), pp. 82-102.
- Shepard, F. P. (1963). "Submarine Geology." 557 pp. Harper and Row, New York.
- Shepard, F. P., and Wanless, H. R. (1971). "Our Changing Coastlines." 579 pp. McGraw-Hill, New York.
- Shideler, G. L., and Swift, D. J. P. (1972). Seismic reconnaissance of Quaternary deposits of the Middle Atlantic continental shelf—Cape Henry, Virginia, to Cape Hatteras, North Carolina. *Marine Geol.* **12**, 165-185.
- Shideler, G. L., Swift, D. J. P., Johnson, G. H., and Holliday, B. W. (1972). Late Quaternary stratigraphy of the inner Virginia continental shelf: A proposed standard section. *Geol. Soc. Am. Bull.* (in press).
- Sloss, L. L. (1962). Stratigraphic models in exploration. *J. Sed. Petrol.*, **32**, 415-422.
- Smith, J. D. (1969). Geomorphology of a sand ridge. *J. Geol.* **77**, 39-55.
- Stanley, D. J., Fenner, P., and Kelling, G. (1972). Currents and sediment transport at the Wilmington Canyon shelfbreak, as observed by underwater television. In "Shelf Sediment Transport: Process and Pattern" (D. J. P. Swift, D. B. Duane, and O. H. Pilkey, eds.). Dowden, Hutchinson & Ross, Stroudsburg, Pennsylvania.
- Stanley, D. J., and Kelling, G. (1968). Sedimentation patterns in the Wilmington submarine canyon area. In "Transactions of the National Symposium on Oceanic and Sciences and Engineering of the Atlantic Shelf" (A. E. Margulies and R. C. Steere, eds.) 366 pp.
- Stearns, F. (1967). "Bathymetric Maps of the New York Bight, Atlantic Continental Shelf of the United States, Scale 1:125,000." National Ocean Surv., National Oceanic and Atmospheric Admin., Rockville, Md.
- Stefansson, V., Atkinson, L. P., and Bumpus, D. F. (1971). Hydrographic properties and circulation of the North Carolina shelf and slope waters. *Deep-Sea Res.* **18**, 383-420.
- Swift, D. J. P. (1968). Coastal erosion and transgressive stratigraphy. *J. Geol.* **76**, 444-456.
- Swift, D. J. P. (1970). Quaternary shelves and the return to grade. *Marine Geol.* **8**, 5-30.
- Swift, D. J. P., and Heron, S. D., Jr. (1969). Stratigraphy of the Carolina Cretaceous. *Southeastern Geol.* **10**, 201-245.
- Swift, D. J. P., Dill, C. E., Jr., and McHone, J. (1971b). Hydraulic fractionation of heavy mineral suites on an onconsolidated retreating coast. *J. Sed. Petrol.* **41**, 683-690.
- Swift, D. J. P., Holliday, B. W., Avignone, N. F., and Shideler, G. L. (1972). Anatomy of a shore-face ridge system, False Cape, Virginia. *Marine Geol.* **12**, 59-84.
- Swift, D. J. P., Sanford, R. B., Dill, C. E., Jr., and Avignone, N. F. (1971a). Textural differentiation on the shore face during erosional retreat of an unconsolidated coast, Cape Henry to Cape Hatteras, western North Atlantic shelf. *Sedimentology* **16**, 221-250.
- Tanner, W. F. (1960). Expanding shoals in areas of wave refraction. *Science* **132**, 1012-1013.
- Tanner, W. F. (1961). Offshore shoals in an area of energy deficit. *J. Sed. Petrol.* **31**, 87-95.
- U.S. Army Corps of Engineers (1955). New York District. Atlantic Coast of Long Island, New York, "Fire Island Inlet and Shore Westerly to Jones Inlet." Beach Erosion Control Rept. on Cooperative Study. 16 pp. (unpublished).
- Uchupi, E. (1965). "Map Showing Relation of Land and Submarine Topography Nova Scotia to Florida." U.S. Geol. Surv., miscellaneous geological investigations map 1-451.
- Uchupi, E. (1968). "Atlantic Continental Shelf and Slope of the United States—Physiography." U.S. Geol. Surv. Prof. Paper 529-C, 30 pp.
- Uchupi, E. (1970). "Atlantic Continental Shelf and Slope of the United States—Shallow Structure."

- U.S. Geol. Surv. Prof. Paper 529-1, 44 pp.
- Veatch, A. C., and Smith, P. A. (1939). "Atlantic Submarine Valleys of the United States, and the Congo Submarine Valley." Geol. Soc. Am. Spec. Paper 7, 101 pp.
- Weigel, R. L. (1964). "Oceanographical Engineering." 532 pp. Prentice Hall, Englewood Cliffs, New Jersey.
- Weinman, Z. H. (1971). Analysis of littoral transport by wave energy: Cape Henry, Virginia to the Virginia, North Carolina Border. Masters thesis, Old Dominion University, Norfolk, Virginia (unpublished).
- Wicker, C. F. (1951). History of New Jersey coastline. Berkeley, Calif., *Proc. First Conf. Coastal Eng.* pp. 299-319.
- Widmer, K. (1964). "The Geology and Geography of New Jersey." 193 pp. Van Nostrand, New York.

A HARD LOOK AT OCEANS FROM SPACE

John R. Apel, Ph.D.

Atlantic Oceanographic & Meteorological Laboratories
Environmental Research Laboratories

National Oceanic and Atmospheric Administration
15 Rickenbacker Causeway, Virginia Key
Miami, Florida 33149

ABSTRACT

A critical assessment is made of the problem of observing the oceans from spacecraft. Estimates are given of the directions that a satellite oceanography program might take during the next decade. Using both active and passive sensors in the visible, near- and thermal-infrared, and microwave frequency regions, it appears possible to determine several geophysical and biological variables of interest; these include the marine geoid, sea surface temperature, currents, wave heights and spectra, winds, storm surges, tsunamis, tides, ice, chlorophyll concentrations, red tides, sediment transport, and shallow bathymetric features. There are large benefits to marine and coastal interests and to weather forecasting from such information.

I. Introduction

The exhilarating photographs of oceans and estuaries taken during the Gemini and Apollo flights have demonstrated that interesting oceanographic information can be obtained from visible imagery taken from spacecraft. It has been an open question, however, as to whether this information was sufficiently quantitative to warrant anything like an oceanographic satellite based on optical images alone.

As sensor development has proceeded and as the classes of instruments available have expanded from passive visible and infrared devices into the active microwave and laser regimes, it has become apparent that considerably more than simple blue-green gradations in the color of sea water can be determined. In fact, the list of ocean parameters potentially observable via remote sensing has lengthened to respectable proportions as the level of instrument sophistication has grown. The implications which these data have on the problems of long-term weather forecasting, location of fisheries, marine hazard warning, ship routing, and oceanographic and meteorological research are large indeed. This paper will attempt to briefly assess the categories of oceanographic measurements or observables that may be determined from space, the types of sensors useful for making those observations, and the benefits that might accrue to both science and society from a satellite that would do for the oceans what the NIMBUS and theITOS/NOAAseries have done for the atmosphere. The assessment will prove to be much to the positive. The

time appears propitious, then, to call for the development of a dedicated oceanographic satellite system, similar in spirit to those generated for meteorological, earth resources, and extraterrestrial observations, but optimized for viewing the oceans--the fourth member of the ancient elemental quartet of air, earth, fire, and water.

II. Two-Dimensional Oceanography

By and large, satellite oceanography is confined to surface and near-surface phenomena. This constraint is not as severe as it appears at first glance, because surface data taken from spacecraft can be appended with other, conventionally-derived subsurface measurements of certain parameters (say, vertical current or temperature profiles) in order to construct a more nearly three-dimensional view of the ocean. In addition, near-surface data are useful in their own right, since the coupled, nonlinear interaction between ocean and atmosphere largely takes place in the few tens of meters above and below the sea-air interface; man's marine activities are mostly limited to that surface as well, so the kind of two-dimensional oceanography one can pursue from spacecraft is highly relevant.

The problems that may be so addressed group themselves into those relating to: (a) visible images and ocean color; (b) ocean brightness temperature; (c) sea surface topography; and (d) surface or subsurface data collection and relay. It is chiefly the physical state of the ocean surface that appears amenable to such measurement-at-a-distance, although one may also derive some biological, chemical, and atmospheric information, especially from *in situ* sensors that relay their data through satellite telemetry channels.

A. Visible Imagery and Ocean Color

Following the visible and IR color photography taken during the manned space flights have been multispectral images obtained from the ERTS-1 satellite; these have shown a surprising amount of ocean detail, especially when one considers the fact that the ERTS sensors were optimized for terrestrial, not oceanic targets. Figure 1 shows a 180 x 180 km² scene of the New York Bight taken in the light of 600-700 nm solar illumination at about 10:30 a.m. on August 16, 1972. The picture has been exposed to bring out oceanographic features, the most obvious of which are the two U-shaped objects some

15-20 miles southeast of New York City. These are ascribed to (legal) acid waste dumping events occurring eight and 20 hours before the overflight. Just north of these is a more obscure sewage sludge dump. In the southeast corner, a train of long-length gravity waves, either surface or internal, is incident upon the continental shelf and may be seen advancing in the deeper water over the submerged Hudson Valley at a larger phase velocity than in the more shallow regions surrounding that ancient depression. Sediment plumes from the Hudson River and from Barnegat Bay are also to be seen, even though the tide was coming in. Barely visible in the half-tone reproduction here is a water mass discontinuity running south from Fire Island and associated with the 20°C surface isotherm, and other, more subtle and yet-to-be identified features extending off the Long Island coast.



FIG. 1 ERTS-1 image of New York Bight. Waste dumping, sediments, waves are visible.

In interpreting these features, their variations in the four spectral channels are highly useful; not only does the ocean surface reflectivity differ at different wavelengths, but more importantly, the depth to which one sees into the water varies greatly as well. Atmospheric contributions may also be partially sorted out using several spectral images.

The approach to identifying the nature of objects in an ocean scene is obviously a multispectral one, then, and relies on determining the departure of the water mass from its pristine color state. The color of the ocean is chiefly determined by organic and inorganic particulates of natural and man-made origin; by light reflected from the bottom; by ice, foam, and spray; and by surface illumination conditions. A deep, ultramarine blue is characteristic of sterile, clean, open ocean, while increasing amounts of chlorophyll-

bearing plankton add to the green-yellow and red portions of the spectrum. Sediments tend to be brownish, with little spectrally-differentiated character. The presence of white bottom lightens the general tone of a region with some spectral shift, while vegetation darkens it. Ice is obviously white. As the sun angle and cloud cover vary, surface illumination ranges over all allowable conditions. The appearance of sun glitter in a scene renders that part which images the solar disc useless for water color measurement, although the same scene may be analyzed for surface wind speeds by a combination of photometric brightness and diffuseness of the sun's image there.

These are qualitative statements, however, more appropriate to the marine painter than to the oceanographer. Quantitatively, for example, it appears possible to measure concentration of chlorophyll in approximately one optical absorption depth to better than a factor of two over the interesting range of 0.1 - 10 $\mu\text{g/l}$, using a radiometrically-calibrated multispectral sensor that is corrected for atmospheric effects. This measurement is of great utility in locating fisheries, in biomass assay, and in mapping both sterile western boundary currents such as the Gulf stream, and near-shore circulations, which carry plankton and sediment entrained in them.

The measurement of sediment is less well understood; preliminary USGS estimates from ERTS-1 images over Tampa Bay suggest some quantitative determination of sediment load is possible with multispectral images, provided the general nature of the sediment is known in advance. These data are of importance in studies of estuarine circulation, river plumes, beach erosion, and in littoral (along shore) transport, dredging operations, and formation of shoals and banks.

Ice is obvious enough at visible wavelengths, although from space, distinguishing it from snow is sometimes difficult. Ice assay is of concern to shipping, especially in regions such as the Great Lakes, where operations are conducted as late into the autumn as possible. In another discipline, the weather in polar regions is critically dependent upon the percentage of open water there, because the large difference in the thermal conductivities of ice and water determines the exchange rate of heat between sea and air.

Pollutants have been detected from space, both in estuaries and in the open oceans. It is too soon to attach numerical values to the observable pollutant concentrations, but where the geometric pattern allows an unambiguous identification of the dumping event (such as in Fig. 1, above) some estimates of surface concentrations may ultimately be made; more important, the mixing and dilution rates can probably be estimated by a sequence of images made over several days. Large oil slicks may be

detected, especially under conditions of low illumination angle and dual-polarization viewing.

Shallow water bathymetry is possible in clear water, and semiquantitative values of water depth can probably be obtained down to perhaps 20 m depth in low turbidity regions. More significantly, one may determine the geometric shape of shoals and their variations due to storms and currents; even the discovery of uncharted shoals or the positioning of poorly-located ones is possible.

The discussion so far has shown much useful data on ocean surface and near-surface conditions can be obtained when relatively cloud-free viewing exists. Even in persistently cloudy areas, however, some information can be retrieved by using the device of accumulating, over several days, minimum daily brightness values for a given small geographical area. Such selective techniques have the effect of viewing only when clouds or fog are present in a resolution element in least amount. Since many ocean parameters such as color or temperature change rather slowly, a somewhat blurred but often usable picture of the parameter is obtained. The technique fails, however, in consistently cloudy areas or in the coastal zone, where near-daily information is required.

An ocean color sensor optimized for visible and near-IR images might thus have the following characteristics: A radiometrically-calibrated, multispectral scanner with six to ten spectral channels ranging from about 450 to perhaps 3000 nm wavelength, with an instantaneous field of view of order 1-2 km--perhaps smaller for coastal zone work. A sun-synchronous orbit with about 10:00 a.m. equatorial crossing will allow viewing at nearly constant illumination angle, free of sun glint and with minimal interference from morning fog and convective cloud buildup. The swath width could be about five times as large as that from ERTS-1 while maintaining the same instrumental data rate of about 15 megabits/sec.

Deciphering an array of multispectral images for the information they contain on these variables must obviously be accompanied by a large surface truth effort used in conjunction with quantitative models of the optical/infrared transfer function of both the ocean and the atmosphere. Considerable effort has already gone into atmospheric models and an analogous program, both observational and theoretical, is needed for the sea.

B. Sea Surface Temperature

Spacecraft measurements of ocean surface brightness temperatures with a precision of a very few kelvins have been made using infrared radiometers operating in the 10-12 μm atmospheric window. Since the

emissivity of sea water at these wavelengths is essentially unity, the brightness temperature is approximately the same as the molecular temperature of a thin surface layer of the ocean. With the high resolution (1.0 - 2.5 km) infrared radiometers on the NOAA-1 and -2 meteorological satellites, for example, it is possible to derive sea surface temperatures over limited geographical regions with an rms error of 1-2 K, a useful precision.

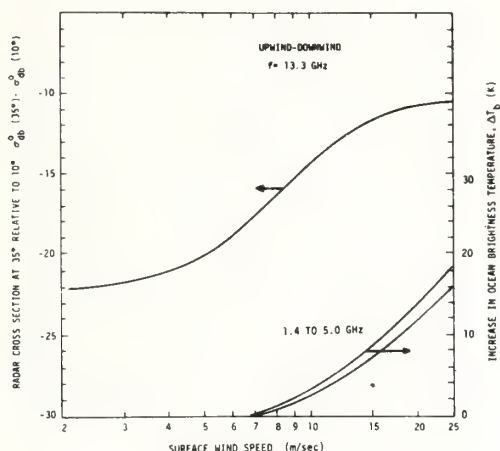


FIG. 2 NOAA-1 thermal IR image of Gulf Stream

Figure 2 is an image of the U.S. east coast and environs, taken on a clear February night in the light of thermal radiation at about 10-12 μm . The Gulf Stream and its meanders are clearly visible, as is a portion of the Gulf of Mexico Loop Current northeast of the Yucatan peninsula. Cold upwellings can also be seen at these wavelengths. Temperature data may thus be composited and published as facsimile maps at five- to seven-day intervals, for use by ships and fishing vessels. Such data are invaluable not only for location of fisheries but for weather forecasting, for location of currents, and for estimating the reservoir of potential energy in the upper mixed layer of the ocean that is available for hurricane intensification.

With less success, microwave brightness temperatures have been determined from aircraft with microwave radiometers, but improvements are forthcoming in the latter instruments which may reduce the errors to several kelvins. At microwave frequencies, the emissivity of ocean water is a sensitive function of frequency, nadir angle, polarization, thermodynamic temperature, salinity, surface roughness, and foam cover; brightness temperatures must therefore be augmented with other environmental para-

meters and with atmospheric data in order to deduce molecular temperatures. It presently appears possible to obtain the required parameters using a multi-frequency, dual-polarization microwave radiometer in conjunction with the other sensors described both above and below. In particular, it may be feasible to determine, even through moderate cloud cover or light rainfall, both molecular temperatures and surface winds; the indicated primary frequency for the radiometer is near 5 GHz. A graph estimating the dependence of ocean brightness temperature on surface wind speed and foam is given on Fig. 3.



Radar cross section of ocean at 35° relative to that at 10°, versus surface wind speed
Increase in ocean microwave brightness temperature due to wind and foam

FIG. 3 Estimated wind speed capabilities of microwave scatterometer and radiometer.

These preliminary data indicate an increased brightness with the onset of whitecapping, which very likely continues on up to speeds approaching hurricane force. Further aircraft flights into storms will be required to refine the estimates.

Measurements of ice cover through clouds is also possible with an imaging microwave radiometer operating near 35 GHz, although the somewhat coarse resolution element of the device (necessitated by the realities of spacecraft antenna sizes) will preclude seeing rifts and cracks smaller than the instantaneous field of view; this may fall between one and 50 km, depending on antenna and frequency.

C. Sea Surface Topography

The ocean surface possesses a variety of topographic features extending over a

wide range of horizontal and vertical scales and varying in both time and space. These undulations arise chiefly from geoidal features, seismic events, geostrophic currents, and atmospheric forcing. The identifiable undulations of natural origin are listed below in approximate order of increasing horizontal dimension, along with their typical vertical scales.

Table 1 Surface Topographic Features

Wind-generated capillary waves (1/10-1 cm)
Wind-generated gravity waves (1-20m)
Slopes due to geostrophic currents (50 cm)
Storm surges (4 m)
Tsunamis (50 cm)
Inverse barometer effect (25 cm)
Wind set-up against shorelines (1 m)
Earth and ocean tides (1 m)
Departures of the marine geoid from the reference ellipsoid (50 m)

Thus a scheme for measuring the horizontal and vertical topographic components of the sea surface would allow observations of important ocean characteristics. There are at least four instruments which at present appear able to make some or other of these measurements; a microwave scatterometer; a bistatic transmitter/receiver; a short-pulse, high precision altimeter; and a coherent imaging radar.

1. Scatterometer

The scatterometer illuminates the sea surface at various angles from nadir and then measures the microwave energy scattered back into the antenna. Energy is preferentially returned from those components of the surface wave spectrum satisfying the Bragg scattering condition, which, for X-band microwave frequencies, are mostly capillary waves; these are coupled to the instantaneous local wind and are essentially independent of the large gravity waves making up the observable sea state. The backscatter also is weakly dependent on the angle between the plane of the beam sweep and the wind direction; this latter can be estimated from ordinary surface pressure charts with sufficient accuracy. Figure 3 also shows a smoothed and normalized functional dependence of the 13 GHz radar cross-section on surface wind speed. Considerations of differential sensitivity and cross-section errors indicate that the scatterometer may be used as an anemometer for wind speeds from near zero to some 15-20 m/sec, with little regard for sea state; the device thus complements the higher-wind anemometric capabilities of the microwave radiometer mentioned previously. It, too, is capable of functioning through clouds and light rain. The scatterometers to be flown on SKYLAB and under the NASA AAFE program should clarify the capability.

2. Bistatic Transmitter-Receiver

The bistatic arrangement uses a ship or buoy equipped with a MF/HF transmitter and

a satellite as a receiver in order to measure the ocean wave spectrum, including the significant wave height. Pulsed radio waves are Bragg-scattered from ocean waves in an elliptical annulus of order 200 km major radius surrounding the buoy, and are received at the satellite along with the directly-transmitted signal. The wave spectrum is then deduced from the Doppler spectrum of the received signals; thus more detail than rms wave height is available from limited regions of the ocean wherever one can position a transmitting platform. The range of the scheme is limited by the necessity for assuming a homogeneous wave field over that range.

3. Short-pulse Radar Altimeter

The short-pulse radar altimeter has two distinct functions: determination of the large-scale roughness of the sea surface, and measurement of the vertical distance between the satellite and that surface. The short pulse feature is required for both functions.

As an example of the roughness measurement, if a radar pulse whose duration is of the order three nanoseconds in time (and hence 50-cm vertical extent in space) is used to illuminate an ocean whose significant wave height exceeds approximately 1/2 meter, the reflected pulse will be broadened by the distribution of reflecting heights presented by the waves. By averaging a few thousand such pulses and measuring the temporal broadening, one may determine the average wave height, i.e., sea state and swell, over the footprint. For typical satellite altitudes of 1000 km and radar beam widths of 1° , the radar footprint diameter on the surface is of order 15 km; an averaging time of 1 sec results in motion of the footprint due to the satellite velocity by one-half of its diameter. Except near the eye of a hurricane, an oceanic wave field is essentially homogeneous over 15 km. Thus sea state and swell can be continuously determined along a 15 km swath spanning the suborbital point, independently of clouds or rainfall. It should be noted that this measurement and the surface wind determination are not redundant, in that while surface wind obviously causes the waves, the resultant wave field is nonlocal in space and time. This means that the wave height at a point depends upon the entire history (duration) and spatial extent (fetch and uniformity) of the wind and not just on its speed and direction at that point. With both wind and waves measured over some region, numerical models of wave propagation can then be used to extrapolate away from and interpolate between satellite orbits. When combined with other data gathered by conventional means, these spacecraft-derived measurements form the basis of a world-wide wind and wave forecast service, disseminated through facsimile maps and radio alerts, and of considerable practical importance. Since much of the world's weather is manufac-

tured over the open oceans, weather forecasting will be enhanced. The time saved by routing ships around storms, by reduction in cargo damage and insurance rates, and by more precise scheduling of ship arrival times are valuable benefits not only to ship owners but to consumers. There are obvious benefits to smaller craft owners and to the ever-enlarging fraction of the population living along the nation's sea coasts as well.

The altitude-measuring function of the altimeter addresses many of the larger scale topographic features on the list above. Measurement of any of these depends upon: (a) very precise orbit determinations relative to the center of the earth (rms errors less than 10-15 cm over ocean-sized arcs); (b) construction of a very precise marine geoid--defined as the surface assumed by a motionless ocean--again to 10-15 cm for all geoidal features of horizontal scale greater than some 10 km; and (c) equally precise measurements of the distance between orbit and sea level, using the altimeter. By differencing the orbit height and the sum of geoid plus altitude heights, one obtains a residual which gives the departure of the dynamic sea surface from the geoid. These elevations may be quantitatively related to the oceanic phenomena listed above. A 1969 NASA-sponsored summer study in earth and ocean physics developed this theme and its importance to geophysics in some detail, and its implementation has been considered by NASA in a forthcoming report on an earth and ocean physics applications program.

Some explanation is in order for the remaining entries on Table I. As regards currents: a moving fluid on a rotating earth develops the horizontal pressure gradient required to balance the horizontal component of Coriolis force, through tilting its surface (relative to the geoid) in an amount proportional to its velocity; this is termed geostrophic flow. Thus such surface slopes measure surface current velocities. Figure 4 shows the calculated, long-time mean surface topography of the western North Atlantic, with elevations above and below mean sea level given in centimeters. The time-averaged Gulf Stream is clearly visible; its instantaneous position may depart from the mean by amounts approaching 100 km, however. Since these departures or meanders occur slowly (5-40 day periods) compared to the times required to map the area with a satellite (a few days), it is felt that not only the mean positions but the important time variations on the major current systems of the world may be determined using altimetry in conjunction with visible and infrared imagery. (This scheme obviously fails in both equatorial and ice-bound ocean regions, however.) Present estimates give roughly 20 cm/sec as the minimum surface speed discernable using satellite altimetry--approximately 10% of the Gulf Stream maximum, for example--and perhaps a few kilometers as the time-averaged

error in the position of the current, using imagery. (There is a genuine synergistic effect that accrues from having several sensors of different types on one spacecraft, e.g., measurement of current speed via altimetry and position via imagery.)

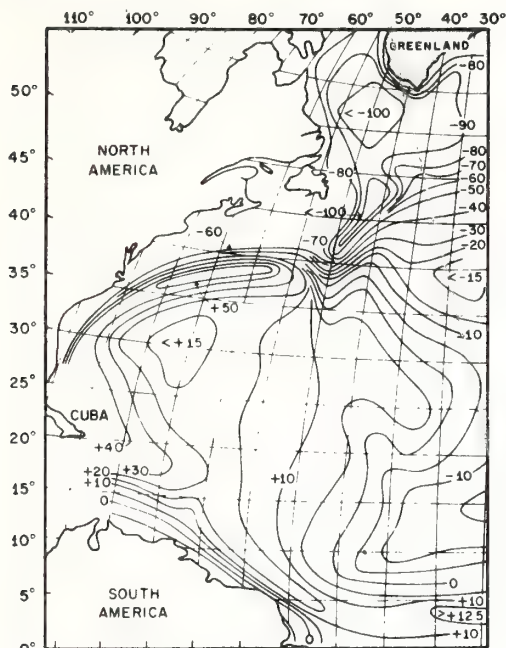


FIG. 4 Calculated topography from geostrophic currents (Defant).

Again, a current monitoring and predictive service can be rendered to marine and weather interests, based on both satellite and surface data. Facsimile maps can be transmitted even to relatively small commercial fishing vessels, who then exploit their knowledge of currents and temperatures in taking fish. Weather services are improved through information on heat transport by boundary currents. Minimum-time ship routing is also enhanced; for example, tankers plying between Arabian oil ports and North American refineries experience variations of several days in their transit times, chiefly due to the Somali-Agulhaus current systems off the African east coast. These currents are driven by the Indian Ocean monsoon, which reverses direction every six months; the current response is dramatic but only poorly known. Even the position of the Gulf Stream, the best-studied of all major currents, is not yet predictable in any useful sense but would become so with a combined satellite-surface based ocean monitoring and prediction program.

Returning to Table I: storm surges develop as an intense wind system approaches land; hurricane Camille in 1969 generated a 9 m surge on the Texas coast, for

example. The surge is usually confined to several hours' time and several tens of kilometers along a coast. Tsunamis are more rare but of greater extent; their amplitudes in mid-ocean have never been measured but theoretically should be of order 1/2 m. Both surges and tsunamis must be considered targets of opportunity for altimetric determination, and their observation as serendipitous events. While a warning system cannot at present be predicated on the basis of satellite systems alone, any data so gleaned would be highly valuable for better understanding of the phenomena.

The inverse barometer effect is due to atmospheric loading on the surface of the ocean and should probably be considered as a correction to be applied to altimeter measurements rather than the converse, a surface barometer. Wind set-up is the piling-up of water near the coasts due to long-term atmospheric stress such as trade winds, and is approximately calculable as a correction factor to the altimeter measurement.

Earth and ocean tides, being driven by astronomical forces at well-defined frequencies, can be extracted from satellite altimetry by narrow-band numerical filtering of the data. For example, a one-meter mid-ocean tide can be estimated from approximately 80 measurements to within about 15%, in the presence of an overall orbit, geoid, and altitude noise level of one meter. This is typical of one year's worth of data gathered over one square degree of surface at mid-latitudes.

Finally, the marine geoid, which is an object of interest in its own right, must be determined in considerable detail before any real confidence can be had in ocean dynamical effects determined through altimetry. Separating the stationary geoid from the time-varying ocean is one technique that can be used; another is correlation of local geoidal features with local sea floor topography and gravity measurements. The separation process will undoubtedly require several years of data and several iterations, but present estimates have it as a feasible task.

4. Coherent Imaging Radar

The coherent imaging radar is probably the microwave instrument having the greatest potential for ocean observations, although an accurate assessment of its capabilities is not yet available. At off-nadir angles, it images the surface of the sea and shows wave-trains and ship wakes in addition to land masses (Fig. 5). It also has a scatterometric mode that functions much as the pure scatterometer described in Section C-1. In addition, at the nadir angle it possesses an altimetric mode whose altitude precision is of order one-half a radar wavelength, or 10 cm; and perhaps a mode that displays the ocean wave spectrum directly.

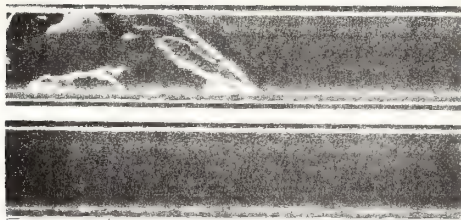


FIG. 5 Images of ocean waves off Kayak Island, Alaska from JPL 25 cm coherent imaging radar. Dimensions: width, 6-8km; length of each strip about 25 km.

In a satellite application, the estimated coherence time for surface gravity waves implies that a minimum resolution element of about 30 m is possible at 1.5GHz, independent of satellite altitude. A low-gain, crudely stabilized antenna is needed; power requirements are of order 30 W. The data rate is near 10Mb/sec for a 200 x 200 km² scene, approximately the same as for the ERTS multispectral scanner; in the spacecraft configuration, most of the data processing takes place on the ground. Assuming the radar lives up to its promise, one could replace all the microwave systems described above, except for the multi-frequency radiometer, by a single instrument that measures surface wind, sea state and wave spectrum, and satellite altitude; an image of the sea, of ice, or the land would be provided as well. Once again it functions through clouds and rainfall. Aircraft missions are currently planned that should delineate some of these claims.

D. Data Relay and Collection

There are several present and planned satellite systems having a data collection and relay capability. Surface data gathered from ships, aircraft, and buoys can be relayed to collection points through these. For purposes of a dedicated oceanographic satellite program, however, several thousand additional channels on the spacecraft would be needed because certain information on effects such as wind velocity, sea state, and tsunamis is highly perishable; hence these data must be handled expeditiously. Programs such as the National Data Buoy Project must be integrated with the satellite system. A central location is envisaged for processing the data, similar to the NOAA National Meteorological Center. Such a center, being the major consumer of the data, can efficiently handle surface-derived information relayed through the satellite as well as remotely-sensed data, and amalgamate them into both synoptic and world-wide overviews of the oceans.

III. Summary of Sensors and Observables

A summary of oceanic candidate sensors and parameters is contained on Table II. Some observables may be viewed by two or more sensors, which are ordered in terms of their general ability in this regard by Primary (P), Secondary (S), and Tertiary (T) labels. In several cases, these capabilities are estimated from preliminary data only, and further investigation will be required; in others, chiefly the visible and infrared imaging radiometers, the instrument capabilities are reasonably well known.

It is clear from the table that techniques now exist for monitoring a wide class of oceanic features from satellites; some observations would be sufficiently quantitative to be graced with the name "measurement". It is also clear that considerable effort would have to be put into data transmission and manipulation, into interpreting that data in geophysical terms, and into disseminating the distilled information to the user in timely fashion. However, much relevant experience has been accumulated in both the meteorological and earth resources programs, and the information flow problem appears solvable with reasonable resources.

IV. Benefits

The benefits to be derived from an oceanographic satellite are many-faceted; several have been touched upon earlier. Some carry large dollar value, while others serve to enhance the general welfare.

A. Improved Weather and Hazard Forecasting

The combination of meteorological and oceanographic satellites should go a long way toward achieving the one-to-two week forecast that appears possible with an adequate, synoptic data base; the remaining observational elements such as buoys and shore-base remote sensors either are or can be assembled. The cost benefits of an improved weather forecast are enormous and have been documented elsewhere. With the increase in the numbers of people living along the coasts, the potential for loss of life and property has been magnified greatly. In many low-lying areas along the East and Gulf Coasts, earlier warning of severe hurricanes is absolutely essential to evacuate the population in time. Ocean-wide observations of surface temperature, wind and sea state, and understanding of the storm surge process will constitute a large step forward in achieving the required warning.

Warning of potential tsunamis based on earthquake monitoring has been reasonably successful, but the problem of over-warning remains. A means of determining the energy content of a tsunami is needed, so as to estimate its capacity for damage. A satellite system will make important

SENSORS OBSERVABLES		TABLE II SUMMARY OF SENSORS AND OBSERVABLES					
		IMAGING RADIOMETERS		SCATTEROMETER	BISTATIC TRANSMITTER	SHORT PULSE ALTIMETER	IMAGING RADAR
		Visible	Thermal IR	Microwave			
Chlorophyll and Red Tides	P	-	-	-	-	-	-
Current Position	S	P	T	-	-	P	P
Current Velocity	-	-	-	-	-	P	P
Estuarine Circulation	P	P	-	-	-	-	-
Fishery Identification	P	P	T	-	-	T	T
Fog	P	S	-	-	-	-	-
Icebergs	P	-	-	-	-	-	P
Ice Cover	P	S	P	-	-	T	P
Marine Geoid	-	-	-	-	-	P	P
Pollutant Identification	P	-	-	-	-	-	-
Salinity	-	-	T	-	-	-	-
Sea State & Swell	T	-	T	-	P	P	P
Sediment Transport	P	-	-	-	-	-	-
Set-up	-	-	-	-	-	P	P
Shallow Water Bathymetry	P	-	-	-	-	-	-
Storm Surges	T	-	-	-	-	P	P
Surface Winds	-	-	P	P	S	S	S
Temperature	-	P	S	-	-	-	-
Tides	-	-	-	-	-	P	P
Tsunamis	-	-	-	-	-	P	P
Upwellings	S	P	S	-	-	-	-
Wave Spectrum	-	-	-	T	P	T	S

contributions toward understanding this phenomenon.

B. Ship Route Forecasting

There is increasing economic and environmental value to optimum ship routing based on sea state and current forecasts. Some 12 to 24 hours' reduction in transit time may be achieved on transoceanic voyages simply by avoiding areas of high sea state. The total savings for world-wide shipping from minimum time routing should approach nine-figure numbers of dollars per year.

C. Fisheries Assessment and Management

Location of fisheries from a knowledge of currents and chlorophyll distributions and from location of upwellings will enhance the open-ocean fish take considerably. A knowledge of the general physical state of the oceans is indispensable to a rational living resources assessment and management program.

D. Beach Erosion, Sedimentation, Bathymetry, and Ice Reconnaissance

The assessment of the effects of storms on coastal properties, and formulation of strategies for placing jetties, channels, and restoration of beaches should be simplified by the large-scale data available from an oceanographic satellite. Monitoring of the conditions and flows in bays and estuaries will also be possible, and from this, rationales may be developed for using these bodies of water in the manifold

of ways required by a high population density. Shoals and shallows may be positioned more accurately. Ice surveys in the oceanic polar regions and lakes will also be made possible by the imaging instruments on the satellite.

E. Research in Oceanography and Meteorology

The global and synoptic views of the oceans and their biological and physical characteristics that will be gained from an oceanographic satellite will be of much value in research. Oceanographers have never been able to gain the necessary overview of their domain required to understand global circulation or large scale processes. A satellite promises this vantage point, as regards those surface oceanographic and meteorological features discussed above, and perhaps other, unsuspected ones as well. It is only through such research that the applied knowledge needed for intelligent management of the oceanic resource can be gleaned.

GENERAL BIBLIOGRAPHY

G. C. Ewing, Ed. Oceanography from Space
Woods Hole Oceanographic Institution,
No. 65-10 (1965)

-----Earth Photographs from Gemini III, IV and V, National Aeronautics and Space Administration, SP-129 (1967).

-----"Man's Geophysical Environment...Its Study from Space", U.S. Department of

Commerce, ESSA, (March 1968)

-----Earth Photographs from Gemini VI through XII, National Aeronautics and Space Administration, SP-171 (1968)

-----"Satellites Capable of Oceanographic Data Acquisition--A Review", U.S. Naval Oceanographic Office, TR-215 (May 1969)

-----"Microwave Observations of the Ocean Surface", U.S. Naval Oceanographic Office, SP-152 (June 1969)

P.C. Badgley, L. Miloy, and L. Childs, Eds., Oceans from Space, Gulf Publishing Co., Houston, Texas (1969)

-----Williamstown Report, "The Terrestrial Environment: Solid Earth and Ocean Physics," NASA CR-1579, prepared by M.I.T., Cambridge, Mass., (April 1970)

O.W. Nicks, Ed., This Island Earth, NASA SP-250, National Aeronautics and Space Administration, Washington, D.C. (1970)

J.R. Apel, Ed., "Sea Surface Topography from Space", Vols. 1 & 2, U.S. Department of Commerce, NOAA, TR ERL 228-AOML 7 and 7-2 (Feb. 1972)

V.E. Derr, Ed. Remote Sensing of the Troposphere, Department of Commerce, U.S. Government Printing Office, Catalog Number C-55.602: T 75 (1972)

ON A DEDICATED OCEANOGRAPHIC SATELLITE

John R. Apel

The capabilities of an ocean-oriented satellite are given in terms of the features that might be observed from spacecraft and the instruments that perform the remote sensing.

INTRODUCTION

In the decade following the advent of meteorological satellites and the synoptic, world-wide data obtainable from them, there occurred a significant enlargement in our understanding of weather processes and a somewhat lesser but still appreciable upgrading in the quality of weather forecasting. If the lessons of the NIMBUS, TIROS, ATS, ESSA, and NOAA series are any guide, one might expect roughly analogous results to follow from a satellite program addressed specifically to the oceans.

To date, in the areas of monitoring and assessment of oceanic conditions, satellites have not yet played a major role. However, as sensor and instrument development have proceeded, it has become apparent that much important and useful data on the oceans can be gathered from space platforms, some of it sufficiently quantitative to be graced with the name "measurement."

These oceanic features have been observed with visible and infrared sensors of a variety of types; but, with a few notable exceptions, such techniques more nearly fall in the category of photo-interpretation than in that of measurement. However, microwave instruments, both passive and active, promise to flesh out the visible-IR imagery with radiometric, surface roughness, and metric (or distance) measurements in a way that could lead to a remarkable flow of useful information about the oceans. Much of this information, ne data, would be due to a genuinely synergistic effect arising out of observations made with an optimum mix of closely coordinated sensors flown on one or more spacecraft. Thus, what is required for serious oceanic observations is a dedicated oceanographic satellite similar in spirit to those generated for meteorological, earth resources, and extraterrestrial observations, but optimized for viewing the seas--the fourth member of the ancient elemental quartet of air, earth, fire, and water.

It is important to understand, however, that an oceanographic satellite would be but a part of a larger system that includes data from surface ships, buoys, aircraft, and from meteorological satellites as well, all used in conjunction with large-scale numerical modeling. It is

only in the context of this extended ocean monitoring and prediction program that the potential benefits discussed here can be realized.

The major impact of such a system, if it is to be rationalized in terms of cost/benefit ratios or the like, would have to be in the areas of marine environmental monitoring, prediction, and resource assessment, rather than simply in oceanographic research--although obviously it would serve such a function as well. The efficacy of a satellite system in monitoring geophysical events such as winds, sea state, temperature, currents, ice conditions, tsunamis, storm surges, and such biological ones as chlorophyll concentrations and fish stocks, would largely justify (or fail to justify) the necessarily large expenditures required to give it birth.

OCEANIC PROCESSES AND OBSERVABLES

The ocean plays as fundamental a role in the natural scheme of things as does the atmosphere, although its functions, being considerably more varied and diffuse, are probably neither as well appreciated nor understood. The sea profoundly affects the weather and in turn is affected by the atmosphere, acting as both a heat reservoir for storing, distributing, and releasing solar energy and as the ultimate source for atmospheric moisture. Photosynthesis by oceanic phytoplankton is one major process for maintenance of atmospheric oxygen. Geological activity on all time and space scales takes place in and under the seas, which serve as the repository for the detritus of man and nature and as an important, practicable source of petroleum and a few useful minerals. Its currents and dilutant powers are called upon to disperse sewage, poisonous and nonpoisonous wastes, solid trash and excess heat, all the while maintaining a role as the aqua viva for an extremely complicated and commercially important food chain, and as a means of recreation and refreshment for people. In the estuaries and the coastal zones, these conflicting demands are especially severe.

By and large, satellite oceanography is confined to surface and near-surface phenomena. This constraint is not as severe as it appears at first glance, because surface data taken from spacecraft can be appended with other, conventionally derived subsurface measurements of certain parameters (e.g., vertical current or temperature profiles) in order to construct a more nearly three-dimensional view of the ocean. In addition, near-surface data are useful in their own right, since the coupled, nonlinear interaction between ocean and atmosphere largely takes place in the few tens of meters above and below the sea-air interface; man's marine activities are mostly limited to that surface as well, so the kind of two-dimensional oceanography that one can pursue from spacecraft is highly relevant.

One finds a diverse list of features, therefore, that enter into oceanic processes. In listing those observables that may potentially be discerned from space, it is convenient to begin at the level of the action of the atmosphere upon the sea, and then follow with the ocean's response--waves and currents--and their effects upon the shore; other

land-sea interactions are then given. Identification of water mass properties established by natural and man-made influences is also discussed. In many cases, quantitative remote measurements of certain features have not yet been accomplished with acceptable precision, but the data available hold enough promise for them to be listed as observables. The instruments that might be used to determine them are listed below in the section on Sensors. The details of the measurements are given in a forthcoming report (Ref. 1). Often, remotely gathered data can be appended and calibrated with in situ measurements relayed through the satellite.

Sea-Air Interactions

Here the observables include solar radiation input, sea temperature, ice cover, surface wind field, wave spectrum, and significant wave height. These data are important in both the extended weather prediction problem and in the forecasting of wave conditions for coastal regions and for the protection of ships at sea.

Currents, Upwellings, and Deep-Sea Tides

The position and surface velocities of the major ocean currents such as the Gulf Stream may be discernable with considerable research into ocean color and temperature signatures and in precision altimetry. The positions and temperatures of upwellings are presently observable. Deep-sea tides are also long-term candidates for measurement via radar altimetry. Knowledge of currents is important for understanding transport of heat and nutrients, for biological and fisheries studies, and for ship routing purposes. Upwellings are of much interest in fish stock assessment.

Sea-Earth Interactions

In this category are grouped such features as wind set-up along a coast, tsunamis, and storm surges, all measurable in principle via altimetry. In addition, wave refraction patterns, beach and shoal dynamics, and shallow water bathymetry may be observed with imaging radar or visible sensors. Near-surface sediment transport is also measurable using the latter instrument. The marine geoid and surface gravity field are decipherable via altimetry.

The importance of the wind, wave, and land interactions is obvious enough in terms of their effects on the coastal environment. An accurate geoid is required for interpreting all altimetric measurements.

Water Mass Identification

Such compositional features as water pollutants, nutrients, salinity, plankton and algae, suspended sediments, and bottom types go into water mass identification and the associated problem of fish stock assessment. Many of these can be determined via ocean color sensors, and others with microwave systems.

INSTRUMENTS AND SENSORS

The list of oceanic features is sufficiently broad so that no one type of sensor is capable of measuring or even observing all of them. The instruments discussed below include those generic types that are known from previous spacecraft or aircraft usage to possess a significant capability in oceanography. A broad spectrum of sensor types is presented without suggesting that a given satellite should fly with all of them; the exact choice of sensors for a mission must await more detailed studies.

Imaging Ocean Color/Thermal Infrared Spectroradiometer (IOCTIS)

This device should yield images of the ocean surface taken by both reflected sunlight and thermal infrared emission. Several radiometric channels having tens of nanometers spectral resolution and 0.25 to 1.0 km spatial resolution are required. A swath width of 500 to 1000 km is indicated.

High-Precision Radar Altimeter (HIPRA)

The high-precision radar altimeter has two distinct functions: measurement of the vertical distance, or altitude, between the satellite and the sea surface, and determination of the large-scale roughness of that surface.

The altitude-measuring function of the altimeter addresses those oceanographic features that lead to departures of the sea surface from the geoid. Measurement of any of these to a level of about ± 10 cm depends upon: (a) precise orbit determinations; (b) derivation of a very precise marine geoid; and (c) equally precise measurements of altitude. From these data one obtains the departure of the dynamic sea surface from the geoid, which may be quantitatively related to oceanic phenomena. The roughness-measuring function yields significant wave height and perhaps some information on wave spectrum along the sub-satellite orbit.

A radar footprint of about 10 km and a pulse length of a few nanoseconds appear acceptable. Further definition of the instrument's characteristics will be possible after analysis of SKYLAB and GEOS-C data.

Microwave Coherent Imaging Radar (MICAR)

The coherent, side-looking radar provides all-weather images of the sea surface with resolutions of order 50 m, from which wave spectra and refraction patterns can be deduced. Existing space-qualified instruments indicate that precision altimetry is also possible, while aircraft data also suggest that scatterometry and detection of oil slicks can be accomplished. A wavelength near 25 cm is useful.

TABLE I

SUMMARY OF SENSORS AND OBSERVABLES

Sensors OBSERVABLES	VISIBLE	Imaging Radiometers		Short Pulse Altimeter	Imaging Radar	Scatterometer
		THERMAL	IR MICROWAVE			
Chlorophyll and Algae	P	-	-	-	-	-
Current Position	S	P	T	P	P	-
Current Velocity	-	-	-	P	P	-
Estuarine Circulation	P	P	-	-	-	-
Fish Stock Location	P	P	T	T	-	-
Fog	P	S	-	-	-	-
Icebergs	P	-	T	-	P	-
Ice Cover	P	S	P	T	P	-
Marine Geoid	-	-	-	P	P	-
Pollutant Identification	P	-	S	-	S	-
Salinity	-	-	P	-	-	-
Sea State and Swell	T	-	T	P	P	P
Sediment Transport	P	-	-	-	-	-
Set-Up	-	-	-	P	P	-
Shallow-Water Bathymetry	P	-	-	-	T	-
Storm Surges	T	-	-	P	P	-
Surface Winds	-	-	P	S	S	P
Temperature	-	P	S	-	-	-
Tides	-	-	-	P	P	-
Tsunamis	-	-	-	P	P	-
Upwellings	P	P	S	-	-	-
Wave Spectrum	-	-	-	T	P	T

Multifrequency Imaging Microwave Radiometer (MIMR)

A multifrequency imaging microwave radiometer can be used to determine several oceanic and atmospheric parameters of interest, even in the presence of cloud cover and light rainfall. Presently, the measurable oceanic variables appear to be surface wind speed, ice cover, sea surface temperature, and surface salinity; the atmospheric variables are the vertical distributions and integrated values of liquid water and water vapor. By using a multifrequency, dual-polarized system operating at selected nadir angles, measurements of acceptable accuracy may possibly be obtained. The indicated frequencies range from 1.4 to 37 GHz.

Microwave Scatterometer

The scatterometer has been shown to be useful for measuring surface winds from aircraft up to perhaps 15 to 20 m/s with auxiliary data on wind direction and cloud cover; wavelengths of about 3 cm are apparently near optimum. SKYLAB has been gathering significant information on the instrument's space capabilities.

Table I below summarizes the applicability of the sensors discussed to the ocean features presented earlier. The letters P, S, and T stand for Primary, Secondary, and Tertiary capabilities, respectively.

BENEFITS TO THE NATION

The benefits that may ultimately be derived from an oceanographic remote sensing system are as many-faceted as the impact of the ocean on the affairs of man. These generally fall in the categories of: protection of life and property along the coasts and at sea; safety and navigation of shipping; increased efficiencies in maritime operations; improved management of marine resources; and enhancement of the quality of the environment.

In more specific terms, they include improved weather forecasting and hazard warnings, ship route forecasting, fish stock location and environmental assessment, pollution monitoring, and the advancement of research.

BIBLIOGRAPHY

1. Apel, J.R., and Sherman, J.W., Monitoring the Seas from Space; AOML-LORS 6.73.1 (to be published, 1973).
2. Man's Geophysical Environment . . . Its Study from Space; U.S. Dept. of Commerce, ESSA, (March 1968).
3. Satellites Capable of Oceanographic Data Acquisition --A Review; U.S. Naval Oceanographic Office, TR-215 (May 1969).
4. Microwave Observations of the Ocean Surface; U. S. Naval Oceanographic Office, SP-152 (June 1969).
5. Williamstown Report, The Terrestrial Environment: Solid Earth and Ocean Physics; NASA CR-1579, prep. by M.I.T., Cambridge, Mass., (April 1970).
6. Apel, J.R., Ed., Sea Surface Topography from Space; vols. 1 & 2, U.S. Dept. of Commerce, NOAA, TR ERL 228-AOML 7 and 7-2 (Feb. 1972).

MONITORING THE SEAS FROM SPACE:
NOAA'S REQUIREMENTS FOR OCEANOGRAPHIC SATELLITE DATA

A Report to the NOAA Satellite Plans and
Requirements Steering Group

JOHN R. APEL

Environmental Research Laboratories
Atlantic Oceanographic and Meteorological Laboratories

JOHN W. SHERMAN, III

National Environmental Satellite Service
Spacecraft Oceanography Project

Report AOML-LORS 6.73.1

June 1973

PREFACE

This report is submitted to the NOAA Satellite Plans and Requirements Steering Group, a committee composed of senior members from each of the major line components of the Agency. It represents the authors' best judgement on the data requirements, instruments, and capabilities of a dedicated ocean satellite surveillance system for the coming decade; such judgement in turn results from the distillation of the work of a large number of investigators throughout the oceanographic and aerospace communities, as tempered by the comments and critiques of many colleagues. Among the latter, we especially acknowledge the contributions of William O. Davis, Alan E. Strong, William H. Stevenson, George A. Maul, Donald V. Hansen, Duncan B. Ross, and Kirby J. Hanson.

The microwave sections of the report are outgrowths of reports from an earlier ad hoc study group, the NOAA Committee on the Usefulness of Microwave Systems in Space. The contributions of this group are being published as a separate appendix, Volume II of the present document. The membership of that committee included: John R. Apel, ERL, Chairman; E. Geoffrey Albert, NESS; John C. Alishouse, NESS; Reed Armstrong, NMFS; Donald E. Barrick, ERL; Bernard H. Chovitz, NOS; Robert D. Cole, NWS; Duane S. Cooley, NWS; Douglas D. Crombie, ITS; William O. Davis, HQ; Earl Estelle, NWS; Lowell Goodman, NOS; David Halpern, ERL; Stacey Hicks, NOS; Robert Junghans, HQ; George A. Maul, ERL; Robert W. McCaslin, NWS; Robert Morrison, NOS; Max W. Mull, NWS; Hyman Orlin, NOS; Jack H. Puerner, NESS; Alan E. Strong, NESS; and Donald J. Williams, ERL.

JRA
Miami, Florida

JWS
Suitland, Maryland

EXECUTIVE SUMMARY

The rationale for requiring oceanographic satellite data is developed in terms of NOAA's programs in Ocean Resources, Environmental Monitoring and Prediction, and Environmental Modification. Problems in achieving established goals in these programs are in part ascribed to insufficient data gathered over the world's oceans. Sea state and current predictions, weather forecasts, and assessment of living marine resources are cases in point. However, satellites are beginning to show their usefulness in delivering some of the required data.

The objectives of an oceanographic satellite are to determine physical and biological parameters remotely, as part of a future environmental monitoring and prediction system that also includes surface vehicles, buoys, and aircraft. Its evolution into an operational system, analogous to the meteorological satellites, is foreseen.

The ocean features to be measured from spacecraft are diverse. They are listed in a sequence that follows cause-and-effect relationships between atmosphere, sea, and land. In air-sea interactions, the observables include sea temperature, surface winds, and solar radiation; then follows surface waves, as described by significant wave height and wave spectrum. Currents, upwellings, and downwellings constitute an important but difficult set of measurements. Open ocean tides are another observable. In the category of sea-earth interactions are found storm surges, tsunamis, wave refraction in shallow water, shoreline dynamics, shoals, and near-surface sediment transport. Ice cover and dynamics may also be studied. The marine geoid is an important quantity to determine, both in its own right and as a reference surface for ocean dynamical effects such as currents. Water mass identification, especially in the coastal zone, leads to requirements on determining suspended sediment, chlorophyll, algae, fish stock locations, pollutants, oil spills and slicks, and salinity. Collection of in situ surface data is also needed as a means of calibration and obtaining information that cannot be sensed remotely. Table I summarizes the importance of these features to NOAA's goals.

The presently known sensors that show promise of yielding the required data are severalfold. In approximate order of priority, they are: (1) an Imaging Ocean Color/Thermal Infrared Spectroradiometer; (2) a High-Precision Radar Altimeter; (3) a Microwave Coherent Imaging Radar; (4) a Multifrequency Imaging Microwave Radiometer; (5) a Microwave Scatterometer; (6) a Bistatic Transmitter-Receiver; (7) a Laser Altimeter; and (8) a Vertical Tropospheric Sounder. The total number of candidate instruments is probably too large and the devices too complex to carry on one spacecraft, so tradeoffs and compromises are required. A summary of sensors and the observables that they might determine is given on Table III.

Satellite orbits are discussed in terms of instrument complements; an ocean color sensor requires a sun-synchronous orbit, while the microwave-equipped satellite could remain below 75°-80° latitude and view during all phases of the diurnal cycle. A preference should be given to coastal zone observations.

Integration of the satellite system into the NOAA program in Ocean Monitoring and Prediction is proposed, with various of the NOAA Major Line Components executing different functions in the process.

The scientific benefits foreseen include improved weather and marine prediction, enhanced hazard warning, ship route forecasting, fisheries environment assessment, and monitoring of pollution. The socio-economic benefits to the nation include protection of life and property in the coastal and marine environment, safety and navigation of ships at sea, increased economies in maritime operations, and enhanced management of marine resources.

TABLE OF CONTENTS

	Page
Chapter I. Introduction and Rationale	1
II. Objectives of an Oceanographic Satellite	3
III. Ocean Features to be Measured	4
IV. Candidate Sensors and Instruments	20
V. Satellite Mission Profiles	33
VI. Integration into an Environmental Monitoring and Prediction System	35
VII. Contributions to NOAA's Missions	36

LIST OF FIGURES

	Page
1. Satellite-derived sea surface temperatures off U. S. East Coast.	6
2. Power spectrum for wind-driven waves vs. wave frequency; wind speed is the parameter.	8
3. Mean surface topography for western Atlantic derived from geostrophic flow calculations. Elevations relative to the geoid in cm.	10
4a. Image of southeast U. S. taken from NOAA-2 during April 1973. Sunlight reflected from rough water defines the Gulf Stream.	11
4b. Thermal infrared image coincident with 4a, with Gulf Stream defined by its higher temperatures.	12
5. Computer-enhanced image of New York Bight taken from ERTS-1, showing oceanographic features.	17
6. Geoidal contours of the western Atlantic at one-meter spacings.	22
7. Average shape of leading edge of short altimeter pulse, for various significant wave heights.	23
8. Coherent, 25-cm radar image of ocean surface waves taken from aircraft altitudes. $\lambda \approx 200$ m.	25
9. Simulated brightness temperature of a rough sea at 37 GHz; polarization and wind speed as parameters.	28
10. Scatterometer cross-section ratio at 13 GHz, vs. surface wind speed.	30

LIST OF TABLES

I. Importance of Satellite Observations in Meeting NOAA Goals	19
II. Characteristics of Multifrequency Imaging Microwave Radiometer	27
III. Summary of Sensors and Observables	32

I. INTRODUCTION AND RATIONALE

A. NOAA Programs to Achieve National Goals

Among its many mission assignments, the National Oceanic and Atmospheric Administration is charged with at least three distinct tasks related to the oceanic domain, which may be broadly divided as follows:

1. Ocean Resources
2. Environmental Monitoring and Prediction
3. Environmental Modification

Implicit in these tasks is the need for environmental measurements and assessments, the prediction of oceanic or atmospheric conditions, the dissemination of forecasts, hazard warnings, charts, and other services, and the husbandry of national resources, both living and nonliving.

B. NOAA Services

To these ends, NOAA attempts to monitor and forecast fisheries environmental conditions, with a view towards increasing the harvest of living marine resources while remaining consistent with wise resource management. The agency develops and maintains weather and marine forecast services that predict meteorological and oceanic events and hazards such as winds, sea state, sea surface temperature, ice cover, tsunamis and storm surge warnings. It also publishes marine charts, tide and current tables, and other aids to navigation that increase safety at sea.

C. Problems in Achieving National Goals

However, because of the great length and breadth of the sea, the difficulties in obtaining detailed, timely information of sufficient observational density across most of its expanse have prevented an effective monitoring and forecasting system for the oceans. Thus the prediction of wave heights for use by ships depends on forecasts of the time and space histories of surface winds--the latter forecasts themselves being fraught with considerable uncertainty, as the loss of ships and oil drilling rigs at sea attests. Similarly, the locations of major ocean currents are known only approximately and the data required for ships to efficiently exploit currents are lacking. The lack of sufficient wind and pressure data over the oceans has precluded an improved, longer-range weather forecast for continental areas.

In order to achieve an effective one- to two-week forecast, observational data are needed over the oceans with about the same frequency and density as now exists in the continental United States. Similarly, wise management and utilization of living marine resources requires timely and repeated assessment of marine

fish stocks and the environment in which they live. Traditional methods of assessing both fish stocks living at or near the ocean surface and their environment must be significantly enhanced in the immediate future in order to supply management with necessary information on these items.

D. Usefulness of Satellites in Programs

The advent of meteorological satellites and the synoptic, world-wide data obtainable from them has resulted in a significant enlargement in the understanding of weather processes. Along with this has gone an enhancement of our ability to forecast meteorological events, especially large systems such as hurricanes and typhoons, and to warn against hazards resulting from them. However, much still remains to be done before reliable, several-day forecasts can be generated even for the continental United States. Overwarning and timeliness are two major problems. Improved data are vital not only to the weather prediction problem, but, in more general terms, for generating a flow of information needed by marine interests and by the ever-increasing fraction of our population living along the seacoasts.

In the area of monitoring and assessment of oceanic conditions and marine resources, satellites have not yet played a major role. However, as sensor and instrument development have proceeded, it has become apparent that much important and useful data on the oceans can be gathered from space platforms. For example, under relatively cloud-free conditions, sea surface temperatures can be derived from infrared radiometers on ITOS/NOAA satellites; some tracking of major ocean currents can be accomplished. Wind speeds from zero to about 15 m/sec can be estimated from the reflection of the sun from the ocean surface, as observed from the same spacecraft. The ERTS-1 satellite is presently showing that many additional features such as ocean color, pollution, and near-surface sediment transport can also be observed. Even more data are expected from SKYLAB, GEOS-C and NIMBUS-G sensors.

II. OBJECTIVES OF AN OCEANOGRAPHIC SATELLITE

The mission of an oceanographic satellite system is to measure from spacecraft such physical and biological parameters of the oceans, lakes, and estuaries as may be remotely determined and to integrate these measurements with other space- and conventionally-derived data so as to define in the near future a system for coastal and global environmental monitoring and prediction and for marine resource assessment.

To this end, research and development efforts in satellites and in sensor technology must be mounted jointly by NOAA, NASA, and other interested agencies. A series of satellites carrying a variety of sensors must be orbited, data must be gathered, and information digested that will lead to the design of an operational prototype system carrying an optimum mix of sensors. The operational version of the ocean satellite and the data from it will then be managed by NOAA in much the same fashion as it now deals with the ITOS/NOAA and SMS/GOES series of weather satellites.

This ocean-oriented satellite thus directly addresses two of the three major NOAA missions--those concerned with Ocean Resources and with Environmental Monitoring and Prediction, and it impacts the third--Environmental Modification--in a somewhat less direct but nevertheless real and valuable fashion.

III. OCEAN FEATURES TO BE MEASURED

The ocean plays as fundamental a role in the natural scheme of things as does the atmosphere, although its functions, being considerably more varied and diffuse, are probably neither as well appreciated nor understood. The sea profoundly affects the weather and in turn is affected by the atmosphere, acting as both a heat reservoir for storing, distributing, and releasing solar energy and as the ultimate source for atmospheric moisture. Photosynthesis by oceanic phytoplankton is one major process for maintenance of atmospheric oxygen. Geological activity on all time and space scales takes place in and under the seas, which serve as the repository for the detritus of man and nature and as an important, practicable source of petroleum and a few useful minerals. Its currents and dilutant powers are called upon to disperse sewage, poisonous and nonpoisonous wastes, solid trash and excess heat, all the while maintaining a role as the aqua viva for an extremely complicated and commercially important food chain, and as a means of recreation and refreshment for people. In the estuaries and the coastal zones, these conflicting demands are especially severe.

One finds a diverse list of features, therefore, that enter into oceanic processes. In listing these observables, it is convenient to begin at the level of the action of the atmosphere upon the sea; then follows the ocean's response--waves and currents --and their effects upon the shore. Other land-sea interactions are then listed. Identification of water mass properties established by natural and man-made influences is discussed next, followed by requirements for in situ measurements of these and other surface observables.

It is obvious that not all of these observables are independent; furthermore, many cannot be discerned from spacecraft. By and large, satellite oceanography is confined to surface and near-surface phenomena. This constraint is not as severe as it appears at first glance, because surface data taken from spacecraft can be appended with other, conventionally derived subsurface measurements of certain parameters (e.g., vertical current or temperature profiles) in order to construct a more nearly three-dimensional view of the ocean. In addition, near-surface data are useful in their own right, since the coupled, nonlinear interaction between ocean and atmosphere largely takes place in the few tens of meters above and below the sea-air interface; man's marine activities are mostly limited to that surface as well, so the kind of two-dimensional oceanography that one can pursue from spacecraft is highly relevant.

In many of the requirements listed below, the parameter specifications are somewhat arbitrary because of the present lack of experience in measuring of some of them on synoptic scales. Thus, they represent a list of desiderata for a coastal and global monitoring system as viewed from a position of relatively imperfect knowledge.

A. Air-Sea Interaction

The transport of matter, momentum and energy across the air-sea interface is chiefly due to solar radiation and atmospheric stress. Such parameters as the air-sea temperature difference, exchange of latent and sensible heat, and the surface vector wind field are the important observables for both meteorological and oceanic forecasting. For spacecraft, the following requirement appears reasonable:

•Requirement:

1. Sea temperature: Measure surface temperature with an instantaneous field of view of 0.25 to 1.0 km, to an rms precision of $\pm 0.5^\circ\text{C}$; composite over one- to two-day intervals and one-km² areas in the coastal zone; over three- to five-day intervals and 100-km² areas in the open ocean; all-weather data desirable. Append with vertical temperature profiles from in situ sensors.

Figure 1 shows satellite-derived surface temperatures off the U. S. east coast, as an indication of the current level of capability.

2. Ocean surface wind field: As referenced to 19.5-m altitude, measure wind speed to ± 2 m/s or $\pm 25\%$ of the actual value (whichever is larger) and wind direction to $\pm 20^\circ$; 25-km resolution near storms and fronts, and 50-to 100-km resolution elsewhere; daily, in near-real time.

3. Radiation input: Spectrally integrated solar radiation absorbed in and reflected by the global ocean, with a precision of 5 to 10 langley/day; with spatial and temporal resolution similar to that for global sea-surface temperature.

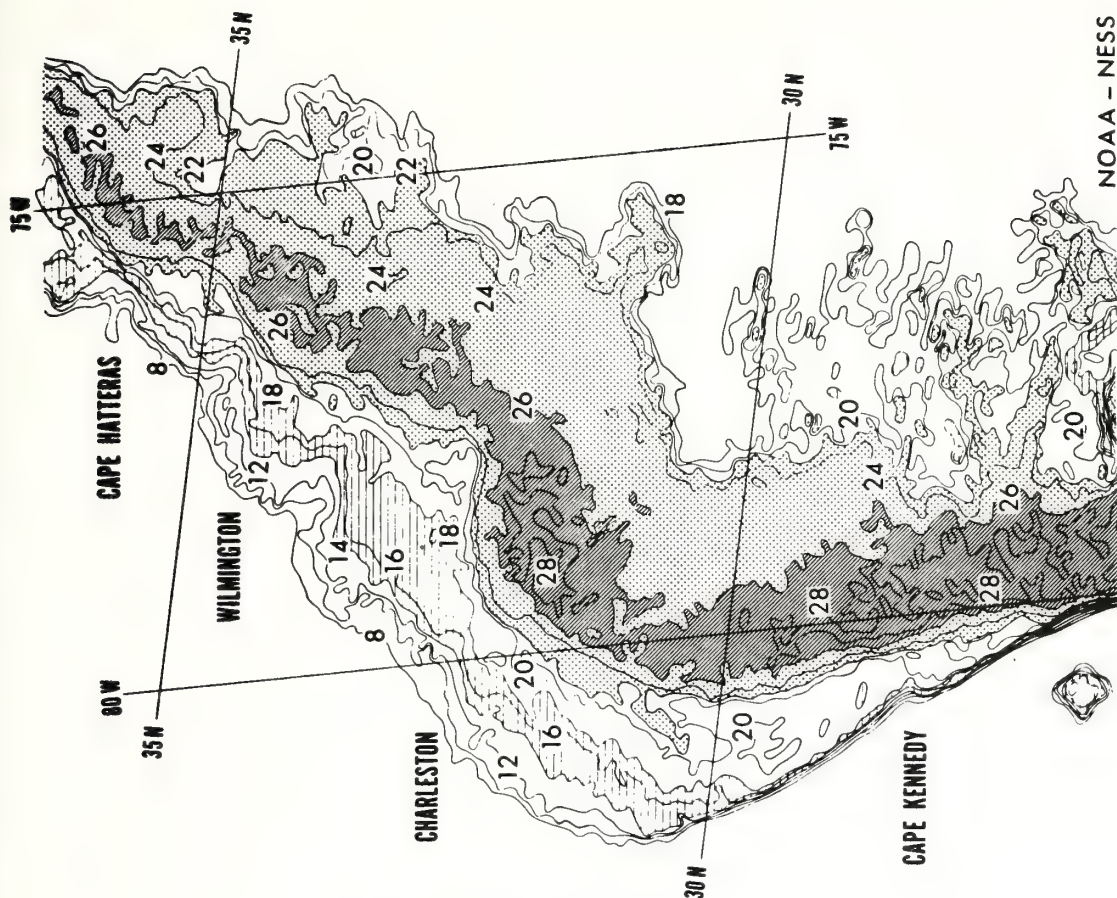
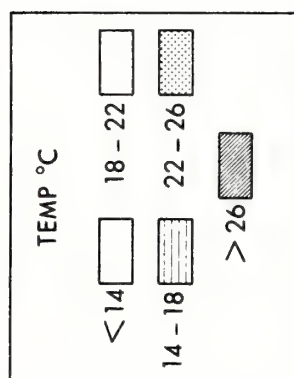
B. Surface Waves and Roughness

There is obviously a strong coupling between the surface wind field and ocean waves, with the wind initially generating short-length capillary waves which then cascade toward longer wavelengths and larger amplitudes, dependent upon the strength, duration, and fetch of the wind. While significant wave height, $H_{1/3}$, is a one-parameter specification of sea state, the proper description of a surface wave field is statistical--e.g., the two-dimensional power spectral density as a function of surface wave vector. A reasonably complete specification of this function near storms, when used as input data to numerical models, would allow wave forecasts to be made at several hundred kilometers distance from the high wind regions.

•Requirement:

1. Measure significant wave height, $H_{1/3}$, with a precision of ± 0.5 m or $\pm 25\%$ of the actual height (whichever is larger) over 100-km resolution elements; globally at 12-hour intervals, on a near-all-weather basis.

**ITOS 1 SRIR DIRECT
15 FEBRUARY 1971
0900 GMT**



2. Power spectrum: square-amplitude measurements consistent with the precision for $H_{1/3}$, above, for all wavelengths between 50 m and the largest observable length; measured at 30° intervals for all angles of propagation; spatial and temporal resolution as for $H_{1/3}$; all-weather capability.

Figure 2 illustrates a typical surface wave frequency spectrum for wind-driven waves, with different wind speeds as the parameter.

C. Currents

Ocean currents are driven by wind stress, tidal forces, and by uneven temperature and salinity distributions in the body of the sea. On the rotating earth, a moving fluid tilts its surface relative to the geoid with a slope proportional to the fluid velocity; this is called geostrophic flow. In the case of western boundary currents--e.g., the Gulf Stream, the slopes are of order 10^{-5} or less; the resultant topographic elevations across the Stream are about one meter or less.

Upwellings and downwellings are slow vertical flows brought about by divergent and convergent surface currents; these conditions are common along coastlines and are the result of wind-driven circulations. Upwellings, in particular, are of interest because the cold subsurface water has a high nutrient level that often leads to a plankton bloom and a resultant enhanced fish population. The speed of the current in an upwelling is not as important as its timely identification and location.

In order to determine the complete dynamical current velocity field, one must measure speed and direction as a function of position and time, so that not only the speed but the location of the current system and its time variations are also required. In addition, the vertical distribution of current velocity throughout the water column is needed for measuring total transports of water, dissolved chemicals, nutrients, etc. Therefore, to any surface current measurements made from spacecraft must be appended subsurface current profiles taken by conventional means.

Present estimates give roughly ± 20 cm/sec as the achievable precision in the determination of surface speed using surface slope measurements and perhaps a few kilometers as the time-averaged error in the position of the current. Nevertheless, surface current speeds, considerably below 20 cm/sec, are found in the ocean and are of interest. As discussed below, no apparent means exist for remotely determining such low speeds from spacecraft. However, drifting Lagrangian buoys may act as water movement tracers for these lower speeds. When equipped with satellite positioning devices and data collection systems, drifting buoys become extremely valuable adjuncts to the remote sensors on board the spacecraft.

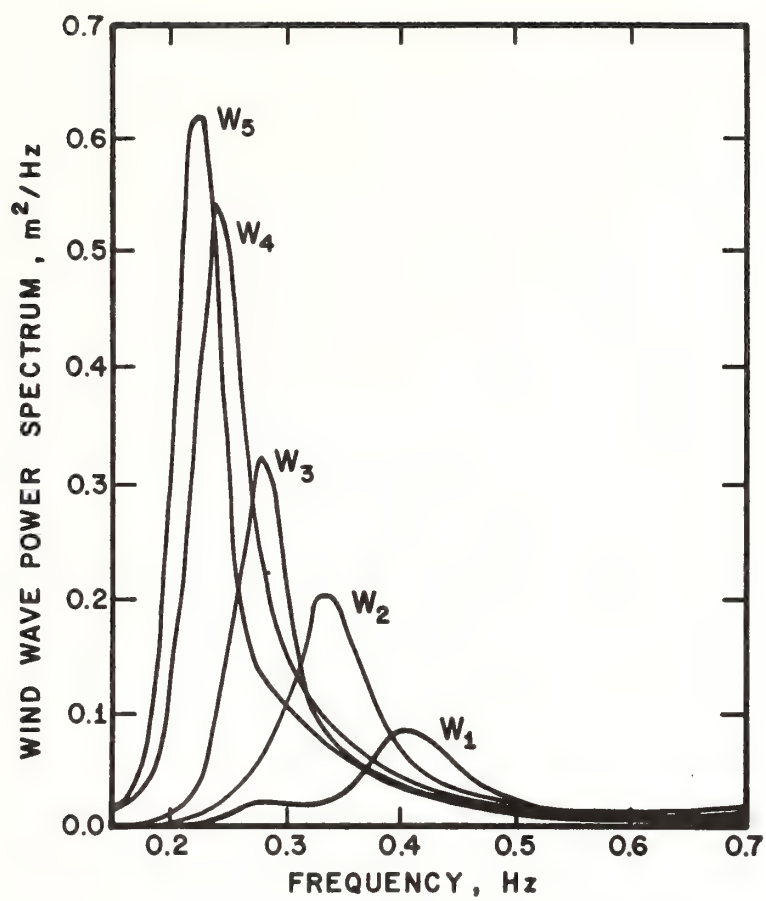


Figure 3 shows the calculated, long-time mean surface topography of the western North Atlantic, with elevations above and below mean sea level given in centimeters. The time-averaged Gulf Stream is clearly visible; its instantaneous position may depart from the horizontal mean axis by amounts approaching 200 km, moving slowly (5- to 40-day periods) compared to the times required to map the area with a satellite (a few days). It is felt that not only the mean positions but the important time variations in the speed and location of the major current systems of the world may be determined using satellite sensors.

Figures 4a and 4b are images of the southeast U. S., taken from the NOAA-2 weather satellite with the VHRR sensor operating in the visible and thermal-infrared bands, respectively; they show the Gulf Stream and other dynamical features.

The above discussion is intended to clarify the requirements below and to indicate that spacecraft remote sensors alone are not expected to deliver the information requested there.

•Requirement:

1. Ocean and estuarine currents: Measure the velocity field in three dimensions, with surface currents to ± 5 cm/sec or $\pm 10\%$ of the actual value (whichever is larger) over a range of 5-500 cm/sec; current profiles to the bottom; positions to 0.25 km in estuaries, 10 km near important ocean current systems, 100 km in open ocean; daily in estuaries, on 3- to 5-day intervals globally.

2. Upwellings: Determine position and areal extent of an upwelling event to 5 km within one to two days of its onset; estimates of surface water speeds and nutrient content.

D. Tides--Open Ocean and Shelf

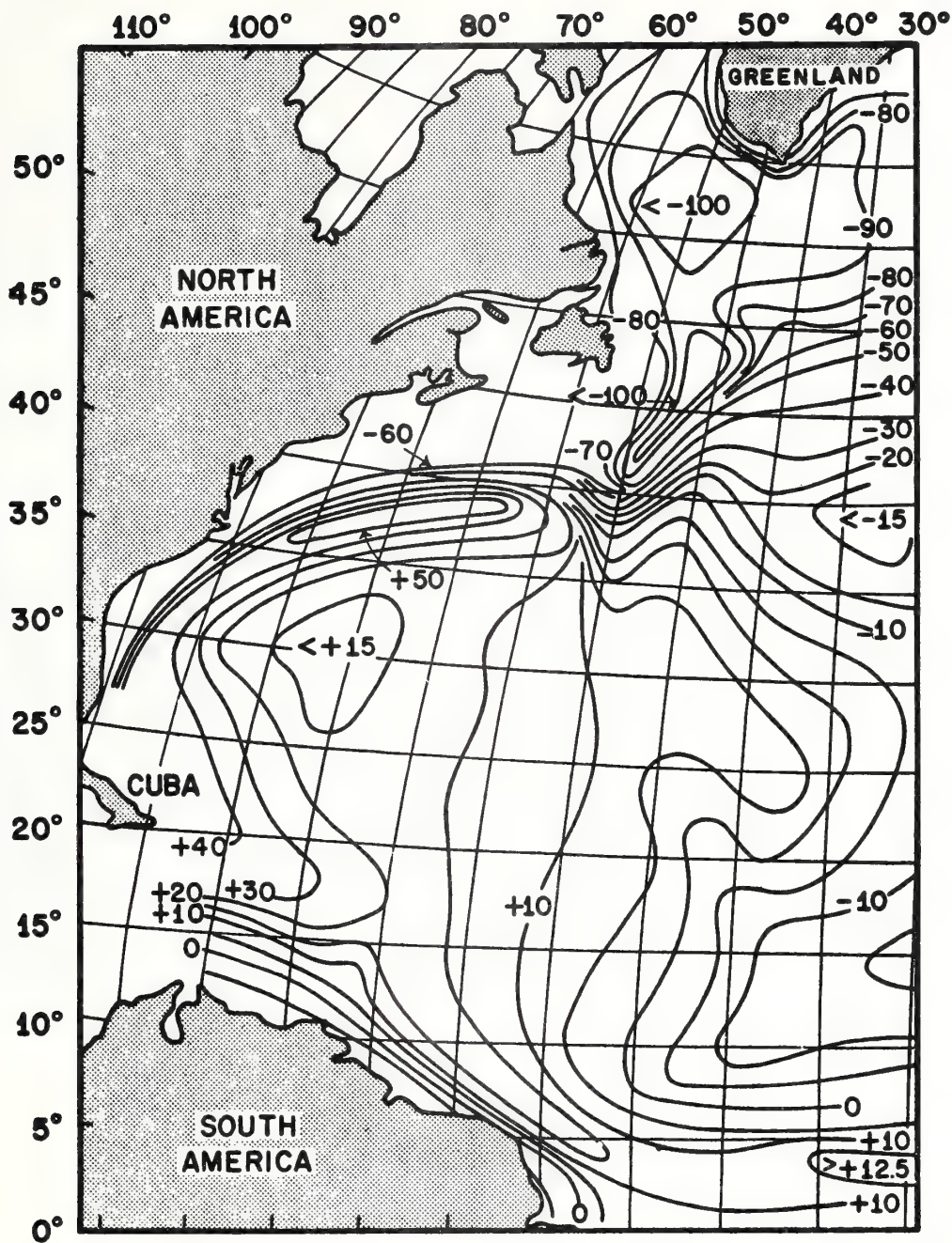
Tides, being astronomically driven by the moon and sun, occur at precise frequencies, some five of which contain about 95% of the tidal energy. Their amplitudes are typically zero to one meter. Open ocean and shelf tides are difficult and time-consuming to measure, and their relationships to coastal tides hard to establish. World-wide deep-sea tidal measurements would aid in the theoretical understanding and prediction of tides at arbitrary locations along the coastlines.

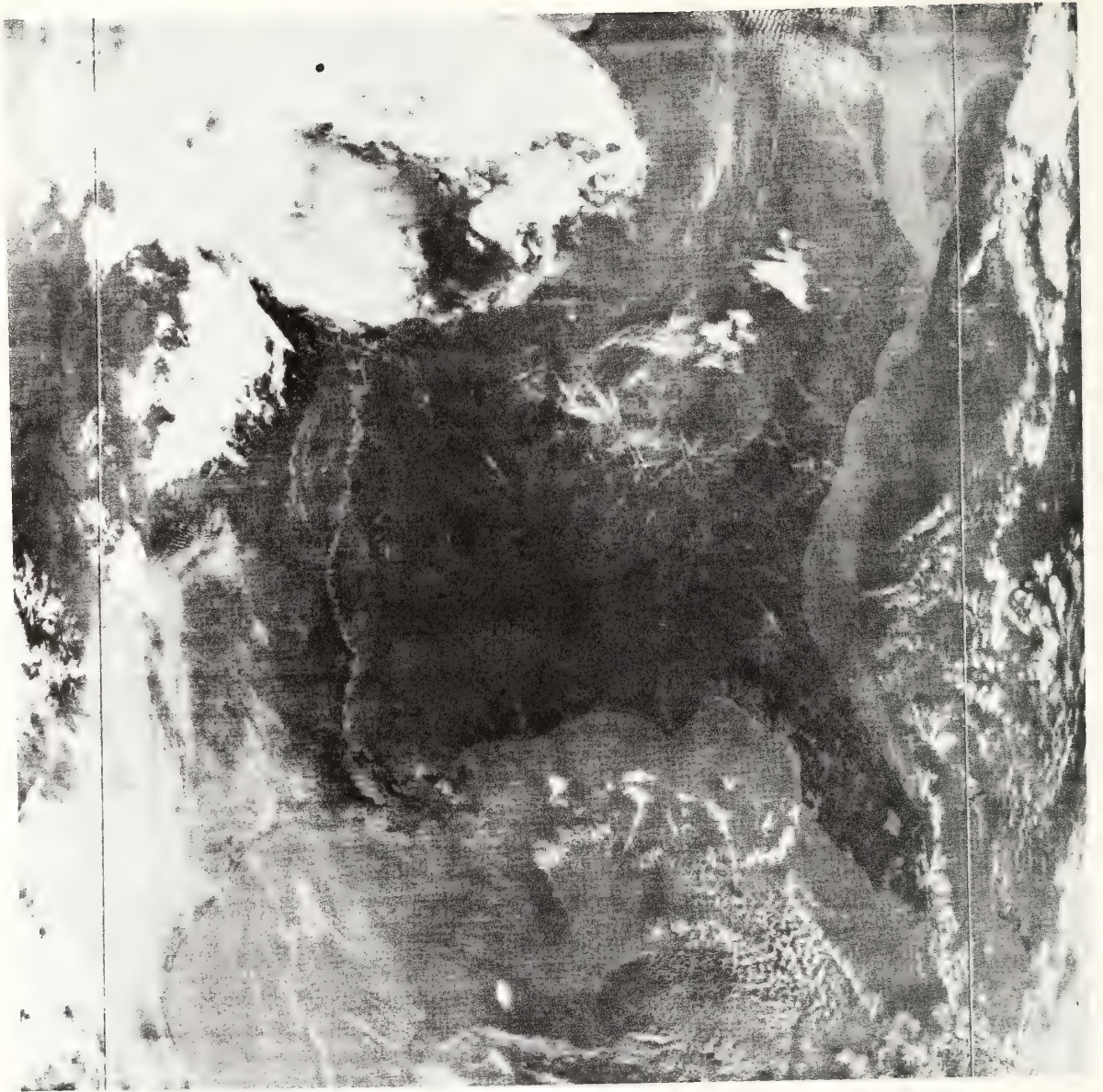
•Requirement:

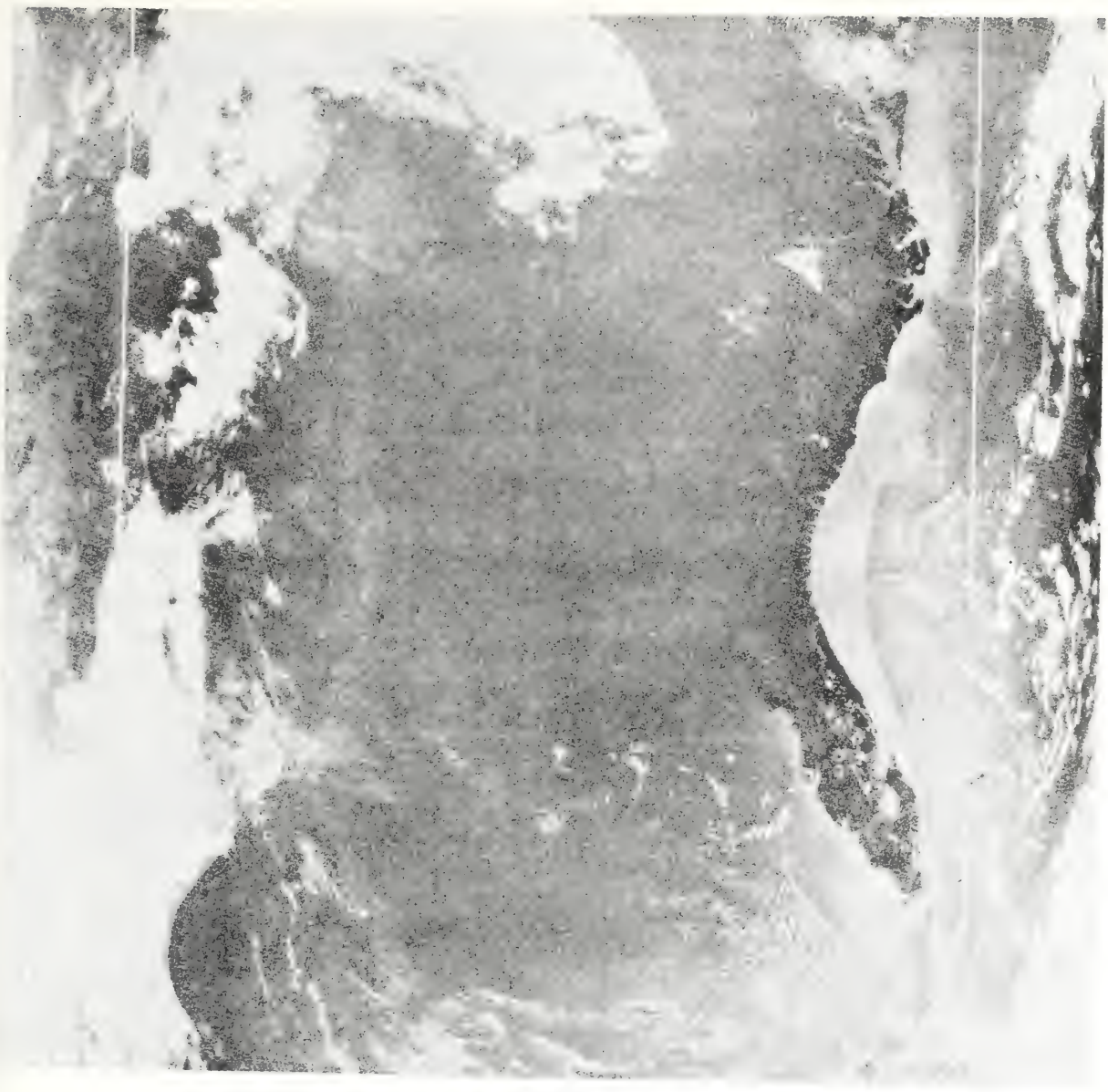
Measure tidal range to ± 10 cm (relative to mean sea level) and phase to $\pm 20^\circ$ for diurnal and semidiurnal periods; 25 km spacing on continental shelves, 100 km spacings globally.

E. Sea-Earth Interactions

In the category of interactions between the ocean and the solid earth are found such a wide diversity of features that no general discussion will suffice. Instead, each observable will be specified individually.







1. Storm surge and wind set-up along a coast. Storm systems pile up water ahead of them as they approach a coastline from seaward. In the case of hurricanes, this surge is often directly responsible for more damage and loss of life than is the wind. They are confined to a few tens of kilometers and a few hours time during the landfall; amplitudes can exceed nine meters.

Wind set-up is the accumulation of water along a coast due to long-term stresses such as trade winds. The elevation is typically one meter.

•Requirement:

Measure storm surge elevations to ± 1 m at several locations in a storm system as it develops; in real time; for arbitrary hurricane-force systems; global; all-weather basis.

2. Tsunamis. These are seismically excited long-length ocean waves capable of great damage. Their peak-to-trough amplitudes in mid-ocean have never been measured, but theoretically should be of order $1/2$ m; wavelengths are a few hundred kilometers and the disturbance ultimately fills an entire ocean basin. As they approach shore, the amplitude may increase to tens of meters. Assessing the energy content of a tsunami is a difficult task and thus much overwarning results.

•Requirement:

Measure tsunami amplitude to ± 10 cm and wavelength to $\pm 20\%$ in the open ocean, in real time, throughout an ocean basin.

3. Wave refraction patterns. Surface waves refract under the influence of shoal water and may converge or diverge, depending on bottom topography. Heavy wave action moves shoals and channels about and damages ocean structures such as jetties and offshore platforms. Wave refraction studies for a given region assist in shoreline protection, channel maintenance, and understanding of wave-driven circulation.

•Requirement:

Image wave refraction patterns for all wavelengths greater than 50 m, over swath widths of up to 500 km, on a selected basis worldwide; some real time requirement; near-all-weather operation.

4. Beach and shoal dynamics. Waves and currents erode and build shorelines and shallow bottom features. Baseline data on shoreline and shoal configurations allow assessment of changes due to wave action.

•Requirement:

Image shorelines and shoal waters with resolutions down to 50 m; image centers located to ± 500 m, over swath widths of up to 500 km, on a selected basis worldwide.

5. Shallow-water charting and bathymetry. The positioning of newly formed or poorly charted shoals and the assessment of their topography are necessary for the safety and navigation of ships at sea.

•Requirement:

Image shoals of depths less than 10-15 meters where possible, with vertical resolutions of 2 to 5 m and horizontal resolutions down to 50 m; with image centers located to ± 500 m, over swath widths of up to 500 km, on a selected basis worldwide.

6. Sediment transport. Wave action, river discharges, tidal flushing, and advection by current systems result in transport of sediments and sands throughout the ocean. Sediment patterns and particulate concentrations are indicators of transport of material.

•Requirement:

Image surface and near-surface sediment patterns with 100-m resolution, over swath widths of up to 500 km; determine concentrations from 0.2 to 1000 mg/m³; one-day intervals on a selected basis.

7. Ice cover, dynamics, and icebergs. Ice cover and ice movements vary greatly with time of the year and with surface wind conditions. The percentage of ice cover in polar regions governs much of the weather there, due to the exchange of heat through open water areas. In coastal areas and the Great Lakes, shipping depends upon an accurate assessment of ice conditions throughout those inland seas. Iceberg tracking and forecasting are vital for protection and navigation of shipping.

•Requirement:

Image ice cover and icebergs with a resolution of 50 m and with image centers located to ± 500 m, over swath widths of up to 500 km; latitudes above 40°N and S; daily intervals; all-weather basis.

8. Marine geoid. In a quite separate category from the previous observables is the marine or ocean geoid, defined as the surface assumed by a motionless, uniform ocean under the influence of gravitational and rotational forces. Geostrophic currents, storm surges, set-up, and waves lead to an ocean surface that has a slope relative to the geoid; the latter must then be known with a precision and on a spatial grid at least as fine as that with which the observable is to be determined.

Because these types of measurements have not been undertaken as of this writing, it is not possible to specify with any great confidence the needed geoidal accuracy. However, studies to date suggest the following tentative requirement.

•Requirement:

Measure height of the ocean geoid above the reference ellipsoid with a precision of ± 10 cm, on a 10-km grid in the vicinity of intense currents and large gravity anomalies and on a 100-km grid elsewhere over the global oceans.

F. Water Mass Identification

Variations in the physical or chemical composition of a water mass lead to variations in its color or reflectivity, for example. These changes can be natural or man-made; in either case, they tend to be more pronounced near continents. The color is determined primarily by nutrients, plankton and algae, suspended sediment load, pollutants, and, where sufficiently shallow, by water depth and bottom type. Other environmental factors such as atmospheric conditions, sun and viewing angles, surface winds, and waves also influence the measurement of ocean color.

Regions of the ocean where surface water convergence and sinking occur tend to be quite sterile biologically, while divergent or upwelling regions are usually biologically active. The major ocean constituent causing color change is the chlorophyll contained in all forms of phytoplankton, with chlorophyll-a being the dominant component. In the open ocean, the ability to detect and quantitatively measure chlorophyll-a is the most important benefit to accrue from the determination of the color of the sea and has much significance in the conservation and development of ocean living resources. In the coastal area, other types of biologically active ocean color producers may be as important to measure as is chlorophyll; these include carotenoids and red and brown algae.

NOAA's responsibilities in the coastal zone require it to emphasize those regions in its research and operational programs. The effective monitoring of water masses out to the continental margins requires concurrent, spatially registered observations of ocean color, temperature, and preferably salinity, made at frequent intervals. The remote observation of these features typically does not provide the distribution of the parameter throughout the water column, but instead yields a weighted-integral estimate of the observable near the top of the column.

An important aspect in the measurement of ocean color is the influence of the orbit on the signal received at the spacecraft. Because the sun angle changes as a function of position of the orbit and season of the year, the system must provide for a variable observation angle, so as to optimize the viewing conditions while avoiding sun glint. Other environmental factors also bear on the problem, such as morning fog and haze as well as afternoon convective build-up of clouds obscuring the surface.

•Requirement:

Image the ocean surface in multiple wavelengths of visible and reflected and thermal infrared radiation (to be discussed below) with 0.25- to 1.0-km spatial resolution over swath widths of 500-1500 km, with the scene center positioned to 0.25 to 1.0 km under nearly constant illumination conditions; observation interval of one to two days in the coastal zone, three to five days in the open ocean, to overcome cloud cover problems.

Measurement of ocean color by acquiring images of the desired scene in several spectral intervals would allow identification of the features listed below. The same sensor may be used to make all the measurements.

1. Suspended near-surface inorganic sediment distribution and concentration between 0.2 and 1000 mg/m³.
2. Chlorophyll₃ distribution and concentration between 0.1 and 20 mg/m³.
3. Yellow-green, red and brown color-bearing plankton distribution and concentration.
4. Fish stock location via relationship to bio-significant observables.
5. Pollutant distribution and concentration.

By viewing toward, rather than away from, the sun, it is possible to observe surface features in the sun glitter due to the changes in surface reflectivity. Thus, in Figure 4a the Gulf Stream is visible not so much because of its deeper blue color but because a northerly wind was increasing the surface roughness over the current as it moves and thereby diffused the reflected sunlight. A variable viewing angle is required to measure either color or reflected sunlight.

•Requirement:

Observe surface features by changes in surface reflectivity.

Viewing up-sun allows determination of the following observables:

1. Oil spills
2. Internal waves via surface slicks
3. Variations in surface roughness

Figure 5 is a computer-enhanced ERTS-1 image of a 180x180 km² sector of the New York Bight, showing suspended sediments from the Hudson River, U-shaped acid-dumping events, water mass variations, and internal waves, the last visible because of sunglint.

A final item in water mass properties is surface salinity. Its distribution is needed because of its effect on the distribution of living marine resources, ice, and ocean dynamics. The requirements for observation are quite similar to those for surface temperature.

•Requirement:

Map surface salinity to ± 1 part per thousand with a resolution of 1 km on one- to two-day intervals, in coastal regions; ± 0.1 ppt and 10-km resolution globally, on three- to five-day intervals.

G. Surface Data Collection

NOAA has programs in data collection from unmanned automatic buoys, both anchored and drifting, with plans for data transmission through such satellites as SMS/GOES and TIROS-N. In addition, it maintains large archives for surface-derived oceanographic and meteorological data under the auspices of the National Environmental Data Service. It is felt that presently planned systems are sufficient to meet the buoy data collection and positioning requirements in the next five years. However, the existence of these programs should not preclude considerations of new satellite data collection systems, especially if such systems allowed otherwise unobtainable information to be gathered.

H. Summary of Ocean Observations and NOAA's Goals

Table I summarizes the importance of each of the ocean features observable from spacecraft to the major NOAA goals listed in the Introduction. The assessments, which are weighted according to Primary (P), Secondary (S), and Tertiary (T) factors, are necessarily qualitative. However, there is little doubt that spacecraft observations will have a significant impact in the areas of Ocean Resources and Environmental Monitoring and Prediction; their influence in the arena of Environmental Modification is not yet clear except perhaps in weather modification, where their impact is somewhat less.

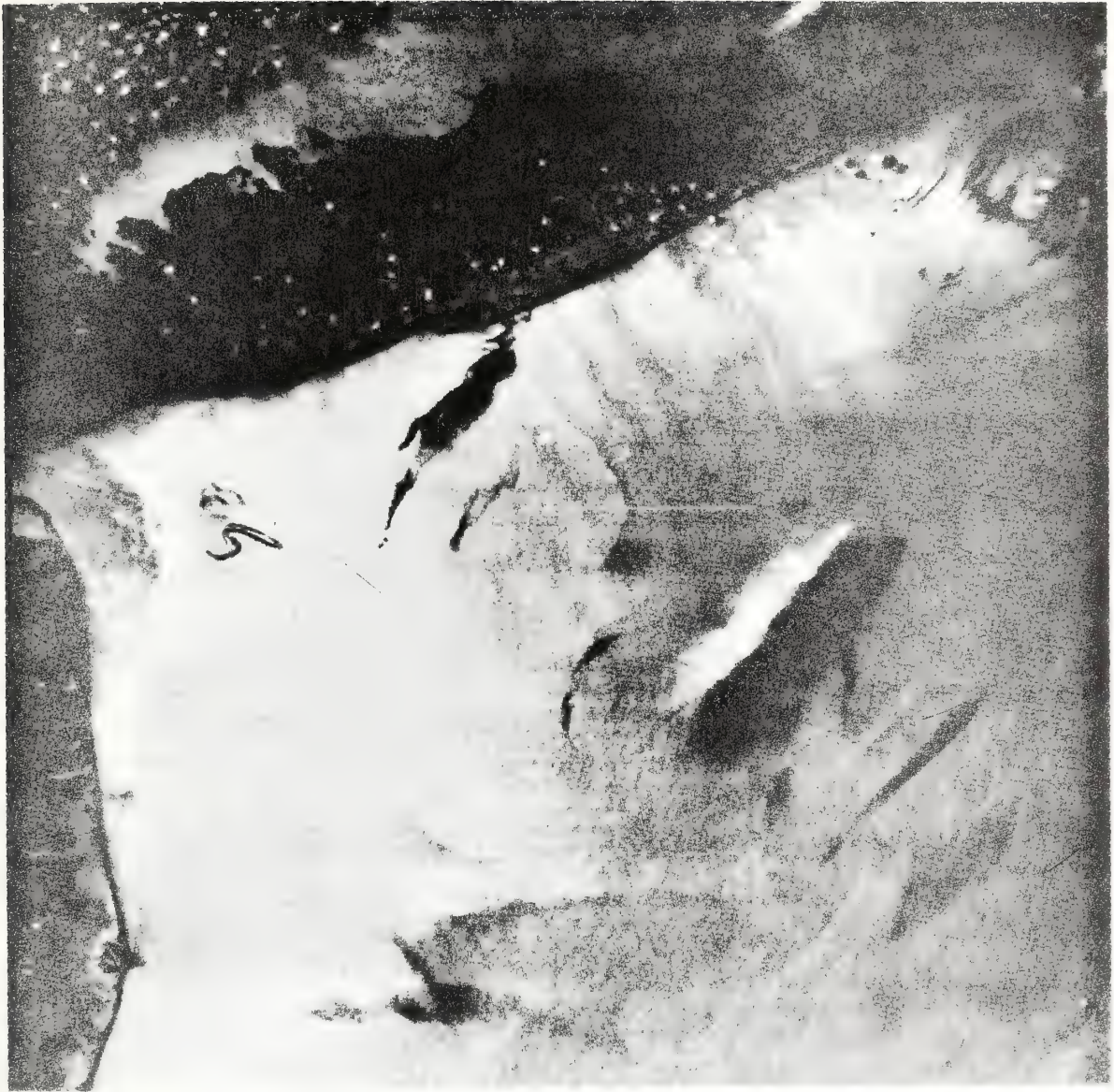


TABLE I

IMPORTANCE OF SATELLITE OBSERVATIONS IN MEETING NOAA GOALS

Ocean Feature Observable From Space	Ocean Resources	Environmental Monitoring and Prediction	Environmental Modification
Air-Sea Interactions	S	P	P
Surface Waves	S	P	S
Horizontal Currents	P	P	S
Upwellings	P	S	S
Tides	S	P	S
Storm Surges	T	P	S
Tsunamis	T	P	T
Wave Refraction	T	P	T
Beach & Shoal Dynamics	S	P	T
Shallow Water Charting	S	P	T
Ice Cover & Icebergs	S	P	T
Marine Geoid	T	P	T
Sea Surface Temperature	P	P	S
Suspended Inorganic Sediment	P	P	T
Chlorophyll, Planktonic Color	P	P	P
Fish Stock Location	P	P	T
Pollutants & Oil Spills	P	P	P
Internal Waves	T	P	T
Salinity	P	P	T
Surface-Derived Data	P	P	P
P-Primary Importance	S-Secondary Importance	T-Tertiary Importance	

IV. CANDIDATE SENSORS AND INSTRUMENTS

The list of observables in Chapter III is sufficiently broad so that no one type of sensor is capable of measuring or even observing all of them. This section discusses those families of sensors known from previous space or aircraft usage to possess a significant capability in oceanography. The list of sensors, while not exhaustive, is in general order of NOAA preference. While this ordering is somewhat a matter of individual taste, it is unlikely that the position of any sensor on the list would change by more than one place in either direction due to individual priorities.

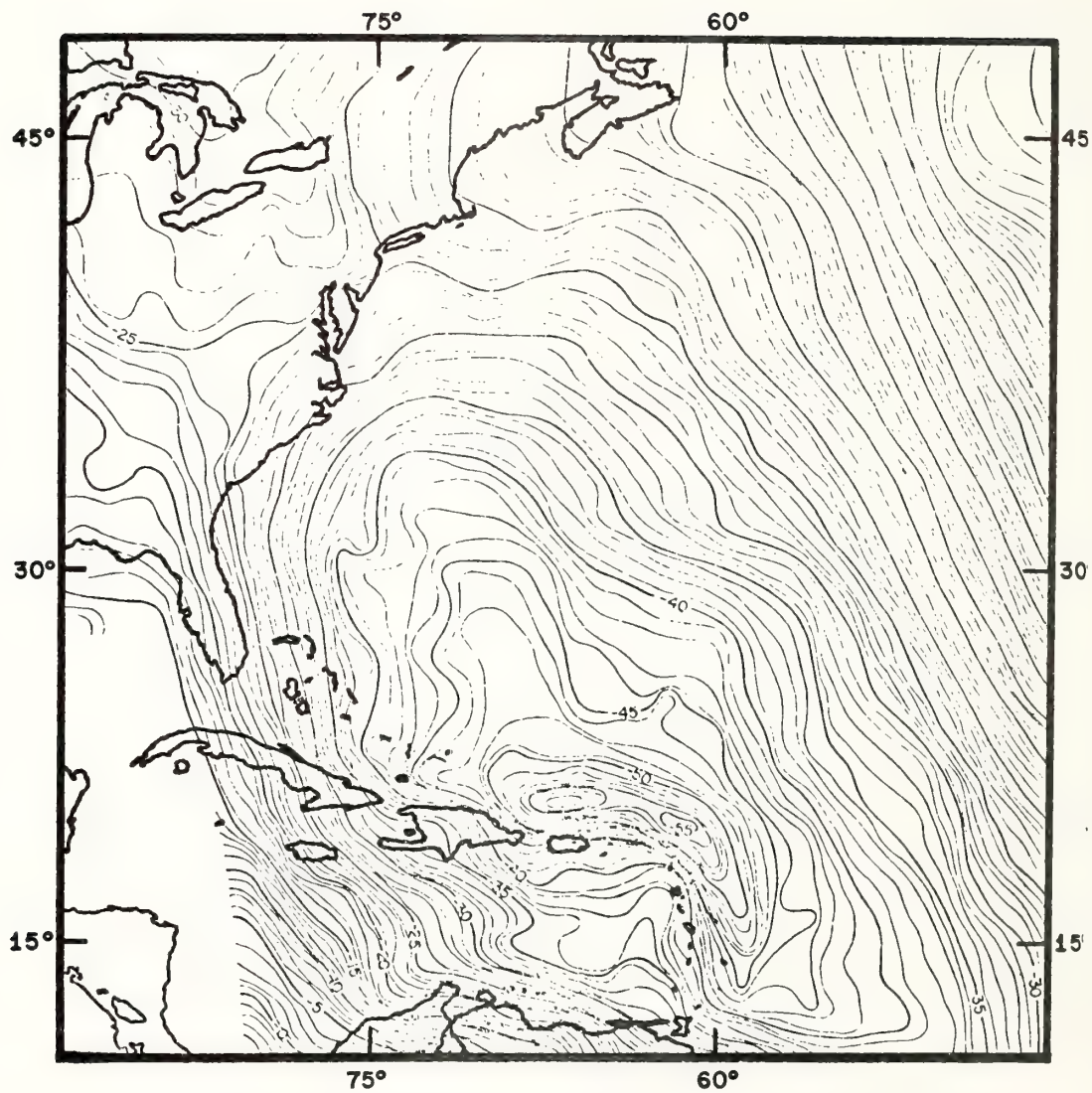
A. Imaging Ocean Color/Thermal Infrared Spectroradiometer (IOCTIS)

This device should yield images of the ocean surface taken by both reflected sunlight and thermal infrared emission. Approximately eight spectral channels of radiometric quality, with a maximum of 30 nm spectral resolution, are required to cover the visible, near infrared, and thermal infrared portions of the spectrum. At least two thermal infrared channels are needed to permit an atmospheric attenuation correction that will yield a precision of $\pm 0.5^{\circ}\text{C}$. The data from all channels must be registered to within one resolution element, which is desired to be between 0.25 and 1.0 km. In spite of atmospheric obfuscation, a blue channel at about 440-450 nm and a green channel at about 520-530 nm are mandatory. Signal-to-noise ratio is considered very important for quantitative chlorophyll measurements, with a minimum of 150-200 being desired. The IOCTIS should scan orthogonal to the flight path but not necessarily symmetrically disposed about the nadir point; scanning about variable angles with respect to the sun is highly desirable. The swath width should be 500 to 1500 km, if data rates will allow. This swath would allow frequent viewing of the open ocean as well as U. S. coastal features. For the coastal zones, daily coverage is desired, while, for the open ocean, several-day revisit times are acceptable.

It is recognized that meeting all of these requirements simultaneously may impose intolerable burdens on the instrument design or the data rate, but the required trade-offs must be made during more detailed engineering studies. Considerable guidance is being gained from the ERTS-1 and NOAA-2 high-resolution scanners that will assist in resolving the conflicts.

In clear or relatively cloud-free areas, the imaging spectroradiometer specified above would be capable of addressing, if not satisfactorily measuring the following features from Table I:

- Horizontal currents (spatial distribution)
- Upwellings and surface convergences (spatial distribution)
- Beach and shoal dynamics
- Shallow water charting
- Ice cover and conditions; large icebergs
- Sea surface temperature (spatial distribution and value)
- Suspended sediment (spatial distribution)
- Chlorophyll (spatial distribution and concentration)



- Fish stock location
- Pollutants and oil spills (distribution)
- Internal waves (distribution)

B. High-Precision Radar Altimeter (HIPRA)

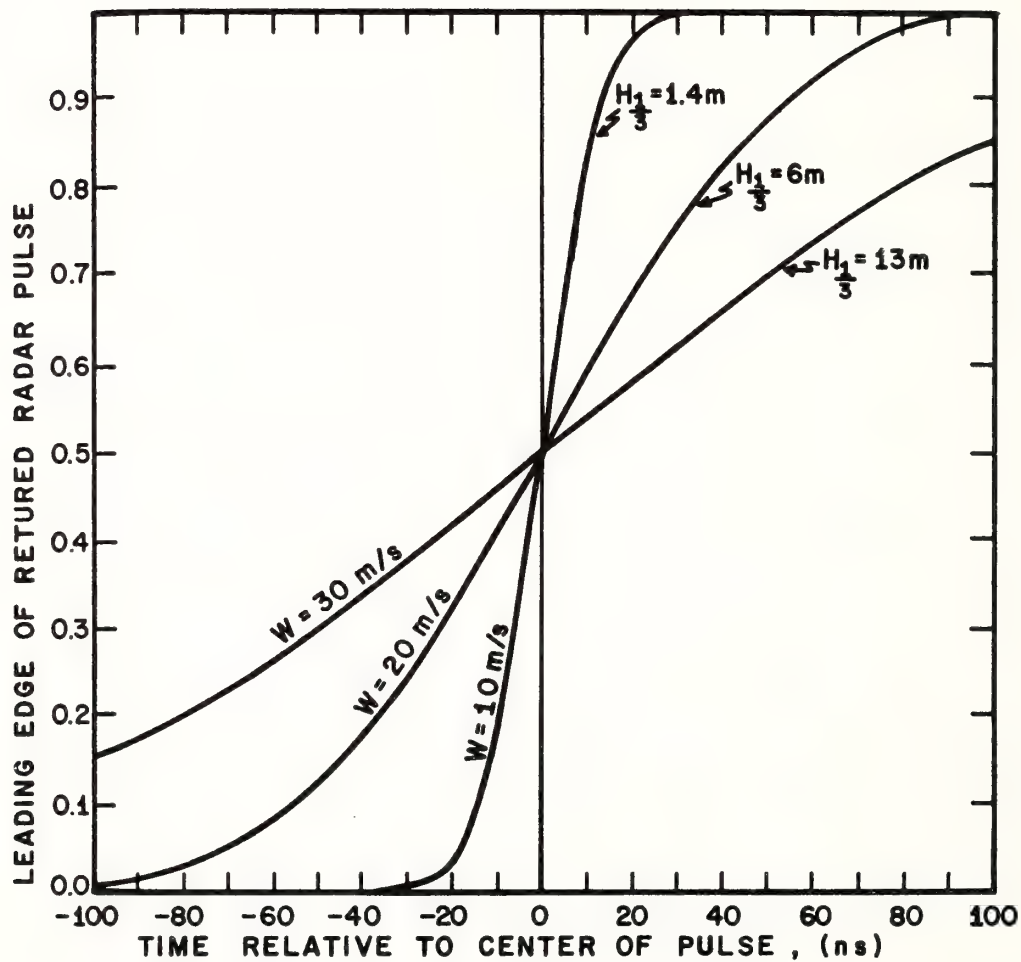
The high-precision radar altimeter has two distinct functions: measurement of the vertical distance, or altitude, between the satellite and the sea surface, and determination of the large-scale roughness of that surface. The high-precision feature is required for both functions.

The altitude-measuring function of the altimeter addresses many of the oceanographic features of Table I that lead to departures of the sea surface from the geoid. Measurement of any of these depends upon: (a) precise orbit determinations; (b) derivation of a very precise marine geoid; and (c) equally precise measurements of altitude. From these data one obtains the departure of the dynamic sea surface from the geoid, which may be quantitatively related to the oceanic phenomena listed in Section A, above. At a level of approximately ± 10 cm precision, measurement of the major geostrophic ocean currents lying between the ice-covered polar regions and the immediate equatorial zones becomes a possibility. Other features such as storm surges, tsunamis, barometric pressure loading, and set-up may be discerned whenever those events are overflown by an active HIPRA.

In addition, earth and ocean tides, being driven by astronomical forces at well-defined frequencies, can be extracted from satellite altimetry by narrow-band numerical filtering of the data.

Figure 6 shows a recent calculation of the geoid in the western Atlantic, with level contours spaced at one-meter intervals. In order to measure geostrophic flow, for example, the topography of Figure 3 will have to be discerned against the geoidal background of Figure 6.

The second function of the HIPRA is measurement of significant wave height. If a nanosecond-pulse radar is used to illuminate an ocean whose significant wave height exceeds approximately one meter, the pulse will be significantly broadened due to the distribution of reflecting heights presented by the waves. By measuring the temporal broadening, one may determine the significant wave height over the radar footprint on the ocean surface. Calculations of the average returned pulse shape as a function of time, with significant wave height as a parameter, are shown on Figure 7. The range of observable heights appears to be of order 0.5 to 20 m with attainable power levels. Since the measurement depends on the shape of the pulse rather than its amplitude, it is essentially independent of atmosphere attenuation and therefore can measure wave height where it is of most concern--near storms. Thus sea state and swell can be continuously determined along a swath spanning the suborbital track.



The features from Table I that may be observed along the suborbital track with the HIPRA are:

- Surface waves (significant height)
- Geostrophic currents (speed only)
- Deep-sea tides
- Storm surges and tsunamis (targets of opportunity only)
- Marine geoid

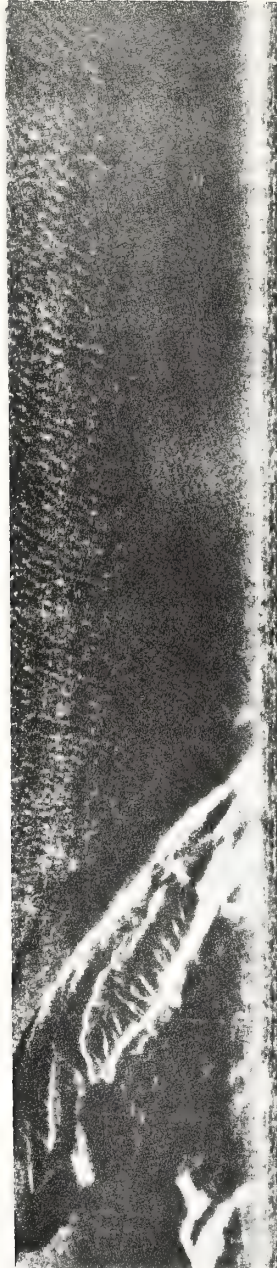
Experience with SKYLAB and GEOS-C radar altimeters will allow a more precise definition of the instrument's required capabilities to be made in the near future. For now, it is sufficient to say that no requirement is apparent that cannot be met within the state of the radar art.

C. Microwave Coherent Imaging Radar (MICIR)

The coherent, side-looking imaging radar is probably the microwave instrument having the greatest potential for ocean observations, although an accurate assessment of all of its capabilities is not yet available. At off-nadir angles, it is capable of imaging the surface of the sea and shows wave trains, ship wakes, and ice, as well as land masses. Figure 8, taken from aircraft altitudes, shows refraction and shortening of a train of 200-m length waves as they approach shore. From satellite altitudes, a radar with a one-second integration time should achieve a resolution element of about 30 m and thus would be capable of viewing ocean waves and other features whose scale exceeds approximately twice that size. From such an image, the two-dimensional power spectrum of the surface wave field can be computed; this is the most fundamental quantity required in wave forecasting. While the data rate is high, on-board processing to yield power spectra can reduce that rate to much smaller values except where detailed imagery is required, as might be the case for wave refraction studies, or where images of ice cover or icebergs are required.

In addition to the imagery and wave-spectrum determination, precision altimetry appears to be possible with the MICIR. Present estimates indicate that the altitude can be measured to a small fraction of a radar wavelength, so that a 25-cm instrument might achieve the required 10-cm level for the altitude precision and thus serve the role of the HIPRA.

A third mode of operation may exist for the MICIR--that of a microwave scatterometer. Such an instrument illuminates the sea surface at various angles off nadir and then measures the microwave energy scattered back into the antenna from capillary and short gravity waves; these are coupled to the instantaneous local wind and are to first order independent of the large gravity waves making up the observable sea state. Measurements of the radar cross-section of the sea surface indicate that the scattering from large angles increases for wind speeds up to perhaps 15-20 m/s.



This effect is visible in the wave images in Figure 8. The backscatter also is weakly dependent on the angle between the plane of the beam sweep and the wind direction; this latter can be estimated from ordinary surface wind charts with sufficient accuracy. Therefore, the scatterometer may function as a low-wind-speed spaceborne anemometer or as an oil slick detector. In an imaging mode, horizontal variations in the wind field or the distribution of oil could be mapped.

Aircraft flights are currently being made that should delineate some of these claims. If they should prove true, the coherent imaging radar should assume higher priority in the sensor list.

Assuming that only the imaging function is served, the MICIR is capable of observing the following:

- Surface waves (height and spectrum)
- Wave refraction patterns
- Ice cover and icebergs

If, in addition, the altimetric mode is capable of sufficient precision, the instrument could further observe:

- Geostrophic currents (speed only)
- Deep-sea tides
- Storm surges and tsunamis (targets of opportunity only)
- Marine geoid

Finally, if the scatterometric mode can be quantitatively implemented in the MICIR, further observables would be:

- Surface wind (distribution and speed)
- Oil slicks (distribution)
- Internal waves (distribution)

Most of these observations could be made on a near-all-weather basis.

D. Multifrequency Imaging Microwave Radiometer (MIMR)

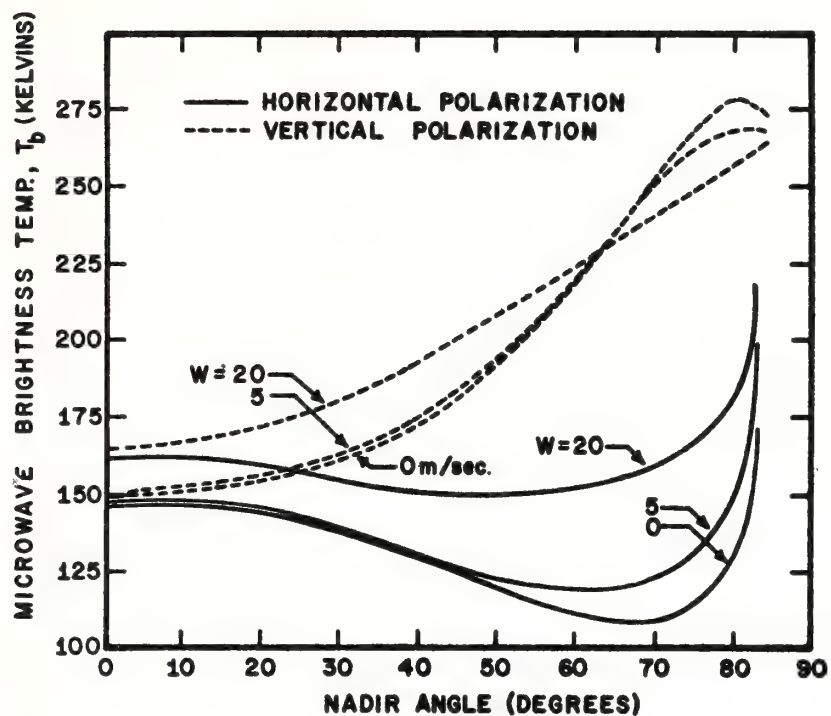
In order to view the surface of the sea through clouds, microwave sensors must be implemented. A multifrequency imaging microwave radiometer can be used to determine several oceanic and atmospheric parameters of interest, even in the presence of cloud cover and light rainfall. Presently, the measurable oceanic variables appear to be surface wind speed, ice cover, sea surface temperature, and surface salinity; the atmospheric variables are the vertical distributions and integrated values of liquid water and water vapor. The accuracy with which these variables may be determined depends upon the microwave opacity of the clouds and the system noise, among other factors.

The emissivity of sea water in the microwave range is a complicated function of frequency, polarization, nadir angle, thermodynamic temperature, salinity, surface roughness, and foam (see Fig. 9). Cloud opacity depends on the vertical distributions of liquid water and water vapor, and water droplet size. The emissivity of sea ice depends on its age and salinity. Nevertheless, by using a multifrequency, dual-polarized system operating at selected nadir angles, in conjunction with atmospheric models based on climatological mean data for a given region of the world, measurements of the geophysical variables apparently may be determined from the microwave brightness with acceptable accuracy until cloud thickness becomes excessive.

Surface wind speed is determined from the enhanced brightness temperature that foam and surface roughness have been observed to possess at frequencies from at least 1.4 to 20 GHz; thus the microwave radiometer is useful for wind speed measurements above some 7-10 m/s, when whitecapping occurs. Sea surface temperature is probably best deduced by observing with frequencies near 5 to 10 GHz. Surface salinity effects may only be seen at or below approximately 2 GHz. Ice observations require higher resolution and only crude radiometric correction; hence 30-60 GHz appears to be a usable range. The exact selection of frequencies, polarizations and nadir angles is still a matter for further research, but in general the lower the frequency, the more immune to atmospheric effects are the oceanic measurements. Table II gives preliminary choices of the dominant frequency required to determine each geophysical variable, along with estimates of the minimum error that might be achieved for each.

TABLE II
CHARACTERISTICS OF MULTIFREQUENCY IMAGING MICROWAVE RADIOMETER

Geophysical Variable	Dominant Frequency, GHz	Nadir Angle, deg	Estimated Error
Salinity	1.4	0-45	± 2 o/oo
Temperature	5.0 & 10.7	45	± 1 Kelvin
Surface Wind Speed	10.7 & 37	0-45	± 2 m/s above 10 m/s
Water Vapor	22.2	0-45	± 300 mg/cm ²
Liquid Water	37	0-45	± 100 mg/cm ²
Sea Ice	37	0-45	---



In a spacecraft application, the optimization of a microwave radiometer to image these variables in a quantitative way is a difficult task. The realities of spacecraft antenna sizes preclude small resolution elements at lower microwave frequencies; furthermore, conical scans are implied for off-nadir, constant-angle viewing. For open-ocean surface salinity and temperature, an instantaneous field of view of about 100 km and a revisit time of a few days are the coarsest measurements acceptable. Surface wind speed and cloud parameters probably require IFOV's of order 25 km and twice-a-day, real-time coverage.

Using such measurements of sea surface and cloud brightness temperatures made at microwave frequencies, the following observables can probably be monitored through moderate cloud cover:

- Ice coverage
- Surface wind speed above 5-10 m/s
- Surface thermometric temperature
- Surface salinity

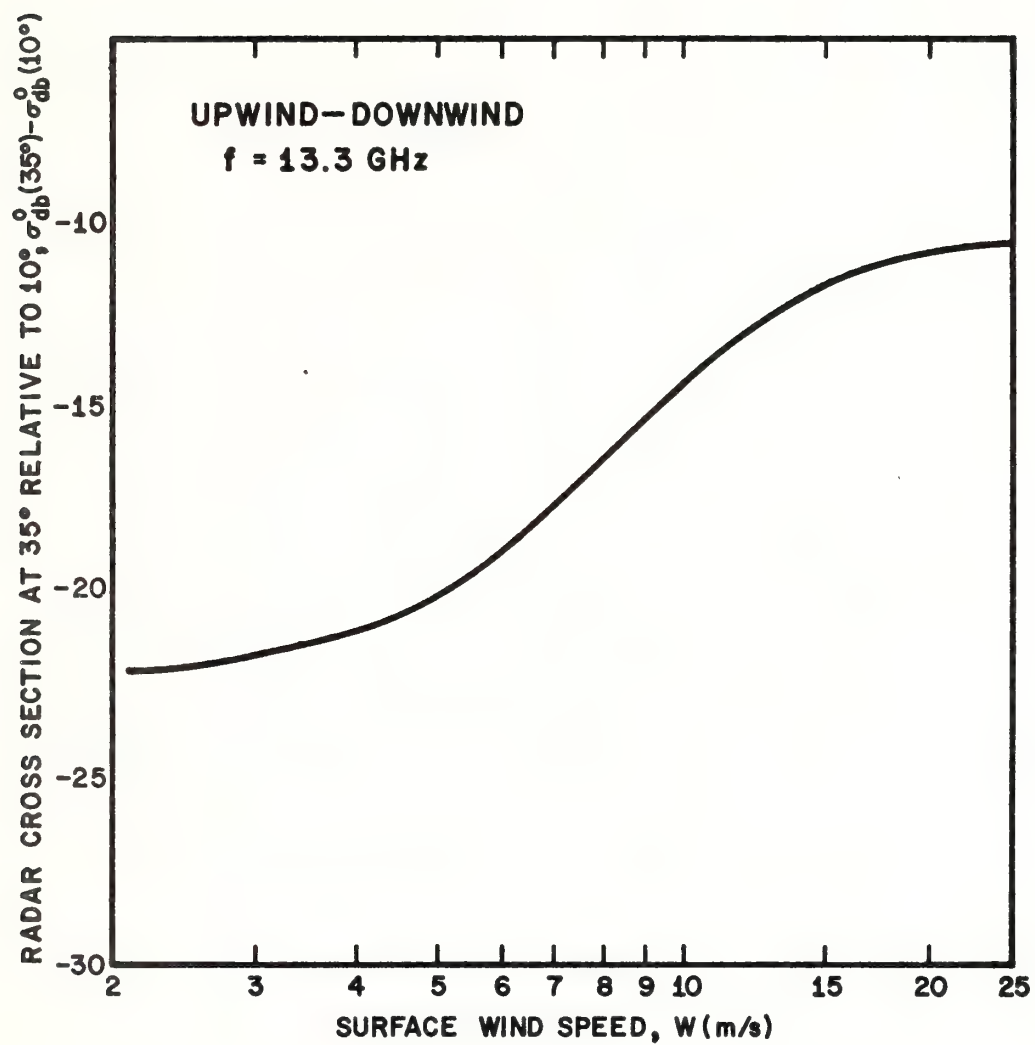
E. Scatterometer

The scatterometer function has been discussed earlier in the section on MICIR. Figure 10 gives a more quantitative estimate of its wind-measuring capabilities; it shows a smoothed and normalized functional dependence of the 13 GHz radar cross-section on surface wind speed. The scatterometer may apparently be used as an anemometer for wind speeds from near zero to some 15-20 m/sec, with only a second-order dependence upon sea state; the device thus complements the higher-wind anemometric capabilities of the microwave radiometer mentioned previously. It, too, is capable of functioning through clouds and light rain. The scatterometers to be flown on SKYLAB and under the NASA AAFE program should clarify the capability.

From satellite altitudes, interpretation of the scatterometer data is more complicated than from aircraft altitudes. At 1000-km altitude, a sweep of $\pm 35^\circ$ about nadir will span approximately ± 570 km of ocean surface, over which the surface wind field must be assumed uniform in order to interpret the scattering according to Figure 10; thus the cross-track scheme fails near storms. Instead, an alternate method is available that determines the scattering and hence wind from a narrow swath along the satellite track thus sacrificing areal coverage for higher resolution.

F. Bistatic Transmitter-Receiver

The bistatic arrangement uses a ship or buoy equipped with an MF/HF transmitter and a satellite with a receiver, in order to measure the ocean wave spectrum, including the significant wave height. Pulsed, swept radio waves of frequencies from approximately 3.5 to 30 MHz are Bragg-scattered off the ocean surface from



an elliptical annulus of order 100 km major radius surrounding the buoy and are received at the satellite along with the directly transmitted signal. The ocean wave spectrum is thus available as an environmental parameter from an in situ transmitting platform.

G. Laser Altimeter

Short-pulse lasers can be used from spacecraft to perform precision altimetry as a means of determining ocean surface topographic features. However, the limited pulse repetition rate of a few per second and the lack of ability to penetrate even modest cloud cover limit their usefulness in oceanographic applications. There appears to be some value in measuring cloud heights along the subsatellite path, however.

H. Vertical Tropospheric and Ionospheric Sounders

In order to correct the precision altitude measurement for tropospheric and ionospheric propagation effects, it is necessary to determine the atmospheric pressure and integrated water vapor content and electron density along the radar propagation path. It appears sufficient to use climatological values of pressure in the correction, but measured values of integrated water vapor are probably necessary to reduce the altitude component of error to below the ± 10 -cm level of precision. Existing vertical water vapor sounders ought to be adequate for the task and should be included in the sensor complement. If 25-cm radars are employed, a two-frequency ionospheric sounder may also be required.

I. Choice of Total Instrument Complement

It is obvious that the sensors listed above cannot all be flown on one spacecraft of moderate size. Thus, choices between sensors will have to be made at a relatively early point in the spacecraft definition phase. These choices will depend upon several users' priorities and will undoubtedly be arrived at by considerations of technical feasibility and suitability of the various instruments in meeting agency goals. The selection process may be assisted by the Summary of Sensors and Observables presented in Table III.

TABLE III

SUMMARY OF SENSORS AND OBSERVABLES

OBSERVABLES	SENSORS	IMAGING RADIOMETERS		SHORT PULSE ALTIMETER	IMAGING RADAR	SCATTEROMETER	BISTATIC TRANSMITTER
		Visible	Thermal IR				
Chlorophyll and Algae	P	-	-	-	-	-	-
Current Position	S	P	T	P	P	-	-
Current Velocity	-	-	-	P	P	-	-
Estuarine Circulation	P	P	-	-	-	-	-
Fish Stock Location	P	P	T	T	-	-	-
Fog	P	S	-	-	-	-	-
Icebergs	P	-	T	-	P	-	-
Ice Cover	P	S	P	T	P	-	-
Marine Geoid	-	-	-	P	P	-	-
Pollutant Identifi- cation	P	-	S	-	S	-	-
Salinity	-	-	P	-	-	-	-
Sea State & Swell	T	-	T	P	P	P	P
Sediment Transport	P	-	-	-	-	-	-
Set-up	-	-	-	P	P	-	-
Shallow Water	-	-	-	-	-	-	-
Bathymetry	P	-	-	-	T	-	-
Storm Surges	T	-	-	P	P	-	-
Surface Winds	-	-	P	S	S	P	S
Temperature	-	P	S	-	-	-	-
Tides	-	-	-	P	P	-	-
Tsunamis	-	-	-	P	P	-	-
Upwellings	P	-	S	-	-	-	-
Wave Spectrum	-	-	-	T	-	T	P

P= Primary
S= Secondary
T= Tertiary

V. SATELLITE MISSION PROFILES

The mission profile for an oceanographic satellite will be partially conditioned by the choice of sensors, which selections in turn reflect the goals that the system is expected to serve. These choices are also matters for interagency negotiation.

A. Orbit and Sensor Selection

The selection of an orbit is a case in point. If the ocean color sensor is to be successfully implemented, a sun-synchronous orbit is the only choice, because of the necessity for a near-constant solar illumination angle. However, it demands approximately a 2800-km sensor swath width in order to achieve daily, overlapping coverage; with sub-kilometer resolution, the accompanying data rates are prohibitively large under those circumstances. It appears that a two-day repeat cycle with a 1200-km swath is a compromise choice and that this width is compatible with both the IOCTIS and the MICIR imagers.

However, the sun-synchronous orbit has at least two disadvantages: 1) the sub-satellite point is always sampled at nearly the same local time, a sequence that could bias the data when observing diurnal effects in the ocean; 2) when performing altimetry from this orbit, the solar components of the earth and ocean tidal signal are aliased into the mean height (and hence into the geoid), an error that is probably on the order of 10-20 cm, or approximately one-sixth of the average mid-ocean tidal range. Thus only the lunar tides could be measured from a sun-synchronous orbit.

If a single satellite is to serve the oceanographic function, the importance to NOAA of color measurements from spacecraft brings down the orbit choice on the side of near or exact sun-synchronism --or thus polar, retrograde orbits, with an altitude choice in the range of 1000 km. Thus the lead instrument in this case is the IOCTIS, and the selection of microwave instruments would be conditioned by considerations of the users' secondary goals, weight, and power.

However, if more than one satellite is simultaneously available for ocean monitoring, the optimum mix of sensors will probably be one in which the microwave systems, both passive and active, find themselves on one platform and the ocean color sensor on another. The ocean color spacecraft should fly sun-synchronous as above, while the microwave-oriented spacecraft can then be orbited so as to precess through the entire day-night cycle during a few days and to remain equatorward of 75°-80° latitude.

Nevertheless, because of the genuinely synergistic effect that accrues from having several different types of sensors view the same phenomenon simultaneously, even a microwave-equipped satellite, in its research phases, should have visible and thermal infrared imagers on board. Such devices are indispensable for positioning currents and spatially interpolating between narrow altimeter swaths, as well as for interpretation of the microwave

signals in terms of currents, clouds, storm cells, land, and ice. A two-channel device such as the NOAA-2 Very High Resolution Radiometer should be adequate for this task. An operational satellite may or may not continue to carry them.

B. Coverage and Geographic Preference

The preferred geographical areas are the coastal waters contiguous to the U. S., out to distances of the order of 500 to 1000 km from shore, and first priority should be assigned there. The remaining systems capability, especially measurements of sea state and wind, can be assigned to the remainder of the world. Thus, any engineering trade-offs required should probably be resolved in favor of the coastal areas.

C. Lifetime

For a research satellite, a one-year lifetime is the minimum acceptable, with two to three years being preferred. Longer lifetimes are indicated for operational systems.

D. Data Requirements

The data rates of imaging sensors are very high, and great care must be exercised in order to request such data properly. Since only limited experience has accrued in sensing the ocean scene quantitatively, the present requirements tend to be somewhat arbitrary. Those measurement requirements found in Chapter III are felt to be proper for the individual observables listed there, but there are variations from feature to feature, so that compromises must be reached during more detailed engineering studies. The way in which a measurement requirement translates over into satellite data requirements is also different for each type of sensor; thus the specifications for the latter type of data must be deferred until selection of the sensors has been made.

In general, it appears difficult to handle routinely data rates above a few times 10^7 bits/sec in real time, even in a direct read-out mode, and therefore efforts to keep the system rate below that number should be made.

VI. INTEGRATION INTO AN ENVIRONMENTAL MONITORING AND PREDICTION SYSTEM

NOAA would expect to handle an oceanographic satellite system in much the same fashion as it now deals with its meteorological satellites--i.e., as a component of a larger observational system composed of surface, airborne, and spacecraft elements. The elements of the ocean system, termed OMAP for Ocean Monitoring and Prediction, are presently in the advanced planning stages. The satellite components would most likely be managed by the National Environmental Satellite Service, and the operational and forecasting functions by the National Weather Service; associated research programs would be undertaken by the Environmental Research Laboratories as well as other NOAA major line activities.

Present NOAA-NASA agreements relating to the research, prototype, and operational phases of the meteorological satellites would serve as guides in formulating the interagency arrangements needed to implement an oceanographic satellite system.

A truly global monitoring and prediction effort for the oceans would entail a significant enlargement of NOAA's responsibilities that would take place over a period of several years, as the system's capabilities warranted it.

VII. CONTRIBUTIONS TO NOAA'S MISSIONS

A. Impact on NOAA Services

It is obvious from both the Introductory section and from Table I of Chapter III that, in the areas of Ocean Resources and Environmental Monitoring and Prediction, an oceanographic satellite capable of the measurements previously discussed offers the potential for real advances in the quality and type of the services that NOAA renders. However, the associated surface systems--buoys, ships, aircraft, and ground stations--must be brought on line in concert with the spacecraft system in order to realize that potential. Most of these required systems are being developed at a rate that will make them available in the same time frame as the satellite component.

B. Contributions to the Performance of NOAA's Missions

The benefits to the nation that may ultimately be derived from an aerospace remote sensing system are as many-faceted as the impact of the ocean on the affairs of man. These generally fall in the categories of: protection of life and property along the coasts and at sea; safety and navigation of shipping; increased efficiencies in maritime operations; improved management of marine resources; and enhancement of the quality of the environment.

Examples of some of the factors that lead to such beneficences are given now.

1. Improved Weather Forecasting: Because of the large area of ocean compared to land and the coupled, nonlinear interactions between ocean and atmosphere, much of the world's weather is created over water or the polar regions. The combination of meteorological and oceanographic satellites should significantly assist in achieving the one- to two-week forecast that appears possible with an adequate, synoptic data base consisting of the kind of information derivable from satellites and surface measurements. The desirability of improved weather forecasts is reasonably obvious.

2. Hazard Warnings: While warnings of hurricanes, typhoons, and high seas have improved considerably with the meteorological satellite programs, it is still extremely difficult to predict, for example, the landfall of a tropical cyclone and the resultant storm surge to within 100 miles, in advance of 24 hours. With the increase in the numbers of people living along the coasts, the potential for loss of life and property has been magnified greatly. In the world's low-lying areas, earlier warning of severe hurricanes is absolutely essential to evacuate the population. Ocean-wide observations of air-sea interactions, surface temperature, wind, and sea state and an increased understanding of the storm surge process will constitute a large step forward in achieving the required warning.

Similarly, improved observations of both ice floes and icebergs would enhance warnings of these hazards by a significant degree. Wave refraction studies would lead to improved designs for harbor entrances, channels, and breakwaters. Actual observations of tsunami amplitudes near their sources would reduce the amount of overwarning that now often occurs.

3. Ship Route Forecasting: With the advent of new ship routes and the extremely large tankers now plying the seas, there is increasing economic and environmental value to optimum, safe ship routing based on sea state, current, and ice forecasts. Variations in transit times of up to six days are experienced by tankers sailing between Arabian oil ports and North American refineries, chiefly due to the Somali-Agulhas current systems and their vagaries under the influence of the Indian Ocean monsoon. In another vein, some 12 to 24 hours' reduction in transit time may be achieved on transoceanic voyages simply by avoiding areas of high sea state. In the area of shipping losses: recent loss rates for seagoing oil drilling rigs have averaged about five platforms and 50 million dollars per year, due to improperly forecast high sea states. The loss of one loaded supertanker per annum and the attendant environmental damage could cost roughly similar amounts. The total savings for world-wide shipping from improved routing, avoidance of breakage or ship loss, reduced insurance rates, and more precise scheduling potentially runs into nine-figure numbers of dollars per year.

The ship-of-opportunity program has established the value of environmental data to shipping interests. However, these data are primarily limited to the heavily traveled corridors of the sea. Satellite observations will yield data away from these corridors as well and thus allow forecasts of sea conditions with sufficient lead time to permit ships to take corrective actions by altering their routes appropriately. Surface-based observation programs will continue as a means of calibrating space systems to insure quality observations and as a way of acquiring otherwise unobtainable data.

4. Fish Stock Location and Environmental Assessment: The detection of environmental conditions--chlorophyll, temperature, salinity and turbidity--in which a particular species of fish is most likely to be found has been shown to be amenable to remote sensing techniques. The acquisition of multispectral imagery from the first Earth Resources Technology Satellite (ERTS-1) has demonstrated that certain water turbidity, color, and chlorophyll boundaries correlate with locations where menhaden fish were taken. These features or others, such as upwellings or plankton blooms, are readily defined by satellite data, so that combinations of ocean color, temperature, and salinity will aid in establishing those areas where specific species of fish are most likely to be found, thus reducing search time and enhancing the fish catch.

Direct detection of fish using photography or imagery is more appropriate for an aircraft than for satellite program. It is presently possible to envision a combined aircraft and satellite system to determine productivity of fishing areas of interest to the U. S., wherein environmental monitoring from the satellite specifies regions and boundaries along which aircraft may then search for specific fish. Predictive models based on satellite data could be used by resource managers and industry to significantly improve the forecasting of fish stocks and locations.

5. Pollution Monitoring: The direct detection of certain ocean pollutants such as sediments, acid wastes, sewage sludge, and ocean outfalls has also been accomplished using ERTS-1 images. It is expected that an optimized oceanographic sensor would be able to monitor these features with considerably more effectiveness than displayed by ERTS; furthermore, it is likely that oil spills can also be observed under the correct conditions. Thus monitoring of foreign substances in the ocean becomes a reality.

6. Advancement of Research: It has almost invariably been the case that the introduction of a significant new instrument technology has yielded for the science to which it was applied a number of unsuspected and often highly significant results. These serendipitous discoveries can surely be expected from an instrument as advanced as an oceanographic satellite. Oceanographers have never been able to gain the overview of their domain required to understand synoptic or planetary scale events in the sea; satellites promise to provide the vantage point for this vision.

Mass and Energy Transports in an Undisturbed Atlantic Trade-Wind Flow

ERNST AUGSTEIN—*Institute für Radiometeorologie und Maritime Meteorologie an der Universität Hamburg, Germany*

HERBERT RIEHL¹—*Department of Atmospheric Science, Colorado State University, Fort Collins, Colo.*

FEODOR OSTAPOFF—*Sea-Air Interaction Laboratory, Environmental Research Laboratories, NOAA, Miami, Fla.*

VOLKER WAGNER—*Institut für Radiometeorologie und Maritime Meteorologie an der Universität Hamburg, Germany*

ABSTRACT—The vertical and horizontal mass and energy transports for the layer between the sea surface and 700 mb are calculated for the first (undisturbed) period of the Atlantic Trade-Wind Experiment 1969. The trade-wind inversion represents a layer with a strong downward mass flux due to the mean motion. The height of the inversion and its thermodynamic properties seem to depend on the balance between the mean atmospheric sinking and the turbulent mixing.

Because of the vertical transport from the sea surface into the atmosphere, this process assures that water vapor is totally accumulated in the layer below the inversion and transported downstream into the equatorial trough region. Thus the effectiveness of the atmospheric heat absorption in the trades as a force for driving the large-scale circulation is closely related to the vertical static structure as well as to the kinematic field of the low-level trade-wind region.

1. INTRODUCTION

Studies by v. Ficker (1936) and Riehl et al. (1951) have shown that the low-level trade-wind regime over the oceans plays an important role in the atmospheric energy cycle. Further investigations, such as those by Riehl and Malkus (1957), Malkus (1958), Aspliden (1971) and Augstein (1972) have confirmed that there is a net gain of energy in the atmosphere between the sea surface and the trade-wind inversion. Malkus (1958) emphasized that the heating mechanism of the trade-wind circulation is determined by a complex interaction between microscale processes near the sea surface, meso-scale convection, and large-scale horizontal transports. This concept of scale interaction has drawn increasing attention during the last decade (Garstang 1972). Progress must depend, in part, upon investigations of the mass, heat, and water vapor fluxes in the entire planetary boundary layer in terms of different levels of atmospheric organization. This study concentrates on the turbulent and mean motion transports in the lower layers of the Atlantic trade-wind flow under relatively undisturbed conditions.

2. THE ATLANTIC TRADE-WIND EXPERIMENT (ATEX)

ATEX was conducted during February 1969 in the Atlantic Northeast trade-wind region. During this experiment, an intensive aerological program, concen-

trated in the lowest 4000 m of the atmosphere, was carried out from three ships (R.V. *Meteor*, R.V. *Planet*, and R.V. *Discoverer*). In the first period of the experiment, a fourth ship, HMS *Hydra*, also participated. *Meteor*, *Planet*, and *Discoverer* formed the corners of an equilateral triangle with sides of about 750 km. This ship array drifted for nearly 3 weeks in a well-developed trade-wind flow. The center of the triangle moved from 13.5°N, 34.7°W on February 6 to 9.5°N, 40.6°W on February 22 (fig. 1). The objectives of the program and details of the measurements are described by Brocks (1972).

Radiosonde and radar wind observations were obtained at the corners of the triangles simultaneously at 3-hr. intervals. Radiosonde releases without wind measurements were made from HMS *Hydra*. In addition to routine deck-level observations (temperature, humidity, wind velocity, cloudiness, etc.), which were carried out at least every 90 min, the turbulent surface fluxes were measured from buoys near *Meteor* and *Planet* by the profile method and the eddy correlation technique. The buoy data were also used as reference values to correct the ship's deck-level measurements for effects caused by the ship's environment.

It is important to note that the ships assembled on three separate occasions for the purpose of intercomparison and calibration. *Hydra* and *Meteor* had two test series of several hours, the first at the beginning of the drift and the second when *Hydra* left the array 14 days later. *Meteor*, *Planet*, and *Discoverer* met for a 1-day intercomparison at the end of the experiment. This com-

¹ Now at the Institut für Meteorologie, Freie Universität Berlin, Germany

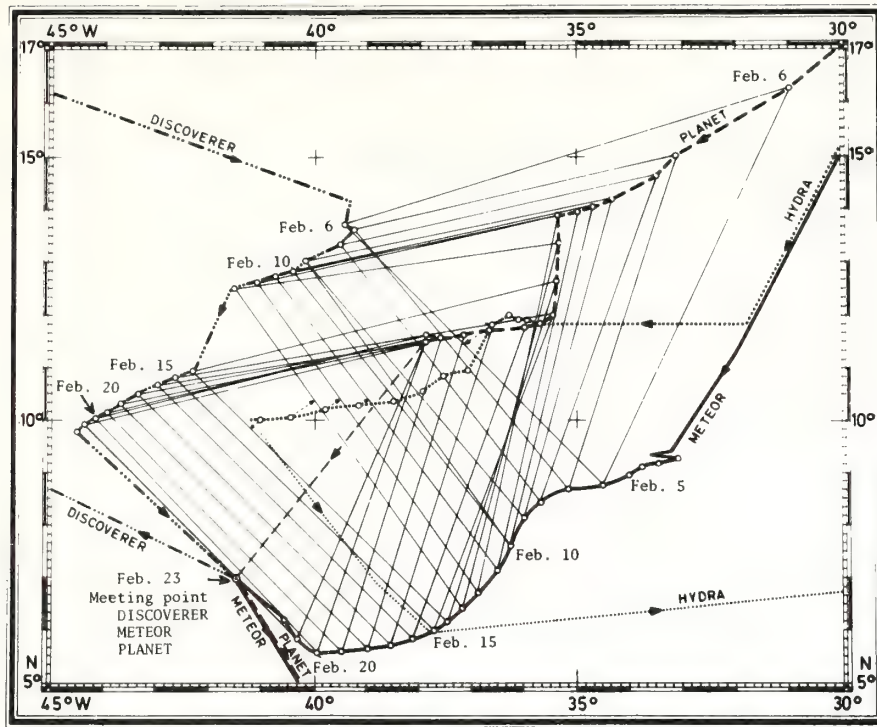


FIGURE 1.—Successive positions of the ATEX triangle Feb. 6–21, 1969. The thin, solid lines show the boundaries of the triangular base for each day.

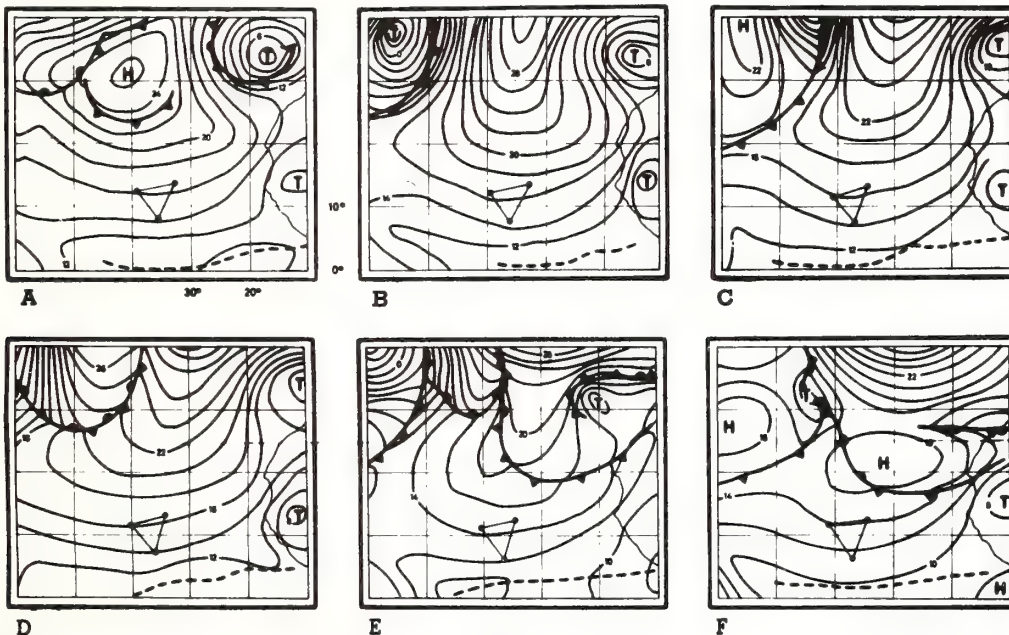


FIGURE 2.—Surface isobars (mb, last two digits only) for (A) Feb. 7, (B) Feb. 8, (C) Feb. 9, (D) Feb. 10, (E) Feb. 11, and (F) Feb. 12, 1969. ATEX triangle is indicated for each day. Conventional frontal symbols and dashed line for equatorial low-pressure trough have been entered.

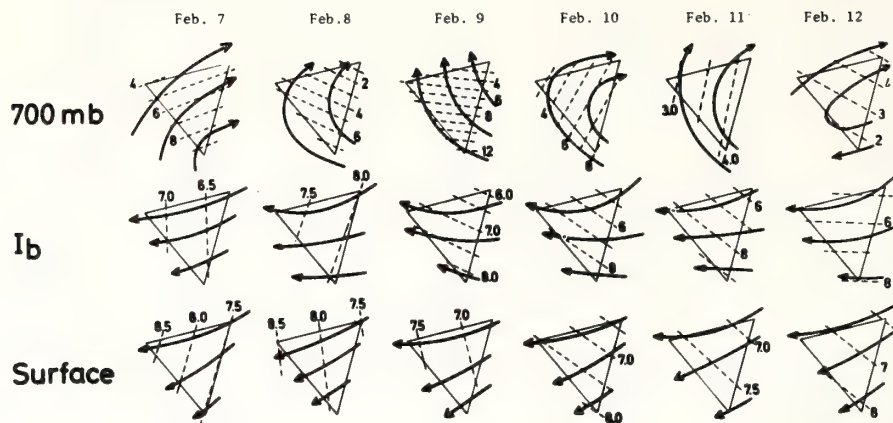


FIGURE 3.—Streamlines (solid) and isotachs (m/s, dashed) for surface, inversion base (I_b), and 700-mb level in the area of the ATEX triangle, Feb. 7–12, 1969.

parison showed substantial differences in the deck-level pressure and temperature readings of the three ships. These deck-level measurements are also used as baseline values for the radiosondes. Corrections based upon the intercalibration test were applied in the subsequent data reduction. The details of the procedures are discussed by Augstein et al. (1973) and Brümmer et al. (1973). Finally, simultaneously tracked balloon targets showed that the statistical noise of the three radars was different. Therefore, filtering methods were applied to achieve compatibility of soundings (Brümmer et al. 1973).

3. THE SYNOPTIC SITUATION

The observational period may be roughly subdivided into two parts. The first period (February 7–12), discussed in this paper, was governed by a well-developed northeast trade-wind flow. Convective activity was weak or absent in the entire area and the trade inversion could be detected in all radiosonde soundings.

The surface pressure field in figure 2, analyzed by Soltwisch (1973), demonstrates that the triangle was embedded in a nearly classical trade-wind situation. The steadiness of the wind field below the inversion may be seen from figure 3. The daily averaged streamline field between the sea surface and the inversion base hardly changed during this period. Air in this layer is always accelerated due to flow toward lower pressure. Contrary to the steady regime in the moist layer below the inversion, strong differences exist from day to day in the wind field above the inversion. These differences are illustrated on the 700-mb charts. The horizontal flow below and above the inversion appeared to be decoupled. This conclusion can also be drawn from the mean wind profile of the triangle in figure 4. While the lower layers were marked by a small standard deviation, time variations increased above the inversion. This is especially true for wind direction. Figure 4 also shows strongest wind speeds in the layer below cloud base. The directional shear was

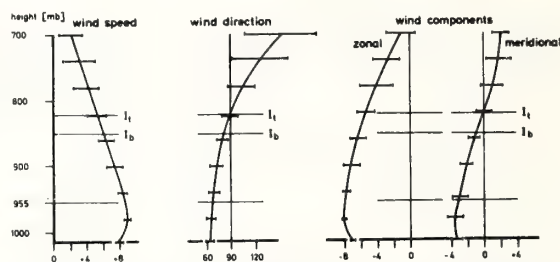


FIGURE 4.—Vertical profiles of wind speed (m/s) and wind direction (deg.) applicable at the center of the ATEX triangle and averaged over the period, Feb. 7–12, 1969. Bars indicate standard deviation and I_b and I_t denote inversion base and top, where the averaging has been performed with respect to the variable positions of the inversion in space and time.

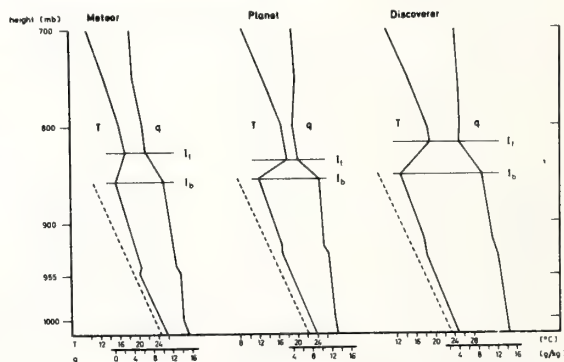


FIGURE 5.—Vertical profiles of temperature, T , and specific humidity, q , averaged as indicated in figure 4. Dashed line denotes dry-adiabatic lapse rate.

small below the inversion ($1^\circ/10$ mb) but increased rapidly in the upper layer ($7^\circ/10$ mb).

The averaged temperature and humidity profiles in figure 5, obtained by a smoothing technique that preserves

the layered trade-wind structure, are in good agreement with measurements of Bunker et al. (1950) and Augstein (1972) in other regions of the Atlantic trade-wind zone. At all ATEX positions, the temperature gradient in the lowest 500 m was almost dry adiabatic and the specific humidity nearly constant with height. The transition zone, characterized by a stable temperature distribution and strong water vapor decrease with height, that generally tops the mixed layer was not always present. This was especially true at the upstream position of *Planet* where it was found in only about 60 percent of the soundings. The inversion was stronger at *Planet* and *Discoverer* and weaker at *Meteor*, which was situated closest to the equatorial trough region (ETR). During the period under discussion, no precipitation was observed on *Planet* and *Discoverer*; only a few small showers were registered in the vicinity of *Meteor*. This fact justifies the assumption that no serious error is introduced if net condensation heating is neglected in the subsequent energy budget calculations.

4. THE ANALYSIS PROCEDURE

The Vertical Scale Subdivision and Averaging Procedures

Following earlier studies, we have divided the layer between the sea surface and 700-mb level into four sub-layers. The lowest one, the subcloud layer, is arbitrarily assigned a thickness of 60 mb, which is approximately supported by observations. Hence, the 955-mb level was taken as its upper boundary. The next layer, extending from 955 mb to the inversion base, is nearly identical with the cloud layer where trade-wind cumuli are usually found. Both the cloud layer and the overlying layer, which was defined by the top and the bottom of the inversion, were subject to much variation. Finally, the top layer is taken from the inversion top to the 700-mb level. Such a vertical subdivision (fig. 5) provides a framework within which we might gain some insight into the interrelation between the horizontal and vertical mass and energy transports and the respective layers of the trade-wind atmosphere. Statistical instrumental errors and small-scale turbulence are smoothed out by averaging each layer in the vertical and in time over 1 day (normally eight soundings). The time scale is also compatible with the scale size of the triangle in view of the mean wind speed.

The Budget Computations

The derivation of the energy equation based on the first law of thermodynamics and the equation of continuity is well known. Referring to unit mass we find

$$\frac{\partial}{\partial t} \rho \left(\frac{v^2}{2} + gz + c_p T \right) = -\text{div} \left[\rho \mathbf{V} \left(\frac{v^2}{2} + gz + c_p T \right) - F\mathbf{V} + \mathbf{R} + \mathbf{C} \right] \quad (1)$$

where $\partial/\partial t$ is the local derivative, ρ is air density, \mathbf{V} is the three-dimensional wind velocity, g is the acceleration of gravity, z is the vertical coordinate, c_p is specific heat at

constant volume, c_p is specific heat at constant pressure, T is temperature, div is the three-dimensional divergence, F is frictional stress, \mathbf{R} is the heat flux due to total radiation, \mathbf{C} is the heat flux due to molecular heat conduction, $c_p T$ is enthalpy, and $c_v T$ is internal energy.

In the following, we will consider kinetic energy, $v^2/2$, frictional force, F , and heat conduction, \mathbf{C} to be small compared to the other terms, assumptions that are supported by the observations.

Integrating eq (1) over a volume V and applying Gauss' theorem to the terms with geopotential energy and enthalpy, one obtains

$$\int_V \frac{\partial}{\partial t} \rho (gz + c_p T) dV = - \int_S \rho \mathbf{V} (gz + c_p T) \cdot \mathbf{n} dS - \int_V \text{div} \mathbf{R} dV \quad (2)$$

where S is the surface of the volume V , $\mathbf{n} = (i n_x + j n_y + k n_z)$ is the vector normal to the surface S and i, j, k are unit vectors of a Cartesian system.

Separating horizontal and vertical components of the first term on the right side of eq (2) and allowing the top and the bottom of the volume to have a slope with respect to the earth's surface, we get

$$\int_V \frac{\partial}{\partial t} \rho (gz + c_p T) dV = - \int_H \rho v (gz + c_p T) n_{xy} dH \quad (3a)$$

$$- \int_{F_t} \rho v (gz + c_p T) n_{xy} dF \quad (3b)$$

$$+ \int_{F_b} \rho v (gz + c_p T) n_{xy} dF \quad (3c)$$

$$- \int_{F_t} \rho w (gz + c_p T) n_z dF \quad (3d)$$

$$+ \int_{F_b} \rho w (gz + c_p T) n_z dF \quad (3e)$$

$$- \int_V \text{div} \mathbf{R} dV \quad (3f)$$

where n_{xy} is the horizontal component of the normal vector, n_z is the vertical component of the normal vector, H is the area of the vertical surface of the volume, F_t is the surface of the top of the volume, F_b is the surface of the bottom of the volume, v is the horizontal wind component, and w is the vertical wind component.

The terms on the right side of eq (3) have the following meaning:

- (3a) Horizontal flux through H .
- (3b) Horizontal flux through F_t .
- (3c) Horizontal flux through F_b .
- (3d) Vertical flux through F_t .
- (3e) Vertical flux through F_b .
- (3f) Divergence of \mathbf{R} in the specified volume.

The terms (3b) and (3c) refer to the flux through the top and the bottom of the volume established by the horizontal wind component. Therefore, if F_t and F_b are parallel to the earth's surface, terms (3b) and (3c) become zero. The equation for the water vapor budget correspond-

ing to eq (3) is expressed by

$$L \int_V \frac{\partial}{\partial t} (\rho q) dV = -L \int_H \rho v q n_{xy} dH \quad (4a)$$

$$-L \int_{F_i} \rho v q n_{xy} dF \quad (4b)$$

$$+L \int_{F_s} \rho v q n_{xy} dF \quad (4c)$$

$$-L \int_{F_i} \rho w q n_z dF \quad (4d)$$

$$+L \int_{F_s} \rho w q n_z dF \quad (4e)$$

$$-L \int_V (q_c - q_E) dV \quad (4f)$$

where q is specific humidity, L is latent heat of vaporization of water, q_c is the water vapor condensed in the volume V , and q_E is the evaporated water in the volume V .

The terms (4a)–(4e) represent the water vapor fluxes in the same way as enthalpy and geopotential energy fluxes are described in terms (3a)–(3e). Term (4f) represents the difference between water vapor loss by condensation and water vapor gain by evaporation within the volume. As already mentioned, however, virtually no precipitation was observed during the period, and there was little change in low-level cloudiness at all stations. Therefore, the last term of eq (4) can be neglected.

To consider mean and turbulent processes separately, we must distinguish between grid and subgrid transports. We therefore use the following notation for a property X :

$$X = \bar{X} + X' \text{ and } X = \tilde{X} + X^*$$

with

$$\bar{X} = \frac{1}{\Delta p} \int_p X dp \quad (\text{vertical average})$$

and

$$\tilde{X} = \frac{1}{F} \int_F X dF \quad (\text{surface average over } F, \text{ which can be the top and bottom of the volume})$$

Asterisked or primed quantities indicate the local deviations from the averages. Furthermore, we assume that the divergence of horizontal subgrid fluxes is small compared to the other terms and can be neglected. Finally, the terms (3a) and (4a) are, in practice, computed by averaging the vertically integrated properties along the connecting lines l_i between the ships. This average is marked by the double bar in eq (5) and (6). This procedure also implies linear changes of the mass flux as well as of other meteorological values. *Hydra*, lying approximately midway between the *Meteor* and the *Discorerer*, provided a partial check on the assumption of linearity, at least in the lower layers. No strong departures from linearity were observed in the data obtained by *Hydra*. Applying the above notation and additional assumptions to eq (3) and (4), we obtain eq

(5) for heat and geopotential energy and (6) for latent heat transports; that is,

$$\begin{aligned} \int_V \frac{\partial}{\partial t} \rho (c_p T + gz) dV &= \frac{1}{g} \sum_{i=1}^3 \overline{(\bar{c}_p \bar{T} + \bar{g} \bar{z}) \bar{v} n_{xy} \Delta \bar{p}}_{l_i} \\ &- [(c_p \tilde{T} + \tilde{g} z)_{\text{top}} \tilde{\rho} \tilde{v}_{\text{top}} n_{xy} F_{\text{top}} \\ &- (c_p \tilde{T} + \tilde{g} z)_{\text{bot}} \tilde{\rho} \tilde{v}_{\text{bot}} n_{xy} F_{\text{bot}}] \\ &- [(\tilde{\rho} \tilde{w})_{\text{top}} (c_p \tilde{T} + \tilde{g} z)_{\text{top}} n_z F_{\text{top}} \\ &- (\tilde{\rho} \tilde{w})_{\text{bot}} (c_p \tilde{T} + \tilde{g} z)_{\text{bot}} n_z F_{\text{bot}}] \\ &- [c_p (\tilde{\rho} \tilde{w})_{\text{top}}^* \tilde{T}_{\text{top}}^* n_z F_{\text{top}} - c_p (\tilde{\rho} \tilde{w})_{\text{bot}}^* \tilde{T}_{\text{bot}}^* n_z F_{\text{bot}}] \\ &- \int_V \text{div } \mathbf{R} dV \end{aligned} \quad (5)$$

and

$$\begin{aligned} L \int_V \frac{\partial}{\partial t} (\rho q) dV &= \frac{1}{g} \sum_{i=1}^3 \overline{(L \tilde{q} \tilde{v} n_{xy} \Delta \bar{p})}_{l_i} \\ &- L [(\tilde{\rho} \tilde{q}_{\text{top}} \tilde{v}_{\text{top}} n_{xy} F_{\text{top}}) - (\tilde{\rho} \tilde{q}_{\text{bot}} \tilde{v}_{\text{bot}} n_{xy} F_{\text{bot}})] \\ &- L [(\tilde{\rho} \tilde{w})_{\text{top}} \tilde{q}_{\text{top}} n_z F_{\text{top}} - (\tilde{\rho} \tilde{w})_{\text{bot}} \tilde{q}_{\text{bot}} n_z F_{\text{bot}}] \\ &- L [(\tilde{\rho} \tilde{w})_{\text{top}}^* \tilde{q}_{\text{top}}^* n_z F_{\text{top}} - (\tilde{\rho} \tilde{w})_{\text{bot}}^* \tilde{q}_{\text{bot}}^* n_z F_{\text{bot}}] \\ &- L \int_V (q_c - q_E) dV. \end{aligned} \quad (6)$$

$\Delta p = p_{\text{top}} - p_{\text{bot}}$ is the pressure at the top minus pressure at the bottom of the volume. Finally, the left sides of eq (5) and (6) are solved under the assumption that the top and bottom of the respective layer volumes may move vertically in time.

Thus, we obtain the relation

$$\begin{aligned} \int_V \frac{\partial}{\partial t} \rho (c_p T + gz) dV &= -\frac{1}{g} \int_F \frac{\partial}{\partial t} (\bar{c}_p \bar{T} + \bar{g} \bar{z}) \Delta p dF \\ &+ \frac{1}{g} \int_{F_{\text{top}}} \frac{dp_{\text{top}}}{dt} (c_p T + gz)_{\text{top}} dF \\ &- \frac{1}{g} \int_{F_{\text{bot}}} \frac{dp_{\text{bot}}}{dt} (c_p T + gz)_{\text{bot}} dF \\ &= -\frac{1}{g} \frac{\partial}{\partial t} (\bar{c}_p \bar{T} + \bar{g} \bar{z}) \Delta p F \\ &+ \frac{1}{g} \frac{dp_{\text{top}}}{dt} (c_p T + gz)_{\text{top}} F_{\text{top}} \\ &- \frac{1}{g} \frac{dp_{\text{bot}}}{dt} (c_p T + gz)_{\text{bot}} F_{\text{bot}} \end{aligned} \quad (7)$$

and

$$\begin{aligned} \int_V \frac{\partial}{\partial t} (\rho q) dV &= -\frac{L}{g} \frac{\partial}{\partial t} \tilde{q} \Delta \bar{p} F + \frac{L}{g} \frac{dp_{\text{top}}}{dt} \tilde{q}_{\text{top}} F_{\text{top}} \\ &- \frac{L}{g} \frac{dp_{\text{bot}}}{dt} \tilde{q}_{\text{bot}} F_{\text{bot}}. \end{aligned} \quad (8)$$

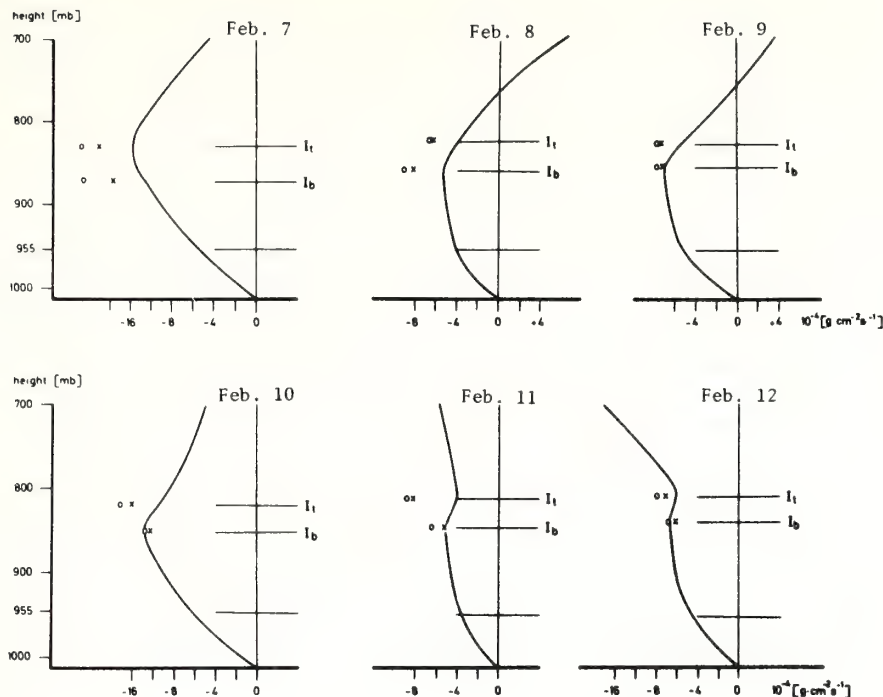


FIGURE 6.—Vertical mass transport averaged on each day for the center of the triangle. The crosses indicate the sum of vertical mass transport due to the vertical motion and the exchange between the layers above and below the inversion (due to the inversion slope in space). The open circles show the total mass transport through the inversion boundaries, including the effect of the vertical movement of the boundaries in time.

Combining eq (5) and (6) with (7) and (8), respectively, we can estimate the mean transports through the surface of the volume, and the local changes, after determining the mean vertical motion \bar{w} . Mean vertical velocity was computed by the kinematic method.

The mass budget was computed by integration of the equation of continuity, assuming stationarity (i.e., $\partial\rho/\partial t=0$). The turbulent, vertical, sensible, and latent heat fluxes are estimated as residuals from the combined eq (5) and (7) and (6) and (8), respectively. The turbulent fluxes at the sea surface were computed by the aerodynamic bulk formulas at each ship and averaged for the triangle. Simultaneous measurements of fluxes by the profile method at *Meteor* have shown that the difference of the daily averages of both values is less than 10 percent.

5. THE MASS TRANSPORT AND MEAN VERTICAL MOTION

In an early study, v. Ficker (1936) suggested that the trade-wind inversion is a layer that separates the air masses embedded in the flow above and below the inversion. Riehl et al. (1951) have clearly shown from measurements over the Pacific Ocean that, dynamically, this assumption cannot be accepted. On the contrary, these authors found that there is a net mass transport downward through the inversion. These results, however, were based on one-

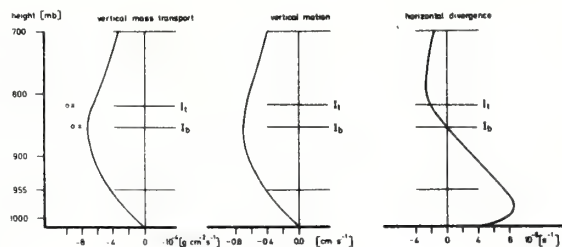


FIGURE 7.—Vertical mass transport, vertical motion, and horizontal divergence for the center of the triangle averaged over the period, Feb. 7-12, 1969.

dimensional divergence computations. The triangular ship arrangement during ATEX offered an opportunity to determine the vertical mass transport in the low-level trade-wind layer without serious restrictions. The results of the daily averaged mean downward mass transports are shown in figure 6. In this graph, the vertical subsidence and the mass flux through the boundary due to the slope effect and the height changes of the inversion are separated. On all days, the curves demonstrate that there is a downward mass transport through the whole regime with a maximum value at the inversion base, decreasing upward and downward. This result implies that the trade

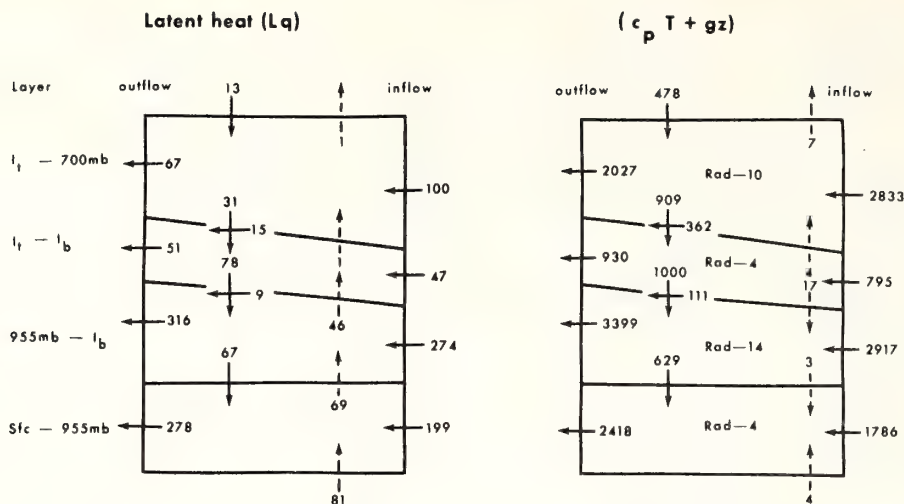


FIGURE 8.—Budgets of latent heat (10^{10} cal/day), and of enthalpy plus geopotential energy (10^{16} cal/day), for the subcloud layer, the cloud layer, the inversion layer, and the layer above the inversion up to 700 mb for the ATEX triangle, Feb. 7–12, 1969. Full arrows indicate transports by the mean motion; broken arrows, the residual turbulent fluxes. Radiation sink is indicated in the sensible heat budget; the net latent heat release is zero for the moisture budget.

inversion is not a solid layer but marks a region of an extremely strong, mean downward mass transport.

The general characteristics of vertical mass flux, vertical motion, and horizontal divergence are clearly reflected in the 6-day average profiles shown in figure 7. Obviously, the layer between the sea surface and the inversion base is governed by a remarkable horizontal divergence while the upper zone, between the inversion base and 700 mb, shows a slight convergence. The strongest horizontal divergence appears to be at approximately 985 mb, where the wind speed also has its maximum.

The coincidence between the inversion base and non-divergence seems to be systematic. Thus, air particles are vertically accelerated downward above and decelerated below the inversion base due to the mean vertical motion field. This is approximately true for every day as may be seen from figure 6.

The inversion height is variable in time, but this layer does not migrate progressively downward with the mean motion. It must, therefore, be balanced by an upward-directed process. As demonstrated by Ball (1960) using meteorological measurements and by Rouse and Dodu (1955) based on laboratory experiments, the most plausible process seems to be upward turbulent mixing leading to the establishment of the inversion base. Since this height generally coincides with the top of trade-wind cumuli, it is suggestive that mainly cumulus convection will achieve the required mixing (Riehl et al. 1951). This argument is reinforced by the water vapor and heat budget calculations presented in the following section. The total mass transport through the inversion boundaries is achieved not only by the large-scale vertical sinking but additionally by the vertical motion of the inversion itself and by its horizontal slope. As indicated in figure 7, these

effects increase the downward mass transport through this layer. During the analyzed period, about one-half of the mass within a column between sea surface and inversion base moving downstream was replaced daily by dry air masses from above. This fact is highly important for water vapor accumulation and cloud development in the lower layers.

6. THE HEAT BUDGET

The Total Budget

The heat budget estimates of the low-level ATEX column are based on the mass transport discussed in section 5 and on the temperature and humidity profiles measured at the corners of the triangle. The transports through the horizontal and vertical surfaces of the different layers averaged over the 6-day period are presented in figure 8. The subgrid-scale fluxes (dashed arrows) are determined as a residual in the budget equations for each horizontal surface of the four layers from the surface to the 700-mb level upward. The radiative cooling was estimated from computations using formulas of Rodgers and Walshaw (1966) for the long-wave component and those from Roach (1961) for the short-wave part. Although a rough correction for cloudiness is made, these values should be considered tentative. However, more precise calculations should not significantly change our results. The numbers, given in 10^{16} cal/day, refer to the surface of the triangular column with a mean base area of $2.2 \times 10^5 \text{ km}^2$. The calculated inflow and outflow values show that there is a horizontal divergence of energy below and a convergence above the inversion layer.

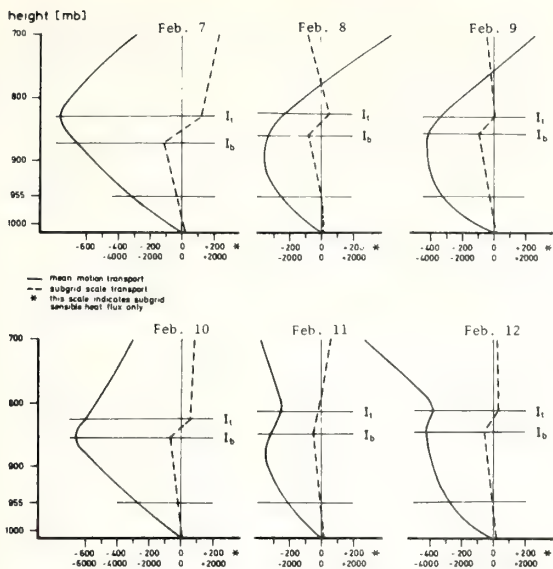


FIGURE 9.—Daily values of the vertical flux of enthalpy plus potential energy (ly/day), notation as in figure 8. The abscissa denoted by asterisks refers to subgrid-scale sensible heat fluxes.

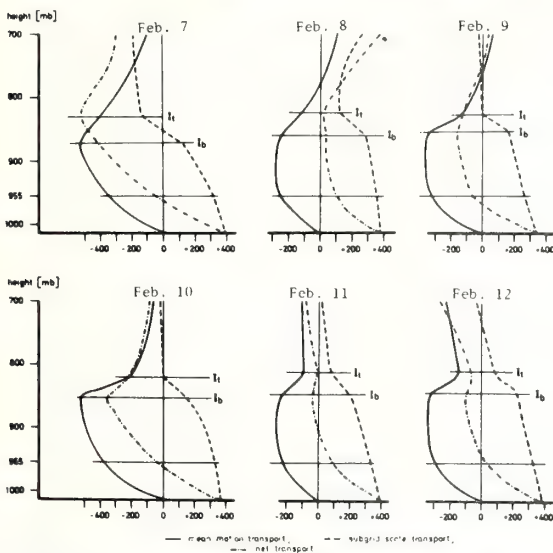


FIGURE 10.—Daily values of the vertical flux of latent heat (ly/day). The dash-dotted line represents the actual transport required for moisture balance.

Vertical Fluxes of Enthalpy and Geopotential Energy

The vertical transports of enthalpy and geopotential energy are portrayed in more detail in figure 9. The shape of the mean downward transport curve is generally governed by a maximum at the inversion. Thus, the low

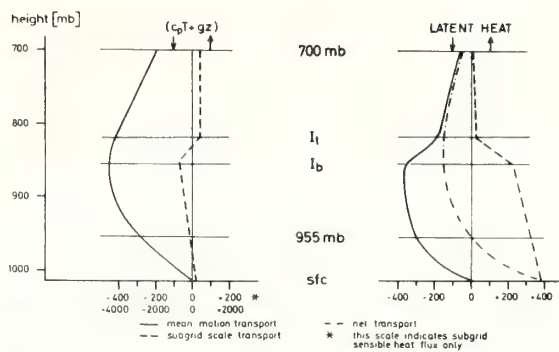


FIGURE 11.—Transports of enthalpy plus potential energy (ly/day), and of latent heat (ly/day), averaged for the period, Feb. 7-12, 1969. Notation as in figures 9 and 10.

troposphere does not receive the major portion of this energy component from the sea surface in any direct sense. Instead, there is an interplay of energy transformation and transport that finally results in the dry downward sinking of air mass in this part of the trades. Although this fact is of great importance to the physical processes in the lower atmosphere, it cannot be interpreted as a net input of energy into the atmosphere at all. Instead, we are observing only one scale of an interacting system. The primary energy source must be attributed to the large convective systems with strong cumulonimbi development, especially in the equatorial trough region. Gray (1971), among many others, recently stated the importance of the heating mechanism due to moist upflow and dry downflow of air.

The residual subgrid flux of sensible heat is a result of a small difference between large quantities. It, therefore, includes a degree of uncertainty. However, we believe that this result supports the conclusion that a balance of our computed $(c_p T + gz)$ budget can be achieved, resulting in reasonable subgrid-scale fluxes.

Vertical Fluxes of Latent Heat

The daily averaged mean downward fluxes of latent heat in figure 10 display similar characteristics to those of $(c_p T + gz)$; but, here, the subgrid-scale values are of the same order of magnitude as the mean transports. The evaporation rate at the sea surface nearly equals the downward water vapor transport due to mean motion at the inversion base. The graphs for the individual days are obviously in good agreement. Therefore, the dominant features will become particularly clear in the profiles averaged over the whole period (fig. 11).

With respect to the vertical latent heat transport, we find an interesting relation between the large-scale and the subgrid-scale fluxes. About 55 percent of the evaporated water at the sea surface is transported upward into the inversion layer by subgrid-scale processes. The rate of upward transport depends on an equilibrium between mean downward sinking and upward

turbulent mixing, which constantly reestablishes and determines the inversion base. Convergence of water vapor in the inversion layer is counteracted by the downward transport accomplished by mean subsiding air in opposition to the upward convective transport of the cloud elements. In fact, there is an additional net moisture input from above the inversion into the cloud layer. Thus, the total input of latent heat from the sea surface is accumulated in the cloud and subcloud layer and transported horizontally into the equatorial trough region.

The Horizontal Transports of Sensible and Latent Heat

The work by v. Ficker (1936), which is based on the *Meteor* observations obtained in 1925–27 and many other studies, indicates clearly that there is a substantial meridional transport of sensible heat, geopotential energy, and water vapor in the direction of the equatorial trough region in the whole trade-wind area. Those findings are supported by our measurements.

Figure 12A shows the downstream transports at the center of the ATEX triangle. The length of the thick horizontal lines indicates the flux magnitude per day across a vertical surface with a base line of 1 cm and the height of the layer. The strongest transports occur in the layer below the inversion. The percentage numbers indicate that portion of latent heat or enthalpy and geopotential energy which contributes to the total transport by horizontal divergence within a column with a length of 500 km. This distance is traversed by an air parcel in about one day. The minus sign means horizontal convergence; that is, the horizontally transported air loses energy. Evidently, the largest gain of energy in the trades is found in the subcloud layer. The layers above the inversion base lose energy downstream.

The zonal and meridional components of the transports, as seen in figure 12B, suggest a strong meridional flow toward the Equator in the lower layers where energy is accumulated, a small equatorward flow in the inversion layer, and a poleward flow above the inversion where energy is extracted. Under these conditions, therefore, a portion of the northwestward transported energy above the inversion moves downward and contributes again to the low-level flow. The region between the sea surface and the trade inversion under undisturbed conditions acts like a channel with a semipermeable top and bottom (with respect to energy) where large amounts of energy are accumulated and transported into the equatorial trough region.

Some Aspects of the Turbulent Flux Mechanisms

While the fluxes at the sea surface were measured or computed by the bulk aerodynamic formulas, the vertical distribution of subgrid-scale fluxes beyond that point could be determined only as a residual of the budget cal-

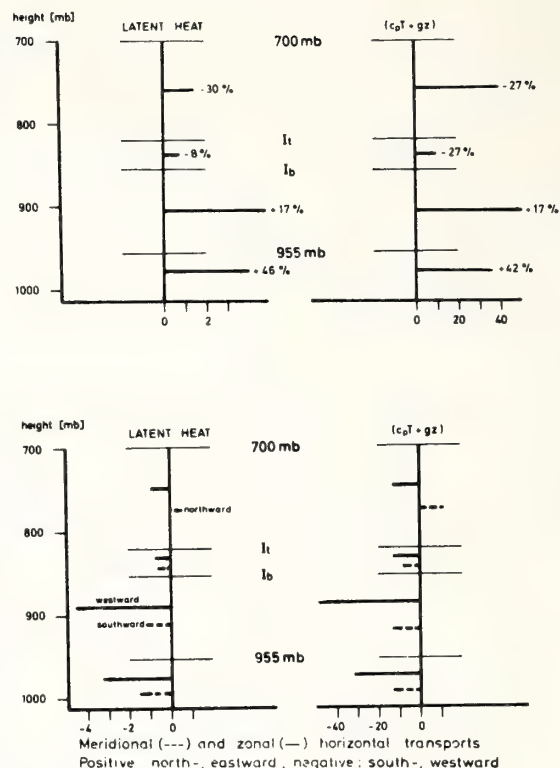


FIGURE 12. —Horizontal, layer-integrated energy transport (10^{10} cal·day⁻¹·cm⁻¹): (A) total downstream transports across a surface with a base line of 1 cm and the height of the layer [percentages indicate the effects of horizontal divergence (+) or convergence (-) relative to the total transport when integrated over a steady-state trajectory of 500-km length] and (B) meridional and zonal transports (positive toward north and east).

culations. Information concerning the mechanisms achieving these transports was not obtained in ATEX, but some qualitative arguments can be offered from the temperature and specific humidity profiles.

In agreement with earlier studies, we find nearly constant potential temperature and small gradients of specific humidity in the layer between 100 and about 500 m. Therefore, microscale processes, as described by the Austausch concept, can hardly be responsible for the vertical turbulent fluxes in this layer. This argument is furthermore supported by the fact that 35 percent of all soundings during ATEX have a constant or even an increasing specific humidity with height in that layer. Hence, organized processes such as dry convection must achieve the subgrid-scale upward transports in the subcloud layer as suggested by Garstang et al. (1970).

As far as the cloud layer is concerned, there is little doubt that cumulus convection is the governing mecha-

nism in the vertical transport of latent and sensible heat. The upward turbulent water vapor flux breaks down in the inversion, where cumulus convection terminates. This fact explains the considerable upward subgrid-scale transports of water vapor into the inversion as well as the strong decrease within the inversion layer. Cumulus convection penetrating the inversion base also permits the calculated downward transport of sensible heat to exist at the inversion base. Such downward transport may be accomplished by at least two processes. On the one hand, cloud air in the inversion is potentially colder than the sinking environmental air; on the other hand, liquid water evaporating in the inversion layer effectively represents downward transport of sensible heat.

A test should be conducted to determine whether or not the large upward turbulent transport of 68×10^{16} cal/day can be accomplished by the cumulus clouds in the convective layer just above cloud base.

The whole area $A = A_a + A_c + A_d$, where A_a is the area of actively ascending towers, A_c is stationary decaying cloud matter, and A_d is the clear area of compensatory descent. From climatic charts and ship observations during ATEX, we find that

$$A_d = A_a + A_c. \quad (7)$$

The upward flux of water vapor by turbulent motions, F_q , is given by

$$F_q = (\rho_{wa} w_a A_a + \rho_{wd} w_d A_d) L \quad (8)$$

if $w=0$ in the area A_c , L is the latent heat of vaporization, w_a is the rate of ascent in the towers, ρ_{wa} and ρ_{wd} are the water vapor densities of the upward- and downward-moving air masses, respectively, and w_d is the rate of descent in the clear area. Since $q = \rho_w / \rho$, eq (8) becomes

$$F_q = \rho(q_a w_a A_a + q_d w_d A_d) L. \quad (9)$$

Here, it is assumed with little error that $\rho_a = \rho_d = \rho$, which follows from $T_a = T_d$ as demonstrated by many aircraft traverses through small cumuli. The equation of mass continuity is given by

$$w_a A_a + w_d A_d = 0 \quad (10)$$

where w_d is additional to the downward mean mass flow discussed earlier. Combining eq (10) and (9), we get

$$F_q = -\rho w_d A_d (q_a - q_d) L$$

or

$$-w_d = \frac{F_q}{\rho A_d (q_a - q_d) L}. \quad (11)$$

By inserting the numbers $F_q = 68 \times 10^{11}$ cal/s, $\rho = 1.1 \times 10^{-3}$ g·cm⁻³, $A_d = 10^{15}$ cm², $L = 600$ cal/g and $q_a - q_d = 2.5$ g/kg, where q_d is the mean specific humidity of the soundings and q_a is the saturation specific humidity at the average temperature, we find that $w_d = -4$ cm/s. This is larger than that obtained by Riehl et al. (1951) because in our case $q_a - q_d$ is much smaller. Nevertheless, the value falls entirely within the reasonable range.

We now wish to compute A_a , given a reasonable estimate of w_a , to see if only a small fraction of the whole area is covered by actively rising towers as observed. Using time-lapse photographs, we estimated w_a to be 1 m/s for trade-wind cumuli. With this value,

$$\frac{A_a}{A} = -\frac{w_d}{w_a} \frac{A_d}{A} = 0.02$$

a very small fraction indeed. We see, therefore, that the normal trade-wind atmosphere can indeed easily produce the transport of water vapor required by our budget calculation. These findings support those of Riehl et al. (1951).

7. CONCLUSIONS

The measurements during ATEX have shown that, under well-developed trade-wind conditions with little convective activity, the trade-wind inversion separates a low-level horizontal divergent layer from a convergent regime above. The maximum divergence tends to coincide with the maximum wind speed near the 400-m height. Using an average of 6 days, we found downward motion over the height range between the sea surface and the 700-mb level over the whole region. Maximum downward motion of about 600 m/day is found at the inversion base. Thus, the inversion is not a solid barrier to the vertical mass and energy transports; it is instead a region of maximum downward fluxes due to mean motion. On the other hand, there is a remarkable vertical subgrid-scale flux of moisture in the layer between the sea surface and the inversion. The turbulent water vapor fluxes into the inversion from below are relatively strong, but they are suppressed in the inversion layer and become nearly zero at its top. This flux convergence counteracts the drying effect of the mean downward motion and preserves the strong humidity gradient in the inversion layer. Furthermore, the combination of mean downward and turbulent upward water vapor flux in the lower layers ensures that the total latent heat input from the sea surface is, in fact, accumulated and transported downstream in the trade-wind flow below the inversion. The warm dry air from above, with its capability to absorb large quantities of water vapor, prevents condensation in the low-level trade-wind air and, therefore, guarantees that a large amount of latent heat is transported from the trade-wind areas into the equatorial trough region.

The upward latent heat flux and the downward sensible heat flux at the inversion base support the contention that cumulus convection is the predominant means of turbulent transfer at this level. Under these undisturbed conditions, the kinematic field and the static structure of the layer below the inversion are marked by only small time and space variations, in contrast to the layer above the inversion.

ACKNOWLEDGMENTS

We wish to thank our colleagues in each of the participating institutions who carried out much of the work during the field experiment and subsequently in the reduction of the data. In particular,

we wish to acknowledge the assistance of A. Ottke for programming and B. Brümmer for the radiation calculations. We are grateful to M. Garstang for fruitful discussions, which proved helpful in the final presentation of our results. Finally, we are deeply indebted to the late K. Brocks, the coordinator of ATEX, who encouraged and supported this international cooperative effort.

This investigation was sponsored by the Deutsche Forschungsgemeinschaft (German Science Foundation) and supported by the U.S. Department of Commerce, National Oceanic and Atmospheric Administration.

REFERENCES

- Augstein, Ernst, "Mass and Heat Budget Estimations of the Atlantic SE Trade Wind Flow at the Equator," *Meteor-Forschungsergebnisse*, Ser. B, No. 8, Borntrager Verlag, Berlin, Germany, **1972**, pp. 31-41.
- Augstein, Ernst, Hoerber, H., and Krügermeyer, L., "Fehler bei Temperatur-, Feuchte- und Windmessungen auf Schiffen in tropischen Breiten," *Meteor-Forschungsergebnisse*, Ser. B, No. 9, Borntrager Verlag, Berlin, Germany, **1973** (in press).
- Aspliden, C. I., "On Energy Distribution in the Tropical Troposphere," *Dissertation*, Florida State University, Tallahassee, **1971**, 232 pp.
- Ball, F. K., "Control of Inversion Height by Surface Heating," *Quarterly Journal of the Royal Meteorological Society*, Vol. 86, No. 370, London, England, Oct. **1960**, pp. 483-494.
- Brocks, Karl, "Die Atlantische Expedition 1969 (GARF) mit dem Atlantischen Passat Experiment (APEX)," *Meteor-Forschungsergebnisse*, Ser. A, No. 9, **1972**.
- Brümmer, Burghard, Ostapoff, F., and Schmidt, H., "The Aerological Measurements During ATEX," *NOAA Technical Report 1973* (in press).
- Bunker, Andrew F., Haurwitz, B., Malkus, J. S., and Stommel, H., "Vertical Distribution of Temperature and Humidity Over the Caribbean Sea," *papers in Physical Oceanography and Meteorology*, Massachusetts Institute of Technology and Woods Hole Oceanographic Institution, Vol. 11, Mass., **1950**, pp. 1-82.
- Ficker, H. v., "Bemerkungen über den Wärmestrom innerhalb der Passatzirkulation," Verlag Akademische Wissenschaften, Berlin, Germany, **1936**.
- Garstang, Michael, La Seur, Noel E., Hadlock, R., "Results From a Comprehensive Tropical Field Experiment," *Proceedings of the International Conference on Tropical Meteorology, June 2-11, 1970*, University of Hawaii, Hawaii, **1970**, pp. 1-7.
- Garstang, Michael, "A Review of Hurricane and Tropical Meteorology," *Bulletin of the American Meteorological Society*, Vol. 53, No. 7, July **1972**, pp. 612-630.
- Gray, William M., "The Magnitude of and the Fundamental Role of the Up-moist and Down-dry Vertical Circulation of the Troposphere," paper presented at the VII Technical Conference on Hurricanes and Tropical Meteorology, December 6-9, 1971, Barbados, West Indies, **1971**.
- Malkus, Joanne S., "On the Structure of the Trade Wind Moist Layer," *papers in Physical Oceanography and Meteorology*, Massachusetts Institute of Technology and Woods Hole Oceanographic Institution, Vol. 13, No. 2, **1958**, pp. 1-48.
- Riehl, Herbert, Yeh, C., Malkus, Joanne S., and La Seur, Noel E., "The North-east Trade of the Pacific Ocean," *Quarterly Journal of the Royal Meteorological Society*, Vol. 77, No. 334, London, England, Oct. **1951**, pp. 598-626.
- Riehl, Herbert, and Malkus, Joanne S., "On the Heat Balance and Maintenance of the Circulation in the Trades," *Quarterly Journal of the Royal Meteorological Society*, Vol. 83, No. 355, London, England, Jan. **1957**, pp. 21-29.
- Riehl, Herbert, and Malkus, Joanne S., "On the Heat Balance of the Equatorial Trough Zone," *Geophysica*, Vol. 6, No. 3/4, Helsinki, Finland, **1958**, pp. 503-538.
- Roach, W. T., "The Absorption of Radiation by Water Vapor and Carbon Dioxide in a Cloudless Atmosphere," *Quarterly Journal of the Royal Meteorological Society*, Vol. 87, No. 373, London, England, July **1961**, pp. 364-373.
- Rodgers, C. D., Walshaw, S. D., "The Computation of Infrared Cooling Rate in Planetary Atmospheres," *Quarterly Journal of the Royal Meteorological Society*, Vol. 92, No. 391, London, England, Jan. **1966**, pp. 67-92.
- Rouse, H., and Dodu, J., "Turbulent Diffusion Across a Density Discontinuity," *La Houille Blanche*, Vol. 10, No. 4, **1955**, pp. 522-532.
- Soltwisch, D., "Die synoptische Wetterlage über dem tropischen Nordatlantik während der Atlantischen Passat Experimente (ATEX/APEX) in Februar 1969 und Zusammenhänge zwischen großräumigen Vorgängen und dynamischen Prozessen der planetarischen Grenzschicht," Thesis, Fachbereich Geowissenschaften, Freie Universität Berlin, Germany, **1973** (in preparation).

[Received August 10, 1972; revised January 16, 1973]

UPPER AIR SOUNDINGS DURING
ATLANTIC TRADE-WIND EXPEDITION (1969) (ATEX)

B. Brümmer, F. Ostapoff, and H. Schmidt

1. INTRODUCTION

In February 1969, an experiment was conducted in the North Atlantic trade-wind region with the primary objective to obtain meteorological observations suitable for divergence calculations as well as budget studies. Results have been reported by Augstein, Ostapoff, Riehl, and Wagner (1971) and by Augstein, Riehl, Ostapoff, and Wagner (1973). The present publication describes the various correction techniques and data reduction schemes and presents the collected data which may be useful to anyone undertaking his own study.

Participating nations in the Atlantic Trade-wind Experiment (ATEX) were: the Federal Republic of Germany which provided the research ships *Meteor* and *Planet*, the United Kingdom which provided the hydrographic ship *Hydra*, and the United States which provided the research ship *Discoverer*. Principal organizations involved in the project were: the Meteorological Institute and the Institute of Radiometeorology and Maritime Meteorology of the University of Hamburg; the Sea-Air Interaction Laboratory of the Atlantic Oceanographic and Meteorological Laboratories, Environmental Research Laboratories, National Oceanic and Atmospheric Administration in Miami, Fla.; and the Hydrographic Office of Her Majesty's Royal Navy and the Meteorological Office in London.

The four ships were positioned to span a triangle with sides about 700 to 750 km long. The location and configuration of the triangular array are shown in figure 1. The size of the triangle was chosen so that divergences could be calculated from routine upper air data. The *Discoverer*, *Meteor*, and *Planet* were equipped with the Selenia Meteor M200 radar for balloon tracking; the antennas were mounted on gyrostabilized platforms on the first two ships, while the *Planet* system removed the ship's motion electronically. Because the *Hydra* did not have wind-finding equipment, it was decided that she would conduct a radiosonde program in the middle of the baseline spanned by the *Discoverer* and *Meteor*.

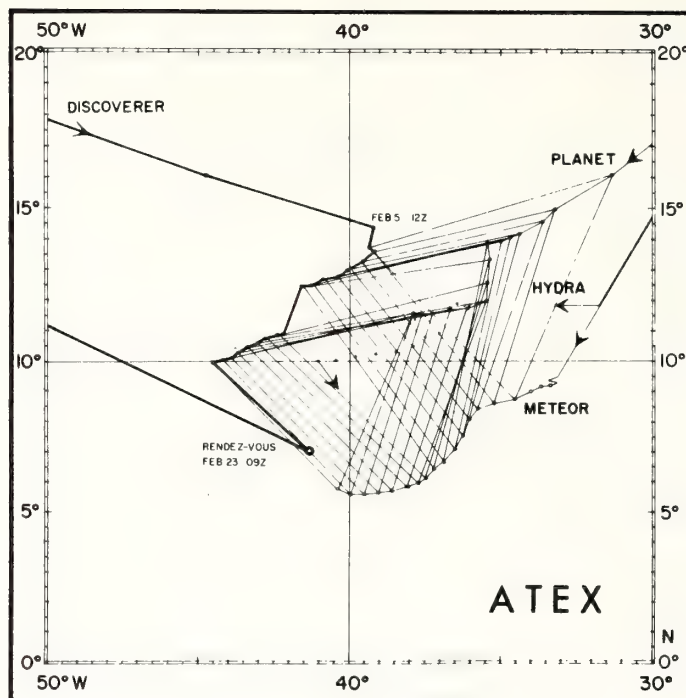


Figure 1. Drift positions of the four ships--Discoverer, Meteor, Planet, and Hydra--participating in ATEX, February 5-23, 1969.

The time schedule of balloon releases was designed to allow the delineation of the semidiurnal pressure wave which is very pronounced in these latitudes. Figure 2 shows schematically the pressure wave as a function of mean local time and the times of the balloon releases. Eight ascents a day were made.

On the *Discoverer* at each ascent, a train was released on a 600-gm balloon (see fig. 3) consisting of two U.S. 403-MHz radiosondes and a radar target. Near 400-MHz, one radiosonde was continuously transmitting relative humidity, interrupted by every fifth contact point (low reference) of which every third one above 30 is high. The other radiosonde, operated at approximately 407 MHz, was continuously recording temperature; it was again interrupted by reference points in the same manner as the humidity radiosonde. Two separate receivers and recorders in the meteorological laboratory were used to record the data on strip charts at a speed of 1 in./min.

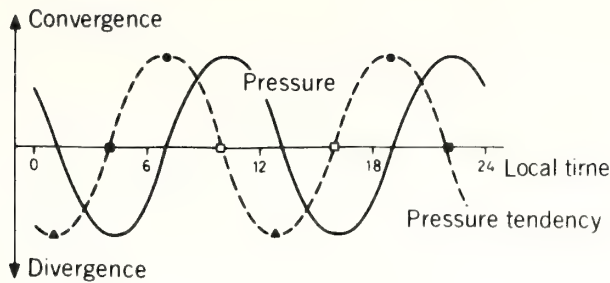


Figure 2. Semidiurnal pressure wave and the scheduled upper air program on the Meteor (M), Planet (P), Discoverer (D), and Hydra (H). Symbols indicate:

- Radiosonde and radar wind on M, P, D; radiosonde only on H.
- ▲ Structuresonde on M, P, H; radiosonde on D; radar wind on M, P, D.
- Structuresonde on M, P, H; radiosonde on D; radar wind up to 7,000 m on M, P, D.
- Radiosonde and radar wind on D; structuresonde and radar wind up to 7,000 m only on M.

On the *Meteor* and *Planet*, regular U.S. 403-MHz radiosondes (single package) were released at 0900 and 2100 Greenwich Mean Time (GMT); at the other release times (0000, 0300, 0600, 1200, 1500, and 1800 GMT), specially developed structuresondes were used. These sondes continuously record temperature and humidity with a time resolution of about 2 s and operate to elevations of about 5,000 m. Similar sondes were also released at the same times from the *Hydra* (but are not published in this report); at 0900 and 2100 GMT, the German M60 radiosondes were used during the normal routine.

Two calibration meetings were originally planned for all ships, but these were not accomplished because of operation difficulties that occurred on the *Discoverer* and *Planet*, both ships having just received their radar sets. Therefore, at the first meeting (January 30-31, 1969), only the *Meteor* and *Hydra* met. But at the second meeting (February 23, 1969), all ships except the *Hydra* were present; that ship had to depart for another project on February 15, 1969. However, as she left the project, the *Hydra* sailed past the *Meteor* for post-calibration purposes.

**RADIOSONDE TRAIN ON
NOAA DISCOVERER OSS 02**

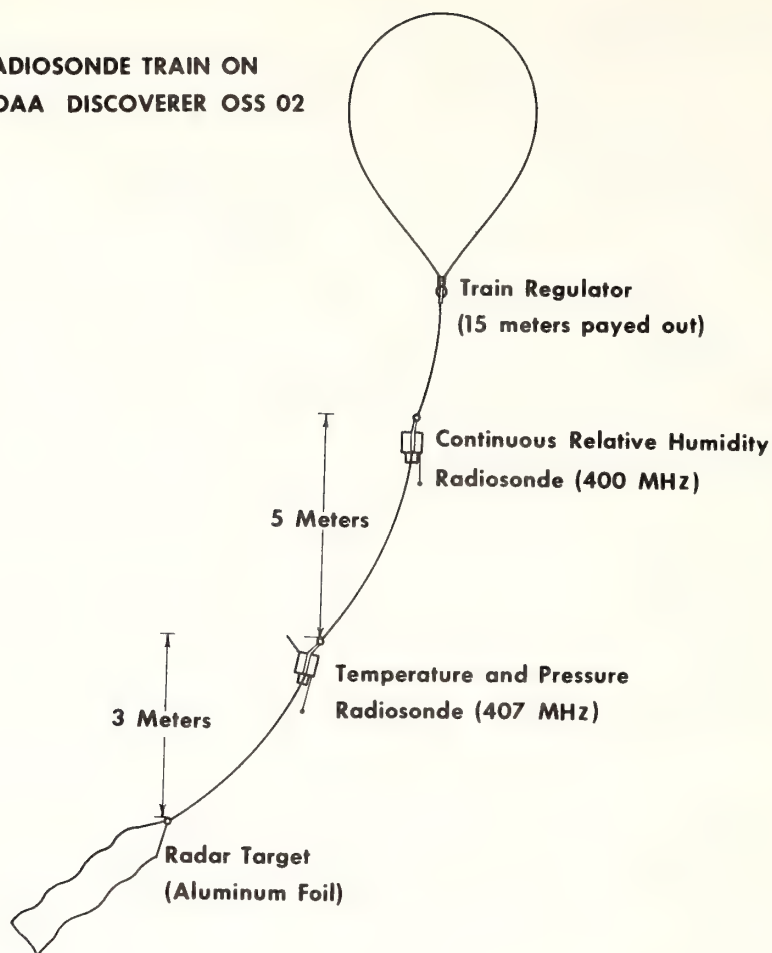


Figure 3. Schematics of balloon system to obtain (almost) continuous soundings of temperature and humidity as used on the Discoverer.

2. U.S. 403-MHz RADIOSONDES

2.1 Data Recording and Reduction

The sensor system of the U.S. 403-MHz radiosonde consists of a rod thermistor, a carbon element to sense relative humidity, and an aneroid to measure pressure. The recording of the radiosonde signal (frequencies) was done on the usual strip-chart recorder. The evaluation of the strip charts followed the procedure established by the various Weather Services, however, with more emphasis on the fine structure of the atmosphere. For this purpose, the temperature (T) and relative humidity (RH) traces were

smoothed piecewise linearly in such a way that for an entire ascent the connected polygon curves, consisting of about 40 to 80 "significant points," would approximate the original traces. Thus, only these "significant points" for temperature and relative humidity were read off the strip charts. With this procedure, the radiosonde trains, as used on the *Discoverer*, proved very useful because significant features--such as the inversion base and top--could be determined in a more reliable way than from routine single-radiosonde ascents.

Each radiosonde is provided with a calibration list giving the pressure as a function of a specified sequence of reference frequencies. A pressure-controlled switch alternates temperature, humidity, and reference frequencies during the ascent. Before the release, this baroswitch is set at the actual surface pressure according to the calibration list. An incorrect surface pressure at this setting influences the pressure measurement of the entire radiosonde ascent. It can be corrected by simple calculations according to the geometry of the baroswitch (equidistant succession of reference switching).

The temperature record is evaluated with the aid of a slide rule (radiosonde temperature evaluator, USWB No. 230 B), using the preflight calibration: When the ordinate value corresponding to one given temperature is determined, the temperatures of the entire ascent are given.

The relative humidity record can be evaluated in a similar manner with the aid of a humidity evaluator (USWB No. 500). In addition to scaling the ordinate values of the humidity trace, a knowledge of the corresponding temperature is required. The slide rule is set according to the calibration check which relates the calibration ordinate value to the given relative humidity at the temperature of the calibration box.

The functional relations for the evaluation of pressure, temperature, and humidity have been programmed for computer use to facilitate the data-reduction process.

The effects of incorrect temperature or humidity readings in the calibration check can be removed by simply correcting the calibration data before computing.

2.2 Additional Data-Reduction Procedures

To minimize instrument and other possible sources of errors, the following procedures were applied.

2.2.1 Pressure Calibration Procedure

During the calibration meetings of the ships, differences in the barometric pressure readings were rescaled as illustrated in figure 4. With the *Meteor* barometric pressure taken as reference pressure, then

$$\begin{aligned} P_{Meteor} - P_{Discoverer} &= 2.2 \text{ mb} \\ P_{Meteor} - P_{Planet} &= 0.4 \text{ mb.} \end{aligned}$$

This error influenced the pressure measurements of the entire radiosonde ascent and has been removed as mentioned in the preceding subsection.

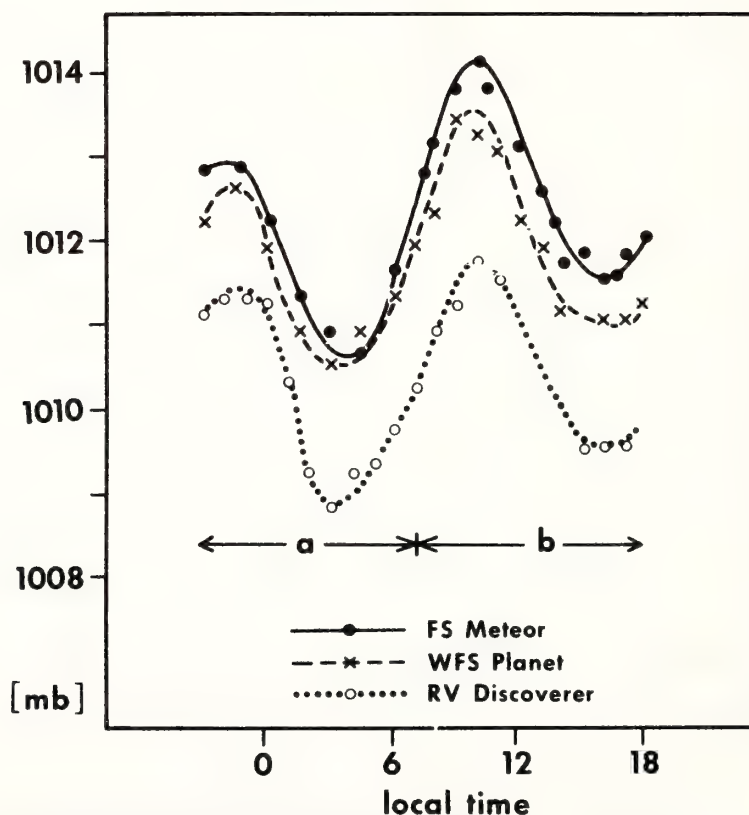


Figure 4. Comparisons of barometric pressure readings on the three ships during the intercalibration meeting on February 23, 1969. Period a: the Discoverer steaming toward the meeting place; period b: all ships at the meeting place.

2.2.2 Relative Humidity Calibration Procedure

The relative humidity is sensed in the U.S. 403-MHz radiosonde by a carbon element (Stine, 1965) which introduces a radiation error during the daytime under sunny conditions (Ostapoff, Shinnars, and Augstein, 1970). This carbon hygistor error has been corrected according to figure 5 (curve 2). This correction was possible during ATEX because the days were essentially cloud free except for fair-weather trade-wind cumuli.

Curve 1 in figure 5 was obtained from intercalibration flights of the U.S. 403-MHz and the German M60 radiosondes; the latter senses humidity by means of a hair hygrometer. Curve 1 also includes humidity values at temperatures below freezing, while curve 2 does not because it was derived from calibration flights in Miami (for more details, see Ostapoff, Shinnars, and Augstein, 1970). For example, if the carbon hygistor registered an RH value of 60 percent on a sunny day, the corrected value from curve 2 reads $RH_c = RH + \Delta RH = 75$ percent.

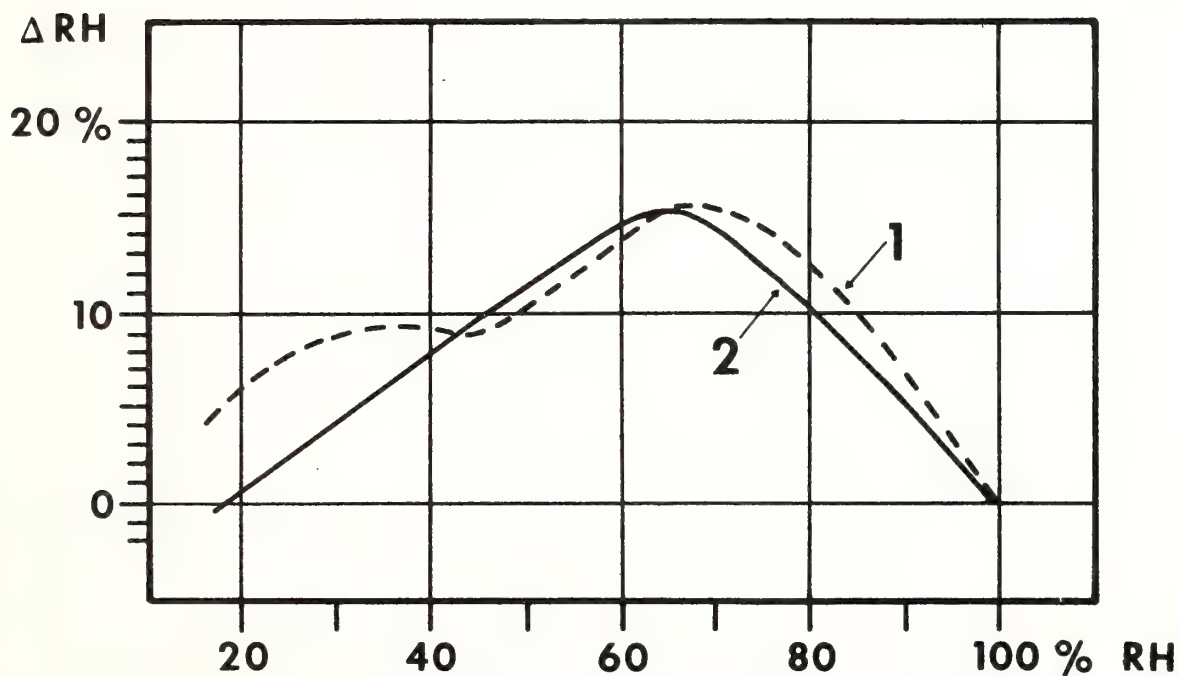


Figure 5. Correction curves for the carbon hygistor error caused by solar heating.

2.2.3 Surface Observations Calibration Procedure

Because of errors introduced by the presence of the ship (such as deck heating and turbulence), the lowest values reported by the radiosonde were not used, but were replaced by specially treated psychrometric observations. These "surface observations" were corrected in two ways.

Firstly, the intercalibration data obtained during the meetings of the ships showed differences in the deck-level readings (see fig. 6). For that reason, average correction values have been applied, with the difference always referring to the *Meteor* values. Table 1 lists the ship differences for the daily means.

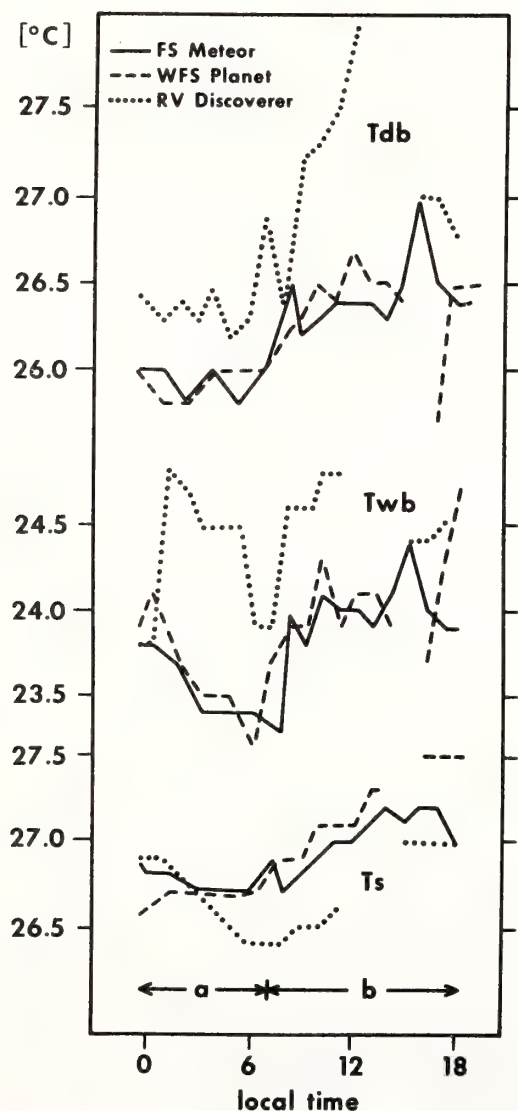


Figure 6. Comparisons of dry-bulb temperature (T_{db}), wet-bulb temperature (T_{wb}), and sea-surface temperature (T_s) for all three ships during the intercalibration meeting on February 23, 1969. Period a: the *Discoverer* steaming toward the meeting place; period b: all ships at the meeting place.

Table 1. Daily Mean Temperature Differences Between Ships

Temperature differences	<i>Meteor-Discoverer</i>	<i>Meteor-Planet</i>
Dry-bulb	-0.6°C	-0.1°C
Wet-bulb	-0.6°C	+0.1°C
Sea-surface	+0.3°C	-0.2°C

Secondly, the routine surface observations onboard the *Meteor* were compared to observations obtained from a profile buoy which floated upwind at a distance about 400 m away from the ship and carried, among other sensors, a temperature sensor with double radiation shields. Comparisons of the average diurnal variation between the ship data and the buoy data show differences in amplitude and phase. Accordingly, a correction was applied that depends on the time of day. Assuming that the true diurnal variation at all ships corresponded to that at the buoy, the surface observations of the ships other than the *Meteor* were corrected in the same manner. The differences are shown in figure 7 (see also Augstein, Hoeber, and Krugermeyer, 1973).

To illustrate the effects of these corrections, figure 8 is presented showing the mean vertical temperature profile averaged over 134 radiosonde ascents from the *Discoverer* before and after the correction. The end points of the horizontal lines give the values of the mean nighttime profile N and daytime profile D. Specifically, the usual "observed" superadiabatic lapse rate below 1000 mb disappears after the corrections have been applied.

2.3 Elimination of the Ship's Influences

Figure 9 shows the mean profiles of the potential temperature, using only part of all structuresonde data from the *Meteor*. The profiles are extended to the sea surface, using mean values for the same time period obtained from the profile buoy. The height scale is logarithmic.

During the daytime and below 30 m, the mean profile M shows a characteristic deviation from the nighttime profile and the buoy profile. A hypothetically correct profile H of the undisturbed (i.e., by the presence of the ship) atmosphere has been added (dashed curve) in figure 9.

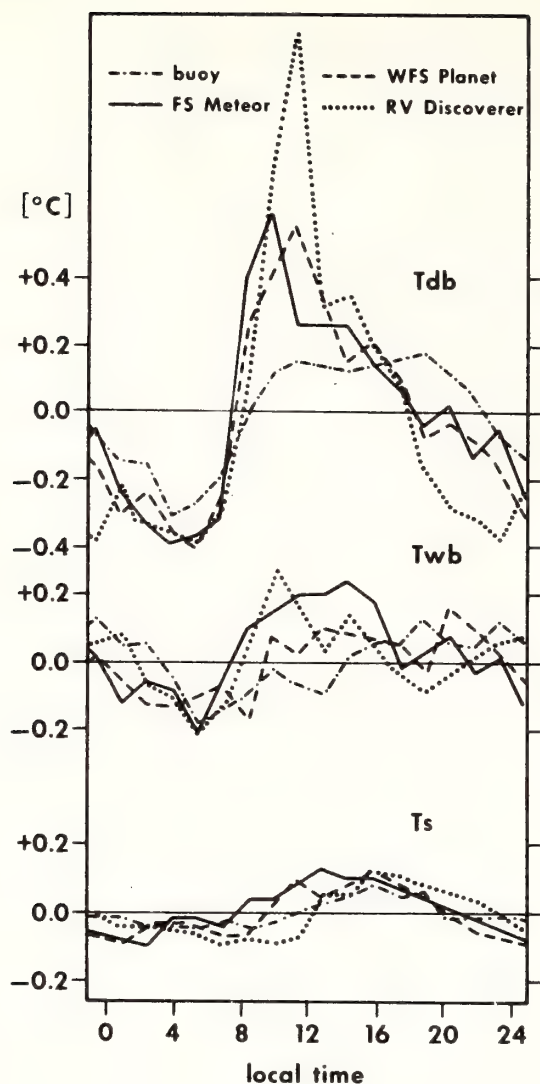


Figure 7. Diurnal deviations from the mean dry-bulb temperature (T_{db}), wet-bulb temperature (T_{wb}), and sea-surface temperature (T_s), averaged over entire ATEX period, for the Meteor, Planet, Discoverer, and for the profile buoy.

In figure 10, the potential temperature difference between profile H and profile M is plotted as a function of time (height). The lowest point of the structuresonde profile M is recorded about 2 s after the release (ascent rate about 4.5 m/s). If one assumes a radiational heating of about 0.5°C above the ambient temperature at the level of release (2 m above the deck at the leeward side of the ship), then the family of curves in figure 10 shows the adjustment time for time constants of $\tau = 2$ s (structuresonde) and 5 and 10 s (routine sonde). This means that the effect of such a heating at the release can still be noticed to a height of about 100 m in the case of the routine sondes.

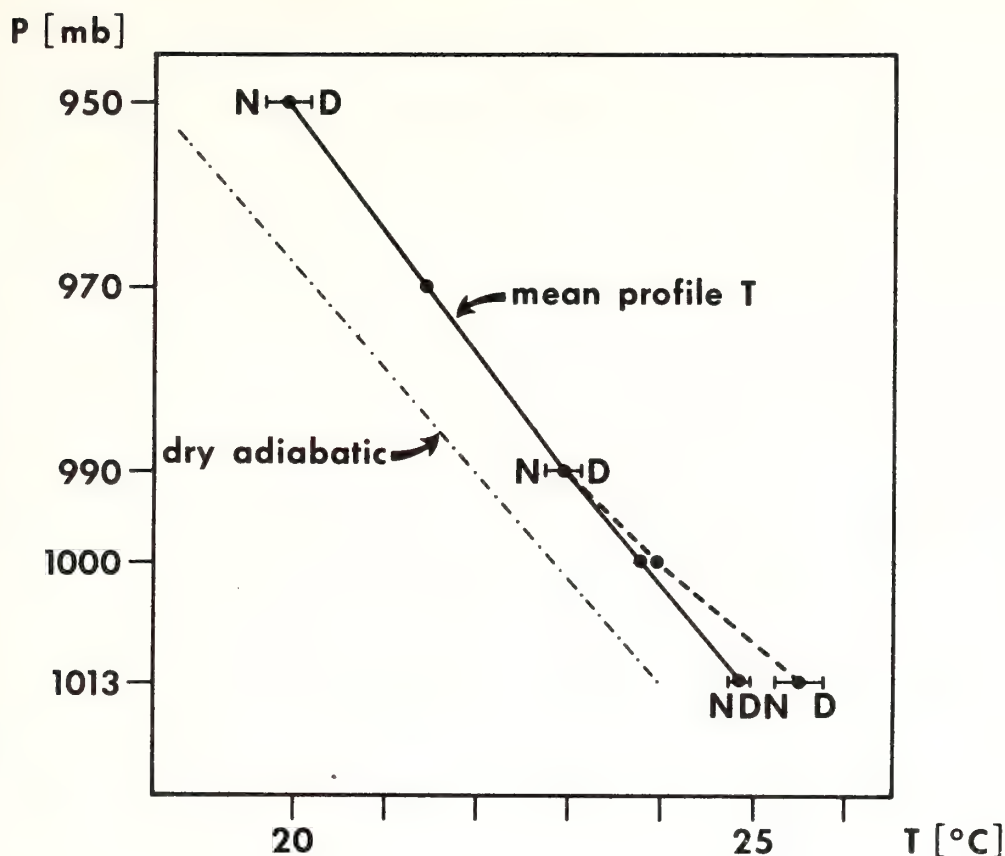


Figure 8. Mean vertical temperature profiles based on the Discoverer radiosonde data. Dashed curve: data before the correction; solid curve: data after the correction; N : mean nighttime profile; and D : mean daytime profile.

On the basis of these considerations and studies of the time constants of the radiosonde (Ostapoff, Shinnars, and Augstein, 1970), the decision was made to ignore all significant points in the routine radiosonde traces below 995 mb. Admittedly, this procedure seems rather crude and eliminates all information about the lowest layer of the atmosphere, but it seems to be justified. Data from the structuresonde still contain the ship's influence in the lowest 30 m.

3. STRUCTURESONDES

The structuresonde, developed at the Meteorological Institute of the University of Hamburg, is equipped with bead thermistors having a diameter

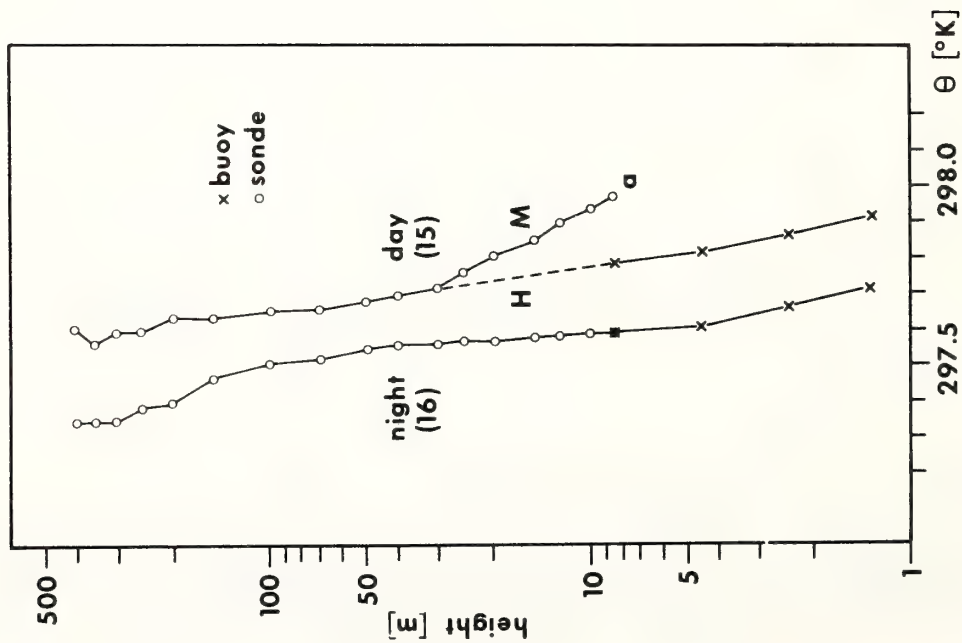


Figure 9. Mean vertical profiles of potential temperature based on structure-sonde data from the Meteor (o) and data from the buoy (x). M: average profile; H: corrected profile.

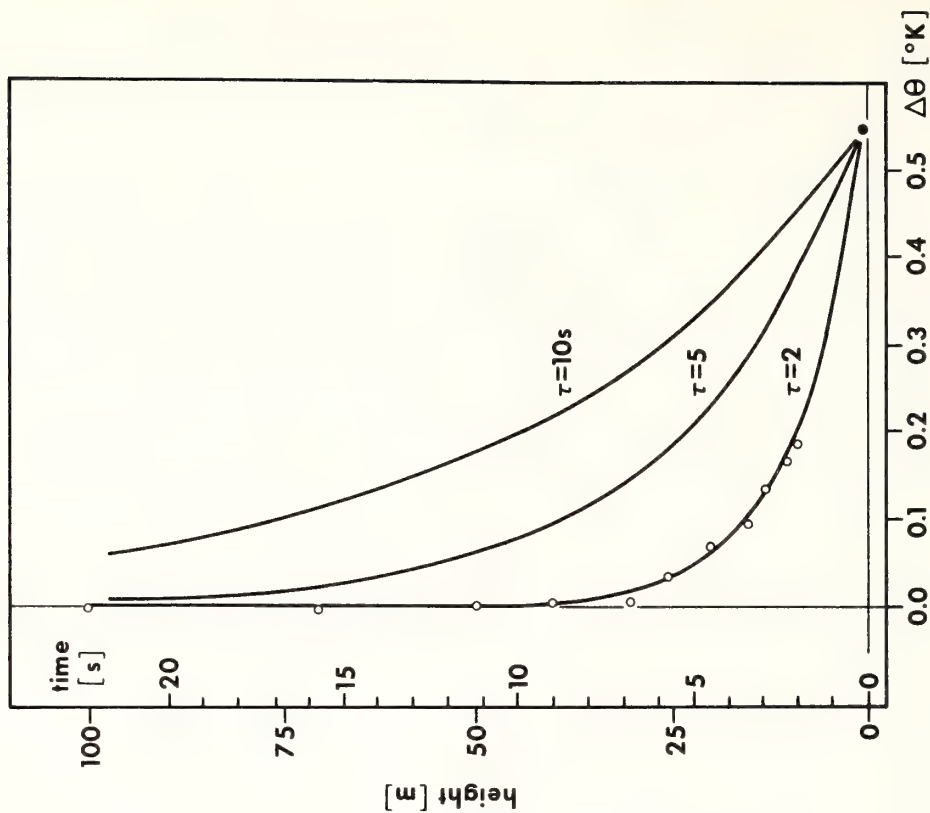


Figure 10. Potential temperature differences between the average profile M and the corrected profile H (see fig. 9) as function of height in the lowest 100 m.

of about 1 mm. The time constant of these thermistors is about 2 s. Therefore, thermodynamic structure can be resolved on a vertical scale of about 10 m. The sensors for the dry- and wet-bulb temperatures are located in a vertical tube made of aluminum with dimensions of 4 x 4 x 20 cm. With this arrangement, a good radiation shielding and sufficient ventilation during the ascent were achieved.

Data transmission is accomplished by means of the frequency triplex method. Two channels transmit the temperature information, while the third channel serves to transmit either the data from a carbon element or from a pressure transducer. The pressure transducer option was used predominately on *Hydra*, but proved unreliable. Therefore, the *Hydra* structuresonde data will not be published in this data publication.

The transmitted signal from the structuresonde was demodulated and recorded on a 3-channel analog recorder. These records were reduced in a similar way to those of the routine radiosonde, but at a higher rate because of the better resolution. In this manner, about 120 significant points between the surface and 5,000 m were obtained. The height and wind data were obtained from the radar tracking.

Before the expedition, the thermistors and the oscillators of the carbon element were calibrated with precision resistances. From the calibration data points, a calibration curve was determined by approximation with a polynomial of the fifth degree. With these calibrations for each structuresonde, the dry- and wet-bulb temperatures-- T and T_w , respectively--were determined as functions of height. Then, the water vapor pressure e was calculated according to the well-known formula:

$$e = E(T_w) - 0.00066 \cdot (1 + 0.00115 T_w) \cdot P \cdot (T - T_w) \quad (1)$$

where $E(T_w)$ is the saturation water-vapor pressure at the wet-bulb temperature T_w and p is the air pressure. The pressure p has been determined by means of the barometric height formula from radar heights and temperature profiles. The virtual temperature contribution was added iteratively with sufficient accuracy by means of an extrapolation method.

The relative humidity RH has then been calculated according to the following equation:

$$RH = \frac{e}{E(T)} \cdot 100 \quad (2)$$

where $E(T)$ represents the saturation water-vapor pressure at temperature T .

A comparison between the relative humidities, as determined by the psychrometric method and using the carbon elements, showed nearly identical values over a wide range after corrections had been applied to the carbon element measurements according to figure 5 (see Ostapoff, Shinnars, and Augstein, 1970). The validity of the calibrations has been verified by baseline checks in a calibration chamber. In cases of discrepancies which occasionally may occur because of the aging of the thermistors, the entire calibration curve has been moved parallel to the temperature axis. This movement was justified on the basis of a number of laboratory tests.

4. CALCULATIONS OF DERIVED VARIABLES

The following variables are tabulated for all radiosonde types:

- p = pressure in millibars (mb),
- T = temperature in Celsius ($^{\circ}\text{C}$),
- RH = relative humidity in percent (%),
- q = specific humidity in grams per kilogram (gm/kg), and
- PHI = geopotential height in geopotential meters (gpm).

The quantities p , T , and RH were observed directly by the routine radiosondes, while q and PHI were calculated. The specific humidity q was obtained from the equation

$$q = \epsilon \cdot e / (p - (1 - \epsilon) \cdot e) \quad (3)$$

where $\epsilon = 0.622$ and e is the partial water-vapor pressure calculated according to equation (2).

The geometric height Z is calculated from p according to the barometric height formula

$$Z = \frac{R}{g(\phi)} \int_{p_0}^p T_v(p) d \ln p, \quad (4)$$

and the inverse is

$$p = p_0 \exp \left[- \frac{R}{g(\phi)} \int_0^Z T_v(z) dz \right] \quad (5)$$

where $g(\phi)$ is the acceleration of gravity as a function of geographic latitude ϕ and is given by List (1951) as

$$g(\phi) = 9.80616 (1 - 0.0026373 \cos 2\phi + 0.0000059 \cos 2\phi). \quad (6)$$

In addition, the slight dependence of g on height has been taken into consideration.

The geometric height Z , calculated according to equation (4), has been recalculated in terms of PHI as

$$PHI = g(\phi) \cdot z/9.80. \quad (7)$$

The structuresonde data were treated in reverse order. The observed values were Z , T , and T_w . From these, the water vapor pressure e has been calculated according to equation (1) and the barometric pressure p according to equation (5). With e and p , the specific humidity q can be obtained from equation (3). And finally, PHI can be found from equation (7).

5. THE REDUCTION OF RADAR WIND DATA

As mentioned in the introduction, the *Discoverer* and *Meteor* were equipped with radar antennas mounted on a gyrostabilized platform, while the *Planet* corrections for ship motion were made by means of an on-line computer. The *Meteor* and *Discoverer* recorded the slant range (SR) between balloon and antenna and the azimuth (AZ) against true north and elevation angle (EL). The *Planet*, however, recorded horizontal distance (HD), azimuth (AZ), and height (HT). These values had to be converted into the same format as the *Discoverer* and *Meteor* data by means of simple calculations, taking into account the spherical shape of the earth and normal refraction. Readings on the *Discoverer* and *Planet* were obtained once every 15 s, while the *Meteor* was able to choose among sampling intervals of 10, 15, 20, or 30 s.

5.1 Intercomparison of Rawins

At the end of the 3-week drift, two intercomparison ascents were made between the radar sets on the *Meteor*, *Discoverer*, and *Planet*. For this purpose, a balloon was released on one of the ships and tracked simultaneously by all radar sets. Ideally, all three sets of radar data should give the same wind profile. This, however, was not the case. From the analysis of the discrepancies, useful guidelines were obtained as to how to reduce the data and, specifically, how to smooth the raw data (SR, AZ, and EL). The smoothing procedure is extremely important if one wants to obtain wind profiles free (or with only a minimum) of instrumental errors.

An example will be discussed using the intercomparison ascent made at 1730 GMT on the February 23, 1969. The balloon was released from the *Discoverer*. The *Meteor* and *Planet* were several hundred meters away. Figure 11 shows the SR's between the balloon and the three ships as a function of time. The ordinate does not represent the SR itself, but the SR after subtraction of a linear trend which is the same for each ship. Therefore, negative values are also possible. The solid curves represent the raw data from each ship. It is apparent that the curve for *Meteor* contains oscillations with a period of about 2 to 3 min that do not appear in the

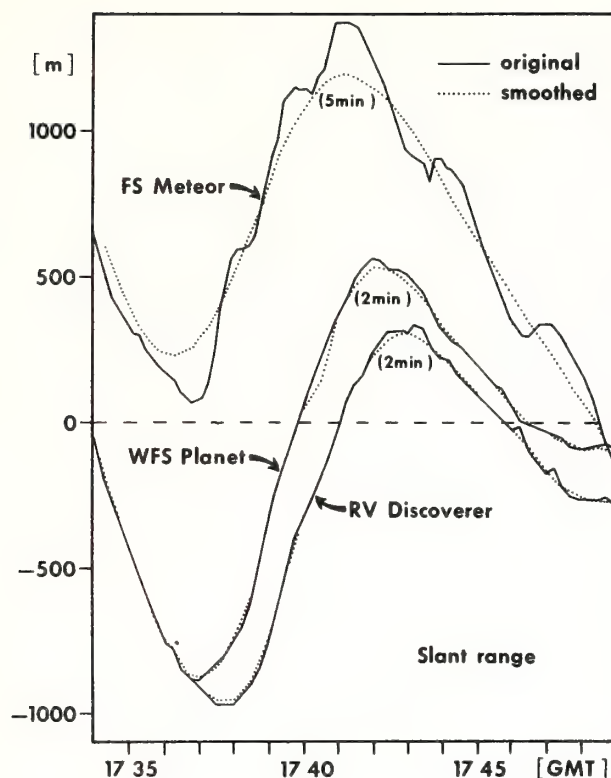


Figure 11. Comparison of radar tracking data between the three ships on February 23, 1969. Slant range data are plotted for the first 15 min into the balloon ascent. Solid curves: raw data; dotted curves: smoothed data.

Discoverer and *Planet* data, indicating that these oscillations in the *Meteor* SR data are not real in a meteorological sense. These periods in the SR's are present in nearly all *Meteor* data. The *Planet* and *Discoverer* SR data do not show any regular periodicity; only the usual scatter is present. Therefore, the *Meteor* SR data were smoothed with a numerical low-pass filter (6-min low-pass filter) which removed oscillations with periods less than 6 min, while it was sufficient to subject the SR data of the *Planet*

and *Discoverer* to a 2-min low-pass filter which removed oscillations with periods less than 2 min (usual scatter). To subject the *Planet* data to the same data-processing method as the *Meteor* data, we also used a 6-min low-pass filter for smoothing the *Planet* SR data. A detailed description of the different filters will be discussed in subsection 5.3.

Using the same ascent, figure 12 presents the respective comparison of the AZ angles. The insert in the lower part of the figure shows an enlarged portion of the record. The solid curves represent the original observed values of AZ and dotted curves represent the smoothed values. The

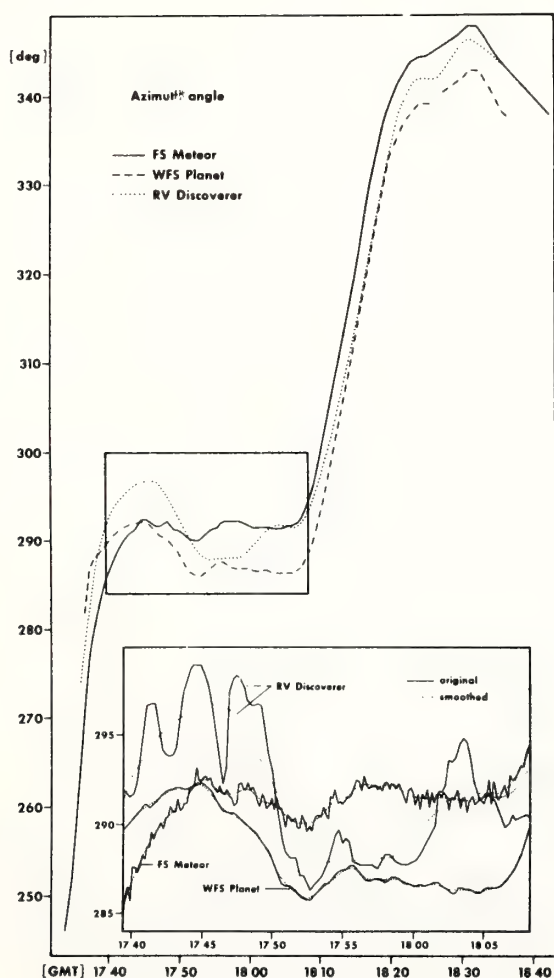


Figure 12. Comparison of radar tracking data between the three ships on February 23, 1969. Azimuth angle data are plotted against time for the first hour into the balloon ascent. Insert gives details of the original and smoothed data for the time period from 1740 to 1808 GMT. Solid curves: raw data; dotted curves: smoothed data.

noise in the original *Meteor* data can be attributed to the 10-s data-acquisition rate for the ship, while on the *Discoverer* and *Planet* the rate was 15 s. From a comparison of all three raw data curves, it is evident that the *Discoverer* AZ data show oscillations with periods of 4 to 6 min that are not present in the data of the other ships. Again, nearly all other *Discoverer* AZ data exhibit such oscillations. They are certainly not real and may be attributed to peculiar electronics behavior of a yet unknown origin. To smooth the AZ data from the *Discoverer*, a numerical low-pass filter was applied that removed oscillations with periods of less than 10 min (10-min low-pass filter). The *Meteor* and *Planet* AZ data were subjected to a 2-min low-pass filter which proved satisfactory to remove the usual scatter. Figure 12 shows the filtered AZ values for each ship as a function of time. The EL data were treated in a similar manner and are shown in figure 13.

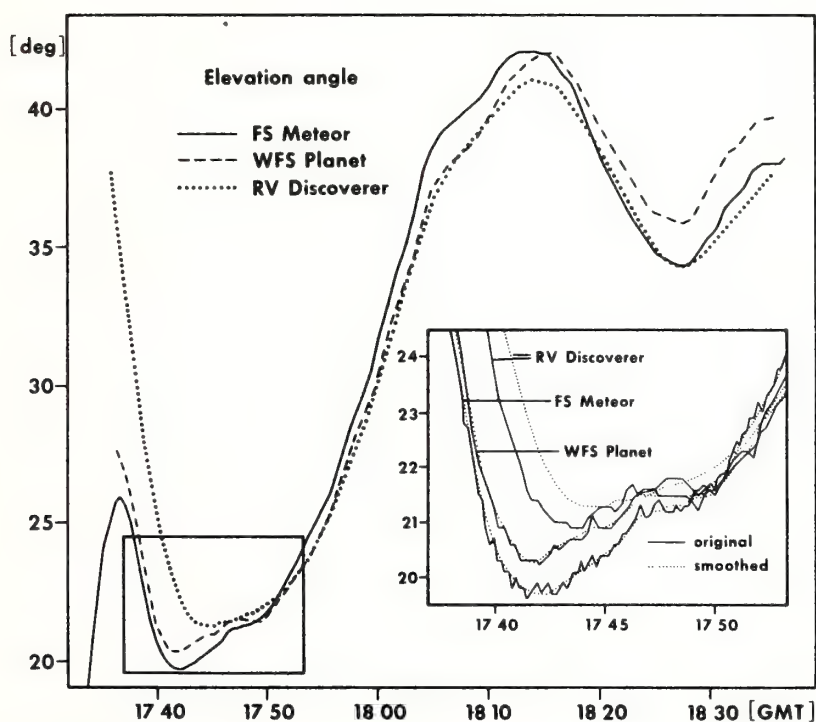


Figure 13. Comparison of radar tracking data between the three ships on February 23, 1969. Elevation angle data are plotted against time for the first hour into the balloon ascent. Insert gives details of the original and smoothed data for the time period from 1740 to 1755 GMT. Solid curves: raw data; dotted curves: smoothed data.

5.2 Smoothing Techniques

The numerical low-pass filters, which were applied to the SR, AZ, and EL data, were designed to satisfy the following requirements:

- (1) All oscillations with periods of less than 2 min should be filtered out to remove instrumental noise with these periods.
- (2) Possible fictitious periods should be removed that were not filtered out in the band covered by requirement (1). (See fig. 11, 12, and 13.)

Table 2 summarizes the low-pass filters used on the data of the three ships. The numbers give the upper cutoff period of the respective filters in minutes; that is, oscillations with periods less than this period are removed from the data.

The 10-min filter, as used on the *Discoverer* AZ and EL data, is given by the following equation:

$$w(k\tau) = 0, \quad |k| > N$$

$$w(k\tau) = \frac{1}{\pi k} \sin 2\pi f_g k\tau, \quad -N \leq K \leq N, K \neq 0 \quad (8)$$

where w is the weighting function, k is the running variable, τ is the time difference between two data points (in this case, $\tau = 15$ s), and f_g is the upper frequency bound of the low-pass filter (i.e., all oscillations with frequencies higher than f_g are removed). $2N + 1$ is the number of weights. The following frequency response $H(f)$, also called damping function, corresponds to the above weighting function $w(k\tau)$:

$$H(f) = w(0) + 2\sum w(k\tau) \cos 2\pi f k\tau \quad (9)$$

where f is the frequency. Figure 14 shows the weighting function $w(k\tau)$ and the corresponding frequency response for the 10-min filter ($f_g = 1/10$). Because the weighting function has a finite number of terms ($2N+1$), the corresponding filter response does not have the form of an "ideal" filter (i.e., that of a gate function). The upper frequency bound f_g is, therefore,

Table 2. Low-Pass Filters in Nimbus Used on the Radar Data of the Various Ships

Ship	Parameters		
	SR	AZ	EL
<i>Meteor</i>	6	2	2
<i>Planet</i>	6	2	2
<i>Discoverer</i>	2	10	10

defined by that frequency where the damping function H has the value $1/2$; that is, the amplitude of an oscillation with frequency f_g is reduced 50 percent.

The construction of the 2-min filter ($f_g = 1/2$) and 6-min filter ($f_g = 1/6$), respectively, proved somewhat more difficult. The *Meteor* data were obtained at several repetitive rates; namely, $\Delta\tau = 10, 15, 20$, and 30 s. Yet, it was required firstly that the time interval $\Delta\tau = 2N\tau$, where the weighting function is different from zero, be the same for all four cases ($\Delta\tau = 2$ min for the 2-min filter and $\Delta\tau = 4$ min for the 6-min filter), and secondly that all four damping functions agree as much as possible. In this way, wind calculations could be made that are more or less independent of the individual data-acquisition rates (t) of the *Meteor*. The filter computation method applied here has been described by Bleck (1965). Briefly, a damping function $H_0(f)$ is prescribed that has a rough similarity to the "ideal" filter. Weighting functions $w(k\tau)$ are determined, with $|k| < N$ and $N = \Delta\tau/2\tau$ corresponding to the damping functions $H(f)$ which best approximate $H_0(f)$ in accordance with chosen minimum conditions (here Gauss' condition was used). Calculations were made with various prescribed $H_0(f)$.

Figures 15 and 16 present those results which seem most applicable to the data concerning the 2- and 6-min filters. In these figures, $w(k\tau)$, $H(f)$, and $H_0(f)$ are plotted, respectively. In some frequency domains, $H(f)$ assumes negative values which are equivalent to a phase shift of 180° (see fig. 13, 14, and 15). These values, however, have no practical consequence as far as the filtered data are concerned. A frequency analysis of the raw data of SR, AZ, and EL revealed that the amplitudes of oscillations, with frequencies near the band where the 180° phase shifts occurred, are smaller

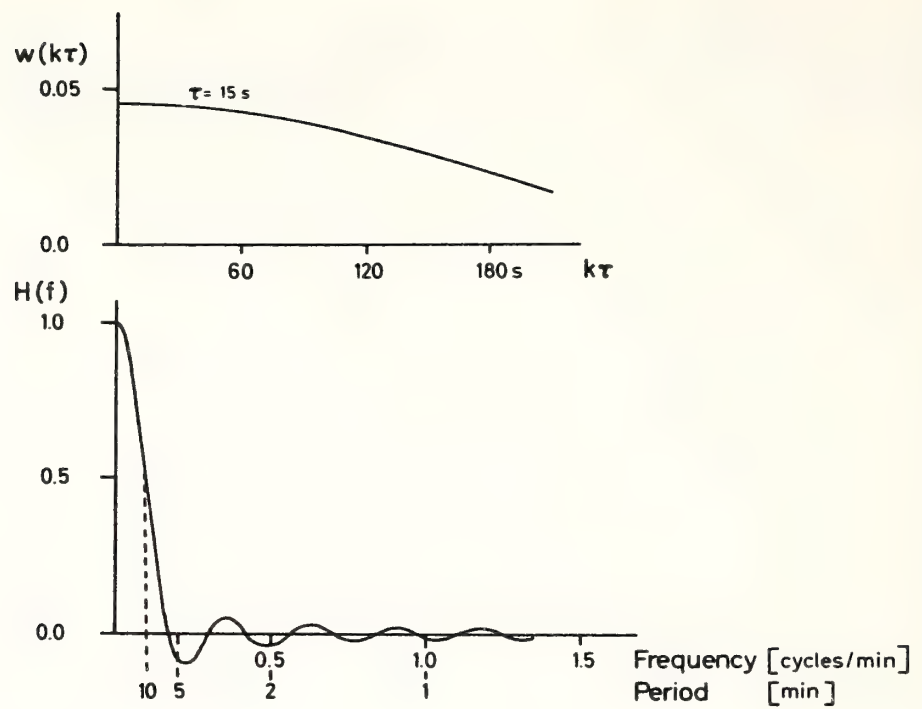


Figure 14. Weighting function (top) and frequency response (bottom) of the 10-min filter.

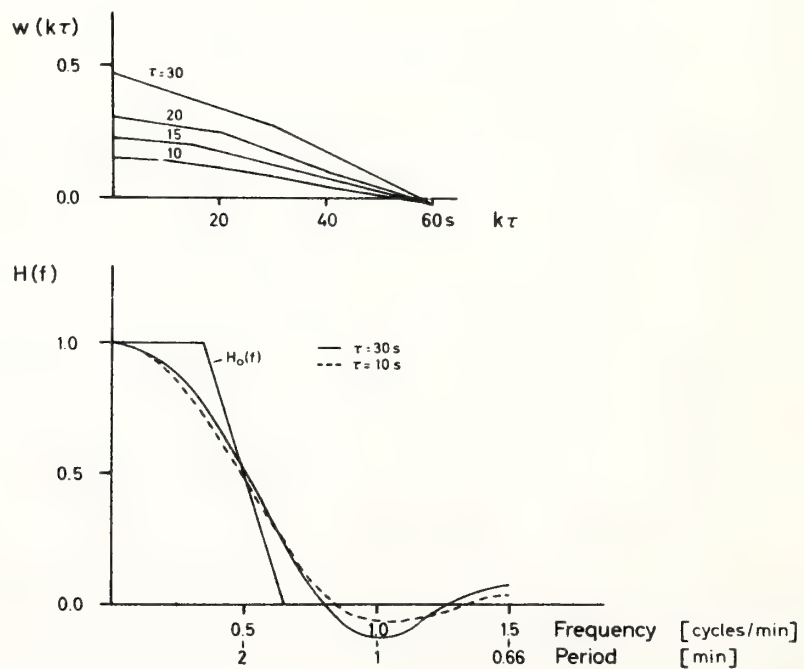


Figure 15. Weighting function (top) and frequency response (bottom) of the 2-min filter.

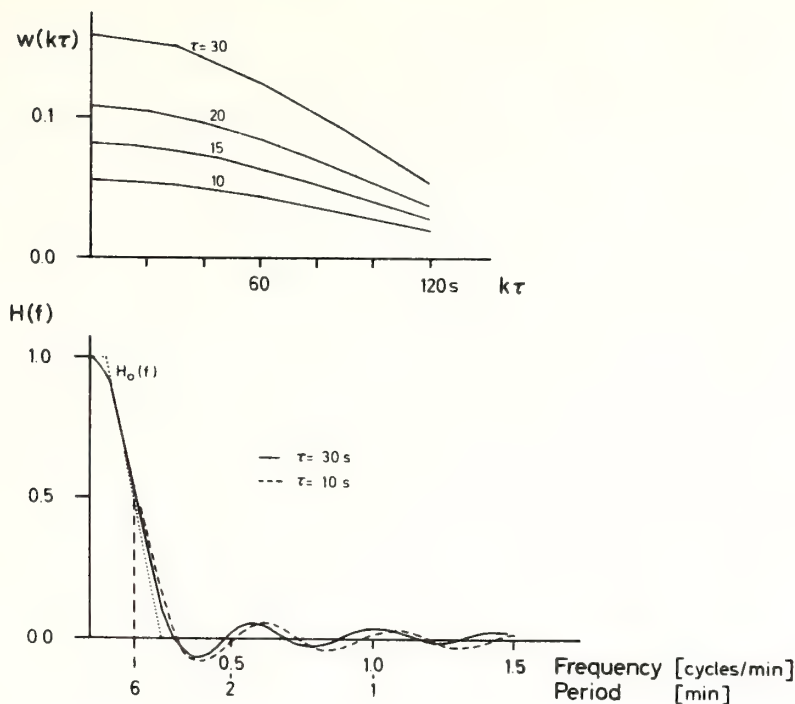


Figure 16. Weighting function (top) and frequency response (bottom) of the 6-min filter.

than one-tenth of the amplitudes in the frequency range $0 \leq f \leq f_g$. In addition, these amplitudes are damped further by a factor of one-tenth or less by the filtering.

If $g(t)$, where t is time, represents the raw data function (i.e., SR, AZ, or EL), then the filtered function $h(t)$ is obtained by the following summation:

$$h(t) = \sum_{K=-N}^N g(t - k\tau) w(k\tau). \quad (10)$$

The smoothed values are computed every 30 s. However, because the first smoothed value is calculated $\Delta\tau/2$ after the first recorded data point, an important portion of information is lost, especially in the lowest layers. Therefore, the missing values at the beginning of a data series were obtained by graphical downward extrapolation. Where there were missing data within a series during the ascent, this procedure was not applied.

5.3 Wind Calculations

Using the smoothed 30-s values for SR, AZ, and EL, the space coordinates (x,y,z) of the target are calculated according to simple geometric formulas. These coordinates are then corrected for the ship's drift or velocity. However, a knowledge of the time difference between the release and the first data point is required. Therefore, a time-height curve was constructed which proved nearly linear. This curve has been extrapolated linearly to the surface. The space coordinates (x,y,z) were again smoothed by a running-smoothing function which consisted of a polynomial of the second degree, using four successive values respectively, each separated by 30 s. The numerical differentiation was performed between the second and third values according to the formula (Zurmuhl, 1965):

$$u\left(\frac{3}{2}\tau\right) = \frac{1}{10\tau} (-3x_0 - x_1 + x_2 + 3x_3)$$
$$v\left(\frac{3}{2}\tau\right) = \frac{1}{10\tau} (-3y_0 - y_1 + y_2 + 3y_3)$$
(11)

where u and v are the zonal and meridional components of the wind, x_0, y_0 ; x_1, y_1 ; x_2, y_2 ; and x_3, y_3 are the components of four successive space vectors, and τ is the time difference between two successive space vectors. The height $z(3/1\cdot\tau)$ is linearly interpolated between z_1 and z_2 . This method does not work at the beginning and at the end of the data series. In this case, a polynomial of the second degree is fitted through five points according to the following equation:

$$u\left(\frac{1}{2}\tau\right) = \frac{1}{35\tau} (-22x_0 + 4x_1 + 15x_2 + 11x_3 - 8x_4).$$
(12)

5.4 Wind Profiles of the Intercomparison Flights

Figure 17 shows the wind profile as obtained simultaneously on all three ships--*Meteor*, *Planet*, and *Discoverer*--during the intercomparison

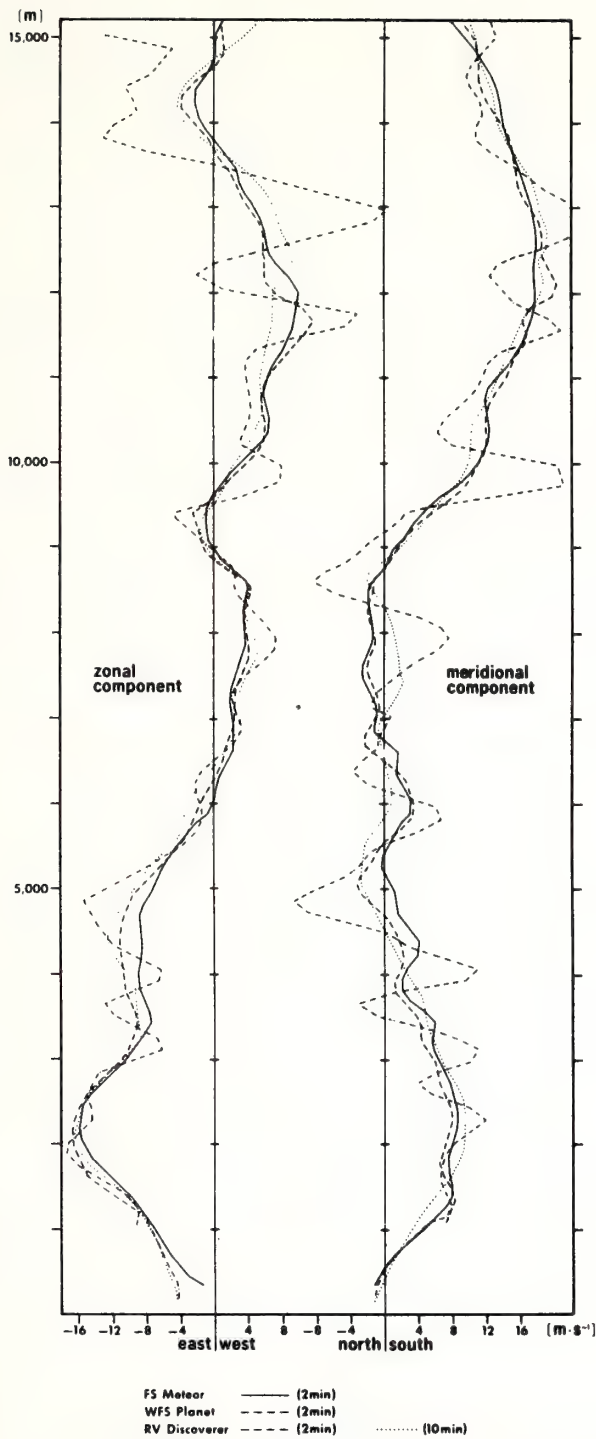


Figure 17. Example of profiles of the u and v components of the wind as obtained during the February 23, 1969, intercalibration meeting of the Meteor, Planet, and Discoverer after subsection to the described filtering technique. Note Discoverer profile using the 10-min filter (.....).

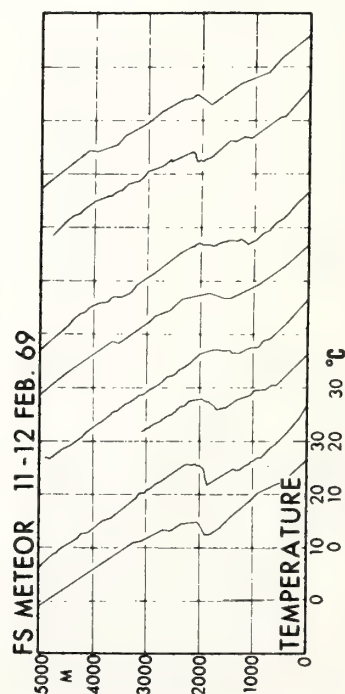
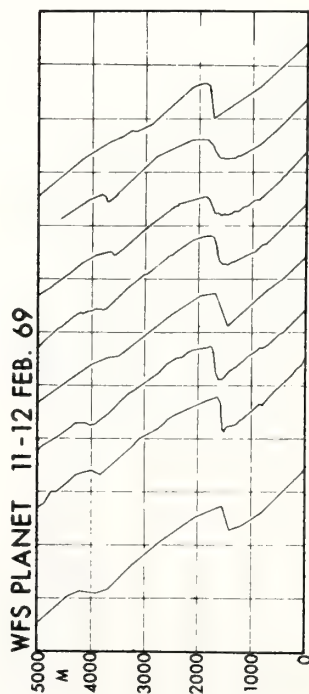
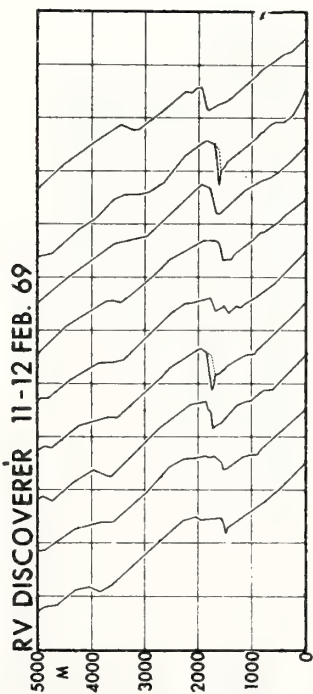


Figure 18. Temperature profiles obtained on February 11-12, 1969, in the lowest 5,000 m. Units in °C.

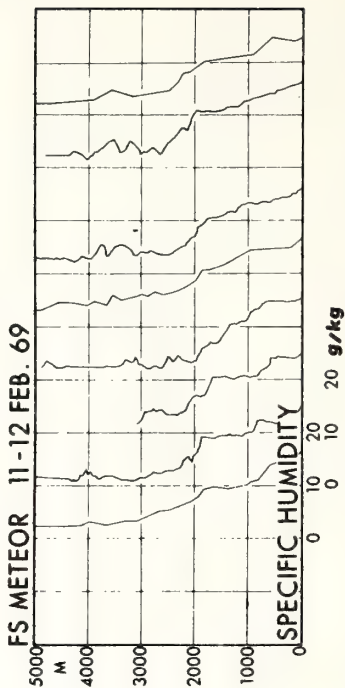
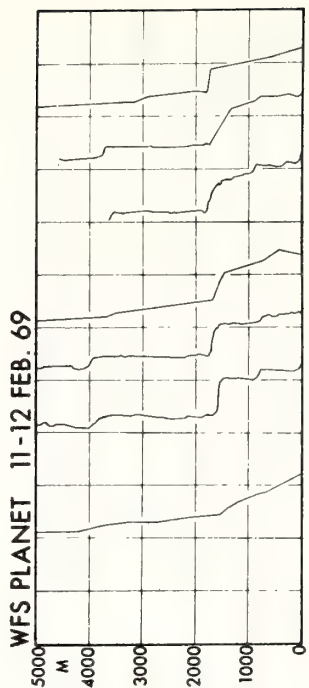
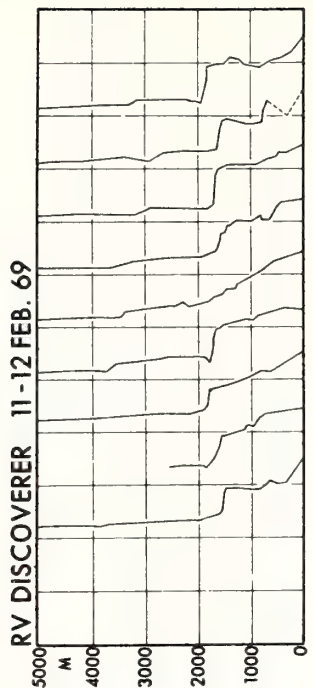


Figure 19. Specific humidity profiles obtained on February 11-12, 1969, in the lowest 5,000 m. Units in g/kg.

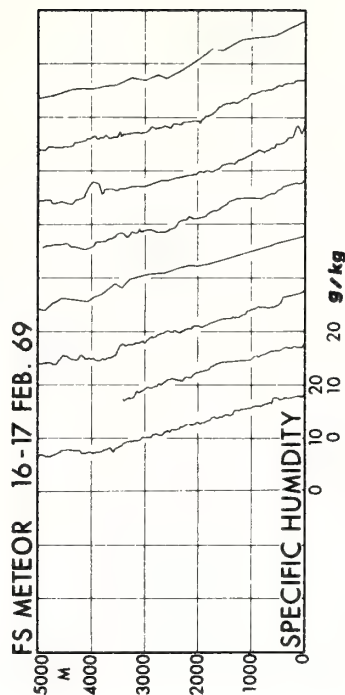
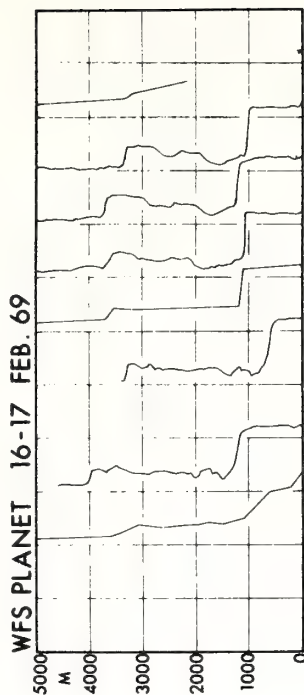
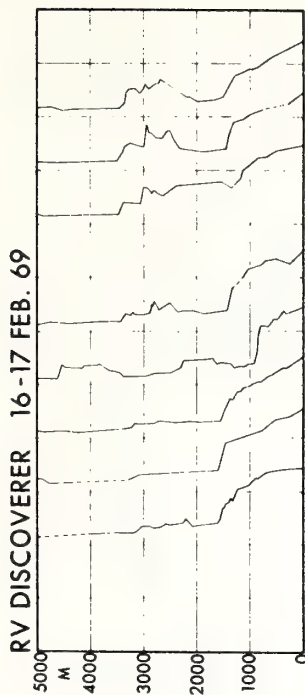


Figure 21. Specific humidity profiles obtained on February 16-17, 1969, in the lowest 5,000 m Units in g/kg.

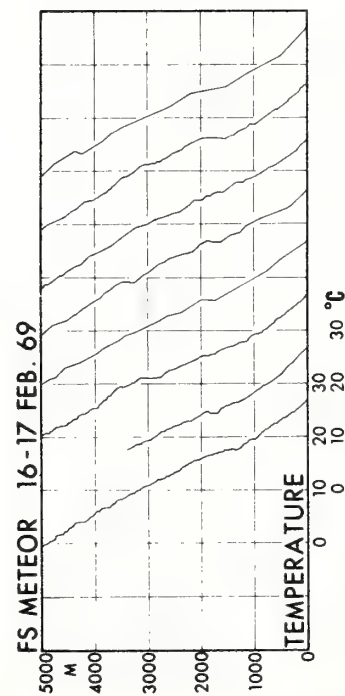
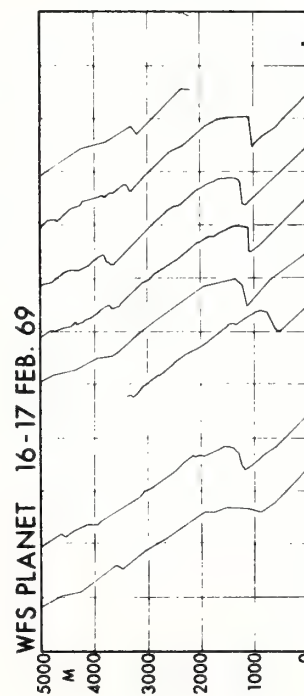
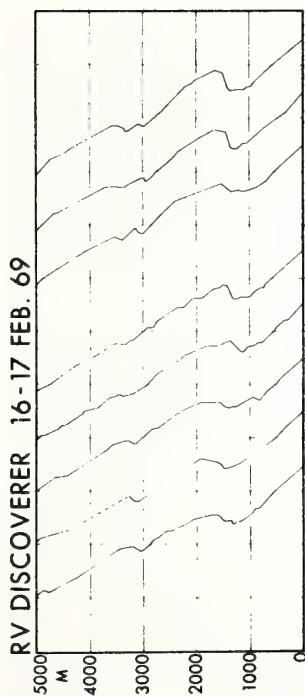


Figure 20. Temperature profiles obtained on February 16-17, 1969, in the lowest 5,000 m. Units in °C.

meeting of February 23, 1969, after being subjected to the smoothing procedures as described above. It is evident that at several levels large differences that amount to as much as 4m/s still occur. In addition, the *Discoverer* wind profile has been included in figure 17. This profile was obtained by smoothing the AZ and EL with the 2-min filter. It is clear that without the intercomparison between the three ships, such errors would be difficult to detect and correct. These results clearly demonstrate the necessity for intercomparisons wherever larger experiments are conducted with a number of different participating platforms.

6. THE TEMPERATURE AND HUMIDITY PROFILES

In the following, a few examples of the tabulated data are presented in graphical form. Figures 18 and 19 show the temperature and specific humidity profiles on February 11-12, 1969, for the first 5,000 m as observed on the *Discoverer*, *Planet*, and *Meteor*. This period was considered as typical for the undisturbed trade-wind conditions, and the mass and energy transports were calculated using these data (Augstein, Riehl, Ostapoff, and Wagner, 1973).

Figures 20 and 21 present the corresponding profiles for February 16-17, 1969. It is apparent that during those days the *Meteor* was situated in the Intertropical Convergence Zone, evidenced by an almost complete absence of the temperature inversion and, most dramatically, by a rather continuous decrease in humidity with height. Notice also the strong inversions in the *Planet* and *Discoverer* profiles and the lower inversion heights as compared to those in figures 18 and 19.

7. ACKNOWLEDGMENTS

We thank our colleagues in each of the participating institutions who carried out much of the work during the field experiment and subsequently during the tedious, time-consuming data-reduction phase. The enormous amount of data collected on all four ships was only possible because of

the enthusiastic cooperation of the crew and officers on each ship for which we are very grateful. The meteorological teams worked untiringly through the experiment on an extremely tight schedule, conscientiously releasing balloon after balloon. It was, indeed, a great cooperative international venture.

We also appreciate the collaboration of all persons in the post-experimental period, especially our colleagues in the United Kingdom who contributed so much to the experiment and who cooperated in the publishing of the data.

The contributions of Cdr. D. MacDonald, Chief Scientist on the HMS *Hydra*, Prof. G. Stilke of the University of Hamburg, and Dr. G. Wurlitzer of the Seewetteramt Hamburg are gratefully acknowledged as well as that of Dr. E. Augstein of the University of Hamburg who helped to develop the aerological program and who took upon himself the enormous task of making the data compatible.

Mostly, we are indebted to the late Prof. K. Brocks, Director of the Meteorological Institute of the University of Hamburg, for his untiring efforts in bringing all diverse research groups successfully together in a truly international cooperative spirit.

8. REFERENCES

- Augstein, E., F. Ostapoff, H. Riehl, and V. Wagnet (1971), Mass and energy transport in the region of the Atlantic tradewind inversion, presented at the Seventh Technical Conference on Hurricanes and Tropical Meteorology, December 6-9, 1971, St. Michael, Barbados. Abstract, *Bull. Am. Meteorol. Soc.*, 52(8):787.
- Augstein, E., H. Riehl, F. Ostapoff, and V. Wagner (1973), Mass and energy transports in an undisturbed Atlantic trade-wind flow, *Monthly Weather Rev.*, 101(2):101-111.
- Augstein, E., H. Hoeber, and L. Krugermeyer (1973), Fehler bei Temperatur-Feuchte- und Windmessungen auf Schiffen in tropischen Breiten, to be published in *Meteor-Forschungsergebnisse*, Ser. B, No. 9, Borntrager-Verlag, Berlin, Germany.
- Bleck, R. (1965), *Lineare Approximationsmethoden zur Bestimmung ein- und zwei-dimensionaler Filter der dynamischen Meteorologie*, Institut für Theoretische Meteorologie der Freien Universität, Berlin, Germany, 86 pp.

- List, R. J. (1951), *Smithsonian Meteorological Tables*, 6th rev. ed., Smithsonian Institution Press, Washington, D.C., 527 pp.
- Ostapoff, F., W. Shinnars, and E. Augstein (1970), Some tests on the radio-sonde humidity error, *NOAA Tech. Rept. ERL 194-AOML 4*, U.S. Dept. of Commerce, Miami, Fla., 50 pp.
- Stine, S. L. (1965), Carbon humidity elements--manufacture, performance and theory, in *Humidity and Moisture: Measurement and Control in Science and Industry*, A. Wexler, ed., Vol. 1, *Principles and Methods of Measuring Humidity in Gases*, R. E. Ruskin, ed., Reinhold Publ. Corp., New York, pp. 316-330.
- Zurmühl, R. (1965), *Praktische Mathematik für Ingenieure und Physiker*, 5th rev. ed., Springer-Verlag, Berlin, 561 pp.

ATTENUATION OF SOLAR RADIATION BY WINDBORNE
SAHARAN DUST OFF THE WEST COAST OF AFRICA

Toby N. Carlson, Joseph M. Prospero, and Kirby J. Hanson

In August 1972, solar radiation was measured aboard ship near the coast of West Africa, using an upfacing Eppley pyranometer and Volz type sunphotometers. A simple radiative transfer model for solar irradiance (the broadband measurements) was used to compute an effective aerosol transmission for essentially cloud-free conditions. The aerosol transmission values showed systematic variations with changes in atmospheric turbidity as measured with the sunphotometers. For a typical hazy day, the mean aerosol transmission was 0.86 (the equivalent of a Volz turbidity of ~ 0.30) and the net depletion of the solar energy due to Saharan dust was estimated to be about 100 lys/day. This amount of heat loss is comparable with the mean depletion of solar energy solely due to cloud cover in this region and suggests that Saharan dust reduces the solar heating of the ocean-atmosphere system, but it probably also decreases the net radiation cooling at mid-levels. The Angstrom turbidity coefficient, α_A , calculated from two pairs of turbidity measurements, was very close to zero for the period, implying a neutral haze extinction.

1. INTRODUCTION

The large-scale transport of Saharan dust from North Africa has received some attention by meteorologists, not only because of the dynamic properties of the layer of air in which the dust is carried, but also because the particulate matter itself appears to alter the large-scale solar energy balance. Thick dust haze associated with a deep layer of Saharan air often covers synoptic scale areas over the equatorial Atlantic Ocean and Caribbean during the summer. The Saharan air layer, which we shall refer to as SAL, originates over the arid stretches of North Africa where prolonged and intense heating produces a deep isentropic mixed (dry convection) layer generally extending to 5 or 6 km during July and August.

The formation processes are continuous and large scale; heated air eventually emerges along the west coast of North Africa and is undercut before reaching the coastline by a layer of cooler and moister maritime air, a branch of the northeasterly trades.

During BOMEX, we (Carlson and Prospero, 1972; Prospero and Carlson, 1972) were able to measure dust concentration aboard the DC-6 aircraft of NOAA's Research Flight Facility (RFF). These studies showed that the SAL was the source of dust material for the lower level air; within the SAL the maximum concentration of dust was generally near 3 km.

The important dynamic influence of the SAL is likely to be the braking effect that the warm base has on the cumulus convection. A warm lid near 850 mb is very apparent in the temperature sounding (fig. 1) near the African coast taken aboard the NOAA Ship *Discoverer* at 21.8N, August 7, 1972. The moist layer is rather shallow and topped by a strong inversion that we refer to as the transition layer. The air within that layer corresponds to air parcels whose origins vary from having crossed the interior of North Africa (at the base of the Saharan layer) to air that moved southward into the tropics without crossing North Africa (the base of the transition layer). Intermediate air parcels in the transition layer have shorter passage times over North Africa than air within the SAL and thus do not achieve as high a potential temperature.

Recent work (Vonder Haar and Cox, 1972) with aircraft radiation measurements made during BOMEX indicates that the amount of absorption of solar radiation by a dusty atmosphere is 25 to 100 percent greater in the lowest 300 mb than would be expected from calculations based upon a clean gaseous atmosphere. Their measurements also suggest that enhanced warming

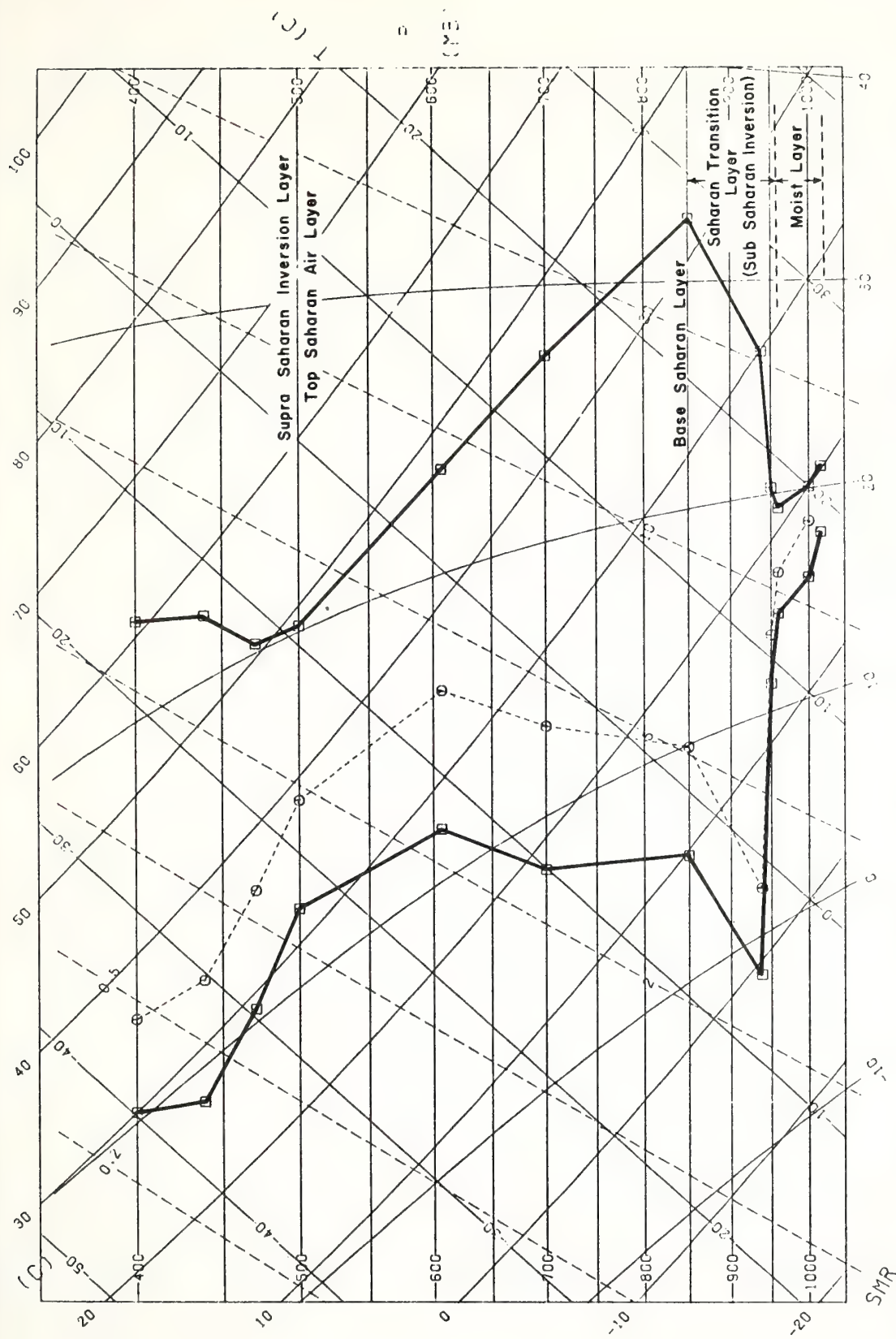


Figure 1. Temperature and dewpoint sounding at 1100 GMT aboard the DISCOVERER, August 7, 1972. Significant features of the sounding are indicated. The dashed line represents the dewpoint corrected for hygrometer error due to radiation and lag.

of the layer is caused by short-wave absorption by aerosols and water vapor and that this warming exceeds the long-wave infrared (IR) cooling for a few hours around solar noon. We would expect a similar situation off the coast of Africa.

During the summer of 1972, we were able to measure radiation and surface air aerosol concentrations aboard the NOAA Ship *Discoverer* during the NOAA TAG (Trans-Atlantic Geotraverse) cruise near the coast of Africa. Dust samples were obtained by paper filters (IPC 1478) in conjunction with a high volume pump. Exposure times for the filter samples were necessarily of several hours duration (generally about 8) in order to deposit a sufficient quantity of material on the filters for later analysis; these exposures were usually made twice a day, once in the morning and once in the afternoon. The filter samples were analyzed for bulk insoluble dust concentrations as well as solubles such as sea salt constituents and sulfates. Only the dust will be considered in this paper.

Atmospheric turbidity was measured with a Volz sunphotometer similar to the type used by Flowers et al. (1969) and by Volz (1970). This instrument records the intensity of a direct solar beam at very narrow wavelength, the most widely used being at 0.5 micron (μ). Some versions of these instruments have the capability to measure two or more wavelengths, at 0.5 μ and at 0.38, 0.85, or 1.07 μ . The instruments used aboard the *Discoverer* operated at 0.5 μ and 1.07 μ but a second vessel, the University of Miami's research vessel *Columbus Iselin* which conducted side-by-side operations during part of August, carried a two-channel sunphotometer operating at 0.5 μ and 0.8 μ . The *Iselin* measurements are included in this paper.

The downward global solar radiation was measured with an upfacing Eppley pyranometer and an upward (reflected) solar radiation with a downfacing instrument. The sensors were mounted at the end of a boom extending from the bow of the *Discoverer* where the field of view was only slightly obscured by the ship. The instrument package is a part of the regular ship program of NOAA's Sea-Air Interaction Laboratory (SAIL) and has been used earlier in 1972 during NOAA's FLARE (Florida Aquanaut Research Expedition) project and during SAIL's IDOE (International Decade of Ocean Exploration) Mixed Layer Experiment in 1971 (Hanson and Poindexter, 1972).

These detectors sense total solar radiation in the spectral interval approximately 0.3 to 3.0μ between about 10 and 90° of the sky dome; accuracy is considered to be within 2 or 3 percent of the solar constant, but relative variations of solar irradiance may be significant to within a percent or two. Output from all the sensors was continuously recorded on a paper chart, a portion of which is shown in figure 2. These records were digitized after the voyage and converted to units of langleys averaged over 3 min intervals.

Our earlier observations in BOMEX (Prospero and Carlson, 1972; Carlson and Prospero, 1972) showed that surface dust measurements made beneath the base of the SAL correlated poorly with the dust loading within the SAL. Remote sensing of the dust layer should offer a particularly useful means of assessing the concentration and size spectra of the dust in a vertical column through the atmosphere. Our primary concern in this paper is with the total downward solar radiation, as measured by the upfacing pyranometer, although surface albedos will be presented without comment.

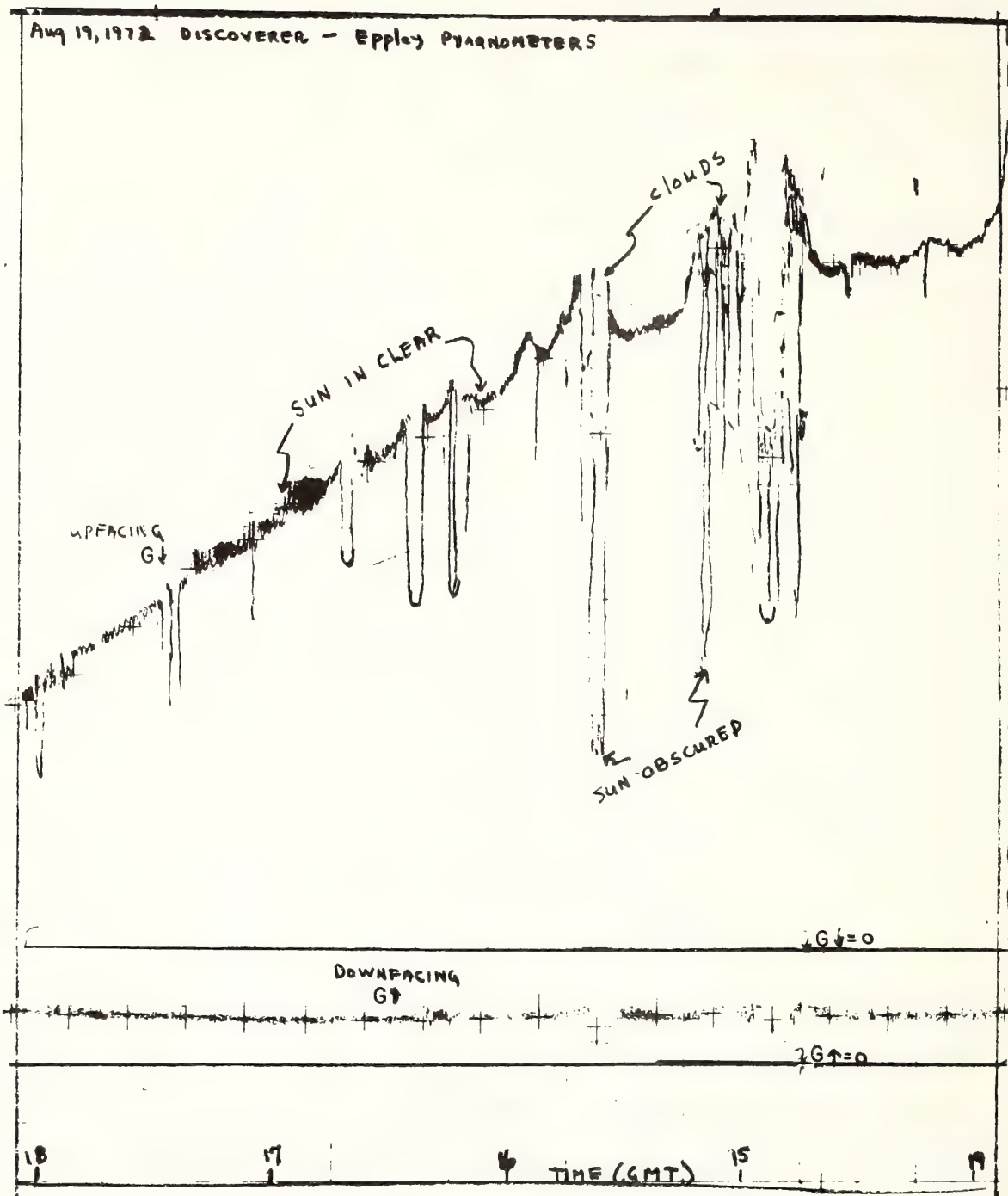


Figure 2. Portion of the original record of pyranometric data for the up-facing Eppley instrument (top trace) and downfacing instrument (below) aboard the DISCOVERER, August 19, 1972.

2. OBSERVATIONAL AND THEORETICAL BACKGROUND

Our intent here is to use the shipboard radiation data to relate fluctuations in broadband extinction to the turbidity. To calculate the solar intensity fluctuations due to the aerosol layer, we consider only the cloud-free cases and treat the measurements similar to G. D. Robinson (1969), Idso (1969), and Unsworth and Monteith (1972). Although no precipitation occurred during leg 2 of the 1972 *Discoverer* TAG cruise, cloudiness was present much of the time. Unlike the sunphotometers, which are able to accurately measure solar intensity at normal incidence to the sun even with clouds in close by, the pyranometer is sensitive, in principle, to incoming solar radiation over the whole sky, both diffuse and direct, and is therefore affected by the distribution of clouds, however scanty.

With the use of whole-sky camera photographs and conventional meteorological observations from the ship, we selected periods when the net cloud cover was no more than a small fraction of the sky. In practice, the net effects of cloud cover are thought to be negligible when the clouds are thin and broken and when there is a wide clearing around the sun's disk; these periods we refer to as *essentially* cloud-free. As shown in figure 2, the presence of clouds close to the sun can actually reflect the light in such a way as to produce temporarily *higher* solar intensities, although with diminishing clouds the "noisiness" of the record diminishes to an almost smooth line, a characteristic that enabled us to further delineate the essentially clear conditions.

If the downward component of the sky (diffuse) radiation is $D\downarrow$, the downward component of direct solar radiation $S\downarrow$, and the global (total)

solar component downward is $G\downarrow$, then for the cloud-free case (super-script ⁰)

$$G\downarrow^0 = S\downarrow^0 + D\downarrow^0. \quad (1)$$

Using standard transmission coefficients for absorption and for Rayleigh scattering in a clean gaseous atmosphere, one can compute the above balance for a cloud-free dust-free case, as denoted in (1b) by the super-script ^{*}. Thus,

$$G\downarrow^* = S\downarrow^* + D\downarrow^*. \quad (1b)$$

The attenuation of a monochromatic radiation at wavelength λ in the cloud free atmosphere on a plane tangent to the earth's surface is

$$S_{\lambda\downarrow}^0 = S_{0\lambda\downarrow} \left[\exp - \{T_\lambda \cdot m\} \right] \cdot \cos Z \quad (2)$$

where $S_{0\lambda}$ is the direct beam solar intensity per unit wavelength interval (centered at wavelength λ) outside the atmosphere, T_λ is the monochromatic optical thickness (attenuation coefficient) of the atmosphere, and m is the path length number (approximately $\sec. Z$ where Z is the solar zenith angle). The value of T_λ depends strongly on wavelength; for molecular (Rayleigh) scattering it is proportional to λ^{-4} . Expanding T_λ for all major atmospheric constituents

$$T_\lambda = T_{R\lambda} + T_{w\lambda} + T_{wa\lambda} + T_{d\lambda} + T_{da\lambda} + T_{oz\lambda} \quad (3)$$

where the subscripts R, w, wa, d, da, and, oz refer, respectively, to Rayleigh scattering, water vapor scattering, water vapor absorption, aerosol scattering, aerosol absorption, and ozone absorption. In (3) we neglect the small amount of absorption by the uniformly mixed gasses such as CO_2 .

The sunphotometer measurements were obtained at normal incidence ($\cos Z = 1.0$); customarily the wavelengths measured by the Volz instrument are in a water vapor absorption window (although this is not quite true at 1.07μ). Neglecting water vapor, we write (2)

$$S_{\lambda\downarrow}^0 = S_{0\lambda\downarrow} \exp - \left[\{T_{R\lambda} + T_{Oz\lambda} + T_{d\lambda} + T_{da\lambda}\} \cdot m \right] \quad (4)$$

which is usually expressed in decadic notation (base 10) as

$$S_{\lambda\downarrow}^0 = S_{0\lambda} \cdot 10^{-\{k_{R\lambda} + k_{Oz\lambda} + B_{\lambda}\} \cdot m} \quad (4b)$$

where B_{λ} is the decadic extinction coefficient (turbidity) for aerosol and $T_{\lambda} = 2.303 k_{\lambda}$. The value of B_{λ} , sometimes referred to as the Volz or Scheupp turbidity (Flowers et al., 1969), is obtained from the sunphotometer measurements, the coefficients k_R and k_{Oz} being calculable from standard tables (Elterman, 1968; Smithsonian Meteorological Tables, 1951). In practice, B_{λ} is calculated without the water vapor scattering correction because it is felt that this effect is insignificant in the visible range.¹

Unsworth and Monteith (1972) attempted to measure the whole spectrum dust extinction T_D as a Linke turbidity factor, which is equal to the sum of the scattering and absorption coefficients for dust. This factor is treated as a whole spectrum (bulk) extinction coefficient which is redefined in terms of an integration over the whole solar spectrum. The

¹Subsequent use is made of a water vapor scattering transmission coefficient for the total solar spectrum. We now feel that this was not fully justifiable and that the scattering due to water vapor alone is negligible.

intensity of direct solar radiation for the entire spectrum is:

$$S\downarrow^0 = S_0\downarrow \cdot \cos Z \cdot \exp - \left[\left\{ T_R + T_w + T_{wa} + T_{Oz} \right\} \cdot m \right] \\ \cdot \exp \left[- T_D \cdot m \right] \quad (5a)$$

$$= S_0\downarrow \cdot \cos Z \cdot a_g(m,w) \cdot a_D = S\downarrow^* \cdot a_D \quad (5b)$$

where $a_g(m,w)$ is the whole spectrum transmission below an atmosphere free of aerosol and a_D is the bulk dust transmission for that atmosphere.

The calculation of a_g is based upon the Smithsonian method (similar to that of Idso (1969)) and uses Houghton's (1954) curves for dry air and water vapor scattering and McDonald's (1960) relationship for water vapor absorption. (Ozone was neglected for the whole-spectrum computations.) A mean solar constant ($S_0\downarrow$) of 1.955 lys/min, divided by r_s^2 , the solar distance squared, was used in place of $S_0\downarrow$. Precipitable water, w , was determined from the 1200 GMT soundings aboard the ship. Dewpoints were corrected for radiation heating of the hygistor; the correction (the difference between the dashed and solid dewpoint curves in fig. 1) was determined by comparing the differences between a large number of day-night paired soundings made during BOMEX and aboard the *Discoverer* during August 1972.²

We next calculate the dust-free, clear-sky diffuse component of downward radiation $D\downarrow^*$. This is not simply given by any relationship; but for isotropic or Rayleigh scatter, where the scattering function is symmetric,

²No sounding was made aboard ship on August 9. The number 61415 in parenthesis in the last column of Table 1 refers to the radiosonde station for Nouadhibou, Mainitania (21.5N, 17.2W).

approximately one-half the scattered radiation will reach the ground and the remainder is backscattered to space. For multiple scattering, slightly less than half the solar radiation scattered will reach the ground, decreasing with increasing zenith angle and optical depth. This can be expressed

$$G_{\downarrow}^* = \frac{S_{00\downarrow}}{r_s^2} \cdot \cos Z \cdot \left[a_g + f_Y(T_{g,m}) \cdot a_{wa}(1 - a_R \cdot a_w) \right] \quad (6)$$

where f_Y is defined as the fraction of the direct solar beam energy scattered that reaches the sensor, i.e., the ratio of forward-to-total scatter.

Robinson (1966) suggests a functional form for f_Y as $0.5 \cos^{1/3} Z$, which was used in subsequent calculations.³ This enables G_{\downarrow}^* to be calculated; whereas, the pyranometer measures G_{\downarrow}^0 , the difference ($G_{\downarrow}^* - G_{\downarrow}^0$) being the amount of energy scattered by the aerosol and lost to space plus the amount absorbed in the aerosol. This can be expressed by expanding the attenuation coefficient for aerosol T_D as

$$T_D = T_d + T_{da} = T_{dd} + T_{du} + T_{da} \quad (7)$$

where the expansion considers an effective attenuation for direct radiation by downward scatter due to aerosol (T_{dd}), by upward scatter to space (T_{du}), and by absorption (T_{da}). Since the pyranometer measures all scatter radiation by reaching the surface, as well as direct radiation, the

³A later examination of calculations made from the exact multiple scattering theory for a Rayleigh atmosphere (Deirmendjian and Srkera, 1954) indicates that the functional form of f_Y used in this paper poorly represents the real atmosphere and its use may significantly underestimate the diffuse radiation for low sun angle. Our future work will contain a more correct multiple scatter parameterization.

difference between measured and calculated solar energy is related to the upwards scatter and the aerosol attenuation as expressed by T_{da} and T_{du} . The net transmission a_{dn} due solely to aerosol is thus defined as the product of the transmission scattering and dust absorption, where

$$G\downarrow^0 = G\downarrow^* \cdot a_{dn}. \quad (8)$$

Admittedly, this treatment is a gross simplification of the exact radiative transfer theory, but it is accurate enough to calculate the net dust transmission to within a few percent. Neglect of ozone and other trace gas absorptions will cause a_{dn} to be underestimated a percent or two, while inaccuracies in f_Y will result in a few percent overestimated for longer path lengths. A more significant error in the absolute sense is in the solar constant, which we chose to be 1.955 lys/min. Robinson (1966) and others suggest a solar constant near 2.00 lys/min, but the lower values used in the literature may reflect a restricted solar constant appropriate to measurements by instruments that do not have 100 percent sensitivity over the whole solar spectrum. To some extent many of these uncertainties will tend to cancel, leaving a residual error of probably no more than a few percent in a_{dn} . This is sufficiently accurate to enable variations in a_{dn} to reflect real changes in the character of the dust layer. An example of a daily profile of the calculated $G\downarrow^*$ is shown by curve A in figure 3.

3. OBSERVATIONAL RESULTS

Profiles of $G\downarrow^*$ were calculated for each of the 20 days in August 1972 that had daily pyranometric records. The 3-min averages of $G\downarrow^0$ were

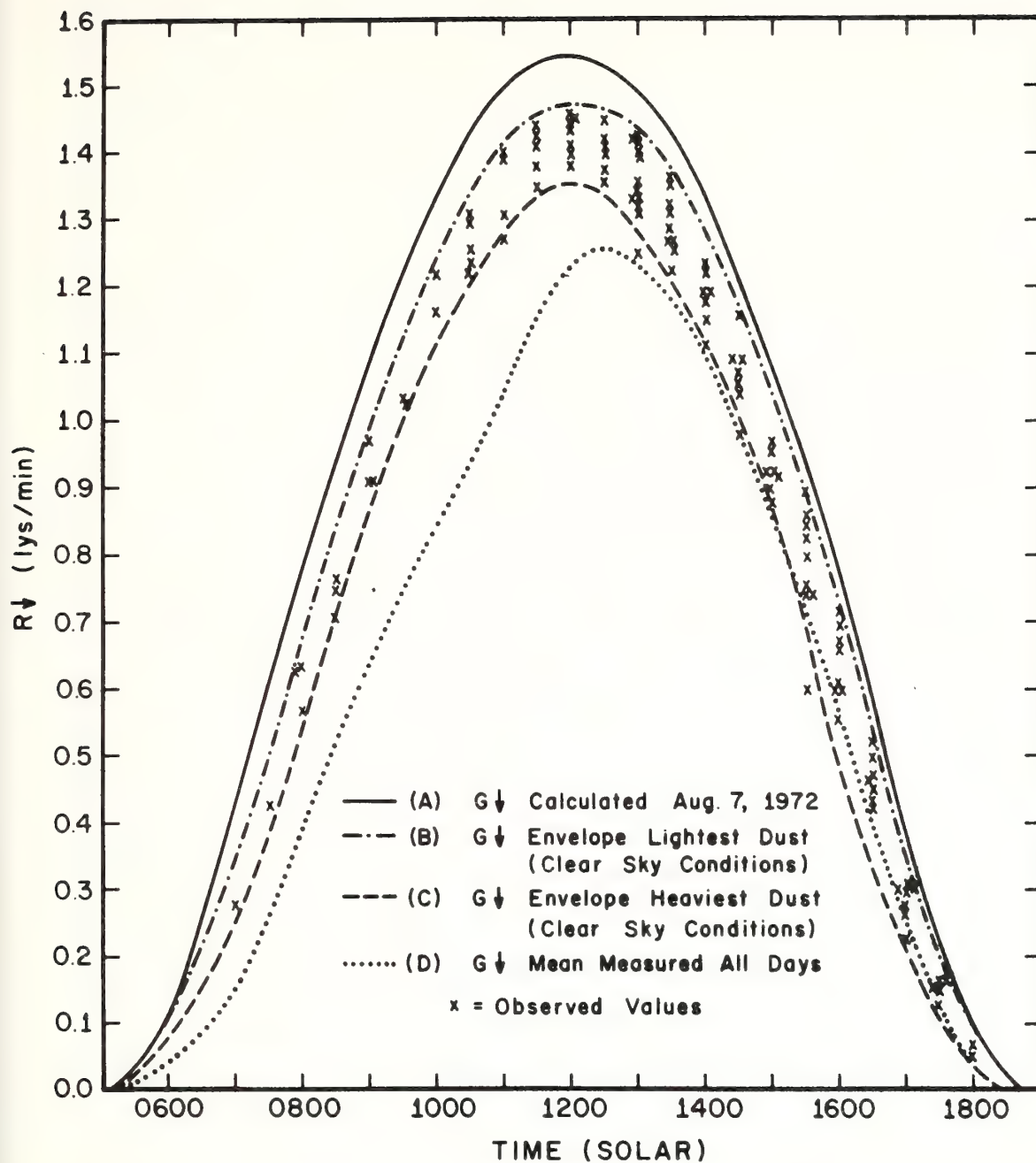


Figure 3. Total solar radiation profiles. Curve A is a calculation of $G \downarrow^*$ for a representative day during August 1972. Curves B and C are the upper and lower envelope of data points (the x's) for all clear-sky measurements of $G \downarrow^0$ (table 1). Curve D is the mean daily profile of net solar radiation for the entire period.

plotted on a series of graphs, one for each day, for periods that were considered essentially cloud-free. The procedure was followed for $G\downarrow^*$, for values of the surface albedo ($G\uparrow^0/G\downarrow^0$), and for the calculated a_{dn} . Smooth curves were drawn through the data points where the data were dense enough and the scatter small enough to define a continuous line. These smoothed values are listed in Table 1 where row A through D, respectively, refer to the calculated net dust transmission (a_{dn}), the total measured solar radiation ($G\downarrow^0$), the surface albedo in percent, and the measured Volz turbidity values ($B_{0.5}$) determined from the sunphotometers (aboard either the *Iselin* or the *Discoverer*) at 0.5μ . Solar noon was calculated from the ship's position and Greenwich time; however, where possible the profile was adjusted so that the apex of the solar intensity profile coincided with calculated solar noon. In some cases, an adjustment of a few minutes was necessary.

The values in Table 1 refer to the smoothed values that were read from the graphs at 1/2 hour intervals from solar noon (except for the turbidities, which were assigned to the closest 1/2 hour). All the 1/2 hour intensities were composited on a single graph, as shown by the x's plotted in figure 3. Except for the fluctuations in precipitable water and the minor changes due to the latitude and seasonal movement, the scatter should represent extremes of dustiness for the period; the upper envelope of these points (curve B) represents an almost dust-free day and the lower envelope (curve C) represents a rather hazy day.

From Table 1 a series of curves of a_{dn} versus solar time were drawn for each of the 16 days having some essentially clear periods. These curves (fig. 4), which are similar to ones presented by Robinson (1962),

Table 1. *DISCOVER Cruise August, 1972 - Data Sheet*

DATE & POSITION	SOLAR TIME										SOLAR TIME										PW	(GMT) SOLAR HOUR	SURFACE DUST CONC $\mu\text{g}/\text{m}^3$	SAL
	0700	0730	0800	0830	0900	0930	1000	1030	1100	1130	1200	1230	1300	1330	1400	1430	1500	1530	1600	1630				
AUG 4																								
237 N, 183 W																								
AUG 5																								
219 N, 191 W																								
AUG 6																								
212 N, 191 W																								
AUG 7																								
218 N, 185 W																								
AUG 8																								
209 N, 172 W																								
AUG 9																								
210 N, 172 W																								
AUG 10																								
217 N, 171 W																								
AUG 11																								
219 N, 185 W																								
AUG 12																								
219 N, 185 W																								
AUG 13																								
190 N, 204 W																								
AUG 14																								
167 N, 217 W																								
AUG 15																								
167 N, 217 W																								
AUG 16																								
164 N, 186 W																								
AUG 17																								
166 N, 202 W																								
AUG 18																								
161 N, 235 W																								
AUG 19																								
162 N, 233 W																								
AUG 20																								
178 N, 225 W																								
AUG 21																								
203 N, 194 W																								
AUG 22																								
216 N, 180 W																								
AUG 23																								
217 N, 178 W																								

A = a_{dn}

B = SG+ (lys/min)

C = SG+SG+ x 100 (surface albedo)

D = Turbidity 0.5 μ

PW = Precipitable water (cm)

Parentheses () indicate interpolated or indefinite values

Letters D and I refer to Ships *Discover* and *Iselin*

AEROSOL TRANSMISSION (a_{dn}) vs. SOLAR TIME and PATH LENGTH (m) FOR DAYS IN AUG, 1972

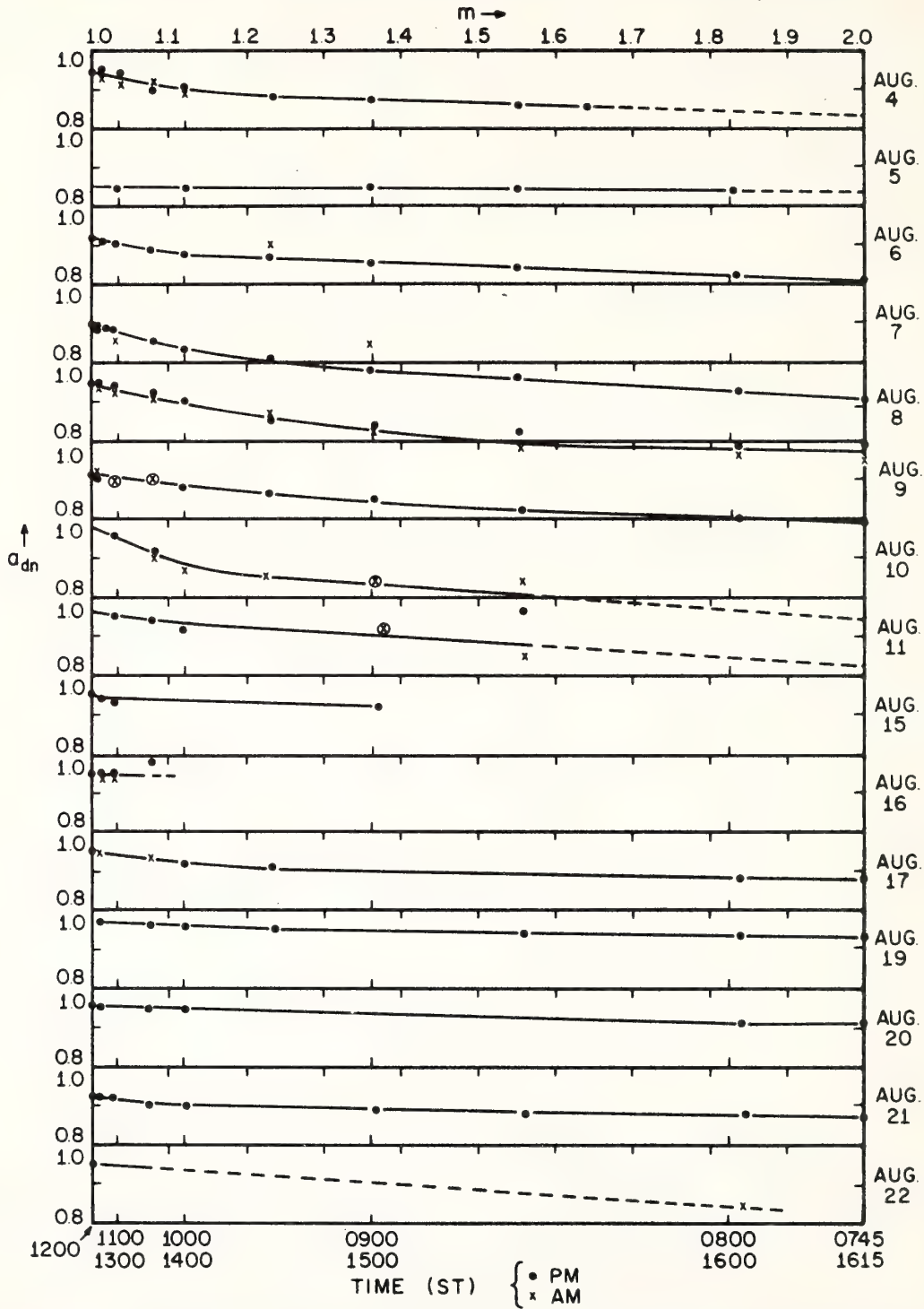
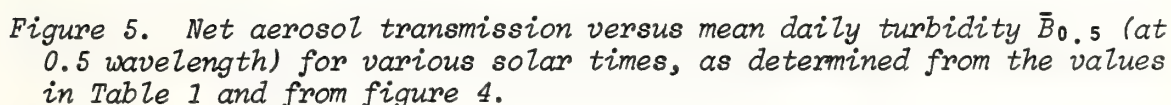


Figure 4. Net aerosol transmission versus path length (solar time) as calculated for both morning (the crossed circles) and afternoon values (filled circles), as listed in Table 1.

AEROSOL TRANSMISSION (a_{dn}) vs. MEAN DAILY
TURBIDITY ($B_{0.5\mu}$) FOR VARIOUS SOLAR TIMES (ST)



through data to intersect the ordinate at a point where $\bar{B}_{0.5}$ is almost zero (but positive). With increasing sun angle, the values of a_{dn} are increasingly sensitive to changes in turbidity.

Figure 6 was constructed directly from figure 5 and shows the family of turbidity curves for a_{dn} versus solar time. Although this figure has been composed of successively smoothed data, it does illustrate the anticipated result; i.e., the net radiation at the surface decreases with increasing turbidity and that the transmission through haze decreases with increasing path length. In contrast, however, there is no systematic relationship between surface level dust concentrations with the turbidity (fig. 7) or with the depth of the Saharan air layer.⁴

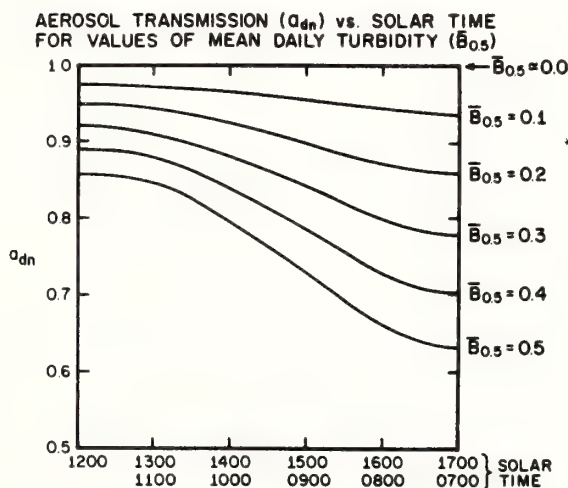


* Figure 6. Net aerosol transmission a_{dn} versus solar time for values of atmospheric turbidity (at 0.5 wavelength), as determined from the lines of the best fit in figure 5.

⁴The lack of variation of atmospheric turbidity with surface dust concentrations may be due in part to the location of the measurements, often very close to the coast, where one could expect local and unrepresentative contamination from shoreline sources. Thus coastal dust would remain in a very shallow layer beneath the SAL.

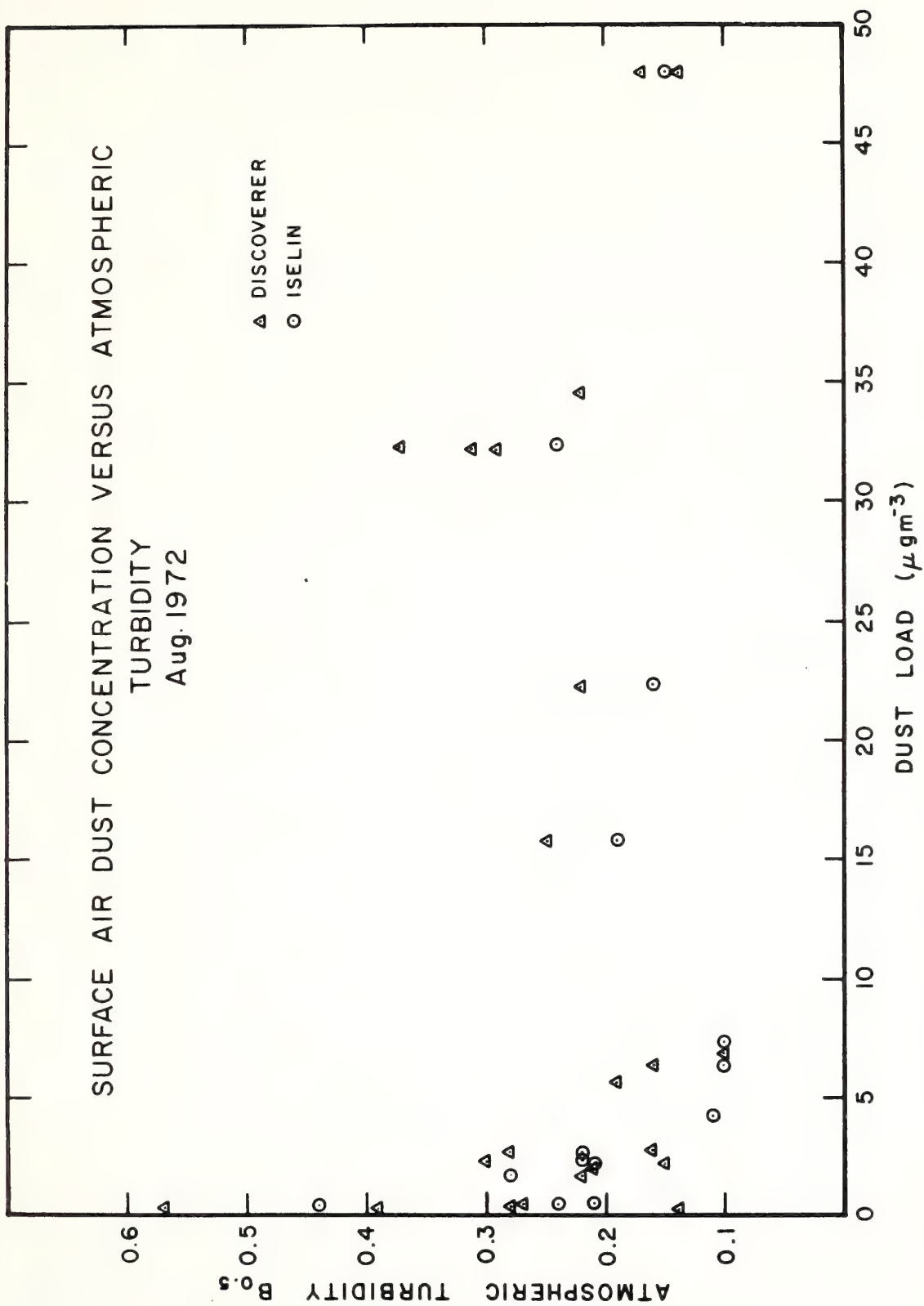


Figure 7. Surface air dust concentration versus atmospheric turbidity, August 1972.

Figure 6 indicates a systematic variation between attenuation of solar radiation reaching the sea and atmospheric turbidity. The broad-band-narrowband relationship is not surprising in view of our turbidity measurements at 0.85 and 1.07 μ , which show B value of a comparable magnitude to those at 0.5 μ .⁵ The Angstrom scattering coefficient α_A (Bullrich, 1964) is therefore close to zero, implying a near *neutral* haze scattering. Calculated values of α_A for both wavelength pairs, 0.5 versus 1.07 μ ($\bar{\alpha}_1$) and 0.5 versus 0.85 μ ($\bar{\alpha}_2$), were generally found to be between -0.2 and +0.3 (Table 2), implying that the haze consists of rather large particles as compared with typical maritime values of α_A which lie between 1.0 and 2.0 (Volz, 1970; Rangarajan, 1972). Small values of α_A associated with large hygroscopic particles downwind from the desert areas have been indicated by the work of Roosen et al. (1973).

4. SIGNIFICANCE OF THE TURBIDITY AND RADIATION MEASUREMENTS

The Volz turbidity is the extinction of solar radiation in a very narrow wavelength caused by total scattering and absorbing by the aerosol. Unlike the Rayleigh scattering, aerosol scattering is very strongly in the forward direction, with the foreshatter-to-backscatter ratio being 5 to 10 to 1; i.e., in our notation $T_{dd} \gg T_{du}$. Large amount of the scattered radiation, as detected by measurements of direct solar radiation, arrive at the pyranometer sensor undifferentiated from direct solar

⁵A slight correction for water vapor absorption applied in calculating the turbidities at 1.07 μ , as suggested by Volz in a private communication.

Table 2. Mean Daily Angstrom Turbidity Coefficients[†]
August 1972

Date	$\bar{\alpha}_1$	$\bar{\alpha}_2$	Date	$\bar{\alpha}_1$	$\bar{\alpha}_2$
4	----	----	14	0.1	-0.4
5	-0.4	----	15	0.1	-0.1
6	0.2	0.2	16	0.1	0.1
7	0.2	----	17	0.4	----
8	0.1	-0.2	18	----	----
9	0.0	0.0	19	0.3	0.0
10	0.1	-0.1	20	0.5	----
11	0.1	-0.2	21	0.3	----
12	0.0	-0.1	22	0.2	----
13	----	----	23	0.3	----

[†] $\bar{\alpha}_1$ Angstrom turbidity coefficient 0.5 versus 1.07μ ; $\bar{\alpha}_2$ for 0.5 versus 0.85μ .

radiation. The correlation between photometer and pyranometer measurements must be due to variations in the component of backscattered and absorbed solar radiation. Although absorption by aerosol may constitute a relatively small percentage of the attenuation of a direct solar beam, its magnitude may be significant (Vonder Haar and Cox, 1972). A reasonable estimate of this absorption given by Robinson (1962) is two-thirds the total beam extinction due to aerosol.

That the backscatter from the Saharan dust layer can be significant is substantiated observationally by examining the ATS-3 meteorological satellite pictures where massive clouds dust, appearing as light toned areas in the photos, periodically advance westward from the African coast in a large-scale plume.⁶ At other times when our measurements show heavy

⁶One such occasion was during March 7-9, 1973, when the dust cloud was so thick it obscured some of the land mass and coastal boundaries.

dust concentrations in the Saharan layer, the dust does not show on the satellite photograph, suggesting that size spectra and hygroscopic properties of the dust particles may be an important factor in its opacity.

We can make a crude estimate of the relative importance of aerosol attenuation on the atmospheric energy balance as compared with the cloud cover. The mean net radiation reaching the sea surface averaged over the entire 20-days was 538 lys/day as represented by the area under curve D in figure 3. The net solar radiation at the sea surface, as calculated for the cloud-free, dust-free case (\bar{G}_\downarrow^*) — the area under curve A in figure 3 — is 719 lys/day, which is 47 lys/day larger than that amount obtained by integrating under curve B, 672 lys/day, in relatively dust-free envelope. A reasonable estimate for the normally hazy case might be obtained by integrating under a curve drawn mid-way between curves B and C in figure 3. This median curve is 617 lys/day, which corresponds to an average aerosol transmission (a_{dn}) of 0.92 at solar noon; on the bases of figure 6 this value of a_{dn} is equivalent to a turbidity value ($B_{0.5}$) of about 0.3.⁷ On such an average hazy day along the African coast, the aerosol depletion is 100 lys/day and the average daily transmission (\bar{a}_{dn}) is equal to 0.86. Figure 3 indicates, however, that an average combination of cloud and dust will deplete about 180 lys/day from the solar beam (the area under curve A minus the area under curve D); this suggests a rough parity between cloud cover and dust in the mean for solar attenuation in that region.

⁷This is roughly comparable with the mean turbidity for the industrial northeastern United States (Flowers et al., 1969).

Our observations of dustiness suggest that the heaviest concentrations of aerosol are to be found in a belt extending southwestward from the African coast between Dakar (14.5N) and Cape Blanc (21.5N) across the Cape Verde Islands. Cloud cover in this region is not scanty in summer but it tends to be broken and rather thin. Consequently, it is not surprising that the Saharan dust layer, which in this area is rather deep and persistent, appears in the mean to be as important as the cloud cover in attenuating solar radiation.⁸

Assuming an average depletion of 100 lys/day by the aerosol, two-thirds of which is absorbed, we find the presence of a Saharan layer will induce a net cooling of the ocean-atmosphere system of about 34 lys/day, a net warming in the lower and middle troposphere of 66 lys/day, and a net cooling of the surface layers. All of which results in a net increase in atmospheric stability below 500 mb. If the tropospheric warming is confined to the dust layer, a depth of 500 mb, the net warming in the SAL will be about 0.5°C/day. Carlson and Prospero (1972) attempted to estimate the net radiative cooling of the SAL by following its isentropic segments over several days and observing temperature changes in the layer. They concluded that the SAL was losing heat at the rate of 0.7 to 0.8°C/day. In the absence of dust, therefore, the present results suggest that the same depth of atmosphere would be losing heat at a rate of 1.2 to 1.3°C/day.

⁸The observed profile of net solar radiation for the period (curve D in fig. 3) has a peculiarity that may be characteristic of this region near the African coast. The cloud cover was usually much heavier in the morning than in the afternoon, and often it dispersed entirely around noon-time. Therefore, the peak solar intensities values were, in the mean, shifted about 30 min past solar noon.

5. CONCLUSIONS

North Africa constitutes a major source of natural aerosols for the equatorial Atlantic, therefore, the extinction of solar radiation by Saharan dust may have a significant effect on the tropospheric heat balance. Pyranometric and sunphotometer measures aboard the NOAA Ship *Discoverer* near the West African coast (16-22N) during August 1972 show variations of the total clear-sky irradiance at the sea surface that relate systematically to changes in the atmospheric turbidity. The turbidity measurements suggest a nearly neutral haze extinction which suggests that the size distribution of particles is skewed toward the large end of the spectrum. Calculations of solar extinction due to backscatter and absorption of dust particles show that the mean daily clear-sky haze transmission under typical haze conditions is about 0.86 in this area. A reasonable apportionment of this attenuated energy between absorption and backscatter would suggest that the Saharan dust cools the ocean-atmosphere system but warms the middle levels.

6. ACKNOWLEDGMENTS

The authors would like to thank Dr. Peter Rona of AOML for inviting us to make use of the *Discoverer's* Trans-Atlantic Geotraverse cruise during the summer of 1972. The pyranometer measurements were obtained through the efforts of Mr. Peter Connors of SAIL who joined the ship for the second leg of the cruise. We are grateful to crew members of both the NOAA Ship *Discoverer* and the University of Miami ship *Columbus Iselin* for their cooperation and particularly to Mssrs. Michael Davidson and

Stellan Ostland who, aboard their respective ships, took the sunphotometer readings and operated the aerosol pumps. The sunphotometers were generously loaned to us by Dr. F. Volz of AFCRL and we wish to thank him for his continuing assistance. The tedious job of digitizing the records was performed by Mr. Bill Mallo. Mr. Dale Martin of NHRL did the drawings.

7. REFERENCES

- Bullrich, Kurt, 1964: Scattered radiation in the atmosphere and the aerosol. *Advances in Geophysics*, 10:99-260, (Academic Press, N.Y.).
- Carlson, T. N., and J. M. Prospero, 1972: The large scale movement of Saharan air outbreaks over the equatorial Atlantic Ocean. *Journal of Applied Meteorology*, 11:283-297.
- Deirmendjian, Diran, and Z. Sekera, 1954: Global radiation resulting from multiple scattering in a Rayleigh atmosphere. *Tellus*, VI:382-398.
- Elterman, L., 1968: UV, visible, and IR attenuation for altitudes to 50 km. *Environmental Research Papers*, No. 285, Optical Physics Laboratory, AFCRL, 68-0153, Bedford, Mass., 49 pp.
- Flowers, E. C., R. A. McCormick, and K. R. Kurfis, 1969: Atmospheric turbidity over the United States. *Journal of Applied Meteorology*, 8:955-962.
- Hanson, Kirby, and M. Poindexter, 1972: Attendance of broad band solar irradiance in the ocean. *Conference on Atmospheric Radiation*, Proceedings, American Meteorological Society, Fort Collins, Colo., August 7-9, pp. 165-168.
- Houghton, H. G., 1954: On the annual heat balance of the Northern Hemisphere. *Journal of Meteorology*, 11:1-9.
- Idso, Sherwood, B., 1969: Atmospheric attenuation of solar radiation. *Journal of the Atmospheric Sciences*, 26:1088-1095.
- McDonald, J. E., 1960: Direct absorption of solar radiation by atmospheric water vapor. *Journal of Meteorology*, 17:319-328.
- Prospero, J. M., 1968: Atmospheric dust studies on Barbados. *Bulletin of the American Meteorological Society*, 49:645-652.
- Prospero, J. M., and T. N. Carlson, 1972: Vertical and areal distribution of Saharan dust over the western equatorial North Atlantic Ocean. *Journal of Geophysical Research*, 77:5255-5265.

- Rangarajan, S., 1972: Wavelength exponent for haze scattering in the tropics as determined by photoelectric photometers. *Tellus*, 24:56-64.
- Robinson, G. D., 1962: Absorption of solar radiation by atmospheric aerosol as revealed by measurements at the ground. *Arch of Meteorology Geophysics and Bioclimatology*, B12:19-40.
- Robinson, N., 1966: *Solar Radiation*. (Elsevier, N.Y.), 347 pp.
- Roosen, R. G., R. J. Angione, and C. H. Klemake, 1973: World-wide variations in atmospheric transmission: 1. Baseline results from Smithsonian Observations. *Bulletin of the American Meteorological Society*, 54:298-306.
- Smithsonian Meteorological Tables*, 1951: Sixth Revised Edition, Smithsonian Institution, Washington, D.C., 527 pp.
- Unsworth, M. H., and J. L. Monteith, 1972: Aerosol and solar radiation in Britain. *Quarterly Journal of the Royal Meteorological Society*, 98:778-797.
- Volz, F. E., 1970: Spectral skylight and solar radiance measurements in the Caribbean: Maritime aerosols and Sahara dust. *Journal of Atmospheric Sciences*, 17:1041-1047.
- Vonder Haar, J., and S. Cox, 1972: Simultaneous measurements of solar radiation from aircraft and satellites during BOMEX. *Proceedings Conference on Atmospheric Radiation*, American Meteorological Society, Fort Collins, Colo., August 7-9, pp. 128-133.

OCEANOGRAPHIC FEATURES IN THE LEE OF THE WINDWARD AND LEEWARD ISLANDS: ERTS AND SHIP DATA

Kirby J. Hanson, Frank Hebard,¹ and Richard Cram,² *Atlantic Oceanographic and Meteorological Laboratories, National Oceanic and Atmospheric Administration, Miami, Florida*

ABSTRACT

Analysis of the ERTS data in portions of the eastern Caribbean are presented for October 1972 showing features which are, as yet, not explained.

Ground truth data obtained in that area during November 1972 are presented. These include vertical temperature structure in the mixed layer and thermocline, and surface measurements of salinity, temperature, and chlorophyll.

1. INTRODUCTION

In previous work in this area, Ingham and Mahnken³ found that tuna schools and bird flocks were concentrated in an area west of St. Vincent Island, Lesser Antilles. They also noted that plankton and primary productivity in the mixed layer were higher in this area than in the Atlantic, and that horizontal temperature differences existed in the upper thermocline in this area which suggested the presence of eddy-like features in the ocean. They suggested the possibility that the increased productivity of this area is a consequence of downstream turbulence on the Caribbean side of St. Vincent Island.

2. ERTS-1 DATA

NASA has collected ERTS-1 MSS Channel 4-7 data over portions of the eastern Caribbean on four cycles in the September-November, 1972 period. For the two ERTS cycles of best photographic coverage, the ERTS photos have been

¹ National Marine Fisheries Service, NOAA, Washington, D. C.

² Rosensteil School of Marine and Atmospheric Science, University of Miami, Coral Gables, Florida

³ Turbulence and Productivity near St. Vincent Island, B.W.I., A Preliminary Report, Contribution No. 42, Tropical Atlantic Biological Laboratory, Bureau of Commercial Fisheries, Miami, Florida 33149

mosaicked and are shown in Figures 1 and 2. The island arc is visible in many of these ERTS photos.

In comparing Figure 1 (October 13-16, 1972) and Figure 2 (Nov. 17-21, 1972), it is clear that there are horizontal differences in the upward spectral radiance from the ocean surface during the October 13-16 period, but such differences are only slightly apparent in the November 17-21 period. These horizontal differences appear in the lee (west side) of each of the major islands of the Lesser Antilles. Figures 1 and 2 have been presented as negative prints of MSS Channel 4.

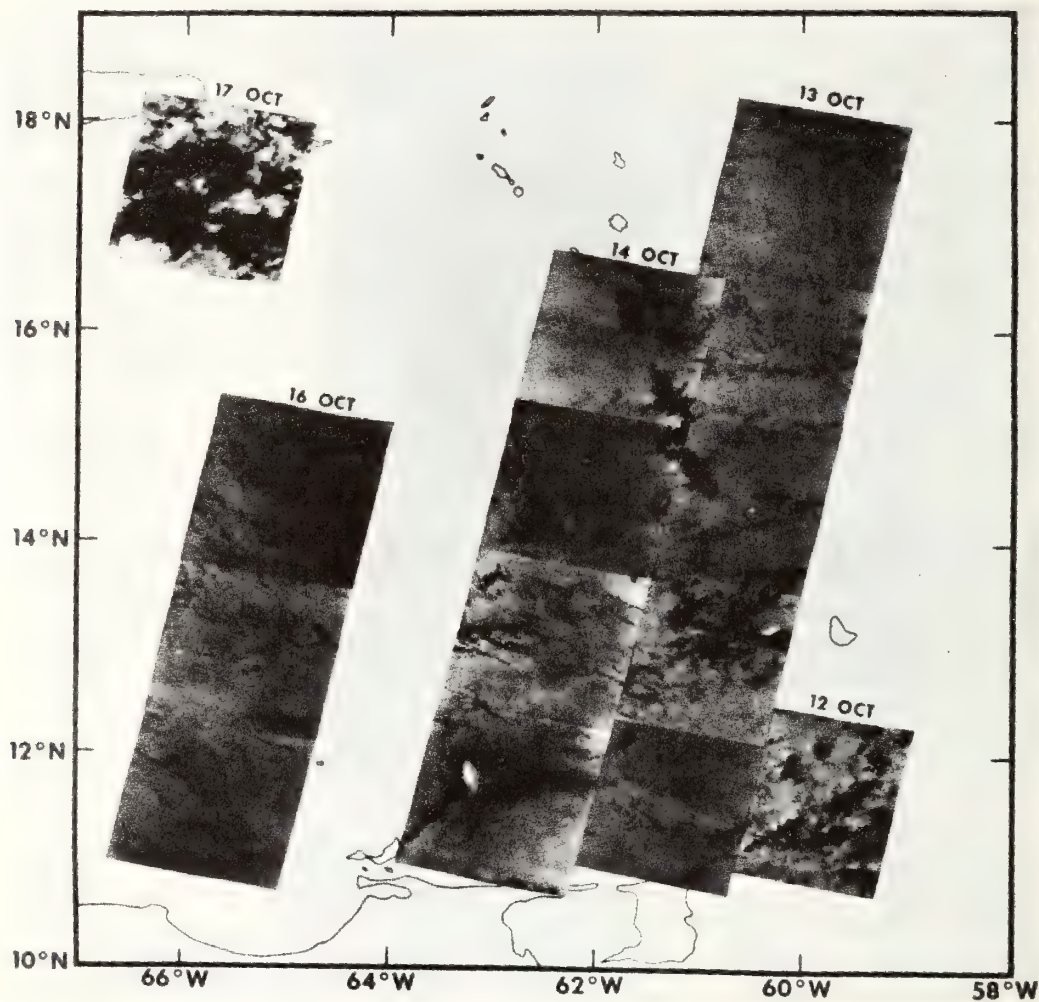


Figure 1. ERTS MSS Channel 4, 13-14, 1972

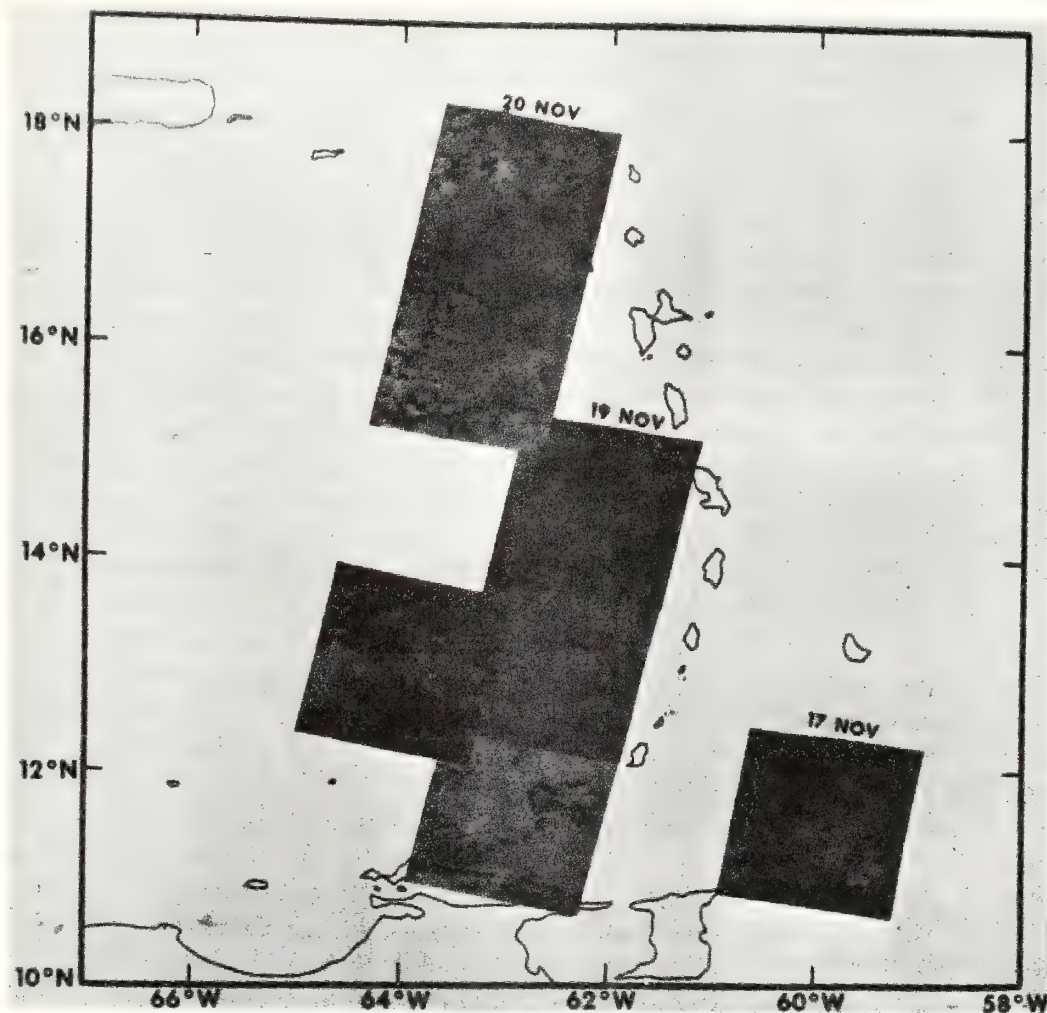


Figure 2. ERTS MSS Channel 4, Nov. 17-21, 1972

The ocean area west of Guadeloupe and Dominica is shown in more detail in Figure 3 and the ocean area west of Grenada and St. Vincent is shown in Figure 4 from the October 14, 1972, MSS Channel 5 data. These same ocean features are visible in MSS Channels 4-7.

3. GROUND TRUTH DATA (Nov. 15-16, 1972)

Ground truth information was obtained in the eastern Caribbean on the NOAA/CARIB cruise of the NOAA ship DISCOVERER. The ship track and times are shown in Figure 5; the hours are GMT. The ocean variables measured were:



Figure 3. ERTS MSS Channel 5, October 14, 1972. Shows Guadeloupe and Dominica and features in the lee of the islands.

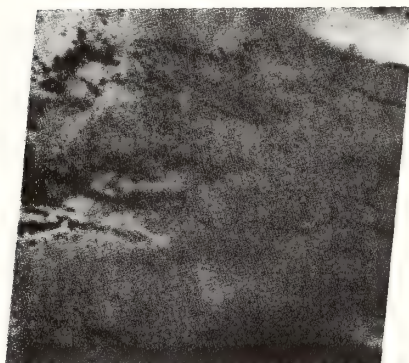


Figure 4. ERTS MSS Channel 5, October 14, 1972. Shows features in the lee of St. Vincent (top) and Grenada (bottom).

1. temperature profile in the mixed layer and thermocline,
2. surface salinity,
3. surface chlorophyll,
4. surface nutrients,
5. upward spectral radiance at the sea surface.

The first three variables have been analyzed and are presented in Figures 6 through 9.

4. DISCUSSION

At the time of collection of ground truth data in the Eastern Caribbean in mid-November, 1972, ERTS data were not yet available to give an indication of

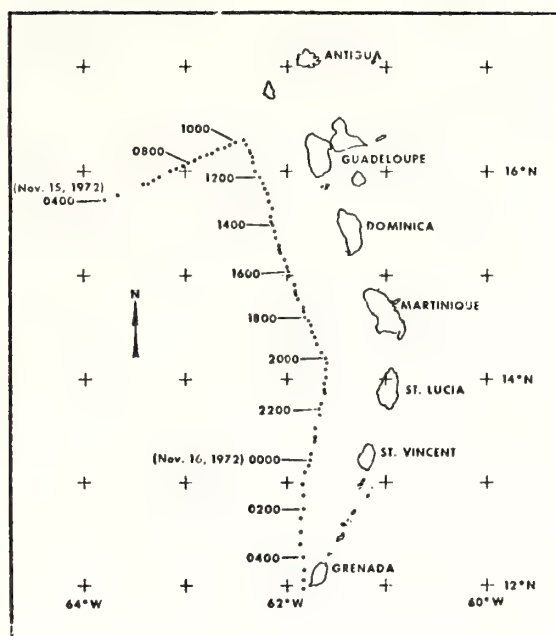


Figure 5. Cruise of DISCOVERER,
Nov. 15-16, 1972

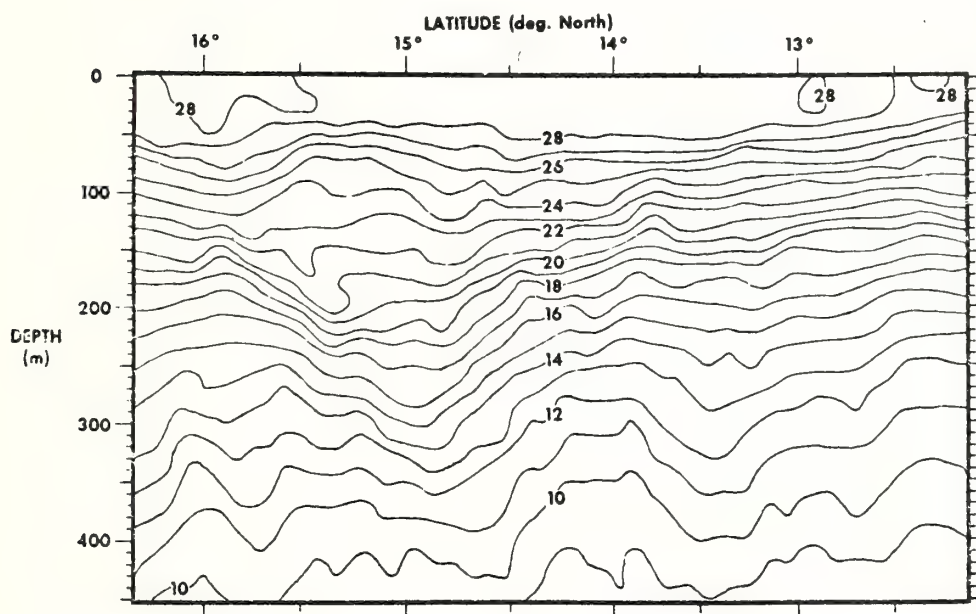


Figure 6. Temperature cross-section along ship track of Figure 5.

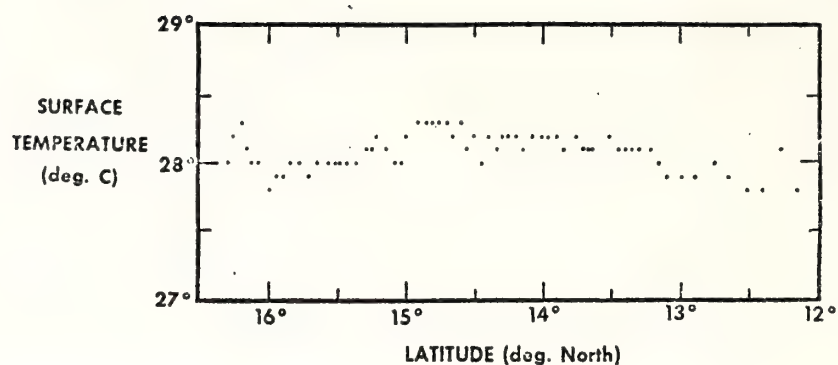


Figure 7. Surface temperature along ship track of Figure 5.

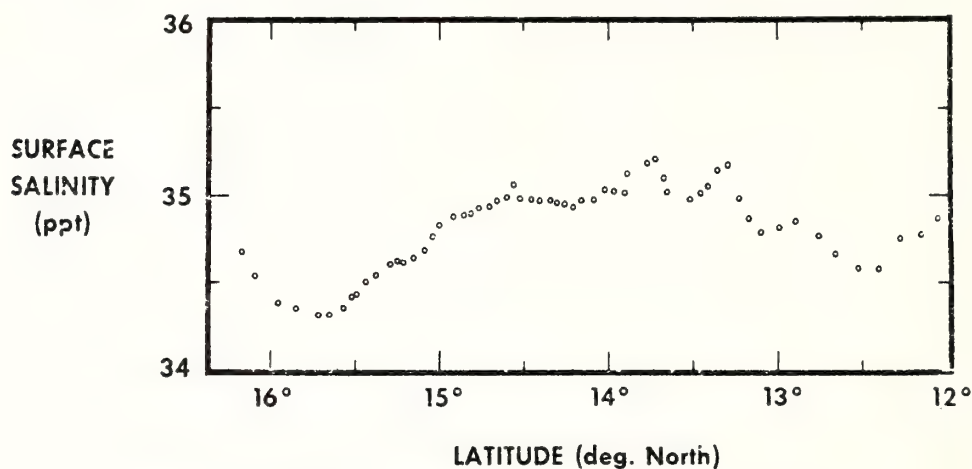


Figure 8. Surface salinity along ship track of Figure 5.

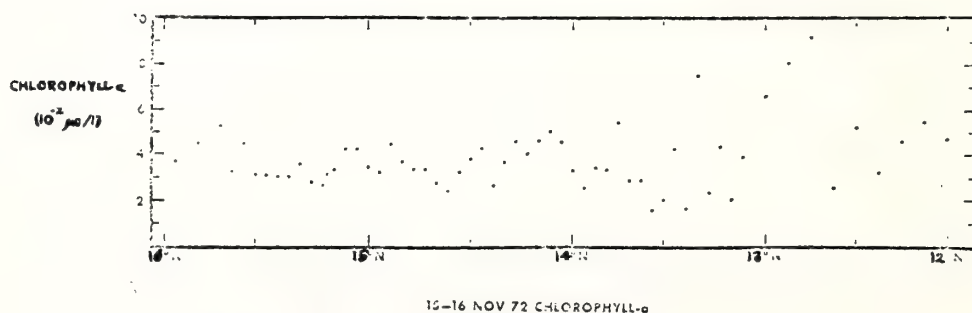


Figure 9. Surface chlorophyll along ship track of Figure 5.

the size and spatial distribution of the features which were apparent in ERTS data, occurring in the lee of each major island in the Antilles arc (Figure 1). Because of this lack of information when the ground truth were collected, only a single north-south cross section was obtained which paralleled the Antilles Island arc.

In the November 19-20, 1972 ERTS data (Figure 2), there are only very small horizontal gradients in image density in the lee of Martinique and Grenada compared to the October 13-14 period. The ground truth data (Figures 6 - 9) obtained four days earlier in that area do not reveal a pattern similar to that of the ERTS data of November 19-20, 1972.

Unfortunately, there were no ground truth taken during the October 13-14, 1972 period which is the only time these ocean features have been clearly apparent in the ERTS data. The features visible in the October 13-14, 1972 ERTS data (Figure 1) may result from one or a combination of causes associated with the atmosphere or ocean. Some possibilities are:

1. The sea state and/or swell is modified in a wind shadow of the island,
2. The run off of island rainfall carries high turbidity water in the mixed layer downstream of the island,
3. The phytoplankton in the mixed layer of the ocean has increased due to increased nutrients associated with upwelling.

We have compared the surface wind observations on the islands during the October 13-14 period with the November 17-21 period and found that the easterly winds were lighter during the October 13-14 period than the November 19-20 period. Thus, the wind observations at the island stations do not support the possible explanation in (1) above, that the sea state is modified due to wind shadow of the island.

In examining the ocean features which are visible in Figure 1, we find that the features are most apparent in channels 5 and 6, and are somewhat less apparent in channels 4 and 7.

Based on the present information, it is not possible to reach a firm conclusion about the cause of the features visible in Figure 1. It is hoped that in the future ground truth in coincidence with the ERTS data, and adequate ERTS data coverage, will resolve the question of the cause of these features.

Heat Flux and Precipitation Estimates from Oceanographic Observations

Abstract. Surface meteorological observations and salinity and temperature profiles were made in the intertropical convergence zone during July 1972. Over an 18-hour period, estimates of the heat budget in the top layer of the ocean and estimates of the total heat flux made by using aerodynamic parameterization equations balance within 10 percent. The salinity budget provides a precipitation estimate. Due to the stable stratification established by the salinity dilution in the wave-mixed layer by rain, the total heat flux to the atmosphere is being extracted from this shallow layer. As a result, large sea surface temperature drops occur regionally and may be capable of inhibiting atmospheric convection.

During the second phase of the Soviet national tropical experiment in July 1972, two of us (Ostapoff and Tarbeyev) had the opportunity to conduct an oceanographic experiment on board the R.V. *Professor Zubov*. The objective of the study was to estimate total heat fluxes from oceanographic measurements on short time scales (less than 1 day) and under the disturbed conditions of the intertropical convergence zone (ITCZ). The *Professor Zubov* was positioned at 5°N, 21°W during the experimental period. The most significant result of this study is the short-term response of the top layer of the ocean to meteorological events such as precipitation from convective systems embedded in the ITCZ.

The meteorological conditions were not completely favorable inasmuch as the ship was at the southern edge of the ITCZ most of the time. Precipitation occurred only on 19 July, and this day was chosen for the analysis reported here as a case study.

The structure of the atmosphere was not typical of deep-reaching convection, as evidenced by the types of clouds, mostly altocumulus and stratocumulus. During 19 July cloud tops

were observed by radar not to exceed 5 km, and the rain was rather steady. A rain bucket mounted on the flying bridge on the starboard side of the ship in lee of the wind collected a total of 17.5 mm of rain between 0923 and 2240 Greenwich mean time.

Surface meteorological observations were made routinely, as well as 2-hourly salinity-temperature-depth (STD) profiles down to 200 m. Here we present the data and compare the estimated budgets for heat and salt in the top layer of the ocean with estimates of the total heat flux made by using aerodynamic parameterization equations (1, 2).

The surface meteorological data obtained aboard the *Professor Zubov* were used to calculate the sensible and latent heat fluxes. The bulk aerodynamic equations were used for the flux calculations. Because relatively large instabilities in the atmospheric boundary layer exist during such events, coefficients were used which depend on the stratification (1-3).

The wind speeds were observed at 28 m (on top of the mast) by means of anemometers, and all other meteorological parameters were observed at a

height of 10 m. Therefore, it was necessary to calculate the wind speed for 10 m, taking into account the stability of the boundary layer (3). Figure 1 shows a diagram of the average radiation, heat, and mass fluxes during the period of interest.

As seen from Fig. 1, the total heat flux for the period amounted to about 246 langleys (ly) per day (4). The mean Bowen ratio for the period was $Q_s/Q_L = 0.196$, where Q_s is the sensible heat flux and Q_L the latent heat flux; the ratio varied from 0.048 to 0.247. A climatological Bowen ratio of this magnitude would be characteristic of higher latitude regions. In the tropics and subtropics, under undisturbed meteorological conditions, a Bowen ratio of 0.05 to 0.10 is more common. However, under the disturbed conditions that prevailed during the observational period, the calculated values of the Bowen ratio are comparable to the results reported by Garstang [table 2 in (5)] and Garstang *et al.* (6). The latent heat flux decreases drastically under conditions of broad light rain due to decreased wind speeds and high humidities. The air temperature drops markedly due to the cold downdrafts associated with the heavy precipitation of the convective clouds (6). Since the wind speed decreases only moderately, the sensible heat flux usually increases. Therefore, the Bowen ratio under disturbed conditions in the tropics typically becomes several times larger than its climatological value.

Although no net radiation was observed on that day, the total incoming solar radiation was measured to be 108 ly/day. The net long-wave radiation was calculated according to the following equation as given by Sverdrup *et al.* (7)

$$Q_{lw} = Q_1[0.56 - 0.08(e)^2](1 - 0.083C)$$

where Q_1 (langleys per day) represents blackbody radiation for the sea surface temperature, e (millibars) water vapor pressure, and C cloudiness on a scale of 1 to 10 (in this case 10). We estimate Q_{lw} to be about 13 ly/day and the reflected short-wave radiation to be approximately 5 percent of the incoming solar radiation, or 5 ly/day. During the period of interest the change in heat storage in the ocean occurs only in the top 11 m, as discussed below, but the solar radiation is absorbed over a much deeper layer. If the incoming solar radiation spectrum was that for a cloud-free day, the radiation passing through the layer of interest would be 22 ly/day

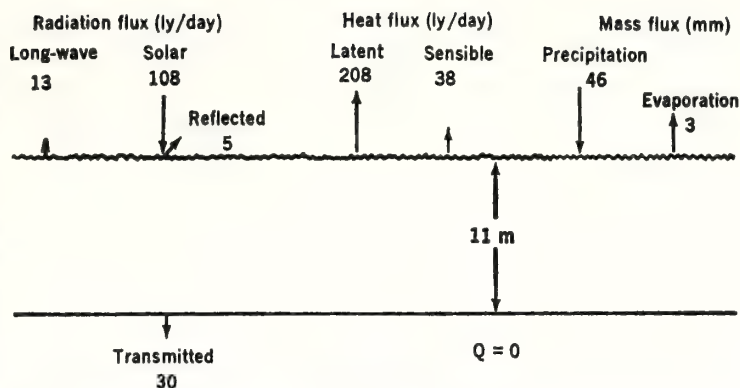


Fig. 1. Schematic diagram of the heat and mass budgets in the upper layer of the ocean on 19 July 1972 during overcast rainy conditions.

(8). However, the clouds substantially decreased the contribution of near-infrared radiation to the total incoming radiation (9). Since the uppermost portion of the ocean absorbs the near-infrared components first, and Jerlov's absorption coefficients (8) apply to a "normal" spectral distribution, we estimate the radiation passing through the 11-m layer to be 30 ly/day. Accordingly, the net radiation absorbed in the layer of interest is about 60 ly/day (see Fig. 1).

The oceanographic soundings at 0830 on 19 July and at 0230 on 20 July are presented in Fig. 2. Within 18 hours the salinity dropped by 0.14 per mil over a layer of about 11 m. This can be attributed to the amount of rain that fell during the period. As mentioned above, 17.5 mm of rain was measured on the ship, while approximately 43 mm is needed to dilute the salinity of 11 m of water from 35.64 to 35.50 per mil. The salinities given here are uncorrected STD values. These differ systematically by about 0.2 per mil when compared with values obtained

by titration methods on board the *Professor Zubov*. However, this difference is immaterial for the purpose of our discussion, since we deal only with differences. The precision of the salinity measurement was ± 0.01 per mil. The depth could be determined to ± 0.5 m. Therefore, for a mean salinity of 35.5 per mil over a depth of 1 m, the measurement error is about ± 3 mm.

Evidently a large discrepancy exists between the rain gauge observations and the values derived from the salinity budget. This could mean that the method of collecting rain on ships is not very accurate, or that more rain fell in the vicinity and the diluted water was advected, or both. Since the precipitation area was rather large (10 to 20 km) and the surface currents rather low (5 to 10 cm/sec), horizontal advection of heat or salt can be neglected on this scale. In other words, we believe that the sampling was representative over an area commensurate with the time and space scales involved.

With the lowering of salinity in the layer stirred by the wind waves, stable

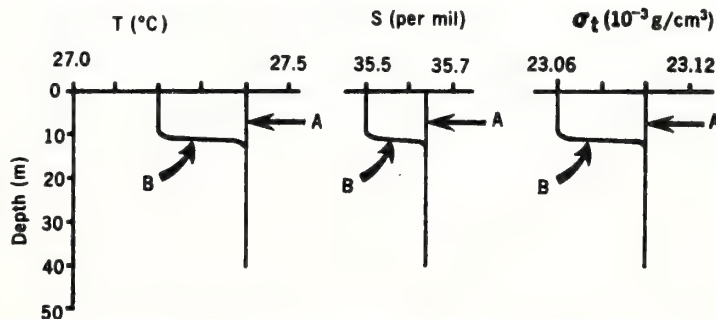


Fig. 2. Temperature (T), salinity (S), and density (σ_t) profiles before and after precipitation: (A) profiles at 0830, 19 July 1972; (B) profiles at 0230, 20 July 1972.

density stratification (see Fig. 2) is set up, limiting vertical convection to that layer. Continuing heat losses to the atmosphere are now derived from a much shallower layer (about 10 m) than the usual mixed layer (about 60 m), and the temperature profiles show dramatically the effects of net heat flux to the atmosphere. This cooling process will continue until the entire mixed layer assumes neutral stratification.

From the 18-hour temperature drop in the surface layer of the ocean, the total heat loss can be calculated as 210 ly/day. We can summarize the heat and precipitation budgets as follows.

Ocean:	
Heat storage change	— 210 ly/day
Atmosphere:	
Total heat flux	246 ly/day
Net radiation	— 60 ly/day
Total:	— 24 ly/day
Ocean:	
Evaporation	+ 3 mm
Net dilution	+ 43 mm
Precipitation	+ 46 mm
Atmosphere	
Precipitation (observed)	17.5 mm

this shows that the heat budget, neglecting advection, can be balanced within about 10 percent. This is definitely within the uncertainty of our STD measurements, while the heat flux calculations made by using the refined bulk equations may be no better than ± 20 percent. Also, the precipitation calculated from the dilution of the top layer is slightly more than $2\frac{1}{2}$ times as high as that observed with the rain gauge. This shows the difficulty of obtaining representative precipitation data aboard ship. It is well known that shipboard rain gauge measurements are inadequate. We suggest that the method outlined above may provide a more reliable precipitation estimate in some situations.

The method presented here for obtaining oceanic heat flux measurements and precipitation estimates independently of meteorological techniques seems to us specifically applicable to tropical regions and experiments such as the global atmospheric research program (GARP) Atlantic tropical experiment (GATE). A method of providing reliable estimates of heat, mass, and mo-

mentum transport across the air-sea interface during a meteorological event is essential. The observations show that on the time scale of a few hours, significant cooling and freshening occurs only over the wave-mixed layer. This allows the temperature of the ocean surface to become much lower than in the case where the heat loss is derived from the entire mixed layer. Since the stratification is stable, the ocean surface remains cool, inhibiting further atmospheric convective development. This air-sea feedback mechanism, which tends to limit the development of atmospheric convective systems, is important to the energetics of the tropical atmosphere. Therefore, this mechanism must be considered if a reliable prediction of long-term atmospheric behavior is to be made.

F. OSTAPOFF

Atlantic Oceanographic and Meteorological Laboratories, Sea-Air Interaction Laboratory, Miami, Florida

Y. TARBIEV

World Meteorological Organization, Geneva, Switzerland

S. WORTHEM

Atlantic Oceanographic and Meteorological Laboratories, Sea-Air Interaction Laboratory

References and Notes

1. K. Brooks and L. Krügermeyer, in *Studies in Physical Oceanography*, A. L. Gordon, Ed. (Gordon & Breach, New York, 1972), p. 75.
2. H. Hoerber, *Meteor. Forschungsverh. Reihe B* 3, 1 (1969).
3. E. Kraus, *Atmosphere-Ocean Interaction* (Oxford Univ. Press, London, 1972), pp. 134-166.
4. The unit 1 langley is equal to 1 cal/cm².
5. M. Garstang, *Tellus* 19, 492 (1967).
6. —, N. LeSeur, K. Warsh, R. Hadlock, J. Petersen, *Amer. Sci.* 58, 482 (1970).
7. H. Sverdrup, N. Johnson, R. Fleming, *The Oceans* (Prentice-Hall, Englewood Cliffs, N.J., 1946), pp. 111-113.
8. N. Jerlov, *Optical Oceanography* (Elsevier, Amsterdam, 1968), pp. 115-132.
9. K. Hanson and M. Poindexter, *NOAA Technical Memorandum ERL-AOML-16* (National Oceanic and Atmospheric Administration, Rockville, Md., 1972), pp. 17-18.
10. F.O. is grateful for the invitation to be a guest on board the R.V. *Professor Zubov* and for the hospitality given him on the ship, especially to Captain O. V. Andriyevskiy and the chief scientist, Dr. M. A. Petrosiants. It was a great pleasure to work with the entire crew, especially the physical oceanography group under the leadership of B. G. Borisov. We also appreciate being provided with the surface meteorological data.
11. December 1972; revised 28 February 1973

85-1

SECTION 85

**OBSERVATIONS OF OCEANIC WHITE CAPS
FOR MODERATE TO HIGH WIND SPEEDS**

by

**Duncan B. Ross
National Oceanic and Atmospheric Administration
Atlantic Oceanographic and Meteorological Laboratories
Sea-Air Interaction Laboratory
Miami, Florida**

and

**Vincent Cardone
Department of Oceanography
and Meteorology
New York University**

A series of photographs of sea surface whitecap conditions for wind speeds of 10 to 25 m/sec has been obtained and analyzed for areal coverage of white water. The results are in good agreement with the semiempirical calculations of Cardone based on the wind speed and the development of the wave spectrum only when the contribution of thin foam streaks oriented in the direction of the wind is neglected. Since both the actively forming whitecaps and the thin foam streaks contribute significantly, though perhaps to a differing degree, to the microwave emissivity of the sea surface, it is important that the foam streaks be included in the theory but differentiated from large white caps and foam patches. A simple relationship that accounts for the foam streaks based on the rate of energy transfer, the windspeed, and the wave spectrum is proposed herein. By means of empirically derived constant terms for the microwave signatures of white caps and foam streaks, this theory is adapted to the prediction of the increase in brightness temperature due to foam, with reasonable results to windspeeds of 20 m/sec.

INTRODUCTION

Current models for the prediction of the marine environment, both atmospheric and in the surface layers of the ocean, utilize many concepts developed from experimental results which are often contradictory. Roll (1965) stated that the most critical deficiency in most models is due to a serious lack of suitable, reliable, and repeatable measurements. A second inadequacy in current predictions is the data base input to the model which is often inferior in both quality and quantity. Thus, in order to improve our forecasting capabilities we must improve the models by means of improved experiments and improve both the quality and quantity of the data base input to the model.

The purpose of this paper is to present results of some studies designed to improve the theoretical concepts of white cap production. The motivation for this effort is that measurements of the microwave emissivity of the ocean are eminently suitable for space applications. Depending on the microwave band chosen, oceanographic parameters of temperature, roughness (including foam as well as RMS wave slope) and salinity greatly modulate the observed emissivity or brightness temperature (Paris, 1969, and 1971, and others). Williams (1969) first demonstrated experimentally the influence of foam on the measured microwave emissivity of the sea surface. Droppleman (1970) and Porter and Wentz (1971) have modeled this dependence theoretically and others (Ross, et al., 1970, Nordberg, et al., 1971, and Williams, 1971) have obtained quantitative field measurements of this foam dependence. Cardone (1969) utilized the fresh water whitecap observations of Monahan (1969) to develop a semi-empirical theory relating fresh water white cap density to the local wind speed and the wave spectrum. From the results obtained during the course of this study, Cardone's theory has been extended to include salt water white caps and to account for the effects of thin streaks which begin to appear to a wind speed between 10 and 12.5 m/sec.

DATA ANALYSIS

A series of photographs has been obtained of a variety of sea conditions for wind speeds of 10-25 m/sec and significant wave conditions of 2.5-8 meters. These photographs, all vertically

oriented and obtained from aircraft, have been analyzed for the percentage of the surface covered by actively forming white caps and new foam patches and thin foam streaks oriented in the direction of the wind. The analysis was accomplished by means of a scanning false color densitometer manufactured by Spatial Data, Inc., of Santa Barbara, Calif. This device scans the photograph and divides the grey scales present into 32 different levels. Each level is assigned a false color and the result is displayed on a color television monitor. This display is then subjectively divided into three categories: (1) actively forming white cap and large new foam patches, (2) thin foam streaks elongated in the direction of the wind, and (3) background foam-free water. Selection of the lines of demarcation between each category is aided by replacing each color in turn with the color black until all white caps and foam patches are blacked out. By means of a planimeter circuit, the coverage of these colors is then obtained. The blacking-out procedure is then continued until the foam streaks are completely filled and the areal coverage of the streaks is obtained. The remaining colors and coverage constitute the background sea conditions. Figure 1 shows a typical photograph along with the enhanced version. Because of deficiencies in the photography, it is not possible to precisely determine the lines of demarcation. In addition, spatial variability in foam conditions is significant. As a result, it is necessary to average a large number of photographs in order to obtain a usefully accurate estimate of the white water coverage.

REFERENCE DATA

As attempt has been made in all instances to suppress the variability in the observations due to windspeed variations with height. This is a necessary procedure, as for example, a 15 m/sec wind measured at an elevation of 10 meters would measure approximately 18 m/sec at 19.5 meters elevation and about 22 m/sec at flight altitudes of 150-400 meters depending on stability criteria (air-sea temperature difference). Therefore, all winds reported here have been adjusted to an anemometer height of 20 meters. For data obtained near ocean station vessels, the winds reported by the weather ship on station are used directly since anemometers on these ships are located at 19.5 meters above mean sea level. Where only flight altitude winds are available, a logarithmic profile was assumed

to hold to an altitude of 43.5 meters (see Moskowitz, 1967) and the measured flight level winds were reduced directly to this elevation and then logarithmically to 20 meters. Table I presents the results of this technique for handling winds when measured by means of an inertial navigation system and referenced to surface anemometer winds. It is evident that the technique give reasonable results.

OBSERVATIONS

A tabulation of all foam cover determinations and associated environmental conditions is shown in Table II. According to the measured air-sea temperature differences, all observations are associated with unstable stratification of varying degree. The wind speeds for the data range from 10-25 m/sec so that the low-level Richardson's numbers, a more fundamental measure of stability, indicate only moderately unstable conditions for most observations. Hence, this data set is not as useful for studying the effects of stability on foam cover as other studies of lower wind speeds which cover both positive and negative air sea temperature differences (e.g. Monahan, 1969).

The range of fetches is quite large - the observations in the vicinity of ocean station "I" and southeast of Cape Fear, North Carolina, represent essentially fully developed sea conditions over the wind speed range 10-17 m/sec as observed significant wave heights were close to values given by the Pierson-Moskowitz fully developed sea formulation. The remainder of the high wind observations represent situations in which the fetch was limited by an upwind shoreline and seas were well below the fully developed stage.

The most striking differences between these observations and those at lower wind speeds are the significant contributions of foam streaks to total foam cover for wind speeds above 12 m/sec and the great variability in both streak and whitecap area coverage. The latter characteristic is also indicated in Figure (1), which shows the distribution of whitecap coverage for a typical photograph.

For most cases, histograms of the data depict a weakly bimodal distribution to the whitecap coverage on individual photographs. An examination of each photograph reveals that typically, the large percentage coverage is caused by the presence of a few very large foam patches associated with the relatively infrequent breaking of

waves of relatively long wavelengths. For low flight altitudes particularly, the observations are subject to considerable sampling variability, as these large foam patches contribute significantly to average whitecap coverage. It is likely, therefore, that the 24.7 and 22.7 m/sec North Sea data are biased toward low foam coverage as no large foam patches were evident in the small number of photographs analyzed, yet they were observed visually (by the authors) on these flights. On the other hand, the absence of large foam patches for the 20 m/sec limited fetch observations at short fetch is probably related to the fact that wave breaking is restricted to the relatively high frequency components in the wave spectrum, as the extremely short fetches restrict the development and saturation of larger wave components. The higher aircraft altitudes and larger area viewed per photograph may also have contributed to the smaller variability for the first two sets of photographs taken on this flight.

DEPENDENCE OF FOAM COVER ON WIND SPEED

As with most other wind-wave interaction phenomena, a meaningful dependence of foam cover on wind speed can be determined only from a set of observations representing similar stages of wave development. The five observations noted above between 10 m/s and 17 m/sec, which represent nearly fully developed seas, are thus suitable for this purpose and are shown in Figure (2).

The indicated variation of white cap coverage is in good agreement with an extensive set of observations of salt water white cap coverage at speeds below 10 m/sec as analyzed by Monahan (1971). The solid curve shown in the figure, which also provides a good fit to the high wind speed data for total foam, was also found by Monahan (1971) to provide a good description of the highest oceanic white cap coverage values observed below 10 m/sec. This curve is one of the results of the semiempirical theory for white cap coverage, proposed by Cardone (1969), initially to explain the dependence of fresh water white cap coverage on wind speed, stability, fetch and duration, but later simply extended (Ross and Cardone, 1970), to include salt water effects in the manner proposed by Monahan (1969).

The observations indicate that total foam coverage increases with wind speed at a greater rate than predicted by Cardone's model. However, the discrepancy is largely attributable to the contribution

to foam cover by the streaks, and a simple way to account for the effect of streaks on total foam cover within the context of Cardone's model is presented below.

The observations of percentage white cap coverage shown in Figure (2) for wind speeds above 20 m/sec lie considerably below what would be expected at these wind speeds for both white cap and total foam cover on the basis of the fully developed sea conditions. This behavior seems to be caused by the fetch limitations associated with these data (as well as a low bias due to sampling) as both Monahan's low-speed white cap data and Cardone's model suggest that for a given wind speed, white cap coverage should increase with increasing fetch and reach a maximum for fully developed seas as seen in Figure (3).

The ratio of streak-to-white-cap coverage for this set of data appears to increase linearly with wind speed. In Figure (4) a simple linear relationship above 9 m/sec is shown to fit the data reasonably well, considering the uncertainty in the observed ratio. A portion of this data was obtained on a flight conducted on 27 January 1971 specifically designed to observe the effect of fetch on the growth of the streak and white cap density and the wave spectrum. The meteorological situation along with the flight track flown are shown in Figure (5). The behavior of the streak and white cap density versus fetch for this flight is shown in Figure (6). It can be seen that the growth of the significant wave height and the white cap and streak density are in reasonable agreement with predictions (solid curves) during the early portion of the flight. However, approximately 120 km offshore, there was a drastic decrease in streak density. Figure (7) is a false color enhancement of the ITOS infrared image of 27 January and shows that the edge of the Gulf Stream lay at approximately this location. Whether this phenomenon is somehow related to the Gulf Stream or perhaps to a mesoscale lull in the wind field is unknown, as the aircraft was not equipped with a navigation system capable of resolving small scale changes in windspeed from the flight altitude flown (the aircraft doppler navigation system is inoperative below 300 meters and the Omega system does not have sufficient sensitivity).

The streak-to-white-cap ratio can be interpreted physically in terms of effective increase in the half-life of whitecaps in surface waters due to the presence of streak producing circulations. The ratio can be employed to extend Cardone's semiempirical theory since, as noted by Monahan, foam coverage is proportional to the product

of the whitecap production rate and the half-life of individual whitecaps. Cardone's model calculates, basically, a measure of the whitecap production rate, with the empiricism entering into the model through a description of the effective half-life.

The success of the relationship depends on the assumption that the streak/whitecap ratio is independent of fetch. While this data set is not entirely conclusive in this regard due to the aforementioned anomaly occurring in the vicinity of the Gulf Stream and to unknowns in the wind field, the dominant effect seems to be windspeed. Further efforts, however, must be expended to verify this assumption.

As mentioned earlier, the Cardone model for white cap production is based on the energy dissipated in breaking waves according to the following equation:

$$E = \rho_w \cdot g \cdot \int_0^\infty B \cdot S \cdot \epsilon \cdot df$$

Where E = energy dissipation (ergs/cm²-sec)

ρ_w = water density

g = gravitational acceleration

B = Miles-Phillips Instability Growth Parameterization

S = Spectral Energy

f = frequency

$$\text{and } \epsilon = \begin{cases} 1 & S \leq S_{\infty} \\ 0 & S > S_{\infty} \end{cases}$$

S_{∞} = Pierson-Moskowitz Fully Developed Spectrum

The empiricism enters in from the data of Monahan and results in the expression for percentage white cap coverage, modified to include salt water effects (Ross and Cardone, 1970), of

$$W_S = .00925 + 1.31 \cdot E$$

Accounting for the streaks by means of the streak/whitecap ratio results in

$$F_T = (1 + R_S)W_S$$

Where F_T = Total Foam Density (% of surface covered by whitecaps plus streaks)

W_S = Salt water whitecap density (%)

R_S = Ratio of streaks to white caps = $-1.99 + .06 \bar{U}_{20}$

\bar{U}_{20} = Average windspeed measured at an altitude of 20 meters (m/sec)

Ross, et al., (1970) and Nordberg, et al., (1971) from data obtained in March, 1969 have shown that K_W , the rate of increase of the brightness temperature with whitecap density at the Nadir viewing angle, amounts to about 1°K for a 1% change in whitecap density at 19.5 GHz. Whether this same figure is correct for the thin foam streaks (which may be largely a single-layered phenomena at the surface) is not known exactly, although it would appear to be somewhat less. Williams (1971), investigating the phenomena in a tank, reports that at 3 cm wavelengths, the emissivity of foam covered water is raised from .4 to .9 with a foam thickness of only 3 mm. This would suggest that the streaks might be equally as important as whitecaps, at least at the higher microwave frequencies. However, it is possible that a streak visible on photography is not altogether a surface phenomena, but also includes light scattered from bubbles suspended just below the surface. If this is the case, streaks would contribute less than whitecaps to changes in the microwave emissivity. In either case, the streak contribution may be represented as some constant, K_S , times the ratio of the streaks to the whitecaps, R_S .

If the whitecap and streak sensitivity are represented in this manner, the change in brightness temperature due to foam may be related to the white cap density according to the expression:

$$\Delta T_B = (K_W + K_S R_S) W_S$$

Using the observations of ΔT_B , K_W , and W_S obtained during the March, 1969 experiment, and the value of R_S determined above, it is possible to solve for K_S . This was done and a value of $K_S = 0.5$ was obtained.

Application of this equation with predicted values of W_S and the empirically-derived constant terms leads, for example, to a ΔT_B of 5.5°K and 14.5°K for fully developed conditions associated with winds of 13 and 16 M/sec respectively, compared to observed differences (Nordberg, et al, 1971) of about 7 and 12°K . For the 20 M/sec case, the calculation leads to a difference of 18°K vs 18°K observed, and for 25 M/sec 70°K calculated vs 22°K observed. Neglecting foam streaks entirely, calculated values of 4, 8.5, 8.5, and 26°K vs observed values of 7, 12, 18, and 22°K are obtained. The following table presents results of calculations of ΔT_B from the above equations and from the photographic observations, compared to observed differences in microwave brightness temperature.

Windspeed (M/s)	ΔT_B Calc. from Ross-Cardone Model (°K)	ΔT_B Calc. from Obs. of W.Cps.&St's (°K)	ΔT_B Observed (°K)
13	5.5	6.0	7.0
16	14.5	10.0	12.0
20	18.0	15.0	18.0
25	70.0	15.0	22.0

While it is recognized that some of the above results may be influenced by invalid atmospheric assumptions, these are judged to be small as the set of observed brightness temperature differences were carefully selected to be from similar atmospheric conditions. Therefore, it would appear that use of the Ross-Cardone model gives reasonable results for windspeeds to 20 M/sec, but may seriously over-estimate ΔT_B for higher winds under fetch-limited conditions. Thus, the thrust of future experiments must be oriented toward the fetch-limited situations and multi-frequency measurements of the microwave signature of foam streaks, and white caps.

85-10

REFERENCES

- Cardone, V. J., "Specification of the wind field distribution in the Marine boundary layer for wave forecasting," Geophysics Sci. Lab., New York Univ., New York, Rep. TR 69-1, December, 1969.
- Droppelman, J. D., "Apparent microwave emissivity of sea foam," J. Geophys. Res., Vol. 75, Jan. 20, 1970.
- Monahan, E. C., "Fresh water whitecaps," J. Atmos. Sci., Vol. 26, No. 9, 1969.
- Monahan, E. C., and Zaitlow, E., "Laboratory Comparisons of Fresh-water and Saltwater Whitecaps," J. Geophys. Res., Vol. 74, No. 28, 1969.

- Moskowitz, L., "Reduction of ocean wind data by use of drag coefficients with application to various wave forecasting techniques," U. S. Naval Oceanographic Office, IMR 0-66-64, Jan., 1965.
- Nordberg, W., Conaway, J., Ross, D.B., and Wilheit, T., "Measurements of Microwave Emission from a foam-covered, wind-driven sea," J. of Atmos. Sciences, Vol. 28, No. 3, April, 1971, pp. 429-435.
- Paris, J. F., "Microwave radiometry and its application to marine meteorology and oceanography", Ref. No. 69-II, Dept. of Ocean., Texas A&M Univ., 1969.
- Paris, J. F., "Transfer of Thermal microwaves in the atmosphere," Dept. of Met., Texas A&M Univ., May, 1971.
- Porter, R. A. and Wentz, F.J. III, Final Report, Radiometric Technology, Inc., Wakefield, Mass., 30 July 1971.
- Roll, H. U., "Physics of the Marine Atmosphere", Academic Press Inc., New York, 1965.
- Ross, D. B., Conaway, J., and Cardone, V. J., "Laser and microwave observations of sea-surface conditions for fetch-limited 17- to 25- M/S winds," IEEE Trans. on Geoscience Electronics, Vol. GE-8, No. 4, Oct., 1970.

85-11

- Ross, D. B., and Cardone, V. J., "Laser observations of wave growth and foam density for fetch-limited 25 m/sec winds," Proc. of the Third Annual Earth Resources Program Review, Rep. No. MSC-03742, NASA, MSC, Houston, Texas, Dec., 1970.
- Williams, G. F., Jr., "Microwave radiometry of the ocean and the possibility of marine velocity determination from satellite observations." J. Geophys. Res., 74, 1968.
- Williams, G. F., Jr., "Microwave radiometry of the ocean, Final Report, Contract N62306-69-C-0301, Rosenstiel School of Marine and Atmospheric Science, Univ. of Mia., Coral Gables, Fla., June, 1971.

TABLE I
LITTON LTN 51 INERTIAL NAVIGATOR WINDS COMPARED TO SURFACE WINDS

Date	Location	Flight Level Wind Speed (m/sec)	Altitude (feet)	Reduced Fit. Level Wind Speed (m/sec)	Measured Surface Wind Speed (m/sec)	Anemometer Height (meters)	Air-Sea Temp. Difference (°C)	Logarithmic Profile Assumption (meters)
3/14/69	N. Sea	25**	500	22.0**	22.7*	20	-3°	45
3/14/69	N. Sea	27.3**	500	25.2**	24.7*	20	-3°	45
3/14/69	N. Sea	27.8**	500	25.8**	25.4*	20	-3°	45
3/14/69	N. Sea	24.2**	500	22.1**	24.0*	20	-3°	45
3/ 6/69	N. Atlantic (I)	17***	1500	15.5	16	20		
3/10/69	N. Atlantic (I)	16***	500	15	16	20	-4°	45
3/11/69	N. Atlantic (I)	20***	750	18	17	20	-3°	45
3/13/69	N. Atlantic (I)	16***	900	13.5	13	20	-2°	45
	N. Atlantic (I)	13.5***	900	13.0	13	20	-2°	45
	N. Atlantic (I)	16.5***	1100	14.8	13	20	-2°	45
	N. Atlantic (I)	15.0***	500	13.5	13	20	-2°	45
3/13/69	N. Atlantic (J)	9***	600	7	6	20	1°	45
2/ 9/70	Hotel	16.5	150	14.8	15.5	20	-1.5°	45
2/11/70	XERBI	5	150	4.5	4	10	0	45
2/16/71	XERBI	7.5	150	7	6-9	Unknown	-2°	45
2/18/71	Hotel	11	150	10	11	20	0	45

* Reduced Geostrophic Winds weighted by Surface Beaufort and Anemometer Winds

** 20 Minute Average

*** 1 Minute Average

TABLE II - SUMMARY OF OBSERVATIONS

DATE	TIME ¹	PLACE	FLIGHT LEVEL(m)	FETCH (km)	A-S ⁵ (°C)	WIND ⁶ SPEED(m/s)	NUMBER of Photos	WHITECAP COVERAGE(%)	WHITECAP STD Deviation	STREAK COVER(%)	STREAK STD. DEV.	TOTAL FOAM Cvt.	RATIO OF STREAKS TO WHITE CAPS
3/10/69	1426-1439	Atlantic ²	150	740	-4	15.5	34	6.7	5.1	7.2	2.8	13.9	1.07
3/11/69	1323-1329	Atlantic ²	230	740	-3	17.0	33	9.0	6.3	10.7	6.8	19.7	1.20
3/13/69	1057-1116	Atlantic ²	270	740	-2	13.4	27	4.2	4.4	3.5	3.2	7.7	.83
3/14/69	1407-1447	North Sea	140	370	-3	24.7	10	7.1	8.7	25.3	7.5	32.4	3.56
3/14/69	1510	North Sea	140	7500	-3	22.7	8	6.4	3.3	17.0	3.1	23.4	2.66
3/19/69	0947-1038	North Sea	140	340	-1	20.6	23	6.2	4.6	18.0	7.0	24.2	2.90
11/16/69	1826-1844	Gulf of Mex.	210	140	-20	13.4	6	4.2	1.1	2.2	2.0	6.2	.69
10/3/70		Caribbean Sea ⁴	420	7800	-1	10.3	13	1.4	.3	0	0	1.4	.00
1/27/71	1452-1454	Atlantic ³	300	6	-8	20.0	49	4.2	2.3	12.8	4.9	17.0	3.00
1/27/71	1503-1504	Atlantic ³	300	75	-8	20.0	13	5.9	2.9	13.1	6.3	19.8	2.36
1/27/71	1513-1515	Atlantic ³	110	148	<-8	20.0	82	4.4	7.0	1.1	3.6	6.3	.43
1/27/71	1522-1524	Atlantic ³	110	204	<-8	20.0	63	4.4	10.2	13.4	7.8	21.8	1.60
1/27/71	1535-1538	Atlantic ³	110	296	<-8	20.0	66	3.8	4.3	14.3	6.4	18.1	3.76

¹All times in Greenwich Mean Time²In the vicinity of ocean station "1"³Downwind of Cape Fear, North Carolina⁴Caribbean Sea⁵Air-Sea temperature difference⁶Adjusted to 19.5 meter level

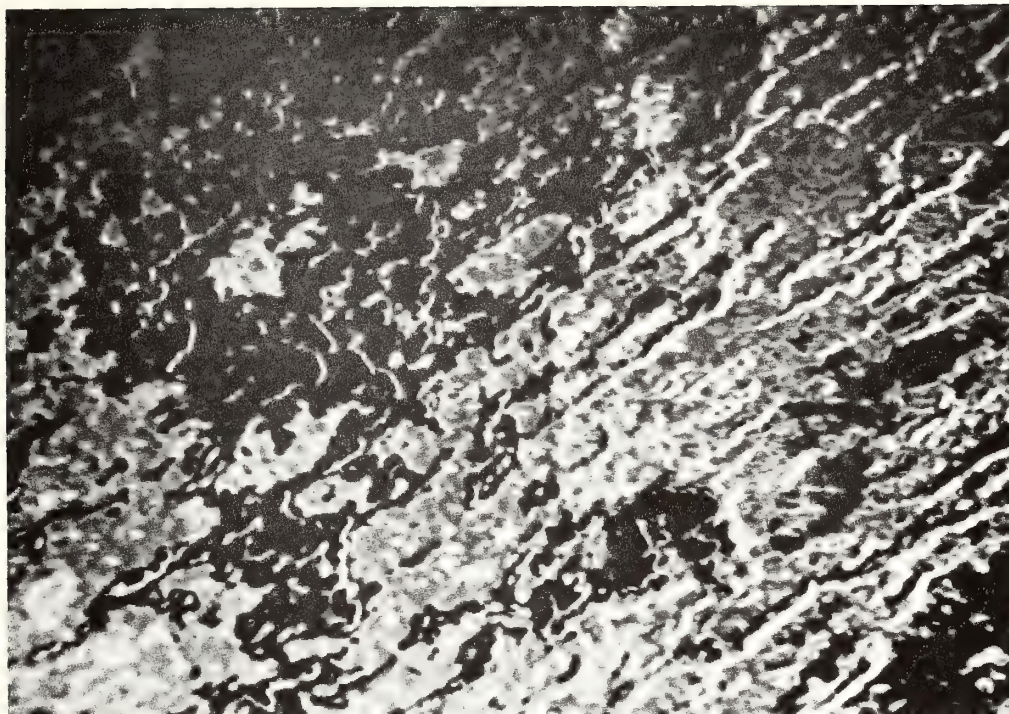


FIGURE 1. False color enhancement of white cap photography for a windspeed of 20 m/s.
White caps have been made black while the thin streaks are gold and orange.

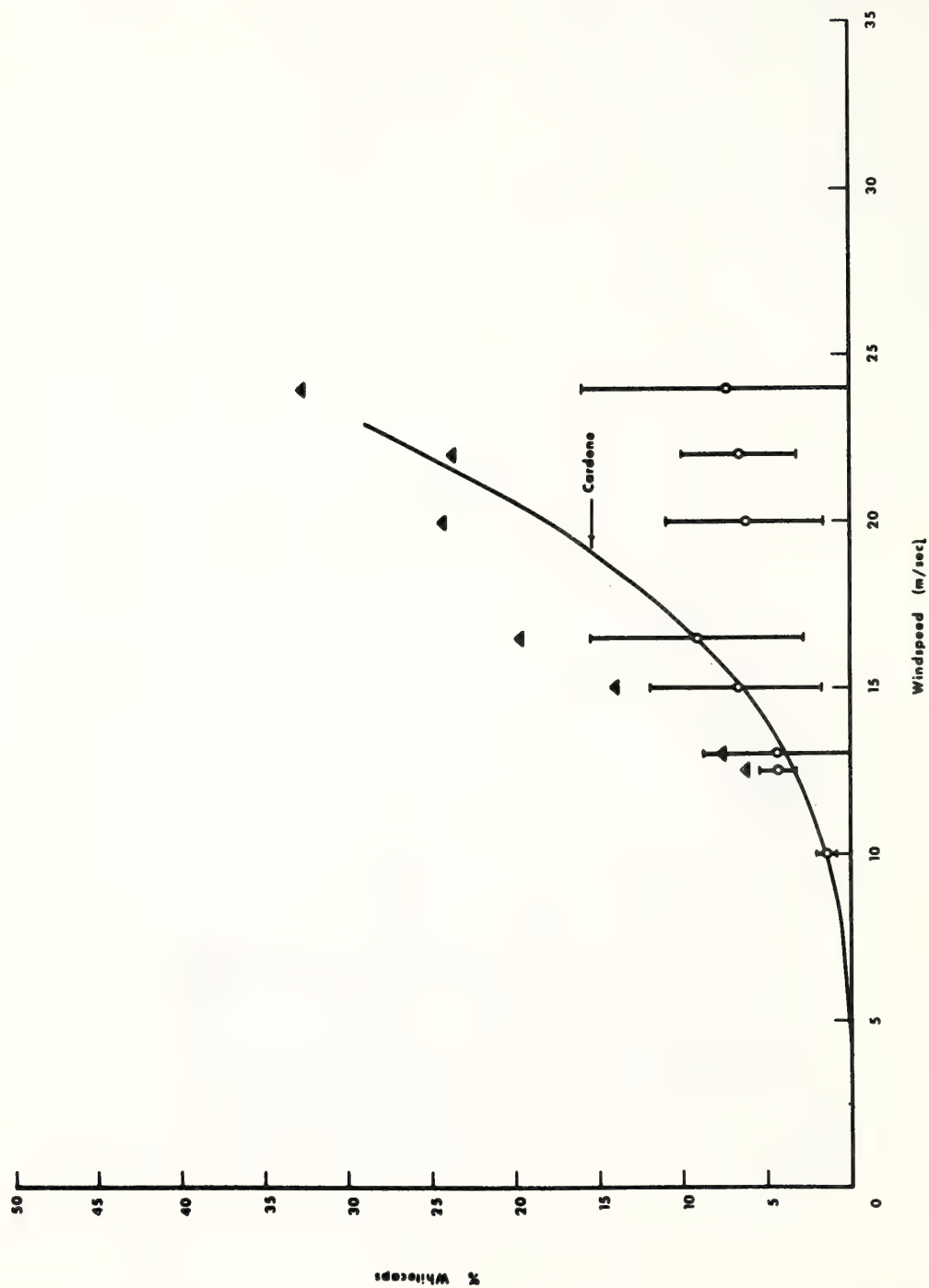


FIGURE 2. Observations of white cap density (open circles) and white caps plus streaks (solid triangles) compared to the predictions of Cardone.

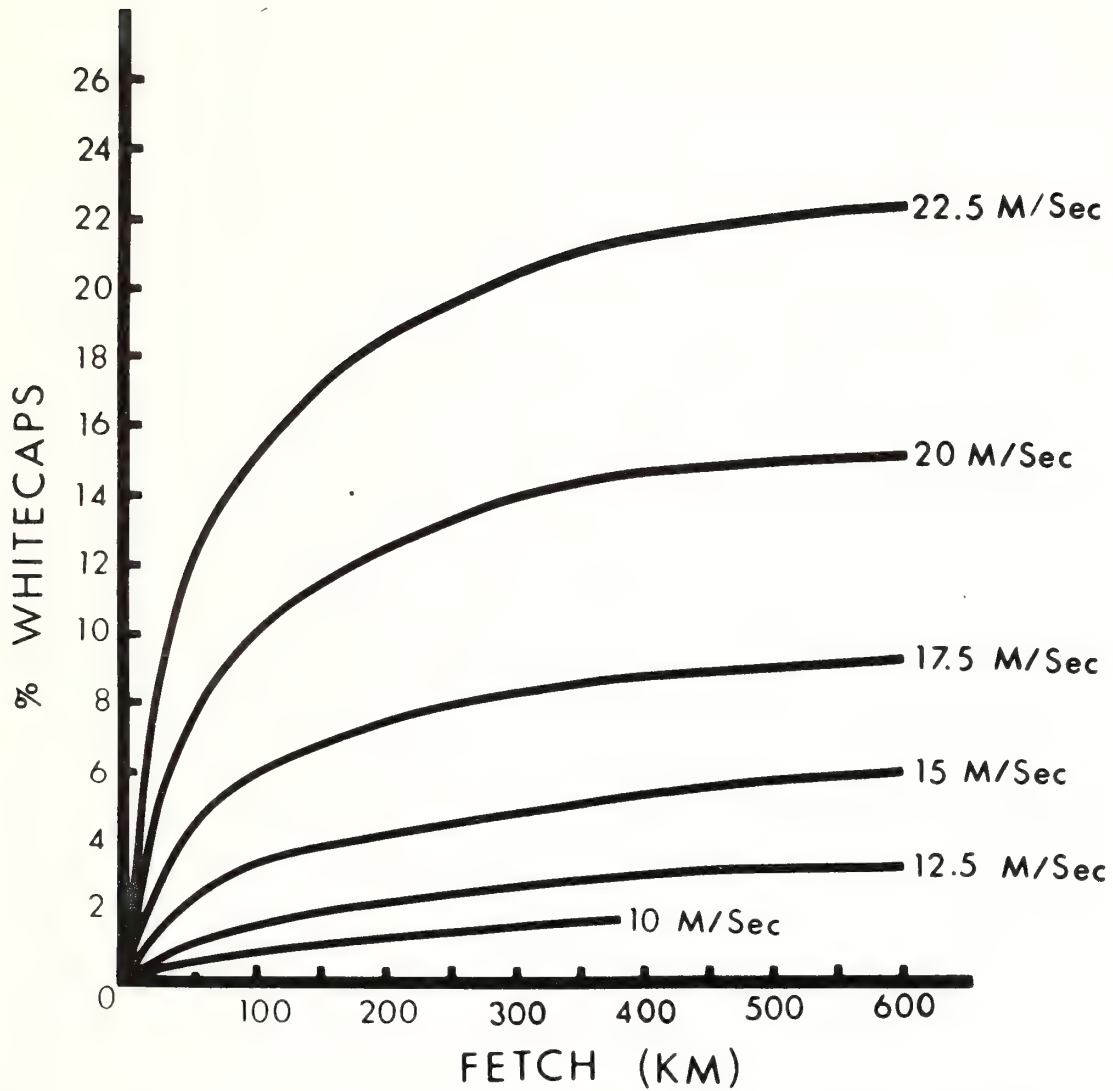


FIGURE 3. Fresh Water White Cap density as a function of fetch according to Cardone (1969).

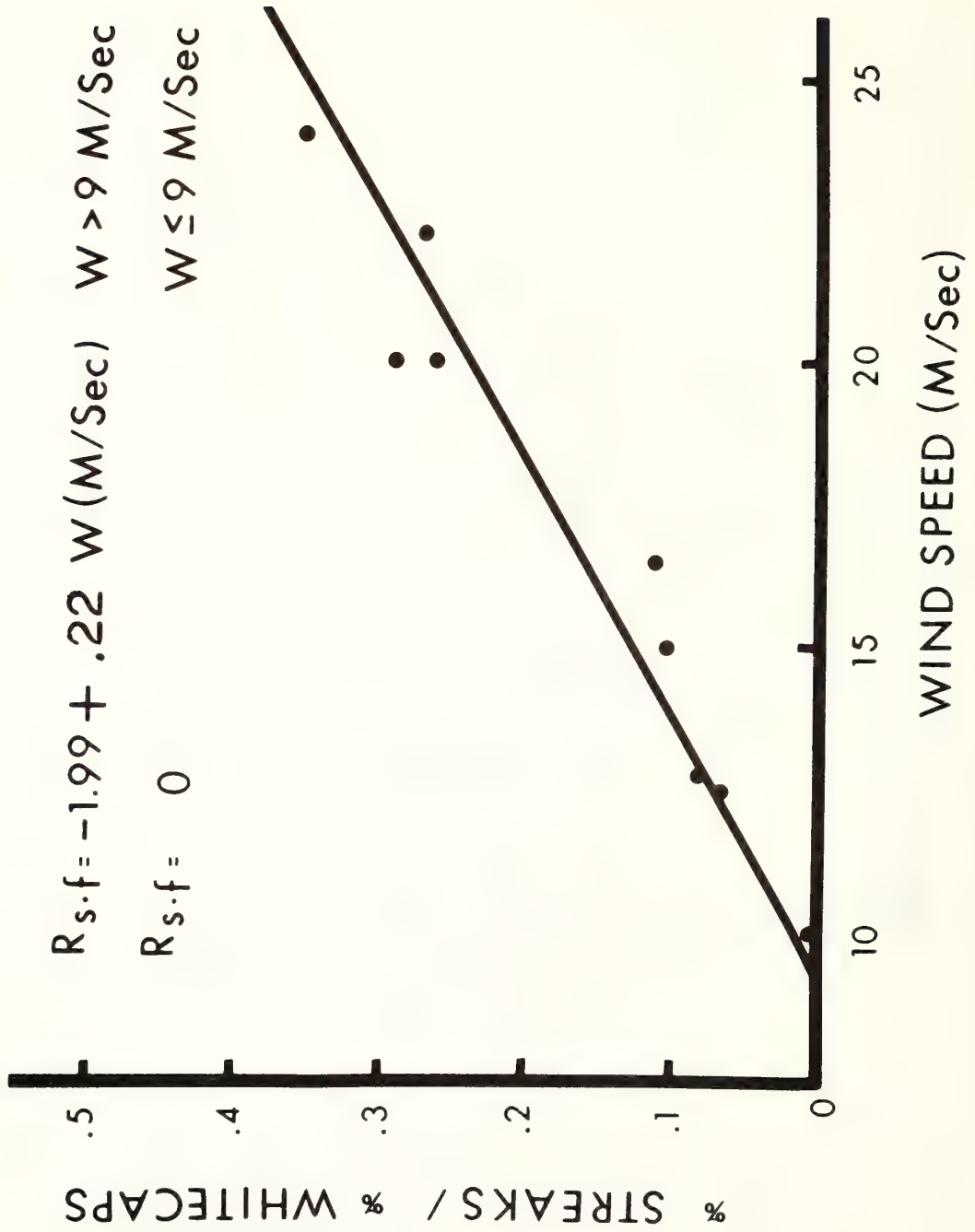


FIGURE 4. Ratio of streaks to white caps vs windspeed.

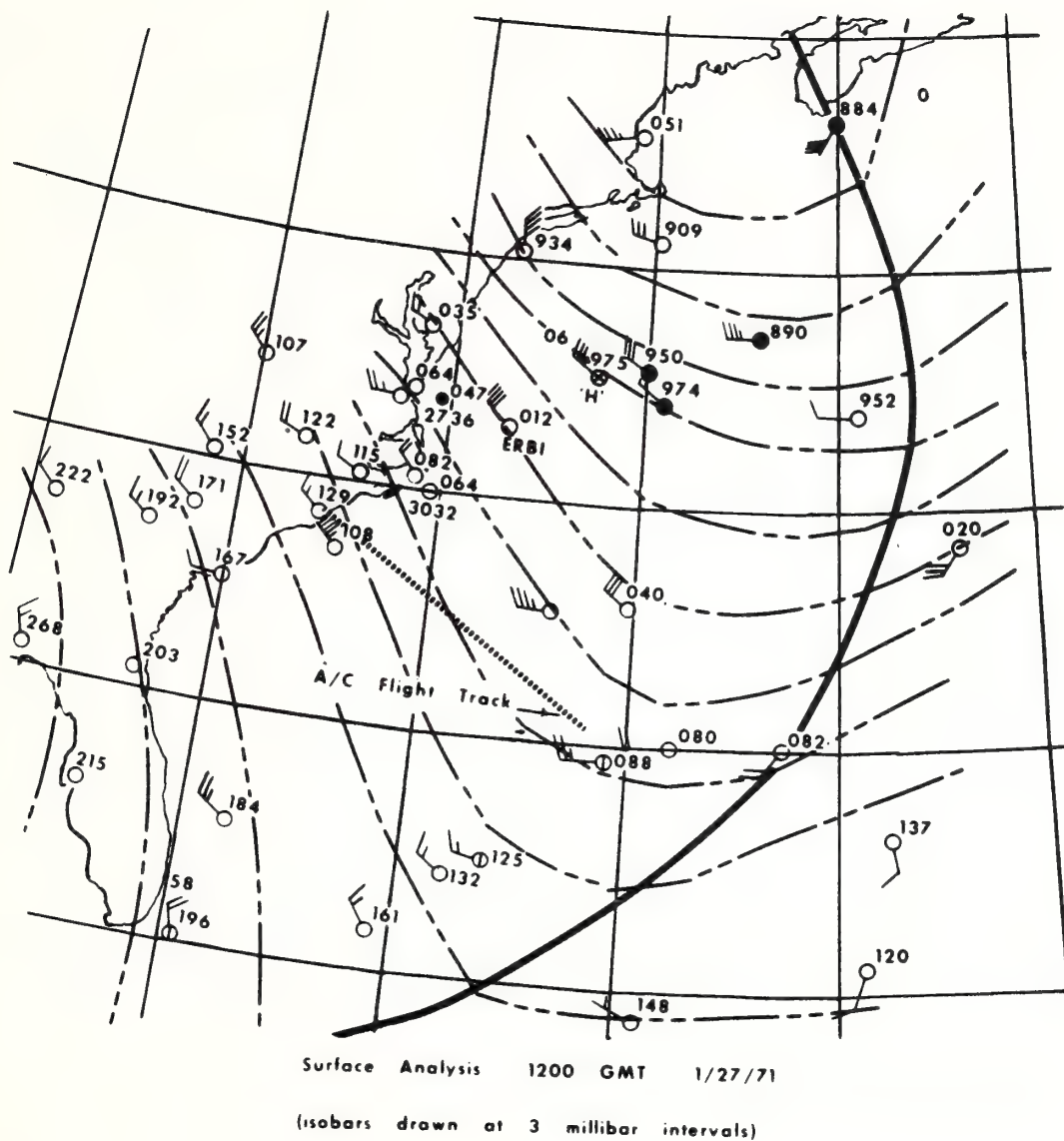


FIGURE 5. Meteorology situation for 27 Jan 71 Fetch Limited Experiment.

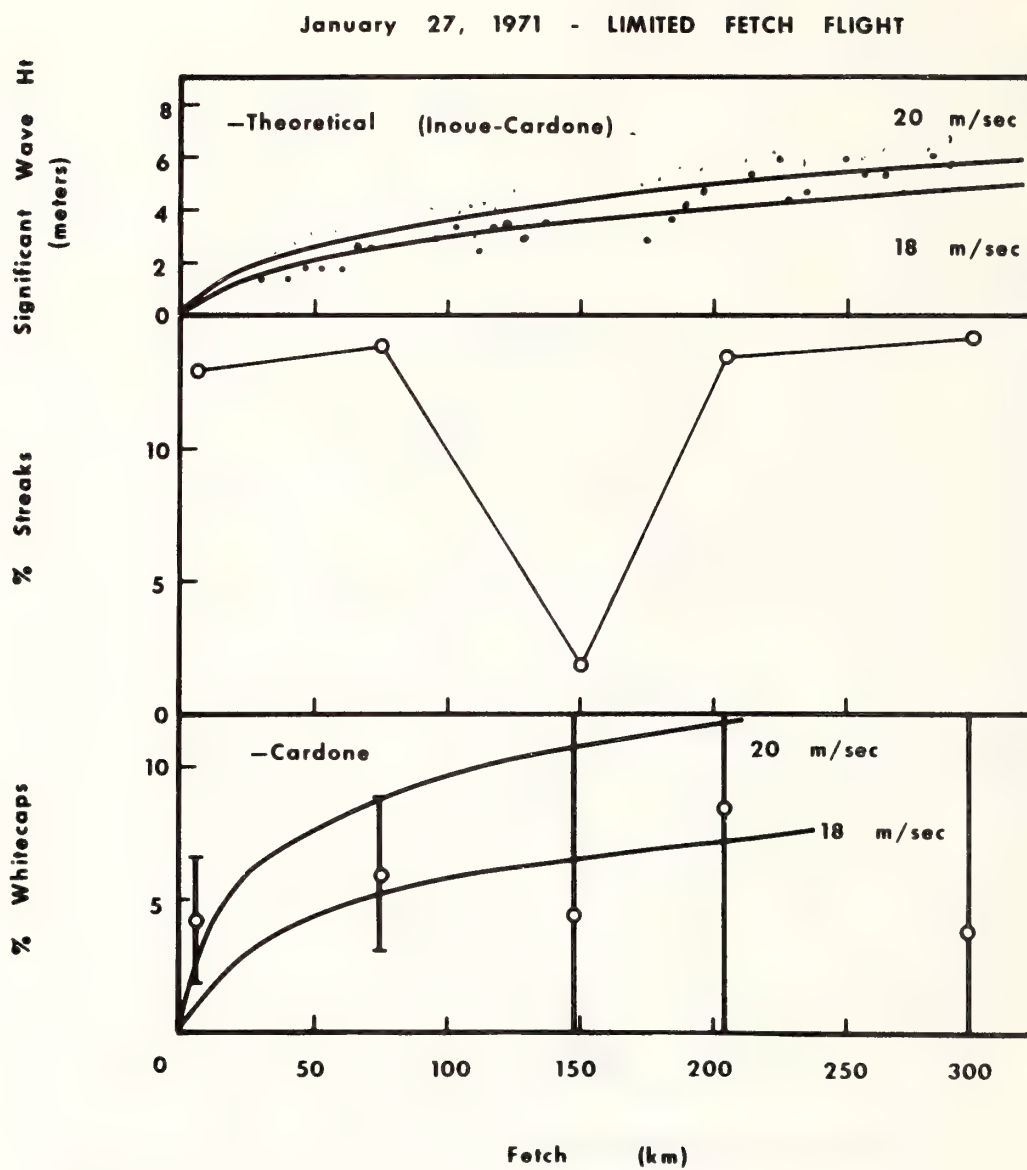


FIGURE 6. Observed behavior of the significant wave height, streak, and white cap density.

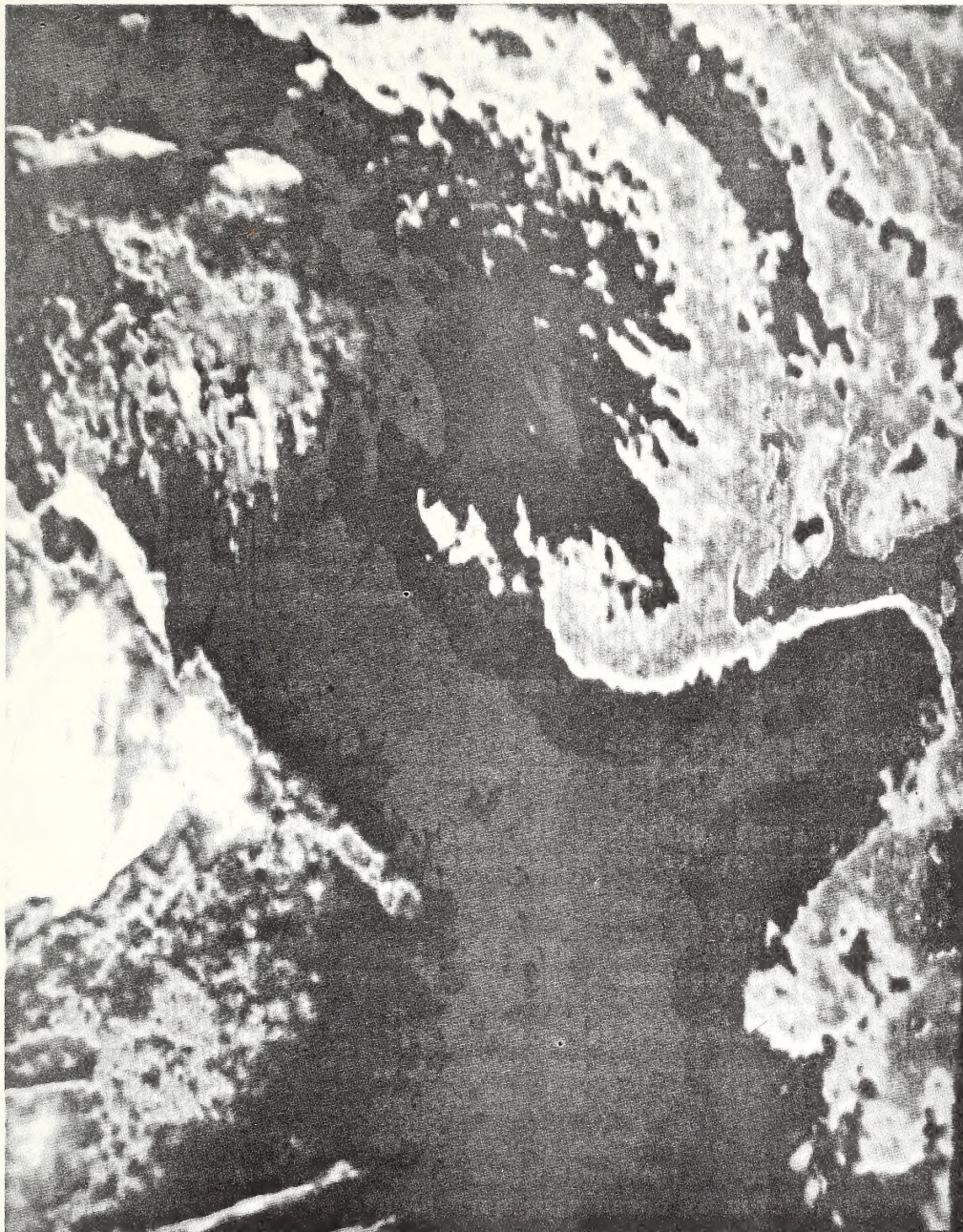


FIGURE 7. 32 level false color enhancement ofITOS HRIR Image of 27 Jan 71 showing warm Gulf Stream in red and light blue and cooler shelf waters in black.

PENN STATE UNIVERSITY LIBRARIES



A000072049679